JAERI-Review
2002-014

JP0250387

研究炉利用における研究成果集

（平成12年度）

2002年8月

（編）高橋　俊行

日本原子力研究所
Japan Atomic Energy Research Institute

本レポートは、日本原子力研究所が不定期に公刊している研究報告書です。
入手の問合わせは、日本原子力研究所研究情報部研究情報課（〒319-1195　茨城県那珂郡東海村）あて、お申し越し下さい。なお、このほかに財団法人原子力弘済会資料センター（〒319-1195　茨城県那珂郡東海村日本原子力研究所内）で複写による実費頒布を行っております。

This report is issued irregularly.
Inquiries about availability of the reports should be addressed to Research Information Division, Department of Intellectual Resources, Japan Atomic Energy Research Institute, Tokai-mura, Naka-gun, Ibaraki-ken 〒319-1195, Japan.

© Japan Atomic Energy Research Institute, 2002
編集兼発行　日本原子力研究所

JAERI－Review 2002－014

研究炉利用における研究成果集（平成１２年度）

日本原子力研究所東海研究所研究炉部
（編）高橋　俊行

（2002年5月16日受理）

平成12年度、研究炉においてはJRR-3の5サイクルとJRR-4の42サイクルの共同利用運転が行われ、中性子散乱実験や放射化分析のための照射等様々な目的に利用された。

本報告書は、実験あるいは照射利用を行った利用者（原研外を含む）から成果の提出を受け、これを分野別に取りまとめたものである。

東海研究所：〒319-1195　茨城県那珂郡東海村白方白根2-4

JAERI－Review 2002－014

Activity Report on the Utilization of Research Reactors (Japanese Fiscal Year, 2000)

(Ed.) Toshiyuki TAKAHASHI

Department of Research Reactor
Tokai Research Establishment
Japan Atomic Energy Research Institute
Tokai-mura, Naka-gun, Ibaraki-ken

(Received May 16, 2002)

This is the third issue of the activity report on the utilization of research reactors in the fields of neutron beam experiments, neutron activation analysis, radioisotope production, etc., performed during Japanese Fiscal Year 2000(April 1, 2000- March 31, 2001).

All reports in this volume were described by users in JAERI and also users in the other organizations, i.e., universities, national research institutes and private companies, who had utilized our research reactor utilization facilities for the purpose of the above studies.

Keywords: Research Reactor, Neutron Scattering, Neutron Radiography, Neutron Activation Analysis, Neutron Beam, Irradiation

目　次

はじめに …… 1
研究成果一覧 …… 3
1. 中性子散乱 …… 25
1) 構造・励起 …… 25
2) 磁　性 …… 79
3) 超伝導現象 …… 179
4) 非晶質・液体 …… 189
5) 高分子 …… 219
6) 生物学 …… 247
7) 基礎物理学・中性子光学 …… 269
8) 装　置 …… 289
9) その他 …… 301
2. 中性子ラジオグラフィ …… 317
3. 放射化分析 …… 347
4. ＲＩの製造 …… 421
5. 原子炉材料照射試験 …… 431
6. 即発ガンマ線分析 …… 437
7. その他 …… 453
謝 辞 …… 486
付 録 …… 487

Contents

Preface 1
Research Reports 3
1. Neutron Scattering 25
1) Structure・Excitation 25
2) Magnetism 79
3) Superconductivity 179
4) Amorphous・Liquid 189
5) Polymer 219
6) Biology 247
7) Fundamental Physics・Neutron Optics 269
8) Instrument 289
9) Others 301
2. Neutron Radiography 317
3. Neutron Activition Analysis 347
4. Produciton of Radio Isotopes 421
5. Irradiation Test of Reactor Materials 431
6. Prompt Gamma-ray Analysis 437
7. Others 453
Acknowledgments 486
Appendix 487

はじめに

平成１２年度には、ＪＲＲ－３において５サイクルの共同利用運転、ＪＲＲ－４において４２サイクルの共同利用運転が行なわれ、これに伴いさまざまな利用が行われた。

本報告書は、利用者（原研外利用者を含む）から当該利用の成果の提出を受け、取りまとめたものである。

提出して頂いた成果の件数は、中性子散乱１９６件、中性子ラジオグラフィ９件、放射化分析２０件、ＲＩの製造３件、原子炉材料３件、即発ガンマー線３件、その他９件で合計２４３件であった。なお、本報告書では下記の報告書の中から一部を転載させて頂いた。

最後に、原稿を提出して頂いた利用者の皆様のご協力に感謝するとともに、今後も研究炉が有効に利用され、種々の研究がさらに進展されることを期待します。

研究炉利用課長
佐川　尚司

---

1) レポート番号：Vol.8（第８巻）
標　　題：ACTIVITY REPORT ON NEUTRON SCATTERING RESEARCH issued by ISSP-NSL,University of Tokyo（東京大学物性研究所発行）
編　　者：Y.Oohara and M.Shibayama （大原泰明，柴山充弘）
発 行 年：２００１年

2) レポート番号：UTRCN-G-30
標　　題：原研施設利用共同研究成果報告書（平成１２年度）
編　　者：東京大学原子力研究総合センター
発 行 年：２００２年

This is a blank page.

研 究 成 果 一 覧

Research Reports

This is a blank page.

No.	「 Title 」	Page
	Neutron Scattering - Structure - Excitation -	
1-1-1	**Neutron Diffraction Studies of Clathrate Hydrates** C.J.Rawn,C.Y.Jones,B.C.Chakoumakos,S.L.Marshall,Y.Ishii,L.A.Stern, S.Circone,S.H.Kirby	27
1-1-2	**Neutron Diffraction Experiments of PZT by Using High Resolution Powder Diffractometer** S.Pongkasem,A.Moriai,Y.Ishii,N.Minakawa	29
1-1-3	**Structure determination of β-Na_xCoO_2** Y.Ono,R.Ishikawa,Y.Miyazaki,Y.Ishii,Y.Morii,T.Kajitani	30
1-1-4	**Jahn-Teller distortion in $La_{1-x}Ca_xMnO_3$ with $0.08 \leqq x \leqq 0.15$** S.Begum,Y.Ono,Y.Ishii,Y.Morii,T.Kajitani	31
1-1-5	**Neutron Diffraction Study of $Sr_2YCu_2FeO_{6+\delta}$** T.Mochiku,Y.Hata,Y.Mihara,J.Suzuki,N.Metoki,K.Kadowaki,K.Hirata	32
1-1-6	**Neutron Diffraction Study of $Sr_2EuCu_2RuO_8$** T.Mochiku,K.Oikawa,N.Metoki,D.P.Hai,K.Kadowaki,K.Hirata	33
1-1-7	**Diffuse Neutron Scattering from CuBr** M.Arai,T.Aung,T.Sakuma,H.Takahashi,Y.Ishii	34
1-1-8	**Diffuse Neutron Scattering from Li_3N** M.Arai,T.Aung,T.Sakuma,H.Takahashi,Y.Ishii	35
1-1-9	**Soft Phonon on the Ferroelastic Phase Transition in $LaNbO_4$** Y.Kuroiwa,S.Aoyagi,A.Sawada,N.Takesue,S.Tsunekawa,Y.Noda	36
1-1-10	**Behavior of Σ_2-Σ_3 Phonon Branches in Low-Temperature Commensurate Phase of Rb_2SeO_4** H.Shigematsu,Y.Nakadaira,T.Matsui	37
1-1-11	**Magnetic Excitations in the Two-Dimensional Spin Gap System $SrCu_2(BO_3)_2$** H.Kageyama,N.Aso,M.Nishi,K.Nukui,T.Yoshihama,K.Kakurai,Y.Ueda	38
1-1-12	**Anomalous Lattice Dynamics due to p-f Mixing Orbital in the Magnetic Polaron States of CeSb** K.Iwasa,M.Kohgi,M.Braden,J.-M.Mignot,H.Kitazawa,T.Suzuki	40
1-1-13	**Acoustic Phonon Softening in the Critical Temperature Region of Charge Ordering of Yb_4As_3** K.Iwasa,M.Kohgi,A.Ochiai,H.Aoki,T.Suzuki	42
1-1-14	**In Situ Study of Structural Change and the Monoclinic-Tetragonal Phase Transition of $YTaO_4$ at High Temperatures** M.Yashima,T.Nogami,K.Ohoyama,Y.Yamaguchi	44
1-1-15	**Neutron Diffraction Studies on Organic-Inorganic Perovskite Structure** Y.Tabuchi,D.Hiroishi,K.Asai	46
1-1-16	**Study on Ti-isotope effects in $PbTiO_3$ by neutron powder diffraction** H.Shigematsu,Y.Nakadaira,T.Nagasaki,T.Matsui,A.Tobo,K.Ohoyama	48
1-1-17	**High-temperature neutron-diffraction study of the structural phase transitions in $CaTiO_3$** R.Ali,M.Yashima,K.Ohoyama,Y.Yamaguchi	49

1-1-18	**Cubic Phase Structure of $CH_3NH_3PbCl_3$** H.Mashiyama,Y.Kawamura,K.Ohoyama	51
1-1-19	**Relation between Thermodynamic Stability,Crystal Structure and Electrode Characteristics of $Li_{1+x}Mn_{2-x}M_yO_4$ as a Cathode Active Material for the Lithium Secondary Battery** Y.Idemoto,T.Ozasa,Y.Tsunoda,N.Koura	52
1-1-20	**Structural refinement with powder neutron diffraction of iron substituted lithium manganese spinel oxides as a positive electrode material for lithium rechargeable batteries** M.Tabuchi,H.Shigemura,A.Hirano,R.Kanno	54
1-1-21	**Structures of new cathode materials for solid state lithium microbattery** H.Kobayashi	55
1-1-22	**Neutron Diffraction Study of Heusler-type $Ni_{2.18}Mn_{0.82}Ga$ Shape Memory Alloy** K.Inoue,Y.Yamaguchi,K.Ohoyama,R.Note,K.Enami	57
1-1-23	**Magnetic Structure in $Eu_3Ir_4Sn_{13}$** K.Kuwahara,K.Iwasa,C.Nagoshi,M.Kohgi,H.Sugawara,Y.Aoki,H.Sato, K.Ohoyama	58
1-1-24	**Structure determination of $Li_3V_2(PO_4)_3$ by Stabilizing Orthorhombic Phase at Room Temperature** M.Sato,H.Ohkawa,K.Yoshida,M.Saito,K.Uematsu,K.Toda	59
1-1-25	**Structure determination of yttrium orthoniobate $Y_{1-x}NbO_{4-1.5x}$,with oxygen defects** M.Honda,K.Toda,M.Sato	61
1-1-26	**Structural Refinement of Nonstoichiometric HT-$LiCoO_2$** N.Imanishi,A.Hirano,Y.Takeda	63
1-1-27	**Neutron Diffraction Study on B-C Network Atomic Arrangements in Tetragonal CeB_2C_2** K.Kaneko,K.Ohoyama,H.Onodera,Y.Yamaguchi	64
1-1-28	**Modulated Structure of the Composite Crystal $Ca_{0.83}CuO_2$** Y.Miyazaki,M.Onoda,S.Shamoto,T.Kajitani	65
1-1-29	**Study of structural change of boron carbide by high-temperature neutorn diffraction** K.Nakamura,M.Yashima,K.Ohoyama,Y.Yamaguchi	66
1-1-30	**Interrelation between Orbital Stability and Charge-Ordering in doped manganites** A.Machida,Y.Moritomo,K.Ohoyama	68
1-1-31	**Neutron Diffraction Measurement of Residual Strain of Partial Penetration Welds for ITER** H.Takahashi,M.Nakahira,N.Minakawa,A.Moriai	69
1-1-32	**Residual Strain Measurement of Functionally Gradient Material by RESA (Ⅱ)** K.Inoue,T.Tsujikami,M.Ohyanagi,M.Sugimoto,M.Komatsu,N.Minakawa, A.Moriai	71

1-1-33	**Measurement of residual stress at the water-jet-peened surface of type 304 stainless steel by neutron diffraction method** S.Okido,T.Yoshimura,K.Enomoto,M.Hayashi,Y.Morii,N.Minakawa	72
1-1-34	**Photo-Induced Structural Change in a Single Crystal Observed by FONDER Diffractometer** T.Ohhara,T.Sosoya,H.Uekusa,T.Ozeki,Y.Ohashi,Y.Noda	73
1-1-35	**Magnetic diffuse scattering in Pt-12 at.% Mn spin-glass alloy** M.Takahashi,T.Sembiring,H.Saitoh,K.Ohshima,Y.Noda,N.Takesue,T.Shishido	74
1-1-36	**Zero Point Distribution of Protons in Ammonium Hexachloroplatinate by Single Crystal Neutron Diffraction** T.Matsuo,N.Onoda-Yamamuro,O.Yamamuro,Y.Fukuda,H.Kimura,Y.Noda	75
1-1-37	**Phonon Measurement on the Spin-Peierls System $CuGeO_3$** M.Nishi,H.Kadowaki,S.Katano,Y.Fujii,K.Kakurai,J.Akimitsu	76
1-1-38	**Magnon gap in single crystals of $La_{1-x}Ca_xMnO_3$ with x=0.15 and 0.20** S.Begum,Y.Ono,Y.Tomioka,Y.Tokura,T.Kajitani	78

No.	「 Title 」	Page
	Neutron Scattering - Magnetism -	
1-2-1	**Magnetic Structure of the Antiferromagnetic Manganese Sulfide $BaLa_2CoS_5$ by Powder Neutron Diffraction Measurements** M.Wakeshima, Y.Hinatsu, Y.Ishii, Y.Shimojo, Y.Morii	81
1-2-2	**Crystal and Magnetic Structures of $Ba_3NdRu_2O_9$** Y.Doi, Y.Hinatsu, Y.Shimojo, Y.Ishii	82
1-2-3	**Magnetic properties of $La_{0.5}Pr_{0.5}CrO_3$** K.Yoshii, A.Nakamura, Y.Shimojyo	83
1-2-4	**Crystal and Magnetic Structures in a localozed 5f system $U_3Pd_{20}Si_6$** N.Tateiwa, N.Metoki, Y.Koike, K.Oikawa, N.Kimura, H.Aoki, T.Komatsubara	84
1-2-5	**Neutron Diffraction Study on the Magneto-structural Phase transition in $La_{1-x}Sr_xMnO_3$: x=0.1** M.Watahiki, J.Suzuki, Y.Yamada, K.Kohn	86
1-2-6	**Neutron Diffraction Study on the Ordered Phases of $Ce_{0.75}La_{0.25}B_6$** K.Iwasa, M.Kohgi, K.Kuwahara, N.Metoki, Y.Koike, S.Kunii	88
1-2-7	**Spin dynamics of hole doped $Nd_{2-x}Ca_xBaNiO_5$** T.Sasaki, T.Yokoo, S.Katano, K.Kakurai, J.Akimitsu	90
1-2-8	**Temperature dependence of the incommensurate peak in $La_{2-x}Sr_xCuO_4$(x=0.12)** K.Yamada, S.Katano, M.Sato, K.Kawashima	91
1-2-9	**Magnetic P-T Phase Diagram and Magnetic Structures of CeSb** T.Osakabe, A.Hannan, N.Tachi, M.Kohgi, H.Kitazawa	92
1-2-10	**Magnetic P-T Phase Diagram of CeP Studied by Neutron Diffraction** A.Hannan, T.Osakabe, M.Kohgi, K.Iwasa	94
1-2-11	**Spin density wave controlled by the superlattice period in Cr(001)/Sn multilayers with Sn monatomic spacer layers** M.Takeda, K.Mibu, K.Takanashi, J.Suzuki	96
1-2-12	**Neutron Scattering Study of a Pressure-Induced Superconductor UGe_2** Y.Koike, N.Metoki, Y.Haga, Y.Onuki	97
1-2-13	**Spin Wave Excitation in a localozed 5f system $U_3Pd_{20}Si_6$** N.Metoki, Y.Koike, Y.Haga, Y.Onuki, K.A.McEwen, N.Aso, M.Kohgi, N.Tateiwa, N.Kimura, H.Aoki, T.Komatsubara	99
1-2-14	**Origin of Weak Antiferromagnetic State in URu_2Si_2:** H.Amitsuka, M.Yokoyama, J.Nozaki	101
1-2-15	**Neutron Diffraction Study of the Magnetic Ordering in $Nd_2MO_2O_7$** Y.Oohara, H.Mochizuki, H.Yoshizawa, Y.Taguchi, Y.Tokura	102
1-2-16	**Magnetic Structure and Excitation of Metallic Phase of $(V_{1-x}Ti_x)_2O_3$** K.Motoya, J.Kikuchi, K.Hioki, S.Tabaru, S.Shin	103
1-2-17	**Neutron scattering study of dipolar spin ice $Ho_2Sn_2O_7$: Frustrated pyrochlore magnet** H.Kadowaki, Y.Ishii, K.Matsuhira, Y.Hinatsu	104
1-2-18	**Spin dynamics in the Zn-Mg-Tb icosahedral quasicrystals** T.J.Sato, H.Takakura, A.P.Tsai, H.Kadowaki, K.Shibata	105

1-2-38	**Neutron Diffraction Study on TbRhGe** M.Kurisu,G.Nakamoto,T.Himi,Y.Andoh,T.Tsutaoka,S.Kawano	129
1-2-39	**Magnetic structures of $Ce(Ni_{0.91}Pd_{0.09})_2Ge_2$ and $Ce(Ni_{0.7}Rh_{0.3})_2Ge_2$** H.Kadowaki,T.Fukuhara,K.Maezawa,N.Aso,H.Yoshizawa,T.Takeuchi, T.Ooshima,M.Ishikawa	130
1-2-40	**Neutron Diffraction Studies of Magnetic Structure of Mn Formate Di-Urea Single Crystal** S.Kawano,T.Kosugi,M.Toda,K.Yamagata	131
1-2-41	**Neutron Powder Diffraction Study of $Sr_{0.5}La_{0.5}RuO_3$** H.Nakatsugawa,Y.Oohara	132
1-2-42	**Neutron Diffraction Studies of Two-Dimensional Magnetic Ordering in $TbRu_2Ge_2$** S.Kawano,M.Toda,M.Takahashi,T.Shigeoka,N.Iwata,T.Kosugi	133
1-2-43	**Anomalous Hall Effect and the Magnetic Structure of $CuCr_2S_4$** S.Iikubo,K.Oda,S.Yoshii,Y.Yasui,M.Kanada,M.Ito,H.Harashina,M.Sato, K.Kakurai	134
1-2-44	**Correlation between the normal-and induced- antiferromagnetic structure in the layer compound $Cs_{0.5}Rb_{0.5}VF_4$** M.Hidaka,M.Yoshimura,H.Akiyama,H.Fujii,S.Watanabe	136
1-2-45	**The Octahedron Frustration system in Mn_3Pt Above Neel Temperature** T.Ikeda,Y.Tsunoda	138
1-2-46	**Coexistence of Ferromagnetic and Antiferromagnetic Clusters in Concentrated Spin-Glass Alloy $Fe_{65}(Ni_{1-x}Mn_x)_{35}$** K.Motoya,K.Hioki	139
1-2-47	**Neutron Scattering Study on the Spin Ice System $Ho_2Ti_2O_7$** M.Kanada,Y.Yasui,Y.Kondo,S.Iikubo,M.Ito,H.Harashina,M.Sato,H.Okumura, K.Kakurai,H.Kadowaki	140
1-2-48	**Spin Dynamics of Magnetically Frustrated Pyrochlore System $Tb_2Ti_2O_7$** Y.Yasui,M.Kanada,M.Ito,H.Harashina,M.Sato,H.Okumura,K.Kakurai, H.Kadowaki	142
1-2-49	**Magnetic Neutron Scattering Measurements in Highly Frustrated $ZnFe_2O_4$ Single Crystal** K.Kamazawa,Y.Tsunoda,K.Kohn	144
1-2-50	**Incommensurate antiferromagnetic transition in substituted spinels of $Zn_{1-x}Cu_xCr_2Se_4$;$0.0 \leq x \leq 0.3$** M.Hidaka,N.Tokiwa,T.T.Wai,H.Fujii,K.Ohoyama	146
1-2-51	**Magnetic Structure of $Y(Co,Ni)_5$** Y.Adachi,F.Ishikawa,M.Ohashi	148
1-2-52	**Magnetic Structures of BaV_6O_{11}Studied by Neutron Powder Diffraction** Y.Kanke,K.Ohyama,Y.Yamaguchi	149
1-2-53	**Magnetic Structures of Quaternary Antiferromagnetic Sulfides $BaNd_2CoS_5$ and $BaNd_2FeS_5$ by Powder Neutron Diffraction Measurements** M.Wakeshima,K.Ino,Y.Hinatsu,A.Tobo,K.Ohoyama,Y.Yamaguchi	150
1-2-54	**Magnetic Structure in the tetragonal compound $Tm^{11}B_2C_2$** K.Ohoyama,K.Kaneko,A.Tobo,K.Indoh,H.Onodera,Y.Yamaguchi	151

1-2-55	**Magnetic Structure of Tetragonal TbB_2C_2 in the Ground State** K.Kaneko,K.Ohoyama,A.Tobo,H.Yamauchi,H.Onodera,Y.Yamaguchi	152
1-2-56	**Neutron Diffraction Study on Ce_3PbC** M.Kosaka,S.Koiwai,Y.Uwatoko,H.Onodera,A.Tobo,K.Ohoyama,Y.Yamaguchi	153
1-2-57	**Magnetic and Neutron Diffraction Study on $(Mn_{1-x}Cu_x)_{66}Ga_{34}$** H.Shiraishi,Y.Iguchi,T.Hori,K.Ohoyama,Y.Yamaguchi	154
1-2-58	**Antiferromagnetic order in the hcp phase of MnAl alloy** S.Tomiyoshi,K.Nakamura,T.Sheo,Y.Yamaguchi	155
1-2-59	**Magnetic structure of the hexagonal $BaFeO_{3-d}$** K.Mori,T.Kamiyama,H.Kobayashi,K.Ohoyama	156
1-2-60	**Powder neutron diffraction study on $TbPd_3S_4$ and $YbPd_3S_4$** E.Matsuoka,F.Takahashi,J.Kitagawa,K.Ohoyama,H.Yoshizawa,M.Ishikawa	158
1-2-61	**Preliminary Study on The Mechanism of Magnetoresistance Behavior of $(Sm,Y)Mn_2Ge_2$ Compound at Room Temperature by Neutron Diffraction Technique** S.Purwanto,A.Purwanto,N.Minakawa,Y.Morii,Y.Hamaguchi,Y.Yamaguchi	160
1-2-62	**Direction of the magnetic moments in UIr** E.Yamamoto,N.Metoki,Y.Koike	162
1-2-63	**Field induced antiferromagnetic ordering in DyB_2C_2** S.Katano,H.Yamauchi,K.Ohyama,A.Tobo,H.Onodera,Y.Yamaguchi	163
1-2-64	**Crystalline Electric Field Excitations in *f* electron compounds $PrCu_6$** Y.Koike,Y.Morii,N.Metoki,Y.Onuki	165
1-2-65	**Static Spin Correlations in Lightly-Doped $La_{2-x}Sr_xCuO_4$** M.Matsuda,M.Fujita,K.Yamada,R.J.Birgeneau,Y.Endoh,G.Shirane	167
1-2-66	**Low energy magnetic fluctuation of $CeNi_2Ge_2$:Origin of non-fermi-liquid behavior** H.Kadowaki,T.Fukuhara,K.Maezawa	169
1-2-67	**Magnetic excitations in the semi-metallic compound YbAs** K.Ohoyama,N.Aso,M.Kohgi,A.Oyamada,T.Suzuki	170
1-2-68	**Magnetic Interfacial Roughness in Co/Cu multilayers -Interfacial roughness and the GMR effect-** M.Takeda,Y.Endoh	171
1-2-69	**Neutron Scattering Study of the Field Induced Antiferromagnetic Order and Magnetic Excitation in Linear Chain Haldane Compound,NDMAP** Y.Koike,N.Metoki,Y.Morii,T.Asano,Y.Ajiro	172
1-2-70	**Neutron Small Angle Scattering Study on $La_{1-x}Sr_xMnO_3$:x=0.1** M.Watahiki,J.Suzuki,Y.Yamada,K.Kohn	174
1-2-71	**Small Angle Neutron Scattering Study on $Pr_{0.7}Ca_{0.3}MnO_3$** Y.Yamada,T.Iwase,M.Watahiki,J.Suzuki	176
1-2-72	**SANS Study of Slow Dynamics in Concentrated Spin Glasses** K.Motoya,K.Hioki,J.Suzuki	178

No.	「 Title 」	Page
	Neutron Scattering - Superconductivity -	
1-3-1	**Neutron Scattering Study on in-plane phonon modes of $YBCO_{6+x}$** M.Ito,H.Harashina,Y.Yasui,M.Kanada,S.Iikubo,M.Sato.K.Kakurai,M.Nishi	181
1-3-2	**Detailed Comparison between Observed and Calculated Magnetic Excitation Spectra of YBa_2Cu_3Oy with Pseudo Gap Behavior** M.Ito,H.Harashina,Y.Yasui,M.Kanada,S.Iikubo,M.Sato.A.Kobayashi,K.Kakurai	183
1-3-3	**Structure and Dynamics of Double Honeycomb Lattice Superconductors** S.Shamoto,Y.Kato,T.Kajitani,K.Ohoyama,Y.Yamaguchi,N.Aso,K.Kakurai	185
1-3-4	**Neutron Scattering Study on the Anomaly in $La_{2-x}Sr_xCuO_4$(x-0.21,y=0.01)** Y.Koike,M.Aoyama,T.Adachi,T.Kawamata,H.Kimura,K.Hirota,K.Yamada, Y.Endoh	186
1-3-5	**Competitive interplay between the charge/spin order and superconductivity in $La_{1.875}Ba_{0.125-x}Sr_xCuO_4$** H.Goka,M.Fujita,K.Yamada,M.Matsuda	187

No.	「 Title 」	Page
	Neutron Scattering -Amorphous・Liquid-	
1-4-1	**The Study of the Structure of Liquid Sn in the Wide Temperature Range due to Neutron Scattering Technique** M.Masaki,S.Munejiri,H.Aoki,T.Kamiyama,T.Itami,Y.Ishii	191
1-4-2	**Hydration Structure of Urea Molecules in Highly Concentrated Aqueous Solutions** Y.Kameda,K.Sugawara,K.Abe,T.Usuki,O.Uemura	193
1-4-3	**Neutron Spin Echo Studies on Bragg Reflections of Magnetite Fine Particles in Ferroliquid due to Dopplar Broadening** N.Achiwa,H.Nishioka,T.Yokoyama,K.Kakurai	195
1-4-4	**Structural Changes in Liquid As-Te Mixtures** K.Maruyama,S.Takeda	196
1-4-5	**Electron-Ion Correlation Liquid Ga by Diffraction Method** S.Takeda,Y.Kawakita,T.Enosaki,K.Maruyama	197
1-4-6	**Elastic neutron scattering from superionic conducting glasses** H.Takahashi,N.Rikitake,T.Sakuma,Y.Ishii	198
1-4-7	**Small angle neutron scattering study on the interdigitation phase transition of dipalmitoylphosphatidylcholine induced by pressure** H.Seto,H.Nobutou,N.Yamada,Y.Kawabata,T.Takeda,M.Nagao	200
1-4-8	**Incoherent Scattering from Water** M.Nagao,M.Shibayama	201
1-4-9	**Small-Angle Neutron Scattering Study on Aggregation in Acetonitrile-D_2O Mixtures** T.Takamuku,A.Yamaguchi,M.Tabata,K.Yoshida,T.Yamaguchi,M.Nagao	203
1-4-10	**Neutron Spin Echo Investigations on the Slow Dynamics in Complex Fluids Involving Amphiphiles** T.Takeda,Y.Kawabata,H.Seto,N.Yamada,M.Nagao	205
1-4-11	**NSE and SANS Studies on the Effects of Temperature and Pressure in a Droplet Microemulsion System** Y.Kawabata,M.Nagao,H.Seto.T.Takeda	206
1-4-12	**Slow Dynamics of n-Butoxyethanol/water Mixture by Neutron Spin Echo Techniques** K.Yoshida,T.Yamaguchi,M.Nagao,Y.Kawabata,H.Seto	208
1-4-13	**Anomalous Dynamics in Liquid Te-Se Mixtures in the Semiconductor-to-Metal Transition Range** M.Yao,Y.Kawakita,Y.Ohmasa,A.Chiba	209
1-4-14	**Neutron Scattering Study on Dynamics of Acetonitrile Molecules in MCM-41** S.Kittaka,S.Takahara,Y.Kuroda,T.Mori,T.Yamaguchi	210
1-4-15	**Low-frequency Dynamics of Cyclooctanol Orientational Glass** O.Yamamuro,H.Yamasaki,Y.Madokoro,T.Matsuo	212

1-4-16	**Neutron Incoherent Inelastic Scattering of Oriented Oleic Acid** T.Yokoyama,N.Achiwa,M.Suzuki	214
1-4-17	**Quasi Elastic Neutron Scattering Measurements on the Liquid Mixture Having Closed Two Phase Region** K.Maruyama,S.Kawase,M.Misawa	216
1-4-18	**Low-energy Excitation in $CaCl_2$ Aqueous Solution Glass** O.Yamamuro,Y.Madokoro,H.Yamasaki,T.Matsuo	217

No.	「 Title 」	Page
	Neutron Scattering - Polymer -	
1-5-1	**Scattering Studies on Hierarchical Structures of Rubber/Filler Systems** T.Hashimoto,M.Takenaka,T.Koga,K.Aizawa	221
1-5-2	**Structural study of the sol-gel transition of linear polyethylene in toluene** Y.Izumi,Y.Jinbo,H.Watanabe,K.Aizawa,H.Tomimitsu	222
1-5-3	**Shear-Induced Ordering of Lamellar Structure Observed in a Nonionic Surfactant / Water System** M.Imai,K.Nakaya	223
1-5-4	**Association Behavior of Amphiphilic Block Copolymer in Solution:The Effect of Crystallization of Core in the Micelle** K.Matsumoto,U.Mizuno,R.Nishimura,H.Mazaki,H.Matsuoka	224
1-5-5	**Equilibrium Elasticity of Diblock Copolymer Micellar Lattice** H.Watanabe,T.Kanaya,Y.Takahashi	225
1-5-6	**Flow-induced structure of poly(styrene-b-isoprene) solutions near ODT** Y.Takahashi,A.Takano,M.Naruse,Y.Matsushita	226
1-5-7	**Studies on aggregated Structure of Globular Protein** S.Takata,T.Norisuye,M.Shibayama	227
1-5-8	**Preparation Temperature Dependence of Frozen Inhomogeneities in Chemically Cross-linked Gels** T.Norisuye,S.Takata	229
1-5-9	**Mechanism of plastic deformation in amorphous polymers** A.Toda	231
1-5-10	**Shear-Induced Transformations in the Lamellar Phase Formed by Nonionic Surfactants** K.Minewaki,T.Kato,M.Imai,Y.Takahashi	232
1-5-11	**Critical Phenomena in Symmetric Poly(deutrated styrene-b-isoprene)/Poly (styrene-b-isoprene) mixture** M.Takenaka,D.Yamaguchi,H.Hasegawa,T.Hashimoto,M.Nagao	233
1-5-12	**Intermediate and Large Scale Structures in Gellan Gum Gels** Y.Izumi,Y.Jinbo,T.Matsugi,M.Hashimoto,T.Takahashi	234
1-5-13	**Effect of Salt for Ovalbumin solution on Heat Denaturation** M.Sugiyama,S.Kuwajima,M.Annaka,K.Hara	235
1-5-14	**Development of Neutron Reflectometer for Air/Water Interface with Imaging Plate** H.Matsuoka,M.Matsutani,E.Mouri,A.Moriai,K.Soyama	236
1-5-15	**Dynamics Study of Amorphous Polystyrene by Quasi Elastic Neutron Scattering near Tg** I.Tsukushi,T.Kanaya,K.Kaji	237

1-5-16	**Pressure Dependence of Gas Permeability in Polyimide and Role of Local Dynamics** T.Miyazaki,T.Kanaya,Y.Ito,A.Shimazu,S.Katayama,K.Kaji	238
1-5-17	**Neutron Reflectivity Study of Time Evolution of Interfacial Structure of (Polystyrene/Deuterated Polystyrene) Bilayer below the Bulk Glass Transition Temperature** T.Kajiyama,D.Kawaguchi,A.Sakai,K.Tanaka,S.Tasaki,A.Takahara	240
1-5-18	**Small-angle neutron scattering and dielectric studies on miscibility of poly (styrene) and poly(vinyl methyl ether) mixtures** H.Takeno,M.Kobayashi,M.Naoki,S.Koizumi	241
1-5-19	**Small-Angle Neutron Scattering Study of Graft-Copolymer Natural Rubber-Styrene** A.Insani,J.Suzuki,S.Koizumi,A.Ikram,Sudirman,A.Purwanto	243
1-5-20	**Small-angle Neutron Scattering Study on Thermal Phase Behavior of NIPA-PEG Diblock Copolymer** M.Annaka,R.Motokawa,T.Nakahira,S.Koizumi	244
1-5-21	**Conformations of a Single Polymer Chain Confined in aMicroemulsion Droplet** K.Nakaya,M.Imai	246

No.	「 Title 」	Page
	Neutron Scattering - Biology -	
1-6-1	**Preliminary Neutron Structure Analysis of Cytochrome c' from Alcaligenes xylosoxidans NCIMB 11015** T.Kohzuma,H.Watanabe,A.Osterman,K.Kurihara,T.Chatake,I.Tanaka,N.Niimura	249
1-6-2	**Phase diagram for B-DNA crystallization systems and its application to make a large crystal of available for neutron diffraction experiments** S.Arai,T.Chatake,Y.Minezaki,Y.Nishimura,N.Niimura	251
1-6-3	**A neutron crystallographic analysis of a rubredoxin mutant** T.Chatake,K.Kurihara,I.Tanaka,M.W.W.Adams,F.E.Jenney Jr.,I.Tsyba,R.Bau, N.Niimura	253
1-6-4	**Data Collection of Neutron Diffraction from a Single Crystal of Hen Egg-White Lysozyme Grown under pH 3.4** S.Fujiwara,M.Maeda,Y.Yonezawa,N.Niimura	255
1-6-5	**Effect of Occlusion of Proteins on AOT Microemulsion Structure** M.Hirai,R.K.Hirai,H.Iwase,T.Hayakawa,M.Nagao,M.Shibayama	256
1-6-6	**Structural analysis of a protein denatured in dodecyl sulfate micelles** Y.Watanabe	258
1-6-7	**Evaluation of the sizes of light-harvesting pigment-membrane protein complexes from a photosynthetic bacterium** Z.-Y.Wang,Y.Muraoka,M.Shimonaga,T.Nozawa	260
1-6-8	**The Ligand Binding-induced Structural Changes in Giant Hemoglobin** M.Harada,N.Shibayama,T.Gotoh	261
1-6-9	**Small Angle Neutron Scattering study of Phosphatidylcholine/ Dimethylsulfoxide/Water System** H.Takahashi	262
1-6-10	**Small-Angle Neutron Scattering of Lipophorin** C.Katagiri,M.Nagao,M.Sato,Y.Ito	263
1-6-11	**Structures of Calmodulin in the Complex with Neutron-Specific Protein NAP-22** Y.Izumi,N.Hayashi,Y.Jinbo,N.Matsushima	264
1-6-12	**Temperature Dependence of Dynamics of Glycosphingolipid (G_{D1a}) Micelle** M.Hirai,H.Iwase,T.Hayakawa,S.Seto,Y.Kawabata,T.Takeda	265
1-6-13	**Neutron Fiber Diffraction of Frog Muscle Combined with the Contrast Variation Measurements** S.Fujiwara,Y.Takezawa,Y.Sugimoto,K.Wakabayashi	266
1-6-14	**Small-Angle Neutron Scattering Measurements of the Native Thin Filaments of Muscle Using Contrast Variation Method** S.Fujiwara,F.Matsumoto,K.Makino	267
1-6-15	**Hydration of Proteins Observed by Small-Angle Neutorn Scattering** S.Fujiwara,Y.Yonezawa	268

No.	「 Title 」	Page
	Neutron Scattering - Fundamental Physics · Neutron Optics -	
1-7-1	**Lattice dynamics of disordered Perovskite $Pb(Zn_{1/3}Nb_{2/3})O_3$** I.Tomeno,S.Shimanuki,Y.Tsunoda,Y.Ishii	271
1-7-2	**Neutron Interferometry at PNO in JRR-3M** H.Tomimitsu,Y.Hasegawa,K.Aizawa	272
1-7-3	**Neutron Diffraction Study on the Texture of Ultrafine-grained Steel** Y.Akiniwa,H.Kimura,K.Tanaka,N.Minakawa,Y.Morii	273
1-7-4	**Evaluation of Fatigue Damage in SiC Particulate Reinforced Aluminum Alloy by Neutron Diffraction** Y.Akiniwa,K.Tanaka,H.Kimura,N.Minakawa,Y.Morii	274
1-7-5	**Measurement of Residual Stress in the Neutron Cold Moderator Cell for High-Intensity Proton Accelerators** A.Moriai,H.Kogawa,K.Yamamoto,M.Kaminaga,N.Minakawa,Y.Horiguchi	275
1-7-6	**Measurement of d_0(A7075) by random rotation goniometer** Bharoto,N.Minakawa	277
1-7-7	**The internal residual stress which evaluated the processing stress of a shrink-fit sample** N.Minakawa,Y.Morii,A.Moriai,K.Kikuchi	278
1-7-8	**Residual strain measurements by neutron diffraction in SiC fiber reinforced Ti-15-3 matrix composite** Y.Tanaka,N.Minakawa,C.Masuda,Y-F.Liu	280
1-7-9	**Measurement of residual strain in a Cu-15 Wt Pct Cr in-situ composite using neutron diffraction** C.Masuda,N.Minakawa,Y.Tanaka	281
1-7-10	**Measurement of Residual stresses of a drawn pearlite steel** T.Suzuki,Y.Tomota,Y.Moriai,N.Minakawa,Y.Morii	282
1-7-11	**Mieze Spin Echo Method Using RF Flippers II** T.Ebisawa,S.Tasaki,N.Achiwa,D.Yamazaki,T.Kanaya,N.Torikai,M.Hino, T.Kawai,K.Soyama	283
1-7-12	**Measurement of spin precession angle of neutron tunneling through a magnetic thin film with absorption** M.Hino,S.Tasaki,T.Ebisawa,T.Kawai,N.Achiwa,D.Yamazaki	285
1-7-13	**Time Beat Neutron Spin Interferometry before or after Analyser** N.Achiwa,G.Shirozu,T.Ebisawa,M.Hino,S.Tasaki,T.Kawai,D.Yamazaki	286
1-7-14	**A novel Jamin-type interferometer for cold neutrons using etalon plates** M.Kitaguchi,H.Funahashi,M.Hino	288

No.	「 Title 」	Page
	Neutron Scattering - Instrument -	
1-8-1	**An Attempt to refrigerate Si-crystal optical component on a Double Crystal Diffractometer II** K.Aizawa,H.Tomimitsu	291
1-8-2	**Stacked Elastically Bent Perfect SI Monochromators for Diffractometers for BIO-Macromolecules (BIX-2 & BIX-3)** I.Tanaka,K.Kurihara,T.Chatake,M.Maeda,N.Niimura	292
1-8-3	**Off-specular reflection from Ni/Ti multilayers** K.Soyama,C.Bin	293
1-8-4	**Enhancement of reflectivity of small d-spacing multilayer mirrors by ion polishing in combination with ion beam sputtering** K.Soyama,W.Ishiyama,K.Murakami	294
1-8-5	**Development of spin flippers with steady current** T.Takeda,H.Seto,Y.Kawabata	295
1-8-6	**Development of Polished Glassy Carbon Mirror for VCN Extraction** Y.Kawabata,M.Hino,H.Unesaki,S.Tasaki,M.Suzuki,A.Wakata	296
1-8-7	**Development of a new spin echo spectrometer using multilayer spin splitters** S.Tasaki,T.Ebisawa,M.Hino,R.Maruyama,N.Achiwa,D.Yamazaki,T.Kawai	297
1-8-8	**Development of 2-dimensional imaging detector based on neutron scintillator with wavelength shifting fibers** K.Sakai,T.Adachi,T.Oku,A.Gorin,T.Ino,K.Kuroda,I.Manuilov,K.Morimoto, A.Ryazantsev,H.M.Shimizu,J.Suzuki,F.Tokanai	298
1-8-9	**A $SrBPO_5:Eu^{2+}$ phosphor for neutron imaging** K.Sakasai,M.Katagiri,K.Toh,H.Takahashi,M.Nakazawa,Y.Kondo	299

No.	「 Title 」	Page
	Neutron Scattering - Others -	
1-9-1	**Commensurate-incommensurate transition in the melting process of orbital ordering in $Pr_{0.5}Ca_{0.5}MnO_3$** R.Kajimoto,H.Yoshizawa,Y.Tomioka,Y.Tokura	303
1-9-2	**Structure and Cathode Properties of Phospho-olivine $LiCoPO_4$ for Lithium Secondary Batteries** S.Okada,S.Sawa,Y.Uebo	304
1-9-3	**Neutron Diffraction Study of Internal Stress Induced by Machining on a Material** Y.Tsuchiya,K.Kikuchi,T.Kato,H.Nakajima,H.Tsuji,N.Minakawa,Y.Morii	306
1-9-4	**Precision Measurement of the Neutron Lifetime** A.Maki	307

No.	「 Title 」	Page
	Neutron Radiography	
2-1	**Liquid Metal Surface Response to Water Jet Impingement** Y.Shibamoto,H.Nakamura,S.Yano,Y.Tsuji,Y.Kukita	319
2-2	**2-dimensional neutron imaging method using scintillators with wavelength shifting fibers** K.Toh,M.Katagiri,K.Sakasai,M.Matsubayashi,A.Birumachi,H.Takahashi, M.Nakazawa	321
2-3	**Development of neutron radiography high resolution imaging asing FOP** M.Matsubayashi,T.Hibiki,K.Mishima,H.Unezaki	322
2-4	**Water Movement in the Vicinity of a Seedling Root with Aluminum Treatment by Neutron Beam Imaging** T.M.Nakanishi,Y.Okuni,J.Furukawa,M.Matsubayashi	323
2-5	**Visualization and Measurement of Thermal Hydraulic Phenomena by Thermal Neutron Radiography** N.Takenaka,H.Asano,J.shirouzu,N.Maeda,S.Hayama,A.hashimoto,H.Hayashi Y.Tagami,T.Fuchimoto	327
2-6	**Development of Refractive neutron Lense** Y.Kawabata,S.Tasaki,K.Yoneda	330
2-7	**Neutron Radiography of Firelock Gun of "Yonezawa-Han" Make** K.Suzuki,I.Araki	334
2-8	**Flow Visualization of Gas-Solid Fluidized Bed** M.Ozawa,H.Umekawa	341
2-9	**Application of Neutron Radiography to observation of Hydrogen Distribution in Distribution in zircaloy Cladding Tubes** R.Yasuda,M.Matsubayashi,M.Nakata,K.Harada,H.Amano	345

No.	「 Title 」	Page
	Neutron Activition Analysis	
3-1	**Behavior of trace elements in the weathered products of volcanic ash** H.Kamioka,Y.Seki,K.Tsukimura,Y.Kanai,Y.Kanazawa,S.Hamasaki,T.Nakajima	349
3-2	**Distribution coefficient Kd of stable elements in surface soils collected in Aomori Prefecture** H.Tsukada,A.Takeda,H.Hasegawa,S.Hisamatsu,J.Inaba	350
3-3	**Fractional crystallization and cumulus processes of granitic magma on the Tottabetsu intrusive body in the Hidaka belt Hokkaido** T.Nakajima,H.Kamiyama,H.Kamioka	351
3-4	**Content levels and dynamics of halogen elements in the soil and plant system of the world -Soils and plants Tunisia-** N.Kihou,K.Yuita,K.Tsuzuki	353
3-5	**Development of the stable ^{41}K tracer methods by using the neutron activation analysis -Labelling the feces and urine (excreta) of the guinea pig by the stable ^{41}K isotope-** N.Kihou,K.Yuita	355
3-6	**Labeling of Heavy Metals in Soil Organic matter with Stable Isotopes** Y.Sakurai,N.Kihou,T.Makino,K.Sugahara	357
3-7	**Determination of sodium and copper in saltwater clam shell by activation analysis** H.Kamioki	358
3-8	**Loss of elements in IAEA standerd soil under ashing conditions** M.Takahashi,S.Kurosawa,M.Magara,S.Sakurai,Y.Hanzawa,S.Usuda, Y.Hatsukawa,Y.Toh,M.Oshima,N.Shinohara,T.Hayakawa	359
3-9	**Minor and Trace Element Determination of Environmental Samples (1)** Y.Miyamoto,Y.Saito,S.Sakurai,S.Usuda	360
3-10	**Determination of long-lived radioisotope, ^{129}I** Y.Hatsukawa,M.Oshima,T.Hayakawa,Y.Toh,N.Shinohara,K.Kushida,T.Ueno	362
3-11	**Geochemical Studies on Cosmic and Volcanism Matters by Instrumental Neutron Activation Analysis(Ⅱ)** T.Fukuoka,K.Nogami,Y.Tazawa,Y.Yokota	363
3-12	**Activation Analysis of Meteorites(Ⅲ)** H.Nagai,M.Honda,H.Sato,M.Ebihara,Y.Oura,M.Setoguchi	367
3-13	**Analysis of the Elements in Plants** T.M.Nakanishi,N.Ikeue,K.Tanoi,H.Yokota,Y.Hayashi,Y.Okuni,J.Furukawa	372
3-14	**Development of New Preconcentration Techniques for Neutron Activation Analysis** S.Abe,M.Endo,S.Funata,A.Miyauchi	375
3-15	**The Activation Analysis of Phosphorescent Phosphor** K.Moriwaki,O.Tsuzukibasi,M.Makimura,S.Sudo,S.Furuyama	379
3-16	**Incorporation of Specified Element to Plant Leaf and Others** S.Masuko,S.Kasahara,T.Ohnishi	387

3-17	**Studies on Cadmium Bioaccumulation in Scallop Mizuhopecten Yessoensis** T.Ohnishi,G.Ohnishi,Y.Noya	392
3-18	**Behavior of Inorganic Elements in Microorganisms** A.Nakajima,Y.Ueda	395
3-19	**Study on Trace Elements in Physiologically Active Substances** Y.Homma,Y.Morita,I.Murakami,K.Ohara	399
3-20	**The Development of Neutron Activation ,Sample Transportation and γ -ray Counting Routine System for Numbers of Geological Samples** S.Shibata,T.Tanaka,M.Minami,R.Senda,M.Takebe,T.Kachi,M.Kondo,S.Oda T.Hayashi,K.Nishizawa,H.Kojima	402

No.	「Title」	Page
	Production of Radio Isotopes	
4-1	**Production of ^{186,188}Re and Recovery of Tungsten from Spent ^{188}W/^{188}Re Generator** K.Kobayashi,S.Motoishi,K.Terunuma,A.A.Rauf,K.Hashimoto	423
4-2	**Development of intravascular irradiation source** H.Kogure,T.Sorita,A.Satoh,S.Izumo	427
4-3	**The Production of Radiopharmaceuticals with Short Lived Radionuclides Produced by Reactor** A.Ando,K.Washiyama,I.Ando	428

No.	「Title」	Page
	Irradiation Test of Reactor Materials	
5-1	**Neutron Irradiation of Lead-Bismuth Eutectic Samples by JRR-4 Neutron Beam Facility** H.Sekimoto,M.Igashira,T.Yano,T.Obara,T.Ohsaki,T.Mori	433
5-2	**Electrical conductivity change under neutron irradiation in single crystal Al_2O_3 containing TiO_2** T.Tanifuji,Y.Katano,T.Nakazawa,S.Jitsukawa	434
5-3	**Tritium Release from Silica Glass** T.Tanifuji,S.Nasu,S.Jitsukawa	435

No.	「 Title 」	Page
	Prompt Gamma-ray Analysis	
6-1	**Neutron-induced Prompt γ -ray Analysis for Volcanic Rocks** T.Fukuoka,T.Hasenaka,T.Sano	439
6-2	**Grompt Gamma-ray Analysis of Meteorite Samples(Ⅱ)** M.Ebihara,S.K.Latif,Y.Oura,G.W.Kallemeyn,S.Yoneda	443
6-3	**Neutron-induced Prompt Gamma-ray Analysis of Solid Environmental Samples and Geochemical Samples** M.Matuo,A.Kuno,K.Kubo,T.Matsumoto,M.Yasoshima,Y.Tanaka, M.Kataoka	447

No.	「 Title 」	Page
	Others	
7-1	**Radiation Damage and Activation of High-Performance Shielding Material** T.Miura,Y.Hirao,T.Ishida	455
7-2	**Installation of experimental equipment for low temperature chemistry at beam guide of JRR-3M and observation of preferential ortho-T_2 formation in recombination reaction of T+T→T_2 in liquid ^{3}He-^{4}He mixture at 1.4-2.5K** Y.Aratono	456
7-3	**Current Medical Setup at JRR-4 for Boron Neutron Captute Therapy (BNCT)** T.Yamamoto,A.Matsumura,Y.Shibata,T.Nose,K.Yamamoto,H.Kumada	457
7-4	**Characterization of Neutron Beams for Boron Neutron Capture Therapy: In-air Radiobiological Dosimetry** T.Yamamoto,A.Matsumura,Y.Shibata,T.Nose,K.Yamamoto,H.Kumada	459
7-5	**In Vivo Neutron Measurement on the Human Brain and Blood Boron Measurement for Intraoprative Boron Neutron Capture Therapy (IOBNCT)** T.Yamamoto,A.Matsumura,Y.Shibata,T.Nose,K.Yamamoto,H.Kumada	463
7-6	**Interim results of the clinical trial for BNCT using the thermal neutron beam mode Ⅰ at JRR-4** A.Matsumura,T.Yamamoto,Y.Shibata,A.Matsushita,S.Yasuda,K.Nakai, T.Yamada,H.Akutsu,T.Nose,K.Yamamoto,H.Kumada,N.Hori	465
7-7	**In vitro NCT comparison study between two Gd targeting compound (Gd-BOPTA and Gd-DTPA)** T.Zhang,A.Matsumura,T.Yamamoto,T.Nose,H.Kumada,K.Yamamoto	467
7-8	**The Influence of Hydrophilic Groups to the Recoil Features of Central Metal Atoms in the Solid System of Water-Soluble Metalloporphyrin Ion Associates** H.Shoji	469
7-9	**Establishment of the System for Observing Boron in Steels Using α -Rays Track** K.Asakura,K.Shibata,S.Harasawa,H.Sawahata,M.Kawate	475

This is a blank page.

1. 中性子散乱 1) 構造・励起

1. Neutron Scattering 1) Structure・Excitation

This is a blank page.

研究テーマ：超低温の導入による中性子散乱の研究
表　題：包接水化物の中性子回折研究

1-1-1 Neutron Diffraction Studies of Clathrate Hydrates

Claudia J. Rawn[1], Camille Y. Jones[1], Bryan C. Chakoumakos[1], Simon L. Marshall[1], Yoshinobu Ishii[2], Laura A. Stern[3], Susan Circone[3], and Stephen H. Kirby[3]

[1]*Oak Ridge National Laboratory, Physical and Computational Sciences Directorate, Oak Ridge, Tennessee 37831 USA*
[2]*Advanced Science Research Center, Japan Atomic Energy Research Institute Tokai-mura, Naka-Gun, Ibaraki, 319-1195, Japan*
[3]*United States Geological Survey, Menlo Park, California 94025 USA*

Neutron diffraction experiments are well suited for the study of clathrate hydrate structures that are primarily built up of a network of H and O atoms. Clathrate hydrates are stable at low temperatures and modest pressures requiring bulky auxiliary equipment and special handling for keeping the samples below the disassociation temperature at 1 atmosphere. Most clathrate hydrates crystallize in one of two cubic structures or a hexagonal structure. The unit cell of the Type I structure contains 46 water molecules comprising two 12-hedron and six 14-hedron cavities, which are each typically occupied by a methane or carbon dioxide molecule. The unit cell of the Type II structure contains 136 water molecules forming sixteen 12-hedron and eight 16-hedron cavities, which are each typically occupied by an oxygen, nitrogen, or propane molecule.

Neutron diffraction experiments were carried out using HRPD installed at JRR-3M to study hydrate samples containing CO_2, tetrahydrofuran (THF), or a mixture of CH_4/C_2H_6 as guest molecules encaged in the hydrogen bonded network. The data collected as a function of temperature will be used to determine the thermal expansion, stability, and decomposition kinetics. The structural models have been refined using rigid body constraints to describe the CO_2, THF, CH_4 and C_2H_6 molecules.

CH_4/C_2H_6 Gas Clathrate Deuterate

Data were collected on a gas clathrate sample, synthesized at the USGS, that contained both methane and ethane as the guest molecules with a gas composition 82%CH_4:18%C_2H_6 at 9, 40, 50, 90, 130, 180, and 190 K. The diffraction pattern at 9 K was dominated by a peak at the diffraction angle of 20.5 degrees. This large peak was not observed in the diffraction pattern for the data collected at 50 K, however, a strong peak at 21.4 degrees was observed. The diffraction pattern from the subsequent data collected at 90 K does not show either of these two unexplained peaks. Figure 1 shows the comparison of the observed neutron powder diffraction data with the calculated pattern. The calculated pattern is based on the Type II structure and includes ice as a secondary phase. The next data set was collected at 40 K where the strong peak at 21.4 degrees was again observed. Table 1 gives the lattice parameters, wt% ice, extra peaks observed, and χ^2 for the Rietveld refinements as a function of temperature.

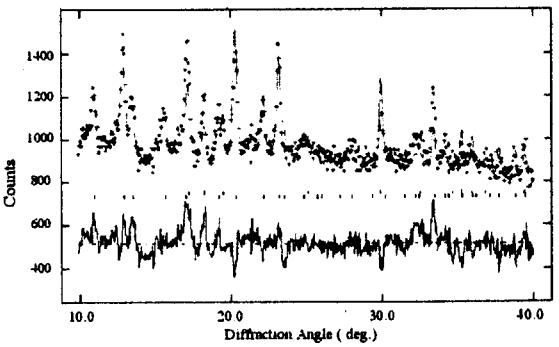


Fig 1. Comparison of the observed neutron powder diffraction data (+) with the calculated pattern and the difference pattern.

Table 1. Lattice parameters, wt% ice, extra peaks, and χ^2 from Rietveld refinements on data of CH_4/C_2H_6 dueterohydrate as a function of temperature.

T (K)	a (Å)	wt% ice	extra peaks	χ^2
8	17.102(3)	10	20.5	7.80
40	17.089(3)	16	21.4	2.93
50	17.086(2)	15	21.4	2.61
90	17.107(2)	18	none	1.88
130	17.138(3)	16	none	1.88
180	17.170(2)	16	none	1.73

原子炉：　JRR-3M　　装置：　HRPD (1G)　　分野：中性子散乱（構造）

CO_2 Gas Clathrate Deuterate

Data were collected on two samples of CO_2 deuterate, $CO_2 \bullet 5.75H_2O$, sample 1 at 8, 60, 100, 140, and 180 K; and sample 2 at 9, 190, 200, and 210K. Data for sample 2 at 210K was above the decomposition temperature of about 205 K, so the 210 K data were recorded 4 times in succession to monitor the kinetics of the transformation of the hydrate to ice + CO_2. Sample 1 exhibited a thermal expansion behavior similar to previous reports[1], but sample 2 exhibited an anomalously small lattice parameter at the lowest T.

Table 2. Lattice parameters from Rietveld refinements on data of CO_2 deuterate (sample1) as a function of temperature.

T (K)	a (Å)
8	11.8145(7)
60	11.8236(7)
100	11.8409(7)
140	11.8646(7)
180	11.8916(8)

Fourier synthesis is being used to create pictures of the nuclear density within the small and large polyhedral cages to understand the preferred orientations of the CO_2 molecules and relate this to the dynamic information derived from inelastic neutron scattering, NMR, and Raman spectroscopy studies. The residual nuclear density in a ΔF Fourier map for the large cage suggests preferred orientations for the CO_2 molecule (Fig. 2).

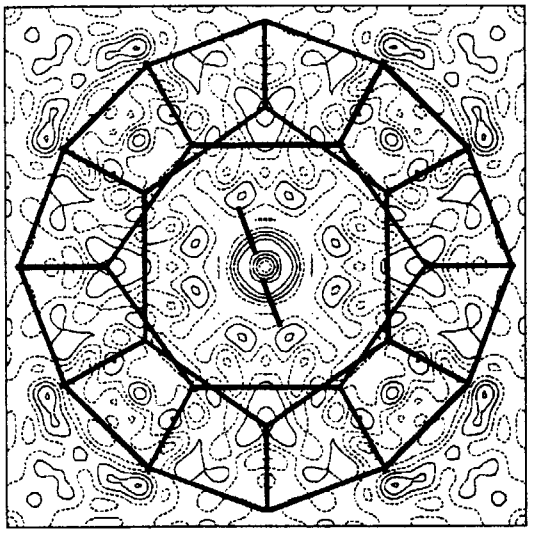


Fig. 2. ΔF Fourier map (100 Å^2) for the large cage in CO_2 deuterate at 100 K. The outline of the large cage is projected on the map and the bold line segments show the size of the CO_2 molecule.

Table 3. Lattice parameters and displacement parameter_for THF deuterohydrate.

T (K)	a (Å)	100 * U_{iso} (Å^2)			
		O_{host}	D_{host}	T_{THF}	L_{THF} (deg^2)
10	17.052(2)	1.1	1.2	5.7	31200
75	17.1180(7)	1.2	1.2	0.0	40600
140	17.1586(8)	2.2	1.8	0.5	36100
205	17.190(2)	0.2	0.4	-0.5	21400
265	17.284(1)	4.2	2.6	0.8	33000

THF Clathrate Deuterate

Data were collected on a tetrahydrofuran deuterohydrate, $C_4H_8O \bullet nH_2O$ ($16<n<17$) at 10, 75, 140, 205, and 265 K. The THF hydrate crystallizes with the Type II structure at ambient pressure. Table 2 gives the lattice parameters and atomic displacement parameters for the THF deuterohydrate. The THF has been modeled using the rigid-body formalism, and isotropic translation and librational terms have been refined. When both the translation and librational parameters are simultaneously refined, the rms displacement of the THF molecule is near zero, and the libration is significant. This is in keeping with the picture of the THF dynamics derived from quasi-elastic neutron scattering.[2]

Acknowledgment

This research was sponsored by the Laboratory Directed Research and Development Program at Oak Ridge National Laboratory, managed by UT-Battelle, LLC for the U.S. Department of Energy under contract no. DE-AC05-00OR22725.

Reference

1) T. Ikeda, S. Mae, O. Yamamuro, T. Matsuo, S. Ikeda and R.M. Ibberson, J. Phys. Chem. A **104** (2000) 10623.
2) K.W. Herwig and C.A. Tulk, personal communication (2001).

研究テーマ：超低温の導入による中性子散乱の研究
表　題　：HRPD による PZT ($Pb_{1-x}Nd_x(Zr_{0.52}Ti_{0.48})_{1-x/4}O_3$) の中性子回折実験

1-1-2

Neutron Diffraction Experiments of PZT by Using High Resolution Powder Diffractometer

S. Pongkasem, A. Moriai[1], Y. Ishii[1], N. Minakawa[1]

Materials Science Group, Physics Division,
Office of Atomic Energy for Peace, Bangkok, THAILAND
[1]Advanced Science Research Center, JAERI, Tokai, Ibaraki, 319-1195, Japan

Objectives

The purpose of my study and training is to understand the system of HRPD and measurement of PZT samples. Therefore, I have studied the HRPD facility at JRR-3M. One of PZT samples (Un-dopant) and the other seven PZT samples with Nd dopant have been measured.

The objective of the measurement is to study the structure of PZT samples with Nd dopant. This study is a collaborative project between our group and the Chemistry Department of the Mahidol University. These samples were prepared by a graduate student. The empirical formula of these samples are $Pb_{1-x}Nd_x(Zr_{0.52},Ti_{0.48})_{1-x/4}O_3$, where x is the mole fraction. Though it was expected that Nd would replace Pb sites, substitution of Nd for Zr and Ti would also be investigated.

Measurement technique

The neutron diffraction experiment was done using HRPD with wavelength • of 1.82268 Å. A powder sample was filled in the 0.05 mm thickness of vanadium foil cylinder with diameter about 10 mm and 45 mm in length. The samples were measured at room temperature and rotated to reduce the preferred orientation effect.

Result and Discussion

We measured respectively the sample of 10.0 mol% and 12.0 mol% of Nd dopant 6.0 mol% 1.2 mol% 0.5 mol% 0.1 mol% 0.01 mol% 0.0 mol%. A measurement result (0.0 mol% and 12.0 mol%) is shown in Fig. 1.

The investigation of the samples with Rietveld method does not yet finish. The refinement of the samples structure does not yield the good results. The investigation will be continued in THAILAND.

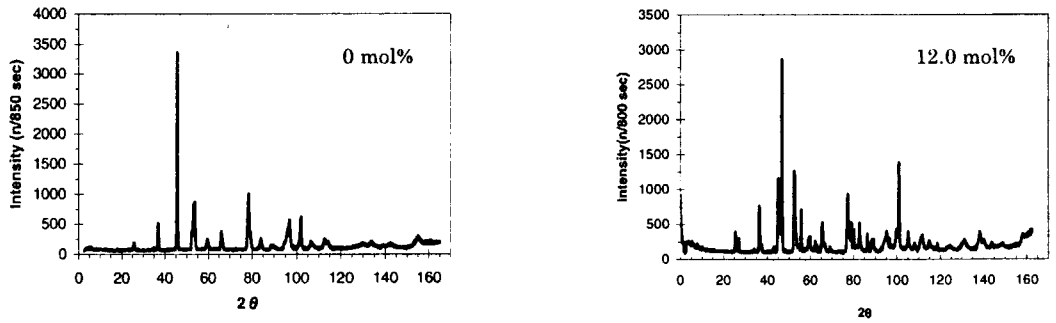


Fig.1. Diffraction pattern of 0mol% and 12.0 mol% Nd dopant PZT.

原子炉：JRR-3M　　装置：HRPD (1G)　　分野：中性子散乱（構造）

研究テーマ： 半磁性電気伝導体の磁性と化学構造

表題 ： β － Na_xCoO_2 の構造決定

1-1-3 Structure determination of β －Na_xCoO_2

Y. Ono[1] , R.Ishikawa[1], Y.Miyazaki[1], Y.Ishii[2], Y.Morii[2] and T. Kajitani[1]

[1] Graduate School of Engineering, Tohoku University, Sendai, 980-8579

[2] Japan Atomic Energy Research Institute, Ibaraki, Tokai, 319-1195

Recently, excellent thermoelectric properties were discovered in a layered cobalt oxide, γ - Na_xCoO_2, which is a member of Na_xCoO_2 oxides containing CdI_2-type CoO_2 layers [1]. There are other three members with different sodium contents, namely, α ($0.90 \leqq x \leqq 1.0$) , α' (x=0.75) and β ($0.55 \leqq x \leqq 0.60$) phases, respectively [2]. The crystal structures of α and α'-phases are believed to be isomorphous to well-known α －$NaFeO_2$ and α'－Na_xMnO_2 [3,4], respectively, while that of β － Na_xCoO_2 was not definitely determined yet.

Polycrystalline samples of β － Na_xCoO_2 were prepared by a conventional solid state reaction. Starting materials, $Na_2O_2$and Co_2O_3, were mixed with a molar ratio of Na:Co=0.70:1.0, pressed into pellets and calcined at 530 ℃ for 12 h in flowing oxygen gas. After intermediate grindings and pelletizing, the product was sintered at 530 ℃ for 24 h in flowing oxygen gas. Powder neutron diffraction measurements were carried out at 10 K and 300 K using HRPD (λ =1.8251 Å) installed at JRR-3M (JAERI).

The structure determination of β － Na_xCoO_2 was performed using a Rietveld analysis program RIETAN [5]. In this study, a monoclinic unit cell with space symmetry, C2/m, was assigned to this compound based on the systematic absence of Bragg reflections, i.e., hkl reflections with h+k=odd number were absent. As shown in Fig.1, the powder neutron diffraction pattern at 10 K, satisfactory agreement between observed and calculated intensities (R_{wp}=7.33%, R_I=2.54%, S=1.32) is obtained.

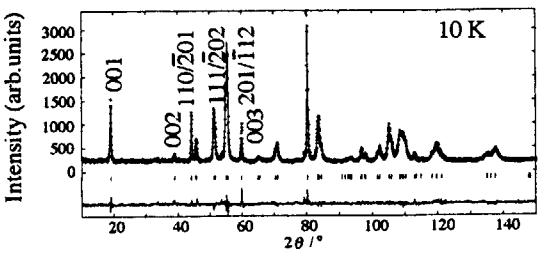


Fig. 1 Observed, calculated and difference neutron diffraction profiles of β － Na_xCoO_2.

Sodium content was determined from the diffraction data to be 0.67(1) at 10 K, which is higher than the earlier report [2]. Oxygen occupancy was also refined, but noticeable oxygen deficiency was not detected. In the refinement for the 300 K data, the sodium and oxygen occupancies were assumed to be identical with those at 10 K. A close similarlity of the structure parameters at 10 K and 300 K is noticed. Figure 2 shows the determined crystal structure at 300 K (a=4.9023(4) Å , b=2.8280(2) Å , c=5.7198(6) Å and β =105.964(6)°). Six oxygen atoms forming a prism coordinate to the sodium ion. The sodium ions are randomely distributed at 8j(x y z) sites with x=0.810(2), =0.097(4) and z=0.495(1). Na-Na distances are in the range from 1.06(2) Å to 1.93(2) Å at 300 K. Judging from the ionic radius of Na^+ for six coordination (1.02 Å [6]), the sodium ions cannot fully occupy the adjacent sites. Six Co-O distances in a CoO_6 octahedron at 300 K, 1.903(3) Å × 2 and 1.909(1) Å × 4, are nearly equal and practically remain unchanged at 10 K.

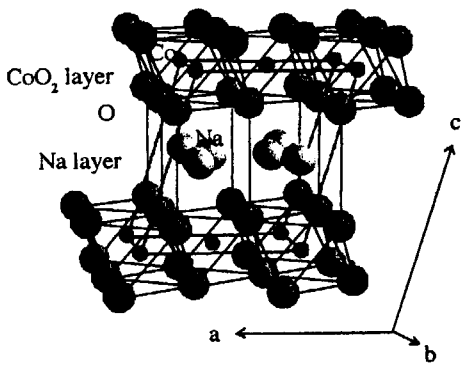


Fig.2 Crystal structure of β － Na_xCoO_2.

References

[1] Terasaki, I *et al.* Phys.Rev.B56(1997)R12865.

[2] Fouassier, C. *et al.* J.Solid State Chem. 6(1973)532.

[3] Wycoff,W.G.. in "Crystal Structures Vol.2", p296. J.Wiley & Sons, New York, 1964.

[4] Parant, J-P. *et al.* J.Solid State Chem. 3(1973)1.

[5] Izumi, F. in " The Rietveld Method"(R.A.Young, Ed.) Chap.13, Oxford Univ. Press, Oxford, 1993.

[6] Shannon, R.D and Prewitt, C.T., Acta Cryst.25(1969)925.

原子炉：JRR-3M 装置：HRPD (1G) 分野：中性子散乱（構造）

研究テーマ： 半磁性電気伝導体の磁性と化学構造

表題 ： $La_{1-x}Ca_xMnO_3$ ($0.08 \leqq x \leqq 0.15$) におけるヤーンテラー歪み

1-1-4 Jahn-Teller distortion in $La_{1-x}Ca_xMnO_3$ with $0.08 \leqq x \leqq 0.15$

Shahnaz Begum[1], Y. Ono[1], Y. Ishii[2], Y.Morii[2] and T. Kajitani[1]

[1] Department of Applied Physics, Graduate School of Engineering, Tohoku University, Sendai 980-8579, Japan

[2]Advanced Science Research Centre, JAERI, Tokaimura, Nakagun, Ibaraki 319-1195, Japan

Attention has been focused to the perovskite-based manganese oxides, $La_{1-x}A_xMnO_3$, (where A = Ca or Sr) because of their colossal magnetoresistance [1], charge ordering (CO) and orbital ordering (OO) of e_g orbitals [2]. We have studied *Jahn-Teller (J-T)* distortion of MnO_6 octahedron of $La_{1-x}Ca_xMnO_3$ with $0.08 \leqq x \leqq 0.15$ by means of neutron powder diffraction.

Powder samples of $La_{1-x}Ca_xMnO_3$ with $0.08 \leqq x \leqq 0.15$ were prepared by a conventional solid state reaction . Neutron powder diffraction experiments were carried out at temperatures from 8 K to the ambient using HRPD (λ =1.8235 Å) . Crystal structures were refined using the Rietveld analysis program, RIETAN'97 (F. Izumi) assuming space group, Pnma. All samples showed reasonable agreement between observed and calculated intensities. Figure 1 shows observed, calculated and difference profiles of powder neutron diffraction intensities of $La_{0.85}Ca_{0.15}MnO_3$ at 8 K. Refined lattice constants for sample with x = 0.15, are, a = 5.4926(1) Å, b = 7.7589(4) Å, c = 5.5056(1) Å with R_{wp} = 11.73 %, R_I = 3.91 %, S = 1.323, at 10 K and a = 5.5005(2) Å, b = 7.7791(3) Å, c = 5.5209(2) Å with R_{wp} = 10.11 %, R_I = 4.93 %, S=1.4146, at 293 K, repectively. A

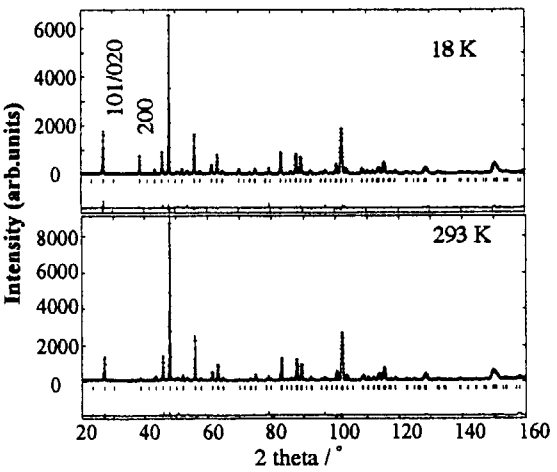


Figure 1 Observed, calculated and difference neutron diffraction profiles of $La_{0.85}Ca_{0.15}MnO_3$.

ferromagnetic contribution was observed below Curie temperature T_c=180 K as an additional increase of the Bragg intensities. Obvious contribution is seen at 200 peak at low temperature. The present sample is ferromagnetically ordered with a

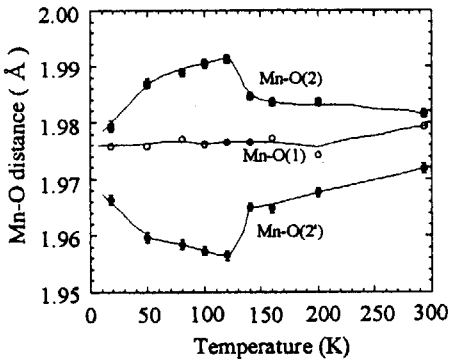


Fig.2 Temperature variations of Mn-O bond lengths in $La_{0.85}Ca_{0.15}MnO_3$.

refined total Mn moment of 3.2(1) μ_B at 10 K , which is less than 3.85 μ_B/Mn, the simple average moment of mixed Mn^{3+}/Mn^{4+} lattice at x=0.15. The decrease of magnetic moment of Mn ion can be understood in terms of canted Mn spins. Figure 2 shows temperature variation of Mn-O bond lengths in the sample with x=0.15. The additional *Jahn-Teller (J-T)* distortion of MnO_6 octahedron was observed at low temperatures below 140 K and become maximum at about 120 K. At 120 K, Mn-O(2') bonds become short by 0.01 Å, which corresponds 0.49 % of Mn-O(2') at 293 K, while Mn-O(2) bonds elongated . But Mn-O(1) distance remains almost unchanged at low temperatures. The *Jahn-Teller (J-T)* distortion of MnO_6 octahedron induces OO of d_{3x2-r2} and or/ d_{3z2-r2} type orbitals. Although it is not clear that which one of the two orbitals is more stabilized for this sample, it may suggest tha d_{3z2-r2} type orbital is little dominant as the larger lattice constant along c (along z) is larger than a and b (along x and y) [3].

References

[1] Millis, A.J. Nature 392(1998)147.

[2] Yamada, Y. *et al.* Phys.Rev.Lett.77(1996)904.

[3] R. Maezono, S. Ishihara, and N. Nagaosa, Phys. Rev. B, 57 (1998) R 13993.

原子炉：JRR-3M 装置：HRPD (1G) 分野：中性子散乱（構造）

研究テーマ：中性子散乱による強相関電子系の研究
表題：$Sr_2YCu_2FeO_{6+\delta}$の中性子回折による研究

1-1-5 Neutron Diffraction Study of $Sr_2YCu_2FeO_{6+\delta}$

T. Mochiku, Y. Hata[1], Y. Mihara[2], J. Suzuki[1], N. Metoki[1], K. Kadowaki[2] and K. Hirata

National Research Institute for Metals, Tsukuba, Ibaraki 305-0047, Japan
[1]Japan Atomic Energy Research Institute, Tokai, Ibaraki 319-1195, Japan
[2]Institute of Materials Science, University of Tskuba, Tsukuba 305-8573, Japan

The substitution of a wide variety of metals (Al, Fe, Co, Ga, Nb, Ru, Ta and so on) for Cu stabilizes $Sr_2YCu_3O_{6+\delta}$ phase, which was sintered only under high pressure [1,2]. However, almost substituted compounds with the composition of $Sr_2YCu_2MO_{6+\delta}$ do not exhibit superconductivity in spite of the treatment under high oxygen pressure, where M is the above metals. Recently, we have discovered superconductivity around 50 K in $Sr_2YCu_2FeO_{6+\delta}$ annealed under N_2 atmosphere and subsequently under O_2 atmosphere [3]. We report neutron diffraction results for the $Sr_2YCu_2FeO_{6+\delta}$ samples at subsequent process of the sample preparation. Neutron diffraction can distinguish between Cu and Fe because the scattering length of Cu differs from that of Fe, while X-ray diffraction can hardly do so. Then, we can analyze the mutual substitution of Cu and Fe.

Samples were prepared by the solid state reaction of stoichiometric amount of $SrCO_3$, Y_2O_3, CuO and Fe_2O_3 powder. The superconducting sample was produced by the process with N_2-annealing, subsequent O_2-annealing and oxidizing under high oxygen pressure. Neutron powder diffraction experiments were carried out using a high-resolution powder diffractometer, HRPD, installed in JRR-3M. Intensity data were collected at room temperature and then were analyzed using the Rietveld refinement program RIETAN on the basis of the tetragonal $Ba_2YCu_3O_{6+\delta}$-type structure model. We also analyzed the sample which is only oxidized without N_2-annealing and subsequent O_2-annealing to compare with other samples. This sample does not exhibit superconductivity.

The total oxygen content, $6+\delta$, determined by the refinements is storongly correlative to the sample preparation process. The $6+\delta$ value decreases by N_2-annealing and increases by O_2-annealing and oxidizing. It is expected that O_2-annealing and oxidizing supply the charge on the CuO_2 sheet. The analysis of the mutual substitution of Cu and Fe indicates that N_2-annealing and subsequent O_2-annealing accelerate the ordered distribution of Cu and Fe. However, the ordered distribution of Cu and Fe is not promoted only by oxidizing without N_2-annealing and subsequent O_2-annealing. Therefore, superconductivity in $Sr_2YCu_2FeO_{6+\delta}$ is caused both by the ordered distribution of Cu and Fe due to N_2-annealing and subsequent O_2-annealing, and by the increase of the oxygen content due to O_2-annealing and oxidizing.

References

[1] P.R. Slater and C. Greaves, Physica C 180 (1991) 299.
[2] T. Den and K. Kobayashi, Physica C 196 (1992) 141.
[3] Y. Hata, to be published.

原子炉：JRR-3M　　装置：HRPD(1G)　　分野：構造

研究テーマ：中性子散乱による強相関電子系の研究
表題：$Sr_2EuCu_2RuO_8$の中性子回折による研究

1-1-6 Neutron Diffraction Study of $Sr_2EuCu_2RuO_8$

T. Mochiku, K. Oikawa[1,*], N. Metoki[1], D.P. Hai[2], K. Kadowaki[2] and K. Hirata

National Institute for Materials Science, Tsukuba, Ibaraki 305-0047, Japan
[1]Japan Atomic Energy Research Institute, Tokai, Ibaraki 319-1195, Japan
[2]Institute of Materials Science, University of Tsukuba, Tsukuba 305-8573, Japan

Coexistence of ferromagnetism and superconductivity has been discovered in $Sr_2GdCu_2RuO_8$ which has a Curie transition around 135 K and a superconducting transition around 15-40 K [1]. A recent study [2] using zero-field muon spin rotation experiments shows that this compound is microscopically single phase with no evidence of spatial separation of ferromagnetic and superconducting phases. On the other hand, antiferromagnetic ordering in $Sr_2GdCu_2RuO_8$ has been reported using neutron diffraction [3]. We report neutron diffraction results for a $Sr_2EuCu_2RuO_8$ sample exhibiting a magnetic transition at 135 K and without superconductivity, which compound has the same structure as $Sr_2GdCu_2RuO_8$.

Sample was prepared by the solid state reaction of stoichiometric amount of $SrCO_3$, Eu_2O_3, CuO and RuO_2 powder. Isotope ^{153}Eu with powder form of Eu_2O_3 was used in stead of natural Eu_2O_3, because the natural Eu has strong absorption for neutron. Neutron powder diffraction experiments were carried out using a high-resolution powder diffractometer, HRPD, installed JRR-3M. Intensity data were collected at room temperature and 10 K, and then were analyzed using the Rietveld refinement program RIETAN on the basis of the tetragonal $Ba_2YCu_3O_{6+\delta}$-type structure model.

The refinements revealed that the position of the O(1) atom from a site (0, 1/2, 0) to a twofold split site (x, 1/2, 0) at both temperatures. This indicates that the O(1) atom displays large thermal motion in the a-direction which is ascribed to the local displacement from ideal position or to the tilt of the RuO_6 octahedra along the c-axis. We could not find the Bragg reflection due to superstructure, which is caused by the tilt of the RuO_6 octahedra. Therefore, at least in our sample there is little possibility of the latter. Although the occupation factor of the O(1) site was refined, we obtained the occupancy deviating substantially from unity. Therefore, we fixed it at 1. The Cu-O(2) distance is much more variable than other distances between room and low temperatures. This indicates that there is possibility of redistribution of the charge between Cu and Ru. We could not find the extra diffraction or the typical change of the intensity due to the magnetic ordering in low temperature study.

References

[1] J.L. Tallon, *et al.*, IEEE Trans. Appl. Supercond. 9 (1999) 1696.
[2] C. Bernhard, *et al.*, Phys. Rev. B 59 (1999) 14099.
[3] J.W. Lynn, *et al.*, Phys. Rev. 61 (2000) 14964.

* Present address: High Energy Accelerator Research Organization, Tsukuba, Ibaraki, 305-0801, Japan

原子炉：JRR-3M　　装置：HRPD(1G)　　分野：構造

研究テーマ：超イオン導電体における構造不規則性と動的性質
表題　　：CuBrの中性子散漫散乱

1-1-7 Diffuse Neutron Scattering from CuBr

M. Arai, T. Aung, T. Sakuma, H. Takahashi[1], Y. Ishii[2]

Faculty of Science, Ibaraki University, Mito 310-8512, Japan
[1]Faculty of Engineering, Ibaraki University, Hitachi 316-8511, Japan
[2]Japan Atomic Energy Research Institute, Tokai 319-1195, Japan

Correlation effects between the thermal displacements of atoms play an important role to explain the oscillatory diffuse scattering in solid electrolytes, CuI and AgBr. The correlation effect is clearly observed in solid electrolytes which have large thermal vibrations of atoms. In order to obtain the dynamical correlation among atoms in CuBr, diffuse neutron background intensity of CuBr has been measured from 300 K to 600 K using a neutron diffractometer HRPD installed at JRR-3 in JAERI. A powder sample of CuBr in a vanadium container with 10 mm in diameter was used. The incident neutron wave length of 1.82 Å was used. Neutron diffraction data were collected for 1 d over the 2θ range of 10° to 150°. Fig. 1 shows the result of the measurement of CuBr at 300 K. Several sharp Bragg lines and a

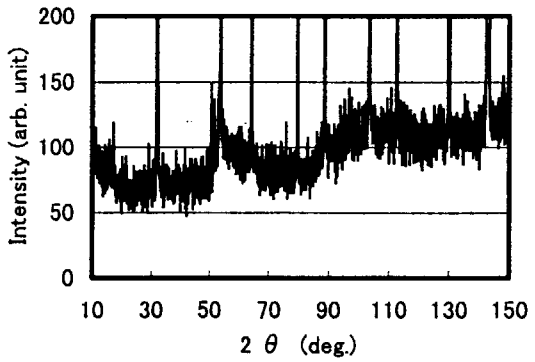


Fig.1 Observed neutron powder diffraction intensity for CuBr at 300 K.

large diffuse scattering were observed. The first and second peak of the oscillatory diffuse scattering appear at 2θ~55° and 110°, respectively in Fig. 1. The temperature dependence of the oscillatory diffuse scattering from CuBr crystals was also confirmed by the measurement.

Numerical calculations of the diffuse background have been made based on zinc blende type structure of CuBr including the correlation between the thermal displacements of atoms. The peak positions of the first and second peak in diffuse scattering of CuBr in fig. 1 are related to the reciprocal of the distance between nearest neighbor atoms; the distance in CuBr is 2.47 Å at 300 K. The main contribution to the oscillatory diffuse scattering of CuI and AgBr was from the correlation among the displacements of cation and anion atoms. The value of the thermal correlation between Cu and Br is about 0.7. It is suggested that the main contribution of CuBr would be from the correlation among the displacements of Cu and Br atoms.

Expected contributions from Cu-Cu, Cu-Br and Br-Br pairs to the diffuse scattering were calculated. The contribution from the correlation among Cu-Cu and Br-Br atoms was very weak to produce the observed oscillating scheme. The main contribution to the observed oscillatory diffuse scattering is from the correlation between the thermal displacements of Cu and Br atoms. The background function including the correlation effect between the thermal displacements of atoms is very effective to treat the diffuse scattering from crystals with the measurement by X-rays and neutrons.

原子炉：JRR-3M　　装置：HRPD (1G)　　分野：中性子散乱 (構造)

研究テーマ：超イオン導電体における構造不規則性と動的性質
表題　　：Li_3N の中性子散漫散乱

1-1-8 Diffuse Neutron Scattering from Li_3N

M. Arai, T. Aung, T. Sakuma, H. Takahashi[1], Y. Ishii[2]

Faculty of Science, Ibaraki University, Mito 310-8512, Japan
[1]Faculty of Engineering, Ibaraki University, Hitachi 316-8511, Japan
[2]Japan Atomic Energy Research Institute, Tokai 319-1195, Japan

There is an amount of interest in the use of solid ionic conductors for a number of practical applications, such as high specific energy storage systems. Lithium is a potentially desirable anode material for use in high specific energy cells. The crystal structure of Li_3N belongs to the hexagonal system with the space group P6/mmm (No. 191). There are two types of positions for Li atoms. One type of positions includes the coordinates for 2c site which form hexagonal Li_2N layers. The other type of positions includes the coordinates for 1b site which form N-Li-N brides.

In order to inspect the existence of the oscillatory diffuse scattering in Li_3N, diffuse neutron background intensity of Li_3N has been measured at 8 K, 150 K, 290 K and 473 K using a neutron diffractometer TAS-1 installed at JRR-3 in JAERI. We used a vanadium container with 10 mm in diameter. The incident neutron energy of 40.80 meV (λ=1.42 Å) was used. Neutron diffraction data were collected for 55 sec/step at 0.1 intervals over the 2θ range from 10° to 108° by step-scan mode. Fig. 1 shows the result of the double-axis measurement of Li_3N at 473 K. Several sharp Bragg lines and a large diffuse scattering were observed at 473 K.

The oscillatory characteristic in the diffuse scattering of Li_3N is not clear. In the case of other super ionic conductor, the temperature dependence of the oscillatory diffuse scattering, which was predicted with the correlation effect between the thermal displacements of atoms, had been confirmed by the diffraction measurements.

Numerical calculations of the diffuse background have been made based on hexagonal system of Li_3N including the correlation between the thermal displacements of atoms. The diffuse scattering is related to the parameters of distance between atoms. As the distance between atoms gets closer, the correlation effect becomes stronger. The distance between first nearest neighbor atoms (Li(1b)-N) and second nearest neighbor atoms (Li(2c)-N and Li(2c)-Li(2c)) are 1.94 Å and 2.11 Å, respectively, at 290 K. As the difference between both distances is small, the contributions to the diffuse scattering from the correlation effect between first nearest neighbor atoms and second nearest neighbor atoms are considered as identical.

The main contribution to the oscillatory diffuse scattering of super ionic conductors was from the correlation among the displacements of cation and anion atoms. The correlation for between Li and Li atoms might contribute to the diffuse scattering intensity of Li_3N in addition to the correlation between first nearest neighbor Li and N atoms.

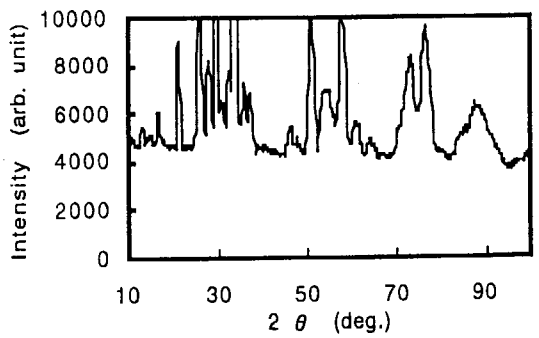


Fig.1 Observed neutron powder diffraction intensity for Li_3N at 473 K.

原子炉：JRR-3M　　装置：TAS-1 (2G)　　分野：中性子散乱 (構造)

研究テーマ：強弾性体 $LaNbO_4$ の格子不安定性と相転移前駆現象
表題：$LaNbO_4$ の強弾性相転移に関するソフトフォノン

1-1-9

Soft Phonon on the Ferroelastic Phase Transition in $LaNbO_4$

Y. Kuroiwa, S. Aoyagi, A. Sawada, N. Takesue,[1] S. Tsunekawa[2] and Y. Noda[3]

Department of Physics, Okayama University, Tsushima, Okayama 700-8530
[1]Neutron Scattering Laboratory, ISSP, University of Tokyo, Tokai, Ibaraki, 319-1106
[2]IMR, Tohoku University, Katahira, Sendai 980-8577
[3]IMRAM, Tohoku University, Katahira, Sendai 980-8577

Introduction

The lanthanum niobate, $LaNbO_4$, undergoes a structural phase transition from a tetragonal phase ($I4_1/a$) to a monoclinic phase ($I2/a$) at T_c = 768K, which has been considered to be a proper ferroelastic phase transition, i.e. the order parameter is the only strain itself. Recently, it has been pointed out that the phase transition is weakly of first-order and precursor phenomena, *e.g.* broadening of the Bragg-reflection profile, are observed prior to the phase transition. The soft phonon at the zone center is considered to provide a key to understand the origin of the phase transition. In the present study, neutron inelastic scattering experiment has been carried out for the first time to investigate the behavior of the soft phonon associated with the ferroelastic phase transition.

Experimental

The single crystal of $LaNbO_4$ with the dimensions of 20mm×10mm×7mm was mounted in a furnace on the triple-axis spectrometer (4G) at JRR-3M of JAERI. The constant q-scan modes with the fixed incident neutron energy E_i = 13.7meV and 30.3meV were employed for the measurements of the TA and TO phonon, respectively, at 820K (T_c + 52K) and 770K (T_c + 2K).

Elastic diffuse scattering and Soft phonon

Anisotropic elastic diffuse scattering was observed at 770K around the Bragg point, showing the Huang-like scattering. It extends to the directions deviated from the b^*-axis by ϕ = 23° on the tetragonal basal plane. In addition, we found that the TA phonon frequencies for the ϕ = 23° direction was remarkably low. The left panel of Fig.1 shows this pronounced soft phonon, and the right panel shows the normal behavior of the TA phonon along the ϕ = 45° direction. The TO phonon shows no softening at any directions. The behavior of the soft phonon obtained in the present study will be connected with the precursor phenomena observed before.

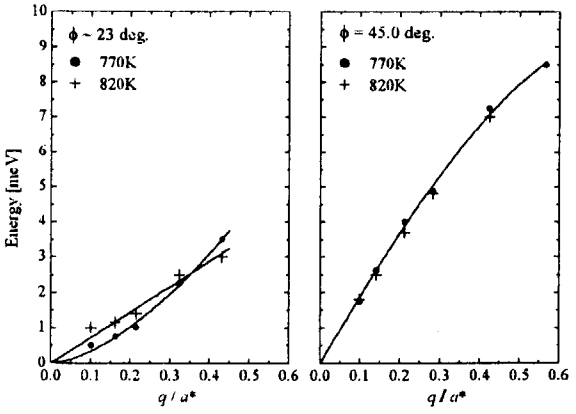


Fig. 1 TA phonon dispersion curves on the tetragonal basal plane above T_c = 768K.

JRR-3M, 4G, 1. Structures & Excitations

研究テーマ：Rb_2SeO_4 のΣ_2 フォノン分枝の振舞い
表題：Rb_2SeO_4 の低温整合相におけるΣ_2-Σ_3 フォノン分枝の振舞い

1-1-10 Behavior of Σ_2-Σ_3 Phonon Branches in Low-Temperature Commensurate Phase of Rb_2SeO_4

H. Shigematsu, Y. Nakadaira and T. Matsui

Department of Quantum Engineering, Nagoya University, Nagoya 464-8603, Japan

Rubidium Selenate, Rb_2SeO_4, belongs to a family of A_2BX_4-type crystals with the β-K_2SO_4 type structure. Many of the A_2BX_4-type crystals transform at lower temperatures to an incommensurate phase with modulation wavevector a-axis. However, no phase transition could occur for Rb_2SeO_4 below room temperature. In the case of Rb_2SeO_4, the calculated dispersion curves included an unstable phonon Σ_2 phonon branch with qualitative and quantitative features similar to those obtained for the prototype incommensurate material K_2SeO_4.

In order to clarify the behavior of the low-energy Σ_2-Σ_3 phonon branches below room temperature, we performed inelastic neutron scattering experiments by using the triple-axis spectrometers (4G and C1-1) at JRR-3M of JASRI. Energy scans were done with the fixed incident neutron momentum k_i = 2.67 Å at 4G and k_i = 1.55 Å at C1-1. The data collections were carried out in the (a^*, c^*) scattering planes.

Figure 1 shows the phonon dispersion curves along the (ξ 0 0) line at 200 K. Two modes, which anticrossed each other at around ξ ~ 0.7, were observed. Figure 2 shows the phonon dispersion curves of the low-energy mode at three temperature below room temperature. Although the behavior of the phonon dispersion curves did not vary down to 100 K, low-energy Σ_2 phonon branch exhibited a softening and decreased more than 15 % as the temperature decreased from 100 K to 30 K.

No phase transition could found between room temperature and 2 K by heat capacity measurement. However, the results of the measurement of the Σ_2-Σ_3 phonon branches showed a clear softening. The soften mechanism in this compound and in K_2SeO_4 is related to an increase of the effective interaction between an acoustic and an optical branch; the phonon branch can be interpreted as that of a one-dimensional 'monoatomic' chain with unit cell a/2.

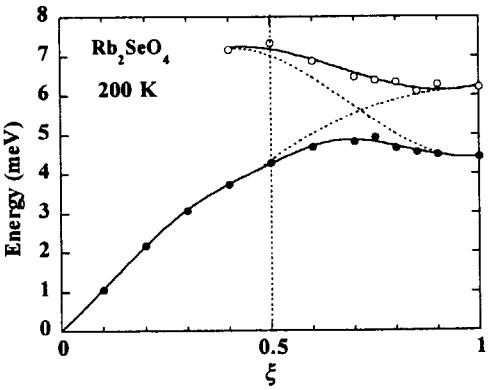


Fig. 1 Phonon dispersion curves in an extended-zone scheme on the (ξ 0 0) line.

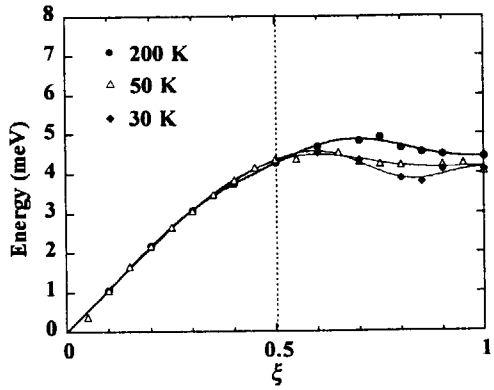


Fig. 2 Phonon dispersion curves of low-energy mode at 30, 50 and 200 K.

JRR-3M, GPTAS(4G) and HER(C1-1), 1. Structures & Excitations

研究テーマ：SrCu2(BO3)2 の磁場下における中性子散乱

表題：２次元量子スピン系 SrCu2(BO3)2 の磁気励起

1-1-11

Magnetic Excitations in the Two-Dimensional Spin Gap System $SrCu_2(BO_3)_2$

H. Kageyama, N. Aso[1], M. Nishi[1], K. Nukui[1], T. Yosihama[1], K. Kakurai[1], and Y. Ueda

Material Design and Characterization Laboratory, Institute for Solid State Physics, University of Tokyo, Kashiwanoha, Kashiwa, Chiba 277-8581, Japan

[1] *Neutron Scattering Laboratory, Institute for Solid State Physics, University of Tokyo, 106-1 Shirakata, Tokai, Ibaraki 319-1106, Japan*

$SrCu_2(BO_3)_2$, which has an orthogonal dimer network of one-half spins, is a 2D spin gap system with the known ground state, i.e., correspondence of the Shastry-Sutherland model [1]. Concerning magnetic excitations, it is theoretically shown that excited triplets are considerably localized. Experimental observation of 1/3, 1/4 and 1/8 plateaux in the magnetization curves are attributed to the localized character. In this study, we performed inelastic neutron scattering to investigate the dynamical properties of the dimer system [2, 3].

Inelastic neutron scattering experiments were carried out on ISSP-PONTA spectrometer installed at 5G beam port of the Japan Research Reactor 3M (JRR-3M) in Japan Atomic Energy Research Institute, Tokai Establishment. The spectrometer was operated in the unpolarized neutron mode with pyrolytic graphite (PG) monochromator and analyzer. The inelastic scans were performed with fixed final energy *E*f=14.7 meV (*k*f=2.67 -1) and horizontal collimations of open(40')-40' -sample-80' -80' . A PG filter was placed after the sample to suppress the higher order contaminations. In order to minimize the neutron absorption by the natural abundance of ^{10}B, ^{11}B-enriched (99.6%) bulk single crystals of $SrCu_2(^{11}BO_3)_2$ were prepared by the traveling solvent floating zone method using $Li^{11}BO_2$ flux. The neutron scattering sample consisted of two single crystals with a total volume of ~1.5 cm^3 well aligned within 20' and it was oriented so as the scattering plane contains a*- and b*- axes or a*- and c*axes.

Shown in Fig. 1 are typical energy scans obtained at 1.7 K and 24 K for a scattering vector of Q=(2, 0). An abrupt growth in intensity below 2 meV is due to the elastic incoherent scattering from the sample. The 1.7 K spectrum consists of three peaks centered at 3.0 meV, 5.0 meV and 9.7 meV (transitions I, II and III, respectively), while that for 24 K no longer has any appreciable peak, indicating that all excitations are of magnetic origin. As already confirmed by other measurements, transition I at 3.0 meV is the excitation of a single triplet from the singlet ground state. Transition II arises from two-triplet excitations and transition III from three- or multitriplet excitations.

The dispersion relation of band I and II for the (H K 0) and (H 0 L) is shown in Fig. 2 (a) and (b), respectively. Interestingly, the energies of the excitation I in both planes are almost dispersionless and change within 0.2 meV at most, indicating the single triplet hardly moves both in the 2D plane and along the c-axis. Miyahara and Ueda theoretically discussed that the dispersionlesss behavior in this compound is not due to the spacial isolation of the dimers but to the orthogonality of the neighboring dimers. They also argued the effects of the interlayer coupling J', showing that the single triplet excitation cannot propagate along the c^* direction, indicating the completely flat dispersion along this direction. This is in contrast to the case of in-plane single triplet excitation where excited triplets can move from the 6th order perturbation calculations. However, comparison the dispersion curves in Figs.

JRR-3M. 5G. 1.structure and excitations

2 (a) and (b) shows that both dispersion energies look almost same. It would be is necessary to perform experiments with a better energy resolution in order to discuss the difference in both dispersions.

Let us move to the second triplet excitation II around 5 meV. Figure 2 shows that the dispersion curve in the *ab* plane is dispersive, while that along the *c* axis is almost flat. This shows that the second triplet excitation can move more easily in the *ab* plane than the single triplet does, but hardly does along the *c*-axis.

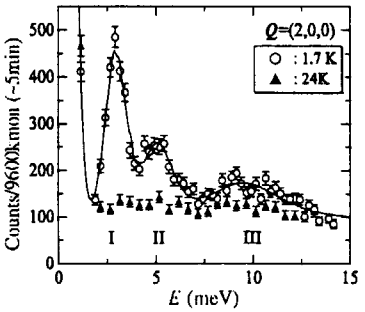


Fig.1 Energy scans at Q=(2, 0. 0) obtained at T=1.7 K (circles) and 24 K (triangles). The excitations are labeled at the bottoms of the figure. The solid curve is the fit to the profile at 1.7 K. The abrupt upturn around the energy zero is due to the incoherent elastic scattering.

References

[1] H. Kageyama *et al.*, Phys. Rev. Lett. **82**, 3168 (1999).

[2] H. Kageyama *et al.*, Phys. Rev. Lett. **84**, 5786 (2000).

[3] N. Aso *et al.*, J. Phys. Soc. Jpn. **70** Suppl. A, 177 (2001).

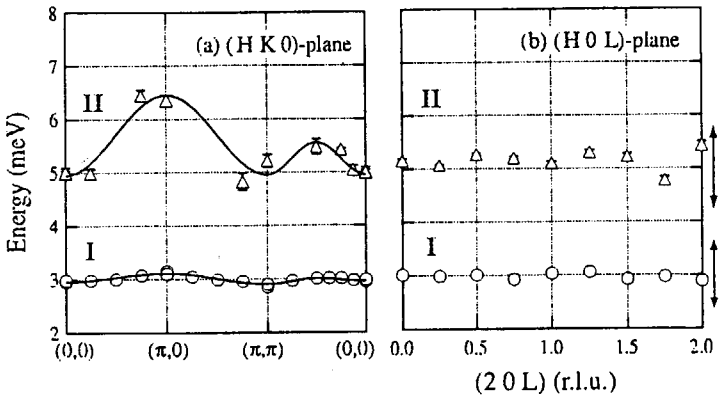


Fig. 2 Q-dependence of the excitation in the (H K 0) plane (left) and (H 0 L) plane (right) obtained at 1.7 K. The solid curves are guided to the eye. The arrows represent the energy resolutions of the instrument (FWHM). The unit cell in the (H K 0) plane (left) by the notation of Weihong *et al.* is used. Q=(2, 0, L) in the right panel correspond to the (0, 0) point in the left one.

研究テーマ：少数キャリアー系 Ce モノプニクタイドの格子振動
表題：CeSb の磁気ポーラロン状態における p-f 混成軌道による異常な格子ダイナミクス

1-1-12 Anomalous Lattice Dynamics due to p-f Mixing Orbital in the Magnetic Polaron States of CeSb

K. Iwasa, M. Kohgi, M. Braden[2,3], J.-M. Mignot[3] H. Kitazawa[4] and T. Suzuki[5]

Department of Physics, Tokyo Metropolitan University, Hachioji, Tokyo 192-0397, Japan
[1] ASRC, Japan Atomic Energy Research Institute, Tokai, Ibaraki 319-1195, Japan
[2] Forschungszentrum Karlsruhe, Institut für Nuklear Festkörperphysik, Postfach 3640, D-76021 Karlsruhe, Germany
[3] Laboratoire Léon Brillouin, CEA/Saclay, 91191 Gif-sur-Yvette Cedex, France
[4] National Institute for Materials Science, Tsukuba, Ibaraki 300-0047, Japan
[5] Tsukuba Institute of Science and Technology, Tsukuba, Ibaraki 300-0819, Japan

A remarkable physical property of cerium monopnictides CeX is the formation of various long-period magnetic structures.[1-4] Ferromagnetic Ce-ion (1 0 0) planes of the NaCl-type crystal structure with a larger magnetic moment of M_L ~ $2\mu_B$ appear in the ordered phases, although the crystal-field ground state in the paramagnetic phase is Γ_7 with a smaller magnetic moment of M_S ~ $0.7\mu_B$.[2, 5] Some of magnetic structures of CeX show a common feature that the Ce-ion planes with paramagnetic state and those with the ordered M_L stack periodically. In the magnetic structures of CeP and CeAs at the lowest temperature, the paramagnetic Ce-ion moments order with M_S. Therefore, the magnetic structures of so-called AFP phases of CeSb can be considered to consist of dominant M_L layers and paramagnetic layers of Γ_7 state.[3] Polarized-neutron experiments on the magnetic form factors of CeP gave direct evidence that the Ce ions with M_L is quite close to the Γ_8 crystal-field state.[6] Thus, the magnetic moment M_L in CeX is caused by the Γ_8–like Ce-ion state. This unusual Ce ion with M_L is considered to be due to the combined effect of strong p-f mixing and localization of low-density carriers (magnetic polaron effect).

The 4f-electron states producing the complex magnetically ordered structures also give crystal lattice anomalies. Low-temperature x-ray diffraction study of CeSb shows the distinct superlattice structures in the ordered AFP phases.[7] The observed satellite-peak patterns are well explained by a model in which two kinds of superlattices are taken into account. One of them is crystal-lattice modulation caused by smaller effective ionic size of the Γ_8-like Ce ions by the order of 10^{-3} than that of the Γ_7 Ce ions. The contraction of ionic size is due to the p-f mixing effect between neighboring Ce and X ions. Another one is the modulation of atomic form factors due to the different 4f-electron orbitals between the Γ_8-like and the Γ_7 Ce ions.

The strong coupling between the 4f-electron states and the inter-atomic distance due to the p-f mixing effect suggests that the lattice dynamics is also affected by the appearance of the unusual magnetic state. In order to study the effects of the p-f mixing on phonons, CeSb has been studied by inelastic neutron scattering performed at TOPAN (6G) installed in JRR-3M and at 1T in Orphée reactor of LLB.

In Fig. 1, inelastic spectra at fixed $\boldsymbol{Q}$ = (4.0, -0.7, -0.7) measured at 4 K in the ordered phase and at 21 K in the paramagnetic region are shown. The data at 4 K shows three peaks at 4, 7 and 9 meV, in contrast to the data at 21 K showing no peak at 7 meV. The peak at 4 meV corresponds to the magnetic excitation reported by Rossat-Mignod *et al.*[8] The peak at 9 meV was detected even at 300 K and is attributed to a transverse

acoustic phonon. The peak at 7 meV is a new excitation appearing in the magnetically ordered phases. From the observation that the intensities at both 7 and 9 meV measured at a smaller Q = (2.0, -0.7, -0.7) were 1/3 of those at Q = (4.0, -0.7, -0.7), the new excitation observed at 7 meV has a phonon character. By the measurement along the [4, ζ, ζ] direction, this new excitation is found to be less dispersive along the [011] direction. Thus, the excitation seems to be a localized one. In order to investigate the eigenvector of atomic displacement of this new excitation, we measured the inelastic response at Q = (4.0, -0.7, -0.7) for the magnetically single-domain sample. In this sample, the magnetic moments were parallel to the [100] direction and the p-f mixing orbital extends within the [010]-[001] plane. As seen in Fig. 2, there was no peak at 7 meV. Thus, based on the phonon cross section of neutron scattering, the atomic displacement is considered to have no component parallel to the ordered-moment direction, but within the *p-f* mixing orbital plane perpendicular to the moment direction.

The above experimental fact indicates that the new phonon at 7 meV is a mode with stretching of inter-atomic distance between the neighboring Ce and Sb ions forming the *p-f* mixing orbital. When the distance is elongated, the *p-f* mixing orbital becomes unstable and the 4*f*-electron state changes to the Γ_7 state. Thus, the observed new excitation can be interpreted as the dynamical transition of the 4*f*-electron state associated with the phonon mode.

References

[1] T. Suzuki: Jpn. J. Appl. Phys. Series **8** (1993) 267.

[2] M. Kohgi *et al.*: Phys. Rev. **B49** (1994) 7068, M. Kohgi *et al.*: J. Phys. Soc. Jpn. **65** (1996) Suppl. B 99, T. Osakabe *et al.*: Physica **B 230-232** (1997) 645.

[3] T. Chattopadhyay *et al.*: Phys. Rev. **B49** (1994) 15096, J. Rossat-Mignod *et al.*: Phys. Rev. **B16** (1977) 440.

[4] H. Bartholin *et al.*: J. de Phys. **C5**-40 (1979) 130.

[5] T. Osakabe *et al.*: JJAP Series **11** (1999) 123.

[6] K. Iwasa *et al.*: Physica B **259-261** (1999) 285, K. Iwasa *et al.*: J. Phys. Chem. Solids **60** (1999) 1185.

[7] K. Iwasa *et al.*: J. Phys. Soc. Jpn. **68** (1999) 2498, to be published.

[8] J. Rossat-Mignod *et al.*: J. Magn. Magn. Mater. **52** (1985) 111.

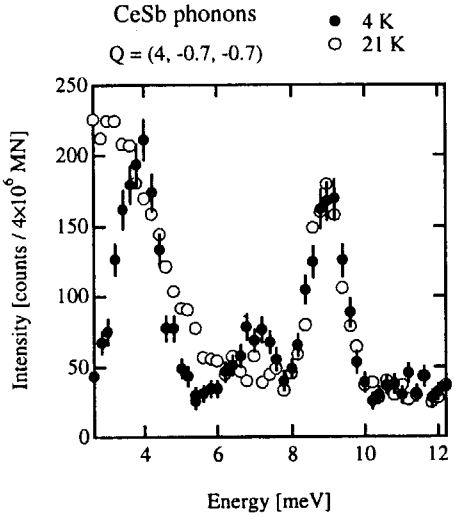


Fig. 1. Inelastic neutron data at Q = (4, -0.7, -0.7) measured at LLB.

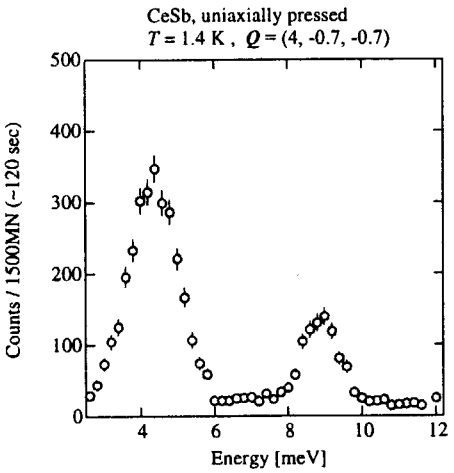


Fig. 2. Inelastic neutron data at Q = (4, -0.7, -0.7) of the single-domain sample measured at JAERI.

研究テーマ：Yb_4As_3の電荷秩序構造相転移とフォノン分散
表題：Yb_4As_3の電荷秩序の臨界温度領域における音響フォノンのソフト化

1-1-13 Acoustic Phonon Softening in the Critical Temperature Region of Charge Ordering of Yb_4As_3

K. Iwasa, M. Kohgi, A. Ochiai[1], H. Aoki[2] and T. Suzuki[3]

Department of Physics, Tokyo Metropolitan University, Hachioji, Tokyo 192-0397, Japan
[1] Center for Low Temperature Science, Tohoku University, Sendai 980-8578, Japan
[2] Max-Planck Institute for Chemical Physics of Solids, D-01187 Dresden, Germany
[3] Tsukuba Institute of Science and Technology, Tsukuba, Ibaraki 300-0819, Japan

The 4*f*-electron properties of the typical low-carrier-concentration system Yb_4As_3 have been attractive, because of its unusual electronic properties like in heavy-fermion compounds and a particular one-dimensional (1D) magnetic character. [1] These behaviors are observed in the charge ordered phase accompanied with a structural phase transition at T_C = 288 K. The crystal structure is an anti-Th_3P_4-type cubic one above T_C, and transforms to a trigonal one below T_C with shrinking slightly along the [111] direction. The 4*f*-electron state is thought to be valence fluctuating in the cubic phase. In the low-temperature phase, the charge-ordered state appears with Yb^{3+} ions aligning along the shrinking [111] direction and Yb^{2+} ions on the other lattice sites, as observed in the polarized-neutron diffraction experiments. [2] Magnetic excitations within this 1D Yb^{3+}-ion chain measured by inelastic neutron scattering are explained by the model of S = 1/2 Heisenberg antiferromagnet, and take important roles in the low-temperature properties in this system. [3] Dynamical properties of crystal lattice of Yb_4As_3 were studied by ultrasonic measurement. [4] The elastic constant, C_{44}, exhibits a strong decrease by 13% from 400 to 300 K in critical region near T_C.

In order to obtain more information about the charge-ordering mechanism in this system, we have measured lower-energy phonons at 300 and 400 K using TOPAN (6G) and HER (C1-1) spectrometers. The temperatures are controlled with the furnace of Tohoku University.

In Fig. 1, inelastic spectra at the reciprocal point $\boldsymbol{Q}$ = (0.15, 2, 2) at 400 and 300 K are shown, which were taken by the cold-neutron spectrometer HER (C1-1). The observed peaks are assigned to transverse acoustic (TA) phonons characterized by a wavevector $\boldsymbol{q}$ = (0.15, 0, 0) which corresponds to the elastic constant C_{44}. It is clearly seen that the phonon softens with decreasing temperature down to T_C. Figures 2 and 3 represent spectra at the reciprocal point $\boldsymbol{Q}$ = (0.125, 2, 2) and $\boldsymbol{Q}$ = (0.10, 2, 2), respectively, which exhibit softening near T_C. In addition to the softening, the peak width at $\boldsymbol{Q}$ = (0.10, 2, 2) at 300 K is larger than that at 400 K. Thus, the TA phonon shows anomalous damping as well as softening. We also measured the temperature variation of TA-phonon spectrum at $\boldsymbol{Q}$ = (0.3, 2, 2) using the thermal-neutron spectrometer TOPAN (6G). Its peak position and the width are independent of temperature between 400 and 300 K. Hence, the TA phonon anomaly occurs at the wavevectors smaller than $\boldsymbol{q}$ ~ (0.2, 0, 0).

Figure 4 represents the peak positions and widths evaluated by a least-squares fitting analysis of Gaussian functions to the data at $\boldsymbol{Q}$ = (0.10, 2, 2). The peak energy at 300 K is 90% compared to that at 400 K. This reduction rate is close to that of $(C_{44})^{1/2}$ obtained by the ultrasonic measurement, which determines the acoustic wave velocity. The peak width, on the other hand,

increases with decreasing temperature. This fact indicates the TA-phonon lifetime shortens near the critical temperature T_C.

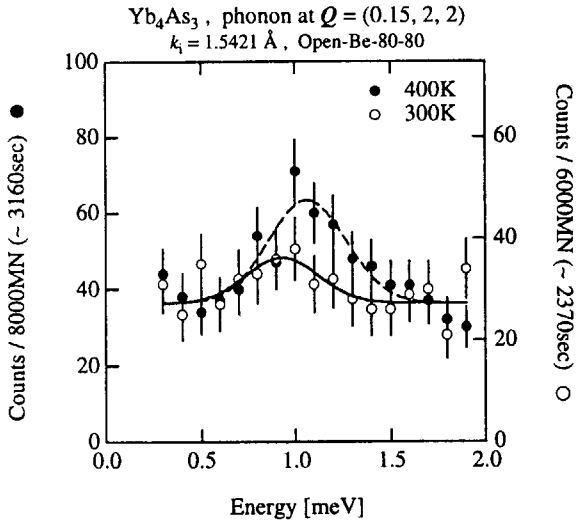


Figure 1. Phonon spectra at Q = (0.15, 2, 2) at 400 and 300 K. Lines indicate the fitted Gaussians.

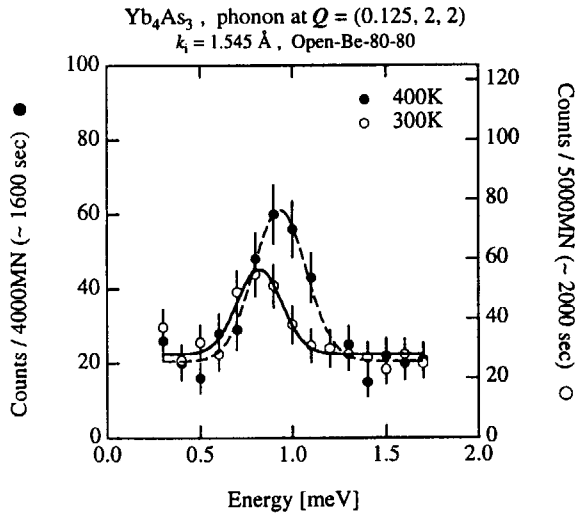


Figure 2. Phonon spectra at Q = (0.125, 2, 2) at 400 and 300 K. Lines indicate the fitted Gaussians.

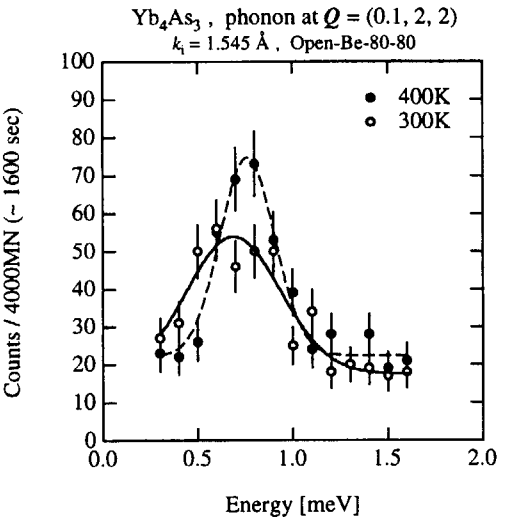


Figure 3. Phonon spectra at Q = (0.10, 2, 2) at 400 and 300 K. Lines indicate the fitted Gaussians.

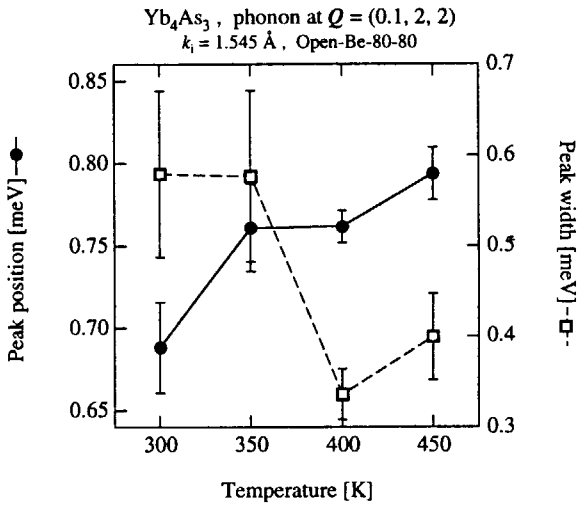


Figure 4. Peak position and width of the phonon spectra at Q = (0.10, 2, 2) as functions of temperature obtained by Gaussian fitting.

References

1) A. Ochiai *et al.*: J. Phys. Soc. Jpn. **59** (1990) 4129.
2) M. Kohgi *et al.*: Physica B **230-232** (1997) 638; K. Iwasa *et al.*: Physica B **281-282** (2000) 460.
3) M. Kohgi *et al.*: Phys. Rev. **B56** (1997) R11388; Phys. Rev. Lett. **86** (2001) 2439.
4) T. Goto *et al.*: Phys. Rev. **B59** (1999) 269.

研究テーマ：螢石関連固溶体の構造変化
表題： $YTaO_4$の構造変化と単斜-正方相転移の高温でのその場研究

1-1-14
In Situ Study of Structural Change and the Monoclinic-Tetragonal Phase Transition of $YTaO_4$ at High Temperatures

M. Yashima, T. Nogami, K. Ohoyama[1], and Y. Yamaguchi[1]

Department of Materials Science and Engineering, Interdisciplinary Graduate School of Science and Engineering, Tokyo Institute of Technology, Nagatsuta, Midori, Yokohama, 226-8502, Japan.
[1]Institute for Materials Research, Tohoku University, Katahira, Aoba, Sendai, 980-8577, Japan.

Stable phase of yttrium orthotantalate $YTaO_4$ at room temperature might be the monoclinic (M) form with a fergusonite structure that could be a fluorite-related structure. The M-$YTaO_4$ exhibits a phase transformation to tetragonal (T) symmetry at a high temperature. However, the structural change and the T-M phase transition of this material have not been known in detail yet. Here we report *in situ* neutron-powder-diffraction study of structural change and of the T-M phase transition of $YTaO_4$ at high temperatures up to 1500°C.

Neutron diffraction measurements were done using the neutron diffractometer HERMES (T1-3) and KSD (T1-2) of JRR-3M research reactor of Japan Atomic Energy Research Institute, using a high-temperature furnace (λ=1.8196Å for HERMES and λ=1.53Å for KSD). M single phase of the $YTaO_4$ was prepared by solid-state reactions. Each neutron-diffraction measurement was done keeping the sample temperature constant. The average heating and cooling rate including the measurements was 3.3°C/min. This rapid heating and cooling rate was very important for this work, because at the slower heating and cooling rate induced the transformation from metastable M to stable M' phase during the measurements. Neutron-diffraction data were analyzed using a Rietveld program RIETAN.

Figure 1 shows temperature dependence of β angle refined through the Rietveld analyses. The β angle decreased continuously with an increase of temperature and became 90 degree at 1400°C. Furthermore there were no hysteresis between heating and cooling. Therefore, the M-T phase transition was strongly suggested to be of second order. Figure 2 shows the temperature dependence of

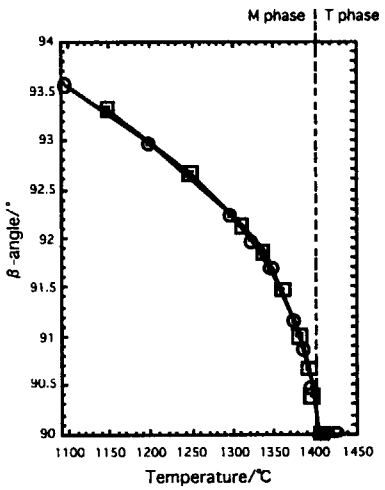


Fig.1: Temperature dependence of β angle. Open circle: data on heating. Open square: data on cooling.

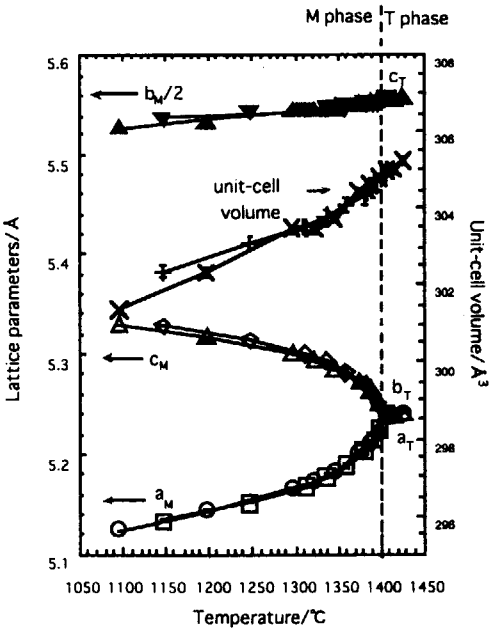


Fig.2: Temperature dependence of unit-cell parameters and unit-cell volume.

unit-cell parameters refined through the Rietveld analyses. The unit-cell volume increased with temperature. The *a* parameter increased while the *c* parameter decreased with temperature. These values approached with temperature and then coincided at the M-to-T phase transition temperature, 1400°C. Phenomenological equation based on Landau's theory for the second-order phase transformation was successfully applied to the temperature dependence of β-angle as shown in Fig. 3. The critical component thus obtained was 0.5 that is the value for typical second-order phase transition. The M-T transition point was estimated to be 1400°C

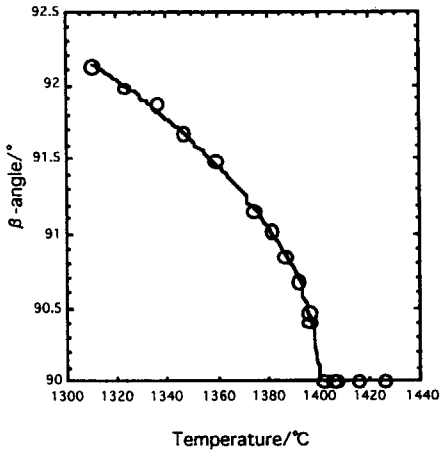


Fig.3: Temperature dependence of β angle. The curve was obtained by fitting the experimental data by an equation based on Landau's phenomenology.

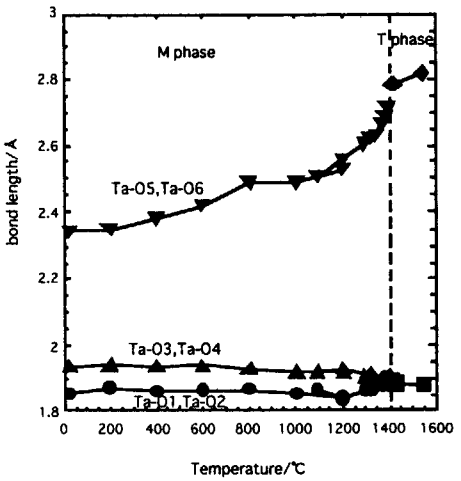


Fig.4: Temperature dependence of interatomic distance between Ta and oxygen O.

Figure 4 shows the temperature dependence of the interatomic distances between Ta and O atoms. The distance between Ta and an oxygen atom O1 is denoted as *r*(Ta-O1) here. The values of *r*(Ta-O1), *r*(Ta-O2), *r*(Ta-O3) and *r*(Ta-O4) changed a little with temperature, while the *r*(Ta-O5) and *r*(Ta-O6) increased considerably with temperature. These results show that the coordination number of Ta changes from 6 to 4 when the temperature was increased from room temperature (See also Fig. 5). The *r*(Ta-O1,O2) and *r*(Ta-O3,O4) seemed to approach each other and coincided at the M-to-T transition point. Figure 5 shows the temperature dependence of the bond angle O-Ta-O'. The bond angle O1-Ta-O2 increased while O3-Ta-O4 angle decreased with temperature, resulting in approaching with temperature and coincidence at the M-to-T transition point. Similarly, the bond angle O1-Ta-O3 and O2-Ta-O4 increased, while O1-Ta-O4 and O2-Ta-O3 angle decreased with temperature, resulting in approaching and coincidence at the M-to-T transition point. These results indicate that the M structure approaches T one with increasing temperature.

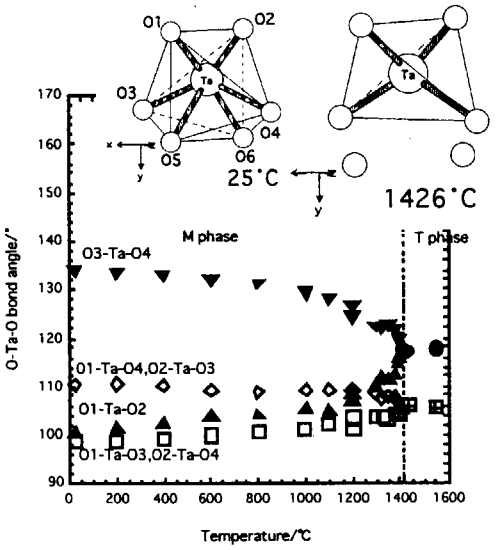


Fig.5: Temperature dependence of bond angle O-Ta-O'. The coordination polyherada around Ta in M- and T-$YTaO_4$ measured at 25°C and 1426°C were depicted above.

研究テーマ：有機・無機層状ペロブスカイト型化合物の構造
表題：中性子回折による有機・無機層状ペロブスカイト型化合物の構造解析

1-1-15

Neutron Diffraction Studies on Organic-Inorganic Perovskite Structure

Y. Tabuchi, D. Hiroishi and K. Asai

Department of Quantum Science and Systems Engineering, The University of Tokyo, Hongo, Bunkyo-ku, Tokyo 113-8656, JAPAN

Introduction

Over the past ten years, more and more attention has been focused on designing and tailoring materials for specific purposes due the prospective use of these materials in electronic and optoelectronic devices. In particular, much attention has been paid to finding suitable materials with high nonlinearity and short responses for optical signal processing and optical computing. However, it is still difficult to realize these systems using conventional nanostructure technology, there are some materials that form low-dimensional structures naturally. The organic-inorganic perovskite compounds examined in this study are such a material naturally forming quantum confinement structures, in which 2D inorganic wells consisting of $[PbBr_6]$ octahedra are sandwiched between organic ammonium, RNH_3^+ layers. The crystal structures of organic-inorganic compounds are generally analyzed using X-ray measurements. However, it is extremely difficult to identify the accurate positions of light atoms such as hydrogen in these compounds. Clear decision of the coordinateness is indispensable for the band calculation.

On the other hand, the neutron diffraction technique plays an important role in solid state physics and material science, providing accurate information regarding crystal and magnetic materials. In comparison to X-ray diffraction, angle-dispersive neutron diffraction has a number of advantages[1], [2]; (1) it allows the positions of light atoms such as oxygen and hydrogen to be determined accurately, in materials containing heavy atoms, (2) the geometry of the diffractometer is relatively simple, and (3) the transmission of neutrons is very high, allowing the use of simple environmental equipment such as refrigerators. In this study, we tried to analyze crystal structure of organic-inorganic perovskites using neutron diffraction measurements.

Experimental

Sample Preparation

$CD_3NH_3PbBr_3$: Gaseous CD_3NH_2 was introduced into an aqueous solution of stoichiometric amounts of hydrobromic acid by bubbling. After this reaction, the water was evaporated out by elevating the temperature, followed by washing with diethylether. The compounds were obtained by mixing purified CD_3NH_3Br with a stoichiometric amount of $PbBr_2$ in N,N-dimethylformamide. The powder samples were obtained as precipitates by pouring the reaction solutions into acetone.

Measurements

The position of hydrogen atoms in the perovskite compounds of $CD_3NH_3PbBr_3$ is determined by neutron diffraction. Thus far, the crystal structure of these compounds has been investigated using crystallographic X-ray measurements. However, it is difficult to accurately determine the structure of all the atoms in the crystal. In particular, it is impossible to determine the position of hydrogen atoms by X-ray diffraction because of their light weight. To determine the position of hydrogen, we used the high-efficiency, high-resolution measurements (HERMES) facility at the JRR-3M reactor in the Japan Atomic Energy Research Institute. Rietveld profile fitting analysis (RIETAN) was

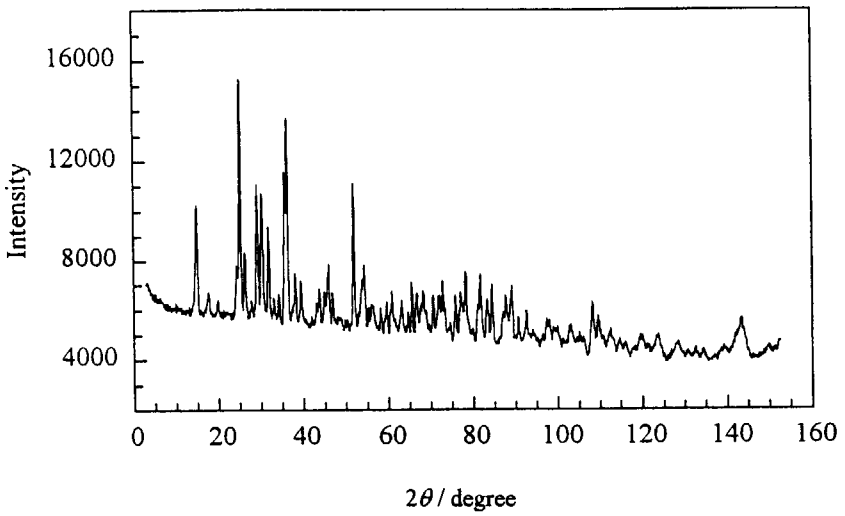


Figure 1 Neutron diffraction patterns of $CD_3NH_3PbBr_3$ powder sample.

used to obtain accurate information. Instrumental details were as follows; Wavelength, λ=1.82 Å at $2\theta_M$ = 90°, Detector: 3He detector x 150 (10 ϕ mm, 8 atm), 2θ range=1.5° - 160°. A powder sample is placed in a cylindrical vanadium cell, which is sealed in a standard aluminum cell with ^4He gas for ideal heat exchange. The diameter of the cylindrical cell is 9 mm for $CD_3NH_3PbBr_3$. Cryostats were used for data collection at low temperature.

Results and Discussion

At first, we used $CH_3NH_3PbBr_3$ as neutron diffraction measurements. However, we can see the background in the diffraction patterns of $CH_3NH_3PbBr_3$ is extremely high. This is due to the great influence of spin incoherent scattering from hydrogen atomic nucleus. In the case of organic compounds that contain large amount of hydrogen, this effect is much greater, and then the contrast of coherent diffraction patterns becomes unclear. As for this case, it is difficult to analyze crystal structure by powder diffraction method without deuteration or using single crystals. For $CH_3NH_3PbBr_3$, the single X-ray crystallographical measurements were already performed, however, the crystal structure of deuterated $CD_3NH_3PbBr_3$ has not yet discovered. Therefore, we estimate the crystal structure of $CD_3NH_3PbBr_3$ by comparing the data of $CH_3NH_3PbBr_3$ obtained from crystallographical measurements.

Figure 1 shows the powder neutron diffraction patterns of $CD_3NH_3PbBr_3$ at 77K obtained using HERMES. By deuteration, the background in the diffraction patterns decreased dramatically in order to distinguish signals to noise.

Analysis of the position of deuterium is under investigation using RIETAN-97β [3], Rietveld profile fitting soft.

REFERENCES

1. K. Ohyama, T. Kanouchi, K. Nemoto, M. Ohashi, T. Kajitani and Y. Yamaguchi, *Jpn. Appl. Phys.*, **37**, 3319 (1998).
2. S. Shamoto, K. Iizawa, T. Kato, M. Yamada, S. Yamanala, K. Ohyama, M. Ohashi, Y. Yamaguchi an T. Kajitani, *J. Phys. Chem. Solids.*, **60**, 1511 (1999).
3. F. Izumi, *"The Rietveld Method"* (Oxford University Press, Oxford, 1993), Chapter 13

研究テーマ：新機能性ペロブスカイト型酸化物の構造相転移に及ぼす同位体効果
表題：中性子粉末回折による $PbTiO_3$ の Ti 同位体効果

1-1-16
Study on Ti-isotope effects in $PbTiO_3$ by neutron powder diffraction

H. Shigematsu, Y. Nakadaira, T. Nagasaki, T. Matsui, A. Tobo[1] and K. Ohoyama[1]

Department of Quantum Engineering, Nagoya University, Nagoya 464-8603, Japan
[1]*Institute for Materials Research, Tohoku University, Sendai 980-8577, Japan*

Lead titanate, $PbTiO_3$, belongs to a family of ferroelectrics with a perovskite ABO_3 type structure and has a transition at about 760 K from cubic high-temperature phase (space group *Pm*3*m*) to ferroelectric tetragonal phase (*P*4*mm*), in which the type of the phase transition is the first-order one. In our previous paper [1], we reported the result on the change of T_C in $PbTiO_3$ produced by the exchange of ^{46}Ti-^{48}Ti isotopes by differential scanning calorimetry and discussed theoretically the isotope effect in relation to T_C displacive-type ferroelectricity: the transition temperature of ^{46}Ti-enriched $PbTiO_3$ was found to be 7.6 K higher than that of ^{48}Ti-enriched $PbTiO_3$.

Furthermore, for the investigation of Ti-isotope effect, we performed neutron powder diffraction experiments using the Kinken powder diffractometer for high efficiency and high resolution measurements, HERMES, of Institute for Materials Research (IMR), Tohoku University, installed at JRR-3M of JASRI. The masses of ^{46}Ti-enriched $PbTiO_3$ and ^{48}Ti-enriched samples were 120 mg and 170 mg, respectively. Therefore, it took us above 12 hours to measure.

Figure 1 shows neutron power diffraction patterns of ^{46}Ti-enriched $PbTiO_3$ and ^{48}Ti-enriched $PbTiO_3$ at room temperature. Although the positions of the reflections are very similar to each other, the relative intensity of reflections is different because of the difference of the neutron scattering amplitude of isotope-enriched Ti.

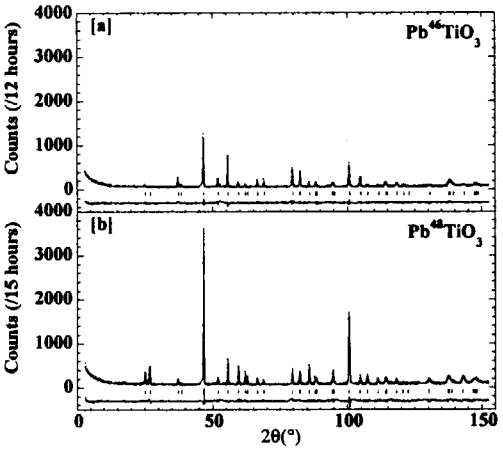


Fig. 1 Neutron powder diffraction patterns of [a] ^{46}Ti-enriched $PbTiO_3$ and [b] ^{48}Ti-enriched $PbTiO_3$.

From the structure analysis below 500 K, we could not confirm the difference in parameters between two samples. The difference is expected to be observed around the phase transition point because of the results by differential scanning calorimetry [1]. The neutron diffraction study at high temperature is now in progress.

References

[1] H. Shigematsu *et al.*: Thermochimica Acta 352-353 (2000) 43-46.

JRR-3M, HERMES(T1-3), 1. Structures & Excitations

研究テーマ：ペロブスカイト関連化合物の構造変化
表題：$CaTiO_3$における構造相転移の高温中性子による回折研究

1-1-17

High-temperature neutron-diffraction study of the structural phase transitions in $CaTiO_3$

Roushown Ali, Masatomo Yashima, Kenji Ohoyama[1] and Yasuo Yamaguchi[1]

Department of Materials Science and Engineering, Interdisciplinary Graduat School of Science and Engineering, Tokyo Institute of Technology, 4259, Nagatsuta-cho, Midori, Yokohama, 226-8502, Japan.

[1] *Institute for Materials Research, Tohoku University, Katahira, Aoba, Sendai, 980-8577, Japan.*

Calcium titanate is well known to be one of the important basic materials of ferroelectric ceramics. $CaTiO_3$ undergoes a sequence of phase transitions like many materials with ABO_3 compounds having perovskite-type structures. A number of researchers have studied the structural changes, but still there are many discrepancies in the number of phase transitions, space group determinations and transition temperatures. Here, we have performed neutron-diffraction experiments of $CaTiO_3$ perovskite at high temperature.

Neutron-diffraction data were collected using the powder diffractometer HERMES installed at JRR-3M in JAERI under the experimental conditions; 2θ range of 20° to 152°; step width 0.1°; wave length 1.8196Å; temperature range 23° to 1447°C. Structural refinements were done using Rietveld analysis RIETAN-2000.

Figure 1 shows temperature dependence of $\{120, 210\}_{Pbnm}$ and $\{121, 103, 211\}_{Pbnm}$ profiles. These two profiles disappeared at two different temperatures 1250° and 1374°C, respectively, clearly indicating two phase transitions.

Rietveld refinements were performed successfully with the space group *Pbnm* for the data obtained 23° to 1200°C. The *R* factors and agreement between observed and calculated patterns confirmed that the compound was

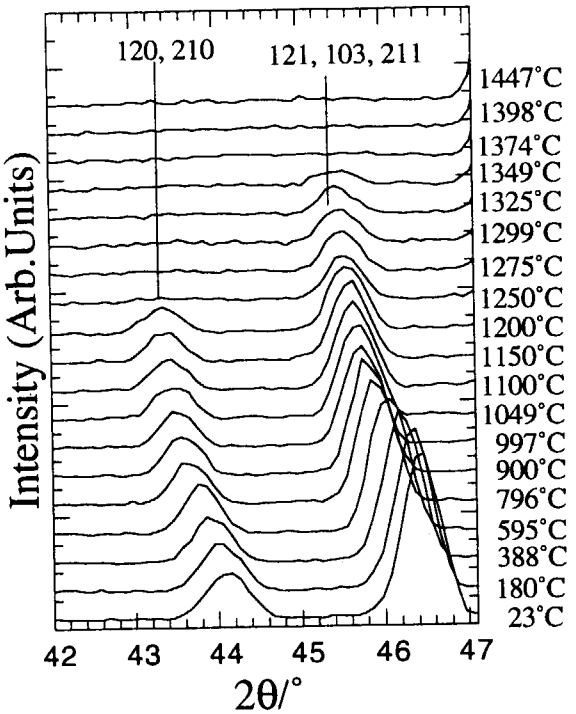


Fig.1 Temperature dependence of neutron-diffraction profile around 120, 210 and 121 103, 211 reflection peaks.

orthorhombic symmetry (*Pbnm*) up to 1200°C. The crystal structure of the intermediate phase was tried to refine using the space groups *P4/mbm*, *Cmcm*, *I4/mcm*, $R\bar{3}c$, and *Imam*, possible space groups between orthorhombic *Pbnm* and cubic $Pm\bar{3}m$. In the analyses Bragg reflections indicated clearly that *P4/mbm*, *Cmcm* and *Imam* space groups were

Reactor: (JRR-3M) Facility: HERMES(T1-3) Field: (1. Structure & Excitations)

Table I: Positional parameters, R factors and GoF values for the three structures obtained from the Rietveld analysis.

		Orthorhombic *Pbnm* (23°C)	Tetragonal *I4/mcm* (1325°C)	Cubic $Pm\bar{3}m$ (1447°C)
Ca	x	0.0350(4)	0.0	0.0
	y	0.25(9)	0.5	0.0
	z	-0.0063(7)	0.25	0.0
Ti	x	0.5	0.0	0.5
	y	0.0	0.0	0.5
	z	0.0	0.0	0.5
O1	x	0.4830(3)	0.0	0.5884(7)
	y	0.25	0.0	0.5
	z	0.0712(5)	0.25	0.0
O2	x	0.2893(3)	0.2683(4)	
	y	0.0374(2)	0.7683(4)	
	z	0.7112(3)	0.0428(6)	
R_p		5.41	5.74	5.70
R_{wp}		7.25	7.68	7.50
GoF		1.55	1.69	1.64

inappropriate for the intermediate phase, because there were some additional or missing peaks compared with the observed peaks. The remaining two space groups *I4/mcm* and $R\bar{3}c$ produced Bragg reflections that were consistent with those of the observed peaks. But Rietveld refinement resulted in a little better R factors and goodness of fit values for *I4/mcm* space group compared with $R\bar{3}c$. Furthermore, split atom model was considered for both *I4/mcm* and $R\bar{3}c$ space groups. Appreciably better agreement was obtained between the observed and calculated profiles in case of the statistical arrangement of O2 in *I4/mcm* space group. No better results were obtained considering split atom model for $R\bar{3}c$ space group. These facts strongly suggested that *I4/m c m* is the appropriate space group for the intermediate phase of $CaTiO_3$. The high-temperature (>1374°C) data were refined through the cubic structure with $Pm\bar{3}m$ space group. The analyses yielded the best fit when the split atom model was considered for the cubic phase. Structural parameters obtained from the analyses are given in Table 1 and temperature dependence of lattice parameters is shown in Fig.2. Cell parameters increased with increasing temperature. The a parameter increased considerably compared with b parameter, consequently with increasing temperature a and b parameters approached each other and coincided around 1250°C where orthorhombic symmetry transformed to tetragonal structure. Since the $\{121, 103, 211\}_{Pbnm}$ peaks disappeared at 1374°C, the data from 1374° to 1447°C were successfully analyzed with cubic ($Pm\bar{3}m$) structure. We conclude here the following sequence of phase transitions for $CaTiO_3$ compound:

$$Pbnm \xleftrightarrow{1200°-1250°C} I4/mcm \xleftrightarrow{1349°-1374°C} Pm\bar{3}m.$$

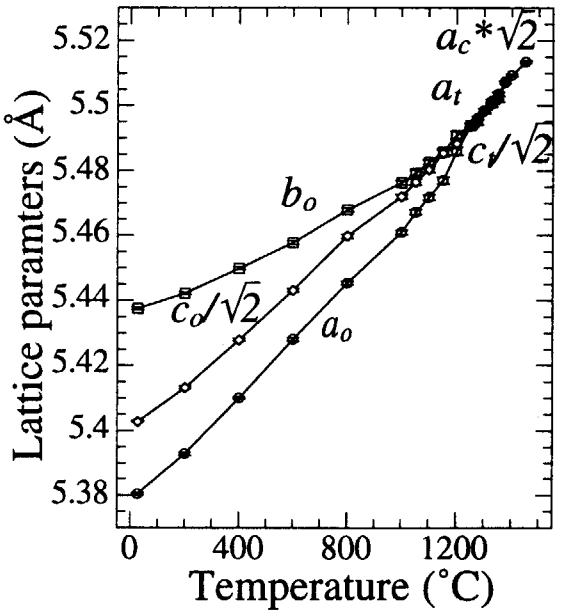


Fig.2 Temperature dependence of lattice parameters. Subscripts o, t and c denote orthorhombic, tetragonal and cubic phases, respectively.

研究テーマ：メチルアンモニウム基をもつペロブスカイト型誘電体の構造と相転移機構
表題：$CH_3NH_3PbCl_3$の立方相の構造

1-1-18 Cubic Phase Structure of $CH_3NH_3PbCl_3$

H. Mashiyama, Y. Kawamura and [1]K. Ohoyama

Faculty of Science, Yamaguchi University, Yamaguchi 753-8512

[1]Institute for Materials Research, Tohoku University, Sendai 980-8577

Methylammonium trihalogenoplumbate(II) $CH_3NH_3PbX_3$ (X=Cl, Br, I) has been interested widely,[1,2] because of disorder of methyl-ammonium ion (abbreviated as *MA*, hereafter) in the cubic perovskite structure. Three kind of structures and the ordering processes of *MA* have been proposed from the transition entropy analysis.[2] We have tried to determine the cubic structure by the use of X-ray single crystal diffractometry.[3] Although the <110>-orientation model seems to be most probable, the difference in the R-factors is minor among the <100>-, <110>- and <111>-orientation models. To clarify the orientation of *MA* in the cubic phase, we investigate the Cl salt by neutron powder-diffraction methods.

The crystal was milled and dried before canning in a vanadium cell, which was set on a goniometer. The measurements were carried out by using HERMES of IMR in JRR-3M. The wave length of neutron was 1.8196A. The scattered intensity of 1500 points with a 0.1° step was obtained during 14 hours. A profile fitting program system RIETAN-94[4] was used to determine the crystal structure.

Since the crystal contains protons, the back-ground level of the observed data is very high. We consider a sphere of radius b and mass m_1 collides with other sphere of mass m_2. The scattering probability at angle $\Theta=2\theta$ is calculated for impact parameter p by classical mechanics:

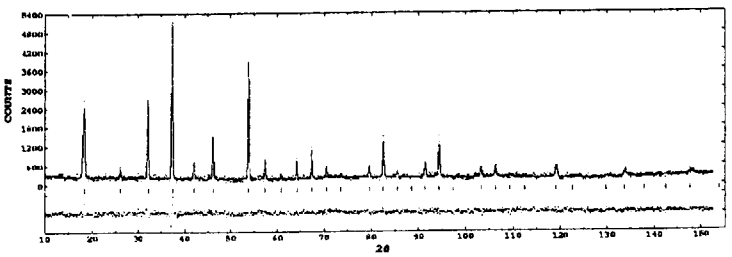


Fig. 2 Profile fitting for the <110> model of the cubic phase of MAPbCl_3.

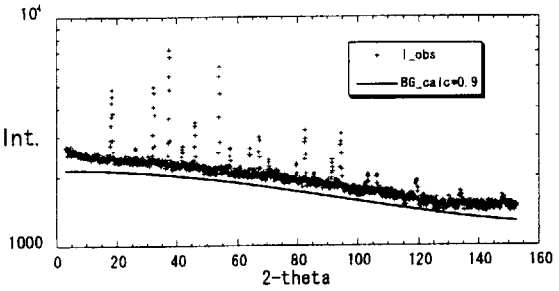


Fig.1 BG-fitting for MAPbCl_3 at RT.

$$\sigma(\Theta)=BX/\sin^3\Theta/\{2[X/(1-X)]^{1/2}+[(2X-1)/(1-X)]\cot\Theta\},$$

$$X=\{1-\mu\sin^2\Theta+\cos\Theta\,(1-\mu^2\sin^2\Theta)^{1/2}\}/2,$$

where $\mu=m_1/m_2$ and $B=(p/b)^2$.are determined by fitting data. Figure 1 shows the observed intensity and calculated background (10% reduced); the effective mass of target proton is 2.70 times heavier than the free proton.

After the back-ground was subtracted, the structure of phase I ($Pm3m$, Z=1, RT) was analyzed. The least-squared calculations converged at Rf= 12.9%, 12.3% and 12.6% for the <100>-, <110> and <111>-orientation models, respectively. Although the difference in Rf is not much, the <110> model is superior and is consistent to the tetragonal structure at low temperature. Though *MA* ions are disordered in the cubic phase, Cl atoms behave as displacive particles if the neutron data was analyzed. Further study is still on progress.

References 1) A. Poglitsch & D. Weber: J. Chem. Phys. **87** (1987) 6373. 2) N. Onoda-Yamamuro, T. Matsuo & H. Suga: J. Phys. Chem. Solids **51** (1990) 1383. 3) H. Mashiyama, Y. Kurihara & T. Azetsu: J. Korea Phys. Soc. **32** (1998) S156. 4) F. Iizumi: *The Rietveld Method*, ed. by R.A.Young, (Oxford Univ. Press, 1993) Chap.13.

JRR-3M, HERMES, 1. Structure

研究テーマ：リチウム二次電池正極材料 $LiMn_{2-x}M_xO_{4-\delta}$の結晶構造,安定性と電池特性
表題：リチウム二次電池正極活物質 $Li_{1+x}Mn_{2-x-y}M_yO_{4-\delta}$の結晶構造,熱力学的安定性と電極特性の関係

1-1-19

Relation between Thermodynamic Stability, Crystal Structure and Electrode Characteristics of $Li_{1+x}Mn_{2-x}M_yO_4$ as a Cathode Active Material for the Lithium Secondary Battery

Y. Idemoto, T.Ozasa, Y.Tsunoda and N. Koura

Faculty of Science and Technology, Science University of Tokyo
2641 Yamazaki, Noda-shi, Chiba 278-8510, JAPAN

The relation between crystal structure, thermodynamic stability and electrode characteristics of the spinel $Li_{1+x}Mn_{2-x-y}M_yO_{4-\delta}$ (M=Al, Co,; x=0, 0.1, y=0, 0.2, 0.5) was investigated.

The samples were prepared by mixing $^7Li_2CO_3$, MnO_2, $Al(NO_3)_3 \cdot 9H_2O$ and $Co(OH)_2$, so as to avoid the high neutron absorption of ^6Li. The Mn valence was controlled by the substitution. Mn valence was determined by the chemical analysis. Each obtained samples were confirmed the single-phase samples of spinel structure by powder X-ray diffraction. The Mn valence and lattice parameter *a* changed with changing of substitution contents.

The neutron powder diffraction was performed using HERMES. Data were corrected at room temperature and 200K. The crystal structure was refined with the Rietveld techniques (Rietan 2000).

First, analyses of the $^7LiMn_{1.8}Al_{0.2}O_4$, $^7Li_{1.1}Mn_{1.7}Al_{0.2}O_4$, and $^7LiMn_{2-x}Co_xO_4$ (x=0.2, 0.5) diffraction data at room temperature were carried out using an initial cubic structure (space group: Fd3m) with oxygen deficiency model. Second, the 200K data were analyzed starting from a cubic (Fd3m) phase or orthorhombic (Fddd) phase with oxygen deficiency model. From these results, we compared the goodness-fit indicator, $S=R_{wp}/R_e$. The S value for the orthorhombic $^7LiMn_2O_4$ is lower than that of cubic one at 200K. On the other hand, the S of cubic for substitution samples are lower than that of orthorhombic one at 200K. From the results, $^7LiMn_2O_4$ is orthorhombic at 200K whereas substitution samples retain its room temperature cubic phase down to 200K. Hence, the crystal structure is more stable at low temperature by the substitution of Al, Li and Co for Mn. The lattice parameter *a*, the bond lengths of Li (8a)-O and Mn [Mn, Al; Mn, Al, Li; Mn, Co] (16d)-O decreased with increasing Al, Li, or Co content. Mn valence and the absolute value of lattice energy, which was calculated by Fourie method, increased with increasing Al, Li, or Co content. Accordingly, the crystal structure is more stable by the substitution of a part of Mn with Al, Li, or Co. Moreover, the analysis data of $^7LiMn_{1.5}Co_{0.5}O_4$ suggested that substituted of Co for not only 16d site but also 8a site.

The effect of electrode characteristics for the positive electrode active materials was investigated over the 4V range. Increase of substitution of Al, Li, or Co content brought to a good cycle performance in spite of some decrease on the initial capacity.

Furthermore, the standard enthalpies of

JRR-3M, HERMES, 1.Structure&Excitatitions

formation, $\Delta_f H^0$, and the enthalpy change of reaction, ΔH, were calculated form the heat of dissolution. Thermodynamic stability was examined by these parameters. These thermodynamic data was compared with the calculated one of samples to partially replace Mn by Al, Li or Co. When $\Delta_f H^0$ and ΔH decreased, it brought to a good cycle performance.

Accordingly, it is suggested that the stability of the host structure brought to improvement for the cycle performance.

研究テーマ：次世代リチウムイオン二次電池正極材料鉄含有リチウムマンガンスピネル酸化物のイオン分布解析
表題：リチウムイオン二次電池正極材料鉄含有リチウムマンガンスピネル酸化物の粉末中性子回折を用いた構造の精密化

1-1-20

Structural refinement with powder neutron diffraction of iron substituted lithium manganese spinel oxides as a positive electrode material for lithium rechargeable batteries

M. Tabuchi[1], H. Shigemura[1], A. Hirano[2], and R. Kanno[3]

[1] Special Division of Green Life Technology, National Institute of Advanced Industrial Science and Technology, Osaka, 563-8577, JAPAN
[2] Faculty of Engineering, Mie University, Mie, 514-8507, JAPAN
[3] Interdisciplinary Graduate School of Science and Engineering, Tokyo Institute of Technology, Yokohama, 226-8502, JAPAN

Introduction

Lithium manganese spinel oxide, $LiMn_2O_4$, is a candidate for the 4 V-positive electrodes for rechargeable lithium batteries. The appearance of operating voltages around 5 V were reported for transition metal substituted spinel, $LiMn_{2-x}M_xO_4$ (M = Cr and Co; $0 \le x \le 1.0$, M = Fe, Ni, and Cu; $0 \le x \le 0.5$). Recently, the charge and discharge process of 5 V- spinels has been studied by X-ray diffraction (XRD), neutron diffraction (ND), X-ray absorption, and so on. We have investigated the structure, electrochemical property, and charge and discharge mechanism of Fe substituted spinel, $LiFe_xMn_{2-x}O_4$. It is considered that the crystal structure, especially cation distribution, is significantly related to the electrochemical property. In this study, structural refinement was done using ND Rietveld analysis.

Experimental

Solid state solution of $LiFe_xMn_{2-x}O_4$ (x = 0, 0.1, 0.3, 0.5) were prepared by heating the mixture of $MnCO_3$, FeOOH, and $LiOH{\cdot}H_2O$ in stoichiometric ratio at 1023 K in Oxygen flow. ND measurements were carried out with using of powder neutron diffractometer, HERMES, of Institute for Materials Research, Tohoku University, in JAERI, Tokai. The ND data were analyzed by Rietveld method using RIETAN 2000 program [1].

Results

Figure 1 shows observed and calculated ND pattern of $LiFe_{0.5}Mn_{1.5}O_4$. All peaks were indexed in cubic space group, Fd-3m. We compared the fitting results obtained from three cation distribution models of the normal spinels which are (1) $(Li)_{8a}[Fe_xMn_{2-x}]_{16d}O_4$; Li occupies tetrahedral site 8*a* and Mn and Fe occupy octahedral 16*d* site, (2) $(Li_{1-y}Fe_y)_{8a}[Fe_{x-y}Mn_{2-x}Li_y]_{16d}O_4$; Fe and Li exist in both 8*a* and 16*d* sites, and (3) $(Li_{1-y}Mn_y)_{8a}[Fe_xMn_{2-x-y}Li_y]_{16d}O_4$; Mn and Li exist in both 8*a* and 16*d* sites. For $x \ge 0.1$, the R_{wp} parameter and goodness of fit, S were smaller in the model (2) with $y \le 0.023$ than those in model (1) and in the model (3) with unaccountably large y values. This indicates that a small amount of Fe occupy tetrahedral 8*a* site in the Fe substituted samples. The final obtained results are given in Table I. The adopted cation distribution model (2) is supported by ^{57}Fe Mössbauer spectra at 300 K which was composed of two symmetric doublets with different isomer shifts of +0.35 and +0.22 mm/s.

Reference

[1] F. Izumi, in: R. A. Young (Ed.), The Rietveld Method, Oxford University Press, Oxford, 1993, Chapter 13.

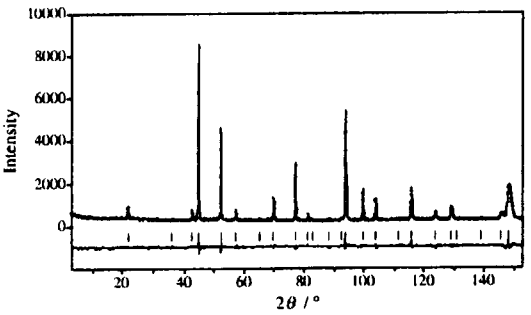


Figure 1 Observed (•), calculated (-) and difference plots for $LiFe_{0.5}Mn_{1.5}O_4$.

Table I The lattice parameters, a, and cation distributions of $LiFe_xMn_{2-x}O_4$ (x = 0, 0.1, 0.3, 0.5) refined by neutron diffraction Rietveld analysis.

x	a / nm	Cation distribution
0	0.82312(4)	$(Li_{1.000})_{8a}[Mn_{2.000}]_{16d}O_4$
0.1	0.82354(4)	$(Li_{0.985}Fe_{0.015(18)})_{8a}[Mn_{1.9}Fe_{0.085}Li_{0.015}]_{16d}O_4$
0.3	0.82391(4)	$(Li_{0.973}Fe_{0.027(14)})_{8a}[Mn_{1.7}Fe_{0.273}Li_{0.027}]_{16d}O_4$
0.5	0.82447(3)	$(Li_{0.971}Fe_{0.029(12)})_{8a}[Mn_{1.5}Fe_{0.471}Li_{0.029}]_{16d}O_4$

研究テーマ：薄膜リチウム二次電池用正極材料のリチウムディインターカレーション伴う結晶構造変化の解明

表題：リチウムマイクロ電池用正極材料の結晶構造

1-1-21
Structures of new cathode materials for solid state lithium microbattery

H. Kobayashi

National Institute of Advanced Industrial Science and Technology, Special Division of Green Life Technology, 1-8-31 Midorigaoka, Ikeda, Osaka, 563-8577, Japan

Introduction

Li_2MO_3 (M=Ru,Ir,Pt,Mo) have a cubic close-packed oxide-ion lattice with basal planes of octahedral interstices filled alternately by Li^+ only and by $1/3Li^+$, $2/3M^{4+}$. The layered Li sites which are nearly identical to the α-$NaFeO_2$ structure might allow reversible electrochemical extraction with fast electrode kinetic. Of these compounds, the Li/Li_2RuO_3 cell showed good cycle reversibility with the capacity of 160 mAh/g [1]. We reported on structural studies for systematic substitution of Fe for Ru in Li_2RuO_3 and clarified that these substitutions caused structural change from monoclinic to rhombohedral symmetry [2]. However, Fe-doped Li_2RuO_3 showed less cycle capacity. We synthesized new material of Co/Ni-doped Li_2RuO_3 and clarified that Li/Co-doped Li_2RuO_3 cell showed reversible charge-discharge characteristics in the voltage range, 2.0-4.4 V and the capacity of 170 mAh/g. In this study, Co/Ni-doped Li_2RuO_3, which was substituted by Co/Ni for Ru, was characterized by neutron Rietveld analysis. A Further, the relationship between structure and electrochemical property was investigated.

Experimental

Co/Ni-doped Li_2RuO_3 was synthesized at 1273 K for 72 h. Samples were checked by X-ray diffraction measurement. The ratios of Li/Ru/M (M=Co,Ni) were determined by ICP spectroscopy. Structural parameters were refined by neutron Rietveld analysis using the computer program RIETAN97-beta [3]. The powder neutron diffraction data was collected at room temperature using HERMES at JRR-3M reactor at JAERI, Tokai, Japan.

Results and discussions

Co-doped and Ni-doped Li_2RuO_3 was synthesized from the approximately mixture ratio 6:3:1 and 2:1:1, respectively, of Li_2CO_3, RuO_2, Co_3O_4 and NiO at 1273 K for 72 h in air. The ratio of Li:Ru:Co and Li:Ru:Ni was determined to be 62:18:20 and 57:20:23 by ICP emission spectrometry. Neutron Rietveld analysis clarified that Co-doped and Ni-doped Li_2RuO_3 had layered structure with the α-$NaFeO_2$-type and could be represented as $[Li]_{3a}[Li_{0.24}Ru_{0.41}Co_{0.35}]_{3b}O_2$ and $[Li]_{3a}[Li_{0.13}Ru_{0.47}Ni_{0.40}]_{3b}O_2$, respectively. The lattice parameters refined were a = 0.287867(5) and c = 1.43380(3) nm and a = 0.294091(6) and c = 1.43938(4) nm, respectively. Figure 1 shows the relationship between lattice parameters and 3d-transition metal ions. Ni-doped Li_2RuO_3 showed smaller lattice parameter, c. For Ni-doped Li_2RuO_3, a small amount of Ni was observed at 3a cite. These results correspond to our electrochemical results, showing the less cycle reversibility for Ni-doped Li_2RuO_3 than that for Co-doped Li_2RuO_3.

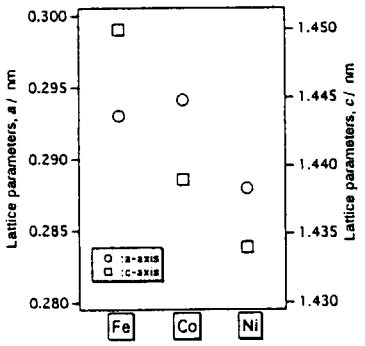


Fig.1 Relationship between lattice parameters and 3d-transition metal ions

References

[1] H. Kobayashi *et al.*, *Solid State Ionics*, 82, 25 (1995).
[2] H. Kobayashi *et al.*, *J. Power Sources*, 68, 686 (1997).
[3] F. Izumi, The Rietveld Method, in: R. A. Young (Ed.),

in Fig. 3(a). The change of mass fraction of each structure is shown in Fig. 3 (b). In Fig. 3 (b) we see that mass fraction of martensitic phase, which consists of a monoclinic structure and an orthorhombic structure, begins to decrease at around 332 K. This temperature should be an austenite

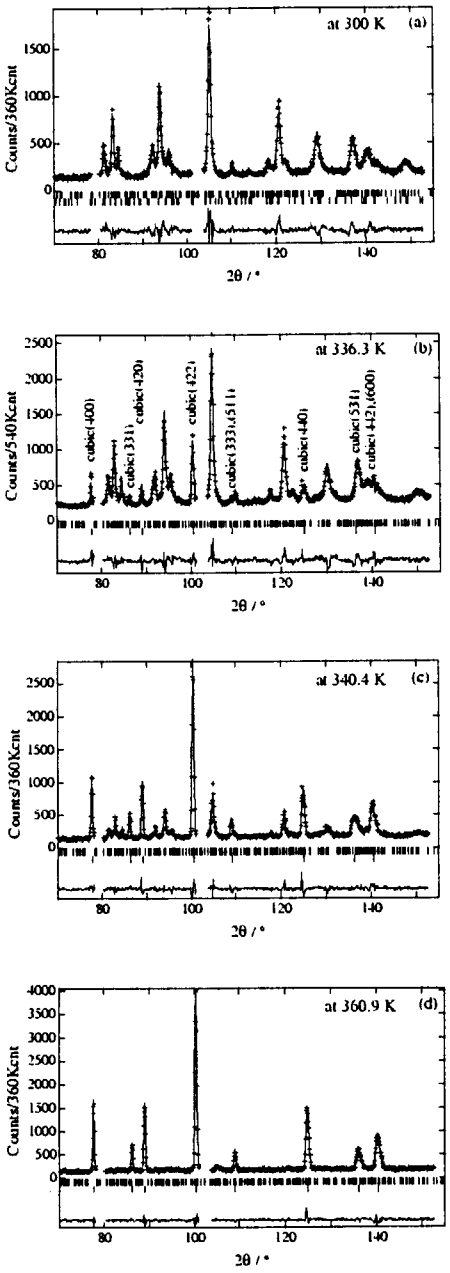


Fig. 2. Diffraction patterns and the results of Rietveld analysis at (a) 300 K, (b) 336.3 K, (c) 340.4 K and (d) 360.9 K.

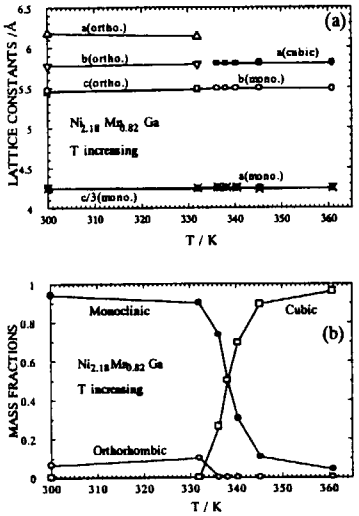


Fig. 3. (a) Lattice constants and (b) massfractions of each structure plotted versus temperature.

start (A_s) point. On the contrary, the mass fraction of cubic Heusler structure begins to increase at the same temperature. The austenite finish (A_f) point seems to be around 345 K.

Conclusion

From these experimental results, the abrupt shape change of a needle-type crystal of $Ni_{2.18}Mn_{0.82}Ga$ alloy at 339 K shown in Fig. 1 is revealed to be owing to the shape memory effect due to martensitic transformation. We found from Fig. 3 (b) that the shape memory effect occurs when the mass fractions of martensitic phase and the mother phase become fifty-fifty.

References

1) K. Inoue, K. Enami, Y. Yamaguchi, K. Ohoyama, Y. Morii, Y. Matsuoka and K. Inoue: J. Phys. Soc. Jpn. **69** (2000) 3485-3488.
2) K. Inoue, K. Enami, M. Igawa, Y. Yamaguchi, K. Ohoyama, Y. Morii, Y. Matsuoka and K. Inoue: to be published in International J. Appl. Electromagnetics and Mechanics (2001).
3) K. Inoue, Y. Yamaguchi, K. Ohoyama, K. Enami and K. Inoue: submitted to Proc. 4th Pacific Rim Int. Conf. on Advanced Materials and Processing. (2001)
4) F.Izumi, H.Asano, H.Murata and N.Watanabe: J.Appl.Crystallogr. **20** (1987) 411.

研究テーマ：形状記憶合金の中性子回折

表題：ホイスラー型 $Ni_{2.18}Mn_{0.82}Ga$ 形状記憶合金の中性子回折

1-1-22

Neutron Diffraction Study of Heusler-type $Ni_{2.18}Mn_{0.82}Ga$ Shape Memory Alloy

K. Inoue[1], Y. Yamaguchi[2], K. Ohoyama[2] R. Note[2] and K. Enami[1]

[1]*Faculty of Science and Technology, Ryukoku University, Seta, Otsu 520-2194, Japan*

[2]*Institute for Materials Research, Tohoku University, Aoba-ku, Sendai 980-8577, Japan*

Introduction

Heusler-type $Ni_{2.18}Mn_{0.82}Ga$ alloy is made by changing the concentration of the composite elements of Ni_2MnGa alloy off-stoichiometrically.[1,2] From the temperature dependence of electrical resistivity and magnetization, we had found that $Ni_{2.18}Mn_{0.82}Ga$ alloy has a thermoelastic martensitic transformation temperature coincident with the Curie temperature at around 340 K. We had succeeded in observing the shape memory effect of a single crystal-like material of this alloy with increasing temperature, as shown in Fig. 1.[3] The crystal was made from the same ingot that was used for the present powder neutron diffraction. We compare this shape memory phenomenon with the result of neutron diffraction.

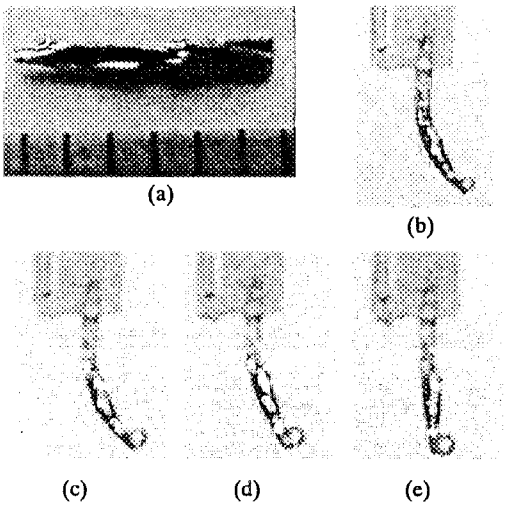


Fig.1. (a) A single crystal-like $Ni_{2.18}Mn_{0.82}Ga$ alloy picked out from the arc-melted ingot, shown with a 1 mm scale ruler. (b) The crystal at 305.0 K, which was bent at room temperature of 301.0 K. The crystal at the temperatures of (c) 333.0 K, (d) 339.0 K and (e) 339.5 K, observed with increasing temperature. The shape is suddenly recovers above 339 K.

Experimets

We have carried out a powder neutron diffraction with increasing temperature from 300 K to 361 K, using the HERMES diffractometer installed at the JRR-3M reactor. We have cared not to make very fine powder like for X-ray diffraction, because the martensitic transformation temperature changes extreamly due to the size effect.[2] The neutron wave length was 1.8196Å. We have performed Rietveld analysis of the observed diffraction patterns using the computer program, RIETAN97-β.[4]

Experimental Results

The crystal structure of martensitic phase was determined by Rietveld analysis performed at larger angle than $2\theta=70°$, because at small 2θ angle the effect of ferromagnetic scattering is not negligible. It was found that in the martensitic phase, two crystal structures coexist. One is an orthorhombic structure distorted from the cubic Heusler structure and the other is a monoclinic structure with the shuffling of a 6-layers period of the (220) plane of the orthorhombic structure.[1]

With increasing temperature, the diffraction pattern alters gradually according to the phase transformation. The diffraction patterns and the results of Rietveld analysis at typical temperatures are shown in Fig. 2 (a) to 2(d). In Fig. 2 (b), the indices of the newly appeared cubic Heusler structure are cited. We can see that the crystal structure gradually changes to cubic Heusler structure with increasing temperature.

The change of each lattice constant is shown

研究テーマ：$Eu_3Ir_4Sn_{13}$の磁気構造
表題：$Eu_3Ir_4Sn_{13}$における構造相転移と競合しうる反強磁性構造

1-1-23 Magnetic Structure in $Eu_3Ir_4Sn_{13}$

K. Kuwahara, K. Iwasa, C. Nagoshi, M. Kohgi, H. Sugawara, Y. Aoki, H. Sato, K. Ohoyama[1]

Department of Physics, Tokyo Metropolitan University, Hachioji, Tokyo 192-0397, Japan
[1]Institute for Materials Research, Tohoku University, Sendai, 980-8577, Japan

$Eu_3Ir_4Sn_{13}$ crystallizes in $Pr_3Rh_4Sn_{13}$-type cubic structure (space group $Pm\bar{3}n$) with a lattice constant a = 9.76Å. This material undergoes a structural phase transition at $T_O = 55$ K and an antiferromagnetic ordering at $T_N = 12$ K. To investigate these phase transitions, we have performed powder neutron diffraction experiments on $Eu_3Ir_4Sn_{13}$.

Single crystals of $Eu_3Ir_4Sn_3$ were grown by the molten tin solution method. Natural abundant Eu isotopes which have large neutron absorption cross sections for thermal neutrons were used. The powder sample prepared from the single crystals was filled up in a specially designed cylindrical vanadium cell for neutron diffraction of strong absorption materials. The experiment has been done using the diffractometer HERMES at the JRR-3M, Tokai. The wavelength of the incident neutron was λ = 1.8196Å. The high performance of HERMES diffractometer enabled us to perform the high resolution powder neutron experiments with natural Eu compounds in which a neutron diffraction is usually difficult.

Figure 1 shows the neutron diffraction patterns of $Eu_3Ir_4Sn_{13}$ at 2.2 K ($< T_N$), 25.6 K ($T_N < T < T_O$) and 70.0 K ($> T_O$). The patterns at 25.6 K and 70.0 K show no difference from each other, at least within experimental error. Below T_N, on the other hand, we have found the antiferromagnetic Bragg peaks with a propagation vector $\boldsymbol{k}$ = [1, 1/2, 1/2]. The magnetic reflections are denoted by the letter M. The detailed analysis of this magnetic structure is now in progress.

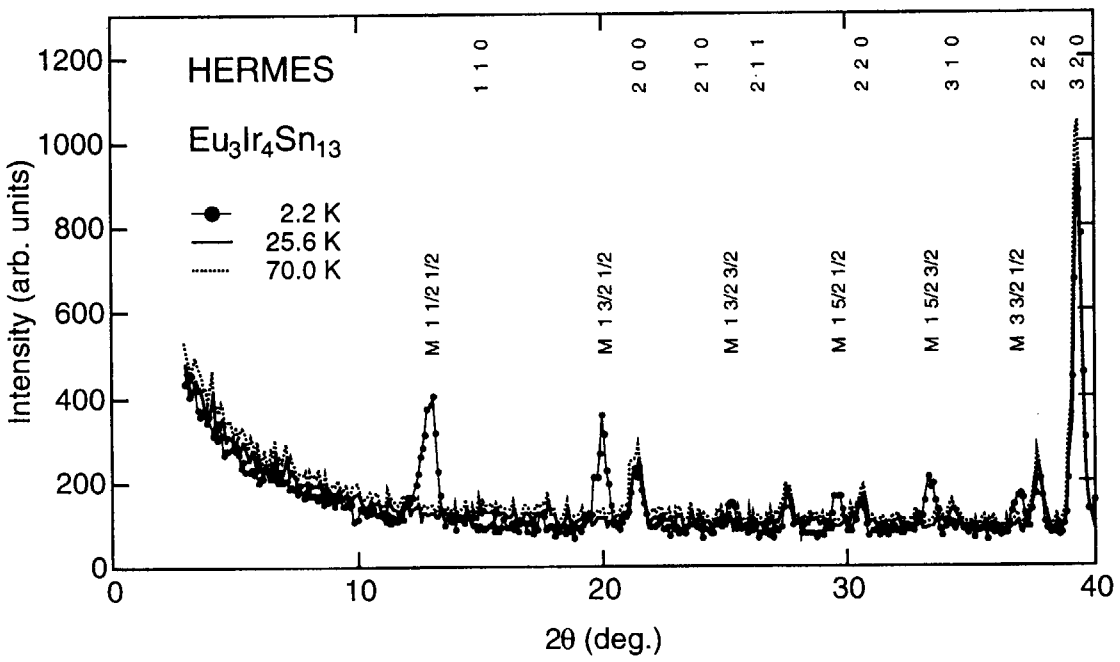


Figure 1 Neutron powder diffraction patterns of $Eu_3Ir_4Sn_{13}$ at 2.2 K, 25.6 K and 70.0 K.

JRR-3M, HERMES, 1.Structures & Excitations

研究テーマ：三次元骨格を有するリチウムインターカレーション材料の探索
表題：室温で安定化した斜方晶 $Li_3V_2(PO_4)_3$ の結晶構造決定

1-1-24

Structure determination of $Li_3V_2(PO_4)_3$ by Stabilizing Orthorhombic Phase at Room Temperature

Mineo Sato, Hirokazu Ohkawa, Kenji Yoshida, Mai Saito, Kazuyoshi Uematsu and Kenji Toda

Department of Chemistry and Chemical Engineering, Faculty of Engineering, Niigata University, Ikarashi 2 no-cho 8050, Niigata, Niigata 950-2181, Japan

Introduction

$Li_3Sc_2(PO_4)_3$, known as a lithium ionic conductor with β -$Fe_2(SO_4)_3$-type, has three structural modificantions. The phase transitions are all reversible. The γ -phase exhibits what is called superionic conductivity. In the previous study [1], we reported that the γ -phase was successfully stabilized at room temperature by substituting aliovalent ions such as Ti, Zr, Nb, Ta and Mg for Sc sites. In our preliminary experiment, it was found that $Li_3V_2(PO_4)_3$ also has the same reversible phase transitions as $Li_3Sc_2(PO_4)_3$ does. The γ -phase stabilized $Li_3V_2(PO_4)_3$, if possible, thus can provide a considerable enhancement of the cathode performance of $Li_3V_2(PO_4)_3$.

In this study the stabilization of γ-phase of $Li_3V_2(PO_4)_3$ at room temperature was succeeded by substituting Zr for V sites. The cathode performance was discussed on the basis of the γ -phase stabilized $Li_3V_2(PO_4)_3$ structure, which was refined by X-ray diffraction and neutron diffraction methods.

Experimental

The crystal structure of each phase found in the samples was refined by the Rietveld method by neutron diffraction. Powder neutron diffraction patterns for the refinement were recorded using the PKD (HERMES) diffractometer installed at JRR-3M Guide Hall in the Japan Atomic Energy Research Institute (TAERI). An incident neutron wavelength λ =1.8196Å was obtained from a Ge(311) monochromater. The powder sample was enclosed in the cylindrical vanadium vessel and mounted on a double-axis diffractometer. The data were collected on thoroughly ground powders by a multi-scanning mode in the 2θ range from 5° to 155° with a step width of 0.05° and a monitoring time of 16 min. The powder patterns obtained were analyzed using the RIETAN97 profile refinement program [2].

Results and Discussion

Rietveld analysis for the neutron diffraction pattern was carried out on the data sets measured at room temperature for the 10% Zr-substituted sample. An initial site assignment was referred to the single crystal data of orthorhombic $Li_3Sc_2(PO_4)_3$ [3], i.e., the refinement was based on an orthorhombic symmetry with *Pbcn* (standard expression of *Pcan*). The M site in the $Li_{2.8}(M)_2(PO_4)_3$, where $M=V_{0.9}Zr_{0.1}$, was asigned as a mixed species with atomic ratio of V : Zr =0.9 : 0.1. Initially, scale and background parameters were refined, followed by subsequent iterations using cell, peak shape, atomic coordinates and isotropic thermal parameters. In the early refinement stages, the R factor of the weighted pattern fitting, R_{wp}, was reasonably reduced to about 10%, but both a large negative thermal parameter and quite large standard deviations for the coordinates were observed for the M sites. Considering a quite small neutron scattering factor for V atom and a small amount of Zr substitution ratio, one should not obtain any precise information on the M site. Therefore, the coordinates of this site were obtained from the Rietveld analysis for the X-ray diffraction pattern, and the values thus obtained were used as invariant parameters in the following neutron refinement stages. In the next stage, the refinement was first done by assuming the site occupancy ratios for Li(1), Li(2) and Li(3) sites as fixed values of 1.0, 0.25 and 0.25, respectively, and then refined as variant parameters under the condition of the total lithium amount equal to 2.8. Finally, the site occupancy ratio and the isotropic thermal parameters for these three lithium sites were simultaneously refined.

The cell parameters and the positional parameters finally refined are listed in Table 1. The distance values between oxygen and cations except Li are all reasonable ones; the distance of M-O bond are in the range of 1.944-2.052 Å, and the one of P-O bond in the range of 1.506-1.548 Å. The lithium ions are located almost within the bc plane in the orthorhombic unit cell with x～1/4 and 3/4. There are some interesting differences between the orthorhombic disordered γ-phase of $Li_3Sc_2(PO_4)_3$,

so called superionic conducting phase, and the orthorhombic disordered γ -phase of $Li_{2.8}(V_{0.9}Zr_{0.1})_2(PO_4)_3$. First, all the lithium sites are partially occupied (Table 1) even in the $Li1_o$ site which seems to be fully occupied in the γ-phase of the unsubstituted sample at high temperature. This may correspond to introducing additional vacancies into the lithium sites by substituting Zr^{4+} for V^{3+} due to charge compensation. Second, quite short distance values are observed in the Li-Li bond, particularly the bonds concerning $Li1_o$ which has the highest occupancy ratio being very short. Although neutron diffraction gives us only static, average information on ion location, but no dynamic information, this fact may imply an image of "dynamical exchange" of lithium ions between the $Li1_o$ site with the highest lithium occupancy ratio and $Li2_o$ or $Li3_o$ site with a relatively low occupancy ratio. These features could be the most responsible to both enhancement of discharge capacity and good cycle performance observed in the Zr-substituted $Li_3V_2(PO_4)$ cathode material.

Conclusions

The stabilized γ -phase of $Li_3V_2(PO_4)$ exhibited not only the enhancement of the discharge capacity but also disappearance of the two-plateau boundary in the charge/discharge curves[11], which was originally observed in the pure material.

The Rietveld analysis by neutron diffraction confirmed that such improvement of the cathode performance should come from the highly disordered arrangement of the lithium ions over the available lithium sites in the β-$Fe_2(SO_4)_3$-type structure.

Acknowledgments

This work was supported by the "Research for the Future, Preparation and Application of Newly Designed Solid Electrolytes (JSPS RFTF96P00102)" program from the Japan Society for the Promotion of Science (JSPS), and also by a Grant-in-Aid (08455405) from the Ministry of Education, Science and Culture.

REFERENCES

[1] T. Suzuki, K. Yoshida, K. Uematsu, T. Kodama, K. Toda, Z.-G. Ye, M. Ohashi, and M. Sato, Solid State Ionics, 113-115, 89(1998).

[2] F. Izumi, in R. A. Young (ed.), The Rietveld Method, Oxford University Press, Oxford, 1993, Chp. 13.

[3] K. S. Nanjundaswamy, A. K. Padhi, J. B. Goodenough, S. Okada, H. Ohtsuka, H. Arai, and J. Yamaki, Solid State Ionics, 92,1(1996).

[4] M. Sato, H. Ohkawa, M. sato, K. Uematsu, M,saito K. Toda, Solid State Ionics, 137-142, 135(2000)

Table 1. Structural parameters refined for $Li_{2.8}(V_{0.9}Zr_{0.1})_2(PO_4)_3$ by neutron diffraction. The unit cell parameters are a=12.1005(5) Å, b=8.6539(4) Å, c=8.6546(4) Å, and Z=4 for *Pbcn* space group. The reliable factors are R_{wp}=5.69%, R_p=4.49%, S=1.63, R_I=2.32%, and R_F=1.17%.

Atom	Site	g	x	y	z	B/Å^{-2}
Li1	*8d*	0.72(1)	0.324(1)	0.286(1)	0.285(2)	0.3(2)
Li2	*8d*	0.33(1)	0.300(2)	0.120(3)	0.357(4)	0.3(2)
Li3	*8d*	0.34(1)	0.231(2)	0.424(3)	0.270(3)	0.3(2)
M[1)]	*8d*	1.0	0.1134(4)	0.247(1)	0.4641(4)	0.3(1)
P1	*8d*	1.0	0.1476(3)	0.1067(4)	0.1054(5)	1.00(9)
P2	*4c*	1.0	0.5	0.0419(8)	0.25	1.67(1)
O1	*8d*	1.0	0.3404(3)	0.4310(4)	0.1011(4)	1.54(9)
O2	*8d*	1.0	0.2732(4)	0.3245(5)	0.4835(5)	2.2(1)
O3	*8d*	1.0	0.0312(3)	0.1545(5)	0.0661(4)	1.8(1)
O4	*8d*	1.0	0.0741(3)	0.4436(5)	0.3538(6)	1.96(9)
O5	*8d*	1.0	0.4221(3)	0.1446(5)	0.1582(5)	1.69(9)
O6	*8d*	1.0	0.1829(3)	0.1583(5)	0.2694(4)	1.6(1)

研究テーマ：フラックスを用いての非化学量論希土類オルソニオブ酸塩の合成と物性

表題：酸素欠損を持つイットリウムオルソニオブ酸塩 $Y_{1-x}NbO_{4-1.5x}$ の結晶構造決定

1-1-25

Structure determination of yttrium orthoniobate $Y_{1-x}NbO_{4-1.5x}$, with oxygen defects

Masahito Honda [a], Kenji Toda [b], Mineo Sato [b]

[a]Department of Active Material Chemistry, Graduate school of Science and Technology, Niigata University
Ikarashi 2-nocho 805ɔ, Niigata 950-2181, Japan

[b]Department of Chemistry and Chemical Engineering, Faculty of Engineering, Niigata University
Ikarashi 2-nocho 8050, Niigata 950-2181, Japan

Introduction

The phase relation Y_2O_3 – Nb_2O_5 system including stoichiometric $YNbO_4$ compound has been reported by many investigators. In the Y_2O_3 – Nb_2O_5 system, it is well known that the rare earth niobates are thought to be candidates for new ionic conductor ferroeloetrics and phosphors [1]. However, their phase diagrams are not well understood and no direct experimental evidence of the non-stoichiometry in the rare earth orthoniobate $YNbO_4$ crystal.

In this report, we disclose the existence of non-stoichiometric rare earth orthoniobate phase. In order to examine the non-stoichiometry in orthoniobate crystal, we used the Rietveld analysis neutron diffraction patterns.

Experimental

The stoichiometric compound was synthesized at 1373 K for 10 h. The non-stoichiometric $Y_{1-x}NbO_{4-1.5x}$ was synthesized at 1173 K for 4 h by using the excess Rb_2CO_3 flux (1.3 mol).

In order to clarify the atomic position of oxygen atoms and lattice defective condition in the non-stoichiometric compound, the crystal structure of each phase was refined by the Rietveld method [2] with neutron diffraction patterns.

Powder neutron diffraction patterns for the refinement were recorded using the PKD (HERMES) diffractometer installed at JRR-3M Guide Hall in the Japan Atomic Energy Research Institute (TAERI). An incident neutron wavelength λ =1.8196Å was obtained from a Ge(311) monochromater. The powder sample was enclosed in the cylindrical vanadium vessel and mounted on a double-axis diffractometer. The data were collected on thoroughly ground powders by a multi-scanning mode in the 2 θ range from 5° to 155° with a step width of 0.05° and a monitoring time of 16 min.

Results and Discussions

The non-stoichiometric yttrium orthoniobate of reaction equations can be expressed as:

$$Nb_2O_5 + Rb_2CO_3 \rightarrow 2RbNbO_3 + CO_2 \quad (1)$$

$$2RbNbO_3 + (1-x)Y_2O_3 \rightarrow 2Y_{1-x}NbO_{4-1.5x} \quad (2)$$

The reactive intermediate, $RbNbO_3$, in second step produces the non-stoichiometric products and regenerates the Rb_2CO_3 flux. For the starting composition of $Y_{1-x}NbO_{4-1.5x}$ ($0.0 \leqq x \leqq 0.6$), compounds crystallized in the fergusonite-related structure. It was confirmed by powder neutron diffraction that that all composition can be indexed in monoclinic space group without any impurities. The refinement was based on a monoclinic symmetry with space group $I2_1/c$ (No. 15, #3

setting) for the room temperature data of the non-stoichiometric sample. Two types of defect models were considered for the origin of non-stoichiometry and the solid solution mechanism of $YNbO_4$. (1) substitution model and (2) rare earth vacancy model are considered to explain the rare earth deficient solid solution. Each model requires a sufficient amount of the associated defects such as the rare earth vacancy and/or the oxygen vacancy to maintain the electrical neutrally. In the substitution model, niobium ions partially substitute the rare earth sites. The positions of atoms were initially assumed to be in ideal fergusonite phase. As a result of Rietveld refinement, it was found that the oxide ion in the non-stoichiometric compound has two defect sites and these sites were lacked equally. The distribution of the oxygen vacancy and amount of the oxygen defect were determined with extreme accuracy from neutron diffraction study. The crystallographic data are listed in Table 1. The oxygen atoms and rare earth cations were proposed for the first time to be located with randomly distributed vacancies based on the vacancy model.

Table 1. Crystallographic data for yttrium niobate, $Y_{0.6}NbO_{3.4}$

Atom	g	x	y	z
Y	0.6	0.25	0.6053(4)	0.0
Nb	1.0	0.25	0.1285(6)	0.0
O(1)	0.788(8)	-0.0386(6)	0.0312(3)	0.2558(7)
O(2)	0.756(7)	0.5027(6)	0.2097(3)	0.3410(6)

Space group I2/*a* (no.15-3)

Lattice parameter

a = 5.0717(3) Å, b = 10.9479(7) Å

c = 5.2988(3) Å, β = 94.517(3)°

Reliable factors

Rwp = 10.62%, R_I = 6.09%, R_F = 3.76%

Conclusion

In the present study, the non-stoichiometric compounds, $Y_{1-x}NbO_{4-1.5x}$ has been obtained for the first time using Rb_2CO_3 as reactive flux. Lattice constants extend with increasing oxygen defect. Large amounts of oxygen vacancies in this compound lead to the relaxation of distorted structure. These non-stoichiometric compounds with random oxygen defect sites have the potential to act as new oxide ion conductor and phosphor for practical use [3,4].

ACKNOWLEDGEMENTS

The authors thank to Tokuyama Science Foundation for financial support of this work. It was also partly supported by the 'research for the Future, Preparation and Application of newly Designed Solid Electrolytes (JSPS RFTF96P00102)' program of the Japan Society for the promotion of Science (JSPS).

REFERENCES

[1] J-H. Lee, M. Yashima, M. Kakihana and M. Yoshimura, Am. Ceram. Soc., 81, 894 (1998)

[2] Y. -I. Kim and F. Izumi, J. Ceram. Soc. Jpn., 102, 401 (1994).

[3] K. Toda. M. Honma, Y. Ishimoto and M.Sato, Key engineering Materials., 217-220, 181-182 (2000).

[4] K. Toda. M. Honma, Y. Ishimoto,Z-G. Ye and M.Sato, Solid State Ionics,25-30,136-137(2000).

研究テーマ：$LiCoO_2$のホストゲスト反応に及ぼす結晶構造の影響
表題：非化学量論組成 HT-$LiCoO_2$の構造解析

1-1-26 Structural Refinement of Nonstoichiometric HT-$LiCoO_2$

Nobuyuki Imanishi, Atsushi Hirano and Yasuo Takeda
Department of Chemistry, Mie University
1515 Kamihamacho, Tsu, Mie 514-8507, Japan

Introduction

$LiCoO_2$ is a commercially used positive electrode of lithium ion battery. The structure of high temperature $LiCoO_2$ shows alternately arranged lithium and cobalt layers. $LiCoO_2$ has been believed to always occur in stoichiometric form, which makes a contrast to the identical structural material, $LiNiO_2$ that contains cubic domains according to the synthetic temperatures. There were few studies about detailed structure of $LiCoO_2$ from the aspect of nonstoichiometry. Recent studies, however, show preparation of Li_xCoO_2 with x>1, when initial nominal composition is set at Li/Co>1. It is reported that oxygen defects are generated in a lithium-rich Li_xCoO_2 together with the occurrence of divalent Co^{2+}. In our study the relation between synthetic condition, nonstoichiometry, cation distribution and electrode characteristics of $LiCoO_2$ is discussed.

Experimental

LiOH and Co_3O_4 were mixed well in an agate mortar at nominal compositions, Li/Co=1.02, 1.05, 1.10, 1.15, 1.20, 1.25, 1.30. Six-hour calcination of the mixture was done at 750℃, followed by 24 hour annealing at 850℃ in air atmosphere.

The structure was analyzed by normal powder X-ray diffraction method. Since the product contains lithium atom with poor scattering ability, neutron diffraction data was used to determine lithium position precisely. The stoichiometry of products was determined from ICP and iodometric titration. From the former data, Li/Co molar ratio was calculated. Cobalt valence or Co/O ratio was decided from the latter results.

Two-electrode test cell was used to examine galvanostatic charge-discharge behaviors. Lithium sheet was used as negative electrode. The lithium cobaltite mixed with acetylene black and binding agent, PTFE, was used as positive electrode. 1M-$LiPF_6$/PC+DMC (vol 1:1) was used as the electrolyte solution. The prepared cell was cycled in the range of 4.3～2.5V at a constant current of 300μAcm^{-2}.

Results and discussion

X-ray and neutron diffraction data strongly suggests the excess amount of lithium go into the cobalt layers in replace of cobalt atoms. The formula of the product can be expressed as $Li_{3a}[Co_{1-x}Li_x]_{3b}O_2$. The solid solution limit of excess lithium is found around Li/Co=1.15. These products contain oxygen defects in order to maintain electronic neutrality.

The determined stoichiometries of Li/Co and cobalt valences from results of ICP, iodometry show that the cobalt valences are categorized into two groups; in Li/Co<1.15 they are around 3.0, while in Li/Co>1.15, they take lower values around 2.9. The discontinuity at Li/Co=1.15 is interpreted as the solid solution limit. This is consistent with the composition that the lattice constant stops decreasing shown in a separate experiment.

The reversible capacity shows dependence on the composition and the highest one as much as 140mAhg^{-1} was obtained at Li/Co=1.10. The capacity linearly decreased with Li/Co ratio beyond 1.10 due to decreasing amount of cobalt in the products. The sample of Li/Co=1.10 also shows better cycling performance with the reversible capacity of ca. 160mAhg^{-1}, when the higher cut off voltage as 4.52V was set for the charge process. Stoichiometric $LiCoO_2$ undergoes the phase transformation at $Li_{0.5}CoO_2$ from rhombohedral to monocolinic structure. This does not appear in Li/Co=1.10 due to the deviation from the ordered ideal structure. It is concluded that the phase change accompanied by the structural rearrangement becomes disadvantage for a long cycle life and can be prevented by doping lithium into cobalt layers.

研究テーマ：正方晶RB_2C_2化合物の結晶構造
表題：正方晶CeB_2C_2におけるB-Cネットワーク内原子配列の中性子散乱による研究

1-1-27
Neutron Diffraction Study on B-C Network Atomic Arrangements in Tetragonal CeB_2C_2

K. Kaneko, K. Ohoyama, H. Onodera and Y. Yamaguchi

Institute for Materials Research, Tohoku University, Sendai 980-8577, Japan

There is an upsurge of interest for well-localized 4*f* compounds RB_2C_2 (R=rare earth) because of its relatively strong antiferroquadrupolar interactions. DyB_2C_2 undergoes an antiferroquadrupolar (AFQ) order transition at T_Q=24.7 K and a successive transition to an antiferromagnetic (AFM) state at T_N=15.3 K[1]. Moreover, HoB_2C_2 also shows an AFQ order transition at T_Q= 4.5 K[2] below T_N=5.9 K, that is, the AFQ order in HoB_2C_2 is realized in the magnetic ordered state. In order to make clear a nature of AFQ interactions in this system, precise knowledge on their crystal structures is indispensable for quantitative discussion.

Our previous neutron diffraction experiments on poly-crystalline $Ce^{11}B_2C_2$ and $Nd^{11}B_2C_2$ indicates that the crystal structure of RB_2C_2 is a tetragonal one belonging to the symmetry group *P4/mbm*, for which the R atoms occupy the 2(*a*) sites, while the B and C atoms occupy the 4(*h*) sites with different positional parameters[3]. Since ^{10}B is a strong absorber for neutrons, measurements were performed on the sample including 99.5 % of ^{11}B to avoid the significant attenuation. However, this enrichment makes it hard to distinguish between B and C, because the coherent scattering length of ^{11}B is $b_{^{11}B}$=6.65x10^{-13} cm, is nearly the same as that of C, b_C=6.646x10^{-13} cm. This work aims, therefore, to verify the precise positional parameters of B and C in CeB_2C_2. For this reason, we dared to use a sample including natural B. Neutron diffraction experiments at room temperature were carried out at Kinken powder diffractometer HERMES (T1-3) on CeB_2C_2.

At first, we estimate the reflection intensity depending on the configuration of B and C. There are two kinds of the arrangements for the 4(*h*) sites: Site 1 with x_1=0.361 and Site 2 with x_2= 0.161. The two models projected onto the *c* plane are illustrated in Fig. 1. In Model I, the B atoms occupy Site 1 and the C atoms are at Site 2. In Model II, the positions of B and C are replaced with each other. The difference between the two models clearly appears in the reflections with *h+k=odd* whose intensities are only come from B and C

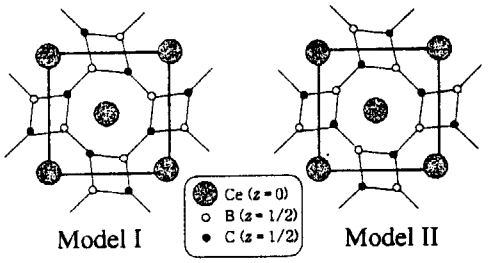


Fig.1 Possible arrangements of B and C atoms in CeB_2C_2.

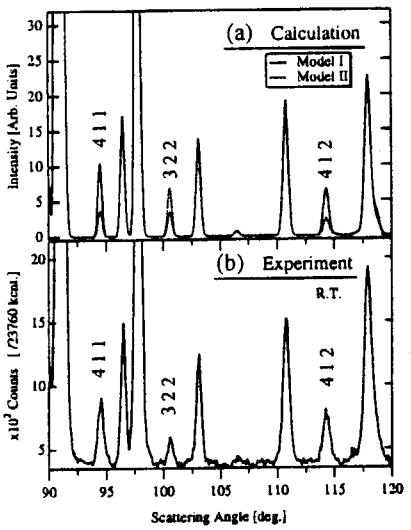


Fig.2 (a) Calculated neutron diffraction patterns for Model I and II. (b) Neutron powder diffraction pattern of CeB_2C_2 observed on HERMES.

because of the extinction rule for rare earth cites. These reflections can be seen particularly in the 2θ range of 90° to 120°, where the 4 1 1, 3 2 2 and 4 1 2 reflections exist. In Model I, the calculated intensity ratio for these peaks is I_{411}:I_{322}:I_{412}=100:35.6:84.1. On the other hand, the ratio differs drastically in Model II and is I_{411}:I_{322}:I_{412}=49.6:100:41.5. Therefore, the observed data giving the ratio of I_{411}:I_{322}:I_{412}=100:32.4:87.6 shown in Fig. 2(b) agrees with that of Model I.

Reference

[1] H. Yamauchi *et al.*: J. Phys. Soc. Jpn. **68** (1999) 2057.
[2] H. Onodera et al.: J. Phys. Soc. Jpn. **68** (1999) 2526.
[3] T. Onimaru *et al.*: J. Phys Soc. Jpn. **68** (1999) 2287.

研究テーマ：準1次元銅酸化物 $(Ca,Y)_{0.82}CuO_2$ の磁気構造
表題：複合結晶 $Ca_{0.83}CuO_2$ の変調構造

1-1-28
Modulated Structure of the Composite Crystal $Ca_{0.83}CuO_2$

Y. Miyazaki[1], M. Onoda[2], S. Shamoto[1] and T. Kajitani[1]

1 Department of Applied Physics, Graduate School of Engineering, Tohoku University, Aramaki Aoba, Aoba-ku, Sendai 980-8579, JAPAN
2 Advanced Materials Laboratory, National Institute for Materials Science, 1-1 Namiki, Tsukuba, Ibaraki 305-0044, JAPAN

Quasi one-dimensional (1D) cuprate $Ca_{0.83}CuO_2$ has recently attracted much interest owing to its unique magnetism. The magnetic behavior can be well described as a diluted 1D $S = 1/2$ system; a mixture of Curie-Weiss, spin dimer and/or alternating Heisenberg chain components [1]. The crystal structure of the compound, on the other hand, has not yet been fully determined due to its incommensurate superstructure. We have refined the crystal structure of the compound by means of a four-dimensional superspace group approach.

Polycrystalline samples were prepared by the standard solid-state reaction method. Neutron powder diffraction (ND) data were collected at room temperature using HERMES diffractometer, installed at the JRR-3M reactor in JAERI. The ND data was analyzed using a Rietveld refinement program PREMOS 91 [2] designed for modulated structure analyses.

The structure model was constructed on the basis of our previous report [3]. We assigned the CuO_2 chains to subsystem 1 and the Ca atoms to subsystem 2. From the observed systematic absences, we adopted suitable superspace group of $F2/m(1+\alpha\ 0\ \gamma)0s$. In Fig. 1 we show the observed, calculated and difference profiles for the ND data. Short vertical lines below the patterns indicate the peak positions of main (upper) and satellite (lower) reflections for the two subsystems. The final R_{WP} factors were 9.8 %. Lattice parameters were refined to be a_1 = 2.8043(2) Å, b = 6.3179(2) Å, c_1 = 10.5744(5) Å and β_1 = 90.10(1)° for subsystem 1 and a_2 = 3.3652(2) Å, c_2 = 10.5893(5) Å and β_2 = 93.04(1)° for subsystem 2. The resulting a_1/a_2 (= α) ratio of 0.8333(2) corresponds to the stoichiometry of the sample, $Ca_{0.8333}CuO_2$.

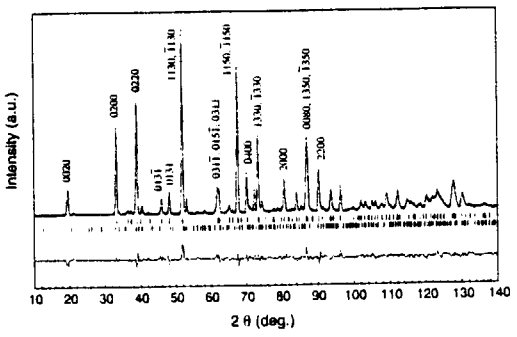


Fig. 1 Observed, calculated and difference neutron diffraction profiles for $Ca_{0.83}CuO_2$.

In Fig. 2 we show the refined modulated crystal structure of $Ca_{0.83}CuO_2$ viewed in perspective from the a-axis. One might recognize markedly waved rows of the O atoms forming "CuO_2-ribbons" along the a-axis. In contrast, the Ca atoms appear to fluctuate mainly in the c-axis. These displacive modulations are originated from the interactions between the two subsystems, namely the CuO_2 chains and the Ca atoms, which have different periods along the a-axis.

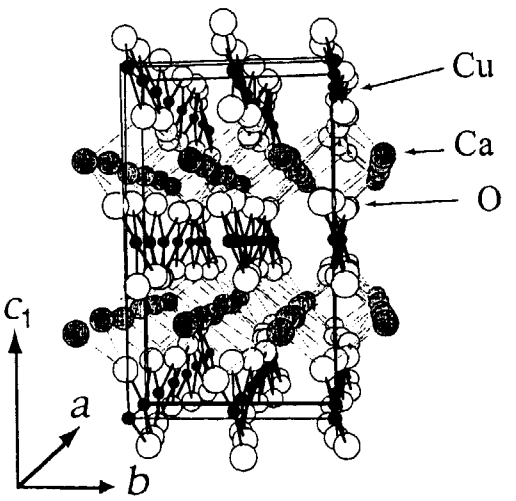


Fig. 2 Refined modulated structure of $Ca_{0.83}CuO_2$ viewed in perspective from the a-axis.

References

[1] see for example, Z. Hiroi et al., *J. Phys. Soc. Jpn.* **69** (2000) 1824.
[2] A. Yamamoto, *Acta Cryst. A* **49** (1993) 831.
[3] Y. Miyazaki et al., *J. Phys. Soc. Jpn*, in press.

研究テーマ：中性子粉末回折用高温電気炉の開発
表題：高温中性子回折による炭化ホウ素の構造変化の研究

1-1-29 Study of structural change of boron carbide by high-temperature neutron diffraction

Kazumasa Nakamura, Masatomo Yashima, Kenji Ohoyama [1]and Yasuo Yamaguchi[1]

Department of Materials Science and Engineering Interdisciplinary Graduate School and Engineering, Tokyo Institute of Technology, 4259, Nagatsuta-cho, Midori, Yokohama, 226-8502, JAPAN

[1] Institute for Materials Research, Tohoku University, Katahira, Aoba, Sendai, 980-8577, JAPAN

As boron carbides are materials with wide applicability due to their refractory and mechanical properties, it is very important to study structural changes of the materials at high temperatures. However little studies on neutron diffraction have been done for boron carbides because the isotope ^{10}B is a strong absorber of neutron. Furthermore, there have been no high-temperature neutron diffraction studies in the literature. Here, we have used ^{11}B-enriched B_4C sample ($B_{0.807}C_{0.193}$, ^{11}B purity 99.68At%) to minimize the effects of neutron absorption. The purpose of this work is to study the structural change of ^{11}B-enriched B_4C by neutron powder diffraction from 23 to 1173℃.

Neutron diffraction data were collected in the temperature range of 23 to 1173℃ using the powder diffractometer HERMES installed at JRR-3M in JAERI[1]. The data collections were done over the 2 θ range of 20.0 to 152.0° with the step width 0.1° . The powder diffraction data were analyzed using a Rietveld analysis program RIETAN94[2]. Here, the Rietveld refinements were done assuming the CCC chain model where three carbon atoms lie along the rombohedral's longest diagonal[3]. Atomic coordinates of B_4C (space group: $R\bar{3}m$) for the CCC chain model are: B1 and B2 on (x, $-x$, z), C1 on (0, 0, z) and C2 on (0, 0, 0.5). So the atomic coordinates x(B1), z(B1), x(B2), z(B2) and z(C1) were refined in the Rietveld analyses where x(B1) denotes the atomic coordinate x for B1 atom.

Figure 1 shows the profile fit and difference patterns of Rietveld analysis for the powder neutron data of boron carbide measured at 993℃. The profile fitting results obtained from the analyses were, Rwp=15.89, 9.56, 15.09,

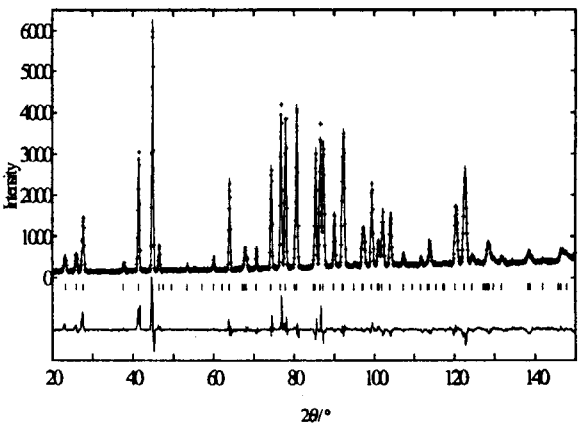


Fig.1 Observed (crosses), calculated (solid) and difference (solid, lower) profiles for boron carbide mesured at 993℃. Positions of the Bragg reflections are marked with vertical lines.

Reactor: (JRR-3M) Facility: HERMES(T1-3) Field: (1. Structure & Excitations)

11.81, 13.77, 11.20, 12.75 (%); R_p=12.64, 7.92, 11.76, 8.03, 10.51, 7.55, 9.60 (%) and S=2.93, 2.08, 2.80, 2.63, 2.92, 2.55, 2.94 for 23, 182, 402, 585, 825, 993 and 1173℃, respectively. As shown in Fig.1, the refinements were successfully performed by a single phase of trigonal structure (space group: $R\bar{3}m$).

Figure 2 shows the variation of refined lattice parameters of this material with temperature. The *a* and *c* parameters increased linearly with increasing temperature.

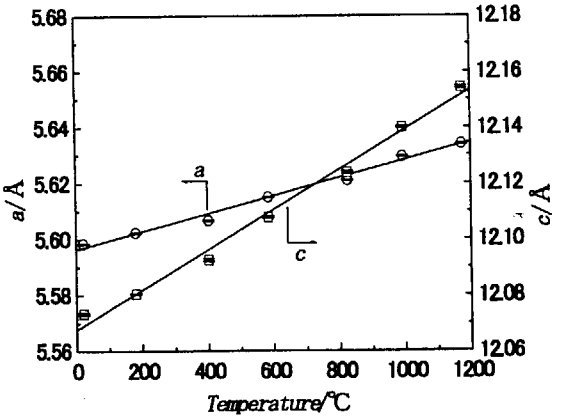


Fig.2 Relationship between refined lattice parameters and temperature (error bars are smaller than the size of the symbols). Linear lines were obtained by the least-squares method.

The expansion coefficients calculated using lattice parameters from 23 to 825℃ were $\alpha_a=(5.2\pm0.4)\times10^{-6}℃^{-1}$ and $\alpha_c=(5.4\pm0.3)\times10^{-6}℃^{-1}$ for *a* and *c* parameters, respectively. Thus the anisotropy for the thermal expansion was not observed. These values exhibited good agreement with the value ($\alpha=5.2\times10^{-6}℃^{-1}$) obtained by a dilatometry.

Figure 3 shows the relationship between refined atomic coordinates and temperature. All atomic coordinates were almost constant from 23 to 1175℃.

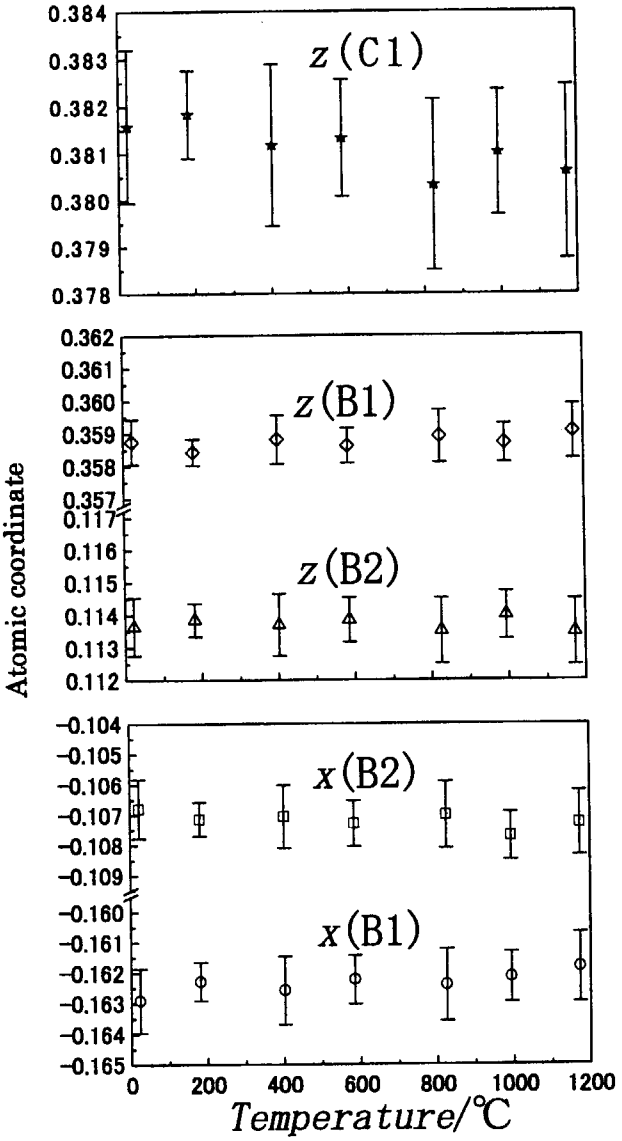


Fig.3 Relationship between refined atomic coordinates and temperature.

References

[1] K. Ohoyama, T. Kanouchi, K. Nemoto, M. Ohashi, T. Kajitani and Y. Yamaguchi, *Jpn. J. Appl. Phys.* 37, 3319-3329 (1998).

[2] F. Izumi, "*The Reitveld Method*", Oxford University Press, Oxford (1993), Chapter13.

[3] B. Morosin, A. W. Mullendore, D. Emin and G. A. Slack, *Am. J. Phys.*, 64, 70-86(1986).

研究テーマ：層状マンガン酸化物の化学圧力効果
表題　：マンガン酸化物の軌道安定性と電荷整列相転移

1-1-30 Interrelation between Orbital Stability and Charge-Ordering in doped manganites

A. Machida[1], Y. Moritomo[2] and K. Ohoyama[3]
[1]Department of Crystalline Materials Science, Nagoya University, Nagoya 464-8601, Japan
[2]CIRSE, Nagoya University, Nagoya 464-8601, Japan
[3]IMR, Tohoku University, Sendai 980-8577, Japan

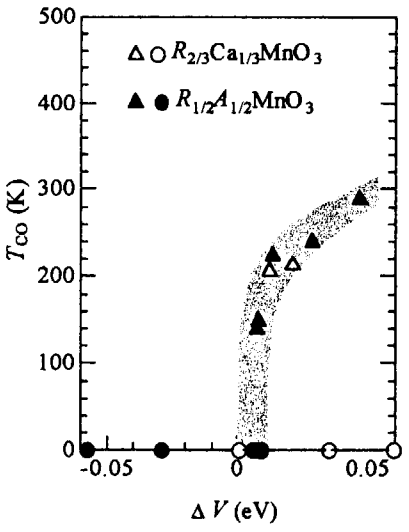
Perovskite-type doped manganites have three-dimensional networks of the MnO_6 octahedra. By changing the averaged ionic radius r of the perovskite A-site, the Mn--O--Mn angle, or the transfer integral t between the neighboring Mn sites, is modified (*chemical pressure*). It is well known that the Curie temperature T_C is suppressed with decrease of r. Similar to the case of the Curie temperature, the chemical pressure effect on the critical temperature T_{CO} for the charge-ordering transition have been regarded as control of t.

In the doped manganites, it is established that the charge-ordering transition accompanies $d(3x^2\text{-}r^2)/d(3y^2\text{-}r^2)$ orbital alternation and that the shape of MnO_6 octahedra relates to the stability of the Mn e_g. To confirm that trend is applicable to the cubic perovskite system, we have extended our research to the cubic perovskite system at $x = 1/2$ and 1/3. We found a close correlation between the orbital stability, which was estimated from the shape of the MnO_6 octahedra in an electrostatic manner, and the charge-ordering transition. This result indicates that the orbital stability is an important factor for the charge-/orbital-ordering transition of doped manganites.

A series of ceramics compounds, $R_{1/2}Ca_{1/2}MnO_3$, $R_{1/2}Sr_{1/2}MnO_3$ and $R_{2/3}Ca_{1/3}MnO_3$, was synthesized by solid state reaction in an air atmosphere. Neutron powder diffraction measurements were performed with the Kinken powder diffractometer for high efficiency and high resolution measurements (HERMES) installed at the JRR-3M reactor at the Japan Atomic Energy Research Institute, Tokai, Japan. We have analyzed the neutron powder patterns at room temperature with RIETAN-97 β program, and have found that the investigated compounds were single phase without detectable impurities. The crystal symmetry is orthorhombic (*Pbnm*; $Z = 4$). The atomic sites are *R*/Ca 4*d*[*x*, *y*, 1/4], Mn 4*b*[1/2, 0, 0], O(1) 4*d*[*x*, *y*, 1/4], O(2) 8*d*[*x*, *y*, *z*]. T_{CO} and T_C are the charge-ordering and Curie temperatures, respectively.

To estimate the relative stability of the respective e_g-orbitals, that is, $d(3x^2\text{-}r^2)$, $d(3y^2\text{-}r^2)$ and $d(3z^2\text{-}r^2)$, we have calculated the electrostatic potentials, V_x V_y and V_z based on the structural data. The larger V_i are, the more stable the corresponding orbital becomes. The stability of the $d(3x^2\text{-}r^2)/d(3y^2\text{-}r^2)$ orbital alternation can be estimated from the difference of the potentials: $\Delta V = (2V_z - V_x - V_y)/2$

In the Figure, we plotted T_{CO} against ΔV. Triangle shows the charge-ordering transition, while circle does not show it. If one sees the phase diagram from left to right (the stability of the $d(3x^2\text{-}r^2)/d(3y^2\text{-}r^2)$ orbital alternation increases.), the COI state appears and T_{CO} increases. However, there are exceptions on this trend (see open circles at $\Delta V = 0.034$ and 0.06), suggesting that an extra factor is needed for the charge-ordering transition. We mapped the data points against ΔV and $|V_x - V_y|$ and found that the data gather in the lower right corner. This suggests that the large ΔV as well as the small $|V_x - V_y|$ are necessary conditions for the charge-ordering transition.



研究テーマ: ITER 真空容器の研究

表題:ITER 真空容器における部分溶け込み溶接の残留応力測定

1-1-31

Neutron Diffraction Measurement of Residual Strain of Partial Penetration Welds for ITER

Hiroyuki Takahashi, Masataka Nakahira, Nobuaki Minakawa[1], Atsushi Moriai[1]

Reactor Structure Laboratory, Department of Fusion Engineering Research in JAERI

[1] Research Group for Neutron Scattering, Advanced Science Research Center in JAERI

The vacuum vessel of International Thermonuclear Experimental Reactor is a double-walled "doughnut" structure made of stainless steel SS316L(N)-IG with D-shaped cross section with approximately 6.5m in width and 11.3 m in height. The outer shell (40-60mm plates) is jointed to the rib by welding. The development of the Partial penetration welding by through-wall electron beam welding (EBW) is carried out for the T joint of ITER, because it has advantage from accuracy and cost points of view. In this study, neutron diffraction measurement of residual strain of this new welding had been carried out in order to investigate an applicability of the welding to the vessel. The configuration of weld and the measurement positions of residual strain are shown in Fig. 1. RESA (Neutron Diffractometer for REsidual Stress Analysis) in the JRR-3 is used for the measurement. The measurement was necessary for a long time, because the decrement of neutron was large due to thick stainless steel. Therefore one directional measurement was selected to obtain the residual strain, because the measurement time was short. The conditions and results of the tests are shown in Table 1 and Fig.2. And the tests are continued in the next year.

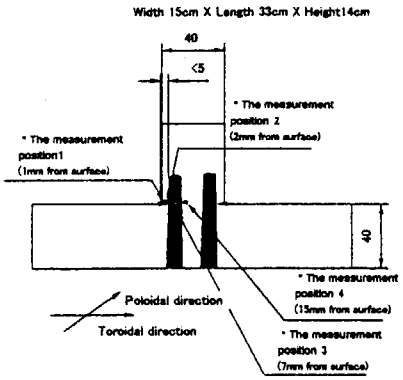


Fig.1 The configuration of weld specimens and the measurement positions

Table.1 Neutron diffraction conditions for the tests

Crystal structure (Miller index)	Wave length of neutron (Å)	Slit(mm)	Interplanar spacing without strain (Å)
Face-centered cubic lattice, fcc (220)	2.0994147	Toroidal 2W X 4h Poloidal 3W X 10h	1.270153146

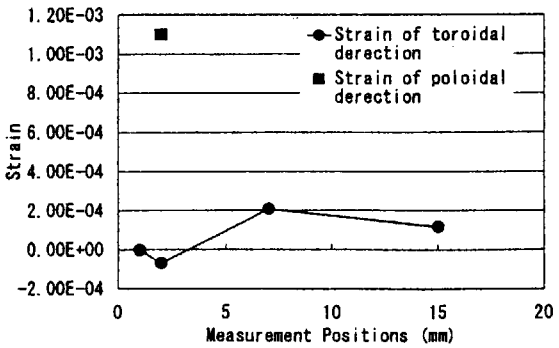


Fig.2 Strain in partial penetration welding by EBW

原子炉：JRR-3M　　装置：RESA (T2-1)　　分野：中性子散乱（構造）

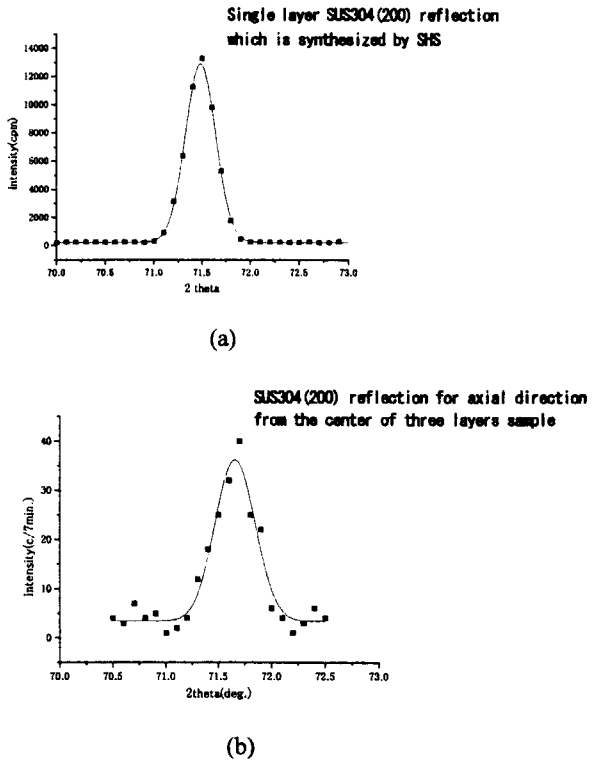


Fig. 2 SUS304 (200) reflection (a) from the rotating single layer SUS304 sample and (b) from the center of three layers sample for axial direction.

gle compared to the peak of single layer one in Fig. 2 (a) means that the middle SUS304 layer in three layers sample is compressed for axial direction at the center of the sample.

The strains estimated for three directions at each position are shown in Figs. 3 (a) to (c). We see that the strain is compressive for axial direction and tensile for radial and hoop directions. However, they change drastically at the position of 15-16 mm from the center. In case of radial direction, it suddenly becomes compressive. These complicate changes of strain relate presumably with the fact that this three layers [WC-10mass%Ni]-[SUS304]-[WC-10 mass%Ni] sample is easy to break, compared to

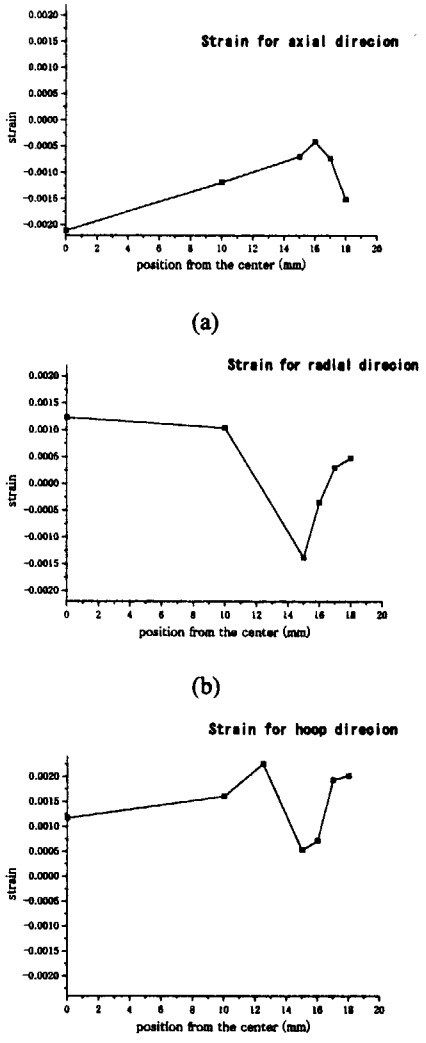


Fig. 3 The strain for three directions at each radial position from the center of three layers sample, estimated from the SUS304 (200) reflection.

[WC-10mass%Ni]-[Ni]-[WC-10mass%Ni], the middle [Ni] layer of which has almost no strain.[1)]

Reference

1) T. Tsujikami, K. Inoue, M. Kawagai, M. Ohyanagi and N. Minakawa, Y. Morii and T. Saitoh, J. Phys. Soc. Jpn., **70** (2001) Suppl. A 523-525.

研究テーマ：三層構造傾斜機能材料の残留ひずみ測定
表題：RESA を用いた傾斜機能材料の残留ひずみ測定

1-1-32

Residual Strain Measurement of Functionally Gradient Material by RESA (II)

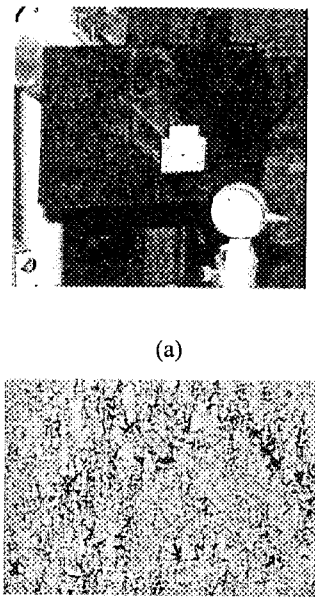
K. Inoue, T. Tsujikami, M. Ohyanagi, M. Sugimoto, M. Komatsu, N. Minakawa[1] and Y. Moriai[1]

Fac. Sci & Tech. Ryukoku Univ. Seta, Otsu 520-2194, Japan
[1]Japan Atomic Energy Research Institute, Tokai, Ibaraki 319-1195, Japan

An internal residual strain of the three-layer functionally gradient material, [WC-10mass%Ni] -[SUS304]-[WC-10mass%Ni], was measured by neutron diffraction with a detection system, RESA. The sample was prepared by self propagating high temperature synthesis (SHS), where the suitable amount of pressed powder elements, WC and Ni, placed on both sides of SUS304 plate are heated up to 2000-3000 ℃ and cooled down rapidly under the static high pressure of 25 MPa. The composite material, [WC-10mass%Ni], is a substitute of a super hard alloy, [WC-10 mass% Co]. We avoided a material containing Co element, because the absorption of thermal neutron by Co nucleus is rather large.

The three layers sample in front of the incident neutron beam and the SEM image of composite [WC-10mass%Ni] layer are shown in Figs. 1 (a) and (b). The diameter of this three layers sample is about 40 mm and the thickness of each layer is about 4 mm. In Fig. 1 (b), the white particle is composed of WC, of which size is several μ m, and the black region is composed of Ni.

The SUS304 (200) reflection from each position of 0, 10, 15, 16, 17 and 18 mm from the center of the sample was measured for axial, radial and hoop directions. The size of the slits for both incident and reflected beams was 2×2 mm^2. The (200) reflection from the rotating SUS304 single layer sample synthesized by the same SHS method was measured with incident beam size



(a)

(b)

Fig. 1 (a) [WC-10mass%Ni]-[SUS304]-[WC-10mass% Ni] in front of the incident beam and (b) the SEM image of the [WC-10mass%Ni] layer.

of 19×19 mm^2 and reflected beam slit of 18×18 mm^2. It was used as a standard for estimating the strain. The SUS304 (200) reflections from the rotating standard sample and from the center of the three layers sample for axial direction are shown in Figs. 2 (a) and (b). In Fig.2 (b), as it takes 7 minutes to obtain one datum point, it takes about three hours to obtain one peak. The fact that the peak of three layers sample in Fig. 2 (b) shifts slightly to higher an-

原子炉：JRR-3M　　装置：RESA(T2-1)　　分野：中性子散乱（構造）

研究テーマ：中性子回折による構造物の残留応力測定
表　　題：中性子回折によるウォータージェットピーニング表面の残留応力測定

1-1-33 Measurement of residual stress at the water-jet-peened surface of type 304 stainless steel by neutron diffraction method

S.Okido, T.Yoshimura, K.Enomoto, M.Hayashi, Y.Morii[1] and N.Minakawa[1]

Mechanical Engineering Research Laboratory, Hitachi Ltd. Hitachi, Ibaraki 317-8511
[1] ASRC, JAERI, Tokai, Ibaraki 319-1195

X-ray or synchrotron diffraction has been used to measure residual stress in the vicinity of a surface. Removing the surface by electrochemical polishing has been necessary when using these methods to measure the stresses in the direction of depth. So residual stress measurement by neutron diffraction was discussed.

A specimen of water-jet-peened type-304 stainless steel was used. Water-jet-peening (WJP) improves the mechanical characteristics of the some materials by deforming the surface plastically applying the pressure arising from the collapse of cavitaties in the highly pressurized water. As a result, compressive residual stress was induced in the vicinity of the surface.

RESA was used in the measurement of lattice strain. The 111 diffraction of γ-Fe in type-304 steel was used in the measurement of strain. The wavelength, λ, was 0.20995 nm. Measurements were performed in steps of 0.1 mm to a depth of 0.4 mm and in steps of 0.2 mm to a depth of 2.0 mm-depth. Cadmium masks were inserted in both the incoming beam and the diffracted beam to define a sampling volume of 0.5x0.5x13 mm^3. The stresses were obtained from Hooke's law using lattice strains in three directions. For 111 diffraction the Young's modulus, E_{111}, was 231 GPa and the Poisson's ratio, ν_{111}, was 0.19. The characteristic x-ray of Cr K_β was used in the x-ray diffraction measurements. The stress constant, K, was –366 MPa/deg.

The results on surface residual stress that were obtained are shown in Fig. 1. At a depth of 0.125 mm the respective values of residual stress at X and Y directions were compressive and at about 400 MPa and 200 MPa. These compressive stresses decreased rapidly and changed to tensile at a depth of 0.3 mm. The values of residual stress in the Y direction fluctuated in comparison with those in the X direction. The value of residual stress in the Z direction at the surface was 0MPa and appeared to tensile stress by a depth of 0.5mm. These stresses, in all directions, disappeared at depths greater than 1 mm.

The values of residual stress obtained by x-ray diffraction are also shown in Fig. 1. It was found that the result for residual stress as obtained by neutron diffraction agreed with those from x-ray diffraction. This result suggests that it should be possible to measure the value of residual stress at the surface by neutron diffraction.

Peak broadening of diffraction curve results from strain gradients within the sampling volume. Fig. 2 showed the difference between the peak widths for peened and non-strained material. This result showed that these were strain gradients at the surface and at a depth of 0.3 mm. Also, the peak width in the Y direction was greater than that in the X direction. These results explain the phenomena seen in Fig. 1. In residual stress measurement at the surface, it should be necessary to evaluate the peak width as a way of grasping the accuracy of measurement by neutron diffraction.

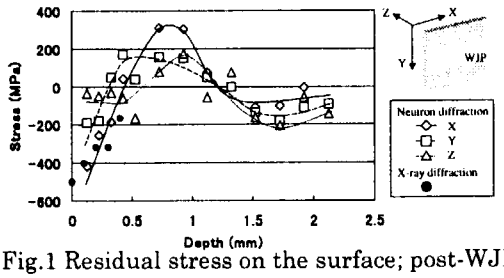


Fig.1 Residual stress on the surface; post-WJP

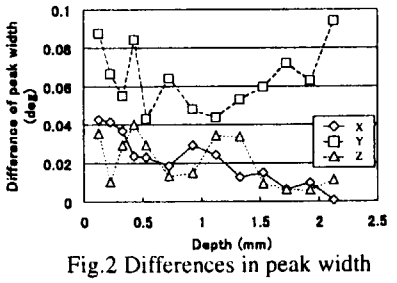


Fig.2 Differences in peak width

原子炉：JRR3M　　装置：RESA(T2-1)　　分野：中性子散乱（構造）

研究テーマ：γ-α 光異性化反応における水素移動の機構解明

表題：単結晶内での光反応による構造変化の FONDER による観察

1-1-34

Photo-Induced Structural Change in a Single Crystal Observed by FONDER Diffractometer

T. Ohhara, T. Sosoya, H. Uekusa, T. Ozeki, Y. Ohashi and Yukio Noda[1]

Department of Chemistry and materials Science, Tokyo Institute of Technology, Meguro-ku, Tokyo 152-8551, Japan; [1] Institute of Multidisciplinary Research for Advanced Materials Tohoku University, Aoba-ku, Sendai 980-8577, Japan

Introduction

The chiral 1-cyanoethyl group bonded to the cobalt atom in some cobaloxime complex crystals was racemized with retention of the single crystal form when the crystal was irradiated with a xenon lamp.[1] Recently the bulkier bis(ethyoxycarbonyl)ethyl group was found to be racemized with out degradation of the single crystal from. Since the bis(ethoxycarbonyl)ethyl group is too bulky to rotate in the crystalline lattice, the inversion of the group was assumed to occur in the different process. In order to make sure the mechanism, the hydrogen atom bonded to the chiral carbon atom of the bis(ethoxycarbonyl)ethyl group was replaced with the deuterium atoms as shown in Fig. 1(a) and the complex crystal after irradiation was analyzed by neutron diffraction.

Experimental

A crystal was irradiated with the xenon lamp for three days. The structure was analyzed by X-rays using a small part of the irradiated crystal. About 50 % of the *(R)*-bis(ethyoxy-carbonyl)ethyl group was inverted to the opposite configuration. The remaining part of the irradiated crystal was mounted on the FONDER diffractometer at T2-2 port. The three dimensional intensity data were collected with the diffractometer. The wave length was 1.5729 Å. The structure was analyzed using the data. Since full of the intensity data was not obtained yet, the positional and thermal parameters of non-hydrogen atoms and the occupancy factor of the produced *(S)*-bis(ethyoxycarbonyl)ethyl were fixed in the refinement.

Result and Discussion

The deuterium atom bonded to the chiral carbon atom is preserved after the group was inverted to the opposite configuration as shown in Fig. 1(b). This result clearly indicates that the inversion of the bulky bis(ethyoxy-carbonyl)ethyl proceeds in the same way as that of the small cyanoethyl group.

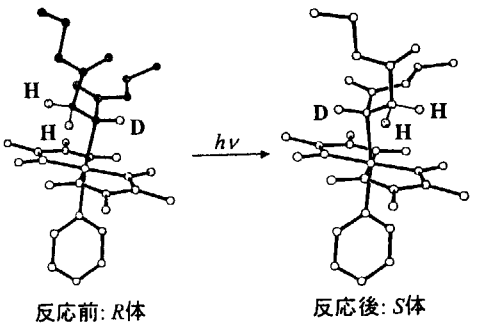


Fig. 1 (a) (b)

[1] Takashi Ohhara, Jun Harada, Yuji Ohashi, Ichiro Tanaka, Shintaro Kumazawa and Nobuo Niimura, *Acta Cryst.*, **B56**, 245-253 (2000).

研究テーマ ： Pt, Pd-M 合金(M=Cr,Mn)の構造揺らぎと磁性との関連性についての研究
表題：スピングラス合金 Pt-12 at.%Mn からの磁気散漫散乱

1-1-35
Magnetic diffuse scattering in Pt-12 at.% Mn spin-glass alloy

M. Takahashi, T. Sembiring, H. Saitoh, K. Ohshima, Y. Noda[1], N. Takesue[2] and T. Shishido[3]

Institute of Materials Science, University of Tsukuba, Tsukuba 305-8573, JAPAN, [1]Institute for Multidisplinary Research for Advanced Materials, Tohoku University, Sendai 980-8577, JAPAN, [2]Neutron Scattering Laboratory, Institute of Solid State Physics, University of Tokyo, Ibaraki 319-1195, JAPAN, [3]Institute for Materials Research, Tohoku University, Sendai 980-8577, JAPAN

We have performed neutron scattering measurements on a single crystal of Pt-12 at.% Mn alloy, annealed at 673 K and gradually cooled to room temperature, in order to observe magnetic diffuse scattering. A spectrometer FONDER was used for this purpose, which is installed at T2-2 beam port of the thermal guide at the JRR-3M research reactor of JAERI. Fig. 1 shows observed intensity contour map around (1/2,0,0) on $(0\bar{1}1)$ reciprocal plane at 10 K. The wavelength of the incident beam was 2.44 A and the contamination of higher-order high energy neutrons was eliminated by a pyrolytic graphite filter. The data show twofold splitting, whose maxima are centered at (1/2,±0.06,±0.06). From the scan along $[01\bar{1}]$ direction, the diffuse maxima are also observed at (1/2,±0.06,∓0.06). This was confirmed by the measurement of the pattern on (100) plane. The maxima are decreasing with increasing temperature and disappear at room temperature. On the other hand, we could not find such diffuse maxima at (1/2, 0, 0) for the quenched sample.

In order to explain the splitting, a Fermi surface imaging idea is introduced. The spin-density wave peaks appear in the reciprocal lattice at the position given by a wave-vector Q spanning the flat portion of the Fermi surface. In the annealed sample, ABC_6 type atomic order, whose structure was determined by X-ray and electron diffraction methods, has new Brillouin zones in compared with those for the disordered FCC structure. Around the 1/2,0,0 position, Fermi vectors from two reciprocal lattice points, 0,0,0 and 1,0,0, contribute to construct the splitting. The results indicate a strong relation between an atomic order and the spin structure of SDW in the alloy.

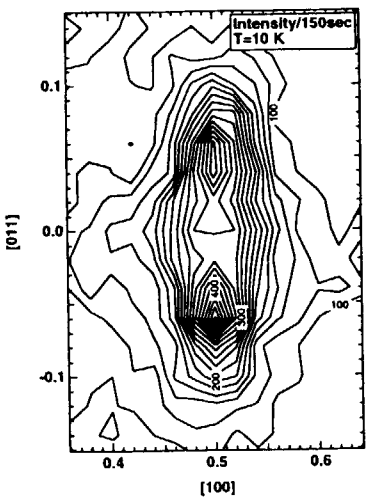


Fig. 1 ： Magnetic diffuse intensity distribution around (1/2,0,0) on the (110) plane taken at 10 K for the annealed sample.

JRR-3M, FONDER, 1. Structures & Exicitations

研究テーマ：アンモニウム塩におけるプロトンゼロ点分布の単結晶に中性子回折法による研究
表題：ヘキサクロロ白金酸アンモニウムにおけるプロトンゼロ点分布の単結晶中性子回折による研究

1-1-36
Zero Point Distribution of Protons in Ammonium Hexachloroplatinate by Single Crystal Neutron Diffraction

T. Matsuo[1], N. Onoda-Yamamuro[2], O. Yamamuro[1], Y. Fukuda[3], H. Kimura[3] and Y. Noda[3]

1) Department of Chemistry, Graduate School of Science, Osaka University, Toyonaka, Osaka
2) Department of Natural Sciences, College of Science and Engineering, Tokyo Denki University, Saitama
3) Institute of Multidisciplinary Research for Advanced Materials, Tohoku University, Katahira, Sendai

Introduction

Some of the deuterated ammonium hexachlorometallates undergo phase transitions at low temperature which the corresponding normal ammonium compounds do not[1]. The transition entropy depends on the metal element in the complex anion, but it is invariably larger than R (= 8.3145 J / K mol). This suggests an interesting possibility that each of the protons belonging to the ammonium ions are distributed over a set of positions dictated by the cubic symmetry. For deuterated ammonium ions the multiple positions are a consequence of orientational disorder. For the hydrogenous ammonium compounds, the crystal symmetry is cubic even at the lowest temperature. Therefore, a multi-maximum proton distribution, if actually observed, should be a characteristic of the ground state of the crystal. As this is a hitherto unknown aspect of a crystal structure, we regard the possibility worth pursuing by neutron diffraction. We have performed a low temperature neutron diffraction on ammonium hexachloroplatinate single crystals, using the recently completed diffractometer FONDER at JRR-3M.

Experiment

The sample ($(NH_4)_2PtCl_6$) was prepared from ammonium chloride and hexachloroplatinic acid dissolved in water by slow evaporation of the solvent. Single crystals of an appropriate size (ca. 3.5mm) was chosen and fixed to the cold finger of a closed-cycle refrigerator mounted on the diffractometer. Diffraction data were collected at T = 7 and 35 K. The neutron wavelength was 1.5729 Å. In total 71 (*hkl*) peak intensities were determined. Because of the high symmetry of the crystal, several equivalent Bragg peaks occurred within the available ranges (2θ<=150 deg.) of the diffraction angle for many of the indices. All peak intensities were collected, equivalent ones compared to check the consistency and then averaged.

Results

All the peaks observed were consistent with the $Fm3m$ symmetry. The cubic lattice constant was 9.766 A and 9.772 Å at 7 and 35 K, respectively. The lattice constant from high resolution neutron powder diffraction is 9.7429 Å at 6 K in good agreement with the present values.
Determination of the structure is in progress and will be reported in due course.

[1] T. Matsuo, A. Inaba, O. Yamamuro and N. Onoda-Yamamuro, *J. Phys.*: Condensed Matter, **12**, 8595-8606 (2000).

研究テーマ：ＣｕＧｅＯ₃の中性子非弾性散乱
表題：スピン・パイエルス系ＣｕＧｅＯ₃のフォノン測定

1-1-37 Phonon Measurement on the Spin-Peierls System $CuGeO_3$

M. Nishi[1], H. Kadowaki[2], S. Katano[3], Y. Fujii[1], K. Kakurai[1] and J. Akimitsu[4]

[1]*Neutron Scattering Laboratory, ISSP, University of Tokyo, 106-1, Shirakata, Tokai-mura, Ibaraki*
[2]*ASRC, JAERI, Tokai-mura, Ibaraki*
[3]*Dept. of Physics, Tokyo Metropolitan University, Hachiohji, Tokyo*
[4]*Dept. of Physics, Aoyama-Gakuin University, Chitosedai Setagayaku, Tokyo*

Magnetic energy of the dimerized singlet pair is lower than that of homogeneous antiferromagnetic system theoretically. Spin-Peierls transition is the magnetic phase transition from the paramagnetic state to the singlet ground state in S=1/2 spin system with the lattice dimerization simultaneously. With the discovery of the first inorganic spin-Peierls compound $CuGeO_3$ by Hase *et al.* in 1993 [1], many efforts to clarify the spin-Peierls mechanism were performed theoretically and experimentally. The soft phonon mode which is expected in the standard spin-Peierls transition by Cross and Fisher [2] has not been observed. In the case of organic spin-Peierls compound $MEM(TCNQ)_2$ (T_{sp}=19 K), a soft phonon mode with the energy of 1.05 meV was observed by Raman scattering [3]. In the TTF-CuBDT (T_{sp}= 11 K) the energy of soft mode was also obtained to 1.4 meV by x-ray diffuse scattering [4]. Then we expect to find the soft mode of $CuGeO_3$ with the energy of about 1 meV in considering the spin-Peierls transition temperature of 14 K. Recently, the longitudinal optical phonon dispersion along b*-axis was determined by the inelastic neutron scattering [5] which mode behaves like acoustic phonon branch with small energy difference. Inelastic neutron scattering is performed to measure the low-lying phonon of $CuGeO_3$. ISSP-HER triple axis spectrometer was used for the experiment at C1-1 port of guide hall at JRR-3M of JAERI in Tokai. The experimental condition with the horizontal focussing analyzer with no collimation was used. The temperature dependence of the phonon spectrum at (0, 3, 0) was measured below 250 K. (0, 3, 0) is not superlattice point but in the case of the order disorder transition of $KDCO_3$ critical diffuse

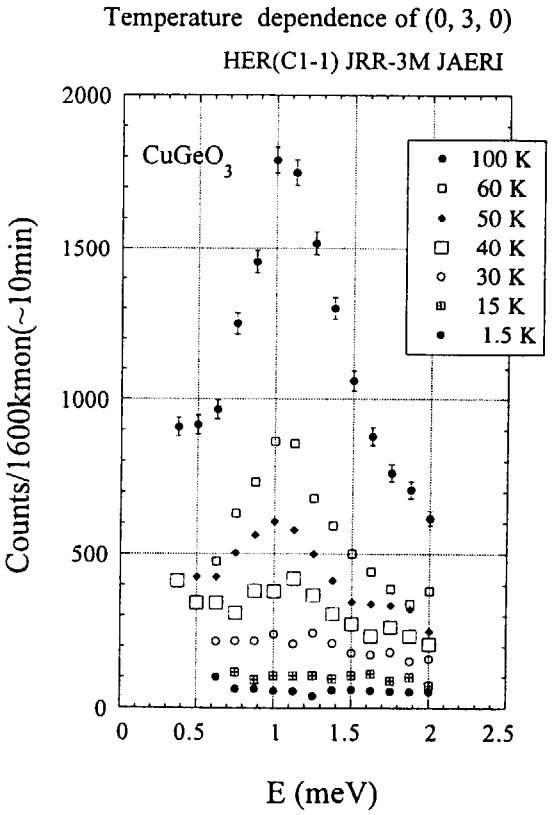


Fig. 1. The temperature dependence of the phonon peak profiles at Q=(0,3,0) at sevral temperatures.

scattering intensity around main peak is stronger than that around superlattice peak [6]. The full width of half maximum (FWHM) (~0.2 meV) and the central energy (~0.9 meV) of the phonon peak does not depend the temperature. Usually the temperature dependence of phonon intensity is described by Bose factor and the intensity decrease from 250 K to 100 K is consistent to the formula. However, below 60 K the integral intensity of phonon spectrum decrease abruptly in discrepancy from Bose factor curve. From the mode analysis the anomalous decrease of phonon intensity is speculated to stem from the short-range order of the lattice dimerization along *c*-axis. The spin-Peierls transition of $CuGeO_3$ is not displacive type but order-disorder type due not to be able to observe the soft phonon mode.

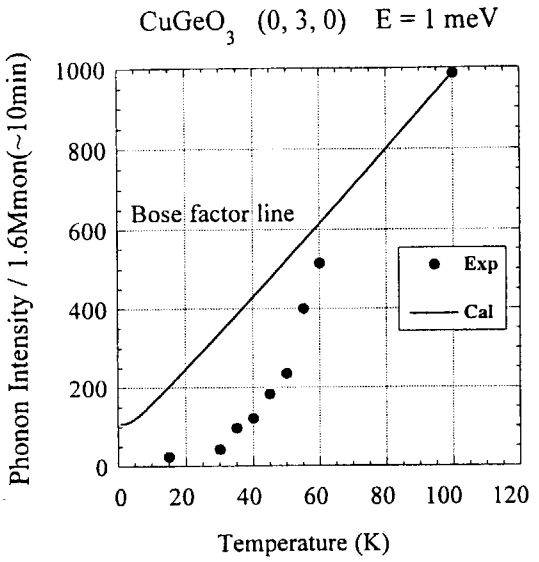


Fig. 2. The temperature dependence of phonon intensity of (0,3,0) as shown by closed circles. The intensity decrease from 250 K to 100 K is consistent to the Bose factor.

Reference

[1] M. Hase, I. Terasaki and K. Uchinokura, Phys. Rev. Lett. **70** (1993) 3651.

[2] M. Cross and D. S. Fisher, Phys. Rev. **19** (1979) 402.

[3] Y. Tanaka, N. Satoh, K. Nagasaka, J. Phys. Soc. Jpn. **59** (1990) 319.

[4] D.E. Moncton, R.J. Birgeneau, L.V. Interrante and F. Wudl, Phys. Rev. Lett **39** (1977) 507.

[5] M. Nishi, K. Kakurai, Y Fujii, S Katano, J Akimitsu, M Yethiraj and JA Fernandez-Baca, J. Phys. Chem. Solids **60** (1999) 1109.

[6] K. Kakurai, T. Sakaguchi, M. Nishi, C.M. E. Zeyen, S. Kashida and Y. Yamada, Phys. Rev. **B 53** (1996) R5974.

研究テーマ：層状熱電変換材料 Na_x $(Co_{1-y}Mn_y)_2O_{4-\delta}$の精密構造決定と磁気励起
表題：$La_{1-x}Ca_xMnO_3$単結晶 (x= 0.15 および 0.20) のマグノンギャップ

1-1-38 Magnon gap in single crystals of $La_{1-x}Ca_xMnO_3$ with x= 0.15 and 0.20

Shahnaz Begum[1], Y. Ono[1] , Y. Tomioka[2], Y.Tokura[2,3] and T. Kajitani[1]
[1] Department of Applied Physics, Graduate School of Engineering,
Tohoku University, Sendai 980-8579, Japan
[2]Joint Research Centre for Atom Technology (JRCAT), Tsukuba, 305, Japan
[3] Department of Applied Physics, University of Tokyo, Tokyo 113-0033.

Neutron scattering is a powerful tool to study the staic and dynamic properties of perovskite manganites $La_{1-x}A_xMnO_3$ (A= Sr, Ca etc.) which renewed interest after the discovery of colossal magnetoresistance (CMR) near Curie temperature T_c. A gap of 1.2 meV was observed at low temperature in the spin wave dispersion curve for $La_{1-x}Ca_xMnO_3$ sample with x=0.05 and 0.08 [1]. The uniaxial anisotropy, a consequence of the ordering of the d_z^2 orbitals, is resposible for the spin gap in an insulating samples and thus no gap in spin excitation is expected for the FM manganites because rapid hopping of d_z^2 electrons in the metallic phase renders spin space isotropic. Recently, it has been suggested that the onset of metalic state is hindered even when x = 0.25 due to the formation of non-percolating FM clusters [3]. So it may not be plausible to observe large gap at $x \leqq 0.2$.

We performed inelastic neutron scattering experiments on $La_{1-x}Ca_xMnO_3$ with x=0.15 and 0.20 single crystal samples to study the low energy excitation or spin dynamics of this system $La_{1-x}Ca_xMnO_3$. Single crystal samples were prepared by Y. Tomioka, using the travelling solvent floating zone (TSFZ) method. Neutron scattering experiments were carried out using the TOF-type cold neutron spectrometer AGNES (λ =4.22 Å), installed at JRR-3M reactor in JAERI.

Figures 1 and 2 show the temperature dependent changes of the inelastic scattering intensities of $La_{1-x}Ca_xMnO_3$ with x = 0.15 and x=0.20 respectively, in the counter group situated at 2-theta = 29-37 degrees (Q= 1/2 0 1/2 reciprocal point) . Inelastic peaks are observed only in the FM region and smearing in the PM region.

The observed peaks at -1.0 meV for x=0.15 and at 0.9 meV for x=0.20 me V are the evidence of magnon gap due to single ion anisotropy term in the Heisenberg Hamiltonian, i.e., $-D\sum_i S_{iz}2$ (z axis along c) [1, 2]. It has been suggested that the gap energy decreases with increasing x, indicating a strong decrease of anti-ferromagnetic coupling by doping [1, 2].

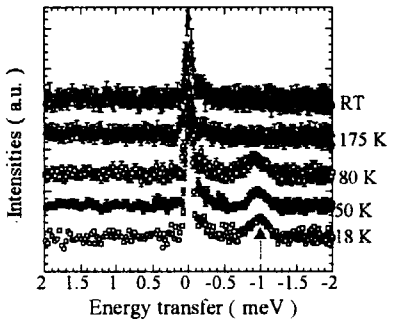


Figure 1 : Temperature dependence of the scattering intensities observed at the counter group situated at 2-theta=29-37 degree (Q= 1/2 0 1/2).

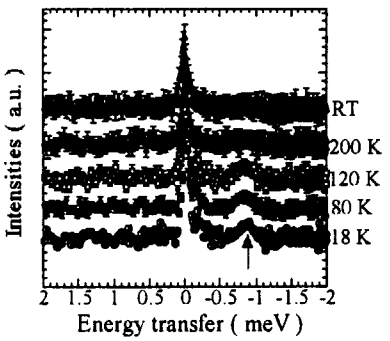


Figure 2 : Temperature dependence of the scattering intensities observed at the counter group situated at 2-theta=29-37 degree (Q= 1/2 0 1/2).

References :

[1] F. Moussa et al. Phys. Rev.B, 60 (1999) 12299.
[2] F. Moussa et al. Phys. Rev.B, 54 (1996) 15149.
[3] J. Alonso et al. Phys. Rev.B, 62 (2000) 11328.

1. 中性子散乱 2) 磁　性

1. Neutron Scattering　2) Magnetism

This is a blank page.

研究テーマ：ﾗﾝﾀﾉｲﾄﾞ－白金元素を含む複合酸化物の磁気構造
表　題　：反強磁性ｺﾊﾞﾙﾄ硫化物$BaLa_2CoS_5$の磁気構造

1-2-1 Magnetic Structure of the Antiferromagnetic Manganese Sulfide $BaLa_2CoS_5$ by Powder Neutron Diffraction Measurements

M. Wakeshima, Y. Hinatsu, Y. Ishii[1], Y. Shimojo[1] and Y. Morii[1]

Division of Chemistry, Graduate School of Science, Hokkaido University, Sapporo 060-0810, Japan
[1] Japan Atomic Energy Research Institute, Tokai-mura, Ibaraki 319-1195, Japan

A quaternary cobalt sulfide $BaLa_2CoS_5$ has a tetragonal structure with space group *I*4/*mcm*. Its magnetic susceptibility showed that the Co^{2+} ions were in the antiferromagnetic state below 63 K [1].

Powder neutron diffraction patterns of $BaLa_2CoS_5$ were measured at 10 K and room temperature (RT) using a High Resolution Powder Diffractometer (HRPD) in the JRR-3M reactor with a neutron incident wave length (λ = 1.823 Å). The Rietveld analyses were performed with the neutron diffraction data.

Figure 1 shows the observed and calculated diffraction patterns for $BaLa_2CoS_5$ at 10 K and RT. The calculated pattern at RT is in good agreement with the observed one (R_{wp} = 13.61 %, R_I / % = 4.34). Compared with the pattern at RT, no additional peaks appear, but some peaks are observed to be much stronger in intensity at 10 K. This result indicates that the Co^{2+} ions in $BaLa_2CoS_5$ has a long-range magnetic orderings. The magnetic structure of Co^{2+} at 10 K was determined to have a collinear antiferromagnetic structure (space group $I\bar{4}$) as shown in Fig. 2. The magnetic moment of Co^{2+} is estimated to be 3.53 μ_B and determined to lie in a parallel direction with the *c*-axis. The reliability factors R_{wp} and R_I for 10 K are 14.80 and 3.43 %, respectively.

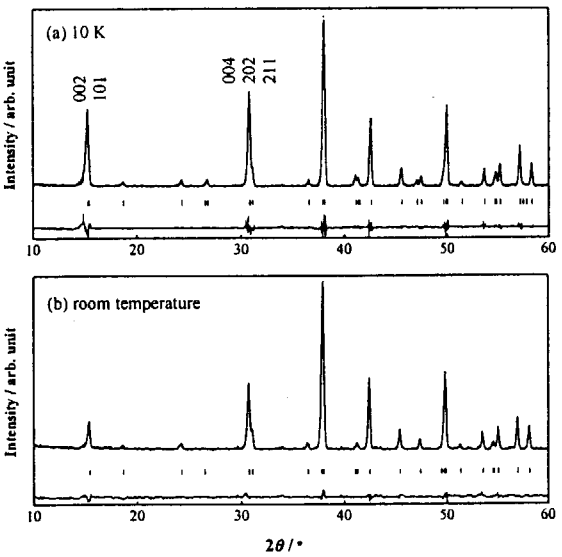


Fig. 1 Powder neutron diffraction patterns fitting for $BaLa_2CoS_5$.

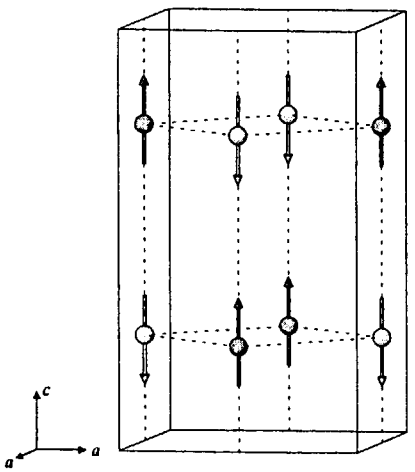


Fig. 2 Magnetic structure for $BaLa_2CoS_5$.

Reference

1) M. Wakeshima and Y. Hinatsu, J Solid State Chem., **159**, (2001) 163-169.

原子炉：JRR-3M　　装置：HRPD (1G)　　分野：中性子散乱（磁性）

研究テーマ：ランタノイド-白金族元素を含む複合酸化物の磁気構造
表題：$Ba_3NdRu_2O_9$の結晶構造と磁気構造

1-2-2 Crystal and Magnetic Structures of $Ba_3NdRu_2O_9$

Y. Doi, Y. Hinatsu, Y. Shimojo[1] and Y. Ishii[1]

Division of Chemistry, Graduate School of Science, Hokkaido University, Sapporo 060-0810, Japan
[1]Japan Atomic Energy Research Institute, Tokai-mura, Ibaraki 319-1195, Japan

A quaternary oxide $Ba_3NdRu_2O_9$ has a 6H-perovskite structure with space group $P6_3/mmc$ at room temperature. Its magnetic susceptibility and specific heat showed that the crystal phase transition and magnetic transition occurred at *ca.* 120 K and 24 K, respectively [1].

In order to determine the crystal and magnetic structures at low temperature, powder neutron diffraction patterns of $Ba_3NdRu_2O_9$ were measured at 10 K, 60 K, 180 K, and room temperature using a High Resolution Powder Diffractometer (HRPD) in the JRR-3M reactor with a neutron incident wave length (λ = 1.82268 Å). The Rietveld analyses were performed with the neutron diffraction data.

Figure 1 shows the observed and calculated diffraction patterns. The crystal structures at 180 K and room temperature are the 6H-perovskite structure (a = 5.9319(1) Å and c = 14.7589(3) Å at room temperature; z = 2). Data collected at 10 K and 60 K indicate that the crystal structures at these temperatures have a lower symmetry than that at 180 K. It has been found that the analysis using a structure model, which has a monoclinic symmetry with space group $C2/c$ (No. 15), gives a good agreement with experimental data (a = 5.9173(3) Å, b = 10.2425(5) Å, c = 14.7663(9) Å, and b = 90.819(2)° at 180 K; z = 4). The crystal structure at 60 K is illustrated in Fig. 2. Data collected at 10 K show that $Ba_3NdRu_2O_9$ has a long-range ferromagnetic ordering of Nd^{3+} ions. The ordered magnetic moment of Nd^{3+} ions is 1.65(8) μ_B. The direction of ordered moments is parallel to the c-axis.

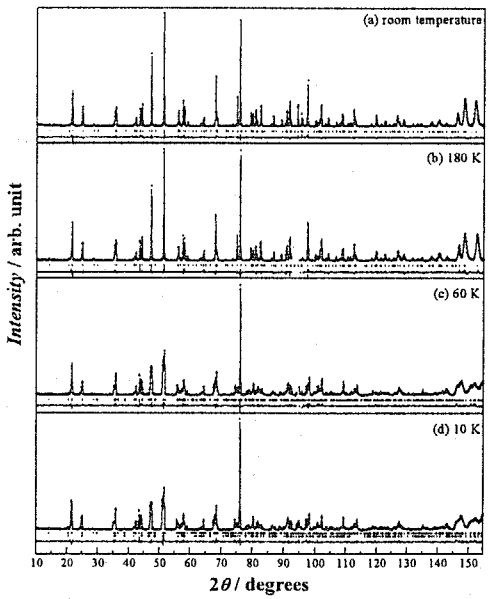


Fig.1 Powder neutron diffraction patterns fitting for $Ba_3NdRu_2O_9$.

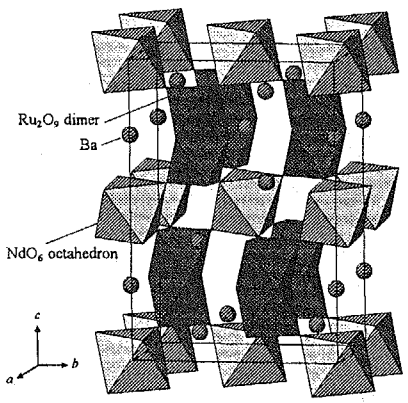


Fig.2 The crystal structure of $Ba_3NdRu_2O_9$ at 60 K.

Reference

1) Y. Doi, Y. Hinatsu, Y. Shimojo, and Y. Ishii, J. Solid State Chem. in press.

原子炉：JRR-3M　　装置：HRPD (1G)　　分野：中性子散乱（磁性）

研究テーマ：中性子散乱による強相関電子系の研究
表題：$La_{0.5}Pr_{0.5}CrO_3$の磁性

1-2-3 Magnetic properties of $La_{0.5}Pr_{0.5}CrO_3$

K. Yoshii, A. Nakamura [1], Y. Shimojyo [2]
Synchrotron Radiation Research Center, Japan Atomic Energy Research Institute (JAERI), Mikazuki, Hyogo 679-5148, Japan
[1] *Department of Materials Science, Japan Atomic Energy Research Institute (JAERI), Tokai, Ibaraki 319-1195, Japan*
[2] *Advanced Science Research Center, Japan Atomic Energy Research Institute (JAERI), Tokai, Ibaraki 319-1195, Japan*

Perovskite chromium oxides $LnCrO_3$ (*Ln*: lanthanides) have an orthorhombic crystal structure (space group *Pnma*) and exhibit so-called canted-antiferromagnetic order of the localized Cr^{3+} moments ($3d^3$) at Néel temperatures (T_N) of ~110-280 K [1]. In this work, magnetic properties of a solid solution between $LaCrO_3$ (T_N~280 K) and $PrCrO_3$ (T_N~240 K), $La_{0.5}Pr_{0.5}CrO_3$, have been investigated. [1)]

Figure 1 shows the magnetization plotted against temperature, which was measured in a field-cooled mode with the applied field of 100 Oe. [1)] A canted-antiferromagnetic transition is observed at T_N~260 K. The magnetization exhibits a negative polarity below ~160 K, indicating that its direction is opposite to that of the applied field. Such a state is not in a thermal equilibrium. The largest absolute value of the negative magnetization (at 2 K) is ~30-40 times as large as that of positive magnetization observed at ~220 K.

To determine magnetic structures at low temperatures, powder neutron diffraction measurements were performed with a high resolution powder diffractometer (HRPD). Figure 2 shows the result at 4 K. A Rietveld analysis using the program RIETAN provided the lattice parameters of a=5.4722(2), b=7.7255(3) and c=5.4740(2) Å (space group *Pnma*), and an antiferromagnetically ordered Cr^{3+} moment of 2.50(5) μ_B/Cr along the b-axis. A weak ferromagnetic component plausibly contributing the negative magnetization has not been clearly observed. Further studies are required to reveal the origin of the characteristic magnetic behavior of this compound.

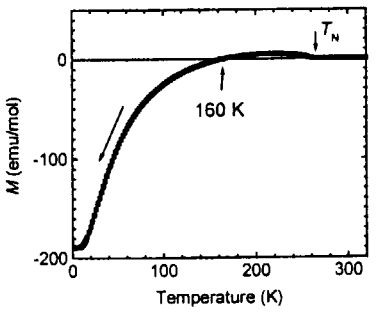


Fig. 1 Magnetization plotted against temperature.

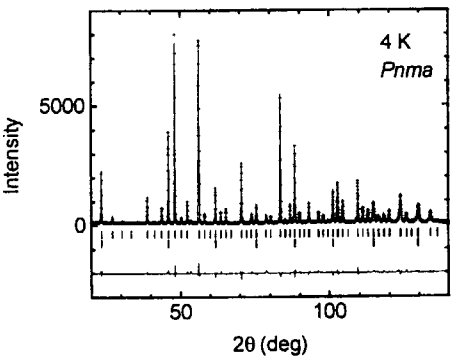


Fig. 2. Powder neutron diffraction patterns at 4 K. The largest magnetic Bragg peak is observed at 2θ~23.5°.

Reference

1) K. Yoshii and A. Nakamura, J. Solid State Chem., **155** (2000) 447-450.

原子炉：JRR-3M　　装置：HRPD(1G)　　分野：中性子散乱（磁性）

研究テーマ：量子凝縮相の基礎研究
表　題　　：$U_3Pd_{20}Si_6$の結晶及び磁気構造

1-2-4 Crystal and Magnetic Structures in a localozed 5f system $U_3Pd_{20}Si_6$

N. Tateiwa[1], N. Metoki[2], Y. Koike[2,3], K. Oikawa[4], N. Kimura[5], H. Aoki[5], and T. Komatsubara[5]

[1]*Graduate School of Science Department of Physics, Osaka University, Toyonaka, Osaka 560*
[2]*Advanced Science Research Center, JAERI, Tokai, Ibaraki 319-1195*
[3]*Japan Science and Technology Corporation, Kawaguchi, Saitama 332-0012*
[4]*Institute of Materials Structure Science, High Energy Accelerator Research Organization 1-1 Oho, Tsukuba, Ibaraki 305-0801*
[5]*Center for Very Low Temperature Science, Tohoku Univ., Sendai 980-8545*

Recently we found a new uranium compound $U_3Pd_{20}Si_6$ and reported its physical properties[1,2]. Two successive magnetic transitions were found at T = 19 K and 2 K, respectively in the electrical resistivity, magnetic susceptibility and specific heat measurements. We studied detailed crystal and magnetic structure of this compound.

Neutron scattering experiments were carried out at the research reactor JRR-3M in Japan Atomic Energy Research Institute (JAERI). Powder diffraction profiles were measured using high-resolution powder diffractometer (HRPD). The elastic neutron scattering experiments of polycrystalline as well as single crystal samples were carried out using triple-axis-spectrometers TAS1 and LTAS, respectively.

Fig.1 shows the high-resolution neutron powder diffraction data of $U_3Pd_{20}Si_6$. The observed profiles were well described by the diffraction pattern of $R_3Pd_{20}X_6$ structure and aluminum sample can. No impurity peak was detected within an experimental accuracy. The refined crystal parameters have been published elsewhere.[2] The crystal structure is schematically shown in Fig. 2.

Fig. 3 shows the powder pattern observed at 7 K, which is the intermediate temperature between the lower and upper transition temperature. After subtracting the powder pattern at 25 K from the data obtained at 7 K, we found the increase of the Bragg intensities with odd integer reflection indices like, (111), (311), (331), etc. The result of this neutron powder diffraction is explained in terms of the magnetic sublattice ordering of the uranium spins on the 8*c*

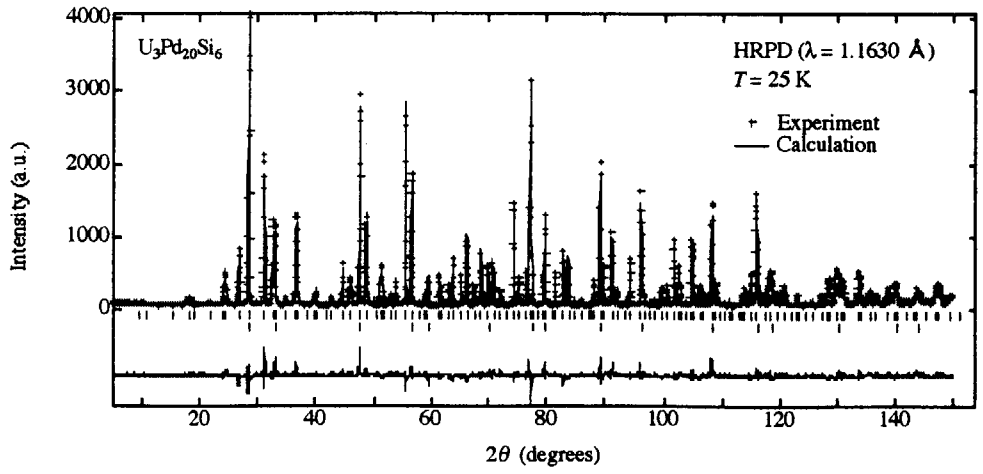


Fig. 1. The high-resolution neutron powder diffraction pattern of $U_3Pd_{20}Si_6$.

原子炉：JRR-3M　装置：HRPD(1G)・TAS-1(2G)・LTAS (C2-1)　分野：中性子散乱(磁性)

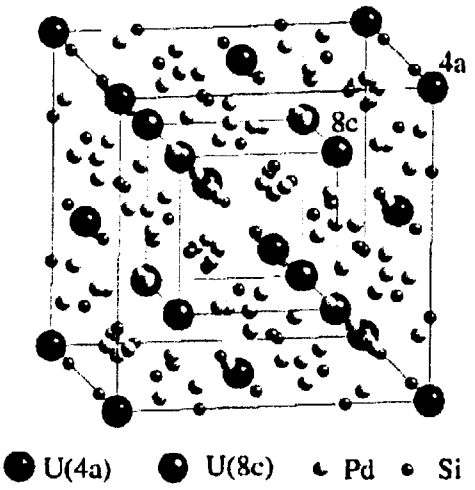


Fig. 2. The crystal structure of $U_3Pd_{20}Si_6$.

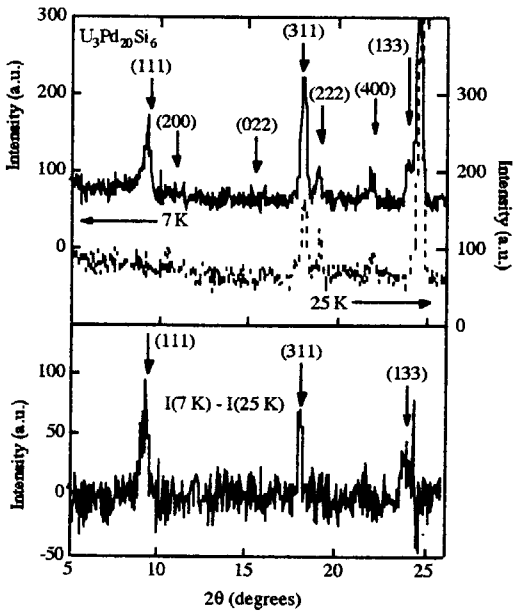


Fig. 3 The powder diffraction profiles at 7 K and 25 K.

site with the propagation vector [111]. From the model calculation the size of the magnetic moment of uranium atoms on 8*c* site was estimated to be 1.73 μ_B/U at 7 K. The direction of the uranium spin can not be determined from the powder diffraction experiments because of the cubic symmetry.

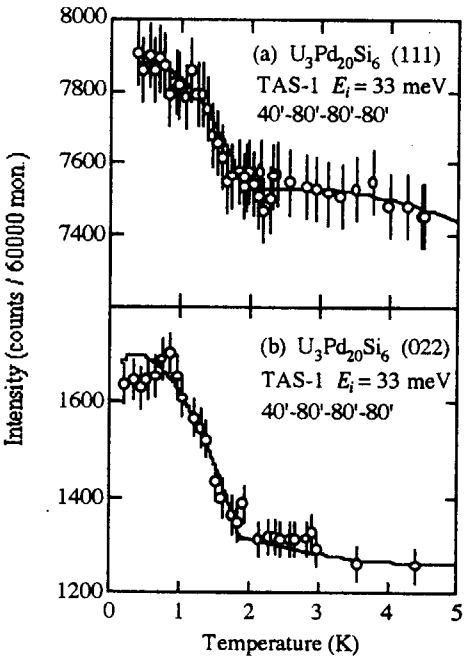


Fig. 4 The temperature dependence of the (111) and (022) peak intensities.

The elastic scattering experiments were also carried out using a single crystal sample with temperature down to 0.2 K. As shown in Fig. 4, the odd and even integer reflections like (111) and (022) showed a steep increase below 2 K. The increase of intensities with even indices reflections is evidence for the existence of the ferromagnetic component below 2 K. These results indicates that the ferromagnetic ordering of uranium spins on 4*a* site below T_C = 2 K.

The detail of the magnetic structure can be studied with single crystal domain sample under magnetic field. This should be studied further to reveal the origin of the unusual coexistence of the rather independent sublattice ferromagnetic and antiferromagnetic ordering.

References

[1] N. Tateiwa et al., J. Phys. Soc. Jpn. **69** (2000) 1517.
[2] N. Tateiwa et al., J. Phys. Soc. Jpn. **70** (2001) 2425.

研究テーマ：中性子散乱による強相関電子系の研究

表　　題：中性子回折による $La_{1-x}Sr_xMnO_3$: x=0.1 の磁気－構造ゆらぎの研究

1-2-5 Neutron Diffraction Study on the Magneto- structural Phase transition in $La_{1-x}Sr_xMnO_3$: x=0.1

M. Watahiki[1,2], J. Suzuki[1], Y. Yamada[1,3], K. Kohn[3]

[1]Advanced Science Research Center, Japan Atomic Energy Research Institute, Tokai- mura, Ibaraki 319-1195, Japan

[2]Japan Science and Technology Corporation, Kawaguchi, Saitama 332-0012, Japan

[3]Advanced Research Center for Science and Engineering, Waseda University, Shinjuku- ku, Tokyo 169-8555, Japan

$La_{1-x}Sr_xMnO_3$ (LSMO: x) has been investigated in connection with its interesting physical properties including CMR effect, charge / orbital ordering, J-T ordering[1)-3)] etc.. In the low concentration range of $x \leq 0.2$, the phase diagram shows complicated features exhibiting the characteristics of strongly correlated electron systems.

We carried out neutron diffraction studies of magneto- structural phase transition in LSMO: 0.1 with TAS- 1 spectrometer installed at JRR3M. A cylindrical sample with size of 15mm × 5mm ϕ were encapsuled in a aluminum sample container with [100]- axis vertical. We used vertically bent PG monochrometer with x=0.23 / nm and 0.151nm. The collimation is 17'- 40'- 40'- B. Fig 1(a) shows the profile of (0, 4, 4) reflection scanned along the b^*- direction. The intensity increases sharply around 100K indicating the on- set of ferromagnetic ordering. In contract, the profile of (0, 3, 4) reflection shows splitting into two peaks peaked at (0, 3, 4) and (0, 3.05, 4). (See Fig. 2(a))

The temperature variation of the integrated intensities of the both spectra are summarized in Fig. 2(b).

Our tentative interpretation is as follows at low temperatures (T≤100K), the system stays in 'two- phase coexistent' state: the one is the ferromagnetic phase, and the other is an antiferromagnetic phase where the magnetic period is doubled along the b - direction as referred to the simple cubic unit cell. At the same time, the lattice of the latter would be slightly distorted as compared with the former. Since the k- odd reflections such as (0, 3, 4) are contributed by the antiferromagnetic structure which are embedded on the slightly strained lattice relative to the mother matrix, the (0, 3, 4) peak would split into two components corresponding to the different lattices of the two phases. In contrast, the k- even reflections such as (0, 4, 4) show a single peak at the 'averaged'

原子炉：JRR-3M　　装置：TAS-1 (2G)　　分野：中性子散乱（磁性）

lattice through out the whole system. Similar behavior has been observed in Martensitic phase transformation in alloys[4]. Further detailed investigations should be necessary to establish the above model.

References

1) Y. Moritomo, A. Asamitsu, and Y. Tokura, Phys. Rev. **B56** (1997) 12190.

2) H. Kawano, R. Kajimoto, K. Kubota, and H. Yoshizawa, Phys. Rev. **B53** (1996) 14709.

3) Y. Yamada, O. Hino, S. Nohdo, R. Kanao, T. Inami, and S. Katano, Phys. Rev. Lett. **77** (1996) 904.

4) W. Lin, H. Spalt, and B. W. Batterman, Phys. Rev. **B13** (1974) 5158.

5) H. G. Smith, N. Wakabayashi, W. P. Crummett, and R. M. Nicklow, Phys. Rev. Lett. **44** (1980) 1612.

6) S. M. Shapiro, Y. Noda, Y. Fujii, and Y. Yamada, Phys. Rev. **B30** (1984) 413.

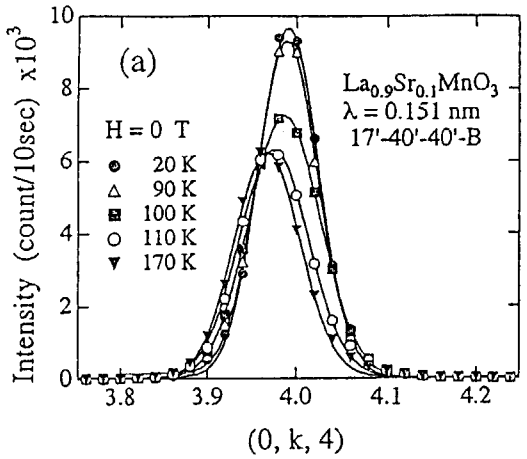


Fig. 1 (a)

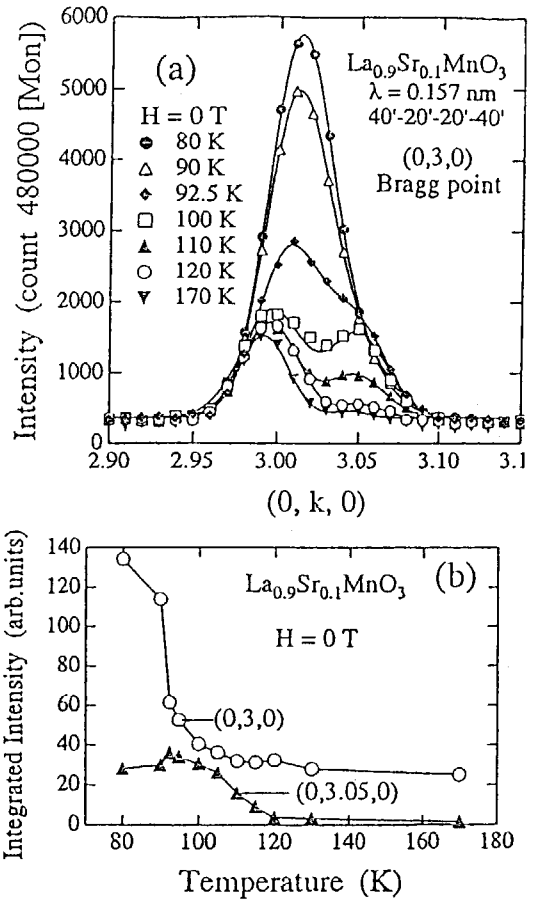


Fig. 2

研究テーマ：中性子散乱による強相関電子系の研究
表　題　：　$Ce_{0.75}La_{0.25}B_6$の秩序相についての中性子散乱研究

1-2-6 Neutron Diffraction Study on the Ordered Phases of $Ce_{0.75}La_{0.25}B_6$

K. Iwasa, M. Kohgi, K. Kuwahara, N. Metoki[1], Y. Koike[1], S. Kunii[2]

Department of Physics, Faculty of Science, Tokyo Metropolitan University, Tokyo 192-0397
[1] A. S. R. C., Japan Atomic Energy Research Institute, Tokai, Ibaraki 319-1195
[2] Department of Physics, Faculty of Science, Tohoku University, Sendai 980-8578

$Ce_xLa_{1-x}B_6$, which crystallize in a cubic structure, are attractive because of strange phase diagrams and ordering of 4f-electron multipoles.

CeB_6 has two phase transition temperatures T_Q = 3.3 K and T_N = 2.3 K at zero magnetic field.[1] An antiferromagnetic (AF) ordered structure in phase III below T_N was found as neutron diffraction at scattering vectors of (1/4, 1/4, 0) and (1/4, 1/4, 1/2).[2] The neutron diffraction experiment revealed a magnetic-field induced AF structure with a propagation vector $\boldsymbol{k}_Q$ = (1/2, 1/2, 1/2) in phase II ($T_N < T < T_Q$).[2] This fact was interpreted as an evidence for the quadrupole ordering with $\boldsymbol{k}_Q$, which was supported by a theory considering the role of 4f-electron multipole interactions.[3]

The remarkable feature of the diluted system $Ce_xLa_{1-x}B_6$ is a new phase IV appearing in a small region of the phase diagram as depicted in Fig. 1.[4-6] Since the dilution of Ce-ion sites may weaken the quadrupole interaction, a simple AF structure has been expected in phase IV with T_N = 1.6 K at zero field. In contrast to such

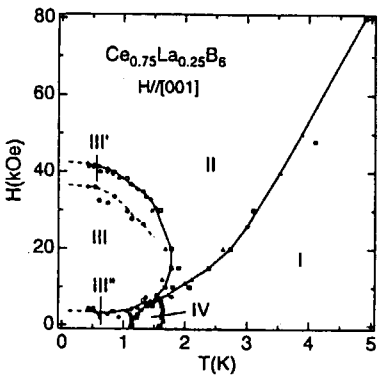


Fig. 1 Phase diagram of $Ce_{0.75}La_{0.25}B_6$ determined by magnetization and sound-velocity measurements.[6]

speculation, no magnetic reflection was observed in our previous neutron-diffraction experiments. The elastic constant C_{44} softening strongly in phase IV indicates that the multipole states take an important role in the nature of phase IV.[6] Magnetization exhibits isotropic behavior in phase IV with a cusp at 1.7 K, while anisotropic larger magnetization is seen in phase III.[5] Recently, magnetization under uniaxial pressure up to 0.1 GPa applied in the [001] direction was measured.[7] The magnetization in

原子炉：JRR-3M　　装置：TAS-1 (2G)　　分野：中性子散乱（磁性）

phase IV under magnetic field H // [001] is almost twice of that under H // [110]. From the pressure-induced anisotropy, a spontaneous magnetic ordering is expected in phase IV. Then, we performed a neutron diffraction experiment for uniaxially pressed $Ce_{0.75}La_{0.25}B_6$.

A single crystal of $Ce_{0.75}La_{0.25}B_6$ enriched with ^{11}B was pressed along the [001] axis up to 0.03 GPa. Temperature was controlled by the dilution refrigerator cryostat. The triple-axis neutron spectrometer TAS-1 was employed with incident energies of 13.7 meV.

We observed magnetic reflections at the scattering vectors Q_1 = (1/4, 1/4, 0) and Q_2 = (1/4, 1/4, 1/2) in phase III. Because these are same as detected for CeB_6,[2] the same AF structure is thought to appear also in phase III of $Ce_{0.75}La_{0.25}B_6$. The behavior that peak intensity at Q_1 saturates below about 0.9 K is similar to the peak at Q_2 from the sample without pressure (measured on the different experiment by TAS-2 spectrometer), as shown in Fig. 2. On the other hand, the peak at Q_2 from the pressed sample increases more gradually with decreasing temperature. The different temperature variations of the peaks at Q_1 and Q_2 indicate that the AF structure suggested for the pure CeB_6[2] is modified due to the diluted and the applied uniaxial pressure. The AF reflections vanish above about 1.2 K, which is consistent with the boundary between phases III and IV determined from the bulk magnetization data. Although we have made careful mesh scans within the reciprocal plane defined by the [110] and [001] axes in phase IV, any magnetic peak was not detected. Thus, phase IV is not a simple magnetically ordered phase.

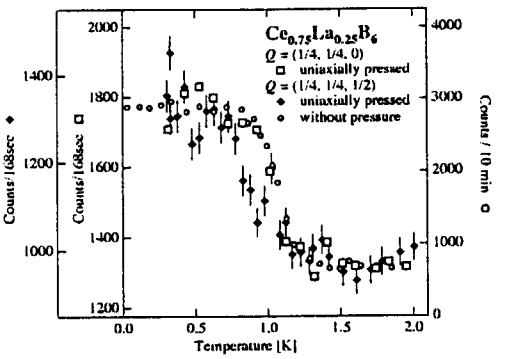


Fig. 2 Temperature dependencies of the AF-peak intensities at Q_1 = (1/4, 1/4, 0) and Q_2 = (1/4, 1/4, 1/2) of $Ce_{0.75}La_{0.25}B_6$.

References

1) N. Sato *et al.*, J. Phys. Soc. Jpn. **53** (1984) 3967-3979, N. Sato *et al.*, *ibid.* **54** (1985) 1923-1932.

2) J. M. Effantin *et al.*, J. Magn. Magn. Mater. **47&48** (1985) 145-148, W. A. C. Erkelens *et al.* *ibid.* **63&64** (1987) 61-63.

3) O. Sakai *et al.*, J. Phys. Soc. Jpn. **66** (1997) 3005-3007.

4) M. Hiroi *et al.*, J. Phys. Soc. Jpn. **66** (1997) 1762-1770.

5) T. Tayama *et al.*, J. Phys. Soc. Jpn. **66** (1997) 2268-2271.

6) O. Suzuki *et al.*, J. Phys. Soc. Jpn. **67** (1998) 4243-4250.

7) T. Sakakibara *et al.*, to be published in Physica B (proceedings of SCES2001).

研究テーマ：中性子散乱による強相関電子系の研究
表　題　：ホールをドープした Haldane 系 $Nd_{2-x}Ca_xBaNiO_5$ のスピン揺動

1-2-7 Spin dynamics of hole doped $Nd_{2-x}Ca_xBaNiO_5$

T. Sasaki, T. Yokoo[1], S. Katano[2], K. Kakurai[2], J. Akimitsu

Department of Physics, Aoyama-Gakuin University
[1]Institute of Materials Structure Science, High Energy Accelerator Research Organization (KEK)
[2]Advanced Basic Research Center, Japan Atomic Energy Research Institute (JAERI)

We report here the single crystal study of $Nd_{1.8}Ca_{0.2}BaNiO_5$ to elucidate the spin dynamics of hole doped Haldane chains. Nd_2BaNiO_5 shows the similar behavior with that of Y_2BaNiO_5 above Néel temperature, on the other hand, Haldane gap suddenly increases below Néel temperature, suggesting that Haldane state coexists with antiferromagnetic state below Néel temperature.

Elastic and inelastic neutron measurements were performed on the TAS-1 triple axis spectrometer at JEARI. The sample was mounted with the (H, 0, L) reciprocal space plane parallel to the scattering plane of the triple axis spectrometer.

In $Nd_{1.8}Ca_{0.2}BaNiO_5$ we have confirmed that the peak at 5.5 meV in $Nd_{1.8}Ca_{0.2}BaNiO_5$ is similar to that of $Y_{2-x}Ca_xBaNiO_5$, although the peak is not distinct, because Haldane gap has dumped and the shoulder of Haldane gap has overlapped for this small peak.

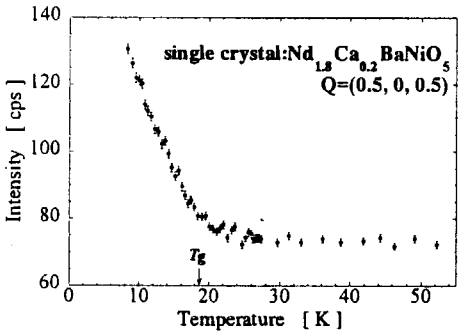


Fig.1 magnetic bragg peak

In $Nd_{1.8}Ca_{0.2}BaNiO_5$ spin-glass like behavior was observed under the zero- and field-cooled susceptibilities at 19K. The temperature is far higher than that of $Y_{1.8}Ca_{0.2}BaNiO_5$. T_N at 19K was determined by measuring the T-dependence of the (0.5, 0, 0.5) magnetic peak (Fig.1), suggesting that spin-glass like state and antiferromagnetic state coexists, and the holes in a Haldane chains influenced by the staggered field have created the ferromagnetic cloud around the holes.

原子炉：JRR-3M　　装置：TAS-1(2G)　　分野：中性子散乱（磁性）

研究テーマ：中性子散乱による強相関電子系の研究
表題：$La_{2-x}Sr_xCuO_4$(x=0.12)の格子不整合ピークの温度依存性

1-2-8 Temperature dependence of the incommensurate peak in $La_{2-x}Sr_xCuO_4$ (x=0.12)

K. Yamada, S. Katano[1], M. Sato[1*], K. Kawashima

Institute for Chemical Research, Kyoto University
[1] Advanced Science Research Center, Japan Atomic Energy Research Institute

It is well known that a static or quasistatic incommensurate magnetic order develops below near the superconducting transition temperature T_c in the underdoped $La_{2-x}Sr_xCuO_4$ (LSCO) and the oxygen-doped La_2CuO_4. To clarify whether the magnetic order spatially coexists or phase separates with the superconducting phase is important for the elucidation of superconducting property and mechanism of high-T_c cuprates.

In both orthorhombic systems, four peaks are observed around the tetragonal (1/2 1/2 0) in the (h k 0) zone and the peak positions are slightly shifted from the corner of the "square" to "rectangle" as shown in the inset of Fig.1(B). We performed neutron scattering study on LSCO with x=0.12 to study the detail of the magnetic order in the superconducting phase, particularly the temperature dependence.

Neutron scattering measurements were carried out on the triple-axis spectrometers TAS-1 installed in the JRR-3M reactor. Incident neutron energy of 14.7meV was selected using the (0 0 2) reflection of a pyrolytic graphite monochromator. To eliminate the higher-order reflected beams pyrolytic graphite filters were inserted at both positions up and down stream of the sample. We measured two single crystals of LSCO (x=0.12) with different T_c, T_c=10K(sample A) and 30K(sample B). The origin of the difference in T_c is not clear at present. The quantity (<<100ppm) of detected impurities cannot cause such difference in T_c. Furthermore, both the structural transition temperature between the tetragonal and orthorhombic structure and the incommensurability of the elastic peak strongly indicate the same Sr-concentration for both crystals. In Fig.1(A) we present the temperature dependence of the incommensurate peak intensity. The onset temperature ~25K for the incommensurate peak of sample A is lower than that of sample B but remarkably higher than T_c. As shown in Fig.1(B) no appreciable temperature dependence of the peak-shift was detected upon heating samples up to near T_c. Therefore, the characteristic energy of the peak-shift is considered to be much larger than T_c. In fact, in the inelastic measurement with w=2meV we observed a similar peak-shift at low temperature.

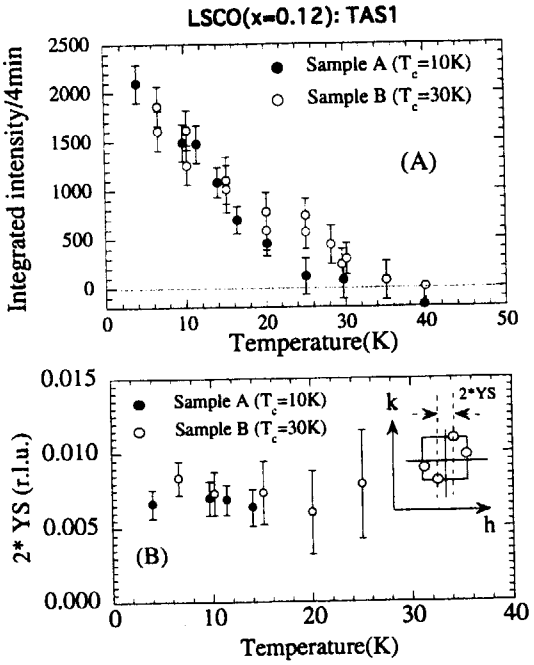


Fig.1(A) Temperature dependence of magnetic peak intensity. (B) Temperature dependence of peak-shift defined in the inset.

*Present address: Experimental Facilities Division, Japan Synchrotron Radiation Research Institute

原子炉：JRR-3M　　装置：TAS-1 (2G)　　分野：中性子散乱（磁性・超伝導）

研究テーマ ： 中性子散乱による強相関電子系の研究
表 題 ： CeSb の圧力-温度相図と磁気構造

1-2-9 Magnetic *P-T* Phase Diagram and Magnetic Structures of CeSb

T. Osakabe, A. Hannan[1], N. Tachi[1], M. Kohgi[1], H. Kitazawa[2]

ASRC, Japan Atomic Energy Research Institute, Ibaraki 319-1195, Japan
[1]Dep. of Physics, Tokyo Metropolitan University, Tokyo 192-0397, Japan
[2]National Research Institute for Metals, Ibaraki 305-0047, Japan

During the past over twenty years, there has been much interest in unusual magnetic and transport properties of semi-metallic Ce monopnictides (CeX ; X=P, As, Sb, Bi), which have simple NaCl-type crystal-structures with extremely low-carrier density ($10^{-2}\sim10^{-3}$ / Ce) [1,2]. Among these compounds, CeSb is well known with its complicated magnetic phase diagrams under high pressure below about 2 GPa as well as under magnetic field below about 10 T [3]. The magnetic structures in the phase diagrams are composed of ferromagnetic (001) Ce layers with Γ_8-like state Ce ions with the moment of 2 μ_B and paramagnetic layers with Γ_7 state Ce ions. On the other hand, above about 1.5 GPa, it was reported that the enormous enhancement of the resistivity appears at around 35 K and at the pressure of about 7 GPa the peak of the resistivity, shifting to higher temperature, reaches a value nearly 20 times as large as that at ambient pressure[5]. Here, we define the temperatures of the onset point of the huge peak on the higher temperature side, and of the inflection point on the lower temperature side, as T_H and T_L, respectively. (T_H and T_L are denoted as T_4 and T_2 in ref. 5), respectively.) Recent high-pressure X-ray diffraction experiments on CeSb above 1.9 GPa by Hannan *et al.* revealed that the sudden shrinking of crystal-lattice appears at a characteristic temperature T_S, which agree well with T_H[6].

In the pressure-temperature phase diagram, there exists some problems to be solved, that is, the existence of the magnetic order in the area between T_H and T_L or below T_L, if the magnetic order exists, the type of the order, and the apparent discrepancy of the phase diagram at around 2 GPa. In order to elucidate these puzzling problems directly, we performed the neutron diffraction experiments on CeSb under high pressure at low temperature on the triple axis spectrometer TAS-1 installed at the 2G beam hole of JRR-3M reactor in JAERI, Tokai. The piston-cylinder clamp-type cell with an alumina cylinder was used for the measurements below 3 GPa[7]. On the other hand, the newly developed sapphire-anvil high-pressure cell, which has the opposite Bridgman-type anvils with 2.5 mm anvil tips and a Cu gasket, was used for the measurements above 3 GPa. The pressure was calibrated by the ruby-fluorescence method in this case.

Fig. 1 shows the new phase diagram of CeSb obtained in this work. The notable facts on the magnetic phase diagram of CeSb are evident from this figure. The phase boundaries of $T_{AF\text{-}I}(P)$ and $T_{AF\text{-}IA}(P)$ are smoothly connected through the all pressure-temperature area investigated in this work. This solves the problem of the discrepancy of the phase diagram at about 2 GPa mentioned above. As pointed out in ref. 6), the shrinking of the crystal lattice at T_S originate from the appearance of the Ce-ions with the Γ_8-like state, which is small in effective ionic size due to the *p-f* mixing effect, among the Ce-ions with the Γ_7 CEF ground state. Since $T_H(P)$ agree well with $T_S(P)$, the huge enhancement of the resistivity is probably caused by the appearance of the Ce-ions with the Γ_8-like state. Concerning the magnetic transition temperatures, $T_{AF\text{-}I}(P)$ agree well with $T_S(P)$ at 0.5 and 1.2 GPa. Although $T_{AF\text{-}I}(P)$ shift to the lower temperature from $T_H(P)$ or $T_S(P)$ with increasing pressure, the development of the AF-I phase is closely related to the huge enhancement of the resistivity. On the other hand, $T_{AF\text{-}IA}(P)$ agree well with $T_L(P)$, indicating the development of the AF-IA phase leads to the drastic decrease of the resistivity. These result indicate that the mechanism of the carrier scattering or the carrier number itself is highly different between the two magnetically ordered

原子炉：JRR-3M 装置：TAS-1(2G) 分野：中性子散乱（磁性）

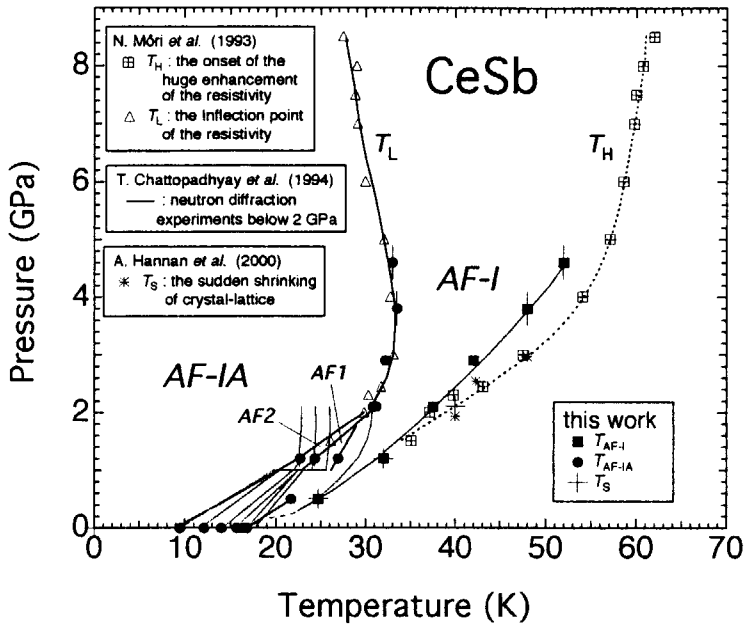


Fig. 1 Magnetic *P-T* Phase diagram of CeSb determined in this work together with the data from the previous neutron diffraction, the electrical resistivity and X-ray diffraction expeiments.

phases of the Ce-ions with the Γ_8-like state, AF-I and AF-IA.

As pointed out in ref. 8) and 9), the physics of Ce-mono-pnictides is probably explained by the model based on the *p-f* mixing effect; the carrier density is a common parameter in the model, although the difference of the CEF splitting between the compounds should be considered. For example, on CeSb, the application of pressure increases the carrier number and cause the enhancement of the *p-f* mixing effect. As a result of this, the paramagnetic Γ_7 Ce (001) planes disappear at around 1 GPa and above 2.1 GPa the same phase diagram as that of CeBi at ambient pressure appears. In ref. 10), Kasuya et al. explained qualitatively the transport and magnetic properties of Ce-monopnictides with the magnetic polaron model as a common physical model, in which the localization of the low-density carrier plays the key role. The development of theoretical works in the future is expected to elucidate the residual problems such as the correspondence between the pressure-induced huge enhancement of the resistivity and the magnetic orders, or the strong stabilization of the AF-I phase by applied pressure in spite of the small difference of the energy between the AF-I and the AF-IA phases at ambient pressure[4].

References

1) see for example, T. Suzuki: JJAP Series **8**, (1993) 267.
2)Y. Haga, Thesis, Tohoku University (1995).
3) see for example, T. Chattopadhyay, P. Burlet, J. Rossat-Mignod, H. Bartholin, C. Vettier, O. Vogt: Phys. Rev. B **49**, (1994) 15096.
4) H. Takahashi, T. Kasuya: J. Phys. C, Solid State Phys. **18**, (1985) 2697, 2709, 2721, 2731, 2745 and 2755.
5) N. Môri, Y. Okayama, H. Takahashi, Y. Haga, T. Suzuki: JJAP Series **8**, (1993) 182.
6) A. Hannan, K. Iwasa, M. Kohgi, T. Suzuki: J. Phys. Soc. Jpn. **69**, (2000) 2358.
7) A. Onodera: JHPI **30**, (1992) 301.
8) T. Osakabe, M. Kohgi, K. Iwasa, K. Kakurai, J.M. Mignot, I.N. Goncharenko, Y. Okayama, H. Takahashi, N. Môri, M. Kubota, H. Yoshizawa, Y. Haga, T. Suzuki: JJAP Series **11**, (1998) 123.
9) M. Kohgi, K. Iwasa, T. Osakabe: Physica B **281-282**, (2000) 417.
10) see for example, T. Kasuya: Physica B **215**, (1995) 88 and references therein.

研究テーマ: Ce 化合物強相関伝導系における特異な磁気相
表　　題: 中性子散乱による CeP の P-T 相図に関する研究

1-2-10 Magnetic P-T Phase Diagram of CeP Studied by Neutron Diffraction

A. Hannan, T. Osakabe[1], M. Kohgi, K. Iwasa
Department of Physics, Tokyo Metropolitan University, 1-1 Minami-osawa, Hachioji-shi, Tokyo 192-0397, Japan
[1]A. S. R. C., Japan Atomic Energy Research Institute, Ibaraki 319-1195, Japan

Various properties of semi-metallic compounds, Ce-monopnictides CeX (X=P, As, Sb, Bi) having very low carrier concentrations (0.3-2.9 %/Ce), have been extensively studied.[1-3] The heavier compounds CeSb and CeBi are well-known to have complex magnetic phase diagrams.[4,5] Magnetic structures in these materials are formed with various sequences of ferromagnetic (001) planes of almost fully polarized Ce ions (moment value~$2\mu_B$). Existence of paramagnetic planes are also found in some of these structures. Microscopic origin of the magnetic properties of CeX is given by the theory considering of p-f mixing state between the neighboring Ce and X ions.[6] High quality single crystals of CeP and CeAs also exhibit complex magnetic phase diagrams with various long-period magnetic structures, which develop at low temperatures under external magnetic fields or under high pressures.[7,8] As shown in Fig.1, the structures of CeP below T_{C1} are formed by ferromagnetically coupled double-layers of cerium ions with magnetic moments of about $2\mu_B$ and the antiferromagnetically coupled single-layers with moments of about $0.7\mu_B$. The Ce ions with $0.7\mu_B$ become paramagnetic between T_{C1} and T_{C2}, while the Ce ions with $2\mu_B$ keep ordering. Goncharenko *et al.*[9] reported the magnetic phase diagram of CeP under pressures up to 5.6 GPa, and some new ordered structures were discovered. However, there are still several unknown regions in the reported phase diagram, which demand further study.

Sapphire-anvil cell was used for generating the pressure with a very small sample (~0.017mm^3) and 4 : 1 deuterated methanol-ethanol solution worked as pressure transmitting medium. Pressure was checked by ruby-fluorescence technique. The experiments were carried out at TAS-1 of JRR-3M reactor in JAERI, Japan. The collimation for the magnetic measurement was Open–Open-Sample – PGF - B_4C mask –Open– Analyzer(flat)-Open. For this measurement the incident neutron energy was 13.7 meV (λ= 2.44Å).

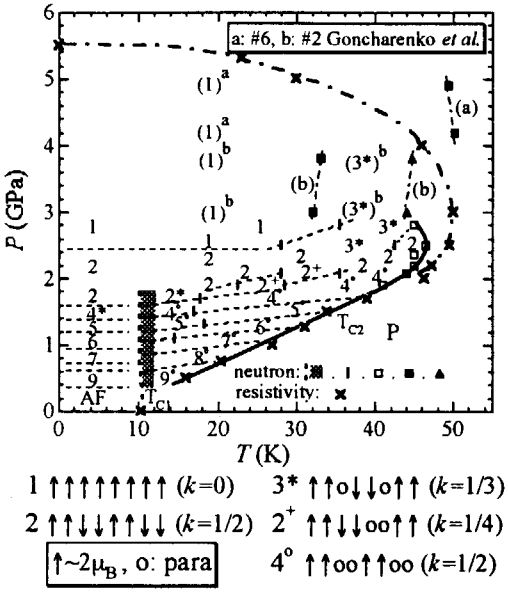


Fig.1: Magnetic P-T phase diagram and magnetic structures (above 1.7 GPa) of CeP.

We have performed experiments at different pressure values using both CeP#2 and CeP#3 samples, and CeP#3 was used for the previous neutron experiments giving the phase diagram up to 1.7 GPa. First we used CeP#2 at 2.0, 2.5 and 3.2 GPa. Due to the observation of sample's batch dependence of the magnetic behaviors under pressure, finally we selected CeP#3 to fill out the remaining part of the phase diagram. Fig.1 shows the P-T phase diagram determined by our recent neutron diffraction experiments along with the previous results up to 1.7 GPa.[7] Higher pressure magnetic phases obtained by Goncharenko *et al.*[9] are also shown in parentheses in the figure. Magnetic structures above 1.7 GPa are

原子炉: JRR-3M　　装置: TAS-1 (2G)　　分野: 中性子散乱 (磁性)

schematically shown at the bottom of the figure. Magnetic structures below this pressure are reported in Ref.7. The magnetic phases observed below T_{C2} are shown in Fig.1 by the Arabic numerals on the line of the pressure under which the experiment was done.

Peak intensities for (-0.5, 2, 0) and (0, 2, 0) reflections at 1.9 GPa increase below about 41 K with decreasing temperature down to 32 K (Fig.2). Then due to the development of another phase which is characterized by the wave vector k=1/4, they decrease with decreasing temperature down

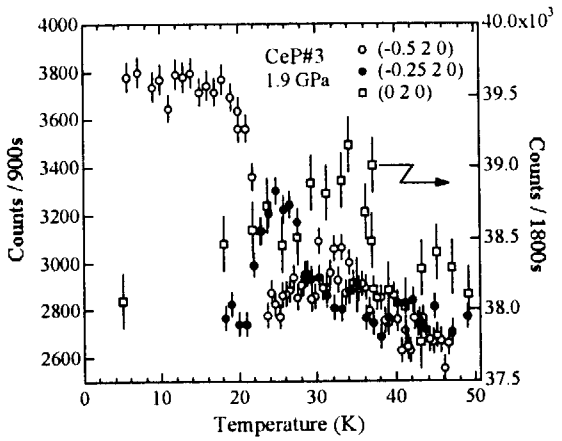


Fig.2: Temperature dependence of intensities for magnetic peaks with wave vectors **k**=[00k] at 1.9 GPa, where k=1/2, 1/4 and 0.

to about 22 K. These results indicate the existence of phase 4° between about 28 and 41 K. The phase with wave vector k=1/4 is a new phase, called phase 2^+ (↑ ↑ ↓ ↓o o↑ ↑) that appears below about 28 K and its existence is observed down to about 22 K. Finally the phase with wave number k=1/2 (so-called phase 2) appears below 22 K. At 2.2 GPa, the observed temperature dependence of intensity reveals the existence of the phase 2 in the whole temperature range below 45 K. We observed this phase also below 45 K at about 2.4 GPa. At 2.5 GPa and between 42.5 K and 46.5 K we observed the phase 2. Between 28 and 42.5 K the existence of phase 3* (k=1/3: ↑ ↑o↓ ↓o) is seen which was observed by Goncharenko *et al.*[9] at higher pressures for CeP#2 as shown in Fig.1. It is difficult to define any boundary line between the phases 3* and 2 in the temperature range 30-40 K, because at around 2.4 GPa they simultaneously appear in this temperature region. The existence of the ferromagnetic phase below 28 K at 2.5 GPa has been found from the increase of intensity of the (0, 2, 0) peak below around this temperature. At 2.8 GPa, similar magnetic phases have been observed as those under 2.5 GPa except the phase 2. It is seen from the phase diagram that the ferromagnetic transition temperature increases with the increase of pressure. If we extrapolate the boundary line between 3* and ferromagnetic phases, it is expected that the phase 3* will disappear at about 3.4 GPa for the present sample (#3). Thus the appearance of this phase in samples from different batches depends on both pressure and temperature.

It is seen that some magnetic phases in CeP above 1.5 GPa are also found in CeSb under magnetic field. The phases of simple ferromagnetic, type-IA antiferromagnetic, 4° (called FP2 in CeSb) are common in both the compounds.[5] This result gives evidence for the increase of carrier number, as well as the enhancement of p-f mixing effect in CeP under pressure considering the fact that the carrier density of CeSb is much higher than that of CeP. From the observed magnetic structures of CeP it is revealed that some common phenomena happen both in CeP above 1.5 GPa and in CeSb under magnetic field.

References

1) T. Suzuki, *Physical Properties of Actinide and Rare Earth Compounds*, JJAP Series 8 (1993) 267.
2) N. Môri, Y. Okayama, H. Takahashi, Y. Haga and T. Suzuki, (Ref. 2) p. 182.
3) T. Suzuki, Physica B **186-188** (1993) 347.
4) J. Rossat-Mignod *et al.*, J. Magn. Magn. Mater. **31-34**, (1983) 398.
5) T. Chattopadhyay *et al.*, Phys. Rev. B **49** (1994) 15096.
6) H. Takahashi and T. Kasuya, J. Phys. C, Solid State Phys. **18** (1985) 2697, 2709, 2721, 2731, 2745 and 2755.
7) M. Kohgi, K. Iwasa and T. Osakabe, Physica B **281-282** (2000) 417.
8) M. Kohgi *et al.*, Rev. High Pressure Sci. Technol. 7 (1998) 221.
9) I. N. Goncharenko *et al.*, Physica B **259-261** (1999) 306

研究テーマ：単結晶 Cr 薄膜及び人工格子の磁気構造とスピン密度波
表　　題：単原子 Sn 層を持つ Cr(001)/Sn 多層膜の人工周期で制御されたスピン密度波

1-2-11

Spin density wave controlled by the superlattice period in Cr(001)/Sn multilayers with Sn monatomic spacer layers

M. Takeda, K. Mibu[1], K. Takanashi[2], and J. Suzuki[3]

Physics Department, Graduate School of Science, Tohoku University, Sendai 980-8578, Japan
[1]Institute for Chemical Research, Kyoto University, Uji 611-0011, Japan
[2]Institute for Material Research, Tohoku University, Katahira Sendai 980-8577, Japan
[3]Advanced Science Research Center, JAERI, Tokai, Ibaraki 319-1195, Japan

The spin density wave (SDW) in Cr films and multilayers is very sensitive to environments such as temperature, thickness, boundary condition of multilayer and so on [1]. Recently we have reported that the wavelength of SDW in Cr/Sn(001) and Cr/Au(001) epitaxial multilayers on MgO(001) substrates with monatomic Sn spacer layers was determined by the multilayer period, Λ [2].

In order to elucidate the influence of multilayer period on SDW of thin film Cr in multilayer systems, we have investigated the SDW in [Cr(t_{Cr} nm)/Sn(0.2 nm)] × N on MgO substrate (t_{Cr} = 4, 8, 10, 12, 14, 16; $t_{Cr} \times N$ =240 nm) by TAS-1. Epitaxial multilayers were prepared by ultrahigh-vacuum deposition. Scans are performed along the axis normal to the sample plane (L direction). The incident neutron energy was fixed at 13.5 meV using a PG(002) monochromator and filtered by the PG filter before the samples.

Figure 1 shows L scans of the Cr(t_{Cr}=12 nm)/Sn multilayer through bcc (010) reciprocal point. This figure indicates that the commensurate antiferromagnetic (CAF) phase at 290 K changed into SDW with the higher order satellites at low temperature. From the separation of the most intense satellites, we fined the dominant SDW period was just the same as the Λ of this sample(=12 nm). This observation suggested that wavelength of the SDW in this multilayer was governed by the Λ. In addition, the existence of the weak higher-order-satellites imply that waveform of the SDWs is not pure sinusoidal, but highly distorted one. No satellite was observed by scans along the in-plane principal axes. Therefore the propagation vector of the SDW is normal to the sample plane.

In the other multilayers the SDWs controlled by the artificial period were also observed, however, the number of nodes in the Cr layers was changed according to threshold value which might be determined by the nesting vector of Fermi surface of Cr in the multilayers (Table 1). This directly indicates that the multilayer period plays an essential role in the SDWs. The details of the experiments will be appeared in Ref. [3].

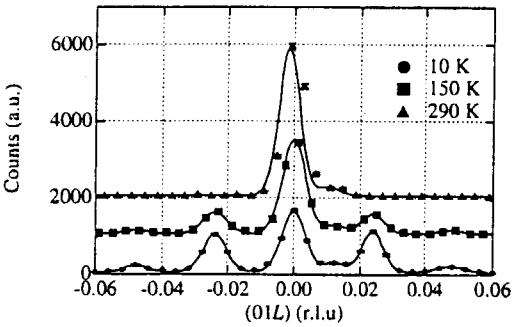


Fig. 1 Temperature dependence of L scans of [Cr(12.0 nm)/Sn(0.2 nm)] × 20 on a MgO substrate, through the (010) position.

t_{Cr} (nm)	wavelength of dominant SDW (nm)		the nuber of nodes
4.0	-	-	0
8.0	16.0	2Λ	1
10.0	10.0	Λ	2
12.0	12.0	Λ	2
14.0	14.0	Λ	2
16.0	11.0	2Λ / 3	3

Table 1 The wavelength of the dominant SDW in the unit of nm and the Λ, and the number of nodes at 20 K.

References

[1] H. Zabel: J. Phys.: Condens. Matter **11** (1999) 9303.
[2] M. Takeda, K. Mibu, K. Takanashi, K. Himi, Y. Endoh, T. Shinjo and H. Fujimori: J. Phys. Soc. Jpn **69** (2000) 1590.
[3] M. Takeda, K. Mibu, T. Shinjo, J. Suzuki and Y. Endoh:Proc ICNS2001 (München) in press.

原子炉：JRR-3M　　装置：TAS-1(2G)　　分野：中性子散乱(磁性)

研究テーマ：量子凝縮相の研究
表題：圧力誘起超伝導体UGe_2の中性子散乱による研究

1-2-12 Neutron Scattering Study of a Pressure-Induced Superconductor UGe_2

Y. Koike[a,b], N. Metoki[a], Y. Haga[a], and Y. Onuki[a,c]

[a] Advanced Science Research Center, Japan Atomic Energy Research Institute, Tokai, Naka, Ibaraki 319-1195, Japan

[b] Japan Science and Technology Corporation, Kawaguchi, Saitama 332-0012, Japan

[c] Department of Physics, Graduate School of Science, Osaka University, Toyonaka 560-0043, Japan

Superconductivity coexisting with ferromagnetism in UGe_2, is the most interesting phenomenum in the field of strongly correlated electron systems. The superconductivity appears under high pressures for p = 1 GPa ~ 1.6 GPa.[1-3] The critical temperature has the maximum about 0.8 K for p = 1.2 GPa, where so called anomaly at T^* disappears. The origin of the T^* anomaly is still an open question. A SDW state of the majority spin is theoretically proposed.[4] However, it has not been experimentally confirmed. The purpose of this study is to reveal the magnetic structure and the nature of the tranition at T^*. It is of particularly important to clarify, whether superconductivity can coexist with a simple ferromagnetic ordering.

A thermal and cold triple-axis-spectrometer were used for experiments. Hydrostatic pressure was applied with use of Macwhan-type cell. The sample was mounted with the a^* and c^*-axes parallel to the scattering plane.

Figure 1 is the temperature dependence of the squared magnetic moment measured at (001) Bragg intensities. At ambient pressure the (001) Bragg intensities showed a sharp increase below T_{Currie} = 54 K. With applying pressure about 0.9 GPa, the T_{Currie} was reduced to 40 K. The magnetic intensity exhibits a gradual increase below T_{Currie} = 40 K. Furthermore a clear increase in the magnetic Bragg intensity was observed at T^* =18 K. At 1.3 GPa the anomaly at T^* disappears. With this pressure the Curie temperature was strongly

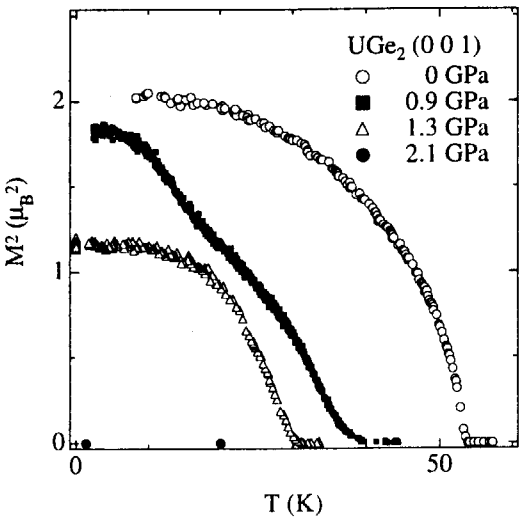


Fig. 1 Temperature dependence of the squared magnetic moment.

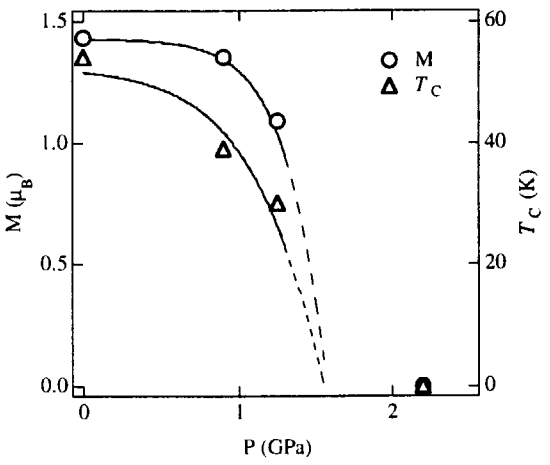


Fig. 2 Pressure dependence of the magnetic moment and Curie temperature.

原子炉：JRR-3M　　装置：TAS-1 (2G), TAS-2 (T2-4), LTAS (C2-1)　　分野：中性子散乱(磁性)

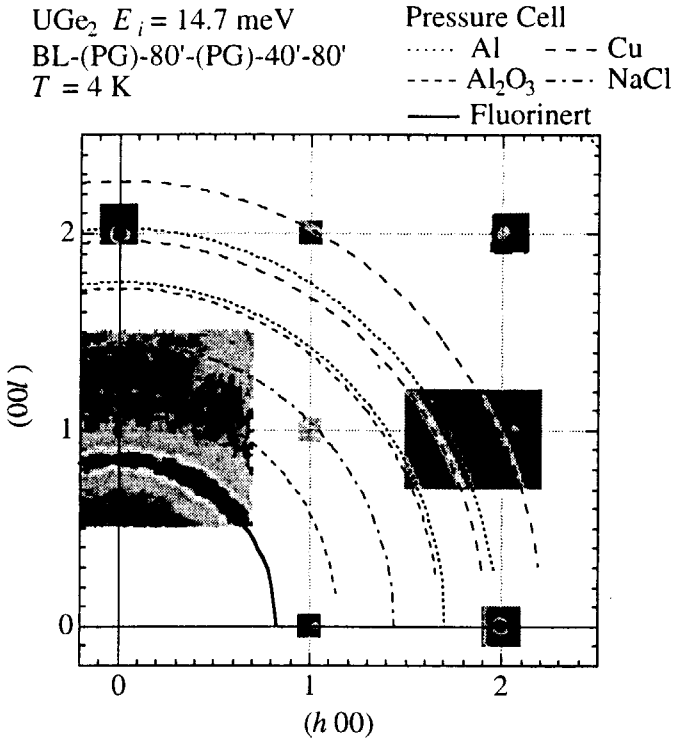


Fig. 3 The contour map of the scattering intensity on the a^*-c^* plane

reduced down to 30 K and the magnetic moment was also suppressed to 1.1 μ_B/U. Above 2.1 GPa we observed no ferromagnetic transition down to 1.3 K.

Figure 2 shows the result of the pressure dependence of the magnetic moment and T_{Currie}. These pressure dependences are in good agreement with other studies.[1-3]

The origin of the unusual behavior of the ferromagnetic order parameter at T^* around 0.9 GPa is an open question. The increase of the magnetization at T is also observed in DC-magnetization measurements[2] and neutron diffraction with different sample.[3] A theoretical study predicted that the magnetic ground state is the SDW state of the majority spin. Elastic scattering experiments were carried out to find satellite peaks due to SDW state.

Figure 3 shows the contour map of the scattering intensity on the a^*-c^* plane. It should be noted that our sample has a large mosaic spread of about 20 degrees along the c^*-axis. Therefore the scattering intensity was integrated over in a relatively large volume in reciprocal space. Up to now we could find no trace of the satellite peak stronger than 10^{-2} of the magnetic scattering at (001) reflection. The rings in Fig. 3 are the scattering from the pressure cell (Al, Cu, Al_2O_3, NaCl) or hydrostatic pressure media. Further diffraction experiments are under planning to survey the satellite peak characteristic to the CDW/SDW state.

References

[1] S.S. Saxena *et al.*, Nature **406** (2000) 587.
[2] N. Tateiwa *et al.*, J. Phys.: Condence. Matter. **13** (2001) L17.
[3] A. Huxley *et al.*, Phys. Rev. B **63** (2001) 144519.
[4] S. Watanabe and K. Miyake, to be published.

研究テーマ：量子凝縮相の基礎研究
表　題　　：$U_3Pd_{20}Si_6$のスピン波励起

1-2-13 Spin Wave Excitation in a localozed 5f system $U_3Pd_{20}Si_6$

N. Metoki[1], Y. Koike[1,2], Y. Haga[1], Y. Onuki[1,3], K.A. McEwen[4], N. Aso[5], M. Kohgi[6], N. Tateiwa[3], N. Kimura[7], H. Aoki[7], and T. Komatsubara[7]

[1]*Advanced Science Research Center, JAERI, Tokai, Ibaraki 319-1195*
[2]*Japan Science and Technology Corporation, Kawaguchi, Saitama 332-0012*
[3]*Graduate School of Science Department of Physics, Osaka University, Toyonaka, Osaka 560*
[4]*Dep. of Physics and Astronomy, University College London, Gower Street, London WC1E 6BT, UK*
[5]*NSL-ISSP, University of Tokyo, Ibaraki 319-1106*
[6]*Department of Physics, Tokyo metropolitan University, Hachioji, Tokyo 192-0397*
[7]*Center for Very Low Temperature Science, Tohoku Univ., Sendai 980-8545*

Recently we found a new localized *5f* uranium intermtallic compound $U_3Pd_{20}Si_6$.[1)] This compound showed very clear crystal field excitation for ΔE ~ 10 - 30 meV, which is direct evidence for the localized character of the *5f* electrons.[2)] The purpose of this study is to look for the spin wave excitation which is the collective magnetic excitation of the localized *5f* spins.

Neutron scattering experiments were carried out at the research reactor JRR-3M in Japan Atomic Energy Research Institute (JAERI). The inelastic neutron scattering experiments on single crystal samples were carried out using triple-axis-spectrometers TAS-1 and LTAS, respectively.

Fig.1 shows the inelastic scattering profile around the magnetic zone center (111). We observed very clear spin wave excitation for ΔE ~ 3 meV. Up to now, only USb [3] had been known which showed a clear spin wave excitation whole in the reciprocal zone. Most uranium compounds shows very weak magnetic response, because of the itinerant character of the *5f* electrons. Therefore we conclude that our result is the strong evidence for the localized character of the *5f* electrons in $U_3Pd_{20}Si_6$.

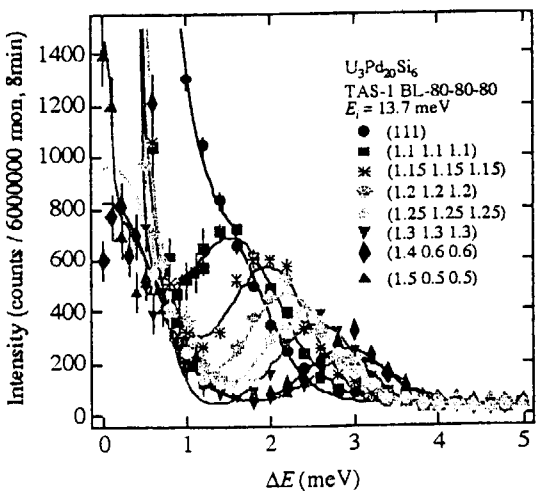


Fig. 1 The neutron inelastic scattering profilrs in $U_3Pd_{20}Si_6$

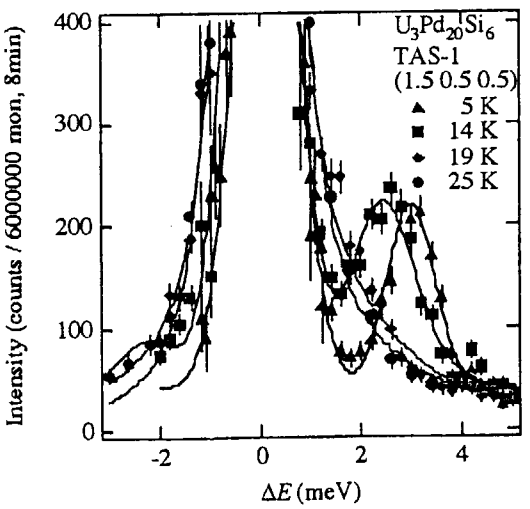


Fig. 2 The temperature dependence of the spin wave excitation in $U_3Pd_{20}Si_6$

原子炉：JRR-3M　　装置：TAS-1(2G)・LTAS (C2-1)　　分野：中性子散乱(磁性)

At higher temperature the inelastic peak becomes weak and broad, and the inelastic response disappear above the Nèel temperature T_N = 19 K (Fig. 2). This temperature dependence is consistent with the one for the spin wave excitation.

Figure 3 shows high-resolution neutron inelastic scatering profile of $U_3Pd_{20}Si_6$ around the zone center (111). It is clearly seen that a weak quasi-elastic response is observed in a very narrow Q-region around the zone center. This quasi-elastic component increases in intensity with elevating temperature. Because of this temperature dependence, we conclude that this component is related to quasi-particle due to hybridization of *5f* with conduction electrons. Very recently a similar response has been observed in UPd_2Al_3 [3] and UGa_3 [4]. In UPd_2Al_3 the quasi-elastic response showed clear gap in superconducting state. The interesting thing is that the quasi-elastic component was observed only at the antiferromagnetic zone center of 8*c* site, but it was not the case for the ferromagnetic zone center of 4*a* site.

Further inelastic scattering experiments are under planing in order to understand the magnetic response of the uranium intermetallic compounds in a systematic manner.

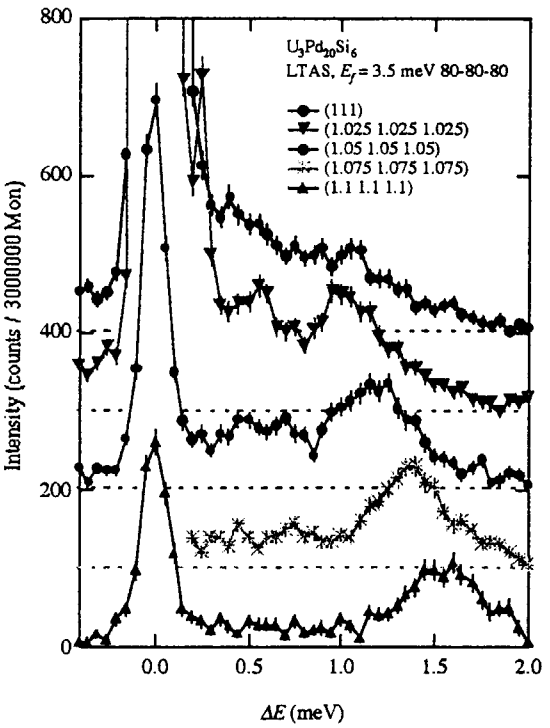


Fig. 3 The high-resolution neutron inelastic scattering spectra in $U_3Pd_{20}Si_6$

References

[1] N. Tateiwa et al., J. Phys. Soc. Jpn. **69** (2000) 1517.
[2] N. Tateiwa et al., J. Phys. Soc. Jpn. **70** (2001) 2425.
[3] G. Lander et al., Phys. Rev. B**21** (1980) 436.
[4] N. Metoki et al., Phys. Rev. Lett. **80** (1998) 5417.
[5] S. Coad et al., Physica B**70**, 200 (2000).

研究テーマ：URu_2Si_2における高温秩序相の解明-四重極秩序の解明
表題：URu_2Si_2における弱い反強磁性状態の起源

1-2-14 Origin of Weak Antiferromagnetic State in URu_2Si_2:

H. Amitsuka, M. Yokoyama and J. Nozaki

Graduate School of Science, Hokkaido University, Sapporo 060-0810, Japan

A puzzling phase transition of URu_2Si_2 at 17.5 K ($\equiv T_o$) is one of the most intriguing issues in heavy fermion physics. A weak antiferromagnetic state (WAF), which is formed of tiny 5f moments ($\mu_{ord} \sim 0.03(1)\ \mu_B$) below around T_o, is apparently unreconciled with large bulk anomalies, and thus possibility of hidden order parameter has been argued. We recently found that WAF is dramatically enlarged by applying hydrostatic pressure[1]: μ_{ord} increases from $\sim 0.017(3)\ \mu_B$ to $\sim 0.25(2)\ \mu_B$, as the pressure P increases from 0 to $\sim$ 1.5 GPa, where the unusual T-linear behavior of $\mu_{ord}(T)$ is unchanged. On the other hand, recent ^{29}Si-NMR measurements have revealed that the resonance line in the paramagnetic state is partly split into two satellites below T_o in the pressure range 0.3 GPa $< P <$ 0.8 GPa[2]. By combining these two experimental results, we can be fairly certain that WAF is not due to a uniform order of the tiny moments, but an inhomegeneous coexistence of normal-moment ($\mu_{ord} \sim 0.3\ \mu_B$) AF phase and a non-magnetically ordered phase. Interestingly, the analyses on the intensity of the NMR signals indicate that the unusual T dependence of μ_{ord} is ascribed to that of the volume fraction of the normal-moment AF domains. To see this aspect, we have measured the correlation length of WAF as a function of temperature. The X-ray magnetic scattering measurements have already reported that the correlation length along the tetragonal c-axis ξ_c is nearly independent of temperature[3]. Here we present the T dependence of the correlation length along the a axis ξ_a, for the first time.

The single crystalline URu_2Si_2 with a cylindrical shape (ϕ7mm × 30mm) was grown by using a tetra-arc furnace, followed by an annealing in an evacuated sealed quartz tube at 1000 °C for ten days. The elastic neutron scattering measurements were performed on the triple axis spectrometer GPTAS(4G) at the JRR-3M reactor, by using neutrons with wave length of 2.3535 Å. Double PG(002) filters and 40'-40'-40'-80' horizontal collimation were adopted.

The experimental results are shown in Fig. 1. ξ_a is very short ($\sim$ 250 Å) and shows no significant T variations below T_o. As is mentioned above, the NMR results predict the "AF volume fraction" to vary in proportion to $\mu_{ord}(T)$. The present results may thus admit of the following two interpretations on the property of WAF in URu_2Si_2: (i) the number of the normal-moment AF domains varies with T, while each domain size is conserved around ξ_a and ξ_c; and (ii) the AF-domain size varies with T, but each domain consists of sub-domains with a size defined by ξ_a and ξ_c. We are planning to perform the similar experiments under hydrostatic and uniaxial pressures to test these two scenarios.

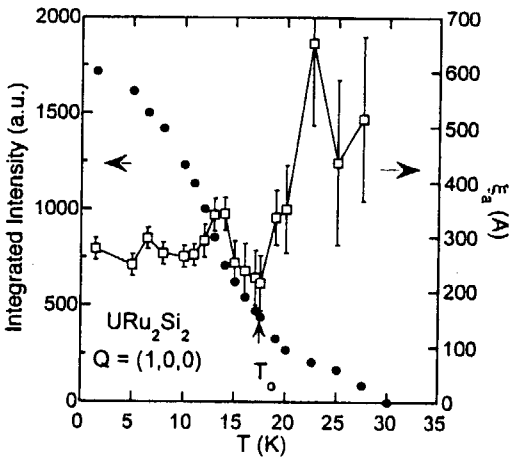


Figure 1: Temperature variations of the integrated intensity of the (100) antiferromagnetic Bragg peak $I(T)$(•) and the a-axis correlation length ξ_a(□) estimated from the same peak.

1) H. Amitsuka *et al.*: Phys. Rev. Lett. **83**(1999)5114; J. Phys. Soc. Jpn. **69**(2000) Suppl. A 5.
2) K. Matsuda *et al.*: to be published in Phys. Rev. Lett.
3) E.D. Isaacs *et al.*: Phys. Rev. Lett. **65**(1990)3185.

研究テーマ：$Nd_2Mo_2O_7$の磁気構造
表題：中性子回折による$Nd_2Mo_2O_7$の磁気構造

1-2-15 Neutron Diffraction Study of the Magnetic Ordering in $Nd_2MO_2O_7$

Y. Oohara,[1] H. Mochizuki,[1] H. Yoshizawa,[1] Y. Taguchi[2] and Y. Tokura[2]
[1]NSL, I.S.S.P., University of Tokyo, Tokai, Ibaraki 319-1106
[2]Department of Applied Physics, University of Tokyo, Tokyo 113-8656

$Nd_2Mo_2O_7$ is a pyrochlore-type magnet. Magnetic ions, Nd^{3+}, and Mo^{4+}, form corner-shared tetrahedra, respectively. It shows ferromagnetism below T_C, 89K, by the double exchange interaction between Mo^{4+} ions. Recently, Taguchi *et al.* demonstrate that $Nd_2Mo_2O_7$ exhibits an anomalous Hall effect due to the spin chirality of its magnetic structure. [1)] To investigate the chirality of the magnetic structure in $Nd_2Mo_2O_7$, we have performed neutron diffraction measurements.

Neutron diffraction measurements were carried out on the ISSP triple-axis spectrometer GPTAS installed at the 4G experimental port in JRR-3M in JAERI(Tokai). We have prepared 0.4 cc of the crystal sample. Magnetic Bragg reflections were observed at (111), (200), (400), (220), $\cdots$, the bcc lattice points, indicating that the magnetic unit cell consists of the Mo and the Nd tetrahedron. Figure 1 shows the temperature dependence of the magnetic intensities at (400), (111) and (200). The intensity at (400) corresponds to the ferromagnetic moment and that at (111) to the antiferromagnetic moment parallel to the ferromagnetic moment, while that at (200) to the moment perpendicular to the ferromagnetic moment. The intensity at (400) and that at (111) appear below T_C, while that at (200) increases rapidly below T^*, 30 K with decreasing the temperature. Consequently, we have concluded that the magnetic structure between T_C and T^* is the ferrimagnetic structure and that below T^* is the umbrella structure.(Fig. 2) The intensity at (400) decreases below T^* with decreasing the temperature. It indicates that the interaction between Nd^{3+} and Mo^{4+} is antiferromagnetic and the ordered Nd^{3+} moment becomes large below T^*. Thus we find that the ordering of the Nd^{3+} moment brings about the umbrella structure.

JRR-3M, GPTAS, 2. Magnetism

References

[1] Y. Taguchi *et al.*: Science **291**(2001)257.

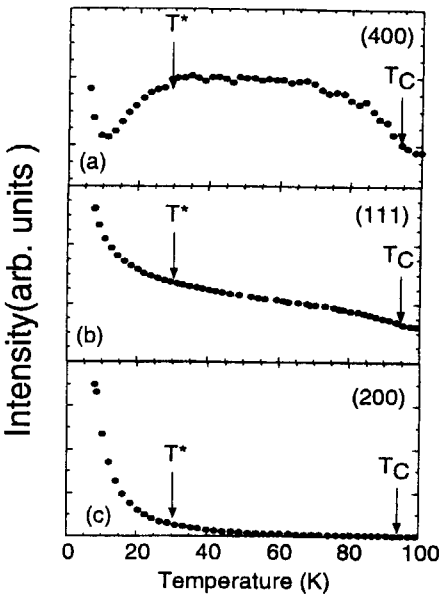


Figure 1: Temperature dependence of the magnetic intensities at (a) (400), (b) (111) and (c) (200).

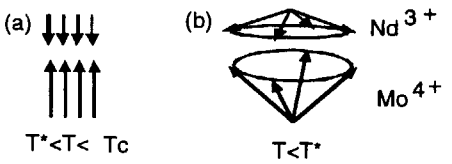


Figure 2: Schematic pictures of the magnetic structure (a) between T_C and T^* (the ferrimagnetic structure) and (b) below T^*(the umbrella structure).

研究テーマ：金属相酸化バナジウムの磁気構造と励起
表題：金属相酸化バナジウムの磁気構造と励起

1-2-16 Magnetic Structure and Excitation of Metallic Phase of $(V_{1-x}Ti_x)_2O_3$

K. Motoya, J. Kikuchi, K. Hioki, S. Tabaru and S. Shin[1]

Department of Physics, Faculty of Science and Technology, Science University of Tokyo, Noda 278-8510

[1]Institute for Solid State Physics, The University of Tokyo, Roppongi, Tokyo 106

A systematic neutron scattering study of a canonical Mott-Hubbard system $(V_{1-x}Ti_x)_2O_3$ has been made. In 2000, four kinds of single crystals with x=0.1, 0.15, 0.2 and 0.3 were synthesized. For the compound with x=0.20, a spin-density-wave (SDW) order characterized by the propagation vector $\mathbf{q}=1.93\mathbf{c}^*$ was observed below T_N=50K. Magnetic structure of this compound is similar but not identical to that of the previously studied x=0.55 compound. The direction of magnetic moments does not change down to the lowest temperature, whereas it rotates from the hexagonal *c*-axis by ~60° below T_R=15K for the x=0.055 compound.

Inelastic neutron scattering patterns taken at various temperatures of $(V_{0.80}Ti_{0.20})_2O_3$ are shown in Fig.1. Constant energy scans show peaks at the positions corresponding to the magnetic Bragg points at temperatures below and even far above T_N. For small energy transfer scans, the width of the peaks in *q*-space is relatively narrow but much wider than the instrumental energy resolution. The width grows wider with increasing energy transfer and/or temperature. Even far above T_N, peaks still exist at magnetic Bragg positions. These characteristics in inelastic scattering properties are similar to those observed in $V_{1.973}O_3$[1] and in $(V_{0.945}Ti_{0.055})_2O_3$.[2] A large fluctuating component, which has been observed in the non-stoichiometric system [1] is also present in this more "homogeneous" system and of which property can be described in terms of the SCR theory for weakly itinerant antiferromagnet. [3]

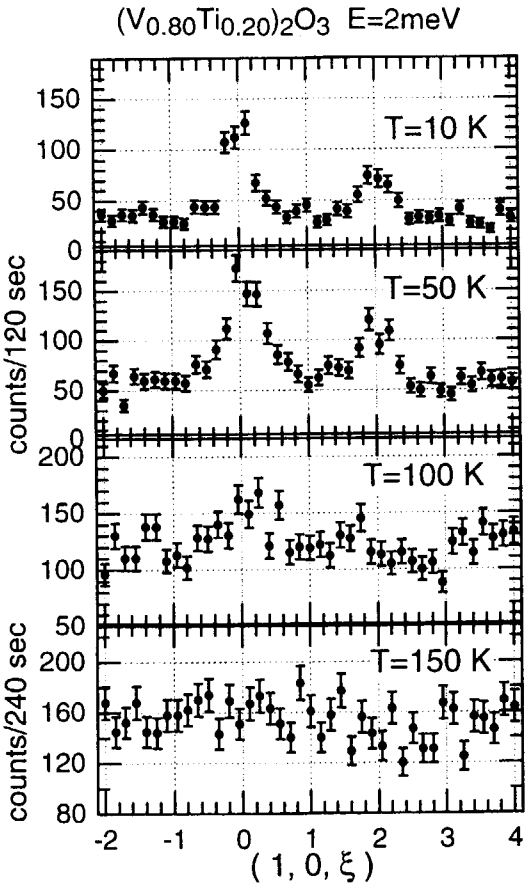


Fig.1 Inelastic neutron scattering patterns from $(V_{0.80}Ti_{0.20})_2O_3$ taken at various temperatures.

References

1) W. Bao et al: Phys.Rev.B **54** (1996) 3726.
2) K. Motoya et al. J.Mag.Mag. Mater. 177-181 (1998) 593.
3) K.Nakayama and T. Moriya: J.Phys.Soc.Jpn. **56** (1987) 2918.

研究テーマ：幾何学的フラストレーションを示す磁性体の磁気揺動
表題：双極子スピンアイス$Ho_2Sn_2O_7$の中性子散乱による研究：フラストレートしたパイロクロア磁性体

1-2-17 Neutron scattering study of dipolar spin ice Ho2Sn2O7: Frustrated pyrochlore magnet

H. Kadowaki, Y. Ishii[1], K. Matsuhira[2], and Y. Hinatsu[2]

Department of Physics, Tokyo Metropolitan University, Hachioji-shi, Tokyo 192-0397
[1]Advanced Science Research Center, Japan Atomic Energy Research Institute, Tokai, Ibaraki 319-1195
[2]Division of Chemistry, Graduate School of Science, Hokkaido University, Sapporo

Discovery of spin-ice model systems, $Ho_2Ti_2O_7$ and $Dy_2Ti_2O_7$, which belong to a series of pyrochlore oxides showing frustrated properties, has renewed interest of ice models. Experimental and theoretical work of these compounds has shown that the spin system freezes into a certain state below a temperature of the order 1 K which has only short range order with macroscopic number of degeneracy, i.e., zero-point entropy. Recently, other pyrochlore compounds $Ho_2Sn_2O_7$ and $Dy_2Sn_2O_7$ were shown to belong to the spin ice families by AC susceptibility measurements [1]. It was shown that $Ho_2Sn_2O_7$ exhibits the slow dynamics below a temperature scale 1.4 K, and that it does not have a magnetic transition to a long-range ordered phase down to 0.15 K. In this work [2], in order to clarify the spin ice behavior of $Ho_2Sn_2O_7$ on a microscopic basis, we have performed neutron scattering experiments on a powder sample.

Neutron scattering experiments were performed on the triple-axis spectrometers HER(C11) and GPTAS(4G). The spectrometers were operated in fixed final energy modes with $E_f = 3.1$ or 14 meV. In Fig. 1 we show Q-scans with an elastic condition at several temperatures down to 0.4 K. One can see from this figure that the magnetic short-range order starts to develop below 20 K. By analyzing the Q-dependence of the intensity on the basis of the mean field theory of the wave-number dependent susceptibility, we obtained convincing evidence that the dipolar interaction is the major inter-spin coupling.

Magnetic inelastic-scattering spectra show that Ho magnetic moments behave as an Ising spin system with the local <111> axes at low temperatures, and that the spin fluctuation has static character. Slow spin dynamics is exhibited as thermal hysteresis and time dependence of the magnetic scattering. We conclude that $Ho_2Sn_2O_7$ belongs to the dipolar-spin-ice family.

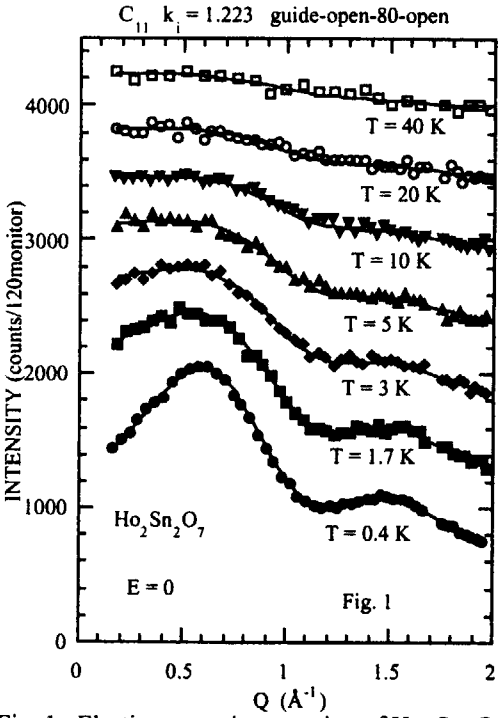


Fig. 1 Elastic magnetic scattering of $Ho_2Sn_2O_7$ as a function of wave number at various temperatures. Data of T = 1.7, 3, 5, 10, 20, and 40 K are shifted by 500, 1000, 1500, 2000, 2500, and 3000 counts, respectively for clarity. Solid lines are fitted curves calculated using the mean field theory.

[1] K. Matsuhira et al., J. Phys. Condens. Matter 12 (2000) L649. [2] H Kadowaki et al., submitted to Phys. Rev B (2001)

研究テーマ: Zn-Mg-(RE,Y) 準結晶の準弾性散乱
表題: Zn-Mg-Tb 正 20 面体準結晶中のスピンダイナミックス

1-2-18 Spin dynamics in the Zn-Mg-Tb icosahedral quasicrystals

T. J. SATO[1], H. TAKAKURA[1], A. P. TSAI[1], H. KADOWAKI[2], and K. SHIBATA[3]
[1]*National Institute for Materials Science and CREST-JST, Tsukuba 305-0047, JAPAN*
[2]*Department of Physics, Tokyo Metropolitan University, Hachioji, JAPAN*
[3]*Institute for Materials Research, Tohoku University, Sendai, JAPAN*

The Zn-Mg-*RE* (*RE*: rare earth) icosahedral quasicrystals have localized $4f$ magnetic moments on the RE sites. Therefore, it provides an opportunity to study dynamics of spins on the quasiperiodic lattice. An initial trial was made to explore the dynamics by using the Zn-Mg-Ho quasicrystal [1], however, its small characteristic energy (inferred by its freezing temperature $T_f \simeq 2$ K) prohibits us to obtain conclusive results. In this study, we used the isostructural Zn-Mg-Tb quasicrystal; its relatively large characteristic energy scale ($T_f \simeq 5.6$ K) enables us to obtain much detailed inelastic excitation spectrum and its $\boldsymbol{Q}$-dependence.

A single crystal of the Zn-Mg-Tb quasicrystal was grown by the Bridgman method. Neutron scattering experiments were performed using the triple-axis spectrometers GP-TAS and HER installed at JRR-3M, JAERI (Tokai). The single quasicrystal was loaded in the standard orange cryostat with the lowest working temperature of 1.4 K, and the 2f plane was selected to be in the scattering plane.

A constant-$\boldsymbol{Q}$ spectrum observed at $\boldsymbol{Q} = (0.55, 0, 0)$ Å^{-1} using GP-TAS is shown in Fig. 1(a) as a typical inelastic scattering spectrum. A broad peak can be seen at $E \sim 2.5$ meV. It should be noted that the spectrum is quite similar to that observed in the Zn-Mg-Ho quasicrystal except for different peak energy (the Zn-Mg-Ho quasicrystal shows a broad peak centered at $E \simeq 0.8$ meV.)

$\boldsymbol{Q}$-dependence of the inelastic peak is studied by several constant-E scans. Typical result is shown in Fig. 1(b), which is for the energy transfer of $E = 3$ meV. It can be seen that the inelastic peak has small $\boldsymbol{Q}$-dependence with noticeable peaks at $Q = 0.5$ and 0.95 Å^{-1}. It should be noted that the elastic diffuse scattering also shows peaks at $Q \sim 0.55$ and

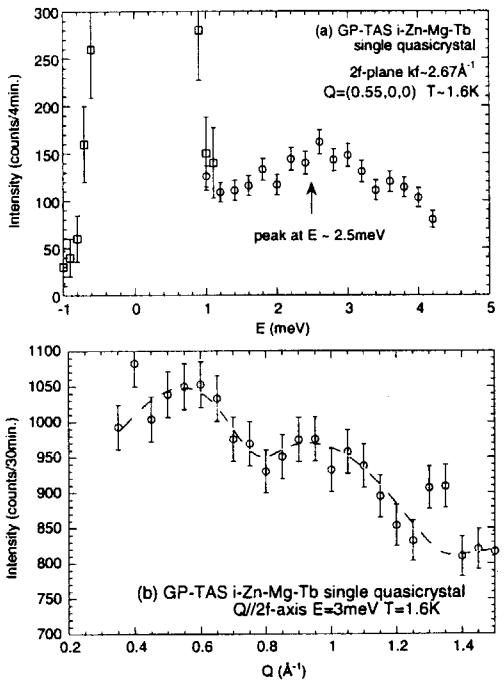


Figure 1: (a) Constant-$\boldsymbol{Q}$ scan at $\boldsymbol{Q} = (0.55, 0, 0)$Å^{-1}. (b) Constant-$E$ scan at $E = 3$ meV.

1.1 Å^{-1} [2]. In view of the low statistics of the inelastic scattering, it is likely that the peak positions are identical for the elastic and inelastic scans. This suggests that dynamic spin fluctuations have weak spatial correlations, which have a similar form to the static short-range ordering. Further study is apparently necessary to elucidate nature of the fluctuations in the icosahedral quasicrystals.

References

[1] T. J. Sato *et al.*, ISSP activity report on neutron scattering research 7 (2000) 159. [2] T. J. Sato *et al.*, Phys. Rev. Lett 81 (1998) 2364; T. J. Sato *et al.*, Phys. Rev. B61 (2000) 476; T. J. Sato *et al.*, Mat. Sci. & Eng. A294 (2000) 481.

JRR-3M, GP-TAS および HER, 2.Magnetism

研究テーマ: 幾何学的三角格子フラストレーションが部分的に解けた Ising 反強磁性体におけるドメインキネティクス
表題 : 幾何学的にフラストレートした二等辺三角格子反強磁性体 $CoNb_2O_6$ における非磁性不純物効果

1-2-19 None-Magnetic Impurity Effects in the Geometrically Frustrated Isosceles Triangular Ising antiferromagnet $CoNb_2O_6$

S. Mitsuda, H. Okano, T. Jogetsu and S. Kobayashi[1]

Department of Physics, Science University of Tokyo, Kagurazaka, Shinjuku-ku, Tokyo 162-8601, Japan

[1]*SVBL, Gunma University, Gunma 376-8515, Japan*

As one of model materials of triangular lattice antiferromagnet with a partially released geometrical frustration, we have studied a quasi-one-dimensional Ising magnet $CoNb_2O_6$, where an isosceles-triangular geometry of frustrated spins provides novel magnetic properties such as propagation-wave-number-dependent magnetic correlation in thermally induced incommensurate (IC) phase and anisotropic domain-growth-kinetics, in antiferromagnetic (AF) phase, with anomalously low growth exponent n ~ 0.2 compared with 0.5 of the conventional Ising magnets.[1,2] This time, using GPTAS and HER, we have performed preliminary neutron diffraction experiments of $Co_{1-x}Mg_xNb_2O_6$ samples under vertical magnetic field up to 600 [Oe] at the temperature down to 1.5 K, to explore how magnetic ordering in AF state with fourfold degeneracy is destroyed on slight substitution as well as how a small amount of Mg^{2+} none-magnetic impurity modifies domain-growth-kinetics. In Fig.1, preliminary results of ac susceptibility as well as neutron scattering measurements are shown, where it can be seen that AF ground state is easily destroyed with only 2 % substitution at least down to 1.5 K. In the sample with x=0.02, down to 1.5 K propagation wave number remains to be incommensurate value of ~ 0.41, accompanied by appreciable broadening of magnetic Bragg peak below ~2K (AF-IC phase transition temperature of x=0.0 sample, $T_{AF\text{-}IC}^{x=0}$). Correspondingly, enhancement of out-of-phase susceptibility χ'' can be seen also below $T_{AF\text{-}IC}^{x=0}$, suggesting that substituted sample still remembers the temperature $T_{AF\text{-}IC}^{x=0}$, in other words, the AF state with fourfold degeneracy. Actually, for the substituted sample with x=0.02 long time evolution of the in-phase ac susceptibility χ', that is characteristic of domain-growth-kinetics in the AF state, is clearly seen below $T_{AF\text{-}IC}^{x=0}$. Furthermore, the growth exponent n ~ 0.16 for the sample with x=0.02 is smaller than that of x=0.0, implying that a small amount of Mg^{2+} none-magnetic impurity prevents domain-growth-kinetics. As for the apparent IC state only below $T_{AF\text{-}IC}^{x=0}$ in the x=0.02 sample, it is speculated from our Monte-Carlo simulation using cluster-heat-bath method that quasi periodic arrangements of the thermodynamically equivalent fourfold degenerate AF domain along the b axis are realized and give rise to apparent IC magnetic Bragg peak with appreciable broadening.

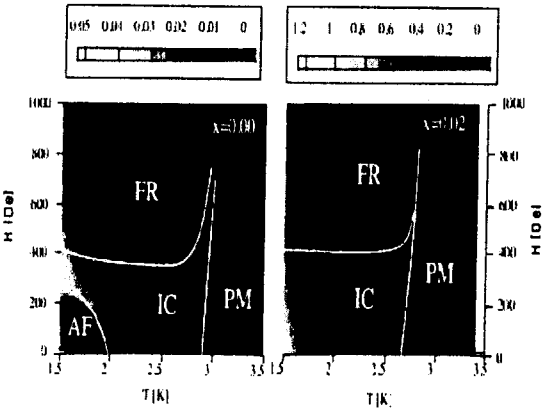


Fig.1 Contour maps of out-of-phase ac susceptibility χ'' on H-T magnetic phase diagram for the samples with x=0.0 and x=0.02. The phase boundaries were determined by neutron scattering experiments

References

[1] S. Kobayashi, S. Mitsuda, M. Ishikawa, K. Miyatani, and K. Kohn, Phys. Rev. B **60**, 3331 (1999).

[2] S. Kobayashi, S. Mitsuda, T. Jogetsu *et al.*, Phys. Rev. B **60**, R9908 (1999).

研究テーマ：Ca_3CoRhO_6の磁性
表題：Ca_3CoRhO_6の磁気構造に関する中性子回折実験

1-2-20 Neutron Diffraction Study of Magnetic Structure in Ca_3CoRhO_6

S. Niitaka, K. Yoshimura, M. Nishi[1], and K. Kakurai[1]

Department of Chemistry, Graduate School of Science, Kyoto University, Kyoto 606-8502, Japan
[1]Neutron Scattering Laboratory, Institute for Solid State Physics, University of Tokyo, 106-1 Shirakata, Tokai, Ibaraki 319-1106, Japan

Ca_3CoRhO_6 with the rhombohedral K_4CdCl_6 structure contains linear chains consisting of alternating face-sharing CoO_6 trigonal prisms and RhO_6 octahedra. The chains along the c-axis are separated by calcium cations, forming a triangular lattice in the c-plane. The magnetic susceptibility *M/H* of Ca_3CoRhO_6 exhibits two anomalies at 90K(=T_1) and 30K(=T_2). The neutron diffraction patterns at 4K below T_2 and 40K between T_2 and T_1 correspond qualitatively with both a ferrimagnetic (FR) structure made up of ferromagnetic Ising spin chains similar to $Ca_3Co_2O_6$ and a partially disordered antiferromagnetic (PDA) structure, where 2/3 of the ferromagnetic Ising spin chains order antiferromagnetically each other and the remaining 1/3 are left incoherent with the other chains. To clarify which magnetic structure is realized, we measured the temperature dependence of the integrated intensity of (110) peak. It is a crucial point in determining the magnetic structure because it includes no magnetic component in the case of PDA, while it does a finite magnetic component in the case of FR structure.

The neutron diffraction experiment was performed for an uncrushed sintered pellet of Ca_3CoRhO_6 using ISSP-PONTA spectrometer in the temperature range of 2-130K under applied magnetic fields of 0-2T after ZFC.

Figure 1 shows the temperature dependence of the integrated intensity of the (110) peak. The intensity at 0T shows no increase below T_1, indicating that there exists no magnetic contribution to the (110) peak. It clearly confirmed that Ca_3CoRhO_6 realizes the PDA state below T_1 instead of the FR state. No magnetic component down to 2K also indicates no magnetic phase transition from the PDA state to the FR state. The intensity at 2T is the same as that at 0T below T_2 and sharply increases above T_2. It can be considered from this result that a state below T_2 is a frozen PDA (F-PDA) state where the Ising spin in the incoherent chains freeze and that a field-induced FR state accompanied with the melting of the frozen spins is realized above T_2. T_1 is the long-range magnetic ordered temperature judging from no difference between the intensities at 0T and 2T above T_1.

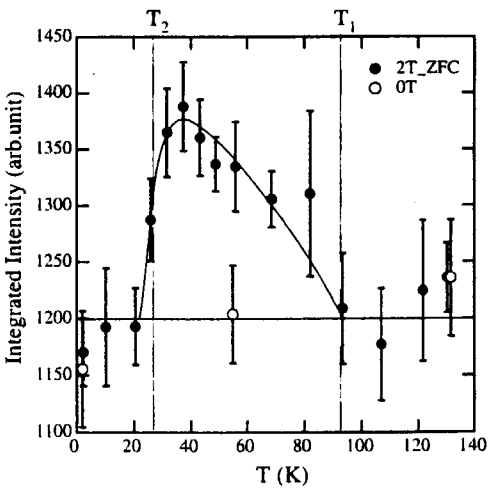


Fig.1 Temperature dependence of the integrated intensity of the (110) peak at 0T(○) and 2T(●). The solid lines are guides to the eye.

テーマ；β-$Na_{0.33}V_2O_5$ の磁気構造及び磁気励起　　表題；β-$Na_{0.33}V_2O_5$ の低温磁気構造

1-2-21 Magnetic Structure of β-$Na_{0.33}V_2O_5$ at Low Temperature

S. Nagai[1], T. Yamauchi[2], M. Nishi[1], J. Yamaura[2], M. Isobe[2], K. Kakurai[3], Y. Ueda[2]
[1]*Neutron Scattering Lab., ISSP, The University of Tokyo, 106 Shirakata, Tokai, Ibaraki, 319-1106*
[2]*Materials Design and Characterization Lab., ISSP, The University of Tokyo, 5-1-5 Kashiwanoha, Kashiwa, Chiba, 277-8581*
[3]*Advanced Science Research Center, JAERI, Tokai, Ibaraki, 319-1195*

β-$Na_{0.33}V_2O_5$ belongs to the β phase of vanadium oxide bronzes β-$A_xV_2O_5$, (A=Li, Na, Ag, Ca, Sr, etc.). In these compounds, metallic atoms of many kinds can crystallize into the tunnels embodied by the characteristic[1] framework of the host oxide (V_2O_5) with a wide composition range of x. The systematic study of compositions with different x[1] revealed that[2] it is only around x= 0.33 that β-$Na_{0.33}V_2O_5$ shows metallic temperature dependence in the electronic conductivity in **b**-direction, and undergoes MI (~136 K) and magnetic (T_N ~24 K) transition. The MI transition is regarded to be due to charge disproportionation[3] (from a mixed valence state to a charge ordered state).

Therefore, although the determination of magnetic structure below 24 K is an interesting subject in itself, we expect it could also provide information of the charge ordering pattern below 136 K.

Experimental

The intensities of magnetic Bragg reflection are expected to be rather weak, since the proportion of V^{4+} sites, which have S=1/2, to the whole vanadium sites is only 1/6. As we couldn't observe any Bragg reflection of a magnetic origin in the neutron powder diffraction experiment on HERMES, the single crystal neutron diffraction experiment was performed on the triple axis spectrometer PONTA, installed at JRR-3M, JAERI (Tokai), with ki = 2.67 ($Å^{-1}$), using 8×5×3 mm^3 β-$Na_{0.33}V_2O_5$ single crystal. Horizontal collimations of open−40′−80′−80′ were chosen. PG-filter was inserted before the sample to suppress the higher order contaminations.

Results

In Fig. 1, the temperature dependence of the magnetic Bragg peak intensity at **Q**=(0, 5/6, 0) is shown. We found satellite peaks appear at such **Q**, displaced by 5/6 **b*** from reciprocal lattice point, with the condition of h+k=even, l=integer below 24 K (see inset of Fig. 1). This reflection condition suggests that the V^{4+} sites form the C-face centered lattice. This is realized, for example, when the V^{4+} occupies half of the V1 zig-zag chain sites. Such linear charge ordering pattern might appear at T~136 K, and helical magnetic ordering on the linear chain sites with the periodicity of six lattice unit in **b**-direction and antiferromagnetic to the neighbouring chain in **a**-direction can explain the observed magnetic diffraction pattern qualitatively.

However, some findings shown below are not compatible with such a simple model.

a) The integrated intensities of the reflections at (0, 5/6, 0), (0, 7/6, 0) are remarkably stronger than others.
b) The intensities at (h, -1/6, 0) do not decrease monotonically with h.
c) Rather weak, but appreciable increase of intensity is found at T_N on the cation ordering superlattice peaks (0, 1/2, 0).
d) A peak structure is seen at (2, 1, 0) and (0, -1/6, 0) below T_N, but not above T_N.

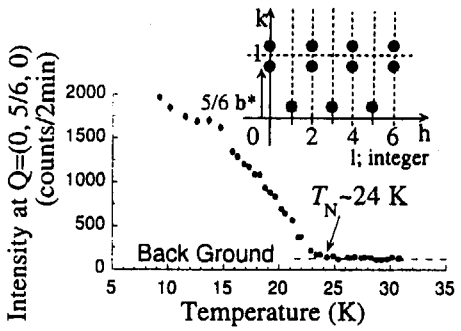


Fig. 1. The temperature dependence of the magnetic Bragg peak at Q = (0, 5/6, 0), which appears at T_N ~24 K. This coincides with the result of the susceptibility measurement[2].

[1]Y. Ueda: J. Phys. Soc. Jpn. **69** (2000) Suppl. B. 149.

[2]H. Yamada and Y. Ueda: J. Phys. Soc. Jpn. **68** (1999) 2735.

[3]M. Itoh, N. Akimoto, H. Yamada, M. Isobe and Y. Ueda: J. Phys. Soc. Jpn. **69** (2000) Suppl. B. 155.

研究テーマ：重い電子系UGe_2の5f電子状態
表題：高圧下におけるUGe_2の磁気形状因子

1-2-22 Magnetic Form Factor in UGe_2 under high pressure

H. Sagayama[1], K. Kuwahara[1], K. Iwasa[1], M. Kohgi[1], K. Kakurai[2], M. Nishi[3], K. Nakajima[3], N. Aso[3], Y. Uwatoko[3], Y. Haga[4], Y. Onuki[2,4]

[1]Faculty of Science Tokyo Metropolitan University, Hachioji, Tokyo 192-0397, Japan
[2]Advanced Science Research Center, JAERI, Tokai, Ibaraki 319-1195, Japan
[3]Insitute for Solid State Physics, University of Tokyo, Tokai, Ibaraki 319-1195, Japan
[4]Faculty of Science Osaka University, Kashiwa, Chiba 277-8581, Japan

UGe_2 crystallizes in the base-centered orthorhombic structure (Cmmm)[1,2]. It is an anisotropic ferromagnetic compound with a Curie temperature of 52 K and has large electronic specific heat coefficient γ of 35 mJ/mol K[2,3,4]. The magnetization along the a-axis, which is the direction of easy axis, shows a spontaneous magnetic moment of $1.43\mu_B$/U, whereas the b- and the c-axis are hard directions for magnetization. The Fermi surface and transport properties of this material are consistent with the 5*f* itinerant picture[4,5,6]. Thermal expansion of UGe_2 shows strong anisotropy[7]. The magnetic form factor of UGe_2 we observed at ambient pressure is similar to that of free ion U^{3+} and U^{4+} in spite of itinerant nature of the 5*f*-electron[8]. Recently, the superconductivity in a single crystal of this material was discovered under high pressure(~1.3 GPa). In order to clarify the difference of the spatial extent of 5*f*-electrons in UGe_2 between at ambient pressure and under high pressure, we have performed polarized neutron scattering experiments under high pressure.

The single crystal of UGe_2 used in the experiment is nearly parallelepiped with the shortest axis oriented to the c-axis (10.00 ×～ 3.5 × 0.50 mm^3). It was placed in a superconducting split-coil magnet with easy magnetization a-axis vertical to the scattering plane. The experiment has been done with the triple-axis spectrometer PONTA(5G) installed at JRR-3M reactor, JAERI. A polarized incident neutron beam with the wavelength of 1.015 Å was produced by the Cu_2MnAl polarizer. A set of collimators of OPEN-40'-80'-OPEN was used. The hydrostatic pressure was made in a clamp cell made of Cu-Be alloy. The experiment was performed at 2 K, by applying a magnetic field of 2 T along the a-axis and a pressure 1.4 GPa.

Figure 1 shows the magnetic amplitudes μf

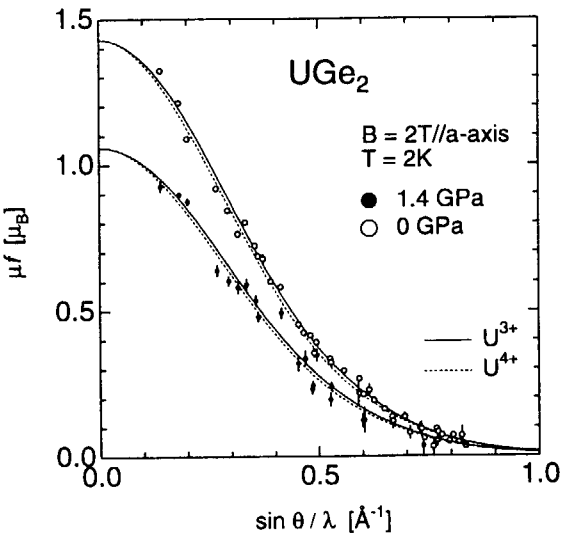


Fig. 1. The magnetic amplitudes μf of UGe_2 as function of $\sin\theta/\lambda$. The closed and open circles denote the observed μf at 1.4 GPa and 0 GPa, respectively. The solid and dashed lines represents fitting by the theoretical 5f form factor of free U^{3+} and U^{4+} respectively.

JRR-3M, PONTA, 2.Magnetism

of UGe_2 under 1.4 GPa as a function of $\sin\theta/\lambda$, where μ is magnetic moment of 5*f* electrons and *f* is the 5*f*-elrctron form factor. For reference, μf of UGe_2 at ambient pressure is also shown. The observed data can be fitted well by the theoretical 5*f* form factor calculated by the dipole approximation that corresponds to the free U^{3+} and U^{4+} in Russell-Saunders ground state but with a reduced magnetic moment. Such a result is also reported in some uranium compounds, for example, the heavy-electron superconductor UPt_3 and UBe_{13}[10]. The value of μ obtained by the fitting is $1.09\mu_B/U$. The result indicates that under the pressure of 1.4 GPa, the magnetic form factor, namely distribution of magnetic moment of 5*f*-electrons in b-c plane shows no large change compared to that at ambient pressure, although the magnetic moment decreases. But it is seen that the scattering of the data points from the calculated values under 1.4 GPa is larger than that at ambient pressure. This might imply that the anisotropy appears by applying pressure, although further analysis is necessary.

Reference

1) K. Oikawa *et al.*: J. Phys. Soc. Jpn. **65** (1996) 3229.
2) P. Boult *et al.*: J. Alloy and compounds **247** (1997) 104.
3) A. Menovsky *et al.*: in *High magnetic Field in High Field Magnetism*, edited by M. Date (North-Holland Publishing Company, 1983)
4) Y. Onuki *et al.* : J. Phys. Soc. Jpn. **61** (1992) 293.
5) Y. Onuki *et al.* : J. Phys. Soc. Jpn. **60** (1991) 2127.
6) K. Satou *et al.* : J. Phys. Soc. Jpn. **61** (1992) 1827.
7) G. Oomi *et al.* : Physica B 186-188 (1993) 758-760.
8) H. Sagayama *et al.* : J. Phys. Soc. Jpn. **70** Suppl. A (2001) 28.
9) S. S. Saxena *et al.* : Nature **406** (2000) 587.
10) C. Stassis *et al.* : Phys. Rev. B **34** (1993) 4382.

研究テーマ：非弾性中性子散乱によるスピンギャップ系$TlCuCl_3$におけるマグノンの質量測定
表題：$TlCuCl_3$における基底1重項状態からの磁気励起

1-2-23
Magnetic Excitations from the Gapped Ground State in $TlCuCl_3$

A. Oosawa, T. Kato[1], H. Tanaka, K. Kakurai[2], M. Müller[3] and H. –J. Mikeska[3]

Department of Physics, Tokyo Institute of Technology, Oh-okayama, Meguro-ku, Tokyo 152-8551
[1]Faculty of Education, Chiba University, Inage-ku, Chiba 263-8522
[2]Neutron Scattering Laboratory, ISSP, The University of Tokyo, Tokai, Naka-gun, Ibaraki 319-1106
[3]Institut für Theoretische Physik, Universität Hannover, Appelstrasse 2, 30167 Hannover, Germany

$TlCuCl_3$ has a monoclinic structure (space group $P2_1/c$). The crystal structure is composed of planar dimmers of Cu_2Cl_6, which are stacked on top of one another to form infinite double chains parallel to the crystallographic a-axis. The double chains are located at the corners and center of the unit cell in the bc-plane, and are separated by Tl^+ ions. Figure 1 shows the projection of Cu^{2+} ions with spin-1/2 on the ac-plane and the exchange interactions between Cu^{2+} ions. From the magnetization measurements, it was found that the ground state of $TlCuCl_3$ is spin singlet with an excitation gap Δ~0.65 meV [1].

Neutron inelastic scattering experiment was performed to investigate the magnetic excitations in $TlCuCl_3$ using the ISSP-PONTA spectrometer installed at JRR-3M, Tokai. The constant-k_f mode was taken with fixed final neutron energy of E_f=14.7meV. Collimations were set as open – monochromater - 80' – sample - 80'- analyzer -80' – detector. Excitation data were mainly collected at T=1.5K. All excitation spectra were taken by the constant-Q energy scan in the energy range of 2~15 meV. We performed scans along (h,0,1), (1,0,l), (h,0,2h+1) and (h,0,-2h+1.4) for $0 \leqq h \leqq 0.5$ and $1 \leqq l \leqq 2$. The present scan area is closer to the origin of the reciprocal space than the previous one [2], so that the magnetic excitations can gain the intensity due to the magnetic form factor.

Figure 2 shows the dispersion relation $\omega(Q)$ in $TlCuCl_3$ for Q=(h,0,2h+1) and (h,0,-2h+1.4). The lowest magnetic occurs at Q=(1,0,1) as observed in $KCuCl_3$. Since the lowest excitation energy E_{min} is lower than 1 meV, we could not determine the excitation energy due to the incoherent scattering and the low energy resolution. In Fig. 2, we substituted the gap energy E_{min} = 0.65 meV, which was evaluated from the magnetization measurement [1]. There is the sharp contrast between the dispersion curves for Q=(h,0,2h+1) and (h,0,-2h+1.4), which are roughly perpendicular to each other. The magnetic excitation is most dispersive along (h,0,2h+1), which is parallel to the cleavage (1,0,-2) plane, and is less dispersive for Q perpendicular to it.

The dispersion date was first analyzed using effective dimmer interactions [2]. The dimer interaction was determined as J=5.68 meV. In order to evaluate individual exchange interactions between dimers, we applied the cluster series expansion up to the sixth order [3]. Solid lines in Fig. 2 are the fits with $J_{(100)}$=0.34 meV, $J'_{(100)}$= 1.70 meV, $J'_{(201)}$= 2.56 meV, $J'_{(1\frac{1}{2}\frac{1}{2})}$= 0.91 meV and $J'_{(1\frac{1}{2}\frac{1}{2})}$= - 0.57 meV. The other interactions are negligible.

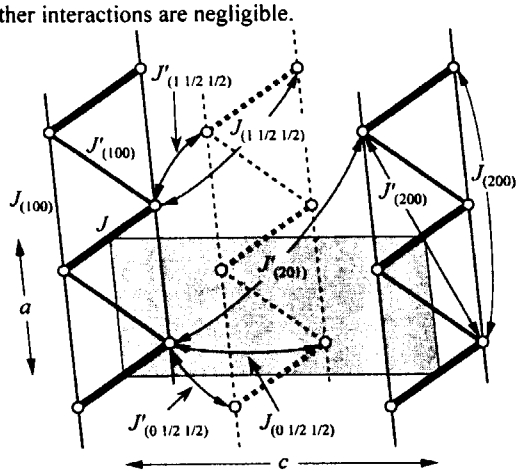


Fig.1. The projection of Cu^{2+} on the ac-plane and the exchange interactions. The double chain located at the corner and the center of the chemical unit cell in the bc-plane are represented by solid and dashed lines, respectively. The shaded area is the chemical unit.

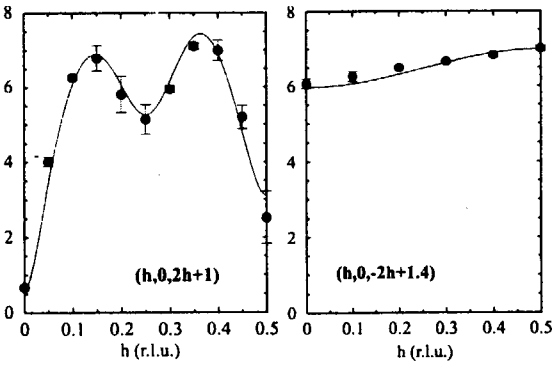


Fig.2. The dispersion relation $\omega(Q)$ in $TlCuCl_3$ for Q=(h,0,2h+1) and (h,0,-2h+1.4). Solid line denotes the fit by the cluster expansion. For the fitting parameters, see text.

Reference

[1] A. Oosawa, M. Ishii and H. Tanaka: J. Phys.: Condens. Matter 11 (1999) 265. [2] A. Oosawa et al.: J. Phys. Soc. Jpn. 70 (2001) Suppl. A 166. [3] M. Müller and H. -J. Mikeska: J. Phys.: Condens. Matter 12 (2000) 7633.

研究テーマ：酸化物磁性
表題：CoOにおけるマグノンギャップの観測

1-2-24 Observation of Magnon Gap in CoO

Keisuke Tomiyasu and Yorihiko Tsunoda

School of science and engineering, Waseda University,
3-4-1 Ohkubo, Shinjuku-ku, Tokyo 169-8555 Japan

The cobalt monoxide CoO belongs to a group of the antiferromagnetic monoxides with the rocksalt structure in the paramagnetic phases like MnO, FeO and NiO. All of their magnetic structures are the type-II fcc, that is, the ferromagnetic sheets of the spins in the (111) planes, antiferromagnetically stacked along the <111> directions. The points of difference among these substances are their distortions; rhombohedral about 0.1% in MnO, FeO and NiO, and tetragonal no less than about 1% in CoO. Furthermore, CoO gradually contracts with the decrease of the temperature from T_N=290[K] to 150[K].

We performed the inelastic neutron scatterting experiments for a single crystal of CoO at the 5G PONTA triple axis spectrometer installed at JRR-3M.

We operated the constant-Q mode for the magnon gap at 260, 230 and 200[K] at (0.5,1.5,1.5) in the reciprocal lattice space, the results are shown in Fig.1. We can say two points from that figure. First, the gap energy is not observed at 260[K] (T/T_N~0.9), becomes lareger as the temperature decreases, and a position of the peak maximum at 200[K] (T/T_N~0.7) is about 18[meV]. Second, the FWHM's are as wide as about 10[meV].

The physical picture of the above is as follows. The gap energy varies with the ratio of c/a because it reflects on an anisotropy energy. Especially, we have to pay attention to the fact that it already looks like zero at 260[K] (T/T_N~0.9) because of too short life time, that is, an overdumping.

We are now calculating exact values of the magnon gap energy at several temperatures corrected for the resolution function.

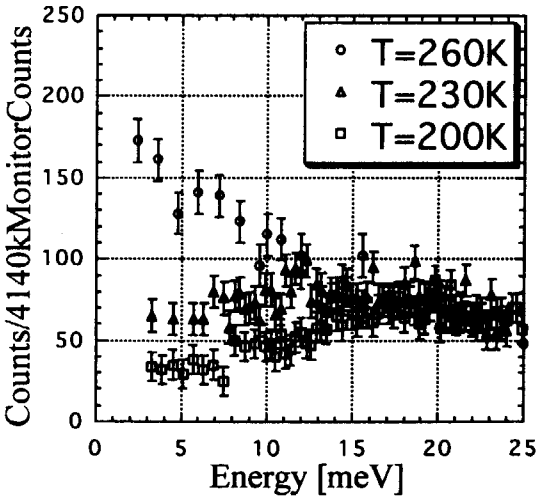


Fig.1 CoO Const-Q at (0.5,1.5,1.5)
T=200,230,260[K] Ef=14.7[meV]
40-F-40-S-40-A-40-C

JRR-3M, PONTA, 2. Magnetism

研究テーマ：磁気フラストレーション系 $Y_2Mo_2O_7$ 単結晶の金属・絶縁体転移
表題：Cr_3Te_4 における異常 Hall 効果と磁気構造

1-2-25 Anomalous Hall Effect and Magnetic Structure of Cr_3Te_4

H. Harashina[1,3], Y. Yasui[1,3], M. Kanada[1,3], S. Iikubo[1], S. Yoshii[3], K. Oda[1], M. Sato[1,3] and K. Kakurai[2,3]

[1]*Department of Physics, Nagoya University, Furo-cho, Chikusa-ku, Nagoya 464-8602*
[2]*Neutron Scattering Laboratory, ISSP, The university of Tokyo, Shirakata 106-1, Tokai 319-1195*
[3]*CREST Japan Science and Technology (JST)*

There is growing interest in the anomalous Hall effect of ferromagnetic systems with nontrivial magnetic structures. It is because there has been made a proposal[1] that anomalous Hall resistivity of $Nd_2Mo_2O_7$ is induced by the spin chirality ordering. Although both of Nd- and Mo- moments have the chirality ordering as was shown by neutron scattering study of the present authors' group[2], it seems that the Hall resistivity ρ_H of $Nd_2Mo_2O_7$ cannot be explained by its single mechanism.[3,4] It does not seem to be able to explained by other existing theories, either.

In order to clarify if the chirality mechanism plays an important role in determining the behavior of ρ_H of systems with nontrivial spin structure, we have studied several ferromagnetically ordered metallic systems. Cr_3Te_4 seems to be one of such systems, with Curie temperature T_C ~ 320K. It exhibits additional superlattice reflections below 80K suggesting that a more complicated magnetic structure is realized.[5]

Figure 1 shows the magnetic field (H) dependence of the Hall resistivity of a polycrystalline sample of Cr_3Te_4 at various temperatures. By using the expression of the Hall resistivity $\rho_H = R_0H + 4\pi R_S M$, with the ordinary and the anomalous Hall coefficients R_0 and R_S, respectively and the experimentally obtained magnetization M, the fittings

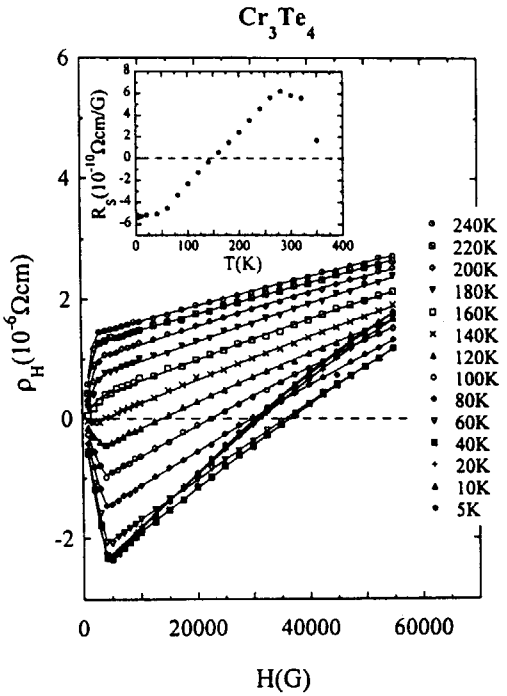


Fig. 1 The magnetic field dependence of the Hall resistivity ρ_H of Cr_3Te_4 at several temperatures. The inset is the T-dependence of Anomalous Hall coefficient R_S.

to the observed data have been carried out. In the inset the temperature (T) dependence of R_S is shown. R_S takes positive values at temperatures just below T_C and decrease with decreasing T and changes sign. It seems to take a finite value even at 0 K, which is unusual because conventional theories predict that anomalous Hall coefficient should exhibit much stronger decrease as T ap-

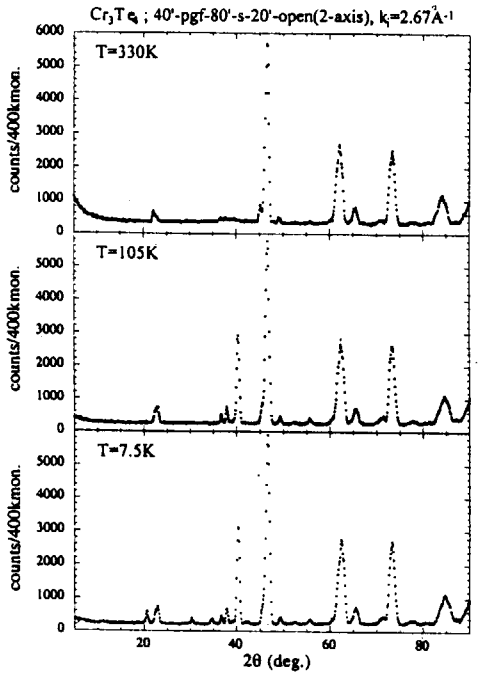


Fig 2 Neutron diffraction data of Cr_3Te_4 taken at 330 K, 105 K and 7.5 K.

proaches zero. At low temperatures, the Hall resistivity apparently has a nonlinear term in H. Are these anomalous transport behaviors related to the change of the magnetic structure?

Neutron powder diffraction experiments have been performed with using of the ISSP PONTA spectrometer installed at JRR-3M of JAERI. Figure 2 shows obtained diffraction patterns at 330 K, 105 K and 7.5 K. In comparison with the data at 330 K, several Bragg intensities increase at 105 K caused by the ferromagnetic ordering. At 7.5 K, additional superlattice reflections were observed. Now, these data are analyzed by using of the program Rietan to determine the magnetic structures. The direction of the ferromagnetic moment at 105 K has been found to be along the c-direction not but along the a-axis which was reported in ref. 5. It is consistent with magnetization measurements carried out in the present study by using of a single crystal. Although analysis of the data at 7.5 K has not been accomplished yet, the pattern of the superlattice reflections seems to indicate that the spin structure is not a ferromagnetic order with simple spin canting. The detailed magnetic structure is expected to give an important information to understanding the unusual behavior of the anomalous Hall effect.

References

1) K. Ohgushi *et al.*: Phys. Rev. **B62** (2000) R6005.
2) Y. Yasui *et al.*: J. Phys. Soc. Jpn. **70** (2001) 284.
3) S. Yoshii *et al.*: J. Phys. Soc. Jpn. **69** (2000) 3777.
4) S. Iikubo *et al.*: J. Phys. Soc. Jpn. **70** (2001) 212.
5) A. F. Andersen: Acta Chem. Scand. **24** (1970) 3495.

研究テーマ:$ZnCr_2O_4$の中性子散乱
表題:$ZnCr_2O_4$単結晶の磁気中性子散乱における電場磁場冷却効果

1-2-26 Field Cooling Effect in Magnetic Neutron Scattering of $ZnCr_2O_4$ Crystal

I. Kagomiya[1], M. Toki[1], Y. Hata[2], E. Kita, K. Kohn[1], K. Siratori[3], K. Nakajima[4] and K. Kakurai[4]

Institute of Applied Physics, Tsukuba University, Tsukuba, Ibaraki 305-8557, Japan,
[1]Department of Physics, Waseda University, Shinjyuku-ku, Tokyo 169-8555, Japan,
[2]Advanced Science Research Center Japan Atomic Energy Institute, Ibaraki, 319-1195 Japan,
[3]Department of Physics, Kyushu University, Fukuoka, 812-8581, Japan,
[4]Institute for Solid State Physics, University of Tokyo, Kashiwa, Chiba 277-8581, Japan

A normal spinel $ZnCr_2O_4$ is a typical example of a geometrically frustrated system. This crystal has a first-order antiferromagnetic transition takes place at T_N=11(±2) K. Our aim is to clarify how the frustration is relaxed at the transition. The magnetic structure is not known, though several magnetic Bragg reflections of the (*h*/2, *k*/2, *l*) and the (*h*/2, *k*/2, *l* /2) types were observed in previous neutron diffraction studies. Possible presence of antiferromagnetic domains makes the problem difficult to be solved. As the first step, we investigate the effect of magnetic and magnetoelectric field cooling in controlling the domains.

We used the PONTA diffractometer installed at JRR-3M in JAERI with the incident wavelength 1.63763 Å. A single crystal sample was set in such a way, as the [001] or [011] direction of the phase was vertical. The integrated intensities of the (3/2,1,0), (1,3/2,0) and (3/2,3/2,0) reflections are compared after cooling from 85 K to 5 K in the following conditions.

a) Cooling in the magnetic field (3 or 5 T) applied along the [100] or the direction ±15° from the [110] (MFC).

b) Cooling in both the magnetic (3 T or 5 T) and the electric (2 kV/cm) fields applied simultaneously (MEFC). The fields are along the [100] or the [110], and along the [00±1] , respectively

c) Cooling in zero magnetic and electric fields (ZFC). It was carried out before and after every MFC or MEFC measurement to certify the effect of the relevant field cooling.

The results are expressed by the difference of the integrated intensities after MFC or MEFC and ZFC, $\Delta I = I_{FC} - I_{ZFC}$.

Figure1(a) shows that MFC approximately along the [110] brings a remarkable change in the integrated intensity, while MFC along the [100] is not effective. This fact suggests that the spin structure possesses a unique axis along the [111], which are equivalent with respect to the [100]. However, the changes in individual reflections are not yet explained in a unified way.

Figure 1(b) depicts ΔI ($=I_{MEFC}-I_{ZFC}$) obtained by ZFC and MEFC. The ΔI was larger than probable error in all the reflections observed. We are now pursuing a model to be consistent with the observed tendencies.

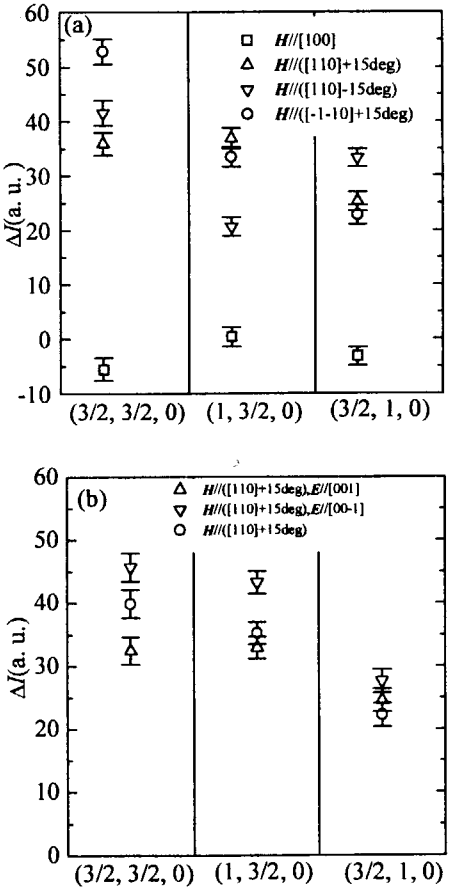


Fig.1 MFC(a) and MEFC effect(b) in magnetic scattering of $ZnCr_2O_4$ single crystal.

研究テーマ：偏極中性子回折法による CeB_6 の四重極秩序の研究
表題：CeB_6 の軌道整列の直接観測

1-2-27 Direct observation of orbital ordering in CeB_6

M. Saitoh [A], H. Takagiwa [A], H. Ichikawa [A], T. Yokoo [A], J. Akimitsu [A], M. Nishi [B], K. Kakurai [B], M. Takata [C], N. Okada [C], M. Sakata [C], S. Kunii [D]

[A] Department of Physics, Aoyama-Gakuin University, 6-16-1 Chitosedai, Setagaya-ku, Tokyo 157-8752, Japan
[B] Neutron Scattering Laboratory, ISSP, University of Tokyo, Tokai, Ibaraki 319-1106, Japan
[C] Department of Applied Physics, Nagoya University, Chikusa-Ku, Nagoya, Aichi 464-8603, Japan
[D] Department of Physics, Tohoku University, Aoba-Ku, Sendai, Miyagi 980-8578, Japan

CeB_6 has been investigated for the last decade as a typical Kondo compound [1-5]. At low temperatures, it exhibits an interesting phase diagram against external magnetic field, which consists of paramagnetic phase (phase I), antiferro-quadrupolar phase (phase II), and antiferro-magnetic phase (phase III). However, nobody has succeeded in directly observing the antiferro-quadrupolar ordering in CeB_6 in the phase II. We report here the trial to observe the antiferro-quadrupolar ordering in CeB_6 in the phase II by the polarized neutron diffraction technique.

Single crystals of CeB_6 were grown by the floating zone method. The polarized neutron diffraction measurements were performed at JRR-3M reactor at Tokai JAERI. The detailed idea and experimental procedures to observe the orbital ordering by the polarized neutron diffraction technique are described in Ref. [6]. The data were taken at 2.3 K under an applied magnetic field of 5.9 T in parallel with <110>-axis. The procedures for correcting the incomplete polarization (neutron polarization P_n ~ 96 %), statistical uncertainly estimation and extinction correction will be published elsewhere.

The final experimental results of the magnetic form factors are shown in Fig. 1 with open circles. The bars indicate the statistical uncertainties. We analyzed the experimental values of the magnetic form factors by the MEM / Rietvelt analysis, so we obtained the spin density distribution in CeB_6. In consequence of the analysis, we obtained the unexpected results that the magnetic moments exist not only at Ce-site but also at between B_6 octahedral and at the center of three bonding of B_6 octahedral. The amounts of each magnetic moment are as follows: Ce-site has 0.77 μ_B, the localized moment inbetween B_6 octahedral has 0.0214 μ_B, the center of three bonding in B_6 octahedral has 0.0218 μ_B. The calculated magnetic form factors are shown as well as the observed value in Fig. 1. The total magnetic moment well corresponds to the experimental values.

In conclusion, we clearly observed the existence of the magnetic moments other than Ce-site by measuring the magnetic form factors using polarized neutron diffraction technique under an applied magnetic field in parallel with <110>-axis. We believe that these magnetic moments dominate the strange physical properties in hexaboride.

JRR-3M, 5G(PONTA), 2. Magnetism

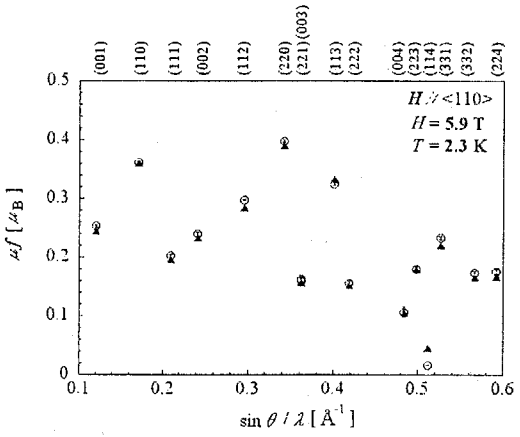


Fig. 1. Comparison between the observed (open circles with bars) and calculated (black triangles) magnetic form factors.

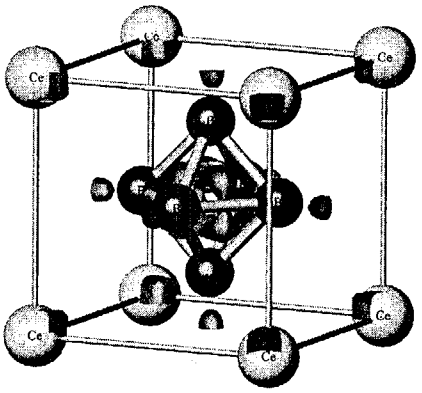


Fig. 2. The magnetic moment in CeB_6.

References

[1] T. Fujita, M. Suzuki, T. Komatsubara, S. Kunii, T. Kasuya, T. Ohtsuka, J. Phys. Soc. Jpn. **35** (1980) 569.

[2] M. Takigawa, H. Yasuoka, T. Tanaka, Y. Ishizawa, J. Phys. Soc. Jpn **52** (1983) 728.

[3] E. Zirngiebl, B. Hillebrands, S. Blumenröder, G. G ntherodt, M. Loewenhaupt, J. M. Carpenter, K. Winzer, Z. Fisk, Phys. Rev. B **30** (1984) 4052.

[4] J. M. Effantin, J. Rossant-Mignod, P. Burlet, S. Kunii, T. Kasuya, J. Magn. Magn. Mat. **47&48** (1985) 145.

[5] S. Nakamura, T. Goto, S. Kunii, J. Phys. Soc. Jpn. **64** (1995) 3941.

[6] Y. Ito, J. Akimitsu, J. Phys. Soc. Jpn. **40** (1976) 1333.

研究テーマ：$(La,Sr)_2MnO_4$のスピンダイナミクスの研究
表題：ストライプ相の$La_{0.6}Sr_{1.4}MnO_4$のスピン波励起

1-2-28 Magnetic Excitations in $La_{0.6}Sr_{1.4}MnO_4$

Kenji Nakajima,[1] Yasuyuki Iihama,[2] Yasuo Endoh[3]
[1] Neutron Scattering Laboratory, Institute for Solid State Physics, University of Tokyo
[2] Department of Physics, Faculty of Science, Tohoku University
[3] Institute for Materials Research, Tohoku University

Exotic phenomena in transition metal oxides triggered by hole-doping have been attracting theoretical and experimental interests recently. One of the fascinating phenomena is charge ordering observed in most of hole-dope transition metal oxides. In La_2MO_4 (M=3d metals), so-called 'hole-stripes' are observed in Ni and Cu systems, and checkerboard-type ordering of Co^{2+} and Co^{3+} is observed in Co system. In $La_{1-x}Sr_{1+x}MnO_4$, also checkerboard-type ordering of Mn^{3+} and Mn^{4+} is observed around x=0.5. [1-3] The complicated phenomena observed in these systems are results of co-playing of spin and charge. Therefore, the spin dynamics provides us information of detail inside of microscopic mechanism hole-doping effects. More over, spin-waves in these systems themselves are interesting since in most of the charge ordered phases, magnetic structure and magnetic correlations are geometrically modulated. In this context, we have been studying spin dynamics in $La_{0.6}Sr_{1.4}MnO_4$.

Neutron scattering experiments were carried out on a triple-axis spectrometer PONTA (5G). Pyrolytic graphite (PG) (002) was used for a monochromator and an analyzer. A PG filter was employed to remove higher order neutron components. A single crystal of $La_{0.6}Sr_{1.4}MnO_4$ (1.4 cm^3 in volume) was set into a ^{4}He closed-cycle refrigerator so as the scattering plane contains [100] (or [010] due to the crystal twining) and [001] (in the orthorhombic notation). Since crystal twining does not allow us to distinguish scattering from a^*-c^* plane from that from b^*-c^* plane, hereafter, we denote (h, 0, l) or (0, h, l) as (h, l). 3D antiferromagnetic (AF) Bragg reflections from ordered Mn^{3+} spins are observed at ((2n+1)/2, (2m+1)/2) (n, m:integer), while no Mn^{4+} origin reflections are observed in (h, l) plane. Therefore, we mainly investigate excitations of Mn^{3+} spins in this plane. In prior to inelastic experiments, we have done elastic work on TOPAN (6G) to characterize the sample. CE-type charge ordering in the sample

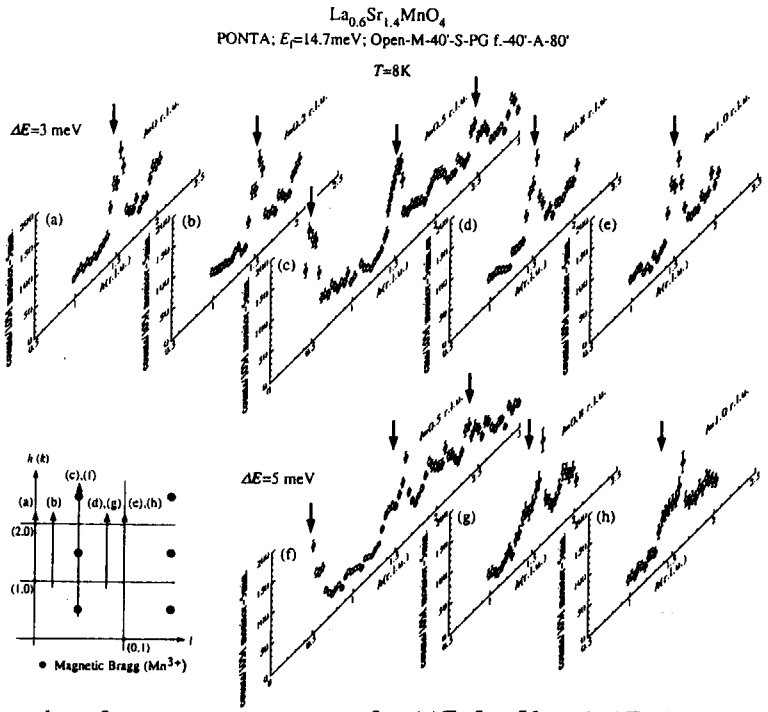


Fig. 1 Typical results of constant energy-transfer (ΔE=3meV and ΔE=5meV) scans at different l positions. Arrows indicate magnetic excitation signals.
JRR-3M, PONTA(5G), TOPAN(6G), 2.Magnetism

was confirmed. Néel temperature (T_N) and charge ordering temperature (T_{CO}) were determined to be T_N=118 K and T_{CO}=231 K.

In Fig. 1, results of Q-scans at constant energy-transfer of ΔE=3 meV and ΔE=5 meV are shown. Scans along (h, 0.5) (Fig. 1 (c) and (f)) shows well-defined peaks at (0.5, 0.5), (1.5, 0.5) and (2.5, 0.5). Since the peak positions coincide with magnetic Bragg positions, we consider that these signals are magnetic excitations of Mn^{3+} spins origin. As one can seen in Fig. 1, signal does not depend on l and the excitation has 2D nature as observed in pure and hole-doped La_2CuO_4 and La_2NiO_4. The 2D AF zone center sifts to the modulated positions, h=(2n+1)/2 (n: integer), from the expected positions in pure $LaSrMnO_4$, h=n (n:odd), as magnetic structure is modulated. That is the same situation of low energy magnons in a stripe phase of nikelate. [4]

By changing transfer-energy, complicated future of the excitations can be seen (Fig. 2 (a)). At low energy region, $\Delta E \leq 4$ meV, the magnetic excitations show well-defined, resolution-limited profiles. A conventional spin-wave theory well works in this region. From the low energy data, $\Delta E \leq 4$ meV, effective exchange interaction is estimated to be J_{eff}=2±0.3 meV. Resulted dispersion relation is depicted in Fig. 2(b). From the known values of La_2CuO_4, La_2NiO_4 and La_2CoO_4, using the relation, $J \propto n^{-2}$, [5] the exchange interaction of Mn^{3+} in pure $LaSrMnO_4$ is estimated to be about J_0=8~7 meV. Therefore, the effective exchange interaction in hole-doped $La_{0.6}Sr_{1.4}MnO_4$ is considered to be renormalized strongly. With increasing the energy, the intensity becomes smaller than expectation from a spin-wave theory. Dashed lines in Fig. 2 (a) are results of simulation using the parameters determined by the fit results of ΔE<4 meV data. At $\Delta E \geq 6$ meV, signal starts to decrease and almost disappears at $\Delta E \geq 10$ meV. Renormalization in exchange energy and decrease of intensity with increasing transfer-energy are same futures as observed in hole-doped La_2NiO_4, [4, 6, 7] and considered to be generic in spin-waves in insulating hole-doped La_2MO_4 systems.

Thedata are contaminated by 'unknown' signal, which becomes prominent at higher energy region (hatched line in Fig. 2(b)). $La_{1-x}Sr_{1+x}MnO_4$ is considered to show microscopic

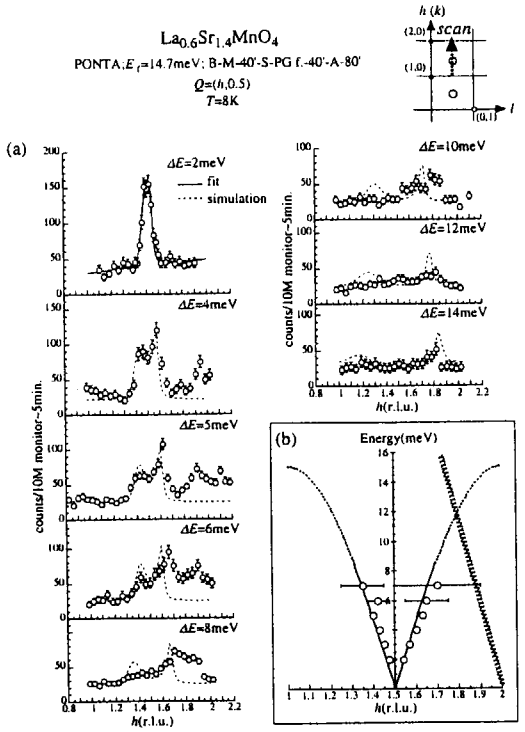


Fig. 2 (a) Constant energy-transfer scans through (1.5, 0.5). A solid line indicates the fit to a spin-wave theory. Dashed lines indicate profiles expected from a spin-wave theory (see text). (b) Resulted dispersion relation. Hatched line indicates the 'unknown' signal (see text).

phase separation into x=0.5 phase and a smaller x phase.[3] The contamination may come from $x \neq 0.5$ phase.

Here, We have studied excitations of Mn^{3+} spins in $La_{0.6}Sr_{1.4}MnO_4$. Further experiments to measure dynamics of Mn^{4+} spins and excitations in different samples of different x are planned. Especially, one of the issues remained is 'where does the magnetic intensity go at higher energy?' Since, in $La_2NiO_{4+\delta}$, unrenormalized spin-waves still remain even in hole-doped systems at higher energy region, [6, 7] we might find a trace of excitations in higher energy, which should be confirmed in further experiments.

[1] B. J. Sternlieb *et al.*: Phys. Rev. Lett. **76** (1996) 2169
[2] Y. Murakami *et al.*: Phys. Rev. Lett. **80** (1998) 1932
[3] S. Larochelle *et al.*: cond-mat/0101294
[4] J. M. Tranquada *et al.*: Phys. Rev. Lett. **79** (1997) 2133
[5] L. J. de Jongh: Solid State Commun. **65** (1988) 963
[6] K. Nakajima *et al.*: J. Phys. Soc. Jpn. **67** (1998) 1552
[7] K. Nakajima *et al.*: J. Phys. Chem. Solids **60** (1999) 1083

研究テーマ：CeB_2C_2での結晶場分裂
表題：正方晶$Ce^{11}B_2C_2$での磁気励起

1-2-29 Magnetic Excitations in the Tetragonal Compound $Ce^{11}B_2C_2$

K. Ohoyama, J. Konno, K. Kaneko, H. Hiraka, K. Hirota[A], H. Onodera, Y. Yamaguchi.

Institute for Materials Research, Tohoku University, Sendai 980-8577
[A]Department of Physics, Tohoku University, Sendai 980-8578

DyB_2C_2 with the tetragonal LaB_2C_2 type structure[1] undergoes an antiferroquadrupolar (AFQ) ordering at T_Q=24.7K and a further transition to an antiferromagnetic (AFM) ordered state at 15.3K[2]. Moreover, an isostructural compound HoB_2C_2 is the unique AFQ material which exhibits AFQ ordering below its magnetic ordering temperature[3]. The most important feature of AFQ ordering in RB_2C_2 system is that the strict ground state by crystal electric field (CEF) effect is a doublet in DyB_2C_2 and a singlet or a doublet in HoB_2C_2; therefore, the strict ground states do not have degree of freedom on quadrupolar moment. We think that the AFQ orderings in this system require a quasi-doublet or quasi-triplet ground state with very small energy gap between the strict ground states and the first excited states. Thus, to understand the mechanism of AFQ ordering in RB_2C_2, it is indispensable to make clear low-lying CEF levels of this system. For this purpose, we performed inelastic scattering experiments on the triple axis spectrometer TOPAN at the JRR3-M reactor of JAERI. Since level schemes in DyB_2C_2 and HoB_2C_2 is expected to be too complicated to clarify, the sample for the present experiments was a polycrystalline sample of $Ce^{11}B_2C_2$ because Ce has the simplest CEF level scheme with only three doublets among the rare earth system. Collimation condition was 30'- 60'-S-PG-100'-B with a constant E_f of 14.7meV.

Fig.1 shows temperature and Q dependence of inelastic scattering spectra of $Ce^{11}B_2C_2$ between 7meV and 13meV obtained on TOPAN. We observed two broad and weak excitations at about 9meV and 11meV. Because of the Q and temperature dependence, the excitations at 9meV and 11meV are probably magnetic. This result is consistent with the fact that temperature dependence of magnetic specific heat indicates a possibility of doublet(s) at about 120K. On the other hand, we also observed another magnetic-like excitation at about 6 meV at T=60 K. The excitation at 6meV, however, is not consistent with the other excitations at 9meV and 11meV; any level scheme model which represents all the three excitations has not been found. To obtain more information of CEF in RB_2C_2 system, inelastic scattering experiments in NdB_2C_2 and ErB_2C_2 are in progress.

References

[1] T. Onimaret al.: J. Phys. Soc. Jpn. 68(1999) 2287.
[2] H. Yamauchi et al. J. Phys. Soc. Jpn 68 (1999) 2057.
[3] H. Onodera et al.: J. Phys. Soc. Jpn. 68(1999) 2526.

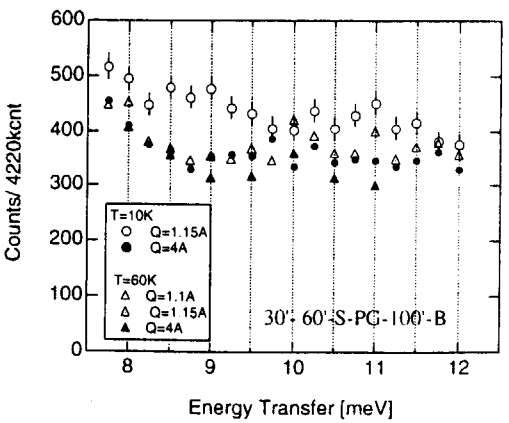


Fig.1 Inelastic scatering spectra from $Ce^{11}B_2C_2$ at 10 K and 60K at several Q values.

JRR-3M, TOPAN (6G), 2: Magnetism

研究テーマ：$Ho^{11}B_2C_2$の磁気相転移
表題：$Ho^{11}B_2C_2$の単結晶中性子散乱

1-2-30 Neutron Diffraction Study on Single Crystal HoB_2C_2

A. Tobo, T. Ohmori, T. Matsumura[A], N. Oumi[A], K. Hirota[A], K. Ohoyama, H. Yamauchi, H. Onodera, Y. Yamaguchi

Institute for Materials Research, Tohoku University, Sendai, 980-8577 Japan

[A]Department of Physics, Tohoku University, Sendai, 980-8578 Japan

The systems showing both of an antiferroquadrupolar (AFQ) ordering and an antiferromagnetic (AFM) ordering have been attracting many interests because of their complicated magnetic behavior. One of those materials is HoB_2C_2. It is reported from magnetization and heat capacity measurements that an AFM transition occurs at T_N=5.9 K and an AFQ ordering transition at T_Q=4.5 K in HoB_2C_2[1]. The most striking feature is that T_Q is lower than T_N. Hence, in the field-temperature phase diagram of HoB_2C_2, we obtained a new intermediate phase, phase IV, between T_Q and T_N.

The neutron diffraction measurements using powdered $Ho^{11}B_2C_2$ sample shows that the magnetic structure between T_Q and T_N is described by propagation vectors of $\boldsymbol{k}_1$=[1 0 0] and $\boldsymbol{k}$=[1+δ δ δ'], where δ~0.1 and δ'~0.04[2]. These propagation vectors indicated phase IV is a magnetic state with long periodicity. In order to clarify the nature of magnetic structure in phase IV, we investigated neutron diffraction measurements around the (1 0 0) magnetic Bragg point on the single crystal $Ho^{11}B_2C_2$ using TOPAN (6G) spectrometer installed at JRR-3M, JAERI.

From the measurements, we saw three type of magnetic components around the (1 0 0) magnetic Bragg point: the (1 0 0) Bragg peak, the (1+δ δ δ') satellite peaks, and the small uniform scattering intensity observed in the region whose vertices are the satellite peaks. In Fig. 1, we show the temperature dependence of these three components. They have different temperature dependency, and the temperature region where the (1+δ δ δ') satellite peaks appear corresponds to phase IV in zero field. Further measurements are needed to understand the nature of the uniform scattering.

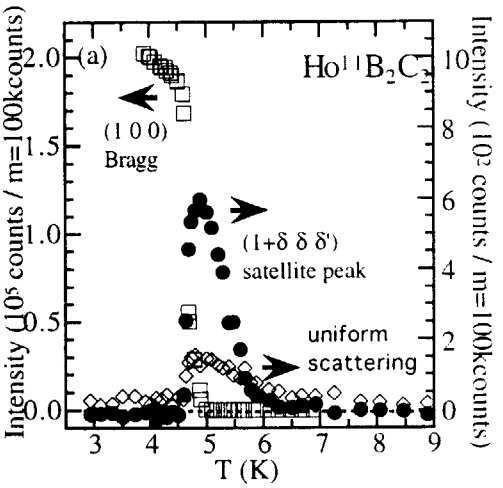


Fig. 1. Temperature dependence of the neutron scattering intensities of three magnetic components around reciprocal lattice points (1 0 0). The magnetic satellite peak component is obtained by subtracting the intensity at (1.02 0 0.04) from that at (1.11 0 0.04). The uniform scattering component is obtained by subtracting the intensity of background from that at (1.02 0 0.04).

[1] H. Yamauchi *et al.*, J. Phys. Soc. Jpn. 68 (1999) 2057.
[2] K. Ohoyama *et al.*, J. Phys. Soc. Jpn. 69 (2000) 3401.

JRR-3M, TOPAN (6G), 2 magnetism

研究のテーマ：中性子回折法による $Lu_2V_2O_7$ の軌道秩序の研究
表題：$Lu_2V_2O_7$ の軌道整列の直接観測

1-2-31 Observation of orbital ordering in $Lu_2V_2O_7$

L. Kano [A], M. Saitoh [A], T. Yokoo [A, B], N. Furukawa [A], J. Akimitsu [A, B], T. Matsumura [C], M. Takeda [C], K. Hirota [C], Y. Taguchi [D], Y. Tokura [D]

Dept. of Phys., Aoyama-Gakuin Univ.[A], *CREST* [B], *Dept. of Phys., Tohoku Univ.*[C], *Dept. of Appl. Phys., Univ. of Tokyo*[D]

The pyrochlore $Lu_2V_2O_7$ (space group: $Fd\bar{3}m$) is a ferromagnetic Mott-insulator with $T_C \simeq 73$ K.

The electronic configuration of V^{4+} ions in $Lu_2V_2O_7$ is $(t_{2g})^1$. A systematic distortion of VO_6 octahedra in pyrochlore produces a trigonal field to a vanadium ion. The existence of "anti-ferromagnetic" orbital ordering has been suggested for the origin of the ferromagnetism.

We investigated the orbital ordering scheme of $Lu_2V_2O_7$ by means of the polarized neutron diffraction method.

Single crystal was grown by the floating zone method. The polarized neutron diffraction measurements were performed at JRR-3M reactor at Tokai JAERI. The energy of the incident neutrons is 80 meV. The data was taken at 3 K under an applied magnetic field of 3 T in parallel with <1 $\bar{1}$ 0>-axis of single crystal specimen. The procedures for correcting the incomplete polarization (neutron polarization P_n ~94.7%), statistical uncertainty estimation and extinction correction will be published elsewhere.

The final experimental results of the magnetic form factors are shown in Fig.1 with squares. The bars indicate the statistical uncertainties.

In order to compare the theoretically suggested orbital ordered configuration of the t_{2g} electron with the experimental results, we calculated the magnetic form factor. The best-fitted wave function is

$$|\Psi\rangle = \sqrt{1/3}|\varphi_{xy}\rangle + \sqrt{1/3}|\varphi_{yz}\rangle + \sqrt{1/3}|\varphi_{zx}\rangle \propto \left|\varphi_{(x+y+z)^2-r^2}\right\rangle$$

for each site in the unit cell. Orbital ordered state shown in Fig.2 indicates that the lobe of each wave function directed for the center of the tetrahedron and the ground state of the wave function of V^{4+} ions is a_{1g}.

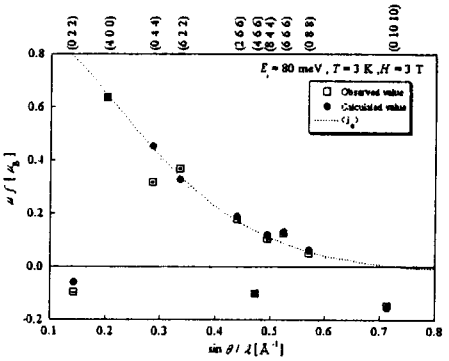


Fig.1. Comparison between the observed (squares with bars) and calculated (circles) magnetic form factors.

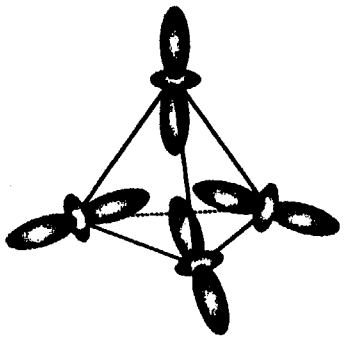


Fig.2. Schematic view of the orbital ordering in $Lu_2V_2O_7$.

研究テーマ：URu_2Si_2の17.5転移に関する研究
表題：重い電子系化合物URu_2Si_2のフォノン分散

1-2-32 Phonon Dispersions in the heavy-electron compound URu_2Si_2

K. Kuwahara, K. Iwasa, M. Kohgi, M. Yokoyama[1], H. Amistuka[1]

Department of Physics, Tokyo Metropolitan University, Hachioji, Tokyo 192-0397, Japan
[1]Graduate School of Science, Hokkaido University, Sapporo 090-0810, Japan

The heavy-electron compound URu_2Si_2 undergoes two successive phase transitions; a second-order phase transition at $T_O = 17.5$ K and a superconducing transition at $T_C = \sim 1.2$ K. It crystallizes in the body-centered tetragonal $ThRu_2Si_2$ type of structure, space group I4/mmm. One of the most interesting issue in this material is the origin of the puzzling phase transition at T_O. Below T_O a simple type-I antiferromagnetic arrangement develops. The problem is that the size of the observed staggered moment is extremely small (~$0.03\mu_B$/U). If this tiny moment is the order parameter of the phase transition at T_O, it is very difficult to explain the observed large anomalies at T_O in various bulk properties of URu_2Si_2. Because of this inconsistency, the possibility that the tiny moment is not the intrinsic order parameter has been argued.

In previous ultrasonic velocity measurements, we have found the weak but distinct softening in the transverse $c_{11} - c_{12}$ mode. This elastic anomaly suggests that U ions have the quadrupolar degree of freedom at low temperatures. If the phase transition at T_O is an antiferoquadrupolar (AFQ) ordering with a propagation vector Q, the transverse acoustic (TA) phonon at $q = Q$ may show a softening near T_O. To check this possibility, we have measured the temperature dependence of the phonon dispersions by inelastic neutron scattering.

Single crystal of URu_2Si_2 was grown in a tetra arc furnace using the Czochralski method. The shape of the crystal is a cylinder (~5mm diameter and ~33mm in length). The inelastic neutron scattering experiment in the (h k 0) scattering plane has been done using the triple axis spectrometer TOPAN (6G) at the JRR-3M, Tokai.

Figure 1 shows the TA phonon dispersions of URu_2Si_2 for q // [h h 0] and q // [h 0 0] directions. The observed dispersion curves are only weakly temperature dependent in contrast to the temperature dependence of the elastic constants. To clarify the order parameter of the phase transition at T_O, measurements of other phonon branch of URu_2Si_2 may be necessary.

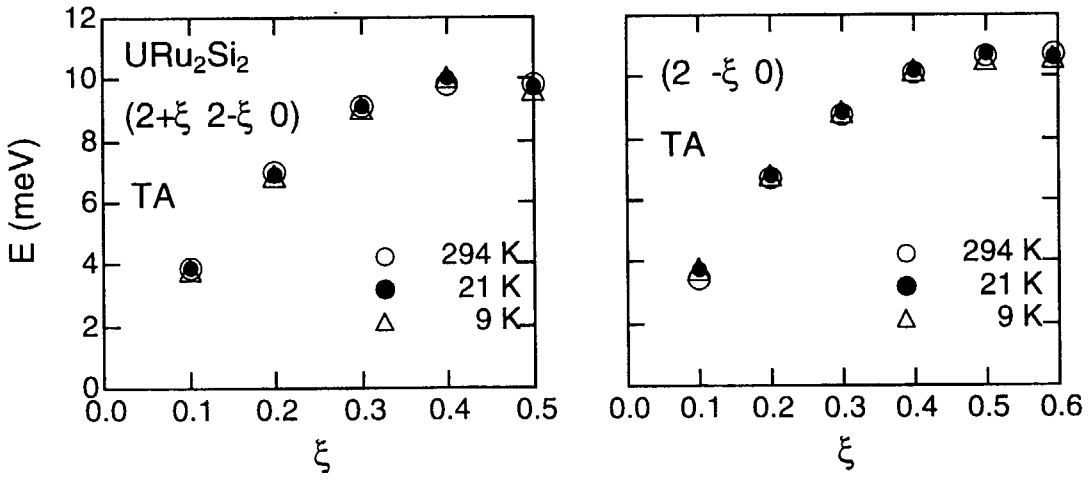


Figure 1 The TA phonon dispersions of URu_2Si_2 for q // [h h 0] and q // [h 0 0] directions.

JRR-3M, TOPAN, 2. Magnetism

研究テーマ: 金属人工格子の磁性
表題 : 単原子制御されたCo/Ru人工格子の反強磁性

1-2-33 Antiferromagnetism of Co/Ru artificial multilayer by monatomic controlled deposition

M. Takeda, K. Himi[1] and K. Takanashi[1]

Physics Department, Graduate School of Science, Tohoku University, Sendai 980-8578, Japan
[1]Institute for Material Research, Tohoku University, Katahira Sendai 980-8577, Japan

Recent development of thin film preparation techniques has made it possible to fabricate ordered alloys with layered structures artificially. In the equilibrium phase, Co and Ru form solid solutions for all the compositions, however, no ordered phase exists. Recently good epitaxial hcp-Co/Ru(0001) films were successfully synthesized and several studies revealed that Co/Ru superlattices with thick Co layer showed a large antiferromagnetic coupling of Co even for a few atomic layers of the Ru thickness[1]. On the other hand, magnetism and magnetic structures of Co/Ru films with thin Co layers are still unknown.

We prepared Co(x ML)/Ru(y ML) multilayers and studied their magnetic structure mainly by magnetization measurements (ML: monatomic layer thickness) [2]. Magnetization curves indicated that only 1 ML difference in the Ru thickness in Co(1 ML)/Ru(y ML) (y = 1- 4) strongly affected on the interlayer magnetic coupling: i.e. ferromagnetic for y = 3, antiferromagnetic for y = 2 and 4 . We have tried to confirm the magnetic structure by neutron diffraction measurements.

Detailed procedures of sample preparation and the magnetization curves were reported in ref. 2. Almost all of Co/Ru films have perpendicular magnetic anisotropy. [Co(1 ML)/Ru(1 ML)] × 100 on the *a* - plane of a sapphire substrate with a Ru buffer layer of 20 nm was used as the first sample to be measured because only this sample has in-plane ferromagnetic components. This enables us to detect magnetic signal without an external magnetic field in the θ -2θ scans normal to the sample plane.

Figures 1 and 2 show the θ -2θ scans by X-ray and neutrons, respectively. The magnetic modulation signal is expected as satellites of CoRu(0001) nuclear peak. However, the peaks at 1.3 and 1.7 Å^{-1} in Fig. 2 has been revealed to come from the sapphire substrate. Furthermore the nuclear peak was not detected in the case of neutrons. In Fig. 1 the ratio of peak height of CoRu(0001) to (0002) is less than 10^{-2}. Thus, we have to improve S/N ratio by reducing the background noise to detect the signals in the next neutron measurements.

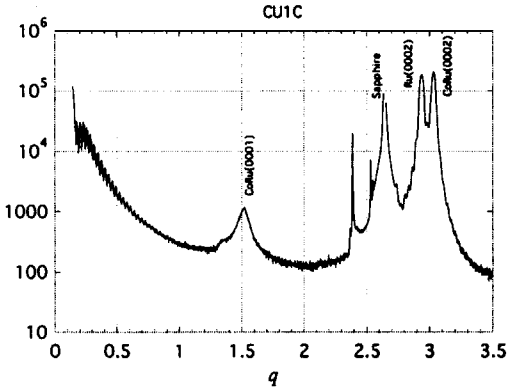


Fig. 1 θ-2θ scans of [Co(1 ML)/Ru(1 ML)] × 100 on a sapphire substrate at ambient temperature by X-ray.

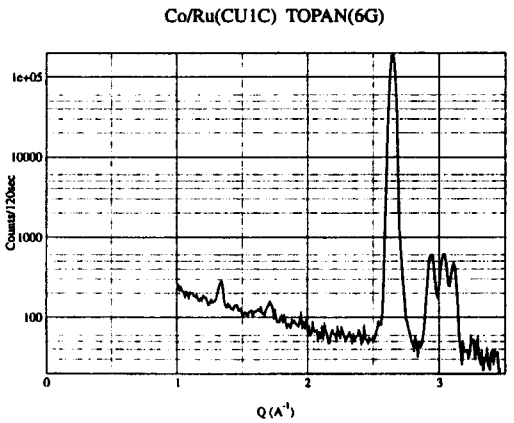


Fig.2 The same scan as Fig. 1 by neutrons.

References

[1] D. Muller, K. Ounadjela, P. Vennegues, V. Pierron-Boshnes, A. Arbaoui, J. P. Jay, A. Dinia, and P. Panissod, J. Magn. Magn. Matter. **104**, 1873 (1992).
[2] K. Himi, K. Takanashi, S. Mitani, M. Yamaguchi, D.H. Ping, K. Hono and H. Fujimori, Appl. Phys. Lett., **78** 1436(2001).

研究テーマ：電子ドープ型銅酸化物におけるスピン揺動と超伝導の相関
表題：電子ドープ型銅酸化物 $Nd_{2-x}Ce_xCuO_4$ における超伝導相境界近傍での反強磁性秩序

1-2-34 Antiferromagnetic Order near the Superconducting Phase Boundary of Electron-Doped $Nd_{2-x}Ce_xCuO_4$

[1]T.Uefuji,[1]M.Fujita,[2]K.Kurahashi,[3]M.Matsuda,[1]K.Yamada,[4]I.Watanabe and [4,5]K.Nagamine

[1]Institute for Chemical Research,Kyoto University,Gokasho,Uji,Kyoto 611-0011,Japan
[2]Department of Physics,Faculty of Science,Tohoku University,Aramaki,Aoba-ku,Sendai 980-8578,Japan
[3]Advanced Science Research Center,Japan Atomic Energy Research Institute,Tokai,Ibaragi 319-1195,Japan
[4]Muon Science Laboratory,RIKEN,Hirosawa,Wako,Saitama 351-0198,Japan
[5]Meson Science Laboratory,KEK,Oho,Tsukuba,Ibaragi 305-0801,Japan

Here we report recent neutron scattering and μSR studies on the electron-doped $Nd_{2-x}Ce_xCuO_4$(NCCO) around the antiferromagnetic(AF)-superconducting(SC) phase boundary to reexamine the phase diagram.

Neutron scattering measurements have been performed on the thermal neutron spectrometers TOPAN and KSD and on the cold neutron spectrometer C11 in JRR-3M. Reduced single crystals were mounted in a closed-cycle ^{4}He refrigerator with the (H0L)-orthorhombic zone parallel to the scattering plane. μSR experiment was performed on the RIKEN muon beam port in Rutherford-Appleton Laboratory in the UK.

The obtained magnetic-superconducting phase diagram of NCCO is shown in Fig.1[1, 2,3]. Below around T_{N1} magnetic Bragg peak intensity starts to develop and the T_{N1} approximately corresponds to the Néel temperature T_N previously determined by Luke *et al.*[4]. In fact, below around T_{N1} a fast exponential-type muon spin relaxation begins to appear in zero-field μSR time spectra. However, the so-called decoupling effect of the londitudinal magnetic field on the μSR time spectra strongly suggests the dynamical nature of the magnetic ordering below T_{N1}. Upon further cooling below around T_{N2} static ordering is found by μSR measurement.

For SC samples near the phase boundary accompanying with the antiferromagnetic order, the q-width of magnetic peak is broader than the instrumental resolution and is temperature dependent. For example, in the SC NCCO with x=0.14 the magnetic peak width along both in-plane and out-of-plane directions gradually increases upon heating and the AF characteristic lengths are determined to be about 100A in both directions from the inverse of the width. On the other hand, in the AF sample with x=0.13 the peak width is almost resolution-limited and is temperature independent.The AF volume fraction in the AF samples estimated from μSR time spectra saturates below T_{N2}, while in the SC samples the volume fraction gradually increases upon cooling.

These systematic studies provide us important information on the interplay between antiferromagnetic order and superconductivity of the electron-doped high-T_c cuprates.

References

[1]T.Uefuji *et al.*,to be published in Physica **C**.
[2]M.Matsuda *et al.*,Phys Rev.**B45**,12548(1992).
[3]M.Matsuda *et al.*,Phys.Rev.**B42**,10098(1990).
[4]G.M.Luke *et al.*,Phys.Rev.**B42**,7981(1990).

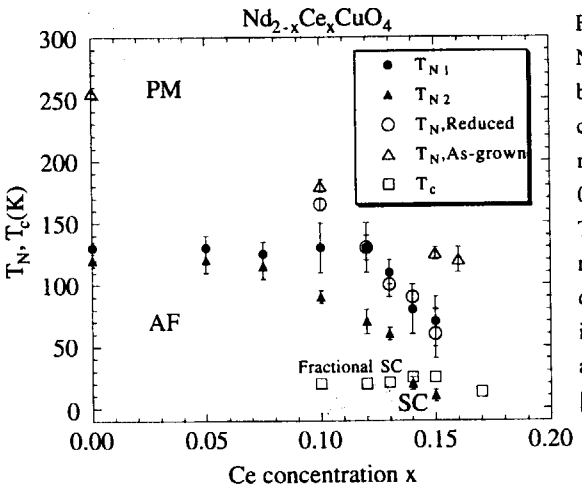


Fig.1 Magnetic-superconducting phase diagram of NCCO single crystals. Both T_{N1} and T_{N2} are determined by μSR measurements. T_N for both reduced and as-grown crystals are determined by neutron scattering measurements. μSR measurements for samples with x=0.000, 0.050 and 0.075 were performed on powder samples. The large difference between neutron scattering and μSR measurements in the lightly doped region possibly be caused by the difference in the oxygen nonstoichiometry in the samples. The data for the as-grown x=0.15 and the as-grown x=0.00 samples are taken from Ref.[2] and [3],respectively.

JRR-3M,TOPAN,HER,KSD,2.Magnetism,3.Superconductivity

研究テーマ：層状マンガン酸化物の軌道秩序
表題：層状ペロブスカイト型マンガン酸化物の軌道状態

1-2-35 Orbital State in Layered-Perovskite Manganite Compound

T. Arima, M. Kushida, A. Nakazawa, K. Ohoyama[1], J. Akimitsu[2], T. Matsumura[3], K. Hirota[3]

Institute of Materials Science, University of Tsukuba, Tsukuba 305-8573, Japan
[1]Institute for Materials Research, Tohoku University, Sendai 980-8577, Japan
[2]Department of Physics, Aoyama-Gakuin University, Tokyo 157-8572, Japan
[3]Department of Physics, Tohoku University, Sendai 980-8573, Japan

Recently, orbital states in strongly-correlated-electron systems have attracted a great deal of attention. We are studying the orbital state in a layered-perovskite manganese oxide compound $La_{2-x}Sr_{1+x}Mn_2O_7$ using a polarized-neutron scattering technique. The spin density distribution should be equivalent to the density distribution of 3*d* electrons, because the manganite compound is half-metallic. The magnetic structure factor obtained by elastic neutron scattering is the Fourier series of the spin density distribution.

Single crystals of $La_{2-2x}Sr_{1+2x}Mn_2O_7$ (x=0.30, 0.40) were melt-grown using a floating-zone furnace. The ratios of magnetic structure factor, F_M, to nuclear structure factor, F_N, for various scattering vectors, Q=($h0l$), were obtained by polarized-neutron scattering measurements using the triple-axis spectrometer TOPAN in JRR-3M of the Japan Atomic Energy Research Institute (JAERI). The measurement was carried out in a magnetic field of 1 T along the *b*-axis. The absolute values of $|F_N|^2+C|F_M|^2$ were obtained by the Rietveld analysis of powder neutron diffraction data, where C is the factor dependent on the angle between the scattering vector and the spin moment. The powder diffraction measurement was carried out using the powder neutron diffractometer, HERMES, which is equipped with multi-detectors with the Ge (331) monochromator (λ=1.819 A) in JRR-3M of JAERI. Magnetic structure factors, $F_M(h0l)$, were calculated from the data of F_M/F_N and $|F_N|^2+C|F_M|^2$. The projection of spin density distribution on the ac plane is obtained by Fourier transformation of the structure factors.

The contour maps of the spin density projection around double Mn ions are shown in Figure 1. Here the contribution of three t_{2g} electrons is subtracted assuming the ionic wave functions. The spin distribution in the x=0.40 compound extends more along the *a*-axis than along the *c*-axis, while the spin distribution of the x=0.30 sample is lower in MnO_2 plane.

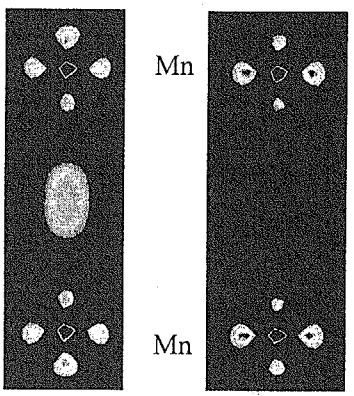


Figure 1 The contour map of the spin density projection on the *ac* plane in $La_{1.2}Sr_{1.8}Mn_2O_7$ for x=0.30 (left) and x=0.40 (right).

研究テーマ：RPdSn (R=Tb,Ho,Er)化合物の磁気構造
表題：HoPdSn の磁気構造

1-2-36 MAGNETIC STRUCTURE OF HoPdSn

Y. Andoh, G. Nakamoto[1], M. Kurisu[1], T. Tsutaoka[2] and S. Kawano[3],

Faculty of Education and Regional Sciences, Tottori University, Tottori 680-8551, Japan
[1]*Japan Advanced Institute of Science and Technology, Ishikawa 923-1292, Japan*
[2] *Graduate School of Education, Hiroshima University, Higashi-Hiroshima 739-8524, Japan*
[3]*Reearch Reactor Institute, Kyoto University, Kumatori, Osaka 590-0494, Japan*

Ternary equiatomic rare-earth compounds, TbPdSn and HoPdSn, crystallize in the orthorhombic (*Pnma*) TiNiSi-type structure. TbPdSn is characterized by three successive magnetic transitions (T_N, T_1 and T_2) and the multistep metamagnetic transition along the *b*-axis at 1.8 K [1]. On the other hand, HoPdSn exhibits two successive magnetic transitions (T_1 = 2.7 K and T_N = 3.6 K). Recently we have performed the measurements of neutron diffraction on single crystals of HoPdSn in the reciprocal a^*-c^* plane. We have found that two propagation vectors k_1= (1, 0, k_{1z}) and k_2= (0.33, 0, 0.93) coexist. The value of k_{1z} changes from 0.38 at 1.8 K to 0.35 at T_1 with increasing temperature.

However, till now, for HoPdSn no information about its spin configuration has been reported. In the present study, we have carried out neutron diffraction studies to reveal the magnetic structure of HoPdSn.

Single crystals of HoPdSn were grown by a Czochralski method. Neutron diffraction measurements were made by using the HQR spectrometer of JRR-3M of JAERI at Tokai in the temperature range from 1.5 K to 5 K.

Figure 1 shows the contour map around at (1 0 0.39) with the propagation vector k_1 in the a^*-c^* plane. Two main magnetic peaks and three satellite peaks are observed at 1.5 K. As the temperature is lowered, the intensities of all peaks are decreased and the number of satellites is changed from three to two but their positions are not changed. At 2.5 K, magnetic peak is not observed at around (1 0 0.39). Instead a new peak appears at (1.02 0 0.36). As Fig.2 shows, there is only single peak in the contour map at around (2 0 0) nuclear reflection, suggesting that the multi-peaks at around (1 0 0.39) are not originated from the grains.

Further diffraction measurements are in progress to clarify the magnetic structure in each phase in the compound.

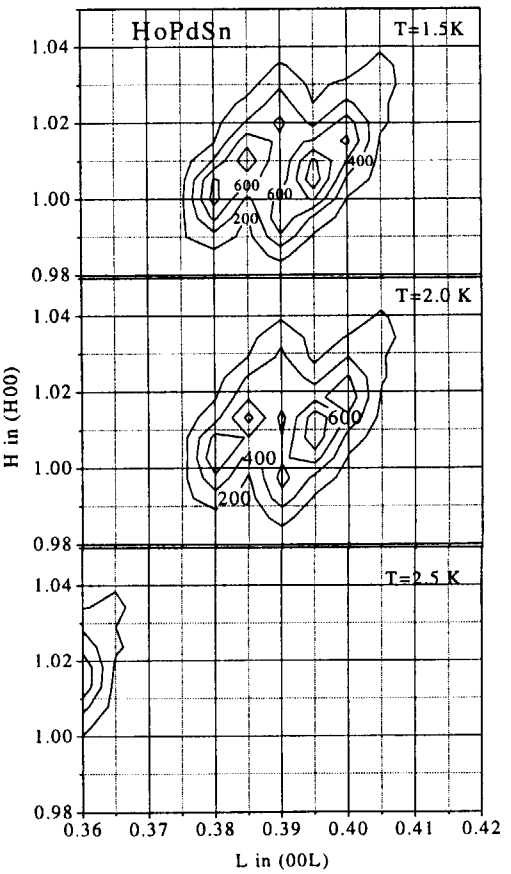


Fig. 1 The contour map around at (1 0 0.39) with k_1 in the a^*-c^* plane at 1.5 K, 2.0 K and 2.5 K.

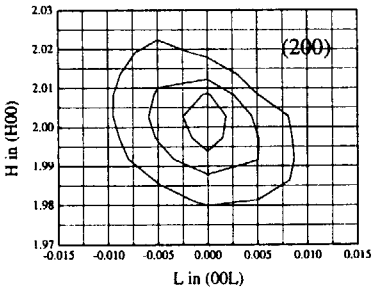


Fig. 2 The contour map at (2 0 0) nuclear position at 2.0 K.

References
[1] Y. Andoh et. al., Meeting Abstract of Phys. Soc. Jpn. **54**, 2 Part 3 (1999) 365

JRR-3M, T1-1, 2. Magnetism

研究テーマ：金属間化合物 R_7Rh_3(R=Nd, Tb, Ho)の磁気構造
表題：Ho_7Rh_3の中性子回折

1-2-37 Neutron Diffraction Studies on Ho_7Rh_3

T. Tsutaoka, T. Tokunaga, Y. Andoh[1], S. Kawano[2],
G. Nakamoto[4] and M. Kurisu[4]

Graduate School of Education, Hiroshima University, Higashi-Hiroshima 739-8524, Japan
[1]Faculty of Education and Regional Sciences, Tottori University, Tottori 680-8551, Japan
[2]Reearch Reactor Institute, Kyoto University, Kumatori, Osaka 590-0494, Japan
[3]Japan Advanced Institute of Science and Technology, Ishikawa 923-1292, Japan

The rare earth compound Ho_7Rh_3 crystallizes in the hexagonal ($P6_3mc$) Th_7Fe_3 type structure. From magnetic measurements, we found that there are two magnetic phase transitions; a paramagnetic to antiferromagnetic (A.F.) at T_N = 34 K, and the A.F. to ferrimagnetic at T_C = 22 K. In the ferrimagnetic phase, small spontaneous magnetization in the *c*-plane and a metamagnetic transition along the *c*-axis were observed. We have made neutron diffraction studies to determine the magnetic structure of Ho_7Rh_3.

Polycrystalline samples were prepared by arc melting of constituent elements of 99.9 % Ho, and 99.96 % Rh using a tri-arc furnace. Neutron diffraction measurements were performed by using the HQR spectrometer of JRR-3M of JAERI at Tokai in the temperature range from 1.5 K to 42 K.

Figure 1 shows the neutron diffraction patterns at several temperatures. The strong $(000)^{\pm}$ reflection is observed at 2θ = 8.724° at 1.5K. The magnetization measurements suggest that the antiferromagnetic component is in the basal plane below T_N. Thus, we assume that the Ho moment in the basal plane is

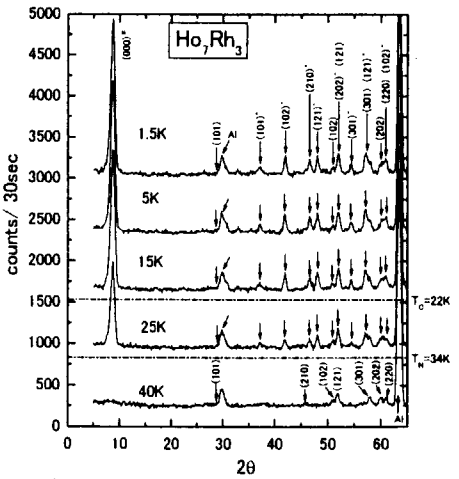


Fig.1 Neutron diffraction patterns at several temperatures.

helically modulated along the *c*-axis at 1.5 K. The propagation vector of this helical component is

Table 1 Observed and calculated values of 2θ at 1.5 K.

h k l	$2\theta_{obs}$	$2\theta_{calc}$	*diff*
$(000)^{\pm}$	8.724	8.72447	0.00047
$(101)^{+}$	37.20	36.5814	-0.6186
$(102)^{-}$	42.10	41.9908	-0.1092
$(102)^{+}$	60.20	60.1337	-0.0664
$(121)^{2-}$	46.50	45.9660	-0.5340
$(121)^{-}$	48.07	48.0502	-0.0198
$(121)^{+}$	57.18	56.9178	-0.2622
$(301)^{-}$	54.30	54.3554	0.0554
$(202)^{-}$	2.10	52.0722	-0.0278
$(210)^{+}$	46.5	46.4965	-0.0035

determined to be $\boldsymbol{Q}$ = (0, 0, 0.3774) from the position of the $(0\ 0\ 0)^{\pm}$ reflection. Using this helical model, we have indexed the magnetic reflections, as shown in Fig. 1 and summarized them in Table 1. Thus, Ho_7Rh_3 has an incommensurate helical magnetic structure. The other peaks can be assigned to nuclear Bragg reflections of the Th_7Fe_3 structure. Lattice constants using this calculation are a = 9.694 Å and c = 6.098 Å. Figure 2 shows the $(0\ 0\ 0)^{\pm}$ reflection intensity and magnetic susceptibility as a function of temperature.

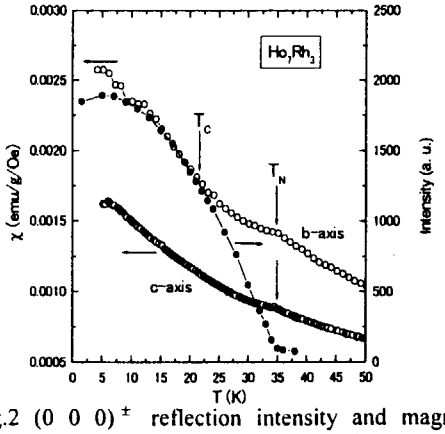


Fig.2 $(0\ 0\ 0)^{\pm}$ reflection intensity and magnetic susceptibility of Ho_7Rh_3 as a function of temperature.

With increasing temperature, the $(0\ 0\ 0)^{\pm}$ reflection peak intensity decreases and vanishes at T_N. More precise investigations using single crystals are in progress.

研究テーマ：TbRhGe 化合物の磁気構造
表題：TbRhGe 化合物の中性子回折

1-2-38 Neutron Diffraction Study on TbRhGe

M. Kurisu, G. Nakamoto, T. Himi, Y. Andoh[1], T. Tsutaoka[2] and S. Kawano[3]

Japan Advanced Institute of Science and Technology, Ishikawa 923-1292, Japan
[1]*Department of Environmental Sciences, Tottori University, Tottori 680-8551, Japan*
[2]*Graduate School of Education, Hiroshima University, Hiroshima 739-8524, Japan*
[3]*Research Reactor Institute, Kyoto University, Osaka 590-0494, Japan*

TbNiSn, TbPdSn and TbRhGe crystallize in the orthorhombic TiNiSi structure among many Tb equiatomic ternary compounds [1]. Magnetic and neutron studies have shown that magnetic properties of TbNiSn and TbPdSn are characterized by successive magnetic phase transitions below 20 K and metamagnetism along the *b*-axis in the ordered states. We have recently found from the magnetic and specific heat measurements on TbRhGe single crystal that it has three successive magnetic phase transitions, T_N =24.0 K, T_2= 15.5 K and T_1 = 13.0 K, and the two step metamagnetic transitions along the *b*-axis [2]. In the present study, we have performed the powder neutron diffraction experiments on TbRhGe to determine the magnetic structure of each phase.

Ingots of TbRhGe were prepared by arc-melting the constituent elements. Neutron diffraction measurements were carried out by using the HQR spectrometer of JRR-3M of JAERI at Tokai in the temperature range from 2 K to 30 K.

Figure 1 shows the powder diffraction pattern at 3.8 K. The low temperature magnetic phase I below T_1 is described by the wave vector of (0, 0.45, 0.11). The wave vectors for the high temperature phase III between T_2 and T_N is (0, 0.45, 0).

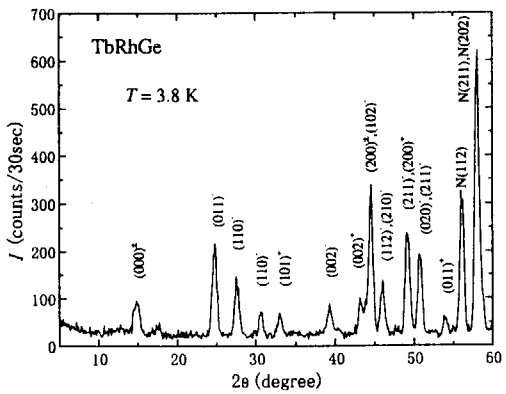


Fig.1. Neutron powder diffraction pattern of TbRhGe at 3.8 K.

We have also examined the intermediate temperature phase II between T_1 and T_2. The temperature variation of the magnetic reflections of (011)* and (110)* and their Q components is given in Figs.2 and 3. The wave vector changes to (0, 0.45, 0.05) at this phase II. It is suggested that there is appreciable change in the direction of the moment in passing through the narrow temperature range of phase II.

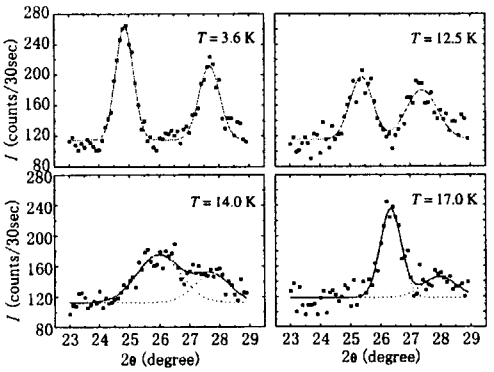


Fig.2. Temperature dependence of (011)* and (110)* magnetic reflections of TbRhGe.

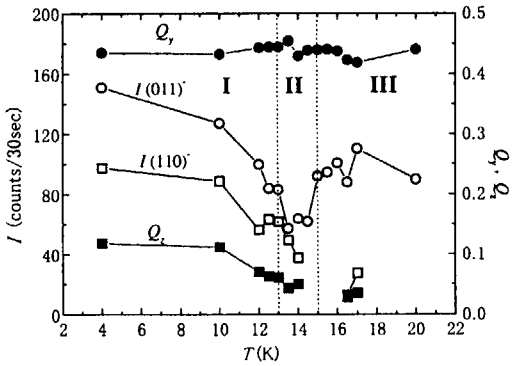


Fig.3. Intensity of (011)* and (110)* and the Q vector of TbRhGe as a function of temperature.

References

[1] D. Gignoux and D. Schmitt, *Handbook of Magnetic Material* Vol.**10** ed. K.H.J.Buschow, (Elsevier) (1997) p.239.
[2] T. Ida, Master Thesis JAIST, (2000).

研究テーマ：反強磁性-非磁性境界付近の重い電子系化合物における反強磁性相関
表題：$Ce(Ni_{0.91}Pd_{0.09})_2Ge_2$と$Ce(Ni_{0.7}Rh_{0.3})_2Ge_2$の磁気構造

1-2-39

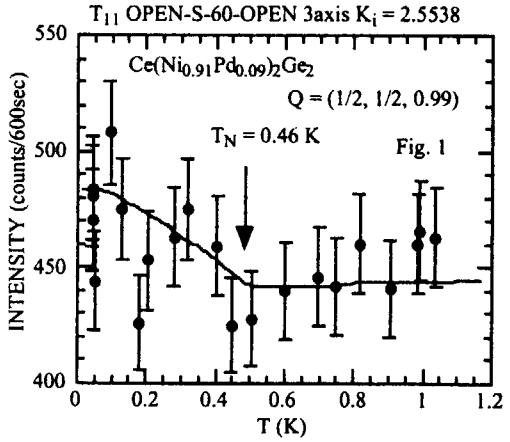
Magnetic structures of $Ce(Ni_{0.91}Pd_{0.09})_2Ge_2$ and $Ce(Ni_{0.7}Rh_{0.3})_2Ge_2$

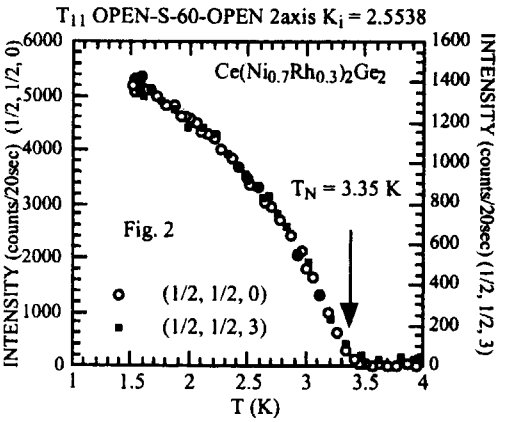
H. Kadowaki, T. Fukuhara[1], K. Maezawa[1], N. Aso[2], H. Yoshizawa[2], T. Takeuchi[3], T. Ooshima[4], and M. Ishikawa[4]

Department of Physics, Tokyo Metropolitan University, Hachioji-shi, Tokyo 192-0397
[1]Department of Liberal Arts and Science, Toyama Prefectural University, Kosugi, Toyama 939-0398
[2]Neutron Scattering Lab., ISSP, University of Tokyo, Shirakata 106-1, Tokai, Ibaraki 319-1106
Low Temperature Center, Osaka University, Toyonaka, Osaka 560-0043
[4]ISSP, University of Tokyo, 5-1-5 Kashiwanoha, Kashiwa, Chiba 277-8581

The paramagnetic heavy-fermion compound $CeNi_2Ge_2$ with a linear coefficient of the specific heat $\gamma = C/T = 350$ (mJ/K^2 mol Ce) and a Kondo temperature T_K about 40 K is located near a magnetic and non-magnetic phase boundary. An intriguing point of this compound is appearance of non-fermi-liquid behavior at low temperatures well below T_K without tuning of magnetic coupling or the Kondo effect by pressure or chemical substitutions. The non-fermi-liquid behavior is expected to be caused by certain low-energy spin fluctuation which has not been found because of weakness of inelastic signal. Substitution of Ni by Pd, Rh or Cu has been reported to induce magnetic long-range orders [1]. In this investigation, we have studied magnetic structures of Pd- and Rh- substituted samples $Ce(Ni_{0.91}Pd_{0.09})_2Ge_2$ and $Ce(Ni_{0.7}Rh_{0.3})_2Ge_2$ to gain insight of the magnetic fluctuation of $CeNi_2Ge_2$.

Neutron diffraction experiments were performed on the thermal-guide triple-axis spectrometer ISSP-HQR(T11). The spectrometer was operated in the double- or triple-axis modes with an incoming neutron energy of 14 meV. For $Ce(Ni_{0.91}Pd_{0.09})_2Ge_2$ we found a magnetic reflection at Q = (1/2, 1/2, 0.99), which indicates a sinusoidally-modulated magnetic-structure with a modulation q=(1/2, 1/2, 0.01). The polarization of the spin is along the [110] direction. In Fig. 1 temperature dependence of the magnetic reflection is shown, which is consistent with $T_N = 0.46$ K determined by a specific heat measurement. For $Ce(Ni_{0.7}Rh_{0.3})_2Ge_2$ magnetic reflections were found at Q=(1/2, 1/2, L) L=integer, which implies a commensurate modulation with q = (1/2, 1/2, 0). The Neel temperature $T_N = 3.35$ K (see Fig. 2) is consistent with bulk measurements. Analysis of the integrated intensities shows that the spin is polarized along the c-axis.





[1] T. Fukuhara et al., Activity Report NSL-ISSP 7 (2000) 95; T. Ooshima et al. Meeting abstracts of JPSJ vol. 55 issue 2 part 3 (2000) 462.

テーマ：2次元スピン格子化合物 $Mn(HCOO)_2 \cdot 2(ND_2)_2CO$ の磁気構造
表題：単結晶 $Mn(HCOO)_2 \cdot 2(ND_2)_2CO$ による磁気構造の中性子回折

1-2-40

Neutron Diffraction Studies of Magnetic Structure of Mn Formate Di-Urea Single Crystal

S. Kawano, T. Kosugi[1], M. Toda and K. Yamagata[2]

Research Reactor Institute, Kyoto University, Kumatori, Sennan, Osaka 590-0494, JAPAN
[1]Graduate School of Human and Environmental Studies, Kyoto University, Kyoto 606-8501, JAPAN
[2]College of Science and Engineering, Iwaki Meisei University, Fukushima 970-8044, JAPAN

Manganese formate di-urea, $Mn(HCOO)_2 \cdot 2(NH_2)_2CO$, belongs to tetragonal $P4_12_12$ symmetry, in which magnetic Mn ions form a two-dimensional layer along the *c*-axis and are basically arranged in the K_2NiF_4 type structure. Magnetization measurements show an antiferromagnetic order below T_N=3.8 K. Recently Kubo et al. [1] have reported from proton NMR measurements that the antiferromagnetic moments of Mn ions within the layer point to the direction rotating by 15 degree around the *c*-axis from a middle direction between [0 0 1] and [-1 0 0] directions. The details of the spin structure are not clear so far.

To determine the magnetic structure and to compare the results of the NMR measurements we have carried out neutron diffraction measurements of the partially deuterated Mn formate di-urea, $Mn(HCOO)_2 \cdot 2(ND_2)_2CO$ single crystal from 1.5 K to 7 K using the HQR spectrometer installed at the $T_{1\text{-}1}$ beam hole of JRR-3M. The data were collected for (*h h l*) and (*h* 0 *l*) type reflections.

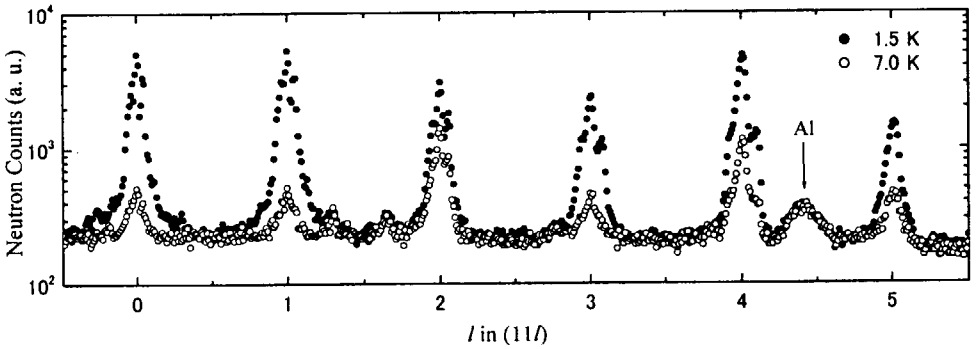


Fig. 1. Neutron diffraction patterns scanning along the c^*-direction for the (1 1 *l*) type reflections at 1.5 K and 7 K. Solid and open circles show the reflections at 1.5 K and 7 K, respectively.

Magnetic Bragg scattering appears for the (*h h l*) reflections with *l*=odd, but not the reflections with *l*=even, and never appears for all (*h* 0 *l*) type reflections. This fact and distribution of magnetic intensities reflect distribution of Mn ion structure factors with a magnetic wave vector $\boldsymbol{Q}$=(1 1 0). And this structure is consistent with the proton NMR results before mentioned. Figure 2 gives the temperature dependence of the (1 1 *l*) reflections with *l*=0, 1, 2 and 3. The Neel temperature is about 4.2 K. Around T_N temperature behavior of intensities of *l*=even seems to be different from the behavior of *l*=odd. This might suggest an effect of the two-dimensional arrangement Mn ions, but the details are unresolved for the present.

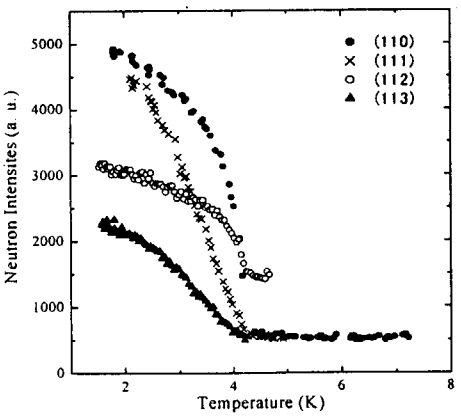


Fig. 2. Temperature dependence of the (1 1 *l*) reflections.

[1] H. Kubo *et al.*, J Phys. Soc. Jpn. **68** (1999) 253.

JRR-3M, HQR($T_{1\text{-}1}$), 2. Magnetism

研究テーマ: $Sr_{1-x}La_xRuO_3$ および $Sr_{2-x}La_xRuO_4$ の磁性

表題: $Sr_{0.5}La_{0.5}RuO_3$ の粉末中性子回折による研究

1-2-41 Neutron Powder Diffraction Study of $Sr_{0.5}La_{0.5}RuO_3$

H.Nakatsugawa[1] and Y.Oohara[2]

[1]*Materials Science, Department of Mechanical Engineering and Materials Science, Faculty of Engineering, Yokohama National University, Tokiwadai, Hodogaya-Ku, Yokohama 240-8501*

[2]*Neutron Scattering Laboratory, Institute for Solid State Physics, University of Tokyo, Shirakata 106-1, Tokai 319-1106*

The perovskite-based ruthenates have been of great recent interest due to coexistence of ferromagnetism and superconductivity in a single structural family. Three-dimensional $SrRuO_3$ is metallic, and ferromagnetic below 160K. Double-layer $Sr_3Ru_2O_7$ has a local moment at high temperatures and develops antiferromagnetic correlations below 15K, but the spins do not order magnetically down to very low temperatures. The single layer compound Sr_2RuO_4 displays no local Ru moment and is superconducting at about 1K.

The ferromagnetism of $SrRuO_3$ is at first unexpected, as according to expectations, the t_{2g} (d^{4+}) – $O2p$ – t_{2g} (d^{4+}) type superexchange interaction in a perovskite structure should be antiferromagnetic. Reports of the earlier crystal-structure investigations indicate that $SrRuO_3$ is orhorhombically-distorted perovskite that has the $GdFeO_3$ structure and the space group *Pbnm* (D^{16}_{2h}), with 4 f.u. per unit cell [1].

In the present study, the structure of La doped $SrRuO_3$, i.e., $Sr_{0.5}La_{0.5}RuO_3$ has been investigate via HQR, which is installed in T1-1 experimental port in JRR-3M at JAERI in Tokai. We have fixed the incident neutron wave number, k_i=2.55 Å^{-1}, from pyrolytic graphite. A polycrystalline sample with a nominal composition of $Sr_{0.5}La_{0.5}RuO_3$ was fabricated through a solid-state reaction using the powder of $SrCO_3$, La_2O_3 and RuO_2. Neutron scattering experiments of powderd samples with a particle size of < 50 micron were performed at room temperature. Based on the neutron diffraction data, the structural analysis were carried out using the Rietveld refinement program; RIETAN-2000.

Figure 1 shows the final fit and the pattern of derivation between calculated intensities and experimental data. The refined values for the lattice parameters were a=5.57605 Å, b=7.88109 Å and c=5.57865 Å which were slightly larger than that of $SrRuO_3$. This slight increase in the lattice was caused by the *A* cation size disorder in $Sr_{0.5}La_{0.5}RuO_3$ The resultant reliability factors were: R_{wp}=18.26%, R_p=12.22%, R_e=11.67%, R_I=5.49% and R_F= 3.41%, where the goodness of fit S (=R_{wp}/R_e) was 1.57.

[1] J.J.Randall and R.Ward, J.Am.Chem.Soc. **81**, 2629 (1959).

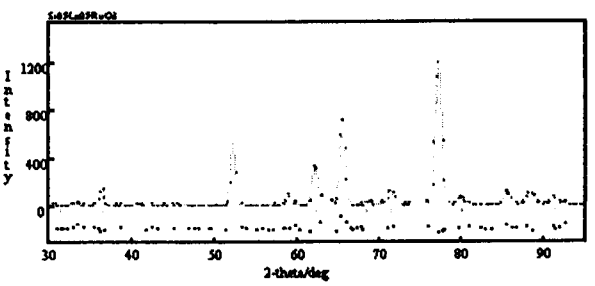


Fig.1 Rietveld refinement of the powder neutron diffraction pattern of $Sr_{0.5}La_{0.5}RuO_3$ at 300K.

テーマ：希土類化合物 $TbRu_2Ge_2$ における低温高次磁気構造
表題：$TbRu_2Ge_2$ における 2 次元磁気秩序の中性子回折

1-2-42

Neutron Diffraction Studies of Two-Dimensional Magnetic Ordering in $TbRu_2Ge_2$

S. Kawano, M. Toda, M. Takahashi[1], T. Shigeoka[2], N. Iwata[2], T. Kosugi[3]

Research Reactor Institute, Kyoto University, Kumatori, Sennan, Osaka 590-0494, Japan
[1]Institute of Materials Science, University of Tsukuba, Ibaraki 305-8573, Japan
[2]Faculty of Science, Yamaguchi University, Yamaguchi 753-8512, Japan
[3]Graduate School of Human and Environmental Studies, Kyoto University, Kyoto 606-8501, Japan

Rare-earth compound, $TbRu_2Ge_2$ crystallizes in the tetragonal $ThCr_2Si_2$ type structure, in which magnetic Tb ions are simply arranged in the body centered tetragonal lattice, and exhibits a successive magnetic transition: T_N=37 K, T_t'=30 K and T_t=4.3 K. At high temperatures $T_N>T>T_t$', two domains with $\boldsymbol{Q}_1=(q_1\ 0\ 0)$, q_1=0.235 and with $\boldsymbol{Q}_2=(q_2\ 0\ 0)$, q_2=0.247 coexist with equal amount, and at intermediate temperatures $T_t'>T>T_t$, the $\boldsymbol{Q}_2$ domain disappears and only $\boldsymbol{Q}_1$ domain is remained. The magnetic structures in these regions are one-dimensional expressed with $\boldsymbol{Q}=(q\ 0\ 0)$ along the a-axis [1]. On the other hand, at low temperatures $T<T_t$, many magnetic satellites are observed on low symmetry lines in the a^*-b^* reciprocal plane as well as on the high symmetry lines in pulsed-neutron diffraction experiments [2]. Those satellites suggest that the spin configuration is not one-dimensional, which has been reported so far [3], but two-dimensional. Since there are some difficulties in the precise estimation of satellite intensities for pulsed-neutron experiments, reactor neutron experiments are necessary.

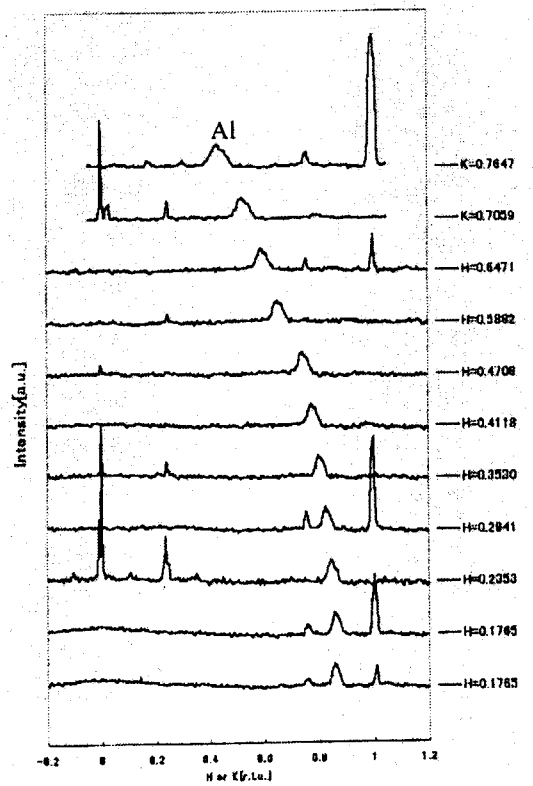


Fig. 1. Several diffraction pattern scanning along the b^* or a^*-direction in the a^*-b^* reciprocal plane at 1.5 K, showing a two-dimensional modulation with the $(1\ 1\ 0)^{(-mq\ -nq\ 0)}$ satellites.

Figure 1 gives diffraction patterns scanning along the a^* or b^*-direction in the a^*-b^* reciprocal plane at 1.5K. The diffusive peaks in the figure are due to scattering from Al of a cryostat. The other peaks can be indexed with odd harmonics components of main satellites from the (2 0 0) or (1 1 0) nuclear reflection. Figure 2 shows the temperature dependence of the $(1\ 1\ 0)^{(-q\ -q\ 0)}$ peak intensity. The intensity disappears around 4.3 K, which is in agreement with T_t indicative of susceptibility anomaly at low temperatures. Those patterns can be described as a model of a $17a\times17a\times c$ magnetic unit cell containing two paramagnetic sites. The paramagnetic sites correspond to node positions of long-period magnetic waves, and also, the positions are strongly frustrated.

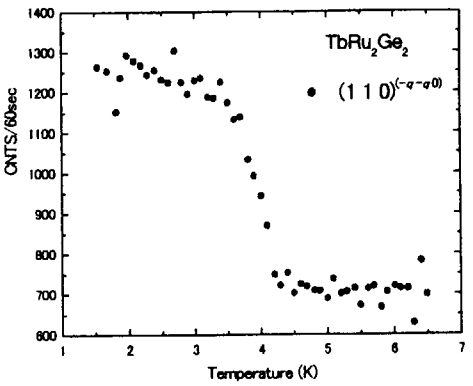


Fig. 2. Temperature dependence of the higher order satellite $(1\ 1\ 0)^{(-q\ -q\ 0)}$.

[1] T. Shigeoka et al., Physica B **237-238** (1997) 572.
[2] S. Kawano et al., J. Phys. Soc. Jpn., **70** suppl. A (2001) 209.
[3] A. Garnier, et al., Phys. Rev. B **57** (11998) 5235.

研究テーマ：磁気フラストレーションを持つ化合物 $Tb_2Ti_2O_7$ における磁性の静的・動的挙動
表題：$CuCr_2S_4$ の異常ホール効果と磁気励起

1-2-43

Anomalous Hall Effect and the Magnetic Structure of $CuCr_2S_4$

S.Iikubo[1], *K.Oda*[1], *S.Yoshii*[2], *Y.Yasui*[1,2], *M.Kanada*[1,2], *M.Ito*[1], *H.Harashina*[1,2]
M.Sato[1,2], *K.Kakurai*[2,3]
[1]*Department of Physics, Division of Material Science, Nagoya University, Furo-cho, Chikusa-ku, Nagoya 464-8602*
[2]*CREST, Japan Science and Technology Corporation (JST)*
[3]*Neutron Scattering Laboratory, ISSP, THE University of Tokyo, Shirakata 106-1, Tokai, Ibaraki 319-1195*

Hall resistivity ρ_H of $Nd_2Mo_2O_7$ has been found to be rather unusual [1-3] and does not seem to be easily explained by classical theories [4,5]. On this problem, a mechanism related to the spin chiral order has been proposed [6]. Although this new mechanism is very attractive, because the system really has, as has been shown by the neutron diffraction study[7], the chiral orders of Mo- and Nd-moments, detailed consideration made by the present authors group indicates that the Hall resistivity can not easily be understood by the single mechanism of the chiral order. Then, to investigate if the chiral order is playing an important role in determining the behavior of ρ_H, we have been experimentally studying various systems which are expected to have nontrivial spin structures.

$CuCr_2S_4$ is one of such compounds, with the spinel type structure where Cr atoms form , as Mo and Nd atoms in $Nd_2Mo_2O_7$, a three dimensional network of corner sharing tetrahedra.

Temperature (T) dependence of the magnetization (M) and the magnetic field (H) dependence of the Hall resistivity ρ_H are shown in Fig. 1 and 2, respectively. The Curie temperature T_C is ~390K and anomalous T-dependence of M is found at T_M ~100K. In the T-region above T_M, the Hall resistivity can be described by the well-known equation $\rho_H=R_0H+4\pi R_SM$, where R_0 and R_S are the ordinary and the anomalous Hall coefficients. At around T_M, the H-dependence of ρ_H begins to deviate from the above equation with decreasing T, which may be related to the observed change of the magnetic structure.

Neutron measurements on a polycrystalline sample of $CuCr_2S_4$ were carried out on the spectrometer T1-1 of the thermal guide of JRR-3M in Tokai. To remove the higher order beam, a PG filter was put in front of the sample. Horizontal collimations were 12'(effective)-open-40'-open (2axis mode). The sample was

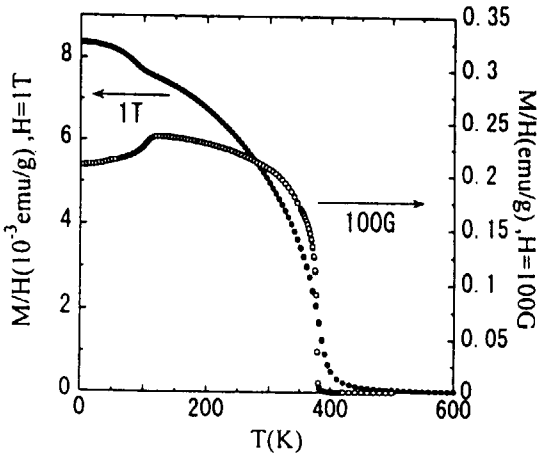


Fig. 1. Temperature dependence of the magnetic susceptibility

JRR-3M, HQR(T1-1), 2.Magnetism

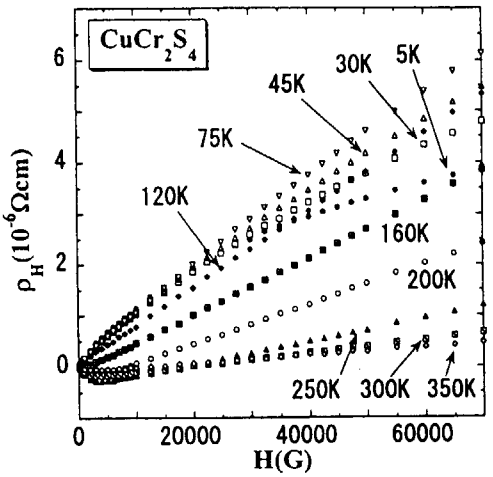


Fig. 2. The magnetic field dependence of the Hall resistivity ρ_H.

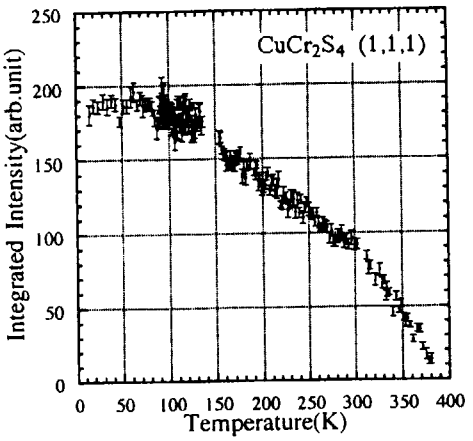


Fig. 3. Temperature dependence of the Integrated Intensity of the 111 reflection

packed in a V-can. We collected the data at 420K, 300K, 137K and 10K. In the measurement of 420K, the sample was set in an electric furnace, and below room temperature, we used a Displex type refrigerator. Below T_C, magnetic reflection intensities were found at the nuclear Bragg positions with indices h, k and l are all even or all odd. We have not found significant change of the intensities at T_M ~100K. Only a small change of the slope of the integrated intensity-T curve at 111 point may be seen as shown in Fig. 3. We analyzed the collected data by Rietveld method with the assumption that Cu and Cr moments take a collinear structure below T_C, as a simple case. R factors obtained by the analysis were shown below.

	Rwp	Re	RI
420K	6.74	5.05	3.15
300K	7.51	5.22	2.25
137K	7.97	5.14	2.49
10K	8.19	5.13	2.31

Although the small values of the obtained R_{WP} might indicate that the assumption of the collinear magnetic structure is correct, there is a possibility that the existence of small tilting of the magnetic moment cannot be detected in the present study. It should be also noted that the obtained value of R_{WP} increases with decreasing temperature. It may be necessary to develop more general fitting program to determine the complicated spin structure.

Effort to obtain more detailed information, including preparing single crystals is now being made.

References

1) S. Yoshii et al., J. Phys. Soc. Jpn. **69** (2000) No.12.
2) S. Iikubo et al., J. Phys. Soc. Jpn. **71** (2001) 212.
3) Y. Taguchi et al., Science **291** (2001) 2573
4) R.. Kurplus and J. M. Luttingerv et al., Phys. Rev. **95** (1954) 1154.
5) J. Kondo et al., Prog.. Theoret. Phys. (Kyoto) **27** (1962) 772
6) K. Ohgushi et al., Phys. Rev. B **62** (2000) R6065
7) Y. Yasui et al., J. Phys. Soc. Jpn. (Supplement) in press.

研究テーマ：層状化合物の低次元磁気特性

表題：層状化合物 $Cs_{0.5}Rb_{0.5}VF_4$ の（非誘起－誘起）反強磁性構造間の相関

1-2-44

Correlation between the normal- and induced- antiferromagnetic structure in the layer compound $Cs_{0.5}Rb_{0.5}VF_4$.

M.Hidaka[1], M.Yoshimura[1], H.Akiyama[2], H.Fujii[3] and S.Watanabe[4]

[1]*Department of Physics, Faculty of Science, Kyushu University,33, Fukuoka 812-0053, Japan.*

[2]*Faculty of Education, Miyazaki University, Miyazaki 812-2192, Japan.*

[3]*Faculty of Education, Oita University, Oita 870-1192, Japan.*

[4]*Neutron Scattering Laboratory, ISSP, University of Tokyo, Tokai,Ibaraki 319-1195, Japan.*

The structure of the layer compound $Cs_{0.5}Rb_{0.5}VF_4$ is mainly characterized by two-dimensional networks of VF_6 octahedra, and Rb^{+1} and Cs^{+1} ions intercalated among these networks. $Cs_{0.5}Rb_{0.5}VF_4$ has structural phase transitions at about 123 K and 368 K[1]. $RbVF_4$ shows the structural phase transitions at about 184 K, 413 K and 482 K[2], while $CsVF_4$ at about 142 K, 425 K, 510 K and 535 K[3]. The difference of these transition temperatures modulates a cooperative tilting of the rigid-like VF_6 octahedra stacked along the c axis, though these compounds have same orthorhombic symmetry structure of space group $P2_12_12$ in lowest-temperature phase. It is considered that a localized structure around V^{3+} ions is slightly different among $RbVF_4$, $Cs_{0.5}Rb_{0.5}VF_4$ and $CsVF_4$. $CsVF_4$ showed an anti-ferromagnetic phase transition at about 43 K, and the magnetic structure depends on the outer magnetic field applied to its single crystal[4,5,6]. For example, the induced magnetic unit cell at 5 K was changed from 2ap x 2bp x 2cp to 2ap x 2bp x cp under 2 T field cooling, where the suffix 'p' means a pseudo unit cell of $TlAlF_4$-type structure. On the other hand, $RbVF_4$ showed the anti-ferromagnetic phase transition at about 45 K. However, $RbVF_4$ did not show the change of the magnetic structure under 3 T field cooling. Recently, we found that there is a anti-ferromagnetic phase transition at about 36 K in $Cs_{0.5}Rb_{0.5}VF_4$[7]. It is therefore considered that the structural modulations made by the successive structural phase transitions affect the magnetic interactions among magnetic moments of V^{+3} ions in the layer compound of AVF_4 having a $TlAlF_4$-type structure.

In order to study the magnetic transition of $Cs_{0.5}Rb_{0.5}VF_4$, we carried out measurements of the intensity of some magnetic reflections as function of the specimen temperature using neutron diffractometer, HQR, in JRR-3. The size of the used single crystal was about 5 x 5 x 3 mm^3 for $Cs_{0.5}Rb_{0.5}V F_4$. The large plane was a nice cleavage (0 0 1)p plane. Figs.1 (a) and (b) show the temperature dependence of the integrated intensity of the $(1/2\ 1/2\ 1/2)_p$ and $(1/2\ 1/2\ 0)_p$ magnetic reflection in $Cs_{0.5}Rb_{0.5}VF_4$, on heating.

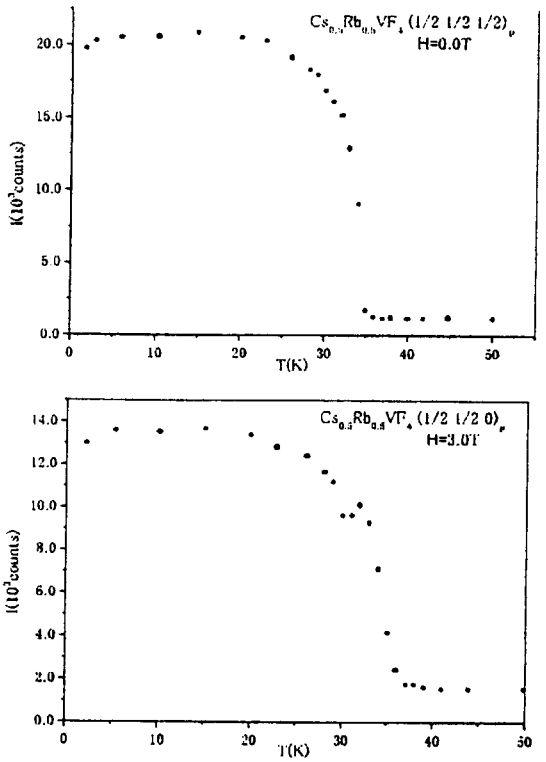


Fig.1. Temperature dependence of the integrated intensity of magnetic reflection;$(1/2\ 1/2\ 1/2)_p$; Hap=0T and $(1/2\ 1/2\ 0)_p$; field-cooling and Hap=3.0T in $Cs_{0.5}Rb_{0.5}VF_4$.

JRR-3M, HQR, 2.Mgnetism

The $(1/2\ 1/2\ 1/2)_p$ reflection was taken under the zero field-cooling and no applied magnetic field, while the $(1/2\ 1/2\ 0)_p$ reflection was taken in the applied magnetic field of Hap=3.0 T after 3.0 T field-cooling from 50 K to 5 K. In the present experiments, the magnetic field was always applied vertically to the (0 0 1)p plane. Therefore, it become clear that the magnetic structure should be the anti-ferromagnetic superlattice structure of G-type in the normal state and C-type in the induced state in $Cs_{0.5}Rb_{0.5}VF_4$. We found by a least-squares refinement to the integrated intensity of several magnetic reflections that the magnetic moments of V^{3+} ions are aligned along the [001]p axis in both magnetic structure.

It is possible to consider that two kinds of the magnetic structures, that is normal and induced anti-ferromagnetic one, co-exist in a single crystal under an adequate strength of the applied magnetic field. Figs.2 (a) and (b) show the integrated intensity of the $(1/2\ 1/2\ 1/2)_p$ and $(1/2\ 1/2\ 0)_p$ magnetic reflection in $Cs_{0.5}Rb_{0.5}VF_4$, on heating. The data were taken by the following procedure. First, the specimen was cooled down from 50 K to 5 K in the applied magnetic field of 3.0 T, that is field-cooling was done. After quickly reducing the magnetic field from 3.0 T to 0.5 T at 5 K, we carried out continuous measurements of maximum peak-intensity of the $(1/2\ 1/2\ 1/2)_p$ and $(1/2\ 1/2\ 0)_p$ as function of the specimen temperature in Hap=0.5 T, on gradually heating up. In the figures, the disappearance of the $(1/2\ 1/2\ 0)_p$ reflection at about 13 K suggests that the induced structure of C-type was almost transformed into the normal one of G-type in the specimen by thermal energy even in Hap=0.5 T. We confirmed the co-existence between the normal and induced magnetic structure below about 13 K. Thus, it is deduced that there is a quasi-stable magnetic phase transition in Hap=0.5 T at about 13 K. We carried out measurements of the temperature dependence of peak intensity for the $(1/2\ 1/2\ 1/2)_p$ and $(1/2\ 1/2\ 0)_p$ in several strength of Hap after field-cooling of 3.0 T, to study the quasi-stable magnetic transition. It became clear that the quasi-stable transition is made by energy balance among multi-magnetic domains, Hap and thermal energy in the specimen.

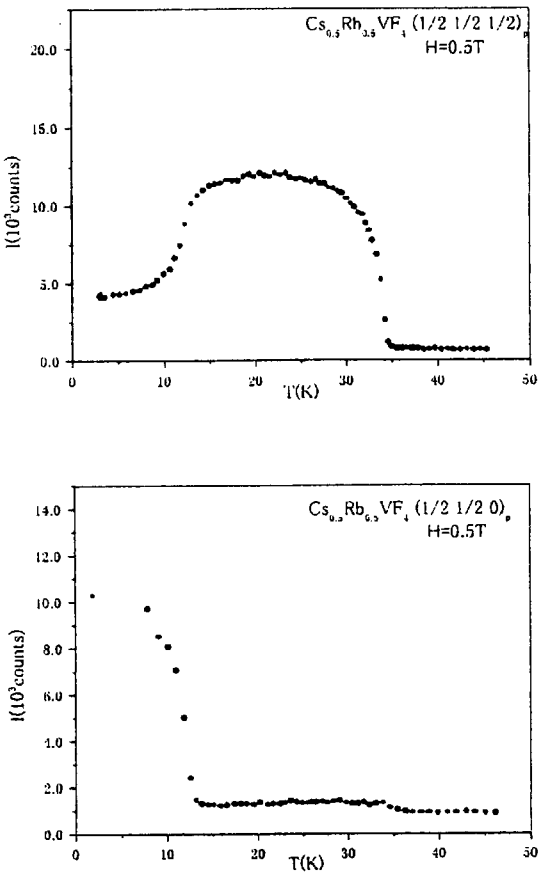


Fig.2. Temperature dependence of peak intensity of magnetic reflection, $(1/2\ 1/2\ 1/2)_p$ and $(1/2\ 1/2\ 0)_p$;Hap=0.5T, in $Cs_{0.5}Rb_{0.5}VF_4$.

References

1) M.Hidaka et.al.:Phys.Stat.Sol.(a)177(2000)375.
2) M.Hidaka et.al.:Phys.Stat.Sol.(a)86(1984)75
3) M.Hidaka et al.:Phys.Stat.Sol.(a)96(1986)415.
4) M.Hidaka et al.:Physica B 160(1990)281.
5) M.Hidaka et.al.:Phys.Stat.Sol.(a)117(1990)563.
6) H.Ikeda et.al.:Physica B 160(1990)287.

研究テーマ：遍歴電子磁性
表題：Mn_3Pt のスピン相関

1-2-45 The Octahedron Frustration system in Mn_3Pt Above Néel Temperature

T. Ikeda and Y. Tsunoda

School of science and engineering, Waseda University,
3-4-1 Okubo, Shinjuku-ku, Tokyo169-8555, Japan.

The ordered alloy Mn_3Pt is an antiferromagnet which undergoes the magnetic transition from a high temperature phase (F-phase) to a low temperature phase (D-phase) at T_t=410K below the Néel temperature T_N=475K. The magnetic structures are triangular below T_t, and collinear between T_t and T_N. At T_t, the volume and the amplitude of magnetic moments of Mn atoms change in order of a few percents. Then, the crystal structure distorts from fcc (D-phase) to fct (F-phase). The similar alloys, however, Mn_3Ir and Mn_3Rh, don't have the collinear magnetic phase, although they have the triangular magnetic structures. Thus, the existence of the collinear magnetic structure is the characteristic of Mn_3Pt alloy. The magnetic structure of F-phase has a special feature that one third of all Mn atoms have no magnetic moments, although all Mn atoms have the magnetic moments in the D-phase. To investigate the dynamical behavior of the special spins (R-Mn) in the F-phase, we performed inelastic neutron scattering measurements at T1-1 triple axis spectrometer. The inelastic diffuse scattering was observed at low excitation energy (3meV). The inelastic diffuse scattering intensities extend along the [010] axis on a plane in reciprocal lattice space. It means that the R-Mn spins have strong correlations along the <100> direction. The R-Mn spins would turn up and down from time to time on keeping the nearest neighbor antiferromagnetic coupling. Since the crystal structure is tetragonal (fct) in the F-phase, the R-Mn spins would partly feel the frustrations. For the cubic structure in the paramagnetic phase above T_N, not only the R-Mn spins but also all Mn spins will feel the frustration. Diffraction pattern obtained by scanning parallel to the [100] axis passing through the 1 0.3 0 RLP on the (001) scattering plane, is given in Fig.1. The data were taken at energy transfer of 3meV by constant E mode of operator. Above T_N, the inelastic diffuse scattering intensities increase three times of those in the F-phase, because the number of the frustrating spins in the paramagnetic phase is three times number of that in the F-phase. Consequently, the behavior above T_N of all Mn spins is considered to be the octahedron frustration system. Further measurements the samples with different atomic order parameter are now in progress.

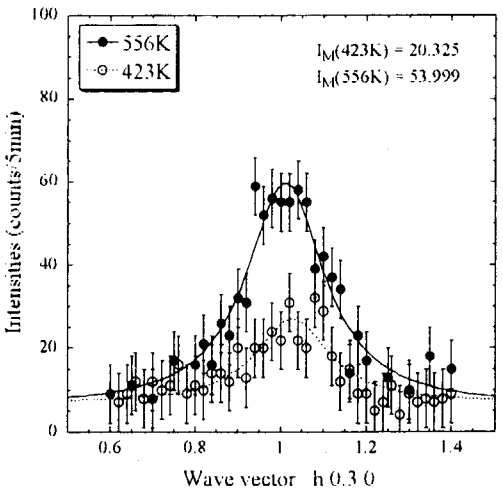


Fig.1 Mn_3Pt Constant E (dE=3meV) around 1 0.3 0

JRR-3M, T1-1, 2 , Magnetism

研究テーマ：高濃度スピングラスにおける磁気クラスターの時間発展
表題：高濃度スピングラスにおける強磁性、反強磁性クラスターの共存

1-2-46 Coexistence of Ferromagnetic and Antiferromagnetic Clusters in Concentrated Spin-Glass Alloy $Fe_{65}(Ni_{1-x}Mn_x)_{35}$

K. Motoya and K. Hioki

Department of Physics, Faculty of Science and Technology, Science University of Tokyo, Noda 278-8510

A previous neutron scattering study showed that ferromagnetic clusters exist in the ferromagnetic as well as in the spin-glass phases of reentrant spin-glass alloys $Fe_{65}(Ni_{1-x}Mn_x)_{35}$.[1] The origin of anomalous temperature variation behavior of spin-wave stiffness and spin-wave intensity observed in this and other spin-glass materials is attributed to the presence of magnetic clusters.[2] We also confirmed by SANS experiment that the slow dynamics in spin-glasses can be explained in terms of the time evolution of magnetic clusters.[3] In the course of these studies, we found that the magnetic clusters with antiferromagnetic correlation (antiferromagnetic clusters) coexist with ferromagnetic clusters in $Fe_{65}(Ni_{0.78}Mn_{0.22})_{35}$ alloy. The alloy of this concentration has been regarded as a spin-glass which transforms directly from paramagnetic to spin-glass phase.

Figure 1 shows an elastic neutron scattering pattern measured around (110) reciprocal lattice point which is an antiferromagnetic Bragg point for the face-centered cubic structure. The line width is much wider than the instrumental resolution width shown by the dotted curve, which indicates that the antiferromagnetic correlation is finite range even at the lowest temperature.

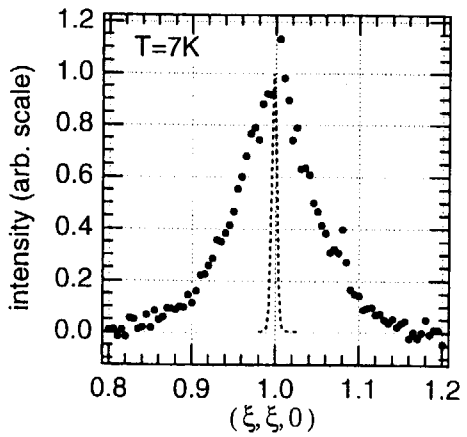


Fig. 1. Neutron scattering pattern from $Fe_{65}(Ni_{0.78}Mn_{0.22})_{35}$ measured around (110).

Figure 2 shows the temperature variation of amplitude and line width of the antiferromagnetic peak shown in Fig. 1.

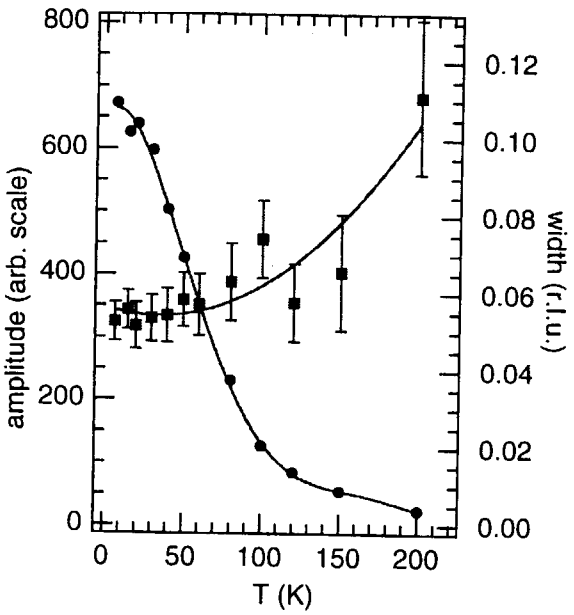


Figure 2. Temperature variation of amplitude and line width of the antiferromagnetic peak.

We remark that the magnetic scattering amplitude arising from antiferromagnetic as well as ferromagnetic clusters (not shown here) develop far above the spin-glass transition temperature T_{SG}=50K. The present observation showed that ferromagnetic and antiferromagnetic clusters coexist in wide temperature range of $Fe_{65}(Ni_{0.78}Mn_{0.22})_{35}$ alloy. Time evolution of these clusters is currently studied.

References

1. K. Motoya and Y. Muraoka: J.Phys.Soc.Jpn. 62 (1993) 2819.
2. K. Motoya, S. Kubota and K. Nakaguchi : J. Phys. Soc. Jpn. 68 (1999) 2351.
3. K. Motoya, K. Hioki and J. Suzuki: J.Phys.Soc.Jpn. suppl.A (2001) 139.

研究テーマ：$Ho_2Ti_2O_7$、および $Dy_2Ti_2O_7$ の磁気的挙動とスピンアイス
表題：スピンアイス系化合物 $Ho_2Ti_2O_7$ の中性子散乱

1-2-47 Neutron Scattering Study on the Spin Ice System $Ho_2Ti_2O_7$

M. Kanada[1], Y. Yasui[1,3], Y. Kondo[1], S. Iikubo[1], M. Ito[1], H. Harashina[1,3], M. Sato[1,3], H. Okumura[2], K. Kakurai[2,3] and H. Kadowaki[4]

[1]*Department of Physics, Division of Material Science, Nagoya University, Furo-cho, Chikusa-ku, Nagoya 464-8602*
[2]*Neutron Scattering Laboratory, ISSP, The University of Tokyo, 106-1 Shirakata, Tokai 319-1195*
[3]*CREST, Japan Science and Technology Corporation (JST)*
[4]*Department of Physics, Tokyo Metropolitan University, Hachioji-shi, Tokyo 192-0397*

Pyrochlore compound $Ho_2Ti_2O_7$ consists of two kinds of three-dimensional networks individually formed by Ho_4 and Ti_4 tetrahedra. The magnetic moments of Ho^{3+} ions have the ferromagnetic nearest neighbor interaction, and each moment is along the principal axis parallel to the line which connects its site with the center of gravity of the corresponding tetrahedron, because the uniaxial anisotropy is very strong. Within a tetrahedron, the magnetic moments tend to have the "two-spin-in two-spin-out" structure, which is shown in Fig. 1. Because the structure has six-fold degeneracy, the total network of the tetrahedra is expected to be highly frustrated. This situation is equivalent to that of solid water, in which the degeneracy exists associated with the arrangements of four hydrogen atoms around an oxygen atom site, and the present system is often called "spin ice". In order to clarify the magnetic behavior of $Ho_2Ti_2O_7$, neutron studies have been carried out.

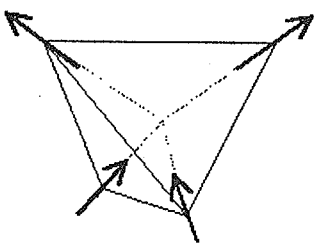


Fig.1 Schematic figure of the Ho moments on a tetrahedron with "two-spin-in two-spin-out" structure.

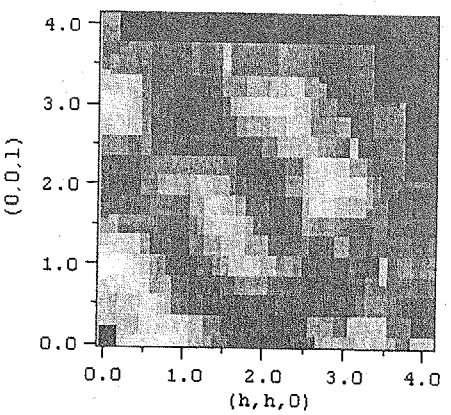


Fig.2 Scattering intensity map with E=0 meV in the (h,h,l) plane. Light position means high intensity in he map.

Neutron measurements have been performed with the T1-1 spectrometer at JRR-3M of JAERI in Tokai. Horizontal collimations were 12'(effective)-open-60'-open and initial neutron energy Ei=13.51 meV was adopted. The energy resolution is about 0.86 meV.

Figure 2 shows the scattering intensity map taken at 0.4 K with the neutron transfer energy E=0 meV in the (h,h,l) plane. In the figure, the magnetic form factor correlation has been made. The magnetic scattering peaks were mainly observed around (0.8,0.8,0), (3.2,3.2,0), (0,0,1), (0,0,3) positions. The Q –dependence of the scattering intensity becomes significant around 30 K with decreasing temperature (T). The magnetic

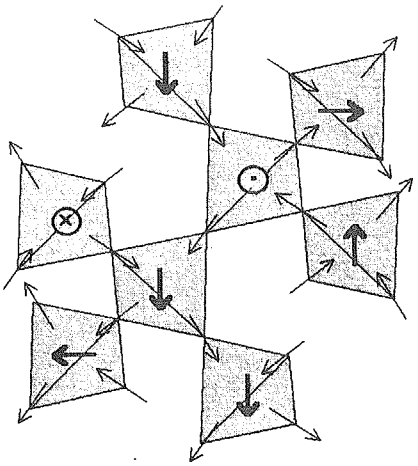


Fig.3 Example of the spin correlation pattern. A big arrows show the net moment of 4 spins on a tetrahedron.

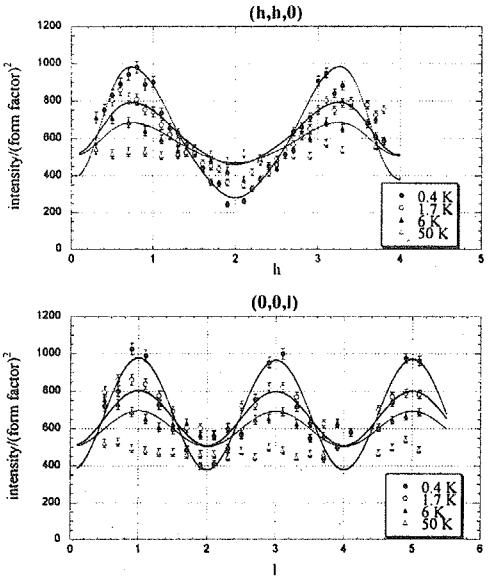


Fig.4 Q –dependence of the scattering intensity with form factor correlation. Solid line shows the results of model calculation

intensity exhibits hysteresis with heating and cooling below T～1.5 K, which suggests that freezing of the moments becomes appreciable at around the temperature with decreasing T.

We have performed model calculations to find the spin correlation pattern, which can explain the observed Q –dependence of the scattering intensity. Twenty-five spins of eight tetrahedra shown in Fig. 3 are considered in the calculation and the condition of "two-spin-in two-spin-out" structure within each tetrahedron is assumed, because if the condition is not kept, the energy increase is ～5 K, much larger than the temperature. The results indicate that several spin correlation patterns which can explain the experimental data exist. The energies of the dipole interaction, which has been pointed out to be the dominant one in the present system, are almost degenerated within the energy of ～0.5 K. Then, the coexistence of these spin correlation patterns tends to persist down to ～0.5 K and before going to the temperature the system begin to freeze due to this coexistence. Figure 3 shows an example of the correlation patterns. We have also calculated the Q –dependence of scattering intensity by considering that the correlation length becomes short with increasing temperature. The Q-dependence of the observed and calculated scattering intensity along (h,h,0) and (0,0,l) directions are shown in Fig.4 for various temperatures. The results of calculation can roughly explain the experimental results.

We have also adopted the mean field analysis. The details of the analysis are described in ref.1. Here, the strong local Ising anisotropy and dipole interaction are adopted. From the analysis, we can see that the calculation roughly reproduces the observed data.

The present studies have shown followings on the magnetic correlation of $Ho_2Ti_2O_7$. The short range correlation becomes appreciable with decreasing temperature around 30K, and with further decreasing temperature , the freezing of the magnetic moments becomes appreciable at ～1.5K due to the coexistence of various short range correlation patterns, whose dipole energies are almost degenerated.

Reference

1) H. Kadowaki, Y. Ishii, K. Matsuhira and Y. Hinatsu: submitted to Phys. Rev. B

研究テーマ：$Ho_2Ti_2O_7$、および$Dy_2Ti_2O_7$の磁気的挙動とスピンアイス
表題：磁気フラストレーションを持つパイロクロア型化合物$Tb_2Ti_2O_7$のスピンダイナミクス

1-2-48

Spin Dynamics of Magnetically Frustrated Pyrochlore System $Tb_2Ti_2O_7$

Y. Yasui[1,2], M. Kanada[1], M. Ito[1], H. Harashina[1,2], M. Sato[1,2], H. Okumura[3], K. Kakurai[2,3] and H. Kadowaki[4]

[1] *Department of Physics, Nagoya University, Furo-cho, Chikusa-ku, Nagoya 464-8602*
[2] *CREST, Japan Science and Technology Corporation (JST)*
[3] *Neutron Scattering Laboratory, ISSP, The University of Tokyo, Shirakata 106-1, Tokai, Ibaraki 319-1195*
[4] *Department of Physics, Tokyo Metropolitan University, 1-1 Minamiosawa, Hachioji 192-0397*

Pyrochlore compound $Tb_2Ti_2O_7$ consists of two kinds of three-dimensional networks individually formed of corner-sharing tetrahedra of Tb^{3+} or Ti^{4+}. Because Tb^{3+} moments have the antiferromagnetic nearest neighbor interaction and do not form a bipartite lattice, the system is expected to be geometrically frustrated and to have strong magnetic fluctuation. For this system, magnetic ordering is not observed down to 70 mK,[1] even though the Weiss temperature is estimated to be as high as ~ -19 K from the magnetic susceptibility data. We have studied the magnetic behavior by means of neutron scattering on a single crystal of $Tb_2Ti_2O_7$.[2,3] Neutron measurements of this compound have been carried out by using the triple axis spectrometer at T1-1 of the thermal guide and at C1-1 of the cold guide at JRR-3M of JAERI in Tokai. The results of measurement at T1-1 have already been reported. In this paper, we present the results obtained by using C1-1 spectrometer with high energy resolution.

In the measurements at C1-1, the crystal was oriented with its $[1\bar{1}0]$ axis vertical to the scattering plane, where the points (h,h,l) in the reciprocal space can be reached. The horizontal collimations in front of the sample were open-20' and after the sample were 420'-open, where a horizontally focusing analyzer was used. The final neutron energy was fixed at 3.10 meV and 2.42 meV, where the energy resolution ΔE was 81 μeV and 46 μeV, respectively.

Figure 1 shows examples of the energy(E)-scan profiles taken at Q=(0,0,2.1) with ΔE=81 μeV. Both the elastic and quasi elastic components exist around E=0 meV. An inelastic scattering peak also exists at the energy of ~1.3 meV and ~1.5 meV at 1.5 K and 15 K. respectively.

Figure 2 shows the T-dependence of the scattering intensities at Q=(0,0,2.1) and (2,2,1.4) measured at E=0 meV with ΔE=81 μeV. The intensities increase with decreasing T down to 30 K in an almost Q-independent manner. Below 30 K, the difference of the observed T-dependences between different Q-points becomes significant. With further decreasing T, a sharp upturn of the intensity at Q=(0,0,2.1) is

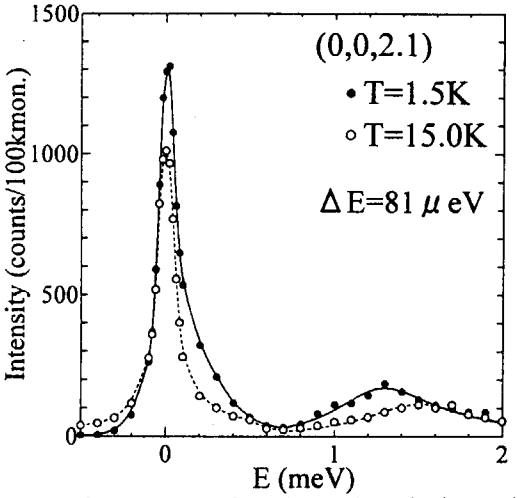


Fig. 1. Scattering profiles observed at Q=(0,0,2.1) at 1.5 K and 15 K with ΔE=81 μeV.

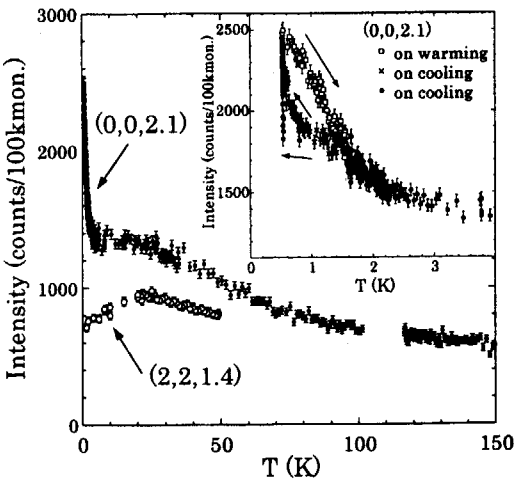


Fig. 2. Temperature dependence of the scattering intensities at Q=(0,0,2.1) and (2,2,1.4) measured at E=0 meV with ΔE=81 μeV.

observed below ~1.5 K. Hysteresis of the intensity-T curve have been observed below ~1.5 K where the temperature is changed up and down, as shown at Q=(0,0,2.1) in the inset of Fig. 2. The intensity profiles in the E-region of -0.2 meV$\leq E \leq$0.6 meV taken with ΔE=46 μeV, have been analyzed by fitting with two components : a Gaussian peak centered at zero energy to represent the elastic scattering and a Lorenzian peak also centered at zero energy to represent the quasi elastic scattering. The profile width of the elastic component are fixed at the resolution width. Then the intensities of these contributions have been separated. Figure 3 and its inset show the T-dependence of the integrated intensities of the elastic and quasi elastic components, respectively, at Q=(0,0,2.1) and (1.5,1.5,1.9). It is found that Q-dependent nature of the elastic and quasi elastic components becomes appreciable at ~1.5 K and ~ 30K, respectively, with decreasing T.

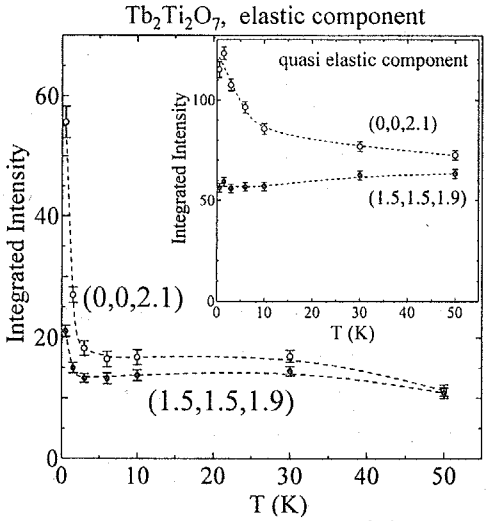


Fig. 3. Temperature dependence of the integrated intensities of the elastic component at Q=(0,0,2.1) and (1.5,1.5,1.9). Inset shows the T-dependence of the integrated intensity of the quasi elastic component.

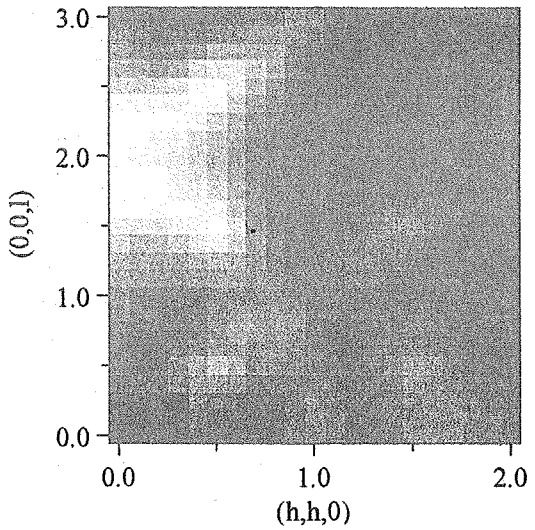


Fig. 4. Scattering intensity map in the (h,h,l) plane in the reciprocal space measured at 0.4 K at E=0 meV with ΔE=81 μeV.

These results are understood as follows. As T decrease from high temperature, the population of the lowest energy level of the 4f electrons of Tb^{3+} ions increases, resulting in the increase of the intensity at around E=0 meV. With decreasing T, the short range correlation of the magnetic moments grows below ~30 K, which induces the Q-dependence of the quasi elastic component. As a results of the spin freezing below ~1.5 K, the rapid increase of the elastic component and the hysteretic behavior appear.

Figure 4 shows the scattering intensity map in the (h,h,l) plane in the reciprocal space measured at 0.4 K at E=0 meV with ΔE=81 μeV. Peak is mainly observed around (0,0,2) (light position in the map). By the profile fittings stated above, the Q-dependence of the intensity of the elastic component is found to be similar to that of the quasi elastic one. Then, the quasi elastic component is considered to be acoustic spin wave of short range order (paramagnon) on the lowest energy level. The inelastic component is considered to be a neutron spin-flip excitation to the first excited state whose z-component of the angular momentum, J_z differ by $\pm$ 1 from that of the ground state.

Magnetic correlation pattern, which can roughly reproduce the elastic and quasi elastic components, is proposed. It is obtained by considering that the system has the antiferromagnetic nearest neighbor interaction as well as a dipole-dipole interaction and a relatively weak uniaxial anisotropy energy. However, the magnetic correlation pattern of the short range order seems not to be unique, and probably, many short range correlation patterns coexist down to the temperature, at which these patterns become frozen and the glassy state is realized.

References

1) J.S. Gardner *et al.*, Phys Rev. Lett. **82** (1999) 1012
2) M. Kanada *et al.*, J. Pys. Soc. Jpn. **68** (1999) 3802
3) Y. Yasui *et al.*, J. Phys. Chem. Solids **62** (2001) 343

研究テーマ：フラストレーション系 $ZnFe_2O_4$ の中性子磁気散乱
表題：3次元スピンフラストレーション系 $ZnFe_2O_4$ のスピン液体

1-2-49 Magnetic Neutron Scattering Measurements in Highly Frustrated $ZnFe_2O_4$ Single Crystal

K. Kamazawa, Y. Tsunoda, and K. Kohn*

Department of Applied Physics, School of Science and Engineering, Waseda University,
3-4-1, Ohkubo, Shinjuku, Tokyo, 169-8555 Japan
*Department of Physics, School of Science and Engineering, Waseda University,
3-4-1, Ohkubo, Shinjuku, Tokyo, 169-8555 Japan

We studied $ZnFe_2O_4$ single crystal in view of the frustration system using neutron scattering measurements. $ZnFe_2O_4$ has a normal spinel structure. The A sites are occupied by Zn^{2+} ions and the B sites by Fe^{3+} ions. The B sites of the spinel structure have special atomic arrangement. The B cations are located at the corners of a tetrahedron and each corner shares with another tetrahedron. If we regard the tetrahedron as a molecule, the B site of spinel is described as an fcc configuration. In other words, one can also regards the third neighbor Fe^{3+} of the B sites as an fcc configuration of the tetrahedral molecules.

Previously we reported that magnetic diffuse scattering distribute along the first fcc Brillion zone boundary. The data indicate that magnetic diffuse scattering is caused by the frustration between the 3rd neighbor Fe^{3+} atoms coupled antiferromagnetically. This time, we found another diffuse scattering around the nuclear Bragg peak positions. The data were taken at T1-1 triple axis spectrometer installed at a thermal guide of JRR-3M, Tokai, Japan. Fig.1 (a) and 1(b) show the temperature dependences of the scan along <111> and <110> directions with constant E-mode operations at an energy transfer of 0meV, respectively. However, around the nuclear Bragg peak points which come from only the A atoms, there is no diffuse scattering. Table 1 shows atomic structure factor in reciprocal space for the spinel lattice. Here we omit oxygen contribution. The diffuse scattering follows the magnetic form factor and depends on a temperature. For this reason, the diffuse scattering is magnetic in origin come from the B atoms. They indicate that the nearest neighbor Fe^{3+} spins couple ferromagnetically and very short range spin correlations exist between these Fe^{3+} spins. The correlation length is estimated to be 5.11 Å at 30K, and is not beyond the distance between 2nd neighbor Fe^{3+} ions; 5.16 Å. In addition, we investigated the energy spectrum of this diffuse scattering. The data were taken at C1-1 triple axis spectrometer with Horizontally Focusing Analyzer (HFA) installed at a cold guide of JRR-3M. The energy resolution of this machine is estimated to be 0.166meV.

Even though very high energy resolution, the energy spectrum of this diffuse scattering is quasistatic (See Fig.2).

We further investigated energy spectra at several points in reciprocal lattice space. The inelastic peak

centered at about ΔE=2meV was observed in various reciprocal lattice points. These data were published in another previous paper. With increasing temperature, the inelastic scattering peaks gradually overdamped around 15K and they become quasielastic scattering peaks at high temperature (See Fig.3). The inelastic scattering does not depend on a Q space. It describes a motion of a local spin such as each Fe^{3+} spin that constructs a tetrahedron. We consider that the origin of this fluctuation arises from the contradiction due to the 3rd neighbor Fe^{3+} spins which couple antiferromagnetically.

Acknowledgements: We would like to thank Dr. H. Kadowaki of Tokyo Metropolitan univ. for lending us with the HFA.

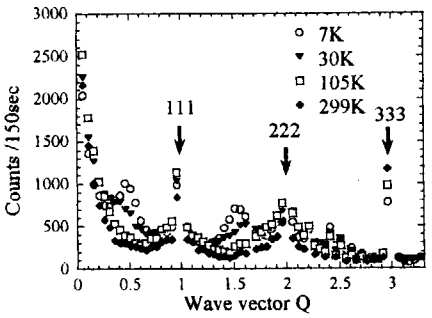


Fig.1(a) Temperature dependences of constant-E scan along <111> direction at an energy transfer of 0meV.

I	111, 331	$B-A/\sqrt{2}$
II	220, 224	A
III	004, 444	2B−A
IV	113, 333	$B+A/\sqrt{2}$
V	222	2B
VI	440	2B+A

Table 1

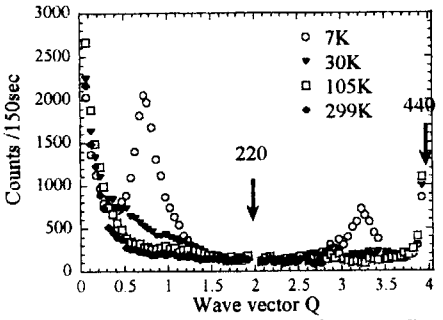


Fig.1(b) Temperature dependences of constant-E scan along <110> direction at an energy transfer of 0meV.

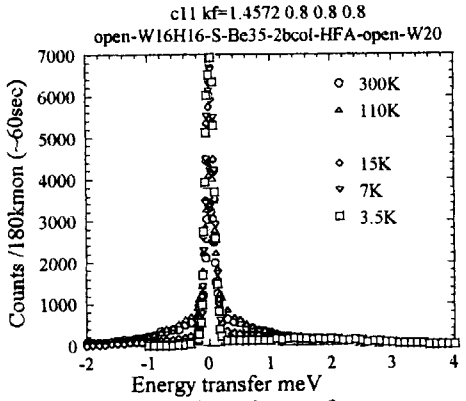


Fig.2 Temperature dependenses of energy spectra studied at Q = (0.8,0.8,0.8).

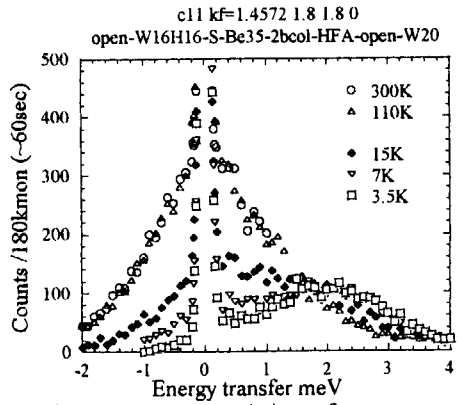


Fig.3 Temperature variations of energy spectra studied at Q = (1.8,1.8,0).

研究テーマ：スピネル化合物の電気的、磁気的性質の強相関係

表題：スピネル化合物 $Zn_{1-x}Cu_xCr_2Se_4$;0.0≦ x ≦0.30 の不整合反強磁性相転移

1-2-50

Incommensurate antiferromagnetic transition in substituted spinels of $Zn_{1-x}Cu_xCr_2Se_4$; $0.0 \leq x \leq 0.3$.

M.Hidaka[1], N.Tokiwa[1], T.T.Wai[1], H.Fujii[2] and K.Ohoyama[3]

[1]*Department of Physics, Faculty of Science, Kyushu University,33, Fukuoka 812-0053, Japan.*

[2]*Faculty of Education, Oita University, Oita 870-1192, Japan.*

[3]*Institute for Materials Research, Tohoku University, Sendai 980-8577, Japan.*

$ZnCr_2Se_4$ and $CuCr_2Se_4$ compounds have a normal spinel-type structure, which is mainly characterized by a strong preference of Cr ions to locate in the octahedral site. It is well known that $ZnCr_2Se_4$ spinel is a semiconductor and an antiferromagnet below 20K with magnetic spiral structure, while $CuCr_2Se_4$ is a metal and a ferromagnet below 420K. However, the substituted spinels of $Zn_{1-x}Cu_xCr_2Se_4$ shows unusual magnetic and electronic properties as a function of Cu-concentration, x. For example, the anti-ferromagnetic semiconductor with $x<0.10$ and ferromagnetic metal with $0.2 \leq x \leq 1.0$. Furthermore, the magnetic property is a spin glass in the region of $0.10<x<0.20$, conical ferromagnet ($0.3<x<0.8$), and uniaxial ferromagnet ($0.9 \leq x \leq 1.0$). The Neel temperature (T_N) is about 20K in $x<0.1$, and the Curie temperature (Tc) is about 380 ~ 400K in $0.3 \leq x \leq 1.0$.The similar x dependence is also observed on the electrical conductivity. Therefore, the $Zn_{1-x}Cu_xCr_2Se_4$ spinels show a good example of strong correlation between the magnetic properties and electronic ones changed by the concentration and the mobility of the current carriers.

We carried out measurements of magnetic and crystallographic reflections using Neutron powder diffraction. The powder diffraction patterns of $Zn_{1-x}Cu_xCr_2Se_4$ with x=0.0, 0.15 and 0.30 were taken using a high-resolution neutron diffractometer, HERMES, in JRR- 3. The used wavelength of incident neutron beams was about 1.820 Å. In Figs. 1(a) and (b), the partial powder diffraction patterns of $ZnCr_2Se_4$ and $Zn_{0.7}Cu_{0.3}Cr_2Se_4$ are shown with thin and thick solid-lines respectively. The diffraction patterns were very similar to those of $Zn_{0.85}Cu_{0.15}Cr_2Se_4$. Therefore, it was confirmed that some magnetic reflections denoted with a notation 'M' appear in the antiferromagntic phase occurring below about 20 K (T_N). The magnetic reflection having a strongest intensity was observed at about 2θ = 4.7 degrees at 2.5 K. Its d-value in $ZnCr_2Se_4$ was about 22 Å and was not an integral multiple to the lattice constant a to be 10.50 Å,

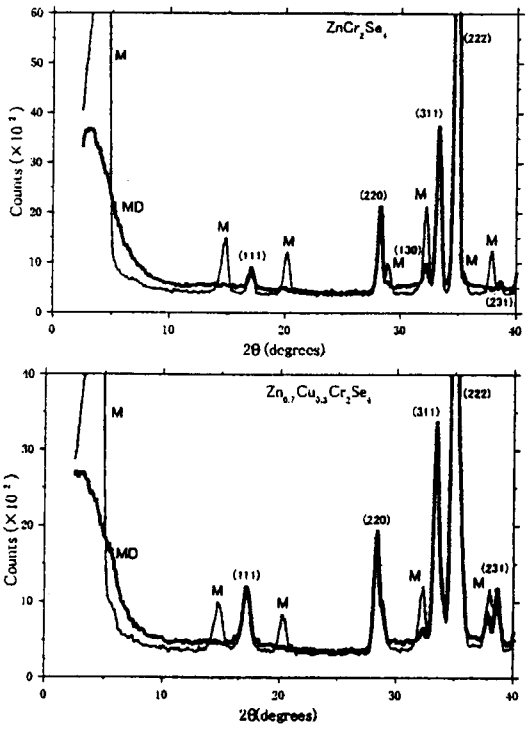


Figure 1. Comparison of partial neutron powder diffraction patterns taken at 2.5 K (thin line) and 40 K (thick line) for $ZnCr_2Se_4$ and $Zn_{0.7}Cu_{0.3}Cr_2Se_4$.

JRR-3, HERMES, Magnetism

which was obtained at 2.5 K. Thus, we considered that its magnetic structure of $Zn_{1-x}Cu_xCr_2Se_4$; x=0.0, 0.15 and 0.30 should be incommensurate. Magnetic diffuse scattering denoted with MD are also observed at 40 K. In the figures, the notations of (1,1,1), (2,2,0), (3,1,1) and (2,2,2) mean indexes of the fundamental reflections calculated by an ideal spinel structure of $Zn_{0.7}Cu_{0.3}Cr_2Se_4$, of which a space group is Fd3m. On the other hand, the (1,3,0) and (2,3,1) reflection having a weak intensity is forbidden in the space group of Fd3m.

In order to index such the magnetic reflections, we deducted the counts of the powder patterns taken at 2.5 K from those taken at 40 K. The deduction curves of the spinels with x=0.0 and 0.30 are shown in Figs.2 (a) and (b). All peaks are the magnetic reflections except a partial peak (P), which results from the difference of the lattice constants at 2.5 K and 40 K. The magnetic diffuse scattering can be also confirmed by negative counts in the figures. In the present investigations, the magnetic reflections could be indexed by ($h \pm Q$, k, ℓ) with Q = 0.470 as shown in Figs.2(a),(b). The calculated peak positions of the magnetic reflections are also shown with thick vertical lines.

The measurements of magnetization and magnetization hysteresis-loops became clear that there is a ferromagnetic phase transition (Curie temperature; T_C) at about 410K and 415K for $Zn_{1-x}Cu_xCr_2Se_4$; x=0.15 and 0.30, respectively. We measured these powder diffraction patterns at 350 K and 430 K, to study the structural modulation related to the ferromagnetic transition. However, we could not find any difference of the powder patterns taken at 350 K and 430 K and any magnetic diffuse scattering in both phases. Thus, we deduced that the Cr^{3+}spin configuration of the conical ferromagnetism in $Zn_{1-x}Cu_xCr_2Se_4$; x=0.15 and 0.30 is not reflected to a long-range periodicity of atomic coordinates in the spinel-type structure and other chemical unit cells.

From the present neutron powder diffraction, we considered that the magnetic phase transition occurring at T_N (~ 20 K) in the substituted spinels of $Zn_{1-x}Cu_xCr_2Se_4$; $0.0 \leq x \leq 0.3$ is mainly induced by the appearance of the spiral spin configuration of the magnetic moments of Cr^{3+} ions. Above T_N, such the spin configuration shows only the short-range order and gradually disappears as increasing the specimen temperature. The evidence implies that the intermediate ferromagnetic phase between T_N and T_C (~ 400 K) in $Zn_{1-x}Cu_xCr_2Se_4$; x=0.15, 0.30 may be related not to the conical long-range order of the Cr^{3+} spins along [100] but strongly to the Cu^{1+}-concentration. The concentration affects the electronic property in $Zn_{1-x}Cu_xCr_2Se_4$; $0.0 \leq x \leq 0.3$. Therefore, it is deduced that the ferromagnetism in $Zn_{1-x}Cu_xCr_2Se_4$ may result from the concentration and the mobility of the current carriers mediating the magnetic interaction among the localized magnetic moments of Cr ions. The current carriers are made to be positive holes by the substitution of Zn^{2+} ions with Cu1+ ion.

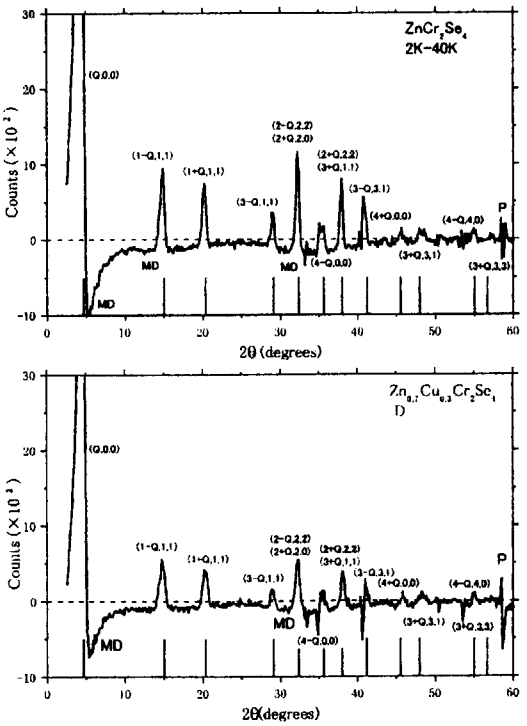


Figure 2. Deducted counts between the powder diffraction patterns taken at 2.5 K and 40 K for $ZnCr_2Se_4$ and $Zn_{0.7}Cu_{0.3}Cr_2Se_4$.

研究テーマ：$Y(Co,Ni)_5$の磁気構造
表題：$Y(Co,Ni)_5$の磁気構造

1-2-51 Magnetic Structure of $Y(Co,Ni)_5$

Y. Adachi, F. Ishikawa[1] and M. Ohashi

Faculty of Engineering, Yamagata University, Yonezawa 992-8510
[1]Ecotechnology System Laboratory, Yokohama National University, Yokohama 240-8501

YCo_5 is a strong ferromagnet with large magnetocrystalline anisotropy. The crystal structure of YCo_5 is the hexagonal $CaCu_5$-type (sapce group P6/mmm), in which there are one site for Y atoms and two sites for Co atoms called 2c and 3g sites. The increase in Ni concetration for the solid solution system $Y(Co_{1-x}Ni_x)_5$ results in the transition from the high moment state to the low moment state. The critical Ni concentration of the transition is x=0.55 in $Y(Co_{1-x}Ni_x)_5$ system.

Polycrystalline samples were prepared by an arc melting method in argon atomosphere and annealed at 1200 K for 24 hours under continuous flow of purified argon gas for homogenization. Neutron powder diffraction experiments were carried out using the powder diffractometer for high efficiency and high resolution measurements (HERMES) installed at JRR-3M in JAERI. The diffraction patterns of $Y(Co_{0.4}Ni_{0.6})_5$ and $Y(Co_{0.5}Ni_{0.5})_5$ were measured using neutrons with wavelength λ=1.8196 Å.

The neutron diffraction patterns of $Y(Co_{0.4}Ni_{0.6})_5$ were obtained at 450 K in a paramagnetic state and at 65 K in a ferromagnetic state, shown in Fig. 1. All reflection peaks are indexed with the hexagonal $CaCu_5$-type structure in both states. Since the magnetic reflection peaks are observed overlapping the nuclear peaks, the magnetic structure seems to be ferromagnetic. We have to calculate the occupation ratios of Co atoms in 2c and 3g sites in order to propose the details of magnetic moments of Co atoms. Analysis of neutron diffraction data is in progress.

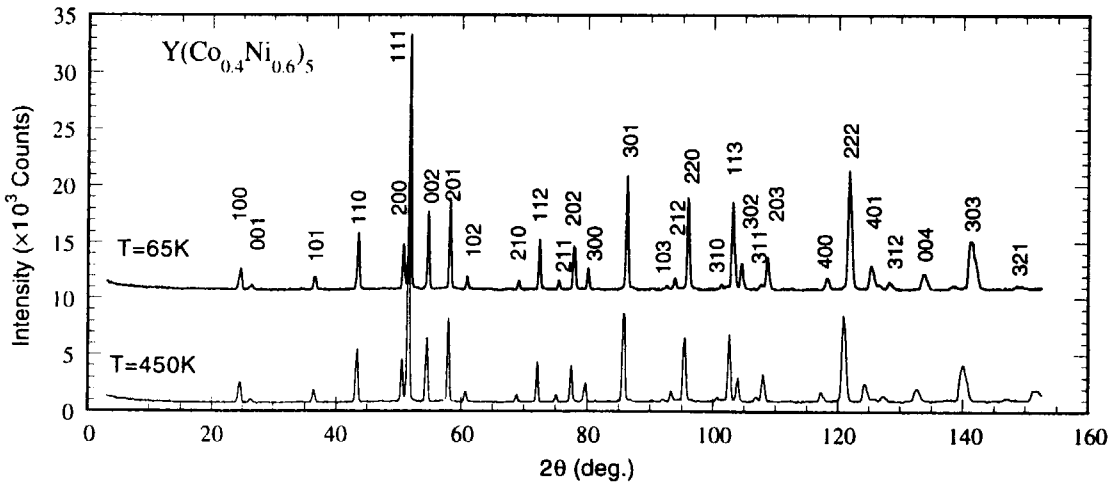


Fig. 1. Netron diffraction patterns of $Y(Co_{0.4}Ni_{0.6})_5$ at 450 K and 65 K.

JRR-3M, HERMES, 2.Magnetism

研究テーマ：AV_6O_{11} (A=K, Ba) 化合物の磁気構造の研究
表題：中性子粉末回折による BaV_6O_{11} の磁気構造の研究

1-2-52 Magnetic Structures of BaV_6O_{11} Studied by Neutron Powder Diffraction

Y. Kanke, K. Ohyama,[a] and Y. Yamaguchi[a]

Advanced Materials Laboratory, NIMS, 1-1 Namiki, Tsukuba, Ibaraki 305-0044, Japan
[a]Institute for Materials Research, Tohoku University, 2-1-1 Katahira, Sendai 980-8577, Japan

Introduction

AV_6O_{11} (A=Na, K, Sr, Ba, Pb) are interesting from viewpoint of possible quantum spin system in *kagomé* lattices, and that of rare "vanadium magnets". The magnetic structures remain open questions. They show Curie-Weiss (CW) paramagnetism and crystallize in hexagonal $P6_3/mmc$, at their highest temperature states. There are three types of V atoms. The $V(1)O_6$ octahedra form a regular *kagomé* lattice. The $V(2)O_6$ octahedra form a face-sharing dimer. The $V(3)O_5$ is a trigonal bipyramid. One formula unit consists of three V(1), two V(2), and one V(3) atoms.[1]

Below T_t, a portion of the CW-spins survives, but the others decrease with decreasing temperature like a spin gap manner. The compounds transform from $P6_3/mmc$ forms to $P6_3mc$ ones. The V(1) atoms form a regular-triangle-cluster. The V(2) atoms branch into the V(21) and V(22) atoms equally. The $V(3)O_5$ trigonal-bipyramid distorts. The *kagomé* V(1) atoms are considered to be mainly responsible for the decreasing spins.

Below T_C, they exhibit individual magnetic order. Spontaneous magnetization extrapolated to 0 K, $M_s(0)$, of BaV_6O_{11} is about 3 times as large as those of the others. BaV_6O_{11} shows three transitions, at T_t (250 K), T_C (115.4 K), and T_m (75 K). At $T_C<T\leq T_t$, the survived CW-spins per formula unit correspond to either five S=1/2 or one S=1+ three S=1/2. $M_s(0)$ values are 4.39 μ_B formula unit^{-1} for above T_m and 4.75 μ_B formula unit^{-1} for below T_m.[2] In this study, magnetic structures of BaV_6O_{11} are investigated by neutron powder diffraction.

Experimental

0.95g of BaV_6O_{11} powder specimen was put into a 9 mm-diameter-vanadium-cell. Diffraction data were collected at 130 K ($T_C<T<T_t$), 85 K ($T_m<T<T_C$), and 13 K ($T<T_m$), by HERMES (λ=1.8196 Å) installed at JRR-3M.

Results and Discussion

Magnetic diffractions were clearly observed at both 85 K and 13K (Fig. 1). Neither super lattice diffraction nor a diffraction violating the extinction rule for $P6_3mc$ ($l\neq$odd if $h=k$) was detected. So the unit cells of both magnetic structure and crystal structure coincide throughout below T_C. There was no $00l$ diffraction, which agrees with that the easy axis is parallel to [001]. The $P6_3mc$ form lacks the inversion center. The situation should be unchanged below T_C. So cant-spin structures are allowed due to Dzyaloshinsky-Moriya interaction, though no $00l$ was observed. The 101 diffraction shows almost same intensity at both 85 K and 13 K. However, 100 is stronger at 13 K than 85 K. Therefore, spin-canting should be larger above T_m than below T_m.

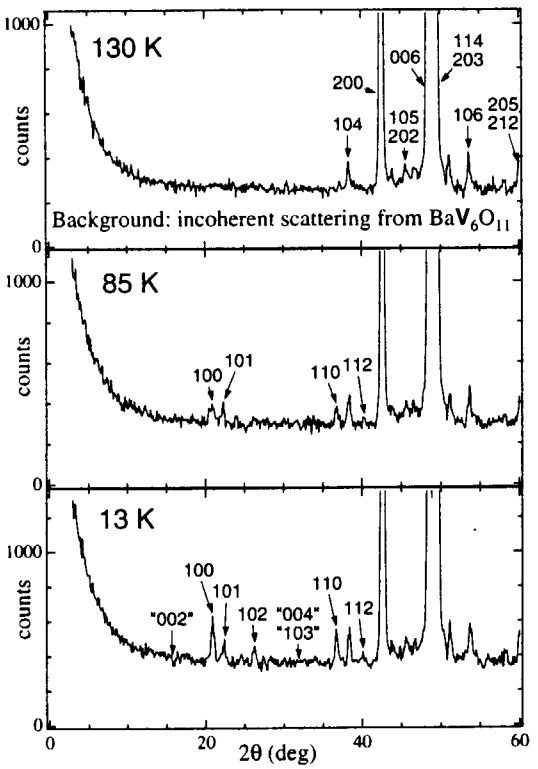


Fig. 1. Neutron diffraction data of BaV_6O_{11}.

The 13 K-data were analyzed by *RIETAN* assuming a co-linear spin structure. Obtained result (V(1): 0.29 μ_B, V(21): 1.86(18) μ_B, V(22): 0.93(17) μ_B, V(3): 1.08(9)μ_B, R_{wp}=5.42%, and S=1.12) is consistent with one S=1+ three S=1/2 for $T_C<T\leq T_t$.

References
[1] Y. Kanke, Phys. Rev. B60, 3764 (1999) and references are therein.
[2] Y. Kanke, submitted.

研究テーマ：希土類元素を含む遷移金属酸化物・硫化物の磁気構造
表題：中性子回折による四元系反強磁性硫化物の磁気構造

1-2-53
Magnetic Structures of Quaternary Antiferromagnetic Sulfides $BaNd_2CoS_5$ and $BaNd_2FeS_5$ by Powder Neutron Diffraction Measurements

M. Wakeshima, K. Ino, Y. Hinatsu, A. Tobo[1], K. Ohoyama[1] and Y. Yamaguchi[1]
Division of Chemistry, Graduate School of Science, Hokkaido University, Sapporo 060-0810, Japan
[1] *Institute for Materials Research, Tohoku University, Sendai 980-8577, Japan*

Quaternary sulfides $BaNd_2CoS_5$ and $BaNd_2FeS_5$ have a tetragonal structure with space group *I*4/*mcm*. Their magnetic susceptibility and specific heat measurements showed that the Co^{2+} and Fe^{2+} ions were in the antiferromagnetic states below 63 and 44 K, respectively. In these compounds, the Nd^{3+} ions show an antiferromagnetic transition at 6 K[1, 2].

Powder neutron diffraction measurements of $BaNd_2CoS_5$ and $BaNd_2FeS_5$ were performed using the high efficiency and resolution powder diffractometer, HERMES, of Institute for Materials Research, Tohoku University, installed at the JRR-3M with a neutron incident wave length (λ = 1.8196 Å). The magnetic structures were determined by the Rietveld method.

Figure 1 shows the diffraction patterns for $BaNd_2FeS_5$ at 2.3, 30, and 60 K. The magnetic reflections observed at 30 K are due to an antiferromagnetic ordering of Fe^{2+}. A collinear magnetic structure of Fe^{2+} with a $\sqrt{2}a \times \sqrt{2}a \times c$ unit cell is determined, which is shown in Fig. 2. The magnetic moment of Fe^{2+} is estimated to be 2.65 μ_B and is determined to lie in a parallel direction with the *c*-axis. The additional magnetic reflections observed at 2.3 K are due to an antiferromagnetic ordering of Nd^{3+}. The magnetic structure of Nd^{3+} is determined to have a noncollinear antiferromagnetic structure with the same unit cell size as that of Fe^{2+} ($\sqrt{2}a \times \sqrt{2}a \times c$).

The magnetic reflections for $BaNd_2CoS_5$ were also observed in the diffraction patterns at 2.3 and 10 K. The diffraction pattern at 10 K indicates that the magnetic structure of Co^{2+} has a collinear antiferromagnetic structure with an $a \times a \times c$ unit cell. The magnetic moments of Co^{2+} (~ 3.66 μ_B) lie in a parallel direction with the *c*-axis, but the magnetic arrangement of the Co^{2+} spins is different from that of the Fe^{2+} spins. The magnetic structure at 2.3 K of Nd^{3+} is found to have the same antiferromagnetic structure as that of the Nd^{3+} in $BaNd_2FeS_5$.

Reference

1) M. Wakeshima and Y. Hinatsu, J Solid State Chem., **159**, (2001), in press.
2) K. Ino, M. Wakeshima and Y. Hinatsu, in preparation.

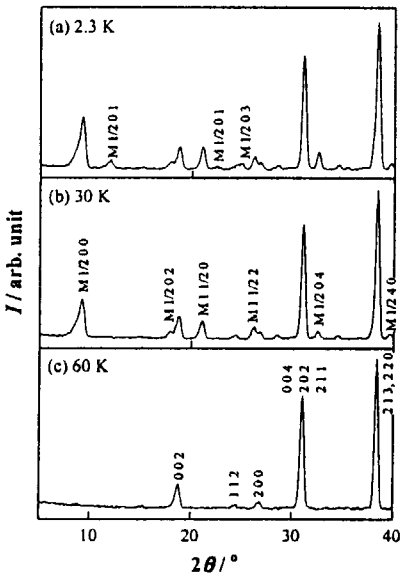


Fig. 1 Neutron powder diffraction patterns of $BaNd_2FeS_5$

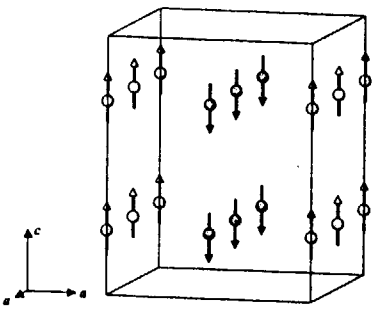


Fig. 2 Magnetic structure of Fe^{2+} in $BaNd_2FeS_5$.

研究テーマ：TmB_2C_2での磁気構造の研究
表題：正方晶$Tm^{11}B_2C_2$の磁気構造

1-2-54 Magnetic structure in the tetragonal compound $Tm^{11}B_2C_2$

K. Ohoyama, K. Kaneko, A. Tobo, K. Indoh, H. Onodera, Y. Yamaguchi,

Institute for Materials Research, Tohoku University, Sendai 980-8577

Magnetic properties in RB_2C_2 compounds (R= rare earth) with the tetragonal LaB_2C_2 type crystal structure[1] attract many interests recently. In particular, DyB_2C_2 undergoes an antiferroquadrupolar (AFQ) ordering at T_Q=24.7K and a further transition to an antiferromagnetic (AFM) ordered state at 15.3K[2]. It should be pointed out that T_Q of DyB_2C_2 is nearly ten times higher than those of other AFQ ordering materials. Moreover, HoB_2C_2 is the unique AFQ material which exhibits AFQ ordering below its magnetic ordering temperature[3]. On the other hand, though other RB_2C_2 compounds show no AFQ ordering, these non-AFQ compounds show various and characteristic magnetic structures including long periodic ones. We think that, to make clear the mechanism of AFQ orderings in RB_2C_2 system, it is indispensable to understand magnetic features in RB_2C_2 system as a whole. This work aims, therefore, at determining magnetic structures in the isostructural compound TmB_2C_2. The temperature dependence of magnetic susceptibility of TmB_2C_2 shows an apparent anomaly at T_N=16.5K which indicates a magnetic transition to an antiferromagnetic state. The magnetic easy axis is the [001] direction in the whole measured temperature range.

Figs.1 show powder patterns of a polycrystalline sample of $Tm^{11}B_2C_2$ on Kinken powder diffractometer HERMES(T1-3) at JRR-3M. Natural boron was replaced by ^{11}B, to avoid the strong neutron absorption effect. Fig.1(a) and (b) are patterns at 2.2K and 25.1K, respectively. Index in Fig.1(b) show nuclear Bragg reflections. As shown in Fig.1(a) and (b), strong magnetic peaks were observed. Fig.1(c) shows the pure magnetic contribution obtained by subtraction of the data at 2.2K and 25.1K ($I_{2.2K}$-$I_{25.1K}$). The magnetic Bragg reflections can be indexed with the propagation vector k=[101/2]. Thus, the magnetic structure in the ground state is a simple AFM one; magnetic couplings in the c-plane and that along the c-axis are both AFQ ones. In fact, Rietveld analysis with this simple magnetic structure model represents the pattern at 2.2K well. The magnetic moment in the ordered state is determined as about 6.5μ_B from Rietveld analysis by FullProf, which is well consistent with the saturation magnetisation. However, the AFM structure with k=[101/2] in TmB_2C_2 is different from those in the ground states of isostructural compounds NdB_2C_2, ErB_2C_2[4]. Since the fundamental AFM correlation in RB_2C_2 is thought to be k=[100] type one, TmB_2C_2 is the unique compound with AFM coupling along the [001] direction among RB_2C_2 system.

References

[1] T. Onimaret al.: JPSJ 68(1999) 2287.
[2] H. Yamauchi et al. JPSJ 68 (1999) 2057
[3] H. Onodera et al.: JPSJ 68(1999) 2526.
[4]K. Ohoyama et al.: JPSJ 69 (2000) 2623

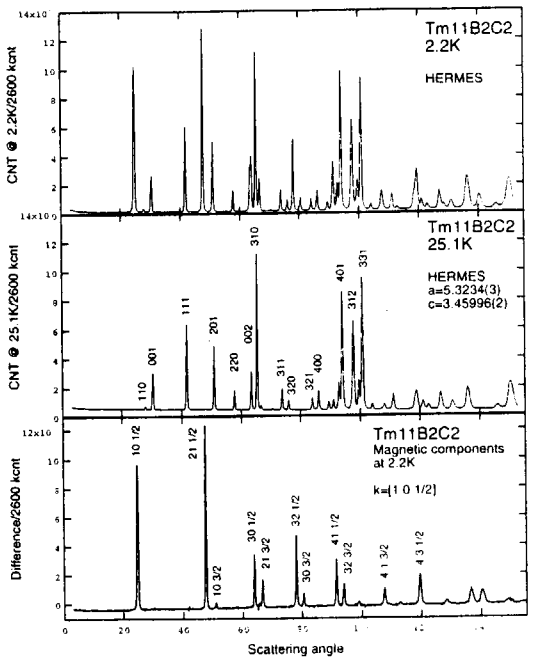


Fig.1 Powder patterns of $Tm^{11}B_2C_2$ at (a) 2.2K, (b) 25.1K on HERMES. (c) is the magnetic contribution pattern obtained by subtraction ($I_{2.2K}$-$I_{25.1K}$). Index in Fig.1(b) indicate nuclear Bragg reflections.

JRR-3M, T1-3, 2: Magnetism

研究テーマ：正方晶TbB_2C_2の磁気構造
表題：正方晶TbB_2C_2の基底状態磁気構造

1-2-55 Magnetic Structure of Tetragonal TbB_2C_2 in the Ground State

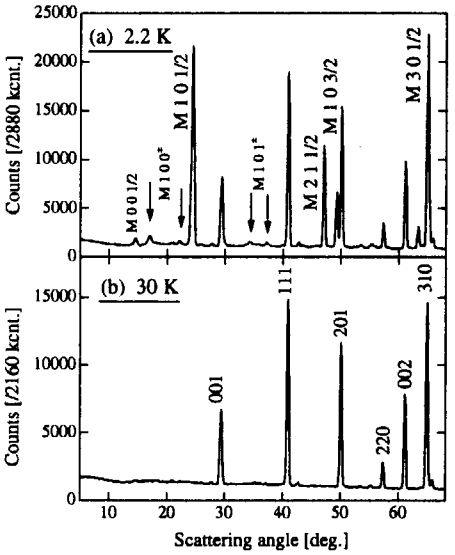
K. Kaneko, K. Ohoyama, A. Tobo, H. Yamauchi, H. Onodera and Y. Yamaguchi

Institute for Materials Research, Tohoku University, Sendai 980-8577, Japan

Recently, rare earth inter-metallic compounds RB_2C_2 with the tetragonal LaB_2C_2-type crystal structure[1],[2] attract our strong interest. In this system, Yamauchi *et al.* reported that DyB_2C_2 is the first material which exhibits an antiferroquadrupolar (AFQ) order transition among tetragonal rare earth compounds; the AFQ order is realized at T_Q=24.7 K with a successive transition to an antiferromagnetic (AFM) state at T_N=15.3 K[3]. Moreover, Onodera *et al.* reported that HoB_2C_2 also shows a AFQ order transition at T_Q = 4.5 K[4]. It should be pointed out that the AFQ order transition in HoB_2C_2 occurs below T_N=5.9 K, that is, the AFQ order in HoB_2C_2 is realized in the magnetic ordered state. To understand the nature of AFQ interactions of DyB_2C_2 and HoB_2C_2, knowledge of magnetic behavior of other RB_2C_2 compounds is also indispensable. As for TbB_2C_2, the magnetic moments lie in the *c*-plane, which is the same as DyB_2C_2 and HoB_2C_2. The aim of this work is, therefore, to determine the magnetic structure of TbB_2C_2 in the ground state.

Neutron powder diffraction experiments were carried out on Kinken powder diffractometer HERMES (T1-3) installed at JRR-3M. Since ^{10}B is a strong absorber for neutrons, measurements were performed on the sample including 99.5 % of ^{11}B to avoid the significant attenuation. Figs. 1 show powder diffraction patterns of $Tb^{11}B_2C_2$ measured at (a) T=2.2 K (below T_N) and (b) T=30.0 K (above T_N). Letter M in Fig. 1(a) indicate magnetic reflections. We observed intense M1 0 1/2, M2 1 1/2, M1 0 3/2 and M3 0 1/2 with a weak M0 0 1/2 at 2.2 K. In addition, weak satellite peaks were also observed around 1 0 0 and 1 0 1 denoted by arrows. These observed magnetic reflections can be described with propagation vectors of dominant $\boldsymbol{k}_2$=[0 1 1/2] with weak $\boldsymbol{k}_4$=[0 0 1/2] and $\boldsymbol{k}_L$=[1±δ ±δ 0] where δ=0.13. The magnetic moments corresponding to $\boldsymbol{k}_2$, $\boldsymbol{k}_4$ and $\boldsymbol{k}_L$ are determined as 5.8(1) μ_B, 1.2(1) μ_B and 1.4(1) μ_B, respectively.

The magnetic structure of DyB_2C_2 and HoB_2C_2 in the ground state which is strongly affected by the AFQ order is characterized by the coexistence of ferromagnetic and AFM coupling along the *c*-axis mainly described with $\boldsymbol{k}_1$=[1 0 0] and $\boldsymbol{k}_2$=[0 1 1/2]. Since only AFM coupling along the *c*-axis with $\boldsymbol{k}_2$=[0 1 1/2] component was observed in TbB_2C_2, the same types of an AFQ order as DyB_2C_2 and HoB_2C_2 is not realized in TbB_2C_2 at least in the ground state. However, $\boldsymbol{k}_1$ component still exists as weak satellite peaks corresponding to $\boldsymbol{k}_L$ in TbB_2C_2. It should be pointed out that the intermediate phase in HoB_2C_2, Phase IV, also exhibits a $\boldsymbol{k}_1$-base incommensurate component which has similar periodicity of $\boldsymbol{k}$=[1±δ ±δ δ'] where δ=0.111 and δ'=0.04. In case of HoB_2C_2, this incommensurate structure is thought to be attributed to effects of AFQ interactions[5]. Therefore, we suppose that effects of AFQ interactions can not be neglected even in the ground state in TbB_2C_2.



Figs. 1 Neutron powder diffraction pattern of $Tb^{11}B_2C_2$ at (a) 2.2 K (below T_N) and (b) 30 K (above T_N). Letter M denotes magnetic reflections and arrows indicate magnetic satellite peaks.

Reference

[1] T. Onimaru *et al.*: J. Phys Soc. Jpn. **68** (1999) 2287.
[2] K. Kaneko *et al.*: J. Phys. Soc. Jpn. **69** (2000) 3762.
[3] H. Yamauchi *et al.*: J. Phys. Soc. Jpn. **68** (1999) 2057.
[4] H. Onodera *et al.*: J. Phys. Soc. Jpn. **68** (1999) 2526.
[5] K. Ohoyama *et al.*: J. Phys. Soc. Jpn. **69** (1999) 3401.

研究テーマ：多段メタ磁性転移を示す Ce_3PbC の磁気構造の決定

表題：Ce_3PbC の中性子回折

1-2-56 Neutron Diffraction Study on Ce_3PbC

M. Kosaka, S. Koiwai, Y. Uwatoko, H. Onodera[1], A. Tobo[1], K. Ohoyama[1] and Y. Yamaguchi[1]

Department of Physics, Saitama University, Urawa 338-8570, Japan

[1] Institute for Materials Research, Tohoku University, Sendai 980-8577, Japan

Ternary compound Ce_3PbC has a simple face-centered cubic $CaTiO_3$-type structure. This crystal structure features that Ce atoms are situated on a face-centered position of an unit cell which occupies 3c tetragonal symmetry site (4/mmm) while the crystal structure is cubic. Ce_3PbC undergoes a transition to an antiferromagnetic state at T_N = 8.3 K and magnetic order-order transition shows at T_t = 5.8 K. The magnetization process shows multi-step metamagnetic transitions at T = 1.5 K. This behavior is similar to that of Ce_3SnC [1].

For sample preparation we used Ce of 99.99%, Pb of 99.999% and C of 99.9995% purity. The compounds are synthesized by a conventional argon arc technique and annealed at 1000 ℃ for a week in tantalum foil, which was sealed in an evacuated quartz tube. Neutron powder diffraction measurements were carried out using the high efficiency and resolution powder diffractometer (HERMES) installed at JRR-3M reactor in the Japan Atomic Energy Research Institute.

Figure 1 shows the neutron diffraction pattern of Ce_3PbC at T = 2.2 K. In the pattern, magnetic reflections are clearly observed (a character N denotes a nuclear reflection). The propagation vector is determined to be q = [½, ½, 0] between T_t < T < T_N. It became clear that the double-q magnetic structure exhibits below T_t which is described by the propagation vectors q = [½, ½, 0] and q = [½, 0, 0]. Abcence of magnetic (½, 0, 0) reflection suggests that a magnetic moment lies along the a-axis. Figure 2 shows the temperature dependence of intensity of representative magnetic reflections (½, ½, 1) and (½, 1, 0) which belong to the propagation vector q = [½, ½, 0] and q = [½, 0, 0], respectively.

Isostructural compound Ce_3SnC shows strange magnetic structure [2]. There are two kind Ce atoms, one has magnetic moment of 2.0 μ_B and the other has no magnetic moment while Ce atoms occupy the same crystallographic site. The reason seems to be that Ce atoms are affected by strong tetragonal symmetry crystalline electric field (CEF). In Ce_3PbC, the magnetic structure described by the propagation vector q = [½, 0, 0] appears blow T_t, this magnetic structure coexists with another magnetic structure between T_t < T < T_N which is expressed the propagation vector q = [½, ½, 0]. Detailed magnetic structure of Ce_3PbC is now in progress.

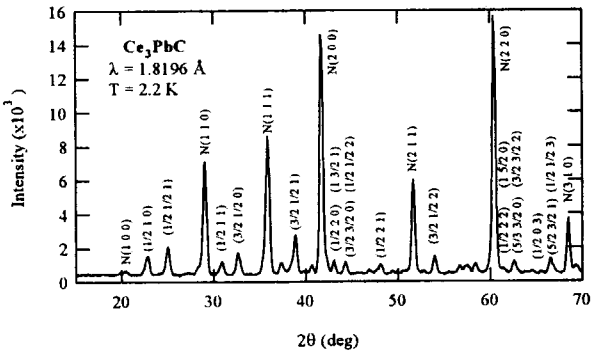


Fig. 1 Neutron diffraction pattern of Ce_3PbC at 2.2K.

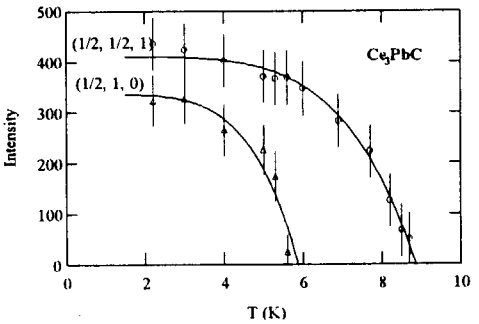


Fig. 2 Magnetic scattering intensity at (½, ½, 1) and (½, 1, 0) as a function of temperature.

[1] M. Kosaka et al., Physica B 284 (2000) 1323.

[2] M. Kosaka et al., Activity Report on Neutron Scattering Research vol.7 (2000) p.100.

研究テーマ：三元系 Ni_2In 型合金の磁性
表題：$(Mn_{1-x}Cu_x)_{66}Ga_{34}$ 合金の磁性と中性子回折による研究

1-2-57
Magnetic and Neutron Diffraction Study on $(Mn_{1-x}Cu_x)_{66}Ga_{34}$

H.Shiraishi, Y.Iguchi, T.Hori, K.Ohoyama [a], Y.Yamaguchi [a]

Shibaura Institute of Technology, Oomiya, Saitama 330-8570, Japan
[a] Institute of Materials Research, Tohoku University, Sendai 980-8577, Japan

The intermetallic compounds $(Mn_{1-x}Cu_x)_{66}Ga_{34}$ of Ni_2In type structure are investigated with magnetmetric and the neutron diffraction experiments in the range of $0.25 \leqq x \leqq 0.35$. The temperature dependence of magnetization σ shows a cusp at T_t after the disappearance of spontaneous magnetization with increasing temperature and the χ^{-1}-T curve shows a bend at T_N as shown in Fig.1.

The neutron diffraction experiments were carried out in order to determine the magnetic structure of $(Mn_{1-x}Cu_x)_{66}Ga_{34}$ compounds with x=0.25 using HERMES of Tohoku University installed in the JRR-3M in JAERI. The atom arrangement corresponding to minimum values of disagreement factor R is as follows: in the Ni_2In type structure, the 2(a) site is entirely occupied by Mn, the 2(d) site by Cu , residual Mn randomly and 2(c) site by Ga. A preferred occupation of Cu on the 2(d) site is observed. Fig.2 shows a part of the diffraction patterns in the low Bragg angle region. In the patterns at T=215 and 293K, the (001) magnetic reflection is observed, indicating the presence of antiferromagnetic component lying in the basal plane. As the magnetic contribution to the (002) reflection is negligible, the ferromagnetic component is parallel to the c axis. From these consideration, the spins at the 2(a) site are thought to be a canted with theferromagnetic components parallel to the c axis and with antiferromagnetic one in the basal plane. The spins at 2(d) site are antiparallel to the ferromagnetic component. This model is similar to that of Ni_2In type CoMnSn and $(Mn_{0.75}Ni_{0.25})_{65}Ga_{35}$ [1]. In the patterns for $T<T_t$ (~208K), satellite lines of (001) and (101) are observed, suggesting the appearance of helical spin structure. The pitch of helix changes $4.12c$ (T=20K) ~ $8.26c$(175K), where c is lattice constant.

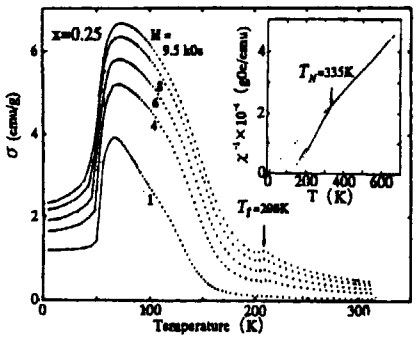


Fig.1. The σ-T curve and χ^{-1}-T curve for x=0.25

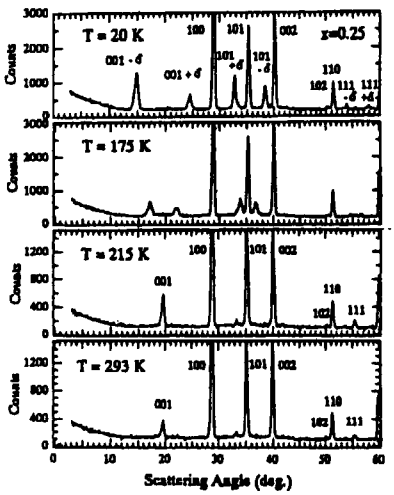


Fig.2. Neutron diffraction patterns in the low Bragg angle region for x=0.25

Reference

[1]H.Shiraishi,H.Niida,Y.Iguchi,S.Mitsudo,Mmotokawa,K.Ohoyama,H.Miki,H.Onodera,T.Hori,K.Kanematsu,. J.Magn.Magn.Mater **196-197**(1999) 660

JRR-3M, HERMES, 2.Magnetism

研究テーマ：MnAl, MnGa合金の磁性と結晶変態の研究
表題　　：MnAl hcp 相の中性子回折による研究

1-2-58 Antiferromagnetic order in the hcp phase of MnAl alloy

S. Tomiyoshi , K. Nakamura, T. Sheo and Y. Yamaguchi
Faculty of Engineering Ehime University Matsuyama 790-8588
IMR, Tohoku University, Sendai 980-8577

The ε -phase of MnAl alloy with the composition of 55 at.% Mn is a disordered alloy with the hcp structure, from which the MnAl permanent magnet is obtained by a suitable heat treatment. This composition of the alloy gives almost zero neutron scattering amplitude which allows the determination of a chemical short range order present in this alloy. The ε MnAl was suggested to be an antiferromagnet with the Néel temperature of 100K, but detail is not known. To investigate the magnetic and crystallographic properties we measured carbon-doped MnAl ε -phase by neutron diffraction using powder diffractometer HERMES.

Figs. 1(a) and (b) show diffraction patterns of the ε -MnAl measured at 220K and 13K. The diffraction patterns consist mainly from sharp Bragg peaks with weak intensity and halo type broad peaks and also the temperature dependent magnetic broad peaks. The sharp Bragg peaks can be indexed by a hexagonal closed packed structure, which could arise because the cancellation of the scattering length is not complete. This result indicates that the lattice of the ε -phase is the disordered hcp structure in consistent with X-ray data. The halo peaks around 30° and 65° originates from a chemical short range order with the B15 type. Present data suggests that B15 type short range order exists in the hcp structure.

Temperature dependence of the pattern indicates a magnetic order in this alloy. Fig. 1(c) shows the magnetic peaks deduced from the subtraction between the intensities measured at 13K and 220K. These peaks can be indexed by doubling the a-axis length of the hcp stucture. The magnetic structure corresponding to these data is that the spins on the a-axis line couple ferromagnetic but the coupling between the adjacent a-axis line is antiferromagnetic. This structure explains well the diffraction pattern given in Fig. 1(c).

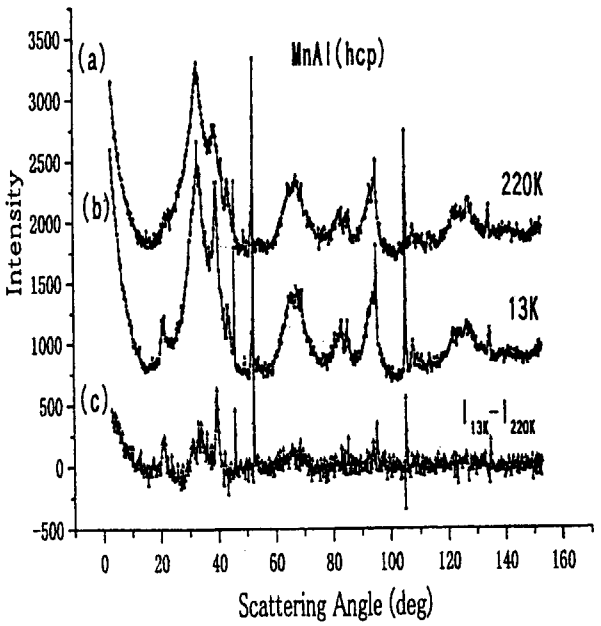


Fig.1 Neutron diffraction pattern of the ε -phase of MnAl at (a) 220K, (b) 13K and (c) the difference between the two. The counts of data (a) is displayed with a bias of 1000.

JRR-3M, HERMES, 2. Magnetism

研究テーマ：Fe^{4+}酸化物における電荷整列の解明
表題：六方晶$BaFeO_{3-\delta}$の磁気構造

1-2-59 Magnetic structure of the hexagonal $BaFeO_{3-d}$

K. Mori, T. Kamiyama, H. Kobayashi [1] and K. Ohoyama [2]

Institute of Materials Structure Science, High Energy Accelerator Research Organization, Tsukuba, Ibaraki 305-0801, Japan
[1] *Department of Physics, Tohoku University, Sendai, Miyagi 980-8578, Japan*
[2] *Institute for Materials Research, Tohoku University, Sendai, Miyagi 980-8577, Japan*

It had been believed that the hexagonal $BaFeO_{3-d}$ showed antiferromagnetic to ferromagnetic transition around 160 K, and the Curie temperature was about 250 K.[1] Recently, however, Iga *et al.* reported that the magnetic state below 160 K is antiferromagnetic-like and that between 160 K and 250 K is paramagnetic from the results of the Mössbauer and the magnetic susceptibility measurement.[2,3] These magnetic properties are very sensitive to the oxygen content. Thus, the extensive studies have been carried out for the hexagonal $BaFeO_{3-d}$ by various authors, but the detail of the magnetic structure is not clear. In this work, we have studied the magnetic structure of the hexagonal $BaFeO_{3-d}$ by neutron powder diffraction experiments.

The powder sample of $BaFeO_{3-d}$ was synthesized by the conventional solid state reaction method from Fe_2O_3 (99.999 %) and $BaCO_3$ (99.999 %). The mixture was fired at 900 °C for 24 h in air, pressed in disks, and heated at 1200 °C for 48 h. Finally, the product was annealed at 900 °C for 24 h in the flowing O_2 gas, then it was gradually cooled to room temperature (RT) for 72 h. The diffraction data were collected on time-of-flight (TOF) neutron powder diffractometer, Vega, at KENS in High Energy Accelerator Research Organization (KEK).[4] To refine the crystal structure of $BaFeO_{3-d}$ the intensity data were analyzed with a Rietveld refinement program RIETAN-2001T developed for Vega.[5] Moreover, to study the magnetic structure of $BaFeO_{3-d}$ the diffraction patterns at low angle region were measured on a neutron powder diffractometer, HERMES, of Institute for Materials Research (IMR), Tohoku University, installed at the JRR-3M reactor in Japan Atomic Energy Research Institute (JAERI).[6]

The crystal structure of $BaFeO_{3-d}$ at RT was refined on the basis of the $P6_3/mmm$ space group (No.194). Figure 1 shows the full pattern of the Rietveld analysis result at RT. An excellent fit was obtained between observed and calculated patterns. R_{wp} and S $(=R_{wp}/R_e)$ values were 5.90 and 1.22 %, respectively. The lattice parameters were a = 5.6725(1) and c = 13.9091(3) Å and the refined structure parameters are listed in Table 1. The oxygen content was estimated from a relation between oxygen one and lattice parameters.[7] Consequently, it was 2.94 and good agreement with the oxygen occupancy refined by the Rietveld analysis.

The neutron powder diffraction data of $BaFeO_{2.94}$ at 10 K collected on HERMES is shown in Fig. 2. In the pattern, all magnetic reflections were index with the propagation vector parallel to the < 001 > direction, whose absolute value δ is $0.44c^*$ at 10 K, where c^* is the reciprocal lattice parameter $(2\pi/c)$. This indicates that the magnetic structure of the hexagonal $BaFeO_{2.94}$ is a helical one. Furthermore, the average magnetic moment on Fe-ion was roughly estimated, and it was about 2.3 μ_B when the spin lies on c-plane. Figure 3 shows the temperature dependence of the magnetic intensity at the 0 0 2-δ reflection between 2.3 and 180 K. The magnetic intensities for all temperature are normalized by that at 2.3 K. As seen from Fig. 3, the intensity of the magnetic reflection 0 0 2-δ gradually decreases from 2.3 K to 100 K. Above 100 K, however, the magnetic intensity drastically reduces with decreasing temperature, and the magnetic reflection disappears over 150 K. It is expected that the Néel temperature exits around 130 K. Recently, it was reported that the Néel temperature is 130 K for the hexagonal $BaFeO_{2.88}$ from results of the Mössbauer measurement.[8]

In conclusion, we have studied the magnetic structure of the hexagonal $BaFeO_{3-d}$ by neutron powder diffraction experiments. We found that the magnetic structure of the hexagonal $BaFeO_{3-d}$ is a helical one with the propagation vector parallel to the < 001 > direction.

Acknowledgements

I wish to acknowledge for Mr. K. Nemoto the help of this work. Furthermore, I thank Dr. O. Yamamuro for experimental help and helpful discussions.

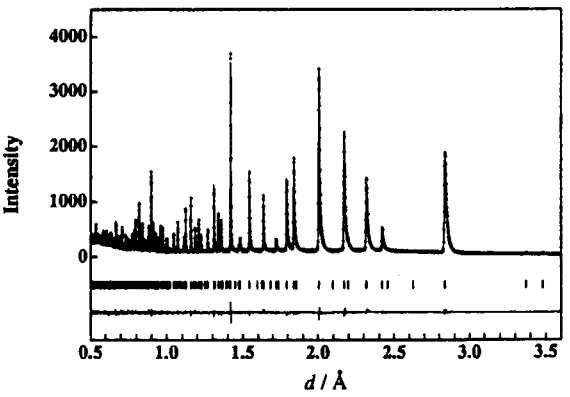


Fig. 1. The full pattern of Rietveld analysis result for $BaFeO_{2.94}$ at RT.

Table 1. Structure parameters determined by the Rietveld analysis for $BaFeO_{2.94}$ at RT.

Atom	site	x	y	z	B	Occupancy
Ba(1)	2*b*	0	0	1/4	0.32(5)	1
Ba(2)	4*f*	1/3	2/3	0.0881(1)	0.48(5)	1
Fe(1)	2*a*	0	0	0	0.58(3)	1
Fe(2)	4*f*	1/3	2/3	0.8467(1)	0.40(2)	1
O(1)	6*h*	0.5208(2)	= - x	1/4	0.89(5)	0.928(4)
O(2)	12*k*	0.8297(1)	= - x	0.0832(1)	0.72(2)	1

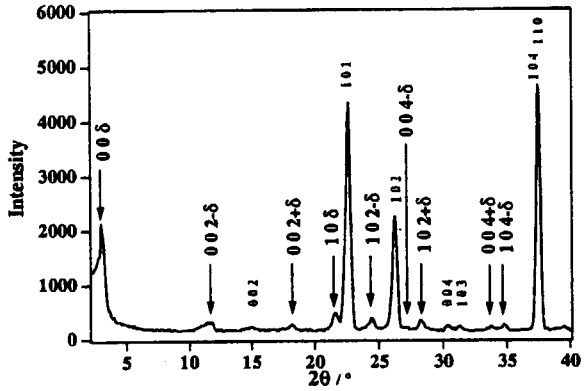


Fig. 2. The neutron powder diffraction data for $BaFeO_{2.94}$ at 10 K. All magnetic peaks were index with the helical spin structure.

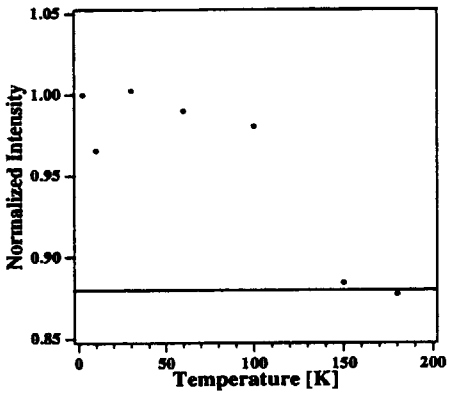


Fig. 3. The temperature dependence of the normalized magnetic intensity at the 0 0 2-δ reflection.

1) S. Mori, J. Phys. Soc. Jpn. 28 (1970) 44.
2) F. Iga, Y. Nishihara. G. Kido and Y. Takeda, J. Magn. Magn. Mater. 104-107 (1992) 1969.
3) F. Iga, Y. Nishihara. T. Katayama, K. Murata and Y. Takeda, J. Magn. Magn. Mater. 104-107 (1992) 1973.
4) T. Kamiyama, K. Oikawa, N. Tsuchiya, M. Osawa, H. Asano, N. Watanabe, M. Furusaka, S. Satoh, I. Fujikawa, T. Ishigaki and F. Izumi, Physica B 213-214 (1995) 875.
5) T. Ohta, F. Izumi, K, Oikawa and T. Kamiyama, physica B 234-236 (1997) 1093.
6) K. Ohoyama, T. Kanouchi, K. Nemoto, M. Ohashi, T. Kajitani, Y. Yamaguchi: Jpn. J. Appl. Phys. Vol37(1998)3319-3326
7) S. Mori, J. Amer. Ceram. Soc. 49 (1966) 600.
8) H. Kobayashi, F. Iga and Y. Nishihara, Nucl. Instrum. Methods Phys. Res. B 76 (1993) 258.

研究テーマ：RPd_3S_4の磁気・四重極子秩序転移に関する研究
表題：$TbPd_3S_4$と$YbPd_3S_4$の粉末中性子回折

1-2-60 Powder neutron diffraction study on $TbPd_3S_4$ and $YbPd_3S_4$

E. Matsuoka, F. Takahashi, J. Kitagawa, K. Ohoyama[1], H. Yoshizawa[2] and M. Ishikawa

Institute for Solid State Physics, University of Tokyo, Kashiwanoha, Kashiwa, Chiba, 277-8581, Japan
[1]*Institute for Materials Research, Tohoku University, Katahira, Aoba-ku, Sendai, Miyagi, 980-8577, Japan*
[2]*Neutron Scattering Laboratory, Institute for Solid State Physics, University of Tokyo, Tokai, Ibaraki, 319-1106, Japan*

We previously reported some physical properties of new series of rare-earth palladium bronzes, RPd_3S_4, which crystallize in the cubic $NaPt_3O_4$ type structure [1]. These compounds exhibited a magnetic transition at low temperatures and another phase transition above the magnetic transition, which was attributed to quadrupolar ordering [1]. In this paper, we report the results of the powder neutron diffraction experiment performed on R = Tb and Yb and propose possible magnetic structures.

The neutron diffraction experiments were performed at the HERMES installed at the T1 thermal neutron guide tube of the JRR-3M reactor in JAERI. The measurement ranges of the temperature and the Bragg angle 2θ were down to 1.3 K and $3° < 2\theta < 153°$, respectively. The wave length of the neutron beam was $\lambda = 1.8196$ Å.

Fig. 1 displays the neutron diffraction patterns of $TbPd_3S_4$ measured at several temperatures shown only for $10°<2\theta<65°$. At $T = 9.0$ K ($> T_Q$, T_N) there are only nuclear reflection peaks with the impurity phases, PdS and Tb_2O_2S and the lattice constant was determined to be $a = 6.632$ Å. At $T = 5.0$ K ($T_N < T < T_Q$) new peaks designated as Q were observed, as shown in the middle panel. Another set of new Bragg peaks designated as M(*hkl*) were observed at $T = 1.3$ K ($< T_N$) with Q peaks unchanged. M(*hkl*) peaks were successfully indexed with the Miller index based on the magnetic unit cell and the wave vector of $\boldsymbol{k} = (1,0,0)$. However, we could not index the Q peaks with a definite wave vector. If T_Q is really a quadrupolar ordering temperature as previously attributed, the Q peaks may be due to a lattice distortion induced at T_Q and there must be a change of the Bragg angles and/or the intensities of the nuclear reflections at $T = 5.0$ K. But we could not notice any changes of the nuclear reflections within the experimental error. The sample used in this experiment contained a very small amount of Tb_2O_2S ($T_N = 7.7$ K [2]). In addition, the Bragg angles of Q agree well with those of the magnetic reflections of Tb_2O_2S observed by neutron diffraction [2]. It is therefore very probable that the transition at $T = 7.5$ K is not a quadrupolar transition but a magnetic one of Tb_2O_2S. In order to make sure ourselves of this problem, we tried to make a cleaner sample by an improved method and succeeded in obtaining such sample. This pure sample exhibits no phase transition around $T = 7.5$ K. Therefore, we attribute the transition at $T = 7.5$ K previously observed in our old samples to the magnetic transition of Tb_2O_2S.

The observed and the calculated intensities of the magnetic M(*hkl*) reflections are tabulated in Table 1(a) with the value of the magnetic moment μ and the reliability factor R defined as $R = \sum|I_{obs} - I_{cal}|/\sum I_{obs}$. The calculation indicates that $TbPd_3S_4$ exhibits a simple type I antiferromagnetic order below $T_N = 2.9$ K. We could not, however, specify unambiguously the direction of the Tb^{3+} magnetic moment in this calculation because the crystal structure has a cubic symmetry.

Fig. 2 displays the neutron diffraction patterns of $YbPd_3S_4$ measured at several temperatures shown only for $5° < 2\theta < 45°$. At $T = 3.6$ K ($> T_Q$ and T_N) there are only nuclear reflection peaks with the impurity phases, PdS and Yb_2O_2S and the lattice constant was determined to be $a = 6.617$ Å. Two sets of new peaks designated as Q and M(*hkl*) appeared at 2.2 K ($T_N < T < T_Q$) and 1.6 K ($T < T_N$), respectively. The M(*hkl*) peaks were successfully indexed with the Miller index based on the magnetic unit cell and the wave vector of $\boldsymbol{k} = (1/2,1/2,1/2)$. The features about Q peaks resemble to those of $TbPd_3S_4$ as discussed above: these peaks were not indexed with a definite wave vector and the variation of the nuclear reflections of the main phase was not observed at 2.2 K within the experimental error. The sample used in this experiment contained a small amount of Yb_2O_2S ($T_N = 2.65$ K [3]) and the Bragg angles of Q agree well with those of the magnetic one of Yb_2O_2S reflections observed by neutron diffraction [3]. It is therefore also very probable that the transition at $T = 2.9$ K is not a quadrupolar transition but a magnetic one of Yb_2O_2S.

We could prepare a cleaner sample by the chemical transport technique using KI. Newly synthesized $YbPd_3S_4$ shows no phase transition at 2.9 K, indicating that the transition at $T = 2.9$ K observed in our old sample was in fact a magnetic transition of Yb_2O_2S. It is noteworthy that the proportion of the Yb^{3+} is only 22 % in the newly synthesized $YbPd_3S_4$.

In order to calculate the peak intensities, we assumed that magnetic Yb^{3+} of 22 % and non-magnetic Yb^{2+} of 78 % are randomly distributed over all Yb sites and the magnetic moments lie along the [111] direction in the magnetic unit cell. In Table 1(b), the observed and the calculated intensities of the magnetic reflections are tabulated with the value of the magnetic moment and the reliability factor defined above. Although the intensity of the magnetic reflections was considerably weak, the agreement of the observed and calculated intensities is fairly good as the reliability factor implies. We could not specify unambiguously the direction of the Yb^{3+} magnetic moment in this calculation for the same reason in the case of $TbPd_3S_4$ mentioned above.

References

[1] K. Abe J. Kitagawa, N. Takeda and M. Ishikawa, Phys. Rev. Lett. **83** (1999) 5366.

[2] Y. Abbas, J. Rossat-Mignod and G. Quezel, Solid State Commun. **12** (1973) 985.

[3] R. Ballestracci and J. Rossat-Mignod, Solid State Commun. **7**, (1969) 1011.

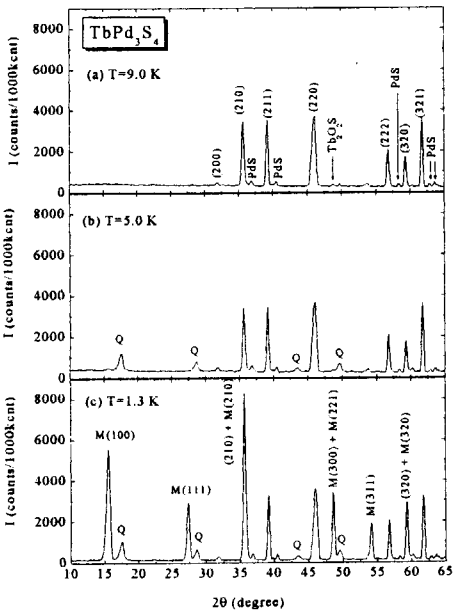


Fig. 1

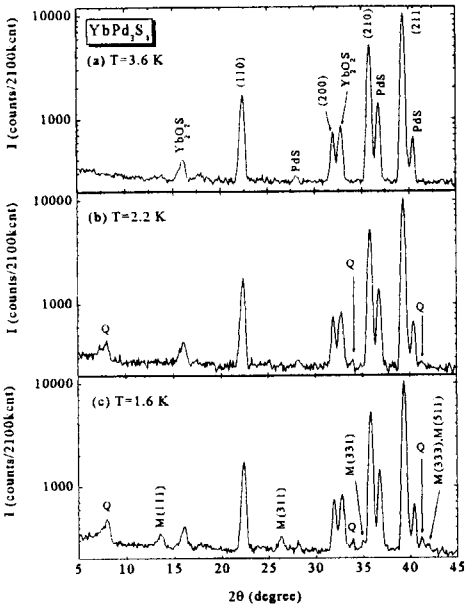


Fig. 2

(*hkl*)	I_{obs}	I_{cal}
(100)	3311	3319
(111)	1350	1335
(210)	2209	2190
(300),(221)	1340	1283
(311)	752	776
(320)	575	609
(410),(322)	807	810
(331)	339	340
(421)	539	578
(500),(430)	289	271
(511),(333)	237	254
(520),(432)	470	508
(441),(522)	294	275
(531)	225	251
(610)	169	116
(540),(621),(443)	367	410
(533)	126	99
(630),(542)	225	291
(700),(632)	241	241
μ (μ_B)	8.16±0.26	
R (%)	3.67	

(a) $TbPd_3S_4$

(*hkl*)	I_{obs}	I_{cal}
(111)	75	78
(311)	56	49
(331)	24	23
(333),(511)	13	17
(531)	16	16
μ (μ_B)	0.66±0.14	
R (%)	8.8	

(b) $YbPd_3S_4$

Table. 1

研究テーマ：超低温の導入による中性子散乱の研究
表　題　：中性子回折による室温での(Sm,Y)Mn_2Ge_2化合物の磁気抵抗の振る舞いに関する予備研究

1-2-61

Preliminary Study on The Mechanism of Magnetoresistance Behaviour of (Sm,Y)Mn_2Ge_2 Compound at Room Temperature by Neutron Diffraction Technique

Setyo Purwanto[1], Agus Purwanto[1], N. Minakawa[2],Y. Morii[2],
Y. Hamaguchi[2], Y. Yamaguchi[3]

[1]Research and Development Center for Materials Science and Technology-BATAN, Serpong-Indonesia
[2]Advanced Science Research Center-JAERI , Tokai-mura, Naka-gun, Ibaraki-ken
[3]Institute For Materials Research, Tohoku Univ. Sendai

1. Introduction

Since the evidence magnetoresistance phenomenon at 125K around 16% under external magnetic field up to 1 Tesla for $SmMn_2Ge_2$ are found by Braber et.al[1],it has been a growing interest to extend the behaviour up to room temperature. We made some modifications of $SmMn_2Ge_2$ by substituting Sm atom with Y atom and measured the magnetoresistance properties at room temperature. We found in (Sm,Y)Mn_2Ge_2 sample there is magnetoresistance effect around 10% at room temperature[2]. To clarify the mechanism on the existence of the magnetoresistance in the sample, we perform neutron diffraction measurement.

2. Experiment Method

The neutron diffraction experiment was done using TAS-2 with wavelength λ of 2.4487Å. A pellet sample with the thickness of 0.3mm under various external magnetic field up to 0.5Tesla was measured at Room Temperature The sample was wrapped with Aluminium foil.

3. Results and Discussion

From the magnetoresistance measurement, we assume that the mechanism might be governed by Mn-Mn coupling. At zero magnetic field, Mn atoms are coupled antiferromagnetically. At H=1.0Tesla, it becomes Ferromagnetic. It was then expected that (111) magnetic peak got weaker and (110) peak became stronger as the magnetic field growing up. We concentrated to search the magnetic contribution around the (110) nuclear peak and (111) reflection index.

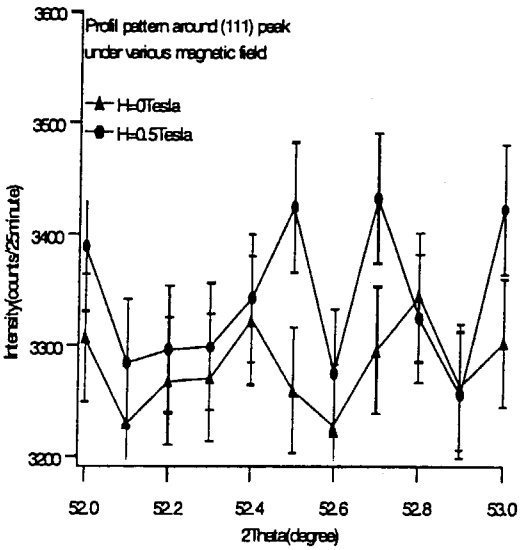


Figure 1. Profile of (111) peak under H=0 Tesla (▲) and 0.5 Tesla(●).

Figure 1 shows part of diffraction pattern around (111) reflection index ($2\theta = 52.4^0$) with H=0 and 0.5 Tesla at room temperature. The signal is too weak to show the magnetic contribution around (111) reflection marker. Figure 2 show part of the diffraction pattern

原子炉：JRR-3M　　装置：TAS-2 (T2-4)　　分野：中性子散乱（磁性）

around (110) nuclear peak for H=0 and 0.5Tesla. The signal difference between (110) peak at H=0 and 0.5T is again too weak to confirm the magnetic contribution from Mn Ferromagnetic coupling, although there is any discrepancy between those peak at around 2θ=51.5°. To overcome this problem, it is necessary to use diluted $(Sm,Y)Mn_2Ge_2$ with Aluminium powder[3] in order to decrease the absorption factor. It is also necessary to increase the magnetic field up to 1 Tesla or more to investigate the critical field of magnetoresistance phenomenon.

References

[1] Braber J.H.V.J et.al, "Giant magneto-resistance in polycrystalline $SmMn_2Ge_2$", J. of Alloys Compounds, 199(1993)L1-L3

[2] Setyo Purwanto et.al, Priority Integrated Research on GMR Materials of $(Sm,R)Mn_2Ge_2$ (in Indonesian), unpublish report,1999-2000

[3] Tomka G.J. et.al ,"Magnetic Structure of $^{154}SmMn_2Ge_2$ as a function of temperature and pressure",Physical Review B Vol. 54,No.10(1998)p.6330

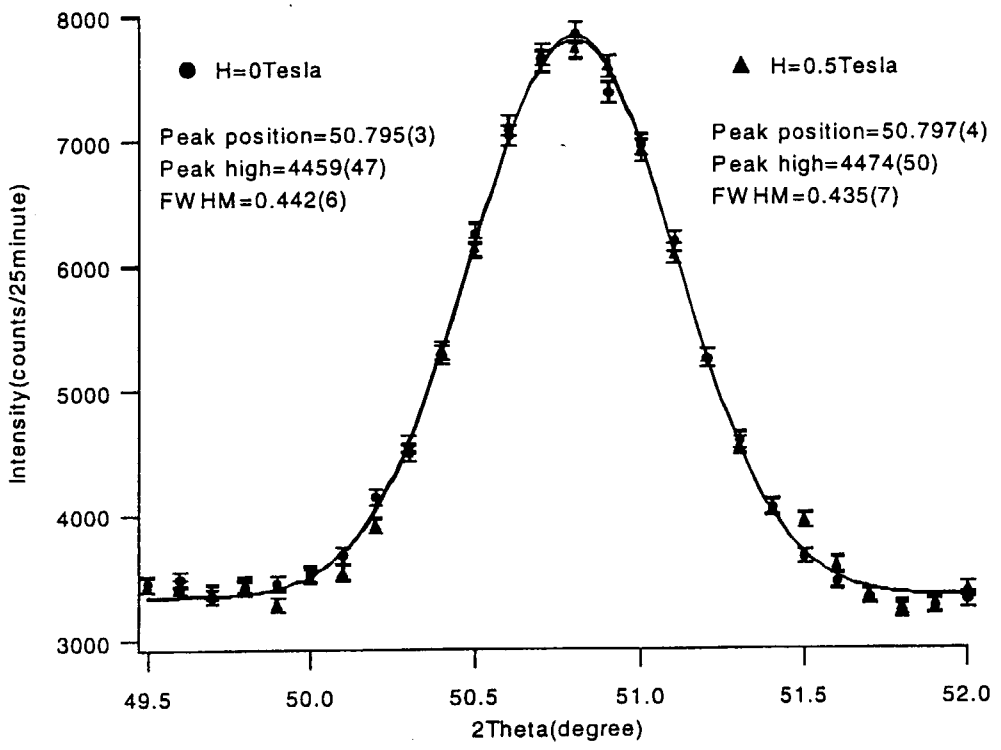


Figure 2. Profile of (110) peak under H=0 Tesla(●) and 0.5 Tesla(▲) with error bar. Gaussian fits for both data sets are approximately coincidence as shown in solid lines.

研究テーマ：中性子散乱による強相関電子系の研究
表　題　　：UIr の磁気モーメントの方向

1-2-62 Direction of the magnetic moments in UIr

Etsuji Yamamoto, Naoto Metoki, Yoshihiro Koike

Advanced Science Research Center, JAERI, Tokai, Ibaraki 319-1195, Japan

UIr is a ferromagnet with the monoclinic structure in space group $P2_1$. Curie temperature T_C is 46 K and a saturated moment is 0.5 μ_B/U and is oriented along the [010] direction.[1] We made high-quality single crystal of UIr and measured the magnetization at 2 K. Contrary to the previous result,[1] the easy axis in the magnetization is found not to be the [010] direction but to be [10$\bar{1}$] direction, which is perpendicular to [010]. The magnetizations along [010] and [101] indicate the usual hard-axis behavior. To confirm the orientation of the magnetic moments, we made the neutron scattering measurement on TAS-2 at JRR-3M. Figure 1 shows the temperature dependence the intensities of scattered neutron at several selected points. UIr is simple ferromagnetic, so that the magnetic scattering occur in the same positions of the nuclear scattering. If the magnetic moments oriented along the [10$\bar{1}$] direction, then $h0\bar{h}$ reflections show no additional magnetic intensity. In order to the neutron fluctuation, the temperature dependence of the intensities are not clear. But it seems that the (060) scattering intensity increases under the T_C, while the (30$\bar{3}$) scattering intensity is not changed.

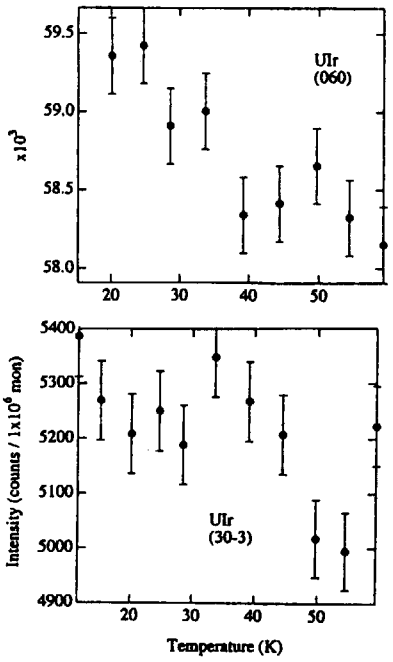


Fig. 1 Temperature of the neutron intensities.

Reference

A. Dommann et al, J. Mag. Mag. Mater., 67 (1987) 323-330.

原子炉：JRR-3 M　　装置：TAS-2 (T2-4)　　分野：中性子散乱（磁性）

研究テーマ：中性子散乱による強相関電子系の研究
表題：DyB_2C_2の磁場誘起反強磁性

1-2-63 Field induced antiferromagnetic ordering in DyB_2C_2

S. Katano, H. Yamauchi[1], K. Ohyama[1], A. Tobo[1], H. Onodera[1], Y. Yamaguchi[1]

ASRC, Japan Atomic Energy Research Institute, Tokai, Ibaraki 319-1195
[1] Institute for Material Research, Tohoku University, Katahira, Sendai, Miyagi 980-8577

DyB_2C_2 is the first tetragonal structural system which shows the AFQ (antiferroquadrupolar) ordering. This compound shows phase transitions from the paramagnetic phase (I) to the AFQ phase at T_Q=24.7 K (II) and further to the AFM (antiferromagnetic) phase at T_N=15.3 K under zero magnetic field [1]. It should be noted that this T_Q of DyB_2C_2 is almost ten times higher than that of previously discovered AFQ compounds (for example, 3.3 K in CeB_6 and 1.8 K in TmTe). Under T_N, the antiferromagnetic order is characterized by the propagation vectors with k_1=[1 0 0], k_2=[0 1 1/2], k_3=[0 0 0] and k_4=[0 0 1/2]. The basic magnetic structure is described by k_1 and k_2 and the moments are aligned antiferromagnetically along [1 1 0] in the c-plane, showing the nearly 90° arrangement along the c axis. The vectors k_3 and k_4 give a slight canting of the magnetic moments from the [1 1 0] direction. This magnetic structure can be considered as a result of competitive coexistence of the AFQ and AFM interactions. The AFQ ordering was confirmed by Tanaka *et al.* [2] and Hirota *et al.*[3], independently, with resonant X-ray scattering technique. Here new experimental evidence for the AFQ order in this compound and novel antiferromagnetic ordering induced under magnetic fields are shown.

The sample was a single crystal with the natural abundant isotopes grown by the Czochralski method with a tetra-arc furnace. Neutron scattering experiments were performed on the triple axis spectrometer TAS-2 installed at the thermal guide of JRR-3M of Japan Atomic Energy Research Institute.

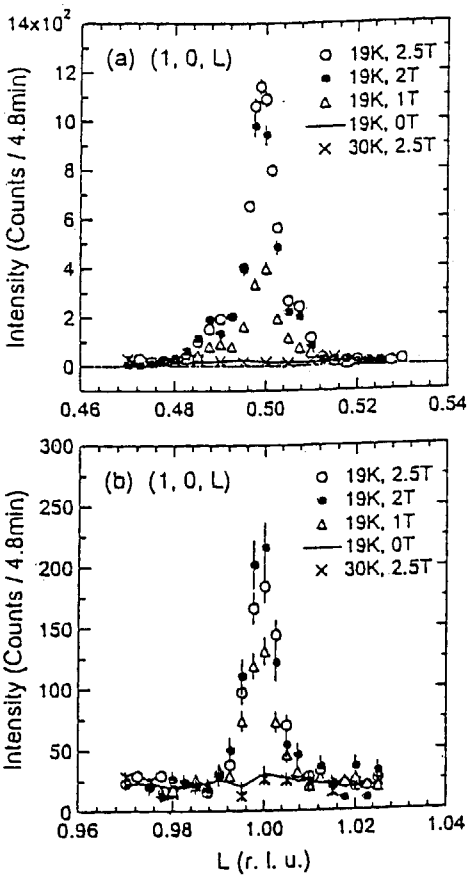


Fig. 1. Antiferromagnetic peaks induced by magnetic fields. (a) (1 0 1/2) and (b) (1 0 1), which were measured along the *l*-direction.

The sample was a rectangle of 5×4×0.5 mm³, and placed in an Al can filled with He gas. The scattering experiments were done with the initial energy of 13.67 meV obtained by a PG monochromator. To reduce the $\lambda/2$

原子炉：JRR-3M　　装置：TAS-2 (T2-4)　　分野：中性子散乱（構造・磁性）

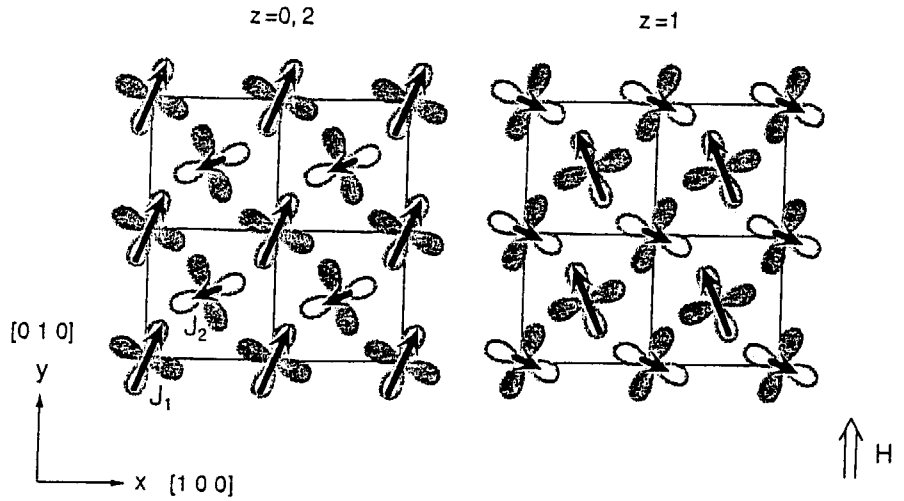


Fig. 2. A model for the antiferromagnetic (AFM) ordering by induced dipole moments under magnetic field H. The figure also shows the antiferroquadrupolar (AFQ) ordering proposed

contamination a PG filter was placed before the sample. The scattering plane was chosen in the a-c reciprocal lattice plane. The experiments under magnetic fields were performed using a He-free type 10 T superconducting magnet [4]. The fields were applied vertically to the scattering plane.

Figure 1 shows the profiles observed along the I-direction. At 19 K under zero field only nuclear reflections were observed. Under the magnetic fields, (1 0 1/2), (1 0 1) and (1 0 3/2) reflections were induced, and they were increased with the field. At 30 K under 2.5 T, in the paramagnetic phase, these peaks were not observable within the experimental accuracy. These results show that the appearance of the additional peaks is due to the AFM moments induced by the magnetic field, and that the antiferromagnetic ordering scheme is related with the underlying AFQ order of this compound.

Figure 2 indicates a model for AFM and AFQ ordering of DyB_2C_2. The underlying AFQ order indicated in this figure is consistent with the antiferromagnetic structure below T_N. Under low magnetic fields two types of magnetic moments, the large J_1 and small J_2, are induced as shown in the figure. When it is assumed that the x and y components are in the relations of $|J_{1x}| \approx |J_{2x}|$ and $|J_{1y}| > |J_{2y}|$, the intensities of the induced AFM reflections are reasonably explained. The experimental results suggests that the canting the quadrupole moments, which is indicated in the figure. However, it is possible that the arrangements of quadrupolar moments is declined by applying magnetic fields from the a or [1 1 0] direction. For precise discussion on this AFQ ordered structure more statistics and the information at the lower fields below 1 T are necessary.

In conclusion the present neutron scattering experiments under high magnetic fields have shown the clear evidence of the AFQ ordering and the field induced novel AFM ordering in DyB_2C_2.

References

[1] Y. Yamauchi *et al.*, J. Phys. Soc. Jpn. 68 (1999) 2057.

[2] Y. Tanaka *et al.*, J. Phys.: Condens. Matter 11 (1999) L505.

[3] K. Hirota *et al.*, Phys. Rev. Lett. 84 (2000) 2706.

[4] S. Katano *et al.*, Proc. of 4th Int. Symposium on Advanced Physical Fields: Quantum Phenomena in Advanced Materials at High Magnetic Fields, 315 (1999).

研究テーマ：量子凝縮相の研究
表題： f電子化合物 $PrCu_6$ の結晶場励起

1-2-64 Crystalline Electric Field Excitations in f electron compounds $PrCu_6$

Y. Koike[a,b], Y. Morii[a], N. Metoki[a], Y. Ōnuki[a,c]

a- Advanced Science Research Center, Japan Atomic Energy Research Institute, Tokai, Naka, Ibaraki 319-1195, Japan

b- Japan Science and Technology Corporation, Kawaguchi, Saitama 332-0012, Japan

c- Department of Physics, Graduate School of Science, Osaka University, Toyonaka 560-0043, Japan

The $PrCu_6$ is known to the enhanced nuclear magnet with $T_N \sim 2$ mK.[1] In the enhanced nuclear system nuclear spins ordered relatively higher temperature than pure nuclear spin systems because the nuclear magnetic moment is enhanced by the hyperfine coupling and RKKY interaction between f electron spins. The Crystalline electric field (CEF) level scheme in $PrCu_6$ has been investigated by using polycrystal samples,[2] while the dispersion has not been measured. We started the neutron scattering study for the low energy magnetic excitations in order to clarify the role for the nuclear magnetic ordering.

Neutron scattering experiments were performed using the thermal and cold neutron triple-axis spectrometers, TAS-2 and LTAS. A single crystal (40 mm in length, 5 mm in diameter) was aligned in (hk0) plane (monoclinic notation; a = 5.09 Å, b = 10.15 Å, c = 8.09 Å, β = 91.33°).

Figure 1 shows the typical constant-Q profiles of $PrCu_6$. We observed clear CEF excitations at the energy about 1.7, 2.7, 5.0, 7.4, and 8.9 meV. The linewidth was almost resolution limited. The observed energy levels are in some part different from a previous polycrystal study.[2] In their paper the excitation at 7.4 meV is interpreted as a transition between 1.5 and 8.9 meV excited levels. This interpretation is obviously wrong, because we observed 7.4 meV peak even at T = 1.5 K. Furthermore the polycrystal study assumed two levels at 1.5 and 1.64 meV. However we believe this is due to mode splitting because $PrCu_6$ has a non-Bravais lattice. The previous polycrystal study proposed a very low CEF level at 0.02 meV. However it is inconsistent with recent specific heat study which reported no Schottky anomaly associated with this level.[3]

No trace of the first excitation was observed, when the scattering vector is parallel to the a-axis, Q = (100), indicating the x-polarization. This is consistent with the susceptibility measurement which shows that the Van-Vleck susceptibility along the a-axis is larger than the other orientations. Similarly the 7.4 and 8.9 meV excitations are considered to have y-polarization, and the 2.7 and 5.0 meV levels have z-polarization.

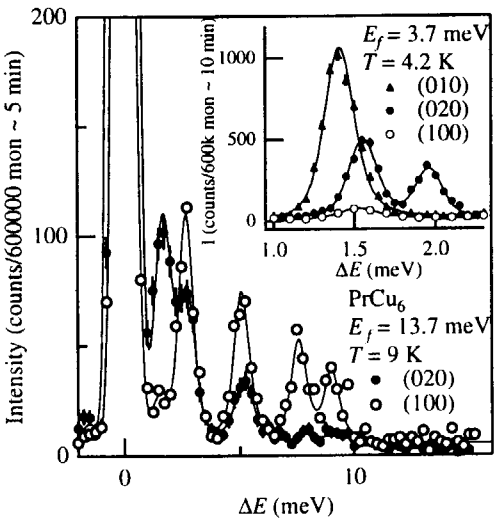


Fig. 1 Constant-Q scans in $PrCu_6$ measured at Q = (100) and (020). Inset is inelastic scattering profiles measured at (100), (020) and (010).

原子炉：JRR-3M　　装置： TAS-2(T2-4), LTAS (C2-1)　　分野：中性子散乱(磁性)

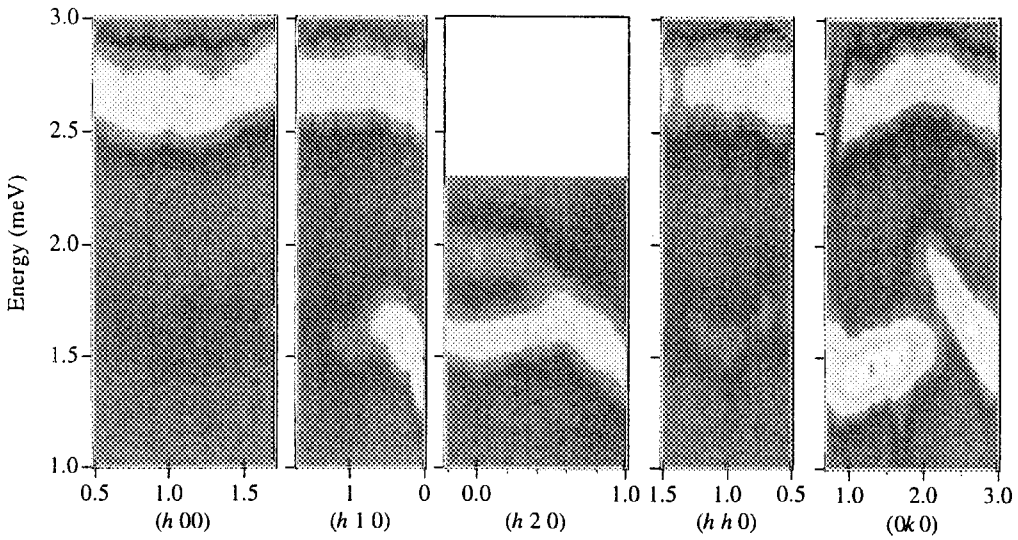


Fig 2 The image plot of dispersion relations.

The image plot of dispersion relations of the lowest two CEF levels are shown in Fig. 2. We observed weak dispersion of the CEF levels, which are due to the RKKY interaction between Pr moments. We found a minimum energy at the forbidden Bragg point (010). We also observed a minimum at the nuclear Bragg point (100). Around the ferromagnetic Bragg point, (020), the first excited level splits into two modes. (See also the inset of Fig. 1). This splitting could be explained in terms of the mode splitting of the optical and acoustic mode in a non-Bravais lattice.

Our data of the dispersion relation and the temperature dependence might suggest that Q = (010) would be the antiferromagnetic propagation vector for the nuclear magnetic ordering of $PrCu_6$. The most interesting point of nuclear magnetism in $PrCu_6$ is existence of the ferromagnetic component along the b-axis.[4] A theoretical model proposed that a canting antiferromagnetic structure could be stabilized by the Dzyaloshinsky-Moriya interaction between the two different Pr cite in a unit cell.[5] It is a future problem to clarify, if the unusual splitting of the dispersion observed at ferromagnetic Bragg point (020) could be explained by the model leading to Dzyaloshinsky-Moriya interaction.

References

[1] J. Babcock *et al.*, Phys. Rev. Lett. **43** (1979) 380.

[2] U. Walter *et al.*, J. Phys. Soc. Jpn. **55** (1986) 650 .

[3] S. Takayanagi *et al.*, J. Phys. Soc. Jpn. **57** (1988) 3552.

[4] H. Inaba *et al.*, Physica B **284-288**, (2000)1692.

[5] H. Ishii and Y. Kinoshita, Phys. Rev. B **63** (2001) 14415 .

研究テーマ：量子凝縮相の研究
表　題　：$La_{2-x}Sr_xCuO_4$低ドープ領域の静的スピン相関

1-2-65 Static Spin Correlations in Lightly-Doped $La_{2-x}Sr_xCuO_4$

M. Matsuda, M. Fujita[1], K. Yamada[1], R. J. Birgeneau[2], Y. Endoh[3], and G. Shirane[4]

Advanced Science Research Center, Japan Atomic Energy Research Institute, Tokai, Ibaraki 319-1195, Japan
[1]Institute for Chemical Research, Kyoto University, Gokasho, Uji, 610-0011, Japan
[2]University of Toronto, Toronto, Ontario M5S 1A1, Canada
[3]Institute for Materials Research, Tohoku University, Sendai 980-8577, Japan
[4]Department of Physics, BNL, Upton, New York 11973, USA

Extensive neutron elastic scattering studies on lightly-doped $La_{2-x}Sr_xCuO_4$ revealed that a diagonal spin modulation, which is a one-dimensional modulation rotated away by 45° from that in the superconducting phase, occurs universally across the spin-glass phase in $La_{2-x}Sr_xCuO_4$ ($0.02 \leq x \leq 0.055$).[1-3] Such diagonal stripes have been predicted theoretically and have also been observed in insulating $La_{2-x}Sr_xNiO_4$.[4] These results lead to the important conclusion that the static magnetic spin modulation changes from being diagonal to parallel at x=0.055±0.005, coincident with the insulator-to-superconductor transition. This establishes an intimate relation between the magnetism and the transport properties in the high-temperature copper oxide superconductors.

It is unknown whether the stripes persist in very lightly-doped $La_{2-x}Sr_xCuO_4$ (x<0.02) which shows a coexistence of a three-dimensional (3D) antiferromagnetic (AF) long-range ordered phase and a spin-glass phase. According to a theory by Kato *et al.*,[5] which has predicted diagonal stripes based on numerical calculations for a simple Hubbard model, the incommensurability of the diagonal incommensurate peaks should change proportionally with hole concentration. Neutron elastic scattering measurements in oxygenated La_2CuO_4 show that a magnetic Bragg peak, which develops below 3D AF transition temperature T_N~90 K, decreases below spin-glass transition temperature T_m~25 K.[6,7] This is ascribed to depression of the 3D AF order because of the reentrant spin-glass transition. Although it is indicated that the two-dimensional AF correlations develops below T_m, no detailed study has been performed.

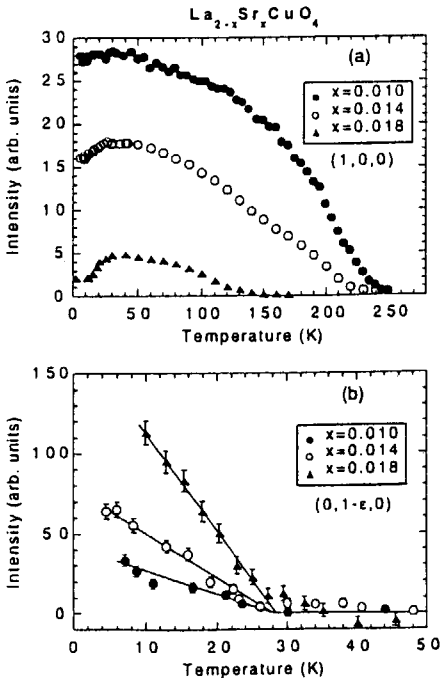


Figure 1 Temperature dependence of the (100) magnetic Bragg intensity (a) and the magnetic intensity at the diagonal incommensurate position (0,1-ε,0) (b) in $La_{2-x}Sr_xCuO_4$ (x=0.01, 0.014, and 0.018).

原子炉：JRR-3M　　装置：LTAS (C2-1), TAS-2(T2-4)　　分野：中性子散乱（磁性）

The elastic neutron scattering experiments were carried out on the cold neutron three-axis spectrometers LTAS and the thermal neutron three-axis spectrometer TAS2 installed in the guide hall of JRR-3M at the Japan Atomic Energy Research Institute (JAERI). Single crystals of $La_{2-x}Sr_xCuO_4$ (x=0.01, 0.014, and 0.018) grown by the TSFZ method were used.

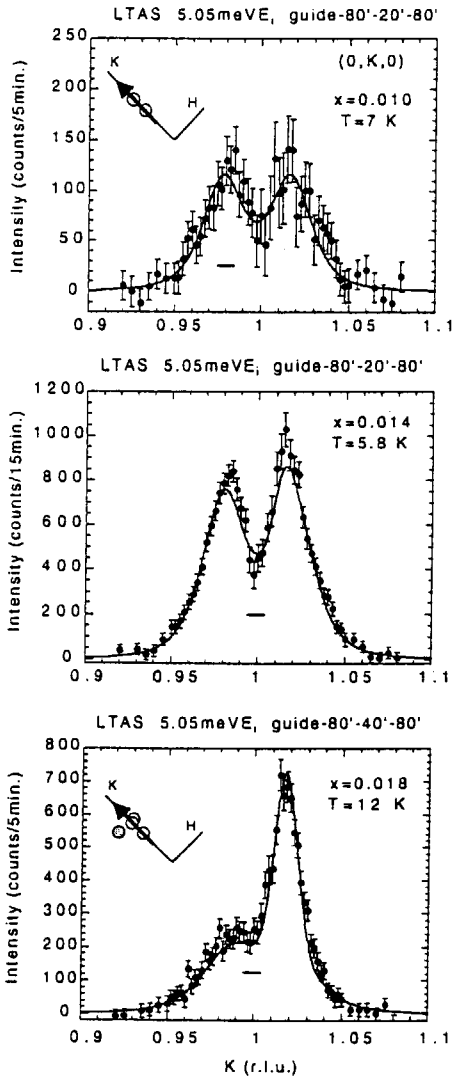


Figure 2 Elastic scans along (0,K,0) in $La_{2-x}Sr_xCuO_4$ (x=0.01, 0.014, and 0.018). The background intensities measured at a high temperature have been subtracted. The horizontal bar in each figure represents the instrumental resolution. The insets show the magnetic peak positions around (0,1,0) in the (HK0) scattering plane. The thick arrows show scan trajectories.

The present elastic neutron scattering study yields important new information on the hole concentration dependence of the magnetic properties in the coexistence phase (x<0.02). First we confirmed the reentrant spin-glass behavior. As shown in Fig. 1(a), at a low temperature of T_m~30 K, the magnetic Bragg intensities decrease in the x=0.014 and 0.018 samples. At the same time diagonal incommensurate peaks, which are similar to those in the pure spin-glass phase in $La_{2-x}Sr_xCuO_4$ ($0.02 \leq x \leq 0.055$), develop. The integrated intensity at the diagonal incommensurate peaks that develops below T_m almost corresponds to that of the (1,0,0) magnetic Bragg peak lost below T_m, indicating that some region of the 3D AF ordered phase turns into the diagonal stripe phase. The volume fraction of the diagonal stripe phase becomes larger with hole-doping. Detailed analysis is now in progress.[8)]

References

1) S. Wakimoto *et al.*, Phys. Rev. B **60**, R769 (1999).; S. Wakimoto *et al.*, Phys. Rev. B **61**, 3699 (2000).

2)M. Matsuda *et al.*, Phys. Rev. B **62**, 9148 (2000).

3)M. Fujita *et al.*, cond-mat/0101320.

4)J. M. Tranquada, D. J. Buttrey, and V. Sachan, Phys. Rev. B **54**, 12318 (1996).

5) M. Kato, K. Machida, H. Nakanishi, and M. Fujita, J. Phys. Soc. Jpn. **59**, 1047 (1990).

6) Y. Endoh *et al.*, Phys. Rev. B **37**, 7443 (1988).

7)B. Keimer *et al.*, Phys. Rev. B **46**, 14034 (1992).

8)M. Matsuda *et al.*, unpublished.

研究テーマ：反強磁性-非磁性境界付近の重い電子系化合物における反強磁性相関
表題：$CeNi_2Ge_2$の低エネルギー磁気揺動：非フェルミ液体の起源

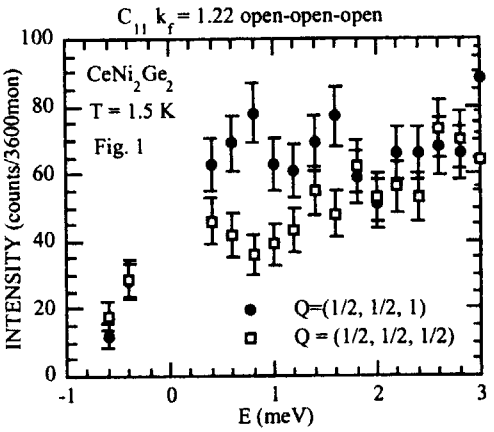
1-2-66 Low energy magnetic fluctuation of CeNi2Ge2: Origin of non-fermi-liquid behavior

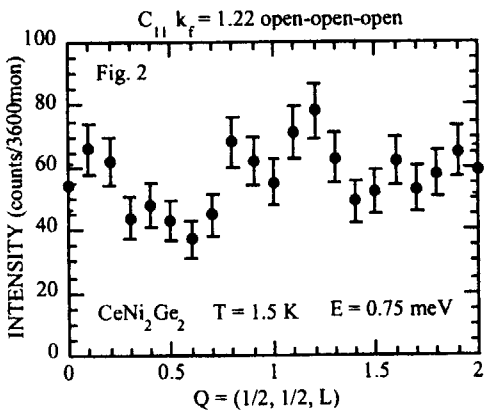
H. Kadowaki, T. Fukuhara[1], and K. Maezawa[1]

Department of Physics, Tokyo Metropolitan University, Hachioji-shi, Tokyo 192-0397
[1]Department of Liberal Arts and Science, Toyama Prefectural University, Kosugi, Toyama 939-0398

The paramagnetic heavy-fermion compound $CeNi_2Ge_2$ with a linear coefficient of the specific heat $\gamma = C/T = 350$ (mJ/K^2 mol Ce) and a Kondo temperature T_K about 40 K is located near a magnetic and non-magnetic phase boundary. An intriguing point of this compound is appearance of non-fermi-liquid behavior at low temperatures well below T_K without tuning of magnetic coupling or the Kondo effect by pressure or chemical substitutions. The magnetic fluctuation corresponding to T_K has been observed around q = (0.23, 0.23, 0.5) with the characteristic energy $\Gamma = 4$ meV [1]. However, certain low-energy spin fluctuation responsible for the non-fermi-liquid behavior has not been found. In the present study, we searched an (h,h,l) scattering plane for the low-energy spin-fluctuation using a single-crystal sample, in which the ^{58}Ni isotope was used to reduce background from large incoherent elastic scattering of Ni nuclei. An important clue of finding the signal was the wave number of the antiferromagnetic ordering of the substituted samples $Ce(Ni_{0.91}Pd_{0.09})_2Ge_2$ and $Ce(Ni_{0.7}Rh_{0.3})_2Ge_2$ [2].

Neutron scattering experiments were performed on the cold-guide triple-axis spectrometer ISSP-HER(C11). The spectrometer was operated in the horizontally focusing analyzer mode with a final neutron energy of 3.1 meV. In Fig. 1 we show typical energy scans taken at Q = (1/2, 1/2, 1/2) and (1/2, 1/2, 1). The spectrum at Q = (1/2, 1/2, 1/2) has a Lorentzian shape with $\Gamma = 4$ meV, and does not show the low energy fluctuation. On the other hand, the energy spectrum at Q = (1/2, 1/2, 1) definitely shows extra spectral weight around 0.75 meV. A Q-scan along a (1/2, 1/2, L) line with E = 0.75 meV is shown in Fig. 2. One can see that the low energy fluctuation is localized in Q-space around q = (1/2, 1/2, 0) which is in good agreement with the wave vector of the substituted samples. Thus we conclude that the non-fermi-liquid behavior $CeNi_2Ge_2$ is caused by the low energy excitation relating to the antiferromagnetic ordering, implying proximity of a quantum critical point.





[1] B Fak et al., J. Phys. Condens. Matter 12 (2000) 5423. [2] T. Fukuhara et al., Activity Report NSL-ISSP 7 (2000) 95; H Kadowaki et al., Activity Report NSL-ISSP 8 (2001)

研究テーマ：少数キャリアー化合物YbX(X=P,As)での抑制された磁気相関
表題：半金属化合物YbAsでの磁気励起

1-2-67 Magnetic excitations in the semi-metallic compound YbAs

K. Ohoyama, [A]N. Aso, [B]M. Kohgi, [C]A. Oyamada, [D]T. Suzuki

Institute for Materials Research, Tohoku University, Sendai 980-8577
[A]Institute for Solid State Physics, University of Tokyo, Tokai, Ibaraki 319-1106
[B]Department of Physics, Tokyo Metropolitan University, Tokyo 192-0397
[C]Graduate School of Human and Environmental Studies, Kyoto University, Kyoto 606-8501
[D]Department of Physics, Tohoku University, Sendai 980-8578

YbX (X= N, P and As), which crystallises in the NaCl structure, is a semi-metallic compound with low carrier density (~0.01 carriers per Yb^{3+} ion). YbX undergoes antiferromagnetic long range ordering at about 0.5 K (H. R. Ott, et al.: Solid State Commun. 55(1985)113). However, the saturation magnetic moment in the ordered state and entropy at the transition temperature are considerably smaller than the expected values of the crystal field ground state doublet Γ_6. The magnetic specific heat shows an anomalously enhanced magnetic specific heat around 5K. In our previous experiments, we observed anomalous magnetic excitations around (1 0 1/2) far above the transition temperature, even at 10 K. To clarify origins of the anomalous excitations, we performed neutron inelastic scattering experiments on a single crystalline sample of YbAs using the triple axis spectrometer (C1-1) installed at the JRR-3M reactor in Japan Atomic Research Institute. Inelastic scattering spectra were obtained under a condition of constant k_i=4.9 meV with collimation of open-open-Be-S-80'-80'. Since the transition temperature is about 0.5K, a dilution refrigerator was used.

Fig.1 and Fig.2 show energy spectra at 100mK ($<T_N$) at (101) zone boundary and the zone boundary along the [110] direcction. A magnon excitation was observed at 1 meV at (101) zone boundary, while a broad excitation was observed around 1 meV at the zone boundary along the [110] direcction, though it was not obvious in comparison with that at (101). It should be pointed out that the excitation energy at the zone boundary (1meV~12K) is much larger than T_N (~0.5K). This indicates that the characteristic energy of exchange interaction in YbAs is about 20 times larger than the transition temperature. This result, thus, is consistent with existence of magnetic excitation far above T_N.

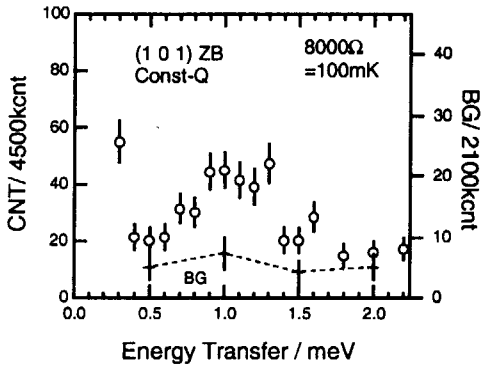


Fig.1 Spin wave excitation in YbAs at 100mK at the zone boundary obtained on C1-1 spectrometer.

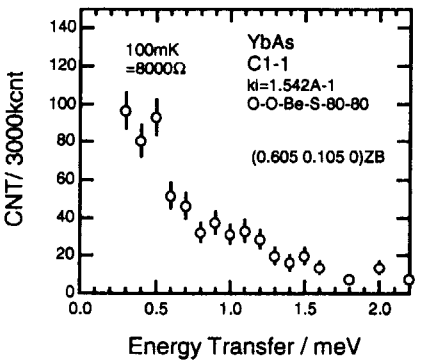


Fig.2 Energy spectrum of YbAs at 100mK at the zone boundary along the [110] direction.

JRR-3M, HER(C1-1), 2: Magnetism

研究テーマ: 巨大磁気抵抗効果と界面の乱れの相関に関する研究
表題 : Co/Cr 人工格子の界面の磁気的な乱れ（界面の乱れと巨大磁気抵抗効果）

1-2-68 Magnetic Interfacial Roughness in Co/Cu multilayers - Interfacial roughness and the GMR effect -

M. Takeda and Y. Endoh[1]

Physics Department, Graduate School of Science, Tohoku University, Sendai 980-8578, Japan
[1]Institute for Material Research, Tohoku University, Katahira Sendai 980-8577, Japan

In order to clarify the role of interfacial roughness in a giant magnetoresistance (GMR) effect we have prepared Co/Cu multilayers whose interface is systematically modified by inserting Co-Cu mixed layers of different thickness, t_{mix} at each interface. The [Co(2.2-t_{mix})/CoCu (t_{mix}) /Cu(1.0 - t_{mix})] × 16 (t_{mix} = 0.0, 0.1, 0.15 and 0.25 nm) with Fe buffer of 5.0 nm on a Si substrate were prepared by a magnetron sputtering. The mixed layer was made by codeposition of Co and Cu targets. The MR ratio of each sample, {ρ (0) - ρ (H >> 1)}/ρ (H >> 1), is 25, 20, 15 and 10 %, respectively.

Interfacial roughness was investigated by the transverse scans along the Q_z = constant line in the reciprocal space. Here the z axis is defined by normal to the sample plane and the Q_z is z component of scattering vector. The sample plane is defined as the xy plane. Assuming no anisotropy in the plane, the component of the scattering vector in the xy plane is denoted by Q_r. The transverse scan and the θ-2θ scan were done by using HER (C1-1) in JRR3-M.

Figures 1 (a) and (b) show the transverse scan of t_{mix} = 0.0 and 0.25, respectively. These scans were done at Q_z = 0.09 Å^{-1} where the antiferromagnetic Bragg peak from antiferromagnetic structure of the Co/Cu bilayer appeared. Thus the profiles give information on correlated magnetic interfacial roughness from the bottom to the top layer.

These data clearly show the different magnetic disorder at the interfaces. On the other hand, the profile at 0.18 Å^{-1} at which the Bragg peak from Co/Cu bilayer itself is observed is less sensitive to the mixing layer. This suggests that the magnetic disorder at the interface plays an important role in the GMR effect. Detailed quantitative analysis is currently in progress.

We would like to express our thanks to Drs. Suzuki M. and Taga Y. in TOYOTA Central Research and Development Laboratories, Inc. for preparation of Co/Cu multilayers for this experiment.

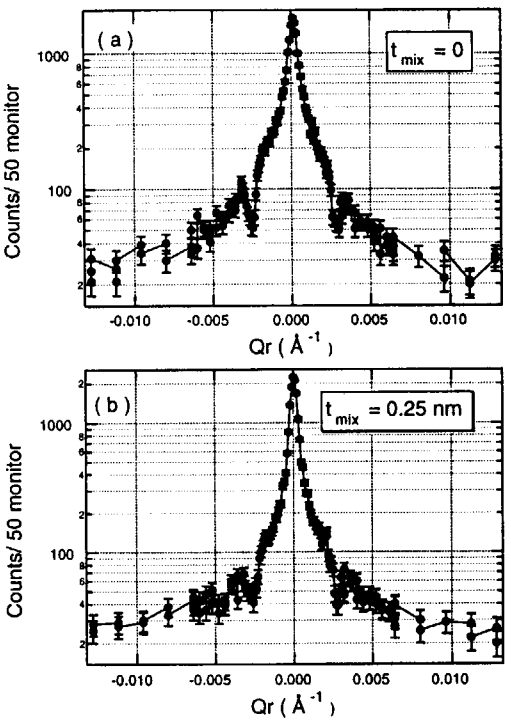


Fig. 1 The transverse scan of Co/Cu multilayer with t_{mix} = 0.0 (a) and t_{mix} = 0.25 nm (b) at Q_z = 0.08 Å^{-1}, the antiferromagnetic Bragg peak position from antiferromagnetic alignment of Co/Cu bilayer.

References

[1] S.S.P. Parkin, Z. G. Li and D. J. Smith, Appl. Phys. Lett. **58** (1991) 2710.
[2] M. Suzuki, Y. Taga, A. Goto and H. Yasuoka, Phys. Rev. **B24** (1994) 18580.
[3] M. Suzuki and Y. Taga, J. Phys. Condens. Matter. **7** (1995) 8497.
[4] S. K. Sinha: Physica B **173** (1991) 25.
[5] D. E. Savage, J. Kleiner, N. Schimke, Y. -H. Phang, T. Jankowski, J. Jacobs, R. Kariotis and M. G. Lagally: J. Appl. Phys. **69** (1991) 1411.

研究テーマ：量子凝縮相の研究
表題：中性子散乱よる直鎖型ハルデン物質 NDMAP における磁場誘起反強磁性秩序と磁気励起の研究

1-2-69

Neutron Scattering Study of the Field Induced Antiferromagnetic Order and Magnetic Excitation in Linear Chain Haldane Compound, NDMAP

Y. Koike[a,b], N. Metoki[a], Y. Morii[a], T. Asano[c] and Y. Ajiro[c]

a- Advanced Science Research Center, Japan Atomic Energy Research Institute, Tokai, Naka, Ibaraki 319-1195, Japan

b- Japan Science and Technology Corporation, Kawaguchi, Saitama 332-0012, Japan

c- Department of Physics, Kyushu University, Fukuoka 812-8581, Japan

The low dimensional quantum spin gap systems attract much interest. The one-dimensional Heisenberg antiferromagnet (1D HAF) with an integer spin number has a spin singlet ground state with spin excitation gap (Haldane gap) [1]. With applying magnetic field, the excited triplet level crosses the singlet ground level. As a result, a three dimensional long-range ordered (3D-LRO) phase is expected to be a ground state above critical field, H_C. In a typical Haldane compound NENP, however, 3D-LRO was not observed because of the anticrossing of the ground and excited level due to the staggered field. [2,3]

In new Haldane compounds, NDMAZ [4] and NDMAP [5], no staggered field is induced on the Ni site because of the equivalent inclination of g-tensor. Consequently, 3D-LRO is developed in these compounds above H_C. [6,7]

We carried out neutron scattering experiments in order to investigate the antiferromagnetic ordering and the magnetic excitation of NDMAP under magnetic field.

A single crystal of NDMAP (0.05 g) was used for experiments. NDMAP has a monoclinic structure (a = 18.092Å, b = 8.670 Å, c = 6.153 Å, $\beta \sim 91°$) below 240 K. Neutron scattering experiments were carried out using a cold neutron triple-axis spectrometer (LTAS) at JRR-3M in JAERI. The experimental setup was the same as the previous studies. [8,9]

Very recently the field induced AFM Bragg peak was observed at the wave vector q= (0 0.5 0.5). [10] We also observed the field induced 3D-LRO in NDMAP. [11] Figure 1 shows the elastic profile along the Q = (0 l l) with applying the magnetic field parallel to the a-axis. We observed a sharp magnetic Bragg peak at Q = (0 0.5 0.5) for H = 10 T but no peak was observed without magnetic field. The inset of Fig. 1 shows the temperature dependence of the AFM Bragg peak intensity measured at (0 0.5 0.5) for H = 10 T. The peak intensity increases steeply below $T \sim$ 1.5 K.

Figure 2 is constant-Q scans at the AFM zone center (0 0.5 0.5). A clear inelastic peak was observed at about 0.4 meV for 0 T, but no trace of the singlet-triplet excitation mode is also observed for 10 T. This behavior is very similar to the one

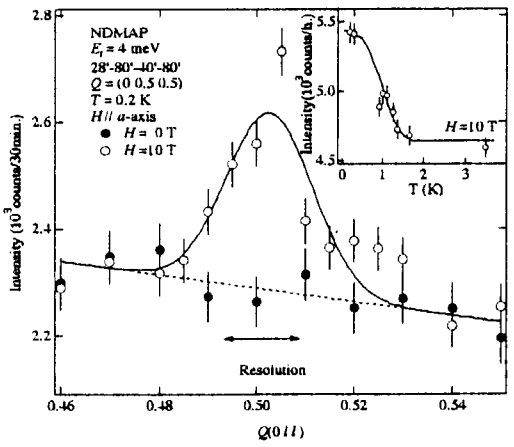


Fig. 1 The elastic profile along the (0 l l). Inset is the temperature dependence of the peak intensity at (0 0.5 0.5) for H = 10 T.

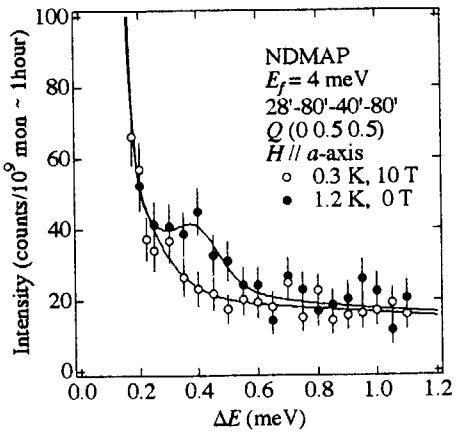


Fig 2 The constant-Q profile at (0 0.5 0.5).

for (0 0 0.5). [8-11]

We found a low-energy excitation in the field induced ordered phase (H = 10 T and T = 0.3 K) as shown in Fig. 3. In the profile at (0 0.5 0.5), no significant signal was observed above H_c within our statistical accuracy. At (0 0.5 0.52), however, it was found that the intensity around 0.2 meV was slightly larger than the background shown by dashed line. The data after the subtraction of the background (solid circle) exhibit a inelastic response at $\Delta E \sim 0.16$ meV. Furthermore, the peak shifts to higher energy with increasing Q. By fitting of the profile, the excitation energy of about 0.23 meV was obtained at (0 0.5 0.54). At (0 0.5 0.56) and (0 0.5 0.58), a very weak peak would be observed around 0.3 meV. From these results, it is considered that a new collective excitation mode appeared in the 3D-LRO phase. It is a future problem to investigate the origin of this excitation.

In conclusion we observed the field induced AFM Bragg peak in NDMAP. We observed a level crossing of the Haldane excitations. Around the AFM zone center, the collective magnetic excitation was found at very low energy. We need to investigate the nature of this new magnetic excitation.

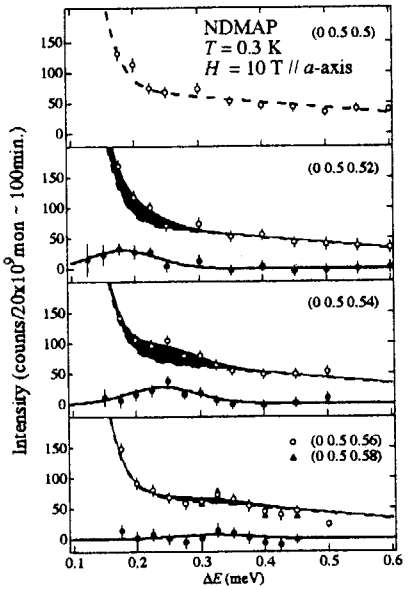


Fig. 3 The constant-Q profile at (0 0.5 0.5), (0 0.5 0.52), (0 0.5 0.54), and (0 0.5 0.56).

References

[1] F.D.M. Haldane, Phys. Lett A**93** (1983) 464.
[2] P.P. Mitra *et al.*, Phys. Rev. Lett. **72** (1994) 912.
[3] T. Sakai *et al.*, J. Phys. Soc. Jpn. **63** (1994) 867.
[4] M. Yamashita *et al.*, Mol. Cryst. Liq. Cryst. **274** (1995) 25.
[5] M. Monfort *et al.*, Inorg. Chem. **35** (1996) 7633.
[6] Z. Honda, *et al.*, J. Phys. Condens. Matter. **9** (1997) L83.
[7] Z. Honda, *et al.*, Phys. Rev. Lett. **81** (1998) 2566.
[8] N. Metoki *et al.*, J. Magn. Magn. Mater. **226-230** (2001) 414.
[9] Y. Koike *et al.*. J. Phys. Soc. Jpn. **69** (2001) 4034
[10] A. Zheludev *et al.*, Phys. Rev. Lett. **86** (2001) 1618.
[11] Y. Koike *et al.*, Phys. Soc. Jpn. **70** (2001) Supple. A 189,

研究テーマ：中性子散乱による強相関電子系の研究

表　　題：中性子小角散乱による $La_{1-x}Sr_xMnO_3$ の磁気ドメインの研究

1-2-70 Neutron Small Angle Scattering Study on $La_{1-x}Sr_xMnO_3$: x=0.1

M. Watahiki[1,2], J. Suzuki[1], Y. Yamada[1,3], K. Kohn[3]

[1]Advanced Science Research Center, Japan Atomic Energy Research Institute, Tokai- mura, Ibaraki 319-1195, Japan

[2]Japan Science and Technology Corporation, Kawaguchi, Saitama 332-0012, Japan

[3]Advanced Research Center for Science and Engineering, Waseda University, Shinjuku- ku, Tokyo 169-8555, Japan

$La_{1-x}Sr_xMnO_3$ belongs to the class of materials which show various interesting physical properties including CMR effect, charge / orbital ordering and J-T ordering etc.. Electron diffraction studies revealed that at lower temperatures, the system stay on a two-phase coexistent state of ferromagnetic metallic phase and antiferromagnetic insulator phase. It is considered that the stability of the two phase coexistence is the essential origin of CMR effect.

In order to study the existence of heterogeneous two phase coexistence, we carried out neutron small angle scattering (SANS) experiments at SANS- J spectrometer installed at JRR3M. The SANS profiles are obtained using neutrons with λ =0.65 and 0.35nm with the band width of 14% and 24%, respectively produced by a mechanical velocity selector. The magnetic field dependence is observed by applying the field up to 5T perpendicular to the incident beam.

The SANS profiles at various temperatures are summarized in Fig. 1. The profiles are composed of the two components with difference q- dependences. In the low- q regime ($q \leq 0.2$nm) the intensities follow q^{-4}-dependence while in the high- q regime, they show Lorentzian distribution. It is inferred that the former is due to the scattering from ferromagnetic cluster of semimacroscopic size embedded in 'non- magnetic' (including antiferromagnetic) medium, while the latter is due to the microscopic ferromagnetic fluctuations.

After subtraction of structural contribution (such as crystal mosaicness) the magnetic SANS spectra are analyzed using the formula,

$$I(q) = \alpha q^{-4} + \frac{I_0}{1+(\xi q)^2},$$

where α is the parameter proportional to the volume fraction of the ferromagnetic cluster and I_0 is proportional to the amplitude of the fluctuations. The results of fitting is shown in Fig. 2. As is shown in Fig. 3, I_0 peaks at the transition temperature while α shows

原子炉：JRR-3M　　装置：SANS-J (C3-2)　　分野：中性子散乱（磁性）

monotonic increase following $M^2(T)$- curve. These results are consistent with the picture described above. It is particularly noticeable that α is completely suppressed as the magnetic field of 5T is applied. This implies that under magnetic field, the system has become homogeneous ferromagnetic (metallic) state. The results seem to support the view that CMR effect is caused by the percolation of metallic cluster within insulator matrix.

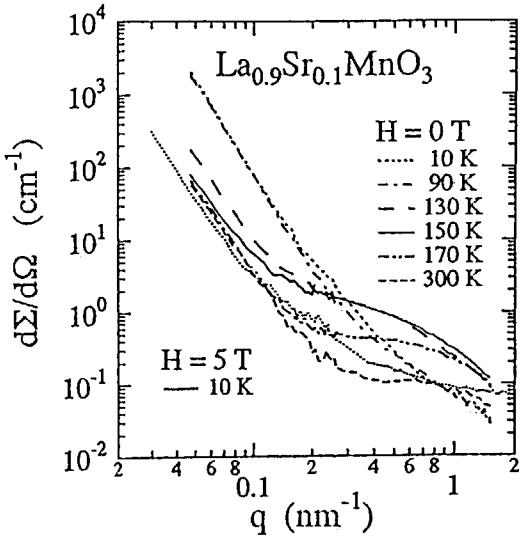


Fig. 1

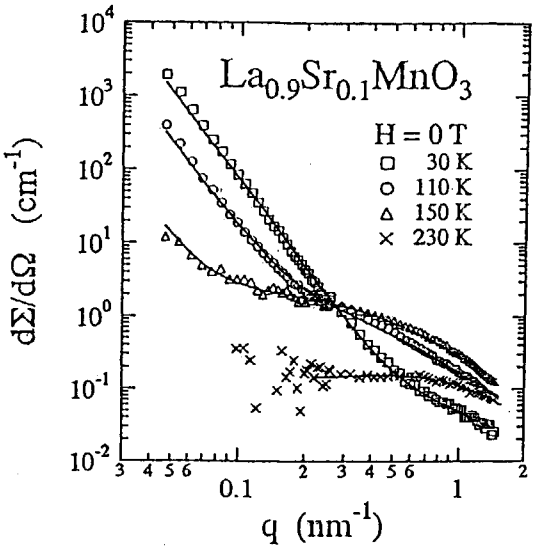


Fig. 2

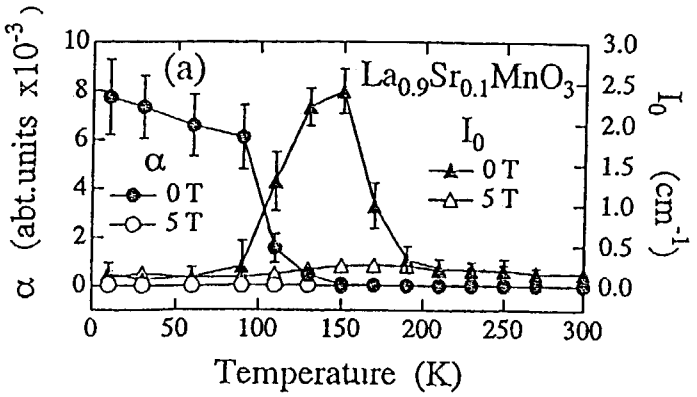


Fig. 3

研究テーマ：中性子散乱による強相関電子系の研究

表　　題：中性子小角散乱による $Pr_{0.7}Ca_{0.3}MnO_3$ の磁気ドメインの研究

1-2-71 Small Angle Neutron Scattering Study on $Pr_{0.7}Ca_{0.3}MnO_3$

Y. Yamada[1,2], T. Iwase[1], M. Watahiki[2], J. Suzuki[2]

[1]Advanced Research Institute for Science and Engineering, Waseda University, Shinjuku- ku, Tokyo 169-8555, Japan

[2]Advanced Science Research Center, Japan Atomic Energy Research Institute, Tokai- mura, Ibaraki 319-1195, Japan

$Pr_{1-x}Ca_xMnO_3$ (x~0.3) is a typical material to exhibit remarkable CMR effect. Electron diffraction studies on various manganites revealed that the CMR manganites tend to stabilize a two-phase coexistent state of ferromagnetic metallic phase and antiferromagnetic insulator phase at low temperatures. It is inferred that stabilization of the coexistent state is essential to exhibit CMR effect since, under such situation, the response of the system upon application of magnetic field is to expand the ferromagnetic metallic phase beyond percolation limit.

In order to investigate semimacroscopic magnetic heterogeneity, we carried out SANS experiment using SANS- J spectrometer installed at JRR3M reactor.

Single crystals of $Pr_{0.7}Ca_{0.3}MnO_3$ with size of 12mm×5mmϕ were used. A single crystal was mounted on the goniometer the C- axis vertical. The magnetic field of 1T applied in horizontal geometry. The two- dimensional detector was set at 1.5m and 10m fight paths depending on the angular resolution needed.

The obtained SANS spectra at various temperatures are summarized in Fig. 1(a) and Fig. 1(b) for H=0 and H=1T respectively. It is noticed that in the low- q range ($q \leq 0.5$nm) the spectra shows q^{-4} dependence (Porod law). At the same time, the temperature variation of the intensity in the low- q regime follows $M^2(T)$- curve (Fig. 2). This indicates that these exist ferromagnetic clusters with smooth surface embedded on 'non-magnetic' (including antiferromagnetic) medium. Detailed numerical analysis showed that the size of the ferro- cluster is of the order of 17nm.

As is clearly seen in Fig. 1(b), when the magnetic field of 1T is applied the intensity in the low- q regime is suppressed drastically by a factor of 10^{-2}. On the other hand, the magnetization itself increases during the same process. Therefore the disappearance of the intensity should suggest that the size of the ferro- cluster is increased beyond the resolution limit of our SANS spectrometer.

These results seem to give support for the mechanism of CMR to be the expansion of ferromagnetic metallic domains beyond the

---

原子炉：JRR-3M　　装置：SANS-J (C3-2)　　分野：中性子散乱（磁性）

percolation limit under magnetic field.

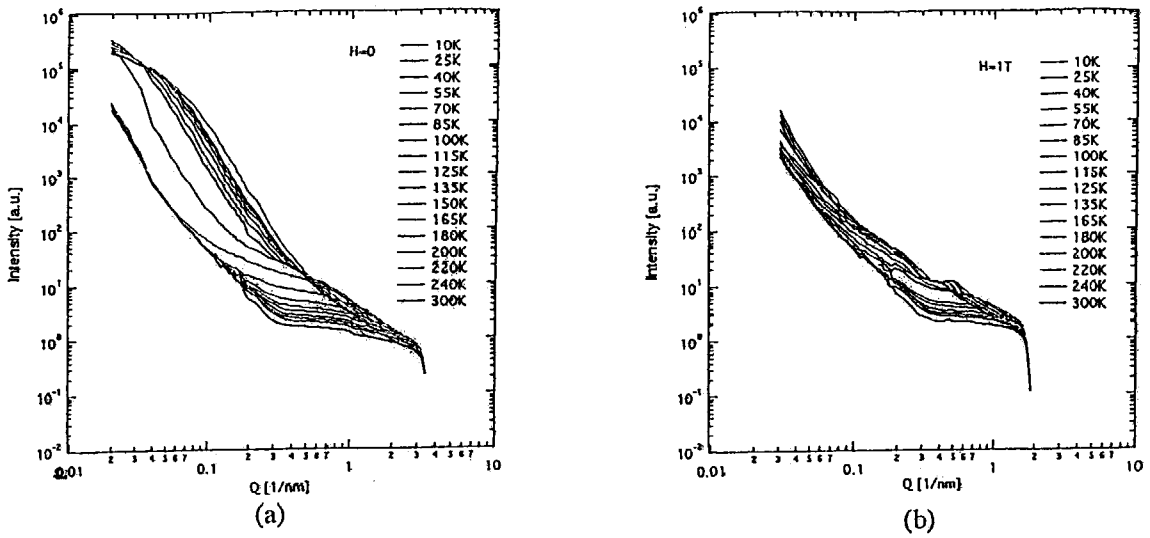


Fig. 1

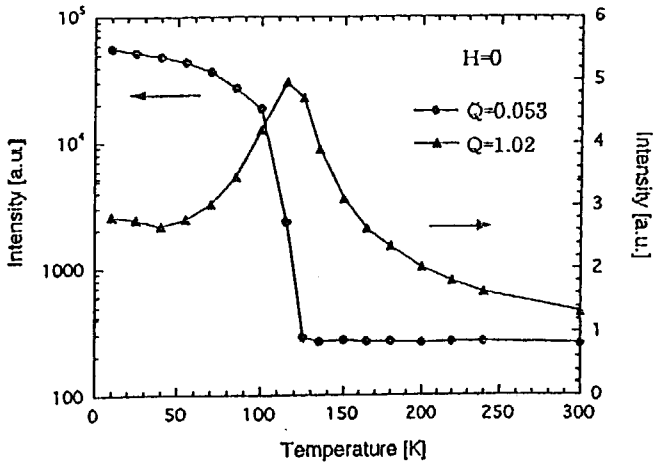


Fig. 2

研究テーマ：高濃度スピングラスにおけるスローダイナミックスの機構

表題：中性子小角散乱法による高濃度スピングラススローダイナミックスの研究

1-2-72 SANS Study of Slow Dynamics in Concentrated Spin Glasses

K. Motoya, K. Hioki and J. Suzuki[1]

Department of Physics, Science University of Tokyo, Noda 278-8510
[1]Japan Atomic Energy Research Institute, Tokai, Ibaraki 319-1195

In the previous neutron scattering studies on concentrated spin-glass alloys we showed that magnetic clusters play an important role for the reentrant spin-glass (RSG) transition, and that a wide variety of spin dynamics observed by inelastic neutron scattering measurements can be attributed to the differences in the size and number of magnetic clusters.[1)] Based on these studies, we speculate that the mechanism of slow dynamics might be closely related to the time evolution of magnetic clusters which can be directly detected by SANS measurement. We made time-resolved SANS experiments on three kinds of concentrated spin glass alloys, of which characteristics in the stationary state have already been clarified in the previous works. In this note, we present a result of $Fe_{0.70}Al_{0.30}$. Results of other samples, $Fe_{65}(Ni_{0.866}Mn_{0.134})_{35}$ and $Cu_2(Mn_{0.7}Ti_{0.3})Al$ have already been reported elsewhere.[2)]

SANS measurements were made utilizing the SANS-J spectrometer installed at the JRR-3M reactor of JAERI-Tokai. The incident-neutron wave-length and band-width ranges used in the experiment are λ=0.45-0.65nm and $\Delta\lambda/\lambda$=0.10-0.14, respectively. The momentum-transfer range of $0.03<q<2$ nm^{-1} was covered. The SANS patterns observed in the RSG phase are well traced by a Lorentzian (LOR) function in the momentum range of $0.06<q<0.3$ nm^{-1}. This is in contrast to the results for previously studied samples, in which the observed patterns cannot be expressed by a single LOR function and can be fitted by the sum of a LOR and a squared Lorentzian (SQL) functions. The simple form of the scattering pattern for the present sample makes it possible to express the time variation of the scattering pattern only by two parameters, the width and the amplitude of the LOR function. In Fig.1, we show the time variation of the line width of the LOR function measured at various temperatures. The width increases with time at T=20K, 30K and 50K, however no detectable change was seen at T=10K and 80K. The time evolution of the line width is well traced by an exponential form with the temperature dependent characteristic time constant t^*. The time constant t^* for T=20K, 30K and 50K are 8.2×10^4, 4.2×10^4 and 2.9×10^4sec, respectively. In the previous neutron scattering works we presented a model that the LOR component of the magnetic diffuse scattering is attributed to the magnetic clusters. Based on this model the present SANS experiment directly showed that the correlation length of the ferromagnetic clusters, in other word the size of the ferromagnetic clusters, decreases with time in RSG phase. The cluster size increases from 8.8×10^{-2} to 9.2×10^{-2} nm^{-1} in 20 hrs at T=50K.

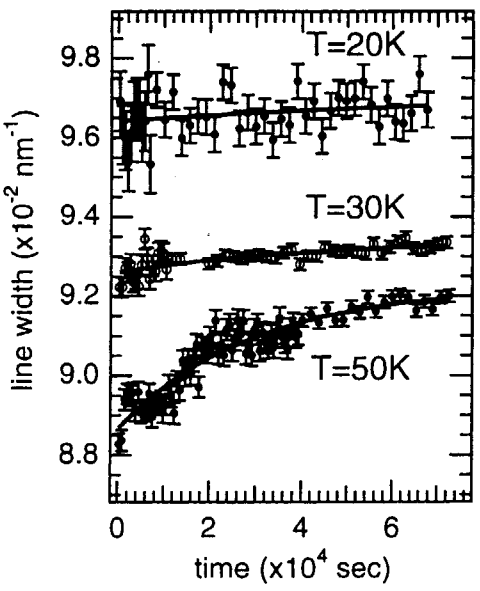


Fig. 1. Time variation of the width of the Lorentzian scattering function measured at various temperatures.

References

[1] K. Motoya et al.: J.Phys.Soc.Jpn. **68** (1999) 2351 and references therin.
[2] K. Motoya et al.: RIKEN Review. No-27 (2000) 29, J. Phys. Soc. Jpn. 70 (2001) suppl. A 139.

原子炉：JRR-3M　　装置：SANS-J (C3-2)　　分野：中性子散乱（磁性）

1. 中性子散乱 3) 超伝導現象

1. Neutron Scattering 3) Superconductivity

This is a blank page.

研究テーマ：$YBa_2Cu_3O_{6+x}$の磁気励起における共鳴ピーク
表題：$YBCO_{6+x}$における面内フォノンの中性子散乱研究

1-3-1 Neutron Scattering Study on in-plane phonon modes of $YBCO_{6+x}$

M. Ito[1], H. Harashina[1,3], Y. Yasui[1,3], M. Kanada[1,3], S. Iikubo[1], M. Sato[1,3], K. Kakurai[2,3] and M. Nishi[2]

1 Department of Physics, Division of Material Science, Nagoya University, Furo-cho, Chikusa-ku, Nagoya 464-8602

2 Neutron Scattering Laboratory, ISSP, The University of Tokyo, Shirakata 106-1, Tokai, Ibaraki 319-1195

3 CREST, Japan Science and Technology Corporation (JST)

The suppression of the superconducting transition temperature T_c at the hole carrier concentration p~1/8 or the "1/8 anomaly" has been found in $La_{2-x}Ba_xCuO_4$ and $La_{2-x-y}Nd_ySr_xCuO_4$. The phenomenon is considered to originate from the static or dynamical "stripes." Various kinds of experiments have been performed to clarify if the dynamical "stripe" ordering exists in other high-T_c Cu oxides and if it contributes to the occurrence of the superconductivity.

For $YBa_2Cu_3O_y$ ($YBCO_y$) system, phonon measurements have been carried out by Mook *et al.* to extract information on the above question.[1-3] They measured the in-plane longitudinal (<B_{2u}/B_{3u}>) modes with the energy of ~(43~52) meV, which have atomic motions along the directions shown in the inset of Fig. 1. Considering that the B_{2u} mode with the motions perpendicular to the dynamical stripes (shown by the solid line in the inset), strongly couple to them, they studied these modes and reported the anomalous wave vector (q)-dependence of the phonon energy broadening of the B_{2u} mode as the experimental evidence for the existence of the dynamical "stripes." Anomalous q dependence of the integrated intensity of the phonon peak has also been reported by their group.

Here, we measured the similar in-plane longitudinal <B_{2u}/B_{3u}> phonon modes with the energy ~(22~32) meV. In the present modes, the atoms in the CuO_2 planes mainly vibrate within the plane. Although the vibration in other layers also exists, the profiles with much finer resolution than the case of Mook *et al.* makes us possible to analyze the phonon behavior more accurately.

Neutron scattering measurements were carried out on the spectrometer ISSP-PONTA installed at JRR-3M of JAERI in Tokai, where single crystals of $YBCO_{6.5}$ (T_c ~52 K and $YBCO_{6.7}$ (T_c ~62 K) were used. Oxygen numbers y of the crystals was controlled by the temperatures of the annealing. The horizontal collimations were 40'-40'-40'-80' and the (002) reflection of the Pyrolytic Graphite was used both for the monochrometer and the analyzer. We measured in-plane phonon modes along Q=(3+h,0,0) in the reciprocal space at several h points ($0 \le h \le 0.45$) at 7 K, by scanning the transfer energy. Profiles calculated by assuming the Lorentzian type phonon broadening are convoluted with the resolution function and then fitted to the observed profiles. Figure 1 shows the obtained dispersion curves of <B_{2u}/B_{3u}> modes for $YBCO_{6.5}$, where the existence of two branches is indicated. In the figure, the twice of the incommensurability δ determined by the measurements of the magnetic excitation spectra $\chi(q,\omega)$ for the same sample is also shown. Anomalous features, if they exist, are expected to appear at around h

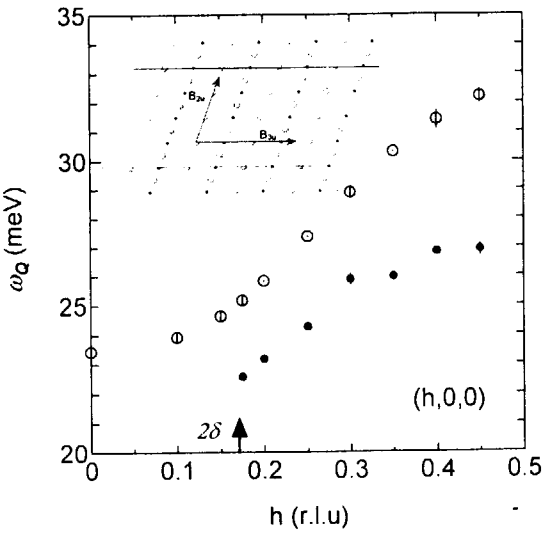


Fig. 1 The dispersion curves of <B_{2u}/B_{3u}> modes obtained for a single crystal of $YBCO_{6.5}$. The inset shows the directions of the vibration for the <B_{2u}/B_{3u}> modes in the CuO_2 plane. Solid line shows the dynamical stripes, if they exist.

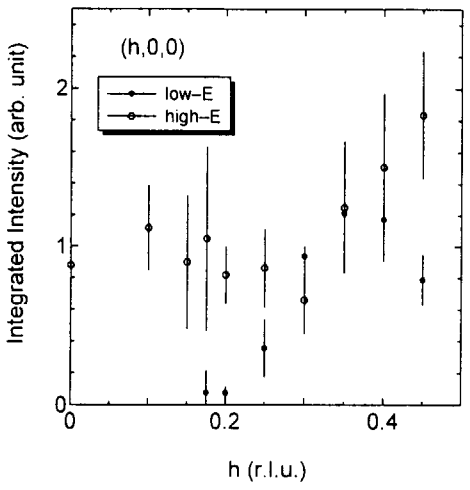


Fig. 2 The h-dependence of the integrated intensity for the <B_{2u}/B_{3u}> modes obtained for a $YBCO_{6.5}$ single crystal.

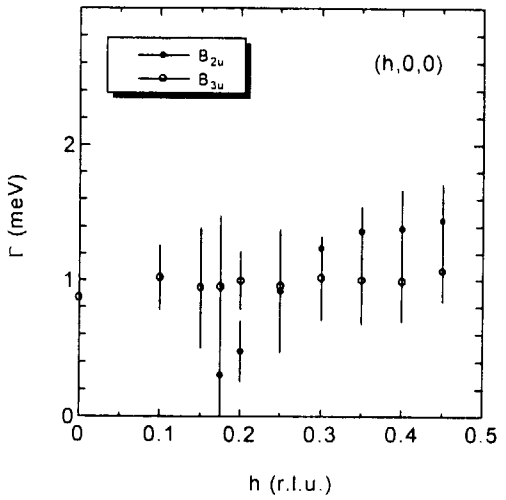


Fig. 3 The h-dependence of the energy broadening Γ obtained for a single crystal of $YBCO_{6.5}$. Open (Solids) circles correspond to B_{3u} (B_{2u}) mode.

~ 2δ. Figures 2 shows the h dependence of the integrated intensity of the phonon peak for $YBCO_{6.5}$. Open (Solid) circles in Fig. 2 correspond to the Open (Solid) circles in Fig. 1. We can see that one of the phonon branches shown by the solid circles exhibits rather irregular h-dependence. On the other hand, another one exhibits regular h-dependence. Considering the vibration pattern that B_{2u} mode has the chain oxygen motion, we think that the B_{2u} mode of the sample (without perfect chain oxygen ordering) exhibits irregular h-dependence of the intensity, while B_{3u} mode (without significant chain oxygen motion) exhibits regular h-dependence. Thus we assigned that Open (Solid) circles in Figs. 1 and 2 corresponds to $B_{3u}(B_{2u})$ modes. We note that any anomalous h-dependence of the sum of the integrated intensities of the B_{2u} and B_{3u} modes at around $h \sim 2\delta$ has not been observed.

The h-dependence of the energy broadening Γ (full width at half maximum) for $YBCO_{6.5}$ is shown in Fig. 3. Unfortunately, the behavior of the B_{2u} mode is quite irregular at the low h region, we cannot recognize the broadening of the profile width in this mode. So the discussion on the existence or non-existence of the effects of the dynamical "stripes" cannot be done for B_{2u} mode. Then we pay attention, here, to the energy broadening for B_{3u} mode, because even for the mode, which vibrates along the direction parallel to the dynamical "stripes," the stripe formation may affect the phonon mode in a significant way. However, as shown in Fig. 3, the energy broadening of the B_{3u} mode is very small (~ 1 meV).

In the case of the single crystal of $YBCO_{6.7}$, we obtained the similar experimental data to those of $YBCO_{6.5}$. We have not observed anomalous features associated with the dynamical "stripes" in the dispersion curves, the energy broadenings and the integrated intensities of <B_{2u}/B_{3u}> modes. We are now planning the experiments on $YBCO_{7.0}$ without the deficiency of chain oxygens, in which both the B_{2u} and B_{3u} modes are expected not to exhibit irregular behavior observed for B_{2u} modes in the present samples.

<Reference>

1) H.A. Mook and F. Dogan: Nature **401** (1999) 145.
2) H.A. Mook, P. Dai, F. Dogan and R.D. Hunt: Nature **404** (2000) 729.
3) H.A. Mook and F. Dogan: Cond-mat/0103037.

研究テーマ：$YBa_2Cu_3O_{6+x}$の磁気励起における共鳴ピーク
表題：$YBa_2Cu_3O_y$の磁気励起スペクトルの構造とその温度依存性

1-3-2 Detailed Comparison between Observed and Calculated Magnetic Excitation Spectra of $YBa_2Cu_3O_y$ with Pseudo Gap Behavior

M. Ito[1], H. Harashina[1,2], Y. Yasui[1,2], M. Kanada[1,2], S. Iikubo[1], M. Sato[1,2], A. Kobayashi[1,2] and K. Kakurai[2,3]

1 Department of Physics, Division of Material Science, Nagoya University, Furo-cho, Chikusa-ku, Nagoya 464-8602

2 CREST, Japan Science and Technology Corporation (JST)

3 Neutron Scattering Laboratory, ISSP, The University of Tokyo, Shirakata 106-1, Tokai, Ibaraki 319-1195

Detailed momentum (q)- and energy (ω)-dependences of the magnetic excitation spectra $\chi''(q,\omega)$ observed by neutron inelastic scattering for $YBa_2Cu_3O_y$(YBCO or $YBCO_y$) single crystals at several temperatures T, have been compared with those deduced by a model calculation, which is essentially based on the band picture. The result shows that the spectral distribution in the (q,ω) space (including the incommensurate-commensurate (resonance peak)-incommensurate variation of $\chi''(q,\omega)$ with varying ω) and its T-dependence can be well reproduced without introducing the dynamical "stripes".

In the calculation, the magnetic susceptibility is expressed as $\chi(q,\omega)=\chi^0(q,\omega)/\{1+J(q)\chi^0(q,\omega)\}$, with the nearest neighbor form of the exchange coupling $J(q)=J(\cos q_x a+\cos q_y a)$, where $\chi^0(q,\omega)$ is the susceptibility for $J=0$ and has been calculated by using effective band parameters $t_0, t_1=-t_0/6$ and $t_2=t_0/5$, which have usual meanings and reproduce the Fermi surface shape of YBCO. The intra atomic Coulomb energy U has been chosen to be zero. Instead, the strong correlation effects are considered by adopting a small effective value of t_0 (~20 meV for y=6.5). Then, by adopting proper values of J, the chemical potential μ and the (d-wave) superconducting gap parameter Δ_0 which is assumed to be T-independent for $YBCO_{6.5}$ considering the pseudo gap behavior above the superconducting transition temperature T_c, the spectral weight $\chi''(q,\omega)$ has been obtained.

Although the results can roughly reproduce the spectra $\chi''(q,\omega)$ observed at low temperatures, much better agreement can be found when the quasi particle broadening $\Gamma(\omega)$, which has been observed by various kinds of studies such as transport, photoemission and optical measurements is taken into account. The broadening is also important to reproduce the quasi particle tunneling spectra observed for underdoped Bi2212 samples in the wide T-region up to room temperature, by using a model that the almost T-independent gap amplitude $|\Delta_0|$ exists.

Several suggestions are given by the above results. (i) The fact that the simple band picture naturally explains the observed spectra of YBCO, indicates non-necessity of the introduction of the dynamical "stripes" to describe $\chi''(q,\omega)$. For the authors, it seems not to be easy to describe the detailed distribution of the spectral weight χ'' in the low energy region by adopting a model of the slowly moving "stripes". (ii) The analyses of the observed $\chi''(q,\omega)$ may present us the opportunity to see the T-dependence of the so-called in-gap states or Zhang-Rice singlets. (iii) The pseudo gap observed even far above T_c can safely be understood as the precursor of

the superconducting gap.

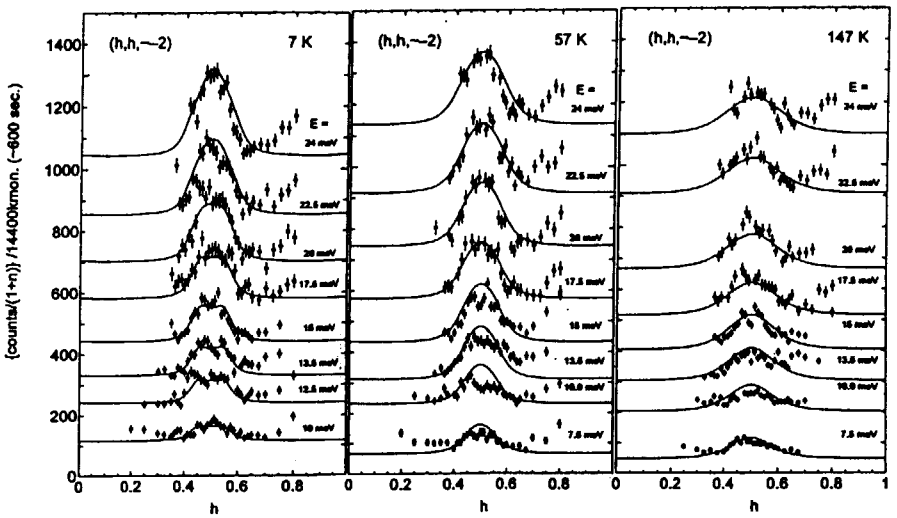


Fig. 1 Results of the fittings to the observed data of $\chi''(q,\omega)$, carried out by using the expression described in the text are shown at 7 K, 57 K and 147 K. In the calculations, effects of the quasi particle damping have been considered by using the broadening Γ, whose T^1 and quasi particle energy-dependence is assumed to roughly reproduce the experimentally observed characteristics.

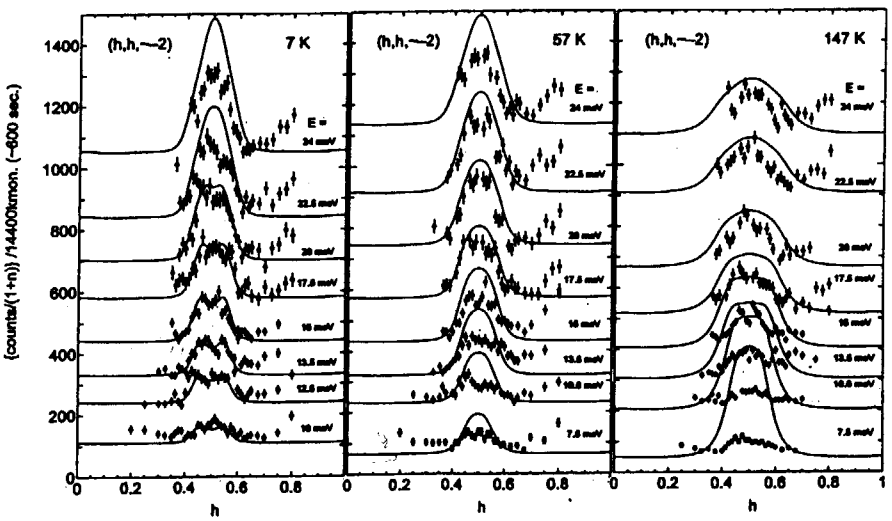


Fig. 2 Results the fittings obtained similarly to the case of Fig. 1, but Γ is just assumed here to have a small T^1 and quasi particle energy independent value.

研究テーマ：二重ハニカム格子超伝導体の構造とそのダイナミクス
表題：二重ハニカム格子超伝導体の構造とそのダイナミクス

1-3-3
Structure and Dynamics of Double Honeycomb Lattice Superconductors

S. Shamoto[a)], Y. Kato[a)], T. Kajitani[a)],
K. Ohoyama[b)], Y. Yamaguchi[b)], N. Aso[c)], and K. Kakurai[c)]

[a)]*Department of Applied Physics, Faculty of Engineering, Tohoku University, Sendai 980-8579*
[b)]*Institute for Materials Research, Tohoku University, Sendai 980-8577.*
[c)]*Neutron Scattering Laboratory, ISSP, The University of Tokyo, Tokai, Ibaraki 319-1106*

Novel layered superconductors, Li_xZrNCl (T_c~15 K), Li_xZrNBr (T_c~13 K), and $Li_x(THF)_yHfNCl$ (T_c~25.5 K), have been discovered by Yamanaka et al. [1]. The basic structure has double honeycomb lattice of $[(Hf, Zr)N]_2$. The conduction band is partially filled by electrons, which are supplied from alkali metals. It is noteworthy that recently discovered high-T_c MgB_2 [2] has similar band structure to the present double honeycomb lattice superconductors but contrasts with that in the sign of doped carriers (electrons for the present system and holes for MgB_2). MgB_2 could be viewed as one of the present compounds family in electronically.

Neutron scattering measurement was carried out using TOF-type spectrometer AGNES at C3-1-1, Triple-axis Spectrometer PONTA at 5G, and Diffractometer KSD at T1-2 of JAERI-JRR3M in Tokai. Specific heat capacity has been measured by Quantum Design PPMS system.

Figure 1 shows generalized phonon density of states, GPDOS, of Li_xZrNBr with x=0 and 0.19 at T~ 270 K, where the arrows are Debye temperatures θ_D of these compounds obtained by heat capacity (higher θ_D is for β-ZrNBr sample). The softening of GPDOS on $Li_{0.19}ZrNBr$ corresponds well to the decrease of θ_D value.

Na_xHfNCl powder sample was pressed uniaxially to be aligned along c-axis. The mosaic spread was estimated to be about 63 degrees by KSD. The phonon mode at E=29.3 meV was investigated at PONTA by rotating crystal angle of the pressed powder sample, as shown in Fig. 2, indicating vibrational mode along c-axis.

JRR-3M, AGNES, PONTA, KSD
3. Superconductivity

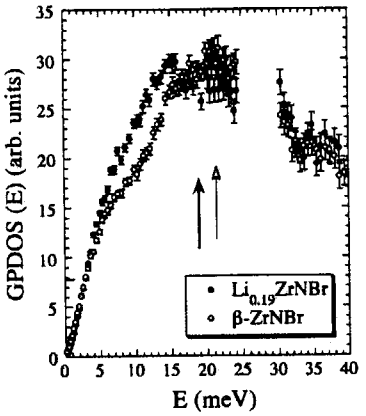


Figure 1. Observed phonon density of states of Li_xZrNBr at T~ 270 K by AGNES [3].

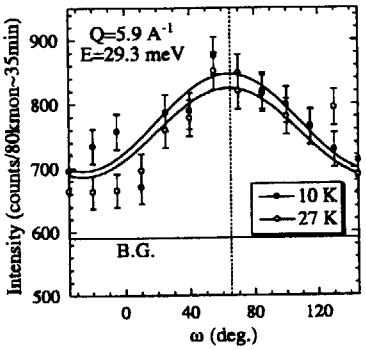


Figure 2. ω-scan of c-axis aligned powder sample at E=29.3 meV and Q=5.9 A^{-1}, where intensity has increased with decreasing temperature from T=25 K to 10 K. Solid lines are theoretically expected ω-dependence.

References

[1] S. Yamanaka, K. Hotehama and H. Kawaji, Nature 392, 580 (1998), and a reference therein.
[2] J. Nagamatsu, N. Nakagawa, T. Muranaka, Y. Zenitani and J. Akimitsu, Nature 410, 63 (2001).
[3] S. Shamoto, Y. Kato, K. Iizawa, T. Koiwasaki, M. Yasukawa, S. Yamanaka, and T. Kajitani, J. Phys. Soc. Jpn. in press (ASR-2000).

研究テーマ：$La_{2-x}Sr_xCuO_4$のオーバードープ領域における電荷・スピン秩序の研究
表題：$La_{2-x}Sr_xCu_{1-y}Zn_yO_4$ (x=0.21, y=0.01)における異常の中性子散乱による研究

1-3-4

Neutron Scattering Study on the Anomaly in $La_{2-x}Sr_xCuO_4$ (x=0.21, y=0.01)

Y. Koike, M. Aoyama, T. Adachi, T. Kawamata, H. Kimura[1], K. Hirota[2], K. Yamada[3] and Y. Endoh[4]

Department of Applied Physics, Tohoku University, Sendai 980-8579, JAPAN
[1]Research Institute for Scientific Measurements, Tohoku University, Sendai 980-8577, JAPAN
[2]Department of Physics, Tohoku University, Sendai 980-8578, JAPAN
[3]Institute for Chemical Research, Kyoto University, Uji 610-0011, JAPAN
[4]Institute for Materials Research, Tohoku University, Sendai 980-8577, JAPAN

Recently, we have discovered anomalous suppression of superconductivity at x = 0.21 in the overdoped region of $La_{2-x}Sr_xCu_{1-y}Zn_yO_4$ single crystals of good quality. This suppression is markedly enhanced through the 1% Zn-substitution for Cu.[1] From the muon-spin-relaxation measurements, the magnetic correlation between Cu spins has been found to be enhanced at low temperatures below 3.5 K in the 1% Zn-substituted crystal with x = 0.21.[2] In order to clarify the magnetic state, we have made the neutron scattering experiment using the 1% Zn-substituted crystal with x = 0.21.[3]

A large single-crystal of $La_{2-x}Sr_xCu_{1-y}Zn_yO_4$ with x=0.21 and y=0.01 was grown by the Traveling-Solvent Floating-Zone method. The size was 5 mm in diameter and 30 mm in length. The neutron scattering experiment was carried out at the triple-axis-spectrometer TOPAN installed at the 6G beam port in JRR-3M. Neutron energy was fixed at 14.7 meV by using PG002 monochromator and analyzer. Incident and scattered beams were filtered by PG crystals in order to eliminate higher order contaminations.

Four incommensurate magnetic peaks around (π, π) were clearly observed as elastic scattering at low temperatures below 20 K, where (π, π) is a propagation wave vector of antiferromagnetic ordering in La_2CuO_4. Typical peak profiles of the incommensurate elastic peaks taken at 1.4 K are shown in Fig. 1. The incommensurability of these peaks is estimated to be 0.135 ± 0.002 r.l.u., which is very similar to that of the peaks observed from the inelastic neutron scattering experiment in the overdoped region of $La_{2-x}Sr_xCuO_4$.[4] The correlation lenth in the CuO_2 plane is estimated from the intrinsic line-width as ca. 70 Å. It is concluded that there is a possibility that the dynamical stripe correlations of holes and spins are pinned by Zn at x = 0.21, leading to a static stripe-order and the marked suppression of superconductivity, as in the case of x ～ 1/8.[5]

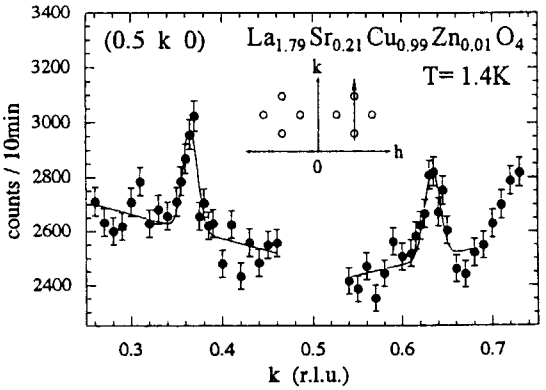


Fig. 1. Incommensurate magnetic peaks observed in the (0.5 k 0) scan at 1.4 K in the elastic neutron scattering experiment for the Zn-substituted single-crystal of $La_{2-x}Sr_xCu_{1-y}Zn_yO_4$ with x=0.21 and y=0.01.

References

1) T. Kawamata, T. Adachi, T. Noji and Y. Koike, Phys. Rev. B 62 (2000) R11981.
2) I. Watanabe, M. Aoyama, M. Akoshima, T. Kawamata, T. Adachi, Y. Koike, S. Ohira, W. Higemoto, K. Nagamine, Phys. Rev. B 62 (2000) R11985.
3) H. Kimura, K. Hirota, M. Aoyama, T. Adachi, T. Kawamata, Y. Koike, K. Yamada and Y. Endoh, J. Phys. Soc. Jpn. (in press).
4) K. Yamada, C. H. Lee, K. Kurahashi, J. Wada, S. Wakimoto, S. Ueki, H. Kimura, Y. Endoh, S. Hosoya, G. Shirane, R. J. Birgeneau, M. Greven, M. A. Kastner, Y. J. Kim, Phys. Rev. B 57 (1998) 6165.
5) Y. Koike, A. Kobayashi, T. Kawaguchi, M. Kato, T. Noji, Y. Ono, T. Hikita, Y. Saito, Solid State Commun. 82 (1992) 889.

JRR-3M, TOPAN, 3.Superconductivity

研究テーマ:$(La,Ba,Sr)_2CuO_4$における結晶構造、電荷・スピン秩序、および超伝導の相関

表題:$La_{1.875}Ba_{0.125-x}Sr_xCuO_4$における電荷・スピン秩序と超伝導の競合的関係

1-3-5
Competitive interplay between the charge/spin order and superconductivity in $La_{1.875}Ba_{0.125-x}Sr_xCuO_4$

H. Goka[1], M. Fujita[1], K. Yamada[1] and M. Matsuda[2]

[1] *Institute for Chemical Research, Kyoto University, Gokasyo, Uji,611-0011, Japan*

[2] *Advanced Science Research Center, Japan Atomic Energy Research Institute (JAERI), Tokai, Ibaraki 319-1195, Japan*

Since the discovery of hole stripe-order in high-T_c superconductor by Tranquada et al. [1], the role of spin/charge stripe correlation for the high-T_c superconductivity has been one of the central issues in this field. In order to clarify the relationship among the crystal structure, spin/charge order and superconductivity, we have been performing neutron scattering experiments using $La_{1.875}Ba_{0.125-x}Sr_xCuO_4$ (LBSCO) single crystals.

We grew single crystas of LBSCO (x=0.05, 0.06, 0.075 and 0.085) by utilizing a traveling solvent floating zone method. Typical size of crystals is 6mm in diameter and 30mm in length (volume~0.8cc). Neutron scattering experiments were carried out at TOPAN, TAS-1 and HER triple-axis spectrometers with the incident neutron energies of 14.7meV, 13.7meV and 5meV, respectively.

Fig. 1 shows the obtained phase diagram of LBSCO. The closed circles represent T_c evaluated from the magnetic susceptibility measurement. Open circles show the low temperature orthorhombic (LTO) to the low temperature tetragonal (LTT) or to the low temperature less orthorhombic (LTLO=*Pccn*) structural transition temperature T_{d2}.

Present study revealed that LTT/*Pccn* structure suddenly disappears with increasing x beyond at x~0.09. In the LTT/*Pccn* phase (x=0.05~0.075) well-defined superlattice peaks corresponding to the incommensurate charge ordering appear below T_{d2}. For the sample near the boundary between LTO and LTT/*Pccn* the same superlattice peak is observed with the peak intensity much weaker than that in the LTT/*Pccn* phase. In the LTO phase on the other hand, it is well known that no well-defined superlattice peak is so far observed. In contrast to the charge peak, incommensurate magnetic peak is observed in all samples. The peak intensity monotonically decreases with increasing x.

As shown in Fig. 1,superconductivity is strongly suppressed in LTT/*Pccn* structure. In LTO structure (x>0.085), T_c is almost constant (around 30K). Above results strongly suggest that the static or quasi static charge order directly suppresses the superconductivity.

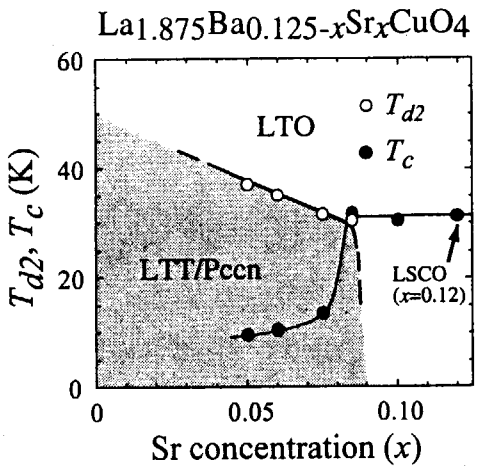


Fig.1 The phase diagram of LBSCO. Closed and open circles represent T_c and T_{d2} respectively. Solid line and broken line are guides to the eye.

References

[1]J. M. Tranquada, et al., Nature(London) 375 (1995) 561

This is a blank page.

1. 中性子散乱 4) 非晶質・液体

1. Neutron Scattering 4) Amorphous・Liquid

This is a blank page.

研究テーマ：拡散現象モデル化及び高精度拡散係数測定
表　題　：中性子回折による広温度範囲での液体錫の構造研究

1-4-1

The Study of the Structure of Liquid Sn in the Wide Temperature Range due to Neutron Scattering Technique

M.Masaki, S.Munejiri, H.Aoki, T.Kamiyama[1], T.Itami[2] and Y.Ishii[3]

National Space Development Agency of Japan(NASDA), 2-1-1 Sengen, Tsukuba, Ibaraki, 305-8505, Japan
1.Invited Researcher of NASDA: Graduate School of Technology, Hokkaido University, N13 W8 , Sapporo, Japan
2. Invited Researcher of NASDA: Graduate School of Science, Hokkaido University, N10W8, Sapporo, Japan
3. Advanced Science Research Center, Japan Atomic Energy Research Institute, Tokai, Ibaraki, 319-1195, Japan

The structure of liquids is the fundamental information for the discussion of the condensed matter science. Particularly in the liquid state the position of atoms is only defined statistically. Therefore, the precise measurement of liquid structures is extremely important. In near future, the big international project "International Space Station(ISS)" starts. The study of diffusion in melts of high melting temperature is an important target for the space utilization program in this ISS. The experiments of diffusion in melts have been suffered from the inevitable convection on the ground in spite of the importance of the exact diffusion data themselves for the many industrial processes. In addition, the problem of diffusion itself is an interesting many body problems in the fundamental science. Also for the understanding of the diffusion in melts from the theoretical point of view, the structure of liquids is an essential knowledge.

We are focussing our attention on the diffusion in melts of the group IVB elements. In these several years, we have performed the study of structures of liquid Sn in the wide temperature range by employing the neutron scattering technique and the *ab-initio* molecular dynamics simulations. Up to the last year the neutron scattering experiments have been performed for the study of $S(Q)$ of liquid Sn at 573 K, 773 K and 1073 K by using the fused silica containers. The shoulders in the high Q side of the first peak of structure factor, $S(Q)$, have been found to be present even at the highest 1073 K. This structure factor of liquid Sn was well reproduced by the *ab-initio* molecular dynamics simulations. This method gave a further microscopic insight; the bond angle distribution function shows a broad peak around 100 degree. The peak of 100 degree may indicate the sign of the fragment of distorted β-Sn structure[1]. At this stage, it is much interested in the question what temperature the anomalous feature of structure of liquid Sn remain to be present until.

In this year, the $S(Q)$ of liquid Sn was measured by the neutron scattering technique at higher temperatures, 1373 K, 1673 K and 1873 K. For the present high temperature experiments, sample containers were newly developed. The sample container was made of the new material, glassy carbon, which is the glass state of carbon and no reactive with corrosive liquid metals. The most striking advantage of glassy carbon container is the absence of Bragg peaks. The size of glassy carbon container is 10 mm(i.d.)×10.6 mm(o.d.)×100 mm(long). The purity of Sn was 99.9999%. The sample was placed in a high temperature radiation furnace with Nb foil heating element (at highest 2100 K), which is constructed by AS Scientific Products.

The neutron scattering experiments were performed by the use of triple axis spectrometer (TAS-1) installed at the JRR-3M in Japan

原子炉：JRR-3M　　装置：TAS-1 (2G)　　分野：中性子散乱（液体・不規則物質）

Atomic Energy Research Institute. The incident wavelengths were 0.85, 0.95 and 2.24 Å, giving a range of scattering vector Q (= $4\pi \sin\theta/\lambda$), of 0.2 to 12.1 $Å^{-1}$, where 2θ is the scattering angle. The height of liquid sample was taken to be about 35mm and the width of neutron window is adjusted to be 14 mm. The data of scattering intensity were acquired with the steps 0.05 and 0.1 $Å^{-1}$ for Q< 6.0 $Å^{-1}$ and Q >6.0 $Å^{-1}$, respectively. Counting time at each temperature was typically 8-12 hours. Neutron scattering data were treated using a standard procedure, which includes subtraction of cell intensities and corrections for absorption and multiple scattering.

Figure 1 shows a typical example of glassy carbon experiments for liquid Sn at 1473 K. This figure shows that the Bragg peak was almost completely removed in the present scattering experiment. Figure 2 depicts the temperature dependence of $S(Q)$ for liquid Sn up to 1873 K. As a first look, the shoulder around the 1st peak of $S(Q)$ seems to be indistinctive with the increase of temperature together with the decrease of its height and the increase of its width. However, the intensity at the Q position of the shoulder of $S(Q)$ is unvaried and the shoulder itself seems to be still present even at 1873 K. The inverse method[2] was applied to obtain the effective pair potential in liquid Sn, which was applied to molecular dynamics simulations in the wide temperature range. Obtained temperature dependence of self-diffusion coefficient well reproduces the temperature dependence under microgravity[3]. In near future, the particular feature of the structures and the microscopic atomic motions are to be extracted more in detail with the use of the present result as a boundary condition.

References

[1] S.Munejiri, T.Masaki, Y.Ishii, T.Kamiyama, Y.Senda, F.Shimojo, K.Hoshino and T.Itami, J.Phys. Soc. Jpn., **79** (2001), A268.

[2] S.Munejiri, F.Shimojo, K.Hoshino and M.Watabe, J. Phys. Soc. Jpn., **64** (1995), 344.

[3] T.Itami, H.Aoki. T.Masaki, et al., J. Jpn. Microgravity Appl., **15** (1998) 225..

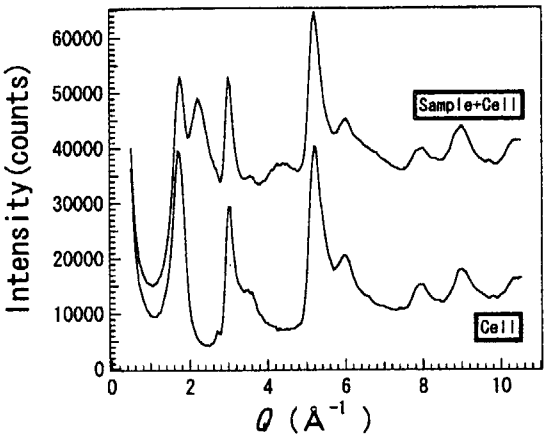


Fig. 1. The intensity of neutron scattering experiment; sample: liquid Sn at 1373 K; cell: glassy carbon.

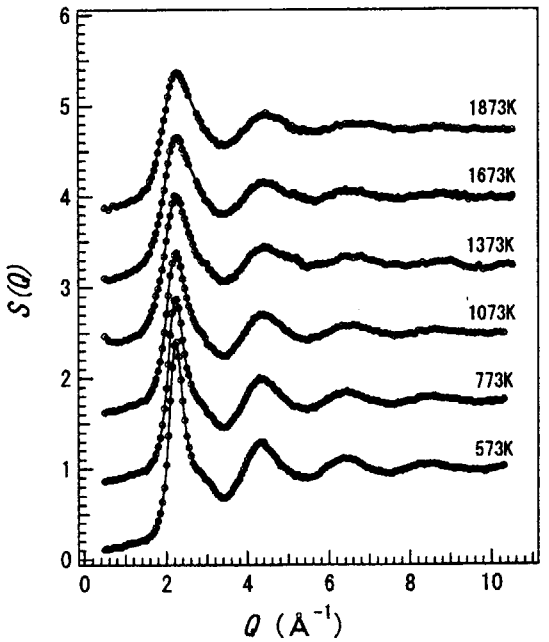


Fig. 2. Temperature dependence of $S(Q)$ for liquid Sn from 573 K to 1873 K

研究テーマ：濃厚尿素水溶液中の分子間水素結合構造
表題：濃厚水溶液中における尿素分子の水和構造

1-4-2
Hydration Structure of Urea Molecules in Highly Concentrated Aqueous Solutions

Y. Kameda, K. Sugawara, K. Abe, T. Usuki and O. Uemura

Department of Material and Biological Chemistry, Faculty of Science, Yamagata University, Kojirakawa-machi 1-4-12, Yamagata 990-8560, JAPAN

Introduction

Urea is one of the most important compounds in extensive fields of chemical and biological sciences. Despite considerable efforts to elucidate the hydration geometry of the urea molecule in aqueous solutions, unambiguous information has not yet been obtained. The first attempt has been conducted by Turner et al., employing neutron diffraction with $^{14}N/^{15}N$ isotopic substitution method,[1] however, a considerable overlap of intra- and intermolecular contributions involved in the observed distribution function around the amino-nitrogen atom, has suffered to obtain precise structural information on the urea hydration.

In the present report, we describe results of neutron diffraction measurements on highly concentrated aqueous 15 mol% urea solutions in which both the isotopic ratios of $^{14}N/^{15}N$ and H/D have been changed. Observed difference functions have been combined to obtain the partial structure factor, $a_{NH}(Q)$. Detailed structural information on the hydration structure around the amino-group within the urea molecule has been deduced.

Experimental

Four kinds of aqueous 15 mol% urea solutions with different $^{14}N/^{15}N$ and H/D isotopic ratios were prepared;

1) $[(^{14}ND_2)_2C{=}O]_{0.15}(D_2O)_{0.85}$ (99.6% ^{14}N, 99.8% D)
2) $[(^{15}ND_2)_2C{=}O]_{0.15}(D_2O)_{0.85}$ (98.0% ^{15}N, 99.8% D)
3) $[(^{14}N^0H_2)_2C{=}O]_{0.15}(^0H_2O)_{0.85}$ (99.6% ^{14}N, 37.5% D, $b_H = 0$)
4) $[(^{15}N^0H_2)_2C{=}O]_{0.15}(^0H_2O)_{0.85}$ (98.0% ^{15}N, 37.5% D, $b_H = 0$).

The sample solution was sealed into a cylindrical fused quartz cell with 11.6 mm in inner diameter and 1.2 mm in thickness. Neutron diffraction measurements were carried out on the ISSP 4G diffractometer installed at the JRR-3M research reactor, JAERI, Tokai, Japan. The incident neutron wavelength of λ = 1.100 ± 0.03 Å was employed. The collimations used were 40'-80'-80' in going from the reactor to the detector. Scattered neutrons were collected over the angular range of $3 \le 2\theta \le 115°$, corresponding to $0.30 \le Q \le 9.63$ Å^{-1}. Measurements of scattering intensities were made in advance for a vanadium rod, an empty cell and a background, respectively. After corrections for absorption and multiple scatterings, the observed neutron count rates were converted to the normalized scattering cross section.

Results and Discussion

The first order difference function,[2] $\Delta_N(Q)$, between corrected scattering cross sections for the sample solutions with the same isotopic ratio for hydrogen atoms and different one for nitrogen atoms, can be expressed as follows,

$$\Delta_N(Q) = A[a_{NO}(Q)-1] + B[a_{NH}(Q)-1] + C[a_{NC}(Q)-1] + D[a_{NN}(Q)-1], \quad (1)$$

where,

$A = 4xb_O(b_{^{14}N}-b_{^{15}N})$, $B = 8x(1+x)b_H(b_{^{14}N}-b_{^{15}N})$, $C = 4x^2b_C(b_{^{14}N}-b_{^{15}N})$, and $D = 4x^2(b_{^{14}N}{}^2-b_{^{15}N}{}^2)$.

x denotes the mole fraction of $(^*N^*H_2)_2C{=}O$ in the solution. Numerical values of the coefficients A—D in eq. 1 are listed in Table 1.

Table 1 Values of coefficients A—D in eq. 1

	A/barns	B/barns	C/barns	D/barns
${}^{D}\Delta_N(Q)$	0.101	0.268	0.018	0.041
${}^{0H}\Delta_N(Q)$	0.099	0.004	0.017	0.041

Since magnitudes of coefficients A and B are much larger than those of C and D in the present experimental condition, the observed $\Delta_N(Q)$ is dominated by the contribution from the amino-nitrogen atom - water correlation. The Fourier transform of $\Delta_N(Q)$ gives the distribution function, $G_N(r)$, around the nitrogen atom,

$$G_N(r) = 1 + (2\pi^2\rho r)^{-1}(A+B+C+D)^{-1} \times \int_0^{Q\max} Q\Delta_N(Q)\sin(Qr)\,dQ. \quad (2)$$

The intramolecular N···X (X: C, O, H and N) contributions within the urea molecule were calculated employing structural parameters reported for the crystalline state,[3] and then subtracted from the total $\Delta_N(Q)$ to obtain the intermolecular difference function, $\Delta_N^{inter}(Q)$. The partial structure factor, $a_{NH}(Q)$, was derived from the second-order difference between observed ${}^{D}\Delta_N^{inter}(Q)$ and ${}^{0H}\Delta_N^{inter}(Q)$ terms.

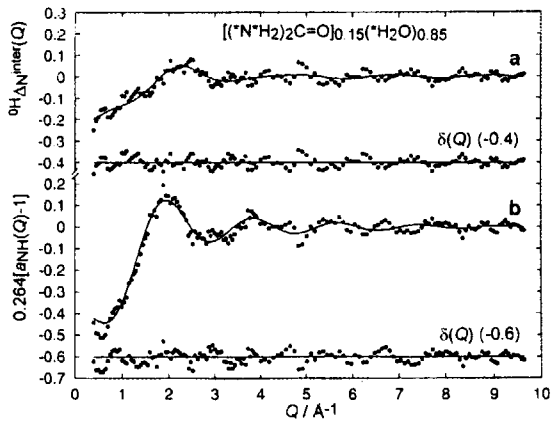


Fig. 1 Observed a) ${}^{0H}\Delta_N^{inter}(Q)$ and b) $a_{NH}(Q)$ for aqueous 15 mol% urea solutions (circles) and the best fit of the theoretical interference functions (solid lines). The residual function, $\delta(Q)$, is shown below.

In order to deduce detailed structural parameters concerning the nearest neighbor N···O(water) and N···H(water) interactions, the least squares fitting analysis has been applied to the observed ${}^{0H}\Delta_N^{inter}(Q)$ ($\approx a_{NO}(Q)$) and $a_{NH}(Q)$ functions, the results of which are indicated in Figs. 1 and 2. The present values for the nearest neighbor N···O(water) and N···H(water) distances, r_{NO} = 2.98(1) Å and r_{NH} = 3.59(1) Å, clearly indicate that water molecules surrounding the amino group of the urea molecule form hydrogen bonds of the N-H···OH_2 type. The tilt angle between the N-H···O axis and the molecular plane of the water molecule is estimated to be 32(4)°.

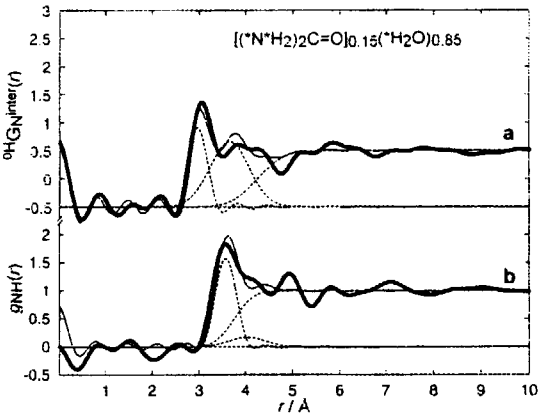


Fig. 2 Distribution functions, a) ${}^{0H}G_N^{inter}(r)$ and b) $g_{NH}(r)$, observed for aqueous 15 mol% urea solutions (circle). Broken lines denote contributions from both the short- and long-range interactions.

References

1) J. Turner, J. L. Finny, J. P. Bouquire, G. W. Neilson, S. Cummings and J. Bouillot, "*Water and Aqueous Solutions*", eds. G. W. Neilson and J. E. Enderby, pp. 277 (1986), Adam Hilger, Bristol, UK.

2) J. E. Enderby, *Chem. Soc. Rev.*, **24**, 159 (1995).

3) S. Swaminathan, B. M. Craven and R. K. McMullan, *Acta Cryst.*, **B40**, 300 (1984).

研究課題：中性子スピンエコー法による重水分散磁性流体磁束のゆらぎ
表題：磁性流体中のマグネタイト微粒子のブラッグ反射中性子スピンエコー

1-4-3 Neutron Spin Echo Studies on Bragg Reflections of Magnetite Fine Particles in Ferroliquid due to Dopplar Broadening

Norio ACHIWA, Heita NISHIOKA, Tomoyuki YOKOYAMA, and Kazuhisa KAKURAI[A]
Department of Physics, Kyushu University, Fukuoka, 8128581, Japan
[A], ISSP Univ. of Tokyo. Japan

Department of Physics, Kyushu University, Fukuoka, 8128581, Japan
[A]ISSP Univ. of Tokyo. Japan

Dopplar broadening of neutron velocity due to brownian motion of magnetite fine particles in ferroliquid have been studied by neutron spin echo(NSE) spectra at Bgagg conditions. The magnetite particle with radius of approximately 10nm with a layer of oleic acid is dispersed in heavy water of which magnetite concentration is about 40 wt% . The powder diffraction patterns of the magnetite in ferrofluid were taken for sample thicknesses of 2mm, 2.5mm and 3mm in thin aluminum containers with rectangular parallelepiped using the ISSP 5G PONTA NSE spectrometer at JRR-3M reactor of JAERI with monochromatic polarized neutron of 2.353 A. Rather high back ground is due to the high incoherent corss-section of hydrogen in oleic acid. NSE measurements were carry out for the ferrofluid sample with the tickness of 2.5mm at the Bragg peaks of (111) ($2\theta = 60.4°$) reflection of aluminum container, (311)(2θ = 55.4°), and (111)2θ = 28.1°) reflections of magnetite up to spin echo time of a order of 10^{-10} s. In these NSE spectra, the the back ground intensity for each Bragg intensity were subtracted. The effects of depolarization in NSE polarization of each magnetite Bragg reflection through ferrofluid were corrected by normalizing it by the NSE polarization of the aluminum reflection of the sample container.

In Fig. 1 normalized NSE visibilities are plotted against spin echo time at three temperatures of 292K, 313K and 333K. The observed NSE polarization at each temperature shows not a simple decay but shows rather oscillatory behavior with increasing of the spin echo time up to 0.1 nsec which means inelastic energy transfer of a order of 10 μeV. The distribution of the velocities of the magnetite particle in ferrofluid might distribute like Brownian motion of the Maxwellian distribution.

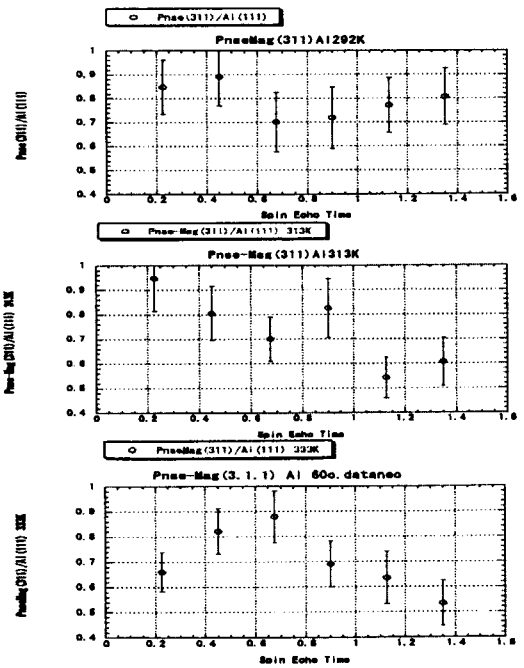


Fig. 1. NSE polarization of magnetite Bragg reflections for (311) normalized by the NSE polarizarion of Al(111) Bragg reflection at temperatures of 292K, 313K and 333K are plotted against spin echo time.

研究テーマ: 高温融点カルコゲン混合系のネットワーク構造
表題: 液体ヒ素－テルル混合系の構造変化

1-4-4 Structural Changes in Liquid As-Te Mixtures

K. Maruyama, S. Takeda[1]

Faculty of Science, Niigata University, Niigata 950-2181, Japan
[1]Faculty of Science, Kyushu University, Ropponmatsu, Fukuoka 810-8560, Japan

Liquid As-Te mixtures show the non-metal to metal transition with increasing temperature. Recent EXAFS study[1] reveals that the network structure of threefold coordinated As and twofold coordinated Te atoms is transformed into the twofold chain structure in the high temperature (metallic) region. In this region, the occurrence of the fluctuation of the interchain correlation is expected. Hence the structural investigation over the scale of about ten ångstroms is inportant. In order to study this structural change, we have performed the neutron scattering measurements for liquid $As_{20}Te_{80}$ and $As_{10}Te_{90}$ by using HERMES spectrometer equipped at JRR-3M in JAERI Tokai.

The samples were sealed in cylindrical fused silica tubes with an inner diameter of 8mm. To decrease the scattering from air and to avoid the damage of the electric heater. the sample environment was exchanged with He gas. The scattering intensity was accumulated for about ten hours for each sample and temperature. After the correction of absorption, scattering from the silica cell and multiple scattering and after the normalization of the efficient of detectors, the structure factor $S(Q)$ was derived as shown in Fig. 1. The obtained $S(Q)$ has enough accuracy for investigation. The disturbance seen in high Q resion is caused by the differnt size of Vanadium rod used for normalization and can be corrected by another Vanadium data. The $S(Q)$ obtained by HIT-II spectrometer with KENS pulsed neutron source is also shown in Fig. 1.

The obtained $S(Q)$ is nearly the same to that from HIT-II except in the low Q region. It is notable that a small but clear prepeak at about Q =1.5Å^{-1} appears in the $S(Q)$. On the other hand, in the $S(Q)$ from HIT-II a prepeak can not be observed. The prepeak is clearer for $As_{20}Te_{80}$ than that for $As_{10}Te_{90}$. And the decrease of peak strength was observed for $As_{20}Te_{80}$ with increasing temperature. The appearance of the prepeak and its behavior is consistent with the model of structure change[1]. As the result, the HERMES spectrometer is very useful for the structural study of the liquid having intermediate range correlation.

In order to investigate the relation between the metal-non metal transition and the structural change, the neutron scattering measirements for wider range of composition and temparature region is planned.

[1]H. Endo., *et al.*, J. Phys.: Condens. Matter, **12** (2000) 6077.

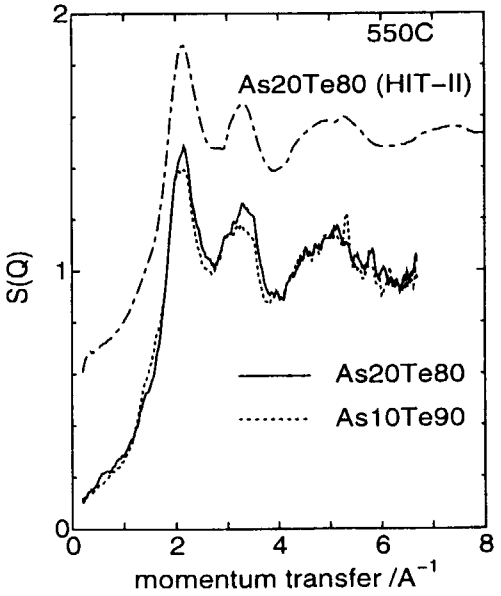


Fig. 1. The structure factor $S(Q)$ for liquid $As_{20}Te_{80}$ and $As_{10}Te_{90}$ at 450°C. The $S(Q)$ obtained by the HIT-II spectrometer is also shown.

研究テーマ：液体金属の電子―イオン相関
表題：回折実験による液体 Ga の電子イオン相関

1-4-5 Electron-Ion Correlation in Liquid Ga by Diffraction Method

S. Takeda, Y. Kawakita, T. Enosaki and K. Maruyama*

Department of Physics, Faculty of Sciences, Kyushu University, Ropponmatsu Fukuoka 810-8560 Japan
** Department of Chemistry, Faculty of Science, Niigata University, Niigata 950-2181 Japan*

Liquid metals can be viewed as a binary mixture between ions and conduction electrons moving nearly freely through an assembly of ions, and many of their physical properties are linked to the corresponding correlation functions. The aim of this study is to report newly measured structural data of neutron diffraction for liquid Ga and provide the electron-ion correlation around Ga^{3+} ion from the diffraction data.

The samples were sealed in thin quartz tubes of inner diameter 8.0mm with 0.3mm wall thickness under a vacuum.

The neutron scattering measurements were carried out at 50 ℃ using the powder diffractometer with a multi detector, HERMES, and the used wavelength was 1.82 Å. The data at high angle region were combined with those observed by TAS-4G previously. In a typical experimental run, counts were taken at 0.5 intervals for $3.0<2\theta<153.0$. The experimental set up and the correction procedures of measured intensity were almost identical to those employed in the previous work for liquid alloys. The experimental uncertainty in the present structural information may be suggested in the following. The accumulated intensity counts are about 8.0×10^4 for sample +cell and 3.8×10^3 for cell in the first peak region. The statistic uncertainty in the structure factor obtained in this work can be estimated to be less than 0.5%.

Figure 1 shows the structure factors of liquid Ga determined by neutron and X-ray diffraction As shown in the figure, the structure factor has an shoulder around Q=3.1 $Å^{-1}$. There has been detected a small but the systematic differences are well appreciated. The quantity of $[S_X(Q)-S_N(Q)]$ evaluated from the two structure factors. The electron charge density around Ga^{3+} ion, $\rho(r)$, the electron-ion correlation function, $g_{ie}(r)$, and metallic form factor, $f_M(Q)$, are evaluated from these small differences. Figure 2 shows the electron-ion correlation function, $g_{ie}(r)$, and the situation is different from the simple metal case.

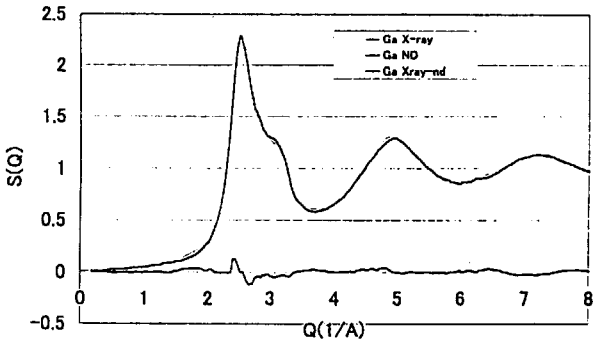


Fig. 1 Structure factors of liquid Ga by X-ray and neutron diffraction, and those differences at 50C.

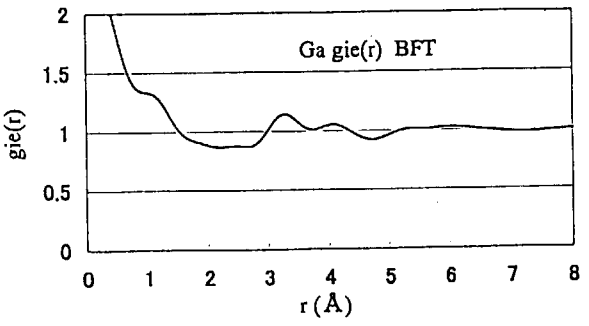


Fig.2 Pair distribution function of ion and electrons, $g_{ie}(r)$, of liquid Ga.

研究テーマ：超イオン導電体における構造不規則性と動的性質
表　　題　：超イオン電導ガラスの中性子弾性散乱

1-4-6 Elastic neutron scattering from superionic conducting glasses

H. Takahashi, N. Rikitake, T. Sakuma[1] and Y. Ishii[2]

Faculty of Engineering, Ibaraki University, Hitachi 316-8511, Japan
[1] Faculty of Science, Ibaraki University, Mito 316-8512, Japan
[2] Japan Atomic Energy Research Institute, Tokai 319-1195, Japan

It is well known that the superionic conductors such as AgI have several common features. It is considered that the random occupation of mobile ions on available sites in the immobile ion cage and the anharmonic thermal vibration of mobile ions are the most promising features for the understanding of conduction mechanism. Superionic conducting glasses also possess high ionic conductivity at ambient temperature. The structural and dynamical features of superionic conducting glasses are very important for understanding of the conduction mechanism. In the structural point of view, it is worth noting that the most of the superionic conducting glasses show pre-peak in low Q region, that is called FSDP. The origin of the FSDP of superionic conducting glasses is considered to be due to the density fluctuation of glass network[1, 2] . In the dynamical point of view, it is suggested that the β glass transition occur at low temperature in AgI-$AgPO_3$ glasses on the basis of specific heat measurement[3] . The purpose of the present study is to obtain information about the thermal vibration and the medium range structure of the superionic conducting glass by the elastic neutron scattering.

Superionic conducting glass $10AgI\text{-}3Ag_2O\text{-}2V_2O_5$ was prepared by melt-quenching method. Powdered glass sample filled into a cylindrical vanadium container of 10 mm diameter was used for neutron diffraction. The measurements were performed on the triple-axis spectrometer TAS-2 with cryostat at JRR-3. The incident neutron wavelength of 2.45 Å is employed. The elastic neutron scattering intensity $I(Q, \omega=0)$ was recorded from 10K up to 300K. The static structure factor was also measured at 300K.

The elastic scattering intensities at several temperatures are shown in Fig. 1. Temperature independent FSDP is seen in the low Q region.

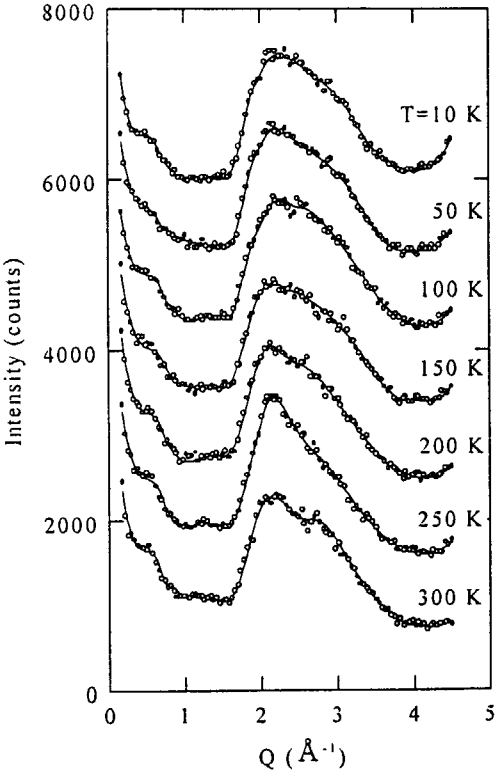


Fig. 1 The elastic scattering intensity for $10AgI\text{-}3Ag_2O\text{-}2V_2O_5$ glass at temperatures of 10, 50, 100, 150, 200, 250 and 300 K.

It is possible to estimate overall Debye-Waller factor using $S(Q)$ and $S(Q, \omega=0)$. Because of relatively narrow Q range of observed structure factor, the effective root-mean-square displacement $\langle u^2\rangle_T - \langle u^2\rangle_{T=10K}$ is evaluated from the $\ln(S(Q, \omega=0)_T / S(Q, \omega=0)_{T=10K})$ versus Q^2 plot. The temperature dependence of the effective root-mean-square displacement is

原子炉：JRR-3M　　装置：TAS-2 (T2-4)　　分野：中性子散乱（液体・不規則物質）

indicated in Fig. 2. It is difficult to extract the individual temperature factor for the multi-component system as in the present glass. So the discussion of thermal vibration is rather tentative at the present stage. The tendency of transition from harmonic to anharmonic thermal vibration or β glass transition is not seen in Fig. 2. The elastic scattering experiments for AgI-free silver vanadate glass are necessary for the detailed discussions of thermal vibration of mobile Ag ion. Figure 3 shows the low Q part of the scattering function. As argued in the previous paper[2], FSDP observed only by X-ray diffraction is originated by the density fluctuation of V-O glass network. While FSDP could not be observed in the static structure factor by neutron diffraction, the elastic neutron scattering detect FSDP around 0.4 $Å^{-1}$ for the first time. The steep increase in X-ray scattering intensity below 0.5 $Å^{-1}$ mainly reflects the range of incident X-ray. FSDP around 0.4 $Å^{-1}$ is considered to result from the incorporated AgI sub-structure having definite dimension. Although, the exact position, the form and the FWHM of FSDP could not be clarified by the insufficient accuracy in the low Q range of the present measurements, the size of AgI sub-structure seems to be estimated at about 15 Å . It is speculated that the reason no FSDP is observed by static structure factor S(Q) is due to the remarkable thermal displacement between Ag and I and resultant damping of FSDP.

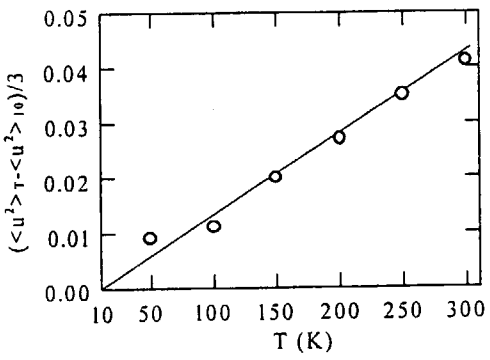


Fig. 2 Temperature dependence of effective root-mean-square displacement.

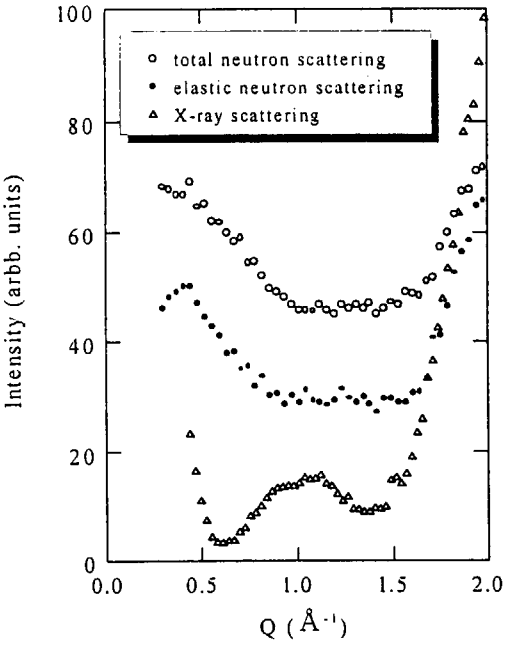


Fig. 3 Low Q part of scattering function of 10AgI-3Ag2O-2V2O5 glass by neutron and X-ray diffraction.

The investigation of the medium range structure characterized by FSDP of AgI doped glasses is interesting for identifying the origin of FSDP and for clarifying the correlation between the medium range glass structure and the high ionic conduction in the superionic conducting glasses. In order to attain above purpose, both the elastic neutron scattering experiments and the static structure factor measurement at low temperature for several glasses including different concentrations of AgI are in progress.

References

1) H. Takahashi et al., J. Mater. Sci., **29** (1994) 2536-2540.
2) H. Takahashi et al., Solid State Ionics, **113-115** (1998) 685-688.
3) M. Nakayama et al., J. Non-Cryst. Solids, **172-174** (1994) 1252-1261.

研究テーマ：マイクロエマルジョンの希薄ラメラ構造の圧力依存性
表題：リン脂質/水系の構造の圧力依存性

1-4-7
Small angle neutron scattering study on the interdigitation phase transition of dipalmitoylphosphatidylcholine induced by pressure.

H. Seto, H. Nobutou[1], N. Yamada[1], Y. Kawabata[1], T. Takeda, M. Nagao[2]

Faculty of Integrated Arts and Sciences, Hiroshima University, Higashihiroshima 739-8521
[1]Graduate School of Biosphere Science, Hiroshima University, Higashihiroshima 739-8521
[2]Institute for Solid State Physics, The University of Tokyo, Tokai 319-1106

An aqueous solution of dipalmitoyl-sn-glycero-3-phosphatidylcholine (DPPC) is known to show a variety of polymorphic phases depending on their environmental conditions such as temperature, composition, salinity, and so on. In many cases, a minimum energy condition requires to form a bilayer structure because of the exclusive force between the hydrocarbon chains and water molecules. However, it is well-known that the lipids conforms non-bilayer structure such as an interdigitated structure ($L_\beta I$) by adopting alcohol. Adachi et al. reported that the alternative arrangement of a set of two alcohol molecules and one phospholipid molecule stabilizes the structure. [1] The molecular packing property could be the origin of the interdigitation phase transition induced by adopting alcohol.

In general, pressure is an important thermodynamic parameter. However, effects of pressure have been less investigated because pressure experiments are more difficult than other experiments such as temperature variation. The situation is the same for the studies on lipid bilayer membranes, which are important for understanding of pressure-anesthetic antagonism, adaptation of marine organisms to extreme depth, and the sterilization by high pressure in food processing Temperature and pressure dependence of the structure of the DPPC aqueous solution was investigated by Winter and Pilgrim by means of SANS (small-angle neutron scattering), and they showed that the pressure induces the $L_\beta I$ phase. [2]

In order to clarify the origin of the pressure-induced phase transition to the $L_\beta I$ phase, SANS experiments were preformed at SANS-U at JAERI, Japan. Because the maximum pressure of our high-pressure cell was about 100 MPa, we prepared aqueous solution of DPPC with adopting small amount of ethanol of 0.8 M and 1.2 M, whose structure at ambient temperature and pressure is L_β'. SANS profiles were collected in the range of $27 \leq T \leq 60$ °C and $0.1 \leq P \leq 100$ MPa. Boththe samples transformed to $L_\beta I$ phase via a transient state. Figure 1 shows a pressure dependence of the SANS profile of the sample with 0.8M ethanol. The structure below 20 MPa was L_α, that at 30 MPa was P_β', and that above 60 MPa was $L_\beta I$. The profiles at 40 MPa and 50 MPa show the transient state existed below the interdigitated structure.

References

[1] T. Adachi, H. Takahashi, K. Ohki, and I. Hatta, Biophys. J., **68** (1995) 1850. See also the references therein.

[2] R. Winter and W. -C. Pilgrim, Ber. Bunsenges. Phys. Chem. **93** (1989) 708.

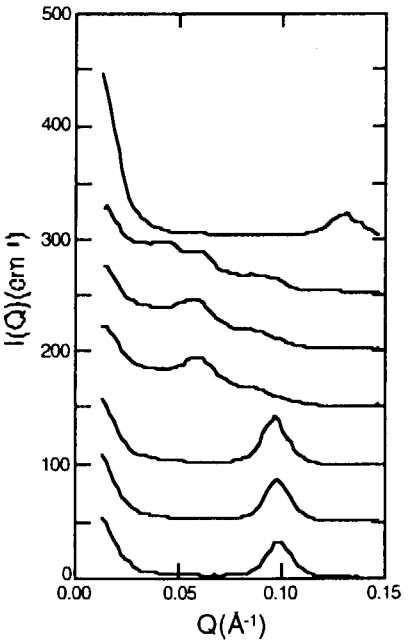


Fig. 1 Pressure dependence of SANS profile of DPPC / D_2O / 0.8M ethanol mixture at T = 318 K.

JRR-3M, C1-2 (SANS-U), 4. Amorphous & Liquid

研究テーマ：マイクロエマルジョンの平均曲率の圧力依存性

表題：水の非干渉性散乱

1-4-8 Incoherent Scattering from Water

M. Nagao and M. Shibayama

Institute for Solid State Physics, The University of Tokyo, 106-1 Shirakata, Tokai 319-1106, Japan

Small-angle neutron scattering (SANS) on hydrogen-containing materials often encounters an uncertainty problem of incohenrent scattering substraction. Wignall et al. reported that the absolute incoherent scattering intensity is not a material parameter but an instrument-dependent parameter. [1] Therefore, it is quite important to evaluate the incoherent scattering intensity properly at the SANS-U spectrometer installed in the guide hall of JRR-3M for quantitative analyses of SANS data. Here, we briefly describe the nature of incoherent scattering based on the incoherent scattering measurement of H_2O/D_2O mixtures.

Mixtures of H_2O/D_2O were filled in quartz cells in order to estimate the incoherent scattering intensity from H and D. The prepared water compositions were varied from 0 to 100 vol.% H_2O. The cell thicknesses were also varied from 0.1 to 0.2, 0.3, and 0.4 cm. The incident neutron wavelength λ was 7.1Å with the wavelength distribution of 10% (FWHM), and the sample to detector distance was 1m. The source aperture was 20mm$^{\phi}$ 4m apart from sample and the sample slit was 5mm$^{\phi}$. The covered momentum transfer was ranged over 0.02 to 0.25Å^{-1}.

The transmission of neutron beam was counted with a ^{3}He detector placed at the center of the transmitted beam just before the 2 dimensional PSD.

In Fig. 1 the obtained transmission is plotted as a function of the volume fraction of water ϕ_H. Introducing Lambert-Beer's relation, the transmission can be written by the following formula,

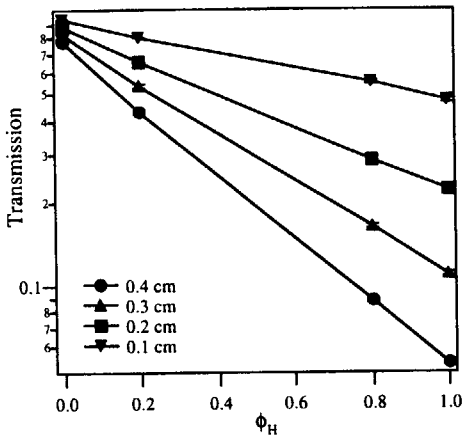


Figure 1: Neutron transmission of water. Legend indicates the thickness of sample cell.

$$T = \frac{I}{I_0} = \exp\left[-d\left\{\mu_H\phi_H + \mu_D(1-\phi_H)\right\}\right], \quad (1)$$

where I and I_0 are the transmitted and incident intensities, T is the neutron transmission, d is the thickness of sample, and μ_H and μ_D are the absorption coefficients of H_2O and D_2O, respectively. Taking logarithm and dividing with d for both sides of Eq. (1), one obtains a linear function of ϕ_H as following;

$$F = \frac{\ln(I/I_0)}{-d} = (\mu_H - \mu_D)\phi_H + \mu_D, \quad (2)$$

The observed values of F were nicely collapsed on a linear function of ϕ_H. The estimated values of μ_H and μ_D for each thickness of sample were summarized in Table 1.

On the other hand, the transmission factor can be written using the scattering

Table 1: Estimated absorption coefficients for H_2O and D_2O. The mean values are μ_H=7.43 cm^{-1} and μ_D=0.70 cm^{-1}.

thickness[cm]	μ_H [cm^{-1}]	μ_D [cm^{-1}]
0.1	7.41	0.69
0.2	7.40	0.69
0.3	7.52	0.70
0.4	7.40	0.73

and the absorption cross sections (σ_s and σ_a) as,

$$T = \exp\Big[-d\Big\{\phi_H\Big[n_H\big(\sigma_s^H+\sigma_a^H\big)\Big] + \Big[n_O\big(\sigma_s^O+\sigma_a^O\big)\Big]\Big\} + \Big\{\phi_D\Big[n_D\big(\sigma_s^D+\sigma_a^D\big)\Big] + \Big[n_O\big(\sigma_s^O+\sigma_a^O\big)\Big]\Big\}\Big]. \quad (3)$$

Here, n_H, n_O and n_D are the number density of H, O, and D, respectively. Hence, μ_H and μ_D can be calculated with known values of σ_s and σ_a. The calculated values of μ_H and μ_D from equation (3) for λ=7.1Å are 5.70 cm^{-1} and 0.70 cm^{-1}, respectively. The observed value of μ_D is excellent agreement with the calculated value. However, that of μ_H from experiment differs significantly from the calculated one. The reason is deduced to be multiple scattering.

In Fig. 2, the observed incoherent scattering from water, $I_{inc,obs}$, is plotted against Q for the case of d = 0.1 cm. The incoherent scattering intensity from H_2O obtained at ILL and NIST are 0.92 and 1.02 cm^{-1}, respectively, and it is consistent with our value; i.e., 0.87 cm^{-1}. It is clear from Fig. 3 that $I_{inc,obs}$ is sample-thickness dependent. Extrapolation of $I_{inc,obs}$ to d = 0 allows one to obtain the incoherent scattering intensity of water independent of the thickness, $I_{inc,0}$.

In Fig. 4, the summarized incoherent scattering intensities are shown. It is clear from the figure that the corrected incoherent scattering is close enough to the calculated values (solid line). In Table 2 the

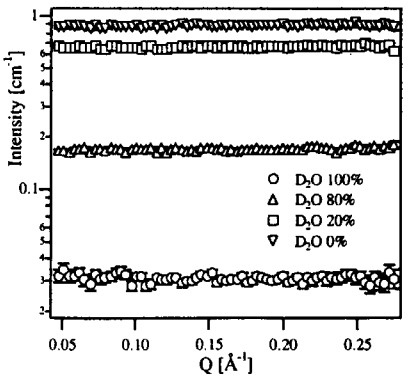


Figure 2: Incoherent scattering intensity from water mixtures for sample thickness of 0.1 cm.

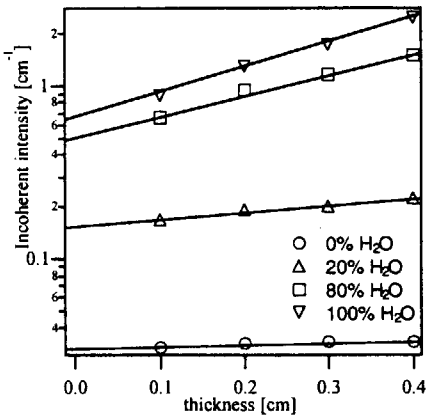


Figure 3: Sample thickness dependence of incoherent scattering intensities from water mixtures.

corrected incoherent scattering intensities, $I_{inc,0}$, and the calculated values are summarized.

From the procedure we can estimate the incoherent scattering intensity from water. The theoretical value we showed is calculated for λ=1.8Å. Therefore, the deviation of the experimental values from the calculated one may be the reason.

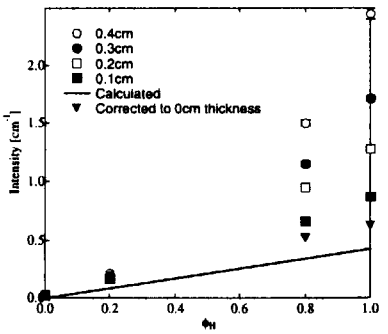


Figure 4: Incoherent scattering intensities from various thicknesses of H_2O and D_2O mixtures. The incoherent scattering intensity calculated with known values for H, D, and O for λ = 1.8 Å are shown with the solid line.

Table 2: Obtained, calculated, and extrapolated incoherent scattering intensities.

	D_2O 100%	D_2O 80%	D_2O 20%	D_2O 0%
0.4 cm	0.034	0.22	1.50	2.44
0.3 cm	0.033	0.20	1.15	1.72
0.2 cm	0.032	0.19	0.95	1.28
0.1 cm	0.031	0.17	0.66	0.87
Extrapolated	0.030	0.16	0.53	0.63
Calculated	0.011	0.094	0.35	0.43

[1] W. S. Dubner, J. M. Schultz and G. D. Wignall, J. Appl. Cryst. **23**, 469 (1990).

研究テーマ：水／エタノール二成分溶液中のキモトリプシン・インヒビター２の中性子小角散乱
表題：中性子小角散乱法によるアセトニトリル－水混合溶液中の会合体形成に関する研究

1-4-9 Small-Angle Neutron Scattering Study on Aggregation in Acetonitrile-D_2O Mixtures

T. Takamuku,[a] A. Yamaguchi,[a] M. Tabata,[a] K. Yoshida,[b] T. Yamaguchi,[b] and M. Nagao[c]

[a]*Department of Chemistry, Faculty of Science and Engineering, Saga University, Honjo-machi, Saga 840-8502*
[b]*Department of Chemistry, Faculty of Science, Fukuoka University, Nanakuma, Jonan-ku, Fukuoka 814-0180*
[c]*Neutron Scattering Laboratory, The Institute of Solid State Physics, The University of Tokyo, Tokai 319-1106*

Introduction

For a long period, microheterogeneity in acetonitrile-water mixtures has often been discussed by many authors on the basis of various physicochemical properties, such as self-diffusion coefficients[1,2] and Kirkwood-Buff parameters.[3] However, no detailed information (size and shape) of microheterogeneity has been reported so far. The small-angle neutron scattering (SANS) method enables us to evaluate fluctuations in density and/or concentration, and the size and shape of aggregates formed in solutions. In particular, the SANS method with H/D substitution is a powerful tool to investigate aggregation in acetonitrile-water mixtures because the scatterings from acetonitrile (CH_3CN) and water (D_2O) have the high contrast due to different scattering lengths of -3.74 and 6.67 fm for H and D, respectively.

In the present study, to clarify microheterogeneity in acetonitrile-water mixtures at the mesoscopic scale, SANS measurements at an ambient temperature have been made on acetonitrile-D_2O mixtures in various acetonitrile mole fractions, x_{AN}. On the basis of the Debye correlation length[4] estimated from the SANS spectra, the mesoscopic order of microheterogeneity has been discussed.

Experimental

Acetonitrile-D_2O mixtures at x_{AN} = 0.1, 0.2, 0.25, 0.3, 0.4, 0.5, 0.6, and 0.8 were prepared in a nitrogen-filled glove box. SANS measurements on the acetonitrile-D_2O mixtures were made at 298.2 ± 0.1 K on SANS-U at a reactor JRR-3M in JAERI, Tokai. The momentum transfer Q (= $4\pi\lambda^{-1}\sin\theta$; λ the wavelength, 2θ the scattering angle) range covered was 0.03–0.15 Å.[5] The SANS intensities on SAUS-U were corrected for background, absorption, and cell scattering and normalized by using the scattering of luporen.[6]

Results and Discussion

Fig. 1 shows the normalized SANS spectra for the acetonitrile-D_2O mixtures at various x_{AN}. As shown in Fig. 1, the scattering intensities at $0.03 \le Q/Å^{-1} \le 0.05$ are most increased at x_{AN} = 0.3 and 0.4 among the acetonitrile mole fractions investigated, while no or less small-angle scatterings are observed at x_{AN} = 0.1, 0.6, and 0.8. It is thus suggested that aggregation in the acetonitrile-D_2O mixtures is most enhanced at x_{AN} = 0.3-0.4.

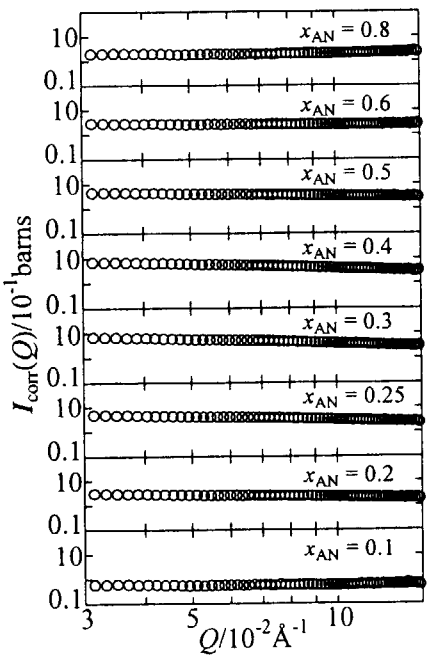


Fig. 1. SANS spectra for the acetonitrile-D_2O mixtures at various x_{AN}.

To elucidate aggregation in the acetonitrile-D_2O mixtures, the Debye correlation length was calculated. Neutron scattering intensities, $I_{corr}(Q)$, in a small Q-range have a linear relation with Q^2 as described by

$$I_{corr}(Q) = I_0\left(1 - \frac{L_D^2}{6}Q^2\right), \quad (1)$$

where I_0 is the scattering intensity at Q = 0 Å^{-1} and L_D is the Debye correlation length.[4] Fig. 2 shows the plots of $I_{corr}(Q)$ for the acetonitrile-D_2O mixtures as a function of Q^2. As seen in Fig. 2, the theoretical values (solid lines) from a least-squares fitting procedure with eq. (1) reproduce well the experimental ones (circles), except for the mixtures at x_{AN} = 0.25, 0.3, and 0.4, where the theoretical values slightly deviate from the straight lines. It is likely that aggregates of several dimension are formed at these compositions, i.e. the multi-dispersive parttern.[7] Hence, the L_D values at the compositions should be regarded as an average one of concentration fluctuations.

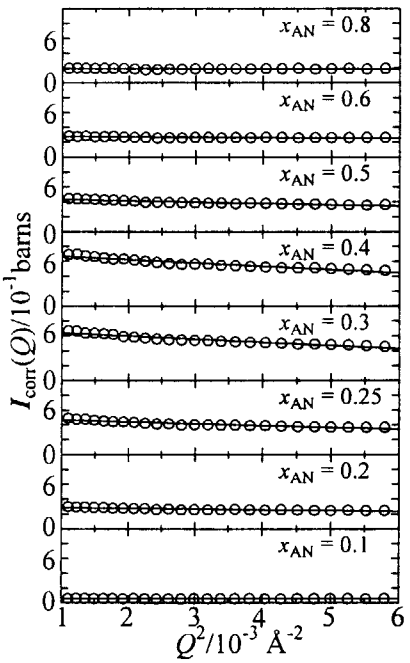


Fig. 2. Plots of $I_{corr}(Q)$ for the acetonitrile-D_2O mixtures as a function of Q^2. The observed values (circles) and least-squares fitted ones (solid lines) by eq. (1).

In Fig. 3, the L_D values determined are plotted as a function of acetonitrile mole fraction. This figure shows that microheterogeneity is most enhanced with L_D~19 Å between x_{AN} = 0.3 and 0.4. It would be reasonable to conclude that the concentration fluctuations arise from microheterogeneity between acetonitrile and D_2O aggregates because the scattering of acetonitrile aggregates has the high contrast from that from D_2O clusters in the present SANS measurements. The present SANS result is in good agreement with the previous results from large-angle X-ray scattering experiments[8] and from the Kirkwood-Buff parameters,[3] which have concluded microheterogeneity at $0.2 \le x_{AN} < 0.6$ with a maximum at x_{AN} = ~0.4. Thus, we can say that the present results are the first direct evidence for microheterogeneity in acetonitrile-water mixtures at the mesoscopic scale.

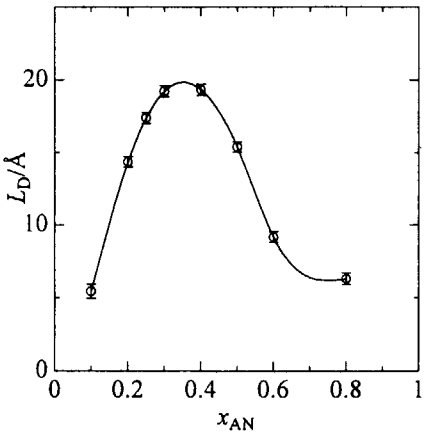


Fig. 3. Debye correlation lengths L_D for the acetonitrile-D_2O mixtures as a function of x_{AN}.

References

1 A. J. Easteal, *Austr. J. Chem.*, **33,** 1667 (1980).
2 E. Hawlicka, *Z. Naturforsch.*, **43a,** 769 (1988).
3 Y. Marcus and Y. Migron, *J. Phys. Chem.*, **95,** 400 (1991).
4 P. Debye, *J. Chem. Phys.*, **31,** 680 (1959).
5 Y. Ito, M. Imai, and S. Takahashi, *Physica B,* **889,** 213 (1995).
6 G. D. Wignall and F. S. Bates, *J. Appl. Cryst.*, **20,** 28 (1987).
7 O. Kratly and O. Glatter, "Small-angle X-ray Scattering", Academic Press, San Diego (1982).
8 T. Takamuku, M. Tabata, A. Yamaguchi, J. Nishimoto, M. Kumamoto, H. Wakita, and T. Yamaguchi, *J. Phys. Chem. B,* **102,** 8880 (1998).

研究課題：両親媒子系複雑液体のスローダイナミックス

表題：中性子スピンエコー法による両親媒子系複雑液体のスローダイナミクス

1-4-10 Neutron Spin Echo Investigations on the Slow Dynamics in Complex Fluids Involving Amphiphiles

T. Takeda*, Y. Kawabata†, H. Seto* Norifumi Yamada† and M. Nagao§

*Faculty of Integrated Arts and Sciences and †Graduate School of Bio-Sphere Science, Hiroshima University, Higashi-Hiroshima 739-8521, Japan

§Institute for Solid State Physics, University of Tokyo, Tokai, Naka Ibaraki 319-1106, Japan

In the dipalmitoylphosphatidylcholine (= DPPC)/water system, the liquid crystalline phase L_α appears above the main-transition temperature T_m (about 41°C). The result obtained from neutron spin echo (NSE) experiments on the sample with a lamellar repeat distance d_l = 54 Å could be explained by a mode with a relaxation rate determined mainly by the friction between the two layers constituting the bilayer[1]. d_l varies greatly with an addition of salt in the DPPC/water system. In order to study the dynamics further in undulation of lipid bilayers, NSE experiments were carried out on the dilute lamellar phase of the DPPC/D_2O /$CaCl_2$ system with d_l longer than 300 Å in order to avoid the effect on the single membrane dynamics from neighbouring sheets of membranes. d_l is roughly in inverse proportion to DPPC concentration as shown in Fig. 1.

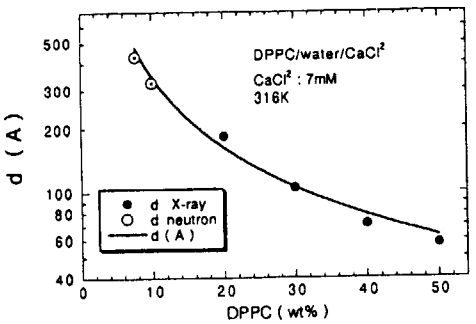


Fig. 1 DPPC cencentration dependence of the lamellar repeat distance d_l obtained from small angle X-ray and neutron scattering experiments. The solid line is a fitting curve to inverse proportion to DPPC concentration.

The scattering vector Q and time t dependent intermediate functions $I(Q,t)$ obtained from the NSE experiments were well fitted to the following equation,

$$I(Q,t) = I(Q,0)\exp[-(\Gamma t)^{2/3}] \quad . \qquad (1)$$

The relaxation rates Γ obtained from the fitting to Eq.(1) increased as Q^3 over the range of Q from 0.05 Å^{-1} to 0.14 Å^{-1}. So with the case of the non-ionic surfactant n-dodecyl pentaoxylethylene glycol ether ($C_{12}E_5$) /n-octane / D_2O system[2], these NSE results supported the theory presented by Zilman and Granek[3]. They considered an ensemble of membrane plaquettes at random orientations and used the Helfrich bending free energy to describe membrane undulations in sponge and lamellar phases and predicted a stretched exponential relaxation of $I(Q,t)$ as follows Eq.(1) where Γ is given by

$$\Gamma = 0.025\gamma(k_BT/\varkappa)^{1/2}(k_BT/\eta)Q^3. \qquad (2)$$

Here, $\varkappa$ is the bending modulus of the membrane and η the viscosity of the surrounding medium. Figure 2 shows an example of the dependence of $\varkappa$ on temperature[4]. $\varkappa$ estimated in the lipid system using their theory. The value of $\varkappa$ estimated decreases monotonically with increasing temperature.

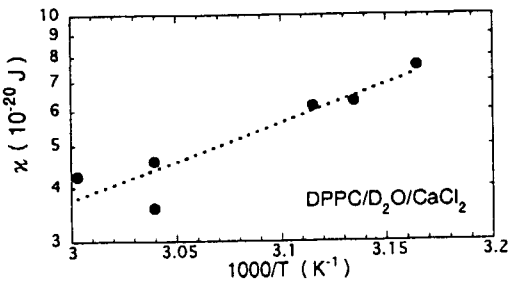


Fig. 2. The dependence of the reduced bending modulus $\varkappa$ of the membrane on the temperature T obtained from NSE experiments for the lipid sample in which 6.3wt% DPPC was dispersed in D_2O solutions with 6.6mM $CaCl_2$.

1. W. Pfeiffer et al: Europhy. Lett. 23 (1993) 457.
2. T.Takeda et al, J. Phys. Chem. Solids 60 (1999) 1375.
3. A. G. Zilman and R. Granek: Phys. Rev. Letters 77 (1996) 4788.
4. T. Takeda et al: J. Phys. Soc. Jpn. 70 (2001) Suppl. A 323.

Facilities and Instruments	Research field
JRR-3M NSE(C2-2)	4. Amorphous & Liquid
JRR-3M SANS-U(C1-2)	

研究課題：中性子スピンエコー法を用いた両親媒子膜の温度、圧力効果
表題：中性子スピンエコー法、小角散乱法を用いたマイクロエマルジョン droplet 系における温度、圧力効果

1-4-11
NSE and SANS Studies on the Effects of Temperature and Pressure in a Droplet Microemulsion System

Y. Kawabata[1], M. Nagao[2], H. Seto[3], and T. Takeda[3]

[1]*Graduate School of Bio-Sphere Science, Hiroshima University,* [2]*Faculty of Integrated Arts and Sciences, Hiroshima University, 1-7-1 Kagamiyama, Higashi-Hiroshima 739-8521,* [3]*Institute for Solid State Physics, The University of Tokyo, 106-1, Shirakata, Tokai, 319-1106*

A mixture of water, n-decane and AOT (dioctyl sulfosuccinate sodium salt) is known to form a water-in-oil droplet microemulsion at room temperature and ambient pressure. A phase transition to a two-phase coexistence with a dilute droplet and a dense droplet phases is known to be induced by temperature and/or pressure [1]. It has been suggested that the mechanism of this phase transition is dominated by the static and dynamic properties of amphiphilic membranes, such as their curvature elasticity.

In this study, we investigated the static and dynamic properties of amphiphilic membranes using small-angle neutron scattering (SANS) and neutron spin echo (NSE) in a dilute droplet system in order to clarify the mechanism of the phase transitions. Dilute systems have been studied by means of SANS and NSE [2-4], and the way to analyze them has been established. Therefore, the system is suitable to investigate the effects of temperature and pressure on the phase transitions.

For our experiments, we used a mixture of 5.4% vol. of AOT (99 % purity, purchased from Sigma Inc.), 4.6% vol. of D_2O (99.9 at.%-D purchased from Isotec Inc.) and 90% vol. of $C_{10}D_{22}$ (99.9 at.%-D, purchased from Isotec Inc.). The composition leads that the radius of water-in-oil droplet is about 33Å at room temperature and ambient pressure, and that the volume fraction of droplets is 10%.

The SANS experiments were carried out at the SANS-U spectrometer at C1-2 port in the cold neutron guide hall of JRR-3M in JAERI, Tokai. The wavelength of the incident neutron beam was 7.0Å with a spread of $\Delta\lambda/\lambda$=10%. The distance from the sample to the 2-dimensional position sensitive detector was 1m and 4m. The momentum transfer Q was covered over $0.01 \leq Q$ [Å^{-1}] ≤ 0.14. The temperature was varied from 23 °C to 80 °C

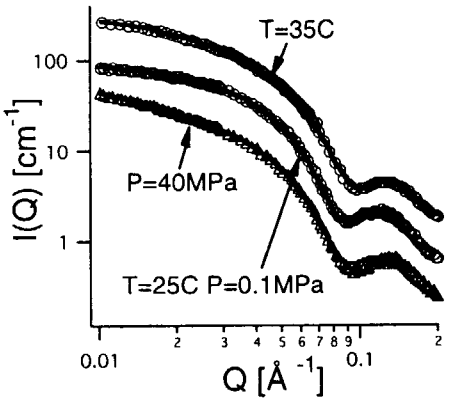


Figure 1: SANS profiles observed at 3 conditions. The SANS profile at T=25°C and P=0.1MPa is shown in the absolute unit. Others are shifted 80 cm^{-1} for better visualization.

with a step of about 3°C. The pressure was varied from 0.1 MPa to 66.5 MPa with a step of about 5 MPa using a high-pressure cell.

The scattering profiles $I(Q)$ obtained from the SANS experiments are shown in Figure 1. It is clear that the spectrum at high temperature is almost the same with that at high pressure. In a dilute droplet system, $I(Q)$ can be expressed as the form factor of spheres. Therefore, we can conclude that the static features of droplets at high temperature are similar with those at high pressure. Note that because of the critical scattering, the scattering intensities at low Q region become larger with increasing temperature and pressure.

The NSE experiments were performed at the ISSP- NSE spectrometer at the C2-2 port in the cold neutron guide hall of JRR-3M. The wavelength of the incident neutron beam was 7.14Å with a spread of $\Delta\lambda/\lambda$=18%. The measured Q ranged over $0.04 \leq Q$ [Å^{-1}] ≤ 0.13 and Fourier time t over $0.15 \leq t$ [ns] ≤ 15. The

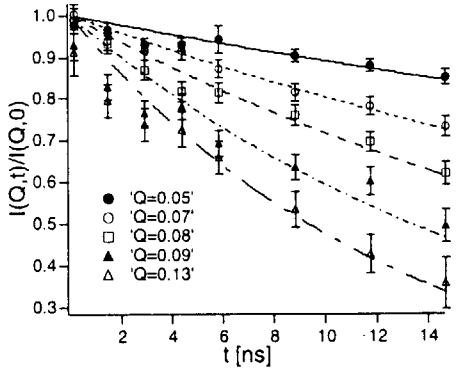


Figure 2: $I(Q,t)/I(Q,0)$ observed from an NSE experiment at room temperature and ambient pressure. Lines are fitting results to Eq. (1).

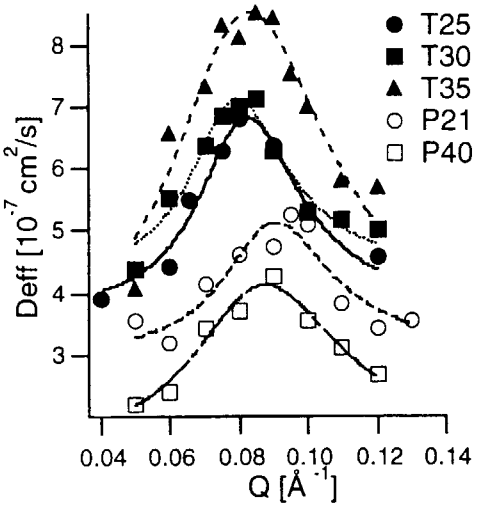


Figure 3: D_{eff} derived from NSE data for various conditions. Lines are preliminary fitting results to a model proposed by Milner and Safran. With increasing temperature, D_{eff} became larger, on the contrary, it became smaller with increasing pressure.

temperature was varied from 25 °C to 35 °C with a step of 5 °C. The pressure was varied from 0.1 MPa to 40 MPa with a step of about 20 MPa with the high-pressure cell for NSE experiments, which was made of non-magnetic Stainless steel and Inconel. However the cell was magnetized slightly, and it caused neutron spin depolarization. We canceled out the magnetic field by increasing the guide magnetic field around the cell using the correction coils.

The intermediate correlation functions, $I(Q,t)/I(Q,0)$, obtained from the NSE experiments are shown in Figure 2. They decay as a single exponential function as follows,

$$I(Q,t)/I(Q,0) = \exp(-D_{eff}Q^2t) \qquad (1)$$

where D_{eff} is the effective diffusion coefficient including the information about the membrane fluctuation and the translational diffusion of droplets [5]. The Q dependence of the obtained D_{eff} is shown in Figure 3. Lines indicate the preliminary fitting results to a model proposed by Milner and Safran [5]. The D_{eff} at high temperature is much larger than that at high pressure. This result indicates that the dynamical features of membranes or those of droplets at high temperature are quite different from those at high pressure.

Combining the NSE and SANS results, we can conclude that effects of temperature and pressure on the dynamics of droplets played opposite roles although the apparent structures of high-temperature and high-pressure phases were quite similar. This fact suggests that the mechanism of the structural formation with increasing temperature is different from that with increasing pressure. Detailed analyses are under way for understanding the membrane dynamics.

References

[1]. Z. Saïdi et al., *J. Phys. D: Appl. Phys.* **28** 2108-2112 (1995).
[2]. J. S. Huang et al. *Phys. Rev. Lett.* **59** 2600-2603 (1987).
[3]. B. Farago et al., *Phys. Rev. Lett.* **65** 3348-3351 (1990).
[4].T. Hellweg and D. Langevin, *Physica A*, **264** 370-387 (1999).
[5].S. T. Milner and S. A. Safran, *Phys. Rev. A* **36** 4371 (1987).

研究テーマ: メゾスケール領域における水／アルコール混合溶液の構造とダイナミクス
表題: 中性子スピンエコー法によるブトキシエタノール／水のスローダイナミクス

1-4-12

Slow Dynamics of *n*-Butoxyethanol/water Mixture by Neutron Spin Echo Techniques

K. Yoshida[1], T. Yamaguchi[1], M. Nagao[2], Y. Kawabata[3], and H. Seto[3]

[1]*Department of Chemistry, Faculty of Science, Fukuoka University, Fukuoka 814-0180, Japan*

[2]*Institute for Solid State Physics, University of Tokyo, Tokai 319-1106, Japan*

[3]*Faculty of Integrated Arts and Sciences, Hiroshima University, Higashi-hiroshima 739-8521, Japan*

n-butoxyethanol/water mixtures undergo phase separation at a lower critical solution temperature (LCST) of 49 °C. Small-angle neutron scattering (SANS) has revealed molecular aggregates in the mixture even less than LCST. The result has suggested that the microscopic structure is related to a microscopic phase separation preceding macroscopic separation. In this study, neutron spin echo (NSE) measurements have been carried out to reveal the mechanism of molecular aggregation in the mixtures.

An NSE spectrometer is equipped at the $C_{2\text{-}2}$ cold neutron guide port of JRR-3M, JAERI. A sample solution is 9 mol% of n-butoxyethanol in D_2O and sealed in a quartz cell of 2 mm thickness. We used the alcohol whose hydroxyl part is deuterated since the hydroxyl hydrogen of the alcohol exchanges with water hydrogen. The temperature was controlled to within±0.1°C with a thermostat to circulate water.

The intermediate correlation function $I(Q,t)$ obtained from the NSE experiments was fitted to the following equation on basis of the Brownian motion,

$$I(Q,t)/I(Q,0) = \exp(-\Gamma t) \qquad (1)$$

where Γ is the relaxation rate. Figure 1 shows the Q-dependence of the relaxation rate Γ. The diffusion coefficient D was obtained from the following equation.

$$\Gamma = DQ^2 \qquad (2)$$

The values of D are 6.6×10^{-7} and 7.8×10^{-7} cm^{-2} s^{-1} at 25 and 37 °C, respectively. These values seem to reflect the motion of molecular aggregates because they are about 10^2 times smaller than those of water and alcohol. The value of D increases with increasing temperature in spite of an increase in the correlation length obtained from SANS [1]. These findings cannot be explained by a Stokes-Einstein model where a stable cluster moves independently as a micelle of surfactants. The averaged activation energy of the diffusion constant is 19 kJ mol^{-1}, which corresponds to the hydrogen bonding energy. This implies the hydrogen bond plays an important role in the mechanism of cluster formation.

In this study, we discussed the temperature dependence of the dynamics of the mixture. The critical phenomena depend on temperature, pressure, and composition. Further experiments as a function of pressure and composition are in progress.

[1] G. D'Arrigo and J. Teixeira, *J. Chem. Soc. Faraday Trans.* **86**, 1503 (1990).

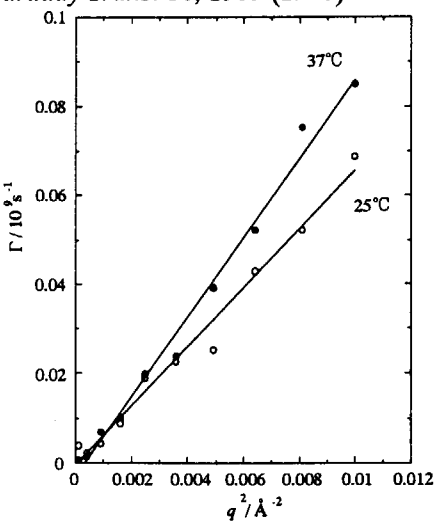


Fig. 1. Q-dependence of the relaxation rate Γ of the 9-mol% *n*-butoxyethanol/water mixture

研究テーマ：液体テルル-セレン混合系の半導体-金属転移領域におけるダイナミクス異常
表題　：液体テルル-セレン混合系の半導体-金属転移領域におけるダイナミクス異常

1-4-13 Anomalous Dynamics in Liquid Te-Se Mixtures in the Semiconductor-to-Metal Transition Range

M. Yao, Y. Kawakita[1], Y. Ohmasa and A. Chiba

Department of Physics, Graduate School of Science, Kyoto University, Sakyo-ku, Kyoto 606-8502
[1]Department of Physics, Faculty of Science, Kyushu University, Ropponmatsu, Fukuoka 810-8560

In the solid state, both Te and Se are semiconductors composed of helical chains in which each atom is bonded to two adjacent atoms by covalent bonds. When Te is melted by heating, it exhibits metallic properties in contrast to Se in which the helical chain structure is more or less preserved even in the liquid state. It is well known that in liquid Te-Se mixtures a semiconductor-to-metal(S-M) transition occurs by raising temperature and that the transition region shifts towards higher temperature as the Se concentration increases. Recently, based upon observations of anomalous sound attenuation, we have suggested that there may occur a slow dynamics with a nanosecond time scale in the S-M transition range. It is interesting to consider how the structural properties correlate with the electronic properties and how the dynamic properties are influenced by the S-M transitions.

In the present study, we have carried out neutron scattering experiments for liquid $Te_{40}Se_{60}$ (l-$Te_{40}Se_{60}$, semiconducting regime) and liquid Te (l-Te, metallic regime) at the fixed temperature, 500 ℃, using the direct geometry neutron spectrometer AGNES installed in the JRR-3M. Figure 1 shows the effective vibrational density of states as a function of energy for l-Te and l-$Te_{40}Se_{60}$ at 500 ℃. In the semiconducting regime (l-$Te_{40}Se_{60}$) a gap appears between 18 and 20 meV and one can distinguish between the bond-stretching (above 20meV) and bond-bending (below 18meV) modes, while in the metallic regime (l-Te) these modes seem to be merged into a broad band and shift to lower energy. This implies that the inter-chain coupling is prominent in the metallic regime. Figure 2 shows $G(Q,E) \approx S(Q,E)E/Q$ of l-Te at 500 ℃. An 'acoustic' phonon dispersion curve extending up to 7 meV with a slightly variable periodicity was observed. The periodicity may be referred to as a quasi-Brillouin zone, near 1 $Å^{-1}$, which originates in the half of the first peak position of $S(Q)$ at 2 $Å^{-1}$.

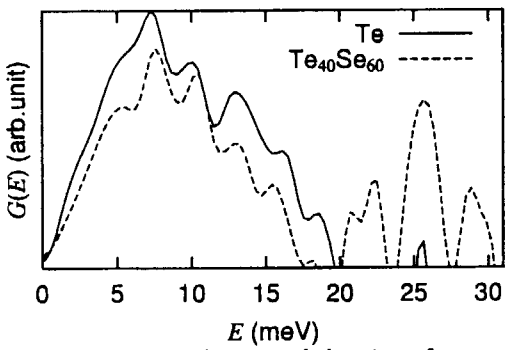


Fig.1: Effective vibrational density of states, $G(E)$ of l-Te (solid line) and l-$Te_{40}Se_{60}$ (broken line) at 500 ℃.

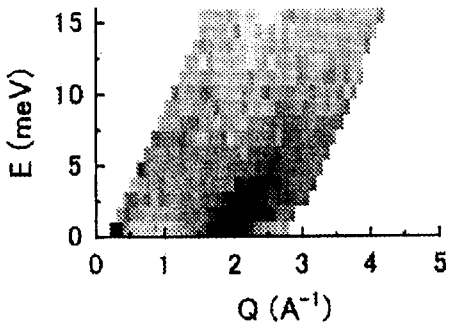


Fig.2: Contour map of $S(Q,E)$E/Q of l-Te at 500 ℃.

研究テーマ：制限空間内における極性分子のダイナミクス
表題：中性子散乱による MCM-41 メソ孔内のアセトニトリル分子のダイナミクスに関する研究

1-4-14
Neutron Scattering Study on Dynamics of Acetonitrile Molecules in MCM-41

Shigeharu Kittaka,[a] Shuichi Takahara,[a] Yasushige Kuroda,[b] Toshinori Mori,[b] and Toshio Yamaguchi[c]

[a] *Department of Chemistry, Faculty of Science, Okayama University of Science, 1-1 Ridaicho, Okayama 700-0005, Japan*
[b] *Department of Chemistry, Faculty of Science, Okayama University, Tsushima, Okayama 700-8530, Japan*
[c] *Department of Chemistry, Faculty of Science, Fukuoka University, Nanakuma, Jyonan-ku, Fukuoka 814-0180, Japan*

Introduction

We have investigated dynamics of water[1] and methanol[2] molecules confined in mesopores of MCM-41 by using neutron scattering, and found that both of rotational and translational motions of these molecules in MCM-41 become slower compared with those in bulk liquid around room temperature. In the present study, dynamics of acetonitrile molecules confined in MCM-41 were investigated by using quasi-elastic neutron scattering (QENS). Acetonitrile molecules do not form hydrogen bonds among them, while water and methanol molecules form hydrogen bond. The aim of this study is to investigate a role of hydrogen bond in molecular motions in confined space. MCM-41 is one of the most suitable samples for studying properties of confined liquid, because it contains highly controlled cylindrical channels with very narrow pore size distribution.

Experimental Section

Two kinds of siliceous MCM-41 samples (C10 and C18) were prepared by the method of Beck *et al.*[3] The pore diameters determined from the N_2 adsorption isotherms were 2.14 (C10) and 3.74 nm (C18). For the neutron scattering measurements, we prepared three kinds of samples having different amounts of adsorption for each MCM-41 sample. (1) pore-filled sample: the mesopores were filled with the adsorbed molecules; (2) monolayer sample: the pore walls are covered with monolayer of the adsorbed molecules; (3) dry sample: MCM-41 samples were evacuated at room temperature to remove physisorbed molecules but chemisorbed species, for example the surface hydroxyls, remained.

QENS measurements were carried out by using time-of-flight type spectrometer AGNES[4] installed at the JRR-3M reactor of Japan Atomic Energy Research Institute. The wavelength of neutron beam was 4.22 Å, the momentum transfer (Q) range 0.68-1.87 Å^{-1}, and the temperature (T) range 100-297 K. A resolution function of the instrument was determined with a vanadium rod.

Results and Discussion

QENS spectra of bulk, pore-filled and monolayer samples at Q = 0.98 Å^{-1} and T = 297 K are shown in Figure 1. Here, the displayed spectra are the difference between raw spectra and spectra of the dry sample, and thus contain the contributions only from the acetonitrile molecules. All the spectra are normalized ones, in which peak maxima have been coincided with each other to emphasize the change in quasi-elastic wings of the spectra. By comparing broadening of the peaks, it is found that motions of acetonitrile molecules become slower in the following order: bulk, pore-filled (C18 and C10) and monolayer samples. On the dry sample, quasi-elastic broadening was not observed (not shown).

Typical examples of Q-dependence of the QENS spectra are shown in Figure 2. The spectra were analyzed by a model in which the diffusive

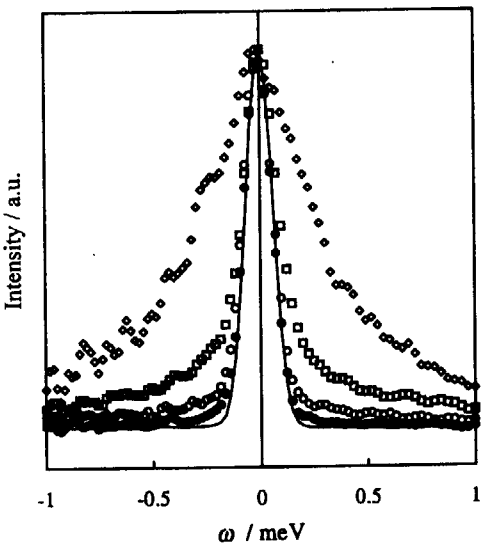


Figure 1. QENS spectra of vanadium (－), bulk (◇), pore-filled (C10:○, C18:□) and monolayer (C10:●) samples at Q = 0.98 Å^{-1} and T = 297 K.

motions of the acetonitrile molecules are composed of the translation, the rotation of the C3 axis and the rotation about the C3 axis. The fitting results are shown with solid lines in Figure 2. The translational diffusion constant D_T and relaxation time τ_R of the rotation of the C3 axis of acetonitrile molecules were determined by the fitting. Figure 3 and 4 show temperature dependence of D_T and τ_R, respectively. As shown in these figures, the translational motion of acetonitrile molecules is decelerated by the confinement in mesopores, while the rotational ones were not changed. This result for acetonitrile is different from the results for water[1] and methanol[2] in MCM-41, i.e., both the translational and rotational motions of these molecules were decelerated by the confinement. The difference can be explained by the fact that cooperativity of molecular motions in acetonitrile is lower than those in water and methanol due to the lack of hydrogen bonds.

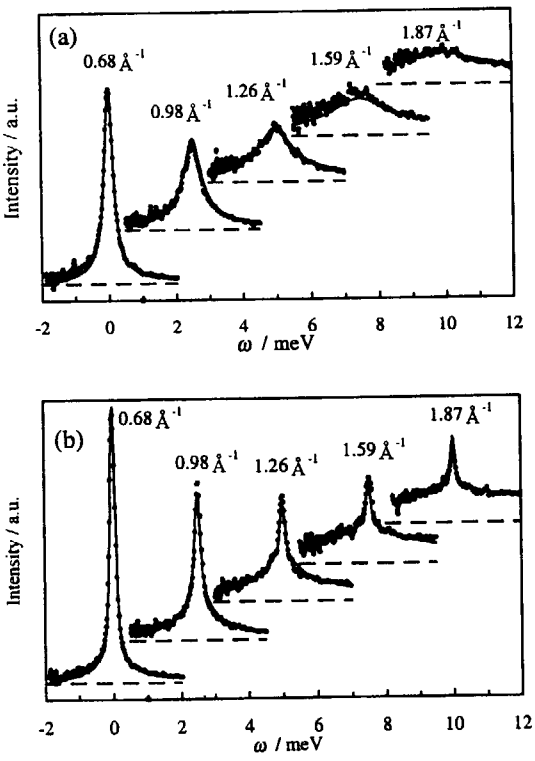


Figure 2. Q-dependence of QENS spectra of the bulk sample (a) and the C18 pore-filled sample (b) at 297 K. Closed circles indicate the experimental data. Solid and broken lines are for the total fit and the background, respectively.

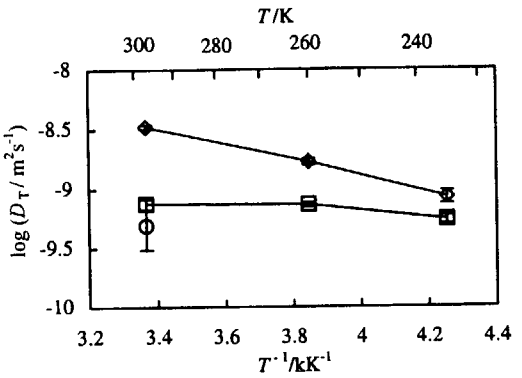


Figure 3. Arrhenius plot of translational diffusion constant of acetonitrile molecules in the pore-filled (C10:○, C18:□) and the bulk (◇) samples.

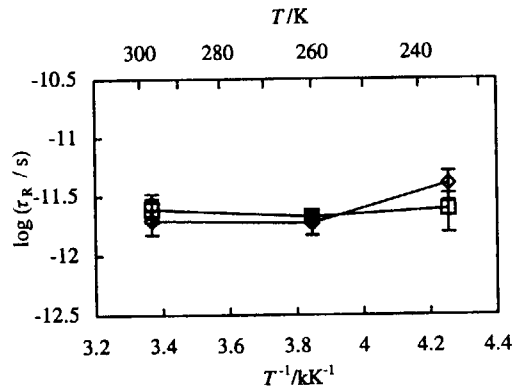


Figure 4. Arrhenius plot of relaxation time of the rotation of the C3 axis of acetonitrile molecules in the pore-filled (C10:○, C18:□) and the bulk (◇) samples.

References

1 Takahara, S.; Nakano, M.; Kittaka, S.; Kuroda, Y.; Mori, T.; Hamano, H.; Yamaguchi, T. *J. Phys. Chem. B*, **1999**, *103*,5814.

2 Kittaka, S.; Serizawa, A.; Iwashita, T.; Takahara, S.; Takenaka, T.; Kuroda, Y.; Mori, T. *Studies in Surface Science and Catalysis* **2001**, *132*, 653.

3 Beck, J. S.; Vartuli, J. C.; Roth, W. J.; Leonowicz, M. E.; Kresge, C. T.; Schmitt, K. D.; Chu, C. T-U.; Olson, D. H.; Sheppard, E. W.; McCullen, S. B.; Higgins, J. B.; Schlenker, J. L. *J. Am. Chem. Soc.* **1992**, *114*, 10834.

4 Kajitani, T.; Shibata, K.; Ikeda, S.; Kohgi, M.; Yoshizawa, H.; Nemoto, K.; Suzuki, K. *Physica B* **1995**, *213&214*, 872.

研究テーマ：分子性配向ガラスの低振動数ダイナミクス
表題：シクロオクタノール配向ガラスの低振動数ダイナミクス

1-4-15 Low-frequency Dynamics of Cyclooctanol Orientational Glass

O. Yamamuro, H. Yamasaki, Y. Madokoro, and T. Matsuo

Department of Chemistry, Graduate School of Science, Osaka University, 1-1 Machikaneyama-cho, Toyonaka, Osaka 560-0043, Japan

Introduction

Globular molecules often crystallize into an intermediate phase in which the molecular center of mass is ordered as in normal crystals while the molecular orientation is disordered as in liquids. This phase is usually called "plastic crystal" based on its plasticity under mechanical stress. Plastic crystals can sometimes be quenched by rapid cooling into a "orientational glass" where the disordered molecular orientations are frozen-in. Orientational glasses have been studies as a simplified model of ordinary structural glasses since orientational glasses have disorder only in molecular orientations [1,2].

The present study deals with the THz dynamics of orientational glasses which has not been studied so far. For the structural glasses, there are two main research subjects in this frequency range; one is the boson peak and the other is the fast β relaxation. The purpose of this study is to examine the existence of the boson peak and fast β relaxation in orientational glasses. We chose cyclooctanol as the material examined in this study, since the plastic phase of cyclooctanol is stable in a wide temperature range and is easily quenched into an orientational glass [3,4].

Experimental

Cyclooctanol (purity: 98 %) purchased from Tokyo Kasei Kogyo Co., Ltd. was dried with molecular sieves and purified by fractional distillation under reduced pressure (19—20 torr).

The neutron scattering experiments were performed using a direct geometry chopper-type TOF spectrometer AGNES [5] installed at the cold neutron guide (C3) of JRR-3M (Tokai, Japan). The elastic energy resolution was ca. 0.1 meV and the energy window was $-3 < E < 20$ meV. In our experiments, 122 ^{3}He tube counters were installed at 2θ = 9—130° at steps of 1°, covering the scattering vector Q region of 0.23—2.70 Å^{-1} for elastic scattering. The liquid sample was confined in a concentric double-cylinder aluminum can. The thickness of the sample was 0.5 mm corresponding to the transmission of neutron beam of 83 %. The data were collected at several temperature in the range 20—335 K.

Results and Discussion

Our recent heat capacity study has revealed that cyclooctanol has two plastic phases designated crystal I and II. Figure 1 shows the $S(Q,E)$ spectra of crystal I at 100, 140, 160, 180, and 261 K obtained by AGNES. These spectra were obtained by summing up the data of the counters with scattering angles of 89—120°; the average Q value for elastic scattering was 2.36 Å^{-1}. A clear boson peak

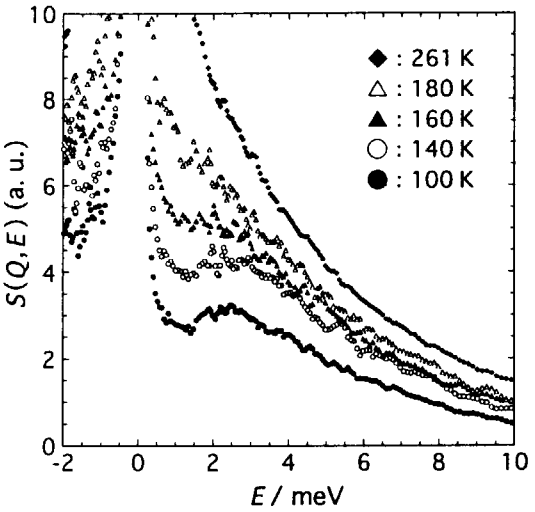


Fig. 1 Dynamic structure factor $S(Q,E)$ of cyclooctanol at several temperatures.

appeared at around 2.5 meV at 100 K. This is the second example of the boson of the orientational glass; the first one is ethanol reported by Ramos et al [6]. A similar boson peak was found also in phase II. A quasielastic scattering appeared in the data above T_g and its intensity increased with increasing temperature.

Figure 2 shows the temperature dependence of the elastic scattering intensity (integrated over -0.2—0.2 meV) divided by that at the lowest temperature (20 K). The data were plotted in a logarithmic scale and against temperature. The open (○, △, □) and closed (●, ▲, ■) symbols represent the data for crystal I and crystal II, respectively. The symbols +, ▽ and ◇ denote the data for liquid. For three different momentum transfer (Q) values, the data lie on a straight line below T_g as expected from the Debye-Waller factor $\exp(-\langle u^2\rangle Q^2)$ and the mean square displacement of a harmonic oscillator ($\langle u^2\rangle \sim T$). Excess decrease of elastic intensity occurred above T_g, corresponding to the quasielastic scattering observed in Fig. 1. The temperature and Q dependence of elastic intensity is quite similar to that due to the fast β relaxation frequently observed in structural glasses and polymer glasses.

For further investigation of the quasielastic scattering, we have calculated the imaginary part of the susceptibility χ'' from the $S(Q,E)$ data at 285 K where both plastic and liquid (supercooled) phases were realized. Figure 3 gives χ'' as a function of frequency for three different Q values. The open and closed symbols denote the data of plastic and liquid phases, respectively. The spectra for plastic and liquid phases are quite similar to each other for all Q values. The peak frequency was ca. 1 THz which is typical value of the fast β relaxation.

From all of the results shown above, we conclude that the quasielastic scattering found in this study is due to the fast β relaxation. This is the first finding of the fast β relaxation in orientational glasses. The appearance of the boson peak and fast β relaxation in cyclooctanol suggests that these phenomena are generally associated with the rotational motions of molecules and polymer segments since orientational glasses have disorder only in molecular orientations.

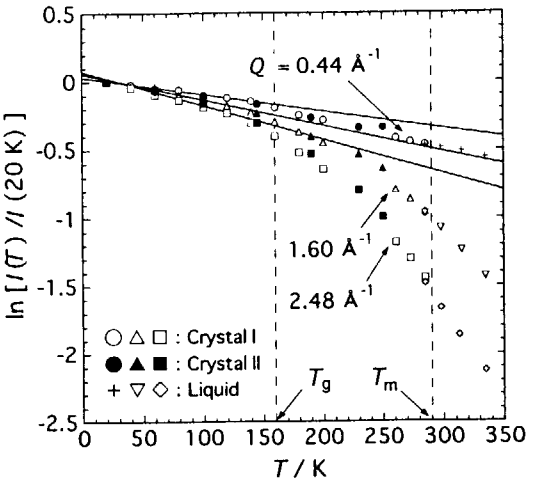


Fig. 2 The temperature dependence of the elastic scattering intensities.

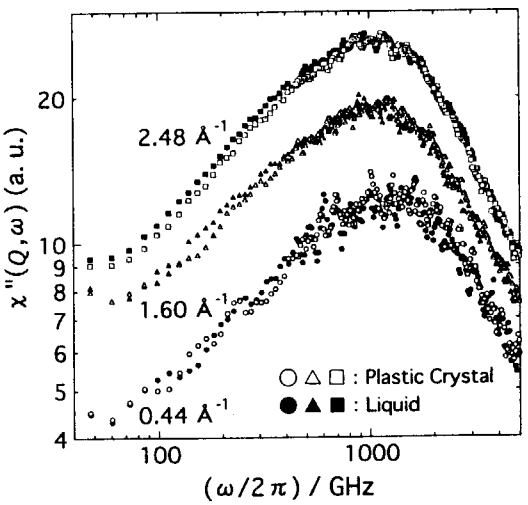


Fig. 3 Imaginary part of susceptibility plotted against frequency.

References

[1] D. L. Leslie-Pelecky & N. O. Birge, Phys. Rev. Lett. **72**, 1232 (1994). [2] R. Brand et al., Phys. Rev. B **56**, R5713 (1997). [3] M. Shablakh et al., J. Chem. Soc. Faraday Trans. 2 **79**, 369 (1983). [4] O. Anderson et al., Mol. Phys. **71**, 523 (1990). [5] T. Kajitani et al., Physica B **213-214**, 872 (1995). [6] M. A. Ramos et al., Phys. Rev. Lett. **78**, 82 (1997).

研究課題：中性子非干渉性非弾性散乱による配向オレイン酸結晶の分子運動
表題：配向オレイン酸の中性子非干渉性非弾性散乱

1-4-16 Neutron Incoherent Inelastic Scattering of Oriented Oleic Acid

Tomoyuki YOKOYAMA, Norio ACHIWA and Masao SUZUKI[A]
Department of Physics, Kyushu University, Fukuoka, 8128581, Japan
[A]Nippon Oil and Fat Co.ltd.,Amagasaki, Hyougo, 580, Japan

§1. Introduction

Oleic acid molecule consists of a couple of finite polymethylene chains connected by ethylene double bond carbon and makes a dimer along the chain axis connected by hydrogen bonds between carboxyl groups in liquid and crystal phases; molecular formula is $CH_3(CH_2)_7CH{=}CH(CH_2)_7COOH$. Oleic acid crystal consists of two dimers in the unit cell. In other word there are four $C(CH_2)_7CH{=}$ groups or two oleic acid molecules units in the unit cell. These units are connected by three kinds of bonds, hydrogen bonds, double bond and non-bond(van der Waals force). So a hierarchical bonding structure of polymethylene chains exists in the crystal. It is expected that it should exist a hierarchical vibrational accordion modes which consist of the accordion modes of dimer, molecular and $C(CH_2)_7CH{=}$ group. We have planned to observe these hierarchical excitations of local modes by using neutron incoherent inelastic scattering of oriented oleic acid in oriented crystal and in liquid phases.

It is interesting to show that these internal molecular, coupled molecular and lattice vibrational modes exist in low frequency region. In liquid phase if any periodic structure does not exist then lattice vibrational modes should disappear. So we are also interested in how these three kinds of mode behave in liquid phase. In our previous study the spectra of oriented oleic acid in low energy region were observed by mean of TOF neutron spectrometer.[1,2] But their bands are broad because of overlapped transitions of many excited levels. Then in order to reduce these overlapped transitions from higher energy levels, the incoherent inelastic scattering spectra have been observed at lower temperature.

§2. Experiments

The inelastic incoherent neutron spectra of the oriented oleic acid were measured with time-of-flight neutron spectrometer AGNES with an incident neutron energy 4.59meV, installed at the cold neutron guide, C3-1-1, in JRR-3M.[3] 118 detectors of the spectrometer cover the angle region from 9° to 130° per 1°. The spectra were measured at each one temperature along two different directions angled 45 degrees, step by step. In the time-of-flight experiment the direction of scattering vector varied according to the time channel of each counter. So the directional dependence of phonon scattering function is obtained by summing up the data in the range of 10 degrees of each Q direction which are distributed over 118 detectors.

§3. Results and Discussions

Figure 1 and 2 show the anisotropic phonon scattering function, which is normalized as follows for the neutron energy gain case,

$$G(Q,\omega) = \frac{4\pi m_n}{Q^2\hbar^2}\frac{\omega}{e^{2W(Q)}n(\omega)}S(Q,\omega) \qquad (3.1)$$

In order to get anisotropic contribution of $G(Q,E)$, it is necessary to select the same Q direction component of $G(Q,E)$ among the all detector data. Since the Q vector is a function of the ξ angle which is the angle between the Q vector and the c-axis, $G(Q,E)$ for each θ direction has some dispersion for the ξ. Now we define a direction components of $G(Q,E)$ for a ξ_0 direction, $D(Q_{\xi_0},E)$, as follows;

$$D(Q_{\xi_0},E) = \sum_{Q}\sigma(\xi-\xi_0)G(Q_\xi,E) \qquad (3.2)$$

When the Q direction is parallel to the ξ_0, the $G(Q_{\xi_0},E)$ is collected as a component of $D(Q_{\xi_0},E)$.

Melting point of oleic acid is 289.6K. The crystal constants of β phase is a=9.3Å b=5.5Å c=35.3Å α=87.9° β=82.8° γ=86.2°. The asymmetric unit contains two crystallographically different dimers in the β crystal unit cell and lamellar interfaces consist of methyl and carboxyl groups. The c-axis is approximately parallel to the molecular chain.

One oleic acid molecule has two finite polymethylene carbon chains of $CH(CH_2)_7C$ which has nine carbon atoms. It is expected that $CH(CH_2)_7C$ of which number called m is a unit of molecular accordion mode. Then an oleic acid molecule is 2m and a dimer is 4m. Since displacement vectors of these modes are parallel to the c-axis, these modes show maximum intensities when the scattering vector is parallel to the c-axis(Q//c). Energy of the molecular accordion modes E_a is given by;[4]

$$E_a = \frac{h\sqrt{E\rho}}{2nL_c} \qquad (3.3)$$

where h is Planck constant, E Young's modulus, ρ density of the crystal (0.98g/cm^3), n the number of carbon atoms and L_c length of inter methylene groups(-CH_2-). The energy of the molecular accordion modes of m, 2m and 4m are estimated by using this equation. Bands around 33.1meV and 31.5meV(Q//c)

JRR-3M, AGNES(C3-1-1), 4.Amorphous & Liquid

were assigned to the molecular accordion modes of $CH(CH_2)_7CH_3$ and $CH(CH_2)_7COOH$, respectively in the crystal. Bands around 66.2meV 15.7meV and 7.3meV(Q//c) were assigned to the molecular accordion modes of $\frac{1}{2}$m, 2m(molecule) and 4m(dimer), respectively in the crystal. Since the sample crystal was not a perfect crystal but an oriented crystal, the c-axis direction had some distribution and some modes was observed the direction perpendicular to the c-axis(Q⊥c).

Band around 1.7meV(Q//c) in the crystal phase is the lowest mode, then it was assigned to a longitudinal component of a zone boundary lattice mode of $4m_c(\pi)$ (c indicates a crystal phonon) of a crystal accordion mode (longitudinal acoustic mode:LA(π)), of which displacement vector is parallel to the c-axis. Band around 3.6meV(Q//c) was assigned to the zone boundary mode of $2m_c$. The energy of this mode is twice as larger as of $4m_c$. In the perfect β crystal the zone boundary mode of $2m_c$ should not exist. But since the crystal stacking packing was disordered, new periodicity of unit cell is 2m a half of the perfect β plane. Then the zone boundary mode of $2m_c$ appears.

Band around $30cm^{-1}$(3.7meV) is a highest energy of the lattice modes, which was by low-frequency Raman scattering spectra of oleic acid in α crystal.[5] Then bands around 2.7meV and 4.4meV(Q//c) in the crystal phase were assigned to longitudinal optical modes(LO) of $4m_c$, which corresponds to q=0 and π, respectively.

In this experiment we observed neutron energy gain spectra, so there are two case of the energy cascade, one is from an excited state to a ground state and the other is an excited state to another excited state which is call intermediate transition. Bands around 5.2meV, 6.1meV, 8.8meV, 12.5meV and 55.7meV(Q//c) in the crystal phase were assigned to the intermediate transition modes, energy level from 7.3meV to 1.7meV (7.3meV-1.7meV), 6.3meV-0.0meV(the ground state), 10.0meV-1.7meV, 15.7meV-1.7meV and 62.2meV-7.3meV, respectively.

It is expected that the energy of twisting mode is lower than that of a transverse component of the crystal accordion mode $4m_c(\pi)$ (transverse acoustic mode:TA(π)) and energy of these modes are lower than that of the other mode. Since the twisting and TA(π) modes are lowest modes whose direction is perpendicular to the c-axis, the lowest bands around 1.9meV and 2.2meV, which show maximum intensities when the scattering vector is perpendicular to the c-axis(Q⊥c), in the crystal phase were assigned to the twisting mode and the transverse component of the crystal accordion mode $4m_c(\pi)$ ($4m_cTA(\pi)$), respectively. Band around 4.5meV(Q⊥c) which is twice as long as the energy of $4m_cTA(\pi)$ was assigned to the transverse component of the crystal accordion mode $2m_c(\pi)$ ($2m_cTA(\pi)$).

On the other hand the lattice modes are depend on the crystal structure. In the liquid phase they should disappear. But some modes, the $4m_c(\pi)$, $2m_c(\pi)$, LO(0), LO(π) and $4m_cTA(\pi)$ modes, were observed at 296K and 318K. Since just above melting point oleic acid molecules have some kind of short range order, the lattice modes were observed.

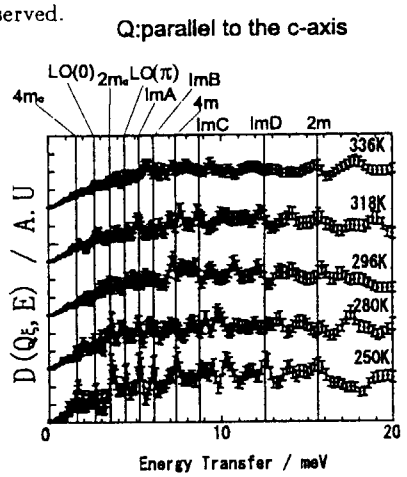


Fig.1. Normalized phonon scattering function at several temperatures for the scattering Q vector parallel to the chain axis c of oleic acid. The melting point of oleic acid is 289.6K. Here, 2m and 4m: the molecular accordion modes of 2m and 4m, $4m_c$, $2m_c$: zone boundary lattice modes of $4m_c$, $2m_c$, LO(0), LO(π): longitudinal optical modes of $4m_c$ which correspond to q=0 and π, ImA: the intermediate transition mode of energy level from 7.3meV to 1.7meV, ImB: the intermediate transition mode of energy level from 6.3meV to 0.0meV, ImC: the intermediate transition mode of energy level from 10.0meV to 1.7meV, ImD: the intermediate transition mode of energy level from 15.7meV to 1.7meV.

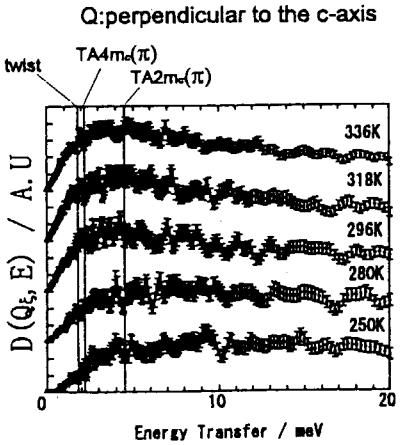


Fig.2. Normalized phonon scattering function at several temperatures for the scattering Q vector perpendicular to the chain axis c of oleic acid. The melting point of oleic acid is 289.6K. Here, twist: the twisting mode, $TA4m_c(\pi)$: the transverse component of the crystal accordion mode $4m_c$, $TA2m_c(\pi)$: the transverse component of the crystal accordion mode $2m_c$.

1) T. Yokoyama, N. Achiwa and M.Suzuki : J. Phys. Chem. Solids 60 (1999) 1519.
2) T. Yokoyama and N. Achiwa : Activity Report on Neutron Scattering Research 6 (1999) 153.
3) T. Kajitani, K.Shibata, S.Ikeda, M.Kohgi, H.Yoshizawa K.Nemoto and K.Suzuki : Physica B213&214 (1995) 872.
4) R. F. Schaufele and T. Shimanouchi : J. Chem. Phys. 47 (1967) 3605.
5) M. Kobayashi, K. Shibata, K. Sato and M. Suzuki : J.Phys.Chem. 90 (1986) 6371.

研究テーマ: 上部および下部臨界温度を持つ混合液体の動的構造
表題: 閉館2相領域をもつ液体混合系の中性子準弾性散乱測定

1-4-17 Quasi Elastic Neutron Scattering Measurements on the Liquid Mixture Having Closed Two Phase Region

K. Maruyama, S. Kawase[1], M. Misawa

Faculty of Science, Niigata University, Niigata 950-2181, Japan
[1]Faculty of Medicine, Niigata University, Niigata 951-8518, Japan

The mixture of glycerol ($CH_2OH - CHOH - CH_2OH$) and guaiacol (o-methoxy phenol $C_6H_4OHOCH_3$) has a closed two phase region in its concentration-temperature phase diagram and has lower and higher critical points at 45°C and about 35 mol % guaiacol, and at 81°C and about 40 mol % guaiacol, respectively. The existence of the lower critical point is peculiar phenomenon according to the usual thermodynamic rules.

Recently we have measured the thermodynamic quantities, such as the Gibbs free energy of mixing, by using Rayleigh-Brillouin scattering measurements. Those studies shown the very small entropy of mixing compared to the ideal mixing in lower temperature region, which suggests the formation of clusters of glycerol or guaiacol molecules.

In order to confirm the existence of the clusters, we have performed quasi elastic neutron scattering measurements of the glycerol-guaiacol mixtures by using AGNES spectrometer equipped at JRR-3M in JAERI Tokai. The used sample cell was an aluminum double cylindrical cell with 0.5mm spacing to avoid multiple scattering by hydrogen atoms. The measurements were carried out in the higher and lower one phase region, at 30 °C and 85°C, respectively, for samples with the composition of 0, 20, 35, 45, 65, 80 and 100 mol% guaiacol.

Figure 1 shows the obtained dynamic structure factor $S(Q,\omega)$ as a function of energy transfer ω. The width of the quasi elastic peak at higher temperature is wider than that at lower temperature, which means slower motion of molecules in lower temperature region. From the Q dependence of peak width, the diffusion constant d was derived. For the samples with the phase separation compositions, the d has low value compared to other samples. These results are consistent with the cluster formation.

We are planning farther experiments with deuterized samples for separating the motion of two components.

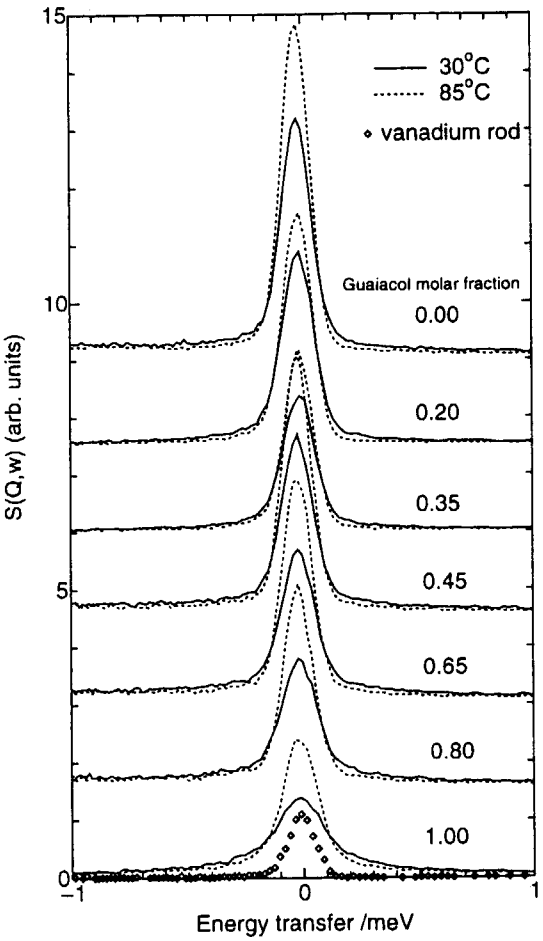


Figure 1. The obtained $S(Q,\omega)$ for glycerol guaiacol mixtures.

研究テーマ：濃厚電解質水溶液ガラスの低エネルギー励起
表題：$CaCl_2$水溶液ガラスの低エネルギー励起

1-4-18 Low-energy Excitation in $CaCl_2$ Aqueous Solution Glass

O. Yamamuro, Y. Madokoro, H. Yamasaki, and T. Matsuo

Department of Chemistry, Graduate School of Science, Osaka University, 1-1 Machikaneyama-cho, Toyonaka, Osaka 560-0043, Japan

Introduction

The glasses of electrolyte aqueous solutions are typical hydrogen-bond network glasses. According to previous neutron diffraction studies [1,2], the cations are strongly coordinated by water molecules and the hydrogen-bond network is partly broken by the added ions. We found a boson peak in $LiCl{\cdot}nH_2O$ (n = 4, 6) glasses by using AGNES last year [3].

The purpose of the present work was to clarify the relation between the boson peak and the connectivity of the hydrogen-bond network. We have performed the neutron scattering measurements on glassy and crystalline $CaCl_2{\cdot}13H_2O$. The coordination of water molecules to Ca ions is known to be weaker than that to Li ions and so the boson peak is expected to change drastically as Li^+ is replaced with Ca^{2+}.

Experimental

The INS experiments were performed using a direct geometry chopper-type TOF spectrometer AGNES [4] installed at the cold neutron guide (C3) of JRR-3M (Tokai, Japan). $CaCl_2{\cdot}13H_2O$ solution was prepared by mixing $CaCl_2{\cdot}2H_2O$ crystal and purified water. The liquid samples were confined in a concentric double-cylinder aluminum can. The thickness of the samples was 0.5 mm corresponding to the transmission of neutron beam of about 80 %. The glassy sample was prepared by a rapid cooling (2 K min^{-1}) and the crystalline sample by annealing the sample at ca. 200 K. All of the samples were measured at 100 K. The duration of the measurement was 40—45 h for each sample.

Results and Discussion

Figures 1 shows the $S(Q,E)$ spectra of glassy and crystalline $CaCl_2{\cdot}13H_2O$. The data of $LiCl{\cdot}nH_2O$ (n = 4, 6) glasses and hexagonal ice are also plotted for comparison. These spectra were obtained by summing up the data from the counters at scattering angles of 89—120°; the average Q value for elastic scattering was 2.35 $Å^{-1}$. The data were scaled by dividing by the integrated intensity for each sample. Glassy $CaCl_2{\cdot}13H_2O$ exhibited a boson peak at around 4 meV as did glassy $LiCl{\cdot}4H_2O$ and $LiCl{\cdot}6H_2O$. The excess density of states of glassy $CaCl_2{\cdot}13H_2O$ (compared with that of hexagonal ice) was 0.03 degrees of freedom per water molecule (cf. 0.10 for glassy $LiCl{\cdot}4H_2O$ and $LiCl{\cdot}6H_2O$). We conclude from the present result that the boson peak is enhanced by broken or weakly connected hydrogen bonds. This is consistent with our recent reports in alcohol glasses [5] and vapor-deposited amorphous ice [6].

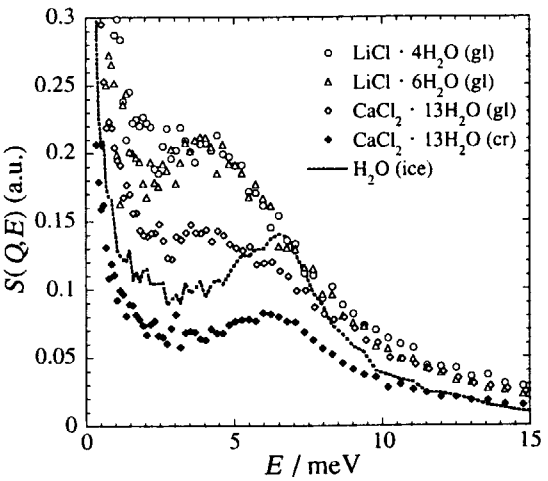


Fig. 1 $S(Q,E)$ spectra of LiCl and $CaCl_2$ aqueous solution glasses and hexagonal ice.

References

[1] S. Ansell et al., J. Phys.: Cond. Matter **9**, 8835 (1997). [2] R. H. Tromp et al., J. Chem. Phys. **96**, 8460 (1992). [3] O. Yamamuro et al., J. Chem. Phys., in press. [4] T. Kajitani et al., Physica B **213&214**, 872 (1995). [5] O. Yamamuro et al., J. Phys.: Cond. Matter **12**, 5143 (2000). [6] O. Yamamuro et al. J. Chem. Phys., in press.

This is a blank page.

1. 中性子散乱 5) 高分子

1. Neutron Scattering 5) Polymer

This is a blank page.

研究テーマ：高分子多成分系のパターン形成に関する研究
表題：散乱法を用いたゴム充填系の階層構造の研究

1-5-1 Scattering Studies on Hierarchical Structures of Rubber/Filler Systems

T.Hashimoto, M.Takenaka, T.Koga[1], and K.Aizawa[2]

Department of Polymer Chemistry, Graduate School of Engineering,
Kyoto University, Kyoto, 606-8501-,Japan
[1]Japan Atomic Energy Research Institute, Tokai, Ibaraki 319-1195, Japan

The incorporation of fillers, such as carbon black or sillica particles, in rubber imporves the mechnical properties of the rubbers. The inprovement depends on the aggregation structures formed by prticles of the fillers in the rubbers. The aggregation structures is expected to have hierarchical structures so that we have to obsertve the wide range of length scale from 1 nm to 10 μm to explore the structure. As shown in Fig.1, in previous study[1], we explored that the poly(styrene-*ran*-butadiene) (SBR) /carbon black (CB) system has the hierarchical structures by combining very small angle neutron scattering (VSANS) and ultra small angle small x-ray scattering (USAXS). In this study, we investigated that the CB fraction dependence of the hierarchical structures of PI/CB system.

We prepared three SBR/CB systems having 15,20, and 25 wt% weight-fraction of CB. VSANS was performed at PNO (3G) in JRR-3M, Tokai. USAXS, SAXS was performed at Hashimoto Polymer Phasing Project, Kyoto. Figure 2 shows VSANS, USAXS, and SAXS profiles of the SBR/CB system. Each profile can be well superimposed so that we obtained the scattered intensity distribution over 4 decade in length scale. This superimposed profile indicates that the PI/CB system has the folowing hierarchical structure:(i) the carbon black forms the primary aggregation structure. (ii) the primary aggregation structure forms the mass-fractal sturcture and the upper limitof the mass-fractal structure can be observed.

We analyzed the data by using the unified Guineir equation[2] to obtain the characteristic length of the hierarchical structures. We can fitted the data with theunified Guineir equation and obtained the size of the primary aggregate and that of upper limit of the mass-fractal stuructures as well as the fractal dimeenssion of the mass-fractal structure. We found that (i) the fractal dimenssion of the mass-fractal sturcutre is independent of the weight fraction and that (ii) the size of aggregate structure increases with the fraction while the upper limit decreases with the fraction.

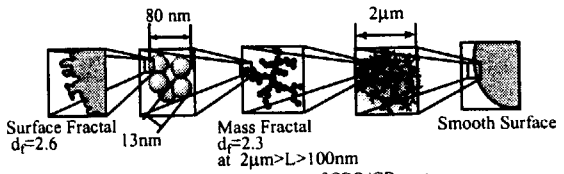


Fig.1 Hierarchical structures of SBR/CB system

Reference
1) M.Takenaka et. al. Polym.Prep.Jpn. **49** (1995) 2482.
2) Beaucage,J.Appl.Cryst.**28**(1995)717.

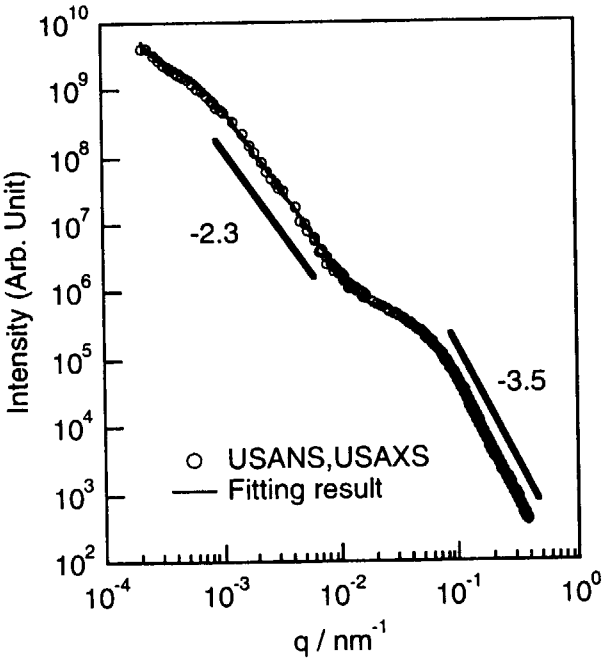


Fig.2 Combined scatering profile for 25wt% system

原子炉：JRR-3M　　装置：PNO(3G)　　分野：中性子散乱（高分子）

研究テーマ：高分子/希釈剤系のゾルーゲル転移に関する研究
表題：散乱法を用いたポリエチレン溶液のゾルーゲル転移の研究

1-5-2 Structural study of the sol-gel transition of linear polyethylene in toluene

Y.Izumi, Y.Jinbo, H.Watanabe, K.Aizawa[1] and H.Tomimitsu[1]
Graduate School of Science and Engineering, Yamagata University,
Yonezawa, Yamagata 992-8510, J apan
[1]Advanced Science Research Center, Japan Atomic Energy Research Institute,
Tokai, Ibaraki 319-1195, Japan

Scattering techniques provide a straightforward method of measuring the essential geometric features of sol-gel transition. They allow in situ measurement and, therefore, are not subject to criticism regarding sample preparation artifacts. In this report, Precise Neutron Optics (PNO) has been applied to specify the geometric features of sol-gel transition of linear polyethylene in toluene.

Linear polyethylene characterized by M_w=3.3x10^4 and M_w/M_n=1.04 was used. The neutron scattering experiments were performed with the PNO at JRR-3M of JAERI (Tokai) in the concentration (c) range from 1.198 to 10.080 g/100cm^3 at 20℃.

Figure 1 shows double-logarithmic plots of the scattering intensity I(q) versus q for quenched samples. In all samples for q values > q_c, a slope of -4 is observed indicating that we are in the Porod regime probing that the surface is smooth. Here, q_c is q at the crossover point between two regimes. For q values < q_c, one can observe a totally different scattering behavior for the sol (open symbols) or gel (filled symbols). A power-law regime appears clearly in the sol. The slope can be interpreted as the negative of the fractal dimension D and yields D=1.4 for c=1.198 g/100cm^3 and 1.8 for c=2.504 g/100cm^3. In order to evaluate the geometric features for all samples, the following equation is used: $I(q)=I(0)/[1+(q\xi)^D]$, for $q_c<q$. Here I(0) is the scattering intensity at q=0 and ξ is a length characterizing spherulites observed in this regime. The results summarized in table 1 suggest that the geometric features change dramatically, as the sol changes gel. The sol is characterized by spherulites with mass fractal of 1.7-1.9, density of about 0.1 and a large ξ. On the other hand, the gel is characterized by spherulites with surface fractal of 2.8-3.6, density of about 5.8-7.5 and a small ξ.

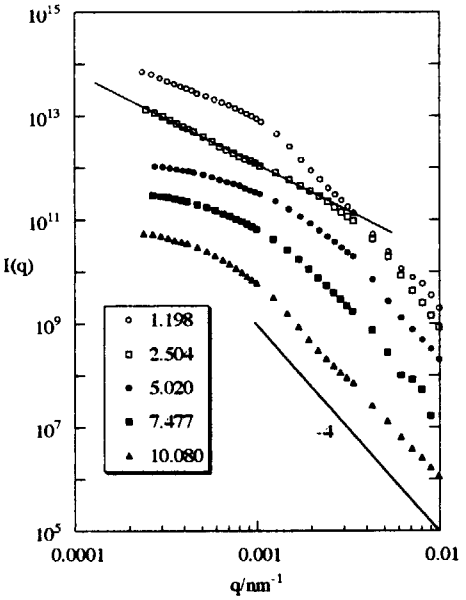


Figure 1 The double logarithmic plots of the scattering intensity I(q) versus q for the quenched samples: c(g/100cm^3)=1.198(○), 2.504(□), 5.020(●), 7.477(■), 10.080(▲).

Table 1

c (g/100cm^3)	10^{-10}I(0)	ξ(nm)	D	q_c (nm^{-1})	I(0)/ξ^3
1.198 (sol)	2.46	7400	1.7	0.0011	0.06
2.504 (sol)	5.4	7400	1.9	0.0025	0.14
5.020 (gel)	1.0	1200	2.8	0.0035	5.8
7.477 (gel)	3.0	1600	3.0	0.0030	7.3
10.080 (gel)	6.0	2000	3.6	0.010	7.5

原子炉：JRR-3M　　装置：PNO(3G)　　分野：中性子散乱（高分子）

研究テーマ：両親媒性分子／水系におけるモルフォロジー転移に及ぼす流動場の影響
表題：非イオン性界面活性剤／水系におけるラメラ相の流動誘起秩序形成

1-5-3 Shear-Induced Ordering of Lamellar Structure Observed in a Nonionic Surfactant/Water System

M.Imai, and K. Nakaya

Department of Physics, Ochanomizu University, Bunkyo, Tokyo 112-0012, Japan

One of the most fascinating properties of surfactant/water systems is their ability to form a variety of ordered mesophases. The shear flow strongly couples with the fluctuations of the ordered mesophases and modifies mesostructures. Then the behaviors of ordered mesophases under shear flow shed light on the stability of the ordered mesophases.

In this study we examined the shear ordering of the lamellar and gyroid phases of a $C_{16}E_7/D_2O$ system. Measurements of SANS under shear flow were carried out on the SANS-U instrument at JRR-3M in Tokai. The Couette shear cell installed by Takahashi's group was used for shear flow experiments.

A series of two dimensional SANS patterns as a function of $\dot{\gamma}$ (shear rate) from 0 to 3.0 s^{-1} at 55°C reveals that the orientation ordering process of lamellae can be classified into three stages. In Figure 1 we plot the shear rate dependence of the scattering intensities in the three principal directions (perpendicular: lamellae parallel to the flow-shear gradient plane, parallel : parallel to the flow-vorticity plane, and transverse: parallel to the shear gradient-vorticity plane). In the stage I ($0 < \dot{\gamma} < 10^{-2}$ s^{-1}) the orientation distribution of the lamellae keeps that at quiescent state although the scattering intensity. Thus shear flow in the stage I hardly affects the orientation of lamellae. In the stage II ($10^{-2} < \dot{\gamma} < 0.3$ s^{-1}), the parallel orientation ordering of lamellae is proceeded preferentially. This tendency is accelerated between $\dot{\gamma}$ = 0.1 and 0.3 s^{-1} and lamellae having the perpendicular and transverse orientations transforms to the parallel orientation lamellae. In the stage III ($0.3 < \dot{\gamma} < 3$ s^{-1}), the population of lamellae having perpendicular orientation starts to increase in the stage III although most of lamellae have the parallel orientation.

In order to elucidate relationship between the orientation of lamellae and undulation fluctuations, we analyzed the scattering functions of oriented lamellae and extract three structural parameters, δ (thickness of membrane), d (membrane distance), and η (Caillé parameter representing rigidity of membrane). Figure 2 shows that in stage II the elastic nature of the membrane drastically changes and subsequently δ and d decrease from the initial values. The derease of η indicates suppression of the undulation fluctuation of the lamellae, i.e. the Maxwell effect. This suppression of undulation fluctuations brings orientation ordering of lamellae to the parallel direction. A simple explanation for this orientation ordering of lamellae is as follows. The stiffening of membranes brings large asymmetry of the mechanical properties between the membrane and the solvent. In the parallel orientation, the strain is expected to be concentrated in the softer water layers, then the membrane layers could avoid bearing their full share of the strain and the overall stress would be lower.

In conclusion shear flow having $0.01 < \dot{\gamma} < 0.3$ s^{-1} suppresses undulation fluctuations of lamellae. This characteristic shear rate brings shear induced lamellae ordering toward a parallel orientation,

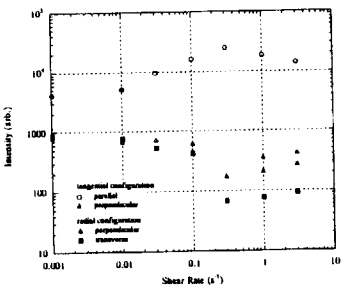


Figure 1 Shear rate dependence of the normalized scattering intensities in the three principal directions.

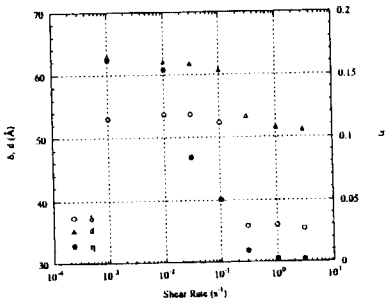


Figure 2 Shear rate dependence of layer thickness δ, layer repeat distance d, and elasticity parameter of membrane η.

JRR-3M SANS-U Polymer

研究テーマ：両親媒性高分子の会合挙動の解析

表題：結晶性両親媒性ポリマーの溶液中での会合挙動における温度の影響

1-5-4 Association Behavior of Amphiphilic Block Copolymer in Solution: The Effect of Crystallization of Core in the Micelle

K. Matsumoto, U. Mizuno, R. Nishimura, H. Mazaki, and H. Matsuoka

Department of Polymer Chemistry, Kyoto University, Kyoto 606-8501, JAPANn

It is well-known that amphiphilic block copolymers self-assemble in selective solvents to form micelles consisting of an inner core composed of insoluble segments and outer shell of soluble segments with the solvent. The shape of the micelle depends on a physical state of the core segment as well as the chemical structure of the copolymer. In this research, we synthesized novel amphiphilic block copolymers consisting of hydrophobic poly(1,1-dimethylsilacycobutane) (polyDMSB) and hydrophilic poly(2-hydroxyethyl methacrylate) (polyHEMA), and examined their association behavior in methanol at various temperatures by small-angle neutron scattering (SANS) measurements.

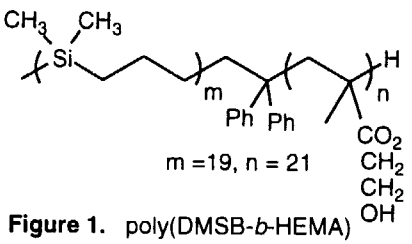


Figure 1. poly(DMSB-*b*-HEMA)

Figure 1 shows the chemical structure of the copolymer. PolyDMSB homopolymer exhibited melt-crystalline transition and the melting point was observed at 29 °C by DSC measurement. The melting point for the polyDMSB segment of the block copolymer in the bulk state was also observed at 22 °C.

Figure 2 shows the SANS profiles for 1wt% methanol solution of the block copolymer at 50 °C, 25 °C, and 13 °C. The scattering curve at 50 °C was well reproduced by the theoretical curve of a core-shell sphere micelle. However, the one at 13 °C showed q^{-2} dependence in the middle angle region, indicating the existence of disk-like aggregates. The scattering curve at 25 °C showed the intermediate shape of those two profiles, which is probably because the co-existence of the sphere micelle and disk-like aggregates. This morphology change of the molecular assembly was caused by the melt-crystalline transition of the core segment in the amphiphilic block copolymer.

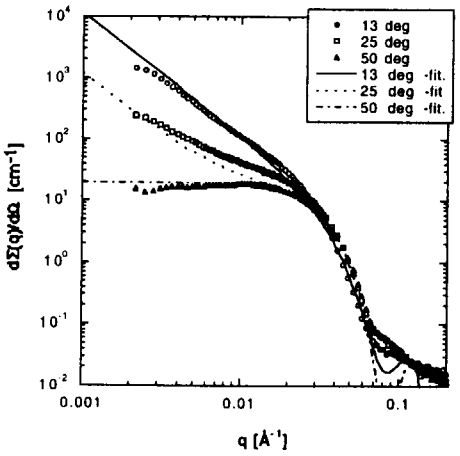


Figure 2. SANS profiles for 1wt% methanol solution of poly(DMSB-*b*-HEMA) at various temperaures.

JRR-3M, SANS-U, Polymer

研究テーマ：共重合体ミセルの構造と物性
表題：ジブロック共重合体ミセル格子の平衡剛性率
使用施設、装置：SANS-U + シアーセル
カテゴリー： Polymer

1-5-5 Equilibrium Elasticity of Diblock Copolymer Micellar Lattice.

H. Watanabe,[a] T. Kanaya,[a] and Y. Takahashi[b]

Institute for Chemical Research, Kyoto University, Uji, Kyoto 611-0011, JAPAN[a] and *Center for Integrated Research in Science and Engineering, Nagoya University, Nagoya, Aichi 464-8603, JAPAN*[b]

Introduction

Styrene-butadiene (SB) diblock copolymers form spherical micelles with S cores and B corona in a B-selective solvent, n-tetradecane (C14). In concentrated solutions, the micelles form cubic lattices because of the osmotic requirement of maintaining the uniform concentration profile in the B/C14 matrix.

This lattice exhibits equilibrium modulus G_e against small strains. If each corona block behaves as an independent entropic strand, G_e obeys the rubber elasticity relationship, $G_e^\circ = \nu k_B T$ with k_B, T, and ν being the Boltzmann constant, absolute temperature, and the corona number density. The measured G_e is proportional to ν but is smaller than G_e° by a factor ~ 10.[1] This difference has been related to defects in the quiescently ordered lattice.

In this study, we test the origin of the difference between G_e and G_e° with the aid of the shear-orientation technique. The shear-orientated micellar lattice includes less defects compared to the quiescently ordered lattice. Thus, G_e should increase significantly on the shear-orientation *if the defects are the main factor raising that difference*. The results of this test are reported below.

Experimental

A SB copolymer composed of deuterated S and protonated B blocks ($M_S = 11 \times 10^3$, $M_B = 23 \times 10^3$) was anionically synthesized in benzene. For a 15 wt% SB/C14 micellar solution, shear-orientation behavior was monitored in a Couette flow cell equipped at the SANS-U beam line at the Neutron Scattering Laboratory, Institute for Solid State Physics, University of Tokyo. The incident neutron wavelength was 0.7 nm, and the sample-to-detector distance was 4.00 m. Linear viscoelastic measurements were conducted before and after the shear orientation.

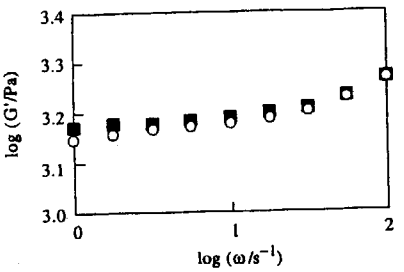


Fig.1 G' of the polycrystalline micellar lattice (■) and shear-oriented lattice (○) in the 15 wt% SB/C14 solution at 25°C.

Results and Discussion

SANS measurements revealed that the SB micelles formed a polycrystalline bcc lattice in the quiescently ordered state at 25°C and a well-oriented lattice was obtained after the shear at a rate of 10 s^{-1}.[2] Figure 1 shows the storage modulus G' measured before and after the shear-orientation. Clearly, the shear hardly affects the G' data and the well-oriented lattice (with a small defect content) has $G_e = [G']_{\omega \to 0} \cong 0.1 G_e^\circ$. Thus the defect is not the main factor raising the difference between G_e and G_e°.

Here, we remember that the B corona blocks in the SB/C14 solution are required to have mutually correlated conformations to maintain the uniform concentration profile in the B/C14 matrix. Thus, by nature, all corona B blocks sustaining the micellar lattice cannot work as the *independent* entropic strands. This argument suggests that the number density ν_{eff} of effectively working entropic strands is smaller than the nominal number density ν of the corona B blocks and G_e of the micellar lattice is given by $\nu_{eff} k_B T$ ($< G_e^\circ = \nu k_B T$). The difference between G_e and G_e° appears to be mainly due to the difference between ν_{eff} and ν.

1. H. Watanabe, *Acta Polym.*, *48*, 215 (1997).
2. H. Watanabe, T. Kanaya, and Y. Takahashi, *Macromolecules*, *34*, 662 (2001).

研究テーマ：ブロック共重合体ミクロドメインの流動配向化に対する粘弾性効果
表題：スチレン－イソプレンブロック共重合体溶液の ODT 近傍における流動誘起構造

1-5-6 Flow-induced structure of poly(styrene-b-isoprene) solutions near ODT

Yoshiaki Takahashi*, Atsushi Takano, Masanori Naruse and Yushu Matsushita
Cent. Integ. Res. Sci. & Eng., and Dept. Appl. Chem., Nagoya Univ.

Introduction

We have been studied the flow effects on lamella structures of symmetric poly(styrene-d_8-*b*-2-vinylpyridine) (DP) in a common good solvent under steady shear flow by small angle neutron scattering (flow-SANS). It was observed that the lamella structure is aligned in so called "perpendicular orientation", i.e., the lamella normal is preferentially oriented to the vorticity direction of shear flow, but such alignment of the structure occurs only in the limited condition. These results of DP are quite different from the data so far published for other diblocks. In this study, therefore, we measure flow effects on the different diblock copolymer, poly(styrene-d_8-*b*-isoprene) solution under the almost the same conditions as used for DP diblock copolymer to compare with above results.

Experimental

The diblock copolymer samples used was a poly(styrene-d_8-*b*-isoprene) , DI10 (M_w=1.15 ⁄ 10^5, M_w/M_n=1.12, ϕ_{PS}=0.5) prepared by anionic polymerization method. Here, M_w, M_w/M_n, and ϕ_{PS} denote the weight-average molecular weight, the molecular weight distribution index and the volume fraction of styrene-d_8, respectively. The solvent used was DOP and the ODT concentration was 27.5 wt.% at 27 ℃. Flow-SANS were measured by SANS Shear Cell attached to SANS-U spectrometer of NSL, ISSP, The University of Tokyo, at JAERI Tokai, Japan with λ = 0.7 nm and the sample to detector distance of 8 m.

Results and Discussions

In the ordered states, spots of strong intensities are observed in the vertical direction denoting perpendicular orientation of lamella domain under steady shear flow. Moreover, flow-induced ordering and alignment of microdomain was observed even in the disordered states close to the ODT. In this case, the anisotoropic intensity due to flow induced microphase separation was almost as strong as that ovserved in the ordered states.

At the lower concentration, (about 5% lower than ODT), anisotropic intensity under the flow were still observed, though, flow-induced ordering did not occur up to 100 s^{-1}.

From above results, it is concluded that the diblock copolymer consist of components having similar rheological properties (DP) are less affected by the flow, compared to the other diblocks such as DI, compared at almost the same experimental condition.

To clarify the reason of such difference in flow-induced structure, it is needed to compare both data based on interaction parameter. More detailed studies are now under the progress.

JRR-3M, SANS-U, Polymer

研究テーマ：球状蛋白質の凝集過程の解析
表題：球状蛋白質の凝集構造の研究

1-5-7 Studies on aggregated Structure of Globular Protein

S. Takata*, T. Norisuye*, and M. Shibayama**

**Department of Polymer Science and Engineering,*
Kyoto Institute of Technology, Matsugasaki, Sakyo-ku, Kyoto 606-8585, Japan
***Neutron Scattering Laboratory, The Institute for Solid State Physics, The University of Tokyo*
Tokai, Naka-gun, Ibaraki 319-1106, Japan

Introduction

β-lactoglobulin (β-LG) has been one of the most popular globular proteins for studying heat induced aggregation.[1~3] It is well-known that the kinetics of aggregate formation and the structure of aggregates are strongly dependent on its environmental factors, such as pH, temperature, and salt concentration. A transparent gel of β-LG can be obtained at pH2 and low ionic strength, whereas the gel becomes opalescent at pH7 and high ionic strength. The mechanism of aggregation, however, has not been fully explicated. In a preliminary experiment, we observed aggregation process of β-LG at pH 2 and 7 by small angle neutron scattering (SANS). SANS results showed that the scattered intensity at pH 2 increased by heat-induced aggregation, while that at pH 7 started to exhibit a distinct maximum at the scattering vector, q = 0.025Å^{-1} by heat treatment. This is due to formation of microphase-separated structure, which is ascribed to denaturation of globular protein. Since dissociated protein molecules exposes their chargeable groups outward, electrostatic interactions are generated and compete against attractive interactions originating from hydrophobic interactions. As a result, a microphase separation undergoes as well as coagguration. In order to clarify the mechanism of this drastic change in protein structure and aggregation, the structure of β-LG aqueous solutions at pH7 was investigated as a function of protein concentration and temperature by SANS.

Experimental

β-lactoglobulin (β-LG), crystallized for 3 times followed by lyophilized, was purchased from Sigma (Lot No. 114H7045), which is known to be a mixture of variants A and B. Solutions of β-LG were prepared by dissolving β-LG in D_2O. The concentrations were C = 0.01 ~ 0.10 g/ml. The pD (pH) of the solutions was adjusted by adding DCl. Each solution was heated in a thermostat bath at 75°C. Small angle neutron scattering (SANS) measurements were carried out with SANS-U spectrometer at the Institute for Solid State Physics, University of Tokyo. The wavelength of neutron beam was 7Å. The observed temperature was 20 and 75°C

Results and Discussion

Figure 1 shows the protein concentration, C, dependence of the normalized scattered intensities $I(q)/C$. The inset shows the C dependence *of* q_{max} and I_{max}. All samples were transparent. However, SANS exhibited a presence of single peak at all *C's* except for the lowest concentration, i.e., C = 0.01 g/ml. In the case of C = 0.01 g/ml, a scattering maximum may exist at a lower q outside the experimental

JRR-3M, SANS-U, Polymer

q window. It is clearly shown that the peak shifts to larger q values with increasing C. The solid lines indicate the theoretical curves for the structure factor of weakly charged polymer solutions in a poor solvent proposed by Borue-Erukhimovich (BE)[4], which is given by

$$I(q)=\frac{K\left(x^2+s\right)}{\left(x^2+t\right)\left(x^2+s\right)+1} \qquad (1)$$

where K is a scaling constant, x is the reduced scattering vector $(\equiv r_0 q)$, and s and t are the reduced charge concentration and the reduced temperature, respectively. The parameter, r_0, is the characteristic scale of screening of Coulombic interaction in polyelectrolytes in a poor solvent. As shown in the figure, the scattered intensities for all of these samples were well reproduced by the BE function. The evaluated values of s and t are $0<s<1$ and $t<0$, respectively. Though the physical meaning of these parameters will be reported elsewhere, this set of s and t indicates that the system behaves as a polyelectrolyte in a poor solvent. In order to examine the stability of this structure, the temperature was lowered to room temperature. Figure 2 shows a comparison of $I(q)/C$s between the two temperatures for the case of C = 0.05g/ml. It is clear from this figure that the heat-induced aggregated structure was thermoset, as was confirmed by the presence of stable peak after quenching to T_{obs} = 25°C. In other words, this aggregation is thermo-irreversible. The detail of the results will be reported in the forthcoming paper.

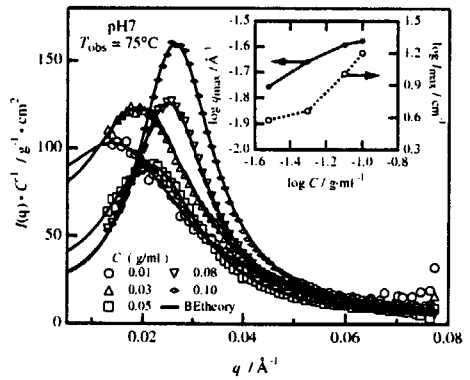


Figure 1. Comparison of the normalized scattered intensities function, $I(q)/C$, for heated β-LG solutions (20h at 75°C) at different protein concentrations, C. The insert figure shows the evolution of q_{max} and I_{max} as a function of C.

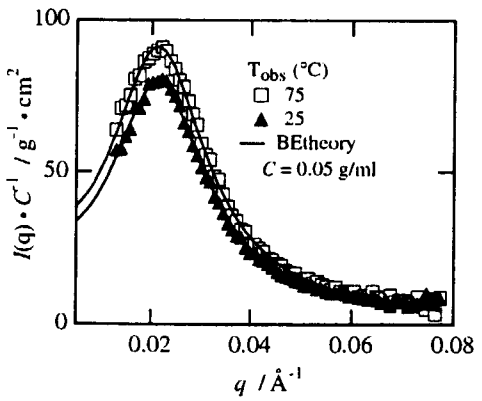


Figure 2. The observation temperature, T_{obs}, dependence of the normalized scattered intensities function, $I(q)/C$.

Reference

1) Griffin, W. G.; Griffin, M. C. A.; Martin, S. R.; Price, J. *J. Chem. Soc. Faraday Trans.* **1993**, *89*, 3395

2) Gimel, J. C.; Durand, D.; Nicolai, T. *Macromolecules* **1994**, *25*, 583.

3) Takata, S.; Norisuye T.; Tanaka, N.; Shibayama, M. *Macromolecules* **2000**, *33*, 5470.

4) Borue, V.; Erukhimovich, I. *Macromolecules* **1988**, *21*, 3240.

研究テーマ：化学架橋ゲルの微視的構造解析と理論検証
表題：化学架橋ゲルの構造不均一性の調製温度依存性

1-5-8 Preparation Temperature Dependence of Frozen Inhomogeneities in Chemically Cross-linked Gels

T. Norisuye and S. Takata

Department of Polymer Science and Engineering,

Kyoto Institute of Technology, Matsugasaki, Sakyo-ku, Kyoto 606-8585, Japan

and M. Shibayama

Neutron Scattering Laboratory, Institute for Solid State Physics,

The University of Tokyo

Tokai, Naka-gun, Ibaraki 319-1106, Japan

Introduction

In our previous studies,[1] we have addressed that structural inhomogeneities of polymer gels are commonly observed in cross-linked system and can be detected by small angle neutron scattering (SANS) as an excess scattering at low scattering angles.[1] With a help of a modern theory proposed by Panyukov and Rabin[2], we succeeded in elucidate effects of cross-links on structural parameters, such as inter-cross-linking distance, N, and interaction parameters, χ, for both chemically cross-linked and radiation cross-linked gels. It was also found that effective number of cross-links incorporated into the network structure has a limited value and depends on the state at sample preparation. We examined SANS scattering functions of chemically cross-linked gels as a function of both cross-linker concentration and preparation temperature in order to clarify the origin of structural inhomogeneities.

Experimental

JRR-3M, SANS-U, Polymer

Poly(*N*-isopropylacrylamide)(NIPAm) gels having different cross-link densities were prepared by polymerizing NIPAm monomer with cross-linker, methylene-bis-acrylamide (BIS) in water at 10, 20, 25 and 27°C. The concentrations of BIS, C_{BIS} were varied from 0 to the critical cross-linker concentration, C_{CST}, which depends on the preparation temperature, while that of NIPAm (C_{NIPA}) was kept to 690mM. For example, in the case of T_{prep}=10°C, C_{CST} was located around 50mM. Details of sample preparation are described elsewhere.[3]

SANS measurements were carried out with SANS-U spectrometer at Institute for Solid State Physics, University of Tokyo in Tokai. The wavelength of neutron beam was 7Å.

Results and Discussion

Figure 1 shows double logarithmic plots of scattered intensity, $I(q)$, having different C_{BIS}'s for a series of PNIPAm gels prepared at (a) 27°C and (b) 10°C. As indicated in the figure,

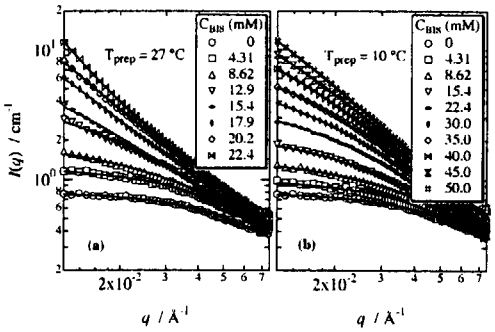


Fig 1. Double logarithmic plots of the scattered intensity functions, $I(q)$, observed at (a) 27°C and (b) 10°C for a series of PNIPA gels having different cross-linking densities.

$I(q)$ increased and became a power law function with increasing C_{BIS} for both T_{prep}'s, where appearance of the power-law function is a signature of the cross-linking saturation threshold, CST. Although such a power-law behavior was universally observed at C_{CST} irrespective of T_{prep}'s, gels prepared at 10°C required a larger number of cross-links than those prepared at 27°C. In other words, a PNIPAm gel becomes more inhomogeneous with increasing T_{prep}. As has been reported in our previous study,[1] scattering functions for a series of PNIPAm gels are well reproduced by the theory proposed by Panyukov and Rabin (PR theory). Similarly, we performed a curve-fitting for the present data and obtained a good agreement between the experimental data and the theory as indicated by the solid lines in the figure. Note that N was the only adjustable parameters, since the interaction parameters at observation, χ, and at preparation, χ_0, were determined from the data for the PNIPAm solution and the gel with highest cross-linking density, respectively.

Figure 2 shows inhomogeneity correlation length, Ξ, as a function of cross-linker concentration. Ξ is the characteristic length at

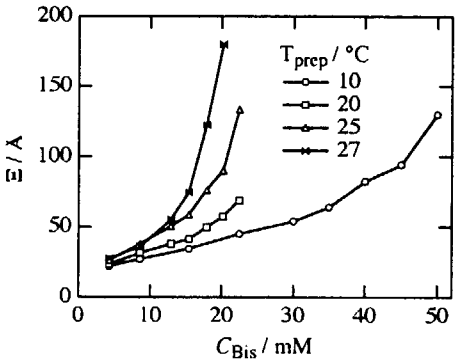


Fig 2. Cross-linking density dependence of inhmogeneity correlation length, Ξ, for PNIPA gels prepared at various temperatures.

gel formation and is calculated with a set of parameters at sample preparation. As shown in the figure, Ξ is an increasing function with C_{BIS} for all T_{prep}'s. A striking feature in this figure is that Ξ increased more abruptly with C_{BIS} by increasing T_{prep}. This means that a lowering T_{prep} enables introduction of a larger number of cross-links. Since effective cross-links are no longer formed at CST, control of the degree of inhomogeneties can be attained by tuning T_{prep}. Hence, it can be concluded that T_{prep} plays an important role on designing the inhomogeneities in gels, which control mechanical properties as well.

Reference

(1) Norisuye, T.; Masui, M.; Shibayama, M.; Ito, S.; Panyukov, S. *Phys. Rev. E.* **2001**, *submitted.*

(2) Panyukov, S.; Rabin, Y. *Macromolecules* **1996**, *29*, 7960.

(3) Shibayama, M.; Takata, S.; Norisuye, T. *Physica A* **1998**, *249*, 245.

研究テーマ：非晶高分子における塑性変形機構

1-5-9
Mechanism of plastic deformation in amorphous polymers

A. Toda

FIAS, Hiroshima University,
Higashi-Hiroshima 739-8521, Japan

Introduction

The physical properties of amorphous polymers depend on its glass transition temperature. The dynamical behavior is also the case. Amorphous polymers do not take complex higher order structure as seen in crystalline polymers, and hence the structural change on plastic deformation is characterized only by the change in molecular conformation and orientation. In order to examine the structural change, we apply a small angle neutron scattering.

It is believed that the deformation of molecular chains follows the deformation of specimen with affine transformation, and many experimental results support this argument. However, an essential question arises on the plastic deformation without fracture even below the glass transition temperature. The neck deformation below its glass transition is supposed to be sustained by the elongation of molecular chains between entanglement points, and superdrawing after the neck deformation gives rise to a slip at the entanglement points. The anisotropy of each molecular chain is accessible by the labeling method in small angle neutron scattering, and hence the deviation from affine transformation and the degree of slip at the entanglement points will be able to be analyzed quantitatively. In this project, we plan to examine the behavior of polymers deformed under various conditions.

Experimental

The original samples are undrawn amorphous poly(ethylene terephthalate) films obtained by quenching. The deformation has been done with an Instron machine under constant speed of deformation below its glass transition point (336 K). The structure before and after the neck deformation has been examined by small angle neutron scattering to determine the anisotropy of radius of gyration in the direction of deformation and its normal. The effects of superdrawing and of annealing above the glass transition to create small crystallites as an entanglement point have also been examined.

The analysis of the experimental results is limited by the weak scattering intensity and needs more data to come, in order to make a definite conclusion on the structural change after those physical treatments.

Acknowledgement

This work has been carried out in cooperation with Mr Nishimura (Toyobo Co. Ltd.).

JRR-3M, SANS-U, Polymer

研究テーマ：界面活性剤が形成する長距離規則構造に対するずり流動場の効果
表題：非イオン界面活性剤が作るラメラ相におけるずり流動場による転移

1-5-10 Shear-Induced Transformations in the Lamellar Phase Formed by Nonionic Surfactants

K. Minewaki, T. Kato, M. Imai[1], and Yoshihiko Takahashi[2]

Department of Chemistry, Tokyo Metropolitan University
[1] Department of Physics, Ochanomizu University
[2]Center for integrated research in Science and Engineering, Nagoya University

In recent years, much attention has been paid to the effects of shear flow on the structure of a lamellar phase by using various scattering techniques as well as microscopy and NMR. In the previous study[1)], we have measured small-angle neutron scattering (SANS) on a nonionic surfactant $C_{16}H_{33}(OC_2H_4)_7OH$ ($C_{16}E_7$)-water system at 55wt% of $C_{16}E_7$ at 55 and 70°C under shear flow for the shear rates $\dot{\gamma}$ = 10^{-3}-10^{2} s^{-1} much lower than those for other studies reported so far. We have found specific shear rate dependences in both the position and the intensity of the first reflection which have not yet reported before. In the present study, measurements have been made for the sample containing 48 wt% of $C_{16}E_7$ at 55°C and 70°C where the lamellar spacing at rest is larger than that at 55wt%.

Measurements of SANS were carried out at the instrument SANS-U of Institute for Solid State Physics of University of Tokyo in JRR-3M at Tokai with a Couette shear cell.

Figure 1 shows shear rate dependence of the lamellar spacing and the peak intensity of the first reflection (20° sector) at 70°C in flow, gradient, and vorticity directions. At lower shear rates less than $0.1s^{-1}$, the peak intensities for both directions decrease with increasing shear rate. In the range 0.1-1 s^{-1}, the lamellar spacing (d) suddenly decreases from 7.2 nm down to 5.1 nm. As $\dot{\gamma}$ increases further, d increases rapidly and then becomes almost constant. At the same time, the peak intensities in gradient and vorticity directions increase with the increase of $\dot{\gamma}$ while that in flow direction does not change very much.

The abrupt decrease in the lamellar spacing was observed at 55wt% also as reported before. In this case, d decreases from 6.5 nm down to 5.1 nm. It should be noted that the minimum values of d at $\dot{\gamma} \cong 1$ s^{-1} for these two samples of different concentrations are the same in spite of the difference of d values at rest, suggesting phase separation induced by shear flow.

1) K. Minewaki, T. Kato, and M. Imai, *Studies in Surface Science and Catalysis*, **132**, 185-188 (2001).

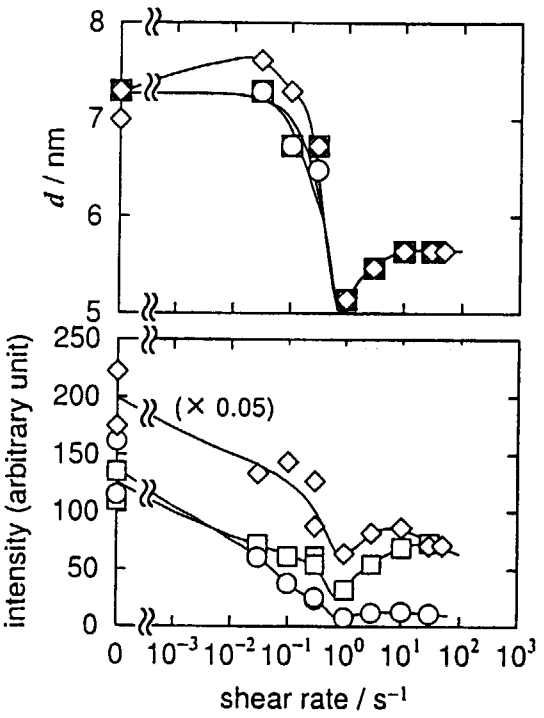


Figure 1 Shear rate dependence of the lamellar spacing (d) and the peak intensity of the first reflection for the sample containing 48 wt% of $C_{16}E_7$ at 70°C in flow (○), gradient (◇), and vorticity (□) directions.

JRR-3M, SANS-U, Polymer

研究テーマ：圧力ジャンプを用いた多成分高分子混合系の濃度揺らぎのダイナミックスの研究
表題：重水素化スチレン－イソプレン／スチレン－イソプレン対称混合系の臨界現象

1-5-11

Critical Phenomena in Symmetric Poly(deutrated styrene-*b*-isoprene)/Poly(styrene-*b*-isoprene) mixture

M.Takenaka, D. Yamaguchi, H.Hasegawa, T.Hashimoto, and M.Nagao[1]

Department of Polymer Chemistry, Graduate School of Engineering, Kyoto University, Sakyo-ku, Kyoto 606-8501, Japan

[1]Neutron Scattering Laboratory, The Institute of Solid State Physics, The Universty of Tokyo, Tokai, Naka, Obaraki, 319-1106, Japan

The multicomponent polymer mixtures provide a rich variety of morphologies induced by self-assembly via "complex phase transition", which means more than two kinds of phase separation are involved in a given system. In this study, we aim to explore the phase behaviors and the self-assembling processes of the complex phase transition in the following binary mixtures of polystyrene(PS)-block-polyisoprene(PI) copolymers: the constituent copolymers designated as SI-60K and DSI-1 are both compositionaly almost symmetric, while their molecular weights are different, i.e., the number-average molecular weights Mn are 6.3×10^4 for SI-60K and 1.0×10^4 for DSI-1.

A phase transition involving macrophase separation between SI-60K and DSI-1 was observed in the SI-60K/DSI-1=20/80(w/w) blend.We measured the temeprature dependence of SANS intensity of the dS-I/B mixture with the SANS-U spectrometer of the Institute for Solid State Physics of the University of Tokyo in JRR-3M at Tokai.

We found that the scattered intensity increases with decreasing temperature at small q-region. We applied Ornstein-Zernike plot to the scattered intensity and obtained the temperature dependencies of the structure factor at q=0, S(0) as shown in Fig.1. The drastic changes in $S(0)^{-1}$ was found at T=180°C. This infdicates that this mixture was found to cause the macrophase separation between two block copolymers, even though there is no segregation interaction in terms of c-parameter.

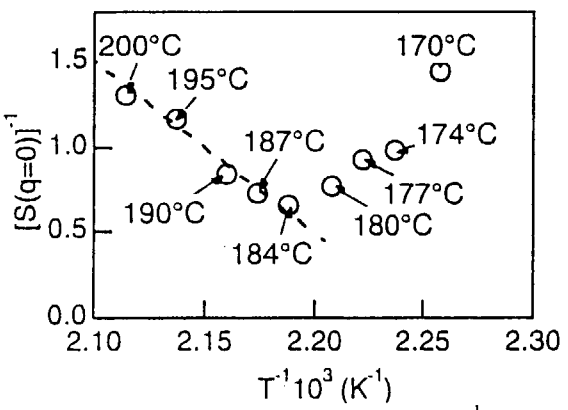


Fig.1 T-dependence f $S(0)^{-1}$

JRR-3M, SANS-U, Polymer

研究テーマ：コントラスト変調法によるジェランガムゲルの秩序構造形成機構解明
表題：コントラスト変調法によるジェランガムゲルの構造

1-5-12 Intermediate and Large Scale Structures in Gellan Gum Gels

Y. Izumi, Y.Jinbo, T.Matsugi, M. Hashimoto[1] and T. Takahashi[1]

Graduate School of Science and Engineering, Yamagata University, Yonezawa, Yamagata 992-8510, JAPAN
[1]Institute for Solid State Physics, University of Tokyo, Kashiwa, Chiba 277-8581, JAPAN

Scattering techniques provide a straightforward method of measuring the essential geometric features of gels. They allow in situ measurement and, therefore, are not subject to criticism regarding sample preparation artifacts. In this report, small-angle scattering (SAS) and ultra-small angle scattering (ULS) studies have been performed in order to reveal the structure of gellan gum gels in the absence of added salts. Furthermore, small-angle neutron scattering (SANS) with the contrast variation method has been applied to reveal the hydrogen-deuterium exchange within the gels.

The gellan gum (NaGG-3) gels were prepared by quenching into cold water after annealing at 90℃ for at least 24h and were maintained at 25℃ for one week. The neutron scattering experiments were performed with the SANS-U and ULS spectrometers (ISSP) installed at JRR-3M reactor of JAERI (Tokai).

The SAS and ULS data are summarized in Fig. 1 which shows the excess scattering intensity vs. the length of the scattering vector, q. The curves have been shifted vertically to match smoothly. For $0.00007 < q < 0.02\,Å^{-1}$, a power-law decay is observed and we obtain 2.4 as the D value. The value agrees well with the previous value (D=2.6) under the different condition, suggesting that the gelation of gellan gum proceeds according to the diffusion limited aggregation mechanism. For $q < 0.00007\,Å^{-1}$, we observe a pronounced upturn from the power-law. For $q > 0.02\,Å^{-1}$, we observe peaks indicating the existence of lamellar structures in the gels. SANS profiles of gellan gum gel in H_2O/D_2O mixtures are shown in Fig. 2. The mean contrast match point obtained from the experiment (60%D_2O) is totally different from the calculated value (40%D_2O) indicating the hydrogen-deuterim exchange within the gel.

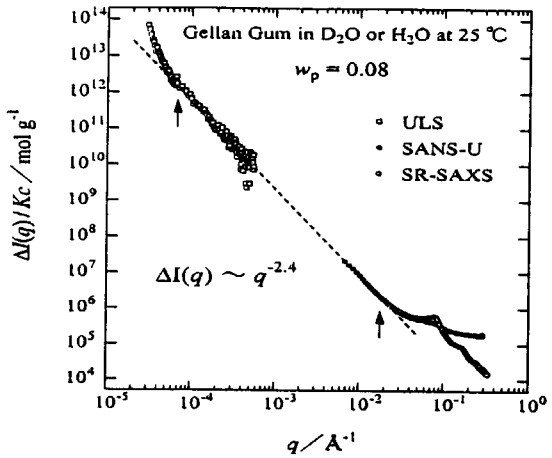


Fig. 1. Combind SAS and ULS profiles for the gellan gum gel in water at the weight fraction of 0.08.

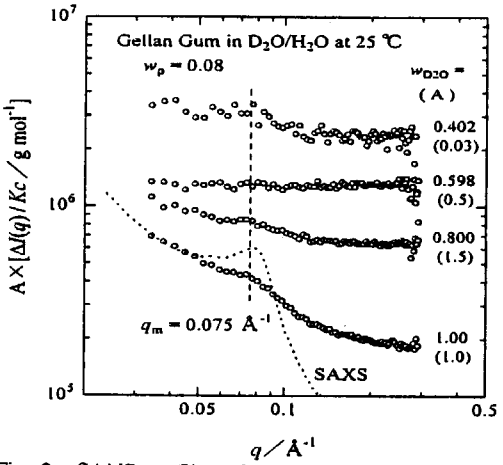


Fig. 2. SANS profiles of gellan gum gel in H_2O/D_2O mixtures.

Reference

1. Y.Izumi, S.Saito, K.Soma, Prog. Coll. Polym. Sci. 114 (1999) 48-55.
2. Y.Izumi, Y.Jinbo, K.Soma, S.Saito, M.Nagao, M.Hashimoto and T.Takahashi, This Report, 6 (1999) 195.
3. Y.Izumi, Y.Jinbo, T.Matsugi, M.Hashimoto and T.Takahashi, This Report, 7 (2000) 234.

JRR-3M, SANS-U & ULS, Polymer

研究テーマ:卵白・Ovalbuminのゲル化における高次凝集構造の形成
表題:OValbuminの熱変成過程における塩添加効果

1-5-13 Effect of Salt for Ovalbumin solution on Heat Denaturation

M. Sugiyama[a], S. Kuwajima[b], M. Annaka[c] and K. Hara[d]

[a]*Department of Physics, Kyushu University, Fukuoka, 812-8581 Japan*
[b]*Department of Polymer Physics, National Institute of Materials and Chemical Research, Ibaraki 305-8565, Japan*
[c]*Department of Materials Technology, Chiba University, Chiba 263-8522 Japan*
[d]*Institute of Environmental Systems, Kyushu University, Fukuoka, 812-8581 Japan*

Ovalbumin (Mw∼45,000), which has a globular shape with a radius of ∼30 Å[1] under watery conditions, is one of a main component of egg white. Therefore, the ovalbumin solution with the concentration of 10 wt% also makes gelation by heat denaturation. On the other hands, the ovalbumin solution with that of less than 5 wt% does not make gelation. However, it was found out that the 5 wt% ovalbumin solution can be made gelation with following procedure; 1)the 5 wt% ovalbumin solution is heated to 90°C, 2)cooled down to room temperature and added with NaCl (0.5M), and 3) reheated to 70°C. Finally, the transparent gel can be obtained.

In order to clarify the structure of the ovalbumin solution on each process, we performed the ultra small-angle neutron scattering experiment with ULS (USANS) spectrometers installed at JRR-3M in the Japan Atomic Energy Research Institute, Tokai, Japan.

As shown in Fig. 1 (a) and (b), the structure of the 5 wt% ovalbumin solution which was heated to 90°C is almost similar to that not-heated. The transparent gel which was made from the 5 wt% ovalbumin solution shows a fractal-like structure as shown in Fig. 1 (c). However the fractal dimension is relatively higher than that of an opaque gel which was made from a 10 wt% ovalbumin solution (Fig. 1 (d)).

1. (a) H. Sobotka and H. J. Trurint, in *Determination of the size and shape of protein molecules*, Ed. by P. Alexander and R. J. Block, Pegamon Press, Oxford, p.232, 1961. (b) T. E.Creighton, in *Proteins: structures and molecular properties* (2nd ed.), W. H. Freeman and Company, New York, p.27, 1993.

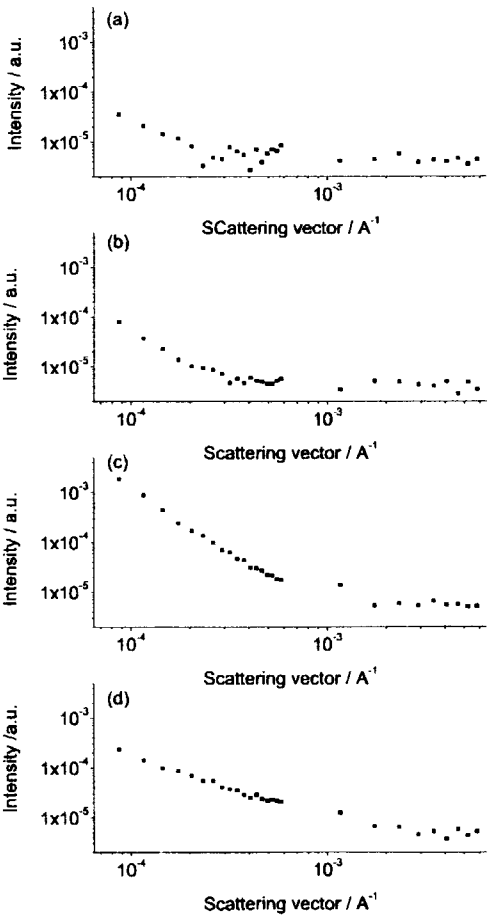


Fig. 1. USANS profiles of the ovalbumin solutions; (a)5 wt% ovalbumin solution, (b)5 wt% ovalbumin solution heated to 90°C, (c)transparent gel of 5 wt% ovalbumin solution (after process 3), and (d)opaque gel of 10 wt% ovalbumin solution, respectively.

JRR3M, ULS, Polymer

研究テーマ：イメージングプレートを用いた気液界面測定用水平型中性子反射率計の開発
表題：イメージングプレートを用いた気液界面測定用水平型中性子反射率計の開発

1-5-14 Development of Neutron Reflectometer for Air/Water Interface with Imaging Plate

Hideki Matsuoka, Mihoko Matsutani, Emiko Mouri, Atsushi Moriai[1], Kazuhiko Soyama[1]

Department of Polymer Chemistry, Kyoto University, Kyoto 606-8501, Japan
[1]Japan Atomic Energy Research Institute, Tokai, Ibaraki 319-1195, Japan

Reflectivity measurement is a powerful tool for the structural study of surfaces and interfaces in nanometer scale. X-ray and neutron reflectivity (XR, NR) are now become a common techniques for surface and interface study. On the other hand, one of the hot topic in this field is a molecular assembly, such as monolayer, on water and its application by functionalization. To know the nanostructure of these systems as basic information, the development of reflectometer for water surface is necessary. In fact, XR technique is often applied to these systems[1]. However, for some systems, especially for complex systems, XR can not give us enough information due to the low contrast of electron density. Hence, NR for water surface should be developed.

For this purpose, we have been continuing the project for construction of NR for water surface. In 1999, we had succeeded to detect a neutron reflection from water (D_2O) by LTAS (C2-1 port) in JRR-3M, Tokai. [2] By IP, the off-specular reflection was also detected. However, the quality of data was not perfectly satisfactory. We thought that this is not sufficient preciseness of the control of sample surface position: different from NR with pulsed neutron, for NR with reactor source, it is necessary to change the sample surface height corresponding to the incident angle change. It was difficult to control the height of water surface in heavy LB trough and also this motion causes the artificial disturbance to water surface.

Hence, in this study, we have tried to develop a new optical system for changing incident angle without changing sample height with utilization of supermirror.

Figure 1 shows the schematic diagram of our new NR setting. The neutron bean from guide was reflected downward by 3Q-supermirror to hit sample surface with required incident angle. By changing the tilt angle of suppermirror, the incident angle can be changed. The position of supermirror was moved horizontally with changing tile angle so that the neutron bean hits just the same position of the sample surface.

Since the mechanical accuracy for the simultaneous control of angle and position of supermirror could not be achieved in this study, we have not obtained the reflection from water surface yet. However, it was confirmed that this optical setting is the most suitable for water surface study.

By independent measurement by using Si wafer, it was confirmed that the reflectivity down to 10^{-4} and up to $Q=0.15Å^{-1}$ can be evaluated by LTAS.

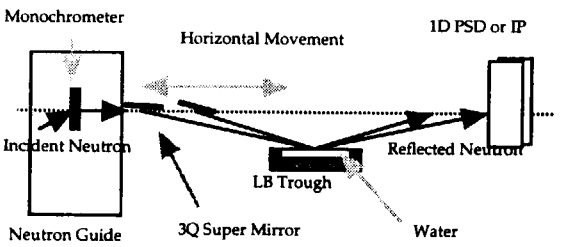


Figure 1 New optical setup of LTAS as a reflectometer for water surface.

Reference

(1) H.Matsuoka, E.Mouri, K.Matsumoto, ***The Rigaku Journal***, in press.
(2) H.Matsuoka, E.Mouri, R.Yoshitome, K.Kago, H.Yamaoka and K.Soyama, ***JAERI-Review***, 1999.

原子炉：JRR-3M　　装置：LTAS(C2-1)　　分野：中性子散乱（高分子）

研究テーマ：スチレン高分子のガラス転移点近傍における高分子化の効果
表題：ガラス転移点近傍での中性子準弾性散乱によるポリスチレンのダイナミクス

1-5-15

Dynamics Study of Amorphous Polystyrene by Quasi Elastic Neutron Scattering near T_g

I. Tsukushi[1], T. Kanaya[2] and K. Kaji[2]

[1]*Chiba Institute of Technology, Shibazono, Narashino, Chiba Pref. 275-0023, Japan*

[2]*Institute for Chemical Research, Kyoto University, Uji, Kyoto-fu 611-0011, Japan*

Glass transiton temperature T_g is a standard point in a study of amorphous solids. For example, temperature is scaled by T_g for Angell plot which shows the viscosity as a function of T_g / T. Its slope at T_g is called fragility which is one of the classification indices for amorphous solids. In this study, we have measured the incoherent neutron scattering of polystyrene, styrene trimer and styrene pentmer at same T / T_g by a time of flight (TOF) spectrometer, AGNES, at JRR-3M, Tokai. The energy resolution (HWHM) of AGNES is 70 μeV. Polystyrene, styrene trimer and styrene pentmer are composed of a same monomer except its polymerization and those T_g are 373 K, 223 K and 235 K, respectively. The investigation of the effect of polymerization may give a hint to the microscopic origin of its phenomena.

Figure 1 shows dynamic scattering law $S(Q,\omega)$ of polystyrene, styrene trimer and styrene pentmer at T / T_g = 0.93. The data are average from 2θ = 10° to 120° , Q_{ave}= 1.5 Å^{-1}. The intensity of $S(Q,\omega)$ is normalized by the area from 0 to 20 meV and corrected by the Debye-Waller factor. All samples have quasielastic scattering component below T_g due to the fast dynamic process which one of the universal features in amorphous solid. The wider of are the longer of main chain of styrene polymers. Comparing at the same T / T_g, the polymerization effect appears in the full width at half maximum (FWHM) of quasielastic scattering. Assuming the relation between macroscopic viscosity and mean-square displacement (MSD) of localized mode, the differences of FWHM correspond to those of fragility.

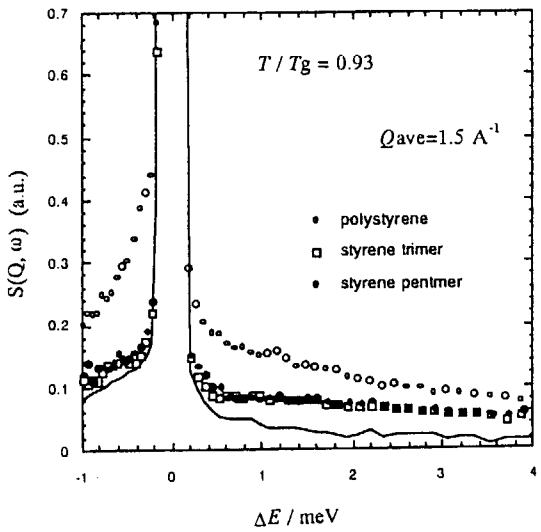


Fig. 1 Dynamic scattering law $S(Q,\omega)$ of polystyrene (open circles), styrene trimer (open squares) and styrene pentmer (solid circles). The solid line is Vanadium shown as a resolution function.

JRR-3M, AGNES, Polymer

研究テーマ：ポリイミド膜の炭化水素ガス透過メカニズムの解明
表題：ポリイミドにおけるガス透過性の圧力依存性と局所運動の役割

1-5-16 Pressure Dependence of Gas Permeability in Polyimide and Role of Local Dynamics

T. Miyazaki, T. Kanaya[1], Y. Ito[2], A. Shimazu, S. Katayama and K. Kaji[1]
Nitto Denko Corporation, Ibaraki, Osaka-fu 567-8680
[1]*Institute for Chemical Research, Kyoto University, Uji, Kyoto-fu 611-0011*
[2]*Research Center for Nuclear Science and Technology, The University of Tokyo, Tokai, Ibaraki-ken, 319-1106*

The permeation properties of propylene and C3 hydrocarbon gases through polymeric membranes are of interest in the development of membrane processes for recovering propylene from C3 hydrocarbon mixtures in the petrochemical industry.

6FDA-based polyimides have been reported to exhibit good performance for the separation of olefin gases from paraffin gases compared with other conventional polymers [1]. However, there have been few studies on this subject. To develop polyimide-based membrane materials for recovering propylene from C3 hydrocarbons, more information including the permeation mechanism is needed. In general, the chain mobility of the polymer matrix is one of the important factors to determine gas permeabilities [2]. In this study, therefore, we have performed quasielastic neutron scattering (QENS) measurements for studying the chain mobility in 6FDA-based polyimide (6FDA-BAAF) as a function of propylene pressure.

The QENS measurements were performed using AGNES spectrometer installed at C3-1-1 cold neutron guide at JRR-3M reactor. The energy resolution of the spectrometer is about 0.1 meV and the Q range is from 0.2 to 2.5 Å^{-1}. For the pressure dependence measurements, we have constructed a pressure cell, which was not equipped with a special pressure device, and hence the maxium pressure is determined by the saturated vapor pressure of propylene P_0. Schematic view of the pressure cell is shown in Fig. 1. Deuterated propylene was used in the experiment in order to reduce the incoherent scattering from hydrogen atoms. All the measurements were performed at 23 °C.

Scattering intensity of propyrene gas is dominated by recoil at a low Q range and rather strong compared to that from the polymer. Hence, in this preliminary report, we focus our attention on the high Q data from 1.9 to 2.5 Å^{-1}.

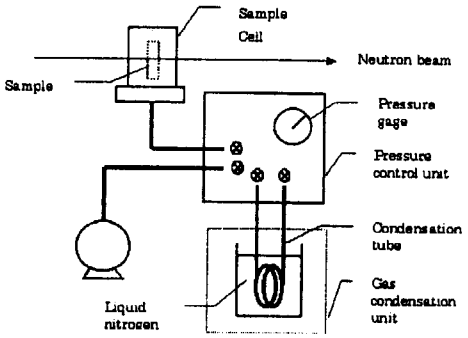


Fig. 1. Schematic view of the pressure control cell.

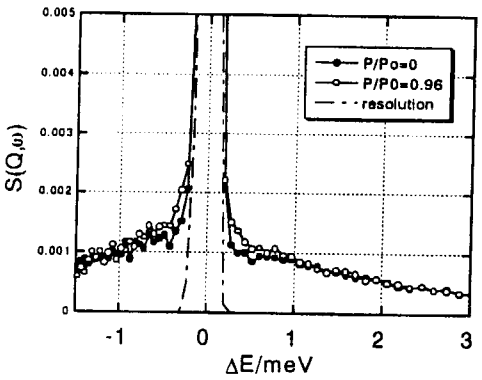


Fig. 2. Dynamic scattering law $S(Q,\omega)$ of 6FDA-BAAF in vacuum and under pressure P/P_0=0.96. The scattering from deuterated propylene gas was subtracted.

The observed scattering law $S(Q,\omega)$ is shown for 6FDA-BAAF in vacuum (P/P_0=0) and under pressure (P/P_0= 0.96) in Fig. 2 where the scattering intensity from the gas has been subtracted. The scattering law

JRR-3M, AGNES, Polymer

$S(Q,\omega)$ for P/P_0=0.96 shows an excess scattering compared with $S(Q,\omega)$ in vacuum in an energy region below about 1.5 meV while $S(Q,\omega)$ is independent of the pressure in the higher energy region.

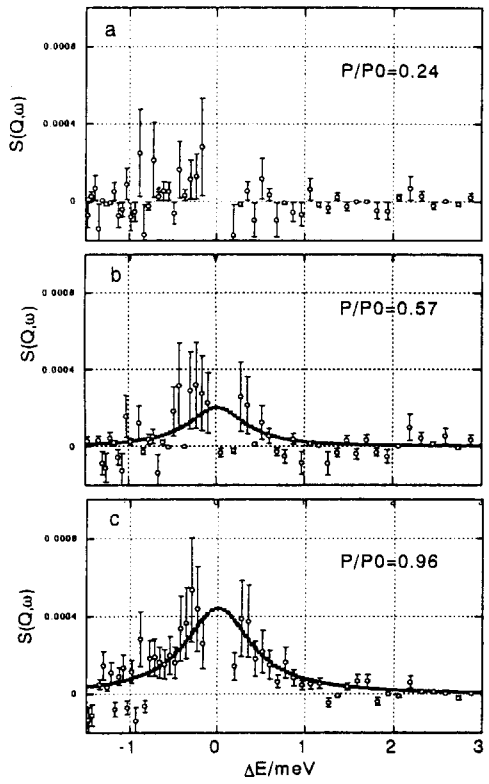


Fig. 3. Difference spectra between $S(Q,\omega)$ under pressure (P/P_0=0.24, 0.57, and 0.96) and in vacuum. Dashed lines are the results of single Lorentzian fits.

In order to see properties of this excess scattering, $S(Q,\omega)$ for P/P_0=0 has been subtracted from $S(Q,\omega)$ for P/P_0=0.24, 0.57 and 0.96, and the difference spectra are shown in Fig. 3a-c. Although the experimental error is rather large, the excess scattering is clearly observed for P/P_0=0.96, and decreases with decreasing pressure. It is slightly observed at P/P_0=0.57, but not at P/P_0=0.24. The excess scattering intensity was fitted to a single Lorentzian to evaluate the spectral width Γ, which corresponds to the relaxation rate, and the fraction A. The results of fits are shown by dashed lines in Fig.3b and c. The evaluated widths and fractions are 0.37 meV and 0.30 meV, and 9.3 x 10^{-5} and 3.1 x 10^{-5} for P/P_0=0.96 and 0.57, respectively. Defining the product of Γ and A as a local flux, which is a measure of the local mobility, we plotted the local flux as a function of P/P_0 in Fig. 4, where the permeability is also shown. The local flux begins to increase at around P/P_0=0.6, which agrees with the onset pressure of the permeability. However, the pressure dependence of the permeability is steeper than that of the local flux. This result indicates that the local mobility of the polymer somewhat contributes to the acceleration of the permeability, but other factors such as an additional layer of the gas on the film [3] and the free volume change [4] also contribute to the acceleration.

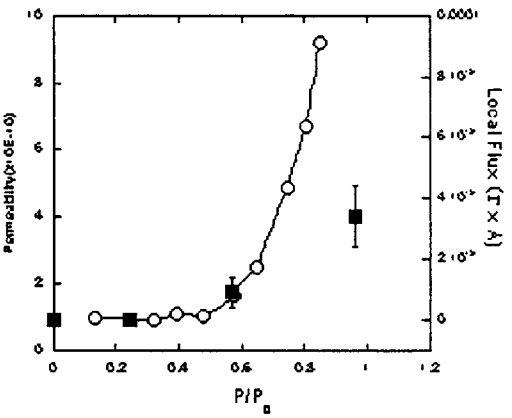


Fig. 4. Pressure dependence of the gas (propylene) permeability (o) and the local flux (=Γ x A) (■)

[1] A. Shimazu, T. Miyazaki, M. Maeda, M. Matsushita, K. Ikeda, J. Polym. Sci., Phys. Ed., **37**, 2941 (1999)
[2] T. Miyazaki, A. Shimazu, K. Ikeda, Polymer, **41**, 8167 (2000)
[3] T. Miyazaki and A. Shimazu, unpublished.
[4] Akira Shimazu, Tukasa Miyazaki, Kenichi Ikeda, Yasuo Ito, Polymer Preprint, Japan, **50**, 4, 731(2001).

テーマ：中性子反射率測定による高分子界面での分子拡散挙動評価
表題：中性子反射率測定による（ポリスチレン/重水素化ポリスチレン）二層膜の界面構造の時間依存性

1-5-17 Neutron Reflectivity Study of Time Evolution of Interfacial Structure of (Polystyrene/Deuterated Polystyrene) Bilayer below the Bulk Glass Transition Temperature

T. Kajiyama, D. Kawaguchi, A. Sakai, K. Tanaka, S. Tasaki*1, and A. Takahara*2

Faculty of Engineering, Kyushu University, 6-10-1 Hakozaki, Higashi-ku, Fukuoka 812-8581, Japan
**1Research Reactor Institute, Kyoto University, Kumatori-cho, Sennan-gun, Osaka 590-0494, Japan*
**2Institute for Fundamental Research of Organic Chemistry, Kyushu University, 6-10-1, Hakozaki, Higashi-ku, Fukuoka 812-8581, Japan*

Molecular motion at polymer surfaces is quite different from that in the bulk region due to the free energy difference between surface and bulk. The purpose of this study is to investigate surface molecular motion based on polymer interdiffusion behavior across a [polystyrene/deuterated polystyrene] (hPS/dPS) interface at a temperature above the surface glass transition temperature, T_g^s and below the bulk glass transition temperature, T_g^b by neutron reflectivity (NR) measurement.

Samples used in this study were monodisperse hPS and dPS with M_n of 190k and 185k, respectively. Each thin film was prepared by the spin-coating method onto a silicon wafer. Then, (hPS/dPS) bilayers were prepared by floating technique as follows. The perimeter of the hPS film was scored with a blade, and then floated it off onto the clean surface of distilled water. Then, the hPS film was picked up onto the dPS film by attaching the dPS film from the air side. For the interdiffusion experiment, the bilayers were annealed at 365 K, which was above T_g^s and below T_g^b for various times.

NR measurement was performed by using the multilayer interferometer for neutrons (C3-1-2, MINE) at the Institute for Solid State Physics, the University of Tokyo. The incident neutrons had the long wavelength of 1.26 nm and the resolution of 3.5 %. The reflectivity was calculated based on the scattering length density profile along the depth direction by using Spreadsheet Environmental Reflectivity Fitting.

Figure 1 shows the neutron reflectivity profiles of the as-prepared (hPS/dPS) bilayer and annealed ones at 365 K for various times. The solid lines denote the calculated reflectivity on the basis of the scattering length density, (b/V) profile along the depth direction. The magnitudes of (b/V) for hPS and dPS were 1.41 x 10^{-4} and 6.46 x 10^{-4} nm^{-2}, respectively. The Kiessig interference fringes shown in Figure 1 were mainly determined by the dPS thickness because of a small contrast qf (b/V) at the (air/hPS) interface. Since the calculated reflectivity curves were in good agreement with the experimental ones as shown in Figure 1, it is considered that the interfacial structure at the (hPS/dPS) interface shown in Figure 2 reflects the real structure. The interfacial broadening discernibly increased by annealing at 365 K, which was below T_g^b, for 2.1 x 10^5 s, and then, the interfacial thickness remained constant even for a longer time. This result indicates that molecular motion at the surface is much enhanced in comparison with its in the bulk.

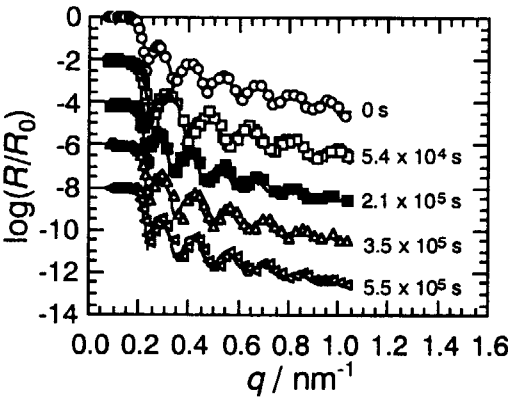


Figure 1. Neutron reflectivity profiles of the as-prepared (hPS/dPS) bilayer and annealed ones at 365 K for various times.

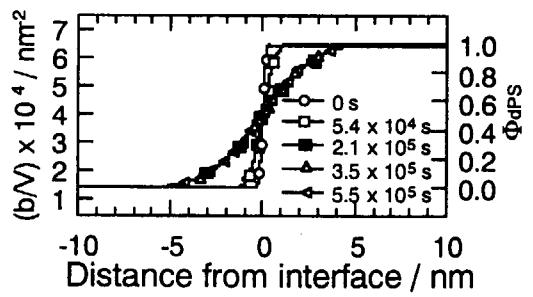


Figure 2. Scattering length density profiles at the as-prepared (hPS/dPS) interface and annealed ones at 365 K for various times.

JRR-3M, MINE, Polymer

研究テーマ：中性子散乱による強相関電子系の研究
表題：ポリスチレン/ポリビニルメチルエーテル混合系の小角中性子散乱及び誘電研究

1-5-18

Small-angle neutron scattering and dielectric studies on miscibility of poly(styrene) and poly(vinyl methyl ether) mixtures

Hiroyuki Takeno, Masaru Kobayashi, Motosuke Naoki and Satoshi Koizumi[1]

Gunma University, Gunma, 376-8515, Japan
[1]Japan Atomic Energy Research Institute, Tokai, Ibaraki 319-11, Japan

In the past several decades, numerous studies have been made on miscibility of polymer mixtures. Nevertheless, miscibility in polymer mixtures seems to be still poorly understood. The Flory-Huggins interaction parameter χ, which characterizes the segregation powers between different components, is a key parameter to understand the miscibility of polymer mixtures, e.g., when the χ parameter becomes large, the segregation powers become large, while in the opposite case the they become small. Apart from original definition of the χ parameter, the χ parameter as obtained by small-angle neutron scattering (SANS) is usually treated as a phenomenological parameter involving all factors which affect the miscibility of polymer mixtures other than combinatorial entropy of mixing. Though the χ parameter for many miscible polymer mixtures has so far been obtained by SANS, physical contents of the χ parameter are very ambiguous.

The molecular motions have been investigated by means of various spectroscopy techniques such as dielectric spectroscopy (DS) inelastic neutron scattering or nuclear magnetic resonance (NMR) techniques and so on. In this work, for polystyrene (PS) and poly(vinyl methyl ether) mixtures, we investigated the χ parameter and localized molecular motions by SANS and DS, respectively. So far, though this mixture has been investigated using SANS or DS by many researchers, to our knowledge, there is no attempt to combine both techniques and understand the χ parameter in terms of the local molecular motions.

We investigated the SANS behavior in the single phase state for deuterated PS (dPS) and PVME mixtures with various compositions. Figure 1 shows the scattering profiles for dPS/PVME =20.3/79.7 (wt/wt%) mixture at various temperatures. The scattered intensity increases with increase of temperature, reflecting that the system has a lower critical solution temperature (LCST) type of phase diagram. We obtained the χ parameter as a function of temperature by best fits of the scattering data with theoretical scattering formula calculated by de Gennes.[1] The χ parameter linearly increases with decrease of reciprocal temperature or increase of temperature. When we compare the χ parameters for various mixtures at a given temperature, as fraction of PS increases, the χ parameter decreases.

On the other hand, in the DS measurements, side group motions of PVME were observed and strongly affected by blending PS, e.g., the relaxation time τ shifted toward higher temperature by blending PS (Figure 2).[2] This result suggests that side group motions of PVME in PS/PVME mixture strongly correlate with PS. Here we compare the composition dependence of the χ parameter with that of the change in τ by blending PS at a given value of τ. We estimated the difference between the temperature position at log $\tau = -4$ in the side group motions for neat

原子炉：JRR-3M　　装置：SANS-J (C3-2)　　分野：中性子散乱（高分子）

PVME and that for the mixture, $\Delta T_{\beta s}$. Figure 3 shows comparison between the composition dependence of the χ parameter and that of $\Delta T_{\beta s}$. Interestingly, until composition of 70% PS, as composition of PS increases, the χ parameter decreases and $\Delta T_{\beta s}$ increases. Both results suggest that interactions between PS and PVME become strong, as composition of PS increase. Thus, the χ parameter and the side group motions of PVME are found to strongly correlate. Namely, side groups of PVME play a significant role in the miscibility of this mixture. Though $\Delta T_{\beta s}$ has a maximum for around PS/PVME = 70/30 mixture, there is no SANS data for the mixture with the composition higher than 70 % PS at the present stage. For further verification of the above speculation, in near future we will carry out the SANS measurement for the mixture with PS composition higher than 70 % PS.

References

1) P. G. de Gennes, *Scaling Concepts in Polymer Physics* (Cornell University: Ithaca, NY, 1979).
2) H. Takeno, M. Kobayashi and M. Naoki, S. Koizumi, J. Chem. Phys. to be submitted.

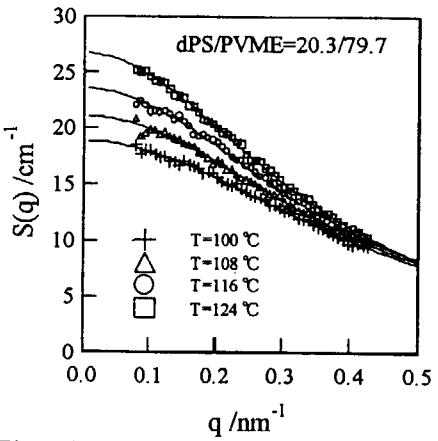


Fig.1 SANS profiles at various temperatures for PS/PVME=20.3/79.7 mixture.

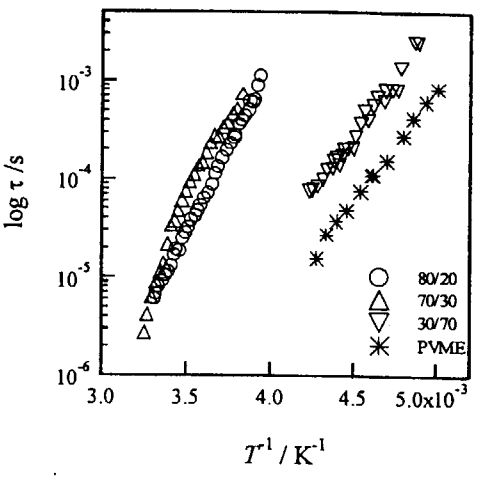


Fig. 2 Plot of logarithmic relaxation time against reciprocal temperature in the side group motions of neat PVME and various mixtures. (Arrhenius plot)

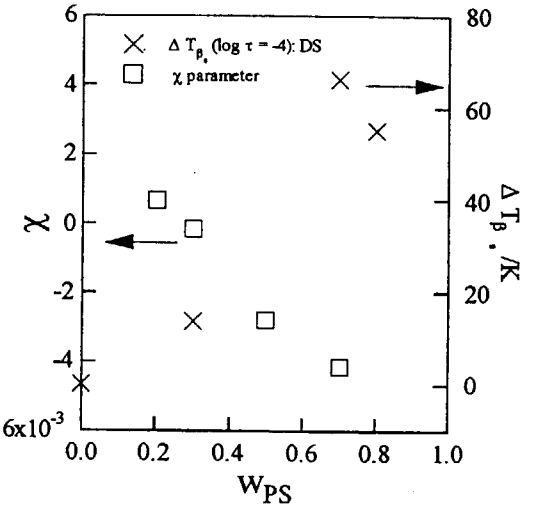


Fig. 3 Comparison between composition dependence of the χ parameter estimated by SANS and that of the difference between the temperature for neat PVME at a given relaxation time (log τ = -4) and that of a given mixture, where w_{PS} represents the weight fraction of PS.

研究テーマ：中性子散乱による強相関電子系の研究
表　題　：共重合体天然ゴムに関する小角散乱の研究

1-5-19 Small-Angle Neutron Scattering Study of Graft-Copolymer Natural Rubber-Styrene

A. Insani[1], J. Suzuki [2], S. Koizumi[2], A. Ikram[1], Sudirman[1], and A. Purwanto[1]

[1]Research and Development Center for Materials Science and Technology, BATAN, Serpong, Indonesia
[2]Advanced Science Research Center, JAERI, Tokai, Ibaraki, 319-1195, Japan

Numerous studies have been made on irradiated copolymerisation of styrene in natural rubber[1)]. Graft-copolymer natural rubber and styrene can be used for gloves, automotive parts, paste of lamellar plank, etc. In the studies of phase separating structure of this materials, it is important to obtain information on the interfacial structure[2)]. The aim of this study is to see the difference of the polydispersion index of the styrene monomer graft in the natural rubber, which depends on dose variation. It is also of interest to compare the data with those obtained by SANS of BATAN, Indonesia.

The natural rubber–styrene (NR-St) copolymer samples has been synthesized by simultaneously mixing and irradiation with gamma-rays[3)]. Small-angle neutron scattering measurements were performed by the SANS-J instrument with λ = 0.706 nm at the JRR-3M reactor in JAERI. Scattering data of NR-St samples were collected for about 2 hours at room temperature. The data were then corrected from background and normalized.

Figure 1 shows the scattering profiles of NR-St at gamma irradiation dosis of 15 kGy, 30 kGy, and 45 kGy. The intensities are approximately proportional to q^{-4} (Porod law), which suggests that the interface between styrene and natural rubber in the samples is smooth. A closer inspection for the sample with dosis of 30 kGy and 45 kGy shows that there are bumps around q = 0.2 nm^{-1}, which does not exist for that with the dose of 15 kGy. More experiments, such as SEM or HRSANS, are necessary to determine the origin these bumps and the mixing structure of the styrene.

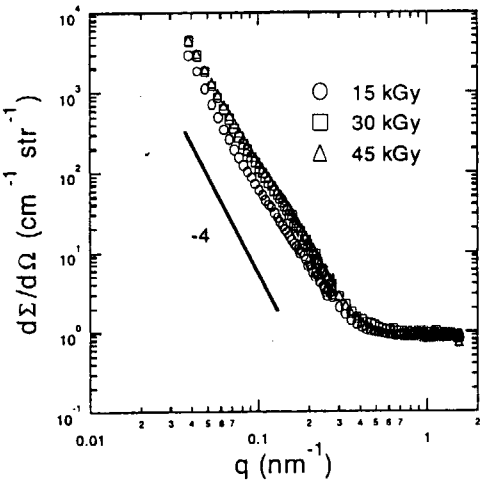


Fig.1 SANS profiles for NR-St with various gamma irradiation dosis. A straight line with a slope of -4 in the log-log plot indicates that the profiles obey the Porod law.

References

[1] Sundardi, F. and Kadarijah, S., J. Appl. Polym. Sci. **29** (1984) 1515.
[2] N. Torikai, Y. Matsushita, S. Langride, D. Bucknall, J. Penfold, and M. Takeda, Physica B **283** (2000) 12-16.
[3] Herwinarni, S., Marga Urama, Kadarijah, S., Made Sumarti, and Sunit Hendrana, Proc. of Simposium Nasional Himpunan Polimer Indonesia, Indonesia (1995).

原子炉：JRR-3M　　装置：SANS-J (C3-2)　　分野：中性子散乱（高分子）

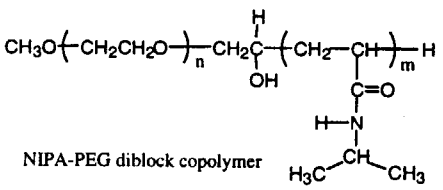
研究テーマ：水溶性ブロック共重合体の自己組織化と機能
表　　題：水溶性ブロック共重合体

1-5-20 Small-angle Neutron Scattering Study on Thermal Phase Behavior of NIPA-PEG Diblock Copolymer

Masahiko Annaka, Ryuuhei Motokawa, Takayuki Nakahira, Satoshi Koizumi[1]

Department of Materials Technology, Chiba University, Inage-ku, Chiba 263-8522, Japan
[1]Advanced Science Research Center, Japan Atomic Energy Research Institute, Tokai-mura, Ibaraki 319-1195, Japan

The self-aggregation of block copolymers has attracted much attention both for its intrinsic scientific interest and for its technological importance. The block copolymer consisting of poly(N-isopropylacrylamide) and poly(ethylene glycol) (NIPA-PEG diblock copolymer) was prepared by using ceric ammonium nitrate (Ⅳ) as a redox initiator.[1)]



An aqueous solution of the block copolymer above a critical concentration experience three distinct phases upon heating. One of the phases is a gel phase that shows reversibility in sol-gel transition without noticeable synerisis. The phase behavior is determined by various factors, i.e. the block ratio, the molecular weight, the concentration and temperature. Block copolymrs exhibit transitions from expanded coil and to collapsed globules and the subsequent aggregation of the collapsed globules to make physical junction.

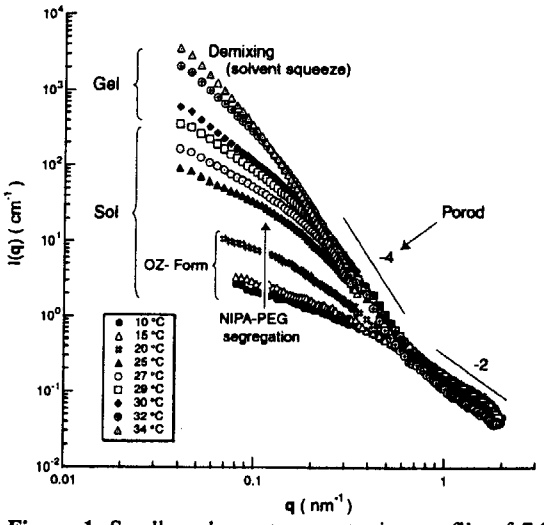


Figure 1. Small angle neutron scattering profile of 7.0 % (w/v) NIPA- PEG diblock copolymer (n:m=2:1 in molar ratio) in D_2O.

We employed small angle neutron scattering (SANS) in order to investigate the microscopic structure.

原子炉：JRR-3M　　装置：SANS-J(C3-2)　　分野：中性子散乱（高分子）

For SANS measurements, we used a wave length of 0.65 nm and two detector position of 1.5 and 9.0 m. Figure 1 shows the SANS profiles for a 7.0 % (w/v) NIPA-PEG diblock copolymer (m:n=2:1) in D_2O. At low temperature below 20 °C, Ornstein-Zernike (OZ) type scattering, which is typical for the semi-dilute polymer solution, was observed. It is interesting to note that the intensity increases abruptly from 15 °C to 25 °C in sol state. We consider that it is precursory phenomenon of gelation; PEG and NIPA chains segregate with themselves, without forming sharp interface. Figure 2 shows a plot of $I(q=0)^{-1}$ vs 1/T. This plot has intended that the segregation is characterized by crossover point in the vicinity of 17 °C, since $I(q=0)^{-1} \sim \chi_{NIPA\text{-}PEG}$ and empirically χ is found to be inversely proportional to temperature[2,3]. Schematic illustration of NIPA-PEG segregation is shown in Figure 3.

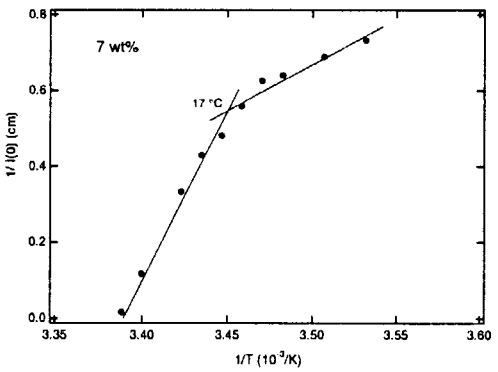


Figure 2. Plot of $I(q=0)^{-1}$ against 1/T, where the extrapolated zero-angle intensity was obtained by Ornstein-Zernike plot.

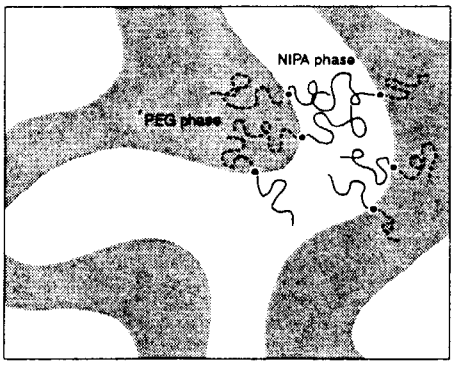


Figure 3. Schematic illustration of the segregation image for NIPA-PEG diblock copolymer (block ratio 2 : 1).

On the other hand, in gel and demixing state we discussed the observed power-low q-behaviors based on the mass and surface fractals and Porod low. Above 30 °C, Porod (q^{-4}) region was shown that is the scattering for reflecting on the microstructure of aggregated NIPA rich domain. The two phases surface structure was characterized by Porod plot and we estimated the characteristic interface thickness and the specific surface area. Details will be discussed in future.

Reference

1) Soundppan and Nagarajan et al., *J. Polymer. Sci., Polym. Part A, Polym. Chem. Ed.* **33**, 2925-2933 (1995).

2) D. Schwahn, S. Janssen, and T.Springer, *J. Chem. Phys.* **97**, 8775-8788 (1992).

3) M.D. Whitemore and J. Noolandi, *J. Chem. Phys.* **93**, 2946-2955 (1990).

研究テーマ：黎明研究（メゾ空間に拘束された高分子の相転移）
表題：マイクロエマルションドロプレット中に閉じ込められた高分子鎖のコンフォメーション

1-5-21 Conformations of a Single Polymer Chain Confined in a Microemulsion Droplet

Kaori Nakaya and Masayuki Imai

Department of Physics, Faculty of Science, Ochanomizu University, Bunkyo, Tokyo 112-0012, Japan

Microemulsions are thermodynamically stable nano-scale structured fluids consisting of water, oil, and surfactants. The microemulsion shows a variety of morphologies such as droplet (sphere), lamellar, and bicontinuous structures as a function of the temperature and the concentration. Among these morphologies, water-in-oil microemulsion droplets provide isolated nano-scale water region separated by continuous oil phase.

When we introduce water soluble polymers into the water-in-oil microemulsion droplet system, polymer chains are subjected to be confined in the droplets. For an ideal chain, the concentration distribution of a polymer chain inside of a droplet is expressed by

$$c(x) \sim \sin^2(\frac{\pi x}{D}) \qquad (1)$$

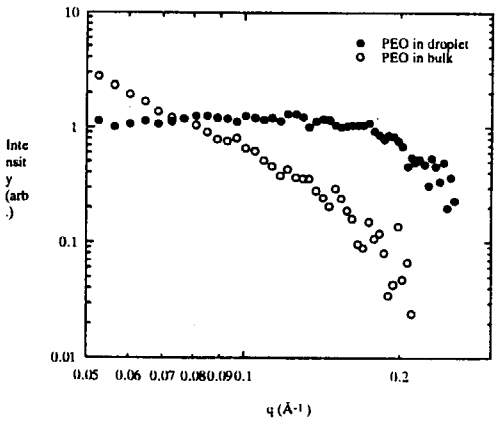
where x is coordinate inside of the droplet and D is the droplet size (wall boundaries are at x=0 and D). Of course this distribution is modified for a real chain. To our knowledge, there are no experimental studies to investigate the concentration distribution inside of the droplet.

A small-angle neutron scattering (SANS) technique is suitable to access this problem because we can focus on the scattering function of a polymer chain inside of a droplet by contrast matching of media and membranes.

In this experiment, we used water-in-oil microemulsion droplets consisting of isooctane, Aerosol-OT (AOT), and water. As confined polymers we adopted gelatin molecules (type A, Bloom 300) having molecular weight of 9.6 $*10^4$. In this study we confined a single gelatin chain into a microemulsion droplet, where the size of the droplet is comparable to the radius of gyration of the gelatin chain in bulk solution state. The SANS measurements were performed using a SANS-J instrument of JAERI at JRR-3M reactor.

Figure 1 shows scattering functions for single gelatin chain confined into a microemulsion droplet (open circle) compared with that in bulk solution state (closed circle). The radius of gyration of a gelatin chain is fairly decreased by the confinement, indicating polymer chain are condensed in the central region of a droplet. We have been investigating the conformations of confined polymer chain in more detail.

Fig. 1 Scattering functions for single gelatin chain confined into a microemulsion droplet (open circle) compared with that in bulk solution state (closed circle).



原子炉：JRR3-M　　装置：SANS-J (C3-2)　　分野：中性子散乱（高分子）

1. 中性子散乱 6) 生物学

1. Neutron Scattering 6) Biology

This is a blank page.

研究テーマ:機能性生体物質の水和構造研究
表　　題:*Alcaligenes xylosoxidans* 由来のチトクローム *c'*の中性子線構造解析

1-6-1

Preliminary Neutron Structure Analysis of Cytochrome c' from *Alcaligenes xylosoxidans* NCIMB 11015

Takamitsu Kohzuma, Hiroyoshi Watanabe, Andreas Osterman[1], Kazuo Kurihara[1], Toshiyuki Chatake[1], Ichiro Tanaka[1], and Nobuo Niimura[1]

Department of Materials and Biological Sciences, Faculty of Science, Ibaraki University, 2-1-1 Bunkyo, Mito, Ibaraki 310-8512, Japan

[1]Advanced Science Research Center, JAERI, 2-4 Shirakatashirane, Tokai, Ibaraki 319-1195, Japan

Gas-sensing heme proteins play a central role in the regulation of important biological processes. NO-, CO-, and O_2-responsive systems have been identified[1]. NO plays a role of cellular signal transduction in mammals, such as the immune response to tumor cells, vasodilation and neuronal synaptic transmission[2]. A number of these biological responses to NO are triggered by an increase in th level of the cellular second messenger cGMP, which is produced by a heme protein, soluble guanylate cyclase (sGC). The sGC is activated by the binding of NO to the heme domain.

Cytochrome *c'* are a class of c-type cytochrome, which have been found in a number of photosynthetic, nitrogen-fixing and denitrifying bacteria. In denitrifying bacteria, Cytochrome *c'* functions as an NO transfer and protecting the organism from potentially toxic levels of NO[3]. It has been demonstrated cytochrome *c'* from *Alcaligenes xylosoxidans* NCIMB 11015 contain a 5-coordinated histidine ligated heme[4] that forms stable adducts with NO accompanied with the dissociation of histidine ligand[5]. The similarities in the distinctive reactivity and the binding modes of NO to the heme center in cytcrome *c'* and that of sGC are very important to reveal the molecular mechanism of the alteration of protein structure caused by the ligand-binding.

Weak interactions involving hydrogen-bonding and stacking interactions between aromatic rings are key interactions to reveal the protein functions[6]. Such hydrogen atoms can be defined *active hydrogen* atoms in the biological relevance. Neutron diffraction technique is the strongest method to obtain precise structural information of such biological *active hydrogen* atoms during the course of the inter-conversion of protein structure.

A preliminary neutron diffraction data set of cytochrome *c'* had been collected at BIX-3 at

---

原子炉：JRR-3M　　装置：BIX-3 (1G-A)　　分野：中性子散乱（生物）

JRR-3M up to a resolution of 2.8 Å. Due to the large unit cell dimension (c = 181. 8 Å) and the relative small crystal volume this data collection represents a challenge for the diffractometer BIX-3. The cytochrome *c*' crystal used in this study belongs to space group $P6_522$ with unit cell parameters, a=b=56.6 Å and c=181.8 Å. The crystal volume is 1.4 mm^3 (1.5 mm × 1.2 mm × 0.8 mm). For the measurement the crystal was sealed in quartz capillary. Neutron diffraction data up to a resolution of 2.8 Å were collected at room temperature at the neutron single crystal diffractometer BIX-3 at JRR-3M (Beam hole 1G). For the data collection the step scanning method was used ($\Delta\varphi$ = 0.3°). The collection time per frame was controlled by the monitor counts of the direct beam in front of the crystal and was about 180 minutes (Fig. 1).

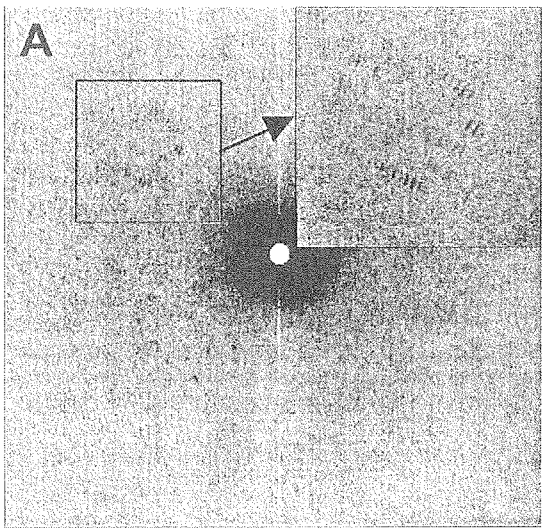


Figure 1. Neutron diffraction of the cytochrome *c*' crystal. The inlay shows the Bragg-reflections of the longest reciprocal axis c*.

The intensities of the reflections were integrated and scaled by the programs DENZO/SCALEPACK. Subsequent data reduction was performed by the CCP4 program TRUNCATE. The preliminary structure refinement and map calculations were done using the program X-PLOR 3.851. As starting model the X-ray structure of cytochrome *c*' form *Alcaligenes xylosoxidans* (PDB accession code 1CGO) was used. The positions of the non-exchangeable hydrogen atoms were generated due to stereochemical information from the topology file. This was followed by a energy minimization for hydrogen atoms with rotational degrees of freedom (methyl-groups) without including the diffraction data. Afterwards a rigid body refinement were performed. An additional data collection is still in progress.

References

(1) K. R. Rodgers, Curr. Opin. Chem. Biol. **3** (1999) 158-167.

(2) J. W. Denninger et al., Biochim. Biophys. Acta **1411** (1999) 334-350.

(3) J. W. B. Moir, Biochim. Biophys. Acta **1430** (1999) 65-72.

(4) J. Dobbs et al., Acta Crystallogr. D**52** (1996) 356-368.

(5) D. M. Lawson et al., EMBO J. **19** (2000) 5661-5671.

(6) T. Steiner et al., J. Mol. Biol. **305** (2001) 535-557.

研究テーマ ： 機能性生体物質の水和構造研究

表 題 ： B-DNA 結晶化の相図及び中性子回折実験に適した巨大結晶育成への応用

1-6-2

Phase diagram for B-DNA crystallization systems and its application to make a large crystal of available for neutron diffraction experiments

Shigeki Arai, Toshiyuki Chatake, Yoshiaki Minezaki, Yoshihiro Nishimura and Nobuo Niimura

Advanced Science Research Center, Japan Atomic Energy Research Institute, Tokai-mura, Ibaraki-ken, 319-1195, Japan

Water molecules affect the structure, stability, polymorphism and flexibility of the DNA double helix. For example, a chain of water molecules is penetrated deeply into the minor groove of the B-DNA duplex, which contributes to the stabilization of DNA conformation[1]. Furthermore, the specific hydration patterns around DNA duplex play a role in nucleotide sequence recognition by proteins and drugs[2]. In those studies, the observed hydration structure was obtained from the network of only the oxygen atoms of water molecules since it is difficult in an X-ray crystallographic analysis to identify the hydrogen atoms. In order to more fully understand the role in nucleotide sequence recognition by proteins, the location of the hydrogen atoms in this network structure of water molecules is important.

In contrast the neutron diffraction is a very powerful method to determine the detailed structure including hydrogen positions[3,4]. Neutron fibre diffraction studies of DNA have been reported and the hydration structure has been described[5], but the resolution of those studies was limited to about 3Å and the information of base pairing specificity is either lacking or very much limited. High-resolution neutron diffraction from a single crystal experiment is indispensable to know the precise network structure of hydration in the minor and major grooves. In order to carry out such a high-resolution neutron experiment, a large single crystal, the volume of which is in excess of 1mm^3, is necessary. Keeping these needs in mind, we attempted to grow millimeter-size single crystal of B-DNA by using the phase diagram technique. So far there have been reports of the phase diagrams of only some DNA oligomers[6-9], although the phase diagram is available for clarification of the crystallization conditions. Moreover, the phase diagram for cation-DNA duplex systems of B-DNA and a large single crystal of available for neutron diffraction experiments has never been reported. We selected the B-DNA decamer d(CCATTAATGG) as a sample because the crystallization conditions of vapor diffusion, for standing drops for this oligonucleotide, have already been reported[10].

Fig. 1 shows a phase diagram for $MgCl_2$-DNA systems determined by the micro-batch method, in which the drops were kept at 6°C for 20 days. pH was being kept constant at 7.0 (using 0.1M sodium cacodylate buffer) and the concentration of MPD (2-methyl-2,4-pentandiol) was held at 30 %(v/v). In the diagram there are three regions, A, B and C, which correspond to the existence of crystals, amorphous precipitate, and a clear solution, respectively. The most distinctive feature of the phase diagram is that

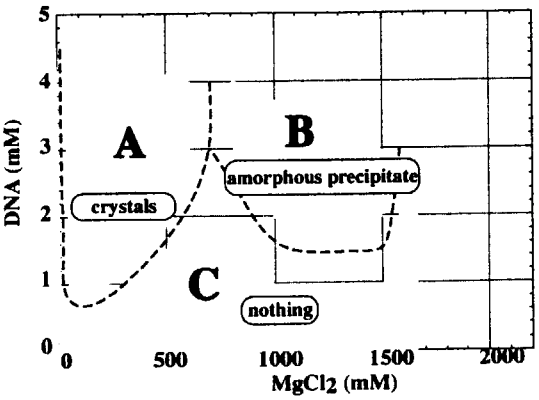


Fig.1 The phase diagram for DNA-$MgCl_2$ systems at 30 %(v/v) MPD.

原子炉：JRR-3M 装置：BIX-3 (1G-A) 分野：中性子散乱（生物）

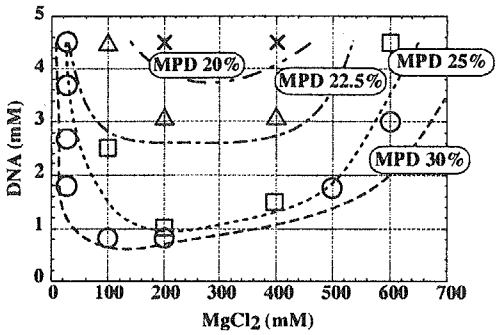


Fig.2 The phase diagram of DNA solubility vs $MgCl_2$ concentration at various MPD concentrations. A circle, a square, a triangle and a cross mean that crystals have appeared at MPD concentrations of 30%(v/v), 25%(v/v), 22.5%(v/v) and 20%(v/v), respectively. The broken lines show the estimated solubility curves at different MPD concentrations.

there is a minimum in the DNA solubility curve, that is, the DNA solubility decreases abruptly to less than 1mM at about a $MgCl_2$ concentration of 100mM and then gradually increases as the $MgCl_2$ precipitant concentration is increased. We found that, in general, crystal quality becomes worse and crystal size becomes smaller as the solution conditions are further moved from the minimum point in Fig.1. And in Fig.2, in which the MPD concentration was varied, it was found that the DNA solubility increased with a decrease of MPD concentration. In addition, crystal quality also decreases as the MPD concentration decreases. Accordingly we have succeeded in growing a large single crystal at conditions near the minimum solubility point.

Fig.3 shows a typical raw data frame of preliminary neutron diffraction pattern from the grown crystal by BIX-3[4] diffractometer at the JRR-3M reactor. The insert in Fig.3 shows a photograph of a single crystal (1.7 x 1.3 x 0.6 mm^3) grown at 0.4 ml D_2O solutions of DNA (1.5mM), MgCl2 (100mM), MPD (30%:v/v) and pD 6.6. This is the largest single crystal of an oligomer B-DNA reported thus far. The reproducibility of our crystals at these solution conditions is quite satisfactory. Fig.3 is confirmed that this crystal is suitable for neutron diffraction analysis, and the collection of a complete data set of Bragg reflections is presently scheduled.

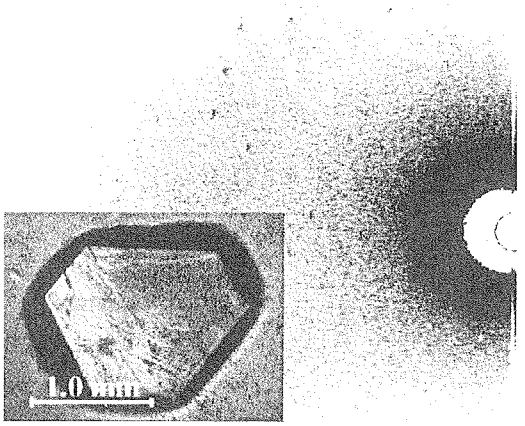


Fig.3 A preliminary neutron diffraction pattern from the grown single crystal. The exposure time is 10 hours. The insert shows a used crystal. In a neutron diffraction experiment, in order to avoid the high background coming from the incoherent neutron scattering of hydrogen atoms, crystallization in D_2O solution.

References

1) H. R. Drew et al., J. Mol. Biol. **151** (1981) 535-556.
2) Z. Owtinowski et al., Nature **335** (1988) 321-329.
3) N. Niimura et al., Nature Struct. Biol. **4** (1997) 909-914.
4) M. Niimura et al., Cuur. Opi. Struct. Biol. **9** (1999) 602-608.
5) M.W. Shotton et al., Biophys. Chem. **69** (1997) 85-96.
6) L.V. Malinina et al., J. Biomol. Struct. Dyn. **5** (1987) 405-433.
7) L.V. Malinina et al., J. Cryst. Growth **110** (1991) 252-257.
8) G. Minasov et al., J. Cryst. Growth **122** (1992) 136-143.
9) P. S. Ho et al., Science **254** (1991) 1003-1006.
10) D.S. Goodsell et al., J. Mol. Biol. **239** (1994) 79-96.

研究テーマ: 機能性生体物質の水和構造研究
表題　　: ルブレドキシン変異体の中性子結晶構造解析

1-6-3 A neutron crystallographic analysis of a rubredoxin mutant

Toshiyuki Chatake, Kazuo Kurihara, Ichiro Tanaka, Michael W. W. Adams[1], Francis E. Jenney Jr.[1], Irina Tsyba[2], Robert Bau[2] and Nobuo Niimura

Japan Atomic Energy Research Institute, Ibaraki 319-1195, Japan
[1]Dept. of Biochemistry, University of Georgia, Athens, GA 30602, USA
[2]Dept. of Chemistry, University of Southern California, Los Angeles, CA 90089, USA

Proteins from thermophilic micro-organisms are especially intriguing because of their unusual thermostability. The X-ray crystal structures of rubredoxins derived from the hyperthermophile *Pyrococcus furiosus* (which can grow at ca. 95°C) (RubPf) and from the mesophilic bacteria *C. pasterurianum* and *D. vulgaris* (which can not grow above 37°C) have been solved, but those results have not yielded enough information to fully explain the thermostabilization mechanism of RubPf. We were hopeful that a detailed knowledge of the hydrogen positions and hydration structure might reveal some hints regarding its thermostabilization mechanism. In this study, the hydrogen positions and solvation pattern of a rubredoxin "triple mutant" (RubMut) of the hyperthermophile *Pyrococcus furiosus* were investigated by neutron crystallographic analysis. RubMut has three mutations (TRP3 to TYR3, ILE23 to VAL23, and LEU32 to ILE32) which make the three core hydrophobic residues identical to those of the mesophilic rubredoxin from *C. pasterurianum*. RubMut is almost as stable as wild-type rubredoxin from *Pyrococcus furiosus* (RubPf) at neutral pH, but less stable at low pH. Our investigation attempts to provide a rationalization of how the introduced residues might make the rubredoxin mutant somewhat less stable thermally.

RubMut was produced and purified as were obtained from D_2O solution under the same condition as those for RubPf (i.e., using 3.6M Na/K phosphate as a precipitant, with seeding) as that for RubPf[3,4]. Prior to the neutron analysis, the X-ray crystal structure of a smaller crystal of RubMut was solved at 1.5 Å resolution with an R-factor of 19.9 % (R_{free} = 22.3 %). The largest crystal available to us (4 mm^3) was used for the neutron experiment. Diffraction patterns were recorded at room temperature on a neutron imaging plate [5] using the new single crystal neutron diffractometer (BIX-3) at the Japan Atomic Energy Research Institute[6]. The neutron beam was monochromatized at 2.35 Å with an elastically bent silicon monochromator [7]. Data collection was carried out up to a maximum resolution of 1.5 Å, and a step-scan method was used in order to get a high signal-to-noise ratio. Exposure time was about one hour per frame, the total time for the two data sets being 30 days. A total of 7,388 independent reflections were obtained with an overall R_{merge} of 12.1 % from 21,513 observed reflections. The structure determination was performed with the refinement program X-PLOR[8] and the graphics program O[9]. The initial model was derived from the X-ray structure of RubMut. The final model included 39 solvent molecules located around the protein (R=22.8 %, R_{free}=26.6 %). Details of the neutron and X-ray experiments

原子炉：JRR-3M　　装置：BIX-3 (1G-A)　　分野：中性子散乱（生物）

The overall structure of RubMut resembles that of wild-type RubPf. The overall root-mean-square-differences (r.m.s.d.) of the main chain and side chain atoms between RubMut and RubPf are only 0.18 Å and 0.37 Å respectively, indicating that dramatic structural changes did not occur by the triple mutation. The three mutated residues in RubMut were found to retain almost the same atomic positions

Table1. Statistics of data collection and refinement

	Neutron	X-ray
Crystal volume	4mm3	0.1mm3
Beam port / radiation	1G (JRR-3M)	CuKα
Diffractometer	BIX-3	DIP-2000
Time	30days	2days
Resolution (A)	50-1.5	100-1.5
Observed ref.	21,620	38,773
Unique ref.	7,402	9,876
Completeness (%)	85.7	98.6
Rmerge	12.7	7.4
R-factor (%)	22.8	19.9
Rfree (%)	26.6	22.3
Non-hydrogen atoms	432	454
Hydrogen atoms	290	
Deuterium atoms	95	
Solvent molecules	39	61

as those of the original three residues of wild-type RubPf. In two of the three (ILE23 to VAL23 and LEU32 to ILE32), there are only small structural differences between RubMut and RubPf, mainly as a result of a methyl group deletion (in the former case) or a methyl group shift (in the latter case) from C_δ to C_γ. However, for TRP3 to TYR3, large structural changes were indeed found, so that their hydrogen bonding schemes are significantly different. In wild-type RubPf, the N_1-D_1 group (TRP3) and the $O_\varepsilon^{\delta-}$ atom (GLU14) are hydrogen-bonded together and moreover one water molecule is hydrogen-bonded to the N_1-D_1 group (TRP3), and atoms $O_\varepsilon^{\delta-}$ (GLU14) and $O_\varepsilon^{\delta-}$ (GLU30) (Fig. 1a). In contrast, the interactions in RubMut seem to be weaker than those in RubPf (Fig. 1b): for example, the hydrogen bond between the 3rd and 14th residues is absent, and is replaced by a hydrogen bond between the O_4-D_4 group (TYR3) and $O_\varepsilon^{\delta-}$ atom (GLU30). However, the density of the D_4 atom in TYR3 is lower than those in other tyrosine residues, and the temperature factor of the carboxyl group in GLU30 is higher than that of GLU14. This suggests that these groups may not be well-ordered and that this hydrogen bond might be fragile. One can postulate, then, that the intramolecular interactions around TYR3 in RubMut are weaker than those around TRP3 in RubPf, a feature that might contribute to the lower thermostability of RubMut at low pH.

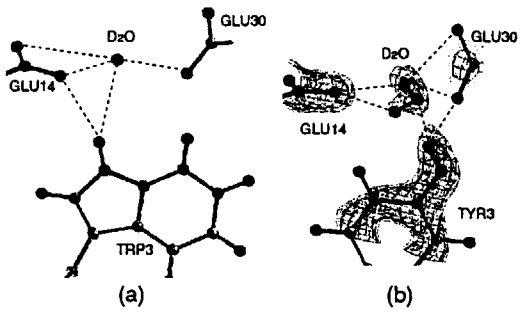


Fig1. Three-dimensional structures around the 3rd residue in RubPf (a) and RubMut (b). Broken lines show hydrogen bonds. In RubMut, the density map is shown with contours at 2.0 σ (dark grey) and 1.5 σ (light grey)

References

1) F. E. Jenney and M. W. W. Adams, Meth. Enzymol. **334** (2001) 45
2) F. E. Jenney et al, in preparation.
3) R. Bau et al., J. Biol. Inorg. Chem. **3** (1998) 484
4) K. Kurihara et al., J. Phys. Soc. Jpn. Suppl. A **70** (2001) 400
5) N. Niimura et al., Nucl. Instrm. Meths. **A349** (1994) 521
6) I. Tanaka et al., J. Phys. Soc. Jpn. Suppl. A **70** (2001) 459
7) I. Tanaka et al., J. Appl. Cryst. **32** (1999) 525
8) A. T. Brunger, X-PLOR, Version 3.1. A (1992)
9) T. A. Jones, J. Y. Zou, S. W. Cowman, M. Kjeldgaard, Acta Cryst. A47, 110 (1991)

研究テーマ：機能性生体物質の水和構造研究
表題：pH 3.4 で調製したニワトリ卵白リゾチーム単結晶の中性子回折のデータ収集

1-6-4

Data Collection of Neutron Diffraction from a Single Crystal of Hen Egg-White Lysozyme Grown under pH 3.4

S. Fujiwara, M. Maeda, Y. Yonezawa[1], and N. Niimura

Japan Atomic Energy Research Institute, Tokai, Ibaraki 319-1195, Japan
[1]Tsukuba College of Technology, Tsukuba, Ibaraki 305-0821, Japan

Hydrogen atoms play essential roles in various aspects of functions of proteins. Moreover, hydrogen bonds between the atoms in the protein as well as hydration are important in the stability of the protein. Locating the positions of hydrogens and hydrated water is therefore important in considering the molecular mechanism of the protein function and the stability of the proteins. Neutron crystallography, which can locate the hydrogens, is one of the important methods to investigate these problems. We have started a project which explore the protonation state of amino acid residues in the protein at various pH, since the charge distribution of the protein, which can be different in different pH, may have important effects on thermodynamic characterization of the protein. As a first step, we collected the neutron diffraction data of the single crystal of hen egg-white (HEW) lysozyme grown in pH 4.9[1-2]. Preliminary structure analysis[3] of these data detected the hydrogen-bond networks including the hydrated water around the active site of this enzyme.

In parallel with the structure analysis, we collected the data from the crystal grown in different pH. Crystals of HEW lysozyme were grown in D_2O at pH 3.4. The space group of the crystals was $P4_32_12$, and the cell parameters were a=b=7.91 nm, c=3.66 nm. Neutron diffraction patterns of the crystal were measured with BIX-II[4]. The oscillation method of 0.4 degrees has been employed. Exposure time per one frame has been 11 hours. Diffraction spots of at least 0.2 nm resolution have been observed. 156 frames of the collected images were used for the data reduction by MAC-DENZO and SCALEPACK[5].

Total of 26733 reflections were observed. The obtained number of independent reflections ($I/\sigma>1$) was 6946, completeness of the data was 78.7% at 0.2 nm resolution, and the overall R_{merge} was 0.273. The data statistics are shown in Table 1. The structure analysis using X-plor[6] is in progress. It is expected that from comparison of the structures at different pH values, protonation states of each residue in the protein can be determined.

Table 1. Data statistics of the collected data

Shell lower limit	Upper limit	Average I	Average error	Norm χ^2	R_{merge}
4.0	0.431	3882.1	415.1	0.536	0.096
0.431	0.342	3255.3	558.4	0.535	0.152
0.342	0.299	2316.6	621.6	0.432	0.227
0.299	0.271	1680.9	706.7	0.395	0.315
0.271	0.252	1607.3	780.9	0.401	0.385
0.252	0.237	1599.4	843.6	0.455	0.415
0.237	0.225	1630.9	964.1	0.424	0.436
0.225	0.215	1637.5	1032.1	0.490	0.457
0.215	0.207	1675.6	963.5	0.586	0.450
0.207	0.200	1833.8	953.6	0.705	0.427
All reflections		2151.6	771.2	0.482	0.273

References

[1] S. Fujiwara et al.: JAERI Review **99-003** (1999) 13.
[2] S. Fujiwara et al.: JAERI Review **2000-005** (2000) 7.
[3] M. Maeda et al.: J. Phys. Soc. Jpn. **70** (2001) Suppl. A 403.
[4] S. Fujiwara et al.: Physica B **241-243** (1998) 207.
[5] Z. Otwinowski and W. Minor: Methods Enzym. **276** (1997) 307.
[6] A. T. Brünger: X-PLOR Version 3.1 (1993) (Yale Univ., New Haven, CT)

原子炉：JRR-3M　　装置：BIX-2 (T2-3)　　分野：中性子散乱（生物）

研究テーマ：逆ミセルの構造ダイナミックスと超酵素活性
表題：AOTマイクロエマルジョン構造にたいする蛋白質の包含の影響

1-6-5 Effect of Occlusion of Proteins on AOT Microemulsion Structure

M. Hirai,[1] R. K. Hirai,[2] H. Iwase,[1] T. Hayakawa[1], M. Nagao,[3] and M. Shibayama.[3]

[1] *Department of Physics, Gunma University, Maebashi 371-8510, Japan.*
[2] *Meiwa Gakuen Junior College, Maebashi, Gunma 371-0034, Japan.*
[3] *Institute for Solid State Physics, University of Tokyo, Tokai 106-1, Japan.*

1. Introduction

We have been studying the relation between w/o microemulsion structure and enzymatic activity of proteins. In our previous studies using synchrotron radiation small-angle X-ray scattering, small-angle neutron scattering (SANS), and neutron spin-echo, we showed the following evidences. 1) Hydrolysis of some esters catalyzed by α－chymotrypsin entrapped in w/o microemulsion is enhanced at a low w_0 range (w_0 ≡ [water]/[AOT]) where the microemulsion is in a transient phase between the oligomeric and monomeric phases [1]. 2) A bending fluctuation of the microemulsions is significantly enhanced at this low w_0 range [2]. 3) Structural properties and phase boundaries between different phases of w/o AOT microemulsions strongly relate to the penetration limits of apolar solvents depending on the linear hydrocarbon chain lengths of those solvents [3].

In the present study, to clarify the location of proteins in w/o AOT microemulsions, we have carried out SANS experiments using the solvent contrast variation method which is well known to have an advantage for determining an internal scattering density distribution of a solute particle.

2. Experimental

AOT was purchased from Nacalai Tesque Inc. Solvents used were 99.9+ % *n*-heptane from Wako Chem. Co., d_{16}-*n*-heptane (99+ atom % D) and deuterium oxide (100 atom % D) from Aldrich Chem. Co. Normal water purified by a Millipore system was used. Type-II α－chymotrypsin from bovine pancreas produced by Sigma Chemical Co. was used without further purification. The α–chymotrypsin was solubilized in D_2O/H_2O mixed water (98 % D_2O v/v) whose scattering density is matched to that of d_{16}-*n*-heptane. The microemulsions were obtained by using an injection method. The fractions of d_{16}-*n*-heptane in the apolar solvent were 100 % v/v, 85 % v/v, and 70 % v/v. The w_0 values were selected to be 12 and 20. The AOT concentrations of all samples were 0.1 M. The concentrations of α–chymotrypsin [E] were 0 M and 1.32 x 10^{-4} M for w_0 = 12, and 0 M and 2.21 x 10^{-4} M for w_0 = 20.

SANS experiments were carried out by using a SANS instrument of JRR-3M of JAERI, Tokai, Japan. The sample solutions were contained in a quartz cell controlled at 25 °C. The standard analyses of SANS data were executed.

3. Results and discussion

Fig. 1 shows the change of the scattering curve $I(q)$ depending on the ratio of [d_{16}-*n*-heptane]/[*n*-heptane] and on the protein concentration. The significant decrease of the scattering intensity below q = 0.03 Å^{-1} is attributed to the presence of a beam stopper. In Fig. 1(a), the scattering curve $I(q)$ varies with decreasing the d_{16}-*n*-heptane concentration, which results from the change of the contrast of the AOT microemulsion. The protein concentration dependence of the scattering curve is shown in Fig. 1(b). Due to the occlusion of the proteins in the

microemulsion, the internal scattering density distribution greatly varies, which results in the change of the scattering curve. As is well known in the solvent contrast variation method, a heterogeneity in the internal scattering density distribution of a solute particle is more clearly reflected with approaching the solvent scattering density to the solute scattering density. In the present case, the effect of the presence of the proteins on the microemulsion structure can be seen most evidently at the low contrast solvent condition, namely, at 70 % v/v d_{16}-*n*-heptane since the contrast matching points of the AOT and protein molecules are lower than 70 % v/v d_{16}-*n*-heptane. The zero-angle scattering intensity $I(0)$ and the radius of gyration R_g of the solute particle were determined by the Guinier plot. The contrast matching point of the solute particle was obtained from the plot of $[I(0)]^{1/2}$ against d-heptane concentration, as shown in Fig. 2(a). As we know the contrast matching point and can calculate the average scattering density of the heptane solvent at each d-heptane fraction, we can plot the Rg^2 against 1/contrast. This plot, so-called the Stuhrmann plot [4], well reflects a heterogeneity of internal scattering density distribution of a solute particle. The negative slope in Fig. 2(b) indicates that the solute particle consists of a high density core surrounded by a low density shell. This agrees with the present microemulsion structure since its water pool contains 98 % D_2O v/v. The decrease of the absolute value of the slope by the occlusion of the proteins also shows that the proteins locate at the center of the microemulsion to descend the scattering density of the water pool.

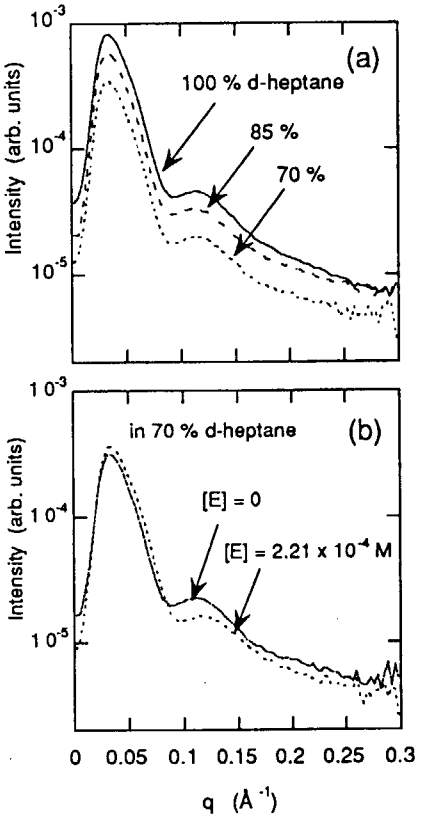


Fig. 1. Change of the scattering curve of AOT microemulsion (w_0 = 20) depending on the d-heptane fraction in the solvent (a) and on the protein concentration (b).

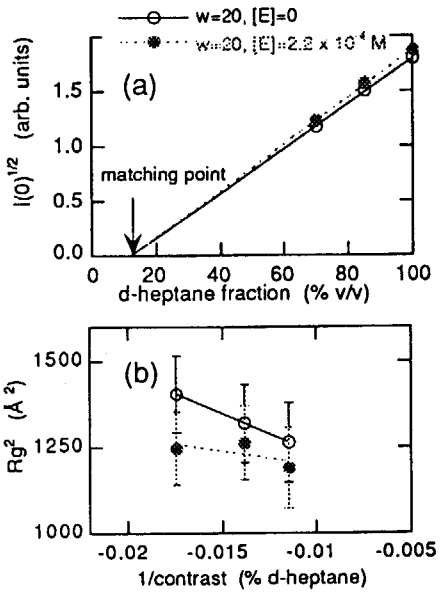


Fig. 2. (a), Square root of the zero-angle scattering intensity plotted against d-heptane fraction. (b), Change of Stuhrmann plot due to the occlusion of the proteins. Marks in (b) are as same as in (a).

References

1. M. Hirai, et al., J. Chem. Soc. Faraday Trans., 91 (1995) 1081.; J. Phys. Chem., 99 (1995) 6652.
2. M. Hirai, et al., J. Phys. Chem. Solids, 60 (1999) 1297.
3. M. Hirai, et al., J. Phys. Chem. B, 103 (1999) 9658.
5. H. B. Stuhrmann, and A. Miller, J. Appl. Cryst., 11 (1978) 325.

研究テーマ：両親媒性環境下のタンパク質の構造特性評価
表題：界面活性剤ミセル中で変性したタンパク質の構造解析

1-6-6
Structural analysis of a protein denatured in dodecyl sulfate micelles

Yasushi Watanabe
National Food Research Institute, Tsukuba, Ibaraki 305-8642, JAPAN

Introduction

A powerful tool for the high-resolution separation of polypeptide chains in protein biochemistry and molecular biology is by its mobility in polyacrylamide gel electrophoresis in the presence of dodecyl sulfate. The electrophoretic mobility of a protein is determined not only by its molecular weight but also by its net charge and its shape. Proteins that interact in the typical manner with dodecyl sulfate also appear to produce complexes with similar shapes and net charge densities on these chains. Although the original conformations of the protein are disrupted by the surfactant, the nature of the conformation they adopt in dodecyl sulfate is not known.

A variety of models such as "rodlike-particle model" (1) and "necklace-model"(2) have been proposed and usefully summarized by Ibel et al. (3). Despite the relatively extensive investigations that have been carried out on the structure of protein-surfactant complexes, definitive results have yet to be obtained. In this study, perdeuterated dodecyl sulfate in neutron scattering experiments was used to determine the size of a protein denatured in the micelles.

Experimental

Small-angle neutron scattering experiments were performed by using a SANS-U spectrometer installed at the C1-2 port of the cold-neutron beam line in the research reactor JRR-3M of the Japan Atomic Energy Research Institute (JAERI). The wavelength was 0.7 nm and the sample to detector distance was 800 cm. The solution samples were contained in flat square-shaped quartz cells of window thickness 1 mm and path length 4 mm. Multiple samples were mounted on a sample changer at 25℃. Sample transmission was taken before and after each measurement to check the material conditions and to correct for absorption of the sample. The buffer solution consisting of 99.8% D_2O, 10 mM MOPS, pD 7.0, 200 mM LiCl, 3.5 mM (above the critical micelle concentration) SD_dS was used as a reference solution for scattering experiments.

Results and Discussion

Figure 1 shows the scattering pattern of perdeuerated dodecyl sulfate in D_2O to confirm its effectiveness in the present experimental condition. It is shown that a 100% D_2O solution matches approximately the scattering length density of perdeuterated dodecyl sulfate, as compared with the scattering curve of a sample. Figure 2 shows a Guinier plot of scattering data reduced carboxymethylated bovine serum albumin (molar

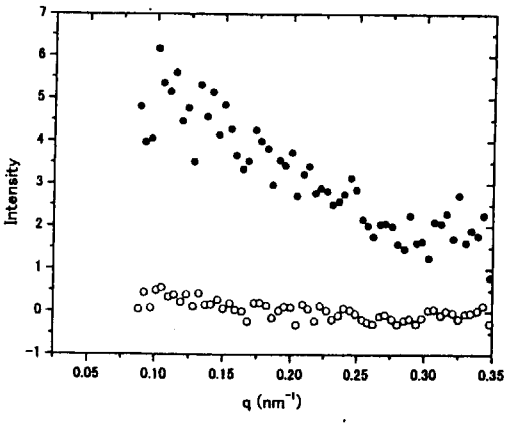


Figure 1. Scattering patterns of perdeuerated dodecyl sulfate (○) and reduced carboxymethylated bovine serum albumin complexed with perdeuerated dodecyl sulfate (●) in D_2O.

JRR-3M, SANS-U, Biology

mass: ～67,000) in perdeuterated dodecyl sulfate micelles. Since a D_2O solution matches approximately the scattering length density of perdeuterated dodecyl sulfate, the scattering obtained in Figures 1 and 2 is assigned to hat derived from the polypeptide chain in dodecyl sulfate micelles. From the slope of the line of Figure 2, the Rg value was estimated to be ～6 nm. Further analysis is in progress to characterize the dodecyl sulfate – protein complexes.

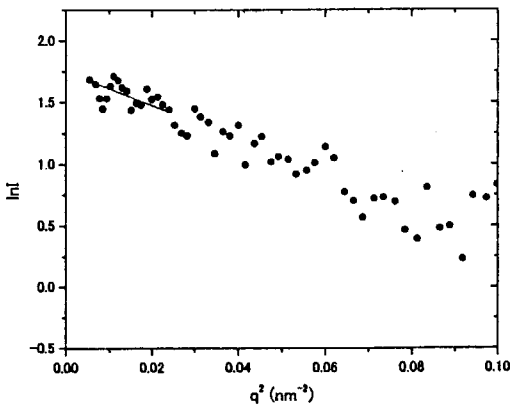


Figure 2. A Guinier plot of scattering data reduced carboxymethylated bovine serum albumin.

References

1. Reynolds J. A., and Tanford C., J. Biol. Chem. 245, 5161(1970).

2 Shirahama K., Tsujii K., and Takagi T., J. Biochem. 75, 309(1974).

3. Ibel K., May R. P., Kirschner K., Szadkowski H., Mascher E., and Lundahl P., Eur. J. Biochem. 190, 311(1990).

Acknowledgements : The encouragement and support of SANS-U IMT members is greatly appreciated. This work was supported in part by a grant of Rice Genome Project PR-2102, MAFF, JAPAN.

研究テーマ：中性子小角散乱による色素膜蛋白質複合体の構造解析
表題：光合成細菌由来光捕集色素膜蛋白質複合体のサイズ評価

1-6-7 Evaluation of the sizes of light-harvesting pigment-membrane protein complexes from a photosynthetic bacterium

Z.-Y. Wang, Y. Muraoka, M. Shimonaga, and T. Nozawa
Department of Biomolecular Engineering, Faculty of Engineering, Tohoku University, Sendai 980-8579 Japan

Light-harvesting (LH) complex serves as a highly efficient molecular machinery for the collection and transfer of solar energy to photochemical reaction centers in photosynthetic organisms. In purple photosynthetic bacteria, the LH complexes are classified into either of two major types, namely, the core (LH1) and peripheral (LH2) complexes, both comprising two small polypeptides α and β along with bacteriochlorophyll (BChl) and carotenoid molecules. The LH1 complex is capable of forming a stable intermediate species, characterized by a near-infrared absorption at approximately 820 nm (referred to as B820), by dissociation of the LH1 with detergent *n*-octyl β-D-glucopyranoside(OG). Although the B820 complex has been considered as a building unit of the LH1, its size and molecular weight remain unclear. Following last year's experiments on OG micelles,[1] we report here the preliminary results of characterization of the B820 along with the LH1 dissolved in deuterated OG using SANS.

SANS measurements were conducted at room temperature (~22°C) with SANS-U(C1-2) at JRR-3M. Neutron wavelength was 7Å. Both native and reconstituted B820 subunits from *Rhodospirillum(R.) rubrum* were dissolved in 4% deuterated OG solution (D_2O). Native and carotenoid-depleted LH1 were dissolved in 1% deuterated OG solution (D_2O). The SANS data were analyzed by using standard Guinier procedure.

Figure 1 shows the Guinier plots for both native and reconstituted B820 subunit complexes. Essentially the same profiles were observed, indicating that both samples are monodispersed and have the same dimension. Guinier analysis yields a R_g=11.0 ±1.0 Å and M_r=11,400±500. The molecular weight is only slightly less than that of calculated with a composition of αβ(BChl *a*)$_2$, giving evidence that the B820 is actually made up by one pair

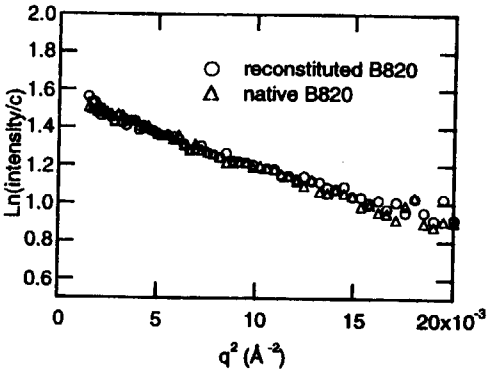


Fig. 1 Guinier plots of SANS profiles for the reconstituted and native B820 subunits.

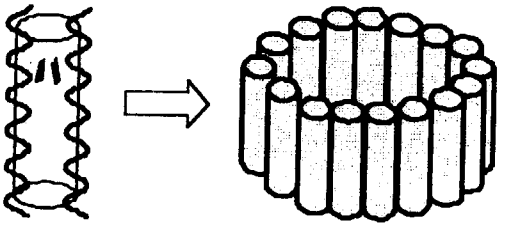


Fig. 2 Schematic representation of B820 subunit and its aggregated form, LH1.

of polypeptides with two pigment molecules. The scattering profiles can be fit using a solid cylindrical model having a particle of 14 Å diameter and length of 40 Å, as shown in Figure 2. The dimension is in agreement with that of a putative subunit of the known crystal structure of LH2. The LH1 complex was determined in a similar way to have a R_g=62±2 Å, corresponding to an aggregated form of the B820 subunits. Electron microscopy of LH1 from *R. rubrum* showed the complex to be composed of 16 αβ pairs, arranged symmetrically in a 116 Å ring with a 68 Å hole in the middle. The observed radius of gyration can account for this organization based on a hollow cylindrical model as illustrated in Figure 2. Further detailed data analysis is in progress.

[1] Z.-Y. Wang, et al. *Act. Rep. Neutron Scat.*,7, 253(2000)

JRR-3M, SANS-U, Biology

研究テーマ：中性子小角散乱による巨大ヘモグロビンの構造（変化）の研究
表題：リガンド結合に伴う巨大ヘモグロビンの構造変化

1-6-8 The Ligand Binding-induced Structural Changes in Giant Hemoglobin

M. Harada, N. Shibayama and T. Gotoh[1]

Department of Physics, Jichi Medical School, Yakushiji 3311-1, Minamikawachi, Kawachi, Tochigi 329-0498, Japan
[1]Department of Life Science, Faculty of Integrated Arts and Sciences, University of Tokushima, Tokushima 770-8502, Japan

Annelid extracellular hemoglobins are giant protein molecules that exhibit a characteristic hexagonal bilayer appearance in electron micrographs and relatively high cooperativity of O_2 binding. They are constructed of approximately 200 polypeptide chains that associate to form a hexagonal bilayer structure. At present, very little is known about the molecular mechanisms of the cooperative ligand binding by these giant hemoglobins because of the lack of information on the ligand binding-induced structural changes. To understand the molecular mechanisms for their cooperative ligand binding, it is necessary to elucidate protein conformational changes associated with ligand binding. In this study, we have explored the possibility of observing any structural changes in the giant molecule by using small-angle neutron scattering (SANS). We present a quantitative comparison of the scattering curves of the giant hemoglobin from the marine worm, *Perinereis aibuhitensis*, both in the deoxygenated and CO-bound states.

Hemoglobin from *Perinereis aibuhitensis* was isolated by the method previously reported [1]. Both the deoxy and CO-bound hemoglobin solutions were made to have the same protein concentration of 13.3 mg/mL in a D_2O buffer (pH 7.4) consisting of 50mM Bistris-propane, (1,3bis[tris(Hydroxymethyl)-methylamino] propane), 0.1 M $MgCl_2$, and 6.7 mM ascorbic acid. These samples were anaerobically transferred into sealed quartz cells of 5 mm path length. The SANS measurements were carried out at 25°C with SANS-U spectrometer of the Institute for Solid State Physics, University Tokyo in Tokai. The wavelength of neutron beam was 7Å.

As shown in figure, there is no difference between the scattering curves of the deoxy and CO-bound states of the giant hemoglobin, although a strong cooperativity was observed in O_2 binding of this hemoglobin under very similar experimental conditions [1]. Thus, substantial alterations in ligand binding affinity of the giant hemoglobin should be associated with conformational alterations that would not lead to major changes of the overall shape and size of its hexagonal bilayer structure. For example, a relative rotation of the two hexagonal rings is a possible conformational alteration.

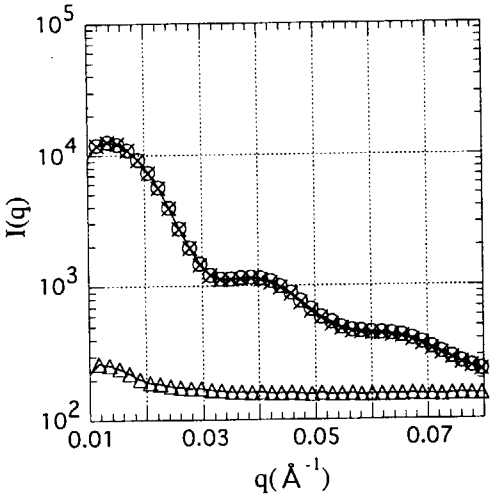


Figure: Scattering curves of the giant hemoglobin samples both in the deoxygenated (○) and CO-bound states(×) at pH 7.4, 25°C, in the presence of 0.1 M $MgCl_2$, along with the scattering curve of the buffer alone (△).

Reference

[1] Tsuneshige, A. et al.: J. Biochem. 106 (1989) 406.

JRR-3M, SANS-U, Biology

研究テーマ：内部コントラスト変化法による液晶状態におけるリン脂質とジアシルグリセロールの混合状態の研究
表題：ホスファチジルコリン/ジメチルスルフォキシド/水系の小角中性子散乱研究

1-6-9

Small Angle Neutron Scattering study of Phosphatidylcholine/Dimethylsulfoxide/Water System

Hiroshi Takahashi

Department of Physics, Gunma University, Aramaki4-2, Maebashi, 371-8510 Japan

Introduction

It is well known that the stability and functions of proteins and biomembranes depend strongly on the solvent composition. Therefore many studies have been conducted to understand the mechanism of the effect of solvent components. Based upon the analyses of chemical potential of solutes and solvents, the concept of preferential solvent interactions has been proposed. According to this concept, for example, in the case of the preferential hydration, water molecules will be bound to biomolecules preferentially over co-solvents.

This is a thermidynamical prediction, however, as far as we know, no structural evidence for the preferential solvent interactions has been reported. We have been studying to get the direct structural evidence for the preferential solvent interaction concept.

In this study, by means of small-angle neutron scattering (SANS), we investigated a ternary system composed of phospholipid, water and dimethyl-sulfoxide (DMSO).

Experimantal

The powders of neutral phospholipid (dimyristoylphosphatidylcholine (DMPC)) were dispersed into the DMSO/water mixture with the weight ratio of DMSO : water = 50 : 50. The lipid concentration was 10 wt%. In order to weaken the intermembrane interactions of DMPC multibilayers, $CaCl_2$ was added to the sample solutions and the concentration was 5 mM. SANS measurements were performed with the SANS-U spectrometer of the Institute for Solid State Physics (ISSP) of the University of Tokyo in JRR-3M at Tokai.

Results and Discussion

For the DMPC/DMSO/Water system, a lamellar diffraction peak was observed clearly at 0.12 A^{-1} (Fig.1). On the other hand, for the DMPC/Water system, no lamellar diffraction peak was observed (Fig.1). This result shows that the effect of Ca^{2+} ions on the intermembrane interaction does not work in the presence of DMSO. It can be interpreted as indicating that DMSO may preferentially bind to the surface of DMPC bilayers and that, as a result, Ca^{2+} ions are not absorbed into the surface of the DMPC bilayers. Further detailed analysis is now in progress.

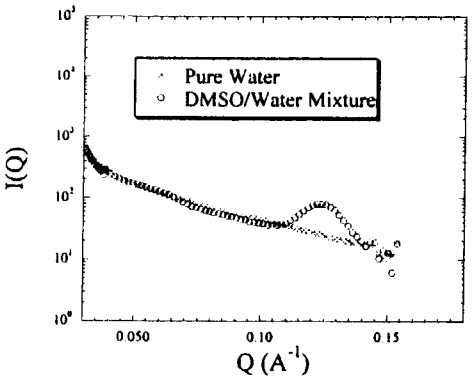


Figure 1 Small angle neutron scattering profiles of DMPC/Water (x) and DMPC/DMSO/Water (O) systems in the presence of 5 mM $CaCl_2$.

JRR-3M, SANS-U, Biology

研究テーマ：中性子小角散乱法による昆虫リポホリンの構造解析
表題：中性子小角散乱法による昆虫リポホリンの構造解析

1-6-10 Small-Angle Neutron Scattering of Lipophorin

C. KATAGIRI, M. NAGAO*, M. SATO† and Y. ITO§

Institute of Low Temperature Science, Hokkaido University, Sapporo 060-0819
**Institute for Solid State Physics, University of Tokyo, Tokai, Naka, Ibaraki 319-1106*
†Graduate School of Integrated Science, Yokohama City University, Yokohama, Kanagawa 236-0027
§Faculty of Education and Human Sciences, Yamanashi University, Kofu 400-8510

Lipophorin is the transport vehicle in insect blood for the water-insoluble lipids from the organs of synthesis to the sites of utilisation. To understand the functions of lipophorin, the chemical composition and the structure have been studied. Lipophorin is a spherelike particle with a particle weight of about 6.0×10^5 and contains two apoproteins and 40-50% (w/w) lipid. A model of three layered lipophorin (diameter = 168Å) was previously proposed based on small-angle X-ray scattering results, which was supported by the small-angle neutron scattering work with H_2O/D_2O contrast variation. The model consists of an inner core of hydrocarbons surrounded by a layer of diacylglycerol and apolipophorin-II ($M_r=8\times10^4$), and a spherical micellar arrangement of the outer hydrophilic surface formed by apolipophorin-I ($M_r=2.5\times10^5$) and polar phospholipid headgroups[1,2,3] Since the closest packing of all the lipophorin constituents makes a sphere with a diameter of about only 135Å, the half of the lipophorin particle could be occupied by water. To examine this hypothesis, we reared American cockroach on D_2O for a month for excluding H_2O from the blood and the lipophorin particle as possible. The prepared lipophorin was subjected to small-angle neutron scattering analyses with H_2O/D_2O contrast variation (Fig. 1). They gave several parameters different from those obtained by the non-treated lipophorin. The model rifinement is now in progress.

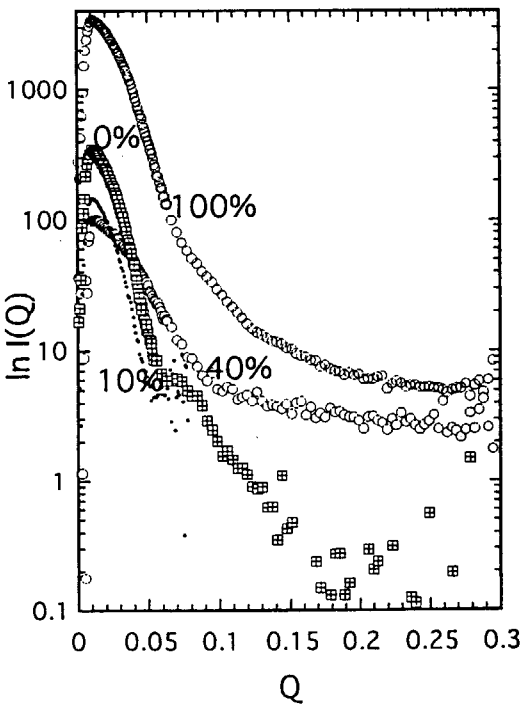


Fig.1 Small-angle neutron scattering curves of the cockroach lipophorin reared on D_2O.

References

1) C. Katagiri *et al.*, *Biochem.* **30** (1991) 9675.
2) C. Katagiri, *J. Crystallographic Soc. Jpn.* **36** (1994) 162 [in Japanese].
3) C. Katagiri *et al.*, *Activity Report on Neutron Scattering Research* **3** (1996) 208.

JRR-3M、SANS-U、 Biology

研究テーマ：コントラスト変調法によるミリストイル化タンパク質とカルモデュリン複合体の溶液構造解析
表題：ニューロン特異的タンパク質NAP-22と複合状態にあるカルモデュリンの構造

1-6-11

Structures of Calmodulin in the Complex with Neuron-Specific Protein NAP-22

Y. Izumi, N.Hayashi[1], Y.Jinbo and N.Matsushima[2]
Graduate School of Science and Engineering, Yamagata University,
Yonezawa, Yamagata 992-8510, JAPAN
[1]Fujita Health University, Toyoake, Aichi 470-1192, JAPAN
[2]School of Health Science, Sapporo Medical University, Sapporo 060-8556, JAPAN

N^{α}-myristoylated CAP-23/NAP-22, a neuron-specific protein kinase C substrate, interacts with calmodulin (CaM) in the presence of Ca^{2+} ions. The myristoyoylated N-terminal nonapeptide of CAP-23/NAP-22 (mC/N9) also binds to Ca^{2+}-bound CaM (Ca^{2+}/CaM)[1]. The binding of one mC/N9 molecule induced an insignificant structural change in Ca^{2+}/CaM. However, the binding of two mC/N9 molecules induced a drastic structural change in Ca^{2+}/CaM. The results suggest that Ca^{2+}/CaM interacts with N^{α}-myristoylated CAP-23/NAP-22 differently than it does with other nonmyristoylated target proteins[2].

In this report, small-angle neutron scattering (SANS) with contrast variation has been utilized to obtain the first low-resolution structure of $4Ca^{2+}$/CaM complexed with N^{α}-myristoylated NAP-22. Deuterated CaM (DCaM) was used. The solutions for the Ca^{2+}/DCaM-N^{α}-myristoylated NAP-22 mixtures with molar ratios of 1:1 and 1:2 were each prepared at a DCaM concentration of 5.0mg/mL. The neutron scattering experiments were performed with the SANS-U spectrometer.

Fig. 1 shows Guinier plots for Ca^{2+}/DCaM-mNAP-22 complex with molar ratio of 1:1 in 0% , 20% and 40% D_2O. The solvent match point is about 40%D_2O, in which one can observe the conformation of DCaM in the complex state. Raidus of gyration, R_g, for 40% D_2O is about 22A, indicating that the conformation of DCaM in the complex is a dumbbell structure.

Fig. 2 shows the basic scattering functions for N^{α}-myristoylated NAP-22 In(q), for DCaM Ic(q) and for the cross-term Icn(q). More detailed analysis requests simply the accumulation for data. The R_g value for 40% D_2O at molar ratio of 1:2 gave unexpectedly a large value, suggesting a large effect of hydrogen-deuterium exchange in the complex.

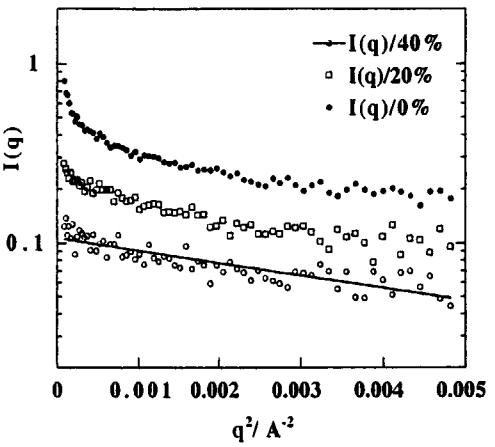


Fig. 1. The Guinier plots for Ca^{2+}/DCaM-mNAP-22 complex with molar ratio of 1:1 in 0% (●), 20%(□)and 40%(○) D_2O at DCaM concentration of 5.0mg/mL.

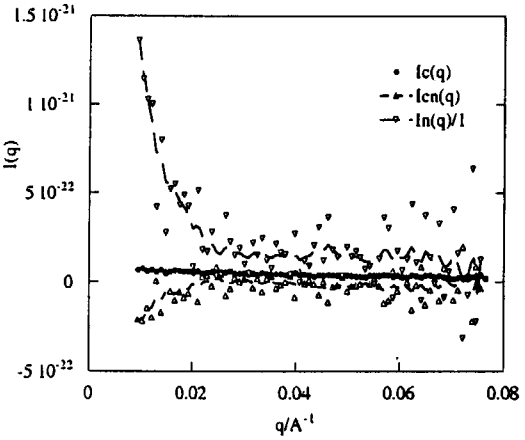


Fig. 2. The basic scattering functions for N^{α}-myristoylated NAP-22 In(q) (▽), for DCaM Ic(q) (●) and for the cross-term Icn(q) (△).

Reference

1. A. Takasaki et al. JBC 274(1999)11848.
2. N.Hayashi, Y.Izumi, K.Titani and N.Matsushima, Protein Sci. 9(2000)1905.

JRR-3M, SANS-U, Biology

研究テーマ：スフィンゴ糖脂質のミクロドメイン形成と生体膜ダイナミックス
表題：スフィンゴ糖脂質 (GD1a) ミセルのダイナミックスの温度依存性

1-6-12

Temperature Dependence of Dynamics of Glycosphingolipid (G_{D1a}) Micelle

M. Hirai,[1] H. Iwase,[1] T. Hayakawa,[1] S. Seto,[2] Y. Kawabata,[2] and T. Takeda.[2]

[1] *Department of Physics, Gunma University, Maebashi 371, Japan.*

[2] *Faculty of Integrated Arts and Science, Hiroshima University, Higashi-Hiroshima 739, Japan,*

1. Introduction Gangliosides are acidic glycosphingolipids, which are involved in various cell surface events such as sorting, signal transduction, and cell adhesion. To understand the physiological role of gangliosides in biomembranes, it is important to elucidate physicochemical characteristics of gangliosides and those aggregates. In our previous studies, we reported that the elevation of temperature ranging from 10 °C to 65 °C induces a shrinkage of the sugar chains of the ganglioside micelle and that this phenomenon accompanies both the extrusion of water from the hydrophilic region and an alteration of micellar surface charge. Then, we have carried out neutron spin echo (NSE) measurements to clarify dynamics of the disialoganglioside (G_{D1a}) micelle depending on temperature elevation.

2. Experimental The sample used was disialoganglioside (G_{D1a}) from bovine brain. The ganglioside powder of 0.5 % w/v was dissolved in 99.9+ atom % D_2O solvent with 50 mM Hepes adjusted to pH 7.0. NSE experiments were carried out at two temperatures by using a NSE spectrometer installed at C2-2 beam port at the research reactor JRR-3M in Japan Atomic Energy Research Institute, Tokai, Ibaraki, Japan.

3. Results and Discussion Fig. 1 shows the Fourier time dependence of the NSE signal amplitude P_{NSE} at 25 °C and 55 °C. The fitting with the equation of $P_{NSE} = \exp(-\Gamma t)$ is well used for microemulsion droplet systems to determine the relaxation rate Γ. However, the observed P_{NSE} functions in Fig. 1 were poorly fitted by this single exponential function, therefore we applied the stretched exponential formula of exponential $P_{NSE} = \exp(-(\Gamma t)^{2/3})$. Fig. 2 shows the q-dependence of the Γ which is mostly proportional to q^3. The present results would suggest that the dehydration and bending of the sugar chains with elevating temperature suppress the modulation of the micellar surface.

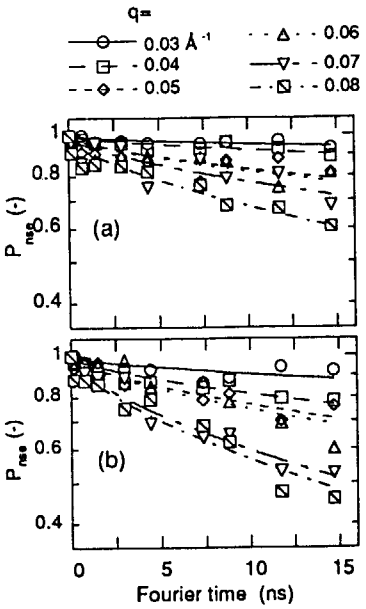


Fig. 1. Normalized NSE signal amplitude P_{NSE} of ganglioside micelle at 25 °C; (b), at 55 °C.

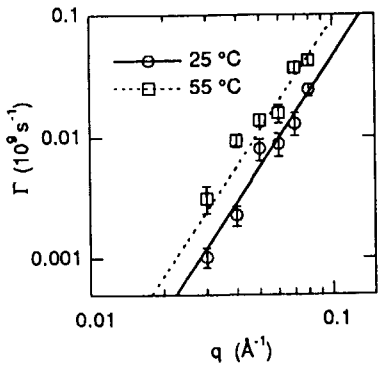


Fig. 2. q-dependence of Γ in log-log scale. The lines indicate the slope of the Γ propostinal to q^3.

JRR-3M, NSE, Biology

研究テーマ：機能性生体物質の水和構造研究
表題：コントラスト変調法を用いたカエル筋肉の中性子繊維回折

1-6-13

Neutron Fiber Diffraction of Frog Muscle Combined with the Contrast Variation Measurements

S. Fujiwara, Y. Takezawa[1], Y. Sugimoto[1], and K. Wakabayashi[1]

Japan Atomic Energy Research Institute, Tokai, Ibaraki 319-1195, Japan
[1]Grad. School of Engineering Science, Osaka University, Toyonaka, Osaka 560-8531, Japan

The contrast variation measurements, which is widely used in the area of neutron solution scattering[1], is applicable to low-resolution neutron crystallography and neutron fiber diffraction as well. We have been explored the possibilities of neutron fiber diffraction combined with the contrast variation measurements. We measured the neutron fiber diffraction patterns of frog sartorius muscles under the relaxed state where no tension of the muscle is produced, in various D_2O concentrations. Integrated intensities of the observed reflections from the muscle were calculated, and its dependence on the D_2O concentrations was investigated[2]. It was shown that there were reflections having different matching points. This indicates that there is a variation of the scattering length density in the unit cell of the muscle structure.

Here we performed similar measurements of the muscle under the rigor state where the myosin heads bind tightly to actin. This state was produced by saponin treatment of freshly dissected muscle under relaxed state, followed by NEM treatment, and final perfusion with rigor solution containing 60 mM K-Propionate, 20 mM HEPES/KOH (pH 7.0), 5 mM EGTA, and 5 mM Mg-acetate under various D2O concentrations (0%, 18.2%, 63.6%, 78.3%, and 99.1%). The neutron fiber diffraction patterns of these samples were measured with the Small-Angle Neutron Scattering Instrument (SANS-J) at the guide hall of the reactor JRR-3M in Japan Atomic Energy Research Institute. Neutrons with the wavelength of 0.706 nm ($\Delta\lambda/\lambda$=12.8%) were employed.

The neutron diffraction patterns in which the reflections on the equator and the meridian were clearly observed were obtained in each D_2O concentration. Figure 1 shows an example of the contrast dependence of the scattering amplitudes of the observed reflections of muscle under the rigor state. The contrast matching points of the equatorial reflections [1,0] and [1,1] were 50.1% D_2O and 40.4% D_2O, respectively. These values are very close to the values obtained in the muscle under the relaxed state, indicating that the regions with different scattering length densities are the same under the relaxed and the rigor states. The detailed analysis using Fourier synthesis is in progress.

(Supported in part by Special Coordination Funds of the Ministry of Education, Culture, Sports, Science and Technology, the Japanese Government)

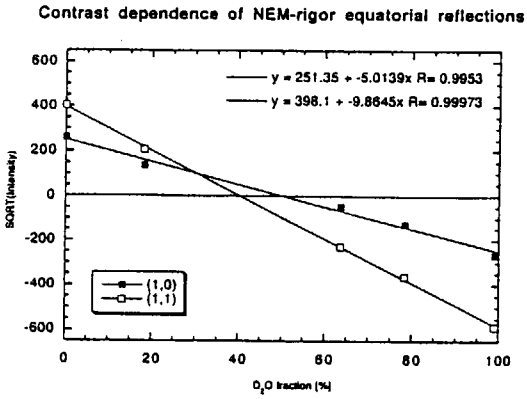


Figure 1. Contrast dependence of the scattering amplitudes of the reflections on the equator. Fitting with straight line is also shown.

References

[1] L. A. Feigin and D. I. Svergun: Structure Analysis by Small-Angle X-Ray and Neutron Scattering (1987) Plenum Press, New York.
[2] S. Fujiwara et al.: J. Phys. Soc. Jpn. **70** (2001) Suppl. A 408-410.

原子炉：JRR-3M　　装置：SANS-J (C3-2)　　分野：中性子散乱（生物）

研究テーマ：機能性生体物質の水和構造研究
表題：コントラスト変調法を用いた筋肉の細いフィラメントの中性子小角散乱測定

1-6-14

Small-Angle Neutron Scattering Measurements of the Native Thin Filaments of Muscle Using Contrast Variation Method

S. Fujiwara[1], F. Matsumoto[1,2], and K. Makino[2]

[1]Japan Atomic Energy Research Institute, Tokai, Ibaraki 319-1195, Japan
[2]RIKEN Harima Institute, Hyogo 679-5148, Japan

Muscle contraction occurs when the two types of the filaments slide past each other. These filaments are called the thin filament, which consists of actin, tropomyosin, and troponin (Tn) complex (composed of TnC, TnI, and TnT), and the thick filament, the main component of which is myosin. The molecular mechanism of the muscle contraction and its regulation is one of the most important problems in biophysics, as it is a typical example of energy transduction mechanisms of living organisms. The regulation of skeletal and cardiac muscle contraction is associated with a Ca^{2+}-dependent structural transition in the thin filament. The trigger of this structural transition is binding of Ca^{2+} to TnC, and subsequent structural changes of TnC, TnI, and TnT. To understand the molecular mechanism of the regulation of the muscle contraction, it is important to obtain structural information of each component of Tn-complex within the thin filaments with and without Ca^{2+}. This is possible only by neutron scattering. Combination of selective deuteration and the contrast matching makes only the component of interest "visible" to neutrons. With this technique, neutron scattering only from the selected component can be measured. We have started a project to obtain *in situ* structural information of TnC, TnI, and TnT within the thin filament using this technique. As a very first step of this project, the contrast matching point of the undeuterated proteins has to be determined. To do this, we performed neutron scattering experiments of the thin filaments purified from muscle.

The "native" thin filaments were purified from bovine cardiac muscle, and suspended in the buffer containing 20 mM Tris (pH 7.5), 100 mM KCl, 5 mM $MgCl_2$, 1 mM EGTA, and 1mM NaN_3, under various D_2O concentrations (0%, 20%, 65%, 80%, and 100%). The small-angle neutron scattering measurements of these solutions with and without 1.1 mM $CaCl_2$ were done with the Small-Angle Neutron Scattering Instrument (SANS-J) at the guide hall of the reactor JRR-3M in Japan Atomic Energy Research Institute. Neutrons with the wavelength of 0.653 nm ($\Delta\lambda/\lambda$=13.8%) were employed. The obtained neutron scattering curves were analyzed by the cross-sectional Guinier plots ($\ln(QI(Q))$ *versus* Q^2, where $Q=4\pi\sin\theta/\lambda$, and 2θ is the scattering angle), to yield the cross-sectional radius of gyration, R_x, and the cross-sectional intensity at zero angle, $I_x(0)$. The obtained R_x values were around 3 nm depending on the D_2O concentration, which are consistent with the reported values[1]. No appreciable changes of R_x were observed with addition of Ca^{2+}. Plotting the square root of $I_x(0)/c$ (c: the thin filament concentration) as a function of D_2O concentration yields the contrast matching point of the thin filament. The contrast matching points of the thin filament without and with Ca^{2+} were estimated to be 40.6% D_2O and 39.6% D_2O, respectively, indicating the condition under which the neutron scattering measurements of the thin filaments containing the deuterated Tn component will be done should be 40% D_2O.

(Supported in part by Special Coordination Funds of the Ministry of Education, Culture, Sports, Science and Technology, the Japanese Government)

References

[1] D. Popp and Y. Maeda: J. Mol. Biol. **229** (1993) 279.

原子炉：JRR-3M　　装置：SANS-J (C3-2)　　分野：中性子散乱（生物）

研究テーマ：機能性生体物質の水和構造研究
表題：中性子小角散乱による蛋白質の水和構造

1-6-15 Hydration of Proteins Observed by Small-Angle Neutron Scattering

S. Fujiwara and Y. Yonezawa[1]

Japan Atomic Energy Research Institute, Tokai, Ibaraki 319-1195, Japan
[1]Tsukuba College of Technology, Tsukuba, Ibaraki 305-0821, Japan

Hydration of protein is one of important factors in the stabilization of the tertiary and the quaternary structures as well as in the interactions between proteins. Recently, a technique to estimate hydration layer around the proteins in solution was proposed[1]. This technique employs X-ray solution scattering and neutron scattering. From the parallel measurements of X-ray and neutron solution scattering of the proteins with known atomic resolution crystal structures in H_2O and D_2O solutions, the average structures of the hydration shell around the proteins can be estimated.

To confirm the applicability of this technique, we performed neutron scattering experiments of the protein hen egg-white (HEW) lysozyme in D_2O and in H_2O. Another purpose of these experiments was to compare the results from solution scattering with the hydration structures determined from neutron crystallography. This is possible since we have ongoing projects to determine the structures of HEW lysozyme under various conditions with neutron crystallography[2-3]. Unfortunately, however, this protein has a strong dependence of its intermolecular interactions on salt concentration in solution. At low salt concentration, scattering curves of this protein show a large decrease in intensity in the small-angle region due to strong repulsive intermolecular interactions. In such cases, proper estimation of the radius of gyration (R_g), a typical structural parameter which is related to the size and shape of the particle, is not possible by the analysis of the Guinier plots (lnI(Q)) *versus* Q^2, where $Q=4\pi\sin\theta/\lambda$, 2θ is the scattering angle, and λ the wavelength). Thus, we first determined the solution condition under which the strong intermolecular interactions can be suppressed. We measured the neutron scattering curves of HEW lysozyme under various NaCl concentrations. The measurements were done with the Small-Angle Neutron Scattering Instrument (SANS-J) at the guide hall of the reactor JRR-3M in Japan Atomic Energy Research Institute. From careful inspection of the scattering curves of HEW lysozyme under various NaCl concentrations, the solution condition under which the experiments were done was determined to be 150 mM NaCl.

We next measured the neutron scattering curves of HEW lysozyme in D_2O and in H_2O at various protein concentrations under this salt concentration. The Guinier analysis of these scattering curves gives R_g at each concentration. Extrapolation of R_g to zero protein concentration gives 1.391 (0.017) nm and 1.392 (0.108) nm for HEW lysozyme in D_2O and in H_2O, respectively, where the values in parenthesis are the standard deviations. These values are contrasted with the reported values of HEW lysozyme, about 1.5 nm, from X-ray scattering[1,4], confirming the applicability of the technique proposed for the estimation for the hydration layer around the proteins.

References

[1] D. I. Svergun et al.: Proc. Natl. Acad. Sci. USA **95** (1998) 2267.
[2] S. Fujiwara et al.: JAERI Review **99-003** (1999) 13.
[3] S. Fujiwara et al.: JAERI Review **2000-005** (2000) 7.
[4] A. Ducruix et al.: J. Crystal Growth **168** (1996) 28.

原子炉：JRR-3M　　装置：SANS-J (C3-2)　　分野：中性子散乱（生物）

1. 中性子散乱 7) 基礎物理学・中性子光学

1. Neutron Scattering 7) Fundamental Physics Neutron Optics

This is a blank page.

研究テーマ：リラクサーPZNのフォノン分散関係
表題：乱れたペロブスカイト $Pb(Zn_{1/3}Nb_{2/3})O_3$ の格子力学

1-7-1 Lattice dynamics of disordered Perovskite $Pb(Zn_{1/3}Nb_{2/3})O_3$

I. Tomeno, S. Shimanuki, Y.Tsunoda[1], and Y. Ishii[2]

Corporate Research and Development Center, Toshiba Corporation, Saiwaiku, Kawasaki 212-8582
[1]School of Science and Engineering, Waseda University, Shinjuku-ku, Tokyo 169-8555
[2]Advanced Science Research Center, Japan Atomic Energy Research Institute, Tokai, Ibaraki 319-1195

The properties of the relaxor $(1-x)Pb(Zn_{1/3}Nb_{2/3})O_3$-$xPbTiO_3$ (PZN-PT) with x~0.1 are appropriate for ultrasonic transducer applications. The donation of 10% Ti atoms to PZN is crucial to piezoelectric enhancement. It is important to investigate the lattice dynamics of the parent material PZN from a microscopic viewpoint, since the Ti-free PZN is also a relaxor. PZN undergoes a structural phase transition from a rhombohedral to a cubic phase at T_C=413 K.

Figure 1 shows the phonon dispersion curves measured at T=423K.[1] The TA phonon branches have flat and isotropic dispersion curves. The TA phonon energies at the zone-boundary M and R points are significantly lower than those for simple perovskite oxides.

The low-lying TO branches drop sharply with decreasing ζ. The constant-Q scans reveal the absence of the well-defined TO spectra in the range $0 \leq \zeta \leq 0.1$. This is similar to the behavior observed for $(1-x)$PZN-xPT with $x = 0.08$.[2]

The TA, TA_2 and TO phonon energies at ζ=0.1 and 0.2 decrease with increasing temperature up to 673 K. Consequently, the phonon hardening toward T_C contradicts the usual soft mode behavior in simple perovskites.

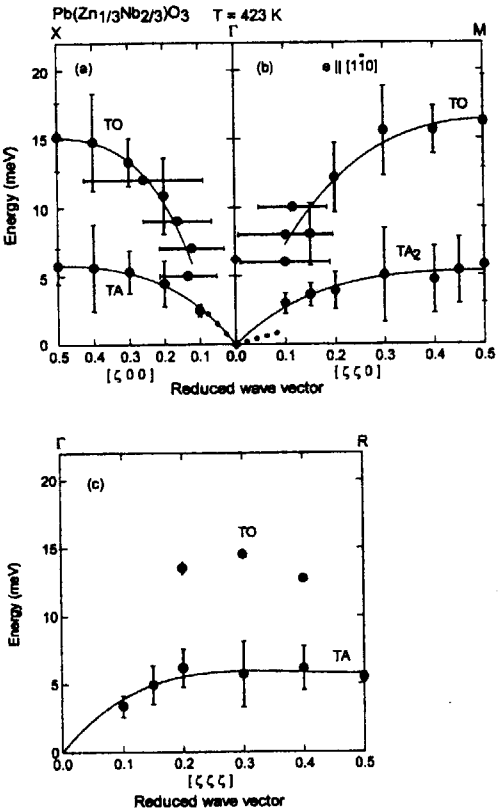


Fig. 1 Phonon dispersion curves for PZN at 423K.

References

1) I. Tomeno *et al.*, J. Phys. Soc. Jpn. 70 (2001) 1444-1447.
2) Gehring *et al.*, Phys. Rev. Lett. 84 (2000) 5216-5219.

原子炉：JRR-3M　　装置：TAS-1(2G)　　分野：中性子散乱（基礎物理）

研究テーマ：超低温の導入による中性子散乱の研究
標　　題：精密中性子光学の研究

1-7-2 Neutron Interferometry at PNO in JRR-3M

Hiroshi TOMIMITSU[a], Yuji HASEGAWA[b] and Kazuya AIZAWA[a]

[a]Advanced Science Research Center, JAERI, Tokai-mura, Ibaraki-ken, 319-1195 Japan
[b]Department of Appl. Phys., Univ. Tokyo, Hongo, Bunkyo-ku, Tokyo 113-8656, Japan

1. Decision of the Sign of the Scattering Length

First in the world, we determined the coherent neutron scattering lengths for ^{202}Hg[1].

With the fitting parameters A~E, the observed intensity I is analyzed by the following function;

$$I = A*\cos(B/(\cos(\alpha + C))+D)+E.$$

The coherent scattering length, b, is then derived through the relation below, with N: atomic number density, t: thickness and λ: wavelength;

$$B = N*b*\lambda* t.$$

Here, we should be careful in deciding the sign of b of an unknown sample. We measured on the following three B's independently;

(1) $B_{(cell)}$: B-value for an empty cell,
(2) $B_{(sample+cell)}$: for the sample within the cell,
(3) $B_{(sample+cell)+(cell)}$: for an extra cell added to (2) above,

and confirmed the relations among them;

$$B_{(sample+cell)+(cell)} = B_{(sample+cell)} + B_{(cell)},\ \text{and}$$
$$B_{(sample+cell)} > B_{(cell)}.$$

Via simple algebra[2], we decided easily that the sample and the cell had the same sign in their b's.

2. Double LL-type Interferometry

In order to use the neutron interferometry much more widely, one of the best solution seems to be the "double LL-type" interferometer, with very large "working area", as shown in Fig.1.

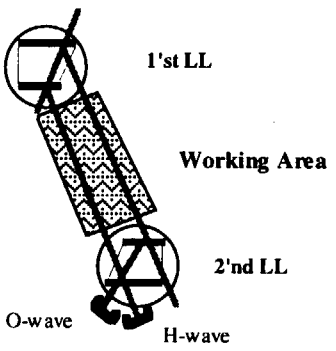


Fig.1 Schematic drawing of the double LL-system

We prepared and started the wide-inquiry on the characteristics of (1) the LL'blocks made from the "imperfect" LLL-interferometers, with 220 reflection, and of (2) the newly made LL'blocks , with 220- and/or 111-reflections.

References

1) H.Tomimitsu, Y.Hasegawa, K.Aizawa: Phys. Lett. **A 274** (2000) 175.
2) H.Tomimitsu, Y.Hasegawa, K.Aizawa: J. Phys. Soc. Jpn **70**(2001) **Suppl. A**, pp.462-464 (Proc. ASR2000).

原子炉：JRR-3M　　装置：PNO(3G)　　分野：中性子散乱（基礎物理）

研究テーマ：構造材料の残留応力と疲労損傷の評価
表　題　：中性子による超細粒鋼の結晶方位測定

1-7-3 Neutron Diffraction Study on the Texture of Ultrafine-grained Steel

Yoshiaki AKINIWA, Hidehiko KIMURA, Keisuke TANAKA,
Nobuaki MINAKAWA[1], Yukio MORII[1]

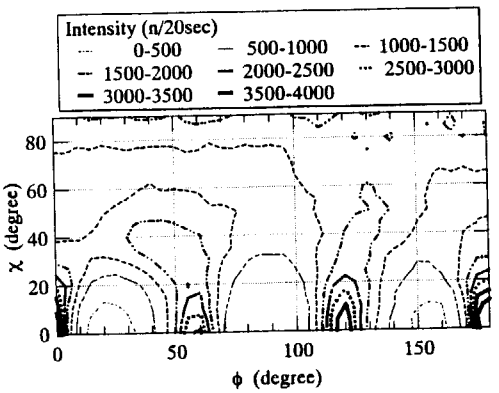
Nagoya University, Nagoya 464-8603, Japan
[1]Japan Atomic Energy Research Institute, Tokai, Ibaraki 319-1195, Japan

Steel plates produced by an advanced thermo mechanical control process have two regions: the ultrafine-grained surface layers with the average grain size of less than 2 μm and the intermediate region with medium-sized grains. The ultrafine-grained steel plates exhibit excellent crack arrestability against brittle crack propagation by forming shear-lips at the surface layers. The fatigue properties are also proven to be superior showing not only higher fatigue limits but also superior crack arrestability against long fatigue cracks due to bifurcation of cracks. The texture of the material is considered to play an important role to form the bifurcation.

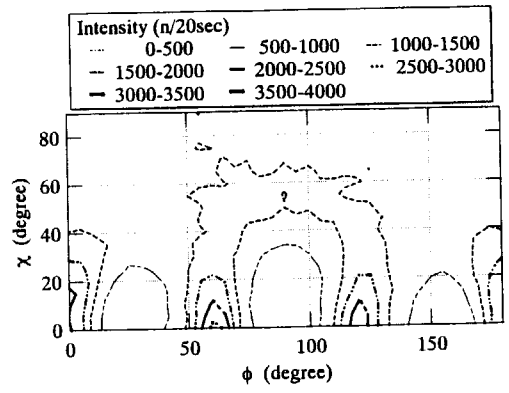
In this study, the textures of specimens prepared from the ultrafine-grained surface layers and medium-grained intermediate region were measured by the neutron diffraction method.

The neutron diffractions from {110} were measured with the scanning range of ϕ from 0 to 180 and of χ from 0 to 90 degrees. The increment of χ and ϕ was 5 degrees with the measurement time of 20 sec.

The result is shown in Fig.1. The intensity of neutron diffractions is plotted as contours in χ-ϕ coordinates. Though the orientation of {110} is the same in (a) and (b), the intensity is higher in (a) indicating that texture is more heavily developed in the ultrafine-grained surface layers.



(a) Ultrafine-grained



(b) Medium-grained

Fig. 1. Contour plot of diffraction intensity.

原子炉：JRR-3M　　装置：RESA(T2-1)　　分野：中性子散乱（基礎物理）

研究テーマ：構造材料の残留応力と疲労損傷の評価
表題：中性子によるSiC粒子強化アルミ合金の疲労損傷評価

1-7-4 Evaluation of Fatigue Damage in SiC Particulate Reinforced Aluminum Alloy by Neutron Diffraction

Yoshiaki AKINIWA, Keisuke TANAKA, Hidehiko KIMURA,
Nobuaki MINAKAWA[1], and Yukio MORII[1]

Nagoya University, Nagoya 464-8603, Japan
[1]Japan Atomic Energy Research Institute, Tokai, Ibaragi 319, Japan

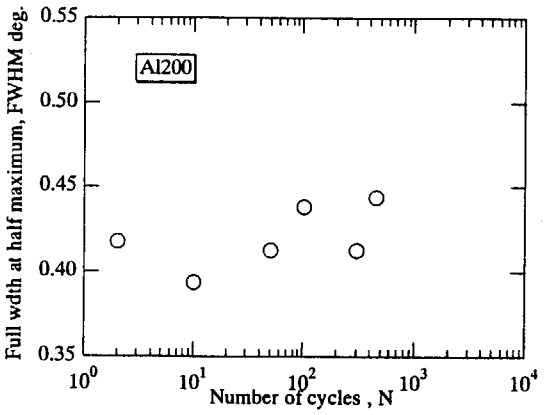
Aluminum alloys reinforced with silicon carbide particles are currently being considered for use as new structural materials in automobile and aerospace industries because of their low weight, high strength and high wear resistance. Structural materials fracture when they are subjected to cyclic loading, even if the load is less than the static strength. This phenomenon is known as fatigue failure. For engineering components, clarification of fatigue properties and development in inspection procedures to detect fatigue damage are very important to obtain a good reliability.

The experimental materials used were aluminum alloy reinforced by silicon carbide particles. The volume fraction of SiC particles of the composite is 20% and their average size is 3 μ m. The composite was fabricated by powder metallurgical processing. An extruded rod of the composite was heat-treated under T6 conditions. The grain size of the matrix is about 5 μ m. The Young's modulus is E=114 GPa, the 0.2% proof strength is $\sigma_{0.2}$=465 MPa and the tensile strength is σ_B=625 MPa.

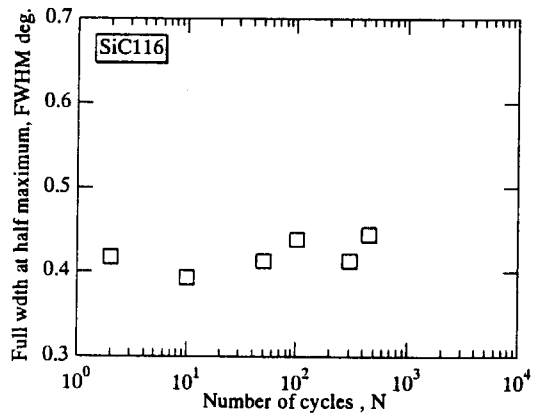
Fatigue tests were conducted using a specially designed mechanical tensile testing equipped machine under a constant amplitude of stress cycling. The stress ratio is R=0.1. The maximum applied stress was 465 MPa.

Neutron diffractions from Al 200 and SiC 116 were used for fatigue damege evaluation. The specimen was uniaxially strained with a tensile testing equipment. The direction of the diffraction plane was parallel to the loading axis. The Full Width at Half Maximum (FWHM) was measured to evaluate the fatigue damege.

Figure 1 (a) shows the change of FWHM with stress cycles obtained for Al 200 phase. FWHM increases with increasing the stress cycles, because the micro strain in the aluminum alloy phase increases during fatigue process. Figure 1 (b) shows the result obtained for SiC 116. The value is also slightly increases with stress cycles. FWHM will be a good parameter to evaluate the fatigue damege in the aluminum alloys reinforced with silicon carbide particles.



(a) Al phase.



(b) SiC phase.

Fig. 1. Change of FWHM with stress cycles.

原子炉：JRR-3M　　装置：RESA(T2-1)　　分野：中性子散乱（基礎物理）

研究テーマ：超低温の導入による中性子散乱の研究
表　題：大強度陽子加速器用中性子冷減速材容器の残留応力測定

1-7-5

Measurement of Residual Stress in the Neutron Cold Moderator Cell for High-Intensity Proton Accelerators

A. Moriai[1,3], H. Kogawa[2], K. Yamamoto[1], M. Kaminaga[2], N. Minakawa[3,1], Y. Horiguchi[1]

[1]*Department of Research Reactor, JAERI, Tokai, Naka, Ibaraki, 319-1195, Japan*
[2]*Center for Neutron Science, JAERI, Tokai, Naka, Ibaraki, 319-1195, Japan*
[3]*Advanced Science Research Center, JAERI, Tokai, Naka, Ibaraki, 319-1195, Japan*

Japan Atomic Energy Research Institute (JAERI) and High Energy Accelerator Research Organization (KEK) are now promoting joint project of constructing the high-energy proton accelerator for comprehensive science and engineering studies, and industrial applications [1]. This project involves construction of the first Japanese spallation neutron source facitities for muon science and neutron scattering research. Neutron cold moderator cell is a device for the neutron source to slowdown fast neutron from the spallation target to thermal neutron provided for diffractometers, spectrometers and other equipments. Supercritical liquid hydrogen and an aluminum alloy are used as moderator and moderator cell material, respectively. The moderator cell is assembled by welding three individual parts shaped from the alloy by machining. It is important to know an initial stress state of the cell for the safety and integrity in the actual operation, because residual stress arising from such manufacturing processing, i.e. welding, machining, and heat treatment etc., often exerts a considerable influence on the service mechanical properties of the engineering components. In this study, residual stress in the base metal near weld was investigated non-destructively by neutron diffraction method [2].

Sample in this study is the neutron cold moderator cell made of an aluminum alloy, JIS A7N01-T6 (7000 series alloy, Al-Zn-Mg-Cu system), as shown in figure 1. The cell looks like a flat water-container, which is consist of complicated curved walls. Wall thickness of the cell is 2 mm for the front wall and 4 mm for the side wall. Circumferential single-vee butt weld was done joining three parts (see figure 1) together by tungsten inert gas welding, TIG, or a combination technique of TIG and YAG laser welding, using an A5356 alloy as a weld metal.

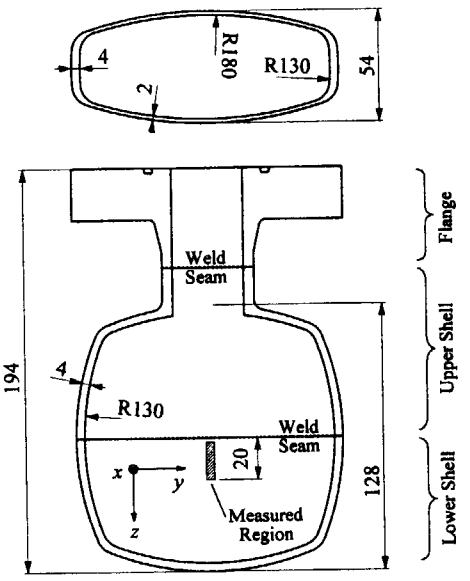


Fig. 1 Cross-sections of the neutron cold moderator cell for high-intensity proton accelerators. A view in the top shows a horizontal-section along the weld seam between the shells.

原子炉：JRR-3M　　装置：RESA(T2-1)　　分野：中性子散乱(基礎物理)

Diffraction strain scanning was made for the shaded region as indicated in figure 1, using the neutron diffractometer for residual stress analysis, RESA, installed at the JRR-3 guide hall of JAERI. Monochromatic incoming neutron with wavelength of 0.2098 nm was used under the beam collimations; 15' in neutron coming into the sample and 20' in the entering the detector. The gauge volume, defined in the measurement region by an intersection between incoming and diffracted neutrons, was limited by cadmium masks with 2 mmØ aperture placed on the path of the both neutrons. The components of strain in the orthogonal x, y and z coordinates of each gauge volumes, ε, were measured as change in the Al (111) lattice plane spacing of d, that is, $\varepsilon = (d - d_0) / d_0$, where d_0 is the lattice spacing of strain-free alloy. In this study, the d_0 was estimated from experimental results by new easy diffraction technique with as-received alloy[3], instead of a conventional diffraction manner with samples subjected to strain relief treatment. As a result, 0.2340547 nm of d_0 in the (111) plane was obtained. Determination of the diffraction elastic constants depending on different lattice planes by neutron experiment during tensile test resulted in 52.8 GPa of Young's modulus and 0.34 of Poisson's ratio in the (111) plane. The stress components in the three coordinates were derived from Hooke's law, using those strains and elastic constants.

Figure 2 shows the residual stress distributions in the base metal near weld of the A7N01-T6 moderator cell. The stresses in all coordinates exhibit tensile response up to the distance of about 5 mm, where the tensile region corresponds to so-called heat affected zone, HAZ. The tensile stresses in each coordinates show the maximum value of about 240 MPa at the distance of $z = 2$ mm, but they do not exceed the 0.2 % proof stress of $\sigma_{0.2} = 295$ MPa and the ultimate tensile strength of $\sigma_b = 365$ MPa as a result of conventional tensile test of the A7N01-T6 alloy at room temperature. On and after the distance of $z = 5$ mm, the stresses in three coordinates turn into compressive response to $z = 20$ mm.

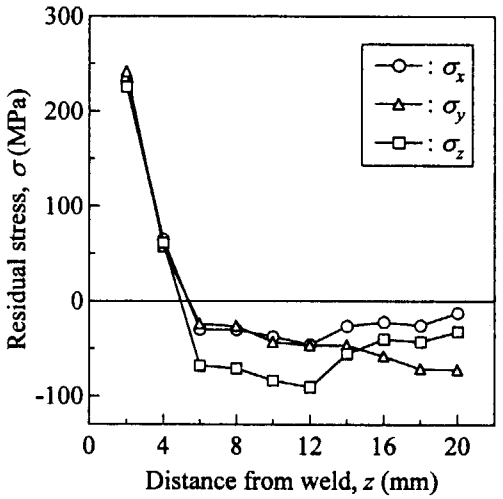


Fig. 2 Residual stress distributions in the base metal near weld of the A7N01-T6 moderator cell.

References

1) The Joint Project for High-Intensity Proton Accelerators, ed. the Joint Project Team of JAERI and KEK, JAERI-Tech 2000-003

2) Measurement of Residual and Applied Stress Using Neutron Diffraction, ed. M. H. Hutchings and A. D. Krawitz, NATO ASI Series (Kluwer Academic Publisher)

3) T. Saito, N. Minakawa *et al.*, J. Soc. Mat. Sci., Jpn., **50** (2001) p. 701

研究テーマ：超低温の導入による中性子散乱の研究
表　題　：ランダム回転ゴニオメーターによるアルミニウム材(A7075)の無歪み状態での面間隔測定

1-7-6 Measurement of d_0 (A7075) by random rotation goniometer

Bharoto[1], N. Minakawa[2]

[1]Research and Development Center for Materials Science and Technology,
National Nuclear Energy Agency of Indonesia.
[2]Advanced Science Research Center, JAERI, Tokai, Ibaraki, 319-1195, Japan

Objectives

The objective of this measurement is to obtain d_0 of Aluminium plug (A7075), which close to standard of Aluminium that no work has been done.

Measurement technique

First, we made goniometer system that can be rotated randomly. The goniometer was driven by pulse generator with 3 kHz of frequency. During experiments, ϕ axis rotates 360° while χ axis rotates from 0° to 90° continuously. ϕ axis was rotating by 5 rpm and χ axis was rotating by 0.08 rpm. Then we measured diffraction pattern of Aluminium (A7075) at (111), (200), (220) and (311) using facility of Residual Stress Analysis (RESA) with λ = 0.2098921 nm at the JRR-3M reactor in JAERI. The diffraction data of samples were collected about 6 minutes for each step.

Result and Discussion

The result of experiment shown in Fig.1 for (111), Fig.2 for (200), Fig.3 for (220) and Fig.4 for (311). From this diffraction pattern, we calculated d_0. The calculated d_0 of each peak is shown in Table 1.

Table 1. d_0 of Aluminium Plug (A7075)

	Aluminium Plug (A7075)			
hkl	(111)	(200)	(220)	(311)
d_0	0.234	0.203	0.143	0.122

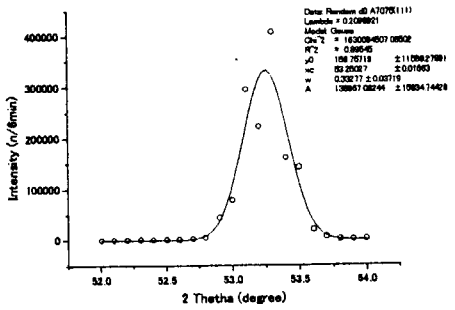


Fig.1. Diffraction pattern of A7075 (111)

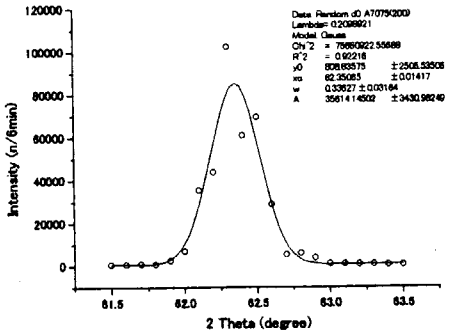


Fig.2. Diffraction pattern of A7075 (200)

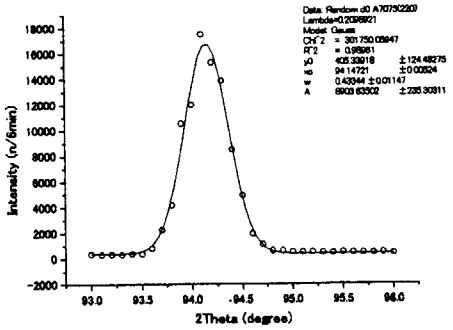


Fig.3. Diffraction pattern of A7075 (220)

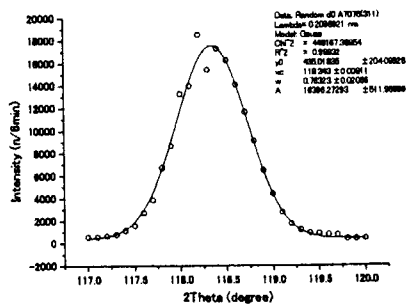


Fig.4. Diffraction pattern of A7075 (311)

研究テーマ：超低温の導入による中性子散乱の研究
表　　題　：冷し填め試料の加工応力を評価した内部残留応力

1-7-7 The internal residual stress which evaluated the processing stress of a shrink-fit sample

JAERI　Nobuaki Minakawa, Yukio Morii, Atsushi Moriai, Kenji Kikuchi

The shrink-fit sample was made by A7075 aluminum material. A shrink-fit sample makes the plug of a somewhat big diameter compared with a ring inside diameter. The plug was contracted by the liquid nitrogen, and it inserts in a ring quickly. After that, the plug left in room temperature swells within a ring, and a big stress generates it into a boundary part. We measured the internal stress distribution after completion, and evaluated the soundness of a design, and the action of a processing stress as compared with the design stress while we measured the inside residual stress of processing when processing a ring and a plug from the base material using RESA.

In order that to measure shrink-fit material by the neutron diffraction, a neutron absorption cross section is small, a cofficient of thermal expansion is large, and it is a necessary condition that a tensile strength is a big material. Therefore, we selected the aluminium alloy material A7075 with which it was satisfied of these conditions. The design stress of a shrink-fit sample was taken as 280MPa of the half of a tensile strength of A7075 material. The design size set the outside diameter to 50mmphi, the height of 50mm, and inside diameter 25mmphi. In order that a sample is a cylindrical, because a stress distribution is equally distributed to the direction of the circumference, it can be measured easily.
The following procedure performed the measurement.
(1) Before combining . plug and a ring, the internal stress distribution generated by each machining was measured.
(2) The spacing of lattice planes in non-strain condition, the characteristic of material, the diffraction pattern, and the measurement of a texture were performed using.a plug.
(3) The internal stress distribution measurement of shrink-fit sample was performed. The non-strain spacing of lattice planes $d_0$measurement of A7075 was performed using χ and ϕ axis continuation rotation goniometer which were newly developed equipment. The measurement Miller indices selected A7075(220).

The strain was calculated by the formula of (4-1) from the measurement result, and used the equation of stress conversion (4-2) and (4-3). An estimate distribution of a hoop direction is shown in Fig. 1. A hoop direction processing residual stress distribution of a ring and a plug is shown in Fig. 2. The surveyed hoop direction residual stress distribution is shown in Fig. 3. The hoop direction residual stress that deducted the processing stress is shown in Fig. 4.

$$\varepsilon_{(h,k,l)} = \frac{(d_{(h,k,l)} - d_{0(h,k,l)})}{d_{0(h,k,l)}} \qquad (4\text{-}1)$$

$d_{0(hkl)}$: Spacing of lattice planes in non-strain condition, $d_{(hkl)}$: Spacing of lattice planes in strain condition, $\varepsilon_{(hkl)}$: Strain

The stress can determine for the hoop and the radial direction by the next following formula.

$$\sigma_H = \frac{E}{1-\nu^2}(\varepsilon_H - \nu\varepsilon_R) \qquad (4\text{-}2)$$

$$\sigma_R = \frac{E}{1-\nu^2}(\varepsilon_R - \nu\varepsilon_H) \qquad (4\text{-}3)$$

σ_H : The hoop stress, σ_R : The radial stress, ν : Poisson ratio, E : Young's modulus

From the measurement result, the hoop direction processing residual stress of a ring is near an inner circumference, and had the elongation stress of about 150MPa. As for the hoop direction processing residual stress

原子炉：JRR-3M　　装置：RESA (T2-1)　　分野：中性子散乱（基礎物理）

of a plug, the elongation stress of about 30MPa remains. By the shrink-fit sample, the hoop direction maximum stresses of a boundary part were about 410MPa. If the processing stress of the circumference part in a ring is deducted, it will become value about equal to 280MPa of a design stress. In the ring of a shrink-fit sample, and the combination of a plug, it has identified that the processing stress of a ring acted as sum.

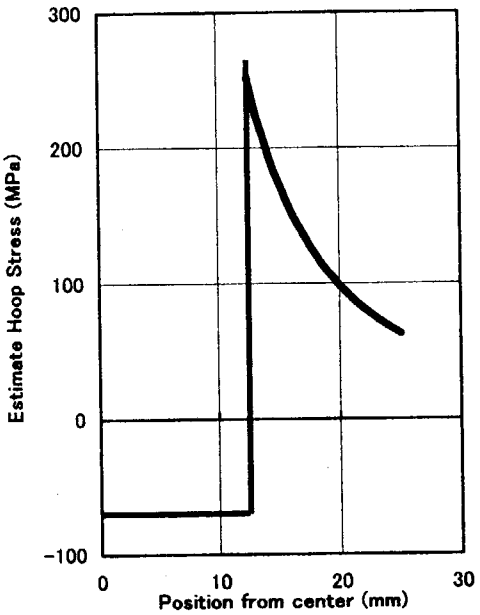


Fig. 1. An estimate distribution of a hoop direction

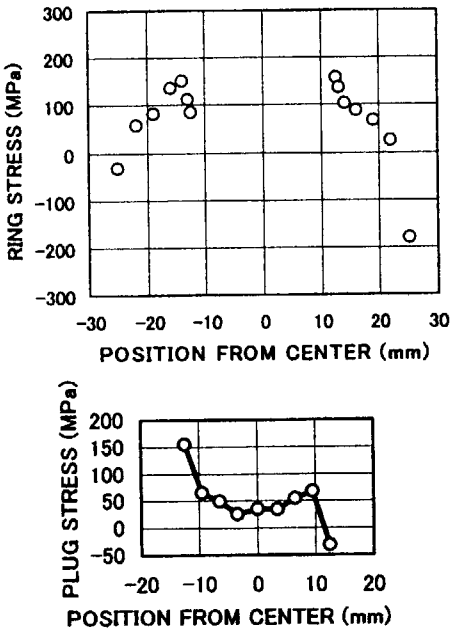


Fig. 2. A hoop direction processing residual stress distribution of a ring and a plug

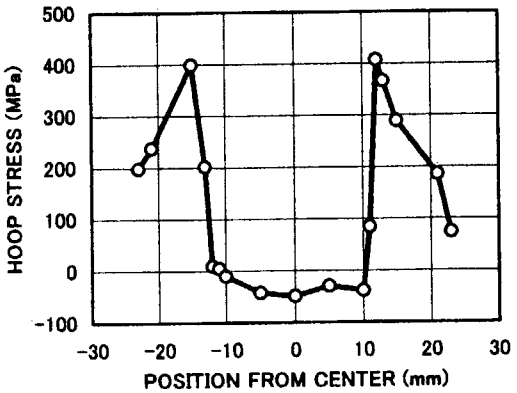


Fig. 3. A residual stress actual measurement distribution of a hoop direction

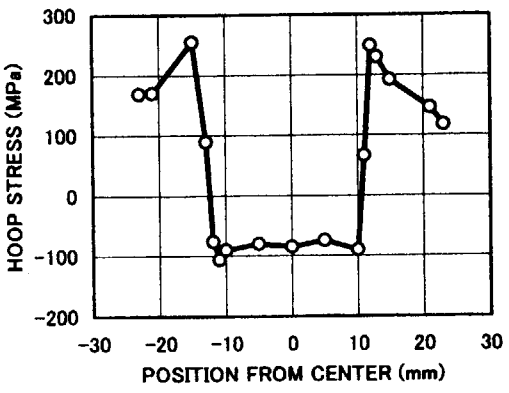


Fig. 4. The hoop direction residual stress that deducted the processing stress

研究テーマ：金属複合材料の力学特性に及ぼす残留応力の影響
表　題　：SiC繊維材とTi-15-3複合材の中性子回折による残留応力測定

1-7-8

Residual strain measurements by neutron diffraction in SiC fiber reinforced Ti-15-3 matrix composite

Y. Tanaka[1], N. Minakawa[2], C. Masuda[1] and Y-F. Liu[1]
[1] National Institute for Materials Science, Tsukuba-shi, Ibaraki 305-0047, Japan
[2] Japan Atomic Energy Research Institute, Tokai-Mura, Ibaraki 319-1195, Japan

Continuous SiC fiber reinforced Ti alloy matrix composites have been candidates for light weight component of gas turbine engines. The composites are expected to be subjected to a fatigue loading condition, therefore, the understanding of fatigue properties becomes an important research subject. When a composite is cooled down to room temperature during the fabrication, thermal residual stress is induced in the composite as a result of the mismatch of the coefficients of thermal expansion between the matrix ($\approx 8.2 \times 10^{-6}$/℃) and the fiber ($\approx 3.6 \times 10^{-6}$/℃). The magnitude of the residual stress may have a very important effect on the yield stress and fatigue strength of the composite[1].

Specimens of continuous SCS-6 fiber reinforced Ti-15-3 (Ti-15V-3Cr-3Al-3Sn) alloy matrix composite containing 6 fiber layers were fabricated by the foil fiber foil consolidation method using HIP was used in this study. The HIP was carried out at 1152K for 5.4 Ks under a pressure of 100 MPa. The matrix processed an equiaxed α microstructure by aging treatment. The volume fraction of the fiber was 0.39. SCS-6 fibers were manufactured via a chemical vapor deposition (CVD) process on an amorphous carbon monofilament core of 30 μm. A pyrocarbon deposited of 3 μm thickness was made so that final diameter of the fiber is about 146 μm. Specimens of the composite measuring 50 mm long, 4 mm wide and 1.2 mm thick, with the fibers oriented in the long direction, were cut from the panel. In addition to the composites, the matrix without the fiber as the same fabrication process and the fibers alone covered with Vanadium sheets were examined to obtain stress-free diffraction patterns. Saito et al.[2] have showed a new technique of measuring the bulk as original process material instead of the powder diffraction method for estimation of stress-free material.

The neutron strain measurements were made using RESA established in JRR-3M. The neutron wavelength was 0.209979 nm. The deep penetration of neutrons into the composite specimen provides simultaneous measurements of bulk average strains for both the matrix and the fibers. Figure 1 shows the neutron diffraction pattern of the composite with scattering vector parallel to the fiber direction. In the fibers the 220 and 311 diffraction was used for strain determination. As the results, the axial strain in the fiber was about –0.0012. The radial and the hoop stresses were compressive in the fiber (-0.0005). The neutron results showed closer agreement to finite element method predictions[3]. The effect of the fatigue loading on the residual strain in the composite will be studied in the future.

References

1) Y. Tanaka, Y. Kagawa, C. Masuda, Y-F. Liu, S.Q. Guo, Metall. Trans. A30 (1999) 221.
2) T. Saito, N. Minakawa, Y. Morii, T. Sasaki, Y. Hirose, J. Soc. Mat. Sci., Japan, Vol.50 (2001) 701.
3) J.-L. Bobet, C. Masuda, Y. Kagawa, J. Mat. Sci. 32 (1997) 6357.

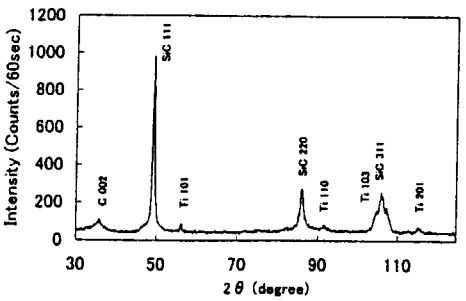


Figure 1 Neutron diffraction pattern of the composite.

原子炉：JRR-3M　　装置：RESA (T2-1)　　分野：中性子散乱（基礎物理）

研究テーマ：金属複合材料の力学特性に及ぼす残留応力の影響
表　題　：Cu-15wt%Crの複合材の中性子回折による残留応力測定

1-7-9

Measurement of residual strain in a Cu-15 Wt Pct Cr in-situ composite using neutron diffraction

C. Masuda[1], N. Minakawa[2] and Y. Tanaka[1]
[1] National Institute for Materials Science, Tsukuba-shi, Ibaraki 305-0047, Japan
[2] Japan Atomic Energy Research Institute, Tokai-Mura, Ibaraki 319-1195, Japan

High strength and high electrical conductive materials are very useful for the application of high field magnets, lead-frame and trolley wire. In Cu-Cr in-situ composite, heavy cold working and aging treatments are the two most important materials processing techniques. By heavy cold working, Cr dendritic structure in the as-cast ingot can be deformed into fibers as the reinforcing elements for obtaining high strength, while by an appropriate aging treatment, high conductivity can be achieved. Thus, the correlation between the cold-working and internal strain becomes very important to study the strength and fatigue mechanisms[1]. In this study, special attention has been focused on the effect of cold working on residual strain in the Cu-Cr in-situ composite.

The Cu-15wt%Cr composite was fabricated by casting method in vacuum condition. After the fabrication and solution treatment the ingot was forged at 1173K and solution treatment was performed at 1273K and quenched into water. The material was cold drawn in the range of drawing strain, η, of 4.6. Finally the material was aged at 800K to improve the electrical conductivity[2]. Figure 1 shows a typical example of the composite at the cold drawing of η=4.6 parallel to the drawing direction. It can be seen that the Cu matrix is reinforced by large fraction of Cr fibers. The chromium fiber surfaces are not smooth and the thicknesses of fibers are not so constant at the cold drawing strain of η=4.6.

The neutron strain measurements were made using RESA established in JRR-3M. The neutron wavelength was 0.209385 nm. Figure 2 shows the neutron diffraction pattern of the Cu-15% Cr in-situ composite at η=4.6. Powder diffraction method was used to determine the stress-free materials of Cu and Cr. In Cr fibers the (110) diffraction was used for strain determination. The average Cr fibers and Cu matrix in the direction of drawing were about 1240 and −1030 $\mu\varepsilon$, respectively. It is suggested that the strains in the Cu-Cr composite are dependent on dynamic process of deformation, recovery, recrystallization with the characteristics of fine grains and subgrains in the Cu matrix after cold drawing, despite the forming total reduction of 99%.

References

1) C. Masuda and Y. Tanaka, ASME Int. Mech. Eng. Conf. DE-Vol. 110 (2000) 73.
2) Y. Jin, K. Adachi, T. Takeuchi and H. Suzuki, Metall. Trans., 29A(1998) 2195.

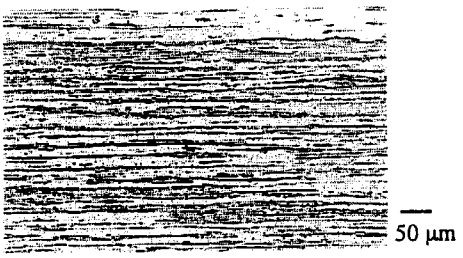


Figure 1 Microstructure of Cu-15Cr composite after cold drawing strain of η=4.6.

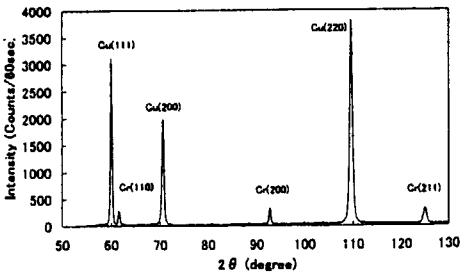


Figure 2 Neutron diffraction pattern of the composite.

原子炉：JRR-3M　　装置：RESA (T2-1)　　分野：中性子散乱（基礎物理）

研究テーマ: 構造材料の残留応力と疲労損傷の評価
表　　題: 伸線パーライト鋼の残留応力測定

1-7-10
Measurement of Residual stresses of a drawn pearlite steel

T.Suzuki, Y.Tomota, Y.Moriai, N.Minakawa and Y.Morii

The Research Center for Superplasticity, Faculty of Engineering, Ibaraki University, Hitachi, Ibaraki 316-8511, Japan.
Department of Materials Science, Faculty of Engineering, Ibaraki University
Japan Atomic Energy Research Institute, Tokai, Ibaraki 319-1195, Japan

The residual phase stress in the ferrite matrix was measured along five directions by using RESA. A hypereutectoid steel with chemical compositions of 0.85C, 0.24Si, 0.82Mn, 0.011P, 0.01S, 0.02Al and 0.05Cr in mass% was used. Hot-rolled rods with 11mm in diameter were patented through an industrial process to produce fully pearlitic structure(P1). They were then drawn to wires with 5.5mm in diameter, where reduction in area was 75%(P2). After that, some of the drawn wires were aged at 423K for 12.6ks (P3) or 698K for 0.6ks (P4: Zn-plating simulated heat) or annealed at 963K for 18ks in order to make cementite particles spherical (P5). Specimens with 5.5 mm in diameter and 30 mm in length were prepared. By using a conventional θ -2 θ method, lattice plane spacings of (110),(200),(220) and (211) ferrite were measured, where a specimen was rotated by 0, 22.5, 45, 67.5 and 90 degrees with respect to the drawing direction. Peak positions of the diffraction profiles were determined by curve fitting with a Gaussian function. Figure 1 shows the results of ferrite 110 lattice plane strain as a function of the measuring direction. As can be seen, the residual elastic strain of P2 and P3 shows strong anisotropy, while that of P1, P4 and P5 is independent of the angle. Such anisotropy in the residual strain was also deserved in P3. This result indicates that the Zn-plating heat treatment relaxed the residual stress produced by the drawing. On the other hand, Table 1 shows the result of tensile and compression test for P1～P5. The yield strength in tension is much higher than that in compression in the cases of P2 and P3. We measured the compression strength of P 1 ～P5 specimens as a function of the angles between the compression direction and drawing direction and found that only P2 and P3 had strength anisotropy. Such anisotropy in the yield strength of pearlite steels can be explained from the results of residual stress shown in Fig.1.

Table 1　Yield stress of the pearlite steels measured by tension or compression tests

	Tension(GPa)	compression(GPa)
P1	1.00	1.05
P2	2.05	1.45
P3	2.15	1.55
P4	1.6	1.6
P5	0.7	0.57

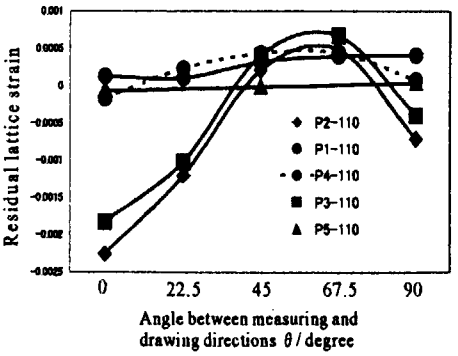


Fig.1 Residual elastic strain in the ferrite matrix As a function of the angle from the drawing Direction.

原子炉: JRR-3M　　装置: RESA(T2-1)　　分野: 中性子散乱(基礎物理)

研究課題: 冷中性子スピン干渉計の開発とその応用 II
表題: RF flipper による冷中性子スピン干渉を用いた分光法の開発 II

1-7-11 Mieze Spin Echo Method Using RF Flippers II

T.Ebisawa, S.Tasaki, N. Achiwa[1], D.Yamazaki[2], T.Kanaya[3], N.Torikai[4], M.Hino, T.Kawai, K.Soyama[5]

Research Reactor Institute Kyoto University
Department of Physics, Kyushu University[1]
Department of Nuclear Engineering Kyoto University[2]
Institute for Chemical Research, Kyoto University[3]
Neutron Science Laboratory, High Energy Accelerator Research Organization[4]
Japan Atomic Energy Research Institute[5]

We have made two improvements for our Mieze spin echo method using RF flipper[1, 2, 3] with regards to the spin echo method and the available neutron intensity.

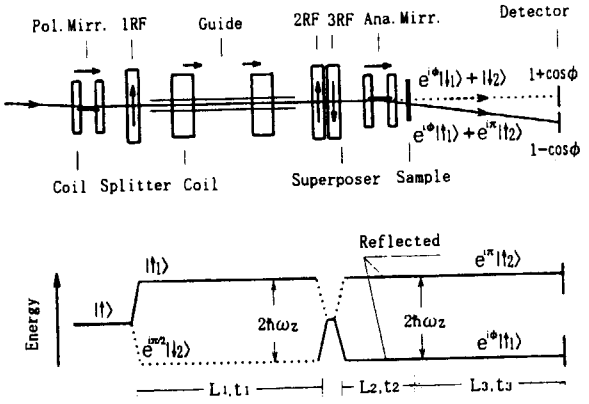


Figure 1: (a) An arrangement of a new modefied Mieze type spin echo method with RF flippers. Direction of magnetic field is shown by bar with arrow. The guide field is applied to the neutron traveling direction. The three RF flippers with magnetic field perpendicular to the guide field, are arranged in the guide field. Non adiabatic changes of the magnetic field at the upward boundary of the first and the downward boundary of the third flippers, function as $\pi/2$ flipper. (b) Illustration of the method from a viewpoint of spin interferometry. The guide field perpendicular to the field of the RF flippers is equivalent to the zero field.

The structure of the new Modefied Mieze spin echo method is shown in Fig.1(a). The guide field is applied to the neutron traveling direction. The three RF flippers are applied to be perpendicular to the guide field. Non adiabatic change of the magnetic field at the upward boundary of the first RF flipper, functions as neutron wave splitter into the two spin eigenstates, which correspond to $|\uparrow_1\rangle$ and $|\downarrow_2\rangle$. Another non adiabatic change at the downward boundary of the third RF flipper, functions as wave superposer into $|\uparrow_1\rangle$, $|\uparrow_2\rangle$ and $|\downarrow_1\rangle$, $|\downarrow_2\rangle$, as shown in Fig.1(a).

This Mieze spin echo method is illustrated by Fig.(b) from a viewpoint of spin interferometry. The guide field perpendicular to the field of the RF flipper give rises to phase shifts between each partial waves. These phase shifts, however, are cancelled in the superposed stage as shown by a little complicated calculation[4]. Consequently such guide field is equivalent to the zero field in the conventional resonance spin echo method[5, 6]. This shows that the above new method brings us spin echo method using RF flipper without magnetic shield.

Neutron intensity reduction caused by the long traveling in the spectrometer would be prevented by neutron guide tube set between the first and second RF flippers.

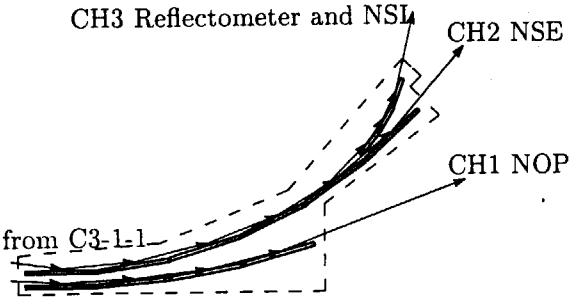


Figure 2: Arrangement of C312 bender and three channel beam ports. Channel 1(CH1) is NOP beam line. CH2 is for new spin echo systems. A reflectometer suitable for low q and a spin interferometer are installed at CH3.

The above spin echo method will be applicable to pulsed neutron source, replacing the conventional RF flippers by new RF flippers suitable for pulsed neutron, which have been developing [7].

The available neutron intensity for the spectroscopy has considerably been improved by the new cold neutron bender using sequential garland reflections, which are installed at C312 port [8, 9].

Table 1: Spectrometers installed at three channel beam ports and typical parameters of the beam ports.

Beam port	CH1	CH2	CH3
Bent angle(degree)	14.5	24.1	35.1
Intensity(/sec.cm^2)	2×10^6	6×10^5	1000
Beam size(mm^2)	42× 8	42× 7	42× 3
Wavelength(Å)	> 9.2	> 10.0	11.0 ± 0.3

The bender system supplies neutron to three channels beam ports, as shown in Fig.2. The new spin echo system is installed at CH2, which supplies neutrons with wavelength longer than 10 Å. Typical parameters and neutron intensities for the three beam ports are summarized in Table 1. Neutron intensities will increase by about 3 times by the replacing to 3Q supermirror of the supermirror used for the bender, which is scheduled in this autumn.

We are going to make two preliminary applications using this spin echo method to two scattering phenomena including inelastic reflection from a polymer with lamellar structure and incoherent inelastic scattering by hydrogen atoms.

The above improvements and measurement schedule will bring us promising future for the development of the new spin echo methods.

References

[1] T.Ebisawa, S.Tasaki, M.Hino, T.Kawai, Y.Iwata, D.Yamazaki, N.Achiwa, Y.Otake, T.Kanaya, K.Soyama, Journal of Physics and Chemistry of Solids 60,(1999) 1569-1572.

[2] T.Ebisawa, S.Tasaki, D.Yamazaki, G.Shirozu, M.Hino, T.Kawai, T.Kanaya, K.Soyama, N.Achiwa. Physica B,276-278(2000),144-145.

[3] T.Ebisawa, S.Tasaki, D.Yamazaki, N.Achiwa, G.Shirozu, T.Kanaya, N. Torikai, M.Hino, T.Kawai, K.Soyama, J. Phys. Soc.Jpn 70(2001)Suppl.A 442.

[4] T.Ebisawa et al, to be published.

[5] W.Besenböck, P.Hank, M.Köppe, R.Gähler, T.Keller, R.Golub, J. Phys. Soc. Jpn. **65** Suppl.A (1996) 215.

[6] M.Köppe, M.Bleuel, R.Gähler, R.Golub, P.Hank, T.Keller, Physica B **266** (1999) 75.

[7] R.Maruyama et al., private comunications.

[8] J.Suzuki, K.Soyama, S.Tasaki, T.Ebisawa, Proceedings of ICANS-XV(2000) 547.

[9] J.Suzuki et al, to be published.

研究課題: スピン干渉と中性子吸収によるトンネル時間の研究
表題: 吸収の強い磁気膜をトンネルする中性子のスピン歳差位相

1-7-12 Measurement of spin precession angle of neutron tunneling through a magnetic thin film with absorption

M. Hino, S. Tasaki, T. Ebisawa, T. Kawai, N. Achiwa[1], D. Yamazaki[2]
Research Reactor Institute Kyoto University
Department of Physics, Kyushu University
Department of Nuclear Engineering, Kyoto University

There has been interest in the notion of tunneling time which measn is that a particle spend in the classically forbidden potential barrier. We take notice of the Larmor clock and measured spin precession of neutrons tunneling through Permalloy45 ($Fe_{55}Ni_{45}$) thin film by means of neutron spin interferometer(NSI) installed at C3-1-2 beam port at JAERI. The spin precession angle is well reproduced by the theoretical phase difference of ↑ and ↓ spin neutron wave functions based on one-dimensional Schrödinger equation. This result shows that tunneling neutron is not a particle but should be considered as a wave. There is no way to determine the path of tunneling neutron in the barrier. Thus we did not say anything concering about the time though we measured precisely spin precession of tunneling neutron and Larmor time which derived from spin precession is indeed used as a correct clock when it is used in non-tunneling case. We introduce the effect of absorption as an additional clock and try to measure average of the time that neutrons spend in the classically forbidden potential barrier.

Figure 1 shows spin precession angle through PA/Gd magnetic thin absorber evaporated on silicon wafer coated with Ti thin film whose thickness is 45nm. The absorber consists of Permalloy45($Fe_{55}Ni_{45}$ and gadolinium elements, the total thickness is estimated to be 23nm. The closed circles are measured and the solid line is calculated from one-dimensional Schrödinger equation using the optical potential barrier with absorption[1]. Here we assume that the value of potential barrier in the magnetic absorber is represented as $V = V_{\rm nucl} \pm \mu B + iV_{\rm ab}$ for ↑ and ↓ spin, respectively, where $V_{\rm nucl} = 220$(neV), $V_{\rm ab} = 10$(neV) and $\mu B = 72.4$(neV) is the average coherent nuclear potential, absorption one, magnetic one, respectively. The critical wavelength for ↑ and ↓ spin neutron correspond to 1.36 and 0.97 degree,respectively. The experimental result is well reproduced by the theoretical line above the critical angle for ↑ spin neutron, that is to say, in non-tunneling case. It is seems to be contrary to non-tunneling and resonant-tunneling case [2], that spin precession of tunneling neutron with absorption is not so reproduced by the plane wave model. It is very interresting if it is ture. We do not confident of this result because intensity of tunneling through the magnetic absorber is very few. Thus we are going to carry out more precisely experiment concering about this.

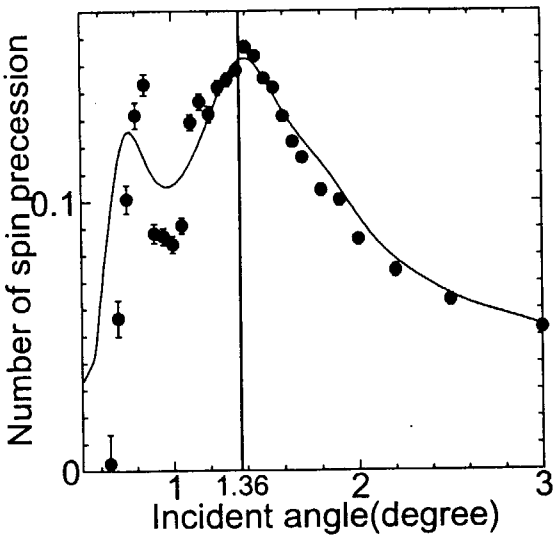


Figure 1: Spin precession of neutron tunneling through magnetic thin film absorber.

References

[1] T. Ebisawa, T. Akiyoshi, N. Achiwa, S. Yamada and S. Okamoto, Annu. Rep. Res. Reactor Inst. Kyoto Univ., **14**, 10(1981).

[2] M.Hino, S.Tasaki, T.Ebisawa, T.Kawai, M.Utsuro, N.Achiwa and D.Yamazaki, Physica B **276-278** 981(2000).

JRR-3M, MINE, Neutron Optics

研究課題：中性子スピン時間干渉計
表題：中性子スピン時間干渉計における試料位置スピンアナライザー前後の意味

1-7-13 Time Beat Neutron Spin Interferometry before or after Analyser

Norio ACHIWA, Gou SHIROZU, Toru EBISAWA[1], Masahiro HINO[1], Seiji TASAKI[1], Takeshi KAWAI[1] and Dai YAMAZAKI[1]

Department of Physics, Graduate School of Science, Kyushu University, Fukuoka, 8128581, Japan
[1]Research Reactor Institute, Kyoto university, Kumatori-cho, Sennan-gun, Osaka 590-0494, Japan

Neutron resonance spin echo method (NRSE) has been developed by Gähler and Golub et al.,[1,2] where spin echo phases are created by radio frequency (RF) flippers. As a modified version of NRSE, they apply the echo of time beat for a TOF neutron spectrometer, MIEZE instrument.[3-5] In the MIEZE spectrometer the sample is downstream of the analyser leaving the signal indifferent to magnetic field and spin flips in the sample. Following their principle, we have developed neutron spin interferometry using these radio frequency flippers.[6-8] In this paper we have firstly demonstrated the dependence of these time beat on the position of a neutron spin depolarizer.

The time beat of neutron intensity at detector position is created by the coherent superposition of the same spin eigenstates of neutrons with different energy states, which are produced with two radio-frequency flippers and polarization analyser.

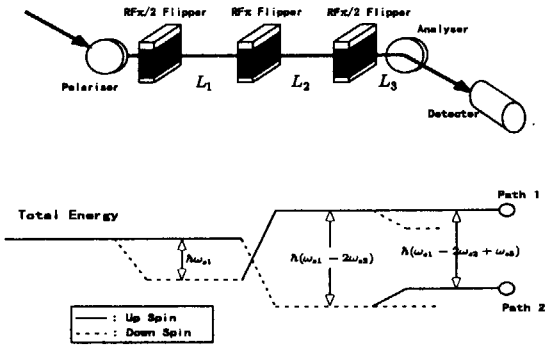


Fig. 1. Arrangement of a time beat neutron spin interferometer with RF spin flippers. The splittings in total energy are given by the exchange of quanta with energies $\omega_{z1}, \omega_{z2}, \omega_{z3}$ by RF flippers.

A simple cold neutron spin interferometer using radio frequency flippers (RF flipper) is shown in Fig.1, which is similar to the MIEZE spectrometer.

Such an interferometer is installed at C3-1-2 cold guide, JRR-3M, JAERI. The RF flippers consist of two coils, that is, one creates a magnetic field B_z parallel to the quantized axis and another one creates an oscillating field $B_x(t)$ perpendicular to the quantized axis. Assuming the resonance condition for the RF flipper and expressing the oscillating field as $B_x(\sin\omega_z t + \Delta)$, the frequency of the oscillating field, ω is given by,

$$\hbar\omega_z = 2\mu B_z \tag{0.1}$$

where μ is the neutron magnetic moment. The RF flippers function as $\pi/2$ and π flippers when the amplitude B_x satisfies Eqs.(0.2) and (0.3), respectively,

$$\frac{l}{v}(\mu B_x) = \frac{\pi\hbar}{2} \tag{0.2}$$

$$\frac{l}{v}(\mu B_x) = \pi\hbar \tag{0.3}$$

where l is the length of the RF-flipper and v the neutron velocity.

We consider the following cases for the magnetic fields of the system,

$$B_{z,1} = B_{z,2} = B \gg B_{z,3} = B_g \tag{0.4}$$

where $B_{z,i}$ is the magnetic field along the z axis of the i th RF flipper and B_g the guide field, respectively. The three RF flippers function as $\pi/2, \pi$ and $\pi/2$ in turn. The polarized neutron is split into the two spin eigenstates with energy difference with $\hbar\omega_z$ by the first RF $\pi/2$-flippers. The spin state and energy difference of these partial waves are reversed by the second RF π-flippers. The third $\pi/2$-flipper supersplits into two $\uparrow$ and two $\downarrow$ spin neutron states which can be selected by analyser to give two $\uparrow$ spin states with different energygiving rise to quantum beats of neutron intensity. The time beat of neutron intensity at the detector positon at $t_d = t_0 + t_1 + t_2 + t_3$ is given by Eqs. (0.5).[9] Here, t_0 is the time when the neutron is incident on RF $\pi/2$-spin flipper, and t_i is given by L_i/v.

$$|\psi_t^{out}(+)|^2 = \frac{1}{2} + \frac{\cos[(2\omega_{z2} - \omega_{z1})t_d + \Delta_0 + \Theta]}{2} \tag{0.5}$$

where the effect of B_g is neglected and the wavelength dependent phase is given by

$$\Theta = \frac{\omega_{z1}L_1 - (2\omega_{z2} - \omega_{z1})(L_2 + L_3)}{v}, \tag{0.6}$$

where L_1 is the length between the first and second RF flippers, L_2 the length between the second RF flipper and the sample, L_3 is the length between the sample and the detector. The phase difference created by the magnetic potential among the flippers is quite analogous to the Larmor precession. Accordingly, this term induces a phase dispersion depending on the velocity spread of the incident neutrons. Condition $\Theta = 0$ is required in order to observe the interference pattern with high visibility.[7,9,10] This condition is equivalent to the time focussing in the MIEZE spectrometer by Gähler et al..[2,11]

JRR-3M Facility:MINES(C3-1-2), Neutron Optics

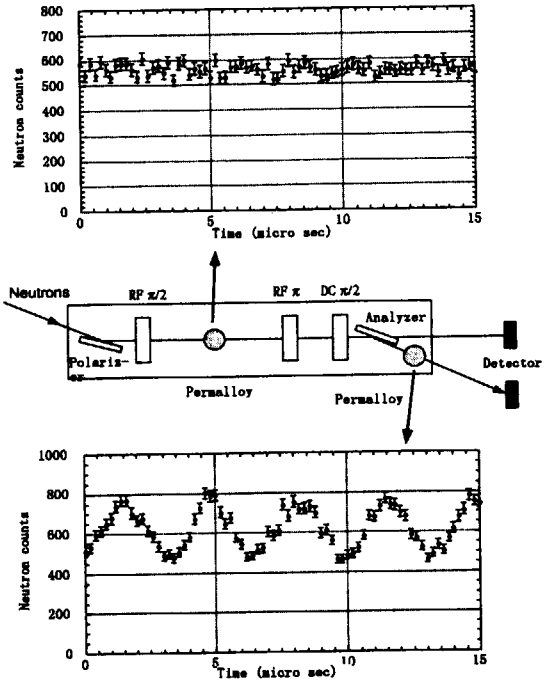


Fig. 2. Two kinds of set up to test the effects of unmagnetized Permalloy sheet of 1 mm thickness inserted upstream of the π flipper or downstream of the analyser as a neutron spin depolariser. The time beat of 400 KHz is completely destroyed by randum magnetic domains in the unmagnetized Permalloy film in the former site while the time beat is unchanged in the latter site. Though as the third flipper, DC $\pi/2$ is used instead of RF $\pi/2$ flipper different from Fig. 3, the role of superslitting into two $\uparrow$ and two $\downarrow$ spin neutron states is similar with each other.

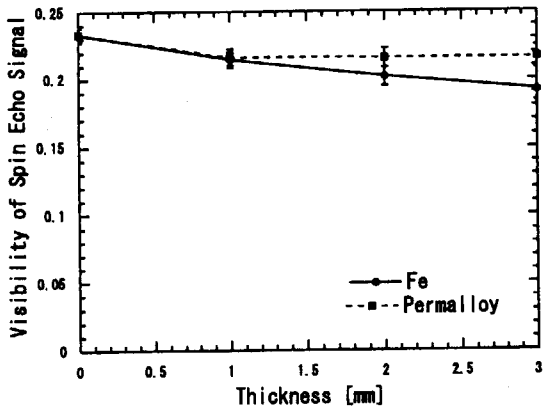


Fig. 3. Tickness dependence spin echo visibility through unmagnetized Permalloy or iron sheet located at behind the analyser for the time beat of 400 KHz

When we insert a magnetic phase shifter between $\pi/2$ and π spin flippers, the phase of time beat is shifted by the following equation.

$$\Delta\Phi = 2\frac{\mu B_z d}{v}. \qquad (0.7)$$

This phase shift corresponds to Larmor precession and it does not depend on the frequency of the RF flippers. In order to measure precisely the phase shift in good visibility of time beat, the frequency is not necessarily high. Here we demonstrate the effect of an unmagnetized Permalloy sheet of 1mm thickness inserted between the $\pi/2$ and the π flippers or inserted between the analyser and the detector as a neutron spin depolariser. The time beat of 400 KHz is completely destroyed by the random magnetic potential of Permalloy domains in the former site while the time beat is almost unchanged in the latter site as shown in Fig. 2.

Thickness dependence of spin echo visibility through unmagnetized Permalloy and iron sheets inserted after the analyser for the time beat of 400KHz is shown in Fig. 3. A small decrease of visibility with increasing thickness was observed both for the iron and the permalloy sheets. Multiple small angle scattering effects by magnetic domains bring path length differences of neutrons in the sample. This might explain the decrease of the visibility. Another possibility is due to the inelastic spin flip multiple scattering. But the frequency dependence of the visibility is required for the proof of these interpretations.

Due to the fact that the time beat of neutron intensity is created by a superposition of $\uparrow$ spin neutron wave functions with different total energies, magnetic potentials downstream of the analyser do not influence the time sygnal. Even if neutron spin is flipped by the random magnetic potentials in the unmagnetized Permalloy sheet, the superposition of both $\uparrow$ spin states changes simultaneously keeping the coherence between them. MIEZE type spectrometer utilizing echo of time beat will be very effective for the measurement of quasi-elastic scattering of ferromagnetic substances and for samples see reference.[12] Similarly, the time beat from the incoherent spin scattering from vanadium sample is demonstrated by Ebisawa in this proceedings.[13]

1) R.Gähler, R.Golub: Z. Phys. **B65** (1987) 269.
2) R.Gähler, R.Golub, T.Keller: Physica B **180 & 181** (1992) 899.
3) M.Köppe, M.Bleuel, R.Gähler, R.Golub, P.Hank, T.Keller: Physica B **266** (1999) 75.
4) P.Hank, W.Besenböck, R.Gähler, M.Köppe: Physica B **234-236** (1997) 1130.
5) J.Felber, R.Gähler, R.Golub, P.Hank, T.Keller, U.Rauch: Foundation of Physics **29** (1999) 381.
6) D.Yamazaki, T.Ebisawa, T.Kawai, S.Tasaki, M.Hino, T.Akiyoshi, N.Achiwa, Physica B 241-243(1998)186.
7) T.Ebisawa, D.Yamazaki, S.Tasaki, T.Kawai, M.Hino, T.Akiyoshi, N.Achiwa, Y. Otake: J. Phys. Soc. Jpn. **67**(1998)1569.
8) T.Ebisawa, S.Tasaki, M.Hino, T.Kawai, Y.Iwata, D.Yamazaki, N.Achiwa, Y.Otake, T.Kanaya, K.Soyama: Journal of Physics and Chemistry of Solids 60,(1999) 1569-1572.
9) D.Yamazaki: private communications.
10) T.Ebisawa, S.Tasaki, D.Yamazaki, G.Shirozu, M.Hino, T.Kawai, T.Kanaya, K.Soyama, N.Achiwa: Physica B,276-278(2000),144.
11) W.Besenböck, P.Hank, M.Köppe, R.Gähler, T.Keller, R.Golub: J. Phys. Soc. Jpn. **65** Suppl.A (1996) 215.
12) W.Besenböck, R.Gähler, P.Hank, R.Hank, M.Köppe, C.-H. de Novion, W. Petry and J.Wuttke: J. of Neutron Research, **7** (1998) 65.
13) T.Ebisawa, S.Tasaki, D.Yamazaki, N.Achiwa, G.Shirozu, T.Kanaya, N.Torikai, M.Hino, T.Kawai, K.Soyama: in this proceedings.

研究テーマ：多層膜冷中性子干渉計の改良 － 経路間隔の拡大 －
表題：エタロンを用いた Jamin 型冷中性子干渉計の開発

1-7-14

A novel Jamin-type interferometer for cold neutrons using etalon plates

M. Kitaguchi [a], H. Funahashi [a], and M. Hino [b]
[a] *Department of Physics, Kyoto Univ. , Kyoto 606-8502, Japan*
[b] *Research Reactor Institute, Kyoto Univ. , Kumatori, Osaka 590-0494, Japan*

A new type of cold neutron interferometer based on a pair of *etalons* has been developed. Neutron interferometry is a powerful technique for studying fundamental physics. The archetype of cold neutron interferometer using multilayer mirrors had been developed to increase the sensitivity to small phase shift[1]. It has advantages in terms of scalability and is highly applicable to long-wavelength neutrons. Later, this kind of interferometer using magnetic multilayer mirrors realized remarkable experiments[2], however, the range of applications of this system is limited due to the small beam separation. The aim of our development is to increase the separation of two coherent beams in a multilayer mirror interferometer in order to broaden the applicability of neutron interferometry.

The new apparatus is a sort of a type of polarization interferometer called a *neutron spin interferometer* [3], which is in a view point of geometrical optics equivalent to a Jamin interferometer, the oldest type of interferometer used practically in optics. It uses several neutron optical components; a neutron polarizer, $\pi/2$ spin flipper coil, π spin flipper coil, phase-shifter coil, $\pi/2$ spin flipper coil, a spin-analyzer mirror, and a path separator. The path separator is composed of a pair of etalons, which are optical components used mainly in the field of laser optics. The parallel planes of etalons are finished to high precision. We made up neutron mirrors on these planes. The reflection off the first etalon divides the incident neutrons into two parallel paths and then the paths are recombined after the reflection off the second etalon (Figure 1). The design of this path separator provides a greater separation between the two paths beyond the limit given by conventional separator. The present interferometer was tested using the 'MINE' cold neutron beam line at the JRR-3M reactor in JAERI. The beam had a wavelength of 12.6Åand a bandwidth of 3.5% (FWHM). Using etalons with 20μm air gap between the parallel planes (20mm clear aperture, roughness RMS 3Å) we observed interference fringes with a contrast of (3.5 ± 0.7)Å(reduced χ^2 value of least-squares fit is 0.9). The results of the five experimental runs were consistent with each other. One of the reasons for the loss of contrast can be attributed to the fact that the undercoat renders one of the four mirrors inadequate. We are currently preparing an experimental apparatus that will use etalon plates without undercoat in order to provide sufficient contrast. We also plan to increase the etalon air gap spacing to 1 mm.

The present results have paved the way for the development a cold neutron interferometer with a large path separation using etalons. The enlargement of the path separation will facilitate high precision measurements and new type of experiments that can not be undertaken using existing interferometeric methods.

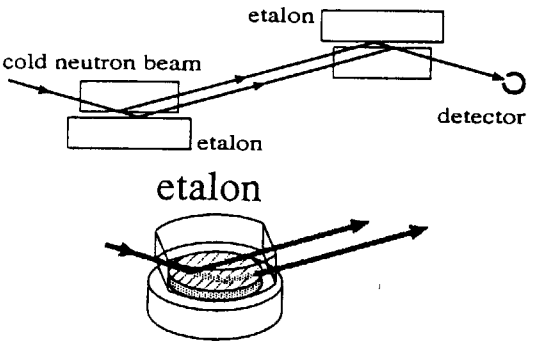


Figure 1: Schematic diagram of Jamin-type interferometer for cold neutrons using etalon plates
Magnetic components are omitted in this figure.

References

[1] H. Funahashi et al. , Phys. Rev. **A54**(1996)649
[2] Y. Otake et al. , Proc. Int. Symp. Foundations of Quantum Mechanics (ISQM-Tokyo '98) pp.323-326
[3] T. Ebisawa et al. , Phys. Rev. **A57**(1998)4720

JRR-3M, C3-1-2 (MINE), Fundamental Physics & Neutron Optics

1. 中性子散乱 8) 装　置

1. Neutron Scattering 8) Instrument

This is a blank page.

研究テーマ：超低温の導入による中性子散乱の研究
表題：2結晶回折計におけるSi光学素子の冷却化の試みII

1-8-1

An Attempt to refrigerate Si-crystal optical component on a Double Crystal Diffractometer II

K. Aizawa and H. Tomimitsu
Advanced Science Research Center, Japan Atomic Energy Research Institute, Tokai, Ibaraki 319-1195, Japan

We have tried removal of thermal diffuse scattering etc. by cooling crystals for the purpose of improving S/N ratio in double crystal diffractometer which used Si-perfect crystals. Previously, we reported a dispersive case which means that d-spacings of first and second crystals are not identical, namely only the second crystal was cooled to 14.78 K. Simultaneous cooling of first and second crystals was tried (non-dispersive setting) and rocking curve of second crystal was measured this time.

The experiment was performed using PNO equipment in JRR-3M at JAERI. A symmetrical (5,-5) setting of 111 reflection was used in this study. The neutron with a wavelength of 0.25 nm was used and the beam was formed 4 mm × 18 mm size at the second crystal position by passing a slit. Our cooling system consists of a conventional compressor-type cryostat and vibration free system to isolate vibration to crystals. The temperature of first crystal was 16.7 K and the second crystal did not get cold enough but was about 120 K. Therefore, unfortunately non-dispersive condition which means that d-spacings of first and second crystals are identical was not realizable. Hereafter, we call this situation low temperature case.

Rocking curves obtained from the low temperature and the room temperature cases are shown in Fig. 1. In the figure, the rocking curve at low temperature is normalized about the peak intensity of that of room temperature. Actually at low temperature, peak intensity decreased to 17.0 cps to that of room temperature being 153.1 cps. Moreover, the ratio of integrated intensity of the low temperature peak to that of the room temperature at this time was reduced to about 43.3%. And the full width at half maximum (FWHM) of obtained rocking curve was about 6.2 sec of arc and it spread by about 3.3 times that of room temperature. Although contribution of dispersive setting is also one of causes of a broadening of FWHM, it is thought that the influence of distortion in crystals by cooling are larger. Moreover, the reduction in integrated intensity is explained because the domains which dynamical diffraction occurs to a certain incident wave vector are decreasing due to distortion in crystals. In a figure, the part where the variation in data is over the error is seen. This is considered because removal of vibration of a cryostat is inadequate.

Although we devised the sample attachment mechanism and the vibration-free mechanism, it is mentioned as a conclusion that it is difficult to measure precise dynamical diffraction by undistorted state at low temperature in a simple compressor-type cooling system which we used. Therefore, in order to reduce thermal diffuse scattering etc., it is considered more realistic to use the optical element which reduced the thickness of slab in ch-cut Si crystal. Now, the experiment using such an optical element is under plan.

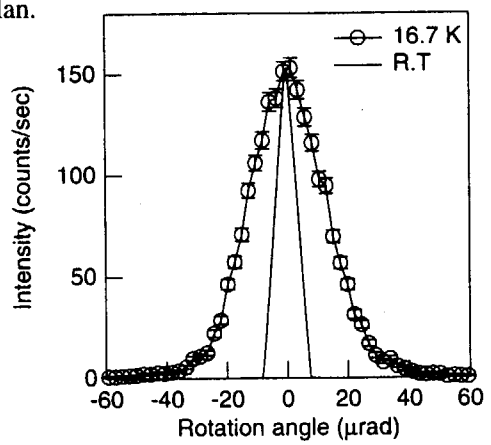


Fig. 1 Rocking curves at 16.7K and room temperature. The peak intensity of 16.7 K data is normalized to that of room temperature.

原子炉：JRR-3M　　装置：PNO (3G)　　分野：中性子散乱（装置）

研究テーマ:機能性生体物質の水和構造研究
表　　題:生体高分子用回折計 BIX-2 および BIX-3 の重ね合せ弾性湾曲完全結晶シリコンモノクロメータ

1-8-2 STACKED ELASTICALLY BENT PERFECT SI MONOCHROMATORS FOR DIFFRACTOMETERS FOR BIO-MACROMOLECULES (BIX-2 & BIX-3)

I. Tanaka, K.Kurihara, T. Chatake, M. Maeda, N. Niimura

ASRC, Japan Atomic Energy Research Institute, Tokai, Ibaraki 319-1195, Japan

Neutrons have a great potential as a probe to investigate hydrogens in biological macro-molecules including bound waters, but the low intensity of incident neutrons is always a big obstacle compared to the intensity of X-rays. In order to gain neutrons at the sample position and to insert a monochromator with the minimum loss of neutrons to the downstream instruments, an elastically bent perfect silicon (EBP-Si) monochromator was used in BIX-2 and BIX-3, diffractometers for bio-macromolecules in JAERI. One of the merits of EBP-Si to be noted here, is to increase reflectivity by stacking Si plates and to be able to select a proper Si(*hkl*) plane corresponding to a necessary wavelength.

Recently at the thermal guide T2 in JRR-3M, nearly half length of the guide tube has been replaced to 2Qc super mirror. As a result the peak spectrum has shifted to lower wavelength. Then the authors must change the wavelength of BIX-2 monochromator from Si(220) of 2.15 Å to Si(311) of 1.83 Å to obtain more neutrons. The reflected intensity for an EBP-Si monochromator of four identical Si(311) planes stacked set at th emonochromator position of TAS-2 was compared with that for single EBP-Si when the incident beam width was 20mm, θ was 34 deg and the distance between monochromator and a detector (neutron IP) was 1.05 m just as BIX-2 MtoS distance. A single plate of Si is 170 x 20 mm^2 surface of Si(311) and 2.5 mm in thickness. Therefore the total thickness of Si was 10 mm. The peak and intensity of four plates EBP-Si were larger by a factor of $2.61 = 1.6^2$ than that of a single plate. This gain factor agrees with the last adjustment of BIX-3 monochromator [1]. And in the real BIX-2 intensity measurement at sample position it was the same intensity as before replacing T2 guide mirrors, which shows the adjustment was acceptable even after considering λ -dependence of reflectivity.

The authors tried to re-adjust an EBP-Si monochromator for BIX-3, which was 2 plates of 5 mm thickness, by the incident beam width of 20 mm with θ of 22 deg, but the gain factor compared to single plate was only 1.1. After checking many points, the authors found the possibility that the bender iron holders might shield incident and reflected beam. From an experiment as Fig. 1, the maximum loss of intensity was about 20 %.

Reference

[1] I. Tanaka, F. U. Ahmed and N. Niimura, Physica B **283** (2000) 295-298.

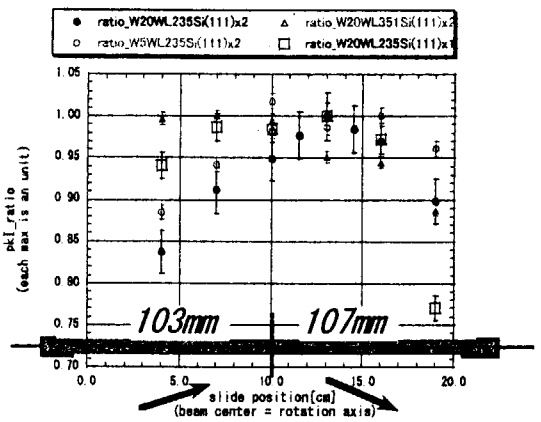


Fig.1. Intensity (reflectivity) difference depending upon the place which part of EBP-Si was irradiated by the incident beam.

原子炉:JRR-3M　　装置:TAS-2(T2-4)　　分野:装置

研究テーマ：偏極ｽｰﾊﾟｰﾐﾗｰの開発
表　題　：多層膜ﾐﾗｰの非鏡面反射に関する開発

1-8-3 Off-specular reflection from Ni/Ti multilayers

Kazuhiko Soyama[1] and Cao Bin[1,2]

[1]Japan Atomic Energy Researeh Institute, Tokai, Naka, Ibaraki 319-1195
[2] Kyushu University, Hakozaki, Higashi, Fukuoka 812-8581

Multilayer mirrors of Ni/Ti with periodical d-spacing in nanometer range, may be utilized for neutron focussing and imaging devices. However, due to the interface roughness of Ni/Ti multilayers, vertical correlation give rise to off-specular (diffuse) scattering which leads to decreasing the resolution of these optical devices. For evaluating and reducing diffuse scattering in a roughness interface, theoretical and experimental study has been started.

Rocking scan was conducted to investigate the specular and off-specular reflections. In the rocking curve geometry, incidence angle and observation angle holds $a_i + a_f = 2\theta$ and the angle of sample which is given by $(a_f - a_i) / 2$ is varied. This type of scan profiles angular distributions of the scattered neutron in a perpendicular to the surface normal. Such a scan allows one to separate out the value of the true specular reflection which appears as an instrument-limited pike above a slowly varying diffuse background.

Rocking curves of Ni/Ti multilayer with d=100 Å and 20bi-layers were measured at small 2θ angles. The sample was deposited using an ion beam sputtering system on Si(111) substrates of 100mm x 100mm with a surface roughness of 3Årms. The base pressure during the operation was 1×10^{-7} Torr, and the sample was grown under an argon pressure of $1x10^{-3}$Torr. The measurements were carried on a reflectometer of the LTAS (C2-1) which was installed at a cold neutron beam line of JRR-3M.

Figure 1 shows the features at the rocking curves. A diffuse intensity above background scattering level is observed over the entire range of q available. The most prominent feature is directed along q_x at constant q_z corresponding to series of closely spaced rocking scan. At the smaller 2θ angle scan, rough interface causes Yoneda peaks to appear, where the incidence angle or exiting angle of neutron approaches the critical angle of the multilayer. It is observed by the intensity of the Yoneda peak varying with the q_z value. With increase the q_z value, the influence of dynamical effects on the transverse scans decrease, which is clearly shown by the small intensity of the Yoneda peaks.

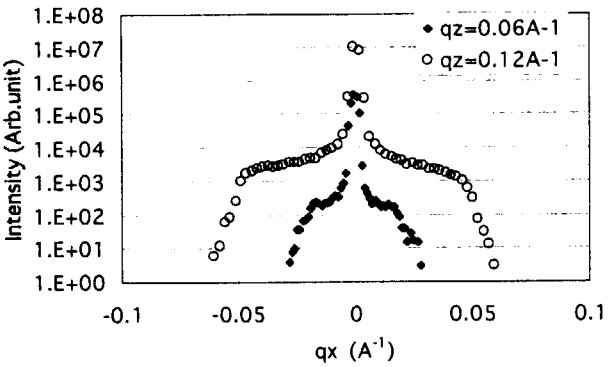


Fig.1 Rocking curve of Ni/Ti multilayer with d=100 Å and 20bi-layers for different qz values.

References

1) C. Bin, K. Soyama, ICANS-XV 2000, JAERI-Conf 2001-002, 592-599

原子炉：JRR-3M　　装置：LTAS(C2-1)　　分野：中性子散乱（装置）

研究テーマ：偏極ｽｰﾊﾟｰﾐﾗｰの開発
表　題　：ｲｵﾝﾎﾞﾘｯｼｭ法による高性能多層膜ﾐﾗｰの開発

1-8-4 Enhancement of reflectivity of small d-spacing multilayer mirrors by ion polishing in combination with ion beam sputtering

K. Soyama, W. Ishiyama[1] and K. Murakami[1]

Japan Atomic Energy Research Institute, Tokai, Naka, Ibaraki, 319-1195 JAPAN
[1]Nikon Corporation, Nishi-ohi, Shinagawa, Tokyo 140 JAPAN

One of the most important problems in producing the small *d*-spacing multilayers is the reduction of the interface roughness that becomes larger with the number of bilayers deposited. We have applied and succeeded in ion polishing in combination with ion beam sputtering deposition for fabricating very small d-spacing multilayers.

Ni/Ti and Ni/Mn multilayers were deposited and ion-polished using an ion beam sputtering system. The ion beam polishing was applied immediately after the deposition of each layer to smoothen the surface of layer. The dependencies of ion polishing time, ion acceleration energy and incidence angle on the interface roughness were firstly studied to optimize the conditions of Ar^+ ion polishing by using X-ray and neutron reflectometry. TEM observation was conducted on these multilayers. It was observed that the reflectivities and the evaluated interface roughnesses of Ni/Ti and Ni/Mn multilayers with d-spacings of 100 Å and 10 pairs were obviously improved by using ion polishing. In the case of ion-polished Ni layers, the evaluated interface roughness σ reaches a minimum value of 3.5 Å at an ion polishing time of 69 sec, ion acceleration energy of 100eV and incidence angle of 10° . On the other hand, a evaluated interface roughness is 7 Å rms in the case without ion polishing.

Smaller d-spacing multilayers were investigated. Ni/Ti and Ni/Mn multilayers with d = 20 ~ 30 Å and N = 50 ~ 300 pairs were deposited and ion-polished. The evaluated interface roughness of the multilayer with d = 31.8 Å and N = 50 pairs decreases to a minimum value of 4.4 Å rms treated by ion polishing. Furthermore, the interface roughness is kept to 4.3 Å rms in the case of d = 29.4 Å and N = 300 pairs. On the other hand, the interface roughness decreases to 8.2 Å r.m.s in case of d = 20 Å. It may be concluded that the intermixing of interface takes place by argon ion bombardment when the layer thickness is 20 Å and the critical boundary of layer thickness at which intermixing takes place may exist between the layer thickness of 20 Å and 26 Å. Finally we would like to discuss about the possibility of multilayer mirrors with d-spacing of less than 20 Å which may realize a normal incidence reflection device for cold neutrons.

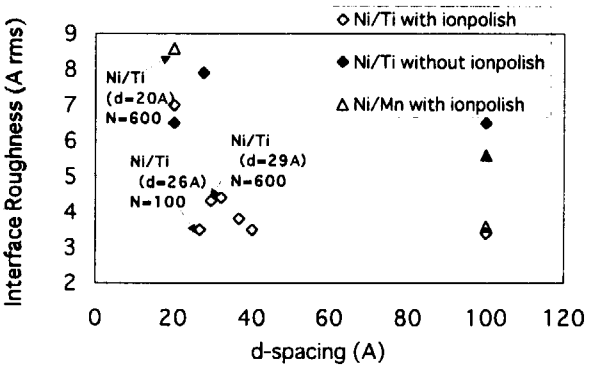


Figure1 Evaluated interface roughness of Ni/Ti and Ni/Mn multilayers with and without ion-polishing as a function of d-spacing.

Reference

1) K.Soyama, W.Ishiyama, K.Murakami, Journal of Physics and Chemistry of Solid, Vol.60 No.8-9 (1999) pp.1587-1590

原子炉：JRR-3M　　装置：LTAS(C2-1)　　分野：中性子散乱（装置）

研究テーマ：中性子スピンエコー分光器
表題：定常電流を用いたスピンフリッパーの開発

1-8-5 Development of spin flippers with steady current

T. Takeda, H. Seto, Y. Kawabata

Faculty of Integrated Arts and Sciences, Hiroshima University, Higashihiroshima 739-8521

New type π and π/2 flippers operated with steady current have been designed. The π flipper consists of a compact modified current sheet and Helmholtz coils. The current sheet produces magnetic fields $\boldsymbol{B}_S$ parallel to the sheet surface without magnetic fields perpendicular to the sheet surface at the surface of the sheet for the neutron beam cross section. The correction field from Helmholtz coils $\boldsymbol{B}_C$ cancel out the perpendicular component of the magnetic field from the precession coils $\boldsymbol{B}_0$ at the current sheet. As shown in Fig. 1, the direction of the magnetic field $\boldsymbol{B} = \boldsymbol{B}_S + \boldsymbol{B}_0 + \boldsymbol{B}_C$ in which neutrons travel rotates slowly and the neutron spin follows the change of $\boldsymbol{B}$ adiabatically outside the current sheet. Crossing the current sheet, the direction of $\boldsymbol{B}$ reverses suddenly without the change in the neutron spin direction. As a result, the above coil system operates as a π flipper without tuning independently of the neutron wavelength. The π/2 flipper consists of a rectangular coil and Helmholtz coils as shown in Fig. 2. The rectangular coil produces magnetic fields $\boldsymbol{B}_r$ perpendicular to the magnetic field from the precession coils $\boldsymbol{B}_0$. The correction field from Helmholtz coils $\boldsymbol{B}_C$ cancel out $\boldsymbol{B}_0$ at the right-side current sheet of the rectangular coil. Crossing the current sheet, the direction of the magnetic field $\boldsymbol{B} = \boldsymbol{B}_r + \boldsymbol{B}_0 + \boldsymbol{B}_C$ turns by π/2 suddenly without the change in the neutron spin direction. As a result, this coil system operates as a π/2 flipper without tuning independently of the neutron wavelength.

A performance test of the new-type π flipper with compact modified current sheet was carried out using ISSP-NSE at JAERI, Tokai Japan. Neutrons with the wavelength λ=7.14 Å (FWHM of its resolution $\Delta\lambda/\lambda$ = 18%) were used. The Mezei-type π flipper was replaced with a new-type one. The current sheet was wound with an Al-conductor wire of 1 mm in diameter and the current density per 1 mm width of the sheet is the followings;
i) I (A/mm) for $-25 \le z \le 25$ (mm),
ii) $2I$ (A/mm) for $-50 \le z \le -25$ (mm) and $25 \le z \le 50$ (mm),
iii) $3I$ (A/mm) for $-75 \le z \le -50$ (mm) and $50 \le z \le 75$ (mm),
iv) $-6I$ (A/mm) for $-100 \le z \le -75$ (mm) and $75 \le z \le 100$ (mm),
where I is current of the Al-conductor wire.
The performance of the new type π flipper was comparable to that of the Mezei-type.

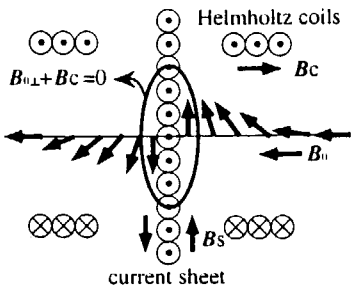


Fig. 1. Direction of the magnetic field $\boldsymbol{B} = \boldsymbol{B}_S + \boldsymbol{B}_0 + \boldsymbol{B}_C$ in the π flipper with a modified current sheet and Helmholtz coils.

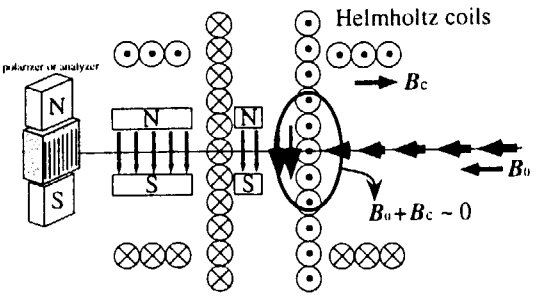


Fig. 2. Direction of the magnetic field $\boldsymbol{B} = \boldsymbol{B}_r + \boldsymbol{B}_0 + \boldsymbol{B}_C$ in the π/2 flipper with a rectangular coil and Helmholtz coils.

JRR-3M, C2-2 (NSE), Instrumentations

研究テーマ：耐放射線性カーボン基盤スーパーミラーの開発
表題：ＶＣＮ導出用研磨グラスカーボン中性子鏡の開発

1-8-6 Development of Polished Glassy Carbon Mirror for VCN Extraction

Y. Kawabata[1], M.Hino[1], H.Unesaki[1], S. Tasaki[1], M.Suzuki[2] and A.Wakata[3]

[1] Research Reactor Institute, Kyoto University, Kumatori, Osaka 590-0494, Japan
[2] Japan Atomic Energy Research Institute, Tokai-mura, Naka-gun, Ibaraki 319-1195, Japan
[3] Gunma R&D Center, Mitsubishi Pencil Co., Tateishi, Fujioka, Gunma 375-8501, Japan

To extract very low energy neutrons, i.e. very cold neutron(VCN) and ultracold neutron(UCN), the neutron mirrors have to be placed into the high irradiation field and the mirrors are exposured with the high irradiation dose and heat cycle. Replica-mirrors have been developed but they easily warp and are very difficult to handle due to the thin thickness. In case of installing a neutron guide tube near to a reactor core, effects of the installing should be as small as possible. To cope with these requirements, we have developed a polished carbon mirror as a new substrate for VCN guide tube.

Carbon plates are baked in an atmosphere of nitrogen to be glassy carbon. The grain size is less than about 5nm. The sample size is 77mm ϕ and 0.8mm thick. The surfaces are polished mechanically by abrasive grains of tiny diamonds in three stages. The sizes of grains in each stage are 2, 0.5 and 0.1 μ m. The surface roughness is very small and parameters are PV = 7.7- 12.5 nm, Ra = 0.62- 0.81 nm, Rq(rms) = 0.78-1.03 nm.

The neutron reflectivity of a caron mirror is measured by the neutron reflectometer at C3-1-2 in JRR-3M. The reflectivity is 0.998±0.004 in the total reflection range (90 - 145 nm) and the critical wavelength is 79 nm. It also corresponds to the potential of 130neV and the carbon density of 1.50 g/cm^3. This density is exactly same with the measured value of this carbon mirror. The high reflectivity shows that this carbon mirror has a good performance as the neutron mirror.

The increase of the beam divergence by the reflection on the carbon mirror is 1.4×10^{-4} rad. This angle is much smaller than the critical angle of the neutron with the wavelength of 0.1nm. It shows the beam spread by the reflection is small enough to be used for thermal neutrons.

Carbon mirror has the irradiation resistance, since it is made of the pure carbon which has small neutron absorption cross section.

JRR-3M, MINE, Instrumentation

A carbon neutron guide tube will be able to be inserted into the reflector region of the reactor core or the accelerator target area. A void in the reflector area will be minimized, because the vacancy will be limited only to the beam extraction size. It also could be minimize the disturbance of the neutron flux distribution.

The main characteristics of carbon mirrors reported in this paper are summarized as follows. 1) They have good surface roughness and neutron reflectivity. 2) They have very good flatness and are hard to bend. This shows the effectiveness for cold and thermal neutrons. 3) Fermi pseudo-potential of carbon for the neutron reflection is high. 4) Carbon has small neutron absorption cross section and the irradiation resistance for fast neutrons and γ ays. 5) Carbon is quite reliable to be used in the core area because of the full experience as reflectors in nuclear reactors.

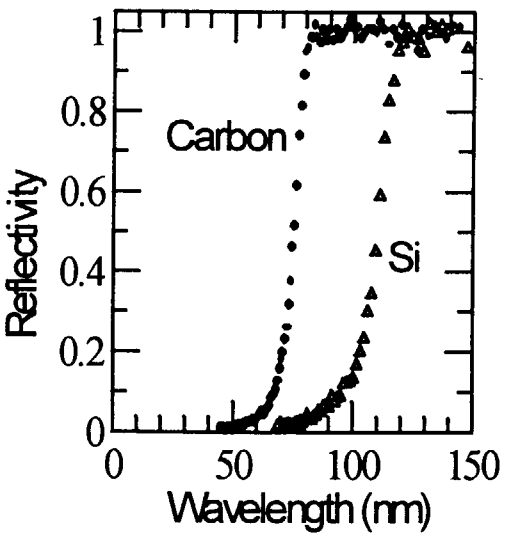


Fig.1. Measured neutron reflectivities of a polished carbon mirror and Si wafer

研究課題: 多層膜スピンスプリッターを用いた中性子スピンエコー分光器の開発
表題: 多層膜スピンスプリッターを用いた中性子スピンエコー分光器の開発

1-8-7

Development of a new spin echo spectrometer using multilayer spin splitters.

S.Tasaki, T.Ebisawa, M.Hino, R.Maruyama, N.Achiwa, D.Yamazaki[1], T.Kawai *Research Reactor Institute Kyoto University*
[1] *Faculty of Science Kyushu University*

The multilayer spin splitter (MSS) is a device, which consists of a magnetic mirror, a gap layer and a non-magnetic mirror. If a Larmor precessing neutron (superposing state of magnetic-parallel and antiparallel spin component) is incident to a MSS, phase difference between the two components proportional to the gap layer thickness is introduced. Such phase difference is equivalent to Larmor precession angle in a magnetic field.

It is expected that if the precession magnets in neutron spin echo (NSE) spectrometer are replaced by sets of MSS's then the spin echo machine will be much smaller than the conventional NSE spectrometers, and it has the possibility of improving the energy resolution of the NSE spectrometer.

The main problems of MSS is the thickness and uniformity of the gap layer. The thickness determines the energy resolution of the spectrometer, and is preferable to be greater than several μm. The uniformity of the gap layer, on the other hand, determines the polarization of the NSE signal, and is preferable to be less than several tens angstroms.

In the present study, we fabricated four MSS's with vacuum evaporation.[1] As non magnetic mirrors, we adopt Ni/Ti multilayer of 180Å-*d*-spacing with number of bilayers of 30. The gap layer is made from Ti with about 10000Å-thickness. For magnetic mirrors, permalloy (PA) and Ge multilayer is adopted with 180Å-*d*-spacing and number of bilayers of 30. The magnetic mirrors are evaporated under 150 Gauss magnetic field in order to be magnetically saturated in less than 10 Gauss. [2]

The check of the gap layer is performed with the arrangement shown in Fig.1. In this set-up, we first measure the NSE signal. Comparing to the NSE signal without MSS's, the polarization reduction of the NSE signal gives uniformity of the gap layer thickness. An example of the comparison is shown in Fig.2. The polarization without MSS is equal to 0.77 and that with MSS's is 0.18, which means the polarization reduction is about 0.48 for each reflection by MSS. This reduction indicates that the uniformity of the gap layer is 66.2Å for each MSS. It is desired that the uniformity should be less than 50Å, to keep the polarization reduction greater than 0.7.

To evaluate the gap layer thickness, shift of the NSE signal is observed by changing the angle of the second MSS. The angle change is the order of 0.002degree, and the shift is 1/10 of the period. From the measurements, the thickness of the gap layer is obtained as about 9000Å, for these MSS's.

In the next step of this study, we will make more uniform gap layer with a help of some polishing technique, and mirrors will be changed to have wider band width.

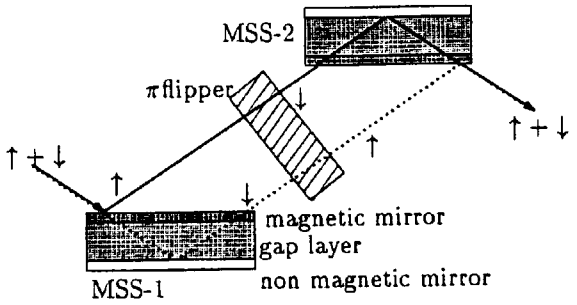


Fig.1 Arrangement for MSS test experiment.

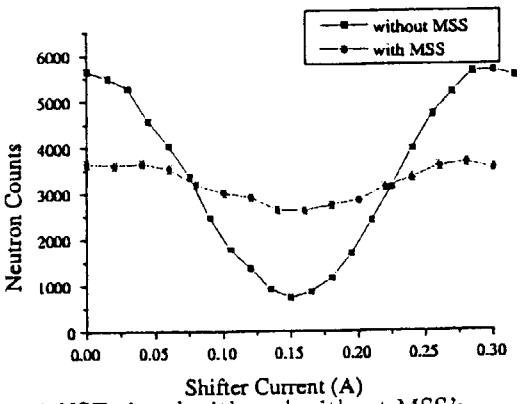


Fig.2 NSE signal with and without MSS's.

References

[1] S.Tasaki, T.Ebisawa, T.Akiyoshi, T.Kawai, and S.Okamoto, *Nucl. Inst. Meth. Phys. Res.*, A355 (1995) 501

[2] T.Kawai, T.Ebisawa, S.Tasaki, Y.Eguchi, M.Hino and N.Achiwa, J. Neutron Research, 5 (1997) 123.

研究テーマ：冷中性子磁気光学系の基礎研究

表　題　　：波長変換ファイバーと中性子シンチレーターを用いた二次元検出器の開発

1-8-8

Development of 2-dimensional imaging detector based on neutron scintillator with wavelength shifting fibers

K. Sakai[1,6], T. Adachi[1], T. Oku[1], A. Gorin[2], T. Ino[3], K. Kuroda[4], I. Manuilov[2], K. Morimoto[1], A. Ryazantsev[2], H.M. Shimizu[1], J. Suzuki[5], and F. Tokanai[1]

[1]*RIKEN(The Institute of Physical and Chemical Research), Wako, Saitama, 351-0198, Japan*
[2]*Institute for High Energy Physics, Protvino, Moscow region, Russia*
[3]*KEK (High Energy Accelerator Research Organization), Tukuba, Ibaraki,305, Japan*
[4]*Advanced Research Inst. for Science and Engi., Waseda University, Tokyo,169-8555, Japan*
[5]*Japan Atomic Energy Institute, Tokai, Ibaraki 319-1195, Japan*
[6]*Department of Physics, Tokyo Institute of Technology, Meguro-ku, Tokyo 152-8551, Japan*

For evaluating neutron optical devices, a neutron detector having a 2-dimensional (2D) imaging capability with a good spatial and temporal resolution is desired. A detector based on neutron scintillator with wavelength shifting (WLS) fibers provides a great advantage in such requirements. The paper reports the development of the detector based on scintillator at RIKEN

In Fig. 1, the detector consists of a neutron scintillator plate for producing charged particles and emitting the scintillation light, and two WLS fiber arrays for transmitting the light to photo-multiplier (MAPMT). As neutron scintillator, a ZnS and ^{6}Li glass with the sensitive area of 50×50 mm^2 were used. Each fiber array optically coupled onto the upper or lower sides of the scintillator consists of 100 fibers with the cross section of 0.5×0.5 mm^2, where every ten fibers at one end of the array was bundled as a belt, and every tenth fiber at the other end was picked up as a stripe to reduce output terminals of signal. As the preliminary result of the feasibility test of the 2D detector with cold neutron beam at the C3-2 beam line of JRR-3M at JAERI, the typical spatial resolution δ≈1.0mm have been obtained. At the present, the study on the detection efficiency and stability of the detector is in progress.

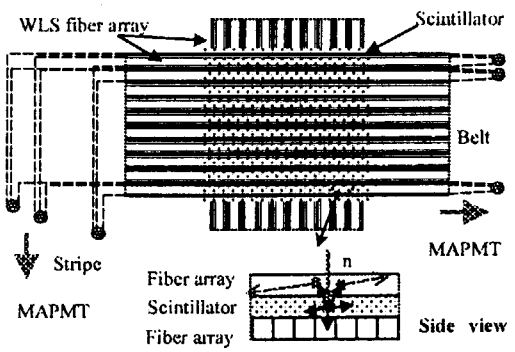


Fig.1 2D detector based on scintillator with WLS fibers

原子炉：JRR-3M　　装置：SANS-J (C3-2)　　分野：中性子散乱（装置）

研究テーマ：パルス中性子イメージング検出法の研究
表　　題：中性子イメージング用 $SrBPO_5:Eu^{2+}$蛍光体

1-8-9 A $SrBPO_5:Eu^{2+}$ phosphor for neutron imaging

K. Sakasai, M. Katagiri, K.Toh, H. Takahashi[1], M. Nakazawa[1], and Y. Kondo[2]

Advanced Science Research Center, Japan Atomic Energy Research Institute, Ibaraki 319-1195, Japan
[1]Dept. of Quantum Science and System Engineering, University of Tokyo, Tokyo 113-8656, Japan
[2]School of Engineering, Dept. of Applied Physics, Tohoku University, Sendai 980-8579, Japan

The neutron imaging plate (NIP) is one of the most promising alternatives to conventional position sensitive neutron detectors (PSNDs). Although the NIP has made a great success in the field of neutron scattering study[1)], there is a disadvantage when the NIP is used for neutron detection in a field where both neutron and gamma ray exist. Since the NIP is sensitive to not only neutron but also gamma ray, it is difficult to discriminate neutron signal from gamma ray one when the NIP is read out. To overcome the problem, the authors have studied a $SrBPO_5:Eu^{2+}$ material as a new neutron storage phosphor consisting of light materials.

The $SrBPO_5:Eu^{2+}$ powder sample was prepared by firing raw materials ($SrCO_3$, H_3BO_3, $(NH_4)_2HPO_3$, and $EuCl_3 \cdot 6H_2O$) in a muffle furnace in a nitrogen atmosphere with a computer-controlled heating schedule at 600°C for 2 hours and at 800°C for 2 hours[2)]. The authors found that this phosphor shows photostimulated luminescence (PSL) at 390 nm by illumination of 635 nm laser light after neutron irradiation without adding any neutron sensitive materials such as Gd.

Figure 1 shows total PSL output per unit neutron fluence as a function of neutron energy, where results of a sample using enriched boron (enrichment: 96%) are also shown. The neutron irradiation was conducted at SANS-J of JRR-3M. As seen in the figure, the PSL output was increased by using enriched boron instead of natural boron. One can also see that the PSL intensity in both samples is proportional to $E^{-0.5}$, where E is neutron energy. This is a rigid evidence that the samples is sensitive to neutron and the PSL output is proportional to amounts of a nuclear reaction of ^{10}B atoms with neutrons because the neutron cross section of $^{10}B(n,\alpha)Li$ is proportional to $E^{-0.5}$. The $SrBPO_5:Eu^{2+}$ phosphor will be a candidate for a new NIP.

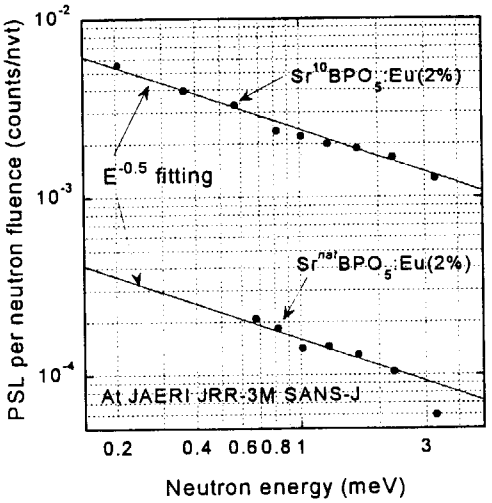


Fig.1 The total PSL output per unit neutron fluence as a function of neutron energy, where results of a sample using enriched boron (enrichment: 96%) are also shown.

References

1) Y. Karasawa et al., Phsica B **213**, 978 (1995)
2) A. Karthiikeyani and R. Jagannathan, J. Lumin., **86**, 79 (2000)

原子炉：JRR-3M　　装置：SANS-J(C3-2)　　分野：中性子散乱（装置）

This is a blank page.

1. 中性子散乱 9) その他

1. Neutron Scattering 9) Others

This is a blank page.

研究テーマ: ペロブスカイト型Mn酸化物における軌道秩序
表題: $Pr_{0.5}Ca_{0.5}MnO_3$における軌道秩序の整合-非整合転移

1-9-1 Commensurate-incommensurate transition in the melting process of orbital ordering in $Pr_{0.5}Ca_{0.5}MnO_3$

R. Kajimoto,[1] H. Yoshizawa,[2] Y. Tomioka,[3] Y. Tokura[3,4]

[1]*Department of Physics, Ochanomizu University, Bunkyo-ku, Tokyo 112-8610, Japan*
[2]*Neutron Scattering Laboratory, I. S. S. P., University of Tokyo, Tokai, Ibaraki, 319-1106, Japan*
[3]*Joint Research Center for Atom Technology (JRCAT), Tsukuba, Ibaraki 305-8562, Japan*
[4]*Department of Applied Physics, University of Tokyo, Bunkyo-ku, Tokyo 113-8656, Japan*

$Pr_{0.5}Ca_{0.5}MnO_3$ is one of the manganites that exhibit the colossal magnetoresistance (CMR) effect and a typical material which shows a so-called "CE-type" charge/orbital/spin ordering. We have studied the melting process of the orbital order in $Pr_{0.5}Ca_{0.5}MnO_3$ single crystal in detail as a function of temperature by neutron diffraction.

In the figure are plotted the T dependences of the order parameter of the orbital ordering observed around Q = (2, −0.5, 0) (a), the orbital order wave vector q_{OO} = (0, δ, 0), and the width (FWHM) of (2, −0.5, 0) orbital order peak (b) with elevating T. We also depicted the T dependences of the scattering vector of the (2, 0, 0) fundamental reflection (c) and the resistivity (d). From the data, the following intriguing picture emerges for the melting process of the orbital ordering in $Pr_{0.5}Ca_{0.5}MnO_3$. The melting process consists of three stages. First of all, the C-IC transition of the orbital ordering begins at T_{C-IC} ~ 215 K [Fig. (b)]. In a very early stage of the C-IC transition, the wave vector is still almost commensurate, but its width increases [Fig. (b)], indicating that the commensurate and nearly-commensurate orbital orders are mixed in the system. In the second stage of the transition, the incommensurability varies quickly, although the width recovers the low T value [Fig. (b)]. The decrease of the superlattice intensity above T_{C-IC} [Fig. (a)] indicates that the number of the orbital-disordered Mn^{3+} ions rapidly increases in the system. In the third stage above $T_{CO/OO}$, the charge ordering and quasi-long-range orbital ordering is destroyed, and their correlation lengths rapidly decrease.

Interestingly, the incommensurate melting of the orbital order induce the rearrangement of the lattice structure [Fig. (c)] and the steep decrease of the resistivity [Fig. (d)] due to partial disordering of the orbital order. This fact is important to understand the nature of manganites, because the CMR effect and accompanied anomalies in the physical properties in manganites have been believed to be induced by the melting of the charge ordering. By careful examination of the melting process of the orbital ordering, however, we succeeded in establishing that the anomalies in the structural, transport and magnetic properties are caused by the change of the orbital order rather than the charge order. The present results indicate that the importance of distinguishing the gradual melting process of orbital ordering from the collapse of charge ordering.

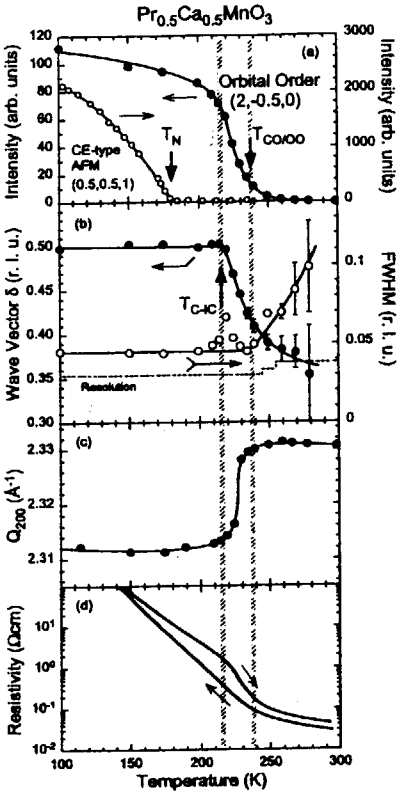


Figure: T dependences of (a) Integrated intensities for (2, −0.5, 0) orbital order peak (closed symbols) and (1/2, 1/2, 1) AFM peak (open symbols). (b) Orbital order wave vector q_{OO} = (0, δ, 0) (closed symbols) and width (FWHM) of (2, −0.5, 0) orbital order peak (open symbols). (c) Scattering vector of the (2, 0, 0) fundamental reflection. (d) Resistivity. In (b), the instrumental resolution is indicated as a dotted line.

JRR-3M, 4G, 9. Others

研究テーマ：リチウム２次電池正極活物質の構造解析
表題：リン酸オリビン $LiCoPO_4$ の構造と正極特性

1-9-2 Structure and Cathode Properties of Phospho-olivine $LiCoPO_4$ for Lithium Secondary Batteries

Shigeto OKADA, Shoichiro SAWA and Yasushi UEBO

Institute of Advanced Material Study, Kyushu University,

Kasuga Koen 6-1, Kasuga 816-8580 Japan

Introduction

In ordered-olivine cathodes with hexagonal closed-packed (hcp) oxygen array, $LiFePO_4$ [1] shows 160 mAh/g on the 3.3 V plateau and exceeds spinel $LiMn_2O_4$ in energy density. In contrast, the other ordered-olivine $LiCoPO_4$ [2] generates 4.8 V versus Li/Li^+ with a discharge capacity of 100 mAh/g after initial charging to 5.1 V and its energy density is comparable to that of layered rocksalt $LiCoO_2$.

Normal spinel $LiMnMO_4$ (M:Co [3], Cr [4]) and inverse spinel $LiNiVO_4$ [5] with 4.5 – 5 V plateau have been investigated as post 4 V cathodes. We anticipates that phospho-olivine $LiMPO_4$ with a theoretical capacity of 170 mAh/g would be a strong candidate for a new high-voltage cathode with superior capacity.
The structure of $LiCoPO_4$ was identify by Neutron diffraction and the cathode properties were revealed using coin cells.

Experimental

Conventional solid-state reactions were employed to synthesize the phospho-olivines. $LiCoPO_4$ were prepared from stoichiometric amounts of reactants Li_2CO_3, P_2O_5 and CoO. The mixtures were presintered at 500 °C for several hours. After firing at 780 – 820 °C for 2 days with an intermittent grinding, the mixtures were quenched using liquid nitrogen. Obtained powder was indexed as orthorhombic in the space group Pnma by XRD (Rigaku RINT2100HLR/PC), using monochromatized CuKα radiation. Neutron diffraction data were taken at powder diffractometer, HERMES [6], at JRR-3M reactor in Japan Atomic Energy Research Institute. The structural parameters were refined by Rietveld analysis using RIETAN 97β [7].

We fabricated the cathodes for electrochemical characterization by blending powders of the active material $LiMPO_4$ with acetylene black (Denki Kagaku Co., Ltd.) and F-210L PTFE Teflon binder (Daikin Industry Ltd.) in a weight ratio of 70 : 25: 5. We measured the cathode properties in a coin-type cell (type 2032 made from SUS316) with a nonaqueous electrolyte (1M $LiPF_6$/EC:DMC = 1 : 1 vol%, Tomiyama Pure Chemical Industries, Ltd.) and polypropylene separator (Celgard 3501) against a Li metal anode.

Results and discussion

Interatomic distances for $LiCoPO_4$ obtained

from Rietveld refinements of neutron diffraction are shown in Table 1 with reported data of $LiFePO_4$ by A.S. Andersson [8]. According to Shannon's ion radius in MO_6, M-O interatomic distances in Table 2 suggest both Co and Fe are 2+ high spin state in initial $LiMPO_4$ olivine matrix. Actually, J.O.Thomas group proved that Fe in $LiFePO_4$ is 2+ high spin state by ^{57}Fe Mössbauer spectroscopy.

Table 1. Average interatomic distances for $LiMPO_4$

Average interatomic distance [Å]	$LiCoPO_4$	$LiFePO_4$ [9]
P-O in PO_4 Tetrahedra	1.54	1.54
Li-O in LiO_6 Octahedra	2.14	2.15
M-O in MO_6 Octahedra	2.12	2.15

Table 2. Shannon's Ion radii in MO_6 Octahedra

6-fold coordinated ion radii [10]	Co^{2+}	Fe^{2+}
High Spin	2.15	2.18
Low Spin	2.05	2.01

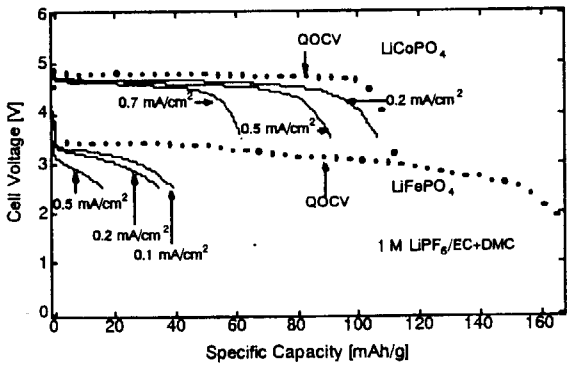


Fig.1 Rate capability of $LiCoPO_4$ and $LiFePO_4$.

The charge-discharge profiles of identified $LiCoPO_4$ and $LiFePO_4$ are shown in Fig.1. However $LiFePO_4$ shows lower discharge voltage than that of $LiCoPO_4$, the capacity of $LiFePO_4$ in the QOCV (quasi open circuit voltage) profile almost reached the theoretical value for 1 Li intercalation per mole of 170 mAh/g. We expect that there is considerable room for improvement up to the theoretical upper limit of about 167 mAh/g for isostructural $LiCoPO_4$, too.

References

1. A.K.Padhi, K.S.Nanjundaswamy and J.B. Goodenough, *J.Electrochem.Soc.*, 144, (1997) 1188.
2. S.Okada, H.Arai and J.Yamaki, *DENKI KAGAKU*, 65, (1997) 802.
3. H.Kawai, M.Nagata, H.Tsukamoto and A.R.West, *Electrochemi. and Solid-State Letters*, 1, No.5, 212(1998).
4. C.Sigala, A.Verbaere, J.L.Mansot, D.Guyomard, Y. Piffard, M.Tournoux, *J.Solid State Chem.*, 132, 372(1997).
5. G.Fey, W.Li and J.R.Dahn, *J. Electrochem.Soc.*, 141, (1994) 2279.
6. K.Ohoyama, T.Kanouchi, K.Nemoto, M.Ohashi, T. Kajitani and Y.Yamaguchi, *Jpn.J.Appl.Phys.*, 37, 3319(1998).
7. F.Izumi, in "The Rietveld Method" (R.A.Young, Ed.), Chap.13, Oxford Univ. Press, Oxford, (1993).
8. A.S.Andersson, Comprehensive Summaries of Uppsala Dissertations from Faculty of Science and Technology 532, (2000).
9. A.S.Andersson, B.Kalska, L.Häggström, and J.O. Thomas, *Solid State Ionics*, 130, 41(2000).
10. R.D.Shannon, *Acta Crystallogr.*, A32, 751(1976).

研究テーマ：超低温の導入による中性子散乱の研究
表題　　：加工により材料に導入される内部応力の中性子回折測定

1-9-3
Neutron Diffraction Study of Internal Stress Induced by Machining on a Material

Y. Tsuchiya*, K. Kikuchi[1], T. Kato[2], H. Nakajima[2], H. Tsuji[2], N. Minakawa[3] and Y. Morii[3]

Faculty of System Engineering, Shibaura Institute of Technology, Saitama 330-8570 Japan
[1]Center for Neutron Science, JAERI, Ibaraki 319-1195 Japan
[2]Naka Fusion Research Establishment, JAERI, Ibaraki 311-0193 Japan
[3]Advanced Science Research Center, JAERI, Ibaraki 319-1195 Japan

A machining induces an internal stress to a material. And the induced stress affects distribution of residual stress. In this study, the induced internal stress by machining was evaluated using neutron diffraction measurement for a conduit material. The result was compared with an estimated value by finite element method (FEM) calculation. The neutron diffraction measurements were performed by neutron diffractometer for the residual stress analysis, RESA, installed at the research reactor JRR-3M guide hall. The wavelength of the incident neutron beam used was 2.07 - 2.08 Å. The reflection of (111) plane was used for the measurement. The data acquisition time was set 2 to 8 hours for a spectrum. The sample is a round-hollowed conduit of INCOLOY908 alloy that shows fcc single phase. The young's modulus of (111) plane was 195 GPa. The conduit has a square cross section of 46 × 46 mm^2 and an inner diameter of 37 mm. An estimation of the induced internal stress by a bending was observed comparing before and after bending conduit. The arc of bent conduit had 500 mm radius. A sampling volume was adjusted for the size of 2 × 2 × 4 mm^3 by the cadmium slits and located at every 1 mm in depth from the outer surface of the sample to the radial direction. The thickness of the measurement region was about 4.5 mm. The code of ABAQUS/Explicit was applied for the FEM calculation.

The internal stresses were measured for the bent and straight conduit individually. Difference of inner stress between bent and straight conduit shows the induced stress to the conduit by bending. Subtractions of internal stress of bent conduit from that of before bending conduit were shown for an axial direction in fig.1. It was found that the compressive stress induced near the outer surface while the tensile stress generated by the bending machining. Measured and calculated stresses showed the same tendency for each other. In the practical material such as the presented bent conduit, it was shown that the affected strain or stress could be estimated by a use of the neutron diffraction together with the FEM calculation.

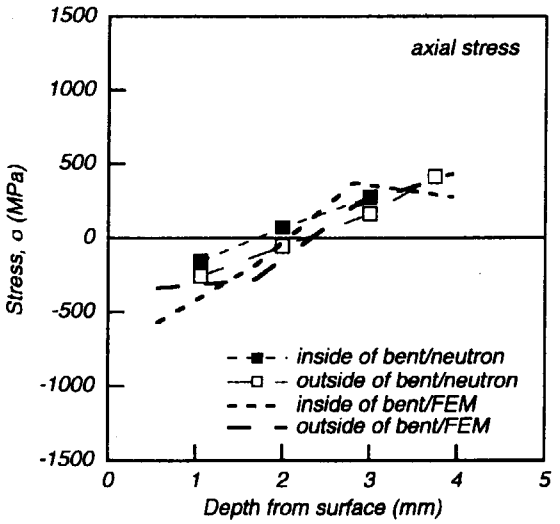


Fig.1 Spatial distributions of the induced stress on the conduit material by bending.

原子炉：JRR-3M　　装置：RESA(T2-1)　　分野：その他

1-9-4

中性子寿命の精密測定

Precision Measurement of the Neutron Lifetime

真木 晶弘
MAKI, Akihiro
高エネルギー加速器研究機構
High Energy Accelerator Research Institute

§1 はしがき

"中性子寿命の精密測定"の研究は，高エネルギー加速器研究機構、佐賀大学，筑波大学，東京家政大学，新潟大学の共同チームによって行われた．チームの構成員は表1に示された通りである。

また，研究経費は平成10年度から12年度の科学研究費補助金（基盤研究（B）（1））を主な財源とし，各参加機関の校費および職員旅費と原研施設利用共同研究旅費によってまかなわれた．

本研究に関する研究発表は表2に与えられている．

§2 研究の目的と意義

1．研究の目的

我々は中性子寿命（τ_nと略す）の値を 0.1%の精度で測定することを目的としている。このため我々は冷中性子ビームを用いた"考え得る限り簡単な実験方法"を世界にさきがけて独自に考案した。この新しい方法によると、従来のビーム法による中性子寿命測定実験における最大の系統誤差の原因であった崩壊体積及びβ線検出の立体角の評価が全く不要となるので、上述の 0.1%の精度で中性子寿命を測定できると考えている。これによって中性子寿命測定の決定版をつくるとともに，併せて世界各地で盛んに行われている超冷中性子貯蔵法による中性子寿命の値のチェックも行う。

2．学術的な特色・独創的な点及び予想される結果と意義

現在の中性子寿命の測定値をみると、約1%程度の不一致が見られる。このことは各測定において系統誤差が正当に評価されていない結果と考えられる。一般に系統誤差の評価は統計誤差に比べて難しく、測定配置や実験操作が複雑になるほど困難となると考えられる。そこで我々は考えられる限り簡単化した冷中性子ビーム法による中性子寿命測定実験を考案した。

即ち、冷中性子ビームを真空槽中を走らせ、プラスチックシンチレーションカウンター系でビームを取り囲む。この真空槽中に ^{3}He ガスを少量（10^{-5}–10^{-4}Torr）入れておく。そしてプラスチックシンチレーションカウンターによって、中性子崩壊からのβ線と ^{3}He(n,p)^{3}H 反応からの陽子を同時に測定する（β線と陽子を区別する方法については、研究計画・方法の項を参照されたい）。このとき中性子の平均寿命τ_nは次の(1)式で与えられる；

$$\tau_n = \frac{N_p \cdot \varepsilon_\beta}{N_\beta \cdot \varepsilon_p} \cdot \frac{1}{\rho \sigma_0 v_0} \qquad (1)$$

ここで N_β、N_p はそれぞれ中性子崩壊によるβ線並びに上述核反応による陽子の計数積分値、ε_β、ε_pはそれぞれβ線並びに陽子の検出効率；ρは1cm^{3}中の ^{3}He 原子（分子）の数、σ_0は速さv_0の中性子に対する ^{3}He(n,p)^{3}H 反応の断面積（これは 1/v 則に従うことが知られているので$\sigma_0 v_0$は定数）である。(1)式にはβ線並びに陽子に対するカウンターの立体角が入っていない。このことは我々の測定配置にお

いては(1)式の分子、分母で相殺するからである。即ち検出立体角を評価する必要がない。この点が我々の測定配置の大きな利点であり、優れた特色といえる。従来ビーム法による中性子寿命の測定における最大の系統誤差の原因であったβ線検出立体角及び崩壊体積の評価が全く不要となった。このことはこの研究の独創的な点であり、大きな進歩と考える。

又，(1)式には中性子の速度 v も現れない．これは，$^{3}He(n,p)^{3}H$ 反応の断面積が 1/v 則に従うため，中性子の測定系内における滞在時間 1/v と相殺するためである．すなわち，本測定方法によれば，中性子ビームのエネルギー分布（速度分布）を知る必要がないということである．このことも，測定精度を高めることに寄与している．

従来のビーム法においては、中性子束の強度の測定の際、$^{3}He(n,p)^{3}H$ 反応からの陽子の検出には比例計数管やドリフト・チェンバー、MWPC などを用いているが、いづれの場合でも一1 気圧のカウンターガスを使用しているため中性子によるバックグラウンドが増える。我々の場合はカウンターガスを一切用いていないので、その心配がない。更に又、我々の実験配置では磁場を用いていないのも特色の一つである。以上述べた特色ある実験によって、0.1%の測定精度で中性子寿命を測ることができれば、素粒子物理学・宇宙物理学におけるその意義は誠に大きいと考える。

例えば宇宙物理学においては、ビッグバン直後における核子合成（Big Bang Nucleosynthesis, BBN）の理論計算が最近精密化されて 0.1%以下の精度となった(R.E.Lopez and M.S.Turner, Phys. Rev. D59(1999)103502-1)。この精度においては原始の ^{4}He 存在比の不定性は主として中性子寿命の実験誤差に因るものとなる由である。世界的に見た τ_n の現在の実験精度は一0.2%であるから、これを更に小さくする必要がある。我々の τ_n 値測定の目標精度 0.1%はこの点からも意義あるものと考えられる。

3. 国内外の関連する研究の中での位置

現在国外ではフランスのグルノーブル，アメリカの NIST，それにロシアの研究所などにおいて超冷中性子や極冷中性子の貯蔵法によって中性子寿命の測定が盛んに行われている。国外におけるビーム法の測定実験は現在のところやられているとの情報はない。

Particle Data Group による 2000 年版の Review of Particle Properties (Eur. Phys. J. C15(2000)1)において中性子寿命のデータとして採用されている10ヶの測定実験（ビーム法によるもの5ヶ、及び貯蔵法によるもの5ヶ）の各々についてのやや詳しい解説については表 2.(1)の 3 の文献を参照されたい。

国内においても京大原子炉実験所や日本原子力研究所において京大原子炉実験所、東北学院大学の研究者が超冷中性子貯蔵法で中性子寿命の測定を計画しているがビーム法による測定計画は我々以外には皆無である。我々は冷中性子ビームを用いて今までなされた、どの実験に比べても遙かに簡単な実験方法を考案した。その意味で、超冷中性子貯蔵法の全盛時代という世界の趨勢の中でユニークな特色ある研究と考えている。

§3. 研究計画の実施

1. 従来の研究経過・準備状況

中性子の寿命は物理学における重要な物理量の一つであることは多言を要しないであろう。この量は弱い相互作用におけるベクトル結合定数と軸性ベクトル結合定数とを決めるために極めて重要である。又、小林—益川マトリックスの C_1 (= cosθ; θは Cabibbo 角)とも密接に関連している。更に宇宙物理学における Big Bang 理論において原始のヘリウム生成量を算定するさい、大事な役割を担っている。更に又、太陽ニュートリノ問題とも上記の軸性ベクト

ル結合定数を通して緊密に関連している。

このような重要な物理量であるにも拘わらず10数年前までは世界の各測定値の間には大きな不一致(－7%)が存在するという好ましくない状況であった。その後世界各地において中性子寿命の研究が盛んに行われた。中性子ビームを用いる"ビーム法"においてはPulsed beamを用いるなど種々の新しい工夫がなされた。他方、極冷中性子や超冷中性子を磁場或いはボトルに閉じ込め、その中の中性子数の減少を測定して中性子寿命を求める"貯蔵法"が長足の進歩をとげた。これらによって10数年前の－7%にのぼる不一致は一応解消された。

2000年版のReview of Particle Properties by PDGをみると，中性子の平均寿命の世界的平均値は886.7±1.9秒である。この平均に用いられた10ヶのデータのうち、5ヶはビーム法を用いており、残りの5ヶは中性子貯蔵法によるものである。これらの測定値の間には上述のように以前ほどの不一致は見られないが、依然として－1%程度のばらつきがみられる。更に、最近は世界的にみて殆ど超冷中性子貯蔵法による中性子寿命測定実験のみが盛んに行われている状況である。これらの貯蔵法による実験を仔細に検討してみると、系統誤差の入る可能性を否定できない。そもそも系統誤差は実験操作が複雑になる程、増加する傾向があることは否めない事実である。

そこで我々は冷中性子ビームを用いる中性子寿命測定の実験において"考え得る限り簡単な実験"を考案した。これは従来のビーム法に伴っていた最大の欠点を全く除去した新しい測定方法に基づいている。この測定配置においては測定操作が簡単なため、格段に系統誤差を減らすことができると考えている。超冷中性子貯蔵法による中性子寿命測定の全盛時代に、敢えて冷中性子ビームによる"最も簡単な実験"を実現したいと考える所以はこれによって系統誤差を極力減らして－0.1 %の精度をもつ中性子寿命の測定を行い、中性子寿命の決定版をつくるとともに、上述の超冷中性子貯蔵法による測定値のチェックを行うためである。

2. 研究計画・方法

先ず研究目的で述べた我々の独自の測定方法に基づく中性子寿命測定装置について以下に説明する。測定装置の略図[横断面(ビーム方向)と縦断面(ビームに平行)]を図1に示す。

主装置は真空槽の中にβ線と陽子を測定するカウンター系を入れたもので、その中心に冷中性子ビームを通過させる。真空槽には 10^{-5}-10^{-1}Torr の圧力の^{3}Heガスを充填する。^{3}Heガスの圧力は高精度圧力測定装置によって測定する。各カウンターは78 x 500 x 6 mm3の板状プラスチックシンチレータから成り、その両端に光導管と光電子増倍管(PMT)がついている。このカウンター4枚を箱型にくんである．この同一のカウンター系によって中性子崩壊によるβ線と^{3}He(n,p)t 反応からの陽子とを識別する方法は次のようである。

1)先ず真空槽をターボ分子ポンプによって充分排気したのち、中性子ビームを通さない状態で測定を行い，環境バックグラウンドのエネルギースペクトルを決める．

2)次に，冷中性子ビームを走らせてカウンター系で中性子崩壊からのβ線を測定し、崩壊β線および冷中性子ビームに伴うバックグラウンドのスペクトルを決める．実際には，われわれはβ崩壊のエネルギースペクトルを知っているので，バックグラウンドに適当な関数を仮定して測定されたスペクトルをフィットすることにより，その形と相対量を決定する．

3)最後に真空槽中に適当量の^{3}Heガスを充填した後、冷中性子ビームを走らせてプラスチックカウンター系で測定する。ここでは，2)のスペクトルに単一エネルギーの陽子のシグナルがピーク(ガウス分布)として重なった分布が得られる．したがって，2)

までで得られた関数と，ガウス関数を用いてこのスペクトルをフィットすることにより，陽子および電子の相対比が求められる．

こうして得られた N_p/N_β を研究目的の項の(1)式に入れると，中性子の平均寿命 τ_n が求められるわけである。もちろん，$\varepsilon_\beta/\varepsilon_p$ の評価も必要になるが，本実験の測定器配置では，その主たる原因と考えられる電子の後方散乱に対しては囲われた配置になっているので，電子を逃す確率はカウンターの端部でのみ考慮が必要となり，結果的に小さな補正となる．

3. 研究計画の実施状況

(1)平成10年度

上述の測定方法を実現するための電子・陽子同時測定用カウンター系の設計のために次の予備実験を行った；

1. プラスチックシンチレータ中の光パルスの減衰長の測定をβ線源を用いて行った。結果は6mm厚さのシンチレーターに対して 60cm、これに 6mm 厚さのアクリルを裏打ちした時には 80cm となった。これによってカウンターの厚さを 6mm とし、これに6mm の厚さのアクリルを裏打ちすることとした。

2. 長さ 50cm のカウンターの両端へのパルスの到達時間差からβ線の入射位置を測定した。

3. 位置の情報と減衰長とを用いて各位置におけるパルス高の補正を行った、その結果両端からのパルスの和をとると、40cm の長さに亙つて補正したパルス高の変動は 2%以下となった。

4. コンピュータ・シミュレーションによってカウンターの厚さが 6mmと12mmとでβ線の検出効率に殆ど差がないことを確かめた。

上述の1－4の結果、カウンター系としては66mm(巾)×6mm(厚)×500mm(長)×4枚のプラスチック・シンチレータを四角形に組み、各シンチレータの両端に光導管と PMT をつける構造とした。β線の後方散乱についてはその角分布を測定し，後方散乱は数%以内であることを確認した。カウンター系のすぐ外側にアンタイ・カウンター系を配置し、これらを内蔵する真空槽及び高真空排気系その他を具備した中性子寿命測定装置一式を製作完成し、KEK に納入された。

(2)平成11年度

11年度は先づ中性子寿命測定装置の中に、電子陽子同時測定用プラスチックカウンター(主カウンター系)及びアンタイ(ベト)カウンターを組み込み、種々の予備テストの後、JRR-3M 原子炉の C2-3 ビームポートに設置し、冷中性子ビームを用いて6月28日から7月30日までの約4週間最初の実験を行った。実験に際しては CAMAC を用いたデータ収集系によってすべてのカウンターの光量とタイミングのデータを記録した。今までのデータ解析によって判ったことは次のようである．

1. $^3He(n,p)^3H$ 反応による陽子ピーク　先づ光電子増倍管のゲインの調整を陽子ピークを用いて行った。次にベト・カウンター系をも併用して宇宙線事象の中、主カウンター系をほぼ鉛直に貫くものを選び出しエネルギースケールを決めた。これによって上記の陽子ピークのエネルギーは電子に換算して 93keV となった。これは既存の半実験的理論式と良く一致している。

2. 中性子ビームの強度　検出された陽子の数と ^3He ガスの圧力とから、冷中性子ビームの強度を見積もった所、大約予想値と一致した。これらの事柄から我々の提案している本測定方法が中性子寿命の精密測定に適している事が確信出来た。しかし乍ら、今回の実験においてはバックグラウンドが未だ多い。このバックグラウンドは(n, γ)によるγ線や散乱中性子によるものと考えられるが、我々は GEANT によるシミュレーションでその場所をつきとめると共に、これに基づきバックグラウンドの少ない測定配置にするため、主カウンター系、及びスリット系などを改造することとした。

(3)平成12年度

1. 平成12年度では先ず11年度の経験とシミュレーションを参考にして、入射中性子ビームに伴うバックグラウンド[(n,n)からのn及び(n, γ)からのγ線]を減らすための改造を行った。(1)カウンターに裏打ちしていたアクリル板を外し，カウンターのサイズを78x500x6と拡張する．(2)四角形に組んだ主シンチレーションカウンターの両端面に、Heavy metal (W が主成分)製のγ線シールド(マウス・ビースと呼んでいる)を設けた。マウス・ビースの中性子ビームに平行な面及び直角な面には ^{6}LiF-テフロン板を貼った。(3) 主真空槽の上流側の真空パイプの長さを、約2倍の 2.7m とし、その内部に3個の中性子コリメータ(^{6}LiF-テフロン板を鉛ブロックで裏打ちしたもの)を分散させて置いた。

2. 平成11年度の実験において、主真空槽と排気系とを仕切るディスク・バルブに ^{3}He ガスのリークがあることが判ったので、従来のものを全金属製ディスク・バルブに取り替えた。又、対流のない真空中で加熱の心配のあった光電子増倍管の電圧分割器の電流を約 1/10 に下げるよう改造した。

3. 我々の中性子寿命測定の精度の目標は～0.1%であるから、主真空槽内に入れる ^{3}He ガスの圧力を 0.1%以下の精度で測定する必要がある。一般には真空の圧力を上記の精度で直接測定する方法はない．10^{-5}-10^{-1} torr の圧力を上述のような精度で測るために我々は次に述べる希釈法による圧力測定法を開発した：小容積に、ある圧力で存在するガスを、高真空に保った大容積の中へ放出するとき生ずる圧力の変化(圧力比)を測定することによって、この2つの容積の体積比を測ることができる。体積比の測定においては、10^{-1}Torr よりずっと高い圧力領域(格段に高い精度の圧力測定が可能)において行った．この測定には半導体を用いたストレイン・ゲージ型圧力計(Druck 社製)を用いた．小容積中の ^{3}He ガスの圧力を精度良く測定した後，τ_n 測定装置本体にガスを拡散させる．上で求めた体積比を使ってτ_n測定装置本体の中の ^{3}He の圧力を充分の精度で推定することができる。われわれは既に希釈法による圧力測定法を確立した。

4. 我々は昨年度と同じく、JRR-3M 原子炉の C2-3 ビームポートに、上述の 1.～3.の改造を施した中性子寿命測定装置を設置してτ_n測定の実験を行った。

§4. 結果とその評価

平成13年2月に行った測定はまだ解析中であるが，図2に示す様に陽子とβ線の信号を確認することに成功している．^{3}He(n,p)^{3}H 反応からの陽子の計数値を用いて，中性子ビームの強度と崩壊β線の計数値を算定した結果大略予想値と一致した．これらのことからわれわれの考案した本測定方法は中性子寿命の精密測定に非常に適していることが判明した．

ただ，この段階では，環境バックグラウンド，ビームに伴うバックグラウンド共に高く，これを軽減させる措置が必要である．しかし、今回のビームに伴うバックグラウンドの源は同定されており，環境バックグラウンドに対する対策と共に準備を進めている[1]．

全般的に見て，我々の提案している、この新しい測定方法が中性子寿命の精密測定に適しているという確かな感触を得ていることを強調しておく。

1) 本報告の執筆時，バックグラウンド対策後の測定が行われているが，環境バックグラウンドは約60%に，ビームに伴うバックグラウンドは約20%に改善された．

図の説明

図1

中性子寿命測定装置の略図．上図は中性子ビームに垂直な面での断面図．下図はビーム軸に沿った断面図．Main Counterは4枚のプラスチックシンチレーションカウンター（各78 x 500 x 6 mm3）が正方形の筒をなしている．中性子はその軸上を通過し，崩壊β線および^{3}He(n,p)^{3}H反応からの陽子は内側からMain Counterに入る．外部からのバックグラウンドを除去するために，Main Counterの外側にはVeto Counter（長さ600 mm）が筒状に取り囲んでいる．全体は300φ x 1500 mmのステンレス製真空容器に納められている．

図2

条件の異なる3つのエネルギースペクトル（4本のMain Counterの出力の和）が重ねて表示されている．すなわち最も低く薄いのがビームを出さない状態でのバックグラウンド（環境バックグラウンド）．真中のスペクトルは^{3}Heガスを充填しない状態でのもの（β崩壊を含む）であり，最大のものは^{3}Heガスを充填したもの（β崩壊と^{3}He(n,p)^{3}Hを含む）である．後者2つは陽子のピークを除いて完全に重なっている．

表1 研究組織

研究代表者:真木 晶弘 (高エネルギー加速器研究機構・素粒子原子核研究所・教授)
研究分担者:安見 真次郎(高エネルギー加速器研究機構・名誉教授)
研究分担者:前澤 秀樹 (高エネルギー加速器研究機構・物質構造科学研究所・教授)
研究分担者:稲垣 洋輔 (東京家政大学・短期大学部・教授)
研究分担者:森 茂樹 (筑波大学・名誉教授)
研究分担者:小林 茂治 (佐賀大学・理工学部・教授)
研究分担者:田村 詔生 (新潟大学大学院・自然科学研究科・教授)

以上の者のほか,以下の大学院生が部分的に参加した.
坂本泰伸(新潟大学),中村雅利(新潟大学),高橋真也(新潟大学),大石龍雄(筑波大学),久良木広司(佐賀大学)

表2 研究発表

(1)学会誌等
1. A. Maki "Neutron Lifetime with Beam", Proc. International Workshop on JHF Science, held at KEK, Tsukuba, March 3-7, 1998; (1998) 227-230.
2. 安見真次郎 "冷中性子ビームを用いた中性子寿命の新しい精密測定法" Nuclear Physics and Fundamental Physics with Neutron IV (KEK Proceedings); 99-4(1999)9-54.
3. 安見真次郎 "中性子寿命" 波紋(日本中性子科学会学会誌);11-2(2001)

(2)口頭発表
稲垣洋輔 "中性子寿命の新しい精密測定法" 日本物理学会講演概要集; 52-1 (1997) 36

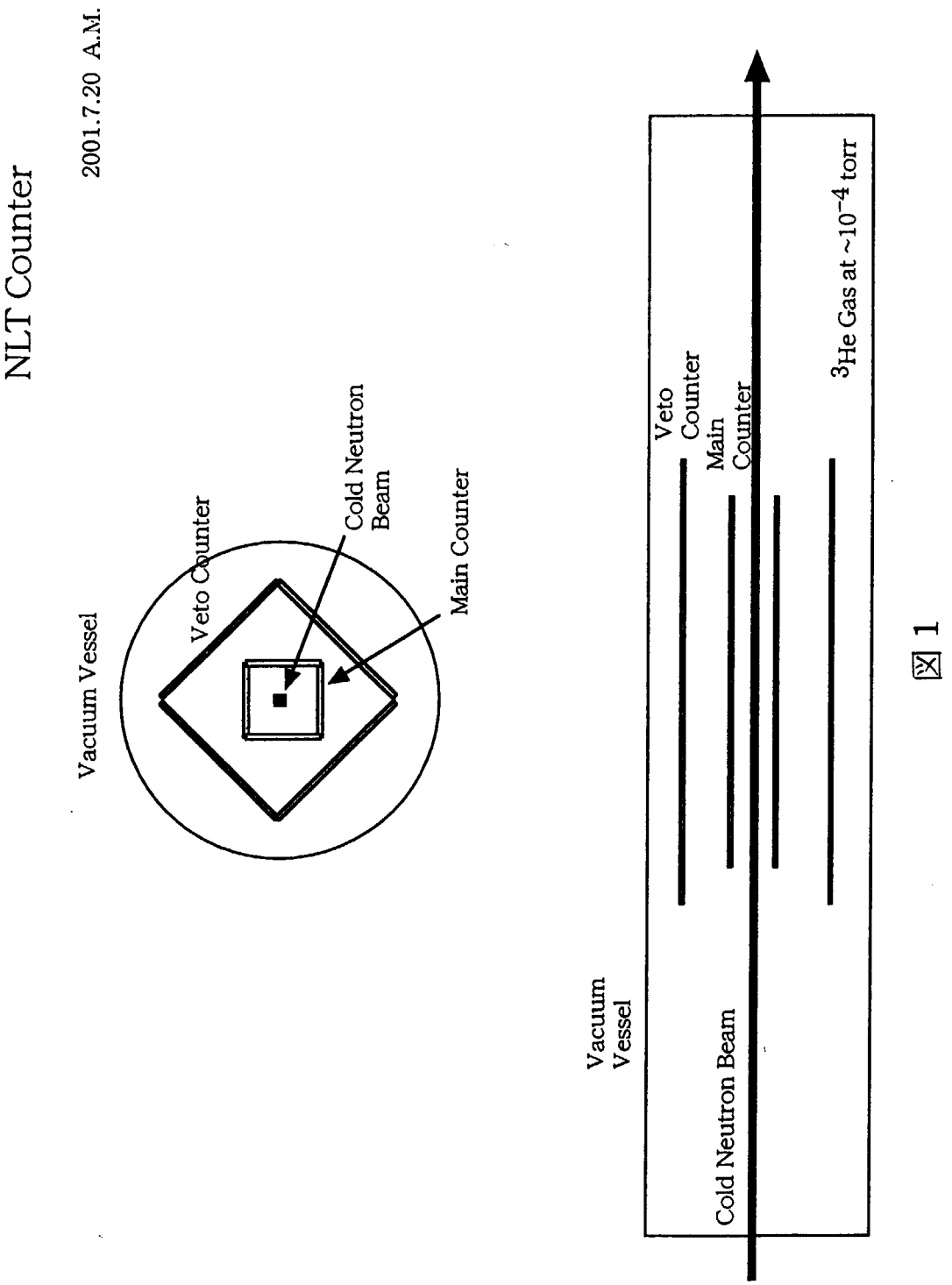

NLT Counter
2001.7.20 A.M.
Vacuum Vessel
Veto Counter
Cold Neutron Beam
Main Counter
Vacuum Vessel
Cold Neutron Beam
Veto Counter
Main Counter
^{3}He Gas at ~10^{-4} torr

図 1

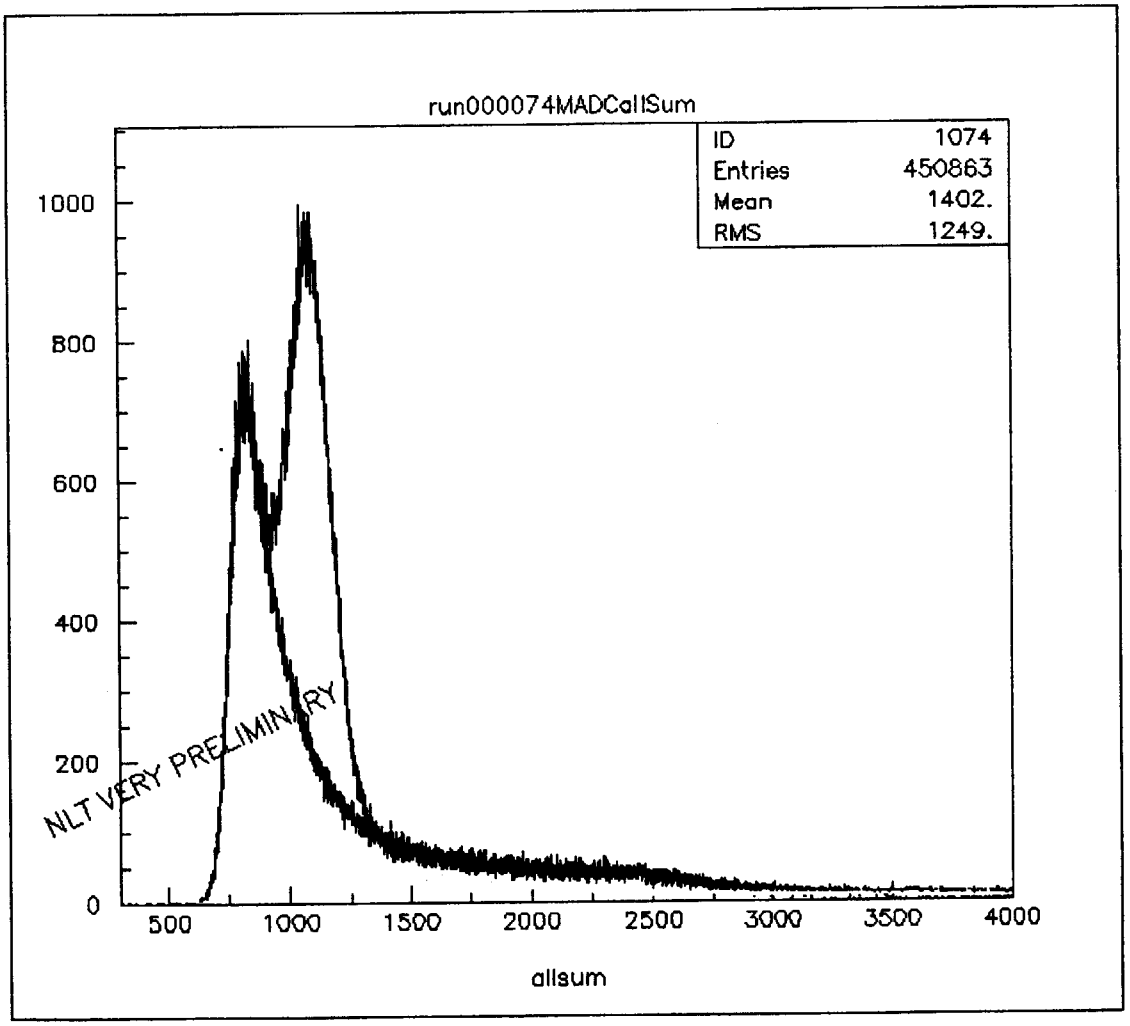

run000074MADCalISum
ID 1074
Entries 450863
Mean 1402.
RMS 1249.
1000
800
600
400
200
0
500
1000
1500
2000
2500
3000
3500
4000
allsum
NLT VERY PRELIMINARY

図 2

This is a blank page.

2. 中性子ラジオグラフィ

2. Neutron Radiography

This is a blank page.

研究テーマ：原子炉シビアアクシデント時の溶融炉心冷却に関する基礎研究
表　　題：溶融燃料／冷却材相互作用の可視化実験

2-1 水噴流衝突時の重液体金属の表面挙動

柴本泰照、　中村秀夫、　矢野早苗[1]、　辻　義之[1]、　久木田豊[1]
日本原子力研究所　東海研究所　原子炉安全工学部
[1]*名古屋大学　大学院工学研究科　エネルギー理工学専攻*

液体金属を利用した直接接触型蒸気発生器の開発や、軽水炉の溶融炉心冷却に関連して、液体金属／水／蒸気混相流の挙動に関心が高まっている。筆者らは、溶融金属（鉛ビスマス）表面に水ジェットを注入させたときの貫入・沸騰挙動を中性子ラジオグラフィ（NRG）により可視化・計測を行ってきた[1]。本報では、ジェット流速や液体金属温度をパラメータとしたこれらの結果を系統的にまとめ、貫入に関わる各種物理モデルを提案する。

実験は、奥行き 10 mm の 2 次元扁平容器に高温鉛ビスマス合金を満たし、一定流速U_jの水をジェット状（円柱：D_j = 6 mm）に衝突させ、NRG により液体金属の表面挙動を観察した（以下 molten Pb-Bi 実験）。実験パラメータは、水ジェットの流速と溶融金属の温度で、前者は Froude 数、

$$Fr_d = \frac{U_j}{\sqrt{D_j g \rho_m / \rho_j}} \tag{1}$$

換算で 6.1～9.8 の範囲となる。後者の温度については、界面接触温度（熱伝導近似式から算出）が均質核生成温度と比して大または小となる 2 種類の条件を設定した。撮像系には、イメージインテンシファイアを用いた高速度ビデオ撮影（1125fps）を採用し、沸騰を伴う高速現象に対応した。また、沸騰の効果を考察にするために、液体金属に水銀を用いた非沸騰実験[2]を 2 次元体系（矩形ジェット：D_j = 5mm）で行い（以下 Hg 実験）NRG の実験結果と比較する。

水ジェット貫入に関わる各種現象について等温 2 次元体系（図 1 参照）を対象にスケーリング則を考察する[3]。まずジェットの貫入速度について、ジェットが直接衝突するよどみ点での圧力バランスは、

$$P'_\infty + \frac{1}{2}\rho_j\left(U_j - U_C\right)^2 + \rho_j g H_C = P_\infty + \frac{1}{2}\rho_m U_C^2 + \rho_m g H_C \tag{2}$$

と表すことができる。U_cはキャビティ底の貫入速度で一定値とした。プールの大きさが無限大で、重力の影響を無視できると仮定すると、U_cはプールとジェットの密度比のみ関数として以下のように近似できる。

$$\frac{U_C}{U_j} = \frac{1}{1+\sqrt{\rho_m/\rho_j}} \cong 0.21 \quad \text{（水銀／水の場合）} \tag{3}$$

次にキャビティ体積の見積もりを行う。キャビティ全体に働く推力は、衝突ジェットとキャビティからの流出水の運動量変化から求めることができ、

$$F_{th} = \rho_j A_j \left(U_j - U_C\right)^2 (1+\cos\theta) \tag{4}$$

流出水が衝突ジェットと反対方向（$\theta = 0$）、かつ$U_C = 0$（定常状態）のときに最大となる。また、キャビティに働く浮力は$F_b = \rho_m V_C g$であり、定常状態では$F_{th} = F_b$となるとするば、キャビティの最大容積を以下のように予測できる。

$$V_C \frac{1}{\delta_C} = \frac{2\rho_j A_j U_j^2}{\rho_m g}\frac{1}{\delta_C} = 2D_j^2 Fr_d^2 \tag{5}$$

ジェット貫入のマクロな不安定現象として、キャビティの中央部がくびれるピンチオフ現象が挙げられる。キャビティ形成からピンチオフに至る時間スケールは貫入速度U_Cとキャビティの深さy、幅W_Cを用いて以下で表される[3]。

$$t = \frac{y}{\beta U_C} + \frac{W_C}{\sqrt{gy}} \tag{6}$$

βは貫入速度に対する補正係数である。この値が極小値（$dt/dy|_{t=t_p} = 0$）になるときに不安定が

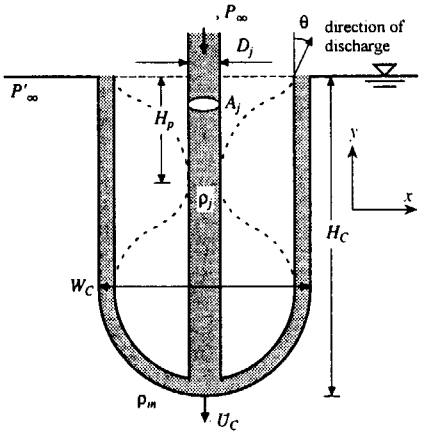


Fig.1 Geometric parameters of the under liquid cavity.

原子炉：JRR3-M　　装置：7R（TNRF）　　分野：中性子ラジオグラフィ（熱水力）

生じるとすると、水面からのくびれ位置の深さ $y=H_p$ とその発生時間 t_p は、貫入速度の式(3)を上式(6)に代入して、

$$\frac{H_p}{D_j}=\left(\frac{1}{2}\beta\gamma\frac{W_C}{D_j}\right)^{2/3}Fr_d^{2/3} \tag{7}$$

$$t_p^*\equiv\frac{t_pU_j}{D_j}=3\frac{1}{\beta(1-\gamma)}\left(\frac{1}{2}\beta\gamma\frac{W_C}{D_j}\right)^{2/3}Fr_d^{2/3} \tag{8}$$

と整理される。ここで、γ は密度比の関数で次式で表される。

$$\gamma=\sqrt{\rho_m/\rho_j}\Big/\left(1+\sqrt{\rho_m/\rho_j}\right) \tag{9}$$

ピンチオフ時の全深 H_C は、$H_C=\beta U_C t_p$ より、

$$\frac{H_C}{D_j}=3\left(\frac{1}{2}\beta\gamma\frac{W_C}{D_j}\right)^{2/3}Fr_d^{2/3} \tag{10}$$

となる。これらの式内に現れるキャビティの幅 W_C は、入射ジェット径 D_j のみの関数として次式で近似できる（2次元の場合）。

$$\frac{W_C}{D_j}=\frac{S+R_j}{R_j}=1+2\pi\cong 7.28 \tag{11}$$

molten Pb-Bi 実験では円柱ジェットを用いており、完全な 2D 体系ではないため（quasi-2D）、上述相関式の適用の際には、式(11)の D_j に対して水力等価直径による補正が必要となる。

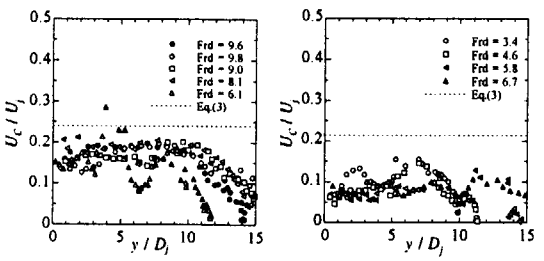
ピンチオフ時には、くびれ部分で後続のジェットが遮られるためキャビティの貫入が停滞する。よって、このときを最大深さと見なすことができ式(10)の相関式が適用できる。また、貫入が定常に達した後では、最大体積の予測式(5)と貫入幅の式(11)から、定常平衡深さは、

$$\frac{H_C}{D_j}=\frac{V_C}{D_j\delta_C W_C}=\frac{2}{1+2\pi}Fr_d^2\cong 0.275Fr_d^2 \tag{12}$$

となる。一方、斉藤ら[4]はフレオン／水実験から貫入深さ（平衡深さ）の経験式として以下を提案している。

$$\frac{H_C}{D_j}=2.1Fr_d \tag{13}$$

提案した理論相関式と実験データの比較を行う。図 2 に、molten Pb-Bi と Hg 実験の界面貫入速度を貫入深さに対してプロットした。両



(a) molten Pb-Bi　　(b) Hg.

Fig.2 Penetration velocities of the cavity bottom.

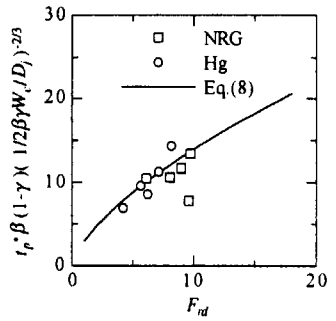
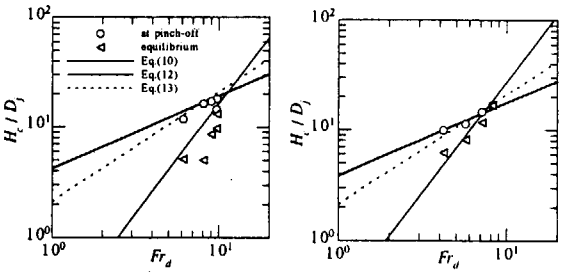


Fig.3 Dimensionless time at pinch-off.



(a) molten Pb-Bi (quasi-2D)　　(b) Hg (2D)

Fig.4 Maximum and equilibrium penetration depths.

者共に貫入速度はほぼ一定で、ピンチオフ時にはゼロに近づく。これより、初期貫入に関しては沸騰／非沸騰の影響は小さいことがわかる。また、両結果とも式(3)の予測値を下回っており、molten Pb-Bi で予測値の 75%、Hg で 50%程度となっている。予測式(3)では、プールが無限に大きくプール内の圧力変化を無視して導出しているが、実験では比較的小さい容器のためこの仮定が成り立たず、このような差が生じた。

以上の貫入速度のズレを考慮して、ピンチオフするときの時刻を図 3 に、またピンチオフ時の深さとその後の平衡状態の深さを図 4 に、それぞれ導いた相関式と共に示す。補正係数 β により貫入速度を式(3)の理論値と適合させることで、時刻・深さの実測値は予測値と良い一致を示した。molten Pb-Bi 実験において平衡深さが予測値よりもやや下回っているが、これは、生成蒸気の吹き上げにより入射ジェットの推力が弱められるためと考えることができる。

以上、ジェット貫入に関わる各種相関式を提案した。これらは、中性子ラジオグラフィから得られた実験値と良い一致を示した。

参考文献

1) Sibamoto et al., Proc. of ICONE-8426 (2000)
2) 矢野他，日本原子力学会中部支部第 32 回研究発表会 (2000), E2.
3) 柴本他，機械学会2001年度年次大会, K-2107.
4) Saito et al., ANS-Proc. National Heat Transfer Conference, (1988), 173-183.

研究テーマ：パルス中性子イメージング検出法の研究
表　　題：シンチレータと波長シフトファイバを用いた２次元中性子イメージング法

2-2

2-dimensional neutron imaging method using scintillators with wavelength shifting fibers

K. Toh, M. Katagiri, K. Sakasai, M. Matsubayashi, A. Birumachi, H. Takahashi[1], and M. Nakazawa[1]

Advanced Science Research Center, JAERI, Ibaraki 319-1195, Japan
[1]Dept. of Quantum Science and System Engineering, Univ. of Tokyo, Tokyo 113-8656, Japan

We have developed a 2-dimensional neutron imaging method using rectangular scintillators and wavelength shifting (WLS) fibers for neutron scattering experiments with a next-generation high-intense pulsed-neutron source as shown in Fig.1. In the method, many rectangular scintillators are arranged at longitudinal direction and transverse direction and WLS fibers are arranged on the four sides of these scintillators. Luminescences generated in the scintillator are absorbed by the four WLS fibers and wavelength-shifted luminescences are detected by multi-channel photomultipliers. The position of incident neutron is decided by coincidence of the four signals. The detection efficiency of 13% for thermal neutron with a coincidence time of 200ns was determined with a preliminary experiment using 5 mm x 5 mm x 2 mm^t ^{6}Li glass scintillators (Bicron, GS-20) and 0.5 mmϕ WLS fibers (Bicron, BCF-92M).

A 4 x 4 ^{6}Li glass scintillator array neutron detection system was fabricated to confirm the effectiveness of the imaging method. Before the neutron imaging experiments, we carried out the experiments to obtain the characteristic of counting rate for this system. The experiments were carried out in the thermal neutron radiography facility of JRR-3M. The thermal neutron flux is 2.0 x 10^8 $cm^{-2}s^{-1}$. The counting rates for a scintillator are shown in Fig.2. One can see that the system has linearity under 5 Mcps for one scintillator in this array. As a next step of the development, we are planning to take a 2-dimesional neutron image with this system.

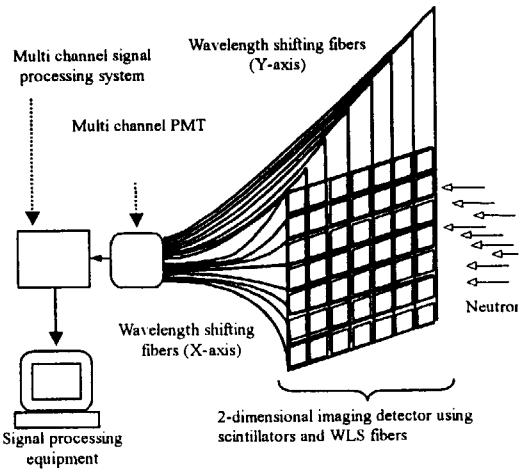


Fig. 1. Illustration of 2-dimensional neutron imaging system using rectangular scintillators with WLS fibers.

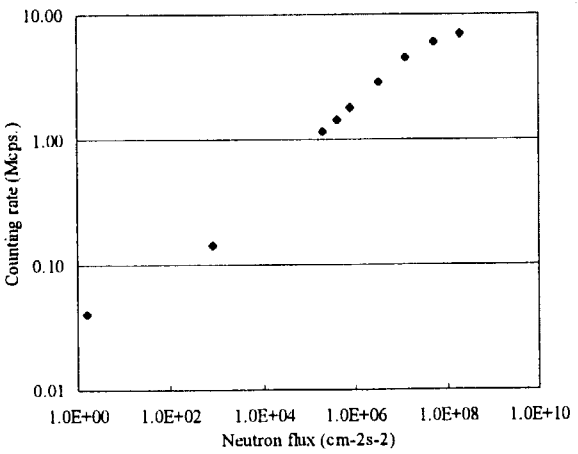


Fig.2 Counting rate for one scintiilator

原子炉：JRR-3M　　装置：TNRF　　分野：中性子散乱（装置）

研究テーマ：中性子ビーム利用技術に関する開発研究
表　　題：FOPを用いた中性子ラジオグラフィ高解像度撮像法の開発

2-3 FOPを用いた中性子ラジオグラフィ高解像度撮像法の開発

松林政仁、日引　俊[1]、三島嘉一郎[1]、宇根崎博信[1]
日本原子力研究所　東海研究所救助　中性子科学研究センター
[1]京都大学　原子炉実験所　核エネルギー基礎研究部門

中性子ラジオグラフィでは蛍光コンバータと撮像デバイスを暗箱の中で光学レンズにより結合した撮像システムが広く用いられている。これに対しFOP (Fiber Optic Plate)を用いた結合法では蛍光体はFOP上の端面に直接塗布されており、FOPの残りの端面がCCD (Charge Coupled Device)チップに直付けされている。このためシンチレータからの発光輸送の光学的ロスが少なく、ファイバーのコアサイズに応じて高解像度が期待できる。前年度までに、5mg/cm^2 のGd_2O_2S(Tb)をシンチレータとしたFOP-CCDカメラシステムにより 35μm の高解像度を達成した。CCDのセルサイズ(約 10μm 角)を考慮すると、ストレートタイプのFOPではこれ以上の高解像度化は困難である。このため今年度は、テーパー型のFOPを用いて高解像度化を進めた。加えて、解像度は劣るものの高い発光輝度が期待できる ^{6}LiF:ZnS(Ag)を用いて実時間撮影(毎秒 30フレーム)の可能性を実験により確認した。[1)]

使用したFOP結合型撮像システム構成はシンチレータ：Gd_2O_2S(Tb)，塗布重量：5 mg/cm^2，FOP(縮小面にシンチレータ塗布)：テーパー比 1:2 又は 1:3，CCD：セルサイズ 11.0μm(H) x 13.0μm(V)，有効画素数 768(H) x 493(V)である。JRR-3M冷中性子ラジオグラフィ装置場でGd製のMTFチャート(10μm LP, 25μm LP, 50μm LP, 100μm LP)を測定した。実時間撮影法への適用可能性のための実験では、コンピュータ用ハードディスク軸受け部を可視化した。

1) MTFチャート撮影結果：テーパー比 1:2 及び 1:3 のFOPそれぞれに対してMTFチャートの撮影を行なった。その結果，どちらのFOPでも 25μm LP まで分離可視化できることを確認した。ストレートタイプのFOPでは、25μm LP の分離可視化は困難であったことから、解像度の向上が確認できた。但し、ストレートタイプに比較して撮影視野が 1/2 あるいは 1/3 と減少するため用途が限定されるのが欠点である。2) 実時間撮影法への適応可能性：CCDに直付けされたFOPに直接 ^{6}LiF:ZnS(Ag)シンチレータを取り付けてハードディスク軸受け部を最高 100Hz まで回転させた状態で可視化を行なった。回転数の変化に応じて潤滑油の分布が変化していく様子を観察することができた。

参考文献

1) 松林政仁、曽山和彦、日引俊、三島嘉一郎、「FOP を用いた中性子ラジオグラフィ高解像度撮像法の開発」、原子力学会 2001 春の年会予稿集

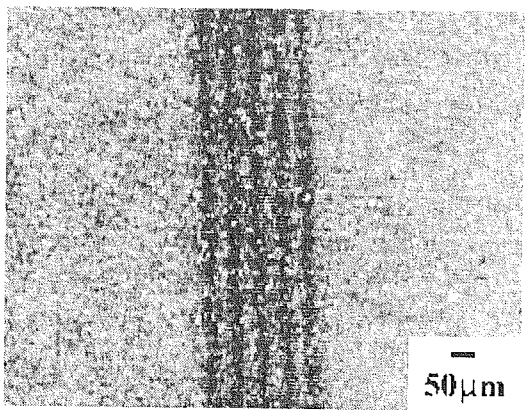


図1 テーパー比 1:3 の FOP を用いて撮影した 25μm LP MTF チャート画像

原子炉：JRR-3M　　装　置：TNRF, CNRF　　分　野：中性子ラジオグラフィ（その他）

2-4

中性子線を用いたアルミニウム添加下における幼植物根近傍の水分動態解析

Water Movement in the Vicinity of a Seedling Root with Aluminum Treatment by Neutron Beam Imaging

中西友子、大國曜子、古川純、松林政仁

T.M.NAKANISHI, Y.OKUNI, J.FURUKAWA, M. MATSUBAYASHI

東京大学大学院農学生命科学研究科

Graduate School of Agricultural and Life Science, the University of Tokyo

日本原子力研究所東海研究所中性子科学研究センター

Japan Atomic Energy Research Institute, Tokai Establishment

1．はじめに

非破壊計測手法としての生体試料の可視化に、X線や中性子線によるイメージングは有効な手法である。X線が重金属等の比較的原子量の大きい元素の検出に適するのに対し、中性子線は水素、リチウム、ホウ素などの軽元素の検出に適している。中性子線による吸収・散乱能はとりわけ水素が高く、重金属に比して1000倍にも及ぶため、中性子線照射によるイメージは水素の分布をよく示すものとなる。生体は60~80%程度が水で構成されているため、非破壊である中性子線を用いたイメージングは、生体試料の水の分布を示すのに適している。我々は、冷却型CCDカメラの撮影像をCT(computer tomography; 断面像)に再構成して、試料の水分分布を3次元的に解析する手法を開発した。

世界の耕地の約40%が、植物の生育を阻害する酸性土壌である。酸性土壌における植物育成の阻害要因には、水素イオンの過剰害やリン、カルシウムなどの栄養不足の他、アルミニウムの過剰害が挙げられる。アルミニウムは、土壌中に7%含まれる主要な構成元素の一つであるが、酸性条件下で様々な化学形態をとってイオン化し、植物の根の伸長阻害、水分および養分の吸収阻害をもたらす。今回、アルミニウムを添加した土壌で栽培した大豆の芽生えを用いて、その根と根周囲の土壌中の水分に着目して、解析を行った。

2．実験手法

播種後3日目のダイズ(*Glycine Max.* Merr., cv. Tsurunoko)幼植物を35mmのアルミニウム製(アルミニウム厚:1mm)の円筒形容器に移し変えた。容器中には豊浦標準砂を充填した。これに重量の15%の0.2 mM $CaCl_2$ 溶液を含ませたものをコントロール区とし、アルミニウム添加区には、$CaCl_2$ 溶液中に終濃度10mMとなるように塩化アルミニウム($AlCl_3$)を添加した。ダイズを移植後、円筒容器は砂の表面からの蒸発を防ぐためにアルミテープでシールし、植物育成器中で温度25℃、湿度70%、照度20000 luxで生育した。移植後2日目から5日目にかけて、試料に中性子線を照射し、冷却型CCDカメラによる撮影を4回行った。撮影用の中性子源には日本原子力研究所(JAERI)東海研究所の研究炉JRR-3Mの熱中性子線を使用し、熱中性子束は 6.0×10^8 n/cm^2 であった。試料は回転台に固定し、試料台を1度ずつ回転させながら各角度において4秒間シャッターを開き、投影画像を撮像した。一つの試料につき180度まで合計180枚の投影画像をCCDカメラで撮像しコンピュータ処理によりCT像を構築した。撮影には1試料当たり90分要した。撮影時の制御および投影画像の再構成、解析に用いたソフトウェアはIPLabSpectrum3.2.4 (Scanalytics, Inc.)であった。

3．結果と考察

CCDカメラによって撮影された180枚の像は、高さ1014ピクセル、幅984ピクセルであった（1ピクセル＝約0.11mm)。これを合成して、各ピクセルの高さにおけるCT像を作成した。さらにこのCT像を1014枚積み重ねることにより、fig.1 (a)のような三次元像を構築した。fig.1 (a)において示された部位のCT像を4日間連続的に示したものが、fig.1 (b)である。各CT像における中央の白い点は、主根である。CT像上の輝度度は、水分量を反映している。水分量が多い所は中性子線が透過しにくいために、より白い像になる。

そこで、各CT像上の主根に相当する輝度値を積分して、植物の主根の体積を計算した。その結果、アルミニウム添加区の根の体積は、コントロール区と比較して低い値を示した（fig. 1(c)）。コントロール区における根の生育はアルミニウム添加区のそれよりも約1日早いことが観察された。主根が円筒容器の底に達した日がコントロール区で2日目であったのに対し、アルミニウム添加区では3日目であり、

側根が伸長を開始したのは、それぞれ 3 日目、4 日目であった。

各 CT 像を、主根を中心に直径 1.6cm の円状に切り出し、主根を除いた部分、すなわち主根近傍の土壌の水分量を、単位面積当たりの輝度値に変換して算出した。また、水の重力による下降や土壌表面からの蒸発などの円筒容器中の不均一な水分分布と区別するために、ブランク値として、同一サンプル中で主根から 1~2cm 離れた部位での土壌水分量も同時に算出した。

fig.2 (a)は、コントロール区 4 日目の根の 3 次元像であり、fig.2 (b)は、fig.2 (a)と高さを対応させた土壌水分量の分布図である。fig.2 (b)は、CT 像から算出された主根近傍の土壌水分量に上述のブランク値を減じた値をプロットし、5 点ごとにスムージング処理を行ったグラフである。グラフの横軸は、水分量の多寡を示している。横軸の 0 はブランク値と同量であり、プラスの点は、主根周囲の土壌がより多くの水分を保持していることを示している。fig.2 (a)の 3 次元像と比較してみると、側根の伸長する部位の主根の周囲は、水分量が多いことが示されている。
そこで、側根の周囲（fig.1 (a)と(b)で左向き矢印）と側根の生えてない部位を（fig.1 (a)と(b)で右向き矢印）5 箇所で 5 ピクセル取りだし、ブランク値を減じた水分量の経日変化を表したものが fig.2 (c)(d)である。

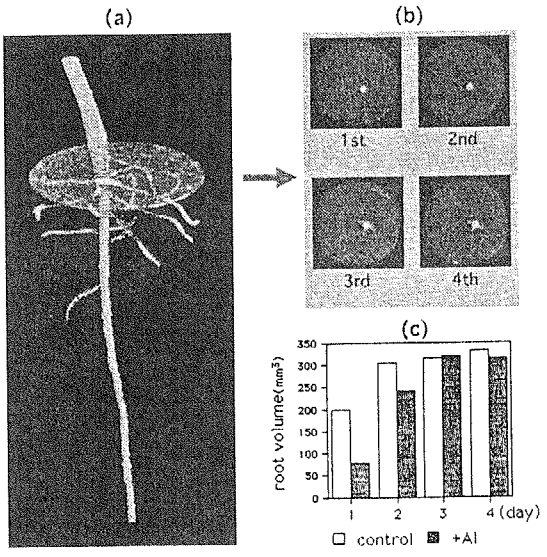


Figure 1: Root growth by image analysis.
(a) A special soybean root image constructed from CT images.
(b) Successive CT images for 4 days at the same height, indicated as a place in (a)
(c) Main root volume calculated through image analysis.

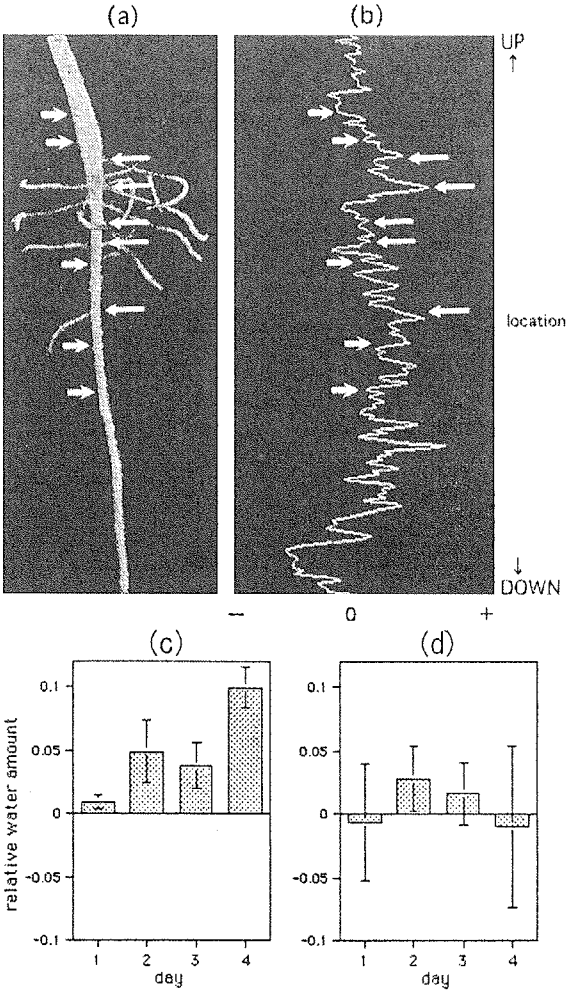


Figure 2: Water profile in the vicinity of a root.
(a) A spacial soybean root image of the control sample on the 4th day.
(b) Water profile along the main root. Water amount far from the root (blank) at corresponding height was subtracted from that mean of the main root, and then the net water amount was plotted. When the net water amount was higher or lower than blank, it was plotted toward + or −as cited down the figure(b).
(c) Water amount around the specific position of the main root where the side root grows. These 5 positions were indicated as left headed arrows (←) in both (a) and (b). The mean water amount of 5 pixels at each site was plotted.
(d) Water amount around the specific position of the main root where the side root did not grow. These 5 positions were indicated as right headed arrows (→) in both (a) and (b). The mean water amount of 5 pixels at each site was plotted.

主根の周囲は、もともと水分が豊富であるが、側根が急激に伸長してくる 3 日目から 4 日目にかけて、側根の生じる箇所の水分量は急激に増加している（fig.2 (c)）。側根の生える箇所以外では、ランダムに点を取ったので誤差が大きいが、概ねブランク値と近い値を示した（fig.2 (d)）。

主根近傍の水分量をより広い範囲を取って分析した。連続した高さの 150 ピクセル分の CT 像において、初日の水分量を 100%とし、その後各日の初日に対する増減率をプロットしたグラフが fig.3 である。両試料において、ブランクではいずれも徐々に水分を減じ、4 日間で初日の 10%程度の水分を失っているが、主根の周囲では水分量は初日よりも増加しており、また

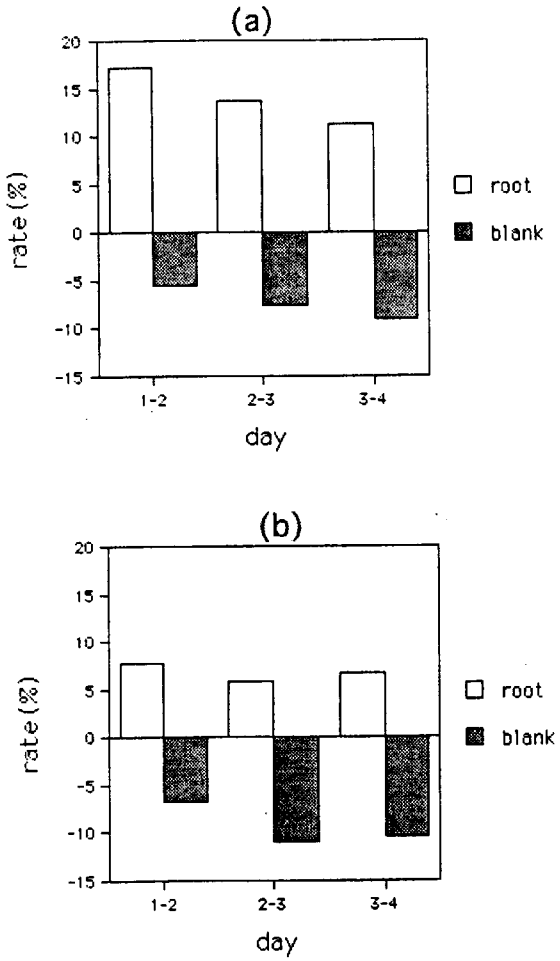


Figure.3: Water moving rate in much wider range.
Water increasing rate, out of 150 CT images, was calculated where the water amount of the first day in soil with root (□)or without root (■) was set as 100%.
(a)control sample (b)Al treated sample

その保持量はコントロール区の方が多かった。1 日目から 2 日目にかけて、両試料で主根水分保持量が増加しているのは、主根が最も急激に伸長したためと考えられる。また、アルミニウム区がコントロール区に比較して水分保持量が少ないことは、アルミニウム添加区の生育が劣ることと相関していると予想される。同時に、根には水分を吸収するだけではなく、水分を積極的に蓄える機能を持ち、アルミニウムがそれを害していることが示唆される。

本研究により、根の水分保持機能は、植物の生育活性を知る上で、重要な指標であることが予想され、今後その機構の解析が期待されるところである。

4． 成果の発表

（論文）

1) T.M.Nakanishi et al. Moisture Imaging of a Camphor Tree by Neutron Beam. Radioisotopes, 47, 387-391, 1998
2) T.M.Nakanishi et al. Three Dimensional Imaging of Moisture in Wood Disk by Neutron Beam During Drying Process. Holzforschung, 52, 673-676, 1998
3) T.M.Nakanishi et al. A Preliminary Study of CT Imaging of Water in Carnation Flower. Nuclear Istruments and Methods in Physics Research A424, 136-141, 1999
4) J.Furukawa et al. Neutron Radiography of a Root Growing in Soil with Vanadium. Nuclear Istruments and Methods in Physics Research A 424, 116-121, 1999
5) T.M.Nakanishi et al. CT Imaging of Water in Root-Soil System by Neutron Beam. Soil Physical Conditions and Plant Growth. J.Jpn.Soc.Soil Phys. 82, 29-33 1999
6) J.Furukawa et al. Water Uptake Activity in Soybean Root Revealed by Neutron Beam Imaging. Nondestructive Test & Evaluation. 16, 335－343, 2001

（発表）

1) 古川他、中性子線を用いた根の水分吸収機構の解析、農芸化学会（名古屋）1998.4.2
2) T.M.Nakanishi . Water Imaging in Living Plant by Nondestructive Neutron Beam Analysis. Proc. of The 23rd Japan Conference on Radiation and Radioisotopes, B125, pp1-18, Tokyo, 1998
3) T.M.Nakanishi . Water Imaging in Living Plant. Proc. of the 3rd Symposium on Radiographic Testing Nov.25-26, Tokyo,1999
4) J.Furukawa et al. CT imaging of soybean root imbedded in soil by neutron beam. World Conference

of Neutron Radiography-6（大阪）1999.5.21
5)古川他、中性子線による植物根近傍の水分動態の可視化、可視化情報シンポジウム(東京)、2000.7.18
6)大國曜子他、日本土壌肥料学会高知大会、「アルミニウム存在下における根近傍の水分吸収動態の解析、中性子線を用いた根－土壌系の経時的な立体像の構築」、高知大学、(2001)
7)大國曜子他、理工学における同位元素・放射線研究発表会、日本青年館、「アルミニウム存在下における根近傍の水分吸収動態の解析」(2001)
8) Yoko Okuni et al., Proc. of XIV International Plant Nutrition Colloquium, The University of Hannover (Hannover,Germany), " Water Uptake Manner and Development of a Living Root through Nondestructive Water Imaging by Neutron Beam." , (July, 2001)
9) Yoko Okuni et al., Proc. Of the 3rd International Congress on Analytical Sciences (ICAS 2001), Waseda University (Tokyo,Japan), " Water Accumulation in the Vicinity of a Soybean Root Imbedded in Soil Revealed by Neutron Beam." (August, 2001)

2-5

熱中性子ラジオグラフィによる熱流動現象の可視化と計測

Visualization and Measurement of Thermal Hydraulic Phenomena by Thermal Neutron Radiography

神戸大学：竹中信幸、浅野　等、白水順一、前田憲男、端山俊輔、橋本章生、林　秀典、田上陽一、淵本　剛

1、序

熱中性子線は、多くの金属をよく透過する一方、水・有機液体や特定の元素によく減衰する特性を有する。

本研究の目的は、機械、化学、原子力工学の分野で重要な熱流動現象を対象として、現在世界最高性能システムの一つである JRR-3M 高束熱中性子ラジオグラフィシステムを用いて、種々の体系についての可視化法と画像処理による計測法を開発し、従来解明されていない熱流動現象を明らかにすることである。

熱中性子の特性を有効に利用した可視化・計測の対象として、特に、今回開発した真影法による定量的なボイド率計測を以下の体系について適用し、それらの熱流動現象の解明を行った。

1、液体金属流れのボイド率計測
2、バンドル内二相流のボイド率計測
3、熱交換器内二相流の可視化とボイド率計測

2、研究方法と結果

ボイド率は二相流における気相の体積割合であり、二相流研究における重要な計測量である。中性子線減衰を冷却型ＣＣＤカメラにより撮像し、ボイド率分布の高分解能計測が期待できる。可視化画像を基に、１、２次元、ＣＴ法による３次元の計測を行った。

ラジオグラフィの画像の輝度は中性子や可視光の散乱成分や多くのノイズを含んでいるため定量化を行うには特別な工夫が必要である。中性子、可視光両方の散乱成分を評価できる方法として真影法を改良した手法を開発し、定量的計測を行った。

液体金属の熱流動現象は、特に原子力工学において重要であるが、液体金属が可視光に不透明であるため流れ場を可視化することは容易ではない。鉛、ビスマス、錫等の重金属合金は、低融点で化学的に不活性であることから熱媒体としての使用が検討されているが、このような液体金属の流れの可視化は中性子線以外では困難であると思われる。

本研究では、すでに開発したトレーサ法による速度計測と今回の定量的ボイド率計測法を用いて、二相流循環冷却型液体金属ターゲットの水力設計の基礎研究を行った。

図１に、加速ビーム方向の管断面１次元ボイド率分布の測定例を示す。液体金属二相流においてこのような計測を行うことは他の方法では困難であり、このような結果をもとに二相循環流のモデリングを行っている。

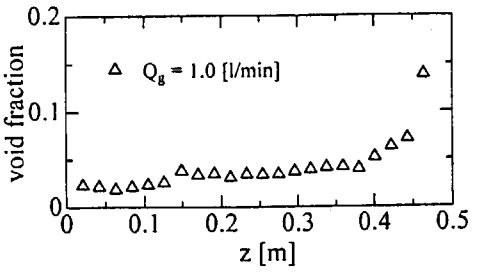


図１　鉛ビスマス溶融合金中の
気液二相流のボイド率分布測定例

大抵の機械は金属で製作され、機器内の水等の流動特性を可視化・計測するには中性子ラジオグラフィが適しており、実際の機械を可視化することにより運転状態の診断も行える。

図２は原子炉の安全研究で重要なロッドバンドル内のスペーサ近傍の気液二相流ボイド率分布をＣＴ法によって３次元計測した例であり、従来完全には

解明されていないスペーサの影響について多くの定量的知見を得た。現在、二相流のモデリングやサブチャンネル解析等を行っている。

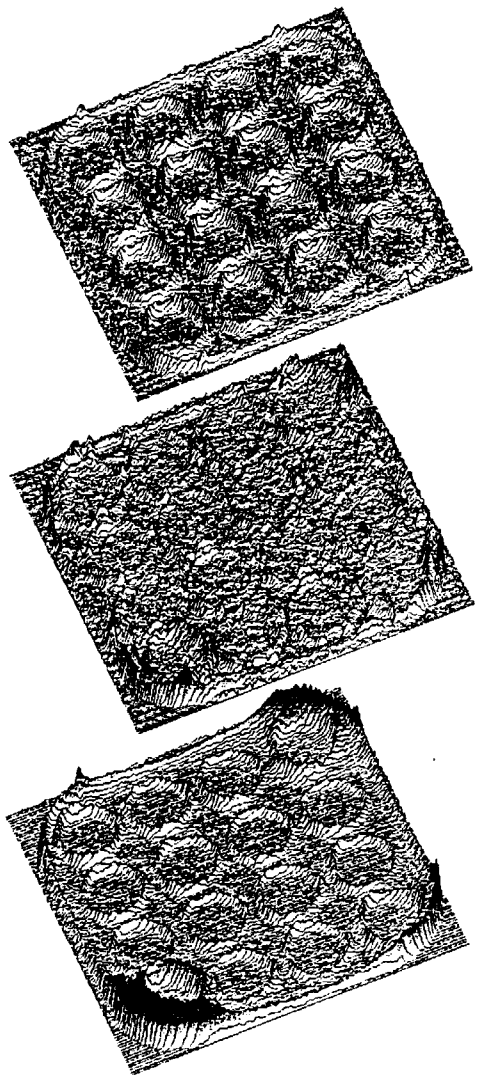


図２　ロッドバンドル内気液二相流の
三次元ボイド率分布測定例

分散型小型エネルギーシステムでは、蒸発部、凝縮部の熱交換器の高性能化が重要である。多数の狭隘チャンネルを持つプレート熱交換器は単相流では高性能であるが、二相流では並列部への分岐の問題がある。二相流の非線形性のため分岐は、非均一性や不安定性を伴うことが一般的であり、分岐部の設計に工夫が必要である。図３はプレート熱交換器内の気液二相流のボイド率を定量的に測定した例であり、このような結果をもとに分岐部の最適設計指針作成を検討している。

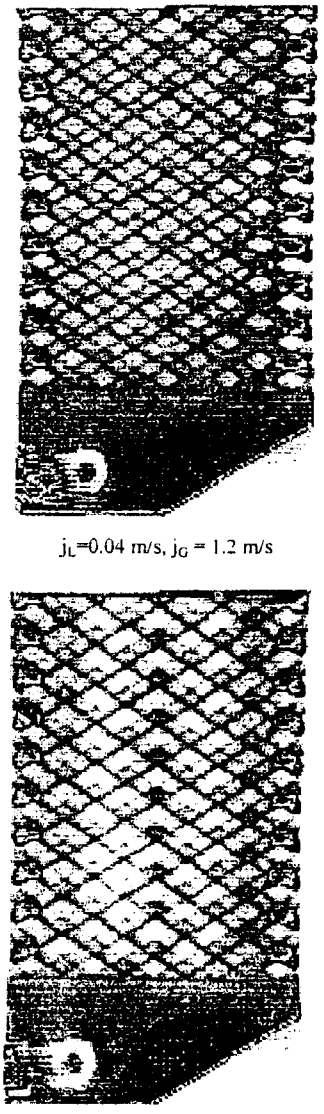


図３　プレート熱交換器内の
２次元ボイド率分布測定結果の例

3、今後の方針

今回の研究により、充分な高精度で液体金属二相流、金属容器内の水等のボイド率計測が行えることを示し、すでに二相流のモデリングや二相流機器の設計指針作成を開始しており、今後さらに研究を継続し、また新たな二相流機器への適用を検討する。

4、成果の公表

本研究で得られた成果をもとに学術雑誌、国際会議で公表された論文を示す。

1. N. Takenaka, H. Asano, T. Nakazawa, H. Umekawa, M. Ozawa,
"Neutron Radiography as a Tool for Multiphase Flow Researches in Industrial Machines", Proc. Asian Symp. on Multiphase Flow, 1999, Nov., Osaka, Japan, pp. 283-287.

2. N. Takenaka, H. Asano, T. Fujii, A. Hashimoto,
"Velocity and Void Fraction Measurement in Molten Lead-Bismuth Two-phase Flow by Neutron Radiography", Proc. JSME-KSME Thermal Eng. Conf. Vol. 1, D115, 2000, Oct., Kobe, Japan, pp. 373-378.

3. H. Asano, N. Takenaka, T. Fujii, N. Maeda,
"Flow Pattern and Void Fraction Distribution of Gas-liquid Two-phase Flow in a Plate Heat Exchanger Measured by Neutron Radiography", Proc. JSME-KSME Thermal Eng. Conf. Vol. 1, G106, 2000, Oct., Kobe, Japan, pp. 591-596.

4. N. Takenaka, H. Asano, T. Fujii, S. Hayama, N. Maeda,
"Void Fraction Distribution of Air-water Two-phase Flow in a Rod Bundle Measured by Neutron Radiography", Proc. JSME-KSME Thermal Eng. Conf. Vol. 2, B213, 2000, Oct., Kobe, Japan, pp. 155-160.

5. N. Takenaka, H. Asano, T. Fujii, M. Matsubayashi,
"A Method for Quantitative Measurement by Thermal Neutron Radiography", Nondestructive Testing & Examination Vol. 16, pp. 345-354.

6. N. Takenaka, H. Asano, T. Fujii, N. Maeda, S. Hayama, M. Matsubayashi,
"Application of Quantitative Measurement Method to Void Fraction of Two-phase Flow in a Rod Bundle by Neutron Radiography", Nondestructive Testing & Examination Vol. 16, pp. 355-362.

7. H. Asano, N. Takenaka, T. Fujii, T. Arakawa, M. Matsubayashi,
"Quantitative Measurement of Void Fraction Distribution of Gas-liquid Two-phase Flow in a Spiral Tube by Thermal Neutron Radiography", Nondestructive Testing & Examination Vol. 16, pp. 363-375.

2-6

屈折式中性子レンズの開発

Development of Refractive Neutron Lense

川端祐司、田崎誠司、米田憲司
京都大学原子炉実験所
Yuji Kawabata, Seiji Tasaki and Kenji Yoneda
Research Reactor Institute, Kyoto University

１．はじめに

中性子ビーム収束は、これまでも中性子ビーム実験の実験効率向上を目的として進められてきた。特に中性子散乱実験効率化を目的としたベントクリスタルによる単色中性子ビームの収束[1]や即発γ線分析に利用することを目的とした白色中性子ビーム収束の試み[2]が盛んである。ここで述べる中性子レンズも白色中性子の収束の一方法であり、マルチキャピラリーを用いた微細ビームの収束[3]や、スーパーミラーによる収束型導管[4]による試みと目的は似ている。

マルチキャピラリーによる収束の場合、入射中性子は平行ビームに限られており、それを束ねた多数の微小径キャピラリーによって収束させることを目的としている。従って、用途は試料に照射するための比較的平行な入射ビームの収束に限られている。また中性子鏡による収束としては、ベンダーによるものとスーパーミラーを用いたものがあり、これらを組み合わせることによりさらに効率よく収束させる試みも有る。この場合も目的はマルチキャピラリーを同じであるが、収束部分の鏡にスーパーミラーを用いることにより、内部を通過する中性子ビームの発散角を増加させ、また通過断面の幅を大きくすることができる。つまりマルチキャピラリーでは照射面積は数十から数百μm程度であるのに対し、この手法では数mmから数cmにまで広げることができる。

これらに対し、画像取得のために利用される集束系としては、反射鏡式と屈折レンズ式がある。反射式のものは超冷中性子を利用した中性子顕微鏡の試みとして進められてきた[5]が超冷中性子源強度の問題から原理実証に止まっている。しかし、冷中性子の利用に向けて、自由形状が可能となるレプリカスーパーミラーの開発[6]も進められている。また屈折式レンズについても画像取得に利用されたものはまだなく、実験効率を上げるために MgF を用いたビーム収束実験を行っている[7]のみである。ここでは、MgF よりも核特性の優れている炭素を利用した微小プリズム式屈折式レンズを提案し、基本となる微小プリズムを試作してその特性を測定した結果を報告する。

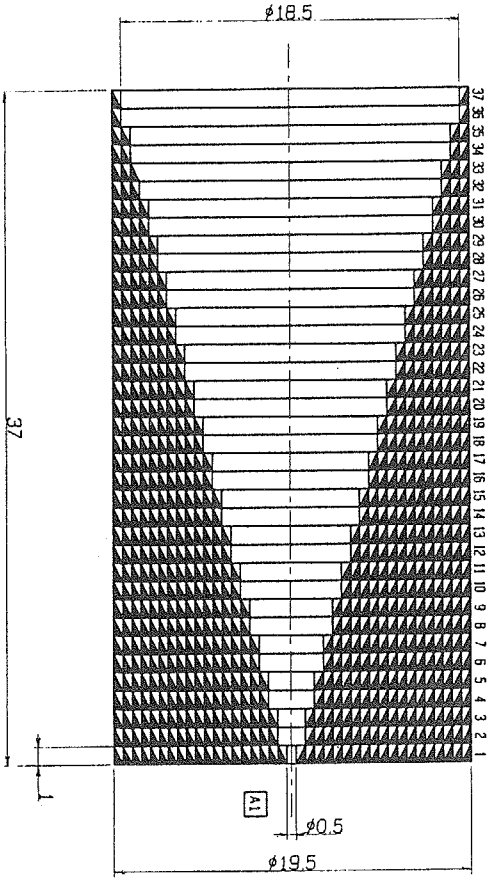
２．屈折式中性子レンズの構造

屈折式中性子レンズの場合、原理的に中性子の入射角に制限がないことが利点であるが、大口径になった場合に外周側で肉厚が厚くなりすぎ透過確率が落ちることが欠点である。しかし反射型の場合、鏡への入射角の制限がない超冷中性子は例外とし、通常反射できる角度制限が厳しく、実製作も容易ではない。それに対して、多プリズム式の本方式では、機械加工による製作が可能であるため、既存の技術により高い製作精度で実現できるため、設計どおりの性能が得られやすいと考えられる。

JRR-3M, 中性子ラジオグラフィ

また即発γ線分析利用のような中性子収束を目的とした場合でも、マルチキャピラリー方式を含む反射型では速度の速い中性子を収束できないため、中性子源のスペクトルが比較的硬い場合には損失が大きくなる。しかし屈折型の場合は、このような速度の速い中性子は光軸上を通過することから利用することができる。即発γ線分析のようにエネルギー分解能が広くとることができる場合には、これが大きな利点となる。

ここでは屈折レンズの材質として、中性子ポテンシャルの大きさと加工性の良さから炭素材を用いることとした。構造は、実際の加工性を考えて黒鉛のくさび形構造の繰り返しとした。その全体構造を第１図に示す。

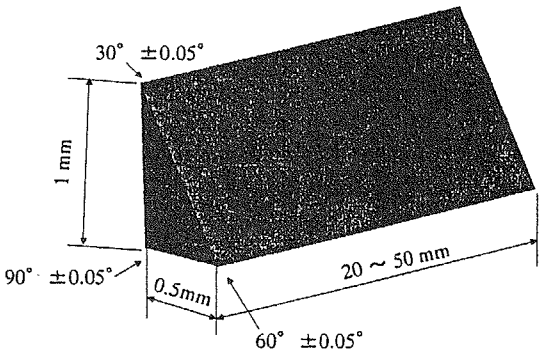


第１図　屈折式レンズ構造

原理的に一回の屈折での曲げ角を大きくできないため、多段構造とした。屈折中の中性子散乱や吸収を少なくするため、一層の厚さは１ｍｍ以下とする。また屈折面がビームラインとなす角を３０°とし、中心にはセンター合わせのため直径 0.5mm の穴をあけるものとする。レンズ直径は 18.5mm で、波長 1.0nm に対して焦点距離を２ｍとするため、３７層構造とする。

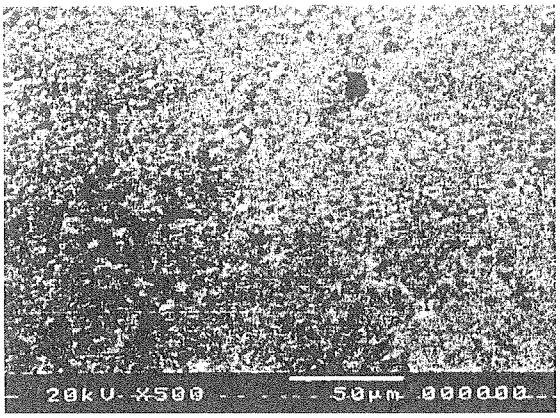
３．微小中性子プリズムの製作

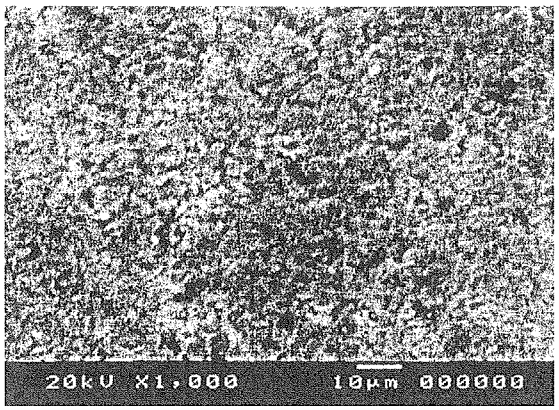
屈折式レンズの要素となる炭素三角柱微小プリズムの試作を行った。その構造を第２図に示す。黒鉛構造を持った炭素柱を加工し、斜面角度を 30° 及び 60° とし、最鋭角部分のＲは 0.05mm 以下とした。炭素密度は約 1.50 g/cm^3 である。純度は Fe, Al, Si, Mg に対しては 500ppm 以下、Cr,Cd,As,Pd に対しては 1ppm 以下であり、不純物の効果は無視できる。



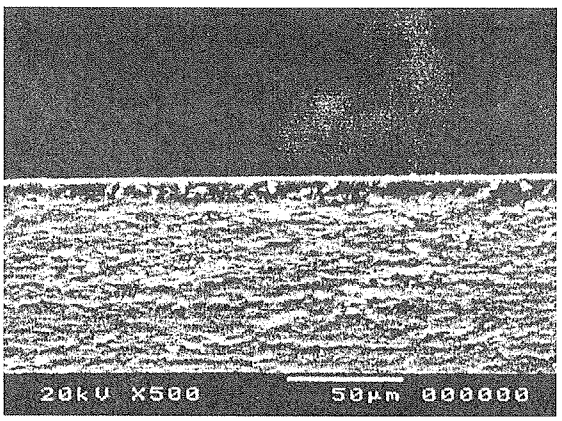
第２図　炭素三角柱微小プリズム

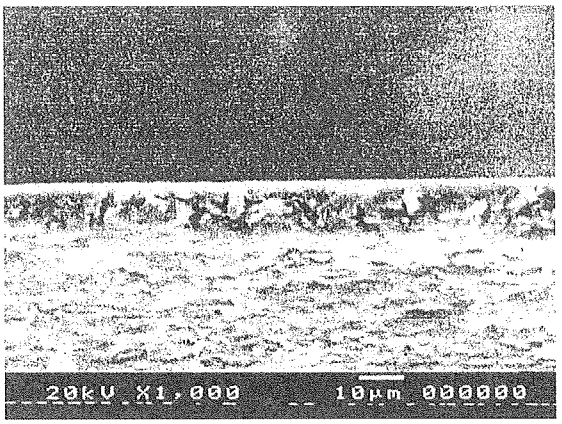
表面の平滑性を SEM で観察した結果を第３図及び第４図に示す。表面における多少の孔構造は観察されるが良好な平面性が得られている。中性子屈折は表面全体で行われるため平面部分と孔部分との面積比が屈折効率となり、形状的には完全な平面でないが、十分な屈折が期待できることがわかった。





第３図　三角柱プリズム表面（１）

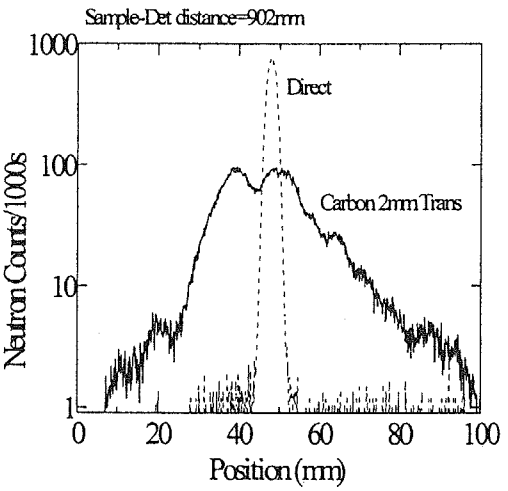




第４図　三角柱プリズム表面（２）

４．材料の小角散乱効果

屈折レンズ用炭素材の中性子透過率をJRR-3M C3-1-2 で測定した。試料は厚さ2mm の平板とし、ダイレクトビーム幅5mm、入射中性子波長 1.26nm 、試料・検出器間距離を 902mm とした場合の中性子透過特性を第５図に示す。



第５図　単色中性子（波長 1.26nm）の炭素素材（厚さ 2mm）透過率

炭素の全断面積から予想される３７層構造屈折式レンズの平均透過率が、入射中性子波長 1.0nm に対して 0.40 と計算されるのに反して、本測定の結果ではわずか 2mm の厚さを透過するだけでダイレクトビームのほとんどが散乱されてしまっていることが明らかになった。

検討の結果、材料中に存在する空孔による小角散乱が、この予想外の散乱の原因であることが判明した。波長 1.0 nm の中性子が入射角 60° で炭素斜面に入射した場合の、一回の屈折によるビーム方向の曲がり角は約 $2x10^{-4}$ rad である。それに対して小角散乱による散乱角の方がはるかに大きいため、入射中性子のほぼすべてが散乱によって除去されてしまうことになる。この結果、物質レンズの材料選定においては、その元素の断面積についての検討をするばかりでなく、材料内の空孔による小角散乱の検討も必須であることが明らかになった。

５．まとめ

炭素材を用いた微小プリズムの組み合わせによる屈折レンズの製作を検討した。その結果、材質の元素固有の断面積ばかりでなく、材質内空孔がもたらす中性子小角散乱が死活的な効果を及ぼすことが明らかになった。このため炭素材料を利用して屈折レンズを製作することは断念し、小角散乱成分を持たない材料の選定から再検討を行った。また微細プリズムの加工についても新たに検討を進めた結果、現在は理化学研究所のグループが中心となって石英を使用したフレネルレンズ型の屈折レンズの開発を進めている。現在その特性測定を進めている段階である。

屈折型の場合、小屈折角に対しては透過レンズ厚みが少ないため中性子損失が少ないが、大屈折角に対しては、透過レンズ厚を極力薄くしても損失が大きくなりやすい。将来的には、大口径部分は反射鏡型とし、小口径部分はレンズとする組み合わせを用いることことにより、より大きな範囲にわたり効率的な収束が可能になろう。

参考文献

[1] P.Mikula et al., ICANS-XV, KEK Proceedings 2000-22, (2000)600-604.

[2] D.Mildner et al., J. of Neutron Reserch 1(1993)1-11.

[3] M.A.Kumakhov et al., Nautre 357(1992)390-391.

H.Chen et al., Nature 357(1992)391-393.

[4] I.S.Anderson, SPIE Vol..983 Thin Film Neutron Optical Devices (1988)84 -92.

[5] A.I.Frank, Nucl. Instr. and Meth. in Phys. Res. A284(1989)161-170.

[6] Y.Kawabata et al., Nucl. Instr. and Meth. in Phys. Res. A420(1999)213-217.

[7] M.R.Eskildsen et al., Nature 391(1998)563-566.

成果の公表

（特許）

清水裕彦、奥隆之、川端祐司

”中性子ビーム制御装置及び中性子エネルギー測定装置”

特許第３０４８５６９号、平成１１年特許第０６０６３０号

（平成１３年度文部科学大臣選定第６０回注目発明）

（研究会発表）

川端祐司、

”炭素研磨鏡及び微小プリズムの開発”

低速中性子制御技術ワークショップ報告書（平成１１年度・第１回） p.99 - 117 、１９９９年.

2-7

中性子ラジオグラフィによる米沢藩火縄銃製造技術の解明

Neutron Radiography of Firelock Gun of "Yonezawa-Han" Make

新潟大学教育人間科学部　鈴木　賢治，荒木一郎
Kenji SUZUKI, Faculty of Education and Human Sciences, Niigata University

1．緒　　言[1]

種子島に伝来した火縄銃の尾栓はねじ加工が施してあり，それにより初めて日本人がねじを知ることになる．その後，鉄砲鍛冶が種子島に誕生し，和泉の堺，近江の国友など火縄銃製造の拠点が形成され，やがて日本全土に火縄銃の製造が広まった．火縄銃は戦国時代の兵法を大きく変革し，日本の歴史において大きい意義をもつ．また，火縄銃の製造技術は，その時々の日本の生産技術の水準を知る上で貴重な歴史資料でもある．

新潟の高田上杉家の家老の直江兼続は鉄砲の威力に着目した一人であり，軍備の増強に熱心であった(1)．そして1592年（文禄元年）に，上杉景勝は豊臣秀吉と共に朝鮮に渡り多いに軍功を上げ，1598年には秀吉の命により上杉景勝は越後から会津若松へ国替えとなり(2)，重臣の直江兼続は米沢に30万石を与えられた．しかし，1600年の関ヶ原の戦いでは上杉氏は石田三成方につき，翌年には徳川家康に降伏し，会津から兼続の所領の米沢藩に移封された．その後も上杉家では鉄砲作りを製造を止めることなく，1614年の大阪冬の陣では徳川方について680挺の鉄砲と50挺の大砲を持って参戦している．徳川時代になり鉄砲製造が下火となってからも幕末まで鉄砲の製造は秘密裏に続けられた．米沢藩火縄銃製造の方法は口伝によるために明確な製造方法や製作図は現存せず，その銃身の尾栓部の構造も不明である．現存する10匁，20匁，30匁銃のすべての尾栓部は固く締結された状態であり，ねじ構造であるのか判明していない．一説によれば，鋳付けであると引用されている文献も見られる(1)．さらに時を経て太平洋戦争の金属拠出，戦後のGHQによる武装解除に伴い，米沢藩火縄銃の数は大幅に減った．

米沢藩古式砲術保存会は，米沢藩火縄銃の保存と稲富流砲術を保存し，現在も銃身に火薬を詰めて実演射撃し，砲術文化を伝承している貴重な団体である(図1)．製造より二百年近く経ており，実射による銃身の経年劣化，製造の完全度も不明であるために，

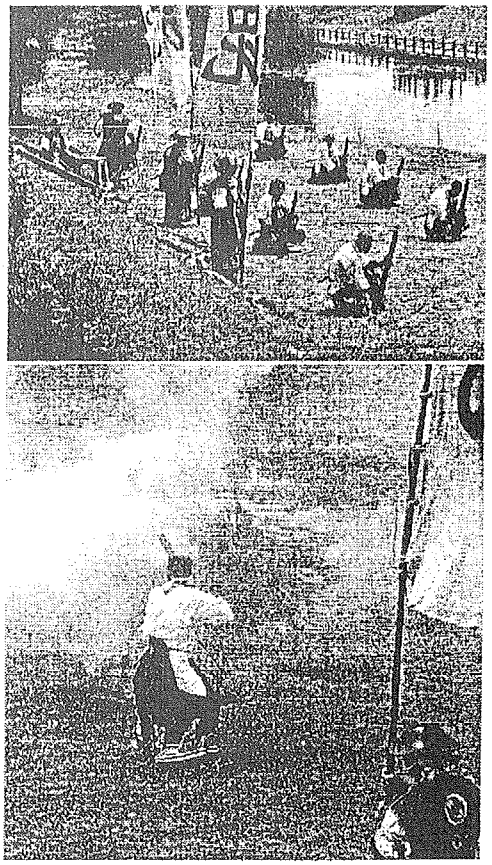


図1: 米沢藩古式砲術保存会

銃身に鍛造割れなどの欠陥がある場合は，重大な事故をまねく心配もある．

数少ない米沢藩火縄銃を切断して，構造や鍛造の検査をすることは文化財の保存の点で行うことはできない．中性子は鉄鋼材料に対する強い透過力をもち，火縄銃などの厚い鍛造品のラジオグラフィに適している．これまで火縄銃の透過写真を撮影した例はなく，火縄銃の中性子ラジオグラフィの有効性についての知見は得られていない．ねじ工業協会が火縄銃ねじ類の調査をした報告(4)があるが，その文献には，種子島博物館所蔵のポルトガル伝来銃と国産第1号の

[1]JRR-3M 7R，中性子ラジオグラフィ装置，技術史

表 1: 調査した米沢藩火縄銃の諸元

	10 匁筒	20 匁筒	30 匁筒
銃身長さ（尾栓を除く）	665 mm	662 mm	632 mm
銃身質量（尾栓含む）	5.1 kg	7.0 kg	10.5 kg
口径	17.7 mm	23.9 mm	28.6 mm
基部外径	43.2 mm	51.0 mm	64.5 mm
先端外径	37.0 mm	42.5 mm	54.0 mm
製作者	岡村九右衛門宗光	不明	不明
製造年	文化 10 年 (1813 年)	不明	文政 2 年 (1818 年)

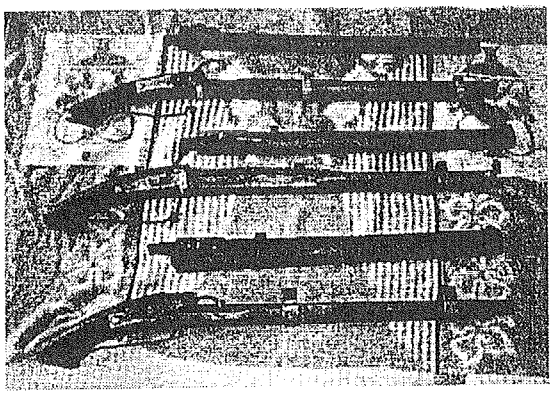


図 2: 米沢藩火縄銃の銃身部（上）とカラクリ・銃床部．上から 10 匁，20 匁，30 匁

火縄銃の調査の顛末が詳しく記されており，尾栓部の分解が実現できなかったこと，この銃の構造解明を目的としたX線ラジオグラフィが未だ実施されていないことが記されている．

以上のことから，米沢藩の火縄銃の中性子ラジオグラフィにより

1. 銃身の構造と銃身鍛造の完成度
2. 銃身尾栓の締結方法，ねじの製造方法
3. 銃身の欠陥等の検査による健全性の評価

を明らかにすることは重要である．本研究では，米沢藩火縄銃の中性子ラジオグラフィを行い，上記の課題を解明する．また，中性子の有効性と特徴も検討する．そのために，中性子に加えてガンマー線検査を同様に行い，中性子とガンマー線の比較も行う．

2．実　験　方　法

2・1　火縄銃

用いた米沢藩火縄銃は，10 匁筒，20 匁筒および 30 匁筒の各 1 本である．その寸法などを表 1 に示す．また，外観を図 2 に示す．これらの火縄銃は現在も実射しているもので，保存の状態も他のものと同様である．火縄銃の機関部，銃床などについては分解組立も行えるが，銃身と尾栓は固く締結され分解はできなかった．

米沢藩火縄銃は文化財であると同時に，銃刀法に登録された銃でもある．火縄銃の銃刀法登録を解除すると廃棄しなければならず，以後実射することは困難となる．そのため，火縄銃を分解し機関部等を外し銃身部のみにし，銃身部を火縄銃の一部品として原子炉に搬入し中性子ラジオグラフィを行うことにした．

2・2　中性子ラジオグラフィ

中性子ラジオグラフィの利用施設は，日本原子力研究所東海研究所の研究用原子炉 JRR-3 である．原子炉特性は，軽水減速冷却プール型，最大熱出力 20MW，20%濃縮燃料，最大熱中性子束 2×10^{14}n/cm^{2}sec である．

中性子ラジオグラフィ装置は，JRR-3 の水平実験孔から導かれた 7R のものを利用した．ラジオグラフィは線強度 1.9×10^8n/cm^{2}sec 中性子束を銃身に 2 sec~12 sec 間照射し，銃身背面に設置した中性子イメージングプレート透過像を記録した．

中性子照射により銃身が放射化するので，照射後の線量を測定し十分安全な強度まで減衰した後，照射室のハッチを開け，イメージングプレートを取り出し，読み取りを行った．中性子照射後，火縄銃の放射線が原子炉から持ち出しできるレベルまで低下するのを確認して管理区域から戻した．

2・3　ガンマー線検査

鋼に対する透過力は，X線，ガンマ線，中性子の順に大きくなる．透過力が足りない場合はラジオグラフィが困難になるが，透過力が過大な場合は画像のコントラストが足りなく細部の様子が得にくくなる．火縄銃の材質・寸法に適した照射線の種類を検討するために，中性子線に加えてガンマ線ラジオグラフィも

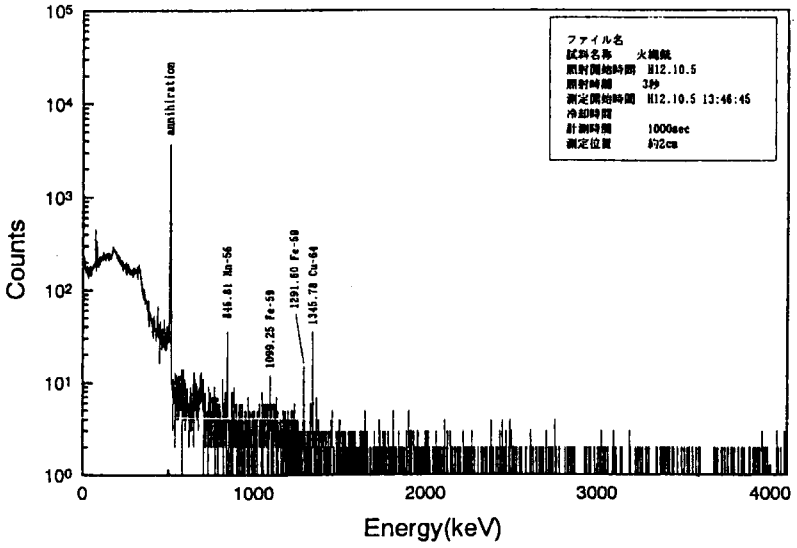


図 3: 火縄銃の中性子照射後の放射線分析

行った．

ガンマ線の線源はイリジウム 192 (^{192}Ir) を用いた．線強度は 250GBq (半減期 72 day)，照射距離 350 mm，照射時間は 8 min (30 匁)，5 min (20 匁)，3.5 min (10 匁) に設定した．画像記録にはガンマー線用感光フィルムを用いた．なお，一般にガンマ線写真はネガ像を用いるが，本研究では中性子画像 (ポジ像) と対応させるためにガンマー線もポジ像にした．

3．実験結果および考察

3・1　中性子とガンマー線ラジオグラフィの比較

中性子を 3 sec 照射した 20 匁銃身の放射線分析結果を図 3 に示す．1000sec の測定で ^{56}Mn (半減期 2.579 hr)，^{59}Fe (半減期 44.6 day)，^{64}Cu (半減期 12.7 hr) の放射性同位元素が生じることがわかった．^{59}Fe の半減期が長いので，長時間中性子照射すると原子炉から火縄銃を取り出せるレベルまで放射冷却の時間が相当かかるので，合計の中性子照射時間を 12 sec 以内とした．

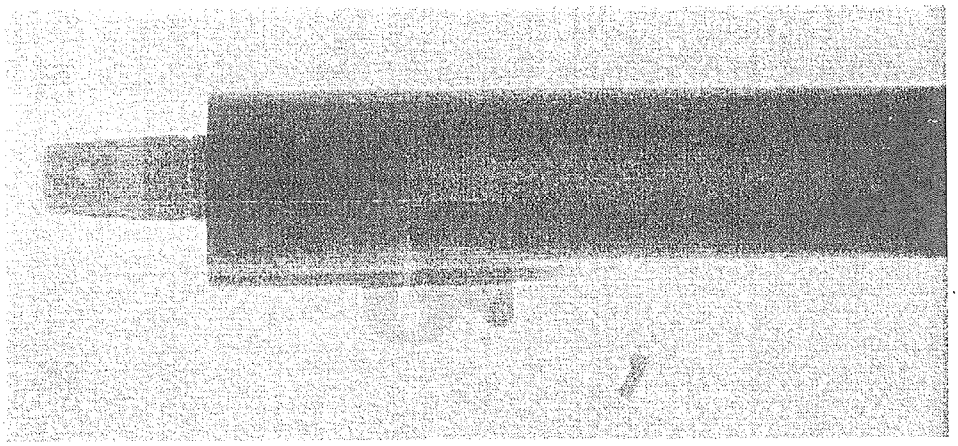
図 4 に 10 匁銃の中性子ラジオグラフィとガンマ線ラジオグラフィを示す．中性子像は鮮明に輪郭が撮像されているが，尾栓部の締結状態は不明である．これに対しガンマ線像は輪郭部は不鮮明であるが，ねじ締結が明瞭に判別できる．また，尾栓部には鍛造割れと思われる縦のき裂が認められる．銃身には鍛造欠陥などは見つからない．中性子よりもガンマ線の方が微妙なコントラストの差が明瞭に判別できることがわかる．しかし，円筒形のために銃身の外周部と中心部では部材の透過厚みが極端に異なるので，ガンマー線ではコントラストが大きくなり，輪郭を判別しにくい．一方，中性子の場合は透過力が大きく外周部と中心部でコントラストの差が出ないので，輪郭が明瞭になっている．

20 匁銃の中性子ラジオグラフィとガンマ線ラジオグラフィを図 5 に示す．この図では，中性子像には尾栓のねじ締結が判別できる．ねじ部のコントラストが生じる撮影条件が見つかれば，中性子でもねじ部の測定が可能である．中性子では，火蓋や火皿の部分がきれいに透過像が得られている．

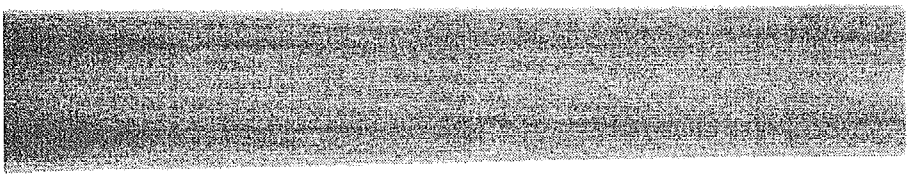
ガンマー線では 10 匁と同様に明瞭に 20 匁のねじ部が判別できるが，火蓋や火皿の部分はほとんどみることができない．ねじ部についてはよい透過像が得られているが，火蓋や火皿や輪郭は像が得られず，中性子とガンマー線を組み合わせることにより銃身全体が把握できる．

30 匁銃の中性子ラジオグラフィとガンマ線ラジオグラフィを図 6 に示す．10 匁銃および 20 匁銃の結果と同様に，ガンマ線では尾栓部のねじ締結が判別できたが，中性子では判別は困難であった．

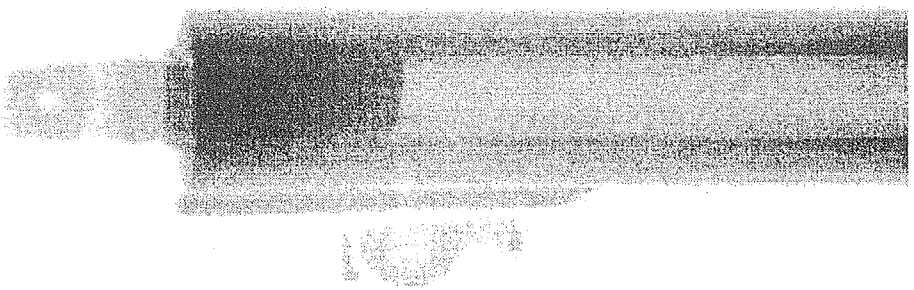
特に，文化財は廃棄処分できないので大量の中性子照射は許されない．そのため，試行錯誤を繰り返して中性子照射時間が長くなることは避けなければならない．中性子ラジオグラフィによる撮影については，種々の撮影条件のデータを系統的に整理されたデータがあるならば，このような撮影の時に適した条件が選定でき大変助かる．文化財などの調査のためにも，



(a) 尾栓部（中性子）

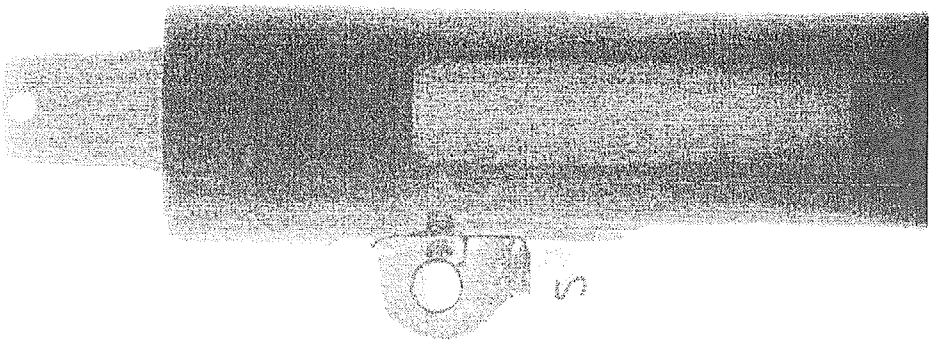


(b) 銃口部（中性子）

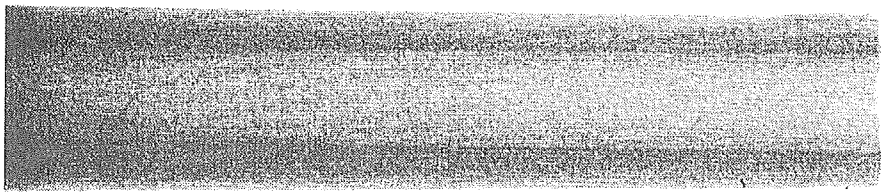


(c) 尾栓部（ガンマ線）

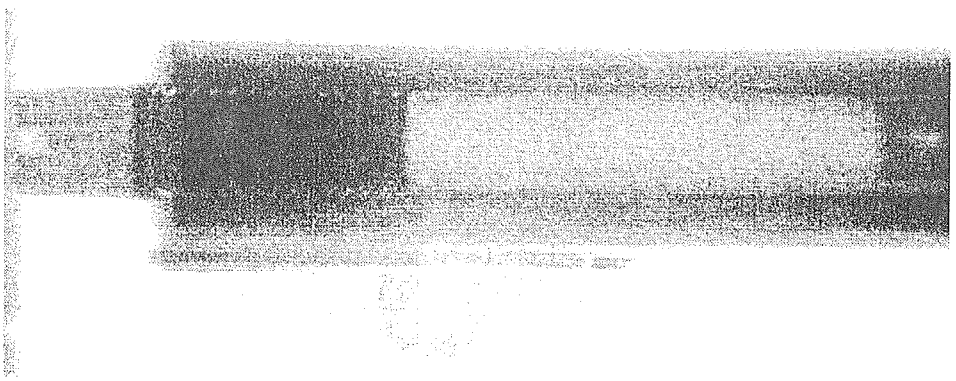
図 4: 10 匁銃身のラジオグラフィ



(a) 尾栓部（中性子）

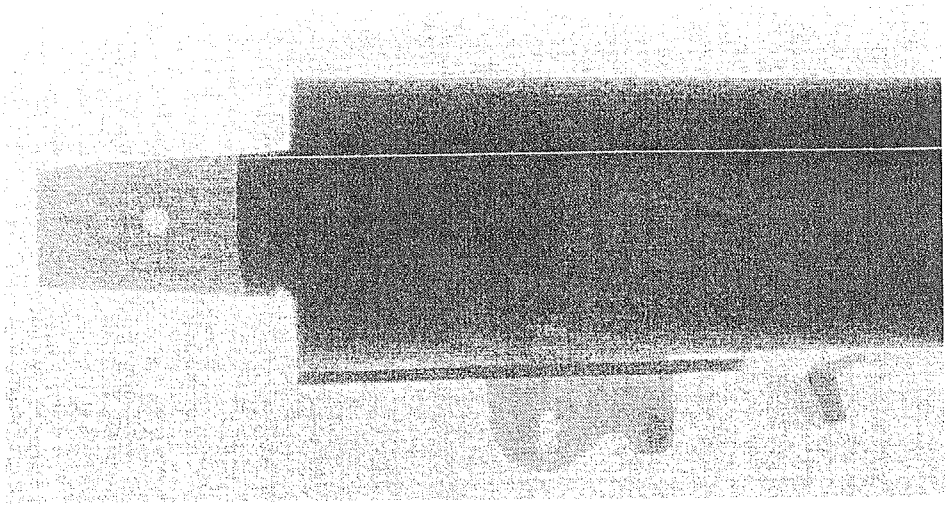


(b) 銃口部（中性子）

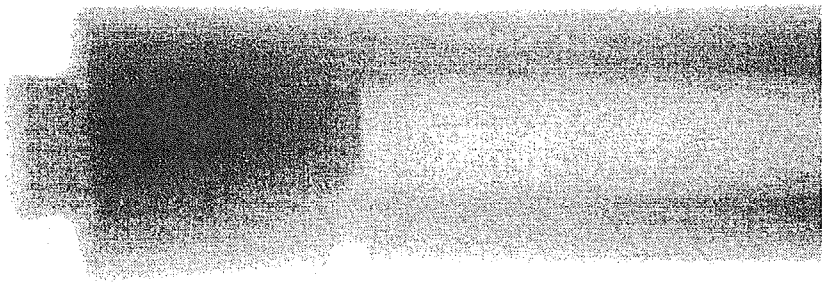


(c) 尾栓部（ガンマ線）

図 5: 20 匁銃身のラジオグラフィ



(a) 尾栓部（中性子）



(b) 尾栓部（ガンマ線）

図 6: 30 匁銃身のラジオグラフィ

そのようなデータベースの構築が望まれる．

米沢藩火縄銃の尾栓は鋳付けという説[3]もあるが，本研究の結果ではねじ締結であることが判明したことは重要な成果である．中性子よりもガンマ線ラジオグラフィの方が，ねじ部の判別には有利であった．輪郭や肉厚変化の大きい物には，透過力の大きい中性子の方が有利である．

3・2　米沢藩火縄銃の製造技術

米沢藩火縄銃の尾栓は，ねじ締結であった．火縄銃のねじの製造方法については，多くの文献があり，加工方法や道具についてもいろいろ研究されている[4],[5]．本研究では，ねじの螺旋の製作法ついて考察する．

表 2: 火縄銃のリード角の比較

	直径 (mm)	ピッチ (mm)	リード角 (deg)
米沢銃 10 匁筒	19.9	3.7	3.39
米沢銃 20 匁筒	25.5	4.5	3.22
米沢銃 30 匁筒	29.5	5.3	3.28
堺鉄砲 [6]	12.3	3.3	4.80
国友鉄砲 [6]	13.5	3.6	4.88
若林家鉄砲 [6]	16.1	4.3	4.86

火縄銃の銃身を上面からガンマ線透過写真を撮影し，さらに銃身を軸まわりに 90° 回転させて透過写真を撮影して撮影することにより，右ねじか左ねじかを判定できる．その結果，米沢藩火縄銃はいずれも右ねじであった．

ねじの外径，ピッチ，リード角の測定結果を表 2 に示す．ねじ山の経やピッチを測定した報告[6]はあるが，リード角に着目した報告はない．表からわかるように米沢藩火縄銃のリード角はほぼ同じ値を持つことから，三角形の型紙を雄ネジに巻き付けねじの螺旋を刻んだことが推測される．堺，国友などの火縄銃のリード角と比較すると，米沢藩火縄銃は細目のねじになっている．現存する火縄銃のリード角を広く測定することで米沢藩火縄銃の製造法の系譜がわかることも考えられる．

4．結　　言

米沢藩火縄銃の 10 匁筒，20 匁筒および 30 匁筒の中性子ラジオグラフィとガンマ線ラジオグラフィを行い，以下の結論が得られた．

1. 米沢藩火縄銃の尾栓はすべてねじ締結であった．
2. 銃身の鍛造の完成度も高く，欠陥は見られなかった．10 匁筒の尾栓には鍛造割れらしきものが確認された．
3. 米沢藩火縄銃のねじはすべて右ねじであった．
4. ねじのリード角はいずれのも同じ約 3.3deg であり，同一の三角形を尾栓に巻いて螺旋を刻んだものと推測される．
5. 国友，堺，若林家鉄砲のリード角と米沢藩火縄銃のリード角は異なり，製造法の系譜が異なる．
6. 中性子線はガンマ線よりも透過力が高くコントラストが少なく，銃身の輪郭を見るのには適しているが，ねじ部のコントラストが小さくねじ山の判別はやや困難であった．
7. ガンマ線はねじ部のコントラストが明瞭であり，ねじ山の判別に適しているが，試料厚さの大きいところと小さいところでコントラストが大きくなり，輪郭などの判定には不適当であった．

中性子ラジオグラフィの手法は科学研究の分野に大きい役割を果たしているが，これらの手法が歴史文化財にも利用され，技術史の解明の手段として広がることを期待する．

最後に，本研究は平成 12 年度原研施設利用総合共同研究（課題番号 185）の援助を得た．また，米沢藩火縄銃は，財団法人宮坂考古館のご厚意により借用させていただいた．以上，記して感謝の意を表します．

5．参 考 文 献

(1) 小野栄，直江兼続の鉄砲製造策，歴史読本，8 号 (1998), p.96.
(2) 花ヶ前盛明，上杉謙信と春日山城，(1984), 新人物往来社．
(3) 岩田勇吉，ねじと鉄砲の文化史，(1994), p.96, 岩田ボルト株式会社．
(4) 相沢富士雄，火縄銃ねじ調査顛末記，日本におけるねじの始まり，(1982), p.101, 日本ねじ工業協会．
(5) 所荘吉，図解古銃辞典，(1987), 雄山閣．
(6) 會田俊雄，わが国におけるねじの起源と火縄銃のねじ，日本におけるねじの始まり，(1982), p.6, 日本ねじ工業協会．

6．成 果 の 公 表

荒木一郎，鈴木賢治，「米沢藩火縄銃の非破壊検査」，新潟大学教育人間科学部紀要，第 3 巻第 2 号，自然科学編，pp. 121-129, (2001).

2-8

熱中性子ラジオグラフィーによる固気系流動層の可視化

Flow Visualization of Gas-Solid Fluidized Bed Using Thermal Neutron Radiography

関西大学工学部機械システム工学科　小澤守，梅川尚嗣

M. Ozawa and H. Umekawa

Dept. Mechanical Engineering, Kansai University

1．研究の目的と意義

近年，石炭や産業廃棄物，さらには一般廃棄物の燃焼炉として流動層が大きな注目を集めている．流動層ではこれら燃料とともにけい砂などの固体粒子を層内に充填し，下部から空気を吹き込むことによって流動化させ，ベッド材の運動による撹拌効果と熱容量によって安定化した燃焼が可能になる．さらに消石灰などの脱硫材を添加することによって炉内脱硫が可能であるだけでなく，ベッド材の熱容量と撹拌効果によって 900℃程度の低温での燃焼が可能となり，環境汚染の元凶でもあるSOx，NOx の排出を極めて低レベルに抑えることができる．さらに燃料の発熱量の変化や負荷変動に対しても柔軟に対応できる装置である．しかしながら内部の流動状態によっては偏析が生じたり，内部の循環不良によるホットスポットの形成とそれに伴う灰溶融，クリンカーの形成，あるいは層内に設置された伝熱管（収熱管）でのバーンアウトを引き起こすことがあり，装置設計上十分な配慮が必要となる．また流動層ボイラや流動層熱交換器においてはその伝熱特性評価に，層材の体積率の時間平均値および変動の周波数や伝熱面近傍での層材の滞留時間の把握が必須である．

そこで本研究ではアルミニウム製容器内に実際の装置で用いられているのと同じ種類，粒度のけい砂をベッド材とした流動層のコールドモデルを構築し，原研の熱中性子ラジオグラフィ装置によって流動化状態にある層材挙動を実時間法にて可視化，録画する．得られた画像データから著者らの所有する画像処理システムによって層材の体積率の実時間での変動特性が定量的に求められる．可視化画像から得られた体積率挙動と，関西大学において行う伝熱実験の結果を総合して流動層内における伝熱特性評価方法を確立するとともに，流動層での層材挙動解析モデル構築のための基礎的資料を得る．

2．研究方法

実験は単一気泡によるベッド材の挙動の解明と気泡流動層内に設置した伝熱管まわりの粒子挙動の解明を目的とした二種類に大別される．従来から気泡流動層中の特性値である気泡の上昇速度の測定や気泡周りのベッド材の動きについての定性的な観測は行なわれているものの，実際のベッド材あるいはエマルジョンの速度の定量的な測定はほとんど行なわれていないこと，そしてそのために粗大粒子が気泡の運動によってどのような影響を受けるのか，定量的な計測データはほとんど得られていなかった．前者はこれらの問題点に対する一つの実証データを与えるものである．また前者の実験を実際の気泡流動層中での粗大粒子の運動にまで拡大して，その粒子の速度変動や姿勢の変化をも調べる．一方，後者の実験では外径 25mm のアルミニウム管を模擬伝熱管として層内に配置し，管まわりのボイド率

JRR-3M7R 中性子ラジオグラフィー装置，熱工学

(空隙率)の時間変化を求める. いずれの場合にも実験装置は同じで, 幅 300mm, 高さ 700mm, 奥行 100mm のアルミニウム製矩形容器内である. ベッド材として 2 種類のけい砂(B 粒子:体面積平均径 218 μm, 密度 ρ_s=2555 kg/m^3 および A 粒子:体面積平均径 62 μm, 密度 2310 kg/m^3).を充填したものを用いた. ベッド材は, コンプレッサからの空気を臨界ノズルと圧力調整バルブによって所定の流量に設定してバッフル板, 分散板を通じて流動層下部から吹き込むことによって流動化される. B 粒子の気泡流動化開始速度は 0.0524 m/s, A 粒子のそれは 0.0068 m/s であった. またそのときのボイド率はそれぞれ 0.44 と 0.57 であった.

テストセクションを構成するアルミニウム板材ならびにベッド材として用いたけい砂は中性子に対してほぼ透明である. そこで気泡挙動をより明瞭に可視化するために, ベッド材に用いたものと同一のけい砂に硫酸カドミウムあるいは硝酸ガドリニウム水溶液でコーティングを施したものを 0.4wt%の割合でベッド材に混入することで中性子に対する色付けを行った. さらにベッド材挙動の観察を容易にするために, B_4Cと粘土を7:3の割合で混合して作成した約 2mm 径のトレーサ粒子をベッド材に混入した. このトレーサ粒子の直径は可視化映像の解像度(約 0.5mm/ピクセル)との兼ね合いで決定したものであるが, ベッド材であるけい砂と比較するとかなり大きな径を有することとなる. 従来の研究から見かけ粘度の値は水と同オーダーから 1 Pa·s 程度であることが報告されていて, 連続体で言えばストークス域にあるとみなしても差し支えないと思われる. したがってトレーサの追従性については本研究の目的に対しては問題がないものとした.

前述の二種類の実験方法についての概略をそれぞれ以下に説明する.

第一番目の実験では, 前述のように気泡, ベッド材ならびに粗大粒子挙動の関係を把握することを目的とした可視化を行った. ここでは外径 38mm のスチロール球の内部にベッド材等を充填することで密度を流動層のバルク密度にほぼ等しい 1500kg/m^3 に調整して粗大粒子として使用した. 実験では, 数個の粗大粒子と, 前述のような色づけ処理を施したベッド材粒子を予め混合した流動層を上記の流動化開始速度のもとで流動化させておく. この状態でエアシリンダと電磁バルブを用いて約 160cm^3 の空気を流動層中央部から急速に注入することで単一気泡を作成した. つまり複数の気泡間の影響が発生しないという点では現実の流動層内部の状態とは異なるが, 気泡, ベッド材ならびに粗大粒子間の挙動を詳細に観察することを念頭においた実験となっている

第 2 番目の実験では層内に中心間距離と管径の比(ピッチ)を 1.2, 1.5, 2.0, 3.0 とそれぞれ 1 列に縦置きの形で配置し, 色付けしたベッド材を充填し, 下部から空気を供給して流動化させた. 可視化については, いずれの実験も日本原子力研究所の JRR-3M 熱中性子ラジオグラフィシステムを用いており, 可視化画像を 30frames/s でビデオ録画している. 得られた画像は, オフセット補正, シェーディング補正を施された後, ボイド率に変換される. また粒子速度の定量化には PTV (Particle Tracking Velocimetry)を用いた. 本実験で得られる情報はあくまでも二次元の投影画像に基づくものであり, 中性子ビームの進行方向(実験装置の奥行き方向)に対する情報は得られない. しかし流動層では主たる挙動は垂直方向(実験装置の高さ方向)に発生すること, ならびに投影画像における気泡の周囲や管周りのベッド材挙動を対象とし, 装置断面 100mm 程度と比較的薄く, ビーム方向にいくつも気泡が重なる場合は比較的少ないことから, ここで得られる情報は充分有益なものであると考えている

3. 実験結果の概要

第 1 番目の実験においては, 層内に混入したトレーサ粒子によって気泡周りのクラウドの速度分布を求めることができた. 層内に混入された粗大粒子の運動は, 気泡および周辺に形成されるクラウドの挙動に強く支配されることが確認された. また粗大粒子の速度, 作用した

力，およびクラウドの速度ベクトルを求めた．また気泡流動化状態においては，粗大粒子の速度そのものは気泡の挙動に依存して大きく変動するが，ほぼ同じ姿勢を保ったまま層内を浮遊することが明らかとなった．なおここで得られたクラウド相の速度分布や，定性的ではあるが粗大粒子の挙動は石炭，RDF などの流動層燃焼炉における層内循環や混合の問題の解明に寄与するものと考えている．

また第 2 の実験では気泡径，気泡の上昇速度，管壁近傍におけるボイド率の変動特性などを求めた．層内に管を配置しない場合には，気泡径は層の厚さ D_t と気相の容積流束 J_G および気泡流動化開始速度 J_{Gmb} から従来より提案されている $1.49[D_t^2(J_G - J_{Gmb})]^{0.4}$ で与えられる結果とよく一致した．一方，伝熱管が挿入されれば有効気泡通過面積が小さくなるため $1.49[D_t H(J_G - J_{Gmb})]^{0.4}$，すなわち管配列のピッチが影響することが明らかになった．また 150mm×140mm の矩形容器内に伝熱管を 3×3 の格子配列にした場合には $1.49[H^2(J_G - J_{Gmb})]^{0.4}$ で評価できる．すなわち管配置を考慮すれば統一的に流動層内の気泡の大きさを決定できることが明らかになった．また気泡は管がなければランダムにその方向を変化させて上昇するが，管が配置されていれば管の存在によって移動方向が制約され，ほぼ垂直に上昇することも明らかとなった．さらに気泡の上昇速度はドリフトフラックスモデルに基づいて精度よく評価できることも明らかとなった．これらの成果は流動層内伝熱管まわりの伝熱特性把握のための基本モデルの構築に有用である．

4. 研究結果に対する評価

今回の成果は流動層における気泡そのものの挙動とそれを支配するベッド材の挙動，ならびに層内に置かれた伝熱管との干渉，粗大粒子と気泡の干渉についてのものである．ここで対象とした現象は基本的には個々の粒子の挙動によるものであるが，それらが集団としてお互いに干渉しあいながら運動する場合には長さスケールが 2 桁程度大きくなり，ここで研究対象とした流動層ボイラなどではさらに装置の長さスケールが 2 桁程度大きくなる．近年離散要素法によって個々の粒子の動力学的干渉を数値的に求め，流動層の基礎現象の解明を行っている研究もあるが，特に本研究で対象とした気泡と粗大粒子の干渉などの問題を扱うにはかなりの困難がある．その意味でもここで明らかにした基本的な特性は流動層の連続体近似およびそれに基づいた二流体モデルに有用な相関式を与えるものとして重要であると考えている．また関西大学において進行中のX線ラジオグラフィーでは困難なベッド材の色付けが中性子ラジオグラフィーでは可能であることから，同じ粒子を用いながら拡散や混合特性を調べることができる点など今後の研究にも大変有利である．ここでは現在進行中の流動層の CT 計測については含まなかったが，これについても平成 13 年度の成果として近く報告できるはずである．学会などを通じての公表に際して，大学における研究者のみならず企業における技術者にもここでの成果が注目されていることを追記しておく．

5. 今後の方針

現在，関西大学において高温流動層の X 線ラジオグラフィによる定量計測が進行中である．これとの関連において熱中性子ラジオグラフィーにおいてはコールドモデルを用いた層内粒子循環特性，前述の流動層の CT 計測，さらに層内における粒子混合と拡散特性などについて平成 13 年度から実験されている．今後これらの成果も合わせて，流動層の数値モデル構築を目指す予定である．

成果の公表

論文(Journal)

(1) H. Umekawa, M. Ozawa, N. Takenaka and M. Matsubayashi, 1999: Visualization of Bed material Movement in a Simulated Fluidized Bed Heat Exchanger

by Neutron Radiography, Nuclear Instruments & Methods in Physics Research, Section A, 424, pp.77-83.

(2) M. Ozawa, H. Umekawa, N. Takenaka and m. Matsubayashi, 2000: Quantitative Flow Visualization of Fluidized-Bed under Normal- and Down-Flow-Mode Operations by Neutron Radiography, Experiments in Fluids, 28, pp.413-424.

(3) 梅川尚嗣，小野寺俊和，小澤守，竹中信幸，2000：二成分系流動層内の気泡と粗大粒子挙動の可視化，混相流（日本混相流学会誌），14-4，pp.451-465.

(4) H. Umekawa, M. Ozawa, T. Onodera, Y. Okura, N. Takenaka and M. Matsubayashi, 2001: Visualization of large-Particle Movement in Fluidized-Bed by Neutron radiography, Nondestr. Test. Eval., 16, pp.377-389.

(5) T. Onodera, H. Umekawa, M. Ozawa, Y. Okura, N. Takenaka and M. Matsubayashi, 2001: Visualization of Bed-Material Movements around Bubble in a Fixed-Bed by Neutron Radiography, Nondestr. Test. Eval., 16, pp.391-402.

論文(Proceedings)

(6) M. Ozawa, H. Umekawa, H., T. Onodera, N. Takenaka and M. Matsubayashi, 1999: Heat Transfer in Cross-Glow Tube-Banks in a Fluidized-Bed with Normal and Down-Flow Mode Operations, PWR-Vol.34, Proc. Int. Joint Power Generation Conference, ASME, Vol.2, 607-613.

(7) M. Ozawa, H. Umekawa and N. Takenaka, 2000: Thermal-Hydraulics in Gas-Fluidized Beds, Proc. of US-Japan Joint Seminar on Two-Phase Flow Dynamics, Santa Barnara, pp.247-263.

(8) M. Ozawa, H. Umekawa, S. Furui, K. Hayashi and N. Takenaka, 2001: Bubble Behavior and Void Fraction in Vertical Tube Banks Immersed in a Gas-Solid Fluidized Bed Model, Proc. Int. Conf. Multiphase Flow, New Orleans, Paper No. 754.

(9) M. Ozawa, H. Umekawa, S. Furui, K. Hayashi and N. Takenaka, 2001: Quantitative Flow Visualization of Fluidized-Bed Heat Exchanger by Neutron Radiography, Proc. Int. Topical Meeting on Neutron Radiography, Pennsylvania, Paper No. 055.

学会発表

(10) 梅川尚嗣，小澤守，小野寺俊和，竹中信幸，松林政仁，1999: 層材流動方向による伝熱特性への影響，第36回日本伝熱シンポジウム講演論文集，403-404.

(11) 梅川尚嗣，小野寺俊和，小澤守，竹中信幸，1999: 流動層内の偏析挙動の可視化，混相流シンポジウム'99講演論文集，127-128.

(12) 小野寺俊和，梅川尚嗣，小澤守，竹中信幸，2000：流動層内縦型管群周りの層材挙動の可視化，日本機会学会関西支部第75期定時総会講演会，No.004-1，pp.5.13-14.

(13) 小澤守，梅川尚嗣，小野寺俊和，古井秀治，竹中信幸，2000：中性子ラジオグラフィによる流動層熱交換器内層材挙動の可視化，可視化情報，Vol.20，Suppl. No.1，pp.343-346.

(14) 林幸一，小澤守，梅川尚嗣，北島哲生，2001：流動層内に設置された垂直管群周りの伝熱特性，日本機会学会関西支部第75期定時総会講演会，No.014-1，pp.6.41-42.

(15) M. Ozawa, H. Umekawa, T. Onodera and N. Takenaka, 2000: Flow Visualization of bubble Behavior in a Fluidized Bed Heat Exchanger Model, 第6回流動層シンポジウム講演論文集，pp.211-217.

(16) 古井秀治，梅川尚嗣，小澤守，2001：流動層内の層材循環の可視化と画像計測，日本混相流学会年会講演会2001，pp.239-240.

研究テーマ：照射後試験及びWASTEF試験に関する技術開発
表　　題：中性子ラジオグラフィによる非破壊試験法の開発

2-9　中性子ラジオグラフィによるジルカロイ被覆管中の水素分布の観察

安田　良，松林政仁[1]，仲田祐仁，原田克也、天野英俊
日本原子力研究所　ホット試験室
1日本原子力研究所　中性子科学センター

本研究では、中性子イメージングプレート法及び中性子断層法(CT 法)の照射後試験に適用することを主な目的として、照射済燃料を模擬した試料を用いて、それらの方法の有効性を検証している。本報告では、水素化物を形成させたジルカロイ被覆管を用いて行った試験の結果について報告する。

原子炉運転中、ジルカロイ被覆管表面の水-ジルコニウム反応により発生した水素は、被覆管中に侵入・拡散し、水素脆化を引き起こすことが懸念されている。そのため、照射済被覆管中の水素の濃度分布は、被覆管の健全性を評価する場合において、重要な知見となる。中性子ラジオグラフィは、水素濃度分布評価法として有効な方法であり、非破壊で濃度分布測定ができる利点がある。そこで、中性子ラジオグラフィの照射後試験へ応用するための基礎データの収集を目的として照射済被覆管を模擬した試料を用いた試験を行った。

本試験では、水素化物を形成したジルカロイ被覆管を用いた。水素化物は、照射済被覆管を模擬するために外周部に偏析させた。試料の水素濃度は、それぞれ異なるように調製した。試験は、JRR-3M 第2撮影室において、中性子イメージングプレート法及びCT 法を用いて行った。イメージングプレート法では、被覆管から長さ5mmに切り出したリング状の試料を用い、リングの中心軸方向から撮影した。CT 試験の場合は、被覆管の側方向から 0°～179° まで 1° おきに回転撮影した。

イメージングプレート法により撮影した画像を図1示す。水素化物が形成している被覆管断面の外周部において、黒化度が他の領域の画像濃度と異なっており、外周部の黒化度が水素濃度の増加とともに大きくなることも確認できる。また、周方向上においても、その濃度が異なっており、水素濃度が形成領域上でも不均一であることが分かる。

水素のCT 法により撮影した画像を図2に示す。イメージングプレートの画像と同様に、水素化物形成領域において、他の領域と画像濃度が異なっている。このCT 試験による水素濃度分布は、文字通り非破壊で得られたものであり、非破壊水素分析の可能性を示唆する重要な結果である。

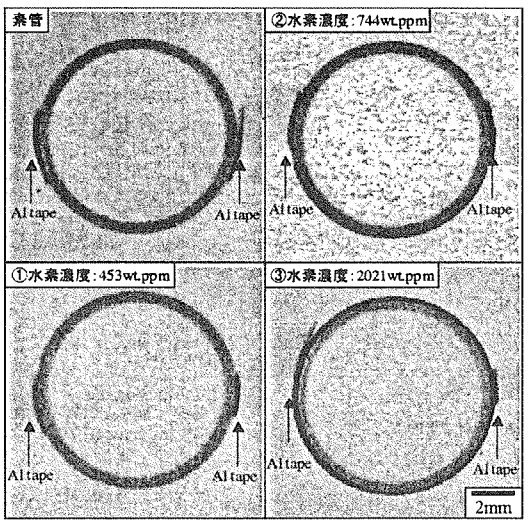


図1　水素化物形成管の中性子イメージングプレート像

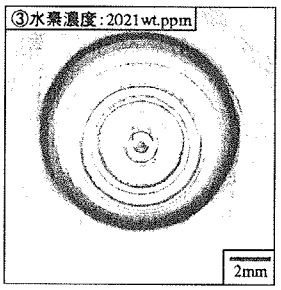


図2　水素化物形成管のCT画像

成果報告論文

(1)題名：Application of Neutron Radiography for Estimating Concentration and Distribution of Hydrogen in Zircaloy Cladding Tubes.

著者：安田　良[a]，松林政仁[b]，仲田祐仁[a]，原田克也[a]

所属　a: 日本原子力研究所　ホット試験室　ホット試験技術

b: 日本原子力研究所　中性子科学センター　中性子利用開発グループ

雑誌：Journal of Nuclear Materials, to be published

(2)題名：中性子ラジオグラフィによる照射済燃料・材料の非破壊試験法の開発(2)
－中性子ラジオグラフィによるジルカロイ被覆管における水素化物及び酸化膜の観察評価－

著者：　安田　良[a]，松林政仁[b]，仲田祐仁[a]，原田克也[a]，安藤均[c]

所属　a: 日本原子力研究所　ホット試験室　ホット試験技術

b: 日本原子力研究所　中性子科学センター　中性子利用開発グループ

c: (財)放射線利用振興協会

レポート：JAERI-Tech 2000-82

(3) 題名：中性子ラジオグラフィによる水素化物及び酸化膜を形成したジルカロイ被覆管の評価

著者：安田　良[a]，仲田祐仁[a]，松林政仁[b]

所属　a: 日本原子力研究所　ホット試験室　ホット試験技術

b: 日本原子力研究所　中性子科学センター　中性子利用開発グループ

2000年原子力学会秋の大会　口頭発表

3. 放射化分析

3. Neutron Activition Analysis

This is a blank page.

研究テーマ：惑星物質における元素の移動・濃集機構の研究
表　　題：岩石風化に伴う微量元素の挙動

3-1 火山灰風化土壌中の微量元素の挙動

上岡　晃、関　陽児、月村勝宏、金井　豊、金沢康夫、濱崎聡志、中嶋輝允

産業技術総合研究所

茨城県の八溝山地南部において、第三紀の凝灰岩風化土壌、第四紀のテフラ（赤城鹿沼軽石層）およびローム（関東ローム層）を採取、粒度分離し、中性子放射化法によって微量元素を中心とする分析を行った。

凝灰岩風化土壌採取地点は、桂村岩船付近の山地斜面、沢の最上流部付近であり、地表から0.2mは黒褐色の腐植質土壌に覆われる。試料は、地表面からの深さ0.1m、0.4mの2箇所から採取した。また、テフラ試料は七会村および笠間市の、ローム試料は笠間市のいずれも八溝層群上に堆積したものを採取した。採取した試料は風乾後ふるいによって、それぞれLL（1～2mm）、L（1/4～1mm）、M（1/16～1/4mm）、さらに水中での沈降速度の差によりS（1/64～1/16mm）、SS（2μm～1/64mm）、CLAY（2μm以下）の6つの粒度フラクションに分離した。これらの試料約100mgずつを、原研ＪＲＲ－４のＴ照射孔で１時間中性子照射し、１週間後および１カ月後の２回、γ線測定を行った。

図１に、深さ0.4mから採取した凝灰岩風化土壌について、Mフラクション中の濃度で規格化した各粒度ごとの元素含有量を示す。REE、Th、Hf、Taなどが細かい粒度、特にCLAYフラクションで濃度が高い。一方Fe、Sc、Cr、Coなど、花崗岩や砂岩風化土壌（98年、99年の年会で発表）で細かい粒度への濃集が顕著であった元素は、凝灰岩風化土壌ではフラクションごとの濃度差が少ない。以上の特徴は、テフラおよびローム試料でも同様である。また、花崗岩や砂岩の風化土壌で見られたジルコンに起因すると思われるHfのSフラクションへの濃集は、いずれの試料でも見られなかった。

REEパターンは、テフラのLLおよびLフラクションにCeの正アノーマリーが特徴的に見られ、酸化的条件下でのREEの溶脱が示唆される（図２）。一方、ロームや凝灰岩土壌では凝灰岩のLLやLフラクションに若干のCeの負アノーマリーが見られるものの、粒度ごとのパターンの差は比較的少ない。

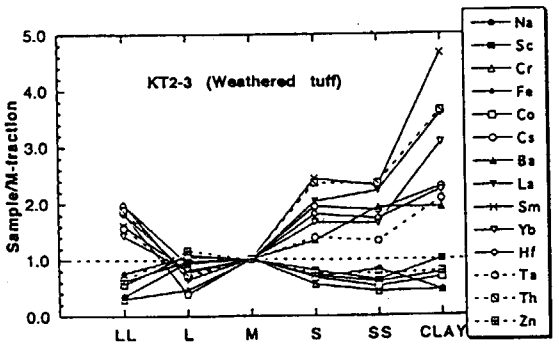


図１　粒度別化学組成

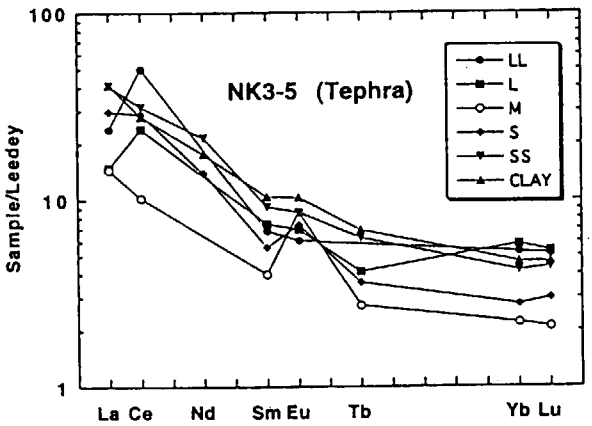


図２　粒度別希土類元素存在度パターン

参考文献

1) 1998年度日本地球化学会年会講演要旨集，（1998），pp.196
2) 1999年度日本地球化学会年会講演要旨集，（1999），pp.160

原子炉：ＪＲＲ－４　　装置：Ｔパイプ　　分野：放射化分析（地球化学・宇宙化学）

研究テーマ：青森県の表層土壌における分配係数
表　　題：青森県の耕作土壌における安定元素の分配係数について

3-2 青森県の耕作土壌における安定元素の分配係数について

塚田祥文、武田晃、長谷川英尚、久松俊一、稲葉次郎
環境科学技術研究所

1. 緒言　土壌に移行した放射性核種は、土壌溶液を介して土壌中を移行し、農作物や地下水へ移行する。そのため、土壌中における固相－液相間の分配係数（Kd 値）は、放射性核種の移行・動態を推測するうえで、極めて重要な環境移行パラメータである。IAEA（1994）によれば、Kd 値は土質に依存した値を示すとされるものの、同類とされる土壌群でも 3～5 桁の変動を示し、移行挙動の評価には、局地域に適した Kd 値を用いることが必要となる。青森県には、多様な土壌群が存在する（12 土壌群）が、そのうち黒ボク土および灰色低地土の耕作土壌を採取し、バッチ法および間隙水法により安定元素の Kd 値を求め、比較・検討を行った。

2. 実験　青森県内で黒ボク土および灰色低地土を、それぞれ 35 および 34 地点から採取した。バッチ法は、土壌試料を 50℃乾燥後、超純水で固液比を 10 とし、20℃で 24 時間接触した後、液相を分離した。一方、間隙水法は、採取後速やかに高速遠心により土壌から間隙水を分離した。土壌および溶液中元素濃度は、放射化分析、ICP-MS、ICP-AES、AAS およびイオンクロマトグラフにより、30 の元素を定量し、Kd 値を求めた。

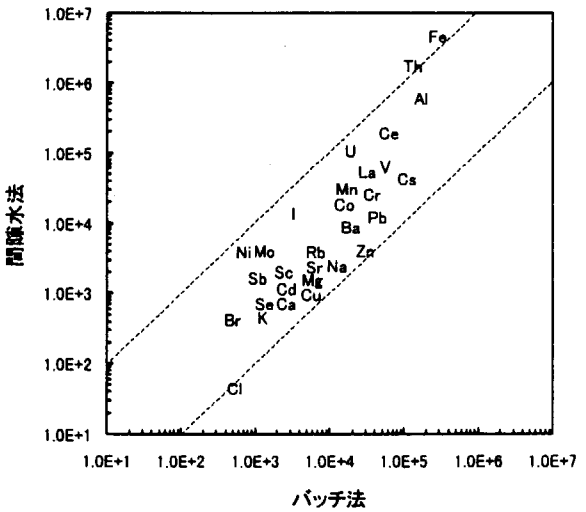


図 1　青森県の黒ボク土におけるバッチ法と間隙水法による Kd 値の比較

3. 結果および考察　Kd 値は、バッチ法により求めることが一般的である。一方、間隙水法は、土壌溶液を高速遠心法によって分離するため、より現実的な値であると言える。ここでは、黒ボク土におけるバッチ法と間隙水法による Kd 値の幾何平均値を比較して図 1 に示した。バッチ法の固液比は 10 としたが、一方、間隙水法に用いた湿土の含水比は 30～90%であり、両者の固液比は 10 倍以上の違いがあった。しかしながら、必ずしも間隙水法に比べバッチ法の Kd 値が高い値を示すのではなく、本研究で求めた 30 元素について両者の Kd 値は、約 1 桁以内で一致した。また、両者の元素間における変動は、類似していた。さらに、灰色低地土についても、同様であった。

バッチ法により求めた Kd 値の±95%の信頼区間は、2 桁以内にあった。以上から、バッチ法により求めた Kd 値は、対象地域において、現実的で、より精度の高い環境移行の評価に適用できることを確認した。

原子炉：JRR-4　　装置：気送管　　分野：放射化分析（環境科学）

研究テーマ：大陸地殻の形成と進化
表　　題：花崗岩マグマの形成と上昇機構

3-3 花崗岩マグマの結晶分化と集積過程：北海道日高帯トッタベツ岩体の例

中島　隆、神山裕幸[1]、上岡　晃

産業技術総合研究所
[1]東京大学地震研究所

本研究は、大陸地殻を構成する花崗岩質岩石がマグマから形成されるプロセスを解明することを目的とし、マグマだまりにおける結晶分化と集積の過程がどのように進行するかを、天然の花崗岩の産状と化学組成から検討するものである。天然の花崗岩としては、かつての地殻断面が現在地表露出していると考えられている北海道日高帯のトッタベツ岩体を選んだ。

トッタベツ岩体は日高地殻断面に貫入した約8kmx10km の深成岩体で、地殻断面の等深面にほぼ平行な層状構造をもち、大局的に下位から上位に向かって苦鉄質から珪長質に移行する。岩体は下位からZone I （層厚7000m）、Zone II （1500m）、Zone III（1500m）に区分される。Zone I, II の構成岩石は Mafic series（斑れい岩，閃緑岩，石英閃緑岩，石英モンゾ閃緑岩）と Felsic series（優白質な閃緑岩および石英閃緑岩）の２岩型に区分され、これらは露頭スケールで互層をなしている。露出の大部分は Mafic series の岩石から成り、Felsic seriesの岩石は通常は1m 以下の薄層として産する。Mafic series の岩石は、Felsic series の岩石との接触部では急冷縁をもつ。Zone III は比較的均質な花崗岩から成る[1]。

これらの各岩相を代表する岩石試料を採取し、全岩粉末試料を調製して中性子放射化分析を行なった。中性子照射は日本原子力研究所の JRR-4 で行ない、測定は地質調査所（現産業技術総合研究所地質調査総合センター）の自動放射化分析装置を用いて、照射１週間後と５～７週間後に行なった。分析工程は 田中ほか (1988)[2] に従った。

分析は Sc, Co, Th など20以上の元素について行なわれたが、本研究では特に希土類元素 (REE) に着目した。REE のうち La, Ce, Sm, Eu, Yb, Lu は中性子放射化分析によって比較的良好な測定が可能であり、これらを地球の仮想始源物質としてのコンドライトにおけるこれらの元素の含有量で規格化した値で、いわゆるREE の存在度パターンを概略的に描くことができる。REE は元素としての性質が似ているため、通常直線的なパターンを示す。一般に珪長質な鉱物は苦鉄質鉱物より軽希土類元素 (L-REE) を多く含む傾向があるので、マグマは分化するほど左上がりの急な直線になる。また、特定鉱物に濃集する元素は直線からはずれた異常を示す。特にEu は斜長石に選択的に濃集する性質があるので、マグマ分化に伴う結晶集積過程の検出に有効である。

今回、トッタベツ岩体の各ユニットの代表的な岩石について得られた希土類元素の存在度パターンを第１図に示す。Mafic series の岩石の中で、細粒急冷組織を示すものは，コンドライト規格化 REE パターンにおいて Eu 異常をほとんど示さない。中粒のもののなかには Eu 正異常を示すものがあり、斜長石の集積が示唆される。一方 Felsic series の岩石は中粒でキュムレート組織を示し、特に斜長石に富む（60～80vol.%）ことが特徴である。全岩化学組成もこれを反映し

原子炉：JRR-4　　装　置：Tパイプ　　分　野：放射化分析（地球化学・宇宙化学）

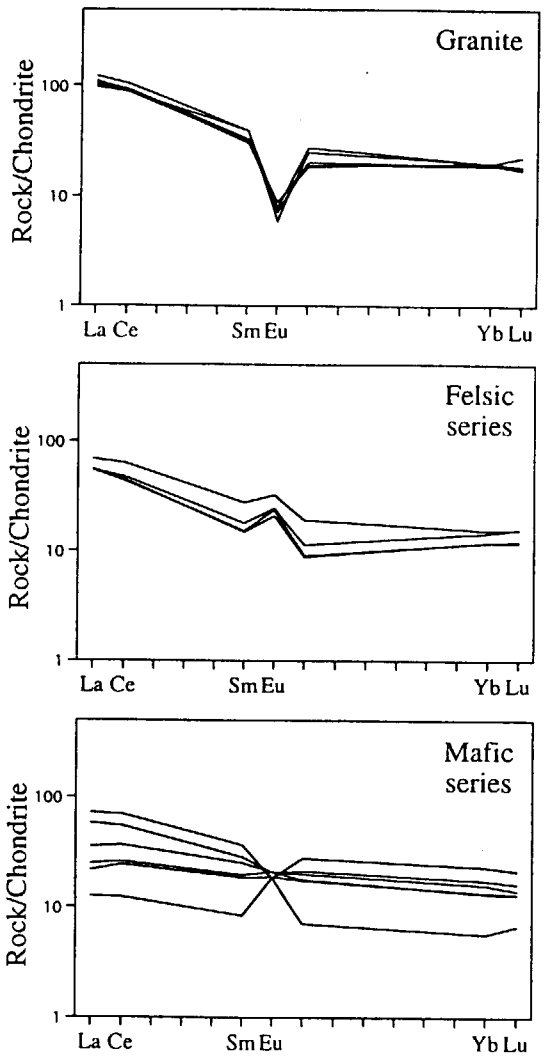


図1　トッタベツ岩体の各ユニットにおける希土類元素の存在度パターン

て，高い Al_2O_3, Na_2O, Sr 量で特徴づけられる。このユニットに例外なく見られる Eu 正異常は Ab 成分に富む斜長石の集積を反映していると考えられ、Felsic series の岩石が珪長質マグマからの集積相であることを示唆する。

以上に述べたトッタベツ深成岩体の層状構造および地球化学的特徴は、分別結晶作用が進行していた珪長質マグマ溜りに繰り返し苦鉄質マグマが注入されたとするモデルで合理的に説明される。このモデルでは、Felsic series の岩石は結晶化が進んでいた珪長質マグマ溜りの底部を構成していた集積岩に相当し、Mafic series の岩石は、マグマ溜りに注入され、その底部に定置・固結した苦鉄質マグマそのもの、あるいはその集積相に相当すると説明される。

一方 Zone III の岩相変化に乏しい花崗岩は、高温マグマの注入が止んだ後の岩体形成の最終ステージでようやく冷えて固結した珪長質マグマに相当するものと考えられ、Zone I, II の岩石と比べて L-REE に富む急傾斜のパターンは、より分化の進んだステージのマグマであることを示す。これらの花崗岩にみられる強い Eu 負異常は、それらが Zone I, II の集積岩と相補的な液に相当することを示すと解釈される。

参考文献

1) 月刊地球，号外 no. 30, (2000), 134-139.
2) 地質調査所月報，vol.39, (1988), 537-557.

研究テーマ：農林生態系におけるハロゲン元素の動態
表　　題：世界の土壌・植物系におけるハロゲン元素の含量レベルと動態の解明

3-4 チュニジア国の土壌および植物

木方展治[1)]、結田康一[1)]、都築克紀[2)]
1）農業環境技術研究所
2）日本原子力研究所（元農業環境技術研究所）

ハロゲン元素(ヨウ素、臭素、塩素)の環境中での易動性は大きく、動植物での欠乏・過剰・汚染問題が生じやすい。

本研究では、これらの元素の高感度・高精度分析法である放射化分析法を用いて、世界各地の土壌・植物系における含量・分布と動態を明らかにする。その中で特に気候や地形条件、土壌や植物の種類、土地利用・農業活動等人為的作用との関連を解析する。

本報ではチュニジア国の土壌と植物を対象とした。

対象土壌と分析法：1)半乾燥ないし乾燥地域(年降水量100～550mm、年可能蒸発量1,200～1,600mm）のチュニジア国内の7地点（図1）の層位別土壌41点とそこに成育する植物（主に葉部）9点を供試。土地利用は、畑地（コムギ，野菜）4、樹園地（オリーブ園）2、自然草原1、砂漠1。土壌中ヨウ素、臭素、塩素の定量：化学分離を伴う放射化分析法。

結果：1)表層土壌中3ハロゲン元素濃度は地点間でかなり大きな差（特に塩素）があるが、平均値はヨウ素6.1，臭素10.5，塩素689mgkg^{-1}乾土で、世界の平均的レベルに比べ、塩素が7倍，臭素は2倍，ヨウ素は1.2倍といづれも高くなっていた（表1）。2）植物葉中3ハロゲン元素濃度は、地点・植物種間で著しい差があるが、平均値ではヨウ素2.7，臭素61.4，塩素17,748mgkg^{-1}乾物で、世界の平均的レベルに比べ塩素は9倍，ヨウ素は7倍，臭素は4倍高くなっていた（表1）。3）かんがい水による3ハロゲン元素の供給がある野菜畑は、降水のみの自然草地に比べて土壌中含量はヨウ素は高く、臭素と塩素は逆に低く、特に塩素は1/10と著しく低くなっていた（図2）。これは、3元素の土壌吸着力の差が反映したもので、土壌吸着力が最も大きいヨウ素は、かんがい水中ヨウ素を吸着することで濃度を高めたのに対し、塩素と臭素、特に塩素はほとんど土壌に吸着されないため、かんがい水と共に下層に浸透したことを示唆していた。4）自然草原（地点1）の塩性植物Salicornia（葉）の塩素，臭素含量は47,341、198mgkg^{-1}乾物と最も高く、オアシス近くの砂漠（地点6）のLygium spartum（葉）はヨウ素含量が9.6mgkg^{-1}乾物と最も高く、臭素，塩素も110、35,581mgkg^{-1}乾物とSalicorniaに次いで高かった。

参考文献

1)結田康一・都築克紀：世界の土壌・植物系におけるハロゲン元素（ヨウ素、臭素、塩素）の含量・分布と動態、－ブルキナ・ファソ、コートジボアール及びチュニジア
日本土壌肥料学会関東支部大会で講演発表(2000)年9月）

原子炉：JRR-3M　　装置：気送管　　分野：放射化分析（環境、農・水産物）

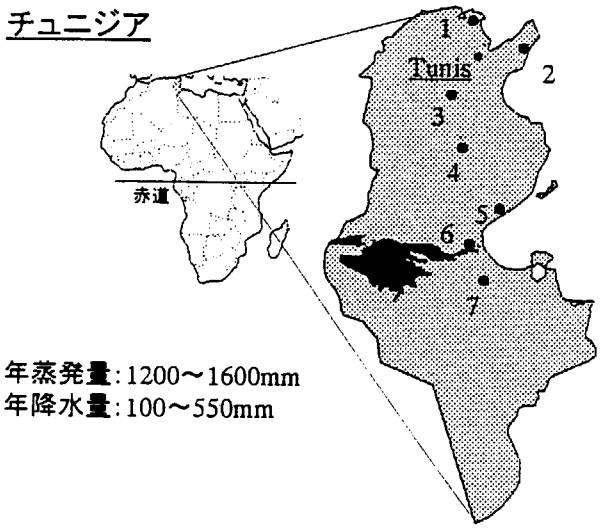
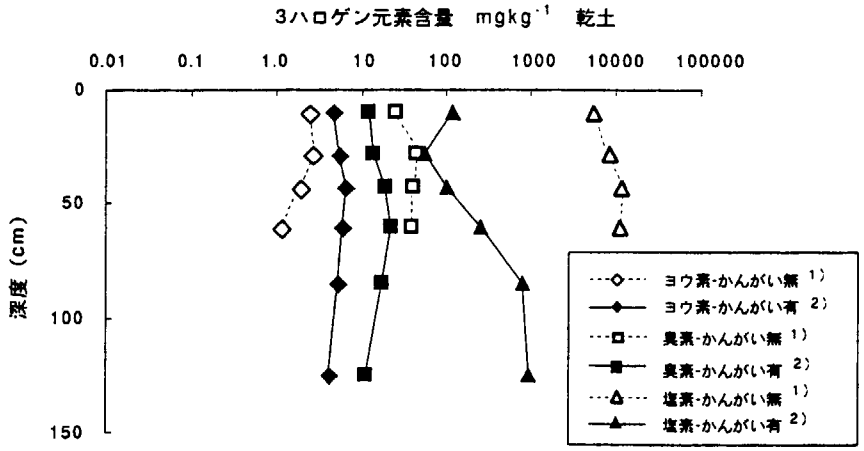


図1　土壌・植物採取地

表1　チュニジアの土壌および植物中のヨウ素、臭素および塩素含量

(試料点数)	表層土壌中含量 mg kg^{-1}・乾土		
	ヨウ素	臭素	塩素
(9)	6.1(2.3～13.7)	10.5(1.5～24.4)	689(7.0～5,259)
世界の平均的レベル	5	5	100
(試料点数)	植物葉中含量 mg kg^{-1}・乾物		
	ヨウ素	臭素	塩素
(6)	2.7(0.22～9.6)	61.4(3.0～198)	17,487(453～47,341)
世界の平均的レベル	0.4	15	2,000



1）自然草原：年平均降水量　470mm、年可能蒸発量　1,350mm、（地点1）、塩類集積が問題

2）野菜畑　：年平均降水量　450mm、年可能蒸発量　1,200mm、かんがい水量が800mm前後あり（地点2）

図2　かんがいによる水供給が土壌（層位別）中ヨウ素、臭素および塩素濃度に及ぼす影響

－非かんがい自然草地とかんがい野菜畑の比較－

研究テーマ：非放射性^{41}Kの長期間追跡のための新たな測定・解析手法の開発

標　　題：放射化分析法利用による安定^{41}Kトレーサ法の開発 3-5 －^{41}Kによるモルモットふん尿の標識化－

木方展治、結田康一
独立行政法人　農業環境技術研究所

三大肥料要素の一つであるカリウムについて、野外環境中で長期かつ自由に使用できる非放射性アイソトープ^{41}Kのトレーサの開発とその利用を図る。

平成12年度は、家畜ふん尿（カリウムが大量に含まれている）の土壌に投与した後の挙動解明に役立つ^{41}K標識物をつくることを目指し、小動物のモルモットを対象に、ふん尿の^{41}Kによる標識化を図った。

実験方法：モルモット（♂3週令、体重250ｇ～）８頭を供試、ルーサン粉末を主体とする配合飼料で１頭毎糞尿分離ゲージに入れて飼育した。毎日１回10時頃（^{41}K投与直後は投与日20時を追加）、糞・尿を採取・乾燥させた後、ミルで十分粉砕・混合した。

^{41}Kトレーサとしては、^{41}K存在比が天然存在比より著しく高いもの（^{41}Kプラス）と、逆に著しく低いもの（^{41}Kマイナスとした）、さらに放射性^{40}Kをトレーサに用いた。これら３種類のアイソトープ（いずれも塩化物）の固体粉末をカプセルにつめ、トレーサとして直接経口投与した。投与したカリウムのアイソトープの内訳を表１に示した。

全カリの分析は、ふん尿試料（尿は固化させた）を灰化、１Ｎ塩酸で抽出した液を炎光光度計で測定した。^{41}Kの分析は、全カリ分析用に調整した１Ｎ塩酸抽出液より、0.1mL秤取後、ポリ袋入りろ紙にしみ込ませたものを作成、非破壊放射化分析法で測定した。^{40}Kはゲルマニウム検出器を用いたガンマスペクトロメトリーによった。

結果および考察

1)糞中の^{41}K存在比（excess％）

糞中の^{41}K存在比（％）（〔糞中の^{41}K含量／糞中の全Ｋ含量〕×100）は、最高で7.71％（0.94excess％）と高く、現在での測定精度excess％＝±0.15の約６倍となっており十分測定可能であった（表２）。［糞中^{41}Kのexcess％／投与した^{41}Kのexcess％］は、最高でも約0.01であり、1/100以下に希釈されたことがわかった。

この希釈率等から算出したモルモットへ投与した^{41}Kの糞への排泄率の経時変化を図１に示した。投与後１～２日後に最大の排泄率を示し、その後は急減し７日後には全く排泄されなくなった。従って、^{41}K標識糞としての利用は、給与後４日までの糞を用いるべきことがわかった。

2)^{41}K，^{40}K，^{15}Nトレーサ実験での検出可能なexcess％

平成12年度以前に実施した^{41}K，^{40}Kのの土壌栽培試験とモルモット標識化実験から検出可能な同位体比変動％を総合的に求めた結果を表３に示した。^{41}Kは0.23～0.15％と^{40}Kより２桁近く低くなっており、今後さらに測定法の改善をはかる必要がある。

なお、本研究は元農水省畜産試験場の宮本進生態機構研究室長と、元農水省果樹試験場の梅宮善章根圏機能研究室長との共同研究として行ったものである。

参考文献

（１）結田康一・宮本進・梅宮善章：非放射性^{41}Kによるカリウムの長期間追跡法の開発－放射性^{40}Kおよび非放射性^{15}Nとの比較－、2000年度日本土壌肥料学会関東支部大会講演要旨集、P35(2000.9.28)

表1　投与したカリアイソトープ

カリウムのトレーサ	カプセルにつめたトレーサ（カプセルで投与）
^{41}K （^{41}Kプラス）	^{41}K存在比95.8%（^{41}K天然存在比6.77%）の^{41}KCl粉末　40mg
^{39}K （^{41}Kマイナス）	^{39}K存在比99.94%（^{39}K天然存在比93.23%）の^{39}KCl粉末　100mg
^{40}K （長寿命放射性）	^{40}K存在比3.15%（^{40}K天然存在比0.0114%）の ^{40}KCl粉末　15mg

表2　モルモット糞中^{41}K存在比%（excess%）と^{41}K存在比で糞での希釈率

試　　料	^{41}K存在比%（excess%）
糞中カリウム	7.71～7.02～6.77（0.94～0.15*）
希釈率（糞中^{41}Kexcess% ／投与^{41}Kexcess%**）	0.0106～0.0017

*excess%±0.15以下は測定が困難　　**^{41}Kexcess%　89.03

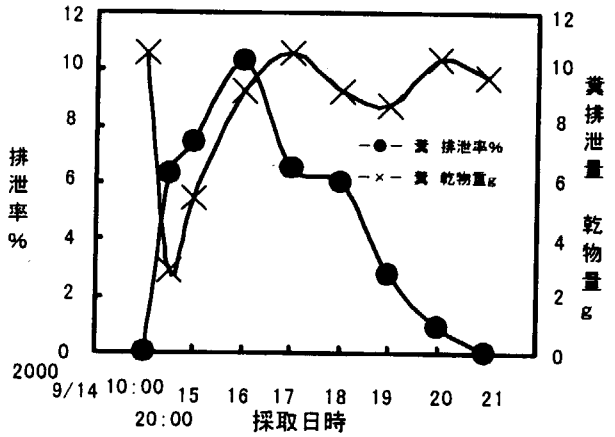


図1　^{41}K標識KCl（カプセル入り）の糞への排泄率（2連の平均値）

表3　^{41}Kと^{40}Kトレーサ実験での検出可能なexcess%

	検出可能な最低同位体比変動%	天然存在比に対する割合
^{41}K	0.23（土耕栽培試験） 0.15（モルモット試験）	0.23／6.77＝0.034 0.15／6.77＝0.022
^{40}K	0.0028. （土耕栽培・モルモット試験）	0.0028／0.0114＝0.25

研究テーマ：中性子放射化分析法の環境影響元素・物質研究に対する新利用法と高度化技法の開発
表　　題：金属元素類（重金属元素等）の同位対比測定法の開発による土壌中の挙動解明

3-6 安定同位体による土壌有機物中重金属の標識化

櫻井泰弘、木方展治、牧野知之、菅原和夫
農業環境技術研究所

環境中の無機元素（Cd, Zn等）の動態解明に資するため、野外での使用が可能である安定同位体(SI)の放射化分析による高精度測定法とSIによる環境物質の標識化法を開発する。本年度は中性子放射化法により検出可能なSIを選定し、これらのSIで土壌有機物（フルボ酸：FA）中の元素を標識化する。

Zn-64(ZnO型)、Cd-108(metal型)およびCd-114(CdO型)を0.1～500 μg g^{-1}の濃度に調製し、ろ紙吸着法で放射化分析により検量線を作成した。土壌有機物は有機物（堆肥、汚泥コンポスト、イナワラ、鶏糞)連用土壌および対照区土壌からアルカリ溶液でFAを抽出した。FA中の元素は陽イオン交換樹脂を用いてSIに置換した。各試料の放射化は日本原子力研究所研究炉JRR-3Mの気送管で5.2×10^{17} $m^{-2}s^{-1}$の熱中性子束を600秒間照射し、1日間冷却後、Ge検出器と波高分析器により生成した放射性核種のγ線スペクトルを計測(200-60000 秒)した。

Zn-64,Cd-114ともに150000 ngまでの検量線が得られ、検出限界はNa-24のバックグラウンド放射のために約30 ngであり、両元素とも放射化分析による検出可能なSIトレーサとして利用可能であることが示された。Cd- 108はZn-64およびCd-114と同一の放射化条件では検出不能であった。有機物連用土壌から抽出・精製したFA溶液を陽イオン交換樹脂を用いてイオン交換するとFA中のCdはほぼ全量、Znは70-84%が脱離した。イオン交換したFA溶液にCd-114、Zn-64の1%硝酸溶液を加え、XAD樹脂に吸着させ精製後、ろ紙法により放射化分析した。FAの単位重量当たりのSI置換量の順を示すと、Cd-114についてはイナワラ施用土壌 FA＞対照区土壌FA＞堆肥施用土壌FA≒汚泥コンポスト施用土壌FA≒鶏糞施用土壌FA、Zn-65についてはイナワラ施用土壌FA＞鶏糞施用土壌FA＞堆肥施用土壌FA＞対照区土壌FAの順であり、施用した有機物の異なる土壌から抽出したFAの各SIに対するキレート能の相違が示唆された。このような方法により土壌FAをSIで標識化し、放射化分析で検出できることが明らかになった。

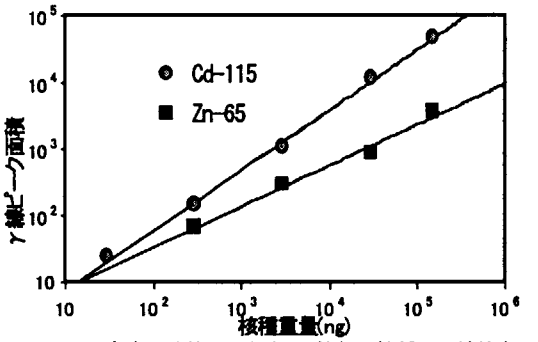


図1　安定同位体から生成した放射化核種のγ線強度による検量線（Cd-115: 0.528MeV, Zn-65: 1.116MeVの各ピークを300秒間積算）

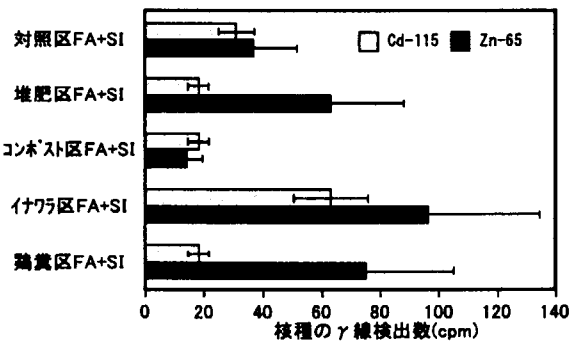


図2　有機物連用土壌から抽出したフルボ酸(FA)の安定同位体(SI)による標識化（図中の標準誤差はZn-65:40%,Cd-115:20%）

原子炉：JRR-3　　装置：気送管　　分野：放射化分析（農・水産物）

研究テーマ:ラジオアイソトープ技術者の養成
表　　題 :実習　放射化分析

3-7 貝殻中の銅・ﾅﾄﾘｳﾑの放射化分析

上沖　寛
国際原子力総合技術センター（東京研修センター）

本研究は、ＲＩ技術者の養成を目的とする研修コースの中で実習教科として行うものである。本報告では、平成12年度の研究炉をもちいた成果として、国内原子力技術および放射線利用に関係する人材養成を行った基礎課程およびアジア・太平洋地域開発途上国の原子力分野人材養成への国際援助としてＪＩＣＡと協力して行った原子力基礎技術コースにおいての実習教科としての放射化分析について報告する。

原子力の基礎として中性子核反応の理論や応用を理解させることは重要である。放射化分析の実際を経験させることはこれらの知識の理解を深めるのに大変重要であり、結果としてガンマ線スペクトル解析による放射能測定法および非密封ＲＩの安全取扱法を習得させることになる。

平成12年度は基礎課程とＪＩＣＡ原子力基礎技術コースの中で5回の放射化分析実習を行った。分析試料は海水産の大アサリであり、炭酸カルシウムをマトリックスにして微量元素を含有する。分析目的核種は、放射化生成核種のガンマ線スペクトルで主成分となるﾅﾄﾘｳﾑ24、放射化生成物が陽電子壊変を伴い陽電子消滅ピークを主要放射線ピークとする銅64である。照射条件は研究炉の気送管で2～5分間照射とし、ナトリウムと銅の標準試料と共に大アサリ貝殻の照射を5回行った。

銅の分析：

銅64の陽電子消滅放射線は、他の放射化生成核種からの高エネルギーガンマ線や宇宙線が物質にもたらす電子対生成による放射線と同一放射線であるから、銅64の分析には化学分離を必要とした。簡単な銅の化学分離法として金属亜鉛により銅イオンを還元させて銅の沈殿分離を行った。この化学分離の操作は、30分間の所用時間で0.1ppm Cu 濃度に対して5%の精度で分析された。本実習は、生成核種を同定および定量することにより核反応の理解を深め、ＲＩ実験における放射線被ばくに対する工夫、除染、サーベイ等、一連の安全取扱いの基礎を習得させるものとして有効であった。

本実験による研修生の被ばく線量は、線源が10^6Bq位に対し最大1μSv程度であった。

原子炉：JRR－3M、JRR－4　　装置：気送管　　分野：放射化分析（環境）

研究テーマ：標準土壌試料の放射化分析
標　　題：標準土壌試料中の微量元素の定量

3-8　灰化による標準土壌中元素の損失率評価＊

Loss of elements in IAEA standard soil under ashing conditions

高橋正人、黒沢節身、間柄正明、桜井聡、半澤有希子、臼田重和
初川雄一[1)]、藤暢輔[1)]、大島真澄[1)]、篠原伸夫[1)]、早川岳人[2)]
環境科学研究部、環境技術開発グループ、
1) 物質科学研究部、原子核科学研究グループ
2) 光量子科学センター、自由電子レーザー研究グループ

極微量元素の同位体組成を高感度で測定できる ICP-MS を環境試料分析に適用する場合には、試料の完全な溶液化が必要となる。試料の溶液化方法についての検討では試料中の不溶解元素量を直接測定することが必要で、これまで非破壊放射化分析法が行われてきた。しかしながら、対象となる環境試料では Na 等の多量に含まれる元素の妨害によって、微量成分のγ線測定による定量が困難である。今回は IAEA 標準土壌試料 soil-7（450℃処理済）を対象として、照射後試料の多重γ線測定[1)]により 18 元素の損失率を同時計測し、溶液化工程の第 1 段階である灰化による元素の損失率を評価した。

試料はマッフル炉にて各温度で 10 時間の灰化処理を行い図 1 に示す重量減少を得た。その後、難溶性の PuO_2 を生じる温度前後（650℃および 850℃）で処理した試料 200mg を分取し、JRR-3 気送管で 10 分間照射、2 日間冷却し密封化処理後、多重γ線測定装置により 1~2 日間測定した。

図 2 に灰化処理後の元素残留割合を示す。図中のプロットは照射試料の単位重量当りの元素含有量にて規格化した値で、エラーバーは灰化処理を行わない試料の測定で得られた含有量のばらつきを示す。650℃処理では、測定した 18 元素の測定精度内での損失は見られなかった。また、850℃処理では約 90%の Br が損失したが、他の元素の有意な損失はみられなかった。植物試料の灰化試験および塩酸系溶液乾固試料での温度処理による元素損失は、650℃以下で As、Br、Cs 等の減少が報告されているが[2),3)]、本土壌試料では、これらの元素の損失は 850℃でも生じていない。これは本試料が花崗岩を主成分とするため、珪素の存在による各元素の化学形態の違いが原因と考えられる。

今後、温度処理後の試料について、酸分解・溶解処理による元素の回収率評価を行うとともに、土壌中に含まれる微量元素の損失の無い溶液化方法を確立していく。

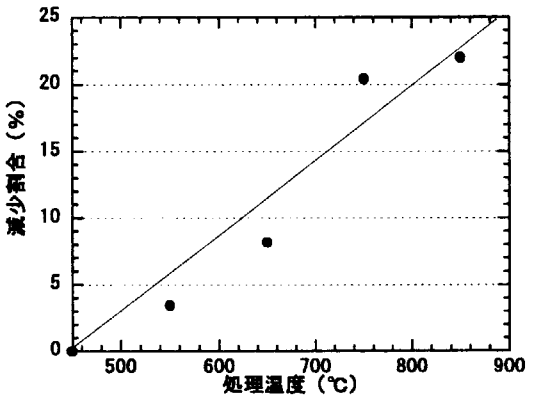


図 1　温度処理による試料の重量減少率（%）

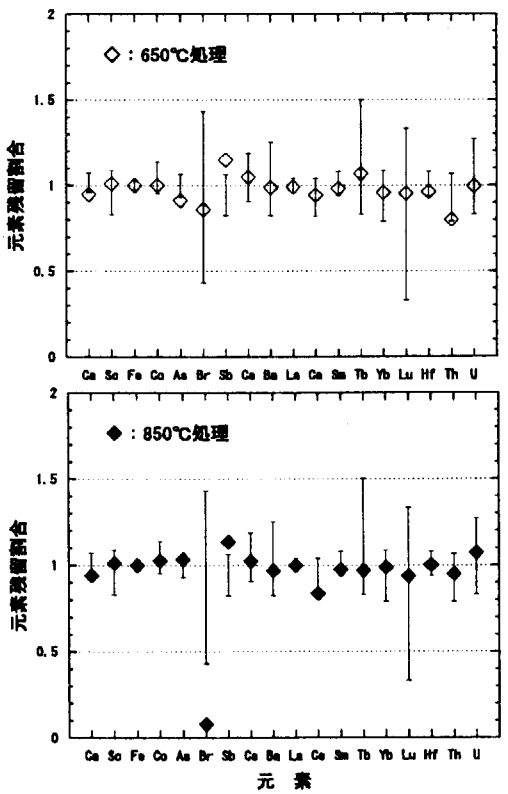


図 2　温度処理前後での元素毎の残留割合

参考文献

1) Application of multidimensional spectrum analysis for neutron activation analysis. Y. Hatsukawa, et. al., J. Radioanal. Nucl. Chem. 248, 121 (2001).
2)「植物試料の乾式灰化に伴う元素の損失」野中信博他　BUNSEKI KAGAKU, 30, 599 (1981).
3)「高温雰囲気中における放射性核種の揮発率の測定」加藤清他　RADIOISOTOPES, 37, 495 (1988).

＊本件は、電源開発特別会計による文部科学省委託研究「保障措置環境分析開発調査」の成果の一部である。

原子炉：JRR-3　　装置：気送管　　分野：放射化分析（環境）

研究テーマ：広域環境モニタリング試料の微量元素分析
表　　題：広域環境モニタリング試料の微量元素分析

3-9 広域環境モニタリング試料の微量元素分析（1）

宮本ユタカ[1]，齋藤陽子[2]，桜井　聡[2]，臼田重和[2]
[1]原研，環境科学研究部，放射性核種データ解析研究グループ
[2]原研，環境科学研究部，環境技術開発グループ

大気に放出された極微量の放射性核種や大気汚染物質の挙動，分布などを評価するために，これらの直接的な輸送媒体である大気浮遊塵の量や組成についてモニタリングすることは重要である。大気浮遊塵はエアーダストサンプラーを使って捕集されることが多い。エアーダストサンプラーは捕集容量や捕集する大気浮遊じんの粒径を分級することができ，目的に応じて大気浮遊じんを捕集することが可能である。また，大気浮遊じんは植物の葉の表面に付着されやすいことが知られている。特に松葉は常緑樹であるため，数年前の松葉を採取することができる。これによって，サンプラーの設置等の手間をかけずに容易に長期間にわたる試料の入手が可能になる。

本研究では，大気浮遊塵の発生起源や環境中における挙動，分布について調べるために，今年度は，放射化分析法を使って次の２点を検討した。①エアーサンプラーで捕集した試料をフィルターと共に照射，分析を行う場合，フィルターに含まれる不純物の量が定量感度や精度に影響を及ぼす。そのため，大気浮遊塵を捕集する際に用いられるフィルターの不純物濃度について分析し，不純物が少ないものを選択する。②松葉表面の付着物を回収し，元素組成分析から付着物の成分を検討する。ここでは，得られた結果の一部を報告する。

フィルターの検討に使った材質の異なるフィルターは，ホウケイ酸ガラス繊維製，シリカガラス繊維製，混合材質，ポリプロピレン製で，1.5cm角に切り，照射試料とした。松葉（クロマツ）は，原研東海研松林で１年目のものを 200 本採取した。得られた松葉は，松葉の表面を洗い落とすために超純水で超音波洗浄し，付着物を回収した。つづいてアセトンにより超音波洗浄し，ワックス層に含まれる付着物を回収した。残った松葉は数日間デシケーター中で乾燥し，細かく切って試料とした。また松葉の付着物との比較のために，アンダーセン型エアーサンプラーで大気浮遊塵を１ヶ月間捕集した。各々の試料は，ポリエチレン製の袋に詰め，JRR-3M の PN-2 で 10 分間または PN-3 で 10 秒間照射した。適当な冷却時間の後，高純度 Ge 検出器で照射試料の放射能測定を行った。比較標準試料に，日本地質調査所製の JB-1a，JA-1，JA-3，JG-1a と NIST 製の Coal Fly Ash (SRM-1633b)を使い，試料とともに照射した。また，Al や Mg 等の放射化分析において，速中性子反応による定量妨害になる Si および Al の影響について高純度試薬による照射により見積もった。

PN-3 照射設備では，Si 1 g の(n,p)反応によって Al 28 μg 相当の Al 定量核種(^{28}Al)が，そして Al 1 g の(n,p)反応によって Mg <3mg 相当の Mg 定量核種(^{27}Mg)が生成することが分かった。ガラス繊維製のものでは Si が主成分であるため，Al の寄与分を補正しなければならない。しかし，Mg については，Al と Mg が同程度含まれている大気浮遊じんや Al に対する Mg の含有量が多い植物では寄与は非常に小さい。

図１にはホウケイ酸ガラス繊維製とシリカガラス繊維製のフィルターに含まれる不純物濃度の結果を示す。ホウケイ酸ガラス繊維の方は，ppm 以上の量で不純物が含まれており，極微量を分析する際には好ましくない。シリカガラス繊維製ならびにポリプロピレン製のフィルターは不純物含有量が少なくこの研究に用いるのに好ましい結果となった。不純物として多く含まれている元素は，分析した全フィルターに，Al は 0.01%-2%，Zn は 10ppm 以上含まれており，ポリプロピレン製では Ti が 0.2%含まれていた。これらの Zn や Ti はフィルターに含まれる白色顔料によるものと思われる。

図２にはアンダーセン型エアーサンプラーで捕集した大気浮遊塵の元素濃度の平均値，松葉表面の付着物，そして松葉について元素の濃度パターンを示す。水およびアセトンから回収した双方の付着物とも大気浮遊じんと類似していることから，回収した付着物は，大気浮遊じんを主な成分としていると推定できる。アセトン回収付着物中の濃度は，超純水回収付着物よりも低いが，これはワックス成分が多く含まれるためである。したがって，水によって松葉表面の多くの大気浮遊じんを回収できることがわかった。

原子炉：JRR-3M　装置：照射設備（PN-2, PN-3）　利用分野：放射化分析（環境）

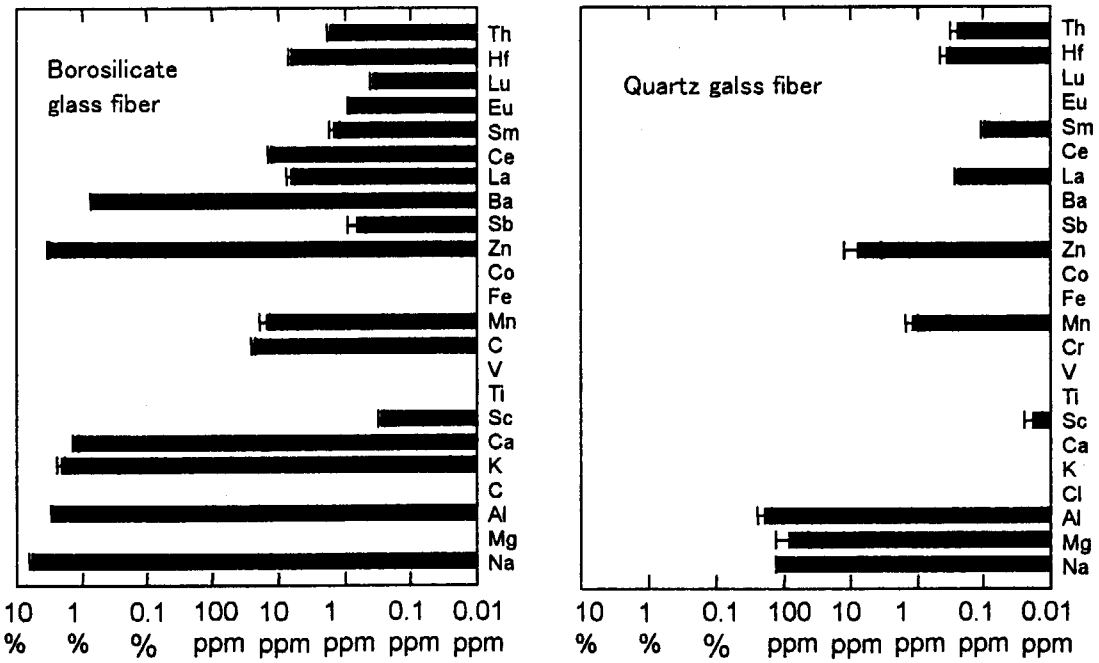
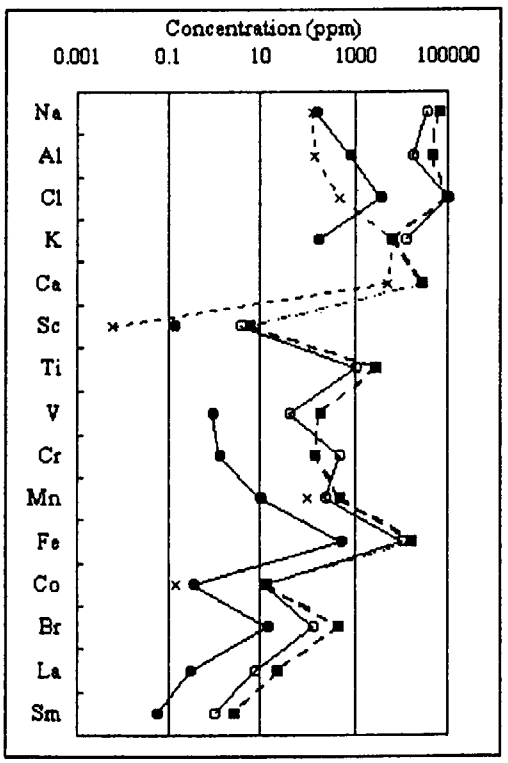


図１　ホウケイ酸ガラス繊維製とシリカガラス繊維製のフィルターの元素濃度



○: Adsorbed compound (Ultra pure water),
●: Adsorbed compound (Acetone),
×:Pine needles, ■:Air particles.

図２　松葉表面の付着物，アンダーセン型エアーサンプラーで捕集した大気浮遊塵，松葉の元素濃度

原子炉：JRR-3M　装置：照射設備（PN-2, PN-3）　利用分野：放射化分析（環境）

研究テーマ：多重ガンマ線分析の分析化学への応用
標　　題：多重ガンマ線分析による長寿命放射性核種の分析

3-10　長寿命核種ヨウ素１２９の分析
Determination of long-lived radioisotope, ^{129}I

初川雄一、大島真澄、早川岳人[1]、藤暢輔、篠原伸夫、櫛田浩平[2]、上野隆[2]

物質科学研究部原子核科学研究グループ

[1]光量子科学センター自由電子レーザー研究グループ

[2]環境科学研究部 陸域環境研究グループ

はじめに

原子核物理の研究において盛んに用いられている、多重ガンマ線検出装置（クリスタルボール）を微量分析に応用することにより、高感度の分析手法を開発した。これを長寿命放射性同位体の測定に応用することにより ^{129}I の検出に成功した。

多重ガンマ線分析

多くの原子核においてはその壊変に伴って複数のガンマ線を放出する。これを同時に複数の検出器で測定を行えば通常の一次元スペクトルと比べて1000 倍のエネルギー分解能が得られることになる。これにより通常の一次元スペクトルではバックグラウンドに隠れてしまうような小さなピークでも分析が可能となることが期待される。この多重ガンマ線の同時検出法はすでに１９６０年代から、いくつもの試みが為されているが、その検出効率の低さのため一般には多く用いられていない。本研究では日本原子力研究所のタンデム加速器に設置されている 12 台の Ge 検出器から成る多重ガンマ線検出装置、GEMINI[(1)]、を用いることにより検出効率の低減をおさえ、尚且つ高い分解能でガンマ線測定を可能にした。

ヨウ素－１２９の分析

この多重ガンマ線分析を中性子放射化分析と組合わせる事により極微量元素分析が可能になる。岩石試料の分析により非破壊分析で含有量４ｐｐｂの Eu の検出にも成功した[(2)]。同様の手法を用いることにより長寿命放射性体の分析にも多重ガンマ線分析と中性子放射化分析を組合わせる事により有効であることが期待される。

1570 万年の半減期を持つ ^{129}I は 37keV のガンマ線を放出するのみであるため、環境中に存在する程度の低レベルの ^{129}I を直接検出することは困難である。最近では加速器質量分析法が開発され高い検出感度での測定が可能になったが、引続き中性子放射化分析は大変有効である。しかし一般には試料中に不純物として含まれる Na などからの生成する放射能によって ^{129}I から生じる ^{130}I からのガンマ線は大きく妨害されてしまい、これを化学操作によって除去しないと ^{130}I を検出することは困難である。そのために行う化学操作は誤差を生じる可能性があり、また作業者の被曝も問題となる。これに関して Ho ら[(10)]はヨウ素の中性子放射化分析の全過程で２０ｍＳｖ程度の被曝の恐れがあると報告している。

本研究では多重ガンマ線分析法を ^{129}I の分析に用いて放射化後の化学分離を行うことなく $^{129}I/^{127}I = 5 \times 10^{-10}$ 程度の低レベルの ^{129}I の測定を可能にした。

^{129}I は天然においては、ウランの自発核分裂や、Xe と宇宙線との核反応によって極僅か生じるが、近年においては核実験や原子力関連施設からの放出が多くなり、環境中の ^{129}I の濃度が注目されている。特にヨーロッパではチェルノブイリ事故や、イギリス、フランスにある再処理施設の影響で濃度は増しており、$^{129}I/^{127}I = 10^{-8} - 10^{-6}$ 程度の高い値が報告されている。[(11)]　一方日本では $^{129}I/^{127}I = 10^{-9} - 10^{-8}$ 程度と報告されている。　また南半球では $^{129}I/^{127}I = 5 \times 10^{-10} - 10^{-9}$ とさらに低い値が報告されている。

本研究では海草試料中のヨウ素－１２９の分析を行った。茨城県内で採取し乾燥させたアラメを約 100 グラム取り、これを灰化させ、化学操作により抽出したヨウ素を PbI_2 にして原子炉で 2－3 時間の中性子照射を行った。

照射した試料を多重ガンマ線検出装置 GEMINI においてガンマ線測定を行った。ガンマ線の同時測定により 2 次元マトリクスを得た。マトリクス中に ^{130}I から発せられた、536-669 keV と 536-740keV のガンマ線ペアが観測されている。このピーク強度と同時に照射した標準試料からのピーク強度との比較により測定試料中の ^{129}I の定量を行った。得られた分析値は $^{129}I/^{127}I = 3.5 \times 10^{-10}$ であった。

また本研究の照射条件や得られたガンマ線の強度から検出限界を考察すると $^{129}I/^{127}I = 10^{-12} \sim ^{13}$ 程度の低レベルの検出が可能であることを示した。

参考文献

１）K. Furumo, M. Oshima, T. Komatsubara., K. Furutaka, T. Hayakawa, M. Kidera, Y. Hatsukawa, M. Matsuda, S. Mitarai, T. Shizuma, T. Saitoh, N. Hashimoto, H. Kusakari, M. Sugawara, T. Morikawa, Nucl. Instr. Mrth. A 421, 211 (1999)

２）Y. Hatsukawa, , M. Oshima, T. Hayakawa, Y. Toh, N. Shinohara, J.Radioanal. Nucl. Chem. **248**(200

原子炉：JRR-3　　装置：気送管

3-11

中性子放射化分析による宇宙・火山起源物質の研究（II）

Geochemical studies on cosmic and volcanism matters by instrumental neutron activation analysis (II)

福岡孝昭[1]　野上謙一[2]　田澤雄二[3]　横田裕子[4]

[1]立正大学地球環境科学部，[2]独協医科大学，[3]京都大学理学部，[4]青山学院大学理工学部

Takaaki FUKUOKA[1], Kenichi NOGAMI[2], Yuji TAZAWA[3] and Yuko YOKOTA[4]

[1]Faculty of Geo-Environmental Science, Rissho University, [2]Dokkyo University, School of Medicine, [3]Faculty of Science, Kyoto University, [4]College of Science and Engineering, Aoyamagakuin University

1．はじめに

本研究の最終目標は、南極を中心とした宇宙塵・隕石の起源を推定するとともに、落下頻度を求めることにある。南極氷床には火山灰層が存在している。これらの給源火山を明らかにすることにより、火山灰の年代を明らかにできる。この年代から氷の年代を求め、宇宙塵・隕石の落下頻度を求めるための時間軸として利用する。南極氷中には世界各地の巨大噴火による火山灰が含まれているはずで、巨大噴火による火山灰の微量元素組成のファイルを作り、氷中の火山灰層のそれとの対比により氷床の年代を求める。

これまでの研究で、宇宙塵等のμgオーダーの微小試料の放射化分析法の手順はほぼ確立した。しかし、宇宙物質としての判定基準になるAu、Ir等親鉄元素用の適当な標準試料がまだない。南極氷中の非溶融宇宙塵はもろく壊れやすいので、高純度の試料の保持体（ポリエチレン等）の開発も必要である。

ここでは、これから一連の研究に関連して過去3年間に行われた研究のうち、第37次南極観測隊（1995-1997年）によって供給された南極ドームFuji基地の生活水造水槽中沈殿物中のガラス質球粒の放射化分析の結果を中心に報告する。

2．試料の純化と分析手順

第37次観測隊によって採取されたドームFuji基地の生活水造水槽の沈殿物が提供された。これは、近年基地周辺に積もった雪100トンを融解した水から得られたものであり、大量の宇宙塵試料が存在すると期待されていた。しかし、沈殿物中には，木片、鉄片、ペンキ片，火山灰、鉱物粒がほとんどで、宇宙塵をすぐに見出すことはできなかった。そこで、図1に示したような純化を行ったところ、非溶融の宇宙塵の他に多くのガラス質球粒の存在が確認された。これらガラス質球粒とJB-1ガラス片（親石元素分析用標準試料）を一粒づつ、約3×3mmの高純度ポリエチレンフィルム袋中に融封し、JRR-3M炉のPN-3（～2×10^{13} n/cm^{2}s）で10分間熱中性子照射し、ポリエチレン袋ごとγ線測定を行い、Al, Mg, Ca, Na, Ti, Mn, V, Dyの分析を行った。その後同一試料についてポリエチレン袋を除去し、合金チップ（親鉄元素分析用標準試料）とともに、1粒づつ高純度合成石英管に融封し、JRR-3M炉HR-1照射孔（1×10^{14} n/cm^{2}s）で70時間熱中性子照射を行った。3日冷却後、石英管から取り出し、3回繰り返しγ線測定を行い、Na, K, Cr, Fe, Rb, Sr, Ba, Sc, REE, Zr, Hf, Th, U, Ta, Co, Au, Ir等の分析を行った。

JRR-4，Sパイプ；JRR-3M，PN-3，HR-1, 2　　宇宙・地球化学試料の放射化分析

表１　INAAにより求められたドームFuji造水槽沈殿物中ガラス質球粒の化学組成

		1	2	3	4	5	JB-1	Error* (%)
Wt	μg	16.8	13.2	12.6	20.1	29.2	45.3	
Al_2O_3	%	15.2	15.5	15.8	14.5	14.9	=14.5	0.5
FeO	%	0.32	0.28	0.33	0.30	0.36	=8.11	6-7
MgO	%	6.9	6.3	6.2	4.5	6.2	=7.7	16-24
CaO	%	37.9	38.7	39.8	35.2	38.7	=9.24	5
Na_2O	%	0.201	0.193	0.205	0.195	0.213	=2.79	0.4-1
K_2O	%	0.35	0.28	0.32	0.33	0.36	=1.42	6-9
TiO_2	%	1.12	1.00	0.89	2.10	0.77	=1.34	13-45
MnO	%	0.16	0.22	0.17	0.15	0.17	=0.16	<3
Cr	ppm	39	25	27	26	30	=414	3-4
V	ppm	1.45	0.22	—	0.136	0.124	=212	5-25
Rb	ppm	6.5	—	6.3	16.9	12.3	=41.2	30-86
Sr	ppm	480	590	450	400	530	=435	17-22
Ba	ppm	760	830	730	690	760	=490	12-16
Sc	ppm	21.2	22.0	22.0	21.1	21.9	=28.9	0.5
La	ppm	51.5	50.9	53.0	50.1	55.5	=38.8	1
Ce	ppm	94.6	97.6	94.5	91.0	100.3	=63	1
Nd	ppm	46.8	46.2	48.4	46.1	51.3	=27	3
Sm	ppm	10.12	9.89	10.39	9.77	10.84	=5.02	0.4
Eu	ppm	2.97	2.86	3.04	2.90	3.22	=1.59	1.2-1.7
Tb	ppm	1.69	1.71	1.77	1.63	1.79	=0.70	5
Yb	ppm	7.7	7.3	8.0	7.3	8.2	=2.4	2-3
Lu	ppm	1.22	1.17	1.27	1.19	1.30	=0.37	3-3.5
Zr	ppm	300	200	410	380	300	=143	26-50
Hf	ppm	5.7	5.8	5.7	5.8	5.9	=3.4	3-4
Th	ppm	13.1	12.7	13.1	13.0	13.3	=9.2	2
U	ppm	8.2	8.2	8.4	8.0	8.7	=1.7	3-4
Ta	ppm	0.31	0.25	0.20	0.27	0.80	=3.6	20-100
Co	ppm	12.1	5.1	1.6	1.7	1.8	=39.1	2-10

* Errors for INAA are due to counting statistics.
1) Totatl iron as FeO.

3．結果と考察

５試料の分析結果を表１に示した。希土類元素（REE）（５試料の平均値）について、C1コンドライト隕石の値で規格化したものを図１にプロットした。一般に宇宙起源である科学的証拠として、Au、Irの存在が挙げられるが、今回の分析結果では検出されなかった。さらにREEパタンは分化したパタンで、コンドライト隕石に見られる未分化で平らなパタンとは異なり、地球物質に見られるものと類似している。これら２点を考えると、ガラス質球粒は明らかに地球起源となる。

ところが、表２で明らかなように、SiO_2含有量が

40%程度である。このような低SiO_2含有量の天然地球物質はマントル物質ということになる。しかし、マントル物質は、Mg、Fe含有量が高くなければならないのに、Feはほとんど含まれず、Mg含有量も低く、Caが異常に高濃度である。地球上の最も普通の人工ガラス（ソーダガラス）の組成はSiO_2とNa_2Oを主成分とし、ガラス質球粒の組成とは大きく異なる（表２）。一方ハンガリーの地層（三畳紀中期～白亜紀後期）中に、形状（しっぽがある（宇宙から地球大気に突入しガラスになったことを想起させる）等）、色等の特徴がそっくり（表３参照）で、主成分化学組成もきわめて類似した（表２参照）ガラス質球粒が存在することが明らかになった。異なる点は、採集された場所（南極とハンガリー）と年代（ドームFujiは現在の積雪、ハンガリーは$65\sim230\times10^6$ YBPの種々の年代）が異なる。これらガラス質球粒の類似性と相違点を考慮すると、その起源候補として彗星が考えられる。それはまだ彗星その物の化学組成が明らかになっていないからである。

４．まとめ

南極ドームFuji基地の生活水造水槽沈殿物から回収されたガラス質球粒は大変興味ある物質である。現段階では宇宙起源か地球物質なのかをはっきりさせることが出来ていない。希ガス組成、同位体分析も含めて今後考察して結論を出したい。

本共同利用研究では、ドームFuji基地の造水槽沈殿物中の非溶融の宇宙塵についても、分析を行い、Au、Irの存在から宇宙起源であることを照明した。しかし、非溶融の宇宙塵は壊れやすく、壊さずに石英管から取り出すことがきわめて困難である。新たな分析技術の開発も必要である。

５．成果の公表

学会誌

1. 田澤雄二・福岡孝昭，物質科学としての宇宙塵研究．地球化学，32，149-159 (1998)

2. Noguchi, T., Imae, N., Nakamura, T., Nozaki, W., Terada, K., Mori, T., Nakai, I., Kondo, N., Sasaki, M., Murakami, T., Fukuoka, T., Nogami, K., Ohmori, R., and Ohashi, H., A consortium study of Antarctic micrometeorites recovered from the Dome Fuji Station. *Antarct. Meteorite Res.*, 13, 270-284 (2000)

学会発表

1. 福岡孝昭・田澤雄二・矢田達・矢野創，南極産非溶融マイクロメテオライトの宇宙起源の化学的証拠．日本惑星科学会1997年秋期講演会，1997年９月．

2. 福岡孝昭・田澤雄二・中村智樹・今栄直也・野口高明・矢野創・中井泉・寺田健太郎・野上謙一・大橋英雄・村上登志男，南極ドームＦ基地造水槽沈殿物中のガラス質球粒の化学組成　—南極宇宙塵予備調査報告—．日本惑星科学会1998年秋季講演会，1998年10月

3. Fukuoka, T., Tazawa, Y., Terada, K., Mori, T., Sano, Y., Nakamura, T., Imae, N., Noguchi, T., Nogami, K., Ohmori, R., Murakami, T., Kondo, N., Nakai, I., and Ohashi, H., Chemical composition of glassy spherules collected at the Dome Fuji Station by the 37th JARE team. The 24th Symposium on Antarctic Meteorites, 1999年６月

4. 福岡孝昭・田澤雄二・野上謙一・横田裕子・野口高明，南極ドームFujiの非溶融マイクロメテオライトの中性子放射化分析．日本惑星科学会1999年秋季講演会，1999年10月

5. Fukuoka, T., Tazawa, Y., Nogami, K., Saito, Y., Noguchi, T., and Yada, T., Instrumental neutron activation analysis of individual Antarctic micrometeorites collected by the 39th Japan Antarctic Research Expedition. The 25th Symposium on Antarctic Meteorites, 2000年６月．

6. 福岡孝昭・田澤雄二・野上謙一・横田裕子，南極ドームFuji造水槽沈殿物中のガラス質球粒の由来．

日本惑星科学会2000年秋季講演会，2000年11月
7. 福岡孝昭，宇宙塵試料の中性子放射化分析．日本物理学会第56回年次大会，2001年3月

出版物
1. 福岡孝昭，微小量試料の機器中性子放射化分析．「放射化分析支援システムの調査に関する報告書」財団法人放射線利用振興協会，315-324（1997）
2. 福岡孝昭，宇宙・地球科学試料のINAAの精度（確度）について．「放射化分析支援システムの調査に関する報告書」財団法人放射線利用振興協会，107-119（1998）
3. 福岡孝昭，宇宙・地球科学試料の機器中性子放射化分析（INAA）．放射化分析，No. 9, 14-23（1998）

表2　ドームFujiとハンガリー地層中ガラス質球粒等の主成分化学組成の比較

	Dome Fuji 5 samples	Hungary (Dosztaly and Don, 1997)	Soda glass
SiO_2*	36-43	37.2-45.5	65-75
Al_2O_3 %	14.5-15.8	8.5-10.6	0.5-4
FeO %	0.28-0.36	0-0.66	<2
MgO %	4.5-6.9	6.5-9.3	0.5-4
CaO %	35.2-39.8	31.1-39.5	5-15
Na_2O %	0.19-0.21	0.28-0.46	10-20
K_2O %	0.28-0.36	0.56-1.23	—
MnO %	0.15-0.22	0.55-1.03	—
BaO %	0.08-0.09	2.18-2.96	—
SO_2 %	?	0.85-1.76	—

*ドームFujiガラス質球粒のSiO_2含有量は他の組成の合計量を100から差し引いて求めた

表3．ドームFujiとハンガリーの地層中ガラス質球粒の化学組成以外の特徴

	Dome Fuji	Hungary (Dosztaly and Don, 1997)
形	sphere, droplet dumb-bell	sphere, droplet dumb-bell
色	yellow, rarely brown	yellow, rarely brown
泡の存在	存在	存在
年代	現在	三畳紀中期～白亜紀後期 (230~65)x10^6YBP)

ドームFuji造水槽沈殿物
（雪100トンの融解）
（木片，鉄片，ペンキ片，火山灰，鉱物がほとんど）
↓
濃　　縮
（サイズ，磁性，沈降速度）
↓
ガラス質球粒のハンドピック
↓
重量測定（マイクロ天秤）
↓
高純度ポリエチレンフィルムに封入
↓
機器中性子放射化分析（INAA）
1. 気送管照射（JRR-3M，PN-3，10分間）
Al，Mg，Ca，Na，Ti，Mn，V，Dy
2. 長時間照射（JRR-3M，HR-1孔，70時間）
Fe，K，Cr，Rb，Sr，Ba，Sc，
La，Ce，Nd，Sm，Eu，Tb，Yb，
Lu，Zr，Hf，Th，U，Ta，Co

図1．試料の純化と分析手順

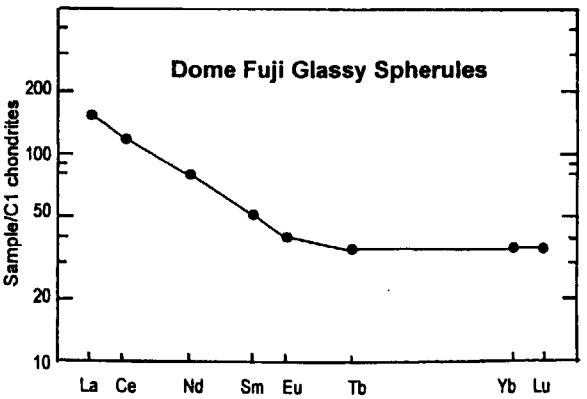


図2．ドームFuji造水槽沈殿物ガラス質球粒の希土類元素パタン

3-12

隕石試料の放射化分析 (III)

永井尚生[1]、本田雅健[1]、 佐藤寛子[1]、海老原充[2]、大浦泰嗣[2]、瀬戸口美奈[2]
([1]日本大学文理学部、[2]東京都立大学理学部)

日本原子力研究所JRR-3M DR-1孔を利用して、鉄を主とする各種の隕石試料中の宇宙線生成核種^{53}Mnの放射化分析に関して、過去3年間の測定結果を報告する。また従来の分析方法に加え、新たに開発した、照射後の化学処理を省略した方法について報告する。

Activation analysis of meteorites (III)

H.Nagai[1], M.Honda[1], H.Sato[1], M.Ebihara[2], Y. Oura[2] and M.Setoguchi[2]
[1] College of Humanities and Sciences, Nihon University,
[2] Faculty of Science, Tokyo Metropolitan University

A long-lived cosmogenic nuclide, ^{53}Mn in extra-terrestrial materials has been determined in the DR-1 hole of the JRR-3M reactor, applying the well-thermalized neutron flux. The neutron flux intensities are variable with the depths whereas the fast thermal ratios are not quite variable. By this method, ^{53}Mn contents in iron meteorites and metal phases in general could be routinely determined in many samples. The chemical separation method has been modified and a convenient short circuit method has been proposed to shorten the process. The short method is to count the activities of ^{54}Mn just after the irradiation without further purification of manganese.

1．はじめに

長半減期宇宙線生成核種としての^{53}Mn($T_{1/2}$: (3.7±0.4)x10^6 y [1]) は鉄に最も近い核種であるために、鉄を主要成分の一つとする地球外物質に多量に含まれており、その測定は重要である。しかしながら中性子不足核であり、EC壊変のみであるので直接放射能測定（Cr KαX線）では感度が不十分であることが多いため、高感度測定法としては現在の所中性子放射化法が賞用されている。その原理は^{53}Mnの中性子捕獲断面積が大きい（80b[1]）ことを利用してその一部を半減期の短い^{54}Mn(312d) に変換し、その835keVγ線測定により、測定感度を2000倍以上にするものである。1965年にH. Millard [2] によって考案された方法であるが、1969年以降今村等[3]によって実用化されてきた。Millardは始め半減期測定に有効であろうと考えた。もし(n, γ)断面積が推定できるなら半減期測定が可能であるはずである。しかしこれは本末転倒であり、半減期が未知であれば、断面積は算定できない。

原子炉中性子は高速中性子を含んでいるた

研究施設・装置
JRR-3M DR-1

研究分野
宇宙化学

めに、普通のマンガン，^{55}Mnが存在すると(n, 2n) 反応によって妨害を受けるが、通常試料中のFe/Mnが100以上で、よく熱化した線束が利用できれば問題は少ない。一般にchondrite（球粒隕石）はこの条件には合わないが、補正により測定は可能である。新3号炉の利用に際しては特にDR孔の上部に照射カプセルを設置することによってこの目的の実現化ををかなり高めることが出来た。

現在chondriteに対しては^{36}Clの場合と同じく、隕石の中から金属鉄の部分をとりだして、鉄隕石とまったく同様に扱って、化学処理する方法をとっているが、これはMnの妨害を押さえるのが主な理由である。^{53}Mnの含量に従って0.1-3 g程度の鉄試料を取り、担体として10-100 μgMn等を加える。以下Mnを分離精製して照射試料とする。従前の方法に従えば、照射後再度Mnの精製を行い担体について化学収率を求めると共に^{54}Mnを計数して標準と比較する。しかしながら最も普通の隕石として存在度の高いchondriteに対してはあと1桁高速中性子束が下げられれば広く適用できるのであるが、残念ながら旧3号炉のような広い利用が出来ない。通常の場合は隕石全体については^{53}Mn(n, γ)による^{54}Mnと^{55}Mn(n,2n)による^{54}Mnとは同程度であるから測定できないわけではない。

2．放射化法による測定実験

1) 標準的な^{53}Mn測定法

(i) 照射前のMnの分離とその後のMnの精製を含めて、Mnの化学収率は50%位であったが、同時に同一試料から^{10}Beや^{26}Al等も測定するし、化学操作の手順が長いので、この程度になるのはやむをえないであろう。精製したMn中の不純物はGe半導体検出器による^{54}Mnのγ線測定に対して殆ど妨害は見られなかった。放射能としては、試料からの、^{192}Ir, ^{51}Cr, ^{58}Co(Niから)、Al箔の不純物からの^{46}Sc, ^{160}Tb, ^{110m}Ag, ^{60}Co, ^{59}Fe, ^{65}Znなどがみられた。

(ii) ^{55}Mn(n,2n)の妨害は担体として加える100μgMn位の共存では、5 dpm程度で、ほとんど問題にならない。化学操作や試料採取におけるMnの汚染は0.1 μgまたは1 ppm以下におさえられるから10 μg以上の担体で十分である。

(iii) 1回の照射に対し20個以上のサンプル処理が実用的におこなわれており手ごろな方法を提供している。

(iv) 照射時間として1サイクル、600時間、25日、を標準としているので、年に1-2回にまとめなければならない。一般に^{60}Coの妨害が低ければ^{54}Mnの半減期に見合った冷却時間が許される。

(v) 照射前のサンプル処理と化学処理及び必要に応じて照射後に化学処理をして精製する。特にFeから^{54}Fe(n,p)^{54}Mnによって副成する^{54}MnはMnの5倍に相当するのでFeは充分除去して10μg以下(equivalent to <50 μgMn)にしなければならないが、この程度のFeの存在は肉眼でも観察できるので通常はほとんど問題にならない。

(vi) Mn/Fe= 0.01を越える試料には適用できないことがある。

(vii) 1 dpm^{53}Mn/kg Fe以下の試料の場合、1g程度の量ではやや感度不足である。

(viii) 立教原研においてCdによる影響を調べた限りでは、epi-thermal neutronの効果は見られなかった。従ってresonance integralは70/2＝35でよいことになる。(G.E. Chart of Nuclides,14th. ed.,1989--)

2) 簡便な^{53}Mn測定法 (Short cut method)

(i) 照射後の化学処理を省略する。

(ii) 照射前の化学処理を十分に行って感度と分解能の優れたGe検出器を使用する。陰イオンカラムの寸法を増倍にするなど、over-loadingを避けることによってCoの除去を完全にする。cooling timeをできるだけ長く（6ヶ月くらい？）とり^{60}Coなど以外の不純物の壊変を待つ。

(iii) 化学収率測定は照射前に行っておく。照射後でもnon destructive INAAの利用ができるが、放射能を更に放射化するのは良い方法ではない。しかし現実にはこの逆になることが多い。収率測定に起因する誤差は大きいことがあるが、この方法によればseparation stepが少な

いので高い収率（70%程度）が期待されるとともに誤差の減少が期待される。
(iv) これによって、hot lab.の操作がいらなくなる。(例えばインドや米国のMn試料もJRR3で照射後、そのまま返送して直接γ測定すれば良い。)
(v) 石英のようなScなどを含まないholderを用いることが望ましいが、Al箔を用いる場合は使用量を減らす（10-20mg, 1cm^{2}程度）ことが要求される。これにより^{46}Sc(1120keV), ^{60}Co (1173 keV) のcompton edgeによる800-900keVのレベルを低下させることができる。
(vi) 通常問題となるのは包装用アルミニウム箔からの^{46}Scと^{160}Tbのほか Fe(1.5-3 μg / 4 cm^2), Ag, Coだけである。分解できない妨害はnatural activity Th系の835.49 keV (^{228}Ac,1.5%)と835.50 keV (^{208}Tl, sum) ぐらいであるが実用的には問題にならない程度である。

このshort cut methodはT9904以降、特別の場合以外に適用されている。

3) 測定結果

最近3年間の分析結果をTable 1に示す。試料は、主として鉄隕石の金属部分であり、その他は鉄隕石の包有物(schribersite, troilite)とchondriteの金属部分である。特に大型の隕石中の表面付近から1000 g/cm^{2}位の深さまでの分布を取っていて^{53}Mnの濃度にして3桁くらいの広い幅をカバーしているのが特徴であり、ほかの放射能の^{10}Be,^{26}Al, ^{36}Cl等のほか、安定な希ガスのデータと比較している。測定値は最高で600 dpm^{53}Mn/kgから、大型の鉄隕石では1 dpm^{53}Mn/kg、^{10}Be,^{26}Alに換算して0.01 dpm/kg, を下回ることも珍しくない。

3．本法の実施状況及び今後の課題

^{53}Mnの重要性については広く認められているが、放射化法の導入実施は容易ではないので広く行われているわけではない。特に適当な原子炉内の照射位置の選択に困難がともない、化学操作が面倒であるために普及していない。近年国外で1985-1990に発表されたJilin chondriteやKnyahinya chondriteの測定結果でも系統的な誤差や再現性にあまりにも問題が多いことが指摘される。我々の1980年に発表したGrant隕石等の内部分布に関する一連の仕事も、相対的な内容については別にしても、絶対値に対して一様に20-30%も過小な値を与えてしまっているのは困ったことである。これらに関して後からきちんと訂正していないことはもっと問題かもしれない。ドイツで始められているように高感度のAMS法に切り替えられる傾向にあるが、精度等にまだ問題が残されている。

1) 測定方法の改良

これまでこの測定の改良と普及が遅れたのは年に1回程度の頻度の実験しかできなかったからである。このために思いきった改良の機会と研究者、特に学生の意欲が損なわれたと考えられる。方法の大筋が1970以来かわって来ていないのはむしろ驚くべきことである。これを解消するにはもっと気軽に頻繁に短時間の照射をも試みるべきであろう。

2) 照射条件

現在の処理能力を抜本的に改善するためには、旧3号炉のように今より桁違いに良い照射位置を見出して含量の低いchondriteでもそのまま測定できるようにすることである。今より２０年前のほうがはるかに進んでいたといえるのは極めて残念である。

3) ^{53}Mn標準試料

現在用いている^{53}Mn標準試料"G-1" solution (Grantより抽出したMn)はほとんどFe, Ir, Co, Ni, Sc, Agのような不純物を含まない優れた標準試料である。放射化分析においては常に^{53}Mnの標準を使用することが望ましいがCo等を利用することも出来る。もちろん濃度既知の鉄隕石を同時に比較試料として使用してもよいが、測定の手順が増加するのであまりよくない。^{53}Mnの標準をいまだに鉄隕石のような天然物から分離したものに頼っていることはおかしなことであり、人工的に調製する方法も可能ではあるが、あまり一般的に行われていない。

絶対値の確定とは別に、相対値の再現性を向上させることも必要である。選ばれた鉄隕石から無担体でMnを分離精製して、比放射能の高

Table 1 隕石中の ^{53}Mn

Run	Name	Class	ID		Source	wt. (mg)	^{53}Mn (dpm/kg)	(±)
T9801	Gibeon	IVA	No.11	m	Casper'97	847.7	4.1	1.2
			No.13	m	Casper'97	252.8	7	3
			No.14	m	Casper'97	706.4	31.2	1.9
			No.1	m	Casper'97	1077.2	53	7
			No.4	m	Casper'97	974.8	4.4	0.7
			No.5	m	Casper'97	1322	[0.3]	0.2
			No.6	m	Casper'97	707	3.8	0.7
			No.7	m	Casper'97	887.6	2.4	0.7
			No.8	m	Casper'97	867.8	1.4	0.7
			No.9	m	Casper'97	738.1	7.2	0.9
			No.12	m	Casper'97	5388.3	2.9	1.6
T9904	Gibeon	IVA	New	m	D.New¬86	2710	2.4	0.2
			L.1	m	Lang'98	7270	0.18	0.12
			98	m	Eisler'98	5020	1.7	0.3
	Nativitas	IIIA	30	m	Huss'63	1482	145	11
			34	m	Huss'63	893.5	134	6
			36	m	Huss'63	1537.6	110	6
	Grant	IIIB	B-281	m	ETH'98	226.8	448	17
T0003	Tawallah Valley	IVB		m	New'87	508.8	415	14
	Canyon Diablo	IA	H37.1078	m	Huss'88	574	259	12
						641.8	231	12
	Odessa	IA	H91.2	m	Huss¬88	807.9	27	5
	Sikhote-Alin	IIB	99.2	m	Eisler'99	20007.5	224	15
				schr.	102.1	216	19	
	Toluca	IA	98	m	Eisler'88	319.9	21	2
	Cape York	IIIA		troil.	Casper'97	862.6	6	1
	Odessa	IA		troil.	Eisler'98	2137.7	17	1
T0009	Gibeon	IVA	99-3	m	Eisler'99	798.9	212	10
	Sikhote-Alin	IIB	9902	schr.	Eisler'99	212	173	8
T0101	DRP78001	IIB	No.59	m	NIPR'00	486.7	87	5
			No.61	schr.		453.6	82	5
	DRP78007		No.75	m	NIPR'00	482.6	125	7
			No.82	schr.		445.7	100	6
	ALH77250*		No.35	m	NIPR'00	548.6	461	17
	Canyon Diablo	IA		m	?	324.7	<3	?
	Allende	C3V	#3529	m	Honda	49.3	209	26
				pentlandite		148.6	183	11
	Gibeon	IVA	L.1	m	Lang'98	3620	0.5	0.2

m: metal fraction, schr.: schribersite fraction, troil.: troilite fraction
*special offer,50g, from NIPR for ^{53}Mn half life determination at TMU.

[postchemistry で収率をおとした,<10%, ため測定不能になったもの]
T9904 run: Odessa,H91.2; Warburton Range, Canyon Diablo 98, Odessa 98, Sikhote-Alin 98, Toluca 98schr., Grant B-281, Odessa 98schr., Canyon Diablo No.4643 [total 9 samples]
T0003 run: Toluca troil.
T0101 run: Gibeon L.3 (too high Ir)
〉DRP〈: Derrick Peak antarctic meteorite,1978;
〉ALH77250〈: antarctic meteorite,1977,

い高純度^{53}Mn試料（G-1と同程度の純度、10ppmMn程度）を研究者に配布出来るような体制を検討すべきであろう。

4) AMS（加速器質量分析）

AMS法は優れた相対値を与えるであろう。比放射能は高くなくても良いので適用範囲が広い。特に濃度の低い大形鉄隕石の深いところの試料、石質隕石、月試料、地球上の試料等、^{53}Mn：^{55}Mn = 10^{-10}以下までも測定できる可能性は放射化法では望むべくもない。ただしそれに見合ったサイズの加速器が必要であり5MV程度では不十分であろう。試料はCrの影響のないものであるほかは特には微量元素の分離はいらないであろう。残る問題は測定の再現性であろう。現在は±15%といわれているが、これまでのAMSの進歩から見ると早晩改良されるであろう。そのような時期迄の間に押さえておくべき問題を解決するのが現状の目標であろう。現在^{10}Beや^{26}Alで求められるAMSの感度に近いものは放射化法で十分実現できるのでテーマによっては、鉄隕石に限ってはそれほど緊急な問題ではない。

5) 異なる標的における^{53}Mnの生成速度

隕石中における^{53}Mnの生成速度の相対比として、これまでNi→^{53}MnはFe→^{53}Mnの約1/3であると報告されている(K.Nishiizumi1987, St Severin metal,high Ni)が、この相対比を正しく見積もることが重要である。原子質量数はそれぞれ56と59に置くことが出来るであろうが、さらにその効果を量的に表現することが求められる。ΔAの違いを遮蔽係数の関数として量的に表現せねばならない。実験的にFe/Niに大きな開きのある試料について比較測定を行いFe/Niの寄与の違いを定量的にする必要がある。

6) Non cosmogenic terrestrial ^{53}Mn

天然に存在する^{53}Mnについては、SCR及びGCRのcosmogenic originを除いては研究が少ない。^{54}Fe(n,2n)^{53}Fe→^{53}Mn, などがinduced reaction productsとして地球物質中で検出されやすいであろう。U, Thからの（α,n）やfission neutronが高い存在度で共存する鉄に作用すれば容易に生成するはずである。問題点は、Mn/Feが高いことと、半減期が長過ぎて良い試料が得られにくいことであろう。^{54}Fe(n,p)による短寿命の^{54}Mnを検出できれば予備実験になるであろう。

[文献]

1) M. Imamura, H.Matsuda, K.Horie and M.Honda (1969) EPSL 6, 165-172.
2) H.T. Millard Jr.(1965) Thermal neutron activation: Measurement of cross section of manganese-53, Science, 147, 503.
3) M.Honda and M.Imamura (1971) Phys. Rev., C4, 1182-1188.

[成果の公表]

1) M.Honda, H.Nagai, and T.Kobayashi, "Cosmogenic Radionuclides in Large iron Meteorites.", 61st Annual Meeting of the Meteoritical Society, (1998.7, Dublin, Ireland)
2) M.Setoguchi, M.Ebihara, H.Nagai, M.Honda, "Measurement for cosmogenic Mn-53 in meteoritic irons.",(abstract), No.34,p.139, 25th Symposium on Antarctic Meteorites, (June 22, 2000, NIPR, Tokyo)Tokyo.
3) 瀬戸口美奈、海老原充、永井尚生、本田雅健,「鉄隕石中における宇宙線生成核種、Mn-53の測定」, 日本地球化学会年会（山形大学）2000年9月山形
4) 本田雅健,「Mn-53の４０年」, 日本質量分析学会同位体比部会, 2000年11月23日, 大分県湯布院

3-13

植物試料の元素分析
Analysis of the Elements in Plants

中西友子、池上奈通子、田野井慶太朗、横田はる美、林芳武、大國曜子、古川純
T.M.NAKANISHI, N.IKEUE, K.TANOI, H.YOKOTA, Y.HAYASHI, Y.OKUNI, J.FURUKAWA
東京大学大学院農学生命科学研究科
Graduate School of Agricultural and Life Science, the University of Tokyo

1．はじめに

植物の生長に関わる無機元素については長い間研究されてきたが、その詳細については未だに明らかになっていない。そこで本研究は、各元素が植物体内でどのように分布し、移行していくのかを明らかにすることで、各無機元素の役割について考察することを目的として、短日植物であるアサガオについて分析を試みた。アサガオ（*Pharbitis nil.* cv Violet）は、特に花について盛んに研究されてきた代表的な短日植物であり、日照条件を制御することで比較的容易に花芽形成を誘導することが可能である。

花芽形成については、環境要因として温度や光が関係するほか、植物体内の生物時計が関与することが報告されている。

以上の背景から、本研究では、明期 12 時間、暗期 12 時間の条件下での栄養成長期から、明期８時間、暗期 16 時間の短日条件に移行させ、花芽形成を誘導する過程での、さまざまな時間に採取したアサガオについて、放射化分析法で無機元素の測定をおこなった。

2．実験

試料のアサガオは、27 度で発芽させ、その後２日目より植物育成器にて栽培した。栽培は水耕（ＭＧＲＬ水耕液）でおこなった。育成条件は、温度27度、湿度75%であった。

３日目の 7 時から最初の 12 時間の明期とし、その後５日目からは明期を８時間に短縮した短日条件区も設けた。

花芽形成を誘導する過程のさまざま時間に 10 個体ずつ採取し、９つの組織に切り分けた（Fig. 1）。10 個体分からなる各組織は 60 度で乾燥し、高純度ポリエチレン袋に封入し、放射化分析に供した。

放射化分析は、日本原子力研究所東海研究所の研究炉 JRR-3M で行った。使用した設備は放射化分析用照射設備（PN-3）であり、熱中性子線束約 2×10^{13} n/cm^2·sec で 10 秒間照射した。

照射後の試料を２分間冷却した後、Pure Ge 検出器（キャンベラ製 GX1519）を用いて元素分析を行った。測定時間は 150 秒間、測定の際の試料位置は検出器表面から 1cm 離れた箇所とした。

ピーク分析には SEIKO EG&G 社製 Spectrum navigator 2ED を用いた。また、各元素の定量には 1014（^{27}Mg）、1525（^{42}K）、1809（^{56}Mn）、3084（^{45}Ca）keV を採用した。なお、濾紙に各元素を一定量マウントしたものを標準試料として調製し、同様の条件下でγ線スペクトロメトリを行った。

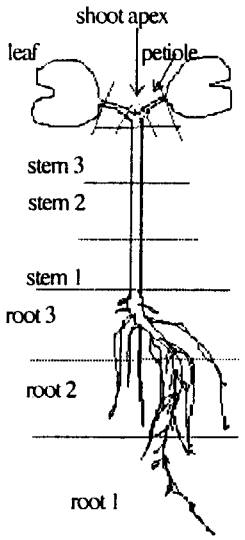


Fig. 1. 植物の切り分け方。

3．結果

数日間にわたる経時的な測定により、無機元素濃度はある周期をもって変化することがわかってきた。Fig. 2 にＣａの濃度変化を示した。

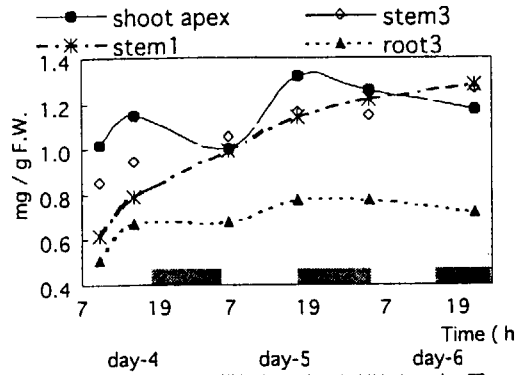


Fig. 2. Ｃａ濃度の変動。横軸上のバーは暗期（19 時ー翌 7 時）を示している。

明期で上昇し、暗期で低下するという濃度変化は特にShoot Apex ではっきりと見られた。

植物体内での分布についても、Stem1 と Root3 の間で大きな濃度差があり、地上部、地下部それぞれではほぼ均一であるという特徴的なものであった。

次に５日目から短日条件に移行した場合の結果を示す(Fig. 3)。短日処理を施した５日目 15 時以降は暗期にもかかわらず低下は見られず、1.3mg/gF.W. 以上を保ち、その後 6 日目の明期に入ると低下を始めた。6 日目 24 時以降は暗期にもかかわらず濃度は上昇し、その後再び明暗の条件に対応するような形の変化に復帰した。

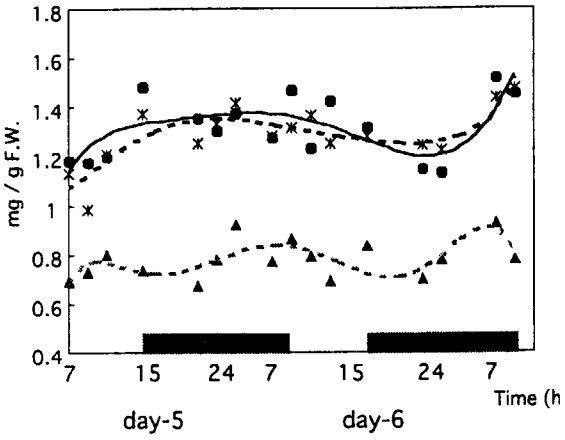


Fig. 3 短日条件下でのＣａ濃度変化。５日目の 15 時から短日処理を施した。横軸上のバーは暗期を示している。6次の近似曲線をもとめた。
● と黒実線：Shoot Apex、
＊ と黒破線：Stem1、
＿ と灰色破線：Root 3 。

Ｍｇにおいても類似の、このような元素濃度の周期的な変動が見られた。Ｃａと異なるのは濃度的な分布であった。

根の上部と地上部の境界付近でＣａ濃度差が大きいのに対し、Ｍｇ濃度は Root3 から Stem3 にかけて段階的に上昇し、特に Shoot Apex において高い値を示した。このことは、同じ２価の多量必須元素であるが、その必須性はそれぞれに特異的であり、濃度分布の制御も異なるということを示している。

Ｍｇの濃度の変動は、通常条件下ではＣａと同様の、明期で上昇し、暗期で低下する傾向を示した。また、短日条件に移行した場合には、やはり規則的な濃度変化は失われるが、Ｃａの場合とは異なる傾向を示した。

また、Ｎａ濃度は地上部では低濃度に保たれており、時間によってもほとんど変化は見られなかった。一方で根においては規則性は見られなかったが大きく変動した。このことは、Ｎａの輸送などの制御が、植物体内のある一ヶ所で強くおこなわれており、その他の部位では特におこなわれていないということを示唆するものである。

この他、Ｋ、Ｍｎについても同様に測定し、それぞれに特徴的な分布を見ることができた。また、Ｃａ、Ｍｇの他に、規則的な濃度変化が見られたのはＡｌであった。Ａｌは必須元素ではないが、植物における毒性の研究は盛んにおこなわれており、未だにその障害機構は解明されていない。Ａｌによる障害は、根の伸長阻害が主なものであるが、今回の測定では、Root1 においてＡｌ濃度が変化する様子が見られた(Fig. 4)。

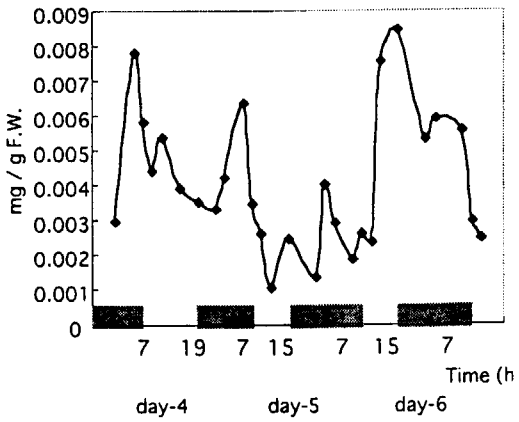


Fig.4 短日条件下での Root1 における Al 濃度変化。５日目の 15 時から短日処理を施した。横軸上のバーは暗期を示している。

実測値を曲線で結んだ。

4．おわりに

以上のような元素濃度の変化が、どのようなしくみでおこなわれているのかはこれからの課題であるが、例えば蒸散流に乗った元素の輸送でも、さまざまな段階で各元素がそれぞれに制御をうけていることが考えられる。

また、今回の実験では、短日処理を施すことによって生長段階を変化させ、元素濃度の変化を調べたが、ＣａとＭｇにおいて特徴的な結果が得られた。Ｃａについてはこれまでも植物の花芽形成への関与が指摘され、研究が続けられていたが、その濃度変化によく対応するような変化がＭｇ濃度において見られたことは、Ｍｇの新たな働きを考える上で非常に重要なものである。

放射化分析を用いることで、同一サンプルから多元素を同時検出した結果、例えばＣａとＭｇで見られたような、植物体内における元素どうしの相関関係を考察することが可能であった。今後は、このような各元素に特異的な分布、役割についてさらに詳細に解明していく。また、現在は得られたデータをもとに、学会発表、論文作成活動をおこなっている。

5．成果の公表

(論文)

1) T.M.Nakanishi et al. Kinetics of Element Profile Pattern during Life Cycle Stage of Morning-Glory. J.Radioanal. and Nuclear Chem., 239(3), 489-494, 1999

2) J.Furukawa et al. A Study of Nutrient Recycling System in a Plant-Soil System using NAA. J.Radioanal. and Nucl. Chem. 244, 283-287, 2000

3) T.M.Nakanishi et al. . Kinetics of Transition Element Profile during the Life Cycle of Morning-Glory. J.Radioanal. and Nucl. Chem., 244, 289-293, 2000

4) 池上奈通子、田野井慶太朗、古川純、横田はる美、大國曜子、中西友子“短日処理を施したアサガオにおけるＭｇ、Ｋ、ＣａおよびＭｎ濃度の日内変動について” RADIOISOTOPES, 50(6), 2001

5) S.Ueoka et al. Multielement Profile Pattern during Life Cycle Stage of Soybean. (1) Determinations of Representative Elements, Na, Mg, Al, K and Ca. J.Radioanal. and Nucl. Chem., in press

6) S.Ueoka et al. Multielement Profile Pattern during Life Cycle Stage of Soybean. (2) Determinations of Transition Elements, V, Cr, Mn, Fe and Zn. J.Radioanal. and Nucl. Chem., in press

7) K.Tanoi et al. . Element Analysis in Cultured Cells, Tabacco and Grape, Treated with Aluminum. J.Radioanal. and Nucl. Chem., in press

8) H.Iikura et al. Al Behavior in Plant Cells by NAA and Staining Method. J.Radioanal. and Nucl. Chem., in press

(発表)

1)池上奈通子、古川純、中西友子 “アサガオの元素分析” 東京大学原子力研究総合センターシンポジウム、2001年1月11日

2)池上奈通子他“アサガオにおける元素動態の日周性に関する基礎研究” 日本土壌肥料学会、講演要旨集第47集、p85)

3) Natsuko Ikeue, et al., Proc. of XIV International Plant Nutrition Colloquium, The University of Hannover (Hannover,Germany), “Chemical Movement of Up-Ground Part of Morning-Glory during Flowering Process.”, (July, 2001)

4) Natsuko Ikeue, et al, Proc. of the 3rd International Congress on Analytical Sciences (ICAS 2001), Waseda University (Tokyo, Japan), “Circadian Rhythm of Ma, Ca and Al Concentration in a Japanese Morning-Glory by Neutron Activation Analysis.” (August, 2001)

3-14

放射化分析のための新規な予濃縮技術の開発

Development of New Preconcentration Techniques for Neutron Activation Analysis

山形大学工学部　阿部重喜、遠藤昌敏、船田俊祐、宮内厚志
Faculty of Engineering, Yamagata Universiity,
ABE, Shigeki; ENDO, Masatoshi; FUNATA, Shunsuke; MIYAUCHI Atushi

1．研究の目的

環境試料などを測定対象とする超微量分析では、マトリックスによる妨害が分析の正確さ及び精度に大きな影響を及ぼす。従って定量操作に先立つ分離及び濃縮技術の確立は、分析法の高感度化に不可欠である。分析の基本的な要素は分離、計測及び特性評価（キャラクタリゼーション）であり、すべての分析法は分離及び計測の対象によって特徴づけられる。本研究では分離モード（物質、エネルギー、時間）に基づき化学分離を併用する中性子放射化分析の役割を学術及び化学教育的な観点から明らかにし、新しい濃縮技術を確立した。

中性子放射化分析法に用いる試料は一般的に薄膜状の固体試料が望ましく、照射後における正確な放射能測定を考慮すると一定のジオメトリーをもつ円板状試料が測定の再現性などの観点から最適であった。本研究では分析対象元素の予濃縮と放射能計測を総合的に一体化した照射試料の簡便な調製技術について基礎的な検討を行った。これまでの原研施設利用共同研究では、放射化分析のための予濃縮技術としてｐ－ノニルフェノールの液滴形成を利用した液－液抽出法及びゲル化剤のＮ－ラウロイル－Ｌ－グルタミン酸－α，γ－ジブチルアミドを用いる金属錯体の固－液抽出法などいくつかの新しい濃縮技術を確立した。特に、後者のチキソトロピーを利用する固－液抽出法は従来の固－液法と異なり、常温での溶媒抽出を可能にした。また、抽出の操作時における器具の破損など不測な事故による放射性物質の飛散を防止する目的に有用であった。本研究では測定対象の放射性核種が低エネルギーのガンマ線のみを放出する場合に、バックグラウンドの軽減が可能な照射試料の作製法を開発し、新規なイオン会合体フィルムの形成を利用する放射化分析法をウラン(VI)の定量に応用した。

ウラン(VI)の放射化分析では^{238}U(n, γ)^{239}Uで生成した^{239}Uのβ$^-$壊変に伴う^{239}Ｎｐのγ線ピークを測定する方法が一般的である。生成した^{239}Ｎｐの放出するγ線エネルギーは106.1（＋103.7）ｋｅＶと低く、測定試料中に他の放射性核種が共存する場合には、高エネルギーγ線のコンプトン散乱などに起因するバックグラウンドが増大し、その影響を排除するためにはマトリックスの分離操作が不可欠であった。

イオン会合体フィルムを利用する疎水性錯体の予濃縮法は試料の中性子放射化及び放射能測定に適した一定厚みの円板状試料の作製が可能であり、従来までに報告した金属錯体の予濃縮

研究施設と装置名
ＪＲＲ－３

研究分野
分離化学・放射化分析

技術（ｐ－ノニルフェノールによる液滴の形成を利用した液－液抽出法あるいはゲル化剤のＮ－ラウロイル－Ｌ－グルタミン酸－α，γ－ジブチルアミドを用いる金属錯体の固－液抽出法）に比べて有利であった。

２．研究の成果

２．１　凝集体フィルム形成剤の選定

陽イオン界面活性剤のセチルトリメチルアンモニウムクロライド（CTAC）などは臨界ミセル濃度以上でミセルを形成することが知られている。ミセルの正電荷はスルホサリチル酸などの添加によって中和され、非電荷型のイオン会合体が凝集体として沈殿した。硝酸セルロースなどの膜フィルタ上に捕集した凝集体は乾燥時に薄膜として簡便に剥離する特性を示した。凝集体のフィルム形成に適した試薬は解離性の官能基団を少なくとも３個以上含み、その内の２個は隣接した位置に存在する芳香族化合物であった。ウラン(VI)の放射化分析には対陰イオンとしてヒドロキノンスルホン酸を使用した。イオン会合体の凝集に最適なCTMA及びヒドロキノンスルホン酸塩濃度はそれぞれ３×１０$^{-4}$M及び３×１０$^{-3}$Mであった。なお、スルファニル酸系では凝集体の生成が認められなかった。

２．２　捕集フィルタの選定

金属錯体を取り込んだ凝集体のろ過媒体として各種のメンブランフィルタを比較した。イオン会合体は硝酸セルロース、酢酸セルロース、再生セルロース及びポリエーテルスルホンなどに捕集できたが、保持媒体からの剥離は硝酸セルロースのみが実用的であった。金属錯体の捕集効率に及ぼすメンブランフィルタの孔径の影響を銅(II)－DDTC錯体について検討した。その結果、０．４５～３μｍの範囲で影響を認めなかった。親水性のＰＴＦＥ型メンブランフィルタを使用した場合には、イオン会合体のろ過後に薄膜の生成は認められず、本実験の目的には硝酸セルロースが最適であった。

２．３　イオン会合体薄膜によるウラン（VI）の放射化分析

ウラン(VI)の捕集剤として４－（２－ピリジルアゾ）レゾルシノール（PAR）を使用した。共存元素の妨害はマスキング剤として１，２－ジ

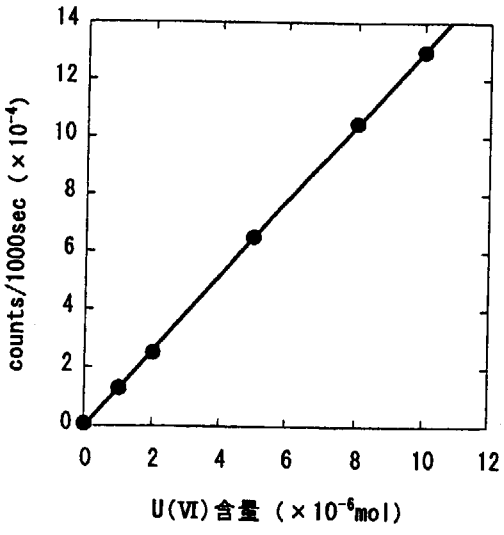


Fig.1　ウランの含量と^{239}Np放射能の関係

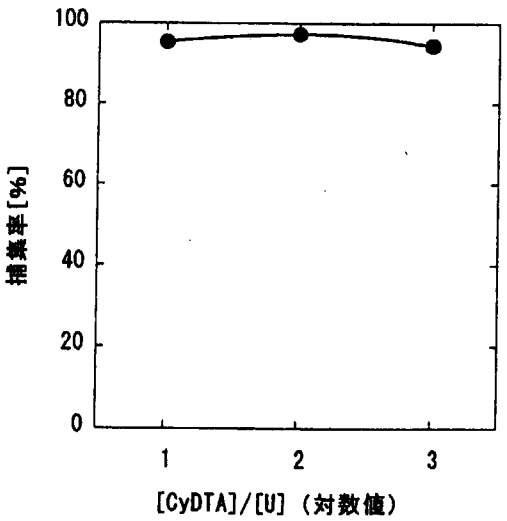


Fig.2　CyDTAの添加効果

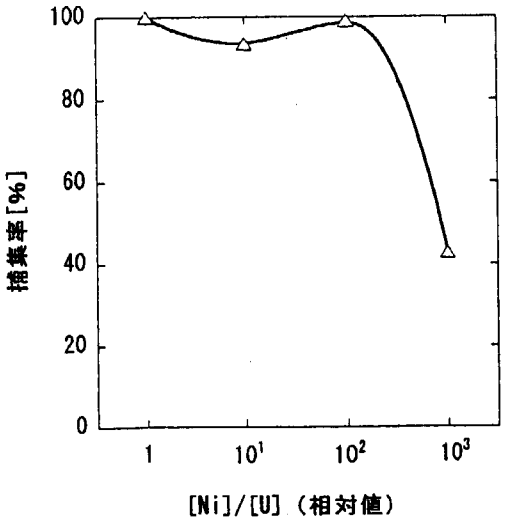


Fig.3 共存元素の妨害効果

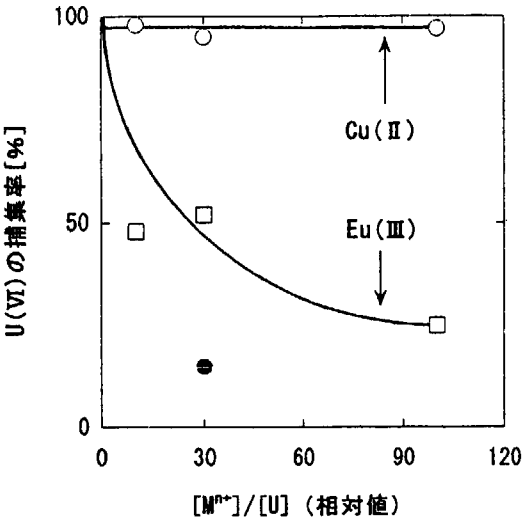


Fig.4 共存元素による妨害効果

○，□：CyDTAの共存下

●　：　CyDTAなし

アミノシクロヘキサンーN，N，N，N－四酢酸（CyDTA）を用いる方法によって排除した。ウラン（VI）を含む試料溶液にCTMA－PAR溶液（１ｍｌ）及び四ほう酸ナトリウム－塩酸緩衝液（２ｍｌ、ｐＨ８）を加えて加温処理（４０℃、５分間）したのち、ヒドロキノンスルホン酸（４ｍｌ）を加えて全容を２５ｍｌとした。恒温槽中で１５分間（１５℃）放置したのち、生成したイオン会合凝集体をニトロセルロース製のメンブランフィルタでろ過した。風乾後に剥離した会合体薄膜は市販のラミネートフィルムで密封したのち、ポリエチレン袋に二重に包装して原子炉照射（JRR-３、５及び１０分間）を行った。なお、共存する重金属イオンはマスキング剤のCyDTAをあらかじめ添加し、その妨害効果を検討した。

ウラン(VI)含量と^{239}Ｎｐ放射能の関係を測定した結果をFig.1に示した。凝集体は薄膜(直径14mm）として定量的に回収され、低エネルギーのγ線測定に対しても良好な直線関係がえられた。本法は厚みの一定な照射試料の調製及び測定ジオメトリーの再現性に優れていることを実証した。妨害イオンのマスキングに用いるCyDTAはウラン（VI)の捕集にほとんど影響を及ぼさなかった。（Fig.2参照）

共存する金属イオンの妨害効果をニッケル、銅、亜鉛、ランタン及びユウロピウムについて検討した。その結果はFig.3～Fig.5に示した。CyDTAを添加しない試料ではバックグラウンドの増大による^{239}Ｎｐの光電ピークの消失など顕著な影響が見られたが、CyDTAの存在下では満足できる結果がえられた。

２．４　中性子束の内部モニタリング法

金属錯体を捕集したイオン会合体の薄膜試料はラミネート被覆法によって乾燥時の破断あるいは外部汚染を防止でき、長期間の試料保存が可能になった。市販のラミネートフィルムは重合触媒のアンチモンを微量含んでおり、ラミネートフィルムを中性子照射した場合、^{122}Ｓｂのγ線ピークが564.2ｋｅＶに観測された。（ｎ，γ）反応で生成する^{122}Ｓｂの半減期は2.8日であり、ウランから生成した^{239}Ｎｐと類似の半減期を示した。ラミネート被覆したウラン（VI）-

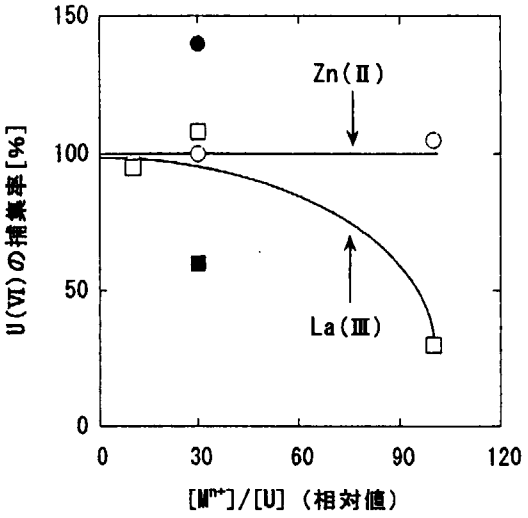


Fig.5 共存元素による妨害効果

○，□：CyDTAの共存下

●　：　CyDTAなし

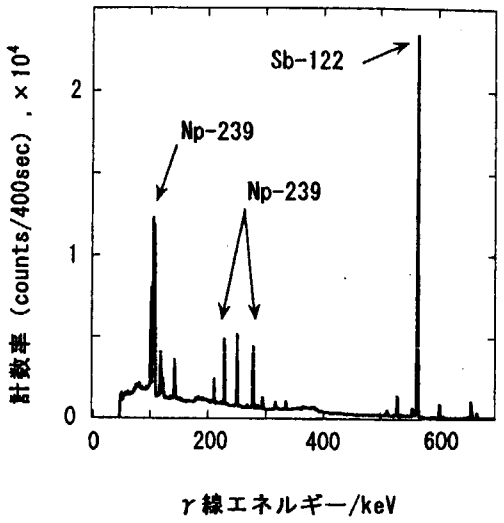


Fig.6 U(VI)錯体のγ線スペクトル

PAR錯体試料のγ線スペクトル例をFig.6に示した。ラミネートフィルムのアンチモン含量は市販製品によって異なっていたが、照射キャプセル内における中性子束の変動は^{122}Sbの光電ピークを利用して補正できた。

3．　結論

中性子放射化分析における試料の濃縮及び放射能測定に適した薄膜試料の新しい調製法を確立した。イオン会合体の凝集体を膜フィルタ上に捕集する本法は金属元素のキレート錯体を濃縮し、同時にγ線スペクトロメトリーの妨害元素を除去する方法として一般的な応用が期待された。特に、ラミネートフィルムで被覆した試料は中性子の照射時におけるキャプセル内での中性子束の変動を補正する目的に有用であり、計数に付随するジオメトリーの問題を解決した。本研究で確立した薄膜試料の作製法は固体試料を用いる色彩計測法に有利であること実証できた。

4．　成果の公表

M. Endo, K. Suzuki, S. Abe, "Novel Preconcentration Technique for Trace Metal Ions by Aggregate Film Formation", Anal. Chim. Acta, 364(1998)13-17.

遠藤昌敏、阿部重喜，"分子会合体を用いる金属錯体の捕集／薄膜試料の放射化分析"、日本分析化学会第48年会(1999年9月)

M. Endo, S. Abe, "Preparation of Aggregate Film for Neutron Activation Analysis of Trace Uranium(VI)", to be submitted in J. Radioanal. Nucl. Chem.

3-15

蓄光性塗料の放射化分析

森脇　一成、続橋　治*、牧村　正治*、須藤貞之[b]、古山俊介[†]

日本大学歯学部 RI,松戸歯学部総合歯科診療学*,RI Center[b], 生理学[†]

The activation analysis of phosphorescent phosphor

K. Moriwaki, O. Tsuzukibasi*, M. Makimura*,S. Sudo[b] and S. Furuyama[†]

Division of RI Research,Nihon University School of Dentistry

* Department of Comprehensive Dentistry, [b] Division of RI Center,

[†] Department of Physiology ,Nihon University School of Dentistry at Matsudo

1　はじめに

日用品に放射性核種が含まれている例としては煙検知器、陶器のうわ薬、夜光時計、避雷針、建築材料や肥料などが知られている[1－3]が、玩具に使われているという報告は見当たらない。我々が入手した Pinbadge に暗室で紫外線を照射すると強く発光したので、Film 上に数時間置いて現像したところ、発光塗料の上に描かれている像だけが抜けて感光した。さらに、少量の塗料を剥離して Scintillator に溶かし、Liquid Scintillation Detector(LSD)で測定した。試料調整直後の測定では高い Count ならびに連続 Spectrum を示した。そこで、放射性物質を疑い、Photo Diode(PD)で発光に対する電流測定を行った結果、放射性塗料ではないことが判った。この塗料の発光物質を同定するため放射化分析を行ったところ、新しい Type の蓄光性塗料であることが判った。

2　方法

① 試料：30 種類の Pinbadge を集め、紫外線下で発光した 8 種類について検討した。

② Film の感光：室内から試料を暗室に移し、X 線 Film の上に 2 時間および 5 時間置いて現像した。(Fig.1)

③ LSD による測定：表面の塗料を直径 1.2mm の打ち抜き器で採取し、8ml の Scintillator に溶かして LSD で LL－UL=0.0kev－18.6kev の Windou 幅で測定した。(Table.1).(Fig.2)

研究施設

JRR－4

研究分野

放射化分析

④ PD による測定：室内から試料を Chamber 内に移し、試料と PD との距離 10ｃｍで 20 分間隔で 60 分まで、以後 1 時間おきに 4 時間測定し、その後試料を取り出して測定した。(Fig.3)

⑤ 放射化分析：日本原子力研究所（JAERI）の 4 号炉（JRR-4）で 10 分間、熱中性子照射（flux:4.5×10^{13}n/cm^2・sec）を行った後、γ-Spectrometry を行った。（Genie-2000, CANBERRA series 35 plus）(Fig.4)

3 結果と考察

蓄光性塗料の蓄光性とは、あたかも光を一時蓄えて発光するかのように見えるので蓄光という言葉が使われており、その発光を燐光とも言う。蓄光性を持つ物質が工業的に生産、使用されたのは２０世紀になってからであり、ZnS:Cu や CaSrS:Bi などの硫化物蛍光体が用いられてきた。しかし、それらは発光時間が短かったり、弱かったため、これに放射性物質を加えて利用されていた。1996 年 Matsuzawa ら（根本特殊化学）が① $SrAl_2O_4$: Eu,Dy ② $Sr_4Al_{14}O_{25}$: Eu,Dy ③ $CaAl_2O_4$: Eu,Nd これらのアルカリ土類アルミン酸塩を主成分とした蓄光性塗料を開発した[4]。

そこで、我々の入手した Pinbadge に使われている塗料がどの Type の蓄光性塗料であるかを確かめるため放射化分析を行った。その際、根本化学から提供された試料も同時に放射化しγ-Spectrometry を行った。この照射条件では Zn や Ca の Peak は認められず 1780keV に ^{28}Al の Photo Peak が認められたので、新しい Type の蓄光性塗料であることが判った。

4 おわりに

夜光塗料には自発光性と蓄光性とがあり、前者は放射性であるが故に用途に制限がある。後者は従来の硫化亜鉛 Type では残光時間や輝度に問題があったが、新しく開発されたアルミン酸塩タイプの蓄光性塗料はこれらの問題をクリアし、現在、時計や交通標識などに全世界的に使われ始めている。

我々は陶歯、陶材中に蛍光剤として添加されている Uranium を定量し、それによる口腔組織の被爆線量を算定して報告してきた[5]。その報告で放射性蛍光剤すなわち Uranium の添加の中止とそれに替わる蛍光剤の開発を勧告してきたが、この蓄光性塗料は陶磁器や Ceramic にも応用できるとされているので、陶歯、陶材の蛍光剤にも利用できるのではないかと考えている。

この研究の一部は原研施設利用総合共同研究により行った。

謝辞

蓄光性塗料の試料を提供して頂いた根本特殊化学（株）に感謝いたします。

研究成果

K.Moriwaki,J.Obata,T.Ezawa, O.Tuzukibashi,Y.Shimpuku,M.Makimura and F.Shiraishi :The activation analysis of the pinbadge paint that is doubted as a radioactive material. Radioisotopes 50,7 (2001) in printing

文献

1) N.Yamagata: Radioactivity in daily goods.Bull.Inst.Publ.Health 26,179-180 (1977)

2) H.Chisaka and Y.Igoshi: Mesurements of radioactive substance and surface dose rate in some wares for health improvements.Radioisotopes27,687-689 (1978)

3) P.Brunner,P.Schneider,H.Schneider and G.Seyoul: Tritium intake by exposure to plastic case watches. Health Physics 70,484-487 (1996)

4) T.Matsuzawa,Y.Aoki,N.Takeuti and Y.Murayama: A New Long Phosphorescent Phosphor with High Brightness, $SrAl_2O_4:Eu^{2+}$, Dy^{3+}.J.Electrochem.Soc.143,8,2670-2673 (1996)

5) E.Sairenji,K.Moriwaki,M.Shimizu , K.noguchi,I.Anzai and N.Ikeda : Determination of uranium content in dental porcelains by means of the fission track method and estimation of radiation dose to oral mucosa by radioactive elements. Health Physics 38,483-492 (1980)

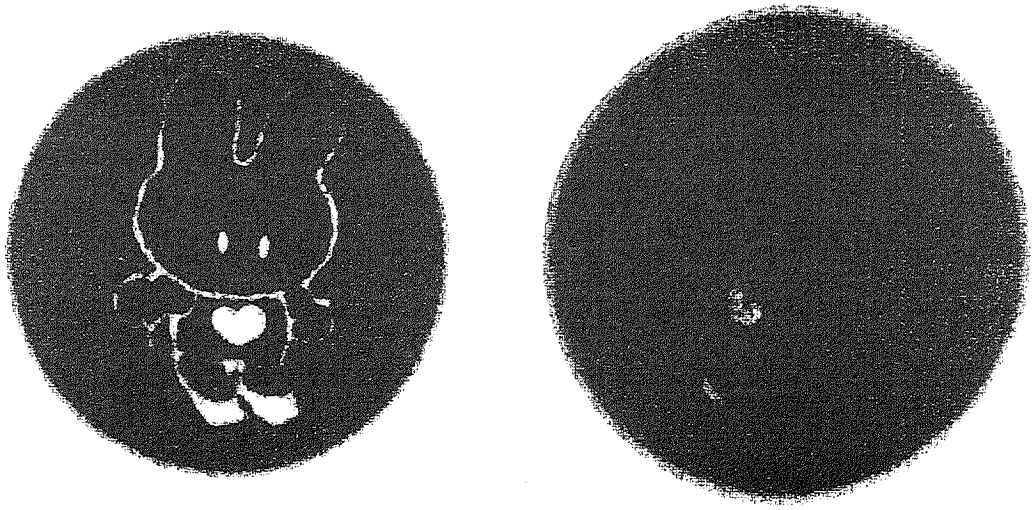


Fig. 1 X ray films that were blackened by the pin badge

Left : contacted with the pin badge for 2 hrs.

Right : contacted with the pin badge for 5 hrs.

Table1 Measurement of phosphorescence by liquid scintillation detector

min	cpm
10	8.9×10^6
20	3.4×10^6
30	1.8×10^6
40	1.1×10^6
50	7.7×10^5
60	5.8×10^5
70	4.5×10^5
80	3.7×10^5
90	3.2×10^5
100	2.7×10^5
110	2.4×10^5
120	2.2×10^5
180	1.3×10^5
240	9.0×10^4
300	6.9×10^4
360	5.6×10^4
420	4.6×10^4
480	4.1×10^4
540	3.6×10^4
1000	6.7×10^3
1440	0

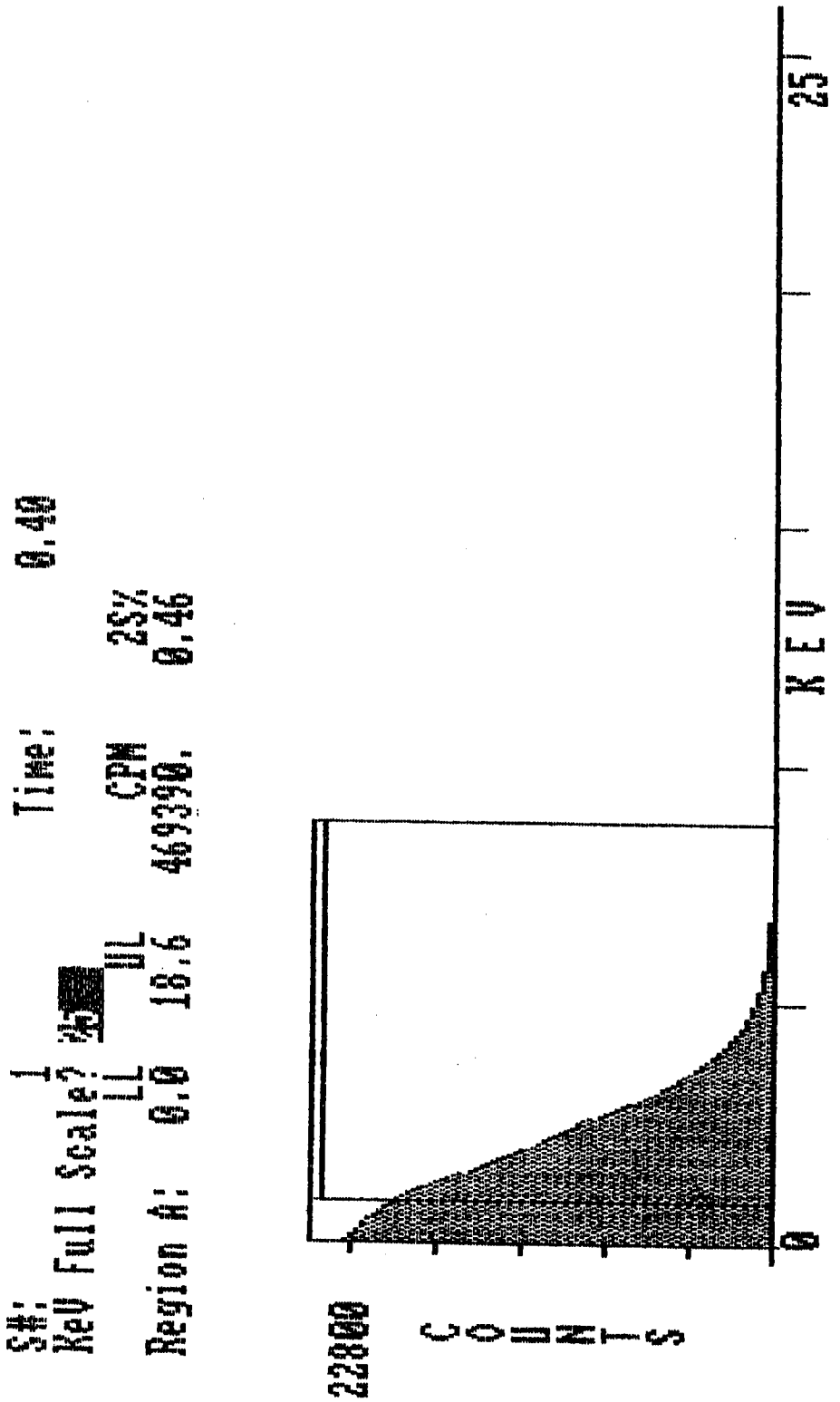


Fig.2 The spectrum was measured by Liquid Scintillation Detector

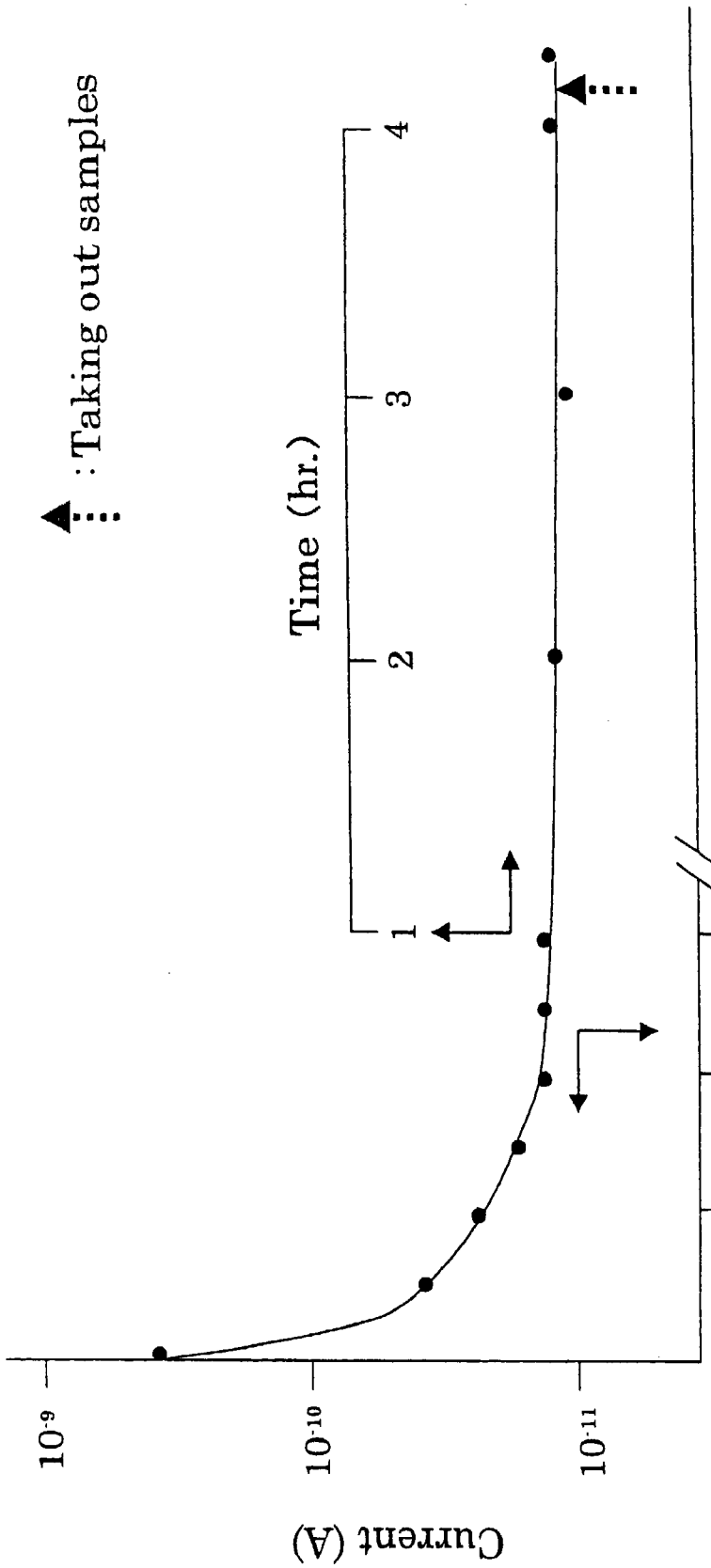


Fig.3 The electric current for emission was decreased drastically till 10 minutes and it was decreased slowly till 4hr..
The current after samples were being taken out was same as the data of 4hr.

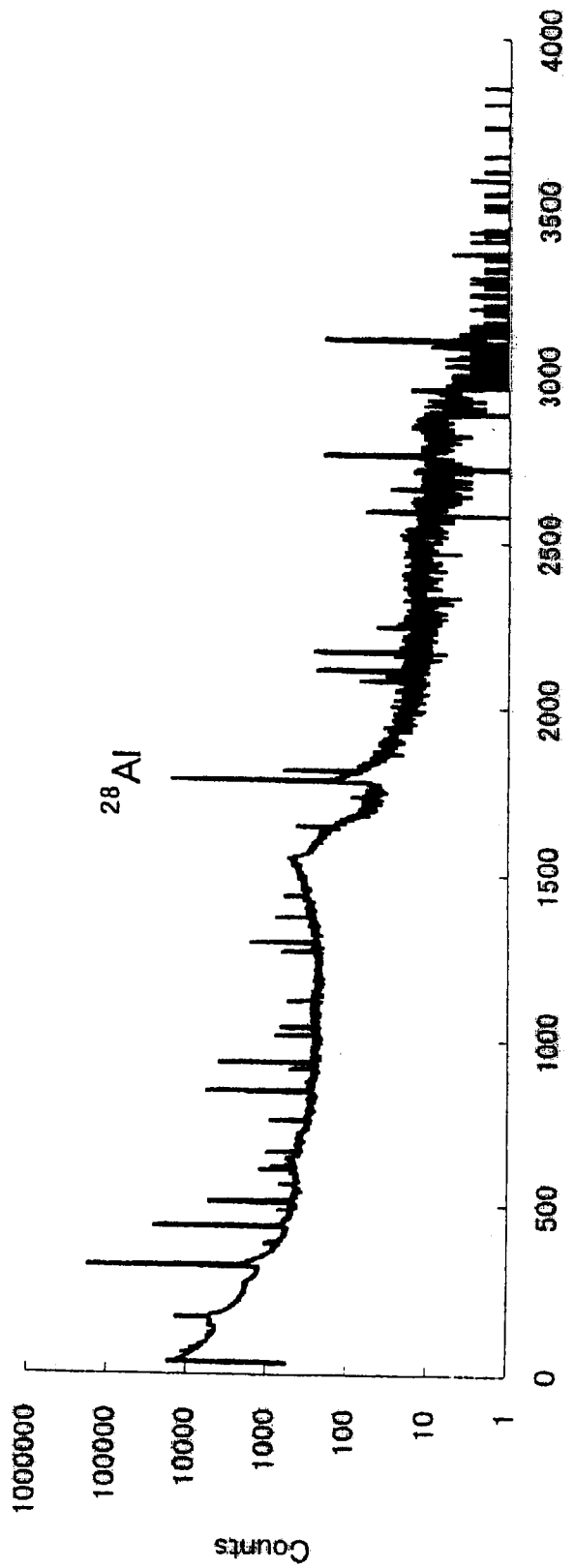


Fig. 4 The badge surface paint samples were irradiated for 10 minutes with thermal neutron, which flux was 4.5×10^{13}n/cm^2・sec by JRR-4 that is installed at JAERI. After irradiation, the radioactivities of samples were measured by Ge detector (CANBERRA series 35 plus). A photo peak at 1780kev for ^{28}Al was detected.

3-16 植物の葉等へ特定元素のとり込み

Incorporation of Specified Element to Plant Leaf and Others

増子捷二、笠原茂、大西俊之
Syouji Masuko，Shigeru Kasahara，Toshiyuki Ohnishi
北海道大学アイソトープ総合センター
Central Institute of Isotope Science ，Hokkaido University

1．はじめに

リョウブの葉は、コバルトを特異的に集積することが報告されている[1]。今回我々は、リョウブ等の根、枝、総状果序等にも葉と同様に集積するかどうかを、中性子照射して放射化して検討した。

リョウブの葉に分布するコバルト元素は報告している。[2] 本報は、

1）リョウブ、オニモミジの根、枝、さく果等に含まれる亜鉛、セシウム、コバルト元素と土壌に含まれる各元素に対する集積割合を検討した。

2）リョウブの枝、葉、総状果序から放出する放射線をメージングプレート（Imaging Plate、以下「ＩＰ」）に露光して元素分布図を検討した。

2．方法

1）土壌に対する集積割合

北海道大学植物園に生育しているリョウブ、オニモミジを採取し、試料とした。これらの試料は以下の方法で測定を行った。

放射化分析法

a　試料の採取後は、蒸留水で洗浄し、６０度で６時間乾燥し、重量を測定した。
b　ポリエチレン袋に葉を封入した。
c　日本原子力研究所（ＪＲＲ－4）Tパイプ、中性子束密度（$n/cm^2.s$）は6.0×10^{13}で、１０分間の中性子照射を行った。
d　試料は６ヶ月間冷却後、ピュアゲルマ半導体検出装置により核種分析を行った。

2）リョウブの枝、葉、総状果序における放射線の分布

北海道大学植物園に生育しているリョウブの枝、葉、総状果序（さく果、果柄、果枝を含む）を採取し、試料とした。これらの試料は以下の方法で測定を行った。

a　葉の採取後は、蒸留水で洗浄し、６０度で６時間乾燥した。
b　ポリエチレン袋に葉を封入した。
c　日本原子力研究所（ＪＲＲ－４）中性子ビーム設備、中性子束密度（$n/cm^2.s$）は2.3×10^{9}で、２４時間の中性子照射を行った。
d　照射後にポリエチレン袋から取り出し、カバーフィルム（粘着力のあるポリエチレン）に挟んだ。
e　５ヶ月経過してから、ＩＰに図１の通り、シールドＢＯＸ内で４４日間露光した（室温）。
f　露光後は、バイオ・イメージングアナライザー（富士フィルムＫＫ，ＢＡＳ－５０００）でＩＰを読み取り、ＭＣＩＤイメージングアナライザー（イメージングリサーチ社）により放射線の分布図を作成した。

3）結果と考察

方法１）の土壌に対する集積割合で測定した結果からは、特に亜鉛、セシウム、コバルト元素に注目し、土壌中の放射線の量と各部位の放射線の量から割合を求め、表１に示す。採取した、土壌、根、枝、葉、さく果の重量を測定し、ついで６０度で乾燥した後に再び重量を測定した。それらの重量の比を乾燥割合とした。乾燥割合は、土壌で６５％、リョウブの枝で４５％、オニモミジの葉で２０％、リョウブのさく果で１３％であった。その結果から

a）リョウブのさく果に含まれるセシウム元素は土壌と比較して１.５倍程集積していることが分かった。
b）リョウブの枝に含まれるコバルトの元素はオニモミジの枝と比較して１０倍程差のあることが分かった。

ＪＲＲ－３　Tパイプ、中性子ビーム設備　放射化分析（環境）

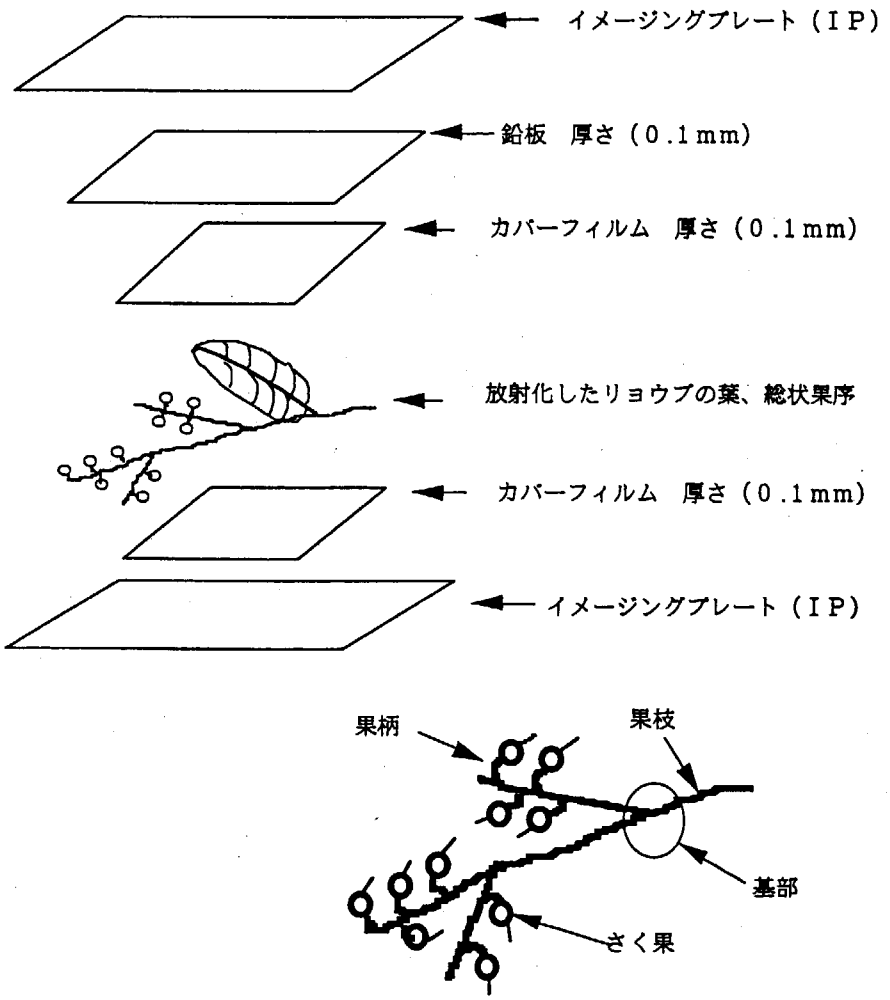


図１．露光詳細図

表１．土壌に対する集積割合（%）

元素	土壌	リョウブ			オニモミジ		
		根	枝	さく果	根	枝	葉
亜鉛	１００	４９	５７	３２	３１	２４	４４
セシウム	１００	５６	１８	１４０	３４	６	２４
コバルト	１００	３６	１６	１９	１５	２	４

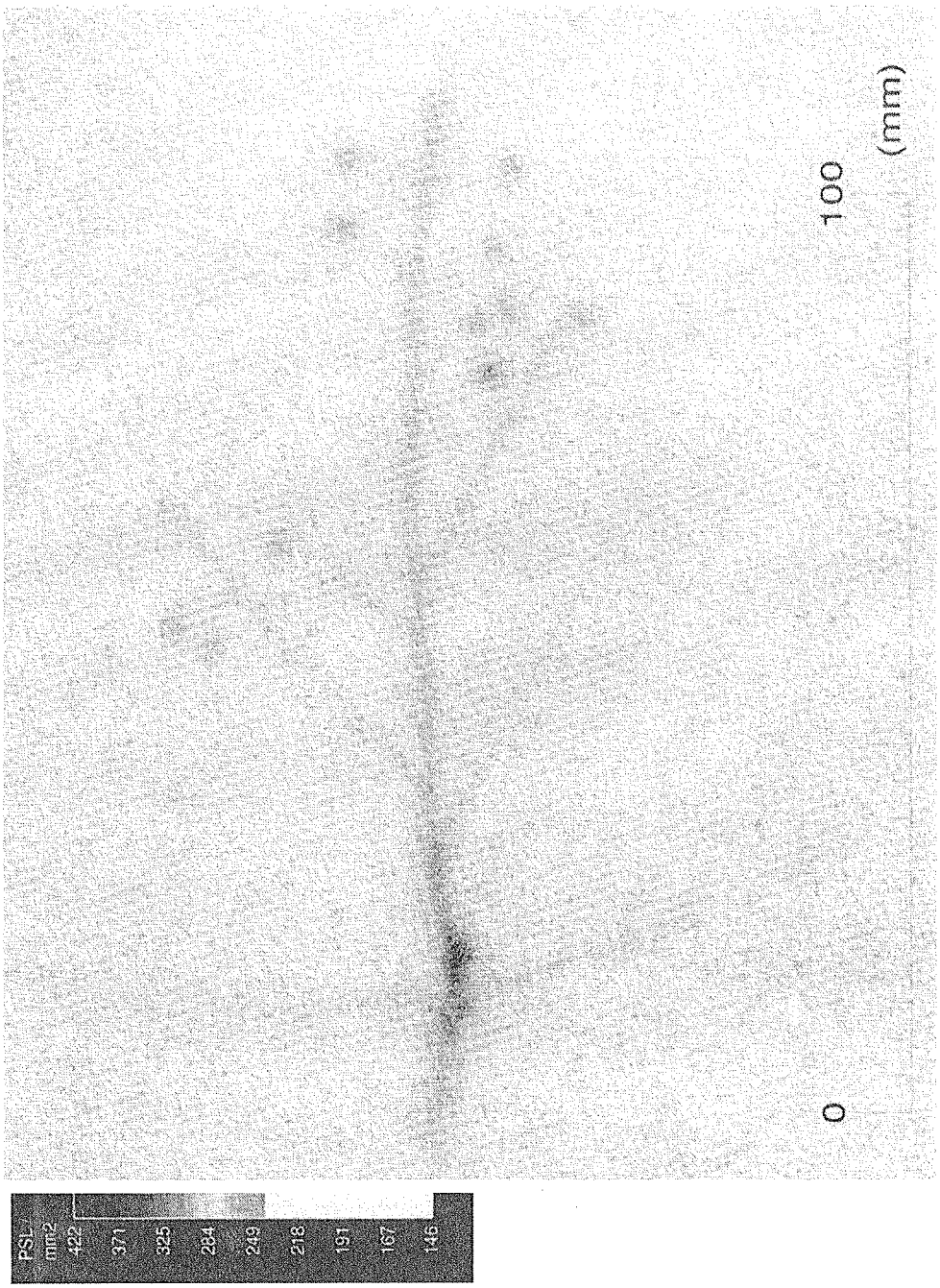


図2．IPによるリョウブの枝、葉、総状果序のγ線画像

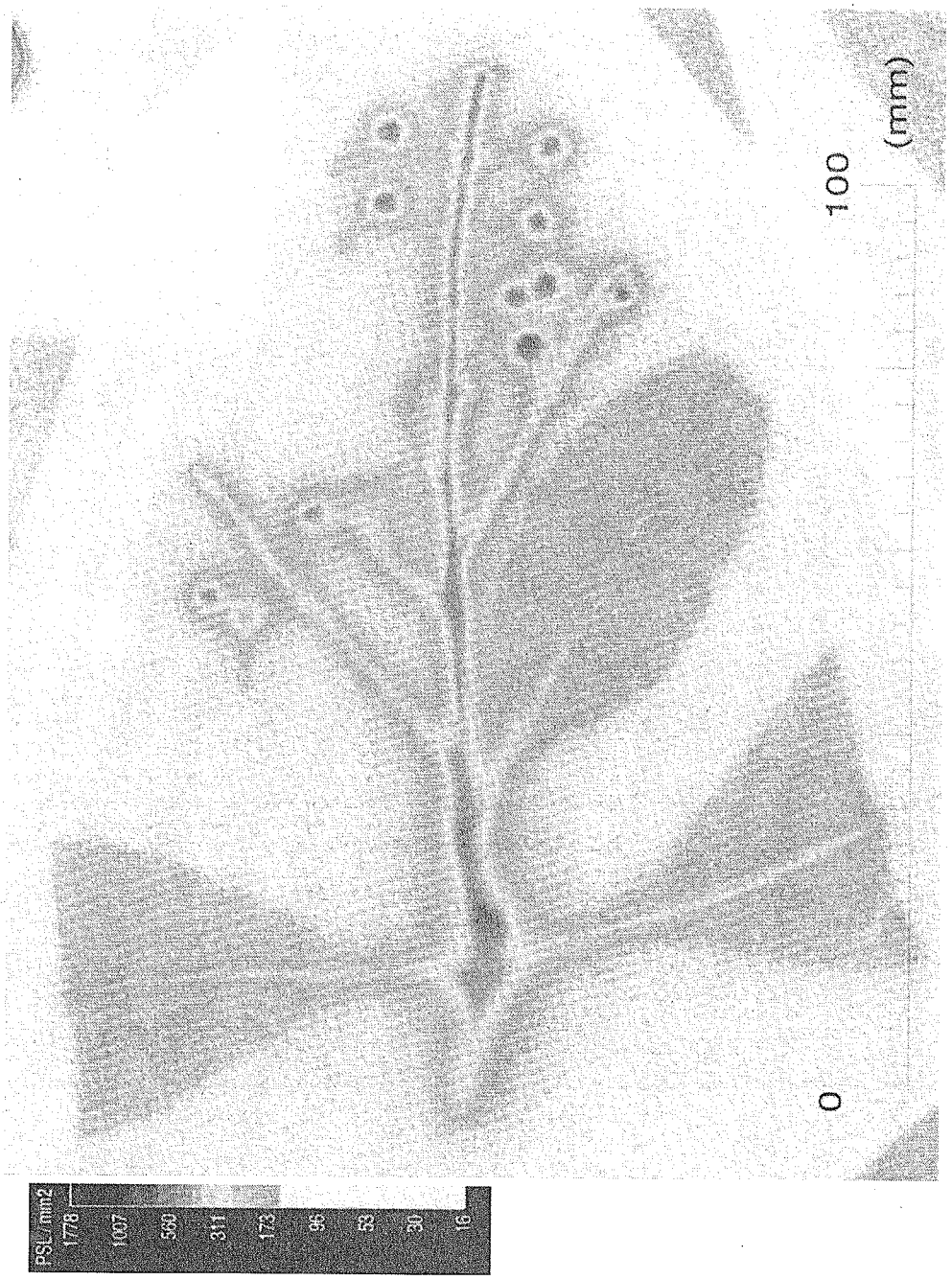


図３．ＩＰによるリョウブの枝、葉、総状果序のβ線、γ線画像

c）リョウブの根、枝、さく果とオニモミジの根、枝、葉に含まれる亜鉛元素の差は少なかった。

方法２）のリョウブの枝、葉、総状果序からの放射線の分布作成にあたっては、前回の「植物の葉に含まれるコバルト分布図の作成」2）の報告より、試料をΦ２５ｍｍ×７５ｍｍの容器に葉を丸めて封入して放射化を行ったが、葉は脆くなり粉砕する傾向にあること、及び前回より大きいサイズの試料であるリョウブの枝、葉、総状果序からの放射線の分布画像を得るには、丸めてΦ２５ｍｍ×７５ｍｍの容器試に封入することができないため、ＪＲＲ－４の照射野の広い中性子ビーム設備で２４時間照射を行った。中性子ビーム設備の中性子束密度（$n/cm^2.s$）は2.3×10^9と小さいため放射化される量は少ない等が予想される。それらを考慮しＩＰに露光する時間を長くすることで、各画像を得ることができた。（図２、３）

今回は、放射化したリョウブの枝、葉、総状果序における放射線の分布画像を作成する方法として、バイオ・イメージングアナライザー（ＢＡＳ－５０００）と画像解析ソフト（ＭＣＩＤ）を用いて行った。

放射化後、放射化したリョウブの枝、葉、総状果序を長期間放置することで短半減期核種の放射能を減衰できることから、５ヶ月経過後、ＩＰに露光した。また、露光中に放射化したリョウブの枝、葉、総状果序が変形する可能性があるので、ＩＰ２枚を同時に露光した。

放射化したリョウブの枝、葉、総状果序から放出するβ線を吸収板（鉛板、カバーフィルム、ポリエチレン板）に吸収させた画像（図２）と吸収板（カバーフィルム）に吸収させた画像（図３）を得た。

図２、図３はバイオ・イメージングアナライザー（ＢＡＳ－５０００）で読み取ったものを画像解析ソフト（ＭＣＩＤ）で画像にしたもので、ＩＰの読み取り条件はGradation;65536、Resolution;25、DynamicRangeSelector;S4000(L5)である。図２は、放射化したリョウブの枝、葉、総状果序から放出する大半のβ線をカットした残りのγ線の画像である。図３は、葉から放出する弱いβ線及びコバルト－６０のβ線の大半をカットした残りのγ線とβ線（セシウム－１３４）の画像である。

図２、図３の結果から

a）総状果枝は全体的にハッキリとした画像になっている。葉枝、果枝の基部の付近に元素を集積している箇所が見受けられた。

b）特にさく果の画像はハッキリした画像になることが分った。これは、土壌に対する集積割合で測定した結果からもセシウム－１３４の放射線が定性されたと考えられる。

この結果、中性子の照射時間や露光の際の吸収板の種類・厚さ等について更に検討する余地があるが、日本原子力研究所（ＪＲＲ－4）中性子ビーム設備を用いて、葉を丸めないでも照射できることができた。基本的にβ線の画像分布の作成が可能であると思われる。

放射化した試料は、前回同様にコバルト元素の他にセシウム元素が予想以上に多く、これをどう分離測定するかが精度を上げる鍵である。また、吸収板の材質についても検討の余地があると思われるので、継続した課題としたい。この成果をもとに研究論文を作成中である。

謝辞

この実験にあたり、貴重な試料を提供して頂いた、北海道大学農学部附属植物園の簾内技術専門職員、谷井技官及び試料調整等の技術指導して頂いた、大学解放研究室の澤幡氏、川手氏に厚くお礼申し上げます。

4.参考文献

1）「微量元素」（山県　登　著）

2）増子捷二、笠原茂,「原研施設利用共同研究成果報告書」平成９年度、７１－７６

3-17

ホタテガイのカドミウム濃縮機序の研究
Studies on Cadmium Bioaccumulation in Scallop *Mizuhopecten Yessoensis*

大西俊之[1)]、大西玄一[2)]、野矢洋一[1)]
Toshiyuki Ohnishi,Gen-ichi Ohnishi,Youichi Noya
1）北海道大学ｱｲｿﾄｰﾌﾟ総合ｾﾝﾀｰ
Central Institute of Isotope Science,Hokkaido University
2）北海道大学歯学研究科
Graduate School of Dental Medicine,Hokkaido University

1．はじめに

ホタテガイは、体内に高濃度のカドミウムを濃縮することが知られている。ホタテガイ中に含まれるカドミウムの多くは、中腸腺や腎臓内で蛋白質に結合して存在していると言われているが[1)、2)、3)]、カドミウム結合蛋白の詳細やその濃縮機構は、未だ解明されていない部分が多い。

今回、ホタテガイに含まれるカドミウム濃度を測定し、カドミウム結合蛋白の分離等の実験により、カドミウム濃縮機構の検討を行ったので報告する。

2．方法

（1）試料

ホタテガイは、北海道岩内郡漁協で購入した３年貝を用いた。購入後、直ちに中腸腺及び腎臓を取り出して、実験開始時まで冷凍保存した。

（2）ホタテガイのカドミウム濃度の測定

ホタテガイの全軟体部及び中腸腺と腎臓は、３～５日間の凍結乾燥後、硝酸－過塩素酸中で加熱分解を行った。これらの試料は石英管に封入して、日本原子力研究所（ＪＲＲ－４）で、中性子束密度５×１０^{13}n/cm^{2}sの条件で４時間の中性子照射を行った。１～２週間の冷却後、ピュアゲルマ半導体検出装置によりカドミウム濃度の測定を行った。

（3）カドミウム結合蛋白の分離

中腸腺に２倍量の５０ｍＭトリス塩酸緩衝液（ｐＨ8.6）を加え、ホモジナイザーでホモジナイズした後、10,000ｇで３０分間遠心分離した。その上澄み液を更に100,000ｇで２時間超遠心分離を行い、上清液と沈殿等に分画した。

得られた100,000ｇ上清液は0.45μｍのメンブランフィルタでろ過した。そのろ液の一部をSephadex G-75を用いてゲルろ過を行った。得られた各フラクションは、280nmの吸光度を測定した後、原子吸光光度計でカドミウム濃度を測定した。メンブランフィルタのろ液の一部をSephacryl S-300ゲルろ過を行い、280nmの吸光度を測定した後、原子吸光光度計でカドミウム濃度を測定した。

100,000ｇ沈殿は、硝酸－過塩素酸中で加熱分解を行った後、原子吸光光度計でカドミウム濃度を測定した。

3．結果

（1）ホタテガイのカドミウム濃度の測定

全軟体部、中腸腺及び腎臓に含まれるカドミウム濃度を放射化分析法で測定し、その結果をTable.1に示す。

Table.1 Cadmium Concentrations in Scallop

項　目	全軟体部	中腸腺	腎　臓
濃　度 (μg/g dry wt)	33.6	136	1290
乾燥重量(g)	10.77	1.28	0.081
含有量(μg)	362	174	104

ホタテガイに含まれるカドミウム濃度はきわめて高く、中腸腺は海水のカドミウム濃度[1)]の100万倍、腎臓に至っては1000万倍の濃縮を示していた。このように高度な濃縮を行う機構を調べるため、中腸腺をサンプルとしてカドミウム結合物質の検討を行うこととした。

（2）カドミウム結合蛋白の分離

中腸腺の100,000ｇ上清液の内、比較的低分子量蛋白（分画範囲70,000以下）をSephadex G-75を用いて、比較的高分子量蛋白（分画範囲30,000～600,000程度）をSephacryl S-300を用いて、それぞれゲルろ過を行った。

a）Sephadex G-75によるゲルろ過の結果をFig.1に示す。

カドミウム濃度は、ボイド体積（２５ｍｌ）に非常に大きなピークが認められた。この部分には分子量70,000以上の物質が含まれており、中腸腺のカドミウムの大部分が高分子量物質と結合していることが分かった。このピークの後、カドミウム濃度は減少し、溶出量５５ｍｌ（分子量10,000程度）付近に小さなピークが認められた。

280nmの吸光度は、カドミウム濃度と同様にボイド体積にピークを示した後、なだらかに減少し、溶出量８０ｍｌ及び９０ｍｌ付近に遊離のアミノ酸[2]によるものと思われるピークを示した。カドミウム濃度に対応した５５ｍｌ付近には、ピークは認められなかった。

分子量70,000以上の物質を検討するため、中腸腺の100,000ｇ上清液をSephacryl S-300を用いてゲルろ過を行った。

b）Sephacryl S-300によるゲルろ過の結果をFig.2に示す。

カドミウム濃度は、ボイド体積（４０ｍｌ）以降、溶出量６０ｍｌ（分子量200,000程度）、７０ｍｌ（分子量90,000程度）、８０ｍｌ（分子量40,000程度）にピークを有するほか、分画範囲を下回る溶出量９５ｍｌにもピークが認められた。溶出量６０ｍｌ及び７０ｍｌのピークはSephadex G-75のボイド体積のピークの主成分に相当すると考えられる。

280nmの吸光度は、カドミウムのピークに対応して溶出量７０ｍｌと８０ｍｌに小さなピークを示した他、分画範囲を下回る１１０ｍｌ、１２０ｍｌ、１３０ｍｌにも明確なピークを示した。１１０ｍｌ以上のピークは、Sephadex G-75の場合と同様、遊離のアミノ酸によるものと思われる

Fig.1 Elution Profiles of Sephadex G-75

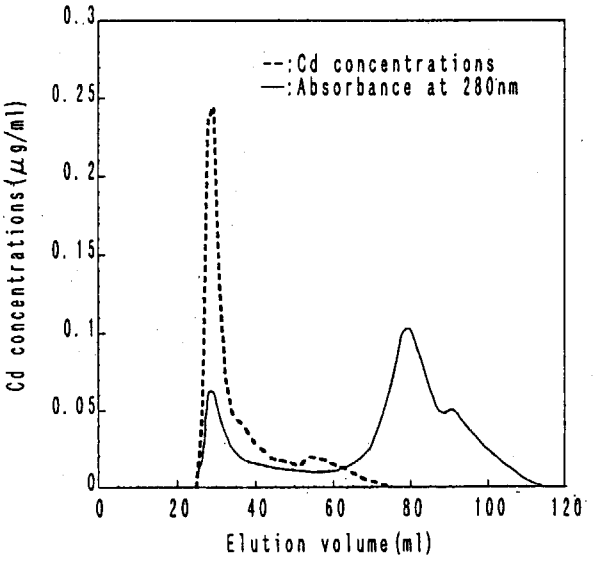
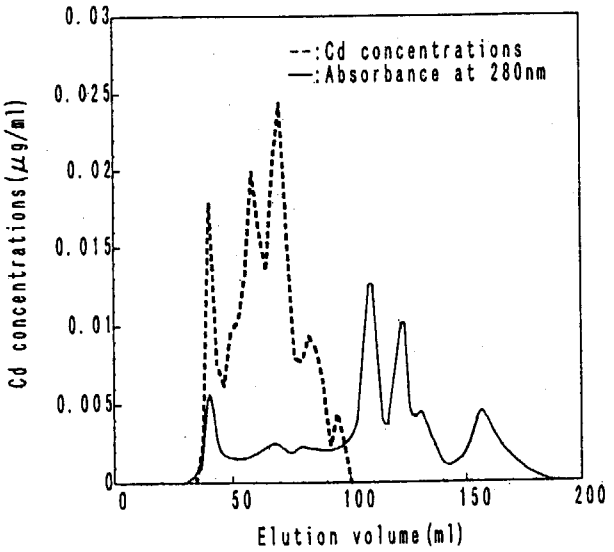


Fig.2 Elution Profiles of Sephacryl S-300



4．考察

Table.1より、ホタテガイ全軟体部に含まれるカドミウムの４８％が中腸腺に、２９％が腎臓に存在していた。両者の合計は７８％に達しており、生殖

腺や貝柱等のその他の部位のカドミウム量の合計は全体の２２％であった。ホタテガイ各部位のカドミウム濃度は以前にも報告したが[1]、中腸腺と腎臓以外の部位では、胃や心臓を含む部位が比較的高濃度（５０μg/g dry wt）であった他は低濃度であり、２～１０μg/g dry wt程度であった。今回の測定でもホタテガイに含まれるカドミウムの大部分が中腸腺と腎臓に含まれることが裏付けられた。

Fig.1及びFig.2のゲルろ過の結果により、ホタテガイ中腸腺に含まれるカドミウムは、分子量１万から２０万程度までのいくつかの蛋白質と結合していることが分かった。カドミウムは中腸腺内で糖蛋白に吸着された状態で存在しているとの報告もあり、本実験で見出された４万、９万及び２０万程度の分子量を持つ物質も糖蛋白である可能性が高い。これらについては、アミノ酸分析を含めて、今後のより詳細な検討が必要である。

Sephadex G-75で溶出量５５ｍｌ（分子量10,000程度）付近に認められたピークは、その分子量と280nmの吸収を有しないことからメタロチオネイン様蛋白質であると考えられた。メタロチオネイン様蛋白質はカドミウム結合蛋白として多くの生物に見出されているが[5]、今回、ホタテガイ中腸腺から検出された量は少なかった。多くの生物と異なり、ホタテガイではより高分子量の４万から２０万程度の蛋白質との結合が、メタロチオネイン様蛋白質より優先される理由は不明である。人為的に多量のカドミウムを摂取させたホタテガイには高濃度のメタロチオネイン様蛋白質が誘導されると報告[1]されている。これに対し、以前に報告[1]したとおり、今回ホタテガイを採取した海域の清浄度は高く、海水中のカドミウム濃度は非常に低い。環境中のカドミウム濃度に応じて存在形態が変わる可能性も有り、そのメカニズムは非常に興味深く、今後の研究課題としたい。

参考文献

1)Ponzano,E.et al.,Polar Biol.,24,147 (2001)
2)中山憲司他,北海道立衛生研究所報,第４５集, 13(1995)
3) Evtushenko,Z.S.et al.,Mar.Biol.,104, 247(1990)
4)野矢洋一他,第３１回理工学における同位元素研究発表会要旨集,p131(1994)
5)Kagi JHR.et al.,Metallothionein.Ⅲ. Birkhauser,Basel,29(1993)

3-18

微生物中無機元素の動態解析

Behavior of inorganic elements in microorganisms

宮崎医科大学医学部化学、精神医学
中島　暉、植田勇人
Akira Nakajima, Yuto Ueda
Department of Chemistry, Department of Psychiatry, Miyazaki Medical College

1. はじめに

微生物のなかには、特定の重金属元素をその体内に集積するものが存在する。これまでの研究で、緑藻類、放線菌、細菌などが、銅、カドミウム、モリブデン、金、ウラン、トリウムなどに対して、優れた集積能を示すことが明らかになっているが、この集積の大部分は、代謝と無関係に細胞の物質と結合しており、生物吸着(Biosorption)と呼ばれている。生物吸着は主に細胞外部に重金属を蓄積し、しかも蓄積容量が大きいことから、水圏中有用金属資源の回収及び環境中有害重金属元素の制御の視点から、近年、活発に研究されている。

本研究では、微生物による重金属生物吸着の機構を解明するとともに、水圏中有用金属資源回収、環境中有害重金属除去を目的とした生物系重金属吸着剤の開発を進めている。微生物の能力を利用する水圏中銅の除去に関する研究は活発に行われているが、微生物による銅吸着機構はいまだ明確ではない[1-3]。とりわけ、微生物に取り込まれた銅のESRによる性状解析については、殆ど行われていない[4,5]。ここでは、中性子放射化分析、電子スピン共鳴(ESR)解析により、細菌による銅生物吸着の機構解析を行ったので報告する。

2. 実験方法

(1) 微生物の培養：東京大学分子細胞生物学研究所IAMカルチャーコレクション(IAM)及び広島大学大学院先端物質科学研究科生命分子機能化学講座(HUT)より分譲された微生物菌株を3日間培養後、遠心分離法またはろ過法で集菌し、後の実験に用いた。培地は、肉エキス 3 g/l, ペプトン 5 g/l, 塩化ナトリウム 5 g/l (細菌)；酵母エキス 4 g/l, 麦芽エキス 10 g/l, グルコース 4 g/l, pH 7.1 (放線菌)；酵母エキス 4 g/l, 麦芽エキス 10 g/l, グルコース 4 g/l, pH 5.7 (糸状菌・酵母)を用いた。

(2) 銅吸着実験：前培養した微生物菌体 20 mg (乾重量として)を40μMの銅を含む溶液(pH 5) 40 mlに懸濁し、銅を取り込ませた。銅塩として硝酸銅を用いた。遠心集菌後、残液中の銅濃度をICP法により測定し、銅吸着量を求めた。また、菌体中の銅量は、中性子放射化分析法により求めた。凍結乾燥した微生物菌体粉末を日本原子力研究所JRR－4炉気送管(中性子束 5×10^{13} n・cm^{-2}・sec^{-1})で1分間照射し、3分及び12時間冷却後、1039.0 KeV (^{66}Cu, 半減期 5.1分) 及び1345.5 KeV (^{64}Cu, 半減期 12.8時間) のγ線を計測した。中性子照射した微生物菌体のγ線スペクトルを図 1 に示す。また、1039.0 KeV (^{66}Cu, 半減期 5.1分)のγ線を用いた場合の検量線を図 2 に示す。

(3) ESR 測定：ESR スペクトルは、以下の条件で測定した。共鳴周波数 9.44 GHz、磁場 310 mT、磁場掃引幅 ±75 mT、磁場変調周波数 100 kHz、磁場変調幅 0.32 mT、マイクロ波出力 5 mW。

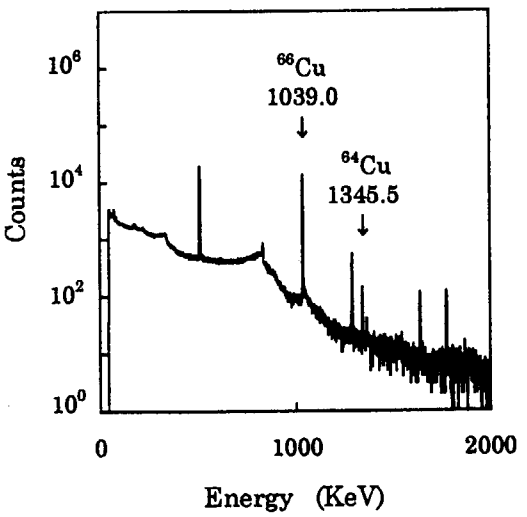


図 1.　中性子照射した銅を含む微生物菌体のγ線スペクトル

研究施設・装置：JRR-4 (気送管)　　研究分野：放射化分析

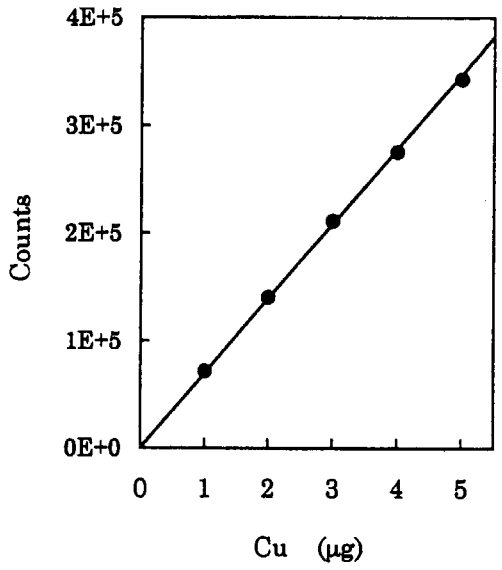


図2. 中性子放射化分析法による銅の検量線(⁶⁶Cuの1039.0 KeV, 半減期 5.1分のγ線)

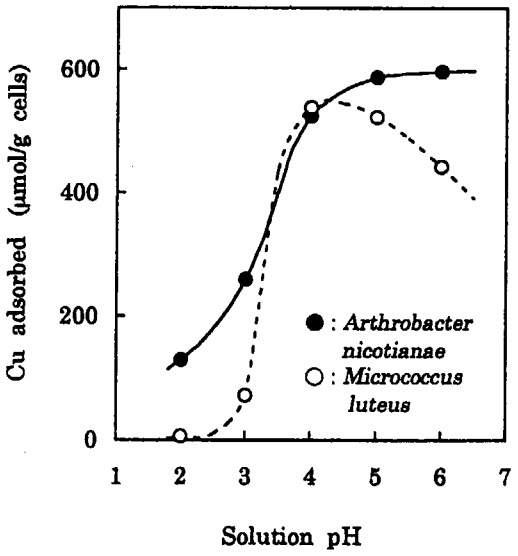


図3. 銅生物吸着に及ぼす溶液のpHの影響
微生物菌体20 mg(乾重量として)を400 μMの銅を含む溶液40 mlに1時間懸濁した。

3. 結果・考察

(1) 微生物による銅生物吸着

細菌、放線菌、糸状菌、酵母の銅生物吸着能を調べた。結果の一部を表1に示す。微生物の銅生物吸着能はその種類によって異なり、*Arthrobacter nicotianae* (IAM 12342), *Micrococcus luteus* (IAM 1056)などの細菌、*Streptomyces flavoviridis* (HUT 6147), *Streptomyces levoris* (HUT 6156)などの放線菌が高い値を示すことがわかった。そこで、細菌類*Arthrobacter nicotianae*, *Micrococcus luteus* について銅生物吸着特性を調べた。両細菌による銅生物吸着は極めて速く、銅溶液接触後数分で平衡に達した。両細菌による銅生物吸着は、溶液のpHの影響を受け(図3)、*Arthrobacter*菌の銅生物吸着量はpH 2～6の範囲でpHとともに増加したが、一方、*Micrococcus*菌はpH 4に極大を持ち、pH 5以上及びpH 3以下で減少した。このように、微生物による銅生物吸着に対する溶液のpHの影響は、微生物の種類によって異なることがわかった。

(2) 微生物菌体中銅(II)のESR

微生物菌体に取り込まれた銅(II)のESRスペクトルは、いずれも典型的な多晶形銅(II)化合物のパターンを示した。図4に銅を吸着した*Arthrobacter nicotianae*のスペクトルを、表1に$g_{//}$と$|A_{//}|$の値の一部を示す。表1より、$g_{//}=2.238\sim2.303$, $|A_{//}|=15.6\sim18.5\ mcm^{-1}$であり、微生物菌体中の銅(II)イオンは窒素原子と酸素原子がドナー原子として配位した歪んだ八面体構造を持つと考えられる[6]。また、*Arthrobacter nicotianae*, *Rhizopus oryzae*などのESRスペクトルは2種類のシグナル(表1のAとB)の重ね合わせであった。*Arthrobacter*菌では、pH 2～3で、新たなシグナル($g_{//}=2.388$, $|A_{//}|=13.0\ mcm^{-1}$)が現れることもわかった。これらのスペクトルの$g_{//}-|A_{//}|$プロットをとると、ほぼ直線になり、この変化は、Glycylglycylglycylglycine銅(II)錯体のpH変化と同じ傾向を示すことがわかった(図5)[7]。これらの結果から、微生物中の銅(II)は、細胞表面蛋白質のアミノ酸残基に結合しており、その配位状態は、微生物細胞表面付近のミクロなpHにより影響を受け、微生物中の銅(II)は、pH変化による窒素ドナーと酸素ドナーの配位能力変化に応じ4N (higher pH), 3N1O, 2N2O, 1N3O, 4O (lower pH) と配位環境が変化するものと考えられた(図6)。

表1. 微生物の銅集積能及び菌体に取り込まれた銅(II)のESRパラメーター

Species		Cu taken up (μmol/g) 4×10^{-5} M	Cu taken up (μmol/g) 8×10^{-4} M	$g_{//}$	$\lvert A_{//} \rvert$ (mcm^{-1})
Bacteria					
Arthrobacter nicotianae IAM 12342	(A)	70.0±1.2	603±5	2.245	18.2
	(B)			2.289	15.9
	(pH 2)			2.388	13.0
Bacillus subtilis IAM 1026		75.1±1.5	327±5	2.242	18.0
Citrobacter freundii IAM 12471		74.2±1.8	212±3	2.254	17.4
Escherichia coli IAM 1268		71.4±1.1	287±2	2.270	16.6
Micrococcus luteus IAM 1056		69.3±2.1	529±3	2.250	17.7
Pseudomonas stutzeri IAM 12097		96.0±2.3	340±4	2.276	17.3
Zooglea ramigera IAM 12136		64.0±1.3	377±3	2.245	17.7
Actinomycetes					
Actinomyces flavoviridis HUT 6147		64.2±0.6	499±9	2.249	17.6
Streptomyces fradiae HUT 6054		72.6±0.8	294±8	2.283	16.5
Streptomyces griseoflavus HUT 6153		68.0±0.8	292±3	2.303	15.6
Streptomyces hiroshimensis HUT 6033		65.3±0.4	309±9	2.266	17.3
Streptomyces levoris HUT 6156		72.2±1.1	551±3	2.249	17.6
Fungi					
Aspergillus niger IAM 2086		38.0±0.2	351±5	2.241	18.5
Penicillium chrysogenum IAM 7114		37.9±1.6	322±7	2.243	18.0
Rhizopus oryzae IAM 6006	(A)	38.0±3.3	382±9	2.253	17.6
	(B)			2.285	16.5
Yeasts					
Candida utilis IAM 4220		64.1±0.7	170±9	2.243	18.0
Cryptococcus laurentii IAM 12264		12.7±0.5	72±6	2.272	17.3
Saccharomyces cerevisiae IAM 4512		56.7±0.4	147±7	2.238	17.8

微生物菌体(乾重量として20 mg)を40 mlのCu溶液 (pH 5) に1時間懸濁した。

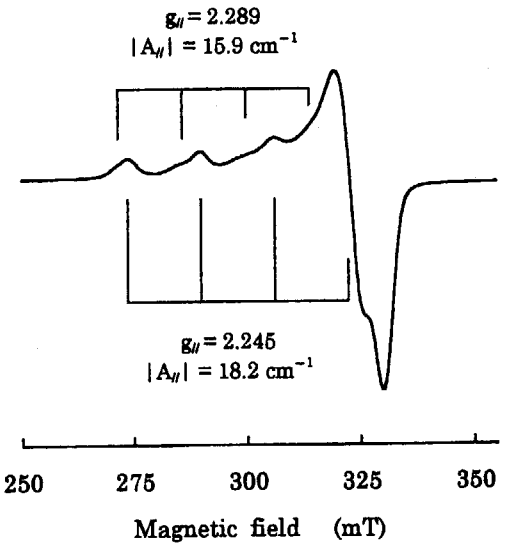


図4. 銅を吸着した微生物菌体のESRスペクトル

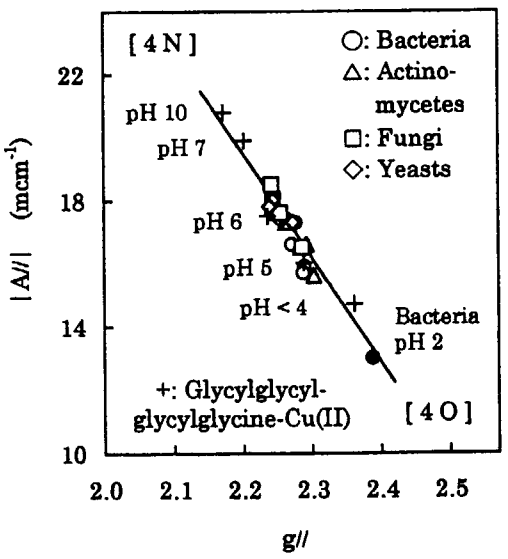


図5. Cu(II)錯体ESRの$g_{//}$－$|A_{//}|$プロット

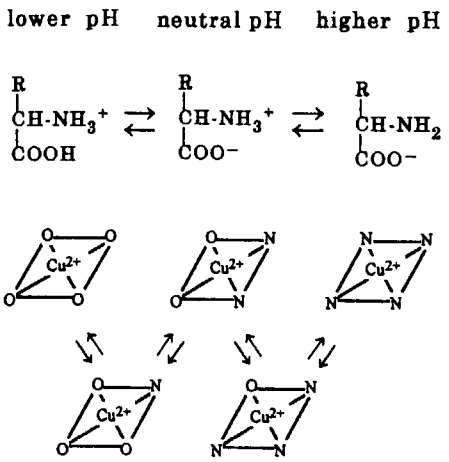


図6. 微生物中のCu(II)の配位環境

5. まとめ

本研究では、中性子放射化分析法、電子スピン共鳴分析法により、細菌類による銅の生物吸着について調べ、*Arthrobacter, Micrococcus*などの細菌が、優れた銅吸着能を持つこと、これら細菌による銅生物吸着は、極めて迅速に行われ、溶液のpHの影響をうけることがわかった。また、電子スピン共鳴解析により、微生物菌体に吸着された銅の大部分が細胞物質に結合しており、細胞物質中酸素及び窒素ドナー原子に配位された歪んだ八面体構造をもつことを明らかにした。今後、研究対象を、他の3d金属元素、希土類金属元素に広げ、中性子放射化分析法、電子スピン共鳴分析法を駆使して、これら金属元素の生物吸着能、吸着機構を解明したい。

6. 文献

(1) Huang, C., Huang, C. P. (1996) Application of *Aspergillus oryzae* and *Rhyzopus oryzae* for Cu(II) removal. Water Research 30 : 1985.

(2) Macaskie, L. E. (1995) Copper tolerance, phosphatase activity and copper uptake by a heavy metal-accumulating *Citrobacter* species. Microbios 84 : 137.

(3) Philip, L., Iyengar, L., Venkobachar, C. (1995) Biosorption of copper(II) by *Pseudomonas aeruginosa*. Int. J. Environ. Pollution 5 : 92.

(4) Tsezos, M., Mattar, S. (1986) A further insight into the mechanism of biosorption of metals, by examining chitin EPR spectra. Talanta 33 : 225.

(5) Lebedev, V. S., Volodina, L. A., Fedorov, Yu. I. (1991) ESR analysis of copper binding sites in intact and N-ethyl-maleimide-modified bacteria *Escherichia coli*. Biophysica 36 : 91.

(6) Peisach, J., Blumberg, W. E. (1974) Structural implications derived from the analysis of electron paramagnetic resonance spectra of natural and artifical copper proteins. Arch. Biophys. Biochem. 165 : 691.

(7) Landolt-Boernstein : Numerical Data and Functional Relationships in Science and Technology, 1984, (Eds. K. H. Hellwege, O. Madelung), Vol.. 12, Magnetic Properties of Coordination and Organometallic Transition Metal Compounds, Subvolume b, Electron Paramagnetic Resonance, Springer-Verlag, Berlin.

7. 成果の公表

［学術論文］

(1) 中島暉、横山秀克、大矢博昭、鎌田仁：微生物に取り込まれた銅(II)イオンのESRによる解析. 磁気共鳴と医学, Vol. 12, 80-83 (2001).

(2) A. Nakajima, M. Yasuda, H. Yokoyama, H. Ohya-Nishiguchi, H. Kamada : Copper biosorption by chemically treated *Micrococcus luteus* cells. World J. Microbiol. Biotechnol., Vol. 17, 343-347 (2001).

［学会発表］

(1) 中島 暉, 鶴田猛彦, 保田昌秀, 横山秀克, 大矢博昭, 鎌田仁：微生物による銅などの重金属元素の回収除去. 日本化学会 第75秋季年会 (松山, 1998年9月).

(2) 中島 暉, 保田昌秀, 横山秀克, 大矢博昭, 鎌田仁：微生物による銅などの重金属元素の回収除去. 2. 日本化学会 第76秋季年会 (横浜, 1999年3月).

(3) 中島 暉：微生物に吸着された銅のESR. 第3回 ESRフォーラム研究会(京都, 1999年6月).

(4) 中島暉, 横山秀克, 大矢博昭, 鎌田仁：微生物に吸着された銅(II)イオンのESRによる解析. 第22回磁気共鳴医学会・第4回SFRRJapan合同学会(東京, 2000年6月).

3-19

生理活性物質中の微量元素に関する研究

Study on trace elements in physiologically active substances.

共立薬科大学　放射薬品学教室
本間義夫、森田裕子、村上　勲、大原久美子
Laboratory for Radiopharmaceutical Chemistry, Kyoritsu College of Pharmacy
Yoshio Homma, Yuko Morita-Murase, Isao Murakami, Kumiko Ohara

1. 研究目的と意義

生体中の微量元素の中には、ヘモグロビンやクロロフィルにおける鉄やマグネシウムのように、活性に極めて重要な役割を果たすものが存在する。

本研究室では、生体内の微量元素の役割を解明する研究の一環として、金属酵素、金属タンパク質など種々の生理活性物質中の微量元素を熱中性子放射化分析により定量し、さらに放射光による回折やNMRなどにより、これらの生理活性物質の構造解析を行う。

本研究により得られる知見は生体内中の微量元素の役割を明らかにする基礎データとして極めて重要である。

2. 研究の方法

精製したタンパク質3～5mgを、よく洗浄、乾燥したポリエチレン袋に二重に封入し試料とした。照射は、東海研究所JRR-3MとJRR-4Mの気送管を利用し、中性子束 1.9×10^{13}～4.5×10^{13} (n/cm²・sec)、照射時間0.5～5分の条件で行った。照射終了3～10分後、あるいは5～6時間後にGe半導体検出器を用いてγ線の測定を行った。測定時間は300秒、dead timeは10%以下であった。

得られたγ線スペクトルから、試料中に含まれる微量元素の同定を行い、さらに定量のための試料の精製、調製を以下のように行った。

精製は遠心式濃縮器を用いて5100rpm、1時間を数回繰り返し、最後に精製濃縮液を1400rpm、2分間で回収した。

液体試料はろ紙に滴下し、乾燥後ポリエチレン袋に二重に封入した。試料は、濃度既知の標準試料とともに照射後、試料については300秒、標準試料は200秒γ線スペクトルを測定し、相対法により、試料の含有微量元素量を求めた。

照射の結果、金属含有量が高い試料については、放射光による構造解析を目的として結晶化を試みた。結晶化のために、まず高分子結晶化試薬クリスタルスクリーニング・キットを用いて、pH、塩、沈殿剤等の結晶化条件を検索した。結晶化法は、密閉容器中にタンパク質溶液と沈殿剤を入れ、蒸気平衡によって結晶化を行うハンギングドロップ蒸気拡散法を用いた。

組織培養用プレートにpH、塩、沈殿剤の異なる98種類の滅菌済試薬を入れ、タンパク質溶液と試薬の混合液（1:1）を載せたカバーグラスを反転させてプレートの上に載せた。密閉を確かなものにするため、シリコングリースでシールして静置した。その後、結晶化の進行状況を顕微鏡で観察した。

3. 結果とその評価

(1) 熱中性子放射化分析によるタンパク質中の微量金属定量結果

多くのタンパク質の中にAg, Ba, Ca, Co, Cu, Mg, Mn, S, V, Znなどの元素がふくまれていることが明らかとなった。標準試料と同時照射する相対法によって得られた定量分析の結果、Cu, Mg, Mn, Znの元素については、試料1mgに対してそれぞれ10^{-4}～10^{-6}mg、10^{-3}～10^{-5} mg、10^{-5}～10^{-7} mg、10^{-3}～10^{-5} mg含まれていることが明らかになった。

遠心式濃縮器による脱塩の操作により、Cl, Naは減少し、その結果、^{38}Cl, ^{24}Naなどによるコンプトンスペクトルの影響が抑えられ、目的核種の光電ピークの定量が容易となった。

(2) タンパク質試料の結晶化

金属元素量として試料1mg中に10^{-4}mg以上の金属元素を含んでいるタンパク質（７種類）を選び、蒸気拡散法による結晶化を試みた。

クリスタルスクリーニングにより、98種類の沈殿剤、pH 等の検討をした結果、３種類のタンパク質について微細な結晶が得られた。それぞれの条件（タンパク質濃度、pH、沈殿剤等）は表にあげた。

さらに、放射光による構造解析に用いるため、良質な結晶を得ようと試みているが、現在までのところ、構造解析に必要な 0.1mm 以上の大きさの結晶には到達していない。

原因としては、試料の精製が不十分であったこと、試料の初期濃度が不適当であったこと、さらに静置時の環境の変動等が考えられる。

現在、これらの点に注意し、再検討を行い、７種類のタンパク質の結晶化を試みている。

また、継続して、さらに広範囲の金属含有タンパク質の探索を行っている。

4. 成果の公表

1) 大原久美子、森田裕子、村上 勲、本間義夫：SODの酵素活性と含有金属量の相関について、原子力研究総合センターシンポジウム（1999年12月）.
2) 大原久美子、森田裕子、村上 勲、本間義夫：金属含有タンパク質の結晶化とその構造解析－１、日本薬学会第121年会（2001年３月）.
3) 大原久美子：酵素中の微量金属の定量と金属含有酵素の結晶化に関する研究、修士論文、共立薬科大学（2001）

表　蒸気拡散法による結晶化の条件

タンパク質	結晶化条件
A	タンパク質濃度：3.275mg/mL 緩衝液：0.1M HEPES-Na（pH7.5） 沈殿剤：2%v/v Polyethylene Glycol 400, 2.0M Ammonium Sulfate
B	タンパク質濃度：1.38mg/mL 緩衝液：0.1M TRIS （pH8.5） 沈殿剤：3.4M 1,6Hexanediol 0.2M Magnesium Chloride hexahydrate
C	タンパク質濃度：2.015mg/mL 沈殿剤：0.4M Potassium Sodium Tartrate tetrahydrate

3-20

地圏環境における元素分布・循環の研究
－原子炉中性子照射，郵送，γ線計測による多試料・多元素分析システムの確立－
The development of neutron activation, sample transportation and γ-ray counting routine system for numbers of geological samples

柴田信之介 (SHIBATA Shin-nosuke)[1]・田中剛 (TANAKA Tsuyoshi)[1]・南雅代 (MINAMI Masayo)[1]・
仙田量子 (SENDA Ryoko)[2]・武邊勝道 (TAKEBE Masamichi)[1]・加地拓哉 (KACHI Takuya)[2]・
近藤正史 (KONDO Masashi)[2]・織田周平 (ODA Shuhei)[1]・林隆正 (HAYASHI Takamasa)[1]・
西澤邦秀 (NISHIZAWA Kunihide)[3]・小島久 (KOJIMA Hisashi)[3]

1）名古屋大学大学院環境学研究科地球環境科学専攻，464-8602　名古屋市千種区不老町
Graduate School of Environmental Studies, Nagoya University, Furo-cho, Chikusa, Nagoya 464-8602, Japan.
2）名古屋大学大学院理学研究科地球惑星理学専攻，464-8602　名古屋市千種区不老町
Graduate School of Sciences, Nagoya University, Furo-cho, Chikusa, Nagoya 464-8602, Japan.
3）名古屋大学アイソトープ総合センター，464-8601　名古屋市千種区不老町
Radioisotope Center, Nagoya University, Furo-cho, Chikusa, Nagoya 464-8601, Japan.

Abstract

A new gamma-ray counting and data processing system for non-destructive neutron activation analysis has been set up in Radioisotope Center in Nagoya University. The system carry out gamma-ray counting, sample change and data processing automatically, and is able to keep us away from parts of complicated operations in INAA.

In this study, we have arranged simple analytical procedure that makes practical works easier than previous. The concrete flow is described from the preparation of powder rock samples to gamma-ray counting and data processing by the new INAA system. Then it is run over that the analyses used two Geological Survey of Japan rock reference samples JB-1a and JG-1a in order to evaluate how the new analytical procedure give any speediness and accuracy for analyses of geological materials. Two United States Geological Survey reference samples BCR-1 and G-2 used as the standard respectively. Twenty two elements for JB-1a and 25 elements for JG-1a were analyzed, the uncertainty are <5% for Na, Sc, Fe, Co, La, Ce, Sm, Eu, Yb, Lu, Hf, Ta and Th, and of <10% for Cr, Zn, Cs, Ba, Nd, Tb and U. This system will enable us to analyze more than 1500 geologic samples per year.

1. はじめに

機器中性子放射化分析法は，試料の化学処理をしないで多数の元素を定量できる方法として広く用いられ，その応用分野は考古学，生物学，地質学・地球化学，犯罪科学，工業製品や医学など多岐に渡っている。その中でも特に，種々の元素が含まれている考古学的・地球科学的試料の多成分分析においては，化学処理なしに多元素の同時定量ができるという点でこの分析法を用いるメリットは大きい。一方，放射化分析に関する教科書（例えば，橋本芳一著「放射化分析の実際」や日下譲著「放射化分析」）はあるものの高度な分析技術を志向するものが多く，分析手法の自動化・平易化を目指したものは少ない。

本研究では地圏環境評価を目的とする河川堆積物の多試料・多元素分析を目的として，試料調製から中性子照射・γ線測定に至るルーチンシステムを開発した。また，岩石標準試料の繰り返し測定・解析によって，新しい分析システムの機能評価を行なった。本研究の主な目標としては，作業手順の単純化，分析精度の向上，より迅速な分析，より多くの試料の分析，一連の分析にかかる諸経費の削減，の5つが挙げられるが，最も重要視したのはそれら全体としてのバランスである。つまり本研究は，容易に・精度良く・早く・多く・安く分析できる最適の放射化分析手法の確立を試みたものである。以下では放射化分析の具体的な手順を試料の準備から測定・解析に至るまで解説するとともに，岩石標準試料の分析結果を報告する。

研究施設と装置名：JRR-3 気送管，JRR-4 気送管・Tパイプ・Sパイプ
研究分野：中性子利用分析・放射化分析，地球化学

2. 原　理

簡単に放射化分析の原理を説明する。試料を高エネルギーの荷電粒子（陽子・α粒子など），中性子，光量子などで照射すると，試料中の元素はその核種の特性に従って核反応を起こす。その結果，不安定な放射性核種が生成され，この放射性核種は核種個有のエネルギーを持ったβ線やγ線等を放出し，それぞれの半減期に従って安定核種へと壊変していく。その放出される放射線のエネルギー（波長）と半減期により核種が同定される。

未知試料中の元素濃度の定量には，一般に既知の元素含有量をもつ標準物質を未知試料と同じ条件で放射化し，標準物質においてピークが同定された核種のγ線のエネルギー強度（ピークの高さ）とそれに対応する元素濃度の比が用いられる。そして，未知試料での各γ線のエネルギー強度から元素濃度を求めることができる。ただしそのときに問題になるのが，中性子照射時における試料の自己しゃへい，及び測定時の試料自身によるγ線の自己吸収や幾何学的配置（ジオメトリー）である。さらに，測定時の検出器の不感時間ならびにγ線スペクトルの形状の違いによる計算処理に起因する誤差を考えると，これらの条件が標準物質と未知試料の間で大きく異なっていては精度の良い分析は期待できない。したがって，標準物質には化学形態，幾何学的形状，化学組成および各元素の絶対量が分析対象とする未知試料とできるだけ類似したものを用いる方がよい。

なお，本研究における測定では標準試料としてBCR-1，G-2，未知試料としてJB-1a，JG-1aを用い，放射化には日本原子力研究所JRR-4炉の熱中性子を用いた。

3. 測定系の概要

名古屋大学アイソトープ総合センター内に設置されているγ線計測システムは，A.　サンプルチェンジャ部，B.　検出器部，C.　波高分析器部，およびD.　データ処理部，より構成される。図1にシステムの全容を，図2にその概略図を示す。

A. サンプルチェンジャ部

A1部分にはチェーンに連結したテーブルが全部で20個あり，それぞれの上にはアクリル製のサンプルホルダが備え付けてある。試料はアーム（A2）によってこのホルダごと測定用しゃへい体A3に自動的に搬入・搬出がなされる。A3内部は外部からの放射線の入射を防ぐために 100 mm 厚の鉛，10 mm 厚の無酸素銅および 5 mm 厚のアクリルで囲われている。内部は 165 mm × 165 mm × 135 mm の空間容積を持つ。A3上部は自動開閉式のスライドシャッタになっており，A1下部にあるサンプルチェンジャ独自のタッチパネル式コントロールパネルで制御できる。またこのコントロールパネルで手動モードにしておくと，サンプル交換に伴う各種操作を任意に行なうことができる。テーブルやアームの位置を初期状態に戻す時も手動モードで「原点」を押せばよい。なお，放射化分析プログラムを用いて自動測定をする場合，「自動」を押し，自動モードに切り替える必要がある。

B. 検出器部

検出器には EG & G オルテック社製の高純度Ge半導体検出器 GEM 35190 型が用いられており，EG & G オルテック社製高圧電源（B1）により通常は 3500 V の電圧をかけて用いる。測定可能なエネルギー範囲は 40 keV ～ 10 MeV であり，エネルギー分解能は 122 keV および 1.33 MeV においてそれぞれ，FWHM が 862 eV および 1.78 keV である。またピーク／コンプトン比は 69.1 ，相対効率は40.1％である。検出器からの信号は EG&G オルテック社製の増幅器（B2）で増幅される。

C. 波高分析器部

検出器部で増幅されたγ線のエネルギーパルスは，マルチチャンネルアナライザ（セイコー EG & G 社製 MCA 7700）によってエネルギーに対応したチャンネルごとにカウントされる。チャンネル数は，256，512，1024，2048，4096，8192，16384　と可変であるが，1チャンネルあたり　0.5 keVの解像度を得るため，および ^{170}Tm の 84 keV から ^{124}Sb の 1691 keV をカバーするために，通常は4096のチャンネル数に設定されている。分析結果はリアルタイムでγ線エネルギースペクトルとしてタッチパネル式の画面に表示され，測定が終了するとそのスペクトルはMCAのメモリに記憶される。なお，測定の開始や終了，ピーク解析などの操作はこのMCAだけを用いても行なうことが可能である。

D. データ処理部

放射化分析システムのメインとなるのがセイコーエプソン社製のパーソナルコンピュータ（D1）で，機器制御および解析プログラム，各種ファイルはすべて内蔵のハードディスクに収められており，スペクトルデータや解析結果の保存などもここに行なわれる。また，このパソコンにインストールされている「ガンマスタジオ」というソフトを用いて

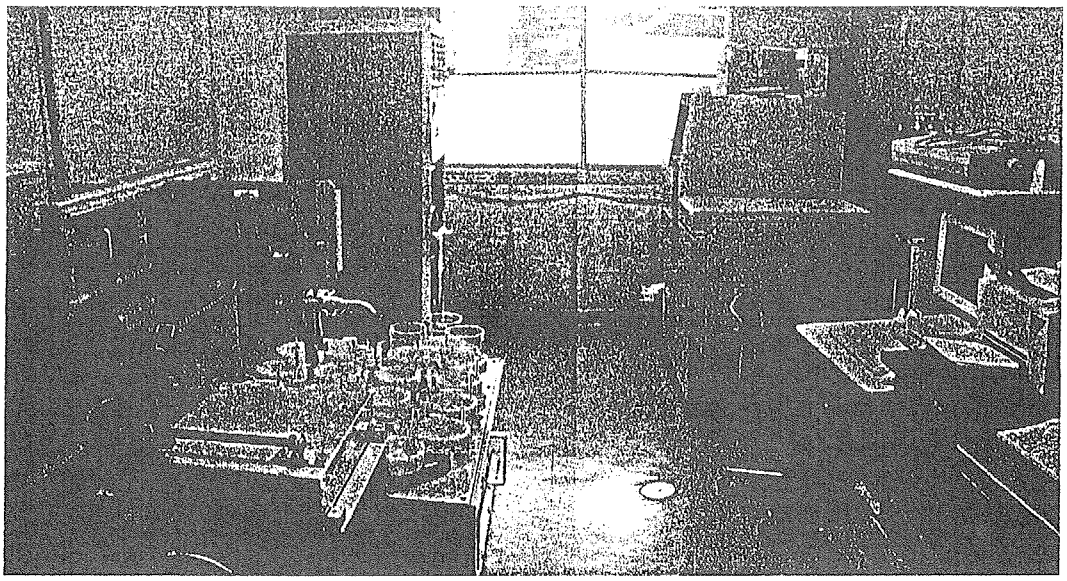


図1-a. 名古屋大学アイソトープ総合センター測定室に設置されている放射線自動測定・解析システムの全容.

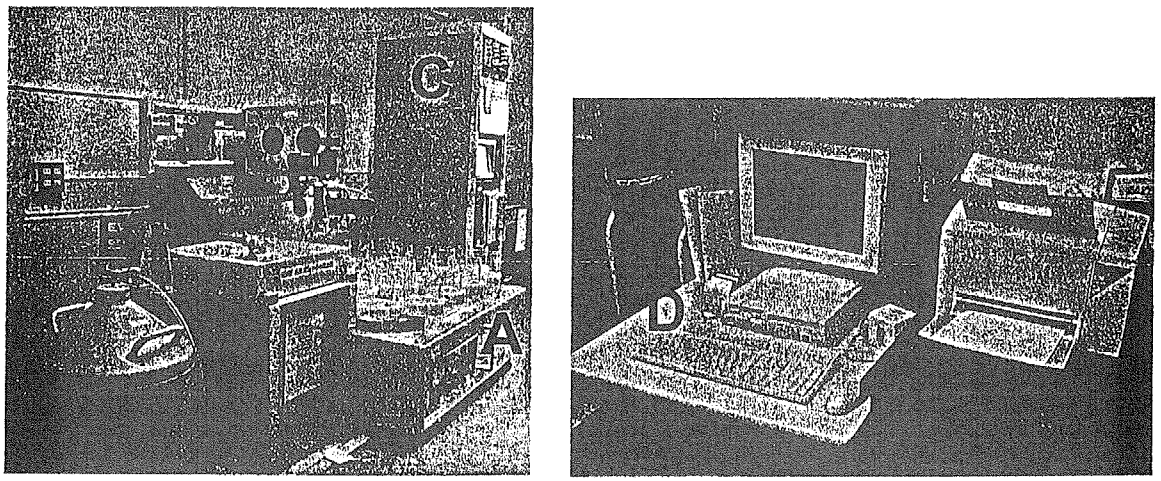


図1-b. 放射線自動測定・解析システムの各部.

A:サンプルチェンジャ部　B:検出器部　C:波高分析器部　D:データ解析部

MCA を制御できるようになっており，実際に放射化分析を行なう場合，ほとんどの操作はこのパソコン上で行なうことになる。得られたγ線エネルギースペクトルは「ガンマスタジオ」でリアルタイムに表示・観察することができ，スペクトルにおけるピークの検出や面積計算，標準試料との比較による濃度換算など，基本的にはこのソフトだけでデータの定性・定量解析を行なうことができる。さらに「ガンマスタジオ」による測定・解析作業を組み込んだ「放射化分析プログラム」を用いれば，必要なデータ（一試料あたりの測定時間，試料の数と重量，中性子照射日時など）が揃っている場合，サンプルチェンジャによるサンプル交換も含め測定から標準試料との比較定量解析，そして備え付けのプリンタ（D2）を通じた解析結果のプリントアウトまでを自動的に行なうことが可能となる。第6節の測定・解析の項では，その「放射化分析プログラム」を用いた自動測定の場合を中心に述べる。

4. 試料調製

岩石粉末試料には比重の異なる様々な鉱物粒子が含まれ，粉体試料中で偏在することが多い。特に酸性岩ではスフェンやジルコンといった希元素に富む副成分鉱物が充分に粉砕されていなかったり，粉砕されても粉体試料中に偏在することがしばしばみられる。従って，その試料が地球化学的に意味を持つためにはできるだけ多量の試料を分析に使用することが望ましい。しかし，試料サイズが大きくなると，中性子照射およびγ線測定時の自己しゃへい・自己吸収，照射時の中性子フラックスの不均一性，さらに測定時の検出器に対する試料の位置（ジオメトリー）の再現性についての問題が無視できなくなる。

岩石粉末試料は，中性子やγ線の吸収が少なく放射化されにくい容器の中に入れて中性子照射される。一般に石英ガラスチューブや，ポリエチレン製の容器またはバッグに封入されることが多い。石英ガラスチューブは熱に強く，試料が少量しかなく充分なγ線強度を得るために長時間の中性子照射が必要な場合には有用である。しかし，その反面やや高価であり力学的破損には注意しなければならない。ポリエチレン製の容器やバッグは静電気による埃の付着などの汚染に留意する必要があり熱に弱いという欠点を持つが，比較的手軽に扱うことができ安価であることから，多数のサンプルを迅速に分析したい場合には有効な素材である。また，後述するように適度な試料量があれば中性子照射時間を短くすることが可能となり，その結果熱の発生は抑えられるため，その点を考慮すれば熱に対する弱さも問題なくなる。本研究では，ポエチレンバッグに封入する方式を採用し，万一のバッグの破損に備え試料を内袋に入れたものをさらに外袋に入れるようにした。また照射後に外袋を交換することによって，取扱いの安全性を増すとともに照射前に外袋に付着した汚染物質の影響を減らしている。

手順の概要を図3に示す。ポリエチレンバッグは内袋にも外袋にも市販のポリエチレンシート（厚さ0.1 mm）を用いた。内袋は2枚重ね合わせたシートを横約 15 mm 縦約 40 mmの長方形の袋ができるようにポリシーラでシールして作成する。外袋も同様にして横の幅が約 20 mm，縦が約 35 mm のものを作成する。岩石粉末試料は予め約 100 mg ずつを薬包紙に計り取り試料名を記しておく。次に，作成しておいたポリエチレンバッグ（内袋）を何も入っていない状態で秤量瓶にセットし重量を計る。秤量瓶には，予め試料名に応じた番号を記しておく。薬包紙から岩石粉末試料をガラス製の小型ろうとを用いて，内袋の底の方に流し入れ，秤量瓶も合わせた全体の重量を計り，そこから先ほど計った空の状態の重量を差し引いて試料の重さを求める。その後，秤量瓶から取り出した内袋の口を試料が付着していない部分でポリシーラによってシールし，内袋はさらに外袋に入れ同様に封入する（内袋が長くなったときは折り畳んで封入する）。なお，試料名は内袋に油性マーカで記入しておく。このようにして封入した試料を，照射用の専用カプセルの中に入れる。そのときなるべく標準物質が中心にくるように配置し，熱によるポリエチレンバッグ同士の癒着を防ぐために，各試料の間には約 1 cm 四方のろ紙または薬包紙を挟んでおく。この専用カプセルにはおよそ20試料まで封入することができるが，10～15試料あたりが最適な試料量である。以上，カプセルへの封入までのすべての作業において，試料を扱うときは汚染をなるべく防ぐためにポリエチレン手袋を着用し，はさみやポリシーラなど用いる道具類も使用前には必ずアルコールで洗浄するよう心掛ける。

5. 中性子照射

分析対象とする放射性核種の半減期から考えると，照射時間が50-60時間位までは照射時間の長さとともに検出感度が向上する。しかし，日本原子力研究所JRR-4による照射経費は照射時間とともに増えること，および必要以上に強い放射能は取扱いの

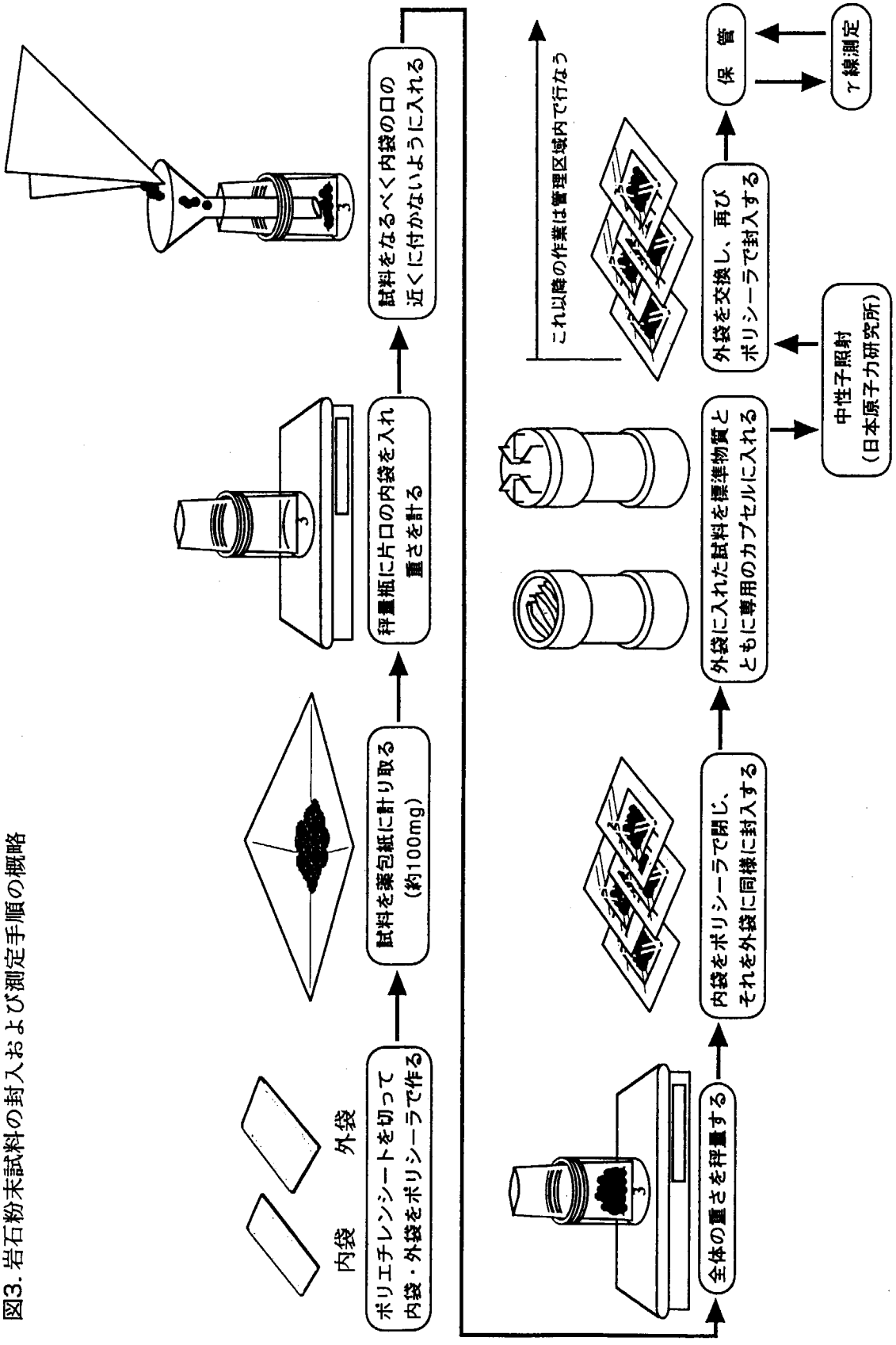


図3. 岩石粉末試料の封入および測定手順の概略

安全上からも好ましくないことから，計測装置の持つ計数速度を充分に発揮し得るのに必要最低量の放射線強度が得られる照射時間を，本研究における最適照射時間とした。この最適照射時間は試料の化学組成，特にスカンジウム，鉄，コバルト等の含有量により変化するが，約 100 mgの岩石粉末試料をJRR-4で気送管照射する場合，5分間の照射で分析対象となるほとんどの元素において，約5日間冷却させた後の測定でも充分なγ線強度が得られることがわかった。必要最低限に照射時間を短くし，放射線量率を低くすることによって，放射性物質の運搬に関する法律に定められている中でもっとも放射線量率が低いL型の放射性輸送物（箱の表面で5μSv/h以下）として郵送による試料の受け渡しが可能となり，経費も大幅に削減されより多数の試料の分析が可能となった。本研究に関する試料においては，中性子照射後5日目の発送を依頼すれば6日目午後にはほぼ入手できており，6日目あるいは翌7日目から測定を開始することができる。

6. 測定・解析

6.1. 測定前の処理

日本原子力研究所から郵送されてきた放射化された試料は，アイソトープ総合センター内に諸手続きを経て持ち込み，予め利用の申請をしてある実験室にて測定前に外袋の交換作業を行なう。万が一の汚染を防ぐため両手にはポリエチレン手袋をはめ，片面がポリエチレンで不透水加工されたシートを敷いた実験台の上でピンセットとハサミを用いて1カプセル分がひとつになっている袋から個々の試料を取り出す。それぞれの試料において内袋からの試料漏れがないか確認した後，充分に注意を払いながら外袋のみを切って内袋を取り出す。それを照射後用のポリエチレンバッグ（比較的薄いものでよい）に入れポリシーラーで封じる。もし内袋から試料が漏れていることが認められる場合は，外袋も切らずにそのまま照射後用のバッグに入れる。このようにして外袋を交換した1カプセル分の試料はひとつの新しいポリエチレン袋にまとめて入れ，カプセル番号を記入し，RI管理番号・核種・保管者の所属及び氏名を明記したラベルを貼付ける（このラベルはアイソトープ総合センターの安全管理室から試料の持ち込み時に支給される）。なお，放射性物質による汚染の危険が伴うこの作業は，万が一のために二人ひと組で行なうのが望ましい（どちらかは必ず汚染の危険がないように作業を分担する）。

6.2. 測定方法

外袋を交換した試料は基本的に素手で触れても放射性物質の付着の恐れはないが，γ線による被曝を最小限に抑えるためにも大きめの袋などに入れてなるべく身体から遠ざけながら測定室に持ち運ぶ。

アイソトープ総合センター1階の測定室には，γ線測定のための高感度Ge半導体検出器が3台設置されているが，岩石粉末試料などの測定に用いているのは中央に位置するオートサンプルチェンジャ付のGEM型高純度Ge半導体検出器である。第3節で述べたように，この検出器で検出されたγ線は，エネルギーごとに割り当てられたチャンネルごとに波高分析器（セイコーEG & G 社製 MCA 7700 ）によってカウントされ，γ線エネルギースペクトルとして記録される。また，オートサンプルチェンジャや波高分析器はパーソナルコンピュータ（セイコーエプソン社製）によって制御することができるようになっており，「放射化分析プログラム」を利用すれば容易に複数個の試料の自動放射化分析が行える。次の項ではオートサンプルチェンジャも含めた具体的な操作手順について説明する。

6.3. 放射化分析プログラム

システム全体の立ち上げはノイズによる誤作動を防ぐため，パソコンが起動し終わってからオートサンプルチェンジャの電源を入れるようにする。通常，波高分析器は常に電源が入れられておりパソコン内のソフトで操作できるので特に触る必要はない。

放射化分析プログラムを利用するにあたって，まずいくつか用意しておかなければならないファイルがある。それは，分析対象核種ごとのエネルギースペクトルや半減期などの情報が入ったファイル（マスターライブラリファイル），分析に使用する標準物質に含まれる既知の元素濃度が入ったファイル（標準試料ライブラリファイル）と，気温や気圧の変化によるγ線検出器自体の状態変化からくるチャンネルとエネルギーのずれを補正するためのファイル（エネルギ校正ファイル）である。これらは「マイコンピュータ」内にあるSegdatフォルダの中の，Livフォルダ，Stdフォルダ，Eneフォルダにそれぞれ保存する。以下に，それぞれのファイルの作成方法について述べるが，一般的な珪酸塩岩石の分析の場合には【3】を除き既存のファイルを用いて充分な分析ができる。

【1】マスターライブラリファイルの作成（図4）

放射化分析プログラムのサブメニューにあるマスターライブラリ編集のボタンをクリックすると「核

種データリスト」というウィンドウが現れる（図4a）。その中にある「周期表」のボタンをクリックすると別ウィンドウに周期表が現れる（図4b）。そこで分析対象となる元素をクリックして選択していくと，各元素に対応した同位体核種が核種データリストのウィンドウにインポートされる（図4c）。同じ核種でも放出されるγ線エネルギーによっては複数登録される場合がある。その中で必要のない核種（γ線の放出率が極端に低いものや半減期が極端に短いもの）については選択状態にした上で，メニューの中の「削除」から「1つだけ削除」を選び削除していく。すべて入力し終わったファイルは，名前をつけてLivフォルダの中に保存する。

もうひとつ，新規にファイルを作る方法として，「ActMaster.LIV」から一核種ずつ選んでインポートしていくこともできる。また予め保存してあるファイルに核種を追加し，別名で保存することにより，新しいマスターライブラリファイルを作ることもできる。対象核種を増やすことで一度に多くの元素分析が行えるが，その分，解析時間が長くなるので明らかに試料中に含まれていない元素や，γ線エネルギースペクトル上でピークの出る見込みのない核種については無駄に登録しない方がよい。なお，岩石などの地質試料を対象とした放射化分析では，すでに作成してあるファイル「Activation.LIV」もしくは「Activation2.LIV」で大部分の元素がカバーできるため，特に新たなマスターライブラリファイルを作成する必要はない。ちなみに，「Activation2.LIV」は「Activation.LIV」に分析対象元素を数種類追加したものである。

【2】標準試料ライブラリファイルの作成（図5）

(1)と同様にサブメニューにある標準試料ライブラリ編集のボタンをクリックすると編集プログラムのウィンドウが現れる（図5a）。左側にある「LIV」ボタンをクリックし，分析対象元素が含まれるライブラリファイルを読み込む。すると左側のカラムに登録されている元素名の一覧が表示される（図5b）。そしてその一覧の中から，分析対象でありかつその標準試料中に含まれる元素を選択し，各元素について既知濃度と単位（%，ppm または ppb）を入力する（図5c）。できあがったファイルは名前をつけてStdフォルダの中に保存する。これも(1)と同様にすでにあるファイルを編集し直し（濃度の値を変更するなど）別名で保存することによって新たな標準試料ライブラリファイルを作ることができる。

【3】エネルギ校正ファイルの作成（図6）

まず，エネルギ校正とは，波高分析器の4096チャンネルに割り当てられるエネルギが室温などの環境変化とともに経時変化するために，測定毎にそれを校正する作業である。

エネルギ校正ファイルの作成には「ガンマスタジオ」というソフトを使用する。メインメニューにある「ガンマスタジオ」のボタンをクリックすると「ガンマスタジオ」が立ち上がる。次に解析対象となる試料の測定日になるべく近い日に測定した試料のスペクトルファイルを読み込む（同じグループの標準試料のスペクトルファイルを用いるのが理想的）。より正確なエネルギ校正を行なうため，なるべく広いエネルギ範囲に渡って多くのピークが検出されているスペクトルファイルを用いるのが望ましい（例としてここでは地質調査所の岩石標準試料JB-1aのγ線エネルギスペクトル（図6a）を用いている）。スペクトルファイルを読み込んだらウィンドウ内のメニューの「計算」をクリックし，現れた項目の中から「平滑化一次微分ピークサーチ」を選択する。それによって検出されたピークには，その形に応じた幅で計算されたピーク面積の領域に色（ROI）がつく（図6b）。スペクトル上で右クリックするかメニューの「校正」の「簡易エネルギ校正」という項目を選択すると（図6c），「ピークサーチ結果を全てエネルギ校正に使用しますか？」というダイアログが出るので「はい」をクリックする。するとエネルギ校正ファイル作成用のウィンドウが現れ，すべてのピークのチャンネル情報が取り込まれる（図6d）。その中から任意の明瞭なピークについて，以前の校正結果を参考にピークに対応する核種を同定し（取り込んだ時点で自動的に同定されることもある），そのγ線のエネルギの値を入力する。ピークが不明瞭なものは選択して削除する。すべてのエネルギの値を入力し終えたら，「ファイル」の「γ線用エネルギ校正ファイル保存」から「Ge検出器による核種分析」を選択し，作成日に基づいた名前（例えば2001年1月1日作成の場合：kousei010101.ENE）をつけて，Eneフォルダの中に保存する。そのとき「コメント」欄に使用したスペクトルファイル名を書いておく（後々その校正ファイルが有効な日時を知るため）。それから「決定」または「キャンセル」ボタンをクリックし，簡易エネルギ校正を終了させる。また，エネルギ校正ファイル作成メモに，作成した校正ファイル名・作成日・作成者名・使用したスペクトルファイル名及び測定日，そして核種ごとのγ線エネルギに対応したチャンネルの値を記録しておく。

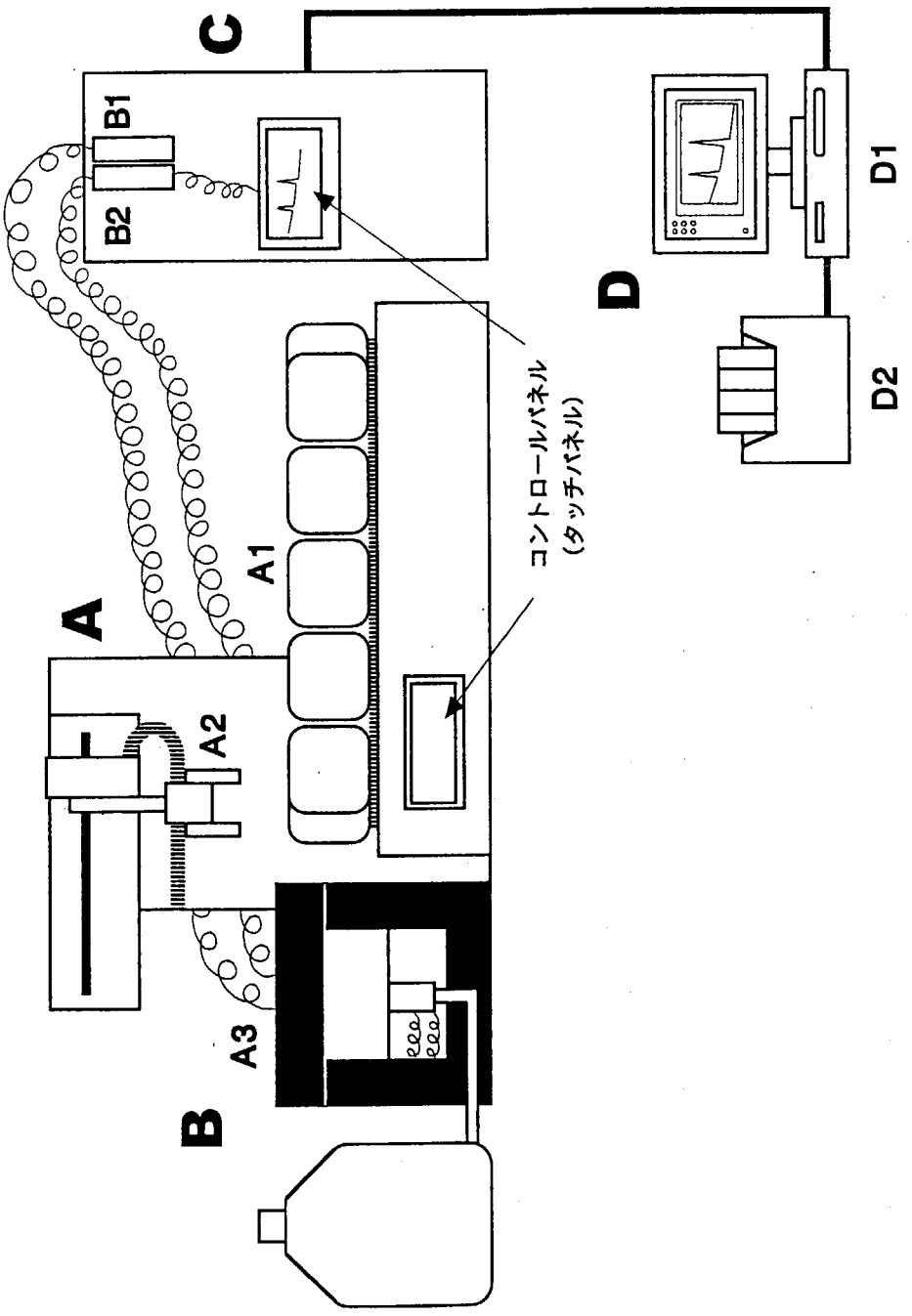
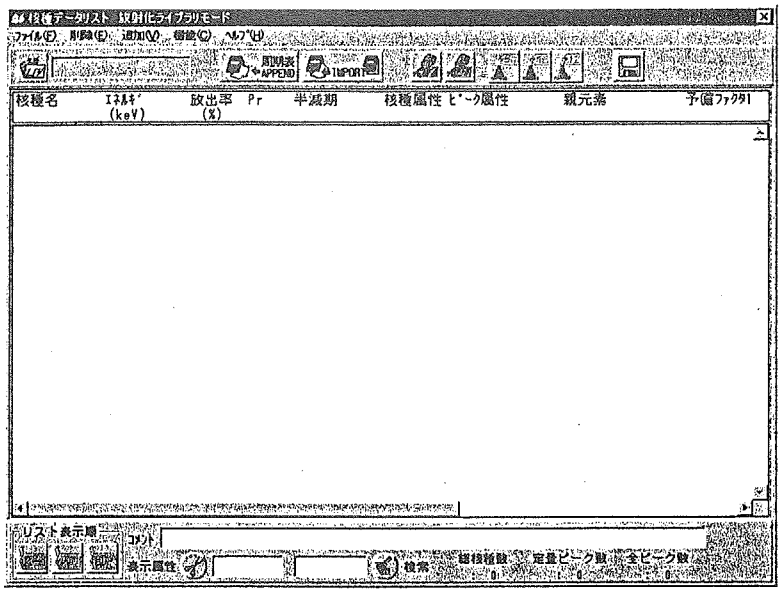
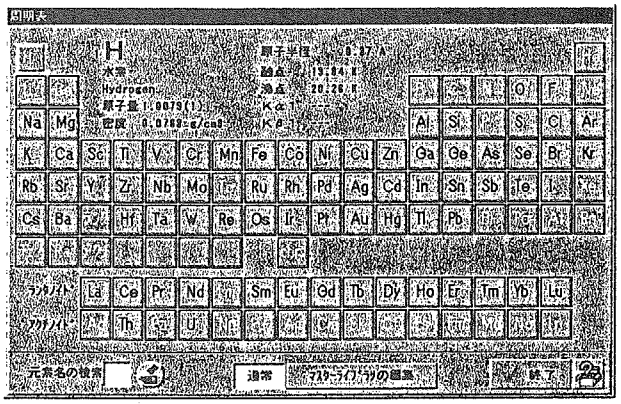


図2. 放射線自動測定・解析システムの概略図（各部の説明は本文参照）

図4. マスターライブラリファイルの作成

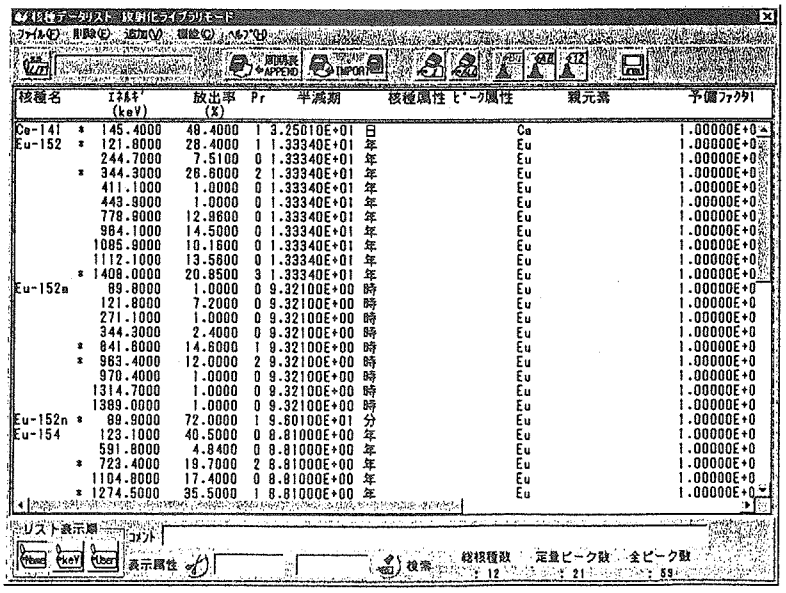


4a　核種データリスト



4b　周期表

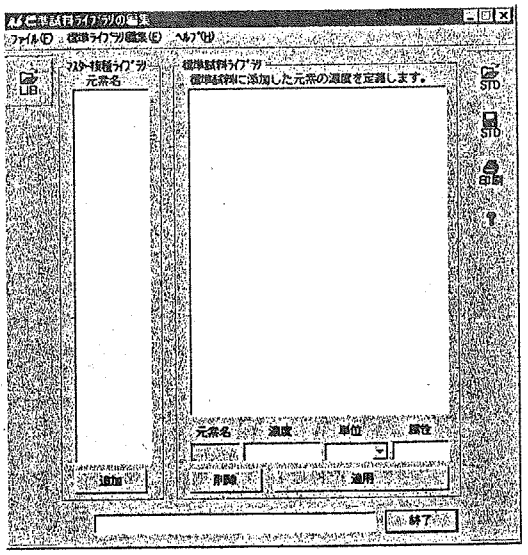
分析対象元素を選択すると、それぞれの核種についての情報がデータリストにインポートされる。



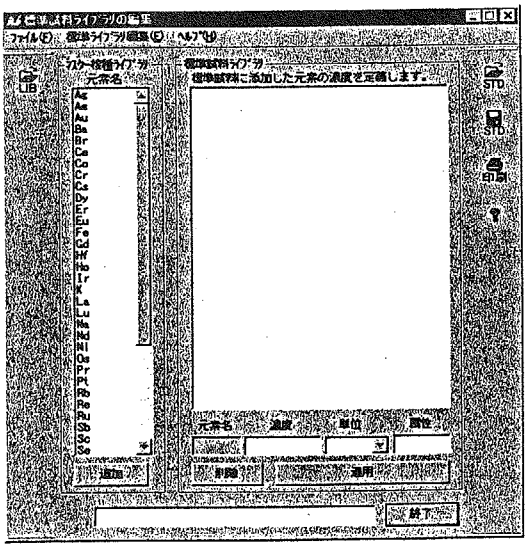
4c

＊がついている核種は、妨害ピーク核種として登録されていることを表す。

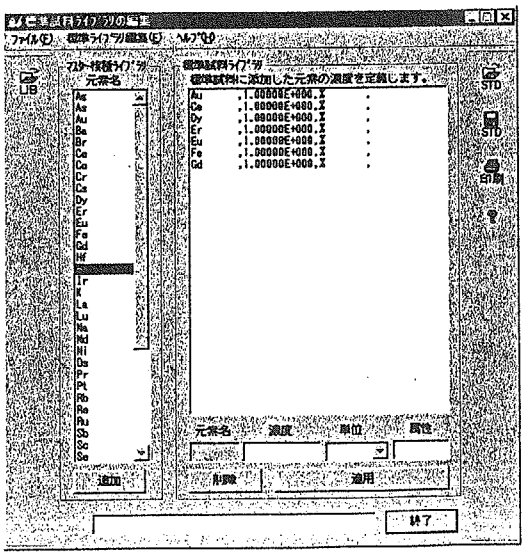
図5. 標準試料ライブラリファイルの作成



5a

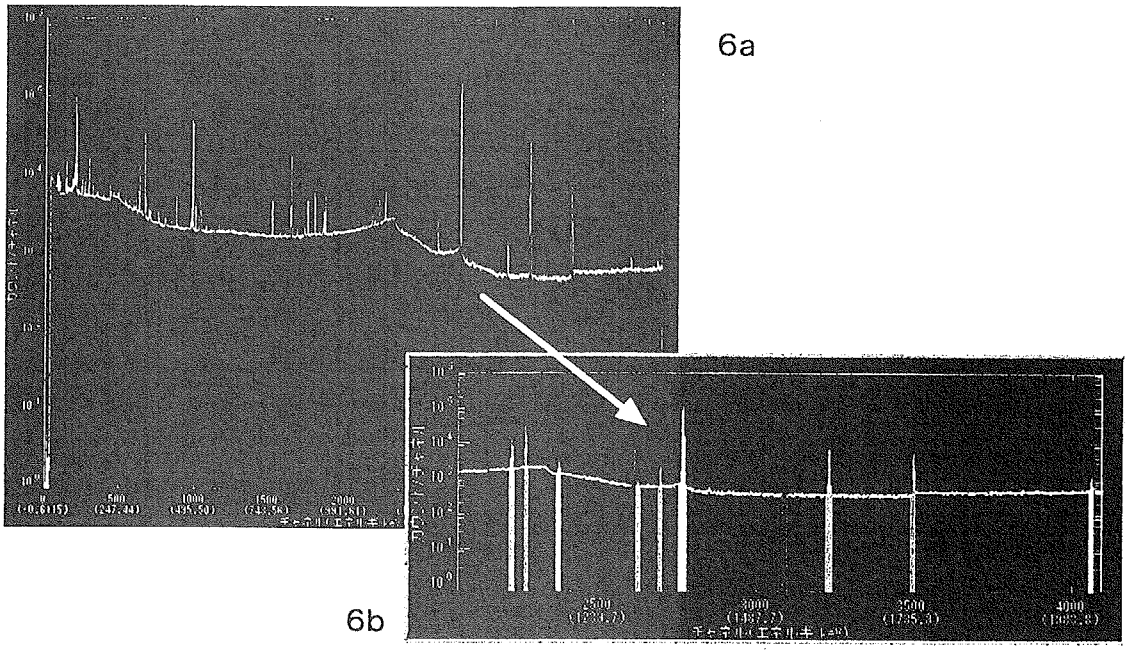


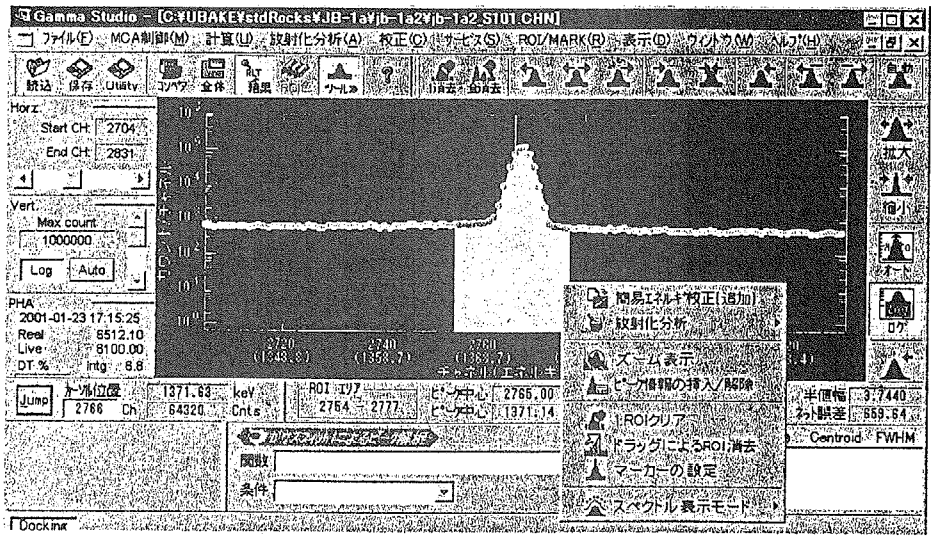
5b

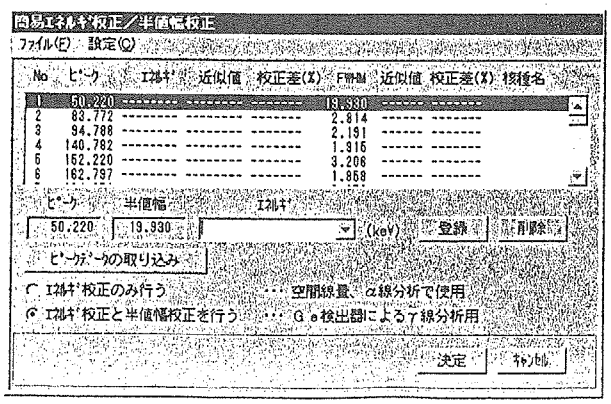


5c

図6.「ガンマスタジオ」を用いたエネルギ校正ファイルの作成







6.4. 自動測定解析（図7）

放射化分析プログラムでは解析に必要な資料（試料の重量などのデータやエネルギ校正ファイル）が揃っていない場合，「測定」のみを実行して，後に「解析」を別に行なうこともできるが，ここでは測定の段階で必要なデータが揃っており，測定と同時に解析を行なう場合について説明する。

まず一連の試料をオートサンプルチェンジャにセットする。サンプルチェンジャには20個のテーブルがあり，その上にはアクリル製のサンプルフォルダが搭載されている。さらにその中央部には適切なサイズのポリエチレン容器がセットできるようになっている部分がある。そのポリエチレン容器のできるだけ中央に試料を入れ，それをアクリルフォルダにセットする。テーブルには「1」から「20」まで番号が記されているが，「1」はバックグランド用のテーブルなので，基本的に何もセットしないで空けておき，以降は「2」番から標準試料，未知試料の順でセットしていく。

試料のセットが完了したらサンプルチェンジャが自動モードであること（チェンジャ本体のコントロールパネルで「自動」ボタンが赤色になっている）を確認して（赤色になっていないときはコントロールパネル上で「自動」ボタンを押して切り替える），パソコンの操作に移る。パソコンのデスクトップ上にある放射化分析プログラムのアイコンをダブルクリックするとメインメニュー画面が現れる（図7a）。その中の「自動測定解析」のボタンをクリックすると，「共通パラメータ登録1」の画面になる。

【共通パラメータ登録1】（図7b）

ここでは「測定グループ」に一連の測定グループ名（例えばカプセル番号など）を入力または選択し，「登録フォルダ」にその測定グループに関するファイルの保存先を指定する。「測定回数」にはその測定が何回目であるかを入力する（ひと組の試料に対して通常短寿命核種を目的とした測定と長寿命核種を目的とした測定の2回の測定を行なう）。「次へ」ボタンをクリックすると「共通パラメータ登録1」は終了し「共通パラメータ登録2」の画面になる。

【共通パラメータ登録2】（図7c）

「検出限界係数」は特に変更しなくてよい。「プリセット（ライブタイム）」には試料一つあたりの測定時間（検出器の不感時間を除く）を，「プリセット（最大カウント）」には同じく最大カウント数を入力する。いずれも入力した値に達したときその試料の測定を終了させるための項目で，通常は最大カウントの値は900000（0～99999999の範囲で入力が可能）にしておき，ライブタイムの値によって試料一つあたりの測定時間を制限する。「標準試料数」にはその測定グループ内で用いている標準試料の数を入力する。「分析試料数」には同じく未知試料の数を入力する。「エネルギ校正ファイル名」はボタンをクリックすると保存されているエネルギ校正ファイルの一覧が表示されるので，その中から最適なもの（通常は最新のもの）を選択する。「マスターライブラリファイル名」も同様にボタンをクリックし一覧の中から選択する。岩石試料の場合は「Activation.LIV」か「Activation2.LIV」でよい（2つのマスターライブラリファイルの違いは単純に分析対象元素の数の違いであり，「Activation2.LIV」の方が若干多い）。「減衰補正基準日」には，通常その測定グループの中性子照射が終了した日時を入力するが，これは別の日時であっても未知試料の元素濃度を知る上では特に関係ない。「次へ」ボタンをクリックすると「共通パラメータ登録2」は終了し，「標準試料登録」の画面になる。ただし，その測定グループについて2回目以降の測定の場合は，ただちに「サンプルチェンジャスケジュール」の画面になる。

【標準試料登録】（図7d）

ここでは用いる標準試料について，重量・単位（通常はmg）・サンプル名を入力する。「フラックス補正係数」は特に変更する必要はない。すべて入力し「次へ」ボタンをクリックすると「標準試料登録」は終了し「分析試料登録」の画面になる。

【分析試料登録】（図7e）

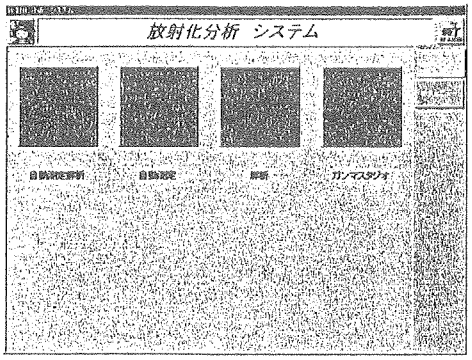
ここでも標準試料と同様に重量・単位・サンプル名を，サンプルチェンジャにセットしたサンプルの順番通りに入力する。「次へ」ボタンをクリックすると「分析試料登録」は終了し，「放射化分析パラメータ登録」の画面になる。

【放射化分析パラメータ登録】（図7f）

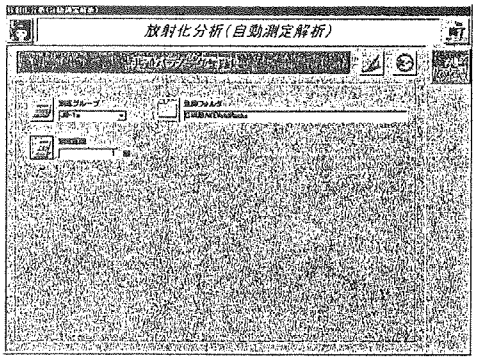
ここでは，元素ごとに分析にどのスタンダードライブラリファイルを用いるかを指定する。「元素名」には予めマスターライブラリファイルから抽出された元素が表示されている。「指定」ボタンをクリックすると保存されているスタンダードライブラリファイルの一覧が表示されるので，その中から適切なものを選択する。標準試料を複数個用いている場合は，分析対象元素が多い順にスタンダードライブラリファイルを「指定」して，元素ごとのスタン

図7. 放射化分析プログラムを用いた自動測定解析の流れ

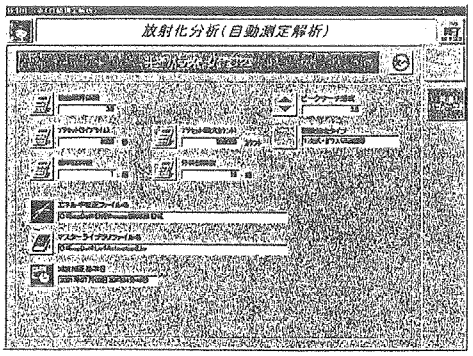
7a



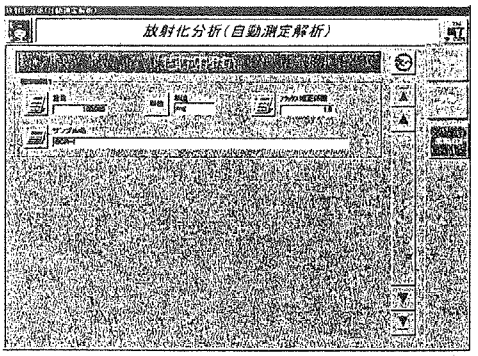
7b



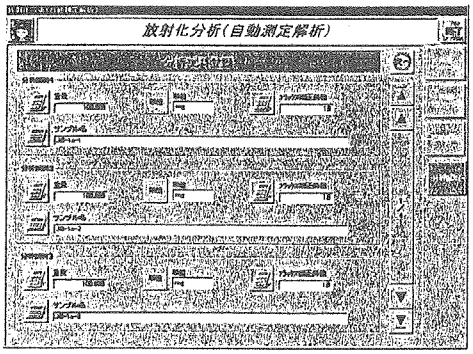
7c



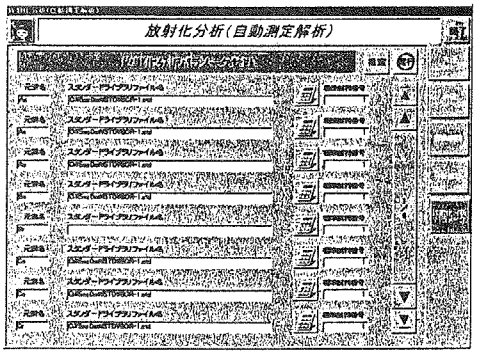
7d



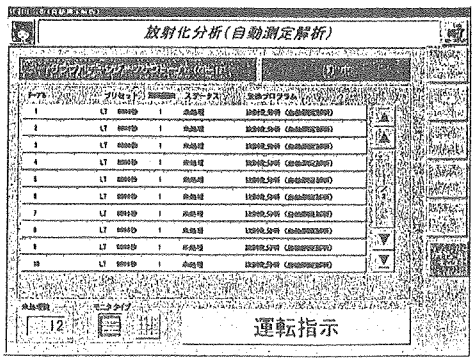
7e



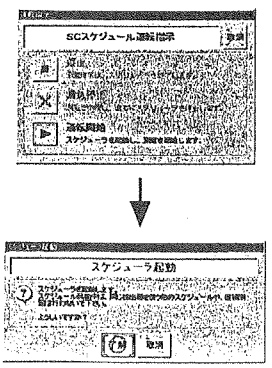
7f



7g



7h



ダードライブラリファイルを置き換えていく（金や白金属元素のように岩石試料中にわずかしか含まれない元素では試薬標準試料を用いる）。そのとき「標準試料番号」も「標準試料登録」画面で登録した番号に合わせて変更する。すべての項目を指定・入力し「実行」ボタンをクリックすると，測定・解析条件が登録され「サンプルチェンジャスケジュール」画面になる。

【サンプルチェンジャスケジュール】（図7g）

ここで「運転指示」ボタンをクリックすると運転指示画面が現れ，さらに「運転開始」「OK」ボタンをクリックすると（図7h），自動的にサンプルチェンジャが作動し，テーブル番号「1」（前述のように通常ここには何も試料をセットせずにバックグランド測定を行なう）から測定が開始される。

その後は，試料が測定される度に自動的に解析がなされ，結果はパソコンに接続されたプリンタからプリントアウトされていく。また複数回の測定を行ないそれぞれの測定で複数のデータを得た測定グループに関しては，サブメニュー内の「まとめの帳表」のボタンをクリックし，「測定グループ」と「測定回数」を指定することによってその回数分の解析結果をもとに各元素について重みづけ平均をした結果をプリントアウトすることができる。

7. 未知試料としての岩石標準試料の分析結果

従来のものに比べて多くの改良が加えられた放射化分析プログラムを含む，放射化分析システム全体としての分析の精度・迅速性・簡便性を総合的に評価するために，アメリカ合衆国地質調査所の代表的な火成岩の岩石標準試料を用いて，日本の地質調査所の岩石標準試料の自動測定解析を行なった。今回標準物質として用いたのは，玄武岩のBCR-1，花崗岩のG-2で，分析試料として用いたのは玄武岩のJB-1a，花崗閃緑岩のJG-1aの2種類の岩石標準試料である。自己しゃへいやγ線の自己吸収の問題から，分析試料と化学組成の類似した標準物質を用いた方が誤差を小さくできることは第2節で述べた通りであるが，そのことを考慮してJB-1aの分析にはBCR-1を，JG-1aにはG-2を，それぞれ標準物質として用いている。

標準物質としてのBCR-1およびG-2中の元素存在度は，それぞれGladney *et al.* (1990)，Gladney *et al.* (1992) による値を用いた（表1）。

JB-1aを10試料とBCR-1を3試料，およびJG-1aを10試料とG-2を3試料，それぞれ1つの同じカプセルに封入し，前者をbasaltグループ，後者をgraniteグループとして中性子照射を行なった。放射化された各グループは前述の手順に従って，1回目は中性子照射後5日～7日間の冷却期間を置いて1試料あたり6000秒，2回目は照射後14日～16日の間に12000秒の合計2回の測定・解析を，それぞれのグループで独立に行なった。

表1．本研究における分析で標準物質として用いた米国地質調査所発行の岩石標準試料BCR-1（玄武岩）およびG-2（花崗岩）中の元素存在度*

element	BCR-1	G-2
Na (%)	2.42	3.02
K (%)	1.40	3.72
Sc (ppm)	32.6	3.5
Cr (ppm)	16	8.7
Fe (%)	9.41	1.88
Co (ppm)	37	4.6
Ni (ppm)	13	5
Zn (ppm)	129.5	86
Se (ppb)	88	0.25
As (ppm)	0.65	0.07
Br (ppb)	72	200
Rb (ppm)	47.2	170
Sr (ppm)	330	478
Zr (ppm)	190	309
Ag (ppb)	27	0.04
Sb (ppm)	0.62	0.07
Cs (ppm)	0.96	1.34
Ba (ppm)	681	1882
La (ppm)	24.9	89
Ce (ppm)	53.7	160
Nd (ppm)	28.8	55
Sm (ppm)	6.59	7.2
Eu (ppm)	1.95	1.4
Tb (ppm)	1.05	0.48
Dy (ppm)	6.34	2.4
Tm (ppm)	0.56	0.18
Yb (ppm)	3.38	0.8
Lu (ppm)	0.51	0.11
Hf (ppm)	4.95	7.9
Ta (ppm)	0.81	0.88
W (ppm)	0.44	0.2
Re (ppb)	0.84	－
Au (ppb)	0.66	1.03
Th (ppm)	5.98	24.7
U (ppm)	1.75	2.07

*Gladney *et al.* (1990; 1992) による

＜basaltグループ＞

まず，BCR-1を標準試料としてJB-1aを分析した結果をImai *et al.*（1995）による推奨値と比較して表2および図8に示した。表2に示した測定値のなかで計数誤差が最も少なく，精度良く測定されているのは，ナトリウム，スカンジウム，鉄，コバルトおよびサマリウムである。これら5元素の測定値における試料間の変動係数（1σ）はそれぞれ2.2%，2.4%，2.7%，2.5%および2.7%である。

次に分析結果を元素ごとに検討する。表2に示されるように，ナトリウム，スカンジウム，鉄，コバルト，ランタン，セリウム，サマリウム，ユウロピウム，イッテルビウム，ルテチウム，ハフニウム，タンタル，トリウムおよびウランは精度・確度ともに高く，本分析は充分信頼するに足るものであることがわかる。これはTanaka *et al.*（1986）によるBCR-1を標準試料に用いたJB-1の分析結果とほぼ同様の傾向であるが，タンタルの確度が向上している点が異なる。この理由として考えられるのは，比較対象として用いたImai *et al.*（1995）による推奨値が1986年当時に用いられていた値（3.6 ppm）よりもより確かなもの（現在は1.93 ppm）になったと考えるのが妥当であろう。

本分析結果の試料間における精度に関しては，TANAKA *et al.*（1986）によるJB-1の分析結果に比べて，最も精度の良かった元素についても約2倍の誤差が認められる。しかし，個々の測定データに附随する計数誤差においてはこれらの元素はどれも1%以下で測定されているため，これは試料の不均一性もしくは測定時におけるジオメトリーの相違を反映しているものと考えられる。ただ，中性子照射時間を36分の1（3時間→5分）にしたことおよび，測定回数を3回から2回にしたことと測定時間を8000秒から6000秒へと短くしたことを考慮すると，2倍の誤差があるとはいえ，多試料の迅速な分析においては，本研究での分析結果は充分に満足すべきものであると言える。

＜graniteグループ＞

G-2を標準物質としてJG-1aを分析した結果を表3および図9に示す。ここに示されるようにほとんどの元素について，JB-1aの分析結果と同様に精度・確度ともに平均値はImai *et al.*（1995）の値の±10%以内に納まっており，満足すべき結果と言える。

JB-1aでは検出できなかったツリウム（Tm）がJG-1aでは測定できているものの，その値は推奨値と大きく異なっている。これは，個々の測定において数十から数百%にもなった計数誤差の大きさのためであると考えられる。ツリウムなどのような中性子吸収断面積が小さい元素は放射化効率が低いために放射性核種が生成されにくく，γ線の放出も微小なものとなり，含有量が少ない場合放射化分析で精度良く定量することは難しいと言える。

ランタン（La）は表2に示すように個々の測定データに附随する計数誤差は小さいものの，測定間のばらつきがJB-1aの場合と比べてわずかではあるが大きいことが注目される。しかもこのランタンに見られる傾向はセリウムおよびサマリウムにも共通して見られる。つまり，ランタンが高めに測定されている試料はセリウム，サマリウムも高めであり，その逆もまた同様である。このことからランタンをはじめとする希土類元素の測定値のばらつきは測定システムに起因するものではなく，試料における元素濃度の偏在（不均一性）を反映しているものと考えられる。

このことは，Kamioka and Tanaka（1989）においても指摘されており，JG-1とJG-1aについて分析結果の比較検証が行なわれている。JG-1aはJG-1と同一露頭から得られた試料であり，その調整にはより注意が払われ，粉砕時の微量元素の混入も少なく，粒度もより細かくなっているとされており，検証のために用いられた試料重量は平均 68.0 mg である。両者の結果の比較によると，偏在するジルコン中に数%含まれるハフニウムについては，JG-1の変動係数（1σ）が12%であるのに対し，JG-1aでは5%と半分以下となって，サンプリングエラーの影響は少なくなっているが，一方希土類元素やトリウムに関しては両者でほとんど差がなく，JG-1aでも計数誤差を大きく超えたばらつきが確認されている。

以上のことから，比較的少量（数十－数百ミリグラム）の試料を用いた酸性岩中の微量元素分析においては，目的元素の濃度や試料粉末の細かさによってはサンプリングエラーの可能性を考慮する必要があり，その試料粉末の均一性には充分過ぎるくらいの注意を払うべきであろう。

表2. 米国地質調査所岩石標準試料BCR-1を標準物質として測定したJB-1aの分析結果

element	1	2	3	4	5	6	7	8	9	10	mean ± σ	ref.*
Na (%)	1.98	2.00	1.92	1.97	1.97	2.03	1.96	1.96	1.87	1.97	1.96 ± 0.04	2.03
K (%)	1.11	1.06	1.14	1.34	1.17	0.99	1.28	1.16	1.07	1.03	1.13 ± 0.11	1.16
Sc (ppm)	27.4	27.3	26.2	27.1	27.2	28.0	26.9	26.9	25.7	27.4	27.0 ± 0.65	27.9
Cr (ppm)	449	435	431	431	441	441	426	426	408	441	433 ± 11.4	392
Fe (%)	6.30	6.25	5.93	6.15	6.14	6.40	6.09	6.12	5.84	6.22	6.14 ± 0.17	6.33
Co (ppm)	36.8	36.5	35.1	35.7	35.9	37.6	35.8	35.8	34.6	37.0	36.1 ± 0.90	38.6
Zn (ppm)	85	87	90	93	100	100	91	145	81	90	92.4 ± 19	82.1
As (ppm)	0.93	0.86	0.90	1.09	0.73	0.99	1.07	0.93	0.75	1.05	0.93 ± 0.13	2.3
Rb (ppm)	34	33	37	29	39	29	37	33	27	44	33.1 ± 5.31	39.2
Sr (ppm)	471	315	292	301	442	361	–	332	275	454	360 ± 76	442
Ba (ppm)	453	471	427	492	451	542	440	483	411	452	462 ± 37	504
La (ppm)	36.7	36.3	35.0	36	36.2	37.6	36.3	35.9	34.5	36.3	36.1 ± 0.87	37.6
Ce (ppm)	65.4	65.8	61.7	64.1	64.0	66.0	62.9	62.5	58.3	65.3	63.6 ± 2.36	65.9
Sm (ppm)	5.22	5.30	4.94	5.06	5.23	5.31	5.19	5.15	4.90	5.12	5.14 ± 0.14	5.07
Eu (ppm)	1.46	1.41	1.23	1.29	1.40	1.45	1.48	1.40	1.39	1.59	1.41 ± 0.10	1.46
Tb (ppm)	0.49	0.59	0.64	0.55	0.67	0.67	0.74	0.80	0.39	0.68	0.62 ± 0.12	0.69
Yb (ppm)	2.00	2.02	1.88	2.03	2.05	2.07	1.92	2.01	1.85	1.89	1.97 ± 0.08	2.1
Lu (ppm)	0.29	0.31	0.25	0.30	0.31	0.30	0.29	0.27	0.28	0.28	0.29 ± 0.02	0.33
Hf (ppm)	3.60	3.41	3.48	3.61	3.61	3.71	3.22	3.38	3.25	3.22	3.45 ± 0.18	3.41
Ta (ppm)	2.23	1.99	1.90	2.02	2.22	2.29	2.20	2.31	1.81	2.26	2.12 ± 0.18	1.93
Th (ppm)	9.19	8.69	8.4	9.22	9.24	9.47	8.85	9.10	8.60	9.28	9.00 ± 0.35	9.03
U (ppm)	1.37	1.45	1.33	1.50	1.15	1.64	1.35	1.69	1.58	1.59	1.47 ± 0.17	1.57

JB-1a (standard : BCR-1)
計数誤差10％以上は2ケタで表示
* Imai *et al.* (1995) による

表3. 米国地質調査所岩石標準試料G-2を標準物質として測定したJG-1aの分析結果

element	1	2	3	4	5	6	7	8	9	10	mean ± σ	ref.*
Na (%)	2.47	2.49	2.52	2.49	2.48	2.49	2.37	2.35	2.40	2.48	2.46 ± 0.06	2.51
K (%)	3.16	3.57	3.39	3.29	3.22	3.15	3.03	2.80	3.22	3.40	3.22 ± 0.21	3.29
Sc (ppm)	6.17	6.30	6.50	6.15	6.36	6.51	5.91	5.89	6.10	6.35	6.22 ± 0.22	6.21
Cr (ppm)	14.5	21.2	14.9	15.7	19.2	18.1	15.5	14.4	15.2	17.8	16.7 ± 2.3	17.6
Fe (%)	1.36	1.40	1.43	1.34	1.42	1.44	1.32	1.31	1.35	1.39	1.37 ± 0.05	1.4
Co (ppm)	5.70	5.18	5.42	5.35	5.57	5.69	4.95	5.10	5.34	5.02	5.33 ± 0.27	5.9
Zn (ppm)	39.8	48.7	45.0	42.7	41.4	46.8	40.2	42.1	41.6	48.7	43.7 ± 3.4	36.5
Rb (ppm)	180	177	179	171	175	184	167	167	165	183	175 ± 6.9	178
Sr (ppm)	124	166	132	134	128	151	134	148	131	216	146 ± 27	187
Zr (ppm)	135	140	–	143	143	180	135	–	136	–	145 ± 16	118
Cs (ppm)	10.2	10.1	10.9	10.2	10.7	10.8	9.58	9.91	10.1	10.35	10.3 ± 0.41	10.6
Ba (ppm)	491	493	498	515	470	506	434	464	516	459	485 ± 27	470
La (ppm)	22.8	22.1	21.2	20.9	21.7	19.5	20.0	19.2	19.1	21.4	20.8 ± 1.3	21.3
Ce (ppm)	47.4	46.5	42.1	43.7	46.4	41.7	39.8	38.5	40.9	43.9	43.1 ± 3.0	45
Nd (ppm)	–	28.6	55	21.7	29.2	–	–	24.2	21.9	–	30.1 ± 4	20.4
Sm (ppm)	4.64	4.75	4.53	4.43	4.69	4.31	4.19	4.17	4.25	4.45	4.44 ± 0.21	4.53
Eu (ppm)	0.78	0.74	0.70	0.74	0.77	0.73	0.62	0.65	0.71	0.79	0.72 ± 0.06	0.7
Tb (ppm)	0.93	1.06	1.04	1.03	1.07	0.99	0.95	0.70	0.92	0.92	0.96 ± 0.11	0.81
Tm (ppm)	0.20	0.25	0.36	0.17	0.16	0.30	0.15	0.15	0.15	0.19	0.21 ± 0.07	0.38
Yb (ppm)	2.86	2.80	2.90	2.95	3.10	2.97	2.80	2.59	2.78	2.94	2.87 ± 0.14	2.7
Lu (ppm)	0.55	0.54	0.62	0.54	0.61	0.58	0.53	0.54	0.52	0.62	0.57 ± 0.04	0.44
Hf (ppm)	3.89	3.67	3.87	4.54	4.03	3.93	3.43	3.09	3.58	4.34	3.84 ± 0.42	3.59
Ta (ppm)	1.74	2.04	2.07	1.82	1.99	1.90	1.65	1.76	1.83	2.06	1.89 ± 0.15	1.9
Th (ppm)	12.3	12.9	12.2	13.6	13.2	11.8	11.5	11.6	12.0	12.1	12.3 ± 0.69	12.8
U (ppm)	3.38	3.47	3.88	3.49	3.34	3.59	3.29	4.99	4.49	3.66	3.76 ± 0.56	4.69

JG-1a (standard : G-2)
計数誤差10％以上は2ケタで表示
* Imai *et al.* (1995) による

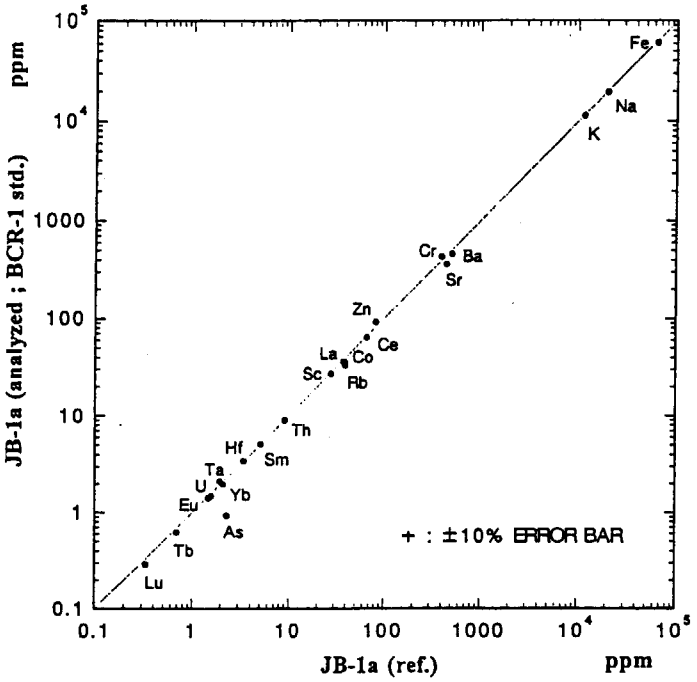


図8. 米国地質調査所発行の岩石標準試料BCR-1（玄武岩）を標準物質としてJB-1a（玄武岩）を分析した結果とJB-1aの推奨値（Imai et al., 1995）との比較図

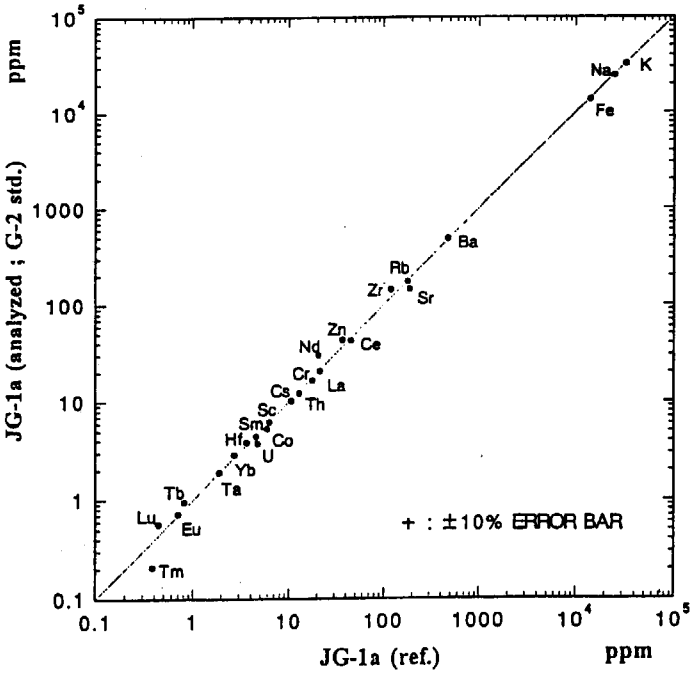


図9. 米国地質調査所発行の岩石標準試料G-2（花崗岩）を標準物質としてJG-1a（花崗閃緑岩）を分析した結果とJG-1aの推奨値（Imai et al., 1995）との比較図

8. 結　論

今回，中性子放射化分析を用いて岩石粉末試料において容易に・精度良く・迅速に・多量に，そしてより安価に多元素の分析を行うことを目的として，以下のことを行なった。

(1) 試料の封入作業の平易化およびルーチンワーク化により，実験者の作業負担を軽減することができた。

(2) 多元素分析において適度な精度が得られる必要最低限の中性子照射時間を見極め，その結果として，取扱いが容易なポリエチレンを用いた試料封入法による短時間照射での放射化分析が可能となった。これは分析試料数を増やせるだけでなく，経費の削減という点においても多大なメリットである。

(3) ハードウェアおよびソフトウェアのバージョンアップを図り，測定・解析における作業の大幅な自動化を行った。これにより測定試料の入れ替えや煩雑な計算に割かれる時間が削減され，時間を有効利用できるようになった。

(4) また，岩石標準試料を実際に用いての放射化分析を行なった結果，玄武岩－花崗岩の化学組成を持つ試料について，ナトリウム，スカンジウム，鉄，コバルト，ランタン，セリウム，サマリウム，ユウロピウム，イッテルビウム，ルテチウム，ハフニウム，タンタル，トリウムについては5％以内の精度および確度で，クロム，亜鉛，セシウム，バリウム，ネオジム，テルビウム，ウランについては10％以内の精度および確度で元素分析が可能であることがわかった。

以上のことから，試料ひとつあたりの中性子照射時間，測定時間および費用と，その結果としての各元素濃度の精度および確度を考慮すれば，今回の結果は多数の地質試料の多元素精密分析においては充分妥当なものだと言える。また以上の改善点によって，地質試料について年間1500試料以上の測定・解析が可能となった。

平成13年度から，本研究により開発された原子炉中性子照射，郵送，γ線計測による多試料・多元素分析システムを用いて河川堆積物の多試料分析を行なう。

参考文献

Gladney, E. S., Jones, E A., Nikell, E. J. and Roelants, I. (1990) 1988 Compilation of elemental concentration data for USGS BCR-1. Geostandards Newsletter 14 : 209-359.

Gladney, E. S., Jones, E A., Nikell, E. J. and Roelants, I. (1992) 1988 Compilation of elemental concentration data for USGS AGV-1, GSP-1 and G-2. Geostandards Newsletter 16 : 111-300.

橋本芳一 (1978)『放射化分析の実際』講談社

Imai, N., Terashima, S., Itoh, S. and Ando, A. (1995) 1994 recommended or preferable values for major, minor and trace elements in five GSJ reference samples. Geostandards Newsletter 19 : 135-213.

上岡　晃 (1989)「機器中性子放射化法による地質試料の分析とその問題点－地質調査所岩石標準試料による検討－」地質学雑誌95，835-850頁

日下　譲 (1973)『放射化分析』共立出版

田中　剛・上岡　晃・山中宏青 (1988)「放射化分析用放射線自動計測・解析システムの開発と岩石標準試料の分析」地質調査所月報39，537-557頁

セイコー・EG & G 株式会社 (2000)『放射化分析プログラム操作説明書 Rev. 1.0』セイコー・EG & G 株式会社

セイコー・EG & G 株式会社 (2000)『Spectrum Navigator オペレーションマニュアルRev. 1.71』セイコー・EG & G 株式会社

セイコー・EG & G 株式会社 (1999)『エネルギ校正オペレーションマニュアル. Rev. 1.30』セイコー・EG & G 株式会社

セイコー・EG & G 株式会社 (1999)『核種ライブラリ作成オペレーションマニュアル. Rev. 2.10』セイコー・EG & G 株式会社

セイコー・EG & G 株式会社 (1996)『7700スーパーグラフィックMCA. Rev. 1.01』セイコー・EG & G 株式会社

本研究に関連した成果の公表

田中　剛・山本鋼志・浅原良浩 (2001)　地球化学図による地圏環境評価手法の研究．岩谷直治記念財団研究報告書，Vol.24, 43-45.

高木真理・田中　剛・浅原良浩・青木和弘・天野健治 (2001)　ストロンチウム同位体の挙動から見た岩石の化学風化：釜石鉱山の地下水による水-岩石反応の研究。地球化学35巻，61-72.

田中　剛・川辺岩夫・山本鋼志・三村耕一・浅原良浩・南　雅代 (2001) 地学野外実習としての地球化学図作成。地質ニュース558号、41-47.

冨樫茂子・今井　登・奥山康子・田中　剛・岡井貴司・狛　武・村田泰章・青山秀喜（2001）日本列島の“クラーク数”若い島弧の上部地殻の元素存在度。地質ニュース 558号、25-32.

Togashi, S., Imai, N., Okuyama-Kusunose, Y., Tanaka, T., Okai, T., Koma, T. and Murata, Y. (2000) Young upper crustal chemical composition of the orogenic Japan arc. Geochemistry, Geophysics and Geosystems(G-cubed), vol.1 no 27, 2000GC000083.

Tanaka, T., Togashi, S., Kamioka, H., Amakawa, H., Kagami, H., Hamamoto,T., Yuhara, M., Orihashi, Y., Yoneda, S., Shimizu, H., Kunimaru, T., Takahashi, K., Yanagi, T., Nakano,T., Fujimaki, H., Synjyo, R., Asahara, Y., Tanimizu, M. and Dragusanu, C. (2000) JNdi-1: A neodymium isotopic reference in consistency with LaJolla Neodymium. Chem. Geol. vol. 168, 279-281.

田中 剛 (2000)多試料多元素分析による地圏の化学環境評価の試みーヒ素のバック グラウンド。立教炉利用共同研究25年誌。p86. 東京大学原子力研究総合センター。

Tanimizu, M. and Tanaka, T. (2000) Ce-Nd-Sr isotope systematics of eucrites and lunar rocks. The Origin of Elements in the Solar System. Kluwer Academic/Plenum Pub. New York, pp. 573-592.

Dragusanu, C. and Tanaka, T. (1999) 1.57-Ga magmatism in the south Carpathians: Implications for the pre-Alpine basements and evolution of the mantle under the Europian continent: A Reply. Jour. Geol. vol.107, 736-738.

Kim, K. H., Tanaka, T., Nakamura, T., Nagao, K., Youn, J. S., Kim, K. R. and Yun,M. Y.(1999) Palaeoclimatic and chronostratigraphic interpretations from strontium, carbon and oxygen isotopic ratios in molluscan fossils of Quaternary Seoguipo and Shinyangri Formations, Cheju Island, Korea. Palaeogeogr Palaeoclimato. Palaeoeco. vol. 154, 219-235.

田中 剛 (1999) 地面の化学バックグラウンドと地球化学図. ぱなんざ 288号, 10-20.

Kim, K. H., Tanaka, T., Nagao, K. and Jang S. K. (1999) Nd and Sr isotopes and K-Ar ages of the Ulreungdo alkali volcanic rocks in the East Sea, South Korea. Geochem. Jour. vol 33, 317-341.

Asahara, Y., Tanaka, T., Kamioka, H., Nishimura, A. and Yamazaki, T. (1999) Provenance of the north Pacific sediments and process of source-material transport as derived from Rb-Sr isotopic systematics. Chem. Geol. vol.158, 271-291.

Dragusanu, C. and Tanaka, T. (1999) 1.57-Ga magmatism in the south Carpathians: Implications for the pre-Alpine basements and evolution of the mantle under the Europian continent. Jour. Geol. vol.107, 237-248.

4. ＲＩの製造

4. Production of Radio Isotopes

This is a blank page.

4-1 Production of ^{186,188}Re and Recovery of Tungsten from Spent ^{188}W/^{188}Re Generator[1,2]

K. Kobayashi*, S. Motoishi*, K. Terunuma*, A. A. Rauf, and K. Hashimoto***

* *Japan Atomic Energy Research Institute, Tokai-mura, Ibaraki-ken, 319-1195 Japan*
** *National Atomic Energy Agency, Serpong Tangerang, 15310 Indonesia*

Received February 9, 2000

Abstract—Production of radioactive rhenium ^{186}Re and ^{188}Re, and recovery of tungsten from spent ^{188}W/^{188}Re generators were studied. Methods were developed for production of ^{186}Re by the ^{185}Re$(n,\gamma)^{186}$Re reaction in a reactor and for production of ^{188}Re by the double neutron capture of enriched ^{186}W, which produces a ^{188}W/^{188}Re generator. For recovery of ^{186}W-enriched tungsten from alumina-based spent ^{188}W/^{188}Re generators, the optimum conditions were determined for reuse of enriched tungsten including the desorption of tungsten from the alumina-based generator and the precipitation of tungsten oxide.

Radioactive rhenium ^{186}Re ($T_{1/2}$ 90.64 h) and ^{188}Re ($T_{1/2}$ 16.98 h) are of current interest for therapeutic applications in nuclear medicine, because of their energetic β-particles and γ-rays suitable for imaging [1–3]. Typical methods of ^{186}Re production are the ^{186}W$(p,n)^{186}$Re reaction with a cyclotron, which can produce carrier-free ^{186}Re, and the ^{185}Re$(n,\gamma)^{186}$Re reaction in a reactor. For carrier-free ^{186}Re, the excitation function of the ^{186}W$(p,n)^{186}$Re reaction was measured and the chemical separation of ^{186}Re from an enriched tungsten target was reported [4]. The main disadvantage of the production of ^{186}Re by the ^{186}W$(p,n)^{186}$Re reaction is the difficulty of large-scale production, because the beam current and bombardment time in a cyclotron are limited. On the other hand, ^{186}Re with high radioactivity can be produced by the ^{185}Re$(n,\gamma)^{186}$Re reaction in a reactor. Therefore, we have produced ^{186}Re using a reactor [5]. Studies on synthesis of labeled compounds with ^{186}Re and on their biodistribution [6–9] have been carried out in Japan using our ^{186}Re products.

Carrier-free ^{188}Re is obtained from β-decay of the long-lived ^{188}W (69.4 days) parent produced by the double neutron capture of ^{186}W in a reactor. ^{188}W/^{188}Re generators are of particular interest [10, 11], since they can produce ^{188}Re repeatedly at a low cost during a long period for the synthesis of labeled compounds [12–14]. Furthermore, the recovery methods of unirradiated ^{186}W from spent alumina-based ^{188}W/^{188}Re generators for the purpose of reuse of tungsten as a target material have been studied [15, 16].

The goal of this study is development of production techniques of ^{186}Re and ^{188}Re using a reactor, and of a method to recover enriched ^{186}W from spent alumina-based ^{188}W/^{188}Re generators.

EXPERIMENTAL

Production of ^{186}Re. The target material was 97.4% enriched ^{185}Re metallic powder (ORNL, 2.6% ^{187}Re). The target (about 5 mg) in a quartz ampule was encapsulated into an aluminum outer capsule shown in Fig. 1, then welded and tested for gas leakage by approved quality assurance procedures before irradiation. Generally, the target in the capsule was irradiated for 4 days in a hydraulic rabbit (HR-1, thermal neutron flux 1.0×10^{14} cm^{-1} s^{-1}) at JRR-3M (Japan Research Reactor no. 3, modification). In some experiments, the target was irradiated for 7–8 days in a hydraulic rabbit (HR-2, thermal neutron flux 2.7 ×

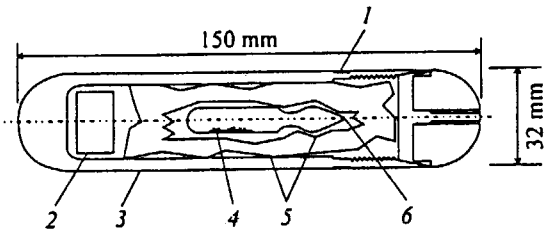


Fig. 1. Capsule for irradiation of Re target: (*1*) cutting mark, (*2*) Pb weight, (*3*) Al capsule, (*4*) Re target, (*5*) Al foil, and (*6*) quartz ampule.

[1] This article was submitted by the authors in English.
[2] Reported at the Japanese–Russian Seminar on Technetium [Shizuoka (Japan), November 29–December 1, 1999].

Target: 5 mg of ^{185}Re (97.4%)
↓
Irradiation (4 days, JRR-3M reactor, ϕ_{th} 1 × 10^{14} cm^{-2} s^{-1})
↓
Decanning
↓
Dissolution (2 ml of 6 M HNO_3, then 5 ml of H_2O)
↓
Evaporation (120°C)
↓
Repeated dissolution in 5 ml of H_2O–evaporation (5 times)
↓
Dissolution in 10 ml of H_2O
↓
^{186}Re product
↓
Quality control, shipment, storage

Flowsheet for the production of ^{186}Re.

Scheme.

10^{14} cm^{-2} s^{-1}) at JMTR (Japan Materials Testing Reactor) in order to obtain a higher specific radioactivity of ^{186}Re.

After the irradiation, the capsule was transferred to the loading–unloading cell in our radioisotope production facility. The irradiated outer capsule was opened using a capsule cutter located in this cell, and the quartz ampule was transferred to the ^{186}Re production cell. Before opening the quartz ampule, the gross radioactivity of ^{186}Re was measured using a well-type ionization chamber calibrated by γ-ray spectrometry with a pure germanium detector and the radiocalorimetric method with a twin-cup heat-flow microcalorimeter [17]. The specific radioactivity of ^{186}Re (Bq/g) was calculated from the gross radioactivity.

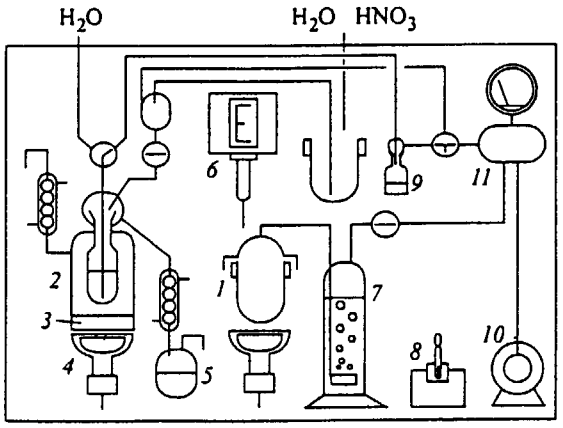


Fig. 2. Schematic diagram of the apparatus used for the production of ^{186}Re: (*1*) dissolver, (*2*) evaporator, (*3*) heat medium, (*4*) heater, (*5*) waste tank, (*6*) buret, (*7*) trap, (*8*) target, (*9*) product bottle, (*10*) vacuum pump, and (*11*) vacuum trap.

The procedure for the dissolution of the irradiated target and the schematic diagram of the apparatus are shown in the scheme and in Fig. 2. The irradiated target was dissolved in 6 M HNO_3. Water was added to the HNO_3 solution, and the solution was evaporated to dryness using tetrachloroethylene (bp 121°C) as a heat medium. The addition of water and evaporation to dryness was repeated five times to totally eliminate HNO_3. Rhenium-186 was taken up in water.

Production of $^{188}W/^{188}Re$ generator. The target material was 99.79% enriched $^{186}WO_3$ (ISOTEC Inc., the United States or Eurisotop, France). The target (about 25 mg) in a quartz ampule was irradiated for one (26 days) or two cycles (26 days × 2, interval 1 month) in JMTR (thermal neutron flux 2.7 × 10^{14} cm^{-2} s^{-1}). The irradiated target was allowed to stand for more than 4 weeks for decay of ^{187}W (23.72 h). The irradiated target was dissolved in 2 M NaOH with heating. The pH of the ^{188}W solution was adjusted to about 2 using HCl. The tungsten solution was loaded onto the alumina column (10 × 60 mm; BIO-RAD, AG-4, 100–200 mesh) which was conditioned with 0.01 M HCl. The column was then washed with 0.9% NaCl. Rhenium-188 was eluted with 0.9% NaCl after the equilibrium between ^{188}W and ^{188}Re had almost been reached.

The adsorption capacity of alumina (BIO-RAD, AG-4, 100–200 mesh) for WO_3 was determined spectrophotometrically. The tungstate stock solution (pH 2) was passed through the alumina column at a constant flow rate of 1 ml/min. The content of tungstate in the eluent was determined by measuring its absorbance at 410 nm after coloration with KSCN/$SnCl_2$.

Recovery of tungsten from spent $^{188}W/^{188}Re$ generators. Mock W/Re generators were prepared using tungsten (natural isotopic abundance: Johnson Matthey "Specpure") solution containing $^{187}WO_4^{2-}$ and $^{186}ReO_4^-$ tracers to study the desorption of tungsten from alumina-based W/Re generators (5 g of alumina). The radioactive tracer of tungstate solution ($^{187}WO_4^{2-}$) was prepared from isotopically enriched $^{186}WO_3$ (99.79%, 2–3 mg) irradiated in the JRR-4 reactor for 10 min under 5 × 10^{13} cm^{-2} s^{-1} thermal neutron flux. To determine the desorption, precipitation, and recovery yields of ^{187}W and ^{186}Re, both γ-peaks at 686 keV of ^{187}W and 137 keV of ^{186}Re were measured by a single-channel analyzer with a well-type NaI detector. Several kinds of eluents: HCl,

HNO_3, H_2SO_4, NaOH and NH_4OH solutions, were used for desorption of tungsten from alumina columns. The precipitate was obtained by adding 6 M HCl to the tungstate solution. For almost complete precipitation, the solution was allowed to stand for 1 day. The precipitate was then filtered and washed with distilled water. For calcination, the precipitate from the eluent was subsequently heated at 600°C in an electric furnace, and then tungsten trioxide (WO_3) was recovered. Impurities in the recovered WO_3 were analyzed by neutron activation analysis and compared with the blank of high-purity WO_3.

RESULTS AND DISCUSSION

Production of ^{186}Re. The natural abundance of ^{185}Re and ^{187}Re is 37.40 and 62.60%, and the cross sections of the thermal neutron capture reaction measured at 2200 m/s are 112±2 and 76.4±1.0 b, respectively [18]. In order to get high radionuclidic purity and high specific radioactivity of the ^{186}Re product, isotopically enriched ^{185}Re (97.4%) metallic powder (ORNL) was used as a target material. However, the radioactive impurity of ^{188}Re in the ^{186}Re product was also formed by the ^{187}Re$(n,\gamma)^{188}$Re reaction due to the presence of ^{187}Re (2.6%) in the target material. The calculated specific activities of ^{186}Re and ^{188}Re produced after 4-day irradiation in JRR-3M are 19 and 0.7 TBq/g Re, respectively. The percentage of ^{188}Re in the ^{186}Re product is about 4% at the end of bombardment (EOB). However, it decreases with elapsed time because the half-life of ^{188}Re (16.98 h) is shorter than that of ^{186}Re (90.64 h). Two days after EOB, the radionuclidic purity of the ^{186}Re product is more than 99%.

The dissolution process of the irradiated target using 30% H_2O_2 was compared with the process using 6 M HNO_3. After dissolution, the solution was evaporated to dryness. The loss of ^{186}Re (max. 60%) was observed during the evaporation using 30% H_2O_2, but the loss was very low (less than 1%) during the evaporation using 6 HNO_3. Therefore, for the dissolution of the irradiated target we used 6 M HNO_3.

The chemical form of the ^{186}Re product, as determined by thin-layer chromatography and ion chromatography, was perrhenate ion ($^{186}ReO_4^-$). At the concentration of ^{186}Re in the final product of 0.4–0.5 GBq/ml, the concentration of rhenium was about 0.3 mg/ml and pH was 3–5. The concentration of NO_3^- in the ^{186}Re product was found by ion chromatography to be less than 10 ppm. Iridium-192 was found as major radionuclidic impurity apart from ^{188}Re. The

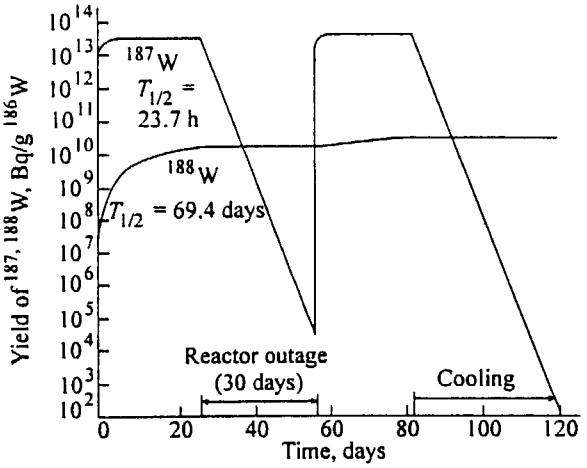


Fig. 3. Calculated yields of ^{187}W and ^{188}W in an enriched ^{186}W (99.79%) target irradiated in JMTR (thermal neutron flux 2.7×10^{14} $cm^{-2}\,s^{-1}$).

percentage of ^{192}Ir in the ^{186}Re product was 1.5×10^{-4}% at EOB. Specifications of the ^{186}Re products per batch are as follows: production yields, 60–90%; specific radioactivity, 17–20 (JRR-3M irradiation) or 65 TBq/g Re (JMTR irradiation); total radioactivity, 50–100 GBq; radionuclidic purity, >99%.

Production of ^{188}W/^{188}Re generator. Rhenium-188 can be produced with a high specific radioactivity by decay of ^{188}W. The parent ^{188}W has produced by the double neutron capture reaction of ^{186}W ^{186}W$(n,\gamma)^{187}$W$(n,\gamma)^{188}$W$(\beta^-)^{188}$Re. The cross sections of the thermal neutron capture reaction of ^{186}W and ^{187}W are 37.9±0.6 b [$(3.79\pm0.06) \times 10^{-23}$ cm^2] and 64±10 b [$(6.4\pm1.0) \times 10^{-23}$ cm^2], respectively [18]. The natural abundance of ^{186}W is not high (28.6%). In order to obtain ^{188}W with a high specific radioactivity and high radionuclidic purity, we used highly enriched (99.79%) $^{186}WO_3$ as a target material. The calculated yields of ^{187}W and ^{188}W at JMTR are shown in Fig. 3. The calculated specific radioactivity of ^{188}W produced after one cycle of irradiation at JMTR is 15 GBq/g ^{186}W, and the calculated activity after two cycles of irradiation is 24 GBq/g ^{186}W. However, the experimental yield was lower (about 70%) than the calculated one. This is probably due to the uncertainty of the cross sections and the contribution of the burn-up cross section of ^{188}W [19]. The total radioactivity of ^{188}W was 200–340 MBq at the end of production.

The ^{188}W/^{188}Re generator was based on an alumina column system [10]. The adsorption capacity of

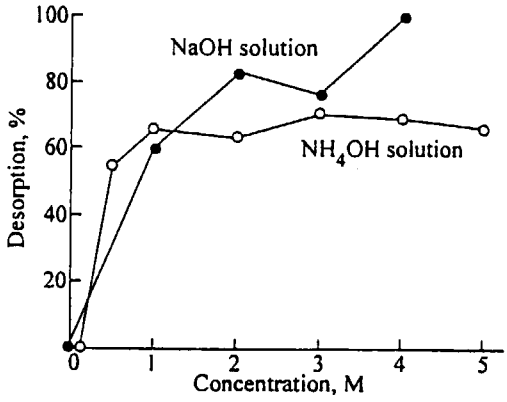


Fig. 4. Desorption of tungsten with NaOH and NH_4OH solutions (10 and 15 ml, respectively).

alumina for WO_3 at pH 2 was found to be about 18–24 mg/g alumina. Rhenium-188 was eluted with 0.9% NaCl from the $^{188}W/^{188}Re$ generator with the very low breakthrough of ^{188}W (less than 5×10^{-6}%). The elution yield of ^{188}Re was about 80%. The radionuclidic purity of ^{188}Re was more than 99.9%; however, ^{60}Co, ^{110m}Ag, $^{141,144}Ce$, ^{140}Ba–^{140}La, etc. were found as the radionuclidic impurities originating from cobalt, silver, uranium, and other impurities in the enriched $^{186}WO_3$ target. The chemical form of ^{188}Re was found to be perrhenate ion ($^{188}ReO_4^-$) by paper chromatography and silica gel thin-layer chromatography.

Recovery of tungsten from spent $^{188}W/^{188}Re$ generators. Tungsten can be desorbed from alumina columns with NaOH or NH_4OH. The desorption yield of tungsten with NaOH or NH_4OH is shown in Fig. 4. The desorption yield was more than 99 and 70% with 10 ml of 4 M NaOH and 15 ml of 3 M NH_4OH, respectively. The desorption yield with NH_4OH was relatively low, but it was increased to 90% by a series of three elutions using 10 ml of 3 M NH_4OH, 10 ml of 0.1 M HCl, and 10 ml of 3 M NH_4OH.

The precipitate was obtained by adding 6 M HCl to the tungstate solution, and the yield was more than 90% after 1-day ripening. The precipitate from the eluent was washed with distilled water to eliminate aluminum and sodium. The precipitate was converted to tungsten trioxide (WO_3) by heating. The chemical form of the recovered tungsten was confirmed to be WO_3 by comparing the specific radioactivity of ^{187}W in a high-purity reagent of tungsten trioxide (WO_3) and the recovered tungsten. The aluminum and sodium content in the recovered WO_3 was less than 0.001%. The high-purity tungsten trioxide ($^{186}WO_3$) can be reused as a target material.

REFERENCES

1. Lewington, Y.J., *Eur. J. Nucl. Med.*, 1993, vol. 20, pp. 66–74.
2. Mausner, L.F. and Srivastava, S.C., *Med. Phys.*, 1993, vol. 20, pp. 503–509.
3. Vera-Ruiz, H., *IAEA Bull.*, 1993, vol. 35, pp. 24–27.
4. Shigeta, N., Matsuoka, H., Osa, A., *et al.*, *J. Radioanal. Nucl. Chem.*, 1996, vol. 205, pp. 85–92.
5. Motoishi, S., Kobayashi, K., Terunuma, K., *et al.*, Abstracts of Papers, *32nd Annual Meet. on Radioisotopes in the Physical Science and Industries*, July, 1995, report 10p-I-3, p. 3.
6. Department of Radioisotopes, Consultative Committee of Research on Radioisotopes, Subcommittee for Production and Radio Labeling, Working Group on Radioactive Rhenium, Development of Pharmaceuticals with Radioactive Rhenium for Cancer Therapy: Production of ^{186}Re and ^{188}Re, Synthesis of Labeled Compounds and Their Biodistributions, *JAERI-Research*, 1998, no. 98-015.
7. Arano, Y., Ono, M., Wakisaka, K., *et al.*, *Radioisotopes*, 1995, vol. 44, pp. 514–522.
8. Kinuya, S., Yokoyama, K., Tega, H., *et al.*, *Jpn. J. Cancer Res.*, 1998, vol. 89, pp. 870–878.
9. Nogawa, N., Momose, S., Miyazawa, K., *et al.*, *J. Radioanal. Nucl. Chem.*, 1999, vol. 239, pp. 385–389.
10. Callahan, A.P., Rice, D.E., and Knapp, F.F., Jr., *Nuc-Compact*, 1989, vol. 20, p. 3.
11. Kodina, G., Tulskaya, T., Gureev, E., *et al.*, *Technetium and Rhenium in Chemistry and Nuclear Medicine 3*, Nicolini, M., Bandoli, G., and Mazzi, U., Eds., Verona: Cortina International, 1990, pp. 635–641.
12. Hashimoto, K., Bagiawati, S., Izumo, M., and Kobayashi, K., *Appl. Radiat. Isot.*, 1996, vol. 47, pp. 195–199.
13. Hashimoto, K., *Appl. Radiat. Isot.*, 1998, vol. 49, pp. 351–356.
14. Hashimoto, K., *Appl. Radiat. Isot.*, 1999, vol. 51, pp. 307–313.
15. Mushtaq, A., *Appl. Radiat. Isot.*, 1996, vol. 47, pp. 727–729.
16. Kobayashi, K., Motoishi, S., Terunum, K., and Rauf, A.A., Abstracts of Papers, *33rd Annual Meet. on Radioisotopes in the Physical Science and Industries*, July, 1996, report 2p-4, p. 156.
17. Geneka, T., Kobayashi, K., and Hagiwara, S., *Int. J. Appl. Radiat. Isot.*, 1987, vol. 38, pp. 845–850.
18. Mughabghab, D.M., *Neutron Cross Sections*, New York: Academic, 1984, vol. 1, part B.
19. Mirzadeh, S., Knapp, F.F., Jr., and Lambrecht, R.M., *Radiochim. Acta*, 1997, vol. 77, pp. 99–102.

研究テーマ：ＲＩ製造技術の開発
表　　題：血管内照用線源の開発

4-2 血管内照射用線源の開発

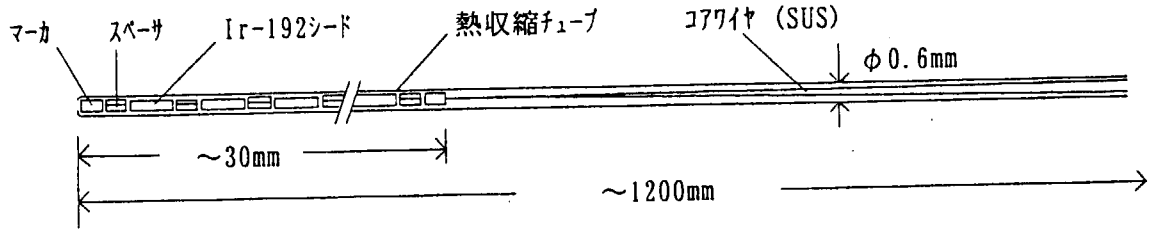
木暮　広人　　反田　孝美　　佐藤　彰　　出雲　三四六
アイソトープ研究開発課

人口の高齢化に伴い、ＰＴＣＡ（経皮的冠動脈形成術）はさらに有用な治療法として普及すると思われる。ＰＴＣＡの問題点は、施行後数ヶ月で３０％程度の高頻度で再狭窄が生じる為に、再びＰＣＴＡを施行しなくてはならないことにある。ステントという金属メッシュを使用する治療法により再狭窄は多少改善したが、まだ十分ではない。再狭窄は、血管壁の損傷に対する内膜増殖で、傷の治癒過程とも言える生物の原始的な反応で、これを抑制することは簡単ではないが、低線量の放射線照射によりそのような細胞増殖を押さえることが可能である。難治性冠動脈狭窄症に対する血管内小線源放射線治療は、再発性冠動脈狭窄症に対する新しい治療法として期待されている。

原研では、「冠動脈再狭窄症に対する血管内小線源療法の安全性と有効性に関する研究」について京都大学医学部と協力研究を行い、Ir-192シード線源を用いた血管内照射用線源の物理的最適デザインのための線量分布測定とその精度評価を行うとともにそれらのデータを基にした臨床用の線源下開発を進めている。

血管内照射用線源の物理的最適デザインは、線源部近傍（血管外膜及び内膜に対して）において線量分布の均一性及び血管内での柔軟性である。この観点から至適なシード線源間隔を求めるため、Seed間隔の異なる（スペーサを使用して間隔を調整）数種の線源を用いて線源近傍の２次元分布測定を行った。線源近傍の線量分布勾配は急峻なため、ワーキング・レンジが大きく、高空間分解能な２次元分布測定器が必要であり、新たに開発されたTL(BaSO4) シートを用いている。線量分布の測定結果は、線源からの距離2mm の距離で評価した結果血管内照射用線源のSeedの至適間隔（スペーサの長さ）は１mm以下となった。

治療の質の向上には正確な線量分布測定が重要であり、その精度評価のため、標準線量計LiF-TLD による線量測定を行いTLシートの測定結果と比較検討を行った。一回目の実験の結果、LiF-TLD の測定可能な領域で、TLシートとLiF-TLD の測定結果は良く一致し、TLシートによる線源近傍の２次元線量分布測定法は簡便で正確な方法であることが示唆された。血管内照射用線源の線源部の概略を以下の図に示す。



原子炉：JRR-3M　　装　置：JRR-3M　HR-1　　分　野：ＲＩの製造（医療用）

4-3

原子炉生産短半減期核種による放射性医薬品の製造法の確立

The production of radiopharmaceuticals
with short lived radionuclides produced by reactor

金沢大学医学部
安東 醇，鷲山幸信，安東逸子

School of Medicine, Kanazawa University
Atsushi Ando, Kohshin Washiyama, Itsuko Ando

目的

核医学の領域では転移性骨腫瘍による疼痛の緩和剤として放射性医薬品を用いる方法が重要になってきた。疼痛緩和用放射性医薬品として ^{89}Sr-chloride, ^{32}P-orthophosphate, ^{117m}Sn-DTPA[1,2], ^{186}Re-HEDP, ^{153}Sm-EDTMP, ^{177}Lu-EDTMP 等の放射性化合物が臨床使用または研究されてきた。この中でも ^{117m}Sn-DTPA は ^{117m}Sn(T=13.60d)が放出する低エネルギー内部転換電子(126.82keV, 151.56keV)による組織中の飛程(0.3mm)が短いために骨髄毒性が小さいという大きな長所を有している。^{117m}Sn イオンは骨集積性があるが、キレート剤の DTPA には骨集積性はない。我々は、高い骨集積性を持つキレート剤である EDTMP と ^{117m}Sn イオンの錯化合物である ^{117m}Sn-EDTMP は ^{117m}Sn-DTPA よりも高い骨集積性を有すると考えて ^{117m}Sn-EDTMP の合成を試みた。またそのための基礎研究を入手しやすい ^{113}Sn (T=115.09d) を使用して行った。まず、^{113}Sn-EDTMP, ^{113}Sn-DTPA の合成の最適条件を求め、ついで原子炉で製造した ^{117m}Sn を使用して ^{117m}Sn-EDTMP を合成した。本研究ではこれら 3 種の化合物の合成条件を調べた。

実験材料および方法

1. ^{113}Sn-EDTMP, ^{113}Sn-DTPA の合成

EDTMP (1-10mg/ml)の 0.1M NaOH 溶液, または DTPA (1-10mg/ml)の 0.1M NaOH 溶液に ^{113}Sn トレーサ溶液と蒸留水を加えて全量を 2.0ml とした。EDTMP ならびに DTPA は(株)同仁科学研究所(熊本県益城町)から購入した。^{113}Sn トレーサ溶液は 4M HCl 溶液中に 740MBq/mg, 635MBq/mg Sn 換算の放射能を持つもの(NEN Life Science Products 社製)を用いた。ついで pH を調整し、室温での撹拌または沸騰水中での過熱を行うことにより、化合物を合成した。次に、これらの反応溶液をミニペーパークロマトグラフ用ろ紙に塗布し展開した。乾燥後、アクチグラムならびにオートラジオグラムを作成し、生成率(使用した放射性スズに対する合成された目的の放射性スズ化合物の割合)を求めた。

またこの際に、^{113}Sn トレーサ溶液とキレート剤のモル比、反応溶液の pH、反応後の室温での撹拌時間または沸騰水浴中での加熱時間を検討した。^{113}Sn-EDTMP, ^{113}Sn-DTPA と未反応の ^{113}Sn トレーサの分離に使用できる展開溶媒を探索した結果、生理食塩水が最も適していたので、これを展開溶媒とするミニペーパークロマトグラフィ[3]で生成率を求めた。

2. ^{117m}Sn の製造

日本原子力研究所の JRR-3M で ^{116}Sn(n, γ)^{117m}Sn の核反応により ^{117m}Sn を製造した。ターゲットは 95.7%濃縮 ^{116}Sn 金属ハク(米国 ORNL 製) 16.6mg を使用し、熱中性子束密度は 9.8×10^{13}(n/cm^{2}sec)、照射時間は 96 時間であった。照射した金属スズ 16.6mg を濃塩酸に溶かした後、塩酸を蒸発乾固して、^{117m}Sn 塩化物とした。このうちの一部を分取し、点線源としてγ線測定を行い生成放射能を求めた。測定には主として金沢大学アイソトープ総合センターの高純度 Ge 半導体検出器 GEM-10220(EG&G ORTEC 社)を使用した。放射能の

研究施設と装置名

JRR-3M HR-2

研究分野名

生物分野に関する放射線効果

定量には158.562keV(分岐比86.4%)のγ線を用いた。

3. ^{117m}Sn-EDTMPの合成

金属スズを溶解し調整した^{117m}Sn塩化物に1.2mlの蒸留水を加え溶かした後、EDTMP(250mg/ml)溶液6.2mlを加えた。1M NaOHでpH6に調整して、沸騰水浴中で30分間加熱して、^{117m}Sn-EDTMPを合成した。合成後は^{113}Sn化合物同様に生成率を求めた。

結果と考察

1. ^{113}Sn-EDTMP, ^{113}Sn-DTPAの合成

反応液のpHと^{113}Sn-EDTMP, ^{113}Sn-DTPAの生成率を調べた。このときの条件は^{113}Sn:EDTMPまたはDTPAのモル比を1:50、沸騰水浴中での加熱を20分とした。3回の実験の平均から、^{113}Sn-EDTMPではpH4～pH8の範囲で99%以上の生成率であるのに対して、^{113}Sn DTPAではpH4での生成率が99%であるがpH5で2.3%, pH6で1.7%, pH7では1.6%と非常に低かった。

次に^{113}Sn:EDTMPまたはDTPAのモル比を1:10, 25, 50, 100, 200と変化させ^{113}Sn-EDTMP, ^{113}Sn-DTPAの合成率の関係を調べた。このときの条件はEDTMPをpH6で、DTPAはpH4で調整し沸騰水浴中での加熱を20分とした。3回の実験の平均から、いずれの条件でも90%以上の合成率を示した。特にモル比が1:25～1:200の範囲では99%以上の合成率であった。

また反応溶液の室温での撹拌時間または沸騰水浴中での加熱時間をそれぞれ10分, 20分, 30分と変化させた場合の^{113}Sn-EDTMP, ^{113}Sn-DTPA合成率を調べた。このときの諸条件は^{113}Sn:EDTMPまたはDTPAのモル比を1:50としEDTMPはpH6で、DTPAはpH4に調整した。^{113}Sn-EDTMP, ^{113}Sn-DTPA共に、室温での撹拌時間または沸騰水浴中での加熱時間が10-30分では99%以上の合成率であった。

したがって以上の結果より^{113}Sn-EDTMP, ^{113}Sn-DTPAの合成では、^{113}Sn-EDTMPの合成にはpH6で, ^{113}Sn DTPAにはpH4で調整し^{113}Sn:EDTMP, DTPAのモル比を1:50とし沸騰水浴中で20分間加熱するのを最適条件とした。

2. ^{117m}Snの製造

^{117m}Sn塩化物の一部を分取し、点線源として高純度Ge半導体検出器でγ線測定を行った。生成放射能は照射終了時で8.15MBq, 比放射能は490kBq/mg Snであった。放射性核種純度は99.9%以上であった。生成放射能から得られた見かけの^{116}Sn(n, γ)^{117m}Sn反応の中性子放射化断面積は5.47±0.03mbであり、これは文献値(6±2mb)[4]と一致する範囲にある。臨床使用に耐えうる放射能量は37MBq(1mCi)程度が望ましいが、今回の条件では比放射能で37MBq/mg Snのものは照射時間がどれだけ長くても熱中性子束の量の制限から作ることが不可能であることが計算により判明した。原研共同試験炉JRR-3Mで利用可能な最大熱中性子束は3×10^{14}(n/cm^2sec)であるが、この場合でも期待される比放射能は最大8MBq(0.22mCi)/mg Snである。

副生成物としては主にスズ箔の構成成分である^{112}Sn, ^{114}Sn, ^{124}Snからの(n, γ)反応等による^{113}Sn, ^{125}Sbが見られた。不純物としては^{46}Sc, ^{59}Fe, ^{60}Co, ^{65}Zn, ^{110m}Ag, ^{140}La, ^{182}Ta, ^{187}Wを認めた。副生成物の^{113}Snは^{112}Snの(n, γ)反応で主に生成する。今回用いた濃縮同位体中の^{112}Sn存在比は0.1%以下であったため、照射終了時においては^{117m}Snの放射化学的純度に寄与せず、生成放射能は照射終了時で0.36kBqであった。しかし、^{113}Snの半減期は115.09日と長いために臨床レベルの^{117m}Sn放射能を使用する場合には最終的に考慮しなければならない核種である。不要な^{113}Snの生成を避けるには^{116}Sn金属ハク中の^{112}Snの存在比をなるべく少なくし、且つ中性子束の高い条件での短時間照射が必要である。不純物に関しては、濃縮同位体を製造する過程でどうしても混入してしまうと考えられるが、これらの核種はいずれも照射後の化学操作で分離が可能であり、また使用においてもその量は実用上ほとんど問題にならない。

3. ^{117m}Sn-EDTMPの合成

合成した^{117m}Sn-EDTMPの比放射能は11.4kBq/mg Sn-EDTMPであった。^{117m}Sn-EDTMPのアクチグラムとオートラジオグラムを図1に示した。いずれの方法でも

^{117m}Sn-EDTMP の生成率はほぼ 100%であった。

まとめ

1. DTPA は非常に限られた pH でのみ ^{113}Sn イオンと安定なキレート化合物 ^{113}Sn-DTPA を形成した。
2. EDTMP は pH4-8 の間で ^{113}Sn と安定なキレート化合物 ^{113}Sn-EDTMP を形成した。
3. ^{113}Sn-EDTMP は 14 日間以上、分解することなく、放射化学的に安定であった。
4. ^{113}Sn-DTPA ならびに ^{113}Sn-EDTMP は容易に合成できるが、^{113}Sn-EDTMP は特に簡単に合成でき、且つ放射化学的に非常に安定であった。
5. ^{117m}Sn は原子炉内での中性子放射化によって簡単に製造できるが、臨床に使用可能な高比放射性 ^{117m}Sn-EDTMP を製造するためには、高濃縮 ^{116}Sn を高い熱中性子束の原子炉で照射する必要がある。

以上より ^{117m}Sn-EDTMP は容易に合成でき、放射化学的にも充分安定あることがわかったが、臨床に使用可能な高比放射性 ^{117m}Sn-EDTMP を製造するためには、高濃縮 ^{116}Sn を高い熱中性子束の原子炉で照射する必要があった。

文献

1) Atkins, H. L., Mausner, L. F., Srivastava, S. C. and Meinken, G. E. et al. (1993) Human biodistribution of Sn-117m(4+)DTPA; a new agent for palliative treatment of painful osseous metastases. *Radiology* **186**, 279-283.
2) Atkins, H. L., Mausner, L. F., Srivastava, S. C. and Meinken, G. E. et al. (1995) Tin-117m(4+)-DTPA for palliation of pain from osseous metastases: a pilot study. *Journal of Nuclear Medicine* **36**, 725-729.
3) 安東醇、真田茂, 安東逸子, 他(1984) ^{99m}Tc 標識医薬品の迅速純度検定法. *Radioisotopes* **33**, 226-229
4) Mughabghab, S. F., Divadeenam, M. and Holden, N. E. (1981) *Neutron Cross Sections*, Vol.1, Part A; Z=1-60. Academic Press, New York.

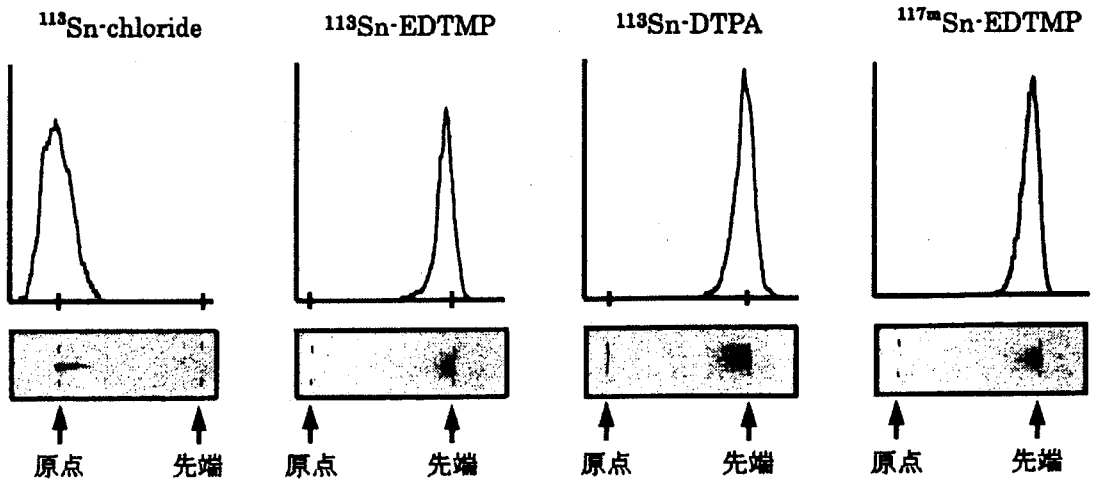


図 1. ^{113}Sn-chloride, ならびに生成された ^{113}Sn-EDTMP, ^{113}Sn-DTPA および ^{117m}Sn-EDTMP のアクチグラムとオートラジオグラム

5. 原子炉材料照射試験

5. Irradiation Test of Reactor Materials

This is a blank page.

研究テーマ：中性子照射により生成する鉛・ビスマス合金中のポロニウム挙動に関する研究
表題：JRR-4 中性子ビーム設備による鉛･ビスマス合金試料の中性子照射

5-1 JRR-4 中性子ビーム設備による鉛･ビスマス合金試料の中性子照射

関本 博、井頭政之、矢野豊彦、小原 徹、大崎敏郎、森 貴正[1]
東京工業大学原子炉工学研究所
[1]日本原子力研究所エネルギーシステム研究部

ナトリウムに代わる液体金属冷却高速炉の冷却材として、また加速器駆動未臨界炉のターゲットとして、鉛･ビスマス液体合金が世界のいくつかの研究機関から提案されている。鉛･ビスマス合金はナトリウムに比べ化学的に不活性で、融点はほぼ同様に低いという利点を有する。しかし、ビスマスの中性子捕獲によりαエミッターであるポロニウムを生成する。本研究は、鉛･ビスマス合金の中性子照射によって生成されたポロニウムの生成率、合金からの放出率及び放出されたポロニウムの各種材料への吸着率を明らかにすることで、鉛･ビスマス冷却高速炉及び加速器駆動未臨界炉でのポロニウムの放出量の定量的評価のための知見を得ることを目的として行われている。

平成 12 年度は、JRR-4 を用いた鉛・ビスマス合金試料の中性子照射と中性子レベルの測定及び加熱溶融装置、α線測定装置の設置調整、特性評価等をおこなった。ここでは、鉛・ビスマス合金試料への中性子照射について述べる。

鉛･ビスマス試料に中性子を照射するにあたり、照射場として JRR-4 中性子ビーム設備熱中性子モードⅠを選んだ。鉛ビスマス合金は高速炉の冷却材として提案されているので、本来なら高速中性子場で実験を行うべきであるが、高速中性子に対するビスマスの中性子吸収断面積は未だ不確定な点があるため、断面積がよく知られている熱中性子による照射を行こととし、熱中性子が多く含まれる照射場を選んだ。

鉛･ビスマス合金は直径約 2cm のアルミナ製のるつぼ内で作成し、アルミナるつぼごと中性子照射を行った。試料内の自己遮へい効果を評価するため日本原子力研究所で開発された連続エネルギーモンテカルロ計算コード MVP を用い、試料内部の中性子束の変化を予測した。その結果、鉛ビスマス内部では中性子束が照射中性子束のおよそ 91%程度になることが分かった。

中性子照射によるポロニウムの生成量を評価するため試料には金線およびカドミウムカバー付き金線を取り付け、中性子フルエンスの測定を同時に行った。照射は試料をファンの取り付けられた弥七と呼ばれる容器に入れて行った。照射した中性子フルエンスから中性子照射を行った鉛ビスマス試料それぞれに含まれるポロニウムの総量の変化を計算によって求めた。5、10、50 分間の照射を行った試料中のポロニウムの量が最大になるのは、それぞれ 24.90、24.89、24.88 日後であり、ポロニウムの最大量はそれぞれ 36.8、79.4、387.8[Bq]と求められた。

引き続き東工大において照射試料の加熱溶融実験を行い、加熱溶融時の鉛・ビスマス合金中のポロニウム挙動に関する実験を行うことを予定している。

本研究は日本原子力研究所の平成 10,11,12 年度「原子力基礎研究推進制度」の支援により実施された。[1)]

参考文献

1) 中性子照射により生成する鉛・ビスマス合金中のポロニウムの挙動に関する研究、(原子力基礎研究(H10-026)、JAERI-Tech (公刊予定)

原子炉：JRR-4　装置：中性子ビーム設備　分野：原子炉燃料・材料（高速炉）

研究テーマ；原子力材料の照射効果の研究
表　　題　；核融合炉用絶縁材料の照射下絶縁劣化特性

5-2 Ti添加Al_2O_3単結晶の中性子照射下その場測定による電気伝導度特性

谷藤　隆昭　片野　吉男　中沢　哲也　實川資朗

日本原子力研究所
物質科学部　材料照射解析研究グループ

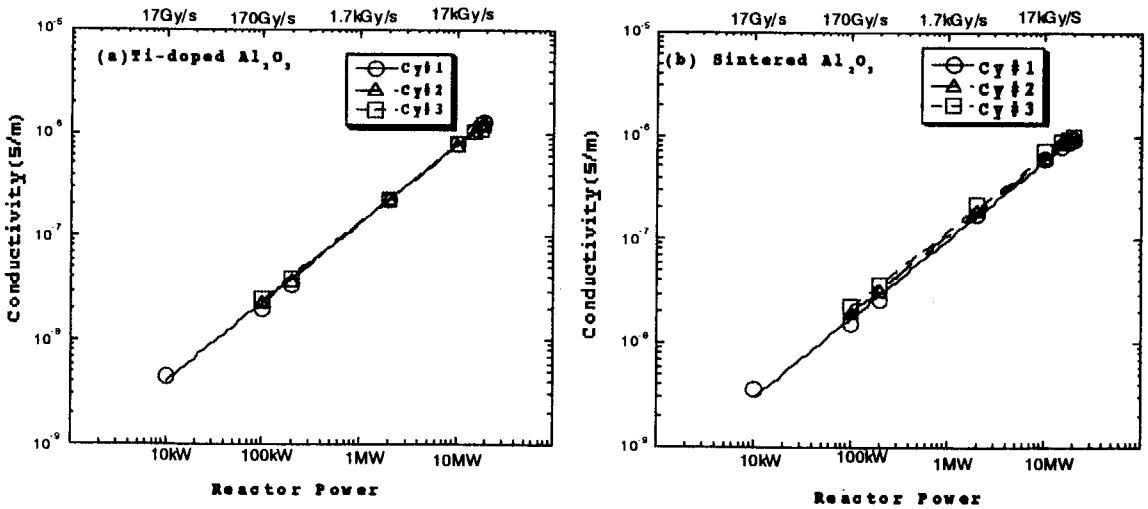
（目的）
核融合炉環境で使用される電気絶縁セラミックスにおいては高エネルギー中性子照射等により電気絶縁特性の劣化が懸念されている。本研究ではTi添加Al_2O_3単結晶及びAl_2O_3焼結体 の二個の試料を同時収納したキャプセルを製作し、JRR-3原子炉を用いた照射下その場測定により電気伝導度特性を評価した。

（実験）
1.8wt%Ti添加Al_2O_3単結晶(レアメタリック製)及びAl_2O_3焼結体 (京セラ製, 測定嵩密度3.97 g/cm^3)の円板試料(寸法 8.5mmΦ×0.2mmt)を用い、それぞれ大気中で1000℃ - 4時間焼鈍後、200nm厚さのPt電極作製処理を施した。照射下実験はJRR－３原子炉内のBR－２孔を用い200-350℃の温度範囲で高速中性子照射束5×1017N/m2s (照射量：0.3dpa) まで照射した。電気伝導測定は印加電圧は直流２０V (DC100V/mm)で中央電極電流、ガードリング電流、高電圧側電流の三点電流を同時測定し電気伝導度を求めた［1］。

（結果）
Ti添加Al_2O_3単結晶とAl_2O_3焼結材のそれぞれの原子炉出力上昇時の各サイクルにおける電気伝導度の変化を図(a)及び図(b)に示す。Ti添加Al_2O_3単結晶では原子炉出力上昇とともに第１サイクルの電気伝導度は4×１０$^{-9}$(S/m)から20MWの最高出力では1.3×１０$^{-6}$ (S/m)に約3桁増加した。第2及び第3サイクルにおいてもほぼ同様の挙動を示した。炉出力上昇に伴う電気伝導度σの増加は炉内のガンマ線の線量率φと相関を示し、$\sigma=\kappa\,\phi^d$で表される。ここでκは定数、d は線量率べき指数である。第1、第2及び第3サイクルのべき指数dは各々0.76、0.76、0.74で殆ど差がなくRIEDは生じていないものと考えられる。また、Al_2O_3焼結材の原子炉出力上昇に伴う電気伝導度の変化は第１サイクルの3×１０$^{-9}$(S/m)ら最高出力の20MWでは1.0×１０$^{-6}$ (S/m)に増加するが第2及び第3サイクルにおいては少し電気伝導度が上昇する傾向を示した。べき指数 d は第1、第2及び第3サイクルの各々0.76、0.75、0.73と減少する傾向を示し微小なRIEDが観察された。これはAl_2O_3焼結材の粒界や粒内の不純物による誘導放射線などに起因するものと考えられる。

一方、既に報告した, 2.8wt%Cr添加Al_2O_3単結晶では、相関指数d が0.8から0.73に減少し、その原因は照射欠陥や照射誘起偏析等の生成に起因していたが、本試料では、殆どこれら照射欠陥生成などが起こり難い事を示唆している。

[1] T. Tanifuji et al., J, Nucl. Mater., 253(1998)156



JRR-3照射下での電気伝導度特性 (a)Ti添加Al2O3単結晶 ，(b)Al2O3焼結体

原子炉；JRR-3M　装置；ＢＲ-2　分野；原子炉燃料・材料（核融合炉）

研究テーマ；原子力材料の照射効果の研究
表　　題　；核融合炉用窓材のトリチウム移行挙動

5-3 石英ガラスからのトリチウム放出

谷藤　隆昭　　那須　昭一 [1)]　　實川　資朗

日本原子力研究所　物質科学部　材料照射解析研究グループ

[1)] 金沢工業大学　　光電磁場科学応用研究所

（目的）

核融合炉の窓材などに使用が検討されている石英ガラスに^{6}Liの核反応による反跳トリチウム(2.7MeV)を原子炉照射により石英ガラスに打ち込み、照射後、等速昇温加熱法によりトリチウム放出挙動を調べた。本研究では、市販の各種石英ガラスからのトリチウム放出特性をスイープ・ガスの効果にも着目して評価した。

（実験）

市販の各種石英ガラス（寸法：10×5×1mm^3）を同様な寸法の酸化リチウム（Li_2O）ペレットに密着させて、JRR-2,HR-8孔で熱中性子照射量約5×10^{18}n/cm^{2}までの照射を行った。照射後の石英ガラス試料を2K/minの昇温速度で加熱し、水素またはアンモニアガスでスイープして放出されるトリチウムを比例計数管に導き測定した。

（結果）

水酸基をあまり含まないSK1300からのトリチウム放出挙動を図1に示す。水素ガスでスイープしたときには約750℃に単一のピークを示すが、アンモニアガスでスイープした場合には主な放出ピークは約850℃となる。これに対して、水酸基を多く含有するSUPRASILからのトリチウム放出は図2に示すように、850℃付近のピークの他に新たに約750℃ピークが観られるようになる。この結果より、750℃付近のピークは石英ガラスに含有している水酸基と密接な関連があることを示唆している。一方、水素ガスでスイープした場合には、SK1300同様、約750℃に単一のピークを示す。水素ガスによるスイープは石英ガラスからのトリチウム放出を約100℃加速し、水素の石英ガラス内への拡散が関与しているものと推定される。

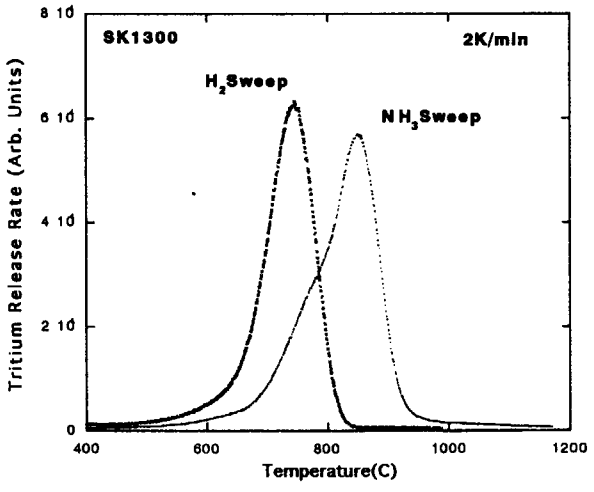


図1．SK1300からのトリチウム放出挙動

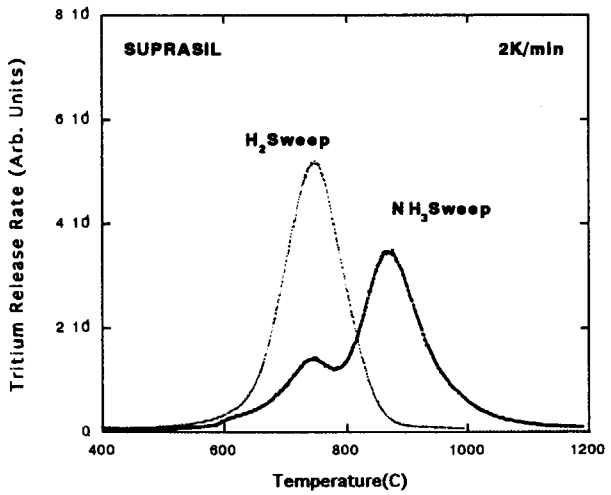


図2．SUPRASILからのトリチウム放出挙動

原子炉；ＪＲＲ-4　　装置；Ｓパイプ　　分野；原子炉燃料・材料（核融合炉）

This is a blank page.

6. 即発ガンマ線分析

6. Prompt Gamma-ray Analysis

This is a blank page.

6-1 火山岩試料の即発γ線分析

Neutron-induced prompt γ-ray analysis for volcanic rocks

福岡孝昭[1] 長谷中利昭[2] 佐野貴司[3]

[1]立正大学地球環境科学部, [2]秋田大学工学資源学部,

[3]京都大学理学部付属地球熱学研究施設（現富士常葉大学環境防災学部）

Takaaki FUKUOKA[1], Toshiaki HASENAKA[2] and Takashi SANO[3]

[1]Faculty of Geo-Environmental Science, Rissho University, [2]Research Institute of Materials and Resources, Akita University, [3]Institute for Geothermal Sciences, Kyoto University

(Present address: College of Environment and Disaster Research, Fuji Tokoha University

1．はじめに

日本の多くの火山のように、島弧火山の岩石中のホウ素含有量は高い。これは、ホウ素を多量に含む深海底堆積物が、プレートのもぐり込みにともない、海溝からマントル中に入り、マグマが生じる時に混入する為と説明されている。しかしこの混入のメカニズムは必ずしも明らかでない。本研究では、このメカニズムを解明するため、海溝の堆積物と島弧火山の岩石試料について、ホウ素含有量を求める。海溝に沿ったあるいは直交する火山の試料について、ホウ素含有量を求め水平方向の変化も明らかにする。また、世界の火山について、どのタイプの火山か不明な火山について、その火山岩中のホウ素含有量を測定して、タイプを明らかにする。

なお、PGA はホウ素だけでなく、INAA では苦手な Gd 等の分析にも感度が良い。本研究では火山マグマの進化を議論するのに有効なホウ素以外の元素についても視野に入れる。

本報告では、一連の研究に関連して過去 3 年間に行われた研究のうち、岩手火山玄武岩マグマに日本海溝堆積物成分がどの程度含まれているかを見積もった研究について報告する。

2．試料と分析法

岩手火山の玄武岩試料 9 試料と日本海溝堆積物コア試料 21 個が分析された。岩手火山の位置と日本海溝堆積物試料の採集地点を図 1 に示した。

主成分元素と K, Ba, Zr 等は蛍光 X 線分析法(XRF)で、B（ホウ素）、Sm, Gd 等は即発γ線分析法（PGA）で分析した。PGA では粉末試料（0.5～0.8 g）をプレス錠剤化し、フッ素樹脂（FEP）フィルムで作製した袋に封入し、日本原子力研究所の JRR-3M 炉の中性子ガイドビームで、He 雰囲気中で 1,000～7,200 秒間照射した。その即発γ線を Ge 半導体検出器と BGO 検出器で測定した。PGA の標準試料として JB-1 と JB-2 を用いた。

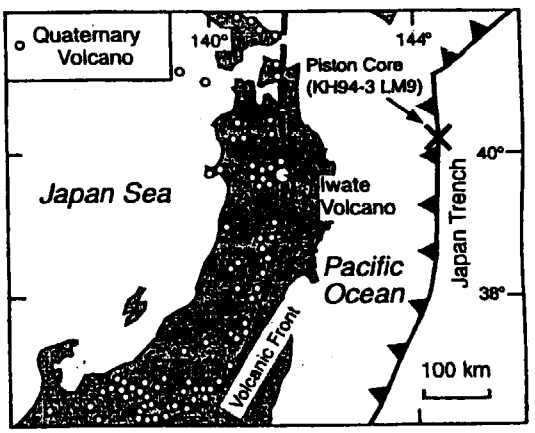


図 1．岩手火山の位置と日本海溝堆積物の採集地点

JRR-3M, 即発γ線分析装置

即発γ線放射化分析（地球化学・宇宙化学）

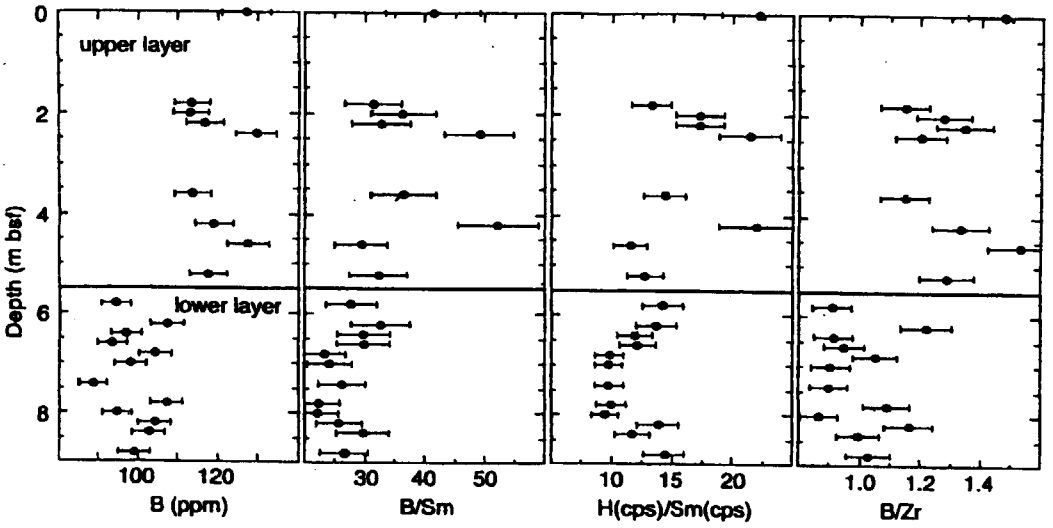


図２．日本海溝堆積物のＢ含有量、B/Sm、H/Sm、B/Zr比の深さ方向の変化

３．結果と考察

日本海溝堆積物中Ｂ含有量、B/Sm、H/Sm、B/Zr比が堆積物の深さ方向にどのように変化するかを図２に示した。各元素の値の結果は調和的である。図３には、岩手火山玄武岩、堆積物、変質玄武岩、地殻岩石中の微量元素含有量をMORBの値で規格化して示した。また、高圧実験によって得られた結果から推定したMobilityも示した。Bの Mobilityが大きいことを示している。

島弧火山マグマ期限のモデルでは、沈み込んだスラブの一部が混入していることになっている。すなわち、海洋プレートを構成する堆積物層と変質玄武岩（AOC）から脱水した流体相がマントルウェッジに存在することになる。今回の分析結果（XRFによるものを含む）とこれまでのほかの研究により報告されているAOCの分析値を用いて、堆積物起源の流体相とAOC起源の流体相中の元素含有量を推定した。その結果、マントルウェッジ中の堆積物起源の流体相とAOC起源の流体相の混合比は10：90と推定された（図４）。岩手火山玄武岩、堆積物起源の流体相、AOC起源の流体相、マントルのB/Sm、Ba/Sm、K_2O/Smを比較した結果、マントルに1%以下の２種類の流体相が存在すれば、岩手火山玄武岩マグマの組成を説明することが可能であることが明らかになった。すなわち、マントルウェッジ中の堆積物起源の流体相の量は、0.1%以下であると考えられる。

４．まとめ

岩手火山マグマに海洋堆積物起源の流体相が約0.1%含まれていることが明らかになった。ホウ素の挙動は^{10}Beのそれと類似していると言われている。今後^{10}Be含有量を知ることにより、サブダクションで沈み込んだスラブの一部がマグマとなり、さらに噴火して地表に出てくるまでの時間軸を明らかにしたい。

本共同利用研究では、岩手山以外の火山についてもホウ素を中心にPGAを行ったが、今後ここで紹介した以外の元素についてもPGAを行い、さらに多くの火山岩試料の分析を行い研究を発展させたい。

５．成果の公表

学術誌

1．佐野貴司，福岡孝昭，長谷中利昭，米沢仲四郎，松江秀明，澤幡浩之，即発γ線による火山岩中ホウ

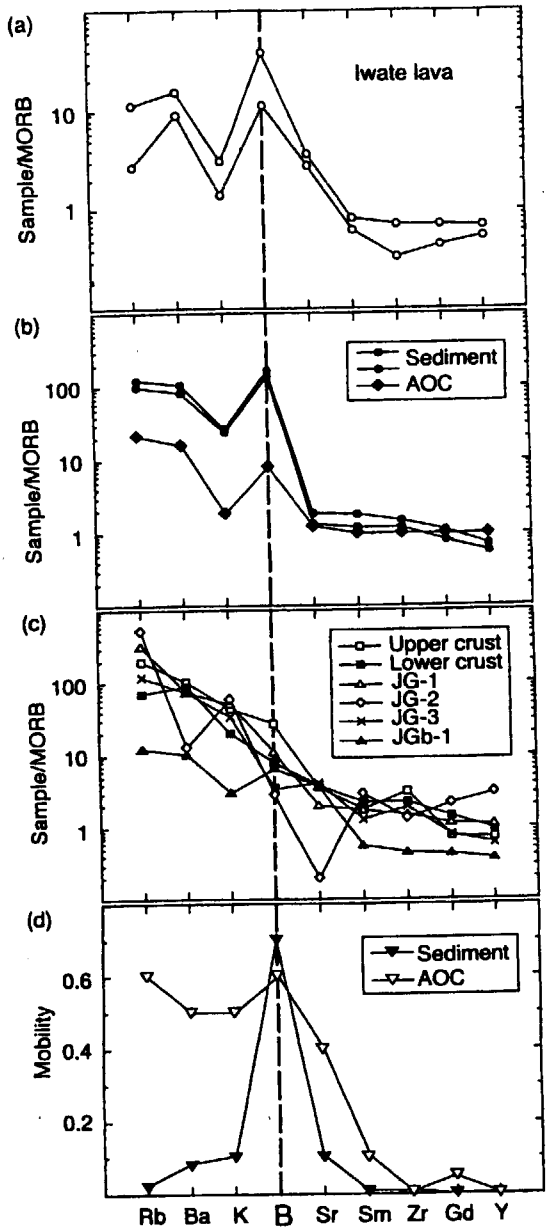


図3．MORBの値で規格化した微量元素含有量とMobility (a) 岩手火山試料、(b) 日本海溝堆積物と変質玄武岩(AOC)、(c) 地殻岩石、(d) 沈み込み帯での脱水過程での各元素のMobility。各元素のMobilityは、脱水過程で失われた量を最初の存在量で割ったものである。

素の分析：ケイ素を用いた内部標準法. *RADIOISOTOPES*, 47, 735-744 (1998).

2. T. Sano, T. Fukuoka, T. Hasenaka, C. Yonezawa, H. Matsue and H. Sawahata, Accurate and efficient determination of boron content in volcanic rocks by neutron-induced prompt γ-ray analysis. *J. Radioanal. Nucl. Chem.*, **239**, 613-617 (1999).

3. T. Sano, T. Hasenaka, A. Shimaoka, C. Yonezawa and T. Fukuoka, Boron contents of Japan Trench sediments and Iwate basaltic lavas, Northeast Japan arc: estimation of sediment-derived fluid contribution in mantle wedge. *Earth Planet. Sci. Letters*, **186**, 187-198 (2001).

学会発表

1. 佐野貴司，福岡孝昭，長谷中利昭，米沢仲四郎，松江秀明，大陸洪水玄武岩および大陸リソスフェア中のホウ素含有量．1999年地球惑星科学関連学会合同大会，1999年6月．

2. 佐野貴司，長谷中利昭，福岡孝昭，島岡晶子，米沢仲四郎，松江秀明，岩手火山のホウ素含有量：沈み込んだスラブに起源をもつ流体相またはマグマのソースへの付加の証拠．1999年地球惑星科学関連学会合同大会，1999年6月．

3. 佐野貴司，福岡孝昭，長谷中利昭，島岡晶子，東北日本弧の火山フロントに噴出した溶岩と日本海溝の堆積物中のホウ素含有量の比較．1999年日本地球化学会年会，1999年10月．

4. 福岡孝昭，佐野貴司，長谷中利昭，島岡晶子，日本海溝堆積物と岩手火山玄武岩中のホウ素含有量の比較：沈み込んだ堆積物起源の流体相の量の見積もり．2000年日本地球化学会年会，2000年9月．

5. 佐野貴司，福岡孝昭，長谷中利昭，大陸下リソスフェアマントルは鉛に富みホウ素に枯渇している：デカン洪水玄武岩を例とした研究．地球惑星科学関連学会2001年合同大会，2001年6月．

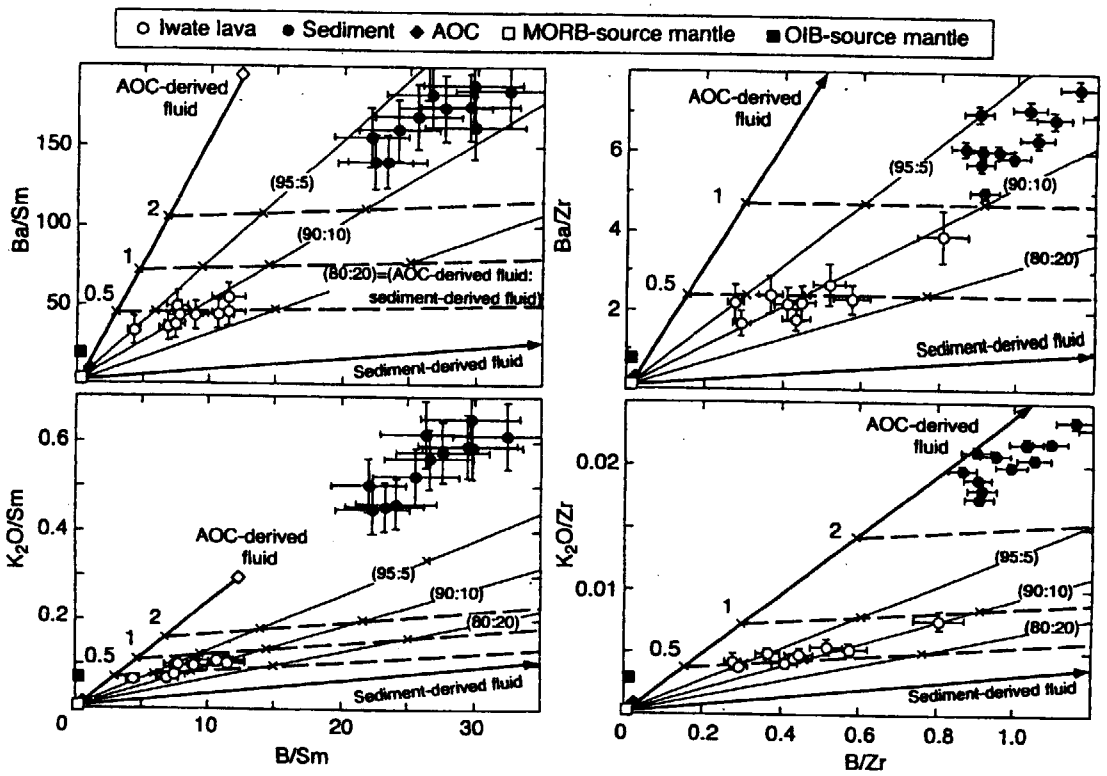


図４．岩手火山玄武岩、日本海溝堆積物の B/Sm 対 Ba/Sm、B/Sm 対 K_2O/Sm、B/Zr 対 Ba/Zr、B/Zr 対 K_2O/Zr 関係。図にはマントルウェッジでの AOC 起源流体相と堆積物起源流体相の重量混合比のモデル計算値を（ ）内に示した。0.5、1、2 と記された点線は、マントルウェッジに対するスラブ起源流体相の付加量（%）を示す。

6-2 隕石試料の即発γ線分析（II）

Grompt gamma-ray analysis of meteorite samples (II)

海老原充、S. K. Latif、大浦泰嗣、G. W. Kallemeyn

M. Ebihara, S. K. Latif, Y. Oura, G. W. Kallemeyn

東京都立大学大学院理学研究科

Graduate School od Science, Tokyo Metropolitan University

米田成一

S. Yoneda

国立科学博物館理工学研究部

Department of Science and Engineering, National Science Museum

1 はじめに

平成10年度から12年度にかけて、標記課題で原研施設を利用した共同研究を行った。これまで同じ研究課題の(I)として、粉末にした隕石試料の元素組成を即発γ線分析で求める研究を実施した。本研究では(I)と同様に隕石試料を研究対象としたが、粉末試料とせず、大きな塊のままの試料を用いて、できるだけ正確な元素組成を測定する方法の確立を目指した。さらに、こうして確立した方法を実際にいくつかの塊状隕石の分析に適用し、結果の評価を行った。

隕石は今から約45-6億年前に起源を持ち、太陽系物質の中で最も古い歴史を持つ物質である。従って、隕石から太陽系初期の様々な情報を知ることができる。従来、隕石試料の元素分析には壊変γ線を利用する中性子放射化分析法、特に機器中性子放射化分析法が多く利用されてきた。即発γ線分析ではホウ素、ケイ素、硫黄など、機器中性子放射化分析法では実質的に分析が困難な元素の定量が可能であり、また、用いる中性子束が壊変γ線を利用する機器中性子放射化分析に比べて遙かに低く、分析終了後、適当な時間冷却すれば生成放射能はほとんど無視できるので、試料の再利用が可能である。隕石試料のように希少な試料には、非破壊分析で、かつ分析後の再利用が可能であるという即発γ線分析は大変有効な分析手段となる。

本研究では、大型の試料を非破壊で分析することが出来るという即発γ線分析の特徴を、隕石試料の分析によって明らかにした。その場合の元素定量法としては、分析しようとする試料と同じ形状の標準試料を準備できないので、いわゆる比較法は適用できない。そこで、かつて考古学的試料に適用された「内部単一標準化法」（internal monostandard method）を隕石試料に適用することを試みた。はじめにこの方法の精度や確度（正確さ）を組成のよくわかっている標準岩石試料で評価し、次いで大型の隕石試料を用いて確認し、最後にいくつかの隕石試料に適用して、文献値との比較を行った。

2 実験

試料の調整　「内部単一標準化法」を適用するための定数を求めるために、定量目的元素の試薬を一定量照射した。「内部単一標準化法」の評価を行うためには、細粒で均一な組成をもつ Allende 隕石標準試料（米国スミソニアン博物館で調整したもの）約250 mg を FEP フィルムに封入した

研究施設と装置名
JRR-3M

研究分野
宇宙化学

試料を用いた。さらに、同法が大型試料の分析にどのくらい適するかを評価するために、大型岩石試料の代わりに、組成のよくわかっている標準岩石試料をテフロン瓶に詰めて元素組成を求めた。実際の大型試料の分析には、主に珪酸塩からなる石質隕石４つと鉄隕石４つを FEP フィルムに包んで、分析に用いた。試料の質量は、粉末標準岩試料の場合 10~15g、塊状石質隕石では 10~50g、塊状鉄隕石では 50~1300g であった。小型試料の場合にはテフロン糸で試料固定架台に吊したが、大型試料の場合には架台につるすことをせず、試料箱に直接据え付けて測定した。

照射と計測　JRR-3M の熱中性子ビームを用いた。本研究の様に大型の試料の場合には冷中性子を用いると放出される即発γ線の強度が強すぎて、測定器の不感時間が大きくなりすぎるのであまり適さない。中性子の照射時間は試料により異なるが、5000~15000 秒であった。測定にはバックグラウンドを下げるために、コンプトン抑制回路つき Ge 検出器を用いた。同様の目的で、試料箱にヘリウムガスを通じて、主に空気中の窒素による妨害を除いた。

データ解析　定量には「内部単一標準化法」を用いた。内部標準元素としては試料に均一に存在する主成分元素がふさわしく、ケイ素と鉄を選んだ。定量目的元素とこれらの内標準元素の元素比 (n^X/n^{Fe}) （ここでは鉄を内標準元素としている）は以下の式で近似的に表される；

$$(n^X/n^{Fe}) = (A^X/A^{Fe}) \cdot (\sigma^{Fe} b^{Fe}(E_\gamma^{Fe})/\sigma^X b^X(E_\gamma^X)) \cdot (\varepsilon^{Fe}(E_\gamma^{Fe})/\varepsilon^X(E_\gamma^X))$$

ここで A は即発γ線のピーク領域、σは中性子吸収断面積、b は中性子吸収あたりの即発γ線の放出率（放出係数）、εは測定器の検出効率をあらわす。b とεの後ろにカッコで示されている Eγは測定に用いる即発γ線のエネルギーをあらわし、そのエネルギーに対応した b、εについての値であることを示す。$\sigma^X b^X(E_\gamma^X)$値は物理定数で、あらかじめ定量目的元素の適当な試薬を用いて求めた。本来中性子エネルギースペクトルに依存するが、測定間の差は無視した。$\varepsilon^X(E_\gamma^X)$は測定条件に依存する数値であり、測定の都度、適当な元素によって測定器の検出効率を求め、その E_γ vs. 検出効率曲線から該当する即発γ線エネルギーの検出効率を求めた。こうすることにより、大型試料中での中性子の吸収や散乱、γ線の吸収の影響を最少に押さえることが可能となる。

結果と考察

精度と確度　Allende 標準隕石試料粉末を用いて、「内部単一標準化法」による定量値の精度と確度を評価した。その結果を Table 1 にまとめる。５回の測定値を加重平均した値は文献値とほとんどの元素で誤差の範囲内で一致する。また、繰り返し精度もホウ素とサマリウムを除いて 10%（1σ）以内であり、精度、確度ともに十分満足できる値であった。

次いで、標準岩石試料である JB-1a を用いて、大きな試料を測定する際の「内部単一標準化法」の有効性を確かめた。Jb-1a を約 14g ほどテフロン瓶にとり、分析した。分析は同一の日に 2 回行ったほか、日を変えて測定を行い、再現性を見た。その結果を Table 2 にまとめる。元素組成を求めるにあたってはケイ素を内標準元素としてもちいた。表で明らかなように、マグネシウムとマンガンで多少の不一致が認められるが、それ以外は文献値と良く一致する。また、3 度の分析による再現性も非常に高い。マグネシウムとマンガンの定量値の不一致は、あらかじめ試薬で求めたσb 値に問題があると思われる。

塊状隕石試料の分析　以上の結果を踏まえて塊状の隕石試料の分析を行った。まず、Allende 隕石を分析した。分析する位置を変えて、2 度分析した。その結果を Table 3 に示す。データは鉄を内標準元素として用いたものである。参考のために、Table 1 で示した粉末試料に対する加重平均値を示した。粉末試料で求められた値とほとんど差のない値が塊状試料でも求められた。従って、Table 2 の結果共々、本「内部単一標準化法」は大きな隕石試料の分析に大変有効な方法であることが明らかとなった。

研究成果（発表論文）

（共同研究の期間に JRR3-M の PGA 装置を用いて得られた成果を報告したもの）

1．S. K. Latif, Y. Oura, M. Ebihara, G. W.

Kallemeyn, H. Nakahara, C. Yonezawa, T. Matsue and H. Sawahata (1999) Propmt gamma-ray analysis (PGA) of meteorite samples, with emphasis on the determination of Si. J. Radioanal. Nucl. Chem. 239, 577-580

2. H. Nakahara, Y. Oura, K. Sueki, M. Ebihara, W. Sato, S. K. Latif, T. Tomizawa, S. Enomoto, C. Yonezawa and Y. Ito (2000) Some basic studies on non-destructive elemental analysis of bulky samples by PGA. J. Radioanal. Nucl. Chem. 244, 405-411.

Table 1
Replicate analyses of the SI Allende meteorite powder by PGA with an internal mono-standard method (Fe as a reference) using thermal neutron beam

Element	Content[a]						
	1st meas.	2nd meas.	3rd meas	4th meas.	5th meas.	Wtd. mean[b]	Literature values[c]
B (ppm)	1.3±0.8	1.2±0.4	n.d.[d]	n.d.	1.9±0.7	1.4±0.3	1-5
Na (%)	(0.20±0.05)[e]	0.33±0.04	0.34±0.05	0.26±0.05	0.28±0.04	0.30±0.02	0.33±0.01
Mg (%)	12±1	11±1	(9±1)	14±2	13±1	13±1	14.8±0.1
Al (%)	1.57±0.20	1.62±0.19	1.79±0.22	1.62±0.21	1.60±0.21	1.60±0.09	1.74±0.04
Si (%)	16.2±13.2	16.0±0.9	15.2±1.1	15.9±1.2	16±1	15.8±0.5	16.0±0.1
S (%)	2.2±0.1	1.9±0.1	1.9±0.1	2.0±0.1	1.9±0.1	1.98±0.04	2.10±0.03
Cl (ppm)	329±87	320±35	277±43	280±54	309±48	302±21	218-320
Ca (%)	1.76±0.15	1.71±0.12	1.62±0.13	1.72±0.15	1.55±0.16	1.68±0.06	1.84±0.05
Ti (ppm)	794±85	732±55	884±86	786±91	811±85	786±64	900±50
Mn (%)	0.12±0.01	0.13±0.01	0.12±0.01	0.12±0.01	0.12±0.02	0.12±0.01	0.145±0.004
Fe (%)[f]	≡23.6	≡23.6	≡23.6	≡23.6	≡23.6	≡23.6	23.6±0.01
Co (ppm)	656±67	666±58	730±67	586±78	659±55	663±28	662±5
Ni (%)	1.56±0.09	1.3±0.07	1.43±0.08	1.59±0.09	1.36±0.08	1.46±0.04	1.42±0.02
Sm (ppm)	(0.53±0.12)	0.32±0.10	0.29±0.12	0.33±0.12	0.29±0.11	0.31±0.06	0.31±0.02

[a]Errors accompanied by data from individual measurements (1st to 5th measurements) are due to counting statistics (1σ). Errors for weighted mean (Wtd. mean) represent standard deviations (1σ). Errors due to standard deviations (1σ) are shown except for B and Cl, for which only ranges of literature values are given because of their large scatterings.
[b]Weighted means of values from 1st measurement through 5th measurement.
[c]Jarosewich et al. (1986); Ebihara et al. (1997); Langenauer and Kraehenbuehl (1993); Dreibus et al. (1979); Kallemeyn and Wasson (1981).
[d]Not detected (below detection limit).
[e]Values in parentheses are not included in calculating weighted means.
[f]A mean value of literature data (23.6%) is used for a reference value.

Table 2
Thermal neutron PGA results for the bottled JB-1a powder sample with an internal mono-standard methods (Si as an internal reference), obtained from different irradiations on the same day (runs 1 and 2) and from different irradiations on different days (days 1 and 2)

Element	Content[a]				
	Day 1			Day 2	Lit. values[b]
	Run 1	Run 2	Mean values		
B (ppm)	7.6±0.6	7.6±0.5	7.6±0.6	8.1±0.8	7.88
Na (%)	1.9±0.1	2.0±0.1	2.0±0.1	2.1±0.1	2.08
Mg (%)	3.8±0.3	3.7±0.2	3.8±0.3	3.5±0.3	4.72
Al (%)	7.9±0.5	8.0±0.5	8.0±0.5	7.4±0.5	7.65
Cl (ppm)	180±15	175±15	178±15	165±20	171
K (%)	1.16±0.05	1.17±0.04	1.17±0.05	1.19±0.05	1.16
Ca (%)	6.7±0.2	6.8±0.2	6.8±0.2	6.4±0.2	6.65
Ti (%)	0.80±0.01	0.80±0.01	0.80±0.01	0.80±0.02	0.77
Mn (ppm)	1000±40	1000±50	1000±50	1000±10	1150
Fe (%)	7.0±0.2	7.0±0.2	7.0±0.2	7.0±0.2	6.33
SM (ppm)	5.1±0.2	5.1±0.2	5.1±0.2	5.4±0.2	5.07
Gd (ppm)	5.7±0.3	5.8±0.3	5.8±0.3	5.2±0.4	4.67
Si (%)[c]	≡24.5	≡24.5	≡24.5	≡24.5	24.5

[a]Errors accomanied by data from individual measurements are due to counting statistics (1σ). Errors for mean values represent larger values of those for runs 1 and 2.
[b]Certified values complied by Imai et al. (1995).
[c]A certified value (24.5%) (Imai et al., 1995) is used for a reference value.

Table 3
PGA results for the Allende meteorite chunk sample (Allende A) with an internal mono-standard method (Fe as an internal reference) using thermal neutron beam

Element	Content[a]				
	1st. meas.	2nd meas.	Mean values	Wtd. means[b]	Lit. values[b]
B (ppm)	1.3±0.4	1.6±0.3	1.5±0.4	1.4±0.3	1-5
Na (%)	0.29±0.02	0.27±0.02	0.28±0.02	0.30±0.02	0.33±0.01
Mg (%)	13.40.6	13.2±0.6	13.3±0.6	13±1	14.8±0.1
Al (%)	1.7±0.1	1.5±0.1	1.6±0.1	1.60±0.09	1.74±0.04
Si (%)	16.9±0.5	16.5±0.5	16.7±0.5	15.8±0.5	16.0±0.1
S (%)	2.12±0.09	2.12±0.09	2.12±0.09	1.98±0.04	2.10±0.03
Cl (ppm)	310±10	290±10	300±10	302±21	218-320
K (ppm)	300±40	370±60	335±60	-[c]	330±80
Ca (%)	31.71±0.07	1.65±0.07	1.68±0.07	1.68±0.06	1.84±0.05
Ti (ppm)	900±30	890±30	895±30	789±34	900±50
Mn (%)	1.39±0.06	1.29±0.07	1.34±0.07	1.20±0.10	1.45±0.04
Fe (%)[d]	≡23.6	≡23.6	≡23.6	≡23.6	23.6±0.01
Co (ppm)	740±30	690±40	715±40	663±28	662±5
Ni (%)	1.60±0.07	1.56±0.06	1.58±0.07	1.46±0.04	1.42±0.02
Sm (ppm)	0.29±0.02	0.33±0.03	0.31±0.02	0.31±0.06	0.31±0.02

[a]Errors for individual measurements (1st and 2nd meas.) and mean values are the same as for Table 5 (Footnote a).
[b]From Table 4.
[c]Not determined.
[d]A mean value of literature data (23.6%) is used for a reference value.

6-3

固体環境試料および地球化学的試料の即発ガンマ線分析（Ⅱ）

Neutron-induced prompt gamma-ray analysis of solid environmental samples and geochemical samples

松尾基之、久野章仁、久保健一、松本　武、八十島光子、田中佑人、片岡正樹[1]
M. Matsuo, A. Kuno, K. Kubo, T. Matsumoto, M. Yasoshima, Y. Tanaka, M. Kataoka[1]

東京大学大学院総合文化研究科広域科学専攻
[1]東京大学大学院理学系研究科化学専攻
Graduate School of Arts and Sciences, The University of Tokyo
[1]Graduate School of Science, The University of Tokyo

1．はじめに

固体環境試料や地球化学的試料中に含有される元素を定量し、その分布を明らかにすることは、試料自体の形成過程を知る上でも、試料の置かれた環境を理解する上でも重要な課題と考えられる。中性子誘起即発γ線分析法(PGA)は、通常の機器中性子放射化分析法(INAA)と同様に、多元素同時定量分析が可能なため、多くの元素の分布を総合的に判断するのに適した分析法と言える。さらにＰＧＡは、ＩＮＡＡでは分析が困難なH, B, S, Si等の軽元素やCd等の有害元素の定量が可能である、試料の誘導放射能が低く同分析法で使用した試料を他の分析法で再使用することが可能である、といった特長を持つ優れた分析法である。本研究では、同法を用いることにより、次の２通りの試料について種々の環境化学的、地球化学的な検討を行った。
①都市河川および干潟において深さ方向に採取した底質のコアサンプル、②古生代／中生代境界直後に遠洋深海で堆積した層状チャート。以下に、それぞれの試料ごとに研究内容およびその結果を報告する。

2．都市河川および干潟底質の即発γ線分析

【序】　河川や干潟の底質は深層になるにつれて還元的雰囲気が強くなり、各元素が特異な反応を起こすなど興味深い場所である。このような底質中で、どのような物質移動や化学変化が起こっているかを明らかにすることは、環境評価の上で重要な情報を与えると考えられる。特に、都市内を流れるいわゆる内部河川の底質中金属元素は次の２点から注目される。
(1)下水処理水などの環境負荷により深層は著しく還元的になり硫化水素などが発生するが、場合によっては金属の硫化物の生成により悪臭発生が抑えられる可能性がある。
(2)河道管理などの観点から浚渫が行われる際、底質の有効利用が図られるべきだが、有害金属の存在量や挙動は正確に把握されねばならない。また、干潟は多くの生物の生活の場であると同時に環境浄化作用を持っており、周辺の水の汚れを除去し、綺麗な水を海へ流し出すことでも注目されている。

上記のような視点から、本研究では、非破壊で、主要元素から微量元素までを同時に測定できる、中性子誘起即発γ線分析法(PGA)および機器中性子放射化分析法(INAA)を、実際に採取された底質コアサンプルに適用し、30数元素の濃度の垂直分布を得た。また、これらの垂直分布について互いの相関行列を作ることなどによって、底質中の各元素の動態の相違について考察を加えた。
【実験】　本研究では、環境負荷の高い都市河川として、東京都の内部河川である北十間川・竪川を選び、また東京湾内でも比較的自然の状態が残っている場所として千葉県谷津干潟（ラムサール条約登録地）を選び、フィールドとした。試料採取にはHR型不撹乱柱状採泥器または塩化ビニル管を用い、垂直方向に得られた約50

研究施設と装置名
ＪＲＲ－３Ｍ、即発γ線分析装置

研究分野
環境化学、地球化学、分析化学

cmのコアを現地で3cmごとに分別し、窒素ガス中に封入した。加圧ろ過（窒素ガス4atm）により間隙水を除いたものを風乾後、めのう乳鉢で粉砕した。その中から約200～400mgを精秤し、錠剤成形器を用いて約100 kgf cm^{-2}の圧力で5分程度置き、直径10mm、厚さ約1mmのペレットに成形した。これを、中性子ビームのサイズである20mm四方以内に収まるように、厚さ12μmのFEPフィルムに封入し、テフロン製の専用ホルダーに固定した上で、日本原子力研究所JRR-3Mの冷中性子ビームガイド（中性子束：1.4×10^{8} n $cm^{-1}s^{-1}$）または、熱中性子ビームガイド（中性子束：2.4×10^{7} n $cm^{-1}s^{-1}$）に設置した即発γ線分析装置にセットし、He雰囲気中で2400秒間（冷中性子）または7200秒間（熱中性子）即発γ線を測定した。熱中性子ビームガイドでの分析感度は冷中性子ビームガイドでの分析感度の約1/10程度であるが、マシンタイムの都合も考慮し、サンプル量を増やして測定時間を短くする方法を選んだため、測定時間をこのように設定した。測定したγ線スペクトルは通常のγ線スペクトル解析プログラム(SEIKO EG&G DS-P 201/MS）でピークサーチとピーク面積の計算を行った。各ピークについて得られた計数率は、中性子束の変動を補正するために、24時間に1回、一定のTiの板(Ti flux monitor）を測定して得られる342keVと1381keVのピークの計数率の平均値で割り、比較標準試料について報告されているTi flux monitorの計数率で規格化した分析感度を用いて各元素の含有量を計算した。INAA法に関しては、立教大学原子力研究所および日本原子力研究所JRR-4にて実験を行った。

【結果及び考察】　北十間川および竪川の底質は、全体的に色が黒っぽく泥質で、粒径は表層で粗く、中層部で細かいという傾向が見られた。表層水の溶存酸素量は2～3mg/l程度であり、谷津干潟の8～9mg/lに比べ低い値であり、より還元的雰囲気にあることが示唆された。谷津干潟には多くの生物が棲息しており、底質中には多くのゴカイが見られた。ゴカイは底質内を移動する際に底質を撹乱することが知られている。^{210}Pb法による年代測定の結果では、竪川は年0.3cmの割合で比較的層状に堆積が起こっていること、それに対し、北十間川と谷津干潟では一度堆積した底質が撹乱されていることが分かった。

PGAおよびINAA法により定量を試みた元素のうち、いくつかのものについては分析したすべての試料で検出限界以下であったが、結局、30数元素の底質中濃度の垂直分布を得ることができた。分析手法の信頼性を評価するため、国立環境研のPond Sediment (NIES CRM No.2)および地質調査所のLake Sediment (JLk-1)を同条件で分析したところ、文献値と一致する結果が得られた。

各元素の垂直分布を見ると、3ヶ所の試料採取地点に共通した特徴も見られ、その特徴に従って元素をいくつかのグループに分けることができた。深くなるに従って減少する元素としてはNa, Ca等が挙げられた。Na, Caは母岩を構成する鉱物中に含まれており、深くなるに伴い溶脱が進んでいるものと解釈された。また、Sc, La等の微量金属の一部は深くなるに従って増加する傾向が見られた。これは底質深層部では粒径が細かく、底質の表面積が大きくなっており、それらの元素の吸着が起こっているためと思われた。Al, Ti, Fe等の元素は深さ方向に変化が少なく、底質中で吸着、溶脱反応は起こっていないと考えられた。

谷津干潟と都市河川を比較すると都市河川では人為起源であると考えられるCrやCdが高濃度であった（図1）。これらの元素は、HやSと同様に中層部で高い濃度を示し（図2）、水酸化物や硫化物の形で存在している可能性が示唆された。また、同じ試料に対して、非破壊で鉄の状態分析ができる^{57}Feメスバウアー分光法を

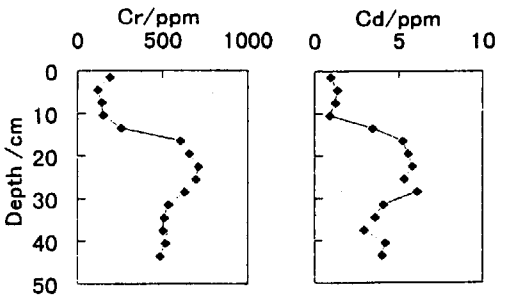


図1 北十間川底質中のCrとCdの垂直分布

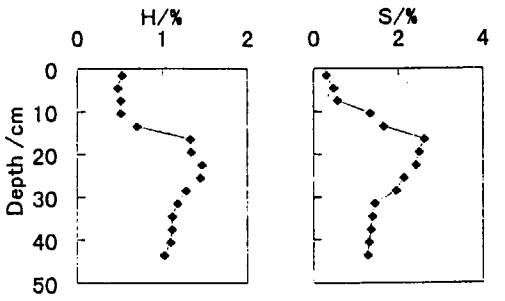


図2 北十間川底質中のHとSの垂直分布

表1 相関行列(北十間川第2コア)

Elements	Ca	Fe	Na	S	Al	Cd	Cr	H
Ca	1.00	0.28	-0.57	-0.78	-0.81	-0.86	-0.92	-0.92
Fe	0.28	1.00	-0.65	-0.18	-0.62	-0.39	-0.37	-0.36
Na	-0.57	-0.65	1.00	0.48	0.63	0.55	0.48	0.49
S	-0.78	-0.18	0.48	1.00	0.56	0.87	0.82	0.84
Al	-0.81	-0.62	0.63	0.56	1.00	0.84	0.83	0.82
Cd	-0.86	-0.39	0.55	0.87	0.84	1.00	0.94	0.94
Cr	-0.92	-0.37	0.48	0.82	0.83	0.94	1.00	1.00
H	-0.92	-0.36	0.49	0.84	0.82	0.94	1.00	1.00

■相関係数0.75以上
■相関係数－0.75以下

適用した結果、パイライト(FeS_2)などの硫化物が中層部で多く検出された。このことは、これらの重金属の硫化物の生成により、硫化水素発生に伴う悪臭が抑えられる可能性を示唆するものである。一方、逆にもしこのような硫化物としてのCdの固定がなかったなら、これらのCdが水中に溶存することになり、生物の生命を脅かすことが想像されるので、このようなCdの固定は一種の自然浄化能と位置づけられる。

次に、元素間の濃度に関する相関係数を計算することにより、コア内各元素の挙動の類似性を数値化することを試みた。各元素間の相関係数の値を表にすることで、底質中で挙動の似た元素同士をおおむね３つのグループに分類することができた。北十間川第２コアにおける結果の主な部分を表１に示す。カルシウムのようなアルカリ・アルカリ土類元素（グループａ）、クロムやカドミウムのような微量元素と水素（グループｂ）、アルミニウムなど環境中で変化の少ない元素（グループｃ）である。グループａは風化反応において固相から溶脱する元素、グループｂは固相にとりこまれる元素というように考えられる。垂直分布と合わせて考えると、中層部で化学風化により底質固相中の元素が溶脱するとともに、水素やそれと同時に水相中の微量元素が取り込まれていると考えられた（式１）。

式1 Ca長石の化学風化による説明

$$CaAl_2Si_2O_8+2H^++6H_2O \rightarrow Ca^{2+}+2Si(OH)_4+2Al(OH)_3$$

b とり込み　a 溶脱　a 溶脱　c そのまま

このように、相関行列分析の結果、グループ分けが数値から成され、多くの元素について底質中で起こっている化学反応の解明に関して有用な情報を得ることができた。

３．遠洋深海性層状チャートの即発γ線分析

【序】　我々はこれまで、古生代／中生代境界（以下Ｐ／Ｔ境界と略記する）直後に遠洋深海で堆積したチャート層中の鉄の化学状態について研究を行ってきた。メスバウアー分光法を用いた測定の結果、チャート中の全鉄に対する２価鉄の割合（以下Fe^{2+}比と略記）は、境界直後の堆積層で１００％を示し、その後徐々に減少して１０～３０％の値に収束することが分かった。このことは、Ｐ／Ｔ境界頃の海洋底が非常に還元的であったこと、そしてその後酸化的な状態に回復したことを示すものと考えられた。しかしながら、海水という複雑な系においては、Fe^{2+}／Fe^{3+}以外にも種々の酸化還元反応が同時に進行している。そして個々の酸化還元反応が互いにリンクし、対象とする系内で平衡が達成されて初めて、海水の酸化還元電位を定量的に推定する意味がある。従って、海洋水の酸化還元環境が変化したことを実証し、さらにその時の酸化還元電位を推定するためには、①他の元素からも酸化還元環境の変化が読み取れること、②それらの示す酸化還元電位が、Fe^{2+}／Fe^{3+}から示される電位を含めて矛盾しないこと、が必要である。そこで今回は鉄以外の元素について分析を行った。酸化還元条件の変化は、元素の価数を変化させると同時に、沈殿や溶出を通じて固相中の各元素の量を変化させる。したがって、種々の元素についての層ごとの分布パターンから、堆積時の酸化還元環境が推定できる。以上の目的で、即発γ線分析および放射化分析による多元素同時定量を行い、各元素の層ごとの分布パターンを明らかにした。

【実験】　分析法としては、中性子誘起即発γ線分析法(PGA)および機器中性子放射化分析法(INAA)を用いた。PGAは原研JRR-3Mのコールドビームを、またINAAは立教大学の原子炉を使用してそれぞれ行った。UおよびSiの定量に関しては、立教炉において熱外中性子を用いた。

試料としては、Ｐ／Ｔ境界直前の試料として丹波帯篠山地域から、またＰ／Ｔ境界直後の試料として美濃帯犬山地域から、それぞれ遠洋深海性のチャートを採取し、新鮮な部分を取り出した上で、粉末にしたものを使用した。

【結果および考察】　PGAおよびINAAにより、23元素についての定量値を得た。それらのうち、Al, Ti, K, Thなど陸源砕屑物に由来し、かつその挙動が酸化還元条件に影響されない元素の分布は互いに高い相関を示した。これは、砕屑物の供給源が時代を通じて一定であったことを示している。一方、Fe, U, S, Mnなど、挙動が酸化還元

条件に敏感な元素は全く異なる分布を示した。これは、酸化還元反応による沈殿や溶出によって堆積物への付加や除去が為された結果と考えられ、海水の酸化還元環境が変化したことを示すものと理解される。次に、図３、４、５にそれぞれU, S, Mnの量をFe^{2+}比に対してプロットした結果を示す。図３、４からは、堆積物へのU, Sの付加は鉄が全て2価に還元された状況でのみ起こっていること、逆に図５からは、Mnの付加はFe^{2+}比が30％以下で起こっていることが分かる。一般にUは、UO_2^{2+}→UO_2の還元反応により、またSは、SO_4^{2-}→H_2Sで生じたH_2SがFe等の金属イオンと反応した結果それぞれ固相に取り込まれると考えられている。またMnは、Mn^{2+}→MnO_2と酸化されて固相に取り込まれると考えられている。熱力学的に求められた標準酸化還元電位を比較すると、SO_4^{2-}／H_2SO_3(0.17v) ＜ UO_2^{2+}／U^{4+}(0.33v) ＜ Fe^{3+}/Fe^{2+}(0.771v) ＜ MnO_2／Mn^{2+}(1.23v)の順であるから、S, Uが還元され始めるのはFeが全て２価に還元されてからであり、またMnが酸化され始めるのはFeがほぼ全部３価に酸化されてからであるという上記の結果は互いに矛盾しないことが分かる。このことは、これら４つの反応の酸化還元電位を用いて、古海水の酸化還元電位を一定の範囲内に限定できることを示している。したがって、今後さらに多くの元素について測定を行い、制約条件を増やしていくことで、古海水の酸化還元電位をより正確に推定できる可能性がある。

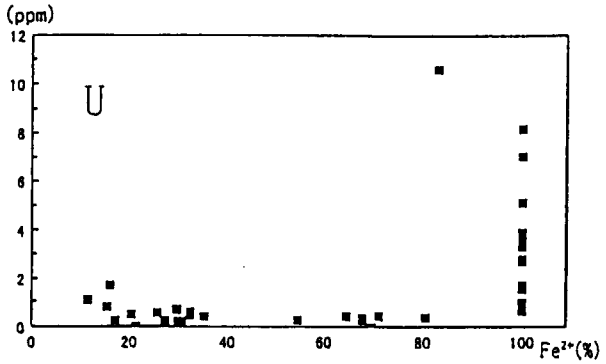


図３．チャート中のU含有量とFe^{2+}比の関係

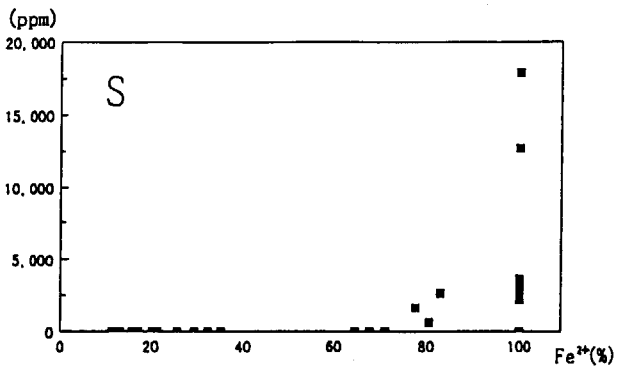


図４．チャート中のS含有量とFe^{2+}比の関係

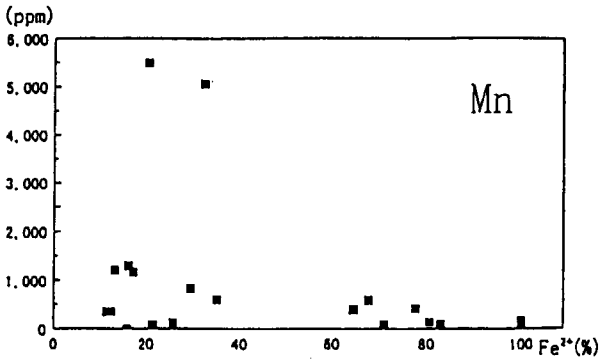


図５．チャート中のMn含有量とFe^{2+}比の関係

４．成果の公表

学術誌

1. A. Kuno, K. Sampei, M. Matsuo, C. Yonezawa, H. Matsue and H. Sawahata, "Vertical distribution of elements in non-polluted estuarine sediments determined by neutron induced prompt gamma-ray and instrumental neutron activation analyses", J. Radioanal. Nucl. Chem., Articles, 239(3), 587-590 (1999)

学位論文

2. 松本　武 "土壌中に含まれる鉄の化学状態と元素分布の植生変動による影響" 東京大学大学院総合文化研究科広域科学専攻 修士論文（1998年2月）
3. 八十島光子 "Uptake of Cu, Zn, Cd, and Hg by Land Snails" 東京大学大学院総合文化研究科広域科学専攻　修士論文（1998年2月）
4. 田中佑人 "河川底質中の元素の分布と化学状態を用いた環境分析" 東京大学教養学部基礎科学科第二 卒業論文Ｉ（1998年11月）
5. 久野章仁 "Non-destructive speciation of solid environmental samples: Fate of heavy metal elements in estuarine sediments" 東京大学大学院総合文化研究科

広域科学専攻　博士論文（2000年11月）

6. 片岡正樹 "干潟堆積物中に含まれる元素の化学状態と垂直分布" 東京大学大学院理学系研究科化学専攻　修士論文（2001年2月）

学会発表

7. 松尾基之・久野章仁 "河口域堆積物中に含まれる元素の垂直分布と鉄の状態分析" 第１回分析化学東京シンポジウム（1997年9月）
8. 松本　武・松尾基之・米沢仲四郎・松江秀明・澤幡浩之 "三宅島土壌中に含まれる鉄の化学状態と元素分布に対する植生の影響" 日本地球化学会年会（1997年9月）
9. 松尾基之・久野章仁・三瓶和巳 "河川および干潟底質中に含まれる鉄化合物の非破壊状態分析" 第２回分析化学東京シンポジウム（1998年9月）
10. 田中佑人・松尾基之 "放射化分析法を用いた都市河川底質中の元素の垂直分布" 第37回理工学における同位元素研究発表会（2000年7月）
11. 松尾基之・田中佑人・片岡正樹・久野章仁 "河川および干潟底質中の元素の分布と化学状態を用いた環境分析" 第４回分析化学東京シンポジウム（2000年8月）
12. 片岡正樹・松尾基之 "谷津干潟底質中の元素の垂直分布とメスバウアー分光法による鉄の状態分析" 第44回放射化学討論会（2000日本放射化学会年会）（2000年9月）
13. 片岡正樹・久野章仁・松尾基之 "谷津干潟底質中の元素の垂直分布とその化学状態の分析" 日本分析化学会第49年会(2000年9月)
14. 田中佑人・松尾基之・金井　豊 "都市河川底質中の金属元素の化学状態に関する研究" 日本地球化学会年会（2000年9月）
15. M. Matsuo, K. Kubo and Y. Isozaki, "Mossbauer spectroscopic study on characterization of iron in the Permian to Triassic deep-sea chert from Japan" International Conference on the Applications of the Mossbauer Effect (ICAME 2001), (Sep. 2001)
16. Y. Tanaka, A. Kuno and M. Matsuo, "A study of environmental analysis of urban river sediments using activation analysis", 2001 Asia-Pacific Symposium on Radiochemistry (APSORC 2001), (Oct. 2001)
17. M. Kataoka, A. Kuno and M. Matsuo, "A study on vertical distribution of elements and their chemical states in Yatsu Tideland sediments", 2001 Asia-Pacific Symposium on Radiochemistry (APSORC 2001), (Oct. 2001)

This is a blank page.

7. その他

7. Others

This is a blank page.

研究テーマ：超小型舶用炉の設計研究
表　　題：高性能遮蔽材の適用性の検討

7-1　高性能遮蔽材の放射線照射損傷と放射化

三浦　俊正、　平尾　好弘、　石田　紀久[1]
船舶技術研究所東海支所　〒319-1195　茨城県那珂郡東海村白方白根2-4
1 日本原子力研究所舶用炉設計研究室　〒319-1195　茨城県那珂郡東海村白方白根2-4

舶用炉の遮蔽構造の軽量・小型化には高性能な遮蔽材の利用が有用である。そこで当所では新しい遮蔽材の開発を試みてきた[1]。本実験の目的は開発中の遮蔽材の放射線損傷並びに放射化を調べることにある。遮蔽材に含まれる元素は主に水素、鉛、硼素、酸素、炭素であり、いずれも放射化断面積が小さく低放射化が期待された。しかし、原子炉で照射し放射化量を測定したところ予想以上の放射化が観測された。ゲルマニウム検出器による放射化分析から原因は鉛材の不純物であるアンチモンの放射化であることが判明した。調査によりガスアトマイズ鉛粉にはアンチモンの含有量が少ないことが判明したので、これを用いて遮蔽材を作成し、照射実験により低放射化が達成されていることを確認した。その後、遮蔽材の試料をＬパイプで照射した。照射量は速中性子束で約 1×10^{14} 及び約 1×10^{14} n/cm^2 であった。放射化量はいずれの場合も 37Bq/g 以下であった。照射試料は全体に多少膨れが見られ、乾いた感じに見えた。これらの試料に対し室温放置又は60 ℃で1時間あるいは 100 ℃で1時間の加熱処理を加えた後で、物性測定を行った。密度測定には空気比較式比重計及び電子天秤を用いた。未照射試料に比べ照射済試料は膨れを生じた分だけ密度が減少した。未照射試料を１とし、照射試料を照射量順に２及び３とすると室温放置で試料1、2、3の密度はそれぞれ2.74、2.29及び1.92であった。しかし照射済みのものは加熱処理を行うことにより膨れが減少し密度は試料2が2.4程度に、又試料3は2.2程度になった。組成分析ではC、H、N、Pb、B、O の割合を調べたが照射による組成成分の変化は見られなかった。水分の含有量は室温放置品で0.37～0.52wt%、高温放置品で0.35～0.50wt%と差はほとんどなかった。試料を200℃まで過熱した場合の重量減少には原子炉照射の影響は見られなっかった。試料の温度を上げると脂肪族炭化水素、脂肪族アクリレートが150℃を越えると急激に発生し、160℃前後でベンジル、ベンゾフェノンが発生した。しかしながら、その発生量は照射試料の方が少なく、何らかの構造変化が起こっていることを示唆した。以上のように今回の照射量の範囲では照射効果が強く現れなかったことと試料のばらつきもあって明瞭な照射効果は得られなかった。しかしながら、遮蔽材の低放射化性が達成されたことを確認した。

参考文献

1)船研報告 第36巻 第3号 p.1 (1999).

原子炉：ＪＲＲ－４　　装置：気送管、Ｌパイプ　　分野：放射線遮蔽

研究テーマ：超流動反応場の原子・分子研究
表　　題：JRR-3Mへの低温化学実験装置の設置と実験

7-2 JRR-3Mビームガイドへの低温化学実験装置の設置及び1.4 - 2.5 K、^{3}He-^{4}He混合液体ヘリウム中でのトリチウムの再結合反応によるオルソT_2の選択的生成

荒殿　保幸
日本原子力研究所　先端基礎研究センター
〒319-1195　茨城県那珂郡東海村白方白根2-4

液体及び固体ヘリウム中の異種原子や分子は、他の媒体中では見られない原子バブルのような特異な構造を示す。又、液体ヘリウムは他の物質には見られない第2の液相、超流動相、の存在する量子液体である。バブル原子ついては、レーザー分光的研究が進み、その構造が次第に明らかになりつつある。一方、そのような特異な形態の原子や分子の再結合反応等による安定化の様式、即ち化学反応の機構等は全くわかっていない。ここで注目されるのは、媒体の温度である。液体ヘリウムは4.2Kの沸点を持つ。従って反応もそれ以下の温度で進行する。いわゆるトンネル効果による反応が支配的となる温度領域である。本報告では、このような低温での化学反応を研究炉を利用して観察するために設置した、「低温化学実験装置」の概要を示す。また、同装置を用いたトリチウムの再結合反応に関する実験結果を述べる。「低温化学実験装置」は，ＪＲＲ-3M中性子ビームガイドホールのＴ１或いはC2の末端に設置しマシンタイムにしたがってT1とC2間を移動する。本装置は、遮蔽体、クライオスタット、ガスハンドリング，温度制御、中性子計測の系より構成されている。遮蔽体は照射の際の誘導γ線、散乱中性子線の遮蔽用で、鉛の内壁を LiF、B_4C 等で内張りしてある。LiF製ビームシャッター、中性子カメラ撮影孔を持つ。クライオスタットは1.3Kで約40時間照射できる。温度は0.001Kの精度で自動制御出来る。ガスハンドリング系は反応ガスの照射容器への導入や生成物回収のためのステンレスチューブ製ラインである。中性子計測系は、^{3}He カウンターであり、ビームシャッターの開閉の確認や照射時間の測定に用いる。本装置を用い、^{3}He-^{4}He の混合液体を照射し、^{3}He(n,p)T で生成するトリチウム同士の再結合反応からのオルソT_2(o-T_2)、パラT_2(p-T_2)の生成割合を調べた結果をテーブル示す。全実験温度領域に渡り、90%以上がオルソT_2である。室温及び実験温度での値は 75%及び 10^{-4}%であり実験値はこれらの値を上回り、オルソ体が選択的に生成していることを示している。Tと同じ核スピンを持つHでも低温でのオルソ体の優先的な生成が報告されており、反応機構の類似性が予想される。反応機構に関しては、実験、理論の面から検討中である。

Fractions of o-T_2 as functions of reaction temperature and atomic fraction of ^{3}He

Temp.(K)	^{3}He/(^{3}He+^{4}He)	o-T_2/(o-T_2+ p-T_2)
1.42	0.38±0.05	1.00±0.00
1.75	1.00±0.00	1.00±0.00
2.00	0.42±0.00	0.98±0.02
2.25	0.40±0.12	0.91±0.06
2.50	0.43±0.00	0.98±0.02

The values are the average of twice experiments.

原子炉 ： JRR-3M　装置 ： 低温化学実験装置　　分類 ： その他(放射化学)

研究テーマ：研究炉利用高度化の技術開発
表　　題：

7-3 Current Medical Setup at JRR-4 for Boron Neutron Capture Therapy (BNCT)

Yamamoto T, Matsumura A, Shibata Y, Nose T, Yamamoto K[1], Kumada H[1]

Department of Neurosurgery, Institute of Clinical Medicine, University of Tsukuba
Department of Research Reactor, Tokai Research Establishment, JAERI[1]

Introduction

In December 1999, a new research protocol on boron neutron capture therapy (BNCT) for high grade glioma (glioblastoma and anaplastic astrocytoma) began at the JRR-4[1]. The primary goals of this project are: (1) establishment of the treatment facility, including the treatment room and anesthesia apparatus, for the performance of intraoperative BNCT (IOBNCT); (2) establishment of the safety and efficacy of BSH-mediated IOBNCT with the mixed thermal-epithermal beam (Thermal neutron beam mode 1: TNB-1) relative to thermal beams used before; (3) cross-calibration of the simulation data by JCDS (JAERI computer dosimetry system) with actual measurement results during IOBNCT; (4) preparation for possible use of the epithermal beam in IOBNCT.

Patient criteria

All patients entered into this study will be seen at the University of Tsukuba Hospital and/or its teaching hospitals. To be eligible, patients have to fulfill the following criteria.

1. Histologic proof of anaplastic astrocytoma or glioblastoma and its variants [3]
2. Karnofsky performance score $\geq$ 70
3. Age 18 to 70 years
4. Supratentorial unilateral tumor no deeper than 6 cm from brain surface
5. Adequate cardiopulmonary, hepatic, renal, and bone marrow functions:
   - SGOT<60 IU/ml, Bilirubin<1.5 mg%
   - BUN<30 mg/dl, Cr<1.5 mg%
   - WBC>2500/mm3, Plt>75000/mm3, no severe anemia
6. No previous chemotherapy or radiotherapy
7. No double cancer and no previous therapy for any other cancers
8. No allergy to BSH
9. Signed informed consent

Facility and procedures of IOBNCT

IOBNCT is comprised of: (1) BSH biodistribution study and the first craniotomy for tumor removal, and (2) a second craniotomy and BNCT with TNB-1 approximately 2 to 4 weeks following the first operation. In the BSH biodistribution study, 1 g of $Na_2{}^{10}B_{12}H_{11}SH$ (BSH) was administrated intravenously 12 h before the first operation, then blood is taken up serially for boron concentration analyses with inductively coupled plasma atomic emission spectroscopy (ICP-AES) method and the prompt gamma-ray analysis (PGA). Specimens from various parts of the brain tumor are also kept for the measurement of boron level. For IOBNCT, 100 mg/kg BW of BSH is given with 500 ml of saline for 1h *via* intravenous drip infusion. The infusion is initiated 12 h before planned irradiation

The medical treatment room was built to reflect a hospital-type operation room that includes an operating table with a carbon head-frame, anesthesia apparatus with several cardiopulmonary monitors, etc. Following craniotomy in the treatment room, a patient under anesthesia is transported into the irradiation room. The operating power of 2MW has been selected to secure measurement time for neutron dose and PGA.

From October 1999 to July 2001, 7 patients with high grade glioma entered to this IOBNCT clinical trial. Interim results suggest the feasibility of treatment facility at JRR-4 and the prolonged survival of the patients. The JCDS and setting system have been experimentally applied in the cases since December 2000.

The management of high grade glioma is complicated by the tumor's low intrinsic radiosensitivity, its rapid proliferation rate, and its pleomorphic property, *i.e.*, the high

mutation rate of this tumor as well as by the presence of microscopic invading cells at distances of 2 to 3 cm or even further around the main tumor bulk that can be clinically identified by contrast enhancement area on computed tomography (CT) and magnetic resonance (MR) image, and/or is found in the microsurgical field[2,3]. The analyses of failure patterns following surgery and conventional radiotherapy revealed that the majority (80-90%) of recurrences occurred within a 2-cm margin of the main tumor, which indicates the need for a therapeutic design for more intensive local control[3]. The results from 3-D conformal radiation therapy showed that the great majority of patient recurrences that occur after high-dose (70 or 80 Gy) conformal irradiation are centrally located and lead to a further dose escalation to 90 Gy and beyond [4]. A dose escalation study of doses up to 90 cobalt gray equivalent with combined proton/photon therapy revealed an improved tumor control rate for the central tumor, despite tumors recurring in the peripheral areas[5]. Therefore, in BNCT, improvement of thermal neutron distribution in deep-seated lesions and the development of a more tumor-selective boron compound are essential to improve local control rates in the treatment of high grade gliomas.

A major advantage of using an epithermal neutrons relates to the enhanced dose delivery to the deep-seated lesion based on the improved penetrability in the first several centimeters of irradiated volume before epithermal neutrons moderated and converted into thermal neutrons, generating the $^{10}B(n, \alpha)$ reaction. Because of their greater penetrability and forwardness, epithermal neutron beams have been employed in the clinical trials of closed-cranium BNCT at the Brookhaven Medical Research Reactor (BMRR), HFR, and the Finnish Research Reactor (FiR-1)[6,7].

The other possible use of epithermal neutron is in IOBNCT. To facilitate neutron penetration, especially to the deep-seated lesion around the bottom of a post-surgical cavity, intraoperative irradiation and insertion of an air-filled balloon as a "void" into the cavity have been utilized as part of the BNCT procedure with thermal beam[1]. Usage of TNB-1 in this clinical trial for IOBNCT can increase thermal neutron distribution in the deep-seated lesion and seems to improve therapeutic efficacy of IOBNCT. When the safety and efficacy of BSH-mediated IOBNCT with TNB-1 relative to thermal beams were confirmed by the long-term follow-up of the treated cases, IOBNCT should be lead to potential application of epithermal beam (Epithermal beam mode: ENB).

REFERENCES:

1. Yamamoto T, et al., Medical setup of boron neutron capture therapy (BNCT) for malignant glioma at the Japan Research Reactor (JRR)-4, in Current Status of Neutron Capture Therapy, IAEA, pp.233-239, 2001.
2. Yaes-RJ: Tumor heterogeneity, tumor size, and radioresistance. Int J Radiat Oncol Biol Phys 17: 993-1005, 1989.
3. Wallner KE, et. al: Patterns of failure following treatment for glioblastoma multiforme and anaplastic astrocytoma. J Radiat Oncol Biol Phys 16: 1405-1409, 1989.
4. Lee SW, et al: Patterns of failure following high-dose 3-D conformal radiotherapy for high-grade astrocytomas: a quantitative dosimetric study. J Radiat Oncol Biol Phys 1: 79-88 1999.
5. Fitzek MM, et al.: Accelerated fractionated proton/photon irradiation to 90 cobalt gray equivalent for glioblastoma multiforme: results of phase II prospective trial. J Neurosurg 91: 251-260, 1999.
6. Chanana AD, et al.: Boron neutron capture therapy for glioblastoma multiforme: Interim results from the Phase I/II dose-escalation studies. Neurosurgery 44: 1182-1193, 1999.
7. Sauerwein W: The clinical project at HFR Petten. A status report. In Larsson B, Crawford J, Weinreich R (eds): *Advances in Neutron capture Therapy: Medicine and physics.* Amsterdam, Elsevier, 1997, vol 1, pp 77-84.

原子炉：JRR-4　　装置：中性子ビーム設備、即発ガンマ線分析装置　　分野：その他

研究テーマ：研究炉利用高度化の技術開発
表　　題：

7-4
Characterization of Neutron Beams for Boron Neutron Capture Therapy : In-air Radiobiological Dosimetry

Yamamoto T, Matsumura A, Shibata Y, Nose T, Yamamoto K[1], Kumada H[1]

Department of Neurosurgery, Institute of Clinical Medicine, University of Tsukuba
Department of Research Reactor, Tokai Research Establishment, JAERI[1]

INTRODUCTION

A mixed radiation field consists of dose components with different LETs and with different efficacies, which are generated in tissue during BNCT (1). The biological effects of BNCT are caused by at least four different dose components that contribute to energy deposition in tumors or healthy tissue. The boron dose, which is the dose from á particles generated by the boron neutron capture reaction, accounts for the majority of the dose in tumor tissue (2). The dose to non-boronated healthy tissue as well as the remaining dose to boronated tumor tissue consist of the other components: The fast neutron recoil, 1H(n, n')p, 0.54 MeV protons from the nitrogen capture reaction, 14N(n, p)14C, the ã ray based on the contamination in the primary beam, and 2.2 MeV, prompt ã rays from the hydrogen capture (3). However, the dose components depend on each neutron energy spectrum of a beam used, e.g., the patterns of the dose components of each "epithermal beam" are not identical among the various institutions. For evaluating the biological response of the tumor and healthy tissue to BNCT, and for comparing the clinical results of BNCT at different institutions with accuracy, all of the dose components of each beam must be determined separately.

This paper will describe the details of radiobiological inter-beam comparison that can be applied to other neutron beams employed in ongoing and planned BNCT clinical trials.

MATERIALS AND METHODS

An epithermal beam (epithermal neutron beam mode: ENB), a mixed thermal-epithermal beam (thermal neutron beam mode 1: TNB-1) and a thermal beam (thermal neutron beam mode 2: TNB-2) under 3.5-MW full-power operation were used as the neutron source for *in vitro* and physical measurements at the beam apparatus.

V79 Chinese hamster cells in the stage of exponential cell growth were preincubated for 6h with boric acid at ^{10}B concentrations up to 15μg^{10}B/ml medium. Boron concentrations in the conditioned medium were measured with prompt γ-ray analysis (PGA) at JRR-4. Cells in suspension in polyethylene cryotubes were irradiated with each neutron beam for the colony formation assay. Cell irradiation and physical measurement were performed using a rotating irradiator to obtain the homogeneous irradiation. Gamma irradiation was carried out at a dose rate of 152 cGy/min using the Gamma Cell 40 system with a ^{137}Cs source at the Isotope Center at the University of Tsukuba.

The relative biological effectiveness (RBE) values for each dose component were estimated using the following assumptions based on the surviving fraction data (4): (a) The total response of the irradiated cells, R_{total}, is expressed as the product of independent responses from each radiation component ($R_{total} = R_{boron} \times R_{neutron} \times R_{gamma}$), which are derived from the boron dose from the boron neutron capture reaction; the sum of the high-LET dose component from hydrogen recoils and nitrogen capture; and γ dose based on the contamination in the primary beam and prompt γ rays; (b) The responses of cells to γ photons derived from neutron irradiation and from a ^{137}Cs unit are identical. To separate the effect due to the boron neutron capture reaction alone from the total effect in the mixed radiation field of BNCT, boronated and non-boronated cells were given identical neutron exposures with the rotating irradiator. R_{boron} was determined by dividing the measured total response of boronated cells, R_{total}, by the measured response of non-boronated cells, R_{beam}.

$R_{neutron}$ was determined by dividing R_{beam} by the cell response to γ-ray, R_{gamma}, which was calculated based on the dose-survival curve of cells irradiated with a ^{137}Cs unit and the γ-ray dose measured. The RBE values for R_{boron} ($^{BA}RBE_{boron}$), $R_{neutron}$ ($RBE_{neutron}$), and R_{beam} (RBE_{beam}) were calculated by comparing the D_0 that reduces survival by 37% of a given survival cell population. The survival curve of V79 cells irradiated with ^{137}Cs showed a D_0 of 150 cGy at 11.45 Gy. The same value was used for the calculation of RBEs so that the calculated RBEs could be compared with RBEs reported in literature based on the same D_0 value for 250 kVp X rays (5). Similarly, D_0 for $^{BA}RBE_{boron}$ was derived by determining the decreased fluence in boronated cells needed to achieve a reduction to 37% of a given non-boronated cell population. Strictly speaking, $^{BA}RBE_{boron}$ is different from true "RBE" which depends only on LET differences (1). $^{BA}RBE_{boron}$ used in this paper, the RBE value that is determined using boric acid as a boron compound, associates with LET and microdistribution of ^{10}B in V79 cells.

RESULTS

The surviving fraction as a function of thermal neutron fluence for ENB, TNB-1 or TNB-2 following *in vitro* irradiation in the presence of varying concentrations of ^{10}B from boric acid is plotted in Figure 1. Both the survival curves of non-boronated and boronated cells indicated that ENB was the most efficient among the three beams.

Figure 2 shows the response per dose of the non-boronated cells to γ rays, JRR-4 neutron beams and a separate, subtracted response to the high- LET components in each beam and an additional boron dose component.

The D_0 values for R_{boron} from the boron dose amounted to 35.1, 40.4, and 102.3 cGy for ENB, TNB-1 and TNB-2, respectively. Comparing these values to the D_0 value of 150 cGy for γ rays, corresponding RBE ($^{BA}RBE_{boron}$) values of 4.07, 3.71, and 1.47 were obtained for the boron neutron capture reaction. The D_0 values for R_{beam} amounted to 122.7, 123.0, and 128.5 cGy for ENB, TNB-1 and TNB-2, respectively, and the corresponding RBE (RBE_{beam}) values of the beam were 1.22, 1.21, and 1.17 for ENB, TNB-1 and TNB-2, respectively. The D_0 values for $R_{neutron}$ amounted to 60.0, 64.4, and 71.9 cGy for ENB, TNB-1 and TNB-2, respectively, and the corresponding RBE ($RBE_{neutron}$) values of the high-LET dose components were 2.50, 2.33, and 2.08 for ENB, TNB-1 and TNB-2, respectively (Table 1).

DISCUSSION

Uncertainty or difficulty in radiobiological inter-beam comparison among different facilities for BNCT is due to this complex mixed radiation field, to different methods of physical dosimetry, different techniques of neutron irradiation, non-uniform boron microdistribution, and the different *in vivo* or *in vitro* biological systems used. In this paper, epithermal, mixed thermal-epithermal, and thermal beams were radiobiologically characterized by separately determining the surviving fraction with the dose components in each beam using a single reactor, the same surroundings for determination and homogeneous neutron irradiation.

The surviving fraction of the neutron beam with or without the presence of ^{10}B depended highly on the neutron beam used, according to the epithermal and fast neutron content in the beam. The slopes with the surviving curve of V79 cells for all dose components were steeper for ENB compared to TNB-1 and TNB-2 (Fig. 7). Because thermal neutron fluence was determined as an integral dose by gold activation in a certain energy range (<0.53 eV), different neutron spectra, especially in the epithermal band, which could not be detected with the gold activation influences RBE values of the dose components (6). The most significant difference was seen in the boron doses, and the $^{BA}RBE_{boron}$ for ENB (4.07) was 2.8-fold higher than that for TNB-2. The RBE values reported in the literature for the boron capture and nitrogen capture reaction using *in vitro* endpoints ranged 2.3 – 3.3 and 1.9 – 2.0, respectively (1,5,7,8). The $^{BA}RBE_{boron}$ of 3.71 for TNB-1 corresponds to the RBE of 3.7 determined by Davis *et al.* (7) for HeLa cells by comparing D_0 values. Although no detailed neutron energy spectra for the beam were mentioned in the study by Davis, the fast neutron dose per thermal neutron flux (0.92×10^{-12} Gy cm^{-2}) for the beam seems to be on a similar level as that of TNB-1 (1.08×10^{-12} Gy cm^{-2}). The

$RBE_{neutron}$ of 2.08 for TNB-2 is in good agreement with the RBE of 2.0 that was determined for the nitrogen capture and the hydrogen capture reactions by Zamenhof *et al.* (9) based on theoretical proton energy deposits, and with the RBE of 1.9 that was determined by Gabel et al. (5) for the nitrogen capture reaction in V79 cells irradiated with a well-thermalized neutron beam.

The $^{BA}RBE_{boron}$ for ENB (4.07) determined in this study is higher than the RBE value of 2.3 reported by Gabel *et al.* (5) and that of 2.2 reported by Vroegindeweif *et al.* (10) for V79 single-cell suspensions. However, the cadmium radio for the BNL beam (~20) used by Gabel is much higher than those for ENB (1.15) and TNB-1 (2.5). Vroegindeweif irradiated cell samples in a cylindrical phantom at different depths with the epithermal beam at HFR; therefore, the beam would be thermalized to a certain degree at the positions of cell samples. $RBE_{neutron}$ of ENB (2.50), TNB-1 (2.33), and TNB-2 (2.08) are considerably lower than the proton RBE of 3.7-3.8 determined by Coderre *et al.* (1) in 9L gliosarcoma cells irradiated with a thermal beam at BNL. The variation of reported RBE values for the dose components in BNCT seems to be partially caused by the nonuniformity of dose distribution, the inhomogeneity in subcellular boron distribution (1), and the different experimental conditions. However, the data in this paper, by comparing different neutron beams with uniform dose distributions and the same experimental conditions, indicate that the neuron energy of a beam is the primary factor for the variation of RBE values. This observation is consistent with the variation of RBE values with energy, which was reported by Hall *et al.* (11).

The experimentally determined RBE values outlined in this paper are comparable to those found for neutron beams at a different facility that were determined by a similar *in vitro* experimental technique. These data are applicable to the dose calculation for each dose component of neutron beams in clinical trials for BNCT at JRR-4 and contribute to the accurate comparison with the variable neutron beams employed in ongoing and planned BNCT clinical trials. The final goal is to evaluate the therapeutic response of the patients treated with BNCT based on the RBEs obtained from this study and to evaluate the accuracy of RBE from the clinical cases.

REFERENCES

1. J. A. Coderre, *et al.*, *Int J Radat Oncol Biol Phys* 27, 1121-1129 (1993).
2. R. F. Barth, *et al.*, *Neurosurgery* 44, 433-451 (1999).
3. C. P. J. Raaijmakers, *et al.*, *Med Phys* 22, 321-329 (1995).
4. V. P. Bond, *et al.*, *Radiat Res* 141, 287-293 (1995).
5. D. Gabel, *et al.*, *Radiat Res* **98**, 307-316 (1984).
6. P. Watkins, *et al.*, In *Advances in Neutron capture Therapy. Medicine and physics. Vol. 1.* (B. Larsson, J. Crawford and R. Weinreich, Eds.), pp. 141-146, Elsevier, Amsterdam, 1997.
7. M. A. Davis, *et al.*, *Radiat Res* **43**, 534-553 (1970).
8. H. Fukuda, *et al.*, *Int J Radiat Biol* **51**, 167-175 (1987).
9. B. W. Zamenhof, *et al.*, *Med Phys* **2**, 47-60 (1975).
10. C. Vroegindeweij, *et al.*, In *Advances in Neutron capture Therapy. Chemistry and Biology. Vol. 2.* (B. Larsson, J. Crawford and R. Weinreich, Eds.), pp. 599-603, Elsevier, Amsterdam, 1997.
11. E. J. Hall, *et al.*, *Radiat Res* **64**, 245-255 (1975).

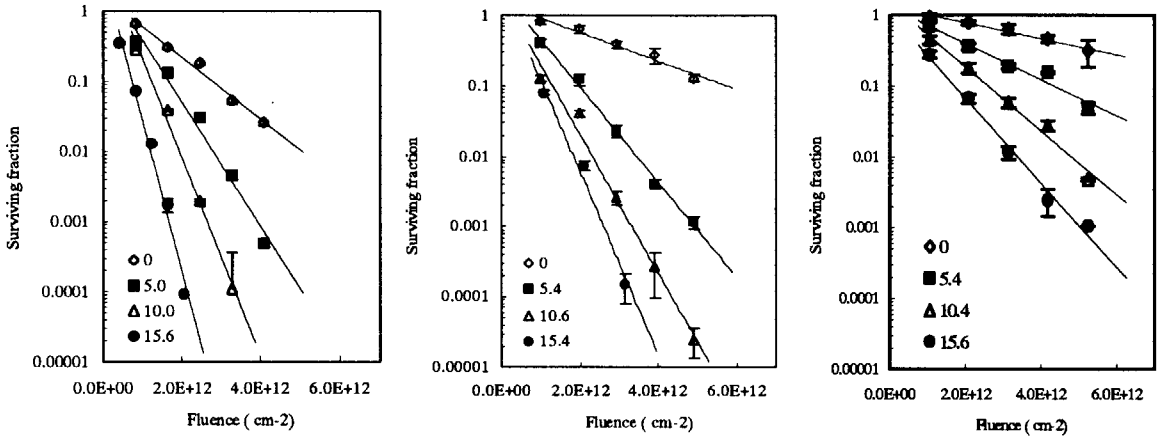


Figure 1. Survival curve of V79 cells incubated with varying concentrations of ^{10}B obtained after irradiation with ENB (a), TNB-1 (b) and TNB-2 (c) at JRR-4. The data were plotted as a function of thermal neutron fluence and were fitted by linear equation. Boron concentrations, in which measurements are performed with the prompt γ-ray analysis (PGA) device at JRR-4, were given in $\mu g^{10}B/ml$ medium. Data points and error bars show the mean value of quintuplicate experiments and their standard deviations, respectively.

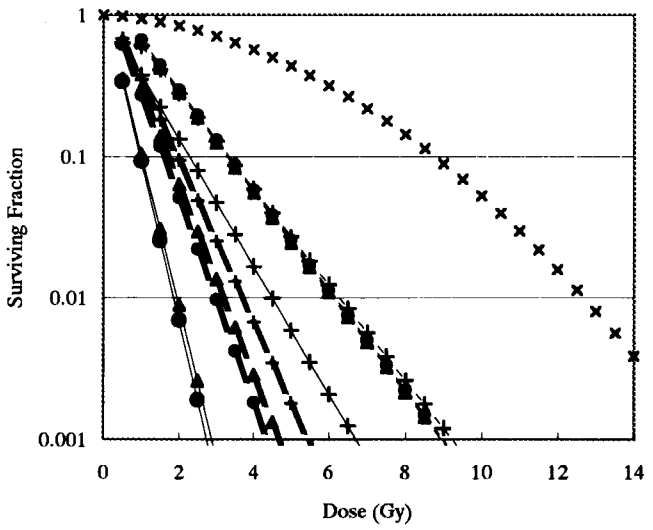


Figure 2. Subtracted, separated response of V79 cells to each dose component in the mixed radiation field of the epithermal neutron beam mode (ENB: ●), the thermal neutron beam mode 1 (TNB-1: ▲), and the thermal neutron beam mode 2 (TNB-2: +), compared with the response to γ ray (x x x). The surviving fraction was plotted as a function of the calculated dose (Gy). Solid, thick broken and dotted line show the separated response of cells to $^{10}B(n, \alpha)^7Li$ reaction, the high-LET components in each beam, and the total response of non-boronated cells to each beam.

	$^{BA}RBE_{boron}$	RBE_{beam}	$RBE_{neutron}$
ENB	4.07	1.22	2.50
TNB-1	3.71	1.21	2.33
TNB-2	1.47	1.17	2.08

Table 1. Relative biological effectiveness (RBE) for the dose componens of JRR-4 neutron beams.

原子炉：JRR-4　　装置：中性子ビーム設備、即発ガンマ線分析装置　　分野：その他

研究テーマ：研究炉利用高度化の技術開発
表　　題：

7-5

In Vivo Neutron Measurement on the Human Brain and Blood Boron Measurement for Intraoprative Boron Neutron Capture Therapy (IOBNCT)

Yamamoto T, Matsumura A, Shibata Y, Nose T, Yamamoto K[1], Kumada H[1]

Department of Neurosurgery, Institute of Clinical Medicine, University of Tsukuba
Department of Research Reactor, Tokai Research Establishment, JAERI[1]

INTRODUCTION

In a clinical trial of the intraoperative boron neutron capture therapy (IOBNCT) for malignant brain tumors, the irradiation time is determined based on the peak vascular dose that is expressed as the product of the maximum boron dose and a vascular geometrical factor[1,2]. Therefore, for precise dose planning, *in vivo* measurement of thermal neutron and blood boron level have critical importance.

MATERIALS AND METHODS

From October 1999 to July 2001, 4 patients with glioblastoma and 3 patients with anaplastic astrocytoma entered to our clinical trial of IOBNCT. Research protocol and a medical setup of the clinical trial was described in detail elsewhere[3]. Two frontal craniotomies (FC), 3 fronto-temporal craniotomies (FTC), 1 frontoparietal (FPC) and 1 occipital craniotomy (OC) were performed at the operation room of JRR-4. The rated output of 2 MW was maintained during each irradiation except for Case 3 who was irradiated with a 1.5 MW operation because of relatively high blood boron level.

Thermal neutron distributions of surgical field are measured with activation gold wires of 0.25 mm in diameter which were arranged on the brain surface and post-surgical cavity. Thermal neutron activation in every 5 or 10 mm were counted with the simultaneous β - γ coincidence counting device. Two of the gold wires were withdrawn 15 min after the beginning of 2 MW operation for determining the irradiation time (intra-irradiation measurement). The final, reporting dose was measured by the gold wires which were irradiated for whole irradiation time (post-irradiation measurement). For drawing isodose lines, a software-based system (G sharp, KGT Co.) and Lagrange's interpolation polynomial in three variables by distance (r) and azimuthal angle (θ) of the gold wire were used (Fig.1)[4].

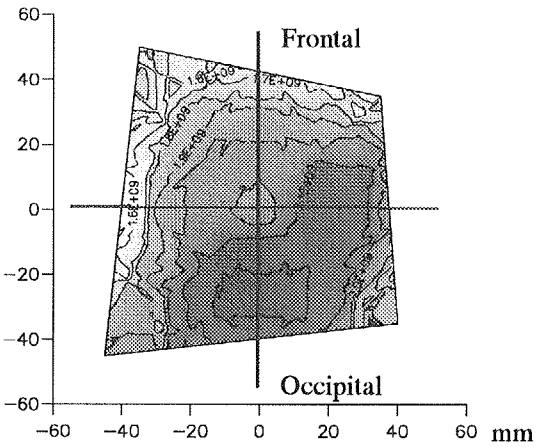


Fig.1 Thermal neutron flux distribution at the brain surface after frontal craniotomy (Case 2). Central circular area shows post-surgical cavity in which thermal neutron flux is relatively low compared to the surrounding brain.

Case	1	2	3	4	5	6	7
Craniotomy	FTC	FC	FC	OCC	FTC	FTC	FPC
Intra-irrad.	2.40	2.24	2.65	2.50	2.60	2.26	2.31
Post-irrad.	2.77	2.50	2.65	2.63	2.61	2.31	2.50
%Difference	+15.4	+11.6	0	+5.2	+0.3	+2.2	+8.2

Table 1 The thermal neutron fluxes (10^9 $cm^{-2}sec^{-1}$) at the brain surface measured with the gold wires which were irradiated for 15 min (Intra-irrad) and a whole irradiation (Post-irrad). *Data were normalized for 2 MW.

In the preliminary distribution study of boron and in the IOBNCT, blood is taken up serially for boron concentration analyses with inductively coupled plasma atomic emission spectroscopy (ICP-AES) method and the prompt gamma-ray analysis (PGA).

RESULTS AND DISCUSSION

The maximum value of thermal neutron fluxes by the intra-irradiation and post-irradiation measurements 2.42 ± 0.16 and 2.57 ± 0.15 E+9 $cm^{-2}sec^{-1}$, respectively (Fig.2). All the post-irradiation measurement found to be more than or equal to those from the

intra-irradiation measurements. In FC cases (case 2 and 3), Skin flap reflected to frontal side tended to increase a port-brain distance at frontal side compared to occipital side, resulting in a heterogeneous thermal neutron distribution at the brain surface (Fig.1).

Because the skin frap was reflected postero-inferiorly in case 3 in which craniotomy was located at more posteriorly compared to that in case 2, a homogeneous distribution was observed. In FTC cases, skin flap and temporal muscle were reflected to frontocaudal side. In case 1, thermal neutron flux in frontal and temporal base was insufficient compared to parietal and occipital side of post-surgical cavity. In the other FTC cases, JAERI computational dosimetry system (JCDS) and a positioning simulator were experimentally introduced to minimize the discrepancy between 15 min data and final data, and to achieve homogeneous thermal neutron distribution.

Radiation necrosis is thought to occur following BNCT at a peak vascular boron dose of approximately 13 Gy or more. At the beginning of the ongoing clinical trial, the peak vascular boron dose of 10.8 Gy (80% dose) by intra-irradiation measurement was employed. Consequently, the differences between intra- and post-irradiation measurement results in each case were varied from 0 to 15.4%. Although this difference, concerning the dose of radiation necrosis, is not critical, further investigation is needed for accurate dose planning and in vivo dosimetry prodedure. In-phantom measurements revealed that the maximum thermal neutron flux for the thermal neutron beam mode I (TNB-1) of JRR-4 was measured approximately at 7 mm from the phantom surface[4]. Because of the thermalization of the beam in surgical drapes and the dura mater, the maximum thermal neutron fluxes for TNB-1 *in vivo* are observed at the brain surface. However, if current neutron fluxes are maintained uniformly at the beam port, the actual thermal neutron flux *in vivo* at post-operative human brain, are influenced by the size and the geometry of bone window, post-surgical cavity and lithium helmet, and by blood and/or cerebrospinal fluid collection, surgical equipments, port-target distance and patient's head position. JCDS and the patient setting system seem to be useful for dose simulation of BNCT patients whose posture and the head position are limited by general

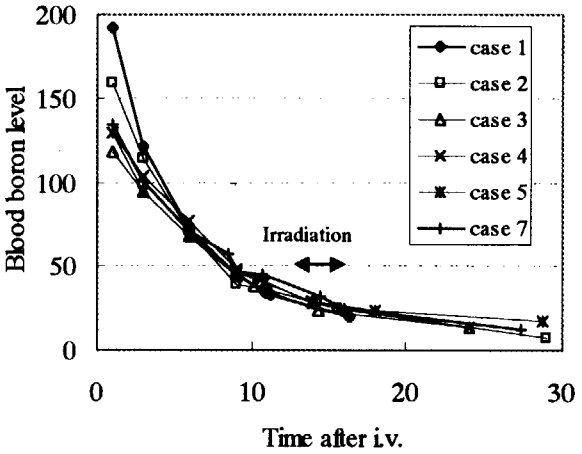


Fig.1 Blood boron level for 6 IOBNCT cases

anesthesia and craniotomy. Moreover, JCDS should be indispensable for the dosimetry of a potential application of an epithermal beam in IOBNCT in which peak vascular dose at the depth are by no means detectable by the similar technique with gold wire arranged on the brain surface.

The PGA results of serial blood boron level for 6 IOBNCT cases were standardized by purity and ^{10}B enrichment based not on instructions by suppliers, but on the comparison between ICP-AES and PGA measurements (Fig.2). In spite of variation of body weight, renal function and other treatment conditions of different cases, the differences in decay of blood boron level among individuals minimized by this standardization. ^{10}B concentration in BSH was varied up to 20% among the different products. The preliminary distribution study should be performed to predict real blood boron level in IOBNCT.

REFERENCES:

1. Nakagawa Y and Hatanaka H, Boron neutron capture therapy: Clinical brain tumor studies, *J Neurooncol* 33, (1997), pp.105-115
2. Matsumura A, *et al.*, The University of Tsukuba BNCT research group; first clinical experiences at JAERI, *Advances in Neutron capture Therapy: Medicine and physics* Vol 1, (1997), pp.46-50
3. Yamamoto T, *et al.*, Medical setup of boron neutron capture therapy (BNCT) for malignant glioma at the Japan Research Reactor (JRR)-4, in Current Status of Neutron Capture Therapy, IAEA, pp.233-239, 2001.
4. Yamamoto K, *et al.*, Measurement of Two-dimensional thermal neutron flux in a water phantom and evaluation of dose distribution characteristics, JAERI-Tech 2001-015, 2001

研究テーマ：研究炉利用高度化の技術開発
表　　題：

7-6 熱ビームIを用いたBNCTの臨床的検討 - 第1報

松村　明、山本哲哉、柴田　靖、松下　明、安田　貢、中井　啓、山田　隆、
阿久津博義、能勢忠男、山本和喜[1]、熊田博明[1]、堀　直彦[1]

筑波大学臨床医学系脳神経外科
日本原子力研究所[1]

はじめに

神経膠芽腫は治療抵抗性であり、日本脳腫瘍統計によれば平均生存期間は約１年、５年生存率は約１０％で、従来の治療に基づく過去２０年間で大きな改善はみられていない(1)．神経膠芽腫に対しては手術療法、放射線療法、化学療法を組み合わせた集学的治療が行われるが、この中で手術での摘出度や６０-６４Gy 程度の外部分割照射を用いた放射線療法により一定の生存期間延長が認められることが知られている(1)．この腫瘍の放射線治療効果は線量依存性であるが、最近の知見では９０Gy の照射を行うことにより腫瘍生後率が著名に改善される一方で、なお腫瘍辺縁部での再発が認められるとされている(2,3)．したがって近年の放射線治療では、正常脳の耐用線量を超えた高線量をいかにして安全に腫瘍に照射するかが一つの課題となっていて、陽子線や重粒子線などの粒子線治療(2)、術中 X 線照射(4)、組織内照射(5)といった方法が試みられてきた．中性子捕捉療法(Boron neutron capture therapy: BNCT)は中性子照射での物理的制御と、α線照射を惹起するホウ素化合物の生物学的な選択性によって腫瘍選択的治療を目指すものである．我々は、日本原子力研究所 JRR-4 号炉の熱中性子ビームモードＩを用いたホウ素中性子捕捉療法(BNCT)の臨床治験を行い、その有用性および手技について検討を行っている(6,7)．

対象と方法

対象は1999年10月より現在までJRR-4号炉にて熱モードＩを用いて術中 BNCT を行った Anaplastic astrocytoma (AA) 3、Glioblastoma (GBM) 4の計７例で、いずれも初発例であり、他の放射線治療は行われていない．年齢は 20-66 才、男性 1、女性 6 である．腫瘍摘出術の際に BSH の distribution study を行った後、原則として 4 週以内に BNCT を施行した．BNCT に用いる BSH は照射開始予定時刻の 12 時間前に投与を開始し、100mg/kgBW を 500ml の生理食塩水に溶解して１時間かけて点滴静注した．照射には熱モード１を２MW 運転で使用し、開頭術野での金線による熱中性子フラックス測定値と全血中 ^{10}B 濃度をもとに算出した血管ホウ素線量 10.8Gy を基準として、照射時間を決定した．

結果と考察

BNCT 後 Follow up 期間は平均 16.8 months (5.8-25.4 months)で、生存期間の median 値は GBM で 19.8 months、4 例中 1 例が遠隔再発により死亡、1 例が腫瘍再発はないものの原疾患以外の原因で 15 months 後に死亡した。2 例は生存中で経過観察中である。AA での生存期間の median 値は 16.8 months であり、3 例中 1 例が原疾患以外の原因で死亡し、残り 2 例は生存中で経過観察中である。GBM では 1 年生存率 75%、AA では 1 年生存率 100%で、現時点のごく短期間の評価として良好な成績と考えられる．

照射時間は平均 117 min (61-171 min)で、血中濃度の予備測定（ICP 法）結果が高かった 1 例で、原子炉運転出力の変更(2MW→1.5MW)が必要であった．照射時間の決定に用いた金線（予定最大出力到達後 15 分間照射）と照射後の評価に用いた金線（全照射時間）の測定によるピーク値はそれぞれ 2.42 ± 0.16 および 2.57 ± 0.15 E+9 $cm^{-2}sec^{-1}$ であり、これによる予測線量と評価線量の違いは 0-15.4 %であった．予測線量と評価線量の違いが個々の症例で異なるのは、照射方向と病変部位（＝開頭方法）によって頭位固定の難易度が異なることが主因と考えられた．また、7 例中線量評価および患者セッティングシステムが試用された 1 例では照射室での頭位設定が容易で、予測線量と評価線量の違いが 2%程度であることから、同システムの有用性が示唆された．

照射中の全血 ^{10}B 濃度は平均 27.2 μg/g(19.7-38.8)であり、1g の BSH を用いた distribution study が照射時の血中濃度の予測に有用であった．個々の症例による BSH 投与後全血 ^{10}B 濃度の減衰の違いは腎機能や脱水の程度、頭蓋内圧降下剤や点滴などによってもたらされる一方、BNCT に用いられた BSH には ^{10}B 含有率にして約 2 割程度の違いがあるため、distribution study の際に純度や濃縮度を把握しておくことが

必要であると考えられた.

BNCTでの熱モードIの利用は、従来の熱ビームに対し熱外中性子によって深部病変での線量分布の改善を狙ったものである.さらに一歩進んで熱外中性子ビームを用いた場合、熱モードIを用いる場合より深部線量が改善されることでより高い治療効果が得られる.BNCTでは、病変部での線量分布はホウ素化合物の血液／腫瘍比や脳／腫瘍比に大きく依存している(生物学的選択性). BNCT では原理上、X・γ線で用いられる多方向照射や回転照射によるconformality(物理学的選択性)は理論上必要としない. しかし、術中 BNCT において熱外中性子ビームを腫瘍摘出後腔に照射した場合、ホウ素化合物の生物学的選択性とは別に、組織内で熱中性子が増加するビーム特性から、腫瘍床近傍に最も高い同心円状の線量分布を示すことが次第に知られてきている. また、中性子遮蔽材料を加工した multileaf collimation も開発中で、将来的にはホウ素化合物による生物学的選択性と中性子線照射制御による物理学的選択性を組み合わせることで、術中 BNCT の効果改善に期待が寄せられている.

むすび

今後さらに症例を重ね、BNCT後の長期成績について評価が必要である.BNCTの治療成績向上のため、照射技術や中線量評価および患者セッティングシステムの開発をはじめ、線量やホウ素濃度測定法においてもさらに改善を進めていきたい.

文献

1. The Committee of Brain Tumor Registry of Japan: Report of brain tumor registry of Japan (1969-1993) 10th edition. Neuro Med Chir, Suppl 40, 2000.
2. Fitzek MM, et al.: Accelerated fractionated proton/photon irradiation to 90 cobalt gray equivalent for glioblastoma multiforme: results of phase II prospective trial. J Neurosurg 91: 251-260, 1999.
3. Lee SW; et al.: Patterns of failure following high-dose 3-D conformal radiotherapy for high-grade astrocytomas: a quantitative dosimetric study. J Radiat Oncol Biol Phys 1: 79-88 1999.
4. Matsutani M, et al.: Intra-operative radiation therapy for malignant brain tumors: rationale, method, and treatment results of cerebral glioblastomas. Acta Neurochir (Wien)131: 80-90, 1994
5. Sneed PK, et al.: Large effect of age on the survival of patients with glioblastoma treated with radiotherapy and brachytherapy boost. Neurosurgery 36: 898-904, 1995.
6. Matsumura A, et al.: The University of Tsukuba BNCT research group: first clinical experiences at JAERI. Advances in Neutron Capture Therapy. Larsson B, Crawford J, Weinrich R eds: Vol.1 Elsevier, Amsterdam, pp46-50, 1997
7. Yamamoto T, et al.: Medical set up of boron neutron capture therapy (BNCT) for malignant glioma at the Japan Research Reactor(JRR)-4. In Current Status of Neutron Capture Therapy, IAEA, Wien, pp233-239, 2001.

原子炉：JRR-4　装置：中性子ビーム設備、即発ガンマ線分析装置　分野：その他

研究テーマ：研究炉利用高度化の技術開発
表　　題：

7-7

In vitro NCT comparison study between two Gd targeting compound (Gd- BOPTA and Gd- DTPA).

Tian Zhang, Akira Matsumura, Tetsuya Yamamoto, Tadao Nose, Hiroaki Kumada[1], Kazuyoshi Yamamoto[1]

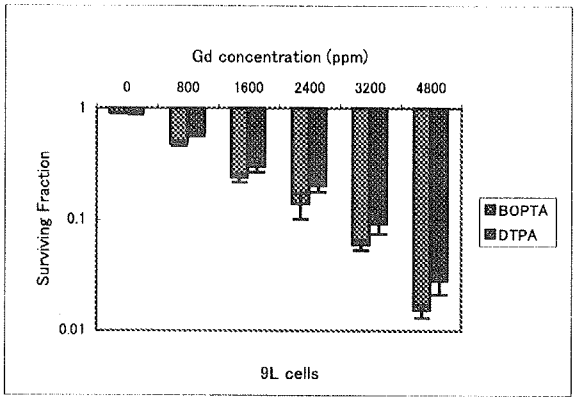
Department of Neurosurgery, Institute of Clinical Medicine, University of Tsukuba
Department of Research Reactor, Tokai Research Establishment, JAERI[1]

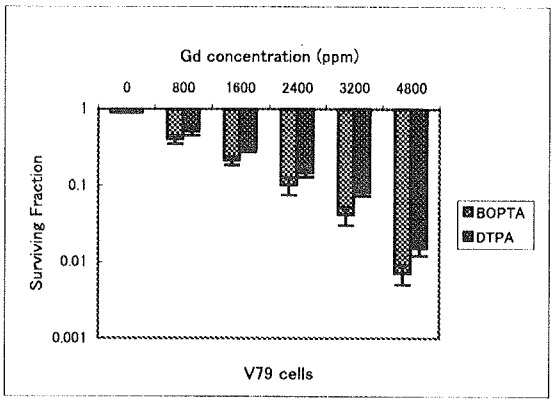
In recent years, some *in vivo* Gd-NCT trials of a targeting Gd compound- Gadopentetate dimeglumine (Gd-DTPA, Magnevist, Schering AG, Germany), which is in common clinical use as a MRI contrast agent, have been conducted. The results of these trials indicated positive irradiation effects. One point of success in the current Gd-NCT trial was maintenance of a sufficient Gd concentration in tumor tissue. Gd-DTPA, which had been used in ordinary Gd-NCT trials, was reported to be eliminated rapidly from tumor tissue after intratumoral (i.t.) administration. A new Gd compound, Gd-BOPTA (Gadobenate dimeglumine, Multihance, Bracoo s.p.a., Italy), used as both a hepatobiliary-specific and extra cellular contrast agent of MRI, was proved to have effective diagnostic value in liver MRI. Moreover, we proved in a previous report that Gd-BOPTA had a significantly greater Gd uptake than that of Gd-DTPA in brain tumor tissue, and Gd was retained longer up to 2 hours after intravenous (i.v.) administration, whereas rapid elimination of Gd-DTPA was seen [1]. Therefore, in the present study, we aimed to investigate whether Gd-BOPTA was a more efficient targeting agent than Gd-DTPA for neutron capture therapy.

9L gliosarcoma cells and Chinese hamster V79 cells lines were used in this trial. The same cell preparation method was used as above. The cell suspensions were diluted to reach a final cell concentration of 10^4 cells/ml, and 1 ml cell suspension was filled into every tube. For the NCT targeting compounds, both Gd- BOPTA and Gd-DTPA, were filled into cell content tubes respectively as same ^{157}Gd concentrations (0, 800, 1600, 2400, 3200, and 4800ppm) for thermal neutron irradiation. Tubes with the same Gd concentration were irradiated together as one irradiation group, which were placed in a rotating irradiation system at JRR-4 (3.5 MW, 8.4×10^9n/cm/S), for 30 minutes thermal neutrons irradiation. After irradiation, the cells were resuspended, diluted with fresh MEM containing 10% FBS, and suitable numbers of cells were plated onto plastic Petri dishes for colony formation assay (n=5). After 7 days the colonies were fixed, stained, and counted. The surviving fractions were calculated for result analysis.

At every equal Gd concentration, Gd-BOPTA showed lower surviving fraction than that of Gd- DTPA group, in both of 9L and V79 cell lines, under thermal neutron irradiation (Fig. 1 and Fig. 2).

Fig.1.





During $^{157}Gd(\ n,\gamma\ )$ reaction, not only gamma-rays were induced, but also include conversion electrons, Auger electrons, and characteristic X-rays. Stasio G et al. [2] proved that Gd-DTPA not only penetrates the plasma membrane of the tumor cell, but also accumulates at a higher concentration in the nucleus than in the cytoplasm, so that a locally intensive destruction of DNA in tumor cells can be made by short range and high linear transfer Auger electrons, which effect is comparable to that of BNCT [3].

The result indicated that at every equal Gd concentration, Gd- BOPTA showed lower surviving fraction than that of Gd- DTPA group, in both of 9L and V79 cell lines. This result supports the possibility of intracellular uptake of Gd-BOPTA (gadobenate ions), which should be investigated in the future. If Gd-BOPTA is proven to reach the intracellular space, more efficiency will be made to induce cell killing with thermal neutron irradiation than extra cellular Gd compounds.

Fig.2.

In conclusion, this is the first report of Gd-NCT by use of Gd-BOPTA to demonstrate that Gd-BOPTA has dual use: as an MRI contrast agent and as an effective targeting compound for neutron capture therapy. This study demonstrated different cytocidal effects among various Gd agents, which has been planned for further investigation.

References

1. Zhang T, Matsumura A, Yamamoto T, et al. Comparison of two brain tumor-localizing MRI agents: Gd-BOPTA and Gd-DTPA. *AJNR*. 2001, in press.
2. De Stasio G, Casalbore P, Pallini R, et al. Gadolinium in human glioblastoma cells for gadolinium neutron capture therapy. *Cancer Res.* 2001; May 15; 61(10): 4272-4277.
3. Brugger RM, Shih JA. Evaluation of gadolinium – 157 as a neutron-capture therapy agent. *Strahlenther Onkol.* 1989, 165: 153-156.

原子炉：JRR-4　　装置：中性子ビーム設備　　分野：その他

7-8 水溶性金属ポルフィリン錯体イオン会合系（固相）における中心金属の反跳挙動に対する異なる親水性置換基の影響

The Influence of Hydrophilic Groups to the Recoil Features of Central Metal Atoms in the Solid System of Water-Soluble Metalloporphyrin Ion Associates

Hitoshi Shoji*
Department of Chemistry, University of Tsukuba

Introduction

In recoil chemistry of metal complexes, complex yields including the retention have been paid much attention to by many researchers. Generally speaking, a complex yields experimentally obtained is not always from a single reaction process, and which is very often the combined result of plural elementary reaction processes. In some cases it is very effective in the analysis of reaction mechanism to adopt bi-component system, which may lead us to the hidden predominant factor of the reaction processes. Mixed crystals of isomorphous metal complexes have been usually used as the bi-component system. It is, however, very difficult to prepare microscopically homogeneous genuine mixed crystals. To avoid such preparative difficulties in keeping the advantage of bi-component systems, the author has been dealing with water-soluble metalloporphyrin ion associates as the bi-component system instead of the mixed crystal. This kind of ion associates was newly obtained by the author's group in the form of precipitates from the aqueous solutions, which are thought to be microscopically homogeneous considering the necessity of mutual electric neutralization. In this study the two series of systems [M(TMPyP)][M'(TCPP)](M, M'=Cu,Zn) and [M(TMPyP)][M'(TPPS)](M, M' = Cu, Zn) were investigated mainly on the influence from the different two kinds of substituted hydrophilic groups with negative charge, where H_2TMPyP = tetrakis(4-N-methylpyridyl)porphine, H_2TCPP = tetra(p-carboxyphenyl)porphine, and H_2TPPS = tetra(p-sulfophenyl)porphine. Their chemical structures are shown in Fig. 1.

Experimental

Materials

Metal free ligands of water-soluble porphyrins were purchased. According to the literature[1,2] the metal free ligand was mixed with small excess of a G.R.-grade metal salt in an appropriate solvent. Then, the solution was refluxed for several hours and the central metal atom was introduced. The water-soluble metalloporphyrin was collected in a form of a precipitate. The aqueous solution of each component metal complex was prepared. After that, the solutions of cationic and anionic component complexes were mixed in (1:1) mole ratio. The mixed solution was left overnight or so. Then the precipitate of the ion associate formed. The ion associate was purified by reprecipitation. The ion associate sample was checked by elemental analysis, spectrometric measurement and powder X-ray

Facilities and Instruments: JRR-3M (Pn-tube), Research Field: Hot-atom Chemistry.
*Present address: 3-46-3 Utsukushigaoka, Aoba-ku, Yokohama 225-0002.

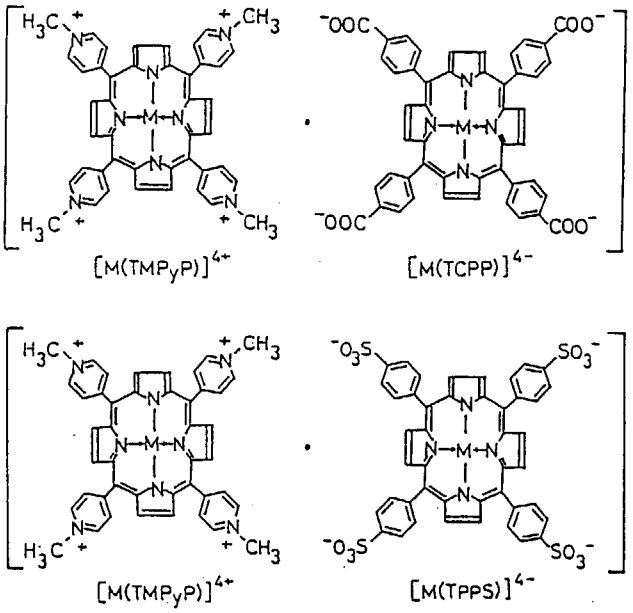


Fig. 1. Structural formulae of water-soluble metalloporphyrin ion associates used. [M(TMPyP)][M'(TCPP)](upper) and [M(TMPyP)][M'(TPPS)](lower).

diffraction before it was subjected to irradiation.

Irradiation

Two kinds of irradiation were carried out, thermal neutron and bremsstrahlung irradiation. The thermal neutron irradiation was done in JRR-3M reactor of Japan Atomic Energy Research Institute, Tokai, Japan. The samples were irradiated in the pneumatic tube at −78℃ for 3 min. The bremsstrahlung irradiation was done in the 300-MeV electron linear accelerator of Tohoku University, Sendai, Japan. The irradiation was carried out using Pt-converter under the following conditions: max energy of photons; 50 MeV, current; 100-150 μA, temperature;<-130℃,irradiation time; 8-10 hours. Unconverted electrons were removed by a sweep magnet.

Chemical Separation

Irradiated samples were dissolved in an ice-cooled mixed solvent of 3M NH_4Cl, 1M ammonia water and ethanol (the volume ratio, (1:1:2) containing the carriers of Cu^{2+}, Zn^{2+} and metal complex ions which had counter central metals to the target sample, if necessary. An aliquot of the sample solution was passed through the cation and anion exchanger columns. In the effluent from the anion exchanger column, the coexisting bare metal ions were removed in a form of the precipitate of metal carbamates by adding the carriers for precipitation and sodium diethyldithio-carbamate.

Activity Measurement

The γ -spectra of these samples were measured using a Ge(Li) or HPGe detector and they were analysed by the connected computer system.

Result and Discussion

The complex yields obtained are shown in Tables 1 and 2. In the case of [M(TMPyP)][M'(TCPP)](M, M' = Cu, Zn) (shown in Table 1) copper nuclides (Cu*) were

preferentially stabilized in the Zn-complex side in both irradiation, while zinc nuclides (Zn*) showed rather uniform stabilization in both sides. This is the fundamental feature in this combination of central metals and ligands. In addition, in thermal neutron irradiation, ^{69m}Zn always showed higher retention value than ^{65}Zn because of the difference of average recoil energy (^{69m}Zn: 166 eV, ^{65}Zn: 446 eV)[3] through the contribution of primary retention part without bond rupture. It is noteworthy that the probabilities of replacement of Zn by Cu* are similar to each other in both irradiation and for all the radiocopper nuclides, which leads us to the already common concept that the recoils react with neighbouring ligands after losing their initial high kinetic energy and/or high charge and that the reaction probabilities are therefore almost independent of the initial recoil energy or the nuclear reaction.

The negatively charged component complex ions were changed from M(TCPP) to M(TPPS) keeping other conditions unchanged. Curiously the preferential substitution of stable

Table 1. Complex Yields(%) in [M(TMPyP)][M'(TCPP)](M,M'=Cu,Zn)

Sample	[Zn(TMPyP)][Cu(TCPP)]		[Cu(TMPyP)][Zn(TCPP)]	
Fraction	M(TMPyP)	M(TCPP)	M(TMPyP)	M(TCPP)
^{64}Cu	9±1	2.8±0.6	2.8±0.4	21±2
	9.1±0.2	3.6±0.1	2.4±0.2	19.7±0.5
^{67}Cu	9.0±0.1	3.0±0.1	2.5±0.1	22.1±0.3
	---	---	---	---
^{62}Zn	2.3±0.4	3.8±0.3	3.3±0.4	4.6±0.5
	---	---	---	---
^{65}Zn	2.2±0.4	3.6±0.5	4±1	4.0±0.7
	2.4±0.1	3.6±0.1	3.3±0.2	2.7±0.3
^{69m}Zn	1.5±0.8	3.9±0.6	4.4±0.8	2±2
	6.8±0.2	3.6±0.2	3.1±0.2	6.9±0.4

Sample	[Zn(TMPyP)][Zn(TCPP)]		[Cu(TMPyP)][Cu(TCPP)]	
Fraction	M(TMPyP)	M(TCPP)	M(TMPyP)	M(TCPP)
^{64}Cu	---	---	2.3±0.4	2.3±0.4
	---	---	2.4±0.1	2.3±0.1
^{67}Cu	5.5±0.2	19.0±0.3	---	---
	---	---	---	---
^{62}Zn	2±1	5±1	---	---
	---	---	---	---
^{65}Zn	3±1	4±1	---	---
	2.4±0.2	2.3±0.2	---	---
^{69m}Zn	3±1	5±1	---	---
	4.2±0.1	4.5±0.1	---	---

Upper value: Bremsstrahlung irradiation below -130°C.
Lower value: Thermal neutron irradiation at dry ice temperature.

Table 2. Complex Yields(%) in [M(TMPyP)][M'(TPPS)](M,M'=Cu,Zn)

Sample	[Zn(TMPyP)][Cu(TPPS)]		[Cu(TMPyP)][Zn(TPPS)]	
Fraction	M(TMPyP)	M(TPPS)	M(TMPyP)	M(TPPS)
^{64}Cu	0.5±0.1	2.5±0.3	0.6±0.3	2.8±0.9
	0.5±0.1	2.2±0.2	1.1±0.1	2.8±0.9
^{67}Cu	0.5±0.1	2.5±0.3	0.5±0.2	2.6±0.2
	---	---	---	---
^{62}Zn	0.5±0.1	2.4±0.2	1.1±0.2	0.7±0.2
	---	---	---	---
^{65}Zn	0.9±0.3	2.7±0.3	1.2±0.4	1.0±0.2
	0.8±0.2	2.5±0.2	1.4±0.2	1.0±0.1
^{69m}Zn	0.6±0.2	2.7±0.2	1.2±0.3	0.8±0.3
	3.3±0.3	2.3±0.1	1.8±0.2	3.4±0.4

Sample	[Zn(TMPyP)][Zn(TPPS)]		[Cu(TMPyP)][Cu(TPPS)]	
Fraction	M(TMPyP)	M(TPPS)	M(TMPyP)	M(TPPS)
^{64}Cu	---	---	0.4±0.1	1.2±0.2
	---	---	2.2±0.1	2.1±0.2
^{67}Cu	1.4±0.5	4.2±0.2	---	---
	---	---	---	---
^{62}Zn	0.7±0.2	1.2±0.3	---	---
	---	---	---	---
^{65}Zn	0.8±0.2	1.0±0.2	---	---
	0.9±0.2	1.1±0.2	---	---
^{69m}Zn	0.8±0.2	1.2±0.3	---	---
	2.2±0.1	2.0±0.1	---	---

Upper value: Bremsstrahlung irradiation below -130°C.
Lower value: Thermal neutron irradiation at dry ice temperature.

Zn central atoms by Cu* disappeared as shown in Table 2. Radiocopper recoils (Cu*) dispersed rather uniformly with showing slight affinity for TPPS ligands in almost all the cases, which reminds us that radiocobalt recoils (Co*) had remarkable affinity for TMPyP ligands in all the cases in the system of [M(TMPyP)][M'(TPPS)](M, M' = Co, Cu). The only remaining common tendency was the influence of average initial recoil energy on the retention of zinc nuclides in thermal neutron irradiation.

As for the stability order among metalloporphyrins in general without consideration of attaching groups to the porphyrin ring, two criteria have been proposed. One is called "Stability Class", which is based on the easiness of demetallization in the treatment with reagents of various reactivity[4,5]. Another criterion is called "Stability Index", the definition of which is valence times Pauling's electronegativity divided by ionic radius[6]. Although at a few points these two criteria have shown inconsistency, they appear

to be consistent with each other in almost all the cases. Here, according to the "Stability Index", we can make stability order of metalloporphyrin complexes whose central metal atom is divalent as in the following:

Pd >Ni >Cu >Pt >Co >Fe >Zn >Sn >

Pb～Hg >Mn >Mg >Cd >Ca >Sr >Ba

In this study Cu- and Zn-complexes were concerned. The Zn-complex is located at a weaker position than Cu-complex, which is consistent with the phenomena of remarkable preferential substitution of Zn central atoms by Cu* in the case of the system of [M(TMPyP)][M'(TCPP)](M, M' = Cu, Zn) (the case shown in Table 1). In the other system of [M(TMPyP)][M'(TPPS)] (M, M' = Cu, Zn) (the case in Table 2) where no above-mentioned preferential substitution was observed, the explanation based on the "Stability Index" or "Stability Class" is not applicable. There must be other predominant factor there, which suppresses the preferential substitution of Zn by the recoil of Cu*, and one candidate of which is thought to be the structural difference between the two kinds of associates.

Although these kinds of water-soluble metalloporphyrin ion associates were obtained in the form of a precipitate, the extent of their crystallization was poor in all the cases even after the mother solution was left for several months or longer. Such a tendency of remaining in the amorphous state was more remarkable in the former kind of ion associates with "TCPP" groups than the latter with "TPPS". The X-ray powder diffraction patterns of typical samples obtained after keeping them in their mother solutions for more than a month are represented in Figs. 2 and 3.

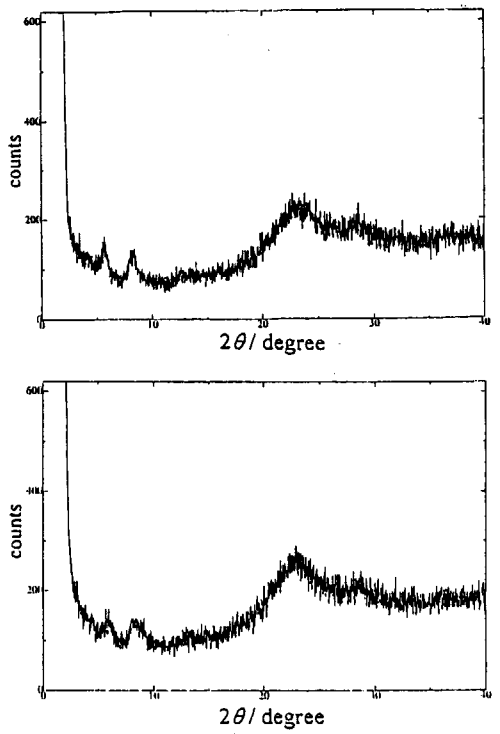


Fig. 2. X-ray powder diffraction patterns of [Cu(TMPyP)][Zn(TCPP)](upper) and [Zn(TMPyP)][Cu(TCPP)](lower).

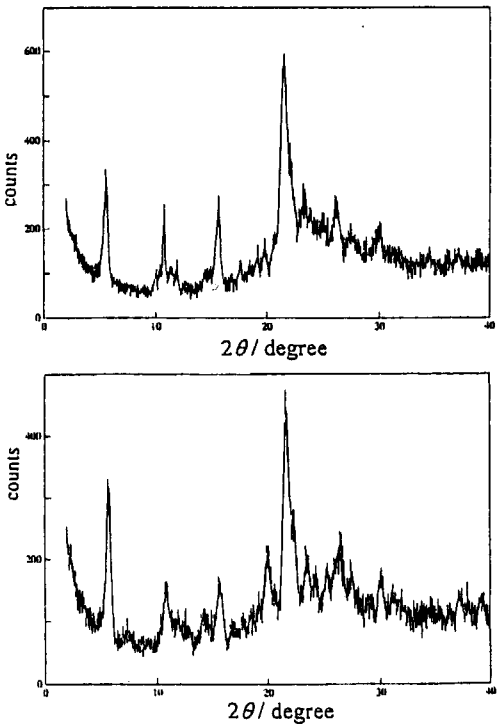


Fig. 3. X-ray powder diffraction patterns of [Cu(TMPyP)][Zn(TPPS)](upper) and [Zn(TMPyP)][Cu(TPPS)](lower).

Figure 2 implies that the former ion associates were almost amorphous with very small crystalline portion and that the exchange of central metal atoms gave no effects to their microscopic structure, while Fig. 3 shows that the latter ion associates were the mixture of crystalline and amorphous portions with little effect of the exchange of central metal atoms. As the crystallization was too poor, the exact comparison of crystal data was unsuccessful between two kinds of ion associates. Although it is clear that the former has much more amorphous part than the latter, the latter also still has its amorphous part. Therefore the difference of amorphous portion between two kinds of ion associates cannot be attributed to the drastic change of the recoil feature in the latter ion associates from the former.

The predominant factor for the rather uniform distribution of the nuclides in the latter case is still in vague, though it is the fact that the change of the hydrophilic group from $-COO^-$ to $-SO_3^-$ in the negatively charged component complex ion plays an important role through some still unknown mechanism.

References

1. 1. A. D. Adler, F. R. Longo, F. Kampas, and J. Kim, J. Inorg. Nucl. Chem., **32**, 2443 (1970).
2. R. F. Pasternack, L. Francesconi, D. Raff, and E. Spiro, Inorg. Chem., **12**, 2606 (1973).
3. Y. Oki, Thesis, University of Tsukuba, 1988.
4. J. W. Buchler, Habilitationsschrift, Technische Hochshule, Aachen, 1971.
5. J. W. Buchler, L. Puppe, K. Rohbock, and H. H. Schneehagee, Ann. N. Y. Acad. Sci., **206**, 116 (1973).
6. K. M. Smith, Porphyrins and, Metalloporphyrins, Elsevier Scientific Publishing Co., Amsterdam-Oxford-New York, 1975.

Publications

1. H. Shoji, "Radioisotope Production Using (n, γ)-recoil in Water- Soluble Metal Phthalocyanines", presented at 5th International Conference on Nuclear and Radiochemistry (NRC5), Pontresina (Switzerland), Sept. 6th, 2000.
2. H. Shoji, "Various Tendencies in the Complex Formation in the Recoil Behaviour of Central Metal Atoms in the Solid System of Water-Soluble Metalloporphyrin Ion Associates", presented at Nuclear and Radiochemistry Symposium (NUCAR 2001), Pune (India), Feb. 8th, 2001.

7-9
α線トラックを利用した鋼中ボロンの状態分布システムの確立

Establishment of the System for Observing Boron in Steels using α-Rays Track.

東京大学大学院工学系研究科金属工学専攻　朝倉健太郎、柴田浩司
立教大学原子力研究所　原澤　進
東京大学原子力研究総合センター東海分室　澤幡浩之、川手　稔
Department of Materials Science, Faculty of Engineering, The Univ. of Tokyo
K.Asakura, K.Shibata
Institute for Atomic Energy, Rikkyo Univesity　S.Harasawa
Research Center for Nuclear Science and Technology, The University of Tokyo
H.Sawahata and M.Kawate

1．研究の目的と意義

1－1．研究の目的

ボロンは極微量でも鉄鋼の性質を向上させることが知られており、非常に多くの鋼で利用されてきたが、今後ますます重要となる環境問題、資源・エネルギー問題に対処できる鋼としてボロン添加鋼の重要性の認識が高まっている。

ボロンの挙動については不明な点が多く、さらに高性能な鋼を開発するためには、鋼中ボロンの挙動の詳細を明らかにする必要がある。そのため日本鉄鋼協会において、平成 11 年度よりボロン添加鋼の研究会（主査：柴田浩司、7 大学、2 国研、鉄鋼企業を含む 12 民間企業）が組織された。

熱中性子とボロン 10 の反応を利用したα線トラックエッチング法は感度に優れると共に、鋼の性質を決定する鋼のミクロ構造（組織）との関わりにおける観察が容易であることから、鋼中ボロンの挙動を観察する最も有力な手法として、多くの鉄鋼研究者に利用されてきた。しかし我が国において、中性子照射を一手に引き受けてきた立教大学原子炉が平成 11 年度をもって閉鎖された。α線トラックエッチング（以下、ATE と略）法が利用できないと、我が国における材料とりわけ鉄鋼材料の基礎研究、開発研究に重要な支障をきたすことは明らかである。

この問題の解決に対応できる我が国唯一の機関は日本原子力研究所である。そこで著者らは、これまで立教大学原子炉（以下、立教炉と略）で行われてきたような便利さで、α線トラックエッチング法が利用できるシステムを立ち上げる計画を立案し、1.5 年間の継続研究において、主として以下の 2 テーマについて研究を遂行した。

【研究 1】：　日本原子力研究所の研究炉 JRR-4（以下、原研炉と略）を利用し、立教炉で行ってきた ATE 法と同じ写真分解能を得るための照射条件および手法を確立する。

【研究 2】：　ATE 法では必須の増感剤塗布の「硝酸セルロースフィルム（Kodak 社製フィルム：CN85）は、メーカー側の都合により製造中止になった。全国の利用者の手持ちフィルムも枯渇化しており、CN85 と同等な特性を有する“代替硝酸セルロースフィルム”の探索を行った。

1－2．意義

原子力発電をはじめとする科学技術の発展を支えていく中心的材料である鉄鋼の基礎研究、開発研究に寄与できる。この照射システムの完成後、多くの鉄鋼材料研究者の利用が期待される。

2．実験方法

2－1．試料

研究に用いた試料の化学成分を Table 1 に示す。12 × 12 × 80mm の大きさの試験片を 1100 ℃× 1h 空冷処理した後、ATE 用試料として 10 × 5 × 1 mm（縦×横×厚さ）の大きさに切断した。

Table 1　照射に用いた試料の化学成分(mass%)

Mark	C	Si	Mn	P	B	Ti	N
B10	0.004	0.21	1.70	0.01	0.0019	0.009	0.043

研究施設：原子力研究所、装置：研究炉 JRR-4（気送管、医療用照射）、研究分野：ボロンの分布観察

2－2．熱処理条件

Table 1に示した化学成分を有する試料を用い、ボライドの固溶化温度を確認するため 950 ～ 1200 ℃、1h 空冷処理後、ATE 観察を行った。この結果、1100 ℃、1h においてボライドが固溶することを確認した。以下、すべての試験において1100 ℃、1h 空冷処理を行った。

2－3．照射用試料の準備

熱処理した試料をファインカッターを用いて約1mm 厚に切り出し、片側のみをエメリー紙研磨（#80 ～#1200）にて粗研磨を行い、その後、バフ研磨（アルミナ粒子：1 μmφ）にて鏡面仕上げを行った。

鏡面仕上げ面に酢酸エチルを滴下した後、増感剤付き硝酸セルロースフィルム（【研究１】は正規フィルム、【研究２】は代替フィルム）を、気泡が入らないように貼り付け、中性子照射を行った。

2－3．照射条件

【研究１】（１）立教大学における照射条件

立教炉での熱中性子束は 1.5 × 10^{10}n・cm^{-2}・sec^{-1} で、12h 照射（カドミ比 100）を行っていた。全熱中性子束は 6.5 × 10^{11}n・cm^{-2} になる。この全中性子束を基準（以下、基準中性子束と略）とし、照射時間を調整した。

（２）原研における照射手段

照射手段は以下のとおりである。

1）気送管による照射

2）医療用照射設備（熱中性子照射モードⅠ）による照射

①照射時間の影響（18h／24h）

②中性子照射の深さ方向における ATE 像の解像度変化

【研究２】

代替フィルムで用いた照射条件は、基本的に【研究１】と同じであるが、放射化分析は以下の照射条件でおこなった。

1）照射設備：JRR-4（気送管）

2）熱中性子束：3.2 × 10^{13}n・cm^{-2}・sec^{-1}

3）照射時間：90sec

4）冷却時間：24h

3．研究成果

【研究１】 照射条件探索のための実験内容は、①照射設備の確定、②照射板の作製と材質の選定、③照射条件の決定を具体的に行った。

3－1．照射設備の確定

（１）JRR-4 簡易照射設備の検討

前述したように、これまで ATE 法を実施してきた立教炉の照射線束を基準にし、原研炉での照射条件を見いだすことを検討した。

これまで立教炉における全熱中性子束は、6.5 × 10^{11}n・cm^{-2} であった。JRR-4 をにおいて同じような照射条件を得るには、N パイプ（1.7 × 10^{10}n・cm^{-2}・sec^{-1}）が考えられた。この照射設備を使って 38sec 照射をすると、熱中性子については同じ中性子束（6.46 × 10^{11}n・cm^{-2}）になるはずである。しかし照射時間を秒単位で制御することは不可能であるとの原研側からの回答を得た。再び照射設備を検討し、Tパイプ－B（4.3 × 10^{13}n・cm^{-2}・sec^{-1}）であれば 10sec ～ 6 h で制御できる（利用カタログに表記）はずであったが、N パイプと同じように秒単位では照射がコントロールできないとの回答を得た。

さらに検討した結果、気送管（4.5 × $10^{13}$$cm^{-2}$・$sec^{-1}$）であれば、1 sec ～ 20min の照射が可能であることが明らかになり、気送管における照射条件で実験を行うことにした。

（２）気送管による照射

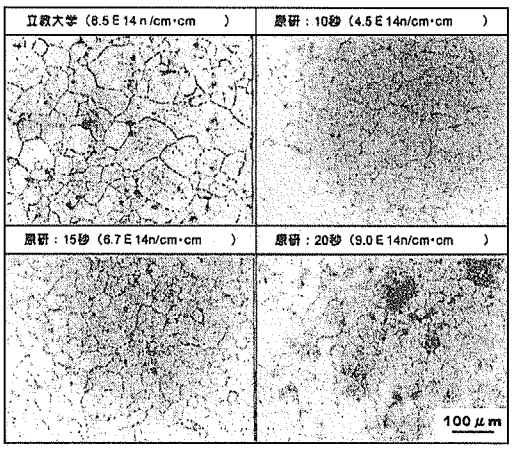
気送管の熱中性子束は 4.5 × 10^{13}n・cm^{-2}・sec^{-1}（カドミ比 3.6）である。基準中性子束（6.5 × 10^{11}n・cm^{-2}）をおおむね合わせるために Table 2 に示した照射時間を設定した。

Table 2. 気送管における照射時間と全中性子束

照射時間(sec)	全中性子束(n・cm^{-2})
10	4.5 × 10^{11}
15	6.7 × 10^{11}
20	9.0 × 10^{11}

立教炉と原研炉（気送管）における ATE 像を比較した結果をFig. 1に示す。立教炉の場合は、まったく問題なく 100 %の確率でトラック像が観察できた。原研炉10sec照射の場合、アルファ線（以下αと略）トラック像のコントラストが薄い、15sec照射の場合は比較的良好であるが、立教炉に比べてトラック像が薄い。20sec 照射の場合は、もっともコントラストが薄く、しみ状のパターンが認められた。しかも気送管の場合、“振動の影響”と考えられるフィルムのはく離が見られた。試料を２個づつ（10、15、20sec）照射したがフィルムのはく離が随所で認められ、αトラック像の観察確率は 45 ～ 50 %程度であった。

さらに立教炉と原研炉（気送管）の結果を解像度の視点から比較しても、明らかに立教炉の方がすぐれていた。



(a)立教炉（基準中性子束）(b) 10sec 照射
(c)15sec 照射　(d)20sec 照射

Fig.1　立教炉と原研炉における ATE 像の比較

この原因は、気送管における秒単位の短時間照射による照射時間の不正確さと、ばらつきが非常大きいことが考えられる。これは炉心に試料が入った時点の時間を検出することができないため、試料が決まったところを通過する時刻を基準として、その点から炉心まの時間を推定して照射時間を決めているためである。ボロンのαトラック像を見るときは正確な照射時間が必要であるが、放射化分析として主に用いられる気送管においては非常に正確な照射量は必要ないため、照射量が敏感なαトラック像の観察には不都合と考えられる。

もう一つの原因は、高速中性子束やガンマ線量が高いことが考えられるが、いずれにしてもボロンのαトラック像の観察には適していなかった。

気送管（原研炉）による問題点を列記すると以下のようになる。したがって気送管による照射を断念せざるを得なかった。

1）試料から硝酸セルロースフィルムのはく離が認められた。落下による衝撃はく離が原因と考えられる。
2）中性子照射源に対して試料が平行／垂直であるという偶然の確率を支配できない。
3）炉心までの時間を推定して照射時間をきめているため、照射時間が不正確である。
4）高速中性子束（ファストニュートロン）やガンマ線量が高いと考えられる。

3－2．医療用照射設備による照射

（1）照射モードの確定と照射時間

熱中性子照射モードⅠの場合（ビスマス表面）、$9.07 \times 10^{9} n \cdot cm^{-2} \cdot sec^{-1}$（カドミ比 2.5）である。立教炉の全熱中性子束に準拠した照射量を基準中性子束として換算すると、Table 3 の全熱中性子束のようになる。この結果から、20h 照射が基準中性子束とほとんど同じ値になるが、6h/day 照射が１単位であるため 3days（18h）照射、あるいは 4days（24h）照射が実質的な照射時間になる。また担当職員の被爆防止という立場から 4days (24h) 照射を検討課題とした。

Table 3. 医療用照射設備による照射時間と全中性子束

照射時間 (h)	全中性子束 ($n \cdot cm^{-2}$)
12	3.92×10^{14}
18	5.88×10^{14}
20	6.63×10^{14}
24	7.84×10^{14}

（2）照射板の作製と材質の選定

本来、医療用照射設備（ホウ素中性子補促療法）は、腫瘍細胞に選択的にホウ素化合物をとり込ませた後、低エネルギー中性子を照射し、ホウ素の

核反応で発生する短飛程のα線で腫瘍細胞を選択的に破壊する治療法として使用されている。したがってカドミニウムシャッタの前にあるビスマス照射口には、ATE 専用の照射板を自前で作製する必要があった。それには放射化しない材質（再利用可能な材質）を探し出さなければならなかった。材質としては、

1）アクリル板
2）段ボール板
3）炭素（カーボン）板

について検討した。

照射板の寸法と試料位置（ナンバリング）の関係を Fig.2 に示す。中性子束のばらつきを避けるため周辺部 150mm を除外し、中心部 300 平方 mm を照射領域とした。試料間隔を 75mm とし、25 個の試料を準備した。当初はポリエチレン袋に入れた試料を専用の粘着テープ（カプトンテープ）で留めて中性子照射に供した。

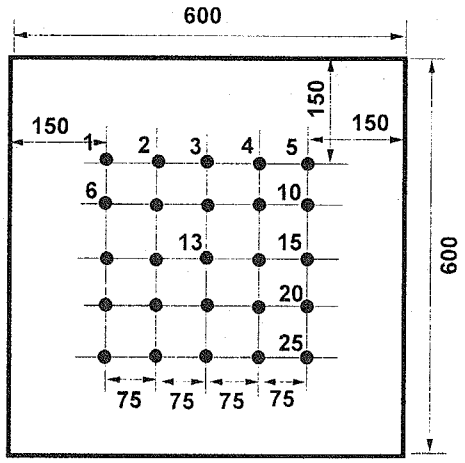


Fig.2　照射板の寸法と試料位置の関係

（3）照射板の放射化分析

放射化分析は、励起する物質に対して透過しやすい中性子を使うために、均一に放射化できる。また検出する物質に対して透過しやすいγ線を使うため、検出の損失が小さいなどの利点が報告されている。試料から放射されるγ線は Ge(Li) 半導体検出器で検出できる。

放射化分析する以前に製作したアクリル製の照射板（購入先などの素性がわからない）は中性子照射による放射化（汚染）が激しかった。γ線サーベによる測定から約 100 ～ 120 μ Sv/hr であった。また、表面を拭き取ることにより、数 10 μ Sv/hr まで落ちたことから、静電気による不純物の付着も考えられ、一概にアクリル板だけの線量ではないと考えられる。あるいは再生材である可能性も考えられる。なお具体的な核種については測定していない。

その後、ATE 専用の照射板を選定するため各種材料について放射化分析を行った。測定対象試料はカーボン 2 種類（新日本炭素㈱購入）、アクリル 5 種類（三菱レイヨン㈱提供）、段ボール板の 7 試料である。その分析結果の代表例を Fig.3 に示す。

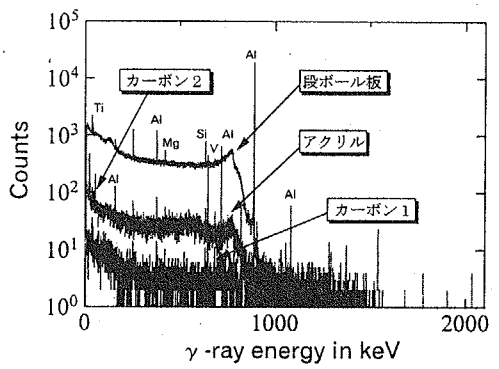


Fig.3　放射化分析による照射板の選択

この結果、カーボン 1 はバックグランドにほぼ等しく、カーボン 2 とアクリルがそれに続いた。これらの結果からカーボン、アクリルについては再利用が可能であることが判明した。段ボール板は Al などの核種が検出され、汚染が激しく再利用が不可能であった。当初、段ボール板については燃焼廃棄処理による「使い捨て」を考えたが、段ボール板の継続的な購入によるランニングコストの負担、製作の煩わしさ、照射後の裁断処理による被爆を避けられないことなどからカーボン板の使用を最優先した。

また三菱レーヨンから提供していただいた一般メタクリル樹脂（ＭＦ）、アクリルライト（Ｅ）、アクリルライト（クリア）および耐熱メタクリル

樹脂（ＶＨ）の素材については、アクリルライトに Bi-214 が認められたが、他の素材に関してはまったく問題がなかった。

３－３．熱中性子モードＩにおけるATE像

（１）１８ｈ照射におけるATE像

Fig.2 のアクリル製照射板に試料を貼りつけて中性子照射した結果を Fig.4 に示す。照射時間は 18hr である。このときの全熱中性子束は 5.9 × 10^{14}n・cm^{-2}・sec^{-1} である。

照射板のエッジ部に相当する試料ナンバー：1, 5, 10,15, 20, 21, 22, 24 および 25 の結晶粒界には“ぼやけ”、ないしは二重線が観察できた。この原因については正確には特定できないが中性子束は均一ではなく、結果にみられるような不均一なビーム特性による、また二重線の生成は irregular beam が散乱されて生じたものと考えられる。したがって均一な中性子束は、照射板の中央部付近（試料ナンバー：７～９、12～14、17～19）で得られるものと確定した。

（２）２４ｈ照射におけるATE像

担当職員の被爆防止という立場から 4days(6h × 4days ＝ 24h)照射について検討した。つまり照射開始の前日である月曜日に試料をセットし、照射終了日の金曜日から次週の月曜日が冷却時間になるため、被爆量をきわめて少量に押さえることが可能になる。つまり中性子の activity が低下した月曜日に試料の出し入れができれば best である。

しかし 24h の全熱中性子束は 13 × 10^{14}n・cm^{-2}・sec^{-1} にもなり、18h 照射に比べて約 2.2 倍のフ

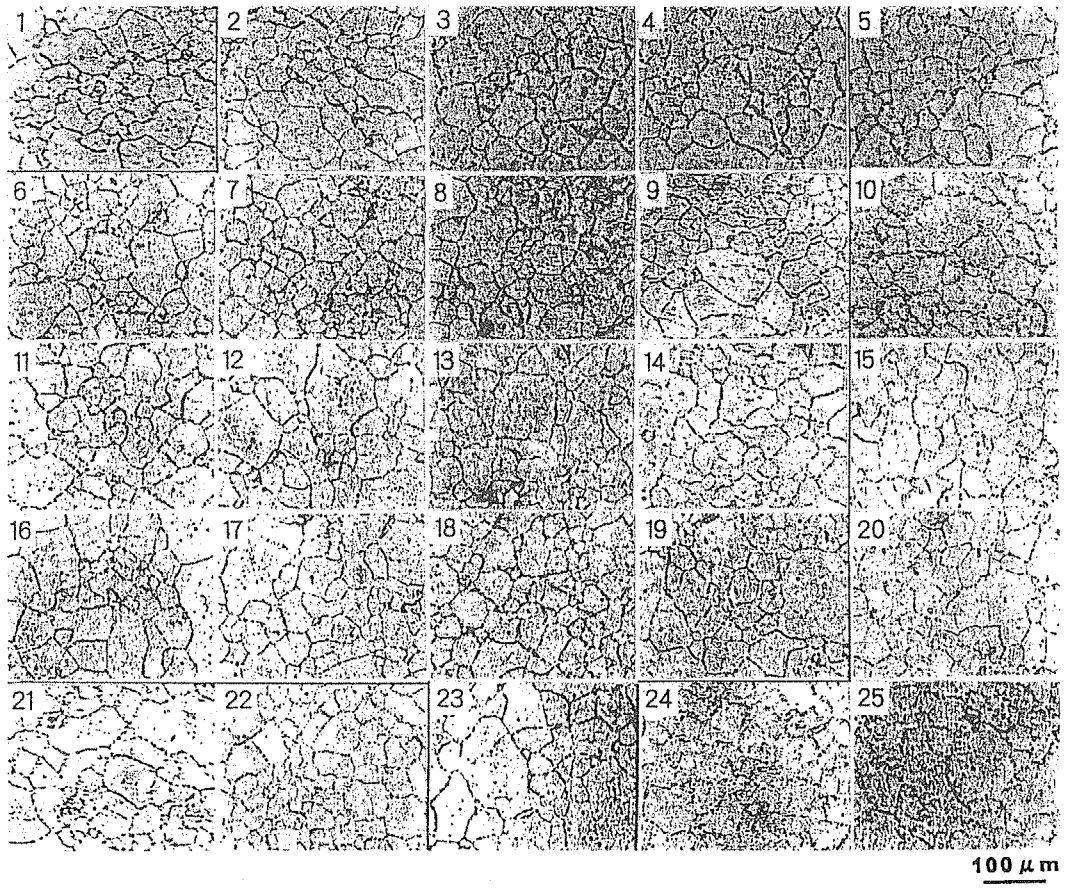


Fig.4　JRR-4（熱中性子モードＩ：照射時間 18h ＝ 5.9 × 10^{14}n・cm^{-2}・sec^{-1}）における ATE 像

ラックス量になる。このためATE像の質(quality)に関しては、図示していないがフラックス量が多いときに観察される“しみ状”のパターンが多数みられた。これらの結果から、24h照射はATE観察にとっては不都合な照射時間（照射フラックス量）であると断定した。

3－4．深さ方向におけるATE像の変化

これまでの実験では平面空間におけるATE像の質について調べた。この結果は前述したとおりである。本節では照射口に対して深さ方向（試料位置を中性子束から遠ざけたとき）におけるＡＴＥ像の変化について調べた。

隔壁板の寸法をFig.5に示す。全体の大きさは120 × 75mm（高さ60mm）である。隔壁の板（斜線部）はFig.5ではわかりにくいが、上下にスライドして取り外せるようにした。試料は照射板から20mm間隔にマークした●印に、粘着テープ(カプトンテープ)で貼り付けた。

深さ方向に対するATE像の変化をFig.6に示す。この結果、40mmと80mm付近にわずかに照射量の高い領域（しみ状の痕跡が一部に認められた）があるものの、全体的には20 ～ 100mmの深さ方向においてATE像をほとんど問題なく観察することができた。

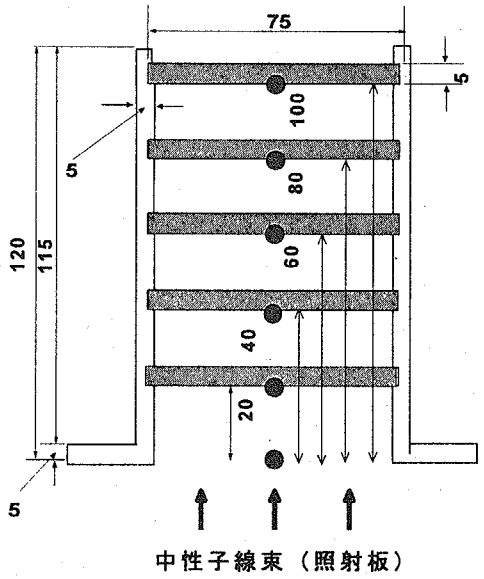


Fig.5　深さ方向のATE像を調べるための隔壁板

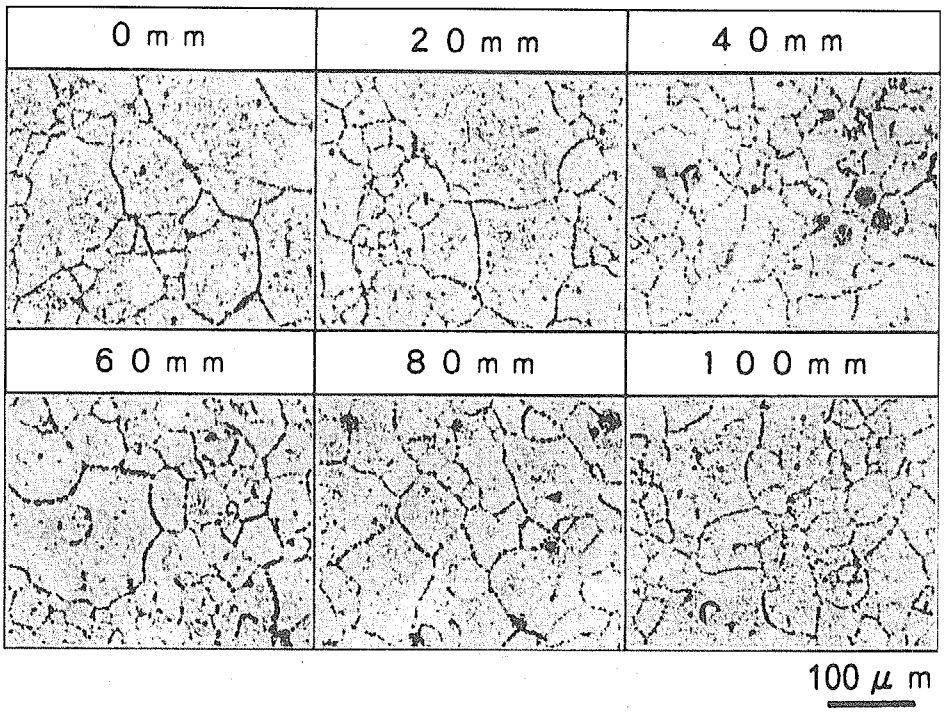


Fig.6　深さ方向（試料位置を中性子束から遠ざけたとき）におけるATE像の変化

実際のアクリル製隔壁板を Fig.7 に示す。この隔壁板を段ボール製の照射板に、アクリル製のビスによって Fig.2 で示した中央部に付けた。

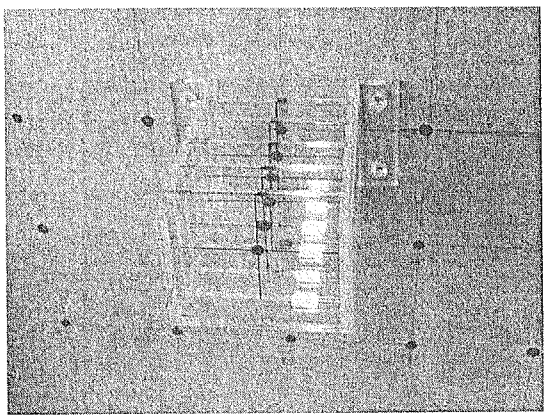


Fig.7　アクリル製隔壁板

現在は Fig.8 に示したカーボン板を照射板として用いている。照射板の大きさは 600 × 700mm（横×縦）で、中央部に相当する領域には約 150 × 10mm（横幅×奥行き）の試料ホルダーを 3 カ所取り付けてある。

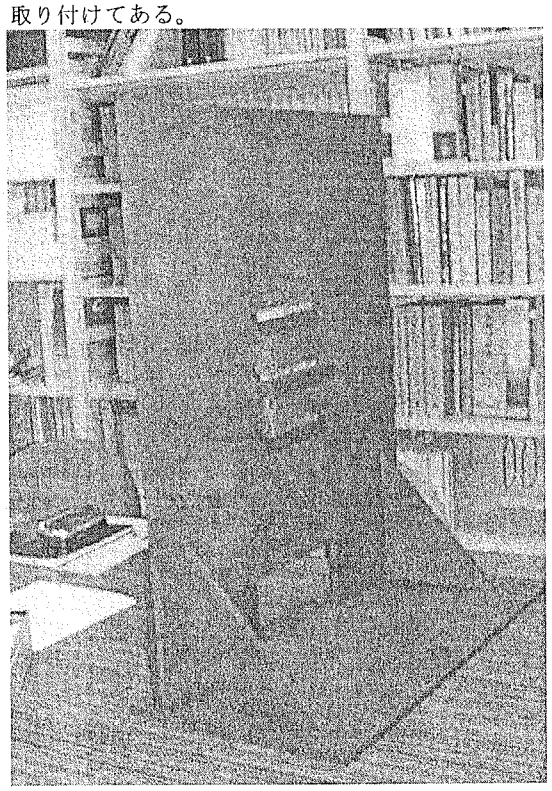


Fig.8　カーボン製の照射板

【研究 2】　前述したように①放射化しないフィルムの探索、②α トラック像が観察できるフィルムの探索について具体的に行った。

3－5．ATE 用フィルムの要求特性と使用した代替フィルム

（1）ATE 用フィルムの要求特性

ATE 用フィルムとして要求される特性は以下のとおりである。これらのどれもが欠如しても使用に耐えることはできない。

1）$^{10}B + n \rightarrow Li + He$（α）反応によって、α トラック像が観察できる。
2）耐中性子照射特性（耐熱性、放射化しない）を有する。
3）平滑性を有する。
4）異物の付着がない。
5）適度な機械的性質を有する。
6）巻き癖カールなどがない。
7）溶剤などによって変質しない。
8）温度・湿度などに対して寸法安定性がよい。

（2）使用した代替フィルム

使用した代替フィルムの名称と略称を Table 4 に示す。供試材としては 9 種類を準備した。INC-1 と INC-2 フィルムの違いは購入先の違いで、フィルム厚さもわずかに異なる。

Table 4　使用した代替フィルムの名称と略称

代替フィルム	略　称
正規フィルム	CN85
工業用硝酸セルロースフィルム	INC-1
〃	INC-2
アセチルセルロース	AC
三酢酸セルロース	TAC
ポリエチレンテレフタレート	PET
ポリエステル	PE
ポリエステルニトリル	PEN
ポリカーボネート	PC

3－6．代替フィルムにおける放射化分析結果

中性子照射後に代替フィルムが放射化するか、しないかを評価するには放射化分析法が適している。その一例を Fig.9 ～ 14 に示す。

（1）正規フィルム（CN85）

正規フィルムの放射化分析の測定結果を Fig.9

に示す。バックグランドの測定結果（コントラストの濃い曲線＝下側）も併せて示しているが、ほとんど重なるような結果を得た。この結果、Na-22は、放射化分析装置を設置している原研ホットラボ内でNa-22を用いた陽電子消滅実験を行っているための影響、K-40は天然に存在する核種、Bi-241は天然のRa系列からの影響であり、比較的長時間測定した際や、検出器の検出効率を高くして測定したときには必ずといってよいほど検出されるものである。これらの結果から、正規フィルムはバックグランドのピークと重なっており、まったく放射化されていないと考えられる。

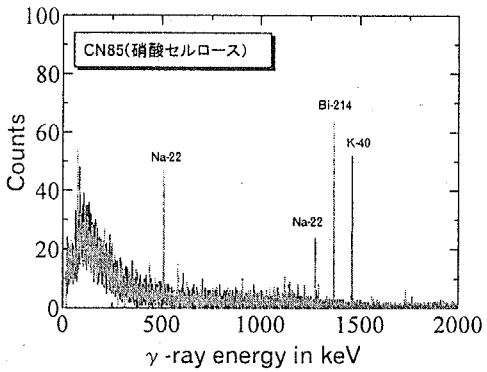


Fig.9　正規フィルムの放射化分析結果

（2）工業用硝酸セルロースフィルム

工業用硝酸セルロースフィルム（INC-1）の放射化分析の測定結果をFig.10に示す。Bi-214のピークがFig.9に比べてわずかに高いが、正規フィルムとほぼ同じ結果であり、まったく放射化されていない。なお図示していないがINC-2の結果も、ほとんど同じであった。

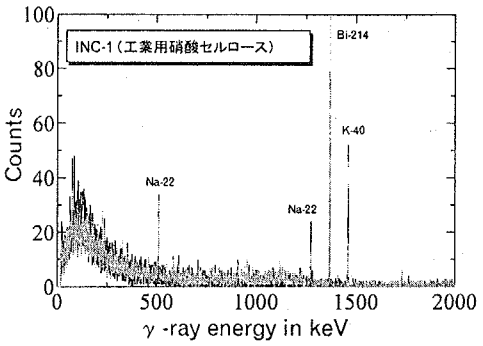


Fig.10　INC-1の放射化分析結果

（3）三酢酸セルロースフィルム（TAC）

三酢酸セルロースフィルム（TAC）の放射化分析の測定結果をFig.11示す。この結果もFig.9の正規フィルムとまったく同じであり、放射化されなかった。

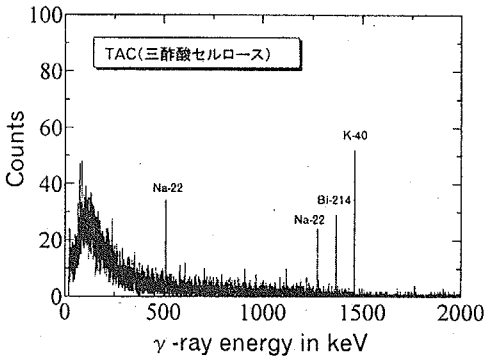


Fig.11　TACフィルムの放射化分析結果

（4）アセチルセルロースフィルム（AC）

アセチルセルロースフィルム（AC）の放射化分析の測定結果をFig.12に示す。正規フィルムとまったく同じ結果であり、放射化されていない。

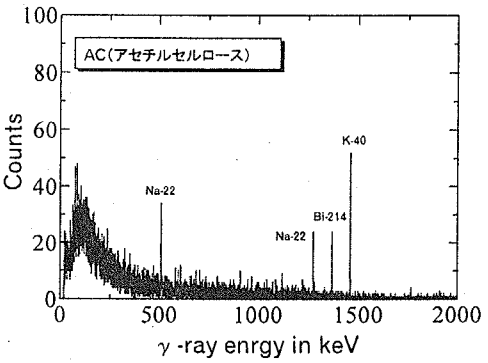


Fig.12　ACフィルムの放射化分析結果

（5）ポリエステルニトリルフィルム（PEN）

ポリエステルニトリルフィルム（PEN）の放射化分析の測定結果をFig.13に示す。バックグラン

ドに比べると Sb-122、Sb-124 および Mn-56 の特異ピークが認められた。なお Mn-56 の半減期は 2.58 日、Sb-122 は 2.8 日、Sb-124 は 60.1 日であり、現在の試料冷却時間（中性子照射後、フィルムはく離するまでの時間）が 48 ～ 72 時間であることから実質的に大きな問題はないが、フィルムの所外持ち出しなどを考えた場合には不都合であることから、放射化するフィルムと判定した。

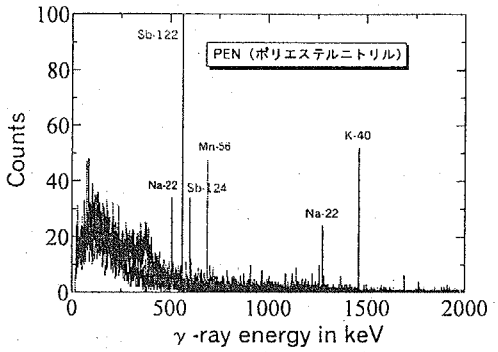


Fig.13　PEN フィルムの放射化分析結果

（5）ポリエステルフィルム（PE）

ポリエステルフィルム（PE）の放射化分析の測定結果をFig.14 に示す。バックグランドに比べると Sb-122、Sb-124、Mn-56 および K-40 の特異ピークが認められた。PE フィルムも放射化するフィルムと判定した。

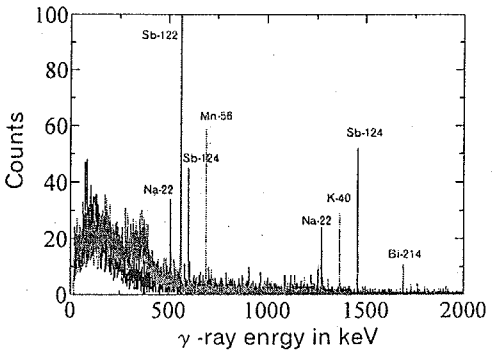


Fig.14　PEN フィルムの放射化分析結果

3－7．$LiNo_3$ 溶液処理した代替フィルム

工業用硝酸セルロースフィルムの表面には、約 50 ～ 100 μm間隔に線条痕が認められる。この状態で ATE 用フィルムとして使用することは不可能であるので、スライドグラスにフィルムを挟み、100 ～ 120 ℃に加熱した恒温装置に 3 ～ 5h 入れて平滑化処理を試み、ある程度の成功を修めた。しかし完全に平滑化するには 500h の加圧・恒温処理が必要であることも明らかになった[1]。

そこで短時間処理によって、すぐれた ATE 像を得るための方法として、$LiNo_3$（硝酸リチウム）溶液で処理した代替フィルムについて検討した。具体的な手順は以下のとおりである。

1）純水中に $LiNo_3$ を 5 ～ 15 %溶融する。
2）各種の代替フィルムを室温において 0.5 ～ 15h 沈漬する。
3）任意の時間沈漬後、強制乾燥（自然乾燥は $LiNo_3$ が再結晶化するため不可）する。
4）試料に貼り付ける。

（1）$LiNo_3$ 無処理における各種フィルムの ATE 像

$LiNo_3$ 処理していない代替フィルムの ATE 像を

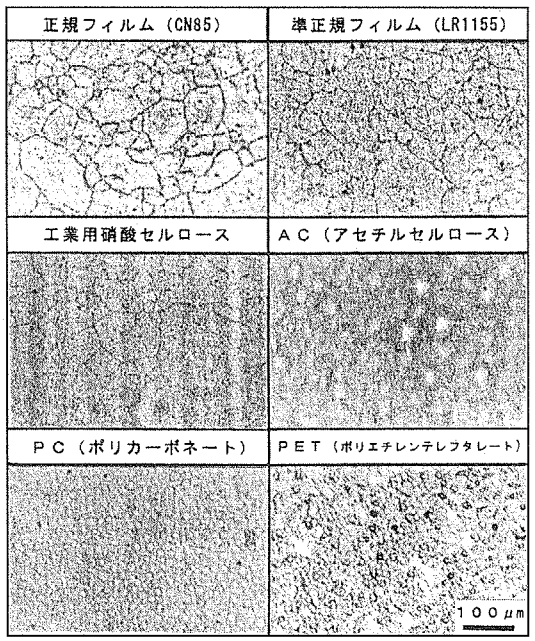


Fig.15　代替フィルム（$LiNo_3$ 無処理）の ATE 像

Fig.15 に示す。正規フィルムおよび準正規フィルム（Kodak 社製の LR1155）では、αトラック像が観察できた。しかし工業用硝酸セルロース（INC-1）フィルム、ないしはアセチルセルロース（AC）フィルムにみられたαトラック像のコントラストはきわめて薄い。ポリカーボネート(PC)、ポリエチレンテレフタレート（PET）の表面には球形構造が観察できたが、αトラック像はまったく観察できなかった。つまり $^{10}B + n \rightarrow Li + He$（α）反応によるαトラック像は生じなかった。

（2）$LiNo_3$ 処理した INC-1 フィルムの ATE 像

$LiNo_3$ 処理した INC-1（工業用硝酸セルロース）フィルムの ATE 像を Fig.16 に示す。左側が濃度 5 %の $LiNo_3$ 溶液中に 1～ 15h 沈漬させたフィルム、右側が濃度 10 %の $LiNo_3$ 溶液中に 1～ 15h 沈漬させたフィルムである。

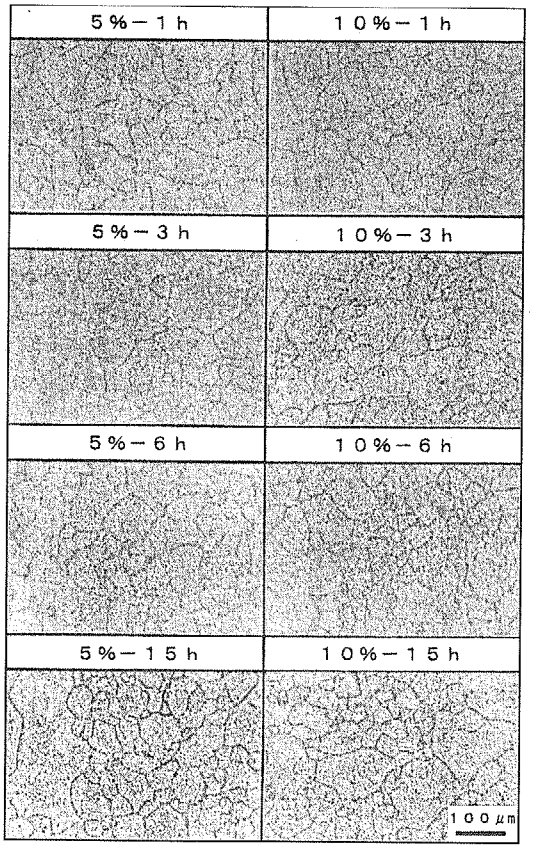


Fig.16 $LiNo_3$ 処理（濃度 5 %、10 %）した INC-1 フィルムの ATE 像

$LiNo_3$ 無処理の工業用セルロースフィルム（INC-1）においては、Fig.15 に示したように線条痕が上下方向に残存していたが、$LiNo_3$ 処理することによって、線条痕は消失するようになる。1～ 15h 沈漬させたフィルムを比較すると、より長時間（15h）沈漬したフィルムにおいて、αトラック像の鮮明度が高かった。

（3）$LiNo_3$ 処理した各種フィルムの表面性状

$LiNo_3$ 処理していない代替フィルムと、$LiNo_3$ 処理した代替フィルムの表面性状を Fig.17 に示す。$LiNo_3$ 無処理フィルムにおける表面性状は凹凸が顕著である。しかし $LiNo_3$ 処理することにより表面性状は平坦になることがわかる。

$LiNo_3$ の濃度が平坦さにおよぼす影響は、5 %よりも 10 %の方が大きかった。また 1 h よりも 15 h 沈漬したフィルムの方が平坦さにすぐれていた。フィルムの表面性状が平坦になった理由はいくつか考えられるが、①フィルムと $LiNo_3$ の化学反応（pH6）であったのか、②フィルム作製時の鏡面ドラムの表面きずを機械的に埋めたのか、③その他であったのかは明らかではない。

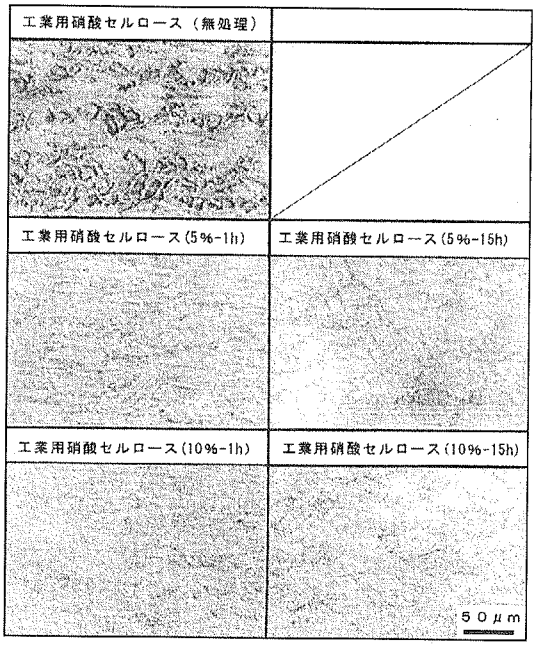


Fig.17 $LiNo_3$ 処理による INC-1 フィルムの表面性状

（4）12h照射効果

2001年3月、原研との打ち合わせにより、「JRR-4医療用照射設備」については重水を使っていないことが判明した。理由は①重水がトリチウム汚染する、②汚染した重水の処理費がかかるなどである。したがって重水を使用しない場合、カドミ比は下がり、総フラックス量があがるため最強モードで照射していたことになる。

そこで照射時間を18時間から、12時間に短縮したATE像をFig. 18に示す。水酸化ナトリウム（NaOH）のエッチング時間は1.5～2倍に増えるが、18時間照射に比べて遜色のない結果が得られた。計算結果とαトラック像の結果から中性子束を類推すると、オーダー的には2倍程度である。

また10%$LiNo_3$溶液に3h沈漬処理した三酢酸セルロース（TAC）フィルムでも、αトラック像を観察することができた。加えてカーボン蒸着を施すことによりコントラストが改善されたが、αトラック像の線幅は太めに見える。

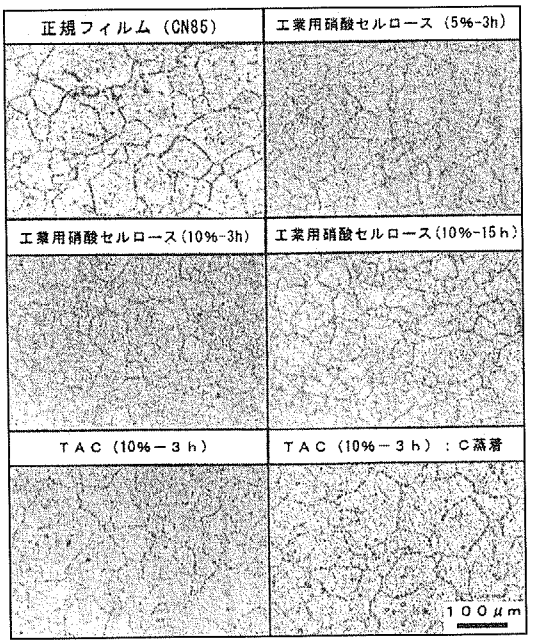


Fig.18　12h時間照射によりATE像

（5）フィルム・エッチング時間の比較

正規フィルム（CN85）のエッチング条件を基準（2.5N － NaOH、30 ℃）にすると、エッチング時間は 60 ～ 90min、工業用硝酸セルロースフィルム（INC）は 30 ～ 45min、三酢酸セルロースフィルム（TAC）は 30 ～ 50 ℃、3 ～ 5h のエッチング時間が必要であった。

4．結果のまとめ

1）気送管による照射は、硝酸セルロースフィルム（Kodak CN85）のはく離、照射時間のばらつきなど不確定な要因が認められた。

2）医療用照射設備（中性子ビーム設備）による照射は、増感剤付き硝酸セルロースフィルム（Kodak CN85）を用いた限り、立教炉に比較しても遜色のないATE像を得ることができた。

3）総合的に考えて、第一候補の代替フィルムとしては硝酸リチウム（$LiNo_3$溶液）の前処理を施した工業用セルロースが推奨できる。

4）次候補の代替フィルムはアセチルセルロース（AC）および三酢酸セルロース（TAC）が推奨できる。

5）12h照射でも、ATEによる鋼中ボロンの状態分析の観察が可能であることが明らかになった。

5．参考文献

1）朝倉健太郎、柴田浩司、原澤　進：α線を用いたボロン分布観察法における代替硝酸セルロースフィルムの有効性評価、CAMP-ISIJ, 11 (1998), 478

6．結果の公表

1）朝倉健太郎、柴田浩司、原澤　進、澤幡浩之、川手　稔：ATEにおける照射条件の探索（原子炉を用いたATEによる鋼中ボロン状態分析システムの確立-1）、CAMP-ISIJ, 14(2001), 699

2）朝倉健太郎、柴田浩司：ATEにおける代替フィルムの探索と硝酸リチウム処理（原子炉を用いたATEによる鋼中ボロン状態分析システムの確立-2）、CAMP-ISIJ, 14(2001), 700

謝辞：代替フィルム、アクリルに関する相談と提供をいただいた原研・鈴木富男氏、帝人㈱平坂雅男氏、コニカ㈱長澤忠広氏、三菱レイヨン㈱森次礼氏に感謝いたします。

謝　辞

本報告書の発刊にあたり、多くの皆様から多大なご協力を頂きました。編集に際し、ご協力頂いた、東京大学物性研究所柴山充弘氏、東京大学原子力研究総合センター高野正美氏、研究炉部長小林晋昇氏、研究炉次長中島照夫、研究炉利用課長佐川尚司氏、原子炉安全工学部ＮＳＲＲ管理室豊田政幸氏に深く感謝致します。

付　録

Appendix

This is a blank page.

付 録(1)

事情により、研究炉利用の成果・連絡票のみの提出となった利用者について、その内容をここに示す。

研究テーマ「表題」	所属 担当者	利用原子炉及び装置名	報告書等	利用分野
ﾊﾜｲﾎｯﾄｽﾎﾟｯﾄ火山地域の起源物質の地球化学的解析－海底玄武岩の希土類元素の定量	熊本大学 理学部 可児 智美	JRR-4 T-Pipe	成果を投稿準備中であり、本年度は間に合わない。	放射化分析

付 録(２)

原研研究炉の利用設備一覧

１．ＪＲＲ－３Ｍ

１）実験設備

実 験 孔	実 験 装 置
１Ｇ	高分解能粉末中性子回折装置（ＨＲＰＤ）
１Ｇ－Ａ	生体高分子結晶構造解析用中性子回折計（ＢＩＸ－Ｉ）
２Ｇ	三軸型中性子分光器（ＴＡＳ－１）
３Ｇ	中性子トポグラフィ及び精密光学実験装置（ＰＮＯ）
４Ｇ	汎用三軸型中性子分光器（ＧＰＴＡＳ）
５Ｇ	偏極中性子散乱装置（ＰＯＮＴＡ）
６Ｇ	東北大学中性子散乱分光器（ＴＯＰＡＮ）
７Ｒ	中性子ラジオグラフィ装置（ＴＮＲＦ）
Ｔ１－１	中性子偏極回折装置（ＨＱＲ）
Ｔ１－２	単結晶中性子回折装置（ＫＳＤ）
Ｔ１－３	粉末中性子回折装置（ＨＥＲＭＥＳ） （ＫＰＤ）
Ｔ１－４－１	即発ガンマ線分析装置（ＰＧＡ）
Ｔ１－４－１Ａ	化学反応実験装置（ＬＣＥ）
Ｔ１－４－３	ＴＯＦ型中性子反射率計（ＴＯＦ）
Ｔ１－４－４	中性子ラウエ回折装置（ＬＡＵＥ）
Ｔ２－１	残留応力測定中性子回折装置（ＲＥＳＡ）
Ｔ２－２	中性子４軸回折装置（ＦＯＮＤＥＲ）
Ｔ２－３	中性子ＩＰ付生体物質中性子回折計（ＢＩＸ－II）
Ｔ２－４	高分解能三軸型中性子分光器（ＴＡＳ－２）
Ｃ１－１	高エネルギー分解能三軸型中性子分光器（ＨＥＲ）
Ｃ１－２	二次元位置測定小角散乱装置（ＳＡＮＳ－Ｕ）
Ｃ１－３	超高分解能後方散乱装置（ＵＬＳ）
Ｃ２－１	冷中性子散乱実験デバイス開発装置（ＬＴＡＳ）
Ｃ２－２	中性子スピンエコー分光器（ＮＳＥ）
Ｃ２－３－１	冷中性子ラジオグラフィ装置（ＣＮＲＦ）
Ｃ２－３－２	即発ガンマ線分析装置（ＰＧＡ）
Ｃ２－３－２Ａ	化学反応実験装置（ＬＣＥ）
Ｃ２－３－４	ＴＯＦ型中性子反射率計（ＴＯＦ）
Ｃ２－３－５	中性子ラウエ回折装置(ＬＡＵＥ)
Ｃ２－３－６	中性子寿命測定装置（ＮＬＴ）
Ｃ２－３－７	パルス中性子機器開発装置（ＣＨＯＰ）
Ｃ３－１－１	高分解能パルス冷中性子分光器（ＡＧＮＥＳ）
Ｃ３－１－２	多層膜中性子干渉計／反射率計（ＭＩＮＥ）
Ｃ３－２	中性子小角散乱装置（ＳＡＮＳ－Ｊ）

2）照射設備

水力照射設備	HR－1，2
気送照射設備	PN－1，2
放射化分析用照射設備	PN－3
均一照射設備	SI－1
回転照射設備	DR－1
垂直照射設備	VT－1，RG－1～4 BR－1～4，SH－1

2．JRR－4

1）実験設備

プール
中性子ビーム設備
散乱実験設備
冷却水循環ループ
医療照射設備（BNCT）
即発ガンマ線分析装置

2）照射設備

簡易照射筒	Tパイプ（水力）
	Sパイプ
	Dパイプ
	Nパイプ
気送管照射設備	PN

This is a blank page.

国際単位系 (SI) と換算表

表 1　SI基本単位および補助単位

量	名称	記号
長さ	メートル	m
質量	キログラム	kg
時間	秒	s
電流	アンペア	A
熱力学温度	ケルビン	K
物質量	モル	mol
光度	カンデラ	cd
平面角	ラジアン	rad
立体角	ステラジアン	sr

表 2　SIと併用される単位

名称	記号
分，時，日	min，h，d
度，分，秒	°，′，″
リットル	l，L
トン	t
電子ボルト	eV
原子質量単位	u

1 eV = 1.60218 × 10^{-19} J

1 u = 1.66054 × 10^{-27} kg

表 5　SI接頭語

倍数	接頭語	記号
10^{18}	エクサ	E
10^{15}	ペタ	P
10^{12}	テラ	T
10^{9}	ギガ	G
10^{6}	メガ	M
10^{3}	キロ	k
10^{2}	ヘクト	h
10^{1}	デカ	da
10^{-1}	デシ	d
10^{-2}	センチ	c
10^{-3}	ミリ	m
10^{-6}	マイクロ	μ
10^{-9}	ナノ	n
10^{-12}	ピコ	p
10^{-15}	フェムト	f
10^{-18}	アト	a

表 3　固有の名称をもつSI組立単位

量	名称	記号	他のSI単位による表現
周波数	ヘルツ	Hz	s^{-1}
力	ニュートン	N	m·kg/s^2
圧力，応力	パスカル	Pa	N/m^2
エネルギー，仕事，熱量	ジュール	J	N·m
工率，放射束	ワット	W	J/s
電気量，電荷	クーロン	C	A·s
電位，電圧，起電力	ボルト	V	W/A
静電容量	ファラド	F	C/V
電気抵抗	オーム	Ω	V/A
コンダクタンス	ジーメンス	S	A/V
磁束	ウェーバ	Wb	V·s
磁束密度	テスラ	T	Wb/m^2
インダクタンス	ヘンリー	H	Wb/A
セルシウス温度	セルシウス度	℃	
光束	ルーメン	lm	cd·sr
照度	ルクス	lx	lm/m^2
放射能	ベクレル	Bq	s^{-1}
吸収線量	グレイ	Gy	J/kg
線量当量	シーベルト	Sv	J/kg

表 4　SIと共に暫定的に維持される単位

名称	記号
オングストローム	Å
バーン	b
バール	bar
ガル	Gal
キュリー	Ci
レントゲン	R
ラド	rad
レム	rem

1 Å = 0.1 nm = 10^{-10} m

1 b = 100 fm^2 = 10^{-28} m^2

1 bar = 0.1 MPa = 10^5 Pa

1 Gal = 1 cm/s^2 = 10^{-2} m/s^2

1 Ci = 3.7 × 10^{10} Bq

1 R = 2.58 × 10^{-4} C/kg

1 rad = 1 cGy = 10^{-2} Gy

1 rem = 1 cSv = 10^{-2} Sv

（注）

1. 表1－5は「国際単位系」第5版，国際度量衡局 1985年刊行による。ただし，1 eVおよび1 uの値はCODATAの1986年推奨値によった。
2. 表4には海里，ノット，アール，ヘクタールも含まれているが日常の単位なのでここでは省略した。
3. barは，JISでは流体の圧力を表わす場合に限り表2のカテゴリーに分類されている。
4. EC閣僚理事会指令ではbar，barnおよび「血圧の単位」mmHgを表2のカテゴリーに入れている。

換　算　表

力	N(=10^5 dyn)	kgf	lbf
	1	0.101972	0.224809
	9.80665	1	2.20462
	4.44822	0.453592	1

粘度　1 Pa·s(N·s/m^2) = 10 P(ポアズ)(g/(cm·s))

動粘度　1 m^2/s = 10^4 St(ストークス)(cm^2/s)

圧力	MPa(=10 bar)	kgf/cm^2	atm	mmHg(Torr)	lbf/in^2(psi)
	1	10.1972	9.86923	7.50062 × 10^3	145.038
	0.0980665	1	0.967841	735.559	14.2233
	0.101325	1.03323	1	760	14.6959
	1.33322 × 10^{-4}	1.35951 × 10^{-3}	1.31579 × 10^{-3}	1	1.93368 × 10^{-2}
	6.89476 × 10^{-3}	7.03070 × 10^{-2}	6.80460 × 10^{-2}	51.7149	1

エネルギー・仕事・熱量	J(=10^7 erg)	kgf·m	kW·h	cal(計量法)	Btu	ft·lbf	eV
	1	0.101972	2.77778 × 10^{-7}	0.238889	9.47813 × 10^{-4}	0.737562	6.24150 × 10^{18}
	9.80665	1	2.72407 × 10^{-6}	2.34270	9.29487 × 10^{-3}	7.23301	6.12082 × 10^{19}
	3.6 × 10^6	3.67098 × 10^5	1	8.59999 × 10^5	3412.13	2.65522 × 10^6	2.24694 × 10^{25}
	4.18605	0.426858	1.16279 × 10^{-6}	1	3.96759 × 10^{-3}	3.08747	2.61272 × 10^{19}
	1055.06	107.586	2.93072 × 10^{-4}	252.042	1	778.172	6.58515 × 10^{21}
	1.35582	0.138255	3.76616 × 10^{-7}	0.323890	1.28506 × 10^{-3}	1	8.46233 × 10^{18}
	1.60218 × 10^{-19}	1.63377 × 10^{-20}	4.45050 × 10^{-26}	3.82743 × 10^{-20}	1.51857 × 10^{-22}	1.18171 × 10^{-19}	1

1 cal = 4.18605 J (計量法)

= 4.184 J　(熱化学)

= 4.1855 J　(15 °C)

= 4.1868 J (国際蒸気表)

仕事率　1 PS (仏馬力)

= 75 kgf·m/s

= 735.499 W

放射能	Bq	Ci
	1	2.70270 × 10^{-11}
	3.7 × 10^{10}	1

吸収線量	Gy	rad
	1	100
	0.01	1

照射線量	C/kg	R
	1	3876
	2.58 × 10^{-4}	1

線量当量	Sv	rem
	1	100
	0.01	1

(86年12月26日現在)

研究炉利用における研究成果集（平成12年度）

R100
古紙配合率100%
白色度70%再生紙を使用しています